The Lecture Notes in Physics

The series Lecture Notes in Physics (LNP), founded in 1969, reports new developments in physics research and teaching-quickly and informally, but with a high quality and the explicit aim to summarize and communicate current knowledge in an accessible way. Books published in this series are conceived as bridging material between advanced graduate textbooks and the forefront of research and to serve three purposes:

- to be a compact and modern up-to-date source of reference on a well-defined topic
- to serve as an accessible introduction to the field to postgraduate students and nonspecialist researchers from related areas
- to be a source of advanced teaching material for specialized seminars, courses and schools

Both monographs and multi-author volumes will be considered for publication. Edited volumes should, however, consist of a very limited number of contributions only. Proceedings will not be considered for LNP.

Volumes published in LNP are disseminated both in print and in electronic formats, the electronic archive being available at springerlink.com. The series content is indexed, abstracted and referenced by many abstracting and information services, bibliographic networks, subscription agencies, library networks, and consortia.

Proposals should be sent to a member of the Editorial Board, or directly to the managing editor at Springer:

Christian Caron
Springer Heidelberg
Physics Editorial Department I
Tiergartenstrasse 17
69121 Heidelberg/Germany
christian.caron@springer.com

More information about this series at http://www.springer.com/series/5304

Yoshihisa Yamamoto • Kouichi Semba
Editors

Principles and Methods of Quantum Information Technologies

Springer

Editors
Yoshihisa Yamamoto
ImPACT Program, Council for Science Technology and Innovation
Tokyo, Japan

Kouichi Semba
National Institute of Information and Communications Technology
Koganei, Tokyo, Japan

ISSN 0075-8450 ISSN 1616-6361 (electronic)
Lecture Notes in Physics
ISBN 978-4-431-55755-5 ISBN 978-4-431-55756-2 (eBook)
DOI 10.1007/978-4-431-55756-2

Library of Congress Control Number: 2015956183

Springer Tokyo Heidelberg New York Dordrecht London

Printed on acid-free paper

Springer Japan KK is part of Springer Science+Business Media (www.springer.com)

Preface

This book presents the research and development results of the "FIRST" Quantum Information Processing Project, which has been conducted from 2010 to 2014 with the support of the Council for Science, Technology and Innovation of the Cabinet Office of the Government of Japan. The project supported 33 research groups and explored five areas: quantum communication, quantum metrology and sensing, coherent computing, quantum simulation, and quantum computing. Part I to Part V of this book, which consist of twenty chapters, focus on the system and architecture aspects of quantum information technologies, and Part VI and Part VII, which consist of eight chapters, discuss the constituent device physics and technologies.

Part I: Quantum Communication is composed of four chapters. Chapter 1 presents the fundamental concepts of quantum information and introduces various protocols of quantum communication. This chapter explains the most general ways to describe quantum states, measurements, and state transformation. The distinction between quantum communication and classical communication, the role of quantum entanglement as a communication resource and the conversion of resources in entanglement sharing, quantum dense coding, and quantum teleportation are then discussed. Chapter 2 overviews advancements in quantum key distribution (QKD) technology. This chapter presents the National Institute of Information and Communications Technology (NICT) perspective on current limitations of the known QKD protocols and future prospects toward merging QKD and modern crypto-technologies. Chapter 3 describes the single photon-based and EPR-Bell photon-pair-based quantum communication technologies developed at Nippon Telegraph and Telephone Corporation (NTT). A particular protocol, called differential phase shift (DPS) QKD, is introduced, and an experimental demonstration of a high-speed and long-distance QKD system is presented. Finally, Chap. 4 reports the recent progress toward solid state (quantum dot spin-based) quantum repeaters explored at Stanford University. Two crucial technologies for this goal are described, which are spin-photon entanglement and coherent single photon frequency down-conversion.

Part II: Quantum Metrology and Sensing is composed of four chapters. Chapter 5 introduces an optical lattice clock operated at the so-called magic wavelength, in which an atomic ensemble trapped in an optical lattice provides a precisely

controlled frequency reference and achieves extremely high accuracy and stability at the level of 10^{-18}. Chapter 6 discusses the cold atom magnetometry on the basis of spinor Bose-Einstein condensates and spin echo techniques, which achieve $10^{-11}\ T/\sqrt{H_z}$ sensitivities at the micron scale. This technique may have various applications for biological imaging, detection of MRI signals, and fundamental science. Chapter 7 describes entanglement-based optical precision measurement techniques with special focus on optical phase measurement beyond the standard quantum limit and quantum optical coherent tomography. The former technique can improve the sensitivity of microscopic imaging beyond the standard shot-noise limit. The latter may cancel out the material dispersion effect and improve the resolution of conventional optical tomography. Finally, Chap. 8 presents an extremely sensitive current measurement apparatus on the basis of mesoscopic quantum dot nanostructures. The apparatus can measure extremely small currents of the order of attoamperes with single-electron resolution and enable bidirectional (forward and backward) electron counting. Various statistical properties, such as frequency spectrum, time-correlation, and full counting statistics, can be elucidated.

Part III: Coherent Computing is composed of four chapters. Chapter 9 reviews the recent progress of approximation algorithms for combinatorial optimization problems, which are most likely NP-hard so that there is no efficient (polynomial time) algorithm to solve them, assuming the widely believed conjecture "P≠NP." Therefore, approximation and polynomial time algorithms have been main targets of interest in applied mathematics and computer science research for the last 30 years. The two main focuses in this article are the edge-disjoint paths problem and the graph coloring problem. The three approaches of combinatorial (graph theoretical) programming, linear programming, and semi-definite programming are discussed, which are central to the recent breakthrough in approximation algorithms. Chapter 10 introduces a coherent Ising machine and XY machine on the basis of an injection-locked laser network, which computes the approximate solutions for NP-hard Ising problems and other combinatorial optimization problems in an extremely short time. The two machines utilize the criticality of a laser phase transition as a computing mechanism and depart from each other via presence or absence of the external injection signal with a reference phase. The basic principle, proof-of-concept experiment, and numerical benchmark study are presented. Chapter 11 describes another coherent Ising machine on the basis of a degenerate optical parametric oscillator (DOPO) network. In contrast to the laser network, the inherent preference of bistability for each DOPO phase makes this system extremely robust against external perturbations and creates quantum entanglement in a transient computational process. The chapter presents the basic principle of a DOPO-based coherent Ising machine, computational experiments for NP-hard MAX-CUT problems, and the idea of physical implementation with a multiple pulse DOPO in a single ring cavity. Finally, Chap. 12 presents a scalable coherent Ising machine on the basis of quantum measurement-feedback control. Instead of connecting DOPO pulses or laser pulses optically, the complex amplitude of each pulse is measured at every round trip by optical homodyne detection, and the mutual coupling among the pulses, which implement the Ising model or XY model, and is realized by

the coherent injection of feedback optical pulses back into the main cavity. The numerical benchmark study for the NP-hard MAX-CUT problems in sparse G-set graphs and dense complete graphs features substantial speedup against the conventional approximation algorithms based on semi-definite programming (SDP) and simulated annealing (SA).

Part IV: Quantum Simulation is composed of five chapters. Chapter 13 reviews the basics of Bose-Einstein condensation (BEC) and introduces two different experimental systems, which provide unique platforms for quantum simulation experiments. A dilute atomic BEC is suitable for implementing an equilibrium many-body system which is well isolated from reservoirs. A dense exciton-polariton BEC is suitable for studying a nonequilibrium many-body system in open-dissipative environments. The chapter covers such topics as the fundamental concepts of BEC, the Bogoliubov theory of interacting particles, superfluidity, and various lattice implementing techniques for atomic and polaritonic BEC. Chapter 14 discusses the recent progress of quantum simulation experiments with ultracold ytterbium (Yb) atoms in optical lattices at Kyoto University. They describe experimental results pertaining to a strongly interacting Bose-Fermi Yb mixture, an SU(N) Mott insulator, an artificial impurity system with Yb-Li (lithium) atomic mixture, flat bands and Dirac cones in nonstandard optical lattices, and optical Feshbach resonance. Chapter 15 reports the recent quantum simulation experiments with trapped Ca^+ ions at Osaka University. They implement the Jaynes-Cummings-Hubbard (JCH) model, which describes an array of coupled cavities with a single two-level atom and thus features strongly correlated phenomena such as quantum phase transition from Mott insulator to superfluid. Chapter 16 discusses the quantum simulation experiments with exciton-polaritons in various two-dimensional lattice structures at Stanford University. In particular, they report the observation of the spontaneously formed high-orbital (p-wave, d-wave, and f-wave) condensation due to the open-dissipative nature of exciton-polaritons. Finally, Chap. 17 presents the theoretical framework for describing the equilibrium BEC, a high-density BCS to nonequilibrium lasing crossover in driven-dissipative semiconductor systems. The gap equation in the BCS theory (GE-BCS) and the Maxwell semiconductor Bloch equation (MSBE) are formulated for the coupled electron-hole-photon system, and their mutual connection is established.

Part V: Quantum Computing consists of three chapters. Chapter 18 introduces the layered architectures for quantum computers and quantum repeaters, where five distinct (physical, virtual, quantum error correcting, logical, and application) layers associated with specialized tasks are synchronously operated to achieve fault tolerance. They report a numerical evaluation for quantum computers and quantum repeaters on the basis of optically controlled quantum dot spins, where a two-dimensional topological cluster state is prepared in a semiconductor quantum dot-planar microcavity structure. This particular hardware technology is very fast, scalable to large problem sizes, and compatible with single photon-based quantum communication. Chapter 19 describes an alternative implementation of fault-tolerant quantum computers on the basis of photon-photon interaction with atom-cavity devices. A three-dimensional topological cluster state is a crucial

part for universal fault-tolerant quantum computation. Chapter 20 discusses a hybrid approach to universal and fault-tolerant quantum information processing. In particular, they propose combined qubit and continuous variable protocols to overcome the limitation of each system.

Part VI: Superconducting Qubits is composed of four chapters. Chapter 21 presents a brief overview of the recent progress in atomic physics and quantum optics experiments using superconducting circuits with Josephson junctions. These circuits provide an unprecedented level of control over quantum states and also enjoy scalability of many qubits integrated on a single chip. Chapter 22 summarizes the experimental efforts toward building a superconducting circuit-based quantum computers. Such topics as various Josephson junction qubits, gate fidelity, decoherence time, integration, implementation of quantum algorithms, and the readout of single qubits are described. Chapter 23 describes the two types of microwave parametric amplifiers on the basis of Josephson junction circuits, which achieve a standard quantum-limited amplification of microwave photons. One is a linear parametric amplifier operated below the oscillation threshold, and the other is a nonlinear parametric oscillator operated above the oscillation threshold. Finally, Chap. 24 reports the recent experimental progress in superconducting flux qubit-diamond NV center hybrid systems. The systems demonstrate the strong coupling between a single superconducting flux qubit and ensemble of NV spins in diamond.

Part VII: Semiconductor and Molecular Spin Qubits is composed of four chapters. Chapter 25 reports the recent progress in semiconductor quantum dot spin qubit technologies. The chapter discusses the experimental schemes of initializing and detecting single qubit gates on the basis of electric dipole-induced spin resonance and implementing two qubit gates on the basis of the exchange coupling between nearby quantum dots. Chapter 26 describes the quantum dynamics of nuclear spins and electron spins associated with an impurity in silicon crystal. In particular, they review the recent nuclear magnetic resonance (NMR)/electron spin resonance (ESR) double resonance experiments using a phosphorus (^{31}P) donor impurity in isotope-purified silicon crystal. Chapter 27 introduces nuclear spins and electron spins in molecules, which have relatively long decoherence time and can be controlled by magnetic resonance techniques. The chapter reports on a newly developed hyperpolarization technique, spin amplification, and an arbitrary waveform pulsed ESR. Finally, Chap. 28 discusses the synthetic approaches to scalable molecular spin-based quantum information processing. The chapter proposes using nuclear spins in the topological network of molecular frames as client qubits and delocalized electron spins as bus qubits, which are simultaneously controlled by RF and microwave pulse techniques.

We hope the research results presented in this book will be a useful source of ideas and knowledge for the future development of quantum information technologies, which are actively being investigated in numerous countries around the world.

Tokyo, Japan
April 24, 2015

Yoshihisa Yamamoto
Kouichi Semba

Contents

Part I
Quantum Communication

Chapter 1
Quantum Information Theory for Quantum Communication

Masato Koashi

1.1 Basic Rules of Quantum Mechanics

We begin by listing a basic set of rules from which all statements in this section should be derived. The choice of this set is by no means unique, and the selection of the properties of quantum mechanics that are used as basic rules, leaving the rest as derived rules, is actually a matter of preference. Our choice here comprises five rules describing states, transformations, measurements, compositions, and causality.

The first of these rules covers the description of the states of a physical system. We call a state *pure* when it is impossible to regard that state as a probabilistic mixture of two or more different[1] states.

Rule 1 A physical system is associated with a Hilbert space $\mathscr{H}$. Every pure state of this system is represented by a normalized vector $|\phi\rangle \in \mathscr{H}$. For any normalized vector $|\psi\rangle \in \mathscr{H}$, it is possible to prepare the system in the state represented by $|\psi\rangle$.

To avoid complications, we assume in this section that the dimension $d = \dim \mathscr{H}$ of the Hilbert space is finite.[2] A physical system with a Hilbert space of dimension d is often called a *d-level* system. Rule 1 dictates that any appropriate

[1] The operational meaning of two states being different is that a measurement exists on the physical system that can show the difference statistically.

[2] Rule 1 also implies that we exclude any cases where a physical law such as the superselection rule imposes an additional restriction on the preparable states.

M. Koashi (✉)
Photon Science Center, Graduate School of Engineering, The University of Tokyo, Bunkyo-ku, Tokyo 113-8656, Japan
e-mail: koashi@qi.t.u-tokyo.ac.jp

Y. Yamamoto, K. Semba (eds.), *Principles and Methods of Quantum Information Technologies*, Lecture Notes in Physics 911, DOI 10.1007/978-4-431-55756-2_1

instruction for preparation of the physical system leads to either a pure state represented by a single vector $|\phi\rangle$ or a *mixed* state represented by an *ensemble* $\{(p_j, |\phi_j\rangle)\}$, which designates the situation where the system is prepared in state $|\phi_j\rangle$ with probability p_j. In either case, the representation is not unique: $|\phi\rangle$ and $e^{i\varphi}|\phi\rangle$ represent the same pure physical state. The different descriptions $\{(p_j, |\phi_j\rangle)\}$ and $\{(q_i, |\psi_i\rangle)\}$ may both refer to the same mixed state. We will introduce an alternative representation of the states, which is unique, in Sect. 1.2.

The next two rules cover the input-output relations of feasible operations on a physical system prepared in state $|\phi_{\rm in}\rangle$. A state transformation refers to the case where the output is the quantum state $|\phi_{\rm out}\rangle$ of the system after the operation. Rule 2 dictates the feasibility of *unitary transformations*, which are, in a sense, a basic set of transformations.

Rule 2 For any unitary operator $\hat{U}$ on $\mathscr{H}$, it is possible to implement a state transformation where every input state $|\phi_{\rm in}\rangle \in \mathscr{H}$ evolves into state $|\phi_{\rm out}\rangle = \hat{U}|\phi_{\rm in}\rangle$.

When the output is a classical variable, we are then referring to a measurement. Rule 3 covers a basic set of measurements called *(complete) orthogonal measurements*.

Rule 3 For any orthonormal basis $\{|u_j\rangle\}_{j=1,\ldots,d}$ of $\mathscr{H}$, it is possible to implement a measurement that produces the outcome $j = 1, \ldots d$ with probability $p_j = |\langle u_j|\phi_{\rm in}\rangle|^2$ when the system is in state $|\phi_{\rm in}\rangle \in \mathscr{H}$ before the measurement is performed.

In this rule, we are not interested in the state of the measured system after the measurement is performed. The two rules above only refer to the feasibility of the limited sets of transformations and measurements. In general, a much wider variety of operations should be available on a physical system, and we will see the whole landscape of these operations in Sect. 1.4.

The next rule is a very special rule that allows us to weave the threads of Rules 1, 2 and 3 into a texture of quantum information with dazzling patterns and colors. This rule tells us how to apply the three rules above when dealing with multiple physical systems. Consider two physical systems, A and B, which are *independently* accessible. For example, the two systems are well separated in space, meaning that one can freely operate on system A without affecting system B at all. We may call this type of operation *local*. In this case, we can treat the whole of systems A and B together as a single physical system (a *composite system* AB), or can focus on one of the two systems (a *subsystem*) with no interest in the other. Rule 4 provides the connection between these different viewpoints.

Rule 4 Suppose that the subsystems A and B are associated with the Hilbert spaces $\mathscr{H}_A$ and $\mathscr{H}_B$, respectively. The composite system AB is then associated with a tensor-product space $\mathscr{H}_{AB} = \mathscr{H}_A \otimes \mathscr{H}_B$. Local operations (e.g., state preparations, state transformations, measurements) are represented by the appropriate tensor products.

Specifically, preparation of system A in state $|\phi\rangle_A \in \mathscr{H}_A$ and system B in state $|\psi\rangle_B \in \mathscr{H}_B$ is equivalent to the preparation of a composite system AB in state

$|\phi\rangle_A \otimes |\psi\rangle_B \in \mathscr{H}_{AB}$. The state that can be written in this form is called a *product state*, and is often abbreviated as $|\phi\rangle_A|\psi\rangle_B$ or even $|\phi\psi\rangle_{AB}$. The unitary transformations $\hat{U}_A$ on system A and $\hat{V}_B$ on B result in the unitary transformation $\hat{U}_A \otimes \hat{V}_B$ on the composite system AB. Performing an orthogonal measurement with basis $\{|u_i\rangle_A\}_{i=1,\ldots,d}$ on system A and another with basis $\{|v_j\rangle_B\}_{j=1,\ldots,d'}$ on system B can be regarded as the performance of a single orthogonal measurement, where the outcome is represented by two numbers (i, j), carried out on the composite system AB with the orthonormal basis $\{|u_i\rangle_A \otimes |v_j\rangle_B\}_{j=1,\ldots,d'}^{i=1,\ldots,d}$ of $\mathscr{H}_{AB}$.

According to Rule 1, we should be able to prepare a state represented by any vector $|\Psi\rangle_{AB} \in \mathscr{H}_{AB}$, possibly by the tailoring of suitable interaction between systems A and B. These vectors include, for example, $(|u_1\rangle_A|v_1\rangle_B + |u_2\rangle_A|v_2\rangle_B)/\sqrt{2}$, which can never be written in the form $|\phi\rangle_A \otimes |\psi\rangle_B$. This type of state is called *entangled*. Similarly, a unitary operator $\hat{U}_{AB}$ acting on $\mathscr{H}_{AB}$ is not necessarily a product $\hat{U}_A \otimes \hat{V}_B$, and the corresponding *global* unitary transformation should be feasible. There are also global orthogonal measurements, for which the orthonormal basis is composed of entangled state vectors.

Since the state of a composite system is not necessarily written as a product form, the definition of 'the state of a subsystem' is something of a moot point. Here, we adopt a definition with a clear operational meaning, called the *marginal* state of a subsystem, which is simply the state that the subsystem would be in if we discard all the other constituent subsystems. With regard to the marginal states, we assume the following.

Rule 5 The marginal state of a subsystem is not changed by operating on other subsystems, as long as no information on the outcome of the operation is referred.

This rule is expected to hold because there would otherwise be a test on system A alone that would give clues on what operations were performed on a remote system B without any communication between them. The rule sets a limitation on the physically allowed state transformations and measurements, which complements the fact that Rules 2 and 3 merely dictate what we can at least do.

1.2 Density Operators

In classical mechanics, a mixed state is simply regarded as a way to formulate an observer's lack of knowledge of the true state of a system. In principle, it is always possible to assume that there is an omnipotent observer who knows the exact state (the pure state) of every system. In quantum mechanics, however, this simple picture does not hold. When a composite system is in a pure state $|\Psi\rangle_{AB}$, we cannot associate the state of the subsystem A with a single vector $|\phi\rangle_A \in \mathscr{H}_A$ unless $|\Psi\rangle_{AB}$ is a product state. Therefore, it is not always possible to assume that every system is in a pure state at the same time. In this subsection, we determine how we can represent the state of a subsystem when it is a part of a composite

system in a pure state $|\Psi\rangle_{AB}$. We will see that the intuitive representation using an ensemble $\{(p_j, |\phi_j\rangle)\}$ is redundant in the sense that different descriptions may refer to the same physical state. This motivates us to introduce a density operator to offer a better representation in this respect. By using a helpful property of bipartite pure states called Schmidt decomposition, we will show that there is a one-to-one correspondence between the density operators and the physical states.

1.2.1 Measurement on a Subsystem

Suppose that the composite system AB is initially prepared in a pure state $|\Psi\rangle_{AB}$, and an orthogonal measurement with a basis $\{|v_j\rangle_B\}_{j=1,\ldots,d'}$ is then conducted on subsystem B, producing an outcome j with a probability p_j. Let us derive a rule to calculate p_j and identify the state of the subsystem A that is conditioned on the value of j.

Our strategy is to observe what happens if we perform a measurement with arbitrary basis $\{|u_i\rangle_A\}_{i=1,\ldots,d}$ on system A. Regardless of the temporal order of the measurements on A and B, Rules 3 and 4 dictate that the joint probability of the two outcomes (i, j) is given by $p_{i,j} = |({}_A\langle u_i| \otimes {}_B\langle v_j|)|\Psi\rangle_{AB}|^2$. Let us introduce the unnormalized vector $|\tilde{\phi}_j\rangle_A := {}_B\langle v_j||\Psi\rangle_{AB} \in \mathscr{H}_A$. We then have $p_{i,j} = |{}_A\langle u_i|\tilde{\phi}_j\rangle_A|^2$ and $p_j = \sum_{i=1}^{d} p_{i,j} = \sum_{i=1}^{d} |{}_A\langle u_i|\tilde{\phi}_j\rangle_A|^2 = |{}_A\langle\tilde{\phi}_j|\tilde{\phi}_j\rangle_A|^2$. Using a normalized vector $|\phi_j\rangle_A := |\tilde{\phi}_j\rangle_A/\sqrt{p_j}$, we obtain an expression for the conditional probability, $p_{i|j} := p_{i,j}/p_j = |{}_A\langle u_i|\phi_j\rangle_A|^2$. Because the choice of the basis $\{|u_i\rangle_A\}_{i=1,\ldots,d}$ was arbitrary, comparison of this relationship to Rule 3 shows that the state of the subsystem A conditioned on the outcome j must be a pure state, which is represented by the vector $|\phi_j\rangle_A$. Noting that the measurement on A can be performed immediately after the preparation of $|\Psi\rangle_{AB}$, we arrive at the following theorem.

Theorem 1. *Suppose that a composite system AB is initially prepared in a pure state $|\Psi\rangle_{AB}$, and that an orthogonal measurement with a basis $\{|v_j\rangle_B\}_{j=1,\ldots,d'}$ is performed on subsystem B. The outcome j then occurs with probability p_j and, conditioned on j, the subsystem A behaves as if it was initially prepared in the pure state $|\phi_j\rangle_A$, where*

$$\sqrt{p_j}|\phi_j\rangle_A = {}_B\langle v_j||\Psi\rangle_{AB} \tag{1.1}$$

holds.

1.2.2 Marginal State of a Subsystem

The argument in the previous subsection immediately provides a description of the marginal state of the subsystem A when the composite system AB is prepared in the pure state $|\Psi\rangle_{AB}$. If the value of the outcome j of the measurement on subsystem B

is unavailable, then the state of system A after the measurement can be described by the ensemble $\{(p_j, |\phi_j\rangle_A)\}_{j=1,\ldots,d'}$, where the probabilities $\{p_j\}$ and the vectors $\{|\phi_j\rangle_A\}$ are calculated from Eq. (1.1). From Rule 5, we see that the marginal state of subsystem A before the measurement was performed is also $\{(p_j, |\phi_j\rangle_A)\}_{j=1,\ldots,d'}$.

On the one hand, this description is helpful because it is sufficient to allow calculation of the statistics of the outcomes of further operations on system A alone. On the other hand, the argument above also shows that the description of a mixed state by the ensemble is by no means unique. If we change the basis $\{|v_j\rangle_B\}_{j=1,\ldots,d'}$ of the measurement to another basis, then the description of the state $\{(p_j, |\phi_j\rangle_A)\}_{j=1,\ldots,d'}$ also changes through Eq. (1.1). This new ensemble should also be a valid representation of the same state.

Lemma 1. *Two ensembles,* $\{(p_j, |\phi_j\rangle_A)\}_{j=1,\ldots,d'}$ *and* $\{(p'_j, |\phi'_j\rangle_A)\}_{j=1,\ldots,d'}$, *represent the same mixed state if a bipartite pure state* $|\Psi\rangle_{AB}$ *and orthonormal bases* $\{|v_j\rangle_B\}_{j=1,\ldots,d'}$ *and* $\{|v'_j\rangle_B\}_{j=1,\ldots,d'}$ *exist that satisfy*

$$\sqrt{p_j}|\phi_j\rangle_A = {}_B\langle v_j||\Psi\rangle_{AB} \quad \text{and} \quad \sqrt{p'_j}|\phi'_j\rangle_A = {}_B\langle v'_j||\Psi\rangle_{AB}. \tag{1.2}$$

1.2.3 Density Operators

Consider a physical system that is associated with a Hilbert space $\mathscr{H}$, and let us call an operator $\hat{\rho} : \mathscr{H} \to \mathscr{H}$ a *density operator* when it is positive ($\hat{\rho} \geq 0$) and of unit trace ($\mathrm{Tr}\ \hat{\rho} = 1$). We associate a mixed state of a system represented by the ensemble $\{(q_i, |\psi_i\rangle)\}_{i=1,\ldots,n}$ with a density operator given by

$$\hat{\rho} := \sum_{i=1}^{n} q_i |\psi_i\rangle\langle\psi_i|. \tag{1.3}$$

One immediate benefit of this representation by the density operator is that the marginal state that was discussed in Sect. 1.2.2 is represented by a unique density operator, i.e.,

$$\hat{\rho}_A = \sum_{j=1}^{d'} p_j |\phi_j\rangle_{AA}\langle\phi_j| = \sum_{j=1}^{d'} p'_j |\phi'_j\rangle_{AA}\langle\phi'_j| = \mathrm{Tr}_B |\Psi\rangle_{ABAB}\langle\Psi| \tag{1.4}$$

that holds under Eq. (1.2). This operator is called the *marginal* density operator of system A for the whole state $|\Psi\rangle_{AB}$.

Because any positive operator $\hat{\rho}$ with a unit trace can be written in a *diagonal* form $\hat{\rho} = \sum_i \lambda_i |u_i\rangle\langle u_i|$ using nonnegative eigenvalues $\{\lambda_i\}$ with $\sum_i \lambda_i = 1$ and orthonormal eigenvectors $\{|u_i\rangle\}$, $\hat{\rho}$ is the density operator for an ensemble $\{(\lambda_i, |u_i\rangle)\}_i$. Therefore, any density operator is associated with at least one physical state.

When an orthogonal measurement with a basis $\{|u_j\rangle\}_j$ is performed on a mixed state $\{(q_i, |\psi_i\rangle)\}_i$, the probability of the outcome j is calculated using Rule 3 to be $p_j = \sum_i q_i |\langle u_j|\psi_i\rangle|^2 = \langle u_j|\hat{\rho}|u_j\rangle$. This shows that the statistics of the measurement outcome depend only on the density operator. This also shows that each physical state is associated with a single density operator. Consider two mixed states with different density operators $\hat{\rho}$ and $\hat{\rho}'(\neq \hat{\rho})$. Because $|u\rangle \in \mathscr{H}$ exists with $\langle u|(\hat{\rho} - \hat{\rho}')|u\rangle \neq 0$, a measurement leading to different statistics between the two states also exists. The two states are therefore distinct. This fact implies that the density operator can be determined using a map from the set of physical states. As shown earlier, this map is surjective.

The remaining question is whether this map is bijective. At this point, it might not be injective, i.e., different mixed states could be associated with the same density operator. We will provide the answer to this question in Sect. 1.2.5, after we discuss the important properties of bipartite pure states in Sect. 1.2.4.

1.2.4 Properties of Bipartite Pure States

First, we consider how a general bipartite pure state $|\Psi\rangle_{AB}$ can be written in terms of the orthonormal bases $\{|u_i\rangle_A\}_i$ and $\{|v_j\rangle_B\}_j$ for the subsystems A and B. Because $\{|u_i\rangle_A|v_j\rangle_B\}_{i,j}$ is a basis of $\mathscr{H}_{AB}$, it is always possible to decompose $|\Psi\rangle_{AB}$ as $|\Psi\rangle_{AB} = \sum_{i,j} c_{i,j}|u_i\rangle_A|v_j\rangle_B$. The special aspect of bipartite states is that a much simpler form of decomposition, $|\Psi\rangle_{AB} = \sum_i c_i|u_i\rangle_A|v_i\rangle_B$, is available if we select $\{|u_i\rangle_A\}_i$ and $\{|v_j\rangle_B\}_j$ appropriately for the given vector $|\Psi\rangle_{AB}$. This decomposition is called *Schmidt decomposition*, and it will be convenient to describe Schmidt decomposition in the form of the following theorem.

Theorem 2. *Let $|\Psi\rangle_{AB} \in \mathscr{H}_{AB} = \mathscr{H}_A \otimes \mathscr{H}_B$ be a normalized vector that represents a pure state of a bipartite system AB. Let $\hat{\rho}_A = \mathrm{Tr}_B|\Psi\rangle_{ABAB}\langle\Psi|$ be the marginal density operator of system A, and let s be the rank of $\hat{\rho}_A$. For any orthonormal set of vectors $\{|u_i\rangle_A\}_{i=1,\ldots,s} \subset \mathscr{H}_A$ that diagonalizes $\hat{\rho}_A$ as $\hat{\rho}_A = \sum_{i=1}^s p_i|u_i\rangle_{AA}\langle u_i|$ with $p_i > 0 (i = 1, \ldots, s)$, there is an orthonormal set of vectors $\{|v_i\rangle_B\}_{i=1,\ldots,s} \subset \mathscr{H}_B$, such that*

$$|\Psi\rangle_{AB} = \sum_{i=1}^{s} \sqrt{p_i}|u_i\rangle_A|v_i\rangle_B. \tag{1.5}$$

Proof. Define the unnormalized vectors $|\tilde{v}_i\rangle_B := {}_A\langle u_i||\Psi\rangle_{AB}$. We then have $|\Psi\rangle_{AB} = \sum_{i=1}^s |u_i\rangle_A|\tilde{v}_i\rangle_B$. We see that ${}_B\langle\tilde{v}_i|\tilde{v}_j\rangle_B = \mathrm{Tr}|\tilde{v}_j\rangle_{BB}\langle\tilde{v}_i| = {}_A\langle u_j|\mathrm{Tr}_B(|\Psi\rangle_{ABAB}\langle\Psi|)|u_i\rangle_A = {}_A\langle u_j|\hat{\rho}_A|u_i\rangle_A = p_i\delta_{i,j}$, where $\delta_{i,j} = 1$ if $i = j$, and otherwise $\delta_{i,j} = 0$. Thus, if we define $|v_i\rangle_B := |\tilde{v}_i\rangle_B/\sqrt{p_i}$, $\{|v_i\rangle_B\}_i$ is an orthonormal set that satisfies Eq. (1.5). □

The number s is often called the *Schmidt number* of the state $|\Psi\rangle_{AB}$. If s is smaller than $\dim \mathscr{H}_A$ or $\dim \mathscr{H}_B$, we can always augment the orthonormal sets to form orthonormal bases.

Next, we introduce a concept that is opposite to the concept of the marginal density operator for a bipartite pure state. For a given density operator $\hat{\rho}_A$ of subsystem A, a *purification* of the density operator is defined to be a pure state $|\Phi\rangle_{AB}$ of the composite system AB that satisfies $\mathrm{Tr}_B|\Phi\rangle_{ABAB}\langle\Phi| = \hat{\rho}_A$. In contrast to the marginal density operator, which is unique to a given state $|\Psi\rangle_{AB}$, the purification of a given density operator $\hat{\rho}_A$ is not unique and there are many bipartite pure states that can be regarded as purifications of $\hat{\rho}_A$. However, they are connected by a simple relation [1, 2] that is given as follows.

Theorem 3. *For any two purifications $|\Phi\rangle_{AB}$, $|\Phi'\rangle_{AB} \in \mathscr{H}_{AB} = \mathscr{H}_A \otimes \mathscr{H}_B$ of the same density operator $\hat{\rho}_A$, there is a unitary operator $\hat{V}_B : \mathscr{H}_B \to \mathscr{H}_B$ such that*

$$|\Phi'\rangle_{AB} = (\hat{1}_A \otimes \hat{V}_B)|\Phi\rangle_{AB}. \tag{1.6}$$

Proof. When we write down a diagonal form $\hat{\rho}_A = \sum_{i=1}^{s} p_i |u_i\rangle_{AA}\langle u_i|$, Theorem 2 ensures that the purifications are decomposed as $|\Phi\rangle_{AB} = \sum_{i=1}^{s} \sqrt{p_i}|u_i\rangle_A|v_i\rangle_B$ and $|\Phi'\rangle_{AB} = \sum_{i=1}^{s} \sqrt{p_i}|u_i\rangle_A|v_i'\rangle_B$. Because $\{|v_i\rangle_B\}_i$ and $\{|v_i'\rangle_B\}_i$ are orthonormal sets, a unitary operator $\hat{V}_B$ exists such that $|v_i'\rangle_B = \hat{V}_B|v_i\rangle_B$ for all i. □

This theorem is quite simple but has deeper consequences. Suppose that Alice holds system A and Bob holds system B, and assume that only Bob knows whether the system AB is in state $|\Phi\rangle_{AB}$ or in state $|\Phi'\rangle_{AB}$. There are then only two possible situations: (i) The marginal density operators of subsystem A are different for $|\Phi\rangle_{AB}$ and $|\Phi'\rangle_{AB}$, and thus Alice can locally distinguish state $|\Phi\rangle_{AB}$ from state $|\Phi'\rangle_{AB}$ to some extent. (ii) The marginal density operators of subsystem A are the same and according to Theorem 3, Bob can switch locally between state $|\Phi\rangle_{AB}$ and state $|\Phi'\rangle_{AB}$. As a result, we see that there is no situation whatsoever in which Alice is unable to distinguish between the two states locally *and* Bob is unable to switch between the states locally. This property has led to the no-go theorem for unconditionally secure bit commitment [3, 4].

1.2.5 Physical States and Density Operators

We are now in a position to prove that there is a one-to-one correspondence between the physical states and the density operators. Consider two states represented by the ensembles $\{(p_j, |\phi_j\rangle_A)\}_{j=1,\ldots,d}$ and $\{(p_j', |\phi_j'\rangle_A)\}_{j=1,\ldots,d'}$, which are associated with the same density operator $\hat{\rho}_A$. We will show that these two states are in fact the same state [1, 2].

Without loss of generality, we may assume that $d \leq d'$. If $d < d'$, we can augment the ensemble $\{(p_j, |\phi_j\rangle_A)\}_{j=1,\ldots,d}$ in an equivalent manner to $\{(p_j, |\phi_j\rangle_A)\}_{j=1,\ldots,d'}$

by adding dummy states $|\phi_j\rangle_A$ with $p_j = 0$. Consider another system B with a Hilbert space $\mathscr{H}_B$ with dimension d', and take an orthonormal basis $\{|v_j\rangle_B\}_{j=1,\ldots,d'}$. We then define the bipartite states $|\Psi\rangle_{AB} := \sum_{j=1}^{d'} \sqrt{p_j}|\phi_j\rangle_A|v_j\rangle_B$ and $|\Psi'\rangle_{AB} := \sum_{j=1}^{d'} \sqrt{p'_j}|\phi'_j\rangle_A|v_j\rangle_B$, which both have $\hat{\rho}_A$ as their marginal density operator. From Theorem 3, there is a unitary operator $\hat{V}_B$ with $|\Psi'\rangle_{AB} = (\hat{1}_A \otimes \hat{V}_B)|\Psi\rangle_{AB}$. We define another orthonormal basis $\{|v'_j\rangle_B\}_{j=1,\ldots,d'}$ using $|v'_j\rangle := \hat{V}_B^\dagger|v_j\rangle$. It is then simple to confirm that the requisite of Lemma 1, Eq. (1.2), holds, and thus the two states are the same state. When combined with the previous observation in Sect. 1.2.3, we can conclude that:

> There is a one-to-one correspondence between the set of physical states and the set of density operators.

Having established that the density operators are conceptually an ideal description of the physical states, it is natural to expect that the basic and derived rules will be equally well stated when using the density operators in place of vectors to represent the physical states. In fact, by carefully following the definition, we obtain the following list of formulas.

Unitary transformation	$\|\phi_{\text{out}}\rangle = \hat{U}\|\phi_{\text{in}}\rangle$	$\hat{\rho}_{\text{out}} = \hat{U}\hat{\rho}_{\text{in}}\hat{U}^\dagger$
Orthogonal measurement	$p_j = \|\langle u_j\|\phi_{\text{in}}\rangle\|^2$	$p_j = \langle u_j\|\hat{\rho}_{\text{in}}\|u_j\rangle$
Local preparation	$\|\phi\rangle_A \otimes \|\psi\rangle_B$	$\hat{\rho}_A \otimes \hat{\rho}_B$
Measurement on subsystem	$\sqrt{p_j}\|\phi_j\rangle_A = {}_B\langle v_j\|\|\Psi\rangle_{AB}$	$p_j\hat{\rho}_A^{(j)} = {}_B\langle v_j\|\hat{\rho}_{AB}\|v_j\rangle_B$
Preparation by mixing	$\hat{\rho} = \sum_i q_i\|\phi_i\rangle\langle\phi_i\|$	$\hat{\rho} = \sum_i q_i\hat{\rho}^{(i)}$
Marginal state	$\hat{\rho}_A = \text{Tr}_B\|\Psi\rangle_{ABAB}\langle\Psi\|$	$\hat{\rho}_A = \text{Tr}_B\hat{\rho}_{AB}$

Distinction is made between the pure and mixed states based simply on the rank of the density operator. The state is pure if and only if the rank of its density operator $\hat{\rho}$ is 1, in which case it can be written as $\hat{\rho} = |\phi\rangle\langle\phi|$ using the normalized vector $|\phi\rangle$. The opposite extreme may be the case of the operators with maximal rank, which is equal to the dimension d of the Hilbert space. Among these operators, the state where $\hat{\rho} = \hat{1}/d$ has the unique property of invariance under all unitary transformations, and is called the *maximally mixed* state.

Classification of the density operator can be related to the classification of the bipartite pure states through purification. The Schmidt number of a specific purification is equal to the rank of the density operator. The purification of a rank-one density operator, $\hat{\rho}_A = |u\rangle_{AA}\langle u|$, is a product state in the form of $|u\rangle_A|v\rangle_B$, while the purification of a nonpure density operator is an entangled state. The purification of a maximally mixed state is called a *maximally entangled* state. Under Schmidt decomposition of Eq. (1.5), a maximally entangled state $|\Phi\rangle_{AB}$ is written as

$$|\Phi\rangle_{AB} = \frac{1}{\sqrt{d}}\sum_{i=1}^{d}|u_i\rangle_A|v_i\rangle_B, \tag{1.7}$$

where d is the dimension of $\mathscr{H}_A$.

1.3 Qubits

The simplest of the physical systems is a two-level system that is associated with a Hilbert space of dimension 2, and is called a qubit. For a qubit, the general states, the orthogonal measurements, and the unitary transformations can be conveniently visualized using a three-dimensional image called the Bloch representation.

1.3.1 Pauli Operators

Consider a qubit and choose an orthonormal basis $\{|0\rangle, |1\rangle\}$ of its Hilbert space $\mathscr{H}$ as the standard basis. We define a set of three operators, called *Pauli operators*, as $\hat{\sigma}_x = \hat{\sigma}_1 := |0\rangle\langle 1| + |1\rangle\langle 0|$, $\hat{\sigma}_y = \hat{\sigma}_2 := -i|0\rangle\langle 1| + i|1\rangle\langle 0|$, and $\hat{\sigma}_z = \hat{\sigma}_3 := |0\rangle\langle 0| - |1\rangle\langle 1|$. In the matrix representation under the standard basis, they are written as

$$\hat{\sigma}_x = \hat{\sigma}_1 = \begin{pmatrix} 0 & 1 \\ 1 & 0 \end{pmatrix}, \ \hat{\sigma}_y = \hat{\sigma}_2 = \begin{pmatrix} 0 & -i \\ i & 0 \end{pmatrix}, \ \hat{\sigma}_z = \hat{\sigma}_3 = \begin{pmatrix} 1 & 0 \\ 0 & -1 \end{pmatrix}. \tag{1.8}$$

They satisfy the following commutation and anti-commutation relations:

$$[\hat{\sigma}_i, \hat{\sigma}_j] = 2i\epsilon_{ijk}\hat{\sigma}_k \ \text{ and } \ \{\hat{\sigma}_i, \hat{\sigma}_j\} = 2\delta_{ij}\hat{1}, \tag{1.9}$$

where $[\hat{A}, \hat{B}] = \hat{A}\hat{B} - \hat{B}\hat{A}$, $\{\hat{A}, \hat{B}\} = \hat{A}\hat{B} + \hat{B}\hat{A}$. The Levi-Civita symbol ϵ_{ijk} is zero, except for $\epsilon_{123} = \epsilon_{231} = \epsilon_{312} = 1$ and $\epsilon_{321} = \epsilon_{132} = \epsilon_{213} = -1$, and the Einstein notation is used to omit the summation.

Together with $\hat{\sigma}_0 := \hat{1}$, we have four self-adjoint and unitary operators. These satisfy the orthogonality relations,

$$\mathrm{Tr}(\hat{\sigma}_\mu \hat{\sigma}_\nu) = 2\delta_{\mu,\nu} \tag{1.10}$$

for $\mu, \nu = 0, 1, 2, 3$. Every linear operator $\hat{A}$ acting on $\mathscr{H}$ is uniquely decomposed as $\hat{A} = (P_0\hat{1} + P_x\hat{\sigma}_x + P_y\hat{\sigma}_y + P_z\hat{\sigma}_z)/2$, where the four complex parameters (P_0, P_x, P_y, P_z) can be determined using $P_0 = \mathrm{Tr}(\hat{A})$, $P_x = \mathrm{Tr}(\hat{\sigma}_x\hat{A})$, $P_y = \mathrm{Tr}(\hat{\sigma}_y\hat{A})$, and $P_z = \mathrm{Tr}(\hat{\sigma}_z\hat{A})$. It is convenient to regard $\boldsymbol{P} := (P_x, P_y, P_z)$ as a three-dimensional vector, and to define $\hat{\boldsymbol{\sigma}} := (\hat{\sigma}_x, \hat{\sigma}_y, \hat{\sigma}_z)$ as well. We denote the inner product between these vectors as $\boldsymbol{P} \cdot \hat{\boldsymbol{\sigma}} := P_x\hat{\sigma}_x + P_y\hat{\sigma}_y + P_z\hat{\sigma}_z$, and the squared norm as $|\boldsymbol{P}|^2 := P_x^2 + P_y^2 + P_z^2$. Using the vector notation, we have

$$\hat{A} = (P_0\hat{1} + \boldsymbol{P} \cdot \hat{\boldsymbol{\sigma}})/2 \tag{1.11}$$

with $P_0 = \mathrm{Tr}(\hat{A})$ and $\boldsymbol{P} = \mathrm{Tr}(\hat{\boldsymbol{\sigma}}\hat{A})$.

Because $\hat{A}^\dagger = (\bar{P}_0\hat{1} + \bar{\boldsymbol{P}}\cdot\hat{\boldsymbol{\sigma}})/2$, $\hat{A}$ is self-adjoint if and only if both P_0 and $\boldsymbol{P}$ are real. For a self-adjoint operator $\hat{A}$, it is simple to show that $\det(\hat{A}) = (P_0^2 - |\boldsymbol{P}|^2)/4$, and that the two eigenvalues of $\hat{A}$ are $(P_0 \pm |\boldsymbol{P}|)/2$. Therefore, $\hat{A}$ is positive if and only if $\boldsymbol{P}$ is real and $P_0 \geq |\boldsymbol{P}|$.

1.3.2 General States of a Qubit

Because a density operator $\hat{\rho}$ is positive and has a unit trace, application of the decomposition of Eq. (1.11) leads to

$$\hat{\rho} = (\hat{1} + \boldsymbol{P}\cdot\hat{\boldsymbol{\sigma}})/2 \tag{1.12}$$

where the real vector $\boldsymbol{P} = \mathrm{Tr}(\hat{\boldsymbol{\sigma}}\hat{\rho})$ satisfies $|\boldsymbol{P}| \leq 1$. We see that the density operators, and thus the general states of a qubit, are uniquely represented by three-dimensional real vectors $\boldsymbol{P} = (P_x, P_y, P_z)$ with lengths no greater than unity. These vectors are called the *Bloch vectors*, and representation of the qubit states using these Bloch vectors is called *Bloch representation*. As shown in Fig. 1.1a, a Bloch vector is visualized in an *xyz*-Cartesian coordinate system as an arrow stemming from the origin and reaching a point (P_x, P_y, P_z) on or inside of a sphere of unit radius, which is called a *Bloch sphere*.

As shown in Sect. 1.2.5, the rank of $\hat{\rho}$ is 1 when it is a pure state, and for a qubit this implies that the smaller of the eigenvalues of $\hat{\rho}$, $(1-|\boldsymbol{P}|)/2$, is zero. A pure state is thus represented by a Bloch vector of length $|\boldsymbol{P}| = 1$, with the vector tip reaching the Bloch sphere. For a mixed (and nonpure) state, the length of the Bloch vector is shorter ($|\boldsymbol{P}| < 1$). The maximally mixed state with $\hat{\rho} = \hat{1}/2$ is represented by the zero vector $\boldsymbol{P} = \boldsymbol{0}$.

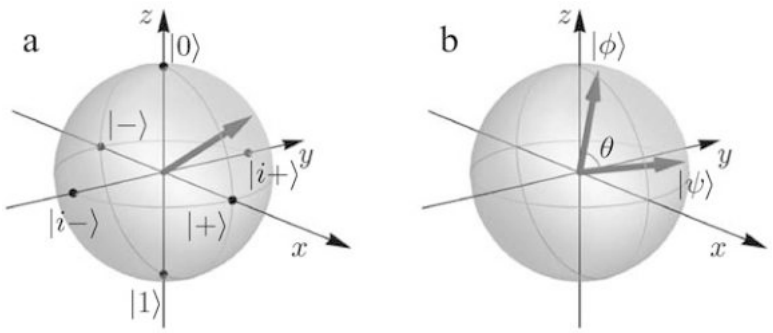

Fig. 1.1 (**a**) Bloch sphere and a Bloch vector. The six pure states on one of the three axes, where $|\pm\rangle := (|0\rangle \pm |1\rangle)/\sqrt{2}$ and $|i\pm\rangle := (|0\rangle \pm i|1\rangle)/\sqrt{2}$, are also shown. (**b**) A pair of pure states $|\phi\rangle$ and $|\psi\rangle$, with $|\langle\phi|\psi\rangle| = \cos(\theta/2)$

Bloch vectors should not be confused with the vectors of the Hilbert space. Bloch vectors belong to a three-dimensional real vector space, while the Hilbert space of a qubit is a complex two-dimensional vector space. Consider two pure states, $\hat{\rho}_\phi = |\phi\rangle\langle\phi|$ and $\hat{\rho}_\psi = |\psi\rangle\langle\psi|$, with Bloch vectors $\boldsymbol{P}_\phi$ and $\boldsymbol{P}_\psi$, respectively. When $\boldsymbol{P}_\phi \cdot \boldsymbol{P}_\psi = \cos\theta$, then the angle between the two Bloch vectors is θ (see Fig. 1.1b). In contrast, based on Eq. (1.10), we have $|\langle\phi|\psi\rangle|^2 = \mathrm{Tr}(\hat{\rho}_\phi\hat{\rho}_\psi) = (1+\boldsymbol{P}_\phi\cdot\boldsymbol{P}_\psi)/2 = \cos^2(\theta/2)$, which implies that the angle between the two vectors of the Hilbert space is $\theta/2$. For two orthogonal pure states, $\theta/2 = \pi/2$ implies that the corresponding pair of Bloch vectors point in opposite directions.

1.3.3 Orthogonal Measurement on a Qubit

Let us interpret an orthogonal measurement using the basis $\{|u_0\rangle, |u_1\rangle\}$ in terms of Bloch representation. We define the Bloch vectors $\boldsymbol{P}_0$ and $\boldsymbol{P}_1$ for the basis states using $\hat{\rho}_j := |u_j\rangle\langle u_j| = (\hat{1} + \boldsymbol{P}_j \cdot \hat{\boldsymbol{\sigma}})/2$. Because the orthogonality $\langle u_0|u_1\rangle = 0$ implies that $\boldsymbol{P}_1 = -\boldsymbol{P}_0$, the orthogonal measurement is completely characterized by the unit vector $\boldsymbol{P}_0$, which is a direction in the three-dimensional space.

Suppose that the measured qubit is initially in the state given by $\hat{\rho} = (\hat{1}+\boldsymbol{P}\cdot\hat{\boldsymbol{\sigma}})/2$. The probabilities of outcome $j = 0, 1$ are then calculated to be $p_j = \langle u_j|\hat{\rho}|u_j\rangle = \mathrm{Tr}(\hat{\rho}_j\hat{\rho}) = (1 + \boldsymbol{P}_j \cdot \boldsymbol{P})/2$, leading to

$$p_0 = (1 + \boldsymbol{P}_0 \cdot \boldsymbol{P})/2 \quad \text{and} \quad p_1 = (1 - \boldsymbol{P}_0 \cdot \boldsymbol{P})/2. \tag{1.13}$$

This shows that the probabilities are essentially determined by projection of the measured Bloch vector $\boldsymbol{P}$ along the direction $\boldsymbol{P}_0$ that was specified by the measurement, with appropriate scaling (see Fig. 1.2a).

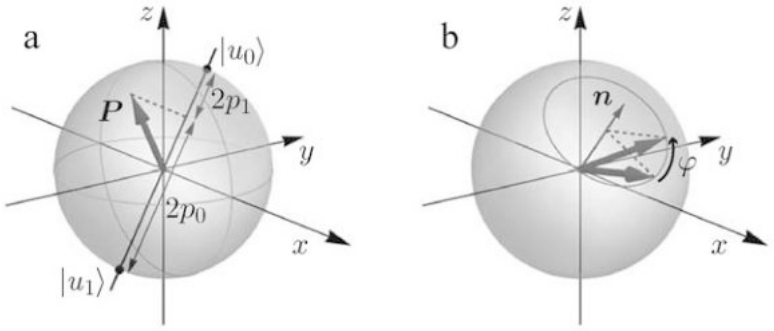

Fig. 1.2 (**a**) Orthogonal measurement with a basis $\{|u_j\rangle\}_{j=0,1}$. The Bloch vector $\boldsymbol{P}$ of the input state determines the probability p_j of the outcome j. (**b**) The Bloch vector rotates in a unitary transformation with $\hat{U}(\boldsymbol{n}, \varphi)$

1.3.4 Unitary Transformation on a Qubit

We now discuss how the Bloch vector of a physical state changes under a unitary transformation. We limit ourselves to the unitary operators $\hat{U}$ that belong to a set called $SU(2)$, and are characterized by the condition $\det \hat{U} = 1$. This does not lose generality because $\hat{U}(\theta) := e^{i\theta/2}\hat{U}$ for real θ transforms the state $\hat{\rho}$ to $\hat{U}(\theta)\hat{\rho}\hat{U}(\theta)^\dagger = \hat{U}\hat{\rho}\hat{U}^\dagger$, which is independent of θ. All $\hat{U}(\theta)$ physically represent the same transformation, and we are thus allowed to choose one that satisfies $\det \hat{U}(\theta) = e^{i\theta} \det \hat{U} = 1$ and thus $\hat{U}(\theta) \in SU(2)$. Note that the correspondence is not one-to-one but in fact two-to-one, because $-\hat{U}(\theta) = \hat{U}(\theta + 2\pi)$ also belongs to $SU(2)$.

The elements of $SU(2)$ are conveniently parametrized as follows. Any $\hat{U} \in SU(2)$ can be written in the diagonal form $\hat{U} = e^{-i\varphi/2}|u_0\rangle\langle u_0| + e^{i\varphi/2}|u_1\rangle\langle u_1|$ with $\langle u_0|u_1\rangle = 0$. We may then write $\hat{U} = \exp(-i\varphi\hat{S}/2)$ with $\hat{S} := |u_0\rangle\langle u_0| - |u_1\rangle\langle u_1|$, which is self-adjoint, traceless, and has eigenvalues of ± 1. Using the decomposition of Eq. (1.11), we find that $\hat{S}$ is written as $\hat{S} = \boldsymbol{P}\cdot\hat{\boldsymbol{\sigma}}/2$ with $|\boldsymbol{P}| = 2$. By introducing a unit vector $\boldsymbol{n} := \boldsymbol{P}/2$, we conclude that the elements of $SU(2)$ can be parametrized as

$$\hat{U}(\boldsymbol{n}, \varphi) := \exp[-i(\varphi/2)\boldsymbol{n}\cdot\hat{\boldsymbol{\sigma}}]. \tag{1.14}$$

We are interested in how the Bloch vector evolves when the density operator evolves under a unitary transformation. Noting that $\hat{U}(\boldsymbol{n}, \varphi+\varphi') = \hat{U}(\boldsymbol{n}, \varphi')\hat{U}(\boldsymbol{n}, \varphi)$ holds in general, we see that it is sufficient to focus on the transformations given by $\hat{U}(\boldsymbol{n}, \delta\varphi)$, where $\delta\varphi$ is infinitesimally small. A general transformation $\hat{U}(\boldsymbol{n}, \varphi)$ is then understood as a result of sequential application of these infinitesimal transformations.

Under the transformation $\hat{U}(\boldsymbol{n}, \delta\varphi)$, a Bloch vector $\boldsymbol{P} := \mathrm{Tr}(\hat{\boldsymbol{\sigma}}\,\hat{\rho})$ evolves into $\boldsymbol{P} + \delta\boldsymbol{P} = \mathrm{Tr}(\hat{\boldsymbol{\sigma}}\,\hat{\rho}')$ with $\hat{\rho}' := \hat{U}(\boldsymbol{n}, \delta\varphi)\hat{\rho}\hat{U}(\boldsymbol{n}, \delta\varphi)^\dagger$. Using $\hat{U}(\boldsymbol{n}, \delta\varphi) \cong \hat{1} - i(\delta\varphi/2)\boldsymbol{n}\cdot\hat{\boldsymbol{\sigma}}$ and collecting the terms up to the first order in $\delta\varphi$, we find that $\delta\boldsymbol{P} = \mathrm{Tr}(\hat{\boldsymbol{\sigma}}\,\hat{\rho}') - \mathrm{Tr}(\hat{\boldsymbol{\sigma}}\,\hat{\rho}) = -i(\delta\varphi/2)\mathrm{Tr}([\hat{\boldsymbol{\sigma}}, \boldsymbol{n}\cdot\hat{\boldsymbol{\sigma}}]\hat{\rho})$. From Eq. (1.9), we obtain $[\hat{\sigma}_i, n_j\hat{\sigma}_j] = 2i\epsilon_{ijk}n_j\hat{\sigma}_k$ under the Einstein notation, which implies that $[\hat{\boldsymbol{\sigma}}, \boldsymbol{n}\cdot\hat{\boldsymbol{\sigma}}] = 2i\boldsymbol{n}\times\hat{\boldsymbol{\sigma}}$. Therefore, $\hat{U}(\boldsymbol{n}, \delta\varphi)$ induces an infinitesimal change in the Bloch vector, which is given by

$$\delta\boldsymbol{P} = \delta\varphi\boldsymbol{n}\times\boldsymbol{P}. \tag{1.15}$$

This is equal to the infinitesimal change in rotation around axis $\boldsymbol{n}$ by the angle $\delta\varphi$. We thus conclude that the Bloch vectors rotate around axis $\boldsymbol{n}$ by angle φ under the general unitary transformation $\hat{U}(\boldsymbol{n}, \varphi)$ (see Fig. 1.2b). Notable examples include the Z gate with $\hat{U}((0, 0, 1), \pm\pi) = \mp i\hat{\sigma}_z$, the X gate with $\hat{U}((1, 0, 0), \pm\pi) = \mp i\hat{\sigma}_x$, and the Hadamard gate with $\hat{U}((2^{-1/2}, 0, 2^{-1/2}), \pm\pi) = \mp 2^{-1/2}i(\hat{\sigma}_z + \hat{\sigma}_x)$.

1.4 Generalized Measurements and Quantum Operations

The basic set of rules that we adopted in Sect. 1.1 dictated that we can carry out unitary transformations and orthogonal measurements on a physical system (Rules 2 and 3). Here, we extend the repertoire of what we can do to a physical system by using an auxiliary system as a workspace. We also clarify how far this extension goes, and draw a clear line between what we can and cannot do.

1.4.1 Use of Auxiliary Systems

Suppose that we want to operate on a physical system A. Let $\hat{\rho}_{\text{in}}$ be the density operator for the initial state of the system A. We first prepare an auxiliary system E, which has a Hilbert space $\mathscr{H}_E$ of dimension s, in a fixed pure state $|\phi_{\text{ini}}\rangle_E$. We then let the systems A and E interact with each other such that the unitary transformation described by the unitary operator $\hat{U}_{AE} : \mathscr{H}_A \otimes \mathscr{H}_E \to \mathscr{H}_A \otimes \mathscr{H}_E$ occurs. Finally, we perform an orthogonal measurement on system E with an orthonormal basis $\{|j\rangle_E\}_{j=1,\ldots,s}$ of $\mathscr{H}_E$. The output of the operation is the classical variable j and the final quantum state $\hat{\rho}_{\text{out}}^{(j)}$ of system A, which may depend on the value of j. This can thus be regarded as conducting a state transformation and performing a measurement at the same time. Using the rules that were summarized in Sect. 1.2.5, we can easily show how the final state $\hat{\rho}_{\text{out}}^{(j)}$ and the probability p_j of obtaining j are related to the initial state:

$$p_j \hat{\rho}_{\text{out}}^{(j)} = {}_E\langle j|\hat{U}_{AE}(\hat{\rho}_{\text{in}} \otimes |\phi_{\text{ini}}\rangle_{EE}\langle\phi_{\text{ini}}|)\hat{U}_{AE}^{\dagger}|j\rangle_E. \tag{1.16}$$

We sometimes encounter a situation where the input and the output are different physical systems. For example, in the photoelectric effect, light is incident on a metal but an electron comes out of the metal. In such a case, we would regard the light field as the input system A, and the metal, including the electron that is eventually emitted, as the auxiliary system E. The whole system is the composite of A and E. The output system, i.e., the electron, is a subsystem of the composite system AE, and we call it system A'. The rest of system AE is then called system E'. In short, we have introduced two different ways to decompose the entire system into two subsystems, AE and $A'E'$. Mathematically, this corresponds to an equivalence relation $\mathscr{H}_A \otimes \mathscr{H}_E = \mathscr{H}_{A'} \otimes \mathscr{H}_{E'}$.

We can now generalize the strategy for use of an auxiliary system to include cases where the output system is not necessarily the same as the input system, as shown in Fig. 1.3. It is convenient to regard the unitary operator $\hat{U}_{AE}$ as a linear map $\hat{U} : \mathscr{H}_A \otimes \mathscr{H}_E \to \mathscr{H}_{A'} \otimes \mathscr{H}_{E'}$, where we dropped the subscript AE. Let s' be the dimension of $\mathscr{H}_{E'}$. The orthogonal measurement is performed on system E' with an orthonormal basis $\{|j\rangle_{E'}\}_{j=1,\ldots,s'}$. Equation (1.16) is then generalized as

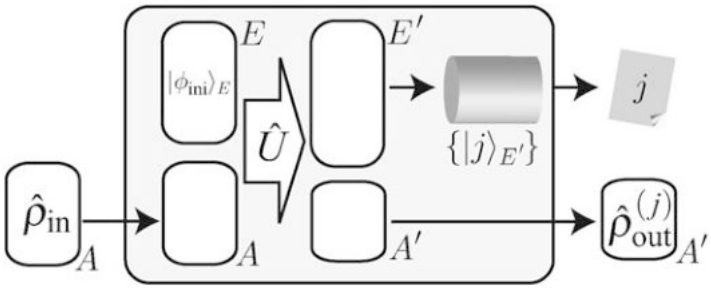

Fig. 1.3 Use of an auxiliary system in operation on the physical system A. An auxiliary system E is prepared in a fixed pure state $|\phi_{\rm ini}\rangle_E$, and the unitary transformation $\hat{U}$ is applied to systems A and E. System A', which is part of the whole system AE, is released as an output. The remaining system, E', is measured to produce the outcome j

$$p_j\hat{\rho}^{(j)}_{\rm out} = {}_{E'}\langle j|\hat{U}(\hat{\rho}_{\rm in}\otimes|\phi_{\rm ini}\rangle_{EE}\langle\phi_{\rm ini}|)\hat{U}^\dagger|j\rangle_{E'}. \tag{1.17}$$

It is convenient to introduce the operators $\hat{M}^{(j)} : \mathscr{H}_A \to \mathscr{H}_{A'}$, which are defined by

$$\hat{M}^{(j)} = {}_{E'}\langle j|\hat{U}|\phi_{\rm ini}\rangle_E. \tag{1.18}$$

Using the relation $\sum_{j=1}^{s'}|j\rangle_{E'E'}\langle j| = \hat{1}_{E'}$, we see that the operators satisfy the normalization condition

$$\sum_{j=1}^{s'}\hat{M}^{(j)\dagger}\hat{M}^{(j)} = \hat{1}_A. \tag{1.19}$$

The set of operators $\{\hat{M}^{(j)} : \mathscr{H}_A \to \mathscr{H}_{A'}\}$ that satisfies the above relationship are often called *Kraus* operators. Using these operators, Eq. (1.17) can be simplified as

$$p_j\hat{\rho}^{(j)}_{\rm out} = \hat{M}^{(j)}\hat{\rho}_{\rm in}\hat{M}^{(j)\dagger}, \tag{1.20}$$

where the input-output relationship is stated without any reference to the auxiliary systems E and E'.

In the above argument, we started with a given operator $\hat{U}$ that represented a unitary transformation of the composite system to determine the Kraus operators for the simplified relationship of Eq. (1.20). As we will see, this process can be reversed, i.e., for any given set of Kraus operators $\{\hat{M}^{(j)}\}$ that satisfies Eq. (1.19), there is[3] a unitary operator $\hat{U}$ that satisfies Eq. (1.18). Let $\{|u_i\rangle_A\}_{i=1,\ldots,d}$ be an orthonormal

[3]Given s', we may choose the dimensions of $\mathscr{H}_E$ and $\mathscr{H}_{E'}$ such that they satisfy $\dim\mathscr{H}_{E'} \geq s'$ and $\dim\mathscr{H}_A\dim\mathscr{H}_E = \dim\mathscr{H}_{A'}\dim\mathscr{H}_{E'}$.

basis of $\mathscr{H}_A$. Then, $\{|u_i\rangle_A \otimes |\phi_{\rm ini}\rangle_E\}_{i=1,\ldots,d}$ is an orthonormal set. We define $|v_i\rangle \in \mathscr{H}_{A'} \otimes \mathscr{H}_{E'}$ by $|v_i\rangle := \sum_{j=1}^{s'} \hat{M}^{(j)}|u_i\rangle \otimes |j\rangle_{E'}$. From Eq. (1.19), it can be shown that $\{|v_i\rangle\}_{i=1,\ldots,d}$ is an orthonormal set. There is thus a unitary operator $\hat{U} : \mathscr{H}_A \otimes \mathscr{H}_E \to \mathscr{H}_{A'} \otimes \mathscr{H}_{E'}$ that connects the two orthonormal sets as $|v_i\rangle = \hat{U}|u_i\rangle_A \otimes |\phi_{\rm ini}\rangle_E$, which leads to Eq. (1.18). We thus conclude that any input-output relationship dictated by the Kraus operators as shown in Eq. (1.20) can be physically implemented by attaching an auxiliary system E, applying a suitable unitary transformation over the composite system, and then measuring the subsystem E'.

1.4.2 Physically Allowed Operations

In Sect. 1.4.1, we extended our ability to operate on physical systems through the rather heuristic use of an auxiliary system. It is natural to expect that the introduction of more complex schemes using two or more auxiliary systems may allow us to further extend the variety of possible operations. Additionally, if we look back on the basic rules in Sect. 1.1, we see that none of the rules require a physical operation to be built up from unitary transformations and orthogonal measurements alone. Nonetheless, we will show here that the input-output relations written in the form of Eq. (1.20) are essentially the only relations that are allowed physically.

Consider a black box that accepts a physical system A as an input, and produces a classical outcome $j = 1, 2, \ldots, s$, while leaving the system A' as an output. Let d be the dimension of $\mathscr{H}_A$. We want to know the way in which the output state $\hat{\rho}_{\rm out}^{(j)}$ and the probability p_j of the outcome are related to a general pure input state $|\phi\rangle_A$. For that purpose, it is convenient to introduce a reference system B with a Hilbert space $\mathscr{H}_B$ of the same dimension d. We take the orthonormal bases $\{|i\rangle_A\}_{i=1,\ldots,d}$ and $\{|i\rangle_B\}_{i=1,\ldots,d}$ for $\mathscr{H}_A$ and $\mathscr{H}_B$, respectively, and suppose that the system AB is initially prepared in a maximally entangled state, $|\Phi\rangle_{AB} = d^{-1/2} \sum_{i=1}^{d} |i\rangle_A |i\rangle_B$.

We now explain a frequently used technique called the *relative* states. For any given state $|\phi\rangle_A$, we define the relative state of system B, with reference to the maximally entangled state $|\Phi\rangle_{AB}$, as

$$|\phi^*\rangle_B := \sum_{i=1}^{d} |i\rangle_B {}_A\langle\phi|i\rangle_A. \tag{1.21}$$

It is then easy to see that

$$d^{-1/2}|\phi\rangle_A = {}_B\langle\phi^*||\Phi\rangle_{AB} \tag{1.22}$$

holds. The definition of the relative state is mutual, i.e., $|\phi^{**}\rangle_A = |\phi\rangle_A$, because $d^{-1/2}|\phi^*\rangle_B = {}_A\langle\phi||\Phi\rangle_{AB}$ also holds.

In light of Theorem 1, this relation has the following meaning. If we conduct an orthogonal measurement on system B with a basis that includes state $|\phi^*\rangle_B$, then the

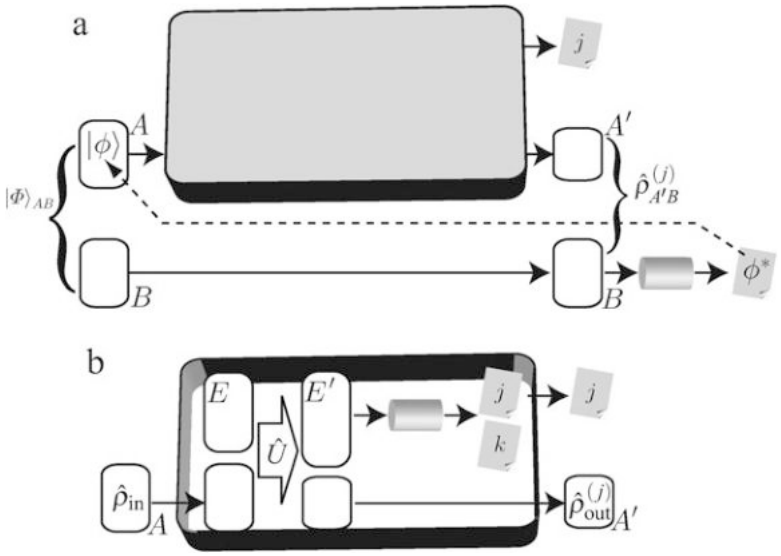

Fig. 1.4 (**a**) Characterization of a physical operation (the *black box*) by feeding in half of a maximally entangled state. Learning the statistics of the outcome j and the states $\hat{\rho}^{(j)}_{A'B}$ then allows us to fully specify the input-output relationship. (**b**) Looking inside the box. Any physical process is implemented in an equivalent manner with an auxiliary system, a unitary transformation, and an orthogonal measurement

corresponding outcome appears with probability $1/d$, and system A then behaves as if it were initially prepared in state $|\phi\rangle_A$. While this is probabilistic, it offers a type of ex post facto method to prepare system A in the arbitrary state $|\phi\rangle_A$.

We now proceed to the analysis of the black box (see Fig. 1.4a). After preparation of $|\Phi\rangle_{AB}$, suppose that system A is fed to the black box, while system B is left alone. After the black box has produced the outcome j, the state of the composite system $A'B$ should be represented by a density operator, which we denote by $\hat{\rho}^{(j)}_{A'B}$. Let q_j be the probability of producing the outcome j. Now suppose that we perform an orthogonal measurement with basis $\{|v_i\rangle_B\}$ on system B, where $|v_1\rangle_B = |\phi^*\rangle_B$. The outcome $i = 1$ should then appear with probability $r^{(j)}$ and this leaves system A' in state $\hat{\rho}^{(j)}_{A'}$, where

$$r^{(j)}\hat{\rho}^{(j)}_{A'} = {}_B\langle\phi^*|\hat{\rho}^{(j)}_{A'B}|\phi^*\rangle_B. \tag{1.23}$$

However, according to Theorem 1, an event with outcomes j and $i = 1$ must be interpreted as follows. With probability d^{-1}, system A is initially prepared in $|\phi\rangle_A$, and is then fed to the black box. This produces outcome j with probability p_j, leaving system A' in state $\hat{\rho}^{(j)}_{\rm out}$. Comparison of the two interpretations leads to $q_j r^{(j)} = d^{-1}p_j$ and $\hat{\rho}^{(j)}_{A'} = \hat{\rho}^{(j)}_{\rm out}$. Using Eq. (1.23), we then have

$$p_j \hat{\rho}_{\text{out}}^{(j)} = dq_{jB} \langle \phi^* | \hat{\rho}_{A'B}^{(j)} | \phi^* \rangle_B. \tag{1.24}$$

Consider a decomposition of the density operator,

$$\hat{\rho}_{A'B}^{(j)} = \sum_{k=1}^{t^{(j)}} |\tilde{\Psi}_k^{(j)}\rangle_{A'BA'B} \langle \tilde{\Psi}_k^{(j)}|, \tag{1.25}$$

where $|\tilde{\Psi}_k^{(j)}\rangle_{A'B}$ is unnormalized. Noting that ${}_B\langle \phi^*| = \sqrt{d}_{AB}\langle \Phi || \phi \rangle_A$, we see that, for fixed values of j and k, the correspondence $|\phi\rangle_A \mapsto \sqrt{dq_{jB}} \langle \phi^* || \Psi_k^{(j)} \rangle_{A'B}$ is a linear map. Thus, an operator $\hat{M}^{(j,k)} : \mathscr{H}_A \to \mathscr{H}_{A'}$ exists such that

$$\sqrt{dq_{jB}} \langle \phi^* || \Psi_k^{(j)} \rangle_{A'B} = \hat{M}^{(j,k)} |\phi\rangle_A. \tag{1.26}$$

Equation (1.24) is now written as

$$p_j \hat{\rho}_{\text{out}}^{(j)} = \sum_{k=1}^{t^{(j)}} \hat{M}^{(j,k)} |\phi\rangle_{AA} \langle \phi | \hat{M}^{(j,k)\dagger} \tag{1.27}$$

for the input state $|\phi\rangle_A$. Then, for the general input state $\hat{\rho}_{\text{in}}$ of system A, the input-output relationship of the black box is written as

$$p_j \hat{\rho}_{\text{out}}^{(j)} = \sum_{k=1}^{t^{(j)}} \hat{M}^{(j,k)} \hat{\rho}_{\text{in}} \hat{M}^{(j,k)\dagger}. \tag{1.28}$$

Taking the trace of Eq. (1.27) and performing a sum over index j, we have $\sum_{j,k} {}_A\langle \phi | \hat{M}^{(j,k)\dagger} \hat{M}^{(j,k)} | \phi \rangle_A = 1$ for arbitrary $|\phi\rangle_A$. Therefore, $\sum_{j,k} \hat{M}^{(j,k)\dagger} \hat{M}^{(j,k)} = \hat{1}_A$ and $\{\hat{M}^{(j,k)}\}$ is a set of Kraus operators.

Equation (1.28) is the most general form of what we can do to a physical system. This equation is merely a trivial extension of Eq. (1.20) in Sect. 1.4.1. Consider a scheme that produces the outcome (j, k) and leaves system A' in state $\hat{\rho}_{\text{out}}^{(j,k)}$, with an input-output relation given by $p_{j,k} \hat{\rho}_{\text{out}}^{(j,k)} = \hat{M}^{(j,k)} \hat{\rho}_{\text{in}} \hat{M}^{(j,k)\dagger}$. As shown[4] in Sect. 1.4.1, this scheme can be implemented by simply attaching an auxiliary system E, applying a unitary transformation, and then performing an orthogonal measurement on system E'. The original black box is then faithfully simulated using this scheme as shown in Fig. 1.4b, by simply discarding the index k and yielding only the index j as the final outcome.

[4]Regard (j, k) as a single index with the values $1, \ldots, s'$, where $s' = \sum_j t^{(j)}$.

1.4.3 Generalized Measurements

By discarding the output quantum state in system A' in the black box that was considered in Sect. 1.4.2, we can obtain the most general form of a physically allowed measurement process, which is called a *generalized measurement*. By taking the trace of Eq. (1.28), we have

$$p_j = \mathrm{Tr}(\hat{F}^{(j)}\hat{\rho}_{\mathrm{in}}), \tag{1.29}$$

where $\hat{F}^{(j)} := \sum_k \hat{M}^{(j,k)\dagger}\hat{M}^{(j,k)}$ is positive and satisfies $\sum_j \hat{F}^{(j)} = \hat{1}_A$. Any measurement must be written in this form.

A set of positive operators $\{\hat{F}^{(j)}\}$ acting on $\mathscr{H}_A$ and satisfying $\sum_j \hat{F}^{(j)} = \hat{1}_A$ is called the *POVM (positive-operator-valued measure)*. For any given POVM $\{\hat{F}^{(j)}\}$, we may define $\hat{M}^{(j)} := (\hat{F}^{(j)})^{1/2}$ and use the argument of Sect. 1.4.1 to construct a generalized measurement that satisfies Eq. (1.29) through the use of an auxiliary system as shown in Fig. 1.3, except that system A' is discarded in this case.

An orthogonal measurement with basis $\{|u_j\rangle_A\}$ is now regarded as a special case of the generalized measurements, when the POVM is chosen to be $\hat{F}^{(j)} = |u_j\rangle_{AA}\langle u_j|$. Note that orthogonal measurements are not necessarily the ideal measurement, and some tasks favor other kinds of generalized measurement. We will provide an example below.

Unambiguous state discrimination. Consider a nonorthogonal pair of qubit states, $\{|\phi_0\rangle_A, |\phi_1\rangle_A\}$, with $c := |\langle\phi_0|\phi_1\rangle| > 0$. Suppose that qubit A has been secretly prepared in $|\phi_0\rangle_A$ or in $|\phi_1\rangle_A$ with an equal probability of $q := 1/2$. Consider the strategy used to distinguish between the two states as follows.

Choose $|\phi_j^\perp\rangle_A$ $(j = 0, 1)$ such that ${}_A\langle\phi_j|\phi_j^\perp\rangle_A = 0$ and ${}_A\langle\phi_0^\perp|\phi_1^\perp\rangle_A = c$. Consider a set $\{\hat{F}^{(j)}\}_{j=0,1,2}$ defined by $\hat{F}^{(0)} := (1+c)^{-1}|\phi_1^\perp\rangle_{AA}\langle\phi_1^\perp|$, $\hat{F}^{(1)} := (1+c)^{-1}|\phi_0^\perp\rangle_{AA}\langle\phi_0^\perp|$, and $\hat{F}^{(2)} := \hat{1}_A - \hat{F}^{(0)} - \hat{F}^{(1)}$. Because $|\phi_0^\perp\rangle_A \pm |\phi_1^\perp\rangle_A$ is an eigenvector of $\hat{F}^{(0)} + \hat{F}^{(1)}$ with eigenvalue $(1+c)^{-1}(1 \pm c) \le 1$, we have $\hat{F}^{(0)} + \hat{F}^{(1)} \le \hat{1}_A$. Therefore, $\{\hat{F}^{(j)}\}_{j=0,1,2}$ is a POVM, and the corresponding generalized measurement is feasible.

When the outcome of this measurement was $j = 0$, we were certain that the prepared state must be state $|\phi_0\rangle_A$, because $\mathrm{Tr}(\hat{F}^{(0)}|\phi_1\rangle_{AA}\langle\phi_1|) = 0$. Similarly, if the outcome was $j = 1$, the prepared state must be state $|\phi_1\rangle_A$. The overall success probability, i.e., the probability of obtaining $j = 0, 1$ is calculated to be $p_{\mathrm{suc}} := \sum_{j=0,1} q\mathrm{Tr}(\hat{F}^{(j)}|\phi_j\rangle_{AA}\langle\phi_j|) = 1 - c$ [5].

If we are to construct a strategy with a similar lack of ambiguity using orthogonal measurements, we must choose either $\{|\phi_0\rangle_A, |\phi_0^\perp\rangle_A\}$ or $\{|\phi_1\rangle_A, |\phi_1^\perp\rangle_A\}$ as the basis. Regardless of how the two orthogonal measurements are mixed, the success probability is $p_{\mathrm{suc}}^\perp := q|{}_A\langle\phi_0^\perp|\phi_1\rangle_A|^2 = q|{}_A\langle\phi_1^\perp|\phi_0\rangle_A|^2 = (1-c^2)/2$. Thus we see that $p_{\mathrm{suc}} > p_{\mathrm{suc}}^\perp$ for $0 < c < 1$.

1.4.4 Quantum Operations

If we discard the outcome j from the black box that was considered in Sect. 1.4.2, then the output density operator of system A' becomes $\hat{\rho}_{\text{out}} := \sum_j p_j \hat{\rho}_{\text{out}}^{(j)} = \sum_{j,k} \hat{M}^{(j,k)} \hat{\rho}_{\text{in}} \hat{M}^{(j,k)\dagger}$. Without loss of generality, we may replace the indices (j,k) with a single index j, which results in the general form of the state transformation,

$$\hat{\rho}_{\text{out}} = \sum_j \hat{M}^{(j)} \hat{\rho}_{\text{in}} \hat{M}^{(j)\dagger} \tag{1.30}$$

with $\sum_j \hat{M}^{(j)\dagger} \hat{M}^{(j)} = \hat{1}_A$. Any physical process that takes system A as an input and leaves the same system or another system A' as an output must be written in this form. This type of process is often called a *quantum operation* or a *quantum channel*. Mathematically, the map $\chi : \hat{\rho}_{\text{in}} \mapsto \hat{\rho}_{\text{out}}$ that is written as per Eq. (1.30) is called a *CPTP (completely-positive trace-preserving) map*.

The argument in Sect. 1.4.1 ensures that the right-hand side of Eq. (1.30) can be rewritten as that of Eq. (1.17) summed over j, i.e.,

$$\hat{\rho}_{\text{out}} = \text{Tr}_{E'}[\hat{U}(\hat{\rho}_{\text{in}} \otimes |\phi_{\text{ini}}\rangle_{EE}\langle\phi_{\text{ini}}|)\hat{U}^\dagger]. \tag{1.31}$$

Operationally, this simply means that the measurement on system E' shown in Fig. 1.3 is unnecessary. Thus, any quantum channel can be equivalently simulated using a simple three-step process, which consists of preparing the auxiliary system (E) in a fixed pure state, applying the unitary transformation, and discarding the subsystem (E'). This property is very helpful when it is necessary to prove that some tasks are physically impossible. This type of argument is vital for establishment of an operationally-defined measure of quantum properties, as indicated in the following example.

Fidelity. In an experimental demonstration, the quality of the final result is often evaluated in terms of the fidelity $F = \langle\phi_{\text{ideal}}|\hat{\rho}_{\text{exp}}|\phi_{\text{ideal}}\rangle$, where $|\phi_{\text{ideal}}\rangle$ is the desired state and $\hat{\rho}_{\text{exp}}$ is the state that was actually obtained in the experiment. The fidelity F between two general states $\hat{\rho}_1$ and $\hat{\rho}_2$ of system A is defined[5] as the maximum overlap between the purifications of these states in a composite system composed of A and an arbitrary system R, i.e.,

$$F(\hat{\rho}_1, \hat{\rho}_2) := \max\{|_{AR}\langle\Psi_1|\Psi_2\rangle_{AR}|^2 : \text{Tr}_R(|\Psi_j\rangle_{ARAR}\langle\Psi_j|) = \hat{\rho}_j, j = 1, 2\}. \tag{1.32}$$

To justify the use of such a quantity in the evaluation of an experiment, we must show that the fidelity $F(\hat{\rho}_1, \hat{\rho}_2)$ is a good measure of the closeness between the two

[5]There is an equivalent method to define the fidelity as $F(\hat{\rho}_1, \hat{\rho}_2) = (\text{Tr}\sqrt{\hat{\rho}_1^{1/2}\hat{\rho}_2\hat{\rho}_1^{1/2}})^2$ [6, 7]. In some of the literature, the quantity $\sqrt{F(\hat{\rho}_1, \hat{\rho}_2)}$ is referred to as the fidelity.

states $\hat{\rho}_1$ and $\hat{\rho}_2$. To enable F to quantify the difficulty in distinguishing between the two states *in principle*, F should not be reduced (and thus the distinguishability should not improve) through the application of any quantum channel χ, i.e.,

$$F(\chi(\hat{\rho}_1), \chi(\hat{\rho}_2)) \geq F(\hat{\rho}_1, \hat{\rho}_2) \tag{1.33}$$

should hold for any CPTP map χ. This can be proved as follows.

Let $|\Phi_j\rangle_{AR}$ be the purifications that achieve the maximum of Eq. (1.32), i.e., $F(\hat{\rho}_1, \hat{\rho}_2) = |_{AR}\langle\Phi_1|\Phi_2\rangle_{AR}|^2$. We consider three different cases separately, corresponding to the three steps that are implied in Eq. (1.31).

(i) $\chi(\hat{\rho}_j) = \hat{\rho}_j \otimes |\phi\rangle_{BB}\langle\phi|$. In this case, $|\Psi_j\rangle_{ABR} := |\Phi_j\rangle_{AR}|\phi\rangle_B$ is a purification of $\chi(\hat{\rho}_j)$. Therefore, $F(\chi(\hat{\rho}_1), \chi(\hat{\rho}_2)) \geq |_{ABR}\langle\Psi_1|\Psi_2\rangle_{ABR}|^2 = |_{AR}\langle\Phi_1|\Phi_2\rangle_{AR}|^2 = F(\hat{\rho}_1, \hat{\rho}_2)$.

(ii) $\chi(\hat{\rho}_j) = \hat{U}_A\hat{\rho}_j\hat{U}_A^\dagger$. In this case, $|\Psi_j\rangle_{AR} := (\hat{U}_A \otimes \hat{1}_R)|\Phi_j\rangle_{AR}$ is a purification of $\chi(\hat{\rho}_j)$. Therefore, $F(\chi(\hat{\rho}_1), \chi(\hat{\rho}_2)) \geq |_{AR}\langle\Psi_1|\Psi_2\rangle_{AR}|^2 = |_{AR}\langle\Phi_1|\Phi_2\rangle_{AR}|^2 = F(\hat{\rho}_1, \hat{\rho}_2)$.

(iii) $\chi(\hat{\rho}_j) = \mathrm{Tr}_{\tilde{A}}(\hat{\rho}_j)$, where $\tilde{A}$ is a constituent subsystem of system A. In this case, $|\Phi_j\rangle_{AR}$ is also regarded as a purification of $\chi(\hat{\rho}_j)$. Therefore, $F(\chi(\hat{\rho}_1), \chi(\hat{\rho}_2)) \geq |_{AR}\langle\Phi_1|\Phi_2\rangle_{AR}|^2 = F(\hat{\rho}_1, \hat{\rho}_2)$.

For a general quantum channel χ, we may decompose the process into the three steps, and the above results demonstrate that F is nondecreasing in each of the three steps. Therefore, Eq. (1.33) holds.

No-cloning theorem. An immediate consequence of the nondecreasing property of the fidelity is the no-cloning theorem. Consider a cloning machine that would transform an arbitrary input pure state $\hat{\rho}_{\mathrm{in},\phi} := |\phi\rangle_{AA}\langle\phi|$ into a duplicated pure state $\hat{\rho}_{\mathrm{out},\phi} := |\phi\rangle_{AA}\langle\phi| \otimes |\phi\rangle_{A'A'}\langle\phi|$. For $0 < |_A\langle\phi|\psi\rangle_A|^2 < 1$, we would have

$$F(\hat{\rho}_{\mathrm{out},\phi}, \hat{\rho}_{\mathrm{out},\psi}) = F(\hat{\rho}_{\mathrm{in},\phi}, \hat{\rho}_{\mathrm{in},\psi})^2 < F(\hat{\rho}_{\mathrm{in},\phi}, \hat{\rho}_{\mathrm{in},\psi}), \tag{1.34}$$

which violates Eq. (1.33). Therefore, this cloning machine could never exist.

1.5 Communication Resources

The task of sending quantum information is essentially different from that of sending classical information, and is achieved using a dedicated quantum channel. Interestingly, transmission of quantum information can also be achieved by supplementing a classical channel with another resource: entanglement. In this subsection, we will see how the three communication resources are related to each other, while focusing our discussion on the ideal cases.

1.5.1 Quantum Channels and Classical Channels

An *ideal classical channel* will transmit a symbol chosen from a fixed set $\{1, 2, \ldots, d\}$ without any error from a sender to a receiver. The number of symbols d stands for the usefulness of the channel as a resource. A channel with $d = 2$ is normally regarded to have a unit of usefulness, called a *bit*. General ideal channels with d symbols have $\log_2 d$ bits. This makes sense because the combined use of a $(\log_2 d)$-bit channel and a $(\log_2 d')$-bit channel amounts to the single use of a $(\log_2 d + \log_2 d')$-bit channel.

In a similar vein, we consider an *ideal quantum channel*, which faithfully transmits the arbitrary quantum states of a d-level physical system that is associated with a Hilbert space of dimension d. Because we have already called the two-level system a qubit, let us define the usefulness of such a channel as $(\log_2 d)$ *qubits*. Because $\dim(\mathscr{H} \otimes \mathscr{H}') = (\dim\mathscr{H})(\dim\mathscr{H}')$, this measure is additive for the combined use of ideal channels.

We now consider how the two types of channels differ. First, a quantum channel can never be simulated using any amount of classical channels. This is because of the no-cloning theorem, as described in Sect. 1.4.4. Because the output of a classical channel can be freely copied, if the receiver were able to reconstruct any input state $|\phi\rangle$, then they could repeat the same procedure to create another copy of state $|\phi\rangle$, which is forbidden by the no-cloning theorem.

In contrast, a $(\log_2 d)$-qubit quantum channel can be used to simulate a classical channel. To simulate a $(\log_2 d')$-bit channel, the sender can encode a symbol $i \in \{1, 2, \ldots, d'\}$ on a quantum state, i.e., the sender transmits the quantum state $\hat{\rho}_i$ via the quantum channel, according to the symbol i that is to be transmitted. The receiver can then perform a measurement of the transmitted state to decode the index i. Encoding on mutually orthogonal states certainly works if $d' = d$, but the user may want to exploit the fact that there are an infinite number of different quantum states to transmit larger numbers of symbols. To deny any such possibility, we recall that any measurement strategy must be described as in Eq. (1.29), using a POVM $\{\hat{F}_j\}$. To simulate an ideal channel, $\mathrm{Tr}(\hat{F}_i\hat{\rho}_i) = 1$ should hold for $i = 1, \ldots, d'$. Because $\{\hat{F}_j\}$ are positive and $\sum_{i=1}^{d'} \hat{F}_i \leq \hat{1}$, we have $d' = \sum_{i=1}^{d'} \mathrm{Tr}(\hat{F}_i\hat{\rho}_i) \leq \sum_{i=1}^{d'} \mathrm{Tr}(\hat{F}_i) \leq \mathrm{Tr}\hat{1} = d$, thus proving the following.

Theorem 4. *Without use of another communication resource, a* $(\log_2 d)$*-qubit ideal quantum channel can never simulate a* $(\log_2 d')$*-bit ideal classical channel if* $d' > d$.

1.5.2 Entanglement as a Communication Resource

We have seen that a quantum channel is qualitatively different from a classical channel. We may then ask what exactly is the difference between the channels, or ask what kind of communication resources may be used to complement a classical

channel to enable it to simulate a quantum channel. It turns out that the entanglement is the answer to these questions.

As an ideal resource of entanglement, let us consider a maximally entangled state with a Schmidt number of d,

$$|\Phi_{0,0}\rangle_{AB} := \frac{1}{\sqrt{d}} \sum_{j=0}^{d-1} |j\rangle_A |j\rangle_B \tag{1.35}$$

where $\{|j\rangle_A\}$ and $\{|j\rangle_B\}$ are the orthonormal bases of $\mathscr{H}_A$ and $\mathscr{H}_B$, respectively. When each subsystem is held by the sender and by the receiver, we can quantify the usefulness of this state as $(\log_2 d)$ *ebits*, which is additive when two or more maximally entangled states are available. Any state that is written as $(\hat{U}_A \otimes \hat{V}_B)|\Phi_{0,0}\rangle_{AB}$ is also a maximally entangled state and is regarded as a resource of the same number of ebits.

If a $(\log_2 d)$-qubit quantum channel is available, then the sender can create state $|\Phi_{0,0}\rangle_{AB}$ locally and transmit system B to the receiver, which produces $(\log_2 d)$ ebits of entanglement resource.

Theorem 5 (Entanglement sharing). *A* $(\log_2 d)$*-qubit ideal quantum channel can be converted into* $(\log_2 d)$ *ebits of ideal entanglement.*

Next, let us compare entanglement with classical channels. First, entanglement does not help in augmentation of a classical channel.

Theorem 6. *Without use of another communication resource, no amount of entanglement can convert a* $(\log_2 d)$*-bit ideal classical channel into a* $(\log_2 d')$*-bit ideal classical channel with* $d' > d$.

Proof. Suppose that the sender chooses a symbol $i \in \{1, 2, \ldots, d'\}$ at random. Assume that it is possible to transmit i faithfully by using a $(\log_2 d)$-bit ideal classical channel and shared entanglement. Because the output of the channel can be guessed correctly with a probability of $1/d$ by random guessing, the receiver can form a strategy, which, without communication, allows the symbol i to be guessed with a success probability of $1/d$. Therefore, $1/d \leq 1/d'$ must hold. □

Entanglement is a *static* resource in the sense that it is simply a correlation and it does not refer to any transfer of information. A classical channel is *dynamic* with regard to its ability to move information around. In this respect, the theorem above may be regarded as a natural example where a static resource cannot be converted into a dynamic resource. However, there is a subtlety here that will be manifest when we see the protocol for quantum dense coding in Sect. 1.5.4.

Finally, we consider the reverse question of how entanglement can be manipulated with unlimited use of classical channels. Suppose that Alice and Bob can freely use classical channels between them in both directions, and they can locally perform any physically allowed measurement or state transformation. This type of framework is called *LOCC (local operations and classical communication)*.

Suppose that Alice and Bob initially share a pure bipartite state $|\Psi\rangle_{AB}$, and try to transform this state into other states under the LOCC framework. Without loss of generality, we may assume that only one party is conducting a local operation at any one time. This means that Alice first conducts a local operation, reveals an outcome to Bob through a classical communication, and Bob then conducts a local operation in turn, and so on. For Alice's turn, her operation is generally written as in Eq. (1.28), with $\hat{M}^{(j,k)}$ acting on Alice's system alone. Although the general description includes the index k, which is discarded, for the purposes of state transformation, Alice may as well record this index. Therefore, we omit k and conclude that, after Alice's first turn, Alice and Bob share state $|\Psi^{(j)}\rangle_{A'B}$ with probability p_j, where

$$p_j|\Psi^{(j)}\rangle_{A'BA'B}\langle\Psi^{(j)}| = (\hat{M}_A^{(j)} \otimes \hat{1}_B)|\Psi\rangle_{ABAB}\langle\Psi|(\hat{M}_A^{(j)} \otimes \hat{1}_B)^\dagger \tag{1.36}$$

and $\hat{M}_A^{(j)} : \mathscr{H}_A \to \mathscr{H}_{A'}$ satisfies $\sum_j \hat{M}_A^{(j)\dagger}\hat{M}_A^{(j)} = \hat{1}_A$. Let $\hat{\rho}_B$ and $\hat{\rho}_B^{(j)}$ be the marginal density operators of system B for $|\Psi\rangle_{AB}$ and $|\Psi^{(j)}\rangle_{A'B}$, respectively. Taking a partial trace and summation over j in Eq. (1.36), we have

$$\sum_j p_j \hat{\rho}_B^{(j)} = \hat{\rho}_B. \tag{1.37}$$

This equation shows that the rank of $\hat{\rho}_B^{(j)}$ never exceeds that of $\hat{\rho}_B$. The Schmidt number of state $|\Psi^{(j)}\rangle_{A'B}$ therefore never exceeds that of the initial state $|\Psi\rangle_{AB}$. A similar argument is applicable to Bob's turns, and we thus see that the Schmidt number never increases under the LOCC framework, even probabilistically. Specifically, no entanglement is generated under the LOCC framework when starting from a product state with a Schmidt number of unity. This is often adopted as a defining property of entanglement when discussing more general cases of mixed-state entanglement.

In view of the relationships between the communication resources, the above argument means that the classical channels do not help to increase entanglement, and this is summarized as follows.

Theorem 7. *Without use of another communication resource, no amount of communication over classical channels can convert a* $(\log_2 d)$*-ebit ideal entanglement into a* $(\log_2 d')$*-ebit ideal entanglement with* $d' > d$.

This theorem implies that entanglement has a nonclassical aspect that cannot be replaced by classical channels. If we combine the two resources, we will obtain a resource that is both dynamic and nonclassical, and we may perhaps simulate a quantum channel. This is indeed true, and will be explained in Sect. 1.5.4 after we summarize the properties of the maximally entangled states in Sect. 1.5.3.

1.5.3 Properties of Maximally Entangled States

Let $\mathscr{H}_A$ and $\mathscr{H}_B$ be Hilbert spaces of dimension d for the systems A and B. Here, we summarize the relevant properties of the maximally entangled states of system AB.

(E1) All maximally entangled states have a common marginal state $d^{-1}\hat{1}_A$ for subsystem A, and a common marginal state $d^{-1}\hat{1}_B$ for subsystem B.

(E2) For any pair of maximally entangled states $|\Phi\rangle_{AB}$ and $|\Phi'\rangle_{AB}$, unitary operators $\hat{U}_A$ and $\hat{V}_B$ exist such that $|\Phi'\rangle_{AB} = (\hat{U}_A \otimes \hat{1}_B)|\Phi\rangle_{AB} = (\hat{1}_A \otimes \hat{V}_B)|\Phi\rangle_{AB}$.

(E3) A maximally entangled state $|\Phi\rangle_{AB}$ specifies a one-to-one correspondence $|\phi\rangle_A \leftrightarrow |\phi^*\rangle_B$ between the pure states of subsystem A and those of subsystem B, as characterized by $d^{-1/2}|\phi\rangle_A = {}_B\langle\phi^*||\Phi\rangle_{AB}$ and $d^{-1/2}|\phi^*\rangle_B = {}_A\langle\phi||\Phi\rangle_{AB}$.

(E4) A maximally entangled state $|\Phi\rangle_{AB}$ specifies a one-to-one correspondence $\hat{M}_A \leftrightarrow \hat{M}_B^{\mathrm{T}}$ between the operators that act on $\mathscr{H}_A$ and those acting on $\mathscr{H}_B$, as characterized by

$$(\hat{M}_A \otimes \hat{1}_B)|\Phi\rangle_{AB} = (\hat{1}_A \otimes \hat{M}_B^{\mathrm{T}})|\Phi\rangle_{AB}. \tag{1.38}$$

Specifically, if $\hat{M}_A$ is unitary then $\hat{M}_B^{\mathrm{T}}$ is also unitary, and vice versa.

(E5) There is an orthonormal basis $\{|\Phi_{l,m}\rangle_{AB}\}_{l=0,\ldots,d-1}^{m=0,\ldots,d-1}$ of $\mathscr{H}_A \otimes \mathscr{H}_B$ where every basis state is a maximally entangled state. This type of basis is called a *Bell* basis.

(E1) is the definition given in Sect. 1.2.5. (E2) is a combination of (E1) and Theorem 3. (E3) refers to the relative states explained in Sect. 1.4.2.

For (E5), a Bell basis that includes state $|\Phi_{0,0}\rangle_{AB}$ of Eq. (1.35) is constructed as follows. For each subsystem, we define unitary operators

$$\hat{X} := \sum_{j=0}^{d-1} |j+1 \ (\mathrm{mod}\ d)\rangle\langle j| \quad \text{and} \quad \hat{Z} := \sum_{j=0}^{d-1} \beta^j |j\rangle\langle j| \tag{1.39}$$

with $\beta := \exp(2\pi i/d)$. Using these operators, we define $|\Phi_{l,m}\rangle_{AB} := (\hat{X}_A^l \otimes \hat{Z}_B^m)|\Phi_{0,0}\rangle_{AB}$. Using the relation $\hat{Z}\hat{X} = \beta\hat{X}\hat{Z}$, it is simple to show that $|\Phi_{l,m}\rangle_{AB}$ is a simultaneous eigenvector of the commuting unitary operators $\hat{X}_A \otimes \hat{X}_B$ and $\hat{Z}_A \otimes \hat{Z}_B^{-1}$ with eigenvalues of β^{-m} and β^l, respectively. Therefore, the d^2 states $\{|\Phi_{l,m}\rangle_{AB}\}_{l=0,\ldots,d-1}^{m=0,\ldots,d-1}$ are all orthogonal. For $d = 2$, the Bell basis consists of the following states.

$$|\Phi_+\rangle = |\Phi_{0,0}\rangle = 2^{-1/2}(|0\rangle_A|0\rangle_B + |1\rangle_A|1\rangle_B) \tag{1.40}$$

$$|\Phi_-\rangle = |\Phi_{0,1}\rangle = 2^{-1/2}(|0\rangle_A|0\rangle_B - |1\rangle_A|1\rangle_B) \tag{1.41}$$

$$|\Psi_+\rangle = |\Phi_{1,0}\rangle = 2^{-1/2}(|1\rangle_A|0\rangle_B + |0\rangle_A|1\rangle_B) \tag{1.42}$$

$$|\Psi_-\rangle = |\Phi_{1,1}\rangle = 2^{-1/2}(|1\rangle_A|0\rangle_B - |0\rangle_A|1\rangle_B) \tag{1.43}$$

(E4) is confirmed as follows. Suppose that $|\Phi\rangle_{AB}$ is decomposed as shown in Eq. (1.7). By applying ${}_A\langle u_i|_B\langle v_j|$ to Eq. (1.38), we see that Eq. (1.38) is equivalent to

$${}_A\langle u_i|\hat{M}_A|u_j\rangle_A = {}_B\langle v_j|\hat{M}_B^{\mathrm{T}}|v_i\rangle_B \tag{1.44}$$

for $i,j = 1,\ldots,d$. This means that the matrix representation of $\hat{M}_B^{\mathrm{T}}$ in the basis $\{|v_i\rangle_B\}$ is the transpose of the matrix representation of $\hat{M}_A$ in the basis $\{|u_i\rangle_A\}$.

As an example of Property (E4), the following relations are worth mentioning:

$$(\hat{X}_A \otimes \hat{1}_B)|\Phi_{0,0}\rangle_{AB} = (\hat{1}_A \otimes \hat{X}_B^{-1})|\Phi_{0,0}\rangle_{AB} \tag{1.45}$$

$$(\hat{Z}_A \otimes \hat{1}_B)|\Phi_{0,0}\rangle_{AB} = (\hat{1}_A \otimes \hat{Z}_B)|\Phi_{0,0}\rangle_{AB}, \tag{1.46}$$

and can easily be confirmed.

1.5.4 Quantum Dense Coding and Quantum Teleportation

In this subsection, we explain two types of scheme in which shared entanglement helps with the conversion between the quantum and classical channels. Every subsystem X that appears in this subsection is a d-level system with Hilbert space of dimension d, and with a standard orthonormal basis denoted by $\{|j\rangle_X\}$. The Bell basis is defined for each pair of subsystems according to the standard bases.

In Theorem 4, we have seen that a one-qubit quantum channel alone can only send one bit of classical information. If the sender and the receiver share entanglement beforehand, then the quantum channel can send more via a protocol called *quantum dense coding* [8].

Theorem 8 (Quantum dense coding). *A* $(\log_2 d)$*-qubit ideal quantum channel and a* $(\log_2 d)$*-ebit ideal entanglement can be converted into a* $(2\log_2 d)$*-bit ideal classical channel.*

A protocol for quantum dense coding can be constructed simply by using the Bell basis $\{|\Phi_{l,m}\rangle_{AB}\}$ of the two d-level subsystems, i.e., Property (E5) in Sect. 1.5.3. We show that Alice can send Bob a symbol (l,m) that was chosen from d^2 candidates $\{(l,m)\}_{l=0,\ldots,d-1}^{m=0,\ldots,d-1}$. Suppose that Alice and Bob shared the entangled state $|\Phi_{0,0}\rangle_{AB}$ initially. Property (E2) ensures that Alice can locally transform[6] the state $|\Phi_{0,0}\rangle$ into the state $|\Phi_{l,m}\rangle$ that is specified by the chosen symbol (l,m). She then sends

[6] An explicit form of Alice's transformation is $|\Phi_{l,m}\rangle_{AB} = (\hat{X}_A^l \hat{Z}_A^m \otimes \hat{1}_B)|\Phi_{0,0}\rangle_{AB}$, which is obtained from Eq. (1.46).

subsystem A, which has a Hilbert space with dimension d, to Bob using the $(\log_2 d)$-qubit quantum channel. Bob, who now holds both subsystems A and B, conducts an orthogonal measurement with the Bell basis $\{|\Phi_{l,m}\rangle_{AB}\}$ to determine Alice's choice (l, m).

This protocol is remarkable in the sense that the static resource of entanglement enhances an ideal channel's ability to achieve the dynamic task of information transmission. This is in stark contrast with what we saw in Theorem 6, i.e., that the static resource of entanglement cannot augment the dynamic resources of classical channels.

Next, we explain the protocol of *quantum teleportation* [9], which combines the nonclassical resource of entanglement and the dynamic resource of a classical channel to achieve faithful transmission of quantum states.

Theorem 9 (Quantum teleportation). *A $(2\log_2 d)$-bit ideal classical channel and a $(\log_2 d)$-ebit ideal entanglement can be converted into a $(\log_2 d)$-qubit ideal quantum channel.*

The protocol proceeds as follows. Suppose that Alice and Bob initially share the entangled states $|\Phi_{0,0}\rangle_{AB}$ of two d-level systems. Alice also holds another d-level subsystem A', and she is supposed to transmit the state of this subsystem to Bob. Alice first performs an orthogonal measurement with the Bell basis $\{|\Phi_{l,m}\rangle_{AA'}\}$ on subsystems A and A', and transmits the outcome (l, m) to Bob through the $(2\log_2 d)$-bit classical channel. Based on the received indices (l, m), Bob then applies a unitary transformation $\hat{U}_B^{(l,m)}$ to subsystem B.

We now consider how we can choose $\hat{U}_B^{(l,m)}$ such that the final state of system B is always identical to the initial state of system A' (see also Fig. 1.5). Consider another d-level system R, and suppose that the system $A'R$ is initially prepared

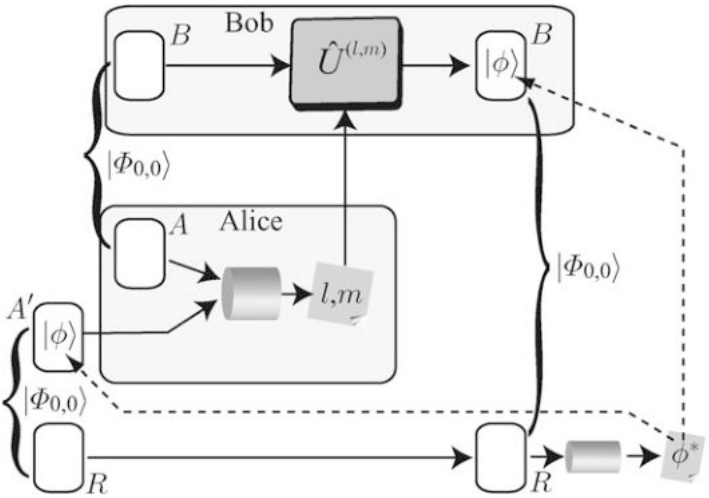

Fig. 1.5 Entanglement swapping and quantum teleportation

in state $|\Phi_{0,0}\rangle_{A'R}$. Later, at the end of this argument, we will use Property (E3) to discuss the case where A' is initially prepared in the general state $|\phi\rangle_{A'}$.

We begin with the following relation, which can be easily confirmed from the definition of Eq. (1.35):

$$d^{-1}|\Phi_{0,0}\rangle_{BR} = {}_{AA'}\langle\Phi_{0,0}||\Phi_{0,0}\rangle_{AB}|\Phi_{0,0}\rangle_{A'R}. \tag{1.47}$$

According to Theorem 1, this shows that if the outcome is $(l, m) = (0, 0)$, then the state of the system BR is $|\Phi_{0,0}\rangle_{BR}$. We want to generalize this relationship to the case where ${}_{AA'}\langle\Phi_{0,0}|$ is replaced by ${}_{AA'}\langle\Phi_{l,m}|$. From Eq. (1.46), we have $|\Phi_{l,m}\rangle_{AA'} = (\hat{X}_A^l\hat{Z}_A^m \otimes \hat{1}_{A'})|\Phi_{0,0}\rangle_{AA'}$ and thus ${}_{AA'}\langle\Phi_{l,m}| = {}_{AA'}\langle\Phi_{0,0}|(\hat{Z}_A^{-m}\hat{X}_A^{-l} \otimes \hat{1}_{A'})$. From Eqs. (1.45) and (1.46), we have $(\hat{Z}_A^{-m}\hat{X}_A^{-l} \otimes \hat{1}_B)|\Phi_{0,0}\rangle_{AB} = (\hat{1}_A \otimes \hat{X}_B^l\hat{Z}_B^{-m})|\Phi_{0,0}\rangle_{AB}$. We therefore obtain

$$d^{-1}(\hat{X}_B^l\hat{Z}_B^{-m} \otimes \hat{1}_R)|\Phi_{0,0}\rangle_{BR} = {}_{AA'}\langle\Phi_{l,m}||\Phi_{0,0}\rangle_{AB}|\Phi_{0,0}\rangle_{A'R}, \tag{1.48}$$

which identifies the state of the system BR after the Bell measurement in the protocol. By setting $\hat{U}_B^{(l,m)} = \hat{Z}_B^m\hat{X}_B^{-l}$, the protocol should leave the system BR in the same state, $|\Phi_{0,0}\rangle_{BR}$, regardless of the value of the outcome (l, m). In summary, if we begin with state $|\Phi_{0,0}\rangle_{A'R}$, the protocol then transforms it into state $|\Phi_{0,0}\rangle_{BR}$, in which the system with which R is entangled changes from A', possessed by Alice, to B, which is held by Bob. This procedure is often called *entanglement swapping* [10].

The case where system A' is initially prepared in the arbitrary state $|\phi\rangle_{A'} = \sum_j c_j|j\rangle_{A'}$ can be analyzed using Property (E3) on the relative states, as in Sect. 1.4.2. After entanglement swapping, the state of the system BR is $|\Phi_{0,0}\rangle_{BR}$. Suppose that we perform an orthogonal measurement on system R with a basis that includes a state $|\phi^*\rangle_R = \sum_j \bar{c}_j|j\rangle_R$. If the corresponding outcome is obtained, then the state of system B becomes its relative state, $|\phi\rangle_B = \sum_j c_j|j\rangle_B$. Because the entanglement swapping protocol starts with state $|\Phi_{0,0}\rangle_{A'R}$ and does not operate on system R, Theorem 1 then dictates that such an event must be consistent with the case where system A' was initially prepared in $|\phi\rangle_{A'} = \sum_j c_j|j\rangle_{A'}$. We thus conclude that if we carry out the protocol with initial state $|\phi\rangle_{A'} = \sum_j c_j|j\rangle_{A'}$, the final state of system B is $|\phi\rangle_B = \sum_j c_j|j\rangle_B$, which is regarded as a faithful transmission of the quantum state.

The existence of this quantum teleportation protocol has profound consequences. Because classical channels are much easier to implement in practice, let us assume that these channels can be used freely in both directions between Alice and Bob. The quantum teleportation protocol and the entanglement sharing of Theorem 5 then imply that one qubit of dynamic resource and one ebit of static resource are freely interconvertible. Because the static resource of entanglement can be stored in quantum memories, this effectively allows dynamic resource storage. If the quantum channels are not ideal but noisy, we may convert these channels into noisy entanglement, which is then distilled into close-to-ideal entanglement and can be

used for faithful quantum transmission. When we wish to concatenate the quantum channels, which will only work probabilistically, as in the case of transmission of photons over an optical fiber, the combination of entanglement sharing and entanglement swapping dramatically improves the process efficiency, as described in Chap. 4. It should also be noted that entanglement has no preferred direction. We can convert a quantum channel from Alice to Bob into a channel from Bob to Alice, through the protocol of entanglement sharing followed by quantum teleportation with backward classical communication.

1.5.5 Conversion Among the Resources

In the preceding subsections, we have described three protocols, entanglement sharing, quantum dense coding, and quantum teleportation, that provide conversion among the three types of communication resources: ebits, bits, and qubits. Because these protocols were introduced in a rather heuristic way, we might expect that there are many other protocols that can be used for resource conversion. Here, we argue that this is not the case. The three protocols in a sense exhaust all possibilities as far as conversion among the three ideal resource types is concerned.

Imagine that Alice and Bob have a right to use E ebits of a shared ideal entanglement, C bits of an ideal classical channel, and Q qubits of an ideal quantum channel, which we denote by the portfolio (E, C, Q). According to Theorems 5, 8, and 9, the three protocols change the portfolio in the following way.

Entanglement sharing (ES)	$(E, C, Q) \to (E+1, C, Q-1)$
Quantum dense coding (DC)	$(E, C, Q) \to (E-1, C+2, Q-1)$
Quantum teleportation (QT)	$(E, C, Q) \to (E-1, C-2, Q+1)$

Let us assume that we start from (E_0, C_0, Q_0). By repeating these protocols N_{ES}, N_{DC}, and N_{QT} times,

$$(E_0, C_0, Q_0) + N_{\mathrm{ES}}(1, 0, -1) + N_{\mathrm{DC}}(-1, 2, -1) + N_{\mathrm{QT}}(-1, -2, 1) \quad (1.49)$$

is attainable. Therefore, if we ignore the fact that only a discrete set of points is attainable, we may say that it is possible to reach anywhere within a triangular pyramid with apex (E_0, C_0, Q_0) and with edges defined by the vectors $(1, 0, -1)$, $(-1, 2, -1)$, and $(-1, -2, 1)$ (see Fig. 1.6).

We are now interested in whether we can reach a point outside this pyramid. We have already derived various restrictions on resource conversion in Theorems 4, 6, and 7, which are summarized as follows.

Theorem 4	$(0, 0, Q) \to (0, C', 0)$ only if $C' \le Q$.
Theorem 6	$(E, C, 0) \to (E', C', 0)$ only if $C' \le C$
Theorem 7	$(E, C, 0) \to (E', C', 0)$ only if $E' \le E$

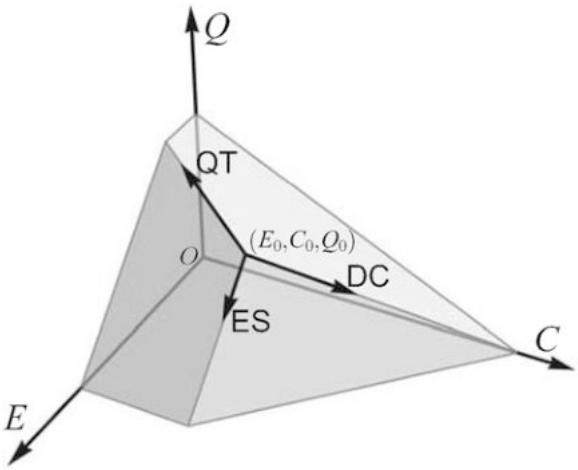

Fig. 1.6 Permitted resource conversion region. *ES*: entanglement sharing; *DC*: quantum dense coding; *QT*: quantum teleportation

Using these theorems, we derive a restriction on a general protocol $\mathscr{P}$ that performs the conversion from $(E_0, C_0, Q_0) \rightarrow (E, C, Q)$. This is done by combining $\mathscr{P}$ with the three protocols, such that the theorems above are applicable to the entire conversion process. For example, we have

$$\begin{aligned}&(0, 0, Q_0 + Q + 2C_0 + E_0 + E) \xrightarrow{\text{ES}} (Q + C_0 + E_0, 0, Q_0 + C_0 + E) \xrightarrow{\text{DC}} \\ &(Q + E_0, 2C_0, Q_0 + E) \xrightarrow{\mathscr{P}} (Q + E, C_0 + C, Q + E) \xrightarrow{\text{DC}} \\ &\quad (0, 2Q + C_0 + C + 2E, 0),\end{aligned}$$

which, from Theorem 4, requires that

$$(E - E_0) + (C - C_0) + (Q - Q_0) \leq 0. \tag{1.50}$$

Similarly, from

$$\begin{aligned}&(Q_0 + Q + E_0, C_0 + 2Q_0, 0) \xrightarrow{\text{QT}} (Q + E_0, C_0, Q_0) \xrightarrow{\mathscr{P}} (Q + E, C, Q) \\ &\xrightarrow{\text{DC}} (E, C + 2Q, 0),\end{aligned}$$

we use Theorem 6 to obtain

$$(C - C_0) + 2(Q - Q_0) \leq 0. \tag{1.51}$$

Finally, by applying Theorem 7 to

$$(Q_0 + E_0, C_0 + 2Q_0, 0) \xrightarrow{\text{QT}} (E_0, C_0, Q_0) \xrightarrow{\mathscr{P}} (E, C, Q) \xrightarrow{\text{ES}} (Q + E, C, 0),$$

we have

$$(E - E_0) + (Q - Q_0) \leq 0. \tag{1.52}$$

It is simple to confirm that Eqs. (1.50), (1.51), and (1.52) correspond to the three faces of the pyramid in Fig. 1.6. It is thus impossible to reach any point outside the pyramid. We see that the three protocols of entanglement sharing, quantum dense coding, and quantum teleportation correspond to the three edges of the achievable region, and form a unique triad that governs the conversions that are allowed among the resources of quantum channels, classical channels, and entanglement.

References

1. N. Gisin, Helv. Phys. Acta **62**(4), 363 (1989)
2. L.P. Hughston, R. Jozsa, W.K. Wootters, Phys. Lett. A **183**(1), 14 (1993)
3. H.K. Lo, H.F. Chau, Phys. Rev. Lett. **78**(17), 3410 (1997)
4. D. Mayers, Phys. Rev. Lett. **78**(17), 3414 (1997)
5. A. Peres, Phys. Lett. A **128**(1), 19 (1988)
6. A. Uhlmann, Rep. Math. Phys. **9**(2), 273 (1976)
7. R. Jozsa, J. Modern Opt. **41**(12), 2315 (1994)
8. C.H. Bennett, S.J. Wiesner, Phys. Rev. Lett. **69**(20), 2881 (1992)
9. C.H. Bennett, G. Brassard, C. Crépeau, R. Jozsa, A. Peres, W.K. Wootters, Phys. Rev. Lett. **70**(13), 1895 (1993)
10. M. Żukowski, A. Zeilinger, M. Horne, A. Ekert, Phys. Rev. Lett. **71**(26), 4287 (1993)

Chapter 2
Quantum Communication for the Ultimate Capacity and Security

Masahide Sasaki, Mikio Fujiwara, and Masahiro Takeoka

2.1 Introduction

Communication theory was born around the same time, 1920s, when quantum mechanics was formulated. It was telegraph transmission theory by H. Nyquist (sampling theorem) and R. V. L. Hartley (transmission rate). Their works inspired C. E. Shannon to formulate the theory of communications. He introduced the mutual information $I(X;Y)$ and provided the formula of the capacity of a channel as [1]

$$C_1 \equiv \max_{P(x)} I(X;Y) = W \log\left(1 + \frac{S}{N}\right) \tag{2.1}$$

where $P(x)$ is a probability distribution of input alphabet x, W a bandwidth of the channel, S an average signal power, N a noise power. Soon after this work, D. Gabor considered how communication theory should be revised when particle nature of electromagnetic field is taken into account [2]. Actually reception of photons causes a new kind of noise in communication. He named it quantum noise. In 1960, T. Maiman succeeded in producing the first beam of laser light. It was a crucial trigger for quantum communication because an energy quanta of laser, photons, is much larger than that of the thermal noise, and hence quantum effect becomes apparent. In 1964, J. P. Gordon considered a photon channel and introduced the von Neumann entropy to the Shannon theory to reformulate the expression of Eq. (2.1) in terms of quantum sates $\hat{\rho}_x$. He conjectured that the capacity can be greater than that of Shannon's formula. But at that time it was not proven because quantum detection theory was not well understood yet. Quantum detection theory was developed in 1970s [3].

M. Sasaki • M. Fujiwara • M. Takeoka (✉)
Quantum ICT Laboratory, National Institute of Information and Communications Technology, Koganei, Tokyo 184-8795, Japan
e-mail: psasaki@nict.go.jp; fujiwara@nict.go.jp; takeoka@nict.go.jp

Y. Yamamoto, K. Semba (eds.), *Principles and Methods of Quantum Information Technologies*, Lecture Notes in Physics 911, DOI 10.1007/978-4-431-55756-2_2

A. S. Holevo applied it to extend the Shannon theory, and gave a rigorous proof on Gordon's conjecture, showing that the quantity introduced by Gordon is the strict upper bound of the mutual information maximized over detection operators $\hat{\Pi}_y$ [4];

$$S\Big(\sum_x p_x\hat{\rho}_x\Big) - \sum_x p_x S(\hat{\rho}_x) \geq \max_{\hat{\Pi}_y} I(X:Y) \geq C_1. \tag{2.2}$$

It's been called the Holevo bound.

In 1980s, the merger was made between quantum mechanics and cryptography by C. H. Bennett and G. Brassard [5], and a notion of quantum key distribution (QKD) was born. QKD provides a means to deliver information-theoretically secure keys, i.e. secure keys against an eavesdropper who has unbounded ability. When the keys are used in the one-time pad (OTP), the unconditional security can be ensured in principle. QKD had attracted less attentions until the middle of 1990s, but has cone into the bloom after 2000s.

In 1990s, on the other hand, it was shown that the Holevo bound is actually the achievable transmission rate when maximized over all possible detection strategies for a given set of quantum states, and hence is the true capacity [6–8]. This capacity is greater than the Shannon limit. So there certainly exists the quantum gain which was not considered explicitly in Shannon's formula. The theories showed that the quantum gain must be due to a collective measurement or a joint measurement on a sequence of signal pulses. In fact, the quantum control of detection process brings a new remarkable effect, when we consider the coding. It is the super-additive coding gain. This can be summarized in the following way. When we increases the transmission resources by n times, then the capacity can increase even more than n times [9]. Classically, however, the capacity increases n times at most, and never more than that (see Fig. 2.1). The very origin of this effect is quantum computing, which is performed prior to the measurement. This kind of new decoding is called quantum collective decoding or simply quantum decoder [10]. The important principle of super-additive coding gain was demonstrated in the laboratory in 2003 [11, 12]. In the experiments, single photon states in the polarization-location coding were used.

In 2004, the general theorem of capacity for a lossy bosonic channel was proved, optimizing not only the receiver structure but also the sender strategy [13]. Let the channel transmittance be η and the frequency cutoff be f_L and f_U. The capacity is given by

$$C_Q = \int_{f_L}^{f_U} df g\left(\eta \cdot \bar{n}(f,\beta)\right) , \tag{2.3}$$

where $g(x) = (x+1)\log_2(x+1) - x\log_2 x$ and $\bar{n}(f,\beta)$ is the optimal photon number determined under the power constraint

$$P = \int_{f_L}^{f_U} df\hbar f\bar{n}(f,\beta). \tag{2.4}$$

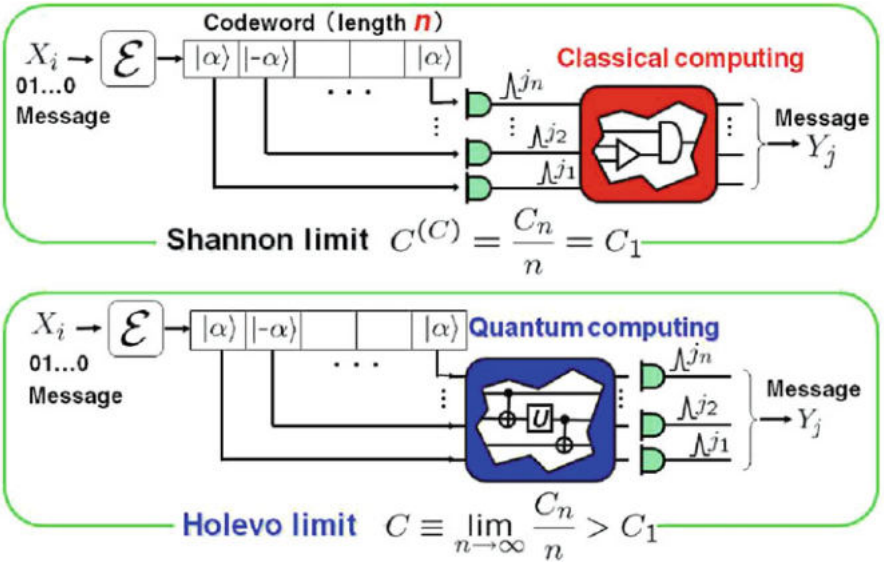

Fig. 2.1 Comparison of quantum and classical decoding schemes

This C_Q was actually the quantity which Gordon derived 40 years ago [14].

Thus in the early 2000s we have known what is the ultimate limit of communications capacity, and how quantum control can be used to reach it. In these two decades QKD has also progressing rapidly from field trials [15–17] to commercial propositions [18]. In this article we present our results on these two topics and then discuss future perspectives.

2.2 Increasing the Capacity of an Optical Channel

Using the formula of Eq. (2.3), we can predict performances of future technologies. A typical example is deep space optical communications where the power feed is very limited but there are no amplifiers. Figure 2.2 shows the transmission rates versus distances in space [19]. The theory tells us that one will be able to extend a Tbps link to Mars if all-band quantum decoder could be realized. Lower curves are realistic simulation with practical technologies, including coherent communication and PPM scheme with 1024 symbols, as well as the Holevo capacity. The bandwidth of 100 GHz is assumed. Up to the moon, coherent communication is better than the PPM scheme. But going beyond Mars, and reaching Jupiter and Saturn, one should use PPM scheme to get closer to the Holevo capacity.

In general, if the power loss is not so severe, we had better to increase spectral efficiency by multi-ary quadrature amplitude modulation with coherent communication. If, on the other hand, the power budget is stringent, we should optimize the energy efficiency by concentrating the energy into a very short time

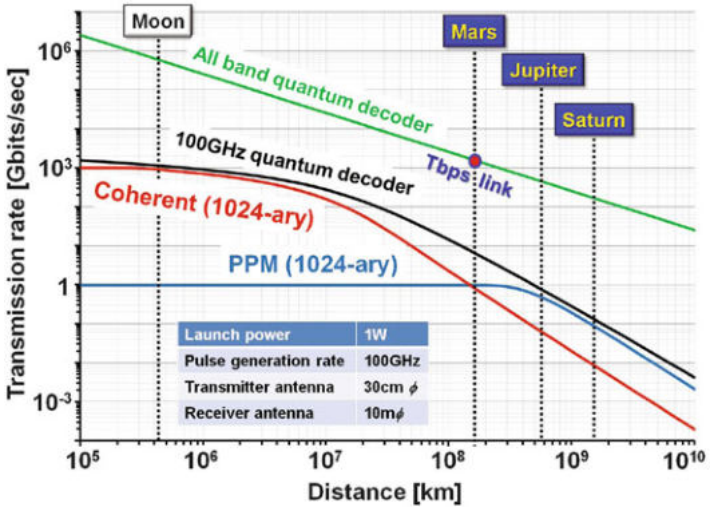

Fig. 2.2 Predictions on the capacities for deep space optical communications

slot with the PPM scheme. For both situations, the transmission rate can be further improved if quantum decoder could be applied.

Unfortunately, however, implementing a quantum decoder for practical coherent-state or PPM signals is still a formidable task. Although the super-additive coding gain was experimentally demonstrated in [11, 12], the decoder used was for single photon states in the polarization-location coding, which is not a practical format for real communications. Current efforts are mainly paid for the very first step for dealing with practical signals of coherent states, i.e. implementing quantum receivers for bit-wise detection with a smaller bit error rate (BER) than current homodyne/heterodyne and on-off detectors. Such quantum receivers would be useful for reducing the decoding complexity when combined with classical coding. It is also true that if a quantum decoder could be realized even in a small scale, it can be used with classical coding to reduce a decoding error with smaller decoding complexity [12].

Let us turn to the topic of practical implementations of quantum receivers. The general theory of detecting (discriminating) quantum signals with minimum error rate was developed by C. W. Helstrom and co-workers [3]. A simple yet practically important example is a discrimination of binary signals $\{|\rho_0\rangle, |\rho_1\rangle\}$. In optical communication, $|\rho_0\rangle$ and $|\rho_1\rangle$ are for example, on-off keyed coherent states or binary phase-shift keyed (BPSK) coherent states. When the two signals occur with equal probabilities, the ultimate quantum limit of the minimum BER (the Helstrom bound) is given by

$$P_e^{\min} = \frac{1}{2}\left(1 - \sqrt{1 - |\langle\rho_0|\rho_1\rangle|^2}\right). \tag{2.5}$$

In contrast, the BER limit in conventional communication theory, often called the standard quantum limit (SQL), is defined by the BER attained by directly measuring the modulation variable, e.g. the intensity and/or phase which is reachable via conventional detectors such as homodyne/heterodyne or on-off photo detectors.

A quantum receiver structure to beat the SQL was first clarified for the BPSK signals by R. S. Kennedy in 1973 [20] and was soon extended by S. Dolinar [21] to reach the Helstrom bound. The operation of the Kennedy receiver is quite simple. First it displaces the BPSK signal from $\{|\alpha\rangle, |-\alpha\rangle\}$ to $\{|2\alpha\rangle, |0\rangle\}$ and then detects them by an on-off detector,

$$\hat{\Pi}_{\text{off}} = |0\rangle\langle 0|, \quad \hat{\Pi}_{\text{on}} = \hat{I} - \hat{\Pi}_{\text{off}}, \tag{2.6}$$

which discriminates zero or non-zero photons. It is well known that the displacement operation $\hat{D}(\alpha)$ can be realized by interfering the signal with coherent state local oscillator (LO) $|\alpha/\sqrt{R}\rangle$ via a beam splitter with reflectance R and set $R \to 0$.

The Kennedy receiver setup is extended to the Dolinar receiver, which *exactly* achieves the Helstrom bound, by introducing a (infinitely) fast electrical feedback to dynamically change the LO amplitude and phase conditioned on the time resolved photo counting [21]. Though Dolinar's original analysis was based on the semiclassical theory, its fully quantum-mechanical description was later given in [22, 23]. It was further shown that the Dolinar scheme can realize not only the Helstrom receiver but also *arbitrary* binary projective measurements [24]. Another scheme of achieving the Helstrom bound based on a nonlinear transformation and conventional detection was also proposed [25].

Though these two receiver schemes enlightened the way to overcome the SQL in optical communication, the optical technologies in 1970s were not enough matured to implement them even in the laboratory. However, thanks to the progress of photon detection and fast feedback electronics, these are nowadays possible to implement in the laboratories. The first experimental demonstration was performed by R. L. Cook et al. [26]. They implemented the Dolinar receiver with avalanche photodiode (APD) and high-speed digital signal processing electronics and demonstrated a discrimination of $|\alpha\rangle$ and $|0\rangle$ with the BER smaller than that of the direct photo detection. Though this was a major experimental progress, its error performance was severely limited by the total quantum efficiency (QE) of the receiver (approximately 0.35) and thus it was difficult to apply it to the BPSK signals.

On the other hand it is natural to ask why the Kennedy receiver for the BPSK signals has not been investigated experimentally despite of its very simple setup and a potential of nearly optimal performance. First, it requires a very high QE photon detectors as is the case for the Dolinar receiver. This could have been overcome these days, with, for example, high QE superconducting detectors. Second, in contrast to the Dolinar or other feedback-based receivers, the Kennedy receiver is not robust against dark counts (DC) (or thermal noises) [27, 28]. Roughly speaking, the error probability is saturated at the DC rate of the receiver which means that the performance of the receiver saturates for higher signal photon number (in fact, it could happen even for few photons per pulse with realistic high QE detectors [28]).

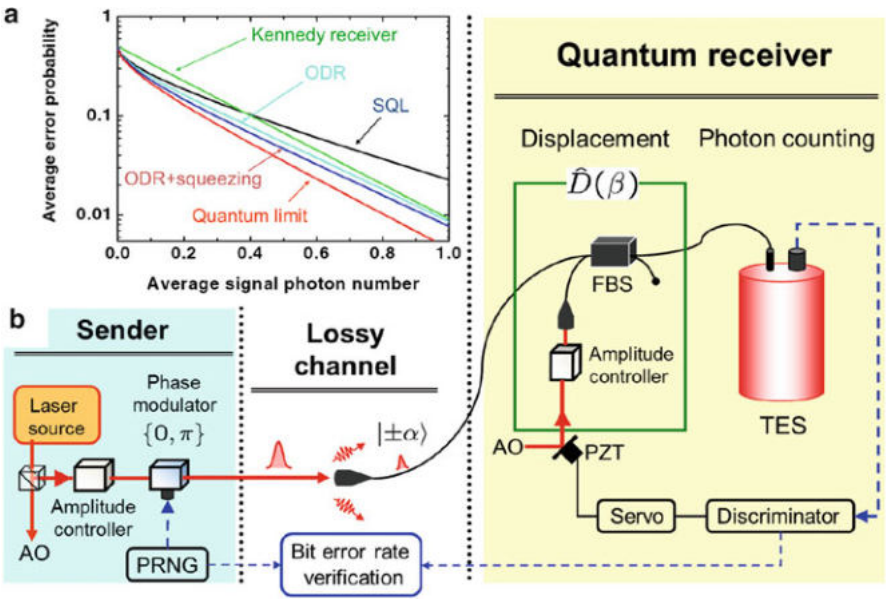

Fig. 2.3 (**a**) Average error probabilities of the SQL, Kennedy receiver, optimal displacement receiver (*ODR*), and the ultimate quantum limit. Note that an installation of the squeezing operation into the receiver slightly improve the error performance [28]. (**b**) Experimental setup of the ODR receiver demonstrated in [30]. *FBS*, fiber beam splitter; *AO*, auxiliary oscillator; *PRNG*, pseudo-random-number generator; *TES*, transition-edge sensor; *PZT*, piezoelectric transducer

Unfortunately, however, the performance of the Kennedy receiver is comparable or even worse than the SQL if the signal photon number is very weak such as less than one (Fig. 2.3a). These situations have prevented the experimental demonstration of the sub-SQL operation of the Kennedy receiver.

The improved scheme to circumvent the problem at the weak signal regime was proposed recently [28, 29]. It is achieved by simply optimizing the amount of displacement instead of simply displacing $|-\alpha\rangle$ to $|0\rangle$. The solid line for the 'ODR' in Fig. 2.3a corresponds to the performance of the receiver in which the displacement is optimized to minimize the error rate (which we call the 'optimal displacement receiver' (ODR)). Its error rate is clearly smaller than the SQL for all α. In particular, the performance at small α is crucial for experimental demonstration of beating the SQL.

A proof-of-principle experiment of the ODR has been performed in [29]. Though the total QE of the receiver was low (55.0 %), the error rates demonstrated were clearly lower than that of the homodyne receiver with higher QE (85.8 %). This result strongly suggests it could be possible to overcome the SQL (i.e. the error rate by a perfect homodyning) if the ODR is implemented with a high QE photon detector. In fact, the first demonstration of the sub-SQL discrimination of the BPSK coherent signals was performed [30] by using a titanium-based superconducting

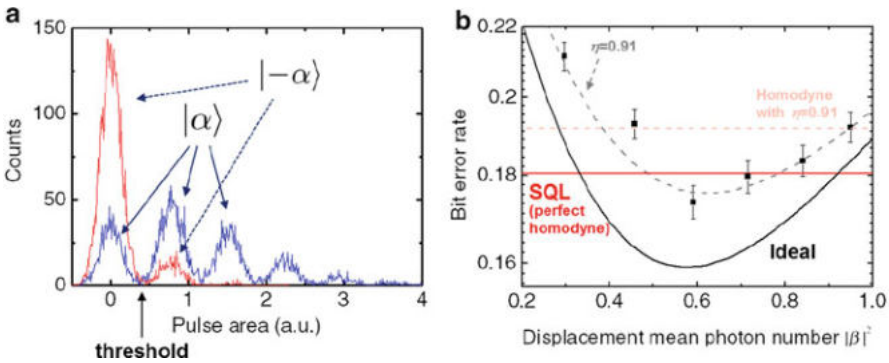

Fig. 2.4 Experimental result [30]. (**a**) The output pulse height distribution of the TES for the signals $|\pm\alpha\rangle$. $|\alpha|^2 = 0.21 \pm 0.01$ and $|\beta|^2 = 0.59 \pm 0.01$. (**b**) The measured BER (average error probability) for various displacements. $|\alpha|^2 = 0.21 \pm 0.01$

transition-edge sensor (TES) which is a photon number resolving detector with QE of 0.95 ± 0.01. The setup is shown in Fig. 2.3b where binary signals are randomly generated and encoded into 20 ns coherent state laser pulses at 853 nm via the BPSK modulation. Figure 2.4a shows the output electrical pulse height distribution from the TES for the BPSK signals $|\pm\alpha\rangle$. Each peak corresponds to different photon number observed at the TES. The signal decision is then made by thresholding the pulse height between the vacuum and one photon and the outcome is verified with the original data at the sender. The result of the average error probability is shown in Fig. 2.4b for various displacement β. It shows that by choosing β appropriately, the error probability clearly surpasses the SQL without compensating any experimental imperfections. Note that the similar technology was applied to the discrimination of the OOK signal and demonstrated the sub-shot-noise-limit performance [31].

Shortly after these works, many experimental studies of implementing quantum receivers for more general purposes have been reported. One natural generalization is to encode more than two signals in phase space. In theory, the Dolinar receiver was extended by R. Bondurant [32] to the near-optimal receiver for the quaternary phase-shift keyed (QPSK) signals. This idea was carefully examined in a more realistic setting with finite number of feedback steps [33, 34] or even without feedback but with the optimal displacement strategy [34]. The former idea was also experimentally implemented with an avalanche photodiode (APD) and an FPGA based feedback system [35] which demonstrated 6 dB gains from the SQL (the theoretical limit of the heterodyne receiver). Furthermore, it was theoretically shown that if the number of feedback step is relatively small, the photon number resolving detector (PNRD) instead of the on-off detector further diminishes the error probability [36]. Another approach hybridizing a homodyne and a displacement-controlled detectors for discriminating the QPSK signals was also proposed and experimentally examined [37].

The receiver was also designed for M-ary PPM signals [38]. In this scheme, the displacement parameter is fixed to make one of the signals into $|0\rangle$ within a whole pulse duration at each time interval but between the time intervals, the nulled pulse is conditioned on the previous measurement outcomes. Furthermore, it is shown that the exact nulling is not optimal and thus further improved by optimizing the amount of displacement.[1] The idea was experimentally demonstrated with an APD and an FPGA based feedback for the conditional nulling [39].

All of the above works are concerning how to minimize the error rate in the coherent state discrimination where the receiver basically works as a *projection* measurement, i.e. the measurement operators are orthogonal projectors. Another direction is to implement a *generalized* measurement where the measurement operators can be nonorthogonal to each other. One of its applications is unambiguous state discrimination (USD) [40] which achieves error-free discrimination of nonorthogonal states by introducing an extra inconclusive result. In practice, it is more appropriate to consider the *intermediate* discrimination (ID) between the minimum error state discrimination (MESD) and the USD where by allowing a small inconclusive probability one can achieve the average error probability smaller than that of the MESD. For binary coherent states, a near-optimal scheme of the ID by using displacement and a PNRD was proposed and demonstrated [41, 42]. The similar approach is extended to more than binary signals [43]. It is worth to note that the ID measurement is useful not only for usual optical communication, but also for QKD or other quantum communication protocols [41–43]

Before closing this subsection, let us briefly discuss the performance gap between the 'quantum receiver' (bit-wise measurement) and the 'quantum decoder' (collective measurement) by comparing their capacity trade-offs between spectral efficiency (SE) [bits/sec/Hz] and the photon information efficiency (PIE) [bis/(received) photon]. Figure 2.5 plots the Holevo bound for various modulation formats and the achievable PIE for various encoding with (non-collective) receivers including the ones we have discussed above (see [44] for the full explanation about the figure). The figure implies that for extremely higher or lower spectral efficiency, the gap between the Holevo limits and the non-collective (i.e. more feasible) receivers is relatively small while the gap is substantial in the intermediate region where the collective quantum decoder will play a crucial role as discussed in Introduction.

[1] It should be noted that in [28, 36, 38] it is shown that the squeezing operation *inside* the receiver also slightly improve the performance of the receivers. Technically this is quite challenging but fundamentally an interesting observation since the squeezing is not useful for the carrier preparation at the sender side but is useful for the carrier processing at the receiver side.

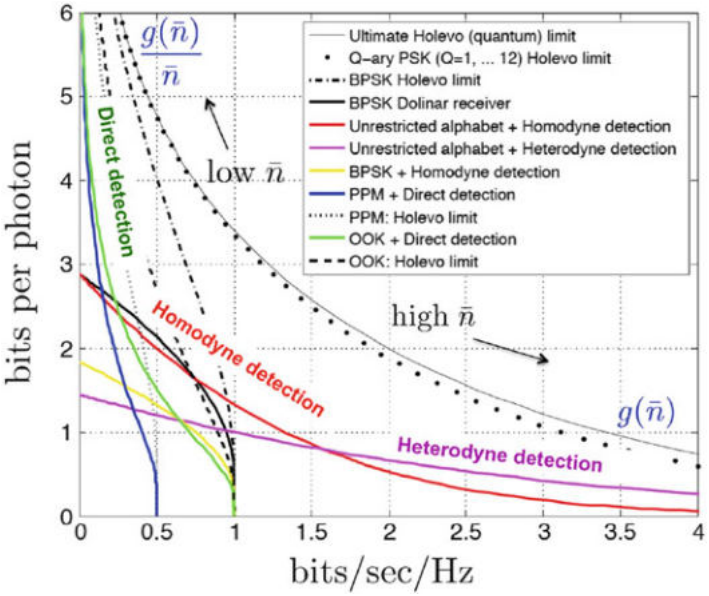

Fig. 2.5 The trade-off between PIE and SE for various choices of modulation formats and receivers [44]. All *solid lines* except the one on the top corresponds to structured optical receivers, whereas the *non-solid lines* and plots correspond to the Holevo capacities constrained to different modulation formats (i.e., with no restrictive assumption on the receiver). The *thin line* on the top is the ultimate capacity limit–no constraint on modulation and receiver–the highest capacity attainable over a pure-loss optical channel

2.3 QKD and Beyond

Current QKD speed and distance are mainly limited by the performance of photon detectors. The maximum count rate is roughly a few hundred counts per sec (cps) for both APD and superconducting nanowire single photon detector (SSPD). The fastest clock rate for current QKD systems is about 1 GHz. Alice should attenuate pulse intensity to be 0.1 photons per pulse, to suppress multi-photon probabilities. Detector efficiency is typically 10 % for APDs. Then a number of signals decrease by the transmission loss as the distance extends. The key distillation usually prunes at least the two third of the received signals. So in a metropolitan scale, we have totally four orders of magnitude reduction. Then the expected secure key rate would be 100 kbps, which may be a kind of limit for a metropolitan scale distance. Further improvement may not be easy, unless the performance of photon detector is dramatically improved.

A straightforward way to increase the key generation rate is to use wavelength division multiplexing (WDM). NEC and NICT developed a WDM-QKD system with maximally 8 wavelength channels [45, 46]. A schematic is shown in Fig. 2.6. The protocol is decoyed BB84. The clock rate is 1.244 GHz. At Alice, optical pulses

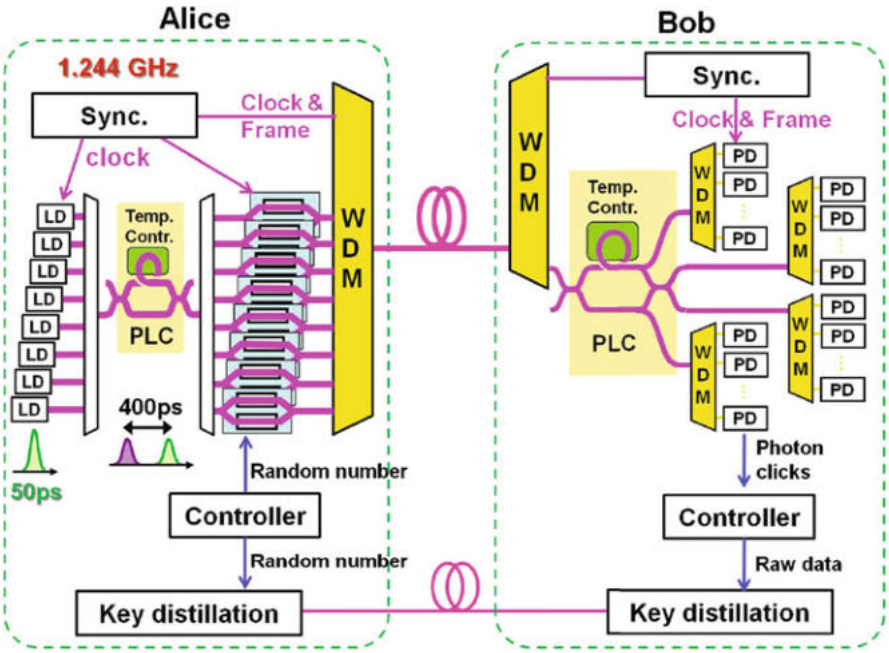

Fig. 2.6 Schematic of WDM-QKD system

of 50-ps-width at this repetition rate pass through a 2×2 asymmetric Mach-Zehnder interferometer of planar lightwave circuit (PLC), and are converted into the time-bin pulses with a 400 ps separation. The time-bin pulses are de-multiplexed, and each wavelength component is independently encoded with the signal and decoy information. The signals are multiplexed again, together with the clock and frame synchronization signal, and input into a single fiber. At Bob, the clock signal is first separated, and the quantum signals pass through the PLC interferometer. They are then de-multiplexed at each of the four ports, and finally detected by the photon detectors.

In this WDM-QKD system, wavelength-dependent phase mismatches always exist. In order to compensate them, phase shifters are added after the encoders. The PLCs are tuned to be polarization-independent, and this enables stable operation even under polarization drift in field fibers [47]. Various device components, synchronization, optical, detector, control units and key distillation engine are assembled into the boards, then mounted to Advanced Telecom and Computing Architecture blades, and finally inserted into 19-inch lacks.

The key distillation process is summarized in Fig. 2.7. Raw key rate is about 1 Mbps per each wavelength channel. A fraction of 10 kbps is spent for frame synchronization. Sifted key rate is roughly 400 kbps. We then make blocks of 1 Mbit size, and the data are processed in this block size. Test bit length is 65kbit, from which the BER is calculated. According to the BER, an appropriate LDPC code is

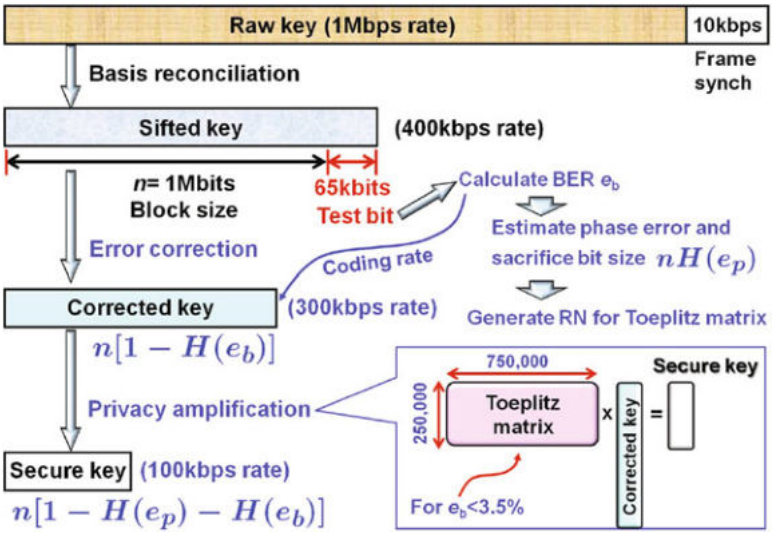

Fig. 2.7 Key distillation flow of the WDM-QKD system and its specifications

chosen from a package of totally 11 code sets. We further estimate the phase error, taking the finite size effect into account. We then determine a size of sacrifice bits, which is typically 2/3 of the corrected key. Then the random numbers are generated for a corresponding Toeplitz matrix, in a size 750k × 250k. The corrected key is multiplied by this, and we distill the final secure key. The secure key rate is typically 100 kbps per channel over a 45 km field fiber.

Then a huge amount of the signals at a rate of 50 Gbps in total should be stored and processed. This is made by a dedicated hardware, the key distillation engine. Raw key rate is roughly 10 Mcps. The sifted key rate is 5 Mbps, and processed in a unit of 1 Mbit block size. The total secure key rate would potentially be 1 Mbps over a 10 dB loss channel.

This system was operated with two WDM quantum channels through a 22-km field fiber. 90 % of the fiber is aerial over poles. The total loss is 12.6 dB. Maintenance-free WDM-QKD operation for 30 days could be demonstrated [48]. Figure 2.8 shows quantum bit error rates (QBERs), sifted key rates and estimated secure key rates for the two channels, at $\lambda_1 = 1547.72$ nm and $\lambda_1 = 1550.92$ nm, for 30 days respectively. In the receiver, two avalanche photodiode (APD) systems were used. The secure key rates are calculated assuming low density parity check code (LDPC) and the three-state decoy protocol for the privacy amplification. We assume a LDPC code applicable up to the error rate of 3 % with coding rate of 0.77, which we have already built separately.

As summarized in Table 2.1, we attained a quantum bit error rate as low as 1.70 % and an estimated secure key rate as high as 112.4 kbps for a record-breaking 291.3 Gbits of estimated secure keys accumulated over an uninterrupted operation

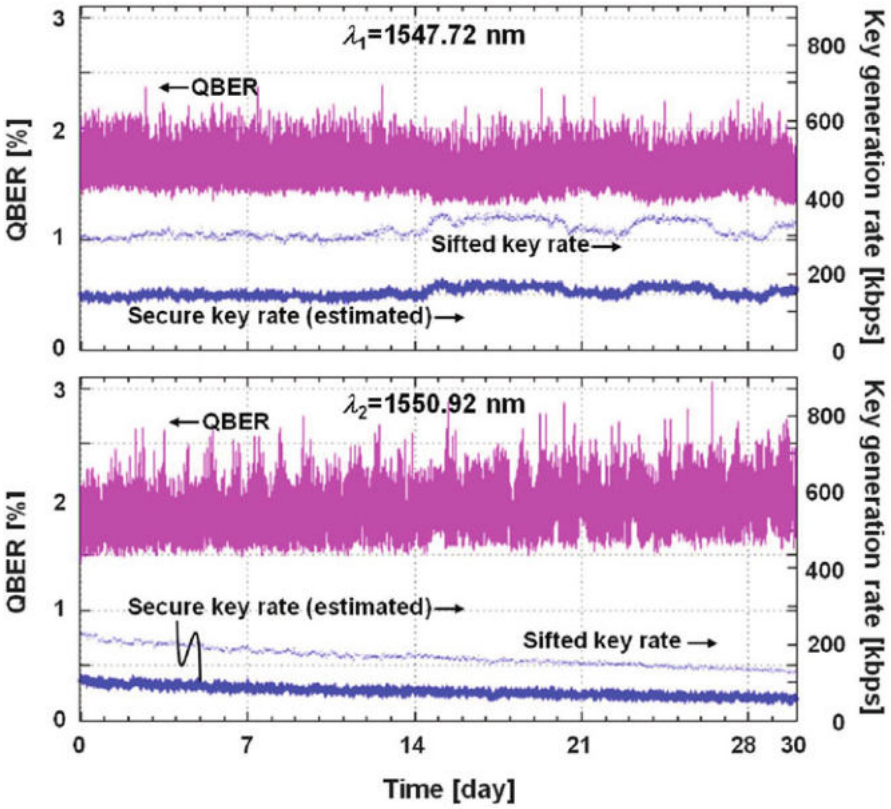

Fig. 2.8 Key generation rate and QBER of WDM-QKD over 30 days at two wavelengths $\lambda_1 = 1547.72$ nm and $\lambda_2 = 1550.92$ nm

Table 2.1 Key generation performance over 30 days

Wavelength (nm)	QBER (%)	Sifted key rate (kbps)	Estimated secure key rate (kbps)
$\lambda_1 = 1547.72$	1.61	315.3	72.6
$\lambda_2 = 1550.92$	1.86	168.0	39.8
Total	1.70	483.3	112.4

period. This was realized by the stabilization technique which adaptively optimize detection timing of the photon detectors, bias voltage of the encoding modulator, temperature of the PLC interferometer, and amplitude of the phase compensation modulator. They were done by software in a period of about 3 minutes. This procedure is executed in parallel with the key generation.

Networking of QKD can be made by key relay via trusted nodes. Namely at each node, secure keys of the neighboring links are stored in the physically protected server called key management agent (KMA). Secure key is encapsulated with the other key, and is relayed securely to the terminal. Each KMA receives the key

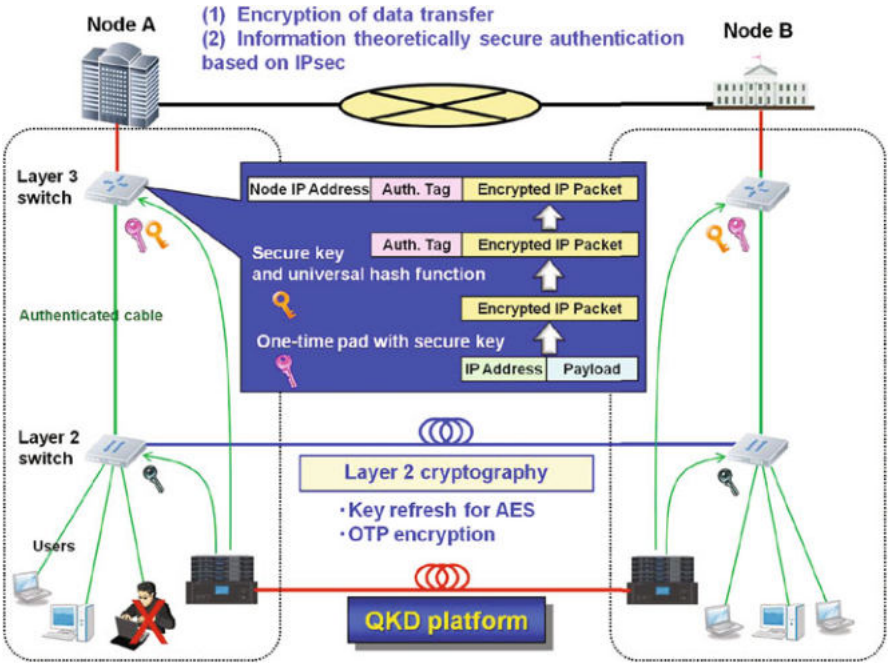

Fig. 2.9 QKD-enhanced Layer-2 and Layer-3 switches

material, resizes and saves them as well as to store quantum BER and key generation rate. The KMAs also have application interfaces and supply secure key to variety of applications in the upper layers. This kind of network with the KMAs can constitute a QKD platform, which is once introduced to a network, then its security can be greatly enhanced.

Actually we have developed QKD-enhanced Layer-2 and Layer-3 switches. A secured network scheme is shown in Fig. 2.9. Layer-2 switches identify the media access control address (MAC address) of both sending and receiving devices, and switch packets in LANs. Secure key from the QKD platform can be used for encrypting MAC address to prevent unauthorized accesses. It also supports key refresh to Layer-2 cryptography which often includes AES (Advanced Encryption Standard) as well as one-time pad (OTP) encryption in Layer 2. Layer-3 switches perform routing based on IP addresses. The QKD-enhanced Layer-3 switch receives two kinds of secure keys. One is used for encrypting payload and IP address by OTP, creating an OTP-encrypted IP packet. The other is used together with universal hash functions such as Wegman-Carter protocol, for generating an authentication tag from that packet. The packet consisting of the encrypted IP packet and the authentication tag is then routed to a terminal node. A key refresh option for symmetric ciphers, such as AES, by QKD is also implemented in the Layer-3 switches. Thus both encryption of data transfer and information theoretically secure authentication based on IPsec can be realized.

A practically important concern is the implementation of countermeasures against side channel attacks. Entanglement based QKD, such as E91, has a great potential for self-testing the presence of side channels, thus offering a qualitatively new insight into cryptography. This scheme is compatible with quantum repeater paradigm. Unfortunately, however, entanglement based QKD is still limited in distance and speed. Quantum repeater is yet to be practical. Quantum relay based on teleportation can be an intermediate option.

In fact we proposed a quantum relay scheme based on teleportation with a gain, called tele-amplification, which can be realized by using a superposition state of coherent states, referred to as a Schrödinger cat state [49]. No quantum memory is required in this tele-amplification scheme. The difficulty is, instead, imposed to the state preparation. The basic scheme is depicted in Fig. 2.10. The receiver prepares a cat state of two waves of 0 and 1, and splits it into beams B and C via a beam-splitter (BS). Beam C is then sent to the sender, where beam C is combined with the input state in beam A. The sender finally measures beams A and C by single-photon detectors. Then, when the sender's detectors register a single photon at beam A and nothing at beam C, the receiver unambiguously restores the input state. Thus by conditioning beam B on the sender measurement result, the receiver can restore the input state with the amplified gain without noise. The tele-amplified gain can be tuned by the reflectance of the two BSs. It can work even for a lossy channel when the input

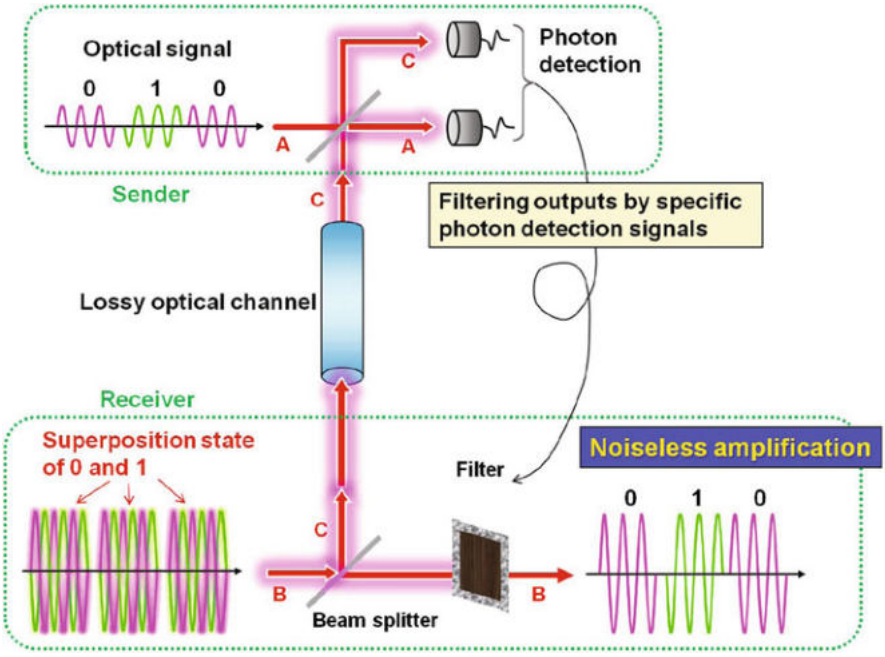

Fig. 2.10 Schematic of quantum tele-amplification

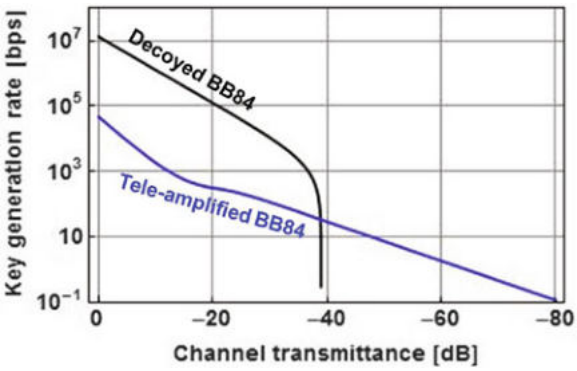

Fig. 2.11 Key generation rates as a function of channel transmittance for decoyed BB84 and tele-amplified BB84. In the tele-amplified BB84, a cat state with 10∼100 photons at 1 GHz repetition rate is assumed

states are restricted to coherent states. This loss-tolerance is brought by the fact that the coherent state is an eigen state of an annihilation operator, i.e. $\hat{a}\,|\alpha\rangle = \alpha\,|\alpha\rangle$.

If the 4-component cat state $|\beta\rangle + i\,|i\beta\rangle - |\beta\rangle - i\,|-i\beta\rangle$ could be prepared, our scheme can be applied to BB84 protocol. Figure 2.11 shows key generation rates as a function of channel transmittance for decoyed BB84 and tele-amplified BB84. Decoyed BB84 hardly generates the secure key as the channel transmittance gets below −40 dB, while tele-amplified BB84 can make a QKD link. As the amplitude of coherent-state superposition could be larger, the relay distance can be extended further in principle. The limit of this scheme is the tradeoff between the distance and the key rate, that is, extending the distance sacrifices the key rate more or less. Details are referred to [49].

2.4 Future Outlook

While QKD can provide the unconditional security, its distance and speed are still limited. This aspect becomes apparent when one consider to apply it to space links in which trusted nodes cannot be made. One may ask whether there are any other ways to secure such links in an information-theoretic way. On occasions the requirement of the unconditional security may be too much. It may be relaxed in a sensible way, while instead pursuing higher rates and distances. Now consider a situation in space optical communications. High speed optical data links between satellites and between satellite and ground are progressing rapidly these days, and are expected to be backbones for global networks. High level security is becoming an important concern. If we insist on QKD for securing those links, no options can be found currently. In Fig. 2.12 we plot the key rate in deep space as a function of the channel transmittance in dB. The dotted line represents the secure key rate of decoyed BB84. The key rate rapidly falls at around −40 dB loss. Total loss for the LEO (low earth orbit)-ground link is typically −50 dB. So it is very difficult to make a QKD link there. The top solid line is the maximum transmission rate for PPM scheme with

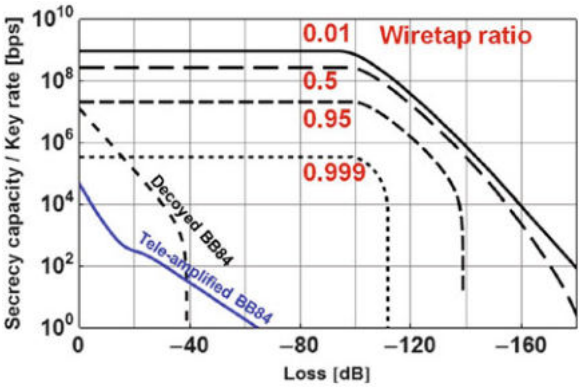

Fig. 2.12 A numerical example of the secrecy capacities for a wiretap channel with various tapping ratio in *red* by an eavesdropper. Pulse position modulation is assumed in free space laser link. In the left corner of figure, typical key rates in quantum key distribution are also shown

transmission power of 1 W and repetition rate 1 GHz. There is no security at all, but just to attain the maximum transmission rate within the available power. As seen there is a huge gap between the performances of these two extreme cases. One might naturally ask whether there are some intermediate schemes, which can provide higher capacity as well as strong enough security. The gap will never be filled merely by improving the currently known QKD schemes.

An option is to compromise the security requirement in a reasonable way. Free space laser link is generally made in large transparent area. If Eve is in the channel, then Alice and Bob can tell Eve is there. So what Eve should do is to hide from Alice and Bob away from the channel, and try to collect scattered light to get information from Alice. Then the transmittance for Eve, η_z, can be smaller than that for Bob η_y. The wiretap ratio is smaller than the unity, $\eta_{zy} = \eta_z/\eta_y < 1$. The degraded condition for Eve can be met, and . this is called a wiretap channel. Then there exists a code that can transmit the following amount of bits faithfully per time, making leaked information to Eve arbitrarily small [50]

$$C_S = \max_{P(x)} [I(X;Y) - I(X;Z)] \tag{2.7}$$

The messages transmitted through such a wiretap channel with an appropriate code can never be broken by any future computers. This scheme is called physical layer cryptography.

We then calculate the secrecy capacity under the cost constraint of transmission power (1 W) and bandwidth (1 GHz). We vary the wiretap ratio from 1 % to 99.9 %. As seen we can cover wide range of larger capacity at longer distances with the information theoretic security.

Wiretap channel coding should include not only redundancy to correct errors but also randomness to deceive Eve. In this way, both reliability and security can simultaneously be realized. The finite length analysis was recently formulated in [51], and was extended to a theory under cost constraint [52], where a dual set of the reliability and security functions, those specify exponentially decreasing rates of Bob's decoding error and leaked information to Eve as n increases, is introduced

to engineer the tradeoff between the reliability and the security. This formulation includes not only the secrecy capacity in the asymptotic limit but also quantifying appropriate reliability and security measures in finite lengths.

These theories on wiretap channel are still within a classical framework based on classical symbols, for given channel matrices. In the quantum setting, given and fixed is a quantum channel (a completely positive trace preserving map), and input states, detection strategy, and coding can be the variables. Extending our theory into the quantum domain remains open, as well as a question of whether the entanglement could be useful for implementing degraded wiretap channel conditions.

Acknowledgements The results on QKD presented here were obtained by the collaboration with NEC Corporation under the NICT Commissioned Research. This work was partly supported by the Quantum Information Processing Project in the Program for World-Leading Innovation Research and Development on Science and Technology (FIRST) and by a National Research Foundation of Korea (NRF) grant funded by the Korean Government (Ministry of Education, Science, and Technology) (No. 2010-0018295).

References

1. C.E. Shannon, A mathematical theory of communication. Bell Syst. Tech. J. **27**, 379–423 (Part I); 623–656 (Part II) (1948)
2. D. Gabor, Communication theory and physics. Phis. Mag. **44**, 1161 (1950)
3. C.W. Helstrom, *Quantum Detection and Estimation Theory* (Academic, New York, 1976)
4. A.S. Holevo, Some estimates for information quantity transmitted by quantum communication channels. Probl. Peredachi Inf. **9**, 3 (1973)
5. C.H. Bennett, G. Brassard, Quantum cryptography: public key distribution and coin tossing, in *Proceedings of the IEEE International Conference on Computers Systems and Signal Processing*, Bangalore (1984), pp. 175–179
6. P. Hausladen, R. Jozsa, B. Schumacher, M. Westmoreland, W.K. Wootters, Classical information capacity of a quantum channel. Phys. Rev. A **54**, 1869 (1996)
7. A.S. Holevo, The capacity of the quantum channel with general signal states. IEEE Trans. Inf. Theory **IT-44**, 269–273 (1998)
8. B. Schumacher, M. Westmoreland, Sending classical information via noisy quantum channels. Phys. Rev. A **56**, 131–138 (1997)
9. M. Sasaki, K. Kato, M. Izutsu, O. Hirota, A demonstration of superadditivity in the classical capacity of a quantum channel. Phys. Lett. A **236**, 1 (1997)
10. M. Sasaki, K. Kato, M. Izutsu, O. Hirota, Quantum channels showing superadditivity in classical capacity. Phys. Rev. A **58**, 146 (1998)
11. M. Fujiwara, M. Takeoka, J. Mizuno, M. Sasaki, Exceeding classical capacity limit in quantum optical channel. Phys. Rev. Lett. **90**, 167906 (2003)
12. M. Takeoka, M. Fujiwara, J. Mizuno, M. Sasaki, Implementation of generalized quantum measurements: superadditive quantum coding, accessible information extraction, and classical capacity limit. Phys. Rev. A **69**, 052329 (2004)
13. V. Giovannetti, S. Guha, S. Lloyd, L. Maccone, J.H. Shapiro, H.P. Yuen, Classical capacity of the lossy Bosonic channel: the exact solution. Phys. Rev. Lett. **92**, 027902 (2004)
14. J.P. Gordon, Noise at optical frequencies; information theory, in *Quantum Electronics and Coherent Light*, ed. by P.A. Miles. Proceedings of the International School of Physics "Enrico Fermi", Course XXXI (Academic, New York, 1964), pp. 156–181

15. C. Elliott, A. Colvin, D. Pearson, O. Pikalo, J. Schlafer, H. Yeh, Current status of the DARPA quantum network, in *Quantum Information and Computation III*, ed. by E.J. Donkor, A.R. Pirich, H.E. Brandt. Proceedings of SPIE, vol. 5815 (2005), pp. 138–149. arXiv:quant-ph/0503058v2
16. M. Peev et al.: The SECOQC quantum key distribution network in Vienna. New J. Phys. **11**, 075001 (2009)
17. M. Sasaki et al.: Field test of quantum key distribution in the Tokyo QKD Network. Opt. Exp. **19**, 10387 (2011)
18. ID Quantique, http://www.idquantique.com/; MagiQ Technologies, Inc., http://www.magiqtech.com/MagiQ/Home.html; QuintessenceLabs Pty Ltd, http://www.quintessencelabs.com/
19. A. Waseda, M. Sasaki, M. Takeoka, M. Fujiwara, M. Toyoshima, A. Assalini, Numerical evaluation of PPM for deep-space links. J. Opt. Commun. Netw. **3**, 514 (2011)
20. R.S. Kennedy, Near-optimum receiver for the binary coherent state quantum channel. Res. Lab Electron. MIT Q. Progress Rep. **108**, 219 (1973)
21. S. Dolinar, An optimum receiver for the binary coherent state quantum channel. Res. Lab Electron. MIT Q. Progress Rep. **111**, 115 (1973)
22. A.S. Holevo, Quantum-probabilistic analysis of counting statistics with an application to the "Dolinar receiver". Izv. Vuz. Mat. **26**, 3 (1982) [Sov. Math. Dolk. **26**, 3 (1982)]
23. M. Takeoka, M. Sasaki, P. van Loock, N. Lütkenhaus, Implementation of projective measurements with linear optics and continuous photon counting. Phys. Rev. A **71**, 022318 (2005)
24. M. Takeoka, M. Sasaki, N. Lütkenhaus, Binary projective measurement via linear optics and photon counting. Phys. Rev. Lett. **97**, 040502 (2006)
25. M. Sasaki, O. Hirota, Optimum decision scheme with a unitary control process for binary quantum-state signals. Phys. Rev. A **54**, 2728–2736, (1996)
26. R.L. Cook, P.J. Martin, J.M. Geremia, Optical coherent state discrimination using a closed-loop quantum measurement. Nature **446**, 774–777 (2007)
27. V. Vilnrotter, E. Rodemich, A generalization of the near-optimum binary coherent state receiver concept. IEEE Trans. Inf. Theory **30**, 446 (1984)
28. M. Takeoka, M. Sasaki, Discrimination of the binary coherent signal: Gaussian-operation limit and simple nongaussian near-optimal receivers. Phys. Rev. A **78**, 022320 (2008)
29. C. Wittmann, M. Takeoka, K.N. Cassemiro, M. Sasaki, G. Leuchs, U.L. Andersen, Demonstration of nearoptimal discrimination of optical coherent states. Phys. Rev. Lett. **101**, 210501 (2008)
30. K. Tsujino, D. Fukuda, G. Fujii, S. Inoue, M. Fujiwara, M. Takeoka, M. Sasaki, Quantum receiver beyond the standard quantum limit of coherent optical communication. Phys. Rev. Lett. **106**, 250503 (2011)
31. K. Tsujino, D. Fukuda, G. Fujii, S. Inoue, M. Fujiwara, M. Takeoka, M. Sasaki, Sub-shot-noise-limit discrimination of on-off keyed coherent signals via a quantum receiver with a superconducting transition edge sensor. Opt. Express **18**, 8107 (2010)
32. R.S. Bondurant, Near-quantum optimum receivers for the phase-quadrature coherent-state channel. Opt. Lett. **18**, 1896 (1993)
33. F.E. Becerra, J. Fan, Baumgartner, S.V.G. Polyakov, J. Goldhar, J.T. Kosloski, A. Migdall, M-ary-state phase-shift-keying discrimination below the homodyne limit. Phys. Rev. A **84**, 062324 (2011)
34. S. Izumi, M. Takeoka, M. Fujiwara, N. Dalla Pozza, A. Assalini, K. Ema, M. Sasaki, Displacement receiver for phase-shift-keyed coherent states. Phys. Rev. A **86**, 042328 (2012)
35. F.E. Becerra, J. Fan, G. Baumgartner, J. Goldhar, J.T. Kosloski, A. Migdall, Experimental demonstration of a receiver beating the standard quantum limit for multiple nonorthogonal state discrimination. Nat. Photonics **7**, 147 (2013)
36. S. Izumi, A. Takeoka, K. Ema, M. Sasaki, Quantum receivers with squeezing and photon-number-resolving detectors for M-ary coherent state discrimination. Phys. Rev. A **87**, 042328 (2013)

37. C.R. Müller, M.A. Usuga, C. Wittmann, M. Takeoka, Ch. Marquardt, U.L. Andersen, G. Leuchs, Quadrature phase shift keying coherent state discrimination via a hybrid receiver. New J. Phys. **14**, 083009 (2012)
38. S. Guha, J.L. Habif, M. Takeoka, Approaching Helstrom limits to optical pulse-position demodulation using single photon detection and optical feedback. J. Mod. Opt. **58**, 257 (2011)
39. J. Chen, J.L. Habif, Z. Dutton, R. Lazarus, S. Guha, Optical codeword demodulation with error rates below the standard quantum limit using a conditional nulling receiver. Nat. Photonics **6**, 374 (2012)
40. D. Ivanovic, How to differentiate between non-orthogonal states. Phys. Lett. A **123**, 257 (1987); D. Dieks, Overlap and distinguishability of quantum states. Phys. Lett. A **126**, 303 (1988); A. Peres, How to differentiate between non-otrhogonal states. Phys. Lett. A **128**, 19 (1988)
41. C. Wittmann, U.L. Andersen, M. Takeoka, D. Sych, G. Leuchs, Demonstration of coherent-state discrimination using a displacement-controlled photon-number-resolving detector. Phys. Rev. Lett. **104**, 100505 (2010)
42. C. Wittmann, U.L. Andersen, M. Takeoka, D. Sych, G. Leuchs, Discrimination of binary coherent states using a homodyne detector and a photon number resolving detector. Phys. Rev. A **82**, 062338 (2010)
43. F.E. Becerra, J. Fan, A. Migdall, Implementation of generalized quantum measurements for unambiguous discrimination of multiple non-orthogonal coherent states. Nat. Commun. **4**, 2028 (2013)
44. M. Takeoka, S. Guha, Capacity of optical communication in loss and noise with general quantum Gaussian receivers. Phys. Rev. A **89**, 042309 (2014)
45. K. Yoshino, M. Fujiwara, A. Tanaka, S. Takahashi, Y. Nambu, A. Tomita, S. Miki, T. Yamashita, Z. Wang, M. Sasaki, A. Tajima, High-speed wavelength-division multiplexing quantum key distribution system. Opt. Lett. **37**, 223 (2012)
46. A. Tanaka, M. Fujiwara, K. Yoshino, S. Takahashi, Y. Nambu, A. Tomita, S. Miki, T. Yamashita, Z. Wang, M. Sasaki, A. Tajima, High-speed quantum key distribution system for 1-Mbps real-time key generation. IEEE J. Quant. Electron. **48**, 542 (2012)
47. Y. Nambu, K. Yoshino, A. Tomita, Quantum encoder and decoder for practical quantum key distribution using a planar lightwave circuit. J. Mod. Opt. **55**, 1953 (2008)
48. K. Yoshino, T. Ochi, M. Fujiwara, M. Sasaki, A. Tajima, Maintenance-free operation of WDM quantum key distribution system through a field fiber over 30 days. Opt. Express **21**, 31395 (2013)
49. J.S. Neergaard-Nielsen, Y. Eto, C.-W. Lee, H. Jeong, M. Sasaki, Quantum tele-amplification with a continuous-variable superposition state. Nat. Photonics **7**, 439 (2013)
50. A.D. Wyner, The wire-tap channel. Bell Syst. Tech. J., **54**, 1355 (1975)
51. M. Hayashi, Exponential decreasing rate of leaked information in universal random privacy amplification. IEEE Trans. Inf. Theory **IT-57**, 3989, (2011)
52. T.-S. Han, H. Endo, M. Sasaki, Reliability and security functions of the wiretap channel under cost constraint. arXiv:1307.0608 [cs.IT]

Chapter 3
Quantum Communication Experiments Over Optical Fiber

Hiroki Takesue

3.1 Evolution of Quantum Key Distribution Systems

Quantum key distribution (QKD) is a method that enables two distant parties to produce a shared random secret key known only to them, and the security of the key is guaranteed by quantum mechanics [1]. Since the invention of the Bennett-Brassard 1984 (BB84) [2] and Ekert 1991 (E91) [3] schemes, QKD has been expected to be the first quantum information processing application to be practically used, because of its simplicity. In fact, many QKD experiments have been performed, ranging from the very first proof-of-principle experiment over 32-cm free-space quantum channel [4] to large scale QKD network experiments over installed fiber networks [5, 6].

As we approach the realization of global-scale secure communication networks, QKD systems will be expected to evolve in the three phases shown in Fig. 3.1 [1]. The first phase is point-to-point systems, which are based on the simple transmission of single photons from Alice, the sender, to Bob, the receiver. Most current practical QKD systems are classified in this phase. In phase-1 systems, the photon loss in the quantum channel limits the key distribution distance; in general terms, when the single photon count rate at Bob is comparable to the dark count rates of the single photon detectors, the error rate increases, and eventually results in no secure key being generated. To increase the distance, we use entanglement as shown in Fig. 3.1b (phase 2). Here, we place an entangled photon pair source between Alice and Bob, and one photon from a pair is sent to Alice and the other to Bob. With this scheme, we can roughly double the key distribution distance of the phase-1 systems (the distance depends

H. Takesue (✉)
NTT Basic Research Laboratories, NTT Corporation, 3-1 Morinosato Wakamiya, Atsugi, Kanagawa 243-0198, Japan
e-mail: takesue.hiroki@lab.ntt.co.jp

Y. Yamamoto, K. Semba (eds.), *Principles and Methods of Quantum Information Technologies*, Lecture Notes in Physics 911, DOI 10.1007/978-4-431-55756-2_3

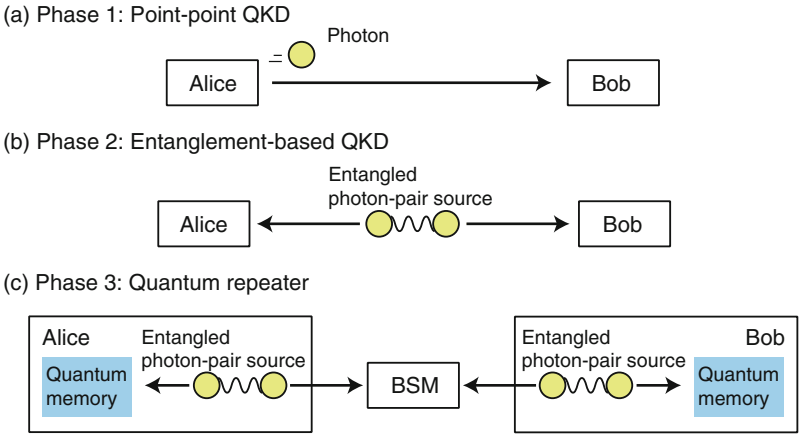

Fig. 3.1 Evolution of quantum communication. *BSM*: Bell state measurement

on the protocol and devices used in the system). In phase 3, we implement "quantum repeaters", by which we can realize fully scalable quantum communication networks [7]. Figure 3.1c shows an example of a basic link in quantum repeater implementation called a "Duan, Lukin, Cirac, and Zoller (DLCZ)" scheme [8, 9]. Here, Alice and Bob are equipped with entangled photon pair sources and quantum memories. By storing a photon from an entangled pair with the memory, Alice and Bob can generate an entanglement between a photon and an internal state of the quantum memory. By undertaking entanglement swapping [10] between the two photon-memory entanglements, Alice and Bob can share an entanglement between the internal states of their memories. A quantum repeater is constructed by concatenating those basic links using the nested entanglement swapping [7]. In the DLCZ scheme, the use of entanglement between quantum memories enables us to avoid an exponential decrease in the rate of entanglement distribution based on entanglement swapping, and thus leads to scalable quantum communication.

In the remainder of this chapter, we will review our efforts to realize those evolutions of QKD systems. In Sect. 3.2, we describe our point-to-point QKD experiments based on the differential phase shift QKD (DPS-QKD) protocol [11]. Section 3.3 focuses on entanglement-based schemes, where we discuss the generation and distribution of telecom-band entangled photon pairs, entanglement-based QKD, and entanglement swapping experiments over optical fiber. In the final section, we briefly discuss the future direction of the research on quantum communication in the telecom band.

3.2 Differential Phase Shift Quantum Key Distribution

3.2.1 Protocol

Since the invention of the first protocols [2, 3], most QKD protocols have been based on the transmission of two-level quantum states, namely qubits. In contrast, DPS-QKD does not use qubits but employs a coherent state that is spanned by many pulses [11, 12]. Figure 3.2 shows a schematic of a DPS-QKD system. Alice is equipped with a light source that emits a coherent pulse train. The phase of each pulse is modulated by 0 or π randomly, and attenuated so that the average photon number per pulse is less than 1 (typically $\sim$0.2 in experiments). The pulse train is sent to Bob through a quantum channel. Bob inputs the received attenuated pulse train into a 1-bit delayed Mach-Zehnder interferometer. When the phase difference between adjacent pulses is 0 (π), a photon is output from Port A (B) and the corresponding detector clicks. Bob records the time instances at which he observed the clicks and which detectors clicked. He then discloses the time instance information to Alice through a classical communication line. From her original modulation data at each time instance, she now knows which detector clicked on Bob's side. By converting the which-detector information into 0 and 1, Alice and Bob now share an identical bit string that can be used as a key for one-time pad cryptography.

The security of the DPS-QKD protocol has been of great interest to the QKD theory community. Since a detailed description of DPS-QKD security is beyond the scope of this chapter, here we briefly consider security against two simple attacks, namely intercept-and-resend (IR) and photon-number-splitting (PNS) attacks, to obtain a rough idea of why this protocol works as a QKD.

The IR attack is the most basic attack against QKD. An eavesdropper (Eve) intercepts photons just after Alice has launched them into the quantum channel, and measures these photons using the same measurement apparatus as Bob. Eve sometimes obtains the phase difference information $\phi_k (= \{0, \pi\})$, where subscript

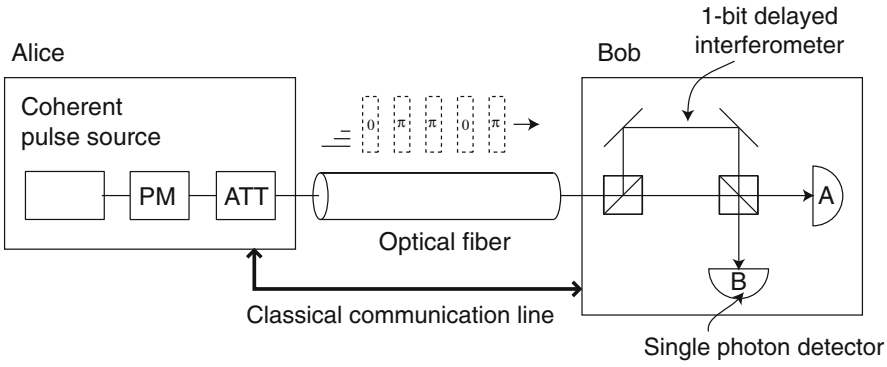

Fig. 3.2 DPS-QKD system. *PM*: optical phase modulator, *ATT*: optical attenuator

k denotes the number of time slots at which Eve's detectors clicked. Then, Eve prepares single photons whose states are given by $(|k-1\rangle + e^{i\phi_k}|k\rangle)/\sqrt{2}$ and sends them to Bob. Here, $|x\rangle$ denotes a state where there is a photon in time slot x. Bob inputs the received photons into a 1-bit delayed Mach-Zehnder interferometer, which converts state $|x\rangle$ to $\frac{1}{2}(|x\rangle_1 - |x\rangle_2 + |x+1\rangle_1 + |x+1\rangle_2)$, where the subscripts denote the output ports of the interferometer. Thus, the state resent by Eve is converted to

$$\frac{1}{\sqrt{2}}\left[|k-1\rangle_1 - |k-1\rangle_2 + (1+e^{i\phi_k})|k\rangle_1 + (1-e^{i\phi_k})|k\rangle_2 \right.$$
$$\left. + e^{i\phi_k}|k+1\rangle_1 + e^{i\phi_k}|k+1\rangle_2\right]. \tag{3.1}$$

This suggests that Bob observes clicks possibly at three time slots, and obtains conclusive results only at the kth time slot. When Bob observes clicks at the $k \pm 1$th slots (with a probability of 1/2), his measurement result is random, leading to a 25 % error rate. Thus, Alice and Bob can detect an IR attack by monitoring the error rate of their quantum transmission.

Next, we consider a PNS attack, which severely limits the key distribution distance of conventional QKD systems [13, 14]. Let us first consider the PNS attack against BB84 QKD systems with attenuated laser sources. Eve performs a quantum non-demolition (QND) measurement [15] on attenuated coherent pulses emitted by Alice, by which she measures the number of photons contained in each pulse (i.e. qubit). When she observes two or more photons in a pulse, Eve extracts one photon and sends the rest directly to Bob so that Eve can force Bob's detectors to click at the pulse where she observed multiphotons. This means that Eve obtains a complete "copy" of the information sent to Bob without causing any errors. The probability of observing multi-photons in a coherent pulse with an average photon number per pulse of μ is approximately given by μ^2. On the other hand, when there is no eavesdropping, Bob's count rate per pulse is given by $\mu\alpha$ (α: quantum channel transmittance including the detection efficiency of the photon detector). This means that when μ^2 is larger than $\mu\alpha$, all the clicks Bob observes can be caused by pulses attacked by Eve. Therefore, μ should be smaller than α in order to obtain a secure key, and thus the secure key rate is proportional to α^2, resulting in a rapid decrease in the key rate at a long transmission distance.

Then, what happens if Eve executes a PNS attack on DPS-QKD? As in the case of BB84, she undertakes the PNS attack on coherent pulses from Alice. If she performs a QND measurement on *each pulse*, it only disrupts the phase coherence between pulses and she does not obtain any phase difference information. If Eve measures the photon number in *two consecutive pulses* using QND, she can obtain a "copy" of a quantum state spanned by two time slots as long as she observes a multiphoton. However, such a QND measurement, which determines the photon number in two specific pulses, changes the initial coherent state spanned by many pulses into photon number states spanned by two pulses. This means that, after the QND measurement, the state sent to Bob is the photon number state that is the same

as the state resent by Eve in the IR attack described above, and thus results in a 25 % error rate as shown in Eq. (3.1). Thus, a PNS attack against the DPS-QKD protocol induces errors, and so the number of bits that can be obtained by this attack is always limited. Eve can reduce the error probability by increasing the number of pulses for the QND measurement, but the probability that Eve obtains the same information as Bob decreases. Therefore, the PNS attack is not effective against the DPS-QKD protocol, which is a significant advantage over practical BB84 QKD systems using attenuated laser sources. We should note that BB84 QKD with attenuated laser sources can be secure against a PNS attack if it is implemented with the decoy state method [16–18], however, it incurs additional system overheads. On the other hand, DPS-QKD is inherently secure against this powerful attack with a very simple setup.

Because of its uniqueness, the DPS-QKD protocol has attracted the interest of many QKD theorists. Several attacks against DPS-QKD [19, 20] and countermeasures [21] have been studied. The DPS-QKD protocol using an attenuated laser source has been proven secure against general individual attacks [22], and intensive efforts to prove unconditional security are under way [23].

3.2.2 *Experiments*

The first DPS-QKD experiment was undertaken in the 0.8 μm band in 2003 [12], and the first experiment over fiber was reported in 2004 [24]. Since then, many record-breaking QKD experiments have been demonstrated using the DPS-QKD protocol. Here, we describe the most representative experiment that achieved the long-distance record in 2007 [25].

Figure 3.3 shows the experimental setup. A continuous light from an external cavity diode laser was modulated into a 20-ps, 10-GHz pulse train using the nonlinear response of an electro-absorption modulator. The pulses were phase-modulated by $\{0, \pi\}$ using a lithium-niobate phase modulator, and attenuated so that the average photon number per pulse was 0.2. Then, the attenuated pulse train was transmitted over 200-km dispersion shifted fiber (DSF) spools, and received by Bob. Bob was equipped with a 1-bit delayed Mach-Zehnder interferometer based

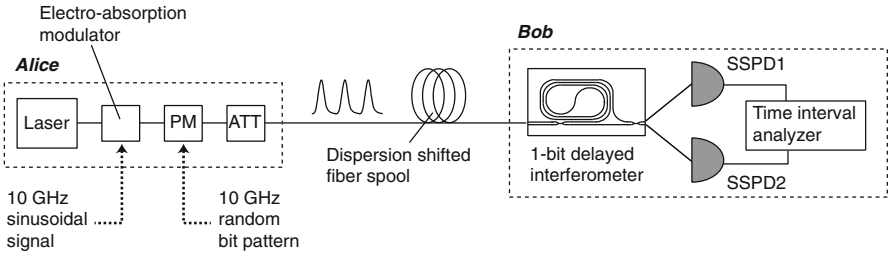

Fig. 3.3 Experimental setup of DPS-QKD

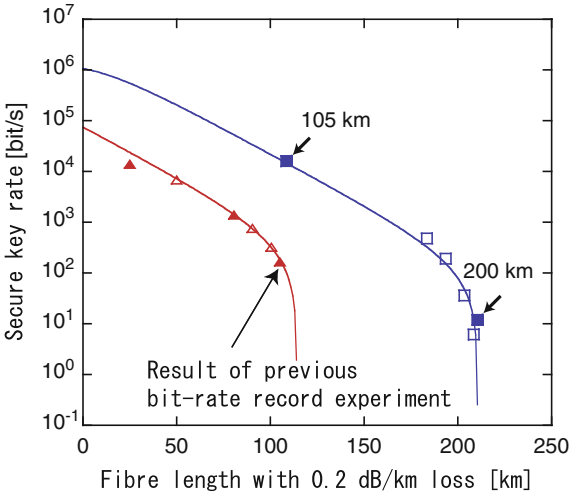

Fig. 3.4 Result of long-distance QKD experiment. *Squares* show the results obtained with the 10-GHz clock DPS-QKD system [25], while the *triangles* shows the results reported in [27]. The *filled* and *open symbols* denote fiber transmissions and optical attenuation, respectively

on a silica waveguide [24], and the interferometer output ports were connected to superconducting single photon detectors (SSPD) [26]. The SSPD was composed of a superconducting niobium nitride nanowire biased slightly below the critical current. When a photon hits the nanowire, the superconducting state is temporarily destroyed and the nanowire becomes resistive, leading to the generation of a voltage pulse. By detecting this voltage pulse, we can detect the arrival of the photon with a very high timing resolution (∼60 ps) with a very low dark count rate. In this experiment, the detection efficiency and dark count probability were 1.5 % and 25 cps for both detectors. The detection signals from the SSPDs were input into a time interval analyzer, which recorded the photon detection times and which detector information.

Figure 3.4 shows the experimental data, which includes the key generation rate as a function of fiber length. Here, the generated key is secure against general individual attacks [22] and the sequential attack considered in [19]. At a fiber distance of 105 km, we achieved a secure key rate of 17 kbit/s, which is two orders of magnitude larger than the previous bit rate record set in 2006 [27]. The maximum secure key distribution distance was 200 km, with a secure key rate of 12 bit/s. Thus, in this experiment we achieved both a significant speed increase and an extension of the key distribution distance, thanks to the high-speed clock implementation and low-noise characteristics of SSPD.

We have undertaken not only laboratory experiments but also the development of QKD systems that can be used in installed fiber networks. In 2010, we participated in a QKD demonstration over a fiber network in Tokyo (Tokyo QKD network) [6]. We developed a DPS-QKD system in which we implemented not only sifted key generation but also other signal processing parts such as error correction and privacy amplification functions. With this system, the NTT team achieved secure communication over a 90-km link between two cities in Tokyo, which was the longest link in the network. We successfully achieved the first demonstration of a QKD-protected TV conference in this demonstration.

3.3 Telecom-Band Entanglement and Applications

3.3.1 Telecom-Band Entanglement Sources

The invention of polarization entangled photon pair sources based on type-II and type-I spontaneous parametric downconversion (SPDC) in bulk crystals [28, 29] triggered a series of important demonstrations of photonic quantum information processing. However, those sources generate photons in short wavelength bands (typically around 800 nm), and thus are not suitable for quantum communication experiments over optical fiber. Starting in the early 2000s, several experiments on telecom-band correlated/entangled photon pair sources were reported. In many of these experiments, photon pairs were generated through spontaneous parametric processes as in the short wavelength band experiments. The important difference between this telecom-band entanglement generation and those in the short wavelengths bands is that we can use technologies such as the optical waveguide devices and narrowband optical filters developed for optical communication systems. Thanks to the optical waveguide devices, we can obtain a high optical power density, which results in a significant enhancement of optical nonlinearity. Thus, highly efficient photon pair generation was possible. The availability of narrowband filters enabled us to use both SPDC and near-degenerate spontaneous four-wave mixing (SFWM) process to generate telecom-band photon pairs, where the wavelengths of the signal and idler photon pairs are closer to that of pump light than in SPDC.

When a pump light is strong and can be regarded as a classical oscillator, the interaction Hamiltonian of the spontaneous parametric process for generating correlated photon pairs is expressed as

$$H_{int} = i\hbar\chi(a_s^\dagger a_i^\dagger - a_s a_i), \tag{3.2}$$

where a_x ($a_x^\dagger$) denotes the annihilation (creation) operator for the mode x ($= s$: signal, i: idler). The constant χ for SPDC and SFWM is expressed as

$$\chi_{SPDC} = c\chi^{(2)}a_p \tag{3.3}$$

$$\chi_{SFWM} = c'\chi^{(3)}a_{p1}a_{p2} \tag{3.4}$$

where a_p, a_{p1} and a_{p2} denote the pump field amplitudes. Using the interaction Hamiltonian given by Eq. (3.2), we can obtain the following state after the time evolution.

$$|\Psi(t)\rangle = \frac{1}{C}\left\{|0,0\rangle + T|1,1\rangle + T^2|2,2\rangle + \cdots\right\} \tag{3.5}$$

Here, $C = \cosh\chi t$, $T = \tanh\chi t$ and t is the time of nonlinear interaction inside the nonlinear medium. $|j,k\rangle$ is a state with j signal and k idler photons. When we use a relatively small pump power, the higher order terms on the right hand side

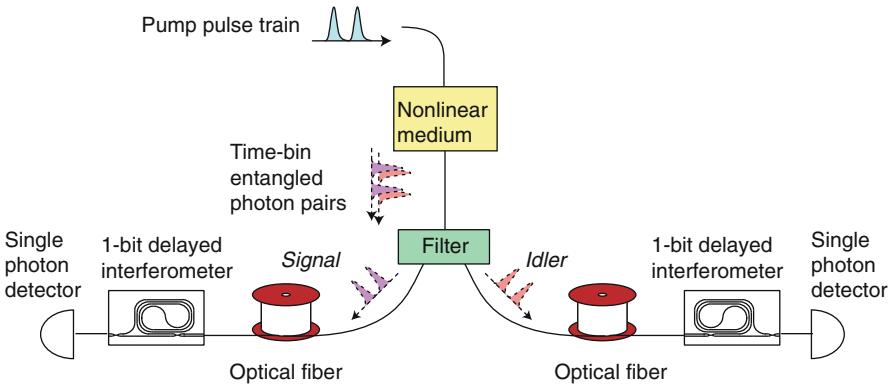

Fig. 3.5 Setup for generating and distributing time-bin entangled photon pairs

of Eq. (3.5) can be neglected, and thus we can selectively observe the photon pair state ($|1, 1\rangle$) by performing coincidence measurements between the signal and idler photons.

We can generate entangled photon pair states based on various parameters such as polarization modes and temporal modes. To date, polarization modes are most widely used in photonic quantum information experiments. However, the polarization of light is hard to stabilize and manipulate in optical fiber, because of the fluctuation in the fiber birefringence caused by changes in the environment such as temperature fluctuations. In contrast, a time-bin entangled state [30], which is a coherent superposition of photon pair states at different temporal modes, is suitable for quantum communication over optical fiber, since a time-bin qubit uses a single polarization mode. The setup for generating time-bin entangled photon pairs is shown in Fig. 3.5. A coherent double pulse is launched into a nonlinear medium. Through SPDC or SFWM processes in the nonlinear medium, we can generate a photon pair state $|k\rangle_s|k\rangle_i$ at the temporal positions of the $k(=\{1, 2\})$th pump pulse. Since the pump pulses are mutually coherent, the relative phase of the photon pair states is fixed. As a result, we can generate a time-bin entangled state given by the following equation.

$$|\Psi\rangle = \frac{1}{\sqrt{2}}(|1\rangle_s|1\rangle_i + |2\rangle_s|2\rangle_i) \tag{3.6}$$

The photons generated from the nonlinear medium are launched into an optical filter to suppress the pump light and separate the signal and idler photons by wavelength. Then, each photon is input into a 1-bit delayed Mach-Zehnder interferometer, whose output port is connected to a single photon detector. The interferometer converts the input state $|k\rangle_x$ into $(|k\rangle + e^{i\theta_x}|k+1\rangle)/2$, where θ_x represents the phase difference between two arms of the interferometer for mode x. This means that the total state $|\Psi\rangle$ is converted to

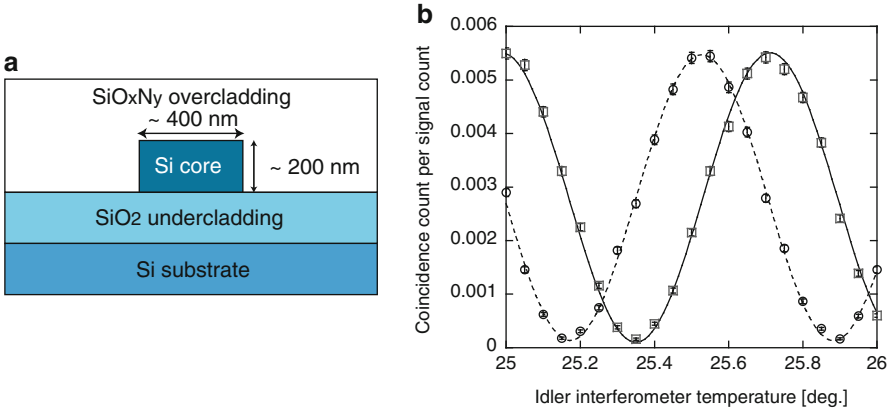

Fig. 3.6 (**a**) Typical cross-section of the structure of a SWW, (**b**) two-photon interference fringes obtained with a silicon-based entanglement source

$$|\Psi\rangle \rightarrow |1\rangle_s|1\rangle_i + (1 + e^{i(\theta_s+\theta_i)})|2\rangle_s|2\rangle_i + e^{i(\theta_s+\theta_i)}|3\rangle_s|3\rangle_i. \tag{3.7}$$

Here, only the terms that contribute to the coincidence counts are shown and the normalization term is discarded for simplicity. The above equation shows that we possibly observe a photon in either of three time slots, and we observe two-photon interference fringes in the coincidence counts at the 2nd time slot.

The NTT team reported several pioneering studies regarding the generation of 1.5-μm band entangled photon pairs. After demonstrating the first polarization-entanglement generation using a DSF [31], we reported the generation of time-bin entangled photon pairs using SFWM in a DSF [32] and SPDC in periodically-poled lithium niobate (PPLN) waveguides [33]. More recently, we reported the first study on entanglement generation using SFWM in a silicon wire waveguide (SWW) [34, 35]. An SWW is a single-crystal, single-mode silicon waveguide whose core size is as small as several hundreds of nanometers. Figure 3.6a shows a typical cross-section of a SWW. Thanks to the tight confinement of light inside of this small waveguide, we can obtain highly efficient SFWM gain and thus realize a correlated/entangled photon pair source whose length can be as small as 1 cm. Two-photon interference fringes obtained from a silicon-based time-bin entanglement source are shown in Fig. 3.6b. The SWW used for the source was 460 nm wide, 200 nm thick, and 1.15 cm long. In the two-photon interference measurement, we used silica-waveguide interferometers that were similar to that used in DPS-QKD experiments. The interferometer phases were tuned by changing the waveguide temperature. The idler interferometer temperature was set at 20.68 °C (squares) and 20.88 °C (circles), which correspond to two non-orthogonal measurement bases. The fringe visibilities were 96.3 % (idler interferometer temperature: 20.68 °C) and 95.2 % (20.88 °C), which confirmed the generation of high-purity entangled photons from the SWW.

3.3.2 *Long-Distance Entanglement Distribution and Entanglement-Based QKD*

The distribution of quantum entanglement is an essential part of quantum communication. The biggest advantage of using telecom-band entanglement sources is that we can distribute entanglement over long distances using optical fiber. Here, we describe our record-setting long-distance entanglement distribution and entanglement-based QKD experiments.

The setup for the entanglement distribution is very similar to that shown in Fig. 3.5, except that a transmission fiber is inserted in each of the signal and idler channels. With this setup, the NTT team set a record distance of 300 km in 2013 [36]. We used SPDC in a PPLN waveguide pumped by 2-GHz clock sequential pulses to generate a high-dimensional time-bin entangled state given by

$$|\Psi\rangle = \frac{1}{\sqrt{N}} \sum_{k=1}^{N} |k\rangle_s |k\rangle_i, \tag{3.8}$$

where N denotes the number of time slots within the coherence time of the pump. The generated photons were separated into the signal (1547 nm) and idler (1555 nm) photons by a wavelength filter. After transmission over 150 km of DSF, each photon was input into a delayed Mach-Zehnder interferometer based on a silica waveguide [24], which is followed by an SSPD. The detection efficiency and the dark count probability per gate of both detectors were 20 % and 10 cps, respectively. We obtained the two-photon interference fringes shown in Fig. 3.7a. Thus, we observed clear sinusoidal modulations in the coincidence counts even after the signal and idler photons were separated by 300 km of fiber. The visibilities of the fitted curves were

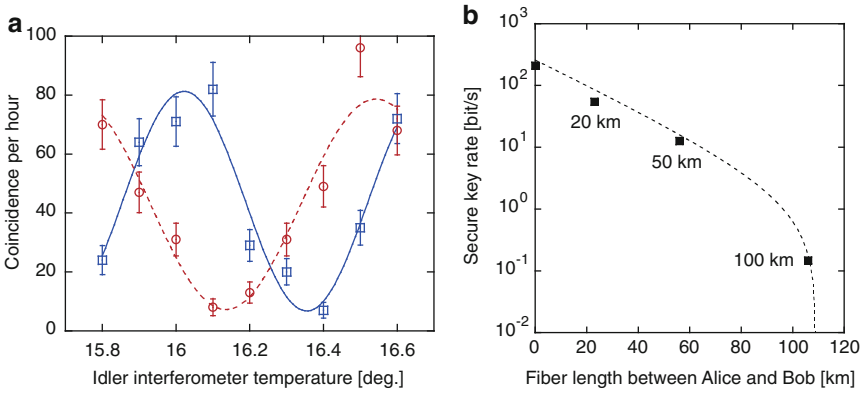

Fig. 3.7 (**a**) Two-photon interference fringes after 300-km distribution over fiber, (**b**) secure key rate as a function of fiber length between Alice and Bob. The *fitted curve* was calculated based on the theory shown in [40]

$86.1 \pm 6.8\,\%$ (squares: idler interferometer temperature 15.35 °C) and $83.7 \pm 9.1\,\%$ (circles: 15.54 °C). We also performed an S value measurement for the CHSH inequality. We obtained $S = 2.41 \pm 0.14$, leading to the violation of Bell's inequality by 2.9 standard deviations.

Our group also implemented QKD based on the Bennett-Brassard-Mermin 1992 (BBM92) protocol using the SWW-based entanglement source described above [37].

In a QKD system based on the BBM92 protocol, the entanglement source is placed between Alice and Bob, and one photon from the source is sent to Alice and the other to Bob. Alice and Bob measure each received photon by using a measurement that is randomly chosen from two non-orthogonal measurement bases. After measuring many pairs, Alice and Bob disclose the measurement bases used for each measurement via classical communication, while keeping the measurement results confidential. According to the nature of maximally-entangled photon pairs, the measurement results obtained by Alice and Bob for a pair of photons are always correlated if their bases coincide. Therefore, they can obtain correlated measurement results by extracting the events when their bases coincide, and the correlated results can be converted into a secret key for one-time pad cryptography.

The experimental setup is similar to that for time-bin entanglement generation shown in Fig. 3.5. In this experiment, the entanglement source generated a time-bin entanglement whose state is shown by Eq. (3.6), and two single photon detectors were connected to the two output ports of each 1-bit delayed interferometer. We implemented two non-orthogonal measurements, namely, "energy basis" and "time basis" measurements, in the following way [38]. As already stated, when a time-bin qubit passes through a 1-bit delayed interferometer, we can possibly observe a click in three time slots. A click in the second time slot is referred to as an "energy basis" measurement, while a click either in the first or third slot is called a "time basis" measurement. The 1-bit delayed interferometers convert a quantum state $|k\rangle_x$ to $\frac{1}{2}\left(|k, p_1\rangle_x - |k, p_2\rangle_x + |k+1, p_1\rangle_x + |k+1, p_2\rangle_x\right)$, where p_1 and p_2 denote the interferometer output ports. Then, Eq. (3.6) is converted to

$$
\begin{aligned}
|\Psi\rangle \rightarrow \frac{1}{4\sqrt{2}} \{ & |1, p_1\rangle_s |1, p_1\rangle_i - |1, p_1\rangle_s |1, p_2\rangle_i - |1, p_2\rangle_s |1, p_1\rangle_i + |1, p_2\rangle_s |1, p_2\rangle_i \\
& + 2|2, p_1\rangle_s |2, p_1\rangle_i + 2|2, p_2\rangle_s |2, p_2\rangle_i + |3, p_1\rangle_s |3, p_1\rangle_1 + |3, p_1\rangle_s |3, p_2\rangle_i \\
& + |3, p_2\rangle_s |3, p_1\rangle_i + |3, p_2\rangle_s |3, p_2\rangle_i \} ,
\end{aligned} \tag{3.9}
$$

where the terms that do not contribute to the coincidences in the matched bases are not shown. The 5th and 6th terms on the right hand side of Eq. (3.9) correspond to the coincidences in the energy basis, while other terms correspond to those in the time basis. This equation shows that we observe a correlation in the "ports" in energy basis measurements, and in the "time slots" in time basis measurements.

Using 100-MHz clock time-bin entangled photon pairs together with 500-MHz sine-wave gated single photon detectors based on an InGaAs/InP APD [39], we undertook a BBM92 QKD experiment [37]. We used a fiber-coupled SWW that

was 460 nm wide, 220 nm thick, and 0.9 nm long. For long-distance key distribution experiments, we inserted DSFs as transmission fibers with lengths of up to 50 km in both arms of the signal and idler channels. The obtained secure key rate as a function of the fiber length between Alice and Bob is shown in Fig. 3.7b. Thus, we successfully distributed keys over 100 km of optical fiber with a secure key rate of 0.15 bit/s. Moreover, we obtained a secure key rate of 208 bit/s, which is larger than the previous record for an entanglement-based QKD experiment using a 1.5-μm entanglement source [41].

3.3.3 *Entanglement Swapping*

As stated in Sect. 3.1, entanglement swapping is an essential ingredient for scalable quantum communication systems based on quantum repeaters. Since an entanglement swapping experiment requires four-photon coincidence counting, it is extremely difficult in the 1.5 μm band where single photon detectors have lower detection efficiencies than the visible wavelength band detectors based on silicon APD. As a result, only a few entanglement swapping experiments have been reported in the 1.5 μm band [42–44]. Here we introduce our experiment in which we realized high-speed entanglement swapping [43].

Figure 3.8 shows our experimental setup. We used two independent high-dimensional time-bin entanglement sources using DSFs pumped by a 500-MHz, 20-ps sequential pulse train. Here, the DSFs were cooled by liquid nitrogen to suppress the noise photons generated by spontaneous Raman scattering [45]. The total state of the photon pairs generated from the two sources is expressed as

$$|S\rangle = \frac{1}{N}\left(\sum_{j=1}^{N}|j\rangle_{1s}|j\rangle_{1i}\right)\otimes\left(\sum_{k=1}^{N}|k\rangle_{2s}|k\rangle_{2i}\right), \tag{3.10}$$

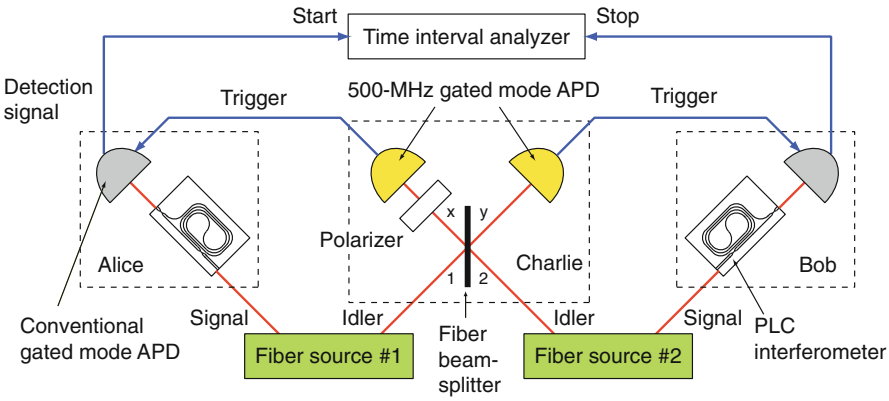

Fig. 3.8 Entanglement-swapping setup

where subscripts 1 and 2 denote the source where the photons with respective quantum state was generated. The signal photons from sources 1 and 2 were sent to Alice and Bob, respectively. Alice and Bob were equipped with 1-bit delayed Mach-Zehnder interferometers followed by single photon detectors based on InGaAs/InP APD operated in a gated mode. On the other hand, idler photons from both sources were sent to the intermediate node Charlie, who was equipped with a fiber beamsplitter (BS) whose output ports were connected to an InGaAs/InP APD operated in a sine-wave gated mode with a 500 MHz frequency [39]. With the BS, the joint state formed by two idler photons was projected to one of the four Bell states. Using the four Bell states $|\Phi_k^{\pm}\rangle = (|k\rangle_{1i}|k\rangle_{2i} \pm |k+1\rangle_{1i}|k+1\rangle_{2i})/\sqrt{2}$ and $|\Psi_k^{\pm}\rangle = (|k\rangle_{1i}|k+1\rangle_{2i} \pm |k+1\rangle_{1i}|k\rangle_{2i})/\sqrt{2}$, the whole state shown by Eq. (3.10) can be rewritten as

$$
\begin{aligned}
|S\rangle \rightarrow \frac{1}{N\sqrt{2}} \Bigg\{ & \sum_{k=1}^{N} |k\rangle_{1s}|k\rangle_{2s}(|\Phi_k^+\rangle + |\Phi_k^-\rangle) \\
& + \sum_{k=1}^{N-1} (|k\rangle_{1s}|k+1\rangle_{2s} + |k+1\rangle_{1s}|k\rangle_{2s})|\Psi_k^+\rangle \\
& + (|k\rangle_{1s}|k+1\rangle_{2s} - |k+1\rangle_{1s}|k\rangle_{2s})|\Psi_k^-\rangle \Bigg\}. \qquad (3.11)
\end{aligned}
$$

Here, the states that are not observed in our coincidence measurements using 1-bit delayed interferometers are discarded for simplicity. At the BS owned by Charlie, an idler state $|k\rangle_{1i}$ ($|k\rangle_{2i}$) is converted to $(|k\rangle_x - |k\rangle_y)/\sqrt{2}$ ($(|k\rangle_x + |k\rangle_y)/\sqrt{2}$), where the subscripts denote the output ports. Therefore, when a Bell state $|\Psi_k^-\rangle$ is input into the BS, the output state is given by $(|k\rangle_x|k+1\rangle_y - |k+1\rangle_x|k\rangle_y)/\sqrt{2}$, implying that only this state gives a coincidence count between detectors x and y, and thus can be distinguished from the other three Bell states. Therefore, we adjusted the temporal position of the detector gates for channels x and y to detect photons in the $(k+1)$th and the kth time slots, respectively, by which we can implement a projection measurement on a portion of $|\Psi_k^-\rangle$ (i.e. $\frac{1}{\sqrt{2}}|k+1\rangle_x|k\rangle_y$). The detection signals from the detectors x and y were used as a gate signal for Alice's and Bob's detectors, respectively. This means that the coincidence events between Alice and Bob's detectors were conditioned by the projection measurement undertaken by Charlie. Then, according to Eq. (3.11), the two signal photons detected by Alice and Bob form an entangled state $(|k\rangle_{1s}|k+1\rangle_{2s} - |k+1\rangle_{1s}|k\rangle_{2s})/\sqrt{2}$.

We first removed the interferometers at Alice and Bob to observe the quantum interference between two photons generated from the independent fiber sources. The result is shown in Fig. 3.9a, where we observed a clear Hong-Ou-Mandel dip whose visibility was 64 ± 8 %, which is larger than the classical limit of 50 %. Thus, we could successfully generate near-indistinguishable photons in the 1.5-μm band using two independent fiber sources.

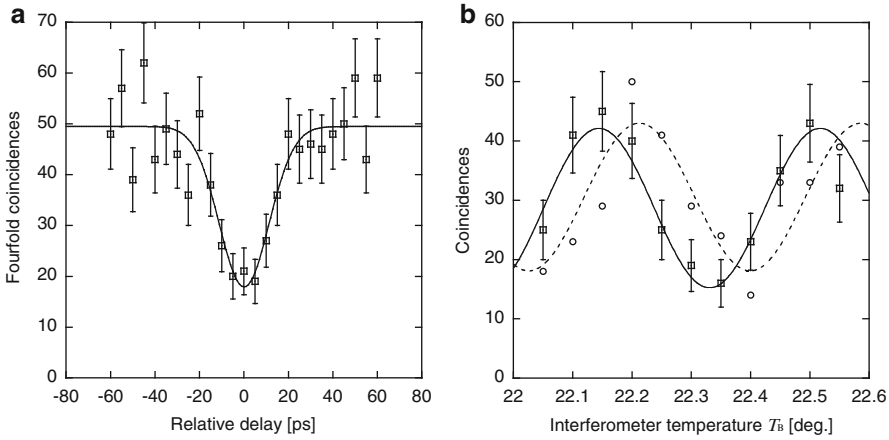

Fig. 3.9 Results of entanglement swapping experiments

We finally inserted the interferometers into the setup, and performed two-photon interference measurements. The result is shown in Fig. 3.9b. Clear sinusoidal modulations were observed in the coincidence counts, implying that the two signal photons coming from independent sources were now correlated. The visibilities of the fringes were 47 ± 7 (Alice's interferometer temperature: 32.25 °C) and 41 ± 9 % (32.35 °C). If we assume the generated state was in a Werner state, a visibility larger than 1/3 implies the existence of entanglement between two photons [46]. Therefore, the present result suggests the formation of entanglement.

We believe this experiment is important because it showed the possibility of developing high-speed quantum communication systems based on multi-coincidences using telecom technologies. The indistinguishable photon generation with externally-modulated pump pulses reported here is expected to become an essential technology. Unfortunately, the fidelity of the entanglement in this experiment was not very good. The biggest reason is the limited detection efficiencies of the detectors in the 1.5-μm band compared with that in the near-visible wavelength bands. Because of this, we needed to increase the average photon number from each source so that we could observe a sufficient number of coincidences. However, there have been several studies that realized telecom-band single photon detectors with near-unity detection efficiencies [47]. With our high-speed indistinguishable photon sources combined with such cutting edge detector technologies, we expect to be able to construct sophisticated quantum communication systems based on multi-photon interferometry in the near future.

3.4 Summary and Future Outlook

This chapter described the progress of technologies related to quantum communication over optical fiber. The development of phase 1 quantum communication systems based on the DPS-QKD protocol is summarized Sect. 3.2. We have achieved QKD over 200 km of fiber, and demonstrated a QKD-protected TV conference using an installed fiber network in Tokyo. With those successful results as well as the development of practical QKD systems by other institutions, we can now say that QKD is the first quantum information technology that can be put to practical use.

The key technology for future quantum communication, namely the generation of 1.5-μm band entangled photon pairs and applications were reviewed in Sect. 3.3. Entanglement sources based on DSFs, PPLN waveguides, and SWWs are now promising candidates for phase-2 quantum communication. It was also shown that quantum entanglement was distributed over long fibers and quantum keys were generated using distributed entanglement. These results indicate that we can extend the quantum communication distance using entanglement. Finally, entanglement swapping was successfully demonstrated using 1.5-μm entangled photon pairs, which will be an important building block of phase 3 quantum communication systems based on the quantum repeater protocol.

An important missing element in terms of realizing quantum repeaters is quantum memory. Many schemes have already been examined, including the use of optical delay lines, electromagnetically induced transparency, and photon echo [48]. Unfortunately, most current quantum memories are for non-telecom wavelength bands, and thus it is difficult to use them directly in quantum communication systems over optical fiber. There have been several reports on 1.5-μm band quantum memories, but characteristics such as efficiency and coherence time are not yet suitable for practical use [49, 50]. An interesting approach is to use quantum frequency conversion (QFC) [51] for connecting short-wavelength photonic quantum systems such as quantum memories and 1.5-μm photons. Several QFC experiments have been reported, including high-efficiency single photon detection [52], phase-sensitive QFC [53], erasure of frequency distinguishability [54], and the frequency downconversion of a single photon [55]. By integrating all these components (entanglement sources, detectors, memories, QFCs), in theory we can realize a quantum repeater. However, further improvements are needed for all these components if we are to realize scalable quantum communication, since the requirements for the components are very demanding.

An interesting research area spun out from telecom-band quantum communication technologies is integrated quantum photonics [56]. The concept is to realize photonic quantum information processing circuits using optical waveguide devices, so that we can increase the integration level with better circuit stability. The NTT team is the first group to use silica waveguide technologies for quantum information experiments, namely QKD [24] and time-bin entanglement measurements [32]. Since these experiments, silica waveguides are now being used in many quantum

information processing studies [56, 57]. As stated in Sect. 3.3, silicon waveguides are also attractive platforms for photonic quantum information processing, since we can realize active components such as entanglement sources on a chip, as described in this chapter [34]. In addition, other functions such as single photon detectors [58, 59] and a buffer [60] integrated on silicon chips have been demonstrated recently. Furthermore, technologies for connecting different waveguides, including silica, silicon and lithium niobate waveguides, are now being developed for optical communication systems [61]. Using these technologies, we may be able to realize advanced quantum information processing based on hybrid photonic quantum circuits.

Acknowledgements The work described here is the result of collaborations with many researchers. I would like to thank all my collaborators, in particular Prof. Kyo Inoue (Osaka University) and Dr. Toshimori Honjo (NTT Laboratories).

References

1. N. Gisin, R. Thew, Quantum communication. Nat. Photon. **1**, 165–171 (2007)
2. C.H. Bennett, G. Brassard, Quantum cryptography: public key distribution and coin tossing, in *Proceedings of IEEE International Conference on Computers, Systems and Signal Processing*, Bangalore, (1984), pp. 175–179
3. A.K. Ekert, Quantum cryptography based on Bell's theorem. Phys. Rev. Lett. **67**, 661 (1991)
4. C.H. Bennett, F. Bessette, G. Brassard, L. Salvail, J. Smolin, Experimental quantum cryptography. J. Cryptol. **5**, 3–28 (1992)
5. M. Peev et al., The SECOQC quantum key distribution network in Vienna. New J. Phys. **11**, 075001 (2009)
6. M. Sasaki et al., Field test of quantum key distribution in the Tokyo QKD network. Opt. Express **19**, 10387–10409 (2011)
7. H.J. Briegel, W. Dur, J.I. Cirac, P. Zoller, Quantum repeaters: the role of imperfect local operation in quantum communication. Phys. Rev. Lett. **81**, 5932–5935 (1998)
8. L.-M. Duan, M.D. Lukin, J.I. Cirac, P. Zoller, Long-distance quantum communication with atomic ensembles and linear optics. Nature **414**, 413–418 (2001)
9. N. Sangouard, C. Simon, H. de Riedmatten, N. Gisin, Quantum repeaters based on atomic ensembles and linear optics. Rev. Mod. Phys. **83**, 33 (2011)
10. J.W. Pan, D. Bouwmeester, H. Weinfurter, A. Zeilinger, Experimental entanglement swapping: entangling photons that never interacted. Phys. Rev. Lett. **80**, 3891–3894 (1998)
11. K. Inoue, E. Waks, Y. Yamamoto, Differential phase shift quantum Key distribution. Phys. Rev. Lett. **89**, 037902 (2002)
12. K. Inoue , E. Waks, Y. Yamamoto, Differential-phase-shift quantum key distribution using coherent light. Phys. Rev. A **68**, 022317 (2003)
13. G. Brassard, N. Lutkenhaus, T. Mor, B.C. Sanders, Limitations on practical quantum cryptography. Phys. Rev. Lett. **85**, 1330–1333 (2000).
14. N. Lutkenhaus, Security against individual attacks for realistic quantum key distribution. Phys. Rev. A **61**, 052304 (2000)
15. N. Imoto, H.A. Haus, Y. Yamamoto, Quantum nondemolition measurement of the photon number via the optical Kerr effect. Phys. Rev. A **32**, 2287–2292 (1985)
16. W.Y. Hwang, Quantum key distribution with high loss: toward global secure communication. Phys. Rev. Lett. **91**, 057901 (2003)
17. H.K. Lo, X. Ma, K. Chen, Decoy state quantum key distribution. Phys. Rev. Lett. **94**, 230504 (2005)

18. X.B. Wang, Beating the photon-number-splitting attack in practical quantum cryptography. Phys. Rev. Lett. **94**, 230503 (2005)
19. M. Curty, L.L. Zhang, H.K. Lo, N. Lutkenhaus, Sequential attacks against differential-phase-shift quantum key distribution with weak coherent states. Quant. Inf. Comput. **7**, 665 (2007)
20. T. Tsurumaru, Sequential attack with intensity modulation on the differential-phase-shift quantum-key-distribution protocol. Phys. Rev. A **75**, 062319 (2007)
21. H. Kawahara, A. Oka, K. Inoue, Differential-phase-shift quantum key distribution with phase modulation to combat sequential attacks. Phys. Rev. A **84**, 052311 (2011)
22. E. Waks, H. Takesue, Y. Yamamoto, Security of differential-phase-shift quantum key distribution against individual attacks. Phys. Rev. A **73**, 012344 (2006)
23. K. Wen, K. Tamaki, Y. Yamamoto, Unconditional security of single-photon differential phase shift quantum key distribution. Phys. Rev. Lett. **103**, 170503 (2009)
24. T. Honjo, K. Inoue, H. Takahashi, Differential-phase-shift quantum key distribution experiment with a planar light-wave circuit Mach-Zehnder interferometer. Opt. Lett. **29**, 2797–2799 (2004)
25. H. Takesue, S.W. Nam, Q. Zhang, R. H. Hadfield, T. Honjo, K. Tamaki, Y. Yamamoto, Quantum key distribution over a 40 dB channel loss using superconducting single-photon detectors. Nat. Photon. **1**, 343–348 (2007)
26. G.N. Gol'tsman, O. Okunev, G. Chulkova, A. Lipatov, A. Semenov, K. Smirnov, B. Voronov, A. Dzardanov, C. Williams, R. Sobolewski, Picosecond superconducting single-photon optical detector. Appl. Phys. Lett. **79**, 705–707 (2001)
27. E. Diamanti, H. Takesue, C. Langrock, M.M. Fejer, Y. Yamamoto, 100 km differential phase shift quantum key distribution experiment with low jitter up-conversion detectors. Opt. Express **14**, 13073–13082 (2006)
28. P.G. Kwiat, K. Mattle, H. Weinfurter, A. Zeilinger, A.V. Sergienko, Y. Shih, New high-intensity source of polarization-entangled photon pairs. Phys. Rev. Lett. **75**, 4337–4341 (1995)
29. P.G. Kwiat, E. Waks, A.G. White, I. Appelbaum, P.H. Eberhard, Ultrabright source of polarization-entangled photons. Phys. Rev. A **60**, R773–R776 (1999)
30. J. Brendel, N. Gisin, W. Tittel, H. Zbinden, Pulsed energy-time entangled twin-photon source for quantum communication. Phys. Rev. Lett. **82**, 2594–2597 (1999)
31. H. Takesue, K. Inoue, Generation of polarization entangled photon pairs and violation of Bell's inequality using spontaneous four-wave mixing in fiber loop. Phys. Rev. A **70**, 031802(R) (2004)
32. H. Takesue, K. Inoue, Generation of 1.5-μm band time-bin entanglement using spontaneous fiber four-wave mixing and planar lightwave circuit interferometers. Phys. Rev. A **72**, 041804(R) (2005)
33. T. Honjo, H. Takesue, H. Kamada, Y. Nishida, O. Tadanaga, M. Asobe, K. Inoue, Long-distance distribution of time-bin entangled photon pairs over 100 km using frequency up-conversion detectors. Opt. Express **15**, 13957–13964 (2007)
34. H. Takesue, Y. Tokura, H. Fukuda, T. Tsuchizawa, T. Watanabe, K. Yamada, S. Itabashi, Entanglement generation using silicon wire waveguide. Appl. Phys. Lett. **91**, 201108 (2007)
35. K. Harada, H. Takesue, H. Fukuda, T. Tsuchizawa, T. Watanabe, K. Yamada, Y. Tokura, S. Itabashi, Generation of high-purity entangled photon pairs using silicon wire waveguide. Opt. Express **16**, 20368–20373 (2008)
36. T. Inagaki, N. Matsuda, O. Tadanaga, M. Asobe, H. Takesue, Entanglement distribution over 300 km of fiber. Opt. Express **21**, 23241–23249 (2013)
37. H. Takesue, K. Harada, K. Tamaki, H. Fukuda, T. Tsuchizawa, T. Watanabe, K. Yamada, S. Itabashi, Long-distance entanglement-based quantum key distribution experiment using practical detectors. Opt. Express **18**, 16777–16787 (2010)
38. W. Tittel, J. Brendel, H. Zbinden, N. Gisin, Quantum cryptography using entangled photons in energy-time Bell states. Phys. Rev. Lett. **84**, 4737–4740 (2000)
39. N. Namekata, S. Sasamori, S. Inoue, 800 MHz single-photon detection at 1550-nm using an InGaAs/InP avalanche photodiode operated with a sine wave gating. Opt. Express **14**, 10043–10049 (2006)
40. M. Koashi, Y. Adachi, T. Yamamoto, N. Imoto, Security of entanglement-based quantum key distribution with practical detectors. arXiv:0804.0891 (2008)

41. T. Honjo, S.W. Nam, H. Takesue, Q. Zhang, H. Kamada, Y. Nishida, O. Tadanaga, M. Asobe, B. Baek, R Hadfield, S. Miki, M. Fujiwara, M. Sasaki, Z. Wang, K. Inoue, Y. Yamamoto, Long-distance entanglement-based quantum key distribution over optical fiber. Opt. Express **16**, 19118–19126 (2008)
42. M. Halder, A. Beveratos, N. Gisin, V. Scarani, C. Simon, H. Zbinden, Entangling independent photons by time measurement. Nat. Phys. **3**, 692–695 (2007)
43. H. Takesue, B. Miquel, Entanglement swapping using telecom-band photons generated in fibers. Opt. Express **17**, 10748–10756 (2009)
44. Y. Xue, A. Yoshizawa, H. Tsuchida, Polarization-based entanglement swapping at the telecommunication wavelength using spontaneous parametric down-conversion photon-pair sources. Phys. Rev. A **85**, 032337 (2012)
45. H. Takesue, K. Inoue, 1.5-μm band quantum-correlated photon pair generation in dispersion-shifted fiber: suppression of noise photons by cooling fiber. Opt. Express **13**, 7832–7839 (2005)
46. A. Peres, Separability criterion for density matrices. Phys. Rev. Lett. **77**, 1413–1415 (1996)
47. F. Marsili et al., Detecting single infrared photons with 93% system efficiency. Nat. Photon. **7**, 210–214 (2013)
48. A.I. Lvovsky, B.C. Sanders, W. Tittel, Optical quantum memory. Nat. Photon. **3**, 706–714 (2009)
49. F. Benabid, P.S. Light, F. Couny, P. St. J. Russell, Electromagnetically-induced transparency grid in acetylene-filled hollow-core PCF. Opt. Express **13**, 5694–5703 (2005)
50. B. Lauritzen, J. Minar, H. de Riedmatten, M. Afzelius, N. Gisin, Approaches for a quantum memory at telecommunication wavelengths. Phys. Rev. A **83**, 012318 (2011)
51. P. Kumar, Quantum frequency conversion. Opt. Lett. **15**, 1476–1478 (1990)
52. C. Langrock, E. Diamanti, R.V. Roussev, Y. Yamamoto, M.M. Fejer, H. Takesue, Highly efficient single-photon detection at communication wavelengths by use of upconversion in reverse-proton-exchanged periodically poled $LiNbO_3$ waveguides. Opt. Lett. **30**, 1725–1727 (2005)
53. S. Tanzilli, W. Tittel, M. Halder, O. Alibart, P. Baldi, N. Gisinand, H. Zbinden, A photonic quantum information interface. Nature **437**, 116 (2005)
54. H. Takesue, Erasing distinguishability using quantum frequency up-conversion. Phys. Rev. Lett. **101**, 173901 (2008)
55. H. Takesue, Single-photon frequency down-conversion experiment. Phys. Rev. A **82**, 013833 (2010)
56. A. Politi, M.J. Cryan, J.G. Rarity, S. Yu, J.L. O'Brien, Silica-on-silicon waveguide quantum circuits. Science **320**, 646–649 (2008)
57. A. Politi, J.C.F. Matthews, J.L. O'Brien, Shor's quantum factoring algorithm on a photonic chip. Science **325**, 1221 (2009)
58. J.P. Sprengers et al., Waveguide superconducting single-photon detectors for integrated quantum photonic circuits. Appl. Phys. Lett. **99**, 181110 (2011)
59. W.H.P. Pernice et al., High-speed and high-efficiency travelling wave single-photon detectors embedded in nanophotonic circuits. Nat. Commun. **3**, 1325 (2012)
60. H. Takesue, N. Matsuda, E. Kuramochi, W.J. Munro, M. Notomi, An on-chip coupled resonator optical waveguide single-photon buffer. Nat. Commun. **4**, 2725 (2013)
61. S. Mino, H. Yamazaki, T. Goh, T. Yamada, Multilevel optical modulator utilizing PLC-$LiNbO_3$ hybrid-integration technology. NTT Tech. Rev. **9**(3), (2011). https://www.ntt-review.jp/archive/ntttechnical.php?contents=ntr201103fa8.pdf&mode=show_pdf

Chapter 4
Spin-Photon Entanglement in Semiconductor Quantum Dots: Towards Solid-State-Based Quantum Repeaters

Kristiaan De Greve and Yoshihisa Yamamoto

4.1 Introduction: Quantum Repeaters

4.1.1 Quantum Key Distribution

Quantum key distribution (QKD), as conceived by Bennett and Brassard in their seminal BB84 proposal [5], provided an elegant, inherently quantum mechanical answer to a canonical problem in cryptography: how can two parties, A(lice) and B(ob), share a secure key without an eavesdropper (Eve) being able to intercept this key? This key sharing is at the very heart of cryptography: when two parties share a secret key that is both truly random, of sufficient length (as compared to the messages they want to share) and used only once, then any message can be safely encrypted and decrypted – the so-called one-time pad protocol [52].

While key sharing can, in principle, be performed in a variety of different ways, many situations require the keys to be shared over publicly accessible channels, which are in principle prone to eavesdropping. Bootstrapping methods (e.g. privacy amplification) do exist, but still require there to be some form of shared,

K. De Greve (✉)
Department of Physics, Harvard University, 17 Oxford Street, Cambridge, MA 02138, USA
e-mail: kdegreve@physics.harvard.edu

Y. Yamamoto
ImPACT Program, Council for Science Technology and Innovation, Tokyo, Japan
e-mail: yyamamoto@stanford.edu

Y. Yamamoto, K. Semba (eds.), *Principles and Methods of Quantum Information Technologies*, Lecture Notes in Physics 911, DOI 10.1007/978-4-431-55756-2_4

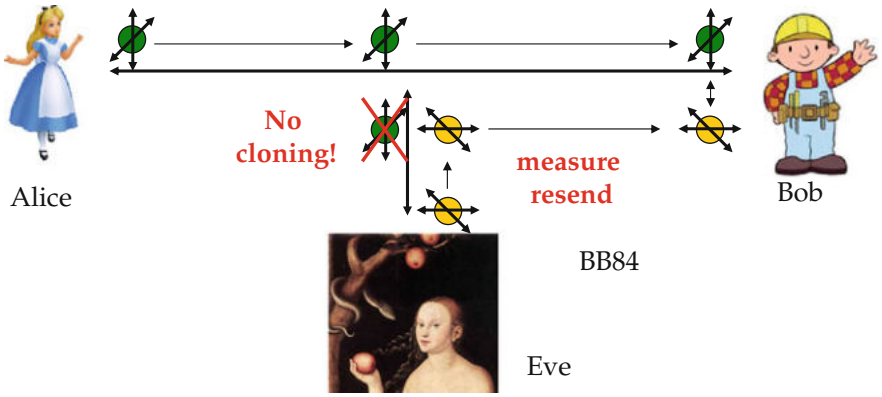

Fig. 4.1 Schematic of the BB84 QKD protocol. Alice and Bob attempt to share a secret key, which Eve tries to intercept. As she cannot clone the qubits used, she attempts to measure and resend them, which leads to detectable errors upon comparing Alice and Bob's code tables (Adapted with permission from [13])

reasonably secure key to start with. Bennett and Brassard's elegant answer to this paradox consisted in exploiting several inherent properties of quantum mechanics: the no-cloning theorem [60], and the Heisenberg uncertainty relationship for non-commuting variables.

The essence of the BB84 protocol is illustrated in Fig. 4.1. Alice and Bob each decide, randomly and independently, to encode and decode every single quantum bit they send each other in one of multiple incompatible (non-commuting) bases, e.g. polarization-encoded photonic qubits along the H/V or A/D ((anti-)diagonal) directions. In view of the no-cloning theorem, Eve is unable to simply copy the quantum bits, and has to therefore resort to an intercept-resend attack. As she has no prior knowledge of which basis Alice or Bob chose individually, she will inevitably make errors in the chosen basis, and, by virtue of the Heisenberg uncertainty principle, will be unable to avoid the back action noise resulting from choosing the wrong measurement basis (reflected in a bit error rate on Bob's side). When Alice and Bob now compare their chosen bases, and compare the values of the shared bits for those cases where the key basis coincides, then the presence of Eve's eavesdropping will reveal itself via the measured error rate.

As the BB84 scheme relies on measured error rates, it is also quite sensitive to the combined effects of photon loss and the system's inherent error rate: in particular, bit errors induced by detector dark counts. There is generally no way to distinguish between the bit error rate due to detector dark counts, and Eve's eavesdropping. Even when using improved protocols, operating at the lowest-loss fiber wavelengths and using the best, state-of-the-art detectors, practical implementations [29, 30] are limited to communication over several 100 km in fiber [55], with free-space schemes (more challenging experimentally, but in principle able to achieve lower system loss) at the time of writing still lagging behind the fiber-based schemes [40, 63].

4.1.2 *Divide and Conquer: Quantum Repeaters*

The obvious solution to the loss-based distance limitation – a divide-and-conquer scheme that divides the link-to-be-established into many shorter links that are established in parallel – suffers from the same no-cloning theorem. A different QKD protocol does lend itself to a repeater-like scheme: the Ekert91 [19] or BBM92 [6] scheme, which relies on the presence of a shared entangled qubit pair on which to perform the random basis choices by Alice and Bob. As an entangled pair has correlations in each basis, the bit error rate for the same choice of basis will again reveal the presence of an eavesdropper.

Such an entanglement based scheme does lend itself to a divide-and-conquer approach by virtue of entanglement-swapping [66], where a joint Bell measurement on the inner two qubits of two sequential entangled pairs results in the establishment of entanglement between the outer nodes. That, in combination with an entanglement purification protocol [4, 7, 8, 41] to correct for practical errors via quantum error correction, is the basis of the quantum repeater [12, 18] as illustrated in Fig. 4.2.

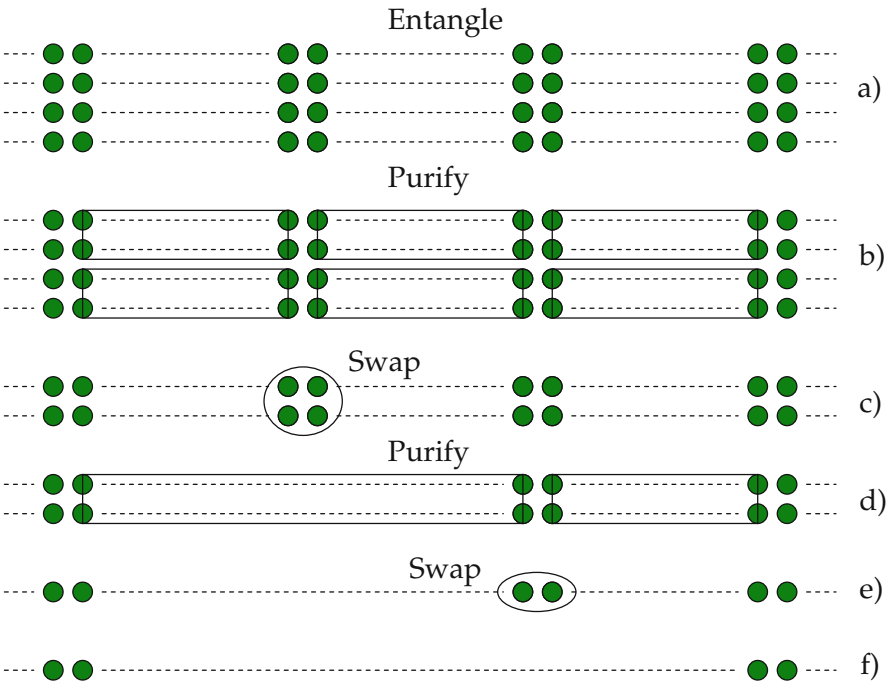

Fig. 4.2 Outline of the quantum repeater, as proposed by [12, 18]. An extended version of the Ekert91/BBM92 QKD scheme is implemented via repeated nested purification (**b**, **d**) and swapping (**c**, **e**) of remotely entangled quantum bits (**a**), resulting in the creation of high-purity, longer-distance entangled qubit pair (Adapted with permission from [13])

First, a series of entangled pairs is created between each of the nodes in the repeater, with multiple links between each set of neighboring nodes used to distill higher-fidelity pairs (Fig. 4.2a, b). Then, entanglement swapping is used to generate entangled links between further remote nodes, which are then subsequently purified further (Fig. 4.2c, d), until finally a high-fidelity, entangled link is established between the outer nodes in the network (Fig. 4.2e, f). The exact order of distillation and swapping, and the overhead needed to perform the distillation, is highly dependent on the details of the implementation, with the overhead scaling dramatically with both the losses between the nodes and the errors in the quantum control used during the swapping/purification [32].

For such a repeater scheme to work, one would require a physical system that would allow the generation of medium-to-long distance entanglement (10s–100s of km) in the first place, which could then be extended by virtue of the nested swapping/purification protocols, provided that such a system is scalable enough to account for the significant overhead required for these operations. For the generation of medium-distance entanglement, a probabilistic version of the entanglement swapping protocol can be used, where two entangled memory-qubit/photon-qubit pairs are used. By virtue of Hong-Ou-Mandel (HOM) interference [27] on a beamsplitter, a probabilistic version of a Bell-state measurement can be performed, which results in the creation of an entangled memory qubit pair (a deterministic version would require number-resolving photon detectors or photonic non-linearities that are, at the time of writing, outside the scope of experimental feasibility). This situation is summarized in Fig. 4.3, which illustrates the essential ingredients for such an elementary network: the robust generation of memory-photon entanglement, low-loss photonic transport (since the same loss mechanisms that limit the QKD distance

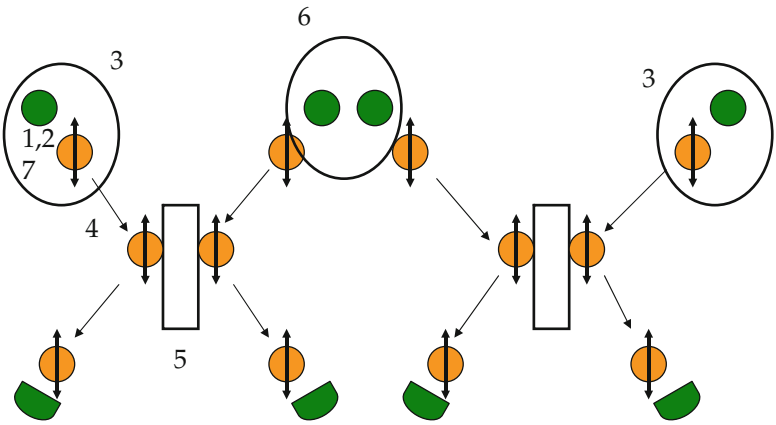

Fig. 4.3 Basic ingredients for a quantum repeater. *Green circles*: memory (spin) qubits; *orange circles*: single photonic qubits; *black-and-white rectangles*: beamsplitters for HOM-measurement; *green boxes*: single-photon detectors; *black-and-white circles*: entanglement operations (Adapted with permission from [13])

also bound the distance over which a single link in the repeater scheme could be established), a fast system (fast repetition rate, operation speed) with sufficient quantum mechanical fidelity to keep the overhead under control, and scalable – the latter in order to perform entanglement purification.

In the remainder, we shall focus on a particular system that, in principle, allows all of the above requirements to be fulfilled: single spins in optically active quantum dots.

4.2 On Quantum Dots and Spins

The spin states of individual electrons or holes in self-assembled, InAs quantum dots (QDs) can be used to encode quantum bits [9, 14, 28, 47]. Such quantum dots are grown via the Stranski-Krastanov growth method, where the strain induced by lattice mismatch between GaAs and InAs induces the formation of small, nm-sized InAs islands on top of a wetting layer, which is subsequently capped by an overgrown layer of GaAs [64]. Figure 4.4a displays an SEM micrograph of uncapped InAs quantum dots. Because of the combined effects of strain and band-structure line-up between InAs and GaAs in both the conduction band (CB) and valence band (VB), these quantum dots offer a new potential well for both electrons and holes – a 3D, nm-scale version of a particle in a box (Fig. 4.4b).

As InAs is a direct bandgap semiconductor, the confinement of both electron and holes results in narrow, well-defined yet fast optical transitions, with the lifetimes of an individual exciton (bound electron-hole pair) on the order of 100 ps–1 ns. For this reason, InAs quantum dots have been extensively studied in the context of single-photon sources [37, 45, 48, 49]. The spin states of an individual electron or hole,

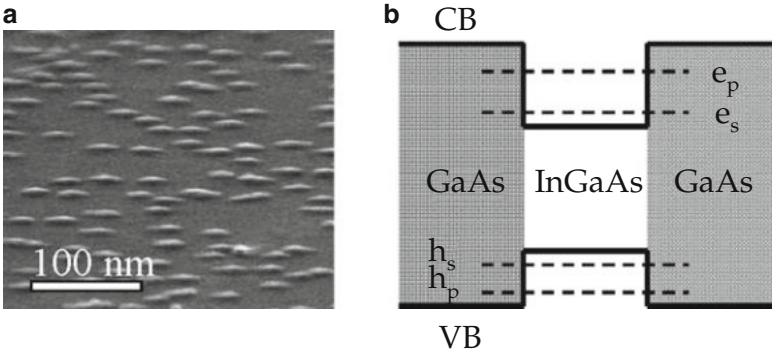

Fig. 4.4 Self-assembled quantum dots: SEM-micrograph of uncapped dots (**a**) and schematic outline of the band- and level structure (**b**). *CB*: conduction band; *VB*: valence band; $e_{s;p}$: s- and p-shell electron states; $h_{s;p}$: s- and p-shell hole states (Adapted with permission from [13])

however, can also be used to encode a quantum bit [3, 28], and the bright optical transitions can be exploited for fast, all-optical manipulation [9, 47].

A magnetic field will lift the degeneracy of the spin states, while the quantum dot confinement helps isolate the quantum bit from the environment [25, 34]. Two distinct magnetic field orientations are generally used: either parallel to the growth direction (Faraday geometry), or perpendicular to it (Voigt geometry). While the former is of particular use for spin-readout [1, 57], it is the latter that allows for all-optical spin manipulation, as well as spin-photon entanglement, which are the focus of the remainder of this chapter.

Figure 4.5a–c displays the level structure of a singly charged InAs quantum dot in the Voigt geometry (the case of a single electron is shown, although the situation for a single hole is equivalent). By δ-doping or tunneling from a nearby

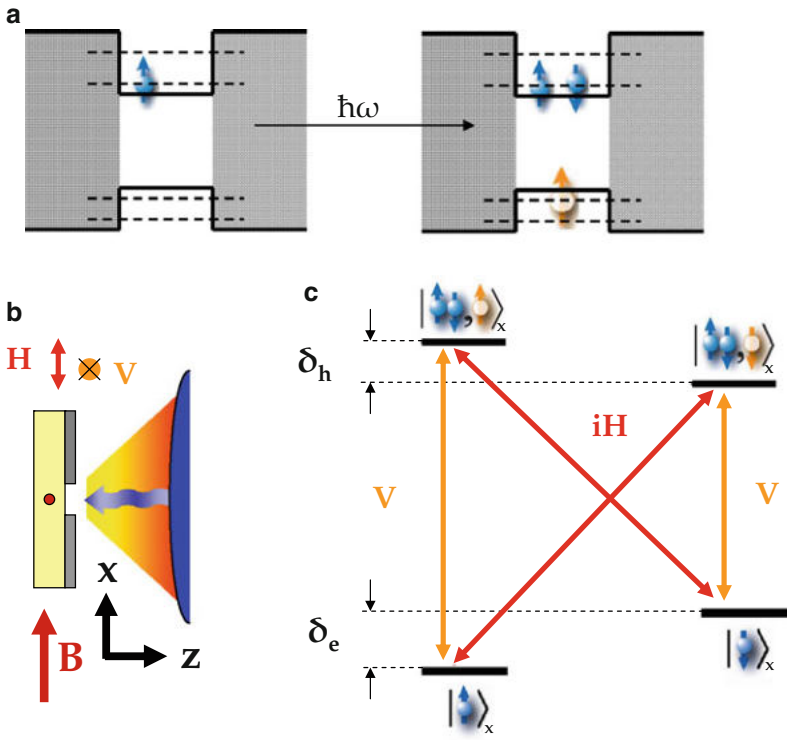

Fig. 4.5 Schematic overview of the level structure of a single-electron-charged quantum dot. (**a**) a single electron is resonantly excited into a trion state: one electron singlet (*blue arrows*) and one unpaired hole (*orange*). (**b**) outline of the Voigt geometry used in this work: the magnetic field is aligned along the x-direction, perpendicular to the growth axis (z); H and V are in the growth plane, respectively parallel and perpendicular to the magnetic field orientation. (**c**) level structure upon application of a Voigt geometry magnetic field; two Λ-systems emerge, which can be used to manipulate the spin state (Adapted with permission from [13])

Fermi-sea [59], a single electron is introduced into the quantum dot, which forms the ground state of the system. The excitation of a single exciton results in the formation of a trion, a three-particle complex consisting of two electrons and one hole. Due to the confinement and interaction effects, the electrons line up as a singlet (the triplets are separated by some 10 meV), and the heavy holes are similarly split from the light holes (also meV scale). With a Voigt-geometry magnetic field (Fig. 4.5b), the simplified level structure of Fig. 4.5c emerges, where each spin state is connected via optical transitions to each of the trion states in a double Λ-configuration. Such a Λ-configuration lends itself to coherent optical manipulation, e.g. via coherent population trapping (CPT) [23], or in the context of electromagnetically induced transparency (EIT) [22].

4.3 All-Optical, Ultrafast Spin Manipulation in Quantum Dots

The strength of the optical transitions in InAs quantum dots, in combination with the good spectral separation, allows for optical manipulation of the spin states of the quantum dot in Voigt geometry with a single, broadband optical pulse [9, 47]. The pulse width must exceed the energy difference between the spin states, and the effects of dephasing via the fast decay of the excited states can be minimized by detuning the pulse energy from the optical transition. By choosing the polarization of the pulse appropriately (circularly polarized light results in constructive interference of both Λ-systems), the spin can be coherently rotated around an axis that, in the lab-frame, corresponds to the propagation direction of the laser pulse, with an angle that depends on the energy of the light pulse. In some sense, the different frequency components of the broadband pulse conspire to jointly execute a stimulated Raman transition.

Figure 4.6 illustrates the coherent spin manipulation of a single quantum dot spin qubit, where optical pumping is used in addition for spin initialization [62], and Larmor precession in the external magnetic field provides rotation around a second, perpendicular rotation axis (Fig. 4.6c). Using these techniques, Press and coworkers [47] were able to generate any coherent single qubit rotation within 20 ps or less, essentially limited by the Larmor precession. Figure 4.7 illustrates the Rabi oscillations, obtained by varying the strength of a single, 3-ps laser pulse. In addition to the speed, their all-optical control also allows for selective manipulation of a single qubit within the diffraction limit of their laser, which would in principle allow for a quantum bit density well beyond $1/\mu m^2$. Using similar techniques, exchange-coupled electron spins in quantum dot molecules could be coherently manipulated, both individually and jointly, resulting in both single-qubit and two-qubit coherent control [33], and the same techniques were also readily applied to hole-doped quantum dots [14].

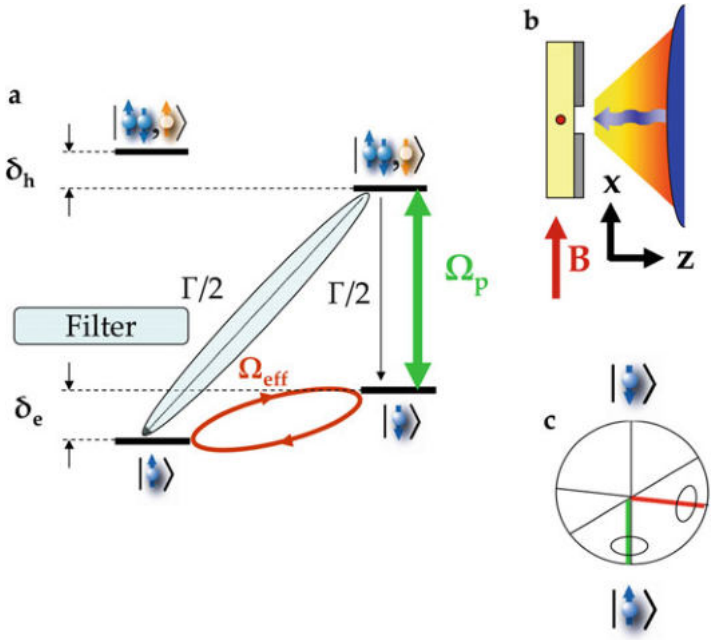

Fig. 4.6 Schematic overview of the coherent manipulation of a single quantum dot spin. (**a**) a narrowband CW laser (Ω_P) is used for optical pumping/initialization of the qubit, as well as readout (detection of a single photon on the Zeeman-energy-split, opposite polarization transition (*blue shaded region*)). A detuned, broadband, circularly polarized pulse provides coherent rotation of the spin. (**b**) Voigt geometry. (**c**) Bloch sphere representation of the spin and the respective rotation axes provided by the fast laserpulse (*red*) and the Larmor precession (*green*) (Adapted with permission from [13])

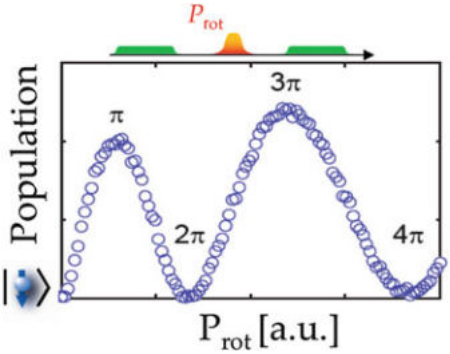

Fig. 4.7 Rabi-oscillations of a single electron spin qubit in an InAs quantum dot. By varying the power (energy) of single circularly polarized rotation pulse, the spin can be rotated over an arbitrary angle. In combination with control over the arrival time of the pulse (rotation axis), full SU(2) control was demonstrated in [47] (Adapted with permission from [46])

Using the same coherent control techniques, Press and coworkers also studied the coherence properties of quantum dot spin-based qubits [46]. A spin-echo coherence time T_2 of around 3 μs was obtained, with a shot-to-shot dephasing time, T_2^*, of less than 2 ns. For the latter, the strong contact hyperfine interaction with the nuclear spins in the quantum dot (some 10^4–10^5, as both In, Ga and As only have non-spin-0 isotopes) is the dominant effect, which also gives rise to a rich and complicated, non-Markovian dynamics due to feedback in the electron-nuclear joint dynamics [26, 35, 36, 58, 61].

For a single hole spin, the p-type wavefunction does not have a contact term in the hyperfine Hamiltonian, which led to predictions of significantly suppressed hyperfine interactions and, consequently, longer coherence times for hole spin qubits [21]. While the weaker hyperfine interaction (essentially dipolar in nature [20]) does indeed lead to a strong suppression of the non-linear, non-Markovian dynamics that are typical for electron spin qubits [14], the coherence times are only comparable or even shorter than those measured for electron spis (T_2 of 1.1 μs, T_2^* of 2 ns as measured in [14]), due to a stronger susceptibility of hole spin qubits to charge noise.

For both electrons and holes, the measured coherence times allow for some 10^5 operations to be performed before decoherence occurs, provided that the fidelity of individual control operations can be increased to the 0.99999 level (currently experimentally limited to 0.95–0.98 as reported in [14, 46]).

4.4 Spin-Photon Entanglement in Quantum Dots

The Λ-systems of Voigt-geometry, charged quantum dots also form a natural interface for the generation of spin-photon entanglement. Upon excitation of one of the trion states (say, $|\uparrow\downarrow\Downarrow\rangle$, see Fig. 4.8), coherent interference between the two spontaneous emission decay pathways automatically results in a state that is entangled in the spin degree of freedom and *both* the polarization and frequency (color) degree of freedom of the spontaneously emitted photon [11, 17, 56]:

$$|\Psi\rangle = \frac{1}{\sqrt{2}}(|\uparrow\rangle \otimes |i\mathrm{H}; \omega + \delta\omega\rangle + |\downarrow\rangle \otimes |\mathrm{V}; \omega\rangle) \tag{4.1}$$

While such entanglement in multiple degrees of freedom does not pose an inherent limitation to the HOM-interference-based entanglement generation schemes described before (provided each photon is *jointly* indistinguishable in both degrees of freedom [38]), it does provide a serious impediment to the *measurement* of the degree of spin-photon entanglement.

In order to prevent which-path information to leak to the environment, obscuring entanglement and resulting in the measurement of a perfectly mixed state, some form of quantum erasure [51] needs to be applied. Measurement of the photonic arrival time with timing resolution, $\Delta t \ll 1/\delta\omega$, can result in such quantum erasure,

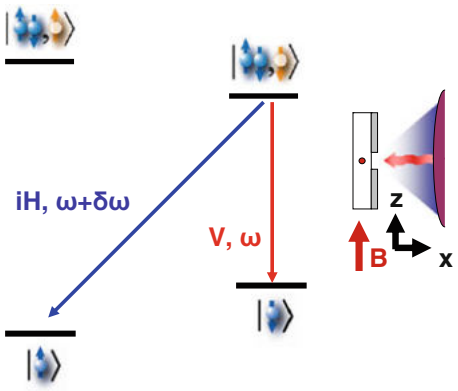

Fig. 4.8 Level-structure of a single-electron-charged quantum dot (the case of a single hole is similar). Upon excitation of one of the excited states, the Λ-level structure ensure that the spontaneously emitted photon is entangled with the spin state. However, this entanglement is both in polarization and the frequency, making it challenging to verify unless quantum erasure techniques are applied (Adapted with permission from [17])

as the bandwidth of such a detection scheme is much wider than the frequency separation of the photons, and is therefore fundamentally unable to distinguish between the different frequencies of the emitted light [17, 24, 50, 56]. For the magnetic fields that are typically used to separate the optical transitions and allow proper spin-polarization via optical pumping, the Larmor precession frequency $\delta\omega/2\pi$ is at several 10s of GHz, corresponding to required detector speeds of 10s of ps; at the time of writing, superconducting nanowire detectors were the only single-photon detectors capable of such timing resolution [24, 50].

Alternatively, a non-linear process can be used to perform an effective measurement of the arrival time of the photon, as was performed in [17]. There, a few-ps optical pulse is mixed with the single photon in a non-linear crystal (PPLN waveguide, in order to increase the interaction strength and work at the single-photon-level [44]). By appropriate choice and filtering of the input- and output frequencies of the converted light, a single 1550 nm photon could be detected, conditional on exact overlap of the spontaneously emitted, QD-photon with the short conversion pulse, thereby providing an accurate measurement of the exact arrival time of the photon. We refer to Fig. 4.9 for a system diagram used in [17] in order to verify spin-photon entanglement using such a time-resolved frequency conversion technique. By combining coherent spin manipulation (in order to change the effective measurement basis of the spin qubit) with the time-resolved, photonic polarization measurement, entanglement between the spin and the photon could be verified with a timing resolution of less than 8 ps [17].

Using tomographic methods, the full density matrix of the spin-photon entangled pair was reconstructed in [15], the results of which are shown in Fig. 4.10. To account for the effect of measurement statistics, an MLE method was used, as

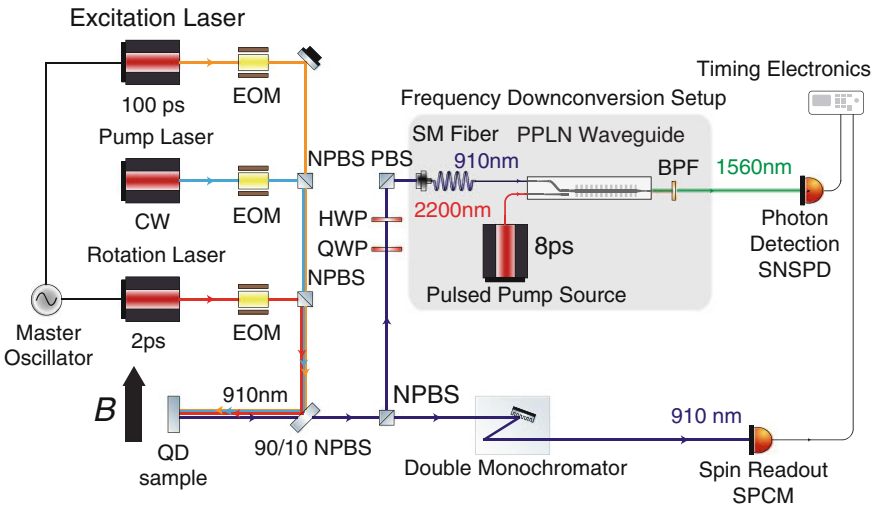

Fig. 4.9 Spin photon entanglement verification: full system diagram. See text for details. *EOM*: electro-optic-modulator; *(N)PBS*: non-polarizing beamsplitter. The *grey shaded box* indicates the frequency quantum erasure setup (Adapted with permission from [17])

described in [31], that enforces positivity of the density matrix (and, therefore, prevents unphysical density matrices that could occur via measurement errors). A spin-photon entanglement fidelity of 0.92 was extracted, still primarily limited by the timing resolution (for the 8 ps used, the theoretical limitation due to timing resolution only would be 0.95, resulting in a bound of the remaining errors – readout, manipulation, dephasing, imperfect generation – of 0.05 or less). This value is comparable, at the time of writing, to the best results obtained in atomic systems, and exceeded only by the trapped ion system [54], and allows for a significant reduction in the amount of overhead required for entanglement purification [15] when compared to lower fidelity systems [24, 50, 56].

4.5 Coherent Frequency/Wavelength Conversion in Quantum Dots

In order to increase the distance over which spin-photon entanglement can be used, which in turn limits the distance between successive nodes in a quantum repeater system, both the decoherence rate of the spin qubit and the loss rate of the photonic qubit need to be addressed. The former can, in principle, be tackled by dynamical decoupling techniques that can increase the the T_2-decoherence time by a series of successive, nested, spin-echo sequences that exploit any slow dynamics of the decohering environment [10]; however, at the time of writing, such dynamical

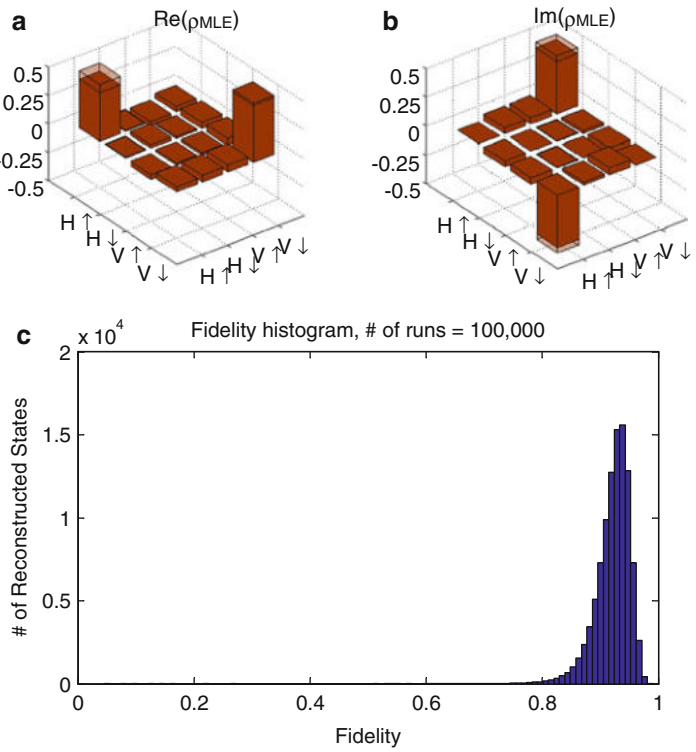

Fig. 4.10 Reconstructed (MLE analysis – see text) density matrices (**a,b**) of the quantum dot spin-photon entangled states. (**c**) Histogram of the obtained fidelity of the entangled state, after analysis (Monte-Carlo simulation) of the propagation of measurement errors (Adapted with permission from [15])

decoupling of quantum dot spin qubits was still an active field of research, and yet to be demonstrated [16].

Reducing the loss of the photonic qubit, however, can be tackled by coherently converting the emission wavelength of the quantum dots (around 900 nm) to the lowest-loss fiber-transmission wavelengths around 1320 and 1550 nm. Coherent frequency conversion at the single-photon level was recently demonstrated by several groups [2, 17, 44, 65], all of whom relied on the enhancement of a non-linear optical process (typically, a $\chi^{(2)}$-type non-linearity in periodically poled lithium niobate, PPLN [43]) in a waveguide that confines the energy and increases the field strength.

The PPLN waveguides used for verification of spin-photon entanglement [17, 44] can be used for transfering the 900-nm spin-photon entanglement to telecom (1550 nm) wavelength, and the frequencies used were chosen accordingly. However, the non-polarization-degeneracy of PPLN waveguides needs to be properly accounted for, and limited the generation of full 1550-nm entanglement in that

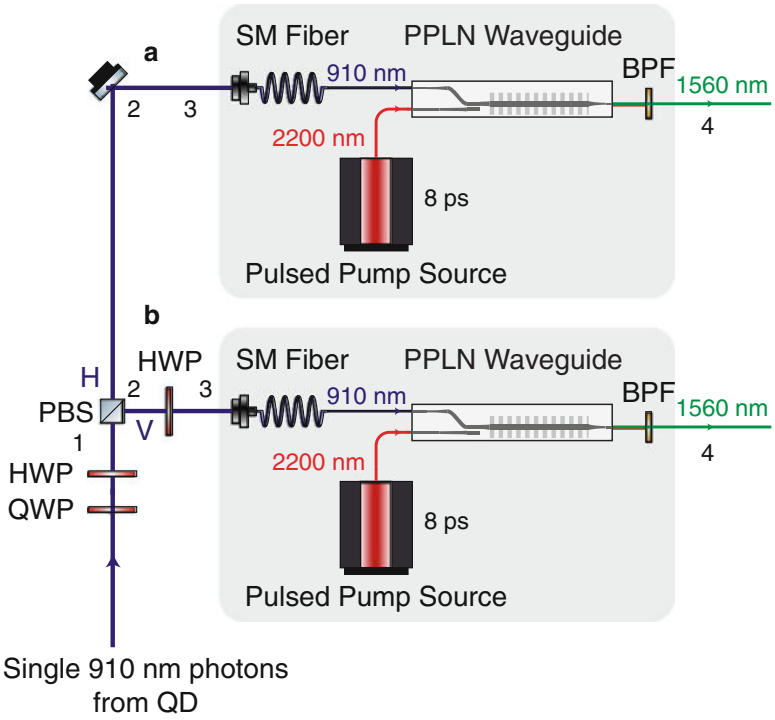

Fig. 4.11 Proposed setup for generation of a full, rail-encoded, 1550-nm photon-spin entangled pair (Adapted with permission from [17])

experiment. Figure 4.11 demonstrates a possible extension of those frequency converters into a dual-rail encoded, full 1550 nm spin-photon entanglement setup. Alternatively, a 1550 nm, polarization-entangled pair setup is illustrated in Fig. 4.12.

As the frequency quantum erasure used in [17] is technically only required for the *verification* of entanglement [38], CW versions of the pulsed converters could be used as well. That way, frequency-entangled spin-photon pairs [24] could be obtained at 1550 nm, where the polarization degree of freedom could be removed by means of recombining both branches of the downconversion setup. Commercial, non-polarization maintaining optical fiber is highly sensitive to polarization fluctuations, whereas the frequency/phase degrees of freedom are rather robust, making such a frequency-encoded qubit attractive from a systems point of view – this is also the basis of DPS-QKD schemes [29].

Another interesting aspect of the demonstrated frequency conversion techniques is that they are in principle capable of overcoming one of the major downsides of self-assembled quantum dots: the inhomogeneous broadening of their emission spectra. As the growth process is stochastic, with essentially different sizes and amounts of strain for each single quantum dot, their quantization energies and emission wavelengths vary drastically from dot to dot. This severely limits their

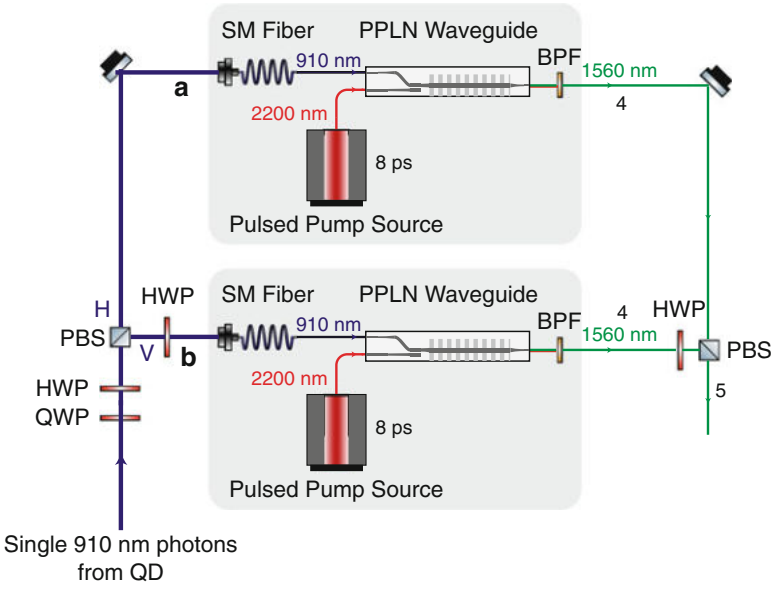

Fig. 4.12 Proposed setup for generation of a polarization qubit at 1550 nm, entangled with the quantum dot spin. Variants of this setup could be used to generate time-bin entangled qubit (frequency quantum erasure as indicated, with variable timing on the 8 ps pulse; removal of the PBS), or 1550-nm frequency encoded qubit (quantum erasure of the polarization degree of freedom, CW frequency conversion) (Adapted with permission from [17])

photonic indistinguishibility, and the first demonstrations of HOM-interference of indistinguishible photons from InAs quantum dots were either performed on successive photons emitted by the same quantum dot [48], or required significant amounts of postselection and in-situ tuning via DC-Stark effects [42]. By appropriately tuning the wavelengths used in the conversion process, nominally frequency-distinguishible quantum dots can be made to emit at the same (converted) wavelength, as shown in [2] for different emission lines from the same quantum dot. This aspect should give a significant boost to the scalability of self-assembled quantum dots in the context of large-scale quantum networks.

4.6 A High-Speed Link to Entangle Quantum Dot Spins

The considerations of both speed, intrinsic scalability, high-fidelity spin-photon entanglement, high-fidelity spin control and coherent frequency conversion all make the charged quantum dot system an interesting candidate for use in large-scale quantum networks and repeaters. While the high intrinsic speed of the quantum dot system would in principle allow an operation frequency (repetition rate) exceeding

1 GHz, the naive implementation illustrated in Fig. 4.3 would drastically lower the operational speed. That is because for every link, the quantum memory (spin) needs to be preserved for the full round trip of (half) the link-length between adjacent nodes: only then is it known whether its photon and that of the neighboring link yielded a proper interference signal and resulted in an entangled link.

In practice, one would want the distance between neighboring links to be as large as possible, to avoid the large overhead associated with a full repeater station as much as possible. Consequently, in realistic scenarios, repeater stations would be positioned 10s–100s of km from each other, which would drastically reduce the clock speed of the system. However, even at the lowest-loss fiber wavelengths, the photon losses are still at 0.2 dB/km, resulting in 20 dB loss over 100 km – in other words, the emitted photons will, most of the time, not interfere at all! Hence, in most cases, the repeater link remains idle for no good reason. Several architectural patches to this problem have been proposed, including using many parallel links and multi-mode quantum memories [39, 53].

Jones and coworkers [32] proposed an interesting variant, that does not require the establishment of many links in parallel, and instead uses a single link between two single-mode memories. The layout of their proposal is illustrated in Fig. 4.13. Instead of having a probabilistic Bell-state analyzer in the middle between the two links (an HOM-analyzer), an entangled-photon-pair source placed in the middle between the two nodes emits entangled photon pairs, one photon each to each node. The repeater nodes, in turn, emit their spin-entangled photons, at the highest rate possible (synchronized to the entangled photon pairs, potentially up to GHz rate). If and only if one photon from the entangled pair arrives at the Bell-state analyzer near the node, the node stops emitting, sends a signal to the other node, and stores the spin state (memory function). Otherwise, the repeater fires again and overwrites the previous memory. This way, the repeater node effectively postselects for those

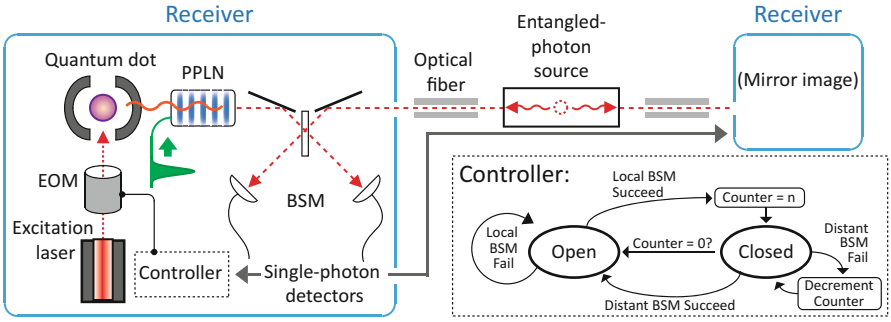

Fig. 4.13 Proposed setup for increasing the probability of success of generating remote entangled pairs in neighboring nodes of a quantum repeater. The use of an entangled photon source in the middle dramatically reduced the down-time of each available photonic link by effectively postselecting for those cases where one half of the photonic entangled pair reaches the repeater node – otherwise, the repeater simply fires with its a priori fast repetition rate. See text for details about this proposed pipelining scheme (Adapted with permission from [32])

events where already half the distance of the link was crossed by the entangled photon before temporarily halting emission. At that time, all depends on what happens to the other half of the entangled pair: if it reaches the other node (now dependent on the other photon only traversing *half* of the link distance), then that node waits as well, sends its signal to the opposite side, and after a round trip, each node is aware of whether entanglement was generated successfully. While a round trip of waiting is still needed to establish entanglement, the repeater now does not need to operate at an a priori low emission rate, and the postselection on arrival of the first photon allows for a scaling improvement as a function of repeater link length, L: $\propto \exp(-L/2)$ i.o. $\propto \exp(-L)$. The only overhead involved in the scheme is the realization of an entangled photon pair source, indistinguishible from the emitted quantum dot photons, and the addition of a second Bell-state analyzer (one HOM-analyzer at each node, rather than a single analyzer in the middle).

4.7 Conclusion

As an inherently scalable, solid-state system, self-assembled quantum dots are expected to be a prime candidate-technology for future quantum repeaters. Their high intrinsic speed, when properly accounted for at the architectural level, and natural photonic interface were exploited in proof-of-principle experiments of all-optical, coherent spin manipulation [9, 47], and high-fidelity spin-photon entanglement [15, 17, 24, 50]. Coherent frequency conversion [17, 44] allows for low-loss photonic transport along commercial optical fiber systems, and helps overcome the inhomogeneous distribution of emission wavelengths among different quantum dots [42, 48]. In this sense, individual building blocks have been demonstrated, with operational fidelities that are, in principle, sufficient for large-scale systems. What remains, is the combination of these building blocks into a working, small-scale and system-level demonstrator – undoubtedly a tremendous engineering challenge, yet likely within reach.

References

1. M. Atatüre, J. Dreiser, A. Badolato, A. Imamoglu, Observation of Faraday rotation from a single confined spin. Nat. Phys. **3**, 101 (2007)
2. S. Ates, I. Agha, A. Gulinatti, I. Rech, M.T. Rakher, A. Badolato, K. Srinivasan, Two-photon interference using background-free quantum frequency conversion of single photons emitted by an InAs quantum dot. Phys. Rev. Lett. **109**, 147405 (2012)
3. M. Bayer et al., Fine structure of neutral and charged excitons in self-assembled In(Ga)As/(Al)GaAs quantum dots. Phys. Rev. B **65**, 195315 (2002)
4. C.H. Bennett, H.J. Bernstein, S. Popescu, B. Schumacher, Concentrating partial entanglement by local operations. Phys. Rev. A **53**, 2046 (1996)

5. C.H. Bennett, G. Brassard, Quantum cryptography: public key distribution and coin tossing, in *Proceedings of the IEEE International Conference on Computers, Systems, and Signal Processing*, Bangalore (1984), p. 175
6. C.H. Bennett, G. Brassard, N.D. Mermin, Quantum cryptography without Bell's theorem. Phys. Rev. Lett. **68**, 557 (1992)
7. C.H. Bennett, G. Brassard, S. Popescu, B. Schumacher, J.A. Smolin, W.K. Wooters, Purification of noisy entanglement and faithful teleportation via noisy channels. Phys. Rev. Lett. **76**, 722 (1996)
8. C.H. Bennett, D.P. DiVincenzo, J.A. Smolin, W.K. Wooters, Mixed state entanglement and quantum error correction. Phys. Rev. A **54**, 3824 (1996)
9. J. Berezovsky, M.H. Mikkelsen, N.G. Stoltz, L.A. Coldren, D.D. Awschalom, Picosecond coherent optical manipulation of a single electron spin in a quantum dot. Science **320**, 349 (2008)
10. M.J. Biercuk, H. Uys, A.P. VanDevender, N. Shiga, W.M. Itano, J.J. Bollinger, Optimized dynamical decoupling in a model quantum memory. Nature **458**, 996 (2009)
11. B.B. Blinov, D.L. Moehring, L.-M. Duan, C. Monroe, Observation of entanglement between a single trapped atom and a single photon. Nature **428**, 153 (2004)
12. H.-J. Briegel, W. Dür, J.I. Cirac, P. Zoller, Quantum repeaters: the role of imperfect local operations in quantum communication. Phys. Rev. Lett. **81**, 5932 (1998)
13. K. De Greve, *Towards Solid-State Quantum Repeaters*. Springer PhD thesis series (Springer, New York, 2013)
14. K. De Greve, P.L. McMahon, D. Press, T.D. Ladd, D. Bisping, C. Schneider, M. Kamp, L. Worschech, S. Höfling, A. Forchel, Y. Yamamoto, Ultrafast coherent control and suppressed nuclear feedback of a single quantum dot hole qubit. Nat. Phys. **7**, 872 (2011)
15. K. De Greve, P.L. McMahon, L. Yu, J.S. Pelc, C. Jones, C.M. Natarajan, N.Y. Kim, E. Abe, S. Maier, C. Schneider, M. Kamp, S. Hoefling, R.H. Hadfield, A. Forchel, M.M. Fejer, Y. Yamamoto, Complete tomography of a high-fidelity solid-state entangled spin-photon qubit pair. Nat. Commun. **4**, 2228 (2013)
16. K. De Greve, D. Press, P.L. McMahon, Y. Yamamoto, Ultrafast optical control of individual quantum dot spin qubits. Rep. Progress Phys. **76**, 092501 (2013)
17. K. De Greve, L. Yu, P.L. McMahon, J.S. Pelc, C.M. Natarajan, N.Y. Kim, E. Abe, S. Maier, C. Schneider, M. Kamp, S. Höfling, R.H. Hadfield, A. Forchel, M.M. Fejer, Y. Yamamoto, Quantum-dot spin-photon entanglement via frequency downconversion to telecom wavelength. Nature **491**, 421 (2012)
18. W. Dür, H.-J. Briegel, J.I. Cirac, P. Zoller, Quantum repeaters based on entanglement purification. Phys. Rev. A **59**, 169–181 (1999)
19. A.K. Ekert. Quantum cryptography based on Bell's theorem. Phys. Rev. Lett. **67**, 661 (1991)
20. P. Fellahi, S.T. Yilmaz, A. Imamoglu, Measurement of a heavy-hole hyperfine interaction in InGaAs quantum dots using resonance fluorescence. Phys. Rev. Lett. **105**, 257402 (2010)
21. J. Fischer, W.A. Coish, D.V. Bulaev, D. Loss, Spin decoherence of a heavy hole coupled to nuclear spins in a quantum dot. Phys. Rev. B **78**, 155329 (2008)
22. M. Fleischauer, A. Imamoglu, J.P. Marangos, Electromagnetically induced transparency: optics in coherent media. Rev. Mod. Phys. **77**, 633 (2005)
23. K.-M.C. Fu, C. Santori, C. Stanley, M.C. Holland, Y. Yamamoto, Coherent population trapping of electron spins in a high-purity n-type GaAs semiconductor. Phys. Rev. Lett. **95**, 187405 (2005)
24. W.B. Gao, P. Fallahi, E. Togan, J. Miguel-Sanchez, A. Imamoğlu, Entanglement between a quantum-dot-spin and a single-photon. Nature **491**, 426 (2012)
25. V.N. Golovach, A. Khaetskii, D. Loss, Phonon-induced decay of the electron spin in quantum dots. Phys. Rev. Lett. **93**, 016601 (2004)
26. A. Greilich et al., Nuclei-induced frequency focusing of electron spin coherence. Science **317**(4), 1896 (2007)
27. C.K. Hong, Z.Y. Ou, Mandel L, Measurement of subpicosecond time intervals between two photons by interference. Phys. Rev. Lett. **59**, 2044 (1987)

28. A. Imamoğlu et al., Quantum information processing using quantum dot spins and cavity QED. Phys. Rev. Lett. **83**, 4204 (1999)
29. K. Inoue, E. Waks, Y. Yamamoto, Differential phase shift quantum key distribution. Phys. Rev. Lett. **89**, 037902 (2002)
30. K. Inoue, E. Waks, Y. Yamamoto, Differential-phase-shift quantum key distribution using coherent light. Phys. Rev. A **68**, 022317 (2003)
31. D.F.V. James, P.G. Kwiat, W.J. Munro, A.G. White, Measurement of qubits. Phys. Rev. A **64**, 052312 (2001)
32. C. Jones, K. De Greve, Y. Yamamoto, A high-speed optical link to entangle quantum dots. arXiv:1310.4609 (2013)
33. D. Kim, S.G. Carter, A. Greilich, A.S. Bracker, D. Gammon, Ultrafast optical control of entanglement between two quantum-dot spins. Nat. Phys. **7**, 223 (2011)
34. M. Kroutvar, Y. Ducommun, D. Heiss, M. Bichler, D. Schuh, G. Abstreiter, J.J. Finley, Optically programmable electron spin memory using semiconductor quantum dots. Nature **432**, 81 (2004)
35. T.D. Ladd, D. Press, K. De Greve, P. McMahon, B. Friess, C. Schneider, M. Kamp, S. Höfling, A. Forchel, Y. Yamamoto, Pulsed nuclear pumping and spin diffusion in a single charged quantum dot. Phys. Rev. Lett. **105**, 107401 (2010)
36. C. Latta et al., Confluence of resonant laser excitation and bidirectional quantum-dot nuclear-spin polarization. Nat. Phys. **5**, 758 (2009)
37. P. Michler, A. Kiraz, C. Becher, W.V. Schoenfeld, P.M. Petroff, L. Zhang, E. Hu, A. Imamoglu, A quantum dot single-photon turnstile device. Science **290**, 2282 (2000)
38. D.L. Moehring et al., Entanglement of single-atom quantum bits at a distance. Nature **449**, 68 (2007)
39. W.J. Munro, K.A. Harrison, A.M. Stephens, S.J. Devitt, K. Nemoto, From quantum multiplexing to high-performance quantum networking. Nat. Photonics **4**, 792 (2010)
40. S. Nauerth et al., Air-to-ground quantum communication. Nat. Photonics **7**, 382 (2013)
41. J.-W. Pan, S. Gasparoni, R. Ursin, G. Weihs, A. Zeilinger, Experimental entanglement purification of arbitrary unknown states. Nature **423**, 417 (2003)
42. R.B. Patel, A.J. Bennett, I. Farrer, C.A. Nicoll, D.A. Ritchie, A.J. Shields, Two-photon interference of the emission from electrically tunable remote quantum dots. Nat. Photonics **4**, 632 (2010)
43. J.S. Pelc, C. Langrock, Q. Zhang, M.M. Fejer, Influence of domain disorder on parametric noise in quasi-phase-matched quantum frequency converters. Opt. Lett. **35**, 2804 (2010)
44. J.S. Pelc, L. Yu, K. De Greve, P.L. McMahon, C.M. Natarajan, N.Y. Kim, E. Abe, S. Maier, C. Schneider, M. Kamp, S. Höfling, R.H. Hadfield, A. Forchel, M.M. Fejer, Y. Yamamoto, Downconversion quantum interface for a single quantum dot spin and 1550-nm single-photon channel. Opt. Express **20**, 27510 (2012)
45. M. Pelton, C. Santori, J. Vuckovic, B. Zhang, G.S. Solomon, J. Plant, Y. Yamamoto, Efficient source of single photons: a single quantum dot in a micropost microcavity. Phys. Rev. Lett. **89**, 233602 (2002)
46. D. Press, K. De Greve, P. McMahon, T.D. Ladd, B. Friess, C. Schneider, M. Kamp, S. Höfling, A. Forchel, Y. Yamamoto, Ultrafast optical spin echo in a single quantum dot. Nat. Photonics **4**, 367 (2010)
47. D. Press, T.D. Ladd, B. Zhang, Y. Yamamoto, Complete quantum control of a single quantum dot spin using ultrafast optical pulses. Nature **456**, 218 (2008)
48. C. Santori, D. Fattal, J. Vuckovic, G.S. Solomon, Y. Yamamoto, Indistinguishible photons from a single-photon device. Nature **419**, 594 (2002)
49. C. Santori, M. Pelton, G. Solomon, Y. Dale, Y. Yamamoto, Triggered single photons from a quantum dot. Phys. Rev. Lett. **86**, 1502 (2001)
50. J.R. Schaibley, A.P. Burgers, G.A. McCracken, L.-M. Duan, P.R. Berman, D.G. Steel, A.S Bracker, D. Gammon, L.J. Sham, Demonstration of quantum entanglement between a single electron spin confined to an InAs quantium dot and a photon. Phys. Rev. Lett. 110, 167401 (2013)

51. M.O. Scully, K. Drühl, Quantum eraser: a proposed photon correlation experiment concerning observation and "delayed choice" in quantum mechanics. Phys. Rev. A **25**, 2208 (1982)
52. C. Shannon, Communication theory of secrecy systems. Bell Syst. Tech. J. **28**, 656 (1949)
53. C. Simon et al., Quantum repeaters with photon pair sources and multimode memories. Phys. Rev. Lett. **98**, 190503 (2007)
54. A. Stute, B. Casabone, P. Schindler, T. Monz, P.O. Schmidt, B. Brandstätter, T.E. Northup, R. Blatt, Tunable ion-photon entanglement in an optical cavity. Nature **485**, 482 (2012)
55. H. Takesue, S.W. Nam, Q. Zhang, R.H. Hadfield, T. Honjo, K. Tamaki, Y. Yamamoto, Quantum key distribution over a 40-dB channel loss using superconducting single-photon detectors. Nat. Photonics **1**, 343 (2007)
56. E. Togan, Y. Chu, A.S. Trifonov, L. Jiang, J. Maze, L. Childress, M.V.G. Dutt, A.S. Sørensen, P.R. Hemmer, A.S. Zibrov, M.D. Lukin, Quantum entanglement between an optical photon and a solid-state spin qubit. Nature **466**, 730 (2010)
57. A.N. Vamivakas, C.-Y. Lu, C. Matthiesen, Y. Zhao, S. Fält, A. Badolato, M. Atatüre, Observation of spin-dependent quantum jumps via quantum dot resonance fluorescence. Nature **467**, 297 (2010)
58. I.T. Vink et al., Locking electron spins into magnetic resonance by electron–nuclear feedback. Nat. Phys. **5**, 764–768 (2009)
59. R.J. Warburton, C. Schäflein, D. Haft, F. Bickel, A. Lorke, K. Karrai, J.M. Garcia, W Schoenfeld, P.M. Petroff, Optical emission from a charge-tunable quantum ring. Nature **405**, 926 (2000)
60. W.K. Wootters, W.H. Zurek, A single quantum cannot be cloned. Nature **299**, 802 (1982)
61. X. Xu et al., Optically controlled locking of the nuclear field via coherent dark-state spectroscopy. Nature **459**(4), 1105 (2009)
62. X. Xu, Y. Wu, B. Sun, Q. Huang, J. Cheng, D.G. Steel, A.S. Bracker, D. Gammon, C. Emary, L.J. Sham, Fast spin state initialization in a singly charged InAs-GaAs quantum dot by optical cooling. Phys. Rev. Lett. **99**, 097401 (2007)
63. J. Yin et al., Quantum teleportation and entanglement distribution over 100-kilometre freespace channels. Nature **488**, 185 (2012)
64. P. Yu, M. Cardona, *Fundamentals of Semiconductors – Physics and Materials Properties*, 3rd edn. (Springer, Berlin/New York, 2001)
65. S. Zaske, A. Lenhard, C.A.J. Keßler, Kettler, C. Hepp, C. Arend, R. Albrecht, W.-M. Schulz, M. Jetter, P. Michler, C. Becher, Visible-to-telecom quantum frequency conversion of light from a single quantum emitter. Phys. Rev. Lett. **109**, 147404 (2012)
66. M. Zukowski, A. Zeilinger, M.A. Horne, A.K. Ekert, "Event-Ready-Detectors" bell experiment via entanglement swapping. Phys. Rev. Lett. **71**, 4287 (1993)

Part II
Quantum Metrology and Sensing

Chapter 5
Optical Lattice Clocks for Precision Time and Frequency Metrology

Masao Takamoto and Hidetoshi Katori

5.1 Introduction

The precision measurement of time and frequency is the foundation of science such as precision spectroscopy [18, 20], determination of fundamental constants [17], precision test of relativity [50] and astronomy [32, 52]. An atomic clock not only gives us an access for studying fundamental science, but also forms the core part of the infrastructure such as the global navigation satellite system (GNSS) and the synchronization of data transfer in broadband networks. The definition of time, the "second", has been given by atomic clocks referencing a microwave transition of cesium (Cs) atoms at ∼9.2 GHz since 1967. With the improvement of accuracies by one order of magnitude every decade, Cs-clocks' accuracies have reached $\sim 10^{-15}$ and some fountain-type clocks have achieved $\approx 4 \times 10^{-16}$ [6, 21]. The invention of the laser and the subsequent development of technologies, such as laser cooling and trapping of atoms [11, 12, 43], optical frequency synthesis with optical frequency combs [15, 56] and stable laser sources with narrow linewidth [61], have opened

M. Takamoto (✉)
Quantum Metrology Laboratory, RIKEN, 2-1 Hirosawa, Wako-shi, Saitama 351-0198, Japan

Innovative Space-Time Project, ERATO, JST, 7-3-1 Hongo, Bunkyo-ku, Tokyo 113-8656, Japan

RIKEN Center for Advanced Photonics, 2-1 Hirosawa, Wako-shi, Saitama 351-0198, Japan
e-mail: takamoto@riken.jp

H. Katori
Quantum Metrology Laboratory, RIKEN, 2-1 Hirosawa, Wako-shi, Saitama 351-0198, Japan

Department of Applied Physics, Graduate School of Engineering, The University of Tokyo, 7-3-1 Hongo, Bunkyo-ku, Tokyo 113-8656, Japan

Innovative Space-Time Project, ERATO, JST, 7-3-1 Hongo, Bunkyo-ku, Tokyo 113-8656, Japan

RIKEN Center for Advanced Photonics, 2-1 Hirosawa, Wako-shi, Saitama 351-0198, Japan

Y. Yamamoto, K. Semba (eds.), *Principles and Methods of Quantum Information Technologies*, Lecture Notes in Physics 911, DOI 10.1007/978-4-431-55756-2_5

up a new area of research in atomic clocks. Optical clocks, which reference optical transitions instead of microwave transitions, are expected to improve the fractional accuracy and stability by 5 orders of magnitude, corresponding to the increase in the transition frequencies. The most promising candidate for optical clocks had been considered to be a singly trapped ion clock that references an optical transition of an ion confined in a Paul trap [13], in which a single ion is trapped near the zero of the quadrupole field, and therefore is ideally isolated from electric perturbations of the trap. Al^+ ion clocks with quantum logic spectroscopy have presented the uncertainty at 8.6×10^{-18} [9]. However, the quantum projection noise (QPN) [25] in observing a single ion requires days of averaging time to achieve their anticipated accuracy. In contrast, optical lattice clocks proposed in 2001 [26, 28] exploit the magic wavelength protocol to facilitate the observation of many atoms N simultaneously, thus reducing the averaging time by a factor of N.

In this review, we outline the principles of optical lattice clocks in Sect. 5.2, and describe the operation of optical lattice clocks, such as the Lamb-Dicke spectroscopy in Sect. 5.3 and the absolute frequency measurements in Sect. 5.4. Section 5.5 describes the frequency comparison of two optical lattice clocks near the quantum projection noise limit. In Sect. 5.6, we present the development of cryogenic Sr optical lattice clocks to reduce the blackbody radiation (BBR) shift to achieve the fractional uncertainty of 10^{-18}. Finally, we discuss the frequency comparison of two remote clocks using an optical fiber link as a tool for relativistic geodesy in Sect. 5.7.

5.2 Operating Principles of an Optical Lattice Clock

An atomic clock provides a reference for frequency, relying on the constancy of atomic transition frequency. The performance of an atomic clock can be expressed by its accuracy and stability. The accuracy is given by a fractional frequency excursion of $\delta\nu/\nu_0$, where $\delta\nu$ is the deviation of clock's frequency from the unperturbed atomic transition frequency ν_0. The frequency deviation is caused by the perturbations such as ambient electro-magnetic fields including BBR, Doppler shifts due to the thermal motions of atoms and atomic collisions. The stability indicates how quickly the clock's frequency settles to the final uncertainty and can be evaluated by the Allan standard deviation. The stability of atomic clocks is limited by the QPN as

$$\sigma_y(\tau) = \frac{1}{K}\frac{\Delta\nu}{\nu_0}\frac{1}{\sqrt{N\tau/T_c}}, \tag{5.1}$$

where τ is the averaging time, K ($\sim$1) is a slope coefficient dependent on the excitation sequence (i.e., Rabi or Ramsey), $\Delta\nu$ the linewidth of the spectrum, N the number of atoms observed in a cycle time of clock operation T_c. In terms of accuracy, a single ion isolated near the zero of the quadrupole field is an ideal

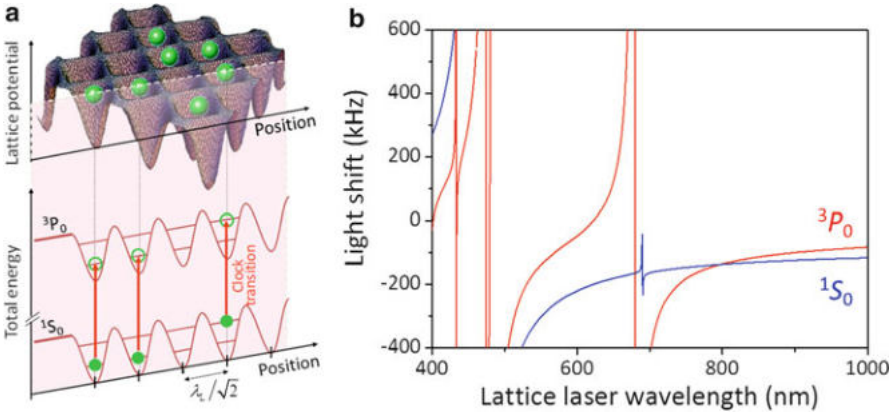

Fig. 5.1 (**a**) Schematic of the optical lattice potentials. The interference pattern of lattice lasers confines a large number of atoms in the Lamb-Dicke regime. (**b**) Calculated lattice light shifts for the $^1S_0$ (*blue line*) and $^3P_0$ (*red line*) states of the clock transition of Sr atoms for the lattice laser intensity $I_L = 10$ kW/cm^2. The magic wavelength λ_m where the light shifts of both states cancel is calculated to be $\lambda_m \sim 800$ nm

reference, however the QPN of observing the ion ($N = 1$) severely limits the stability of such ion clocks. Assuming $\nu_0/\Delta\nu = 10^{15}$, in order to achieve the instability of $\sigma_y \sim 10^{-18}$, ion clocks would require an averaging time of $\tau \sim 10^6$ s ($\sim$10 days). In contrast, optical lattice clocks probe a large number of atoms trapped in an interference pattern of lasers as illustrated in Fig. 5.1a. Such an optical lattice clock would dramatically improve the QPN limit by $1/\sqrt{N}$, which requires only $\tau = 1$ s by interrogating $N \sim 10^6$ atoms simultaneously.

When the atoms are exposed to the light field with an electric field $E(\lambda_L, \mathbf{e}_L, \mathbf{r})$, atoms are subjected to the light shift potential

$$U_i(\lambda_L, \mathbf{e}_L, \mathbf{r}) = -\frac{1}{2}\alpha_i(\lambda_L, \mathbf{e}_L)\,|E(\lambda_L, \mathbf{e}_L, \mathbf{r})|^2, \tag{5.2}$$

where $\alpha_i(\lambda_L, \mathbf{e}_L)$ is the polarizability of atoms in the state i (=g, e), λ_L and $\mathbf{e}_L$ the wavelength and the polarization of the light field respectively, and $\mathbf{r}$ the position of the atoms. By introducing a spatial interference pattern of laser fields as shown in Fig. 5.1a, the atoms can be confined in a region Δx much smaller than the wavelength λ_L in periodic potential wells [22], which is referred to as an optical lattice. Since the confinement Δx is smaller than the wavelength λ_p of a probe laser wavelength, the Lamb-Dicke condition, where the first order Doppler shift is suppressed [14], holds for spectroscopy in an optical lattice.

The electronic states of atoms trapped in an optical lattice are energy-shifted by light shifts. The clock transition frequency $\nu(\lambda_L, \mathbf{e}_L)$ of atoms in the lattice light field

$$\nu(\lambda_L, \mathbf{e}_L) = \nu_0 + \frac{1}{h}\left(U_e - U_g\right) = \nu_0 - \frac{1}{2h}\,\Delta\alpha(\lambda_L, \mathbf{e}_L)\,E^2 + O\left(E^4\right), \tag{5.3}$$

deviates from the unperturbed transition frequency ν_0 by a differential light shift of the trapping potential $(U_e - U_g)/h$, where $\Delta\alpha(\lambda_L, \mathbf{e}_L)$ is a difference of polarizabilities between the ground (g) and excited (e) states of the clock transition. However, if the polarizabilities for the ground and excited states become equal $(\Delta\alpha(\lambda_L, \mathbf{e}_L) = 0)$ by tuning the lattice laser wavelength, the differential light shift of the trapping potential can be cancelled out regardless of the lattice laser intensity. Figure 5.1b shows the light shifts of the ground ($^1S_0$) and excited ($^3P_0$) states of the clock transition for strontium (Sr) atoms for the lattice laser intensity of $I_L = 10$ kW/cm^2. The wavelength where the light shifts get canceled out can be found at $\lambda_L \sim 800$ nm. This particular wavelength is referred to as the magic wavelength λ_m. The light shift dependence on the lattice laser frequency ν_L is calculated to be $d\nu/d\nu_L \approx 1$ Hz/GHz for $I_L = 10$ kW/cm^2 near the magic frequency $\nu_m = c/\lambda_m$, allowing to share the clock's uncertainty of 10^{-18} by sharing the lattice laser frequency with the fractional uncertainty of 10^{-9} [27].

For the choice of atomic species, taking into account the sensitivity to the polarization of lattice lasers $\mathbf{e}_L$, the electronic states of total angular momentum $J = 0$ are attractive to minimize the polarization dependent light shifts and thus to define the magic condition solely by the wavelength [26]. As the transition between the $J = 0$ states is highly forbidden, we rely on the hyperfine mixing by a non-zero nuclear spin I of relevant isotope to obtain a finite transition dipole moment. These conditions are satisfied for the Alkaline-earth (like) atoms in group 2 and 2B, such as Be, Mg, Ca, Sr, Zn, Cd, Hg and Yb, which have two valence electrons. The optimal choice of atomic species might be finally determined by insensitivities to the parameters such as collisions, BBR and hyper polarizability. The optical lattice clocks have been developed with Sr, Yb and Hg atoms thus far.

5.3 Lamb-Dicke Spectroscopy in a Magic-Wavelength Lattice

The first demonstration of optical lattice clocks was performed with ^{87}Sr isotope confined in a one-dimensional (1D) optical lattice (Fig. 5.2a) [55]. The hyperfine mixing induced by the nuclear spin $I = 9/2$ weakly allows the clock transition $^1S_0$ $(F = 9/2)$ – $^3P_0$ $(F = 9/2)$ with a natural linewidth of 1 mHz (Fig. 5.2b). For the preparation of ultracold atomic samples in an optical lattice, the ^{87}Sr are cooled down to $\sim$1 mK by the dipole-allowed transition ($^1S_0$ – $^1P_1$) and the intercombination transition between singlet and triplet states ($^1S_0$ – $^3P_1$) allows cooling atoms further down to a few μK [37].

The optical lattice potential is created by a pair of counter-propagating lasers at the magic wavelength, which forms a 1D standing-wave potential with the depth of $U_0 \sim 10$ μK for the typical laser intensity of $I_L \sim 15$ kW/cm^2 and the typical beam diameter of $\sim$100 μm. The clock laser, which is superimposed onto the lattice laser, excites the atoms confined in the lattice. Along the direction of the clock laser (the x-axis), the amplitude of the atomic motion $\Delta x \sim 40$ nm is less than the clock laser

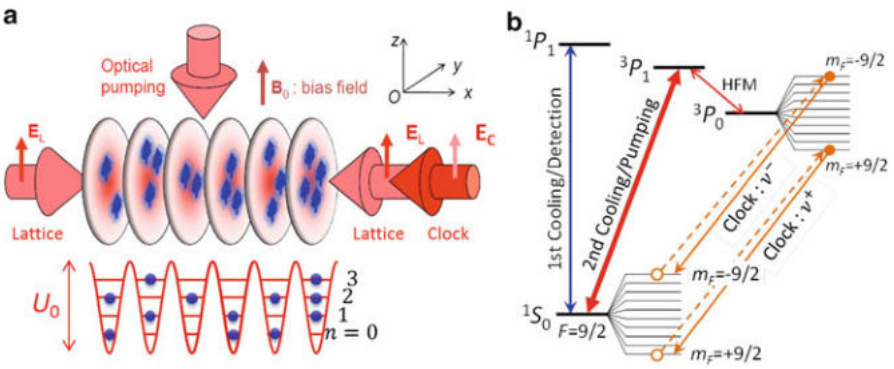

Fig. 5.2 (**a**) Lamb-Dicke spectroscopy in a 1D optical lattice. Atoms trapped in the bound levels of 1D optical lattice with the potential depth U_0 are probed by the clock laser, which is superimposed onto the lattice lasers. Optical pumping laser is irradiated to spin-polarize atoms. (**b**) Energy diagram for ^{87}Sr ($I = 9/2$) atoms. Hyperfine mixing between $^3P_0$ and $^3P_1$ weakly allows the clock transition $^1S_0$ ($F = 9/2$) $-$ $^3P_0$ ($F = 9/2$) with a natural linewidth of 1 mHz. Following the spin-polarization of atoms to the stretched state $^1S_0$ ($m_F = +9/2$ or $-9/2$), the clock transition is probed by the clock laser

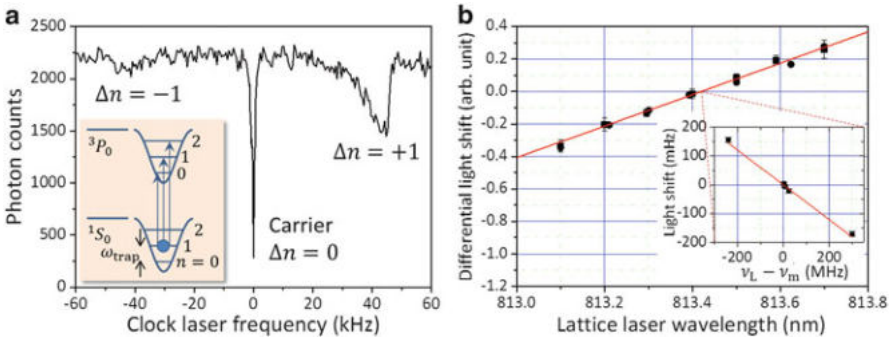

Fig. 5.3 (**a**) Vibrational spectrum of the clock transition. A narrow carrier spectrum with motional sidebands is observed. The *inset* illustrates the vibrational structure of a lattice on the clock transition. (**b**) Determination of the magic wavelength. The differential light shift for two laser intensity is plotted as a function of the lattice laser wavelength λ_L. The magic wavelength where the differential light shift becomes zero is found at $\lambda_m = 813.420(7)$ nm. The *inset* shows the measurement of differential light shift as a function of the lattice laser frequency ν_L ($=c/\lambda_L$) near the magic frequency ν_m

wavelength $\lambda_c = 698$ nm, which guarantees the Lamb-Dicke condition. Figure 5.3a shows the laser-induced fluorescence of atoms on the $^1S_0 - {}^1P_1$ transition as a function of the clock laser detuning. The excitation on the clock transition induces the reduction of the fluorescence, which is referred to as a shelving technique [38]. The spectrum features the vibrational structures due to a quantized atomic motion in a harmonic potential of a lattice. A sideband at higher frequency corresponds to the heating sideband which excites higher vibrational state $\Delta n = +1$, while the

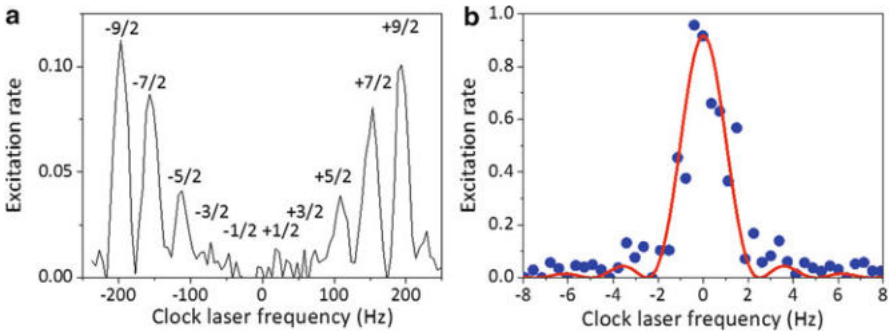

Fig. 5.4 (**a**) Zeeman components of the clock transition with a bias magnetic field of $|\mathbf{B_0}| \sim 50$ μT. (**b**) Rabi spectrum of the clock transition with a Fourier-limited linewidth of 2 Hz

lower one is referred to as the cooling sideband, which excites lower vibrational state $\Delta n = -1$. The central narrow spectrum, which is free from the Doppler shift and photon-recoil shift, allows the high precision spectroscopy in an optical lattice.

In order to determine the magic wavelength, the intensity dependence of the light shifts (dv/dI_L) is measured as a function of the lattice laser wavelength λ_L as shown in Fig. 5.3b. The magic wavelength, where the intensity dependence of light shifts disappears, was determined to be $\lambda_m = 813.420(7)$ nm [54]. Recently, more precise evaluation of the lattice light shifts enabled us to determine the magic wavelength at MHz -level precision (the inset of Fig. 5.3b).

By applying a bias magnetic field $\mathbf{B_0}$, the carrier spectrum splits into ten ($=2I + 1$) Zeeman components for $I = 9/2$ as shown in Fig. 5.4a. The electronic state for clock spectroscopy is prepared by spin-polarizing atoms to the stretched states of either $m_F = +9/2$ or $-9/2$ with optical pumping. By probing the clock transition with a clock laser stabilized to a high finesse cavity, a Fourier-limited linewidth of 2 Hz is observed for a Rabi-π-pulse with a duration of 400 ms (Fig. 5.4b).

5.4 Absolute Frequency Measurement of Optical Lattice Clocks With ^{87}Sr

The absolute frequencies of the ^{87}Sr clock transition were measured by referencing the Cs clocks. At the University of Tokyo, the Sr clock was frequency-linked to the TAI (International Atomic Time) via the National Metrology Institute in Japan (NMIJ) using a GPS carrier phase link [53]. The absolute frequency measurements were performed by three groups, Tokyo-NMIJ [53], JILA [33] and SYRTE [29]. Their measurements were consistent with each other within the fractional uncertainty of 7.5×10^{-15}, which triggered the adoption of the Sr optical lattice clocks as a "secondary representation of the second" in 2006.

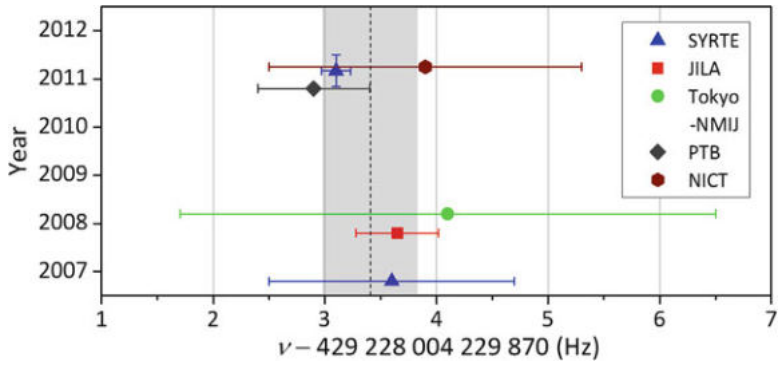

Fig. 5.5 Recent measurements of the absolute frequency of ^{87}Sr clock transition ([3, 7, 16, 24, 29, 58]). The *dashed line* and the shaded area represent the recommended frequency and its uncertainty assigned by the BIPM in 2013

Figure 5.5 summarizes the recent measurements of the absolute frequencies of ^{87}Sr by five groups [3, 7, 16, 24, 29, 58]. The *dashed line* and shaded area represent the recommended frequency $\nu_{\mathrm{Sr}} = 429\ 228\ 004\ 229\ 873.4$ Hz and its fractional uncertainty of 1×10^{-15} assigned by the BIPM in 2013 [4]. Recently, the SYRTE group improved the absolute frequency measurement by comparing the Sr clocks with three primary Cs fountain clocks [30]. This measurement gives the fractional uncertainty of 3.1×10^{-16}, where the measurement uncertainty is limited by Cs clocks. For Yb optical lattice clocks, the NIST group measured the transition frequency of ^{171}Yb to be $\nu_{\mathrm{Yb}} = 518\ 295\ 836\ 590\ 865.2(7)$ Hz [31], which is consistent with the measurements reported by the NMIJ [60] and the KRISS groups [8]. For Hg optical lattice clocks, the SYRTE group measured the transition frequency to be $\nu_{\mathrm{Hg}} = 1\ 128\ 575\ 290\ 808\ 162.0(6.4)$ Hz [35].

5.5 Frequency Comparison of Optical Lattice Clocks Near the Quantum Projection Noise Limit

To evaluate clocks' performance at an uncertainty smaller than that of Cs or any other state-of-the-art clocks, direct comparison between two clocks with similar performance is necessary. We developed two optical lattice clocks with 1D and 3D lattice configurations, which are designed to minimize atomic collisions and lattice polarization effects, and compared them directly [2]. However, the achieved frequency stability of $\sigma_y(\tau) \sim 10^{-14}\ \tau^{-1/2}$ did not exceed the typical stabilities of ion clocks [9]. This is because the stability is degraded by the Dick effect induced by the frequency instability of the clock laser, which masks the QPN limit of optical lattice clocks.

The Dick effect is attributed to the down-conversion of high frequency noise of a clock laser by the sampling process [48]. The stability of a clock laser is

limited by the thermal noise of the reference cavity (e.g. $\sigma_y \sim 1 \times 10^{-15}$ at 1 s for the typical cavity length of 10 cm with ULE mirrors) [41] operated at room temperature. The Dick effect limits the stability to $\sigma_y(\tau) \sim 10^{-14}\ \tau^{-1/2}$, which is two orders of magnitude worse than the QPN limited stability of $\sigma_y(\tau) \sim 10^{-16}\ \tau^{-1/2}$ for $\Delta\nu = 6$ Hz and $N = 10^3$.

We demonstrate frequency comparison between two optical lattice clocks by sharing the clock laser. The response of the atoms to the laser frequency fluctuations $\delta\omega\ (t)$ can be expressed by the sensitivity function $g(t)$. The population fluctuation δp_n of the n-th cycle due to the laser frequency noise $\delta\omega\ (t)$ can be expressed as

$$\delta p_n = \frac{1}{2}\int_{nT_c}^{(n+1)T_c} g(t)\delta\omega(t)\ dt. \tag{5.4}$$

The servo loop converts this population fluctuation δp_n into the frequency fluctuation and degrades the stability of an atomic clock. However, if we interrogate two atomic ensembles synchronously by sharing the clock laser, both atomic ensembles observe the common frequency noise $\delta\omega\ (t)$ and the population fluctuations δp_n correlate for both clocks. Therefore, if we take the beat note of the frequencies of two clocks, the frequency fluctuation, which originates from laser frequency noise $\delta\omega\ (t)$ can be rejected. In this condition, the relative stability of two clocks is solely limited by the QPN of interrogated atoms.

An experimental setup is shown in Fig. 5.6a. A single clock laser with a π-pulse duration of $T_i = 100$–400 ms interrogates the two clock transitions synchronously. The cycle time of $T_c = 1.4$ s includes the time for cooling, trapping and detection. The clock laser's frequency is independently stabilized to the atomic resonance of ^{87}Sr and ^{88}Sr in the 1D and 3D lattice respectively by tuning f_{87} and f_{88} of frequency shifters with digital servo loops. The beat note $f_{88} - f_{87}$ corresponds to the isotope shift $\sim$62 MHz and is used for the evaluation of the clock stabilities.

Figure 5.6b shows the relative stabilities of the 1D and 3D optical lattice clocks. The open circles represent the relative stability for asynchronous interrogations. The short-term stability ($\tau < 10$ s) corresponds to the stability of the clock laser which is limited by the thermal noise of the ULE cavity. After averaging a few tens of seconds, the Allan deviation starts to decrease due to the feedback control to each atomic resonance with the Nyquist frequency of $f_N = 1/(4 \times 1.4\ \text{s})$. For an averaging time $\tau > 50$ s, the Allan deviation decreases with $\sigma_y(\tau) \sim 6.0 \times 10^{-15}\ \tau^{-1/2}$. The closed circles show the relative stability for synchronous interrogations. The Allan standard deviation decreased by $\sigma_y(\tau) \sim 3.7 \times 10^{-16}\ \tau^{-1/2}$ and reached 3×10^{-17} for an averaging time of $\tau = 3\,500$ s. This relative stability is clearly below the Dick effect limit (*dashed line*) owing to cancellation of the clock laser's noise and is approaching the QPN limit for $N = 1 \times 10^3$ and $\Delta\nu = 6$ Hz (solid line, Fig. 5.6b).

Such a stable comparison of clocks is useful to evaluate the systematic uncertainties of optical lattice clocks in a short averaging time as discussed in Sect. 5.6. This scheme is also applicable to the frequency comparison of two remote clocks by sharing the local oscillator with the help of the coherent optical frequency links as discussed in Sect. 5.7.

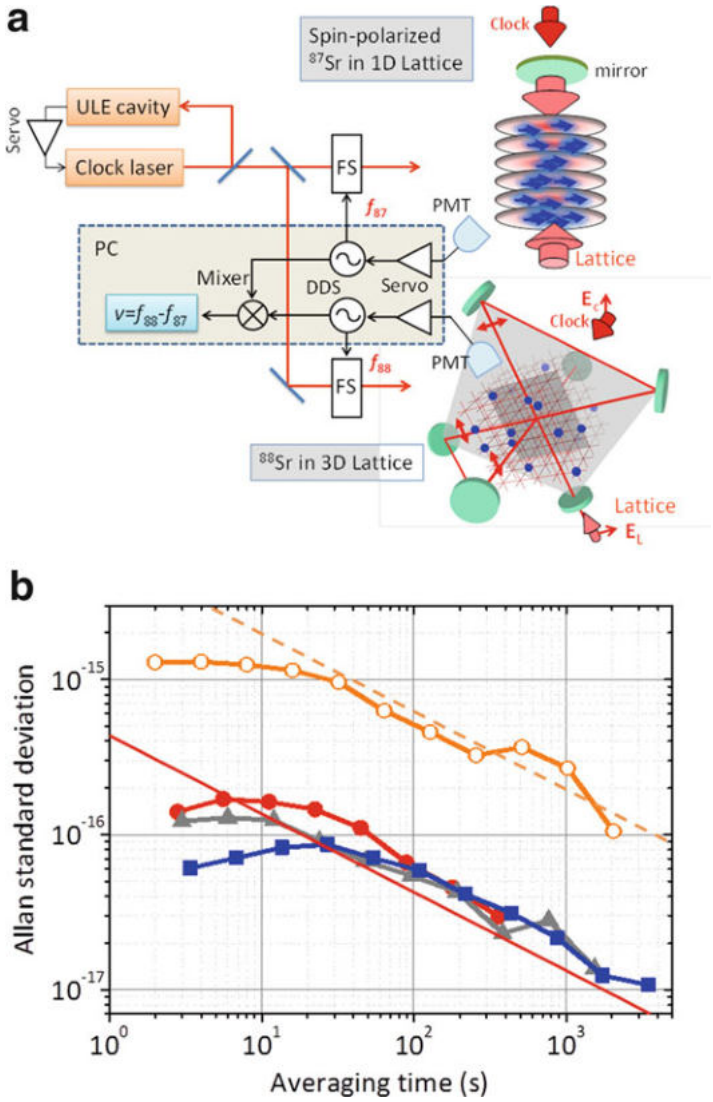

Fig. 5.6 (**a**) Experimental setup for frequency comparison of two optical lattice clocks with 1D and 3D lattice configurations. (**b**) The Allan standard deviation of the frequency difference between two clocks. *Open circles* represent the Allan deviation for asynchronous interrogation. *Closed symbols* represent the Allan deviations for synchronous interrogation with the interrogation time T_i of 100 ms (*closed circles*), 200 ms (*closed triangles*) and 400 ms (*closed rectangles*), respectively. The Allan deviation with $T_i = 400$ ms reaches 1×10^{-17} with the averaging time of 2000 s. The *dashed line* shows the Dick limit for asynchronous interrogations and the *solid line* the QPN limit with $T_i = 100$ ms

5.6 Cryogenic Strontium Optical Lattice Clocks

Nearly QPN limited stabilities for $\sim 10^3$ atoms of $\sigma_y \sim 10^{-16}$ at 1 s have been demonstrated by employing synchronous interrogation scheme as described in Sect. 5.5 or by using clock lasers referencing long cavities [24, 40]. Such high stabilities enable accessing 10^{-18} uncertainty in a few hours of averaging time, allowing extensive studies to unravel systematic uncertainties due to collisions between spin-polarized fermions, hyper-polarizability effects and multipolar interactions of atoms with optical lattices [42, 58]. After careful evaluations of these effects, the frequency shift due to the BBR remains as a dominant source of uncertainty in optical lattice clocks with Sr and Yb.

The BBR shift is given by the Stark shift $h\nu_{\mathrm{BBR}} \approx -\frac{1}{2}\Delta\alpha\langle E^2\rangle_T$, which is induced by the ambient thermal field $\sqrt{\langle E^2\rangle_T} \approx 8.3$ V cm^{-1} at $T = 300$ K, where $\Delta\alpha = \alpha_{\mathrm{e}} - \alpha_{\mathrm{g}}$ is a difference of polarizabilities between the excited and the ground states of the clock transition. The BBR shifts for Sr and Yb atoms are orders of magnitude larger than that of Al^+ ions [46]. Optical lattice clocks based on mercury atoms have been proposed [20] and demonstrated [35], owing to their less sensitivity to the BBR.

The BBR shift for the ${}^1S_0 - {}^3P_0$ clock transition of Sr was calculated [27, 44], and was recently evaluated to be $-2.2778(23)$ Hz at $T = 300$ K based on the measurement of static polarizability difference between the two clock states and a modeling of the dynamic contribution [36]. For Yb atoms, a static polarizability [51] and the dynamic contribution [5] were evaluated experimentally. Such investigations allow correcting the BBR shift at room temperature within an uncertainty of 5×10^{-18} for Sr and 1×10^{-18} for Yb. In order to realize an uncertainty of 1×10^{-18}, the fluctuation and inhomogeneity ΔT of the ambient temperature T has to be controlled to within $\Delta T = 14$ mK for Sr and $\Delta T = 30$ mK for Yb, which remains an experimental challenge. As the BBR energy density $\langle E^2\rangle_T$ varies as T^4 following the Stefan-Boltzmann law, the BBR shift and its temperature dependence ($d\nu_{\mathrm{BBR}}/dT \propto T^3$) rapidly decreases with the surrounding temperature T. For Sr atoms, at the temperature of $T = 95$ K, the BBR shift reduces to -22 mHz. By controlling the temperature of such a cryogenic environment with $\Delta T = 0.5$ K, the fractional uncertainty due to the BBR shift can be reduced to 1×10^{-18}.

Two cryo-clock setups (Fig. 5.7) are developed, namely Sr-1 and Sr-2, with temperature-controlled chambers maintained at T_1 and T_2, respectively. The cryogenic environment is realized by surrounding the region for clock spectroscopy with a cold chamber of volume ~ 6 cm^3. The chamber is cooled down to 95 K by a Stirling refrigerator, which is actively controlled to stabilize the cryo-chamber temperature within a few mK. The measurement uncertainty of the temperature sensors is ~ 22 mK, which corresponds to a fractional frequency uncertainty of 5×10^{-20} at 95 K and is well below the targeted uncertainty of the clock.

Ultracold Sr atoms are transported over 23 mm into the middle of the cryogenic chamber by a moving lattice (Fig. 5.8). In order to introduce the atoms and lasers, the chamber has two apertures with diameters of $\phi_1 = 0.5$ mm and $\phi_2 = 1$ mm. Inside

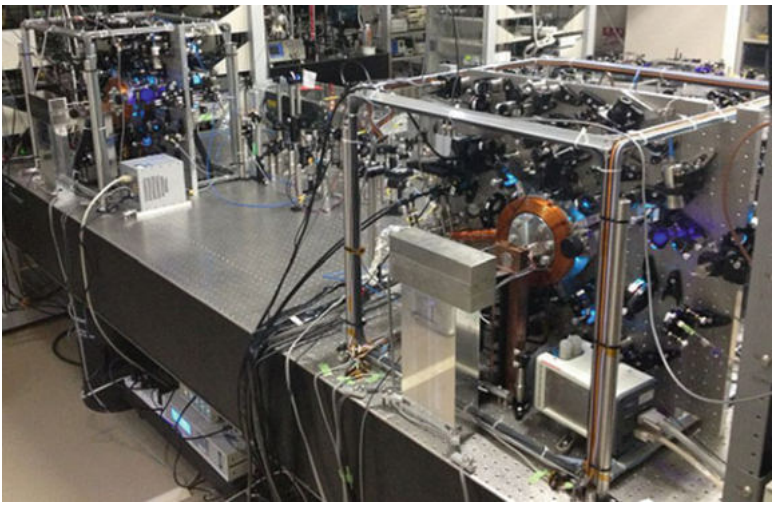

Fig. 5.7 Picture of cryogenic Sr optical lattice clocks. Two setups (Sr-1, Sr-2) are developed to evaluate the BBR shift and the performance of cryogenic clocks from the frequency comparison of the two. Each clock setup is constructed inside a volume of $(60\ \mathrm{cm})^3$

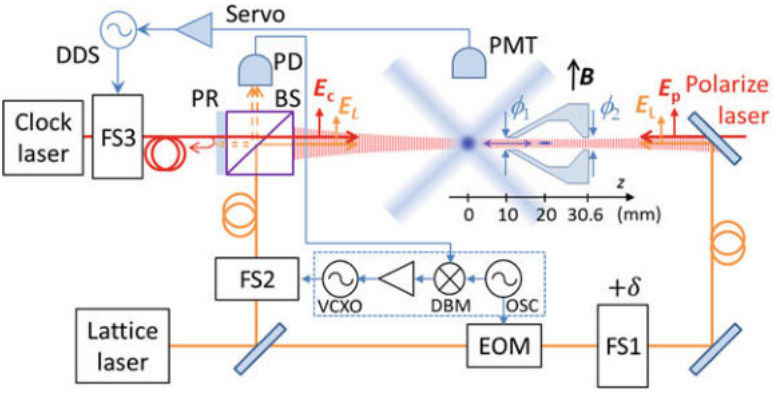

Fig. 5.8 Experimental setup of cryogenic Sr optical lattice clocks. A moving lattice transports atoms from the lattice-loading position (0 mm) to the middle of the cryogenic chamber (20 mm), where the clock transition is probed by a clock laser. After exciting the clock transition, atoms are transported back to the initial position (0 mm) and the excitation fraction is measured from the fluorescence observed by a photomultiplier tube (PMT)

the chamber, the atoms are spin-polarized and then excited by a Rabi π -pulse on the clock transition. After exciting the clock transition, atoms are transported back to their initial position with a moving lattice. The fluorescence of atoms on the ${}^1S_0 - {}^1P_1$ transition is detected to measure the excitation probability on the clock transition.

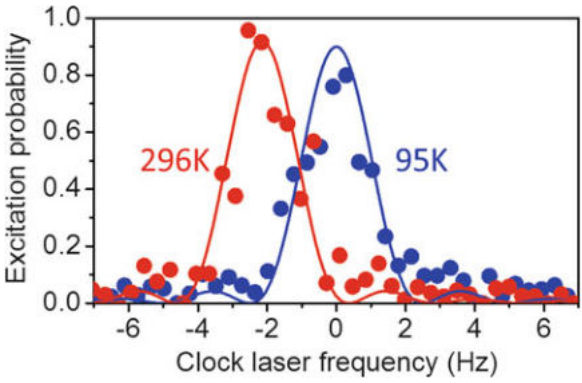

Fig. 5.9 Clock transition spectra for two Sr optical lattice clocks operated at $T_1 = 95$ K and $T_2 = 296$ K. A spectrum with 2 Hz linewidth resolves the frequency shift induced by room-temperature BBR

Figure 5.9 shows the spectra of the clock transitions obtained by scanning the clock laser frequencies simultaneously for Sr-1 and Sr-2. The filled circles show the spectrum of Sr-1 at $T_1 = 95$ K and the empty ones show that for Sr-2 at $T_2 = 296$ K. A Fourier-limited linewidth of 2 Hz clearly resolves the room-temperature BBR shift of about 2 Hz.

To evaluate the uncertainties of cryogenic clocks, both clocks were operated at the cryogenic temperature of $T_1 = T_2 = 95$ K and then compared directly. The Allan deviation reduces with the integration time τ as $\sigma_y(\tau) = 1.8 \times 10^{-16}\ \tau^{-1/2}$ and reaches 2×10^{-18} for $\tau = 6 \times 10^3$ s. The obtained Allan deviation is close to the QPN limit for $T_i = 300$ ms and $N = 10^3$ atoms, which is estimated from the atomic fluorescence. After averaging 11 separate measurements, each of duration $\tau = 4 \times 10^3 - 1 \times 10^4$ s, the frequency difference is measured to be -0.5 ± 0.9 mHz, which corresponds to the fractional frequency difference of $(1.1 \pm 2.0) \times 10^{-18}$. The total systematic correction and uncertainty for the clocks' comparison are evaluated to be 73.9 mHz and 1.9 mHz, respectively. Finally, the agreement between the two cryo-clocks is evaluated to be -0.5 mHz $\pm$ 0.9 mHz (stat) $\pm$ 1.9 mHz (sys) [57].

5.7 Frequency Comparison Between Distant Optical Lattice Clocks Towards Relativistic Geodesy

At the fractional uncertainty of $\delta\nu/\nu_0 \approx 1 \times 10^{-18}$, the gravitational red shift $\delta\nu/\nu_0 = g\Delta h/c^2$ due to the relativistic time dilation becomes measurable even for a height difference $\Delta h = 1$ cm, where $g \approx 9.8$ m s^{-2} is the acceleration due to gravity and c is the speed of light. The height difference of $\Delta h \approx 30$ cm was observed in the frequency comparison of two Al^+ ion clocks [10]. Recently, optical frequency transfer using an optical fiber has been developed extensively for the fiber length up to 920 km [45] and featured a few orders of magnitude better accuracy and stability than the microwave frequency transfer using a satellite link. Such technologies will allow establishing the network of optical clocks to map the earth's gravitational potential. As a step towards the relativistic geodesy, we have

established a 30-km-long optical fiber link between RIKEN and the University of Tokyo (UT) to compare two distant cryogenic Sr clocks at the fractional uncertainty of $\delta\nu/\nu_0 \approx 10^{-18}$ [1]. The straight-line distance and the estimated height difference between the two clocks are ∼15 km and ∼16 m, respectively.

For frequency link using a telecom fiber, a transfer laser at the wavelength around 1.55 μm (C-band) is generally used to take advantage of the low loss of silica-fibers. A frequency comb is then used to bridge the frequency gap between the clock and transfer lasers. However, in this configuration, frequency combs with the typical stability of $\sigma_y \sim 10^{-16}$ at 1 s [39, 49] may degrade the potential link stability. In our transfer setup, we use a transfer laser at 1.397 μm, which is twice the wavelength of the Sr clock transition, to replace a frequency comb by a frequency doubling crystal. For fiber transfer at 1.397 μm, the water-peak attenuation due to the OH radicals in fibers introduces relatively larger absorption loss. In our 30-km-long fiber, the transmission loss of 30.4 dB at 1.397 μm is 7 dB larger than the loss at 1.55 μm, but the loss is small enough for the fiber noise canceller [34] to work.

The experimental setup for the phase-coherent link including a fiber noise canceller is shown in Fig. 5.10a. At the local site (RIKEN), a transfer laser at 1.397 μm is frequency-doubled by a periodically-poled lithium niobate (PPLN) waveguide and is phase-locked to a clock laser at 698 nm. The transfer laser is sent to the remote site (UT) through a 30-km-long fiber. At the remote site, a repeater laser is phase-locked to the transfer laser to boost the received signal intensity. The repeater laser is sent back to the local site through the fiber and a feedback signal for a fiber noise canceller is generated by measuring the beat note between the repeater laser and the transfer laser at the local site. A clock laser at the remote site is phase-locked to the repeater laser. The clock lasers at both sites, therefore, are phase-locked for the servo bandwidth less than ∼800 Hz, which is determined by the bandwidth of the fiber noise canceller.

Figure 5.10b shows the stability of fiber transfer evaluated by the modified Allan deviation (MDEV) [47]. Open circles represent the MDEVs for the free-running fiber, while the closed ones represent those for the noise-cancelled fiber. Although the stability of the noise-cancelled fiber follows the calculation (dashed curve) for short averaging time $\tau < 0.1$ s, it deviates from the calculation due to the clock lasers' instabilities. To evaluate the transfer stability for long averaging time $\tau > 0.1$ s, we connected two fibers at UT to establish a 60-km-long fiber link (closed triangles). The stability of the 60-km-long fiber link is measured to be $4 \times 10^{-17}\ \tau^{-3/2}$, which corresponds to the stability of $1 \times 10^{-17}\ \tau^{-3/2}$ for the 30-km-long fiber link. For averaging time $\tau > 2$ s, the MDEVs have $\sim\tau^{-1/2}$ slopes, which probably result from the white frequency noise caused by the mechanical instability of the interferometer for the beat note measurement.

The clock lasers are stabilized to the Sr clock transitions by applying the offset frequencies δf_{LO} and δf_{RE} to the frequency shifters at local and remote sites, respectively (Fig. 5.10a) . The frequency difference $\delta f = \delta f_{\mathrm{RE}} - \delta f_{\mathrm{LO}}$ gives that of the gravitational shift between the two sites. The timing of the clock sequence is synchronized with a time delay $\tau_{\mathrm{d}} = nL/c \approx 160$ μs, where $L \approx 30$ km is the length of the fiber and $n \approx 1.5$ is the refractive index. We anticipate that the two Sr clocks at RIKEN and UT, 15-km-apart, may be compared with a stability of 1×10^{-17} for

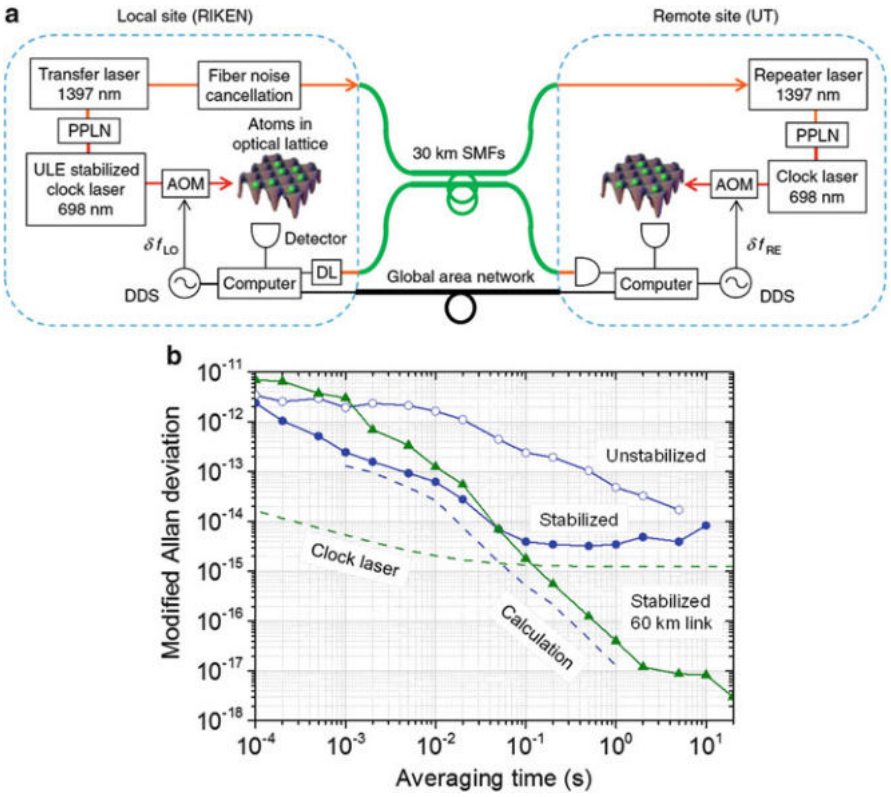

Fig. 5.10 (**a**) Experimental setup for frequency comparison of two distant optical lattice clocks via a phase-stabilized optical fiber link. (**b**) The modified Allan deviation for the fiber transfer. *Open circles* show stabilities of the one-way beat frequency measured with the 30-km-long free-running fiber. *Closed symbols* show those for the stabilized fiber. *Closed triangles* show the stability of the 60-km-long fiber link. A 60-km-link shows the stability of 1×10^{-17} with a few seconds averaging time

1 s averaging time by synchronously operating the two clocks. This clock stability allows detecting gravitational potential difference of 10 cm for a measurement time of 1 s, which will provide clocks with new application as a probe for the geodesy.

5.8 Future Prospects

Optical lattice clocks raised the possibility of ultra-stable and accurate timekeeping by applying the "magic wavelength" protocol on optical lattices. Since the proposal of the scheme in 2001, the optical lattice clocks are being developed by more than 20 groups around the world, and the clocks are surpassing the uncertainty of the current SI second, becoming one of the most promising candidates for the future redefinition of the second. We have demonstrated clock uncertainties approaching

10^{-18} by reducing the BBR shifts and by improving the relative stability of two clocks close to the QPN limit by employing synchronous interrogation scheme.

The accurate clocks and an optical frequency link between the clocks are the essential building blocks for the relativistic geodesy. Armed with these developments, we have started the geodetic demonstrations between RIKEN and the University of Tokyo. The precision of the clock comparison targets 1×10^{-18} that is far beyond the accuracy of the Cs clocks defining the SI second. For a practical use in monitoring the temporal variation of the gravitational potential, long-term continuous operation of the clocks is required, which demands new levels of technical development for stabilized lasers.

In parallel, we are developing technologies to miniaturize optical lattice clocks, aiming at transportable clocks to demonstrate "relativistic" car navigation. Such an endeavor will allow investigating resource mapping, cavities and magma chambers underneath the earth crust by utilizing the measured gravitational red shift caused by the local change of gravitational potential. As a possible direction for the clock miniaturization, we assume the use of a "hollow-core photonic crystal fiber" in which atoms are confined by the magic wavelength lattice. The preliminary experiments are in progress for the "fiber clock". Such transportable ultraprecise atomic clocks will function as a gravitational potential meter.

Acknowledgements This research was supported by the FIRST Program of the Japan Society for the Promotion of Science and by the Photon Frontier Network Program of the Ministry of Education, Culture, Sports, Science and Technology, Japan.

References

1. T. Akatsuka, H. Ono, K. Hayashida, K. Araki, M. Takamoto, T. Takano, H. Katori, 30-km-long optical fiber link at 1397 nm for frequency comparison between distant strontium optical lattice clocks. Jpn. J. Appl. Phys. **53**(3), 032801 (2014). doi:10.7567/jjap.53.032801
2. T. Akatsuka, M. Takamoto, H. Katori, Optical lattice clocks with non-interacting bosons and fermions. Nat. Phys. **4**(12), 954–959 (2008). doi:10.1038/nphys1108
3. X. Baillard, M. Fouché, R. Le Targat, P.G. Westergaard, A. Lecallier, F. Chapelet, M. Abgrall, G.D. Rovera, P. Laurent, P. Rosenbusch, S. Bize, G. Santarelli, A. Clairon, P. Lemonde, G. Grosche, B. Lipphardt, H. Schnatz, An optical lattice clock with spin-polarized ^{87}Sr atoms. Eur. Phys. J. D. **48**, 11–17 (2008)
4. BIPM, in *Report of the 101th meeting of the Comité International des Poids et Mesures (CIPM)* (Bureau International des Poids et Mesures (BIPM), Sevres, Paris Cedex, 2013)
5. K. Beloy, J.A. Sherman, N.D. Lemke, N. Hinkley, C.W. Oates, A.D. Ludlow, Determination of the 5d6s $^3D_1$ state lifetime and blackbody-radiation clock shift in Yb. Phys. Rev. A **86**(5), 051404 (2012). doi:10.1103/PhysRevA.86.051404
6. S. Bize, P. Laurent, M. Abgrall, H. Marion, I. Maksimovic, L. Cacciapuoti, J. Grünert, C. Vian, F.P.D. Santos, P. Rosenbusch, P. Lemonde, G. Santarelli, P. Wolf, A. Clairon, A. Luiten, M. Tobar, C. Salomon, Cold atom clocks and applications. J. Phys. B Atomic Mol. Phys. **38**(9), S449–S468 (2005). doi:10.1088/0953-4075/38/9/002
7. G.K. Campbell, A.D. Ludlow, S. Blatt, J.W. Thomsen, M.J. Martin, M.H.G. de Miranda, T. Zelevinsky, M.M. Boyd, J. Ye, S.A. Diddams, T.P. Heavner, T.E. Parker, S.R. Jefferts, The absolute frequency of the ^{87}Sr optical clock transition. Metrologia **45**, 539–548 (2008). doi:10.1088/0026-1394/45/5/008

8. P. Chang Yong, Y. Dai-Hyuk, L. Won-Kyu, P. Sang Eon, K. Eok Bong, L. Sun Kyung, C. Jun Woo, Y. Tai Hyun, M. Jongchul, P. Sung Jong, K. Taeg Yong, L. Sang-Bum, Absolute frequency measurement of $^{1}S_0$ (F = 1/2) – $^{3}P_0$ (F = 1/2) transition of ^{171}Yb atoms in a one-dimensional optical lattice at KRISS. Metrologia **50**(2), 119 (2013)
9. C.W. Chou, D.B. Hume, J.C.J. Koelemeij, D.J. Wineland, T. Rosenband, Frequency comparison of two high-accuracy Al^{+} optical clocks. Phys. Rev. Lett. **104**(7), 070802 (2010)
10. C.W. Chou, D.B. Hume, T. Rosenband, D.J. Wineland, Optical clocks and relativity. Science **329**(5999), 1630–1633 (2010). doi:10.1126/science.1192720
11. S. Chu, Nobel lecture: The manipulation of neutral particles. Rev. Mod. Phys. **70**(3), 685–706 (1998)
12. C.N. Cohen-Tannoudji, Nobel lecture: Manipulating atoms with photons. Rev. Mod. Phys. **70**(3), 707–719 (1998)
13. H. Dehmelt, in *Mono-Ion Oscillator as Potential Ultimate Laser Frequency Standard*. Thirty Fifth Annual Frequency Control Symposium, 27–29 May 1981 (1981), pp. 596–601. doi:10.1109/FREQ.1981.200532
14. R. Dicke, The effect of collisions upon the Doppler width of spectral lines. Phys. Rev. **89**(2), 472–473 (1953). doi:10.1103/PhysRev.89.472
15. S.A. Diddams, D.J. Jones, J. Ye, S.T. Cundiff, J.L. Hall, J.K. Ranka, R.S. Windeler, R. Holzwarth, T. Udem, T.W. Hänsch, Direct link between microwave and optical frequencies with a 300 THz femtosecond laser comb. Phys. Rev. Lett. **84**(22), 5102–5105 (2000)
16. S. Falke, H. Schnatz, J.S.R.V. Winfred, T. Middelmann, S. Vogt, S. Weyers, B. Lipphardt, G. Grosche, F. Riehle, U. Sterr, C. Lisdat, The ^{87}Sr optical frequency standard at PTB. Metrologia **48**(5), 399 (2011)
17. J. Flowers, The route to atomic and quantum standards. Science **306**(5700), 1324–1330 (2004). doi:10.1126/science.1102156
18. T.W. Hänsch, Nobel lecture: Passion for precision. Rev. Mod. Phys. **78**(4), 1297–1309 (2006)
19. H. Hachisu, K. Miyagishi, S. Porsev, A. Derevianko, V. Ovsiannikov, V. Pal'chikov, M. Takamoto, H. Katori, Trapping of neutral mercury atoms and prospects for optical lattice clocks. Phys. Rev. Lett. **100**(5), 053001 (2008). doi:10.1103/PhysRevLett.100.053001
20. J.L. Hall, Nobel lecture: Defining and measuring optical frequencies. Rev. Mod. Phys. **78**(4), 1279–1295 (2006)
21. T.P. Heavner, S.R. Jefferts, E.A. Donley, J.H. Shirley, T.E. Parker, NIST-F1: Recent improvements and accuracy evaluations. Metrologia **42**(5), 411–422 (2005). doi:10.1088/0026-1394/42/5/012
22. A. Hemmerich, T. Hänsch, Two-dimensional atomic crystal bound by light. Phys. Rev. Lett. **70**(4), 410–413 (1993). doi:10.1103/PhysRevLett.70.410
23. N. Hinkley, J.A. Sherman, N.B. Phillips, M. Schioppo, N.D. Lemke, K. Beloy, M. Pizzocaro, C.W. Oates, A.D. Ludlow, An atomic clock with 10^{-18} instability. Science **341**(6151), 1215–1218 (2013). doi:10.1126/science.1240420
24. F.-L. Hong, M. Musha, M. Takamoto, H. Inaba, S. Yanagimachi, A. Takamizawa, K. Watabe, T. Ikegami, M. Imae, Y. Fujii, M. Amemiya, K. Nakagawa, K. Ueda, H. Katori, Measuring the frequency of a Sr optical lattice clock using a 120 km coherent optical transfer. Opt. Lett. **34**(5), 692–694 (2009). doi:10.1364/OL.34.000692
25. W.M. Itano, J.C. Bergquist, J.J. Bollinger, J.M. Gilligan, D.J. Heinzen, F.L. Moore, M.G. Raizen, D.J. Wineland, Quantum projection noise: Population fluctuations in two-level systems. Phys. Rev. A **47**(5), 3554–3570 (1993)
26. H. Katori, in *Spectroscopy of Strontium Atoms in the Lamb-Dicke Confinement*, ed by P. Gill. Proceedings of the 6th Symposium on Frequency Standards and Metrology (World Scientific, 2002), pp. 323–330
27. H. Katori, M. Takamoto, V. Pal'chikov, V. Ovsiannikov, Ultrastable optical clock with neutral atoms in an engineered light shift trap. Phys. Rev. Lett. **91**(17), 173005 (2003). doi:10.1103/PhysRevLett.91.173005
28. H. Katori, Optical lattice clocks and quantum metrology. Nat. Photon. **5**, 203–210 (2011). doi:10.1038/nphoton.2011.45

29. R. Le Targat, X. Baillard, M. Fouché, A. Brusch, O. Tcherbakoff, G. Rovera, P. Lemonde, Accurate optical lattice clock with ^{87}Sr atoms. Phys. Rev. Lett. **97**(13), 130801 (2006). doi:10.1103/PhysRevLett.97.130801
30. R. Le Targat, L. Lorini, Y. Le Coq, M. Zawada, J. Guéna, M. Abgrall, M. Gurov, P. Rosenbusch, D.G. Rovera, B. Nagórny, R. Gartman, P.G. Westergaard, M.E. Tobar, M. Lours, G. Santarelli, A. Clairon, S. Bize, P. Laurent, P. Lemonde, J. Lodewyck, Experimental realization of an optical second with strontium lattice clocks. Nat. Commun. **4**, 2109 (2013). doi:10.1038/ncomms3109
31. N.D. Lemke, A.D. Ludlow, Z.W. Barber, T.M. Fortier, S.A. Diddams, Y. Jiang, S.R. Jefferts, T.P. Heavner, T.E. Parker, C.W. Oates, Spin-1/2 optical lattice clock. Phys. Rev. Lett. **103**(6), 063001 (2009)
32. C.H. Li, A.J. Benedick, P. Fendel, A.G. Glenday, F.X. Kartner, D.F. Phillips, D. Sasselov, A. Szentgyorgyi, R.L. Walsworth, A laser frequency comb that enables radial velocity measurements with a precision of 1 cm s^{-1}. Nature **452**(7187), 610–612 (2008). doi:10.1038/nature06854
33. A. Ludlow, M. Boyd, T. Zelevinsky, S. Foreman, S. Blatt, M. Notcutt, T. Ido, J. Ye, Systematic study of the ^{87}Sr clock transition in an optical lattice. Phys. Rev. Lett. **96**(3), 033003 (2006). doi:10.1103/PhysRevLett.96.033003
34. L.-S. Ma, P. Jungner, J. Ye, J.L. Hall, Delivering the same optical frequency at two places: Accurate cancellation of phase noise introduced by an optical fiber or other time-varying path. Opt. Lett. **19**(21), 1777–1779 (1994)
35. J.J. McFerran, L. Yi, S. Mejri, S. Di Manno, W. Zhang, J. Guéna, Y. Le Coq, S. Bize, Neutral atom frequency reference in the deep ultraviolet with fractional uncertainty $= 5.7 \times 10^{-15}$. Phys. Rev. Lett. **108**(18), 183004 (2012). doi:10.1103/PhysRevLett.108.183004
36. T. Middelmann, S. Falke, C. Lisdat, U. Sterr, High accuracy correction of blackbody radiation shift in an optical lattice clock. Phys. Rev. Lett. **109**(26), 236004 (2012). doi:10.1103/PhysRevLett.109.263004
37. T. Mukaiyama, H. Katori, T. Ido, Y. Li, M. Kuwata-Gonokami, Recoil-limited laser cooling of ^{87}Sr atoms near the fermi temperature. Phys. Rev. Lett. **90**(11), 113002 (2003). doi:10.1103/PhysRevLett.90.113002
38. W. Nagourney, J. Sandberg, H. Dehmelt, Shelved optical electron amplifier: Observation of quantum jumps. Phys. Rev. Lett. **56**(26), 2797–2799 (1986). doi:10.1103/PhysRevLett.56.2797
39. Y. Nakajima, H. Inaba, K. Hosaka, K. Minoshima, A. Onae, M. Yasuda, T. Kohno, S. Kawato, T. Kobayashi, T. Katsuyama, F.-L. Hong, A multi-branch, fiber-based frequency comb with millihertz-level relative linewidths using an intra-cavity electro-optic modulator. Opt. Express **18**(2), 1667–1676 (2010). doi:10.1364/OE.18.001667
40. T.L. Nicholson, M.J. Martin, J.R. Williams, B.J. Bloom, M. Bishof, M.D. Swallows, S.L. Campbell, J. Ye, Comparison of two independent Sr optical clocks with 1×10^{-17} stability at 10^3 s. Phys. Rev. Lett. **109**(23), 230801 (2012)
41. K. Numata, A. Kemery, J. Camp, Thermal-noise limit in the frequency stabilization of lasers with rigid cavities. Phys. Rev. Lett. **93**(25), 250602 (2004). doi:10.1103/PhysRevLett.93.250602
42. V.D. Ovsiannikov, V.G. Pal'chikov, A.V. Taichenachev, V.I. Yudin, H. Katori, Multipole, nonlinear, and anharmonic uncertainties of clocks of Sr atoms in an optical lattice. Phys. Rev. A **88**(1), 013405 (2013). doi:10.1103/PhysRevA.88.013405
43. W.D. Phillips, Nobel lecture: Laser cooling and trapping of neutral atoms. Rev. Mod. Phys. **70**(3), 721–741 (1998)
44. S. Porsev, A. Derevianko, Multipolar theory of blackbody radiation shift of atomic energy levels and its implications for optical lattice clocks. Phys. Rev. A **74**(2), 020502 (2006). doi:10.1103/PhysRevA.74.020502
45. K. Predehl, G. Grosche, S.M. Raupach, S. Droste, O. Terra, J. Alnis, T. Legero, T.W. Hansch, T. Udem, R. Holzwarth, H. Schnatz, A 920-kilometer optical fiber link for frequency metrology at the 19th decimal place. Science **336**(6080), 441–444 (2012). doi:10.1126/science.1218442

46. T. Rosenband, W.M. Itano, P.O. Schmidt, D.B. Hume, J.C.J. Koelemeij, J.C. Bergquist, D.J. Wineland, Blackbody radiation shift of the $^{27}Al^{+1}S_0 - {}^3P_0$ transition, in *Frequency and Time Forum (EFTF), 2006 20th European*, 27–30 March 2006 (2006), pp. 289–292
47. E. Rubiola, On the measurement of frequency and its sample variance with high-resolution counters. Rev. Sci. Instrum. **76**(5), 054703 (2005). doi:10.1063/1.1898203
48. G. Santarelli, C. Audoin, A. Makdissi, P. Laurent, G.J. Dick, C. Clairon, Frequency stability degradation of an oscillator slaved to a periodically interrogated atomic resonator. Ultrasonics, ferroelectrics and frequency control. IEEE Trans. Ultrason. Ferroelectr. Freq. Control **45**(4), 887–894 (1998). doi:10.1109/58.710548
49. T.R. Schibli, I. Hartl, D.C. Yost, M.J. Martin, A. Marcinkevicius, M.E. Fermann, J. Ye, Optical frequency comb with submillihertz linewidth and more than 10 W average power. Nat. Photon. **2**, 355–359 (2008). doi:10.1038/nphoton.2008.79
50. S. Schiller, G.M. Tino, P. Gill, C. Salomon, U. Sterr, E. Peik, A. Nevsky, A. Görlitz, D. Svehla, G. Ferrari, N. Poli, L. Lusanna, H. Klein, H. Margolis, P. Lemonde, P. Laurent, G. Santarelli, A. Clairon, W. Ertmer, E. Rasel, J. Müller, L. Iorio, C. Lämmerzahl, H. Dittus, E. Gill, M. Rothacher, F. Flechner, U. Schreiber, V. Flambaum, W.-T. Ni, L. Liu, X. Chen, J. Chen, K. Gao, L. Cacciapuoti, R. Holzwarth, M.P. Heß, W. Schäfer, Einstein gravity explorer–a medium-class fundamental physics mission. Exp. Astron. **23**(2), 573–610 (2008). doi:10.1007/s10686-008-9126-5
51. J.A. Sherman, N.D. Lemke, N. Hinkley, M. Pizzocaro, R.W. Fox, A.D. Ludlow, C.W. Oates, High-accuracy measurement of atomic polarizability in an optical lattice clock. Phys. Rev. Lett. **108**(15), 153002 (2012). doi:10.1103/PhysRevLett.108.153002
52. T. Steinmetz, T. Wilken, C. Araujo-Hauck, R. Holzwarth, T.W. Hansch, L. Pasquini, A. Manescau, S. D'Odorico, M.T. Murphy, T. Kentischer, W. Schmidt, T. Udem, Laser frequency combs for astronomical observations. Science **321**(5894), 1335–1337 (2008). doi:10.1126/science.1161030
53. M. Takamoto, F.-L. Hong, R. Higashi, Y. Fujii, M. Imae, H. Katori, Improved frequency measurement of a one-dimensional optical lattice clock with a spin-polarized fermionic ^{87}Sr isotope. J. Phys. Soc. Jpn. **75**(10), 104302 (2006). doi:10.1143/jpsj.75.104302
54. M. Takamoto, F.L. Hong, R. Higashi, H. Katori, An optical lattice clock. Nature **435**(7040), 321–324 (2005). doi:10.1038/nature03541
55. M. Takamoto, H. Katori, Spectroscopy of the $^1S_0$-$^3P_0$ clock transition of ^{87}Sr in an optical lattice. Phys. Rev. Lett. **91**(22), 223001 (2003). doi:10.1103/PhysRevLett.91.223001
56. T. Udem, J. Reichert, R. Holzwarth, T.W. Hänsch, Absolute optical frequency measurement of the cesium D1 line with a mode-locked laser. Phys. Rev. Lett. **82**(18), 3568–3571 (1999)
57. I. Ushijima, M. Takamoto, M. Das, T. Ohkubo, H. Katori, Cryogenic optical lattice clocks. Nat. Photon. **9,** 185–189 (2015). doi:10.1038/nphoton.2015.5
58. P.G. Westergaard, J. Lodewyck, L. Lorini, A. Lecallier, E.A. Burt, M. Zawada, J. Millo, P. Lemonde, Lattice-induced frequency shifts in Sr optical lattice clocks at the 10^{-17} level. Phys. Rev. Lett. **106**(21), 210801 (2011). doi:10.1103/PhysRevLett.106.210801
59. A. Yamaguchi, N. Shiga, S. Nagano, Y. Li, H. Ishijima, H. Hachisu, M. Kumagai, T. Ido, Stability transfer between two clock lasers operating at different wavelengths for absolute frequency measurement of clock transition in ^{87}Sr. Appl. Phys. Express **5**(2), 022701 (2012). doi:10.1143/apex.5.022701
60. M. Yasuda, H. Inaba, T. Kohno, T. Tanabe, Y. Nakajima, K. Hosaka, D. Akamatsu, A. Onae, T. Suzuyama, M. Amemiya, F.-L. Hong, Improved absolute frequency measurement of the ^{171}Yb optical lattice clock towards a candidate for the redefinition of the second. Appl. Phys. Express **5**(10), 102401 (2012)
61. B.C. Young, F.C. Cruz, W.M. Itano, J.C. Bergquist, Visible lasers with subhertz linewidths. Phys. Rev. Lett. **82**(19), 3799–3802 (1999)

Chapter 6
Cold Atom Magnetometers

Yujiro Eto, Mark Sadrove, and Takuya Hirano

6.1 Introduction

Because the magnetic field is a ubiquitous quantity, the improvement in sensitivity and spatial resolution of magnetometers has an impact on various fields ranging from fundamental physics to biomedical engineering. Examples include the search for permanent electric dipole moments [11] to biomagnetic measurements [15]. Recent progress in superconducting quantum interference device (SQUID) magnetometers has opened up novel applications like clinical usage of a magnetoencephalograph system in general hospitals for diagnosis of central nervous system illnesses such as epilepsy or brain tumors [26]. Further progress will enable more detailed identification of electrical activity in the brain and revolutionize medical and neurological research.

Atomic magnetometers offer an alternative to SQUID magnetometers [4]; the advantage of the former is that the optical method doesn't require cryogenic instruments, so small low-cost implementation may be possible. In 2003, Kominis et al. demonstrated magnetic field sensitivity of $5.4 \times 10^{-16}\,\mathrm{T}/\sqrt{\mathrm{Hz}}$ with a measurement volume of $0.3\,\mathrm{cm}^3$ by a spin-exchange relaxation-free atomic magnetometer [16]. They used K atoms heated to 180 °C with a spatial resolution limited by the diffusion of the K atoms. The effect of diffusion can be suppressed by laser cooling techniques and the spatial resolution can be improved by using laser-cooled atoms. Ultimate control over the motion and the position of atoms has been attained for

Y. Eto • T. Hirano (✉)
Gakushuin University, 1-5-1 Mejiro, Toshima-ku, Tokyo 171-8588, Japan
e-mail: eto@qo.phys.gakushuin.ac.jp; takuya.hirano@gakushuin.ac.jp

M. Sadrove
Research Institute of Electrical Communication, Tohoku University, Katahira 2-1-1, Aoba-ku, Sendai-shi 980-8577, Japan
e-mail: mark@cpi.uec.ac.jp

Y. Yamamoto, K. Semba (eds.), *Principles and Methods of Quantum Information Technologies*, Lecture Notes in Physics 911, DOI 10.1007/978-4-431-55756-2_6

quantum degenerate atoms; the atoms are cooled into the smallest phase space volume allowed by Heisenberg's uncertainty relation [13]. Therefore, Bose-Einstein condensates (BECs) offer an ideal testing ground to experimentally study the fundamental performance of optical magnetometers [27].

There are several schemes for BEC magnetometry. One method is to convert the density profile of atoms into the potential energy variations that are created by the magnetic field. Demonstration of 3 μm spatial resolution with 3×10^{-10} T/$\sqrt{\text{Hz}}$ sensitivity was reported in 2005 by Wildermuth et al. [33]. As they discussed in [33], the sensitivity would be improved by two orders of magnitude by utilizing Feshbach resonance [32].The phenomenon of Feshbach resonance itself may be used as a magnetometer by taking advantage of its sensitivity to the magnetic field [29].

The most straightforward scheme for BEC magnetometry may be the measurement of the Larmor precession in a spinor BEC where the spin degrees of freedom are liberated by optically trapping the BEC. One measurement method is the nondestructive phase-contrast imaging of magnetization using off-resonant circularly polarized light. Using this method, Vengalattore et al. reported a field sensitivity of 8.3×10^{-12} T/$\sqrt{\text{Hz}}$ over a measurement area of 120 μm^2 [31].

Another method is based on the spin-echo technique. A very attractive feature of this method is robustness against ambient field fluctuations. By designing the spin-echo sequence, the response function of the magnetometer can be controlled; similar to magnetic resonance techniques, it is possible to cancel the unwanted evolution of atomic spins due to ambient fields fluctuating randomly on timescales longer than the length of the sequence, whereas oscillating magnetic fields matching the echo period constructively affect the spin dynamics [22].

We have demonstrated a magnetic field sensitivity of 12×10^{-12} T/$\sqrt{\text{Hz}}$ over a measurement area of 100 μm^2 using spin-echo BEC magnetometery [5]. In this chapter, we explain the fundamentals of BEC magnetometry using the spin-echo technique. In the following section, the experimental setup and the principle and practice of spin rotations are reviewed. Next, experimental results of Ramsey interferometry [24] and Larmor precession [6] are explained. In the third section, BEC magnetometry is discussed, followed by a summary.

6.2 Control of Spinor Condensates

6.2.1 Experimental Setup

First we briefly introduce our experimental setup and procedure for creation and manipulation of the spinor BEC. Figure 6.1a shows an illustration of the vacuum chamber system to capture and cool the ^{87}Rb atoms [21]. We employed a double magneto-optical trap (MOT) to accumulate the ultracold ^{87}Rb atoms. In order to efficiently load the atoms into the 2nd MOT, the 1st MOT is continuously pushed out by irradiating it with a weak near resonant cw beam (push beam). Using this

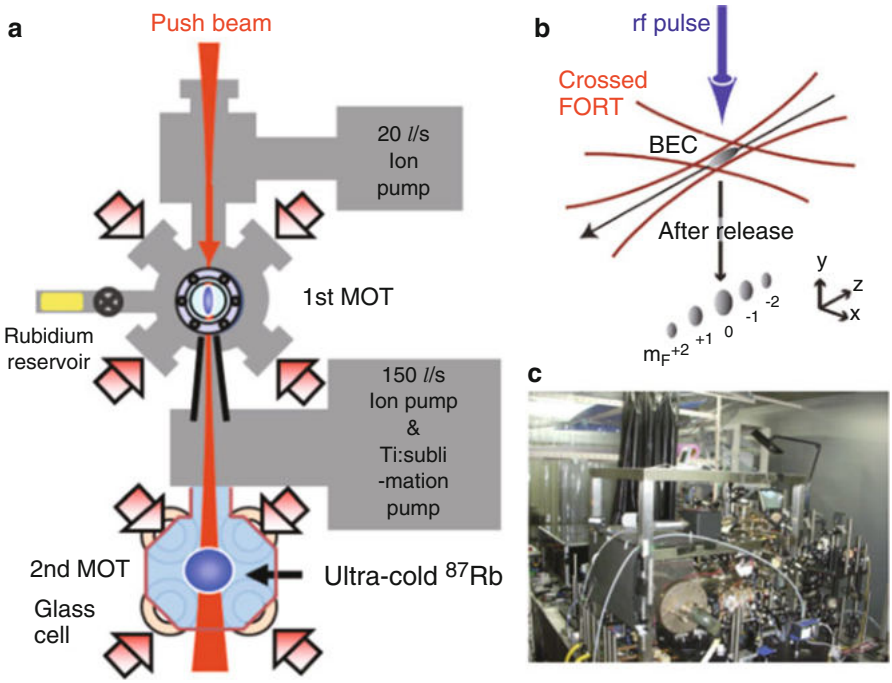

Fig. 6.1 (**a**) Overall experimental setup. (**b**) The BEC is confined in the crossed FORT. After the atoms are released from the FORT, the spin components are separated by the SG method. (**c**) Picture of the experimental setup inside the magnetic shield room

setup, more than 10^9 atoms are collected in the 2nd MOT. The spin state of atoms in the 2nd MOT is converted to the $F = 2$, $m_F = 2$ hyperfine state by optical pumping. After the 2nd MOT is turned off, the spin-polarized atoms are captured in a Ioffe-Pritchard (clover-leaf) type magnetic trap.

A BEC consisting of 10^6 atoms is created using radio frequency (RF) evaporative cooling in the magnetic trap. The BEC is then loaded into a crossed far-off-resonant optical trap (FORT) (Fig. 6.1b), and thereby the spin degrees of freedom are liberated. The axial and radial frequencies of the FORT are 30 and 100 Hz, respectively. After 200 $\sim$ 300 ms hold time in the crossed FORT, typically $3 \sim 4 \times 10^5$ atoms remain in the $F = 2, m_F = -2$ state. The whole experimental setup is installed inside a magnetic shield room whose walls consist of permalloy plates (Fig. 6.1c), and a laser diode source with a low ripple noise of less than 2 μA (Newport 505) is used as the current source for our z-axis Helmholtz coils in order to control the external magnetic field. The magnetic field along the x- and y-direction is carefully compensated by using two Helmholtz coils with similar laser current sources. As shown in Fig. 6.1b, the RF pulses are applied along the y-direction to manipulate the spin state of the BECs. The details of manipulation of spin using the RF pulses are described in Sects. 6.2.2, 6.2.3, and 6.2.4. The techniques of

the Stern-Gerlach (SG) separation and time-of-flight (TOF) absorption imaging are used to measure the atomic density distributions of each m_F component. After a time of flight of 15 ms, the probe beam is incident from the x-direction.

6.2.2 Rabi Oscillations and Ramsey Interferometry

We now begin our discussion of interferometry using an $F = 2$ spinor condensate. For magnetometry applications, the basic phenomenon of interest is Larmor precession of the spin which takes place when the spin is displaced from the magnetic field axis. A classical picture of the precessing spin can provide a good heuristic understanding of the interferometer behaviour and can be shown rigourously to give the same qualitative precession as a full quantum treatment. In particular, the rate of change of angular momentum $\mathbf{S}$ for a magnetic dipole $\boldsymbol{\mu}$ in an external field $\mathbf{B}_0$ is given by

$$\frac{\mathrm{d}\mathbf{S}}{\mathrm{d}t} = \boldsymbol{\mu} \times \mathbf{B_0}, \tag{6.1}$$

where $\times$ is the vector cross product. For the study of spin precession it is permissable to ignore components of the angular momentum other than spin and so we associate the angular momentum $\mathbf{S}$ with the spin of the atoms in the condensate. The Larmor frequency of the precession is given by

$$f_0 = g_F \mu_B B_0 / h, \tag{6.2}$$

where g_F is the g factor, and μ_B is the Bohr magneton. Assuming that only the linear Zeeman effect is present, this frequency also corresponds to the energy spacing between adjacent magnetic sublevels in the atoms of the condensate.

At the beginning of the experiment, atoms in the condensate have their spin anti-aligned to the magnetic field and precession is thus inhibited. Interferometric interrogation of the magnetic field strength, i.e. *magnetometry*, can be achieved if the spin can be misaligned to the field direction or "tipped" to use the term common in NMR literature. The tipped spin is allowed to precess for a given time before it is rotated back into alignment with the field. The interferometric phase acquired during this sequence depends on the Larmor precession rate and thus, by Eq. 6.2 on the ambient magnetic field $\mathbf{B}_0$. Indeed, if there is a way to read out the spin direction periodically, there is no need to perform the second rotation. This fact was used in the first spinor atom interferometer demonstrated which utilized non-destructive imaging to interrogate the spin direction of a spin-1 condensate[31]. Nonetheless, in general at least two rotations are required: one to begin the phase accumulation by tipping the spin and another to read out the phase accumulation.

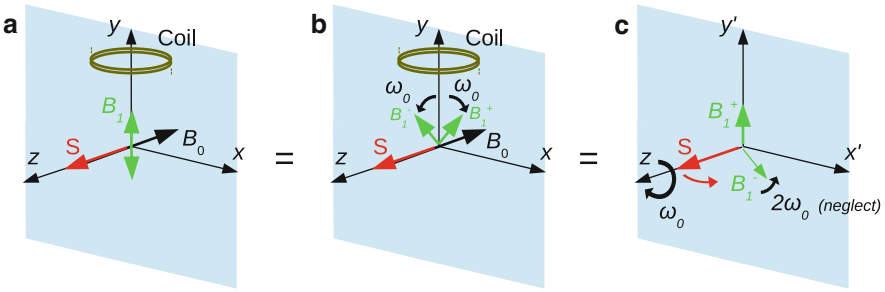

Fig. 6.2 Schematic diagram of the effect of an RF pulse applied by a coil. (**a**) and (**b**) are in the laboratory frame. In (**c**) the system is rotating about the z axis at the Larmor frequency

6.2.2.1 Rotation by Radio Frequency Pulses

We will first consider how a single RF pulse affects the spin of the condensate. We make the following assumptions: (1) The magnetic bias field is small enough that second-order Zeeman effects can be ignored, i.e., the energy spacing between adjacent m_F levels is assumed to be constant and (2) changes to the spin of individual atoms, e.g. through spin-changing collisions can be ignored. Finally (3) the magnetic field is constant across the condensate. As we shall see later, these assumptions are too simple for real experiments and also leave out the possibility of some interesting physics. However, by making the three assumptions above, it becomes possible to construct a simple analytical model for the interferometer.

A resonant magnetic RF pulse (i.e. one whose frequency matches the Larmor frequency) applied by a coil wound about the y axis as shown in Fig. 6.2 rotates the spin in the z-x' plane. The reason that the field due to the pulse, which may be weak relative to the bias field, can effect such a rotation is at the heart of nuclear magnetic resonance (NMR) applications and is explained in various textbooks on the subject using a simple classical model of the spin (see, for example, [7, 12]). We briefly repeat the argument here for completeness.

We identify the unit vectors $\mathbf{x}$, $\mathbf{y}$, and $\mathbf{z}$ with the directions of the x, y and z axes respectively. As shown in Fig. 6.2a, an alternating current of frequency f_0 is applied to the coil producing an alternating magnetic field $\mathbf{B}_1(t) = B_1\mathbf{y}\sin(\omega_0 t)$ along the y axis. (Note that if the coil is far from the origin, so that the RF field propagates in free space before reaching the condensate, a magnetic field along the y direction is not present. In that case, the argument can be made using magnetization instead of the magnetic field itself. See Ref. [7] for details). Figure 6.2b shows a situation equivalent to (a) where the oscillating magnetic field B_1 is replaced by counter-rotating fields $\mathbf{B}_1^+(t) = (B_1/2)[\mathbf{y}\sin(\omega_0 t) + \mathbf{x}\cos(\omega_0 t)]$ and $\mathbf{B}_1^-(t) = B_1/2[\mathbf{y}\sin(\omega_0 t) - \mathbf{x}\cos(\omega_0 t)]$. Since the components aligned along x cancel, the total field is identical to $\mathbf{B}_1(t)$. Finally, we transform to a frame rotating clockwise at frequency ω_0. In this frame, the precession due to the field $\mathbf{B}_0$ is exactly cancelled. This is equivalent to the bias field itself being cancelled and so it is not shown in

Fig. 6.2c. On the other hand, in the rotating frame, $\mathbf{B}_1^+$ is *always* aligned with the y' axis while the $\mathbf{B}_1^-$ component now rotates anti-clockwise at $2\omega_0$. Noting that the effect of the fast rotating $\mathbf{B}_1^-$ component in this frame will average to zero, it is clear that the important field, with respect to its influence on the spin, is the now constant $\mathbf{B}_1^+$ component. Due to this field, the spin will precess about the y' axis in the x'-z plane and thus in the x-z plane in the laboratory frame, with additional free precession about the z axis. Although all of the situations shown in Fig. 6.2a–c are equivalent, only the (c) makes clear the rotational effect of the RF pulse.

6.2.2.2 Mathematical Formalism of Spinor Rotation

Having established that the effect of an RF pulse is to tip the spin in the x-z plane, we can make use of the mathematical formalisms used to describe the rotation of spinors in 3-dimensions. In particular, we note that by decomposing the spin state of the condensate into its magnetic sublevels m_F, we can make use of the Wigner D matrix operators to perform any three dimensional rotation of the spin state. Here, we will focus on the spin-2 case explored in our experiments, but the formalism is valid for any spin. We note that Ref. [30] provides detailed calculations including the form of the D matrices for up to spin $F = 5$. Additionally, we give the form of the Wigner D^2 matrix explicitly in Ref. [24].

In the Euler angle notation, the Wigner matrix for spin-2 is $D^2 \equiv D^2(\alpha, \beta, \gamma)$. It is a function of three angles α, β and γ but only rotations involving β produce couplings between m_F levels [25]. Rotations about the z-axis are parameterized by α and γ and merely change the phase of the spin state.

We also introduce another measure of the spin rotation – the projection of the spin on the z axis which is given by

$$\langle S_z \rangle = \sum_{m_F} |\psi_{m_F}|^2 m_F. \tag{6.3}$$

This is nothing other than the expectation value of the S_z operator over the m_F sublevels. This quantity has the advantage that it undergoes simple sinusoidal variation at the Larmor frequency, rather than the more complicated oscillations of the m_F components themselves.

6.2.2.3 Experimental Verification of Rotation by RF Pulses (Rabi Oscillation)

Having considered theoretically the effect of an RF pulse on the condensate spin and the formalism for spinor rotation, we now consider the experimental verification of the rotation effect of an RF pulse. Practically, the exact rotation effected by an RF pulse of a certain frequency, amplitude and duration is empirically determined by performing experiments while varying the same parameters. Typically, the most convenient parameter to vary is the pulse length t. We can therefore represent the rotation about the y axis as $\beta = \omega_\beta t$, where ω_β is a function of the RF power and the

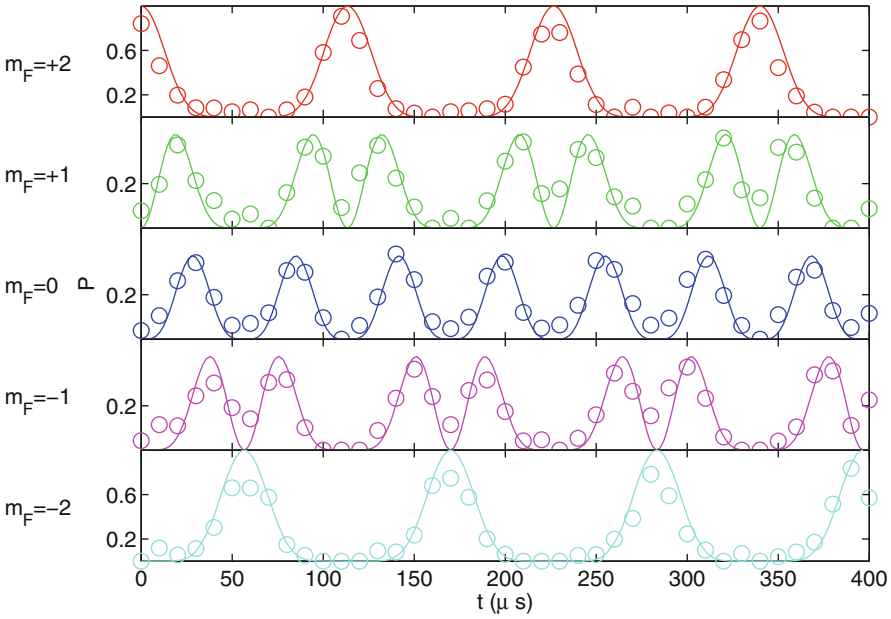

Fig. 6.3 Experimentally measured Rabi oscillation (*points*) of the spinor BEC subject to an RF pulse for time t for m_F levels as indicated to the left of each plot. *Solid lines* show the behaviour predicted by the spin-2 rotation matrix (see text) (This figure is adapted from Ref. [24])

RF frequency. We will explicitly evaluate the frequency dependence later, but the RF power is assumed to be fixed. In the rotating frame, for a given initial wavefunction Ψ_i in the m_F basis, the spin state wavefunction Ψ_f after application of an RF pulse is given by

$$\Psi_f = d^2(\omega_\beta t)\Psi_i. \tag{6.4}$$

Figure 6.3 shows the population of each m_F sublevel after an RF pulse of length t is applied to the condensate. The population of each component is seen to follow the variation predicted by the Wigner rotation matrix with a fitted value of $\omega_\beta = 2\pi \times 8.8$ kHz. This behaviour may be considered to be a multi-level Rabi-oscillation.

We note two types of pulses which are of particular importance to interferometry. Firstly, the $\pi/2$ pulse where $\beta = \pi/2$ rotates the spin by 90° about the y axis leading to precession of maximal amplitude. The $\pi/2$ pulse can also rotate the spin back into alignment with the z axis for readout using the Stern-Gerlach method. Secondly, the π pulse where $\beta = \pi$ is also of importance as we will see in Sect. 6.2.4. Typically, a π-pulse is applied after the spin has already been tipped and it causes the spin to rotate 180° about the y axis. Heuristically, the spin-evolution can be pictured as "reversing" itself after the application of a π-pulse leading to a refocussing of spins precessing at different rates and thus increasing the effective coherence time of the interferometer sequence (see in Sect. 6.2.4). A more rigourous treatment of this so called spin-echo effect may be found in Hahn's seminal publication Ref. [8].

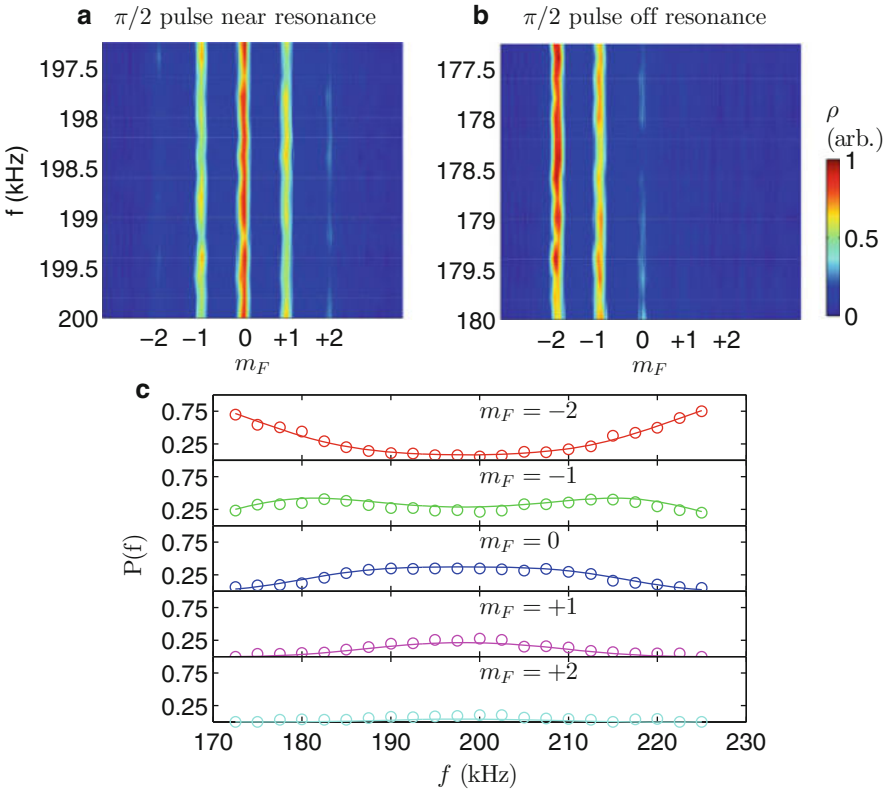

Fig. 6.4 The effect of detuning on the rotation caused by a nominal $\pi/2$ pulse. (**a**) and (**b**) show how the atomic population in each m_F state varies over small frequency ranges close to and far from resonance respectively. (**c**) shows the effect of a nominal $\pi/2$ pulse for each m_F state as indicated over a broad range of frequencies. Experimental results are shown by *circles* whereas *solid curves* show the prediction of Eq. 6.5 (This figure is adapted from Ref. [24])

Finally, before moving on to interferometry, we consider the frequency dependence of the rotation effected by the RF pulse. Due to the resonant nature of the rotation effect, i.e., the need for the RF pulse frequency to match the Larmor frequency of the spin in the magnetic field B_0, we expect that the rotational effect of the pulse will fall off as a smooth function of $|\delta| = |f - f_0|$ over some frequency range Δ. By analogy with the standard Ramsey interferometer [23], we model this frequency dependence by a sinc function:

$$\beta(f) = \beta_0 \eta(f) = \beta_0 \mathrm{sinc}[(f - f_0)/\Delta], \tag{6.5}$$

where β_0 is the rotation caused by the pulse at exact Larmor resonance and $\mathrm{sinc}(x) \equiv \sin(\pi x)/(\pi x)$. The frequency dependent effect of the pulses can now be modeled by the operator $d^2[\beta_0 \eta(f)]$ applied to the initial wavefunction Ψ_i

Figure 6.4 shows the experimentally measured population of each spin state (circles) as a function of the frequency of an applied RF pulse whose pulse duration was empirically set to achieve an approximate $\pi/2$ pulse at resonance. The solid lines in Fig. 6.4 show the fitted frequency response using Eq. 6.5. The fitted parameters were found to be $f_0 = 198\,\text{kHz}$, $\Delta = 37\,\text{kHz}$ and $\beta_0 = 0.95 \times \pi/2$.

6.2.3 Ramsey Interferometry

In typical Ramsey interferometry [23], two $\pi/2$ pulses separated by a constant interrogation time T are applied to a sample and interference fringes are produced by sweeping the frequency of the pulses. To model such an interferometer, we also need to model the phase accumulation due to free precession between pulses and that due to the phase difference between the RF pulses after the interrogation time T has elapsed. In Ref. [24] it was found that these effects could be modeled by rotations about the z axis. Formally, we apply the rotation matrix $D^2(\Phi(f,T), \beta \equiv 0, \gamma \equiv 0)$, where $\Phi(f,T) = 2\pi(f - f_0)T$ is the combined phase accumulation due to Larmor precession and the time between pulses. Since $\beta = 0$, the rotation matrix is diagonal with matrix elements $D^2_{m_F,m_F} = \exp(-\mathrm{i}m_F\Phi)$. Finally, the rotation operator $d^2[(\pi/2)\eta(f)]$ is applied again to give the output state. The interference fringe is given by the absolute value of the complex amplitudes for each m_F component, i.e., the relative population:

$$|\Psi_f|^2 = |d^2[(\pi/2)\eta(f)]D^2(\Phi,0,0)d^2[(\pi/2)\eta(f)]\Psi_i|^2. \tag{6.6}$$

The result of this matrix multiplication is explicitly evaluated in Ref. [24], but we omit the slightly unwieldy expression here since Eq. 6.6 is sufficient for evaluating the fringe profile. To justify Eq. 6.6, we used an argument considered from the point of view of the laboratory frame and ignored the (constant) amount of precession that occurs during the $\pi/2$ pulses. It is, of course, possible to achieve the same expression for the interferometer in the rotating frame introduced earlier. However, the point of view of the laboratory frame makes clear the dependence of the accumulated phase on the *detuning* of f from the Larmor frequency f_0.

In order to see the effect of a Ramsey interferometer sequence on a spin-2 condensate, it is informative to first inspect the raw data in the form of normalized column densities taken from SG measurements of the BEC at various frequencies. Figure 6.5 shows such data taken for an ambient field strength B_0 estimated at 300 mG with $T = 290\,\mu\text{s}$. The applied $\pi/2$ pulses were $29\,\mu\text{s}$ in duration. At the estimated value of B_0, the calculated Larmor frequency is 210 kHz. Figure 6.5 shows that the final spin state rotates from the $m_F = +2$ to the $m_F = -2$ state and back again as the frequency is varied and that it does so with an amplitude that decays as a function of the detuning from the Larmor frequency f_0.

In Fig. 6.6 we show the actual interferometer fringes derived by calculating the population in each m_F state for the data shown in Fig. 6.5. The upper five panels of

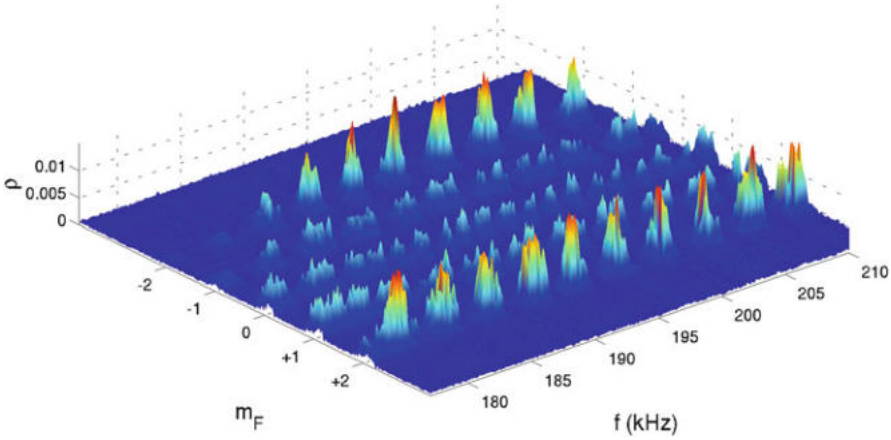

Fig. 6.5 Raw column densities ρ from absorption images of the BEC. The population is seen to oscillate between the $m_F = \pm 2$ states as a function of frequency with the amplitude flowing through the $m_F = +1, 0$, and -1 states (This figure is adapted from Ref. [24])

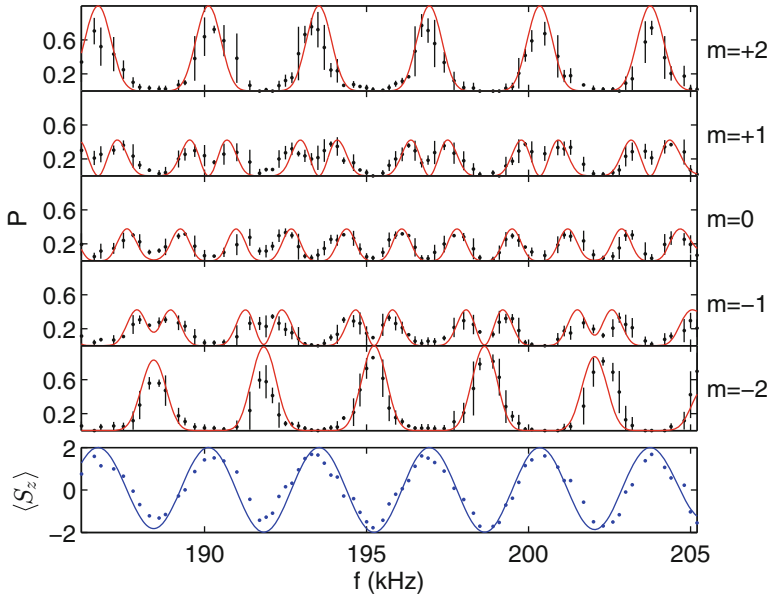

Fig. 6.6 Measured interference fringes. The *top five panels* show relative population measurements P for each m_F component as labelled to the right. Discrete points showing the experimentally measured m_F populations and *solid lines* show the fitted theory from Eq. 6.6 in each case. The *bottom panel* shows $\langle S_z \rangle$ calculated from the data in the upper five panels using Eq. 6.3 (This figure is adapted from Ref. [24])

Fig. 6.6 show the relative populations for each m_F state as a function of frequency while the bottom panel shows $\langle S_z \rangle$. We have also checked the dependence on the interrogation time T and found that the fringe period displayed the expected $1/T$ dependence of a Ramsey interferometer [24].

The experimentally measured fringe pattern for each m_F state shows good qualitative agreement with the predictions of Eq. (6.3). The $m_F = +1$, 0 and -1 component fringes contain oscillations with a smaller period than the fundamental seen for $m_F = \pm 2$. In particular, the $m_F = 0$ fringe oscillates with essentially twice the repetition rate of the principle oscillation. We note that oscillations with shorter period than the fundamental rotation period are also found in multi-beam optical interferometers [9]. Although the individual m_F components show non-sinusoidal variation [24], the expectation value of S_z shows sinusoidal variations at the Larmor frequency as expected.

The sensitivity of the interferometer was estimated by finding the smallest distinguishable phase difference within the experimental error of each point. We calculated the average phase sensitivity to be about 0.6 radians or 10 % of a fringe. We will see in the following Sections that the key to making a magnetometer with better sensitivity is removing sources of dephasing such as magnetic gradient fields inside the vacuum chamber along with using more sophisticated pulse sequences to reduce the effect of dephasing.

6.2.4 Observation of Larmor Precession in an Inhomogeneous Magnetic Field

In Sect. 6.2.2, we assumed that the magnetic field across the BEC was constant. This simplified our treatment of the interferometer and allowed us to arrive at a simple closed form expression for the interferometer fringes. However, in reality, the field experienced by the BEC is never uniform across the entire condensate. This is because inhomogeneities in both the spatial and temporal dependence of the magnetic field are difficult to remove entirely. In this section we review the influence of inhomogeneity of the external magnetic field on the Larmor precession of the BEC spin. The experiments were performed under an external magnetic field of 30 μT with a gradient of 3 μT/cm along the axis of the trap (z direction) [6].

Figure 6.7a shows $\langle S_z \rangle$ measured while changing the interrogation time between two $\pi/2$ pulses, $T + \Delta T$. Here, $T = 130$ μs and ΔT is a small variation in the range of one or two Larmor periods. The clear oscillation indicates that spin precession is successfully observed.

Next we measured $\langle S_z \rangle$ values for various $T + \Delta T$. As shown in Fig. 6.7b, the contrast of the Larmor precession signal, which corresponds to the peak-to-peak values of $\langle S_z \rangle$, was found to decrease with increasing T. This effect can be explained by the increase in spatial variations in the distribution for each m_F component which were experimentally observed to increase with T. This is because

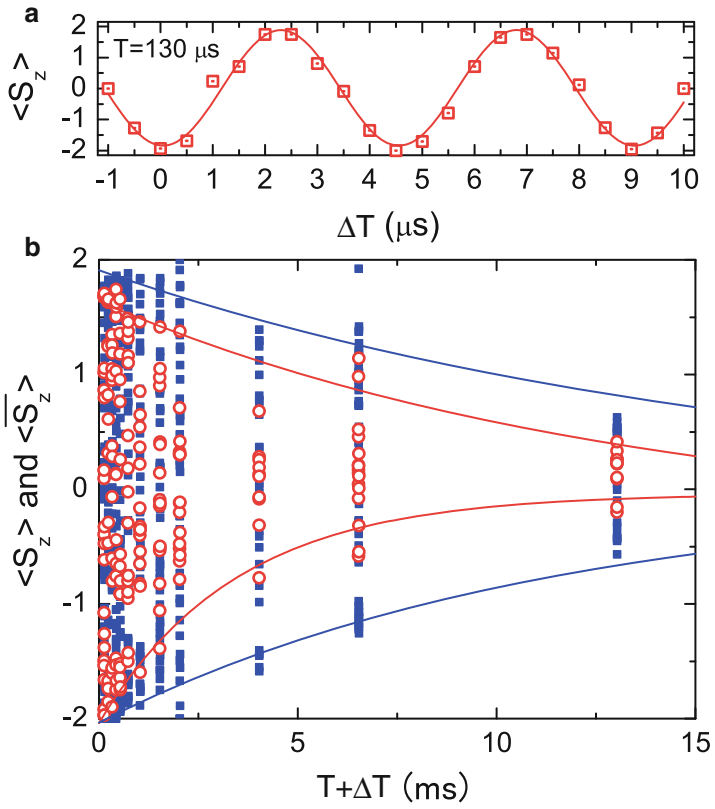

Fig. 6.7 Observation of Larmor precession. (**a**) $\langle S_z \rangle$ as a function of τ at $T = 130\,\mu$s. (**b**) T dependences of $\langle S_z \rangle$ (*filled squares*) and $\langle \bar{S}_z \rangle$ (*empty circles*) for various values of τ. The curves are fitted exponential decay envelopes to guide the eye (Copyright 2013 The Japan Society of Applied Physics)

the observed spatial structure in the density distributions indicates different rates of Larmor precession depending on the position within the BEC. Because $\langle S_z \rangle$ is calculated using the total atom number for each m_F component, and not using the atom number at local position, any variation in the precession rate will eventually lead to dephasing and reduction of the fringe contrast.

In Fig. 6.8a–c typical density distributions for each m_F component are shown by solid curves. The results were obtained for a precession time of $T = 13.03$ ms. The appearance of double peaked distributions in some components (Fig. 6.8a, c) along with a shift in the position of the $m_F = \pm 2$ peaks (Fig. 6.8b) are signatures of the spatial variation of the spin orientation discussed above.

More quantitatively, we can calculate the z-position dependence of $\langle S_z \rangle$ as shown in Fig. 6.8d–f. From these results, we find that the spin orientation clearly depends on the z-position, showing a helical pattern which has also been observed by other groups [2, 10].

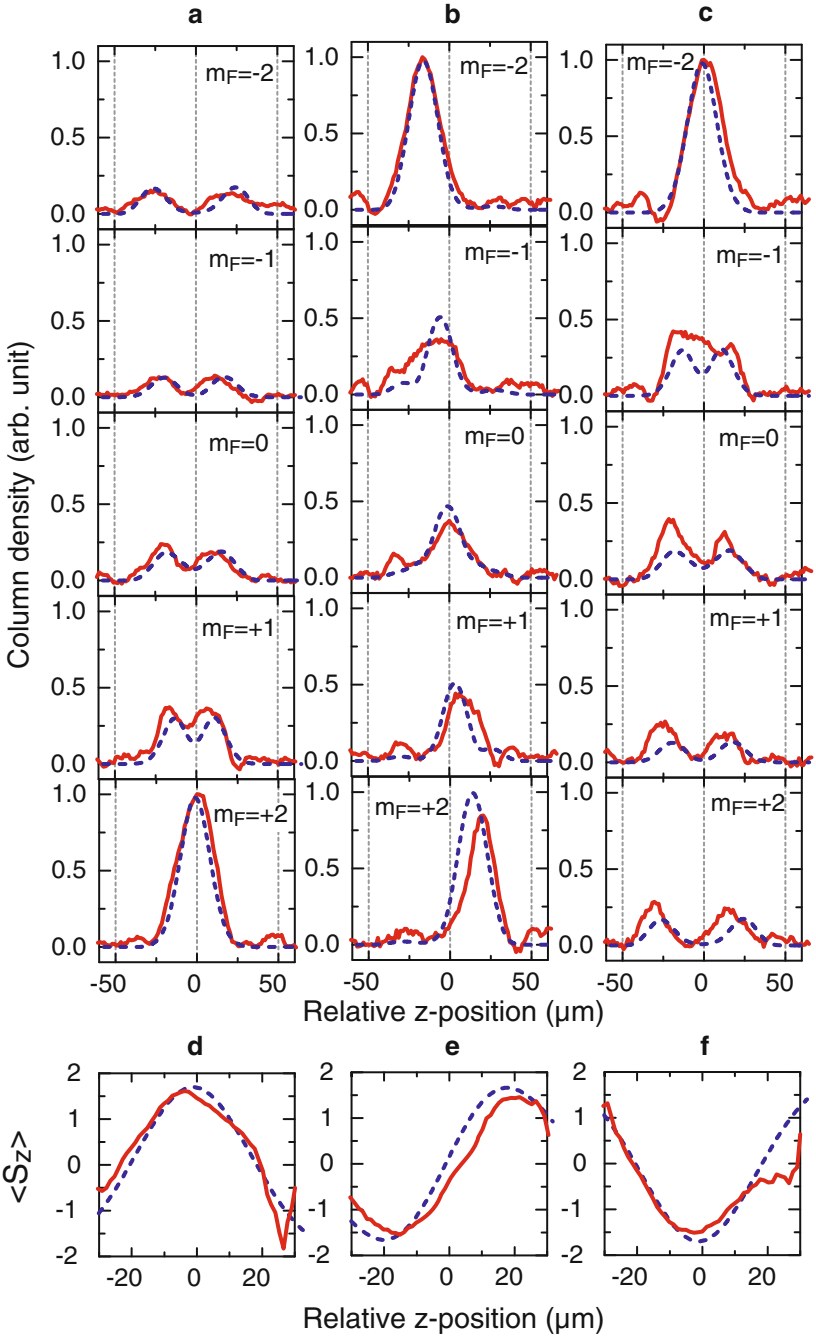

Fig. 6.8 Observation of helical spin texture using the Ramsey interferometer. (**a**)–(**c**) Typical density distributions of each m_F component at $T = 13.03$ ms. (**d**)–(**f**) Spatial profiles of $\langle S_z \rangle$. (**d**)–(**f**) are calculated from (**a**) to (**c**), respectively. The spatial variation of $\langle S_z \rangle$ implies that the spin orientation along the z-axis is twisted. The *solid* and *broken curves* in each figure indicate experimental data and numerical simulation results (from coupled Gross-Pitaevskii equations), respectively (Copyright 2013 The Japan Society of Applied Physics)

For a magnetic field gradient of $dB_z/dz = 30\,\mathrm{mG/cm}$, the distance Δz along which the spin helix is twisted by π for $T = 13.03\,\mathrm{ms}$ is estimated to be $\pi\hbar/[g_F\mu_B(dB_z/dz)T] \simeq 18\,\mu\mathrm{m}$ [6] with g_F and μ_B being the g-factor and the Bohr magneton, respectively, which is comparable to the Thomas-Fermi radius in the z direction $\simeq 21\,\mu\mathrm{m}$.

Inhomogeneity of the magnetic field is not the only cause of fringe contrast decay. We also investigated the effect of temporal fluctuations by considering measurements of $\langle S_z\rangle$ made over different interferometer runs. The empty circles in Fig. 6.7b indicate the average of three $\langle S_z\rangle$ measurements, $\langle \bar{S}_z\rangle$, for the same $T+\Delta T$ [6]. In the absence of time dependent magnetic field fluctuations, $\langle \bar{S}_z\rangle$ would be the same as $\langle S_z\rangle$. However, comparison of $\langle S_z\rangle$ with $\langle \bar{S}_z\rangle$ in Fig. 6.7b shows that the peak-to-peak value of $\langle \bar{S}_z\rangle$ decreases faster than that of $\langle S_z\rangle$, which is halved at $T \sim 4\,\mathrm{ms}$. This difference between $\langle \bar{S}_z\rangle$ and $\langle S_z\rangle$ originates from the temporally fluctuating magnetic field along the z-direction as discussed in Ref. [6]. Under the assumption of Gaussian fluctuation, this behavior of $\langle \bar{S}_z\rangle$ corresponds to a standard deviation of $\sigma_z = 7\,\mathrm{nT}$.

6.2.5 *Effect of Spin Echo for Inhomogeneous Spin Precession*

As shown in the previous section, field inhomogeneities create spin helicity and reduce the repeatability of the precession signal. In this Section we show that these effects induced by the field inhomogeneity can be greatly suppressed by using the technique of spin echo in which a single π pulse is applied in the middle of the interrogation period of length T. These results were first reported in Ref. [6].

Figure 6.9a, b show the τ dependence of $\langle \bar{S}_z\rangle$, where the spin echo technique is applied only for the case of (b). The error bars for each data point show the standard deviation over three measured $\langle S_z\rangle$ values. The error bars in Fig. 6.9b (with spin echo) are smaller than those in Fig. 6.9a (without spin echo). This indicates that the influence of different precession frequencies in each measurement due to the fluctuating magnetic field is reduced by spin echo. Applying the spin echo technique thus improves the repeatability of the experiment [6] and improves the performance of the interferometer.

In order to quantitatively evaluate the effect of spin echo, we estimated the coherence time from the fringe amplitude of $\langle \bar{S}_z\rangle$ measured as a function of τ. We obtained a fringe amplitude of 1.68 ± 0.05 from a sinusoidal fit to the data as shown in Fig. 6.9b. In contrast, the fringe amplitude was 1.14 ± 0.14 when the sequence without spin echo was applied (Fig. 6.9a). Figure 6.9c shows the T dependence of the fringe amplitude. The coherence time, T_2, is estimated by fitting an exponential decay curve to the data, giving $T_2^* = 3.0 \pm 0.4\,\mathrm{ms}$ and $T_2 = 12 \pm 1\,\mathrm{ms}$ in the cases without and with spin echo, respectively. Note that the spin echo can only remove the effect of magnetic field fluctuations which are slower than the time scale set by the interval T between the two $\pi/2$ pulses [28]. Thus, in this experiment, T_2 is limited due to unavoidable rapid temporal fluctuations of the B_z field.

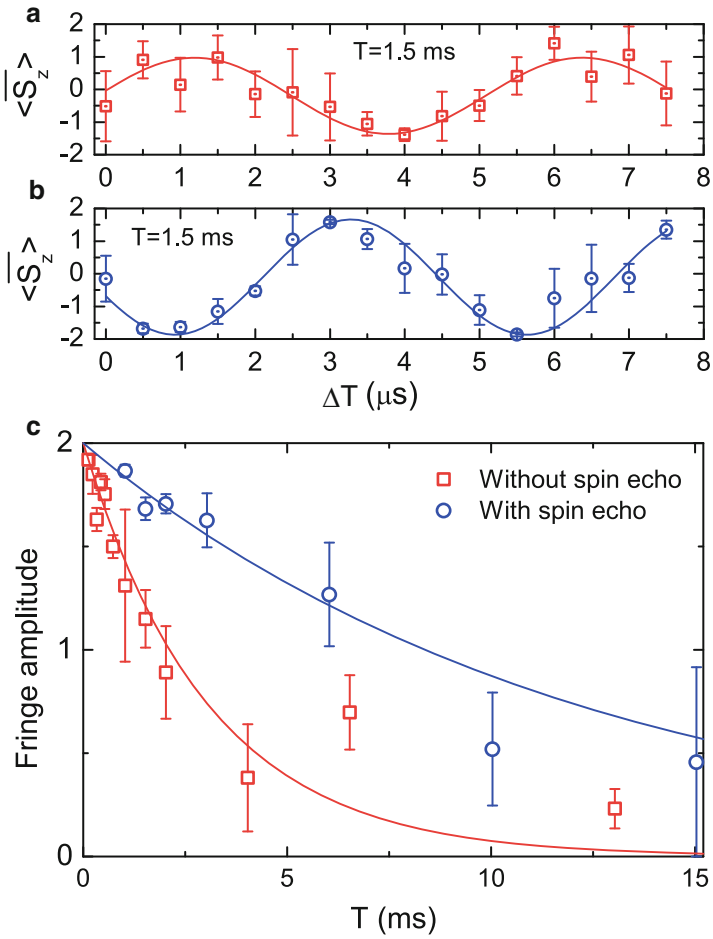

Fig. 6.9 Comparison of spin precession with and without spin echo. (**a**) and (**b**) show the τ dependence of $\langle \bar{S}_z \rangle$ at $T = 1.5$ ms. The spin echo technique is applied only for (**b**). (**c**) T dependence of the fringe amplitude obtained from the sinusoidal fitting seen in (**a**) and (**b**). The curves are exponential functions fitting to the data (Copyright 2013 The Japan Society of Applied Physics)

In Refs. [35, 36], it was theoretically predicted that spin echo can refocus inhomogeneous spin precession due to a gradient magnetic field. We confirmed this effect of spin echo as reported in Ref. [6] by calculating the variance of S_z defined by

$$\langle \Delta^2 S_z \rangle = \sum_{m_F=-2}^{+2} m_F^2 N_{m_F}/N_{\text{total}} - \langle S_z \rangle^2.$$

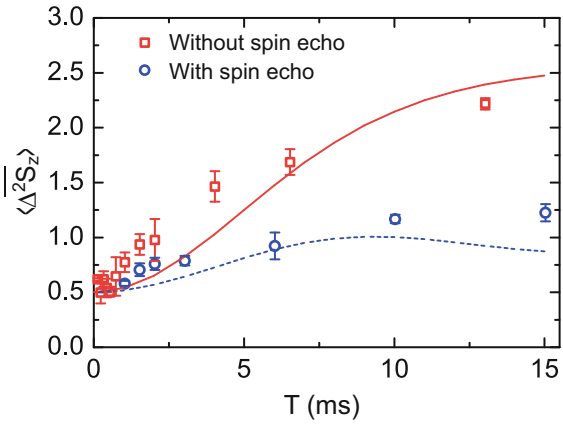

Fig. 6.10 T dependence of $\overline{\langle \Delta^2 S_z \rangle}$. The *squares* and *circles* are the experimental data without and with spin echo respectively. The *solid* and *broken curves* indicate the corresponding numerical simulations (Copyright 2013 The Japan Society of Applied Physics)

The variance, $\langle \Delta^2 S_z \rangle$, takes a value between 0 and 1 for spatially homogeneous spin precession, and the average for one Larmor period, $\overline{\langle \Delta^2 S_z \rangle}$, is 0.5. A helical pattern such as that shown in Fig. 6.8a–c increases the value of $\overline{\langle \Delta^2 S_z \rangle}$. Figure 6.10 shows the experimental values and numerically calculated values of $\overline{\langle \Delta^2 S_z \rangle}$ as a function of T. When spin echo is applied, the experimental values of $\overline{\langle \Delta^2 S_z \rangle}$ are relatively reduced at all T. This indicates that the spin echo refocuses the spatially inhomogeneous precession by the gradient magnetic field.

6.3 Ultracold Atom AC Magnetometry

For the characterization of non-static magnetic fields, magnetometers that have high sensitivity to alternate-current (AC) magnetic fields are necessary. Specialized magnetometers for AC magnetic fields can be constructed using the spin-echo [3, 22, 28] and dynamical decoupling techniques [1, 18, 19], which reduce the effect of slow magnetic field fluctuations, magnetic field gradients and other undesirable inhomogeneous field characteristics.

In this section, we review our study of spin-echo AC magnetometry using a ^{87}Rb $F = 2$ BEC [5]. Using some of the techniques described in the previous sections along with a particular time sequence (described below), we were able to perform magnetometry with a sensitivity of $12\,\mathrm{pT}/\sqrt{\mathrm{Hz}}$ at a spatial resolution of about $100\,\mu\mathrm{m}^2$. As a test of our magnetometer, we detected magnetic field noise synchronous with the power supply line at frequencies of 50 and 100 Hz. It is interesting to note that in the case of this supply line noise, application of a phase reversed magnetic field can suppress the noise down to the order of 1 nT, a fact which should be useful for generating clean magnetic field environments in future studies using BECs.

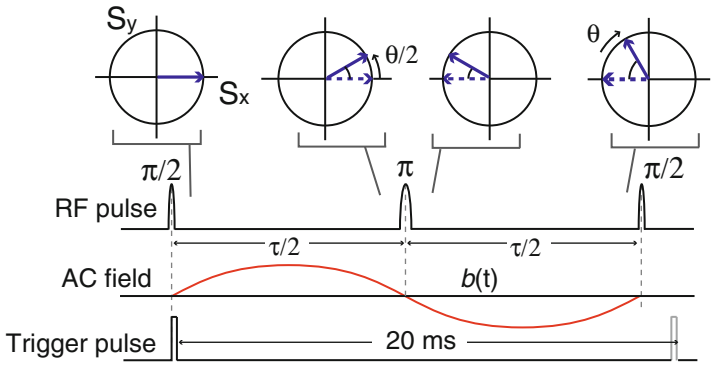

Fig. 6.11 The *upper panel* depicts the evolution of spin direction in x'-y' plane. The *lower panel* shows the RF Hahn-echo pulse sequence used for sensing a weak AC magnetic field (This figure is adapted from Ref. [5])

The specific time sequence used for AC magnetometry has been discussed in Ref. [5] and is depicted in the bottom panel of Fig. 6.11. For completeness, we review the sequence below. The RF Hahn-echo pulse sequence ($\pi/2$-π-$\pi/2$) was applied to an initial $|F = 2, m_F = -2\rangle$ state in the crossed FORT. The first $\pi/2$ pulse rotates the spin vector from the z-direction to the x'-direction and induces Larmor precession in the x'-y' plane as shown in Fig. 6.11. The RF source used to generate our interferometer pulses was synchronized with the 50 Hz AC power line. The upper panel in Fig. 6.11 depicts the evolution of the spin vector in the x'-y' plane between two $\pi/2$ pulses, where the frame is rotating at the Larmor frequency of $f_0 = g_F \mu_B B_z/h$. When we apply a time-varying magnetic field $b(t)$ along the z-direction, the spin direction in the x'-y' plane is changed by $\theta = \frac{g_F \mu_B}{\hbar}[\int_0^{\tau/2} b(t)dt - \int_{\tau/2}^{\tau} b(t)dt]$ relative to the $-x'$-direction due to the presence of the AC magnetic field $b(t)$ (shown by solid arrows in the top panel of Fig. 6.11). The maximum θ variation for a single frequency field, $b(t) = b_{\mathrm{AC}} \sin(2\pi t/\tau_{\mathrm{AC}})$, is reached when the total precession time between two $\pi/2$ pulses, τ, is equal to τ_{AC}. The angle θ yielded by $b(t)$ is converted to S_z, by the application of a second $\pi/2$ pulse, and the relationship between the expectation value of S_z, $\langle S_z \rangle$, and $b(t)$ can be expressed by

$$\langle S_z \rangle = -2 \cos \left\{ \frac{g_F \mu_B}{\hbar} [\int_0^{\tau/2} b(t)dt - \int_{\tau/2}^{\tau} b(t)dt] \right\} . \tag{6.7}$$

In the case that $b_{\mathrm{AC}} = 0$ (shown by dotted arrows in the top panel of Fig. 6.11.), the spin direction returns to the $F = 2$, $m_F = -2$ state ($\langle S_z \rangle = -2$). Therefore measurement of $\langle S_z \rangle$ in principle allows sensitive detection of weak AC magnetic fields.

Our initial tests of the AC magnetometer used a purposely introduced AC magnetic field of adjustable amplitude. Figure 6.12 shows the measured value

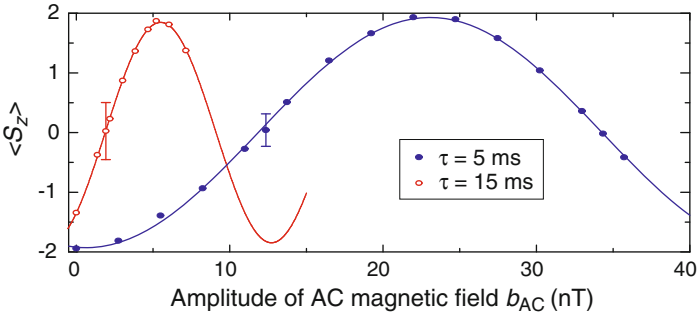

Fig. 6.12 Operation of the AC magnetometer using the Hahn echo sequence. The $\langle S_z \rangle$ values were measured as a function of b_{AC}, where a single frequency AC magnetic field $b(t)$ is applied. Each plotted point represents an average over multiple BEC measurements. The points at $\langle S_z \rangle \sim 0$ and other points are obtained from 60 and 30 times measurement, respectively. The error bars are sample standard deviation calculated from 60 $\langle S_z \rangle$ values (This figure is adapted from Ref. [5])

of $\langle S_z \rangle$ versus b_{AC} for Hahn echo sequences with $\tau = 5\,\mathrm{ms}$ (filled circles) and 15 ms (empty circles), where $b(t) = b_{\mathrm{AC}} \sin(2\pi t/\tau)$, and b_{AC} is the amplitude of the introduced magnetic field. Cosine fits to the data are shown as solid curves. Figure 6.12 shows that the phase variation in the x'-y' plane is consistent with the influence of the AC magnetic field as evidenced by the good agreement of the data with the fitted cosine curves.

We will now discuss the sensitivity of the magnetometer. Firstly, we consider the single measurement sensitivity $\delta b_{\mathrm{min}} = \delta\langle S_z \rangle / (d\langle S_z \rangle / db_{\mathrm{AC}})$, where $\delta\langle S_z \rangle$ is the uncertainty of $\langle S_z \rangle$ in a single measurement. We will assume that $\delta\langle S_z \rangle$ is equal to sample standard deviation calculated from the results of multiple experimental runs. We found that $\delta\langle S_z \rangle$ at $\langle S_z \rangle \sim 0$ was 0.28 and 0.48 at $\tau = 5$ and 15 ms, respectively. From these values, the sensitivity was calculated to be $\delta b_{\mathrm{min}} = 0.97$ and 0.66 nT. As remarked in Sect. 6.2.5, it is important to note that the spin echo technique can only remove the effect of slowly fluctuating ambient magnetic fields whose period is longer than τ. Faster fluctuations that vary for each measurement, cannot be corrected for.

For this reason, we also evaluated the *intrinsic sensitivity* of the magnetometer. This quantity is unaffected by temporal fluctuations which change between measurements. To evaluate the intrinsic sensitivity, we divided the optical density distribution of each m_F component for a single measurement into the three regions as shown in Fig. 6.13a. The value of $\delta\langle S_z \rangle$ is considered as the sample standard deviation calculated from three data points $\langle S_z \rangle_i$, where the subscript $i = 1 \sim 3$ indicates the three regions obtained from a single BEC absorption image. To avoid the effect of temporal magnetic field fluctuations we evaluate $\delta\langle S_z \rangle$ from *a single BEC absorption image*. As discussed in Ref. [5], we theoretically and experimentally confirmed that the shape of the atomic distribution of each m_F component in the optical trap is almost unchanged after a time-of-flight of 15 ms, although the distributions become more spread out. Therefore, each value of $\langle S_z \rangle_i$

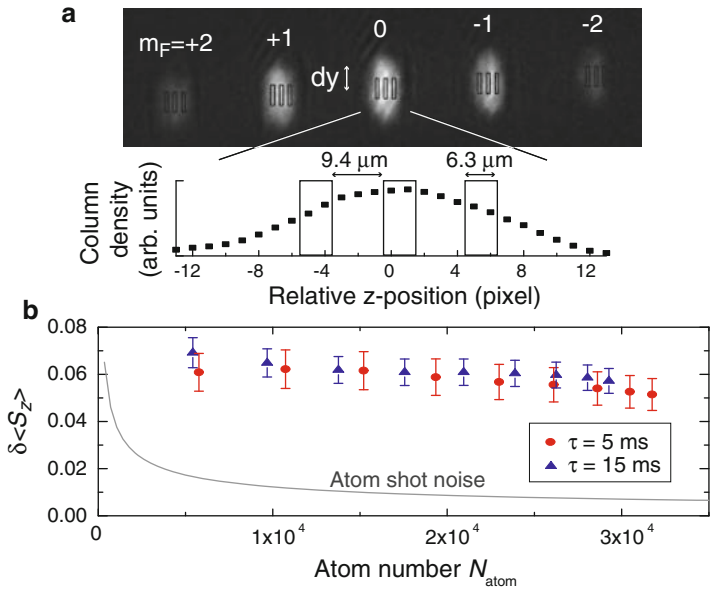

Fig. 6.13 (**a**) The *upper panel* shows a typical optical density distribution measured at $\langle S_z \rangle \sim 0$. The *lower panel* shows the column density, where the optical density along *y*-direction is integrated. The optical density distribution of each m_F component is divided into three regions. Taking into account the finite resolution of our imaging system ($\sim$7.5 μm) [6], each region is separated by 9.4 μm. (**b**) $\delta\langle S_z \rangle$ calculated from single BEC image as a function of the total atom number averaged over three regions, N_{atom}, where the N_{atom} is changed by increasing the region along the *y*-direction, *dy*. The points and error bars indicate the $\delta\langle S_z \rangle$ averaged over the multiple BEC measurements and standard error, respectively (This figure is adapted from Ref. [5])

reflects the value of $\langle S_z \rangle$ in a different *spatial* region of the trapped BEC. Using this method, we evaluated the intrinsic field sensitivity of the magnetometer to be $94 \pm 9\,\text{pT}$ for $\tau = 15\,\text{ms}$ with a corresponding $\delta\langle S_z \rangle$ of 0.069 ± 0.006. This sensitivity corresponded to a region size of $dy \times dz = 15.7\,\mu\text{m} \times 6.3\,\mu\text{m} = 99\,\mu\text{m}^2$, where *dy* and *dz* represent the length along the *y*- and *z*-direction of each region. Finally, the intrinsic field sensitivity for *N* measurements per second was found to be $\delta b^N_{\text{min}} = \delta b_{\text{min}}/\sqrt{N} = 12 \pm 1\,\text{pT}/\sqrt{\text{Hz}}$, where $N = 1/(15 \times 10^{-3})$.

To assess the performance of our magnetometer, it is valuable to compare the observed experimental fluctuations with the standard quantum limited noise floor or shot noise. Figure 6.13b shows $\delta\langle S_z \rangle$ calculated from a single BEC image versus atom number averaged over three regions, $N_{\text{atom}} = \Sigma_{i=1}^{3} \Sigma_{m_F=-2}^{+2} N_{i,m_F}/3$, where N_{atom} is changed by increasing *dy*. The solid curve represents the atom shot noise limited $\delta\langle S_z \rangle$. Fluctuations in excess of atom shot noise limited values have multiple origins including spatial distortion of the atomic distributions and their corresponding optical images, limitations of the spin-echo method in correcting for magnetic-gradient induced dephasing [35], and spontaneous pattern formation

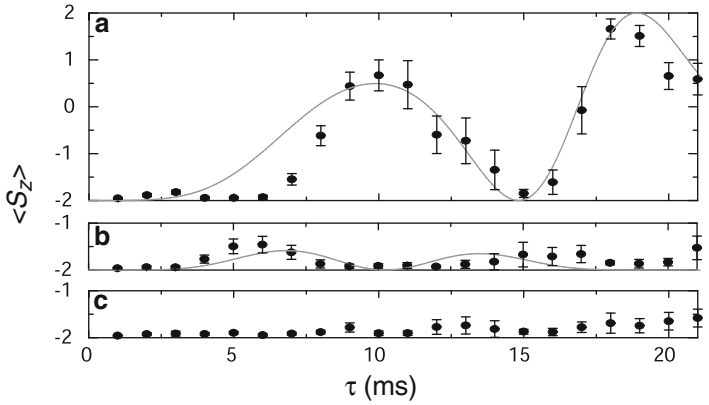

Fig. 6.14 τ dependence of $\langle S_z \rangle$ values after the Hahn echo sequence. Each point represents the average over ten measurements with the error bars giving the standard deviation over those measurements. (**a**) $\langle S_z \rangle$ values measured without the artificial application of the AC magnetic field. (**b**) $\langle S_z \rangle$ values measured with application of an inverse phase magnetic field at 50 Hz (parameters given in main text). (**c**) $\langle S_z \rangle$ values measured with application of an inverse phase magnetic field at 50 and 100 Hz (This figure is adapted from Ref. [5])

[20], along with thermal atoms, whose Gaussian tails reduce the accuracy of discrimination between the m_F components in the Stern-Gerlach separation [5].

Our first practical test of the magnetometer was to use it in the production of a cleaner magnetic field environment which may be useful for future experiments. As shown in Fig. 6.14a, we measured $\langle S_z \rangle$ as a function of τ, this time without an artificially introduced AC magnetic field. If the stray AC magnetic field in the region occupied by the BEC fluctuates in a random manner with respect to amplitude, frequency and phase, then we would expect that the observed values of $\langle S_z \rangle$ would also exhibit a random distribution [5]. However, $\langle S_z \rangle$ was found to exhibit oscillatory behavior indicating a stable AC stray magnetic field in our apparatus. We therefore surmised that the stray AC magnetic field is mainly induced by the magnetic field arising from the electronic devices surrounding the BEC apparatus. The field produced by these devices is expected to be synchronous with the 50 Hz supply line.

Formally, the effect of a stray AC magnetic field is treated by introducing the 50 Hz field $b(t) = b_{20} \sin[2\pi t/(20 \times 10^{-3}) + \theta_{20}]$, into Eq. 6.7. By fitting the resulting expression to our data (solid curve in Fig. 6.14a), we were able to estimate the parameters of the stray AC field. We then applied an AC magnetic field with the same parameters but opposite phase while repeating the experiment. The results, shown in Fig. 6.14b, demonstrate that the variation of $\langle S_z \rangle$ values is clearly suppressed compared with Fig. 6.14a, suggesting that 50 Hz magnetic field noise was reduced.

Further suppression of noise was achieved by fitting Eq. 6.7 to the data shown in Fig. 6.14b, this time assuming the existence of a 100 Hz magnetic field, $b_{10}(t) = b_{10} \sin[2\pi t/(10 \times 10^{-3}) + \theta_{10}]$. Based on the parameter values obtained, we further

applied an inverse phase magnetic field at 100 Hz in addition to the application of that at 50 Hz (Fig. 6.14c). As shown in Fig. 6.14c, $\langle S_z \rangle$ is close to -2 for most values of τ, particularly when $\tau \leq 10$ ms. As we note in Ref. [5], this result indicates that magnetic field noise which is synchronous with the power supply line is strongly suppressed by the application of an inverse phase field with frequency components at 50 and 100 Hz. In particular, at $\tau = 20$ ms, the value of $\langle S_z \rangle$ is -1.7 ± 0.2, consistent with an AC magnetic field $b(t) = b_{20} \sin[2\pi t/(20 \times 10^{-3})]$ with $b_{20} = 1.1^{+0.2}_{-0.4}$ nT, implying that the magnetic field has been suppressed by almost one order of magnitude when compared with the uncompensated case shown in Fig. 6.14a.

6.4 Summary and Future Prospects

We have explained the basics along with the applications of a spin-echo based magnetometer. This magnetometer is sensitive to a specific AC magnetic field, and its response function is adjustable by designing the parameters of the pulse sequence. Because the effect of ambient magnetic fields fluctuating on time scales longer than the length of the sequence is canceled, the magnetometer can operate in realistic environmental conditions. We demonstrated the observation of weak field noise that is synchronous with the power supply line, and by fitting the measured data, we could suppress the synchronous noise down to the order of 1 nT by artificial application of an inverse phase AC magnetic field. We believe this technique will facilitate various research and applications which require a weak magnetic field regime. The sensitivity of the magnetometer is evaluated to be $12 \times 10^{-12}\,\mathrm{T}/\sqrt{\mathrm{Hz}}$ over a measurement area of $100\,\mu\mathrm{m}^2$. This sensitivity is comparable to the atom shot-noise limited value. We may approach closer to the shot noise limit by improving our imaging system and lowering the field gradient [5].

It is possible to go beyond the standard quantum limit by atomic and optical quantum-state control: Quantum noise is present in the atomic system and also in the optical measurement system. The quantum fluctuations of a collective spin system can be reduced below the standard quantum limit for spin squeezed states [14]. Koschorreck et al. reported 1.6 dB enhancement over the projection-noise in broadband atomic magnetometry using laser-cooled thermal ^{87}Rb atoms [17]. In their experiment, atomic spin was read out by quantum nondemolition measurement via Faraday rotation of linearly-polarized incident light in the atomic gas. The shot-noise limit in optical measurement can be overcome with optical squeezing. 3.2 dB improvement in the sensitivity of an optical magnetometer based on the Faraday effect in room temperature Rb atoms was reported by Wolfgramm et al. in 2010 [34]. Simultaneous squeezing of both the atomic spin state and the optical state together with the ultimate control over motion and position of atoms in a BEC will give us a final answer regarding the fundamental sensitivity limit of optical magnetometry.

Acknowledgements We would like to thank H. Ikeda, H. Suzuki, S. Hasegawa, Y. Tomiyama, S. Sekine, and H. Saito for their contribution to the research reported in this chapter. We also thank T. Ichikawa, S. Tojo and T. Kuwamoto for valuable discussions.

References

1. I. Almog et al., Direct measurement of the system-environment coupling as a tool for understanding decoherence and dynamical decoupling. J. Phys. B Atom. Mol. Opt. Phys. **44**, 154006 (2011). doi:10.1088/0953-4075/44/15/154006
2. R.P. Anderson, C. Ticknor, A.I. Sidorov, B.V. Hall, Spatially inhomogeneous phase evolution of a two-component Bose-Einstein condensate. Phys. Rev. A **80**, 023603 (2009). doi:http://dx.doi.org/10.1103/PhysRevA.80.023603
3. G. Balasubramanian et al., Ultralong spin coherence time in isotopically engineered diamond. Nat. Mater. **8**, 383–387 (2009). doi:10.1038/nmat2420
4. D. Budker, D.F.J. Kimball (eds.), *Optical Magnetometry* (Cambridge University Press, Cambridge/New York, 2013)
5. Y. Eto, H. Ikeda et al., Spin-echo-based magnetometry with spinor Bose-Einstein condensates. Phys. Rev. A **88**, 031602(R) (2013). doi:10.1103/PhysRevA.88.031602
6. Y. Eto, S. Sekine et al., Control and detection of the Larmor precession of F=2 ^{87}Rb Bose-Einstein condensates by Ramsey interferometry and Spin-Echo. Appl. Phys. Express **6**, 05280 (2013). doi:10.7567/APEX.6.052801
7. J.N.S. Evans, *Biomolecular NMR Spectroscopy* (Oxford University Press, Oxford/New York, 1995)
8. E.L. Hahn, Spin echoes. Phys. Rev. **80**, 581 (1950). doi:10.1103/PhysRev.80.580
9. P. Hariharan, D. Sen, J. Sci. Instr. **36**, 70 (1959). doi:10.1088/0950-7671/36/2/304
10. J.M. Higbie et al., Direct nondestructive imaging of magnetization in a spin-1 Bose-Einstein gas. Phys. Rev. Lett. **95**, 050401 (2005). doi:http://dx.doi.org/10.1103/PhysRevLett.95.050401
11. L.R. Hunter, Tests of time-reversal invariance in atoms, molecules, and the neutron. Science **252**, 73–79 (1991). doi:10.1126/science.252.5002.73
12. J. Keeler, *Understanding NMR Spectroscopy* (Wiley, Chichester, 2005)
13. W. Ketterle, D.S. Durfee, D.M. Stamper-Kurn, *Making, Probing and Understanding Bose-Einstein Condensates* (1999). arXiv:cond-mat/9904034
14. M. Kitagawa, M. Ueda, Squeezed spin states. Phys. Rev. A **47**, 5138 (1993). doi:10.1103/PhysRevA.47.5138
15. K. Kobayashi, Y. Uchikawa, Development of a high spatial resolution SQUID magnetometer for biomagnetic measurement. IEEE Trans. Magn. **39**, 3378–3380 (2003). doi:10.1109/TMAG.2003.816156
16. I.K. Kominis, T.W. Kornack, J.C. Allred, M.V. Romalis, A subfemtotesla multichannel atomic magnetometer. Nature **422**, 596–599 (2003). doi:10.1038/nature01484
17. M. Koschorreck, N. Napolitano, B. Dubost, M.W. Mitchell, Sub-projection-noise sensitivity in broadband atomic magnetometry. Phys. Rev. Lett. **104**, 093602 (2010). doi:10.1103/PhysRevLett.104.093602
18. S. Kotler et al., Single-ion quantum lock-in amplifier. Nature **473**, 61 (2011). doi:10.1038/nature10010
19. S. Kotler, N. Akerman, Y. Glickman, R. Ozeri, Nonlinear single-spin spectrum analyzer. Phys. Rev. Lett. **110**, 110503 (2013). doi:http://dx.doi.org/10.1103/PhysRevLett.110.110503
20. J. Kronjäger et al., Spontaneous pattern formation in an antiferromagnetic quantum gas. Phys. Rev. Lett. **105**, 090402 (2010). doi:http://dx.doi.org/10.1103/PhysRevLett.105.090402
21. T. Kuwamoto, K. Araki, T. Eno, T. Hirano, Magnetic field dependence of the dynamics of ^{87}Rb spin-2 Bose-Einstein condensates. Phys. Rev. A **69**, 063604 (2004). doi:http://dx.doi.org/10.1103/PhysRevA.69.063604

22. J.R. Maze et al., Nanoscale magnetic sensing with an individual electronic spin in diamond. Nature **455**, 644–647 (2008). doi:10.1038/nature07279
23. N.F. Ramsey, *Molecular Beams* (Oxford University Press, Oxford/New York, 1956)
24. M. Sadgrove et al., Ramsey interferometry using the Zeeman sublevels in a spin-2 Bose gas. J. Phys. Soc. Jpn. **82**, 094002 (2013). doi:10.7566/JPSJ.82.094002
25. J.J. Sakurai, *Modern Quantum Mechanics* (Addison-Wesley, New York, 1993)
26. M. Shimogawara, H. Tanaka, K. Kazumi, Y. Haruta, MEGvision magnetoencephalograph system and its applications. Yokogawa Tech. Rep. **38**, 23–27 (2004). http://www.yokogawa.com/rd/pdf/TR/rd-tr-r00038-006.pdf
27. D.M. Stamper-Kurn, M. Ueda, Spinor Bose gases: symmetries, magnetism, and quantum dynamics. Rev. Mod. Phys. **85**, 1191 (2013). doi:http://dx.doi.org/10.1103/RevModPhys.85.1191
28. J.M. Taylor et al., High-sensitivity diamond magnetometer with nanoscale resolution. Nat. Phys. **4**, 810 (2008). doi:10.1038/nphys1075
29. S. Tojo et al., Controlling phase separation of binary Bose-Einstein condensates via mixed-spin-channel Feshbach resonance. Phys. Rev. A **82**, 033609 (2010). doi:http://dx.doi.org/10.1103/PhysRevA.82.033609
30. D.A. Varshalovich, A.N. Moskalev, V.K. Khersonskii, *Quantum Theory of Angular Momentum* (World Scientific, Singapore, 1998)
31. M. Vengalattore et al., High-Resolution magnetometry with a spinor Bose-Einstein condensate. Phys. Rev. Lett. **98**, 200801 (2007). doi:http://dx.doi.org/10.1103/PhysRevLett.98.200801
32. S. Wildermuth, S. Hofferberth, I. Lesanovsky, S. Groth et al., Sensing electric and magnetic fields with Bose-Einstein condensates. Appl. Phys. Lett. **88**, 264103 (2006). doi:10.1063/1.2216932
33. S. Wildermuth, S. Hofferberth, I. Leanovsky, E. Haller et al., Bose-Einstein condensates: microscopic magnetic-field imaging. Nature **435**, 440 (2005). doi:10.1038/435440a
34. F. Wolfgramm et al., Squeezed-Light optical magnetometry. Phys. Rev. Lett. **105**, 053601 (2010). doi:10.1103/PhysRevLett.105.053601
35. M. Yasunaga, M. Tsubota, Spin Echo in Spinor dipolar Bose-Einstein condensates. Phys. Rev. Lett. **101**, 220401 (2008). doi:http://dx.doi.org/10.1103/PhysRevLett.101.22040
36. M. Yasunaga, M. Tsubota, Magnetic resonance, especially spin echo, in spinor Bose-Einstein condensates. J. Phys. Conf. Ser. **150**, 032127 (2009). doi:10.1088/1742-6596/150/3/032127

Chapter 7
Photonic Quantum Metrologies Using Photons: Phase Super-sensitivity and Entanglement-Enhanced Imaging

Shigeki Takeuchi

7.1 Introduction

Quantum information technology has been attracting a remarkable amount of attention recently. The intrinsic features of quantum particles, like quantum superposition, the uncertainty principle, and quantum entanglement, can be fully utilized to realize novel functions in information processing and communications. Quantum computers can solve some specific problems, such as factoring, much faster than conventional computers. Quantum cryptography utilizes the uncertainty principle to generate secure secret keys which can be shared by distant parties. Since the 1990s, there has been tremendous technological progress towards the realization of these applications.

Recently, "metrology" is emerging as a new target for quantum information science. Some readers may wonder what the connection is between information science and metrology. Suppose you are asked to accurately measure the thickness d of a glass plate. The problem may be interpreted as how one can estimate the parameter d with a variance as small as possible for a given number of physical resources. In other words, the problem is how one can extract the information on d as precise as possible with given experimental data. This example shows that metrology and information science have a close connection. Quantum metrology aims to realize novel functions which are impossible using only classical resources.

In this chapter, we will try to give a brief overview of this emerging field mainly focusing on two topics: Optical phase measurements beyond the standard quantum limit (SQL) and quantum optical coherence tomography (QOCT). The sensitivity of an optical phase measurement for a given photon number N is usually

S. Takeuchi (✉)
Department of Electronic Science and Engineering, Kyoto University, Kyoto-Daigaku-Katsura, Nishigyo-ku, Kyoto 615-8510, Japan
e-mail: takeuchi@kuee.kyoto-u.ac.jp

Y. Yamamoto, K. Semba (eds.), *Principles and Methods of Quantum Information Technologies*, Lecture Notes in Physics 911, DOI 10.1007/978-4-431-55756-2_7

limited by $\sqrt{N}$, which is called the SQL or shot noise limit. However, the SQL can be overcome when non-classical light is used. QOCT harnesses the quantum entanglement of photons in frequency to cancel out the dispersion effect, which degrades the resolution of conventional optical coherence tomography(OCT).

First, the basic concepts of quantum optics will be briefly introduced. Second, we explain why the sensitivity of phase measurements can be improved by utilizing quantum resources. Third, recent experimental results that exceed the SQL [1] as well as an application of this technology for microscopy [2] will be introduced. Fourth, QOCT using frequency-entangled photons is introduced with the latest experimental results [3]. Finally, we summarize this chapter and discuss the future of this field.

7.2 Two Photon Interference

In this section, we briefly explain the basic concepts of quantum optics required to understand the contents of this chapter. First, we introduce the concept of photon number states in spatio-temporal modes, and the so-called "NOON state". Then, we explain the quantum interference of these photon number states at a beam splitter.

7.2.1 Photons in Spatio-Temporal Modes

A k photon state (k photon Fock state) $|k\rangle$ is a state where k photons are in one spatio-temporal mode [4].

$$|k\rangle = \frac{1}{\sqrt{n!}}(a^\dagger)^k|0\rangle \tag{7.1}$$

Here $a^\dagger$ (a) is a photon creation (annihilation) operator and $|0\rangle$ denotes the vacuum state. An arbitrary state of light in one spatio-temporal mode can be written as follows:

$$|\psi\rangle = \sum_{k=0}^{\infty} C_k|k\rangle, \tag{7.2}$$

where C_k is a complex amplitude. For example, a coherent state of light (e.g. laser light) $|\alpha\rangle$ with an amplitude of α can be expressed using Eq. 7.2 with

$$C_k = \exp\left(\frac{-|\alpha|^2}{2}\right)\frac{\alpha^k}{\sqrt{k!}}. \tag{7.3}$$

Suppose we have a superposition of two states: one is the state where N photons are in mode A and 0 photons are in mode B; the other is the state where 0 photons are in mode A and N photons are in mode B. Such a superposition can be written as

$$|\psi\rangle = \frac{1}{\sqrt{2}}\left(|N,0\rangle_{\mathrm{A,B}} + |0,N\rangle_{\mathrm{A,B}}\right), \tag{7.4}$$

where $|N,0\rangle_{\mathrm{A,B}}$ is short hand for $|N\rangle_{\mathrm{A}}|0\rangle_{\mathrm{B}}$. This state is called the "NOON" state due to the form of its equation [5]. Note that the NOON state given in Eq. 7.4 is an "entangled" state since the state cannot be described as a simple direct product of the arbitrary states in the two modes A and B.

7.2.2 *Two-Photon Quantum Interference at a Beam Splitter*

Here we introduce the concept of two-photon quantum interference at a beam splitter. Suppose two 'indistinguishable' photons are incident on a beam splitter with a reflectivity of 50 % (50:50 BS) (Fig. 7.1). If the photons behaved like classical particles, there would be four cases: (1) the left photon is reflected and the right one is transmitted. (2) The opposite case (the right photon is transmitted and the left photon is reflected). (3) Both photons are reflected. (4) Both photons are transmitted. Since a 50:50 BS reflects a photon with a probability of 50 %, it is logical to assume that there is a probability of 50 % that a photon is emitted from both output ports simultaneously. However, this probability is actually 0 due to quantum interference; the probability amplitude of case (3) and case (4) have the same amplitude but opposite sign, and thus completely destructively interfere.

Two-photon quantum interference is not only a typical example of the quantum characteristics of photons, but also a process widely used in quantum information science. This phenomenon is also called Hong-Ou-Mandel (HOM) interference [6].

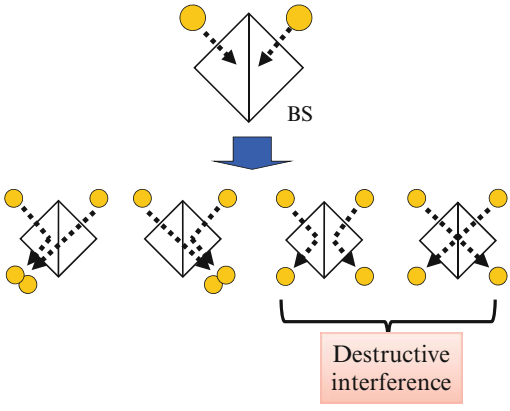

Fig. 7.1 Hong-Ou-Mandel two-photon interference. When two indistinguishable photons enter a half mirror, the two cases shown on the far right do not occur due to quantum interference

7.2.3 Single-Photon and Multi-photon Interferometers

Next, let us consider the effect of phase on multi-photon interference using the multiphoton interferometer depicted in Fig. 7.2. Now we assume a single photon is put into each of the modes, A and B, so that they arrive at the beam splitter at the same time. The two photons are then detected by two photon detectors C and D, which can discriminate the incident photon numbers. A phase plate is used to control the phase difference between mode A and B by altering the optical path length of mode B. Because the total number of photons input to this interferometer is two, there are three cases:

1. Photons are detected by detectors C and D one by one.
2. Both of the photons are detected by detector C.
3. Both of the photons are detected by detector D.

The probability of the first case $P_{1,1}$ is given as follows.

$$P_{1,1} = |\langle 0,0|cda^\dagger b^\dagger e^{i\phi}|0,0\rangle_{A,B}|^2 = 0 \tag{7.5}$$

Here we assume $c = (a + ib)/\sqrt{2}, d = (ia + b)/\sqrt{2}$ at the beam splitter. The probability of the second case $P_{2,0}$ is

$$P_{2,0} = |\langle 0,0|\frac{1}{\sqrt{2}}c^2 a^\dagger b^\dagger e^{i\phi}|0,0\rangle_{A,B}|^2 = \frac{1}{2}. \tag{7.6}$$

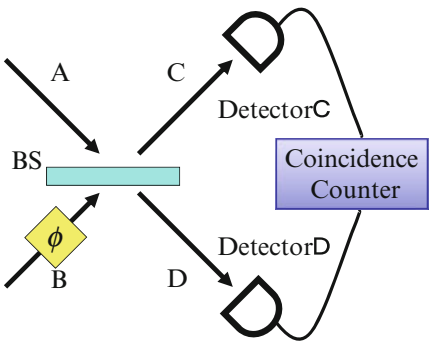

Fig. 7.2 A schematic of a multi-photon interferometer. *BS* is a beam splitter with 50 % reflectivity, and *A, B, C* and *D* denote optical modes. Photons are put into modes *A* and *B*, interfere at the *BS*, and are then detected by photon number discriminating detectors *C* and *D*. The coincidence events of specific outcomes are counted by a coincidence counter. The phase of the photons is shifted by ϕ in mode *B*

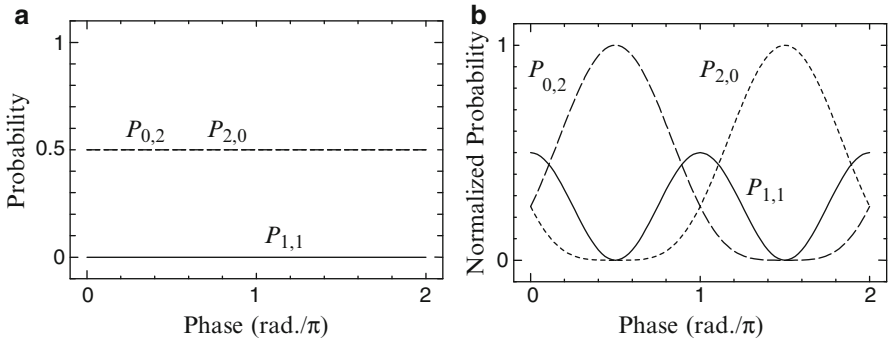

Fig. 7.3 Coincidence probabilities of the multi-photon interferometer in Fig. 7.2. (**a**) Coincidence probabilities with a pair of single-photon states input into modes A and B. (**b**) Normalized coincidence probabilities with weak coherent light input to modes A and B. In both panels, $P_{n,m}$ are the probabilities that n and m photons are detected by detectors C and D respectively

Similarly, it is deduced that $P_{0,2} = 1/2$. This result means that regardless of the phase, both of the photons are output to either mode C or D with a probability of 1/2 (Fig. 7.3a). Note that these results are the mathematical proof of the HOM interference we explained in Sect. 7.2.2.

We can calculate these probabilities when weak coherent light is incident to modes A and B. In this case, the probability $P_{1,1}$ is given as follows.

$$\begin{aligned} P_{1,1} &= |\langle 0,0|cd|\alpha, e^{i\phi}\alpha >_{A,B}|^2 \\ &= |\alpha|^4 \exp(-2|\alpha|^2)\cos^2\phi \end{aligned} \tag{7.7}$$

Similarly, $P_{2,0}$ and $P_{0,2}$ are as follows.

$$P_{2,0} = |\alpha|^4 \exp(-2|\alpha|^2)\frac{1-\sin^2\phi}{2} \tag{7.8}$$

$$P_{0,2} = |\alpha|^4 \exp(-2|\alpha|^2)\frac{1+\sin^2\phi}{2} \tag{7.9}$$

Figure 7.3b is the plot of these probabilities after normalization. The probabilities strongly depend on the phase ϕ, which is completely different from the case for single-photon inputs (Fig. 7.3a). This result can be fully understood in terms of the classical interference of light. Note that the graphs of $P_{0,2}$ and $P_{2,0}$ are the squares of sinusoidal curves because these probabilities are given by the squares of the output intensities.

Next, let us look at the interference patterns caused by NOON states. For a NOON state with an input $N = 1$, $(|1,0\rangle_{A,B} + |0,1\rangle_{A,B})/\sqrt{2}$, the probability $P_{1,0}(P_{0,1})$ of detector C(D) detecting a single photon is shown in Fig. 7.4a. Figure 7.4b is the plot of $P_{1,1}$ and $P_{0,2} + P_{2,0}$ for a NOON state with an input $N = 2$,

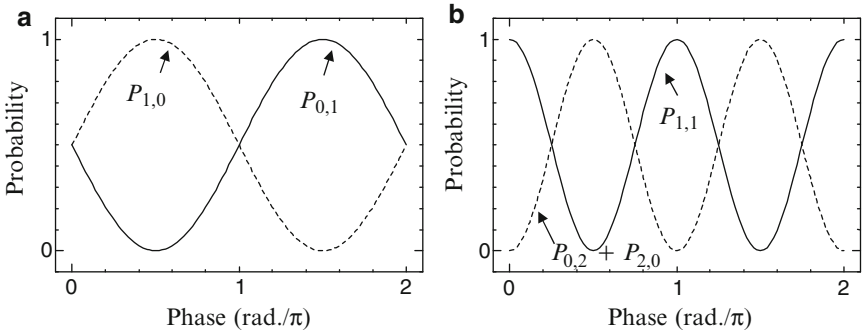

Fig. 7.4 Coincidence probabilities of the multi-photon interferometer in Fig. 7.2. (**a**) Coincidence probabilities with one-photon NOON state input. (**b**) Coincidence probabilities with two-photon NOON state input. $P_{n,m}$ are the probabilities that n and m photons are detected by detectors C and D respectively

$(|2,0\rangle_{A,B} + |0,2\rangle_{A,B})/\sqrt{2}$. Interestingly, the interference fringe periods are both π, a half of the period of $N = 1$ in Fig. 7.4a. When N is increased, the fringe period becomes $1/N$ [7].

7.3 Optical Phase Measurement Exceeding the Standard Quantum Limit

In this section, we will discuss the applications of such multi-photon quantum interference for quantum metrology [1, 8, 9].

Phase measurements using optical interferometry are applicable to many fields, for example, astronomy (gravitational wave detection), engineering (optical fiber gyroscopes) and life sciences (differential interference contrast microscopy). There are two important concepts for such measurements: precision and sensitivity. In principle, precision can be improved by increasing the probe light intensity or the number of measurements made. However, the sensitivity is fundamentally limited by the precision per unit power or the number of photons provided by the probe light.

Suppose we are trying to detect a small phase shift using an optical interferometer as shown in Fig. 7.2. With classical light or single-photon inputs, we observe the typical interference fringe shown in Fig. 7.4a. When we set the bias phase to that where the slope of the interference fringe is maximized, so the change in output due to a slight phase shift is also maximized; thus, the highest sensitivity is achieved. For a classical light source, the sensitivity limit is given by $1/\sqrt{N}$ where N is the number of photons in a given state. This limit is called the standard quantum limit (SQL), or shot-noise limit.

In more detail [1, 10, 11], the precision of the phase measurement $\Delta\phi$ can be written as

$$\Delta\phi = \frac{\Delta n}{|\partial n/\partial\phi|}, \tag{7.10}$$

where n is the number of output photons and Δn is the deviation of n. For coherent light, $\Delta n/n = 1/\sqrt{n}$ due to the shot-noise. The slope normalized by the amplitude is

$$\frac{|\partial n/\partial\phi|}{n}, \tag{7.11}$$

of which the maximum is 1. Thus, the precision of a phase measurement using coherent light can be written as follows.

$$\Delta\phi_{\mathrm{SQL}} = 1/\sqrt{n} \tag{7.12}$$

This is the SQL.

However, as we saw in the previous section (Fig. 7.4b), for an N-photon NOON state input the fringe period becomes $1/N$ of that for the single-photon input case. For the same total photon number N, the number of measurements m becomes $m = n/N$ because we use N photons for one measurement. Thus, the fluctuation $\Delta m = \sqrt{n/N}$. The maximum of the normalized slope of the fringe for N-photon NOON state interference is

$$\frac{|\partial m/\partial\phi|}{m} = N, \tag{7.13}$$

since the fringe period is $1/N$ of the coherent light inputs as seen in Fig. 7.4. As a result, the precision of a phase measurement using an N-photon NOON state interferometer is as follows.

$$\Delta\phi_{\mathrm{NOON}} = \frac{\Delta\phi_{\mathrm{SQL}}}{\sqrt{N}} \tag{7.14}$$

This means that the sensitivity is improved by a factor of $\sqrt{N}$.

Recently, we demonstrated four-photon interference exceeding the SQL [1]. Using parametric fluorescence and a stable displaced Sagnac interferometer (Fig. 7.5), we observed one-photon, two-photon and four-photon interference fringes with high visibilities (Fig. 7.6). The visibility V is a parameter describing the quality of the interference as follows:

$$V = \frac{I_{\max} - I_{\min}}{I_{\max} + I_{\min}}, \tag{7.15}$$

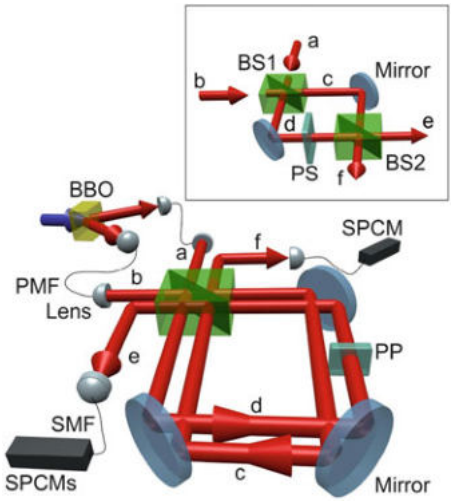

Fig. 7.5 Experimental setup for a four-photon NOON state interferometer [1]. *BBO* is β-Barium Borate, *PMF* is a polarization maintaining fiber, *SPCM* is a single-photon counting module, and *PP* is a phase plate. *Inset*: a Mach-Zender interferometer which corresponds to the displaced Sagnac interferometer in the main panel. *BS* denotes beam splitter and *PS* denotes phase shifter

where $I_{\max}$ and $I_{\min}$ are the maximum and minimum photon counts. The sensitivity degrades when the visibility is lower because the maximum of the normalized slope (Eq. 7.13) is reduced. The sensitivity also depends on the method used to observe the correlation of the photons at the output.

Figure 7.6 shows the results of the multi-photon interference experiments [1]. Figure 7.6a is a simple single-photon interference fringe, and Fig. 7.6b, c are the multi-photon interference fringes using the $N = 2$ and $N = 4$ NOON states, respectively. The interference fringe period of Fig. 7.6b is half of that in Fig. 7.6a, for the reasons described in the previous section (Fig. 7.4). It should also be noted that the fringe period of the four-photon NOON state interference (Fig. 7.6c) is a quarter of that of the single-photon interference.

Let us explain in more detail how we obtained these multi-photon interference fringes. In order to obtain the results shown in Fig. 7.6b, we input $|11\rangle_{ab}$ into the interferometer, which is then converted to $(|20\rangle_{cd} + |02\rangle_{cd})/\sqrt{2}$ by the first beam splitter. Then, we measured the coincidence counts using two single photon detectors in the output modes (e and f).

For the four-photon interference fringe (Fig. 7.6c), the input state $|22\rangle_{ab}$ is converted to the following state by the beam splitter.

$$\frac{\sqrt{6}}{4}(|4,0\rangle_{\mathrm{c,d}} + |0,4\rangle_{\mathrm{c,d}}) + \frac{1}{2}|2,2\rangle_{\mathrm{c,d}} \tag{7.16}$$

This is a superposition of a four-photon NOON state and the $|2,2\rangle_{\mathrm{c,d}}$ state. Interestingly, the interference can be 'extracted' solely from the four-photon NOON state by selecting certain coincidence events as follows.

After the second beam splitter, the four-photon NOON state $(|4,0\rangle_{\mathrm{c,d}} + |0,4\rangle_{\mathrm{c,d}})$ is converted to a state which contains $|3,1\rangle_{\mathrm{e,f}}$. On the other hand, $|2,2\rangle_{\mathrm{c,d}}$ is converted to a similar state shown in Eq. 7.16 and consequently $|3,1\rangle_{\mathrm{e,f}}$ will never

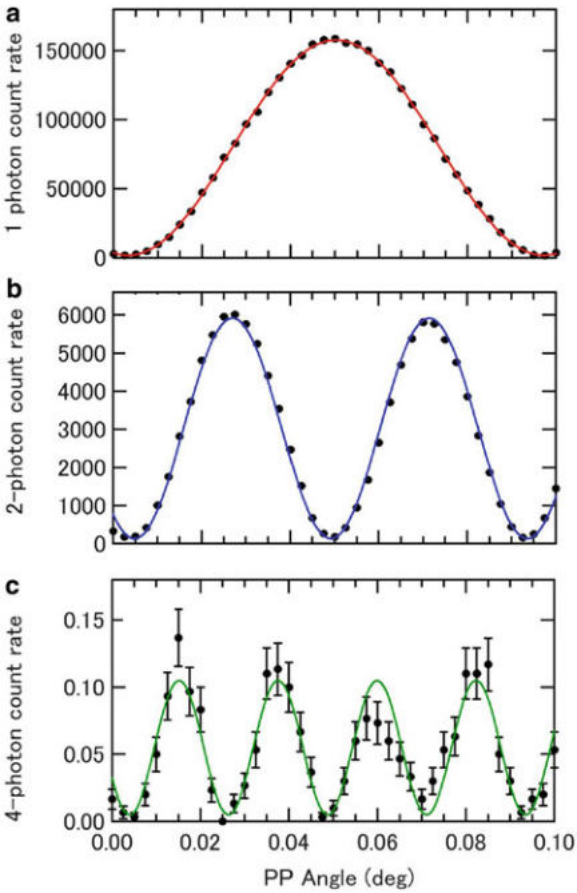

Fig. 7.6 Experimental results of the multi-photon interference fringes [1]. (**a**) Single-photon count rate in mode e as a function of phase plate (PP) angle with a single-photon input $|10\rangle_{ab}$. (**b**) Two photon count rate in modes e and f for the input state $|11\rangle_{ab}$. (**c**) Four photon count rate of three photons in mode e and one photon in mode f for the input state $|22\rangle_{ab}$. Accumulation times for one data point were (**A**) 1, (**B**) 300, and (**C**) 300 s

appear after the conversion by the second beam splitter. Thus, by detecting the events where three photons and one photon are in modes e and f, respectively, the four-photon NOON interference fringe can be observed. The efficiency of this event post-selection η is $3/8$. For this scheme with $\eta = 3/8$, the threshold visibility required to surpass the SQL is 82 % [10]. The visibility of the four-photon interference fringe shown in Fig. 7.6c was 91 ± 6 % [1], clearly exceeding the threshold of 82 %.

7.4 An Entanglement-Enhanced Microscope: Application of the Phase Super-sensitivity to Microscopy

Optical phase measurements are playing an important role in microscopy. Differential interference microscopes (DIM), which detect the optical path-length difference between two adjacent optical paths at the sample, are widely used for the evaluation

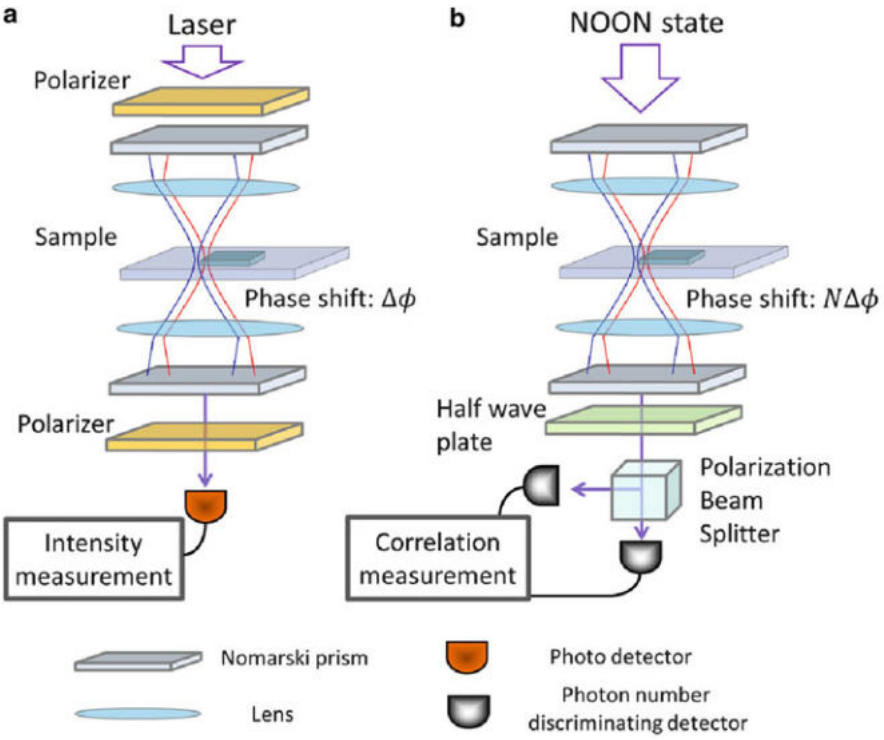

Fig. 7.7 LCM-DIM and the entanglement-enhanced microscope [2]. (**a**) Illustration of LCM-DIM (**b**) Illustration of the entanglement-enhanced microscope. The *red* and *blue lines* indicate horizontally and vertically polarized light

of opaque materials or the label-free sensing of biological tissues. A laser confocal microscope (LCM) combined with a DIM (LCM-DIM, Fig. 7.7a) has recently been used to observe the growth of ice crystals with a single molecular step resolution [12]. The depth resolution of such measurements is determined by the signal-to-noise ratio (SNR) of the measurement, which is in principle restricted by the SQL.

Recently, we proposed and demonstrated an entanglement-enhanced microscope which is based on a LCM-DIM (Fig. 7.7b) [2]. Instead of laser light and an intensity measurement, entangled photons (in the NOON state) and a coincidence measurement were used. The SNR of an entanglement microscope is $\sqrt{N}$ times better than the conventional LCM-DIM restricted to the SQL.

In the experiment, we used a two-photon NOON state ($N = 2$) source as the probe (Fig. 7.8). The sample was a glass plate with a Q shape on its surface, carved in relief with an ultra-thin step of $\sim$17 nm using optical lithography (Fig. 7.8a, b). Figure 7.8c, d show the two-dimensional scan images of the sample using entangled photons and single photons, respectively. The step of the Q-shaped relief is clearly seen in Fig. 7.8c, whereas it is unclear in Fig. 7.8d. The average total

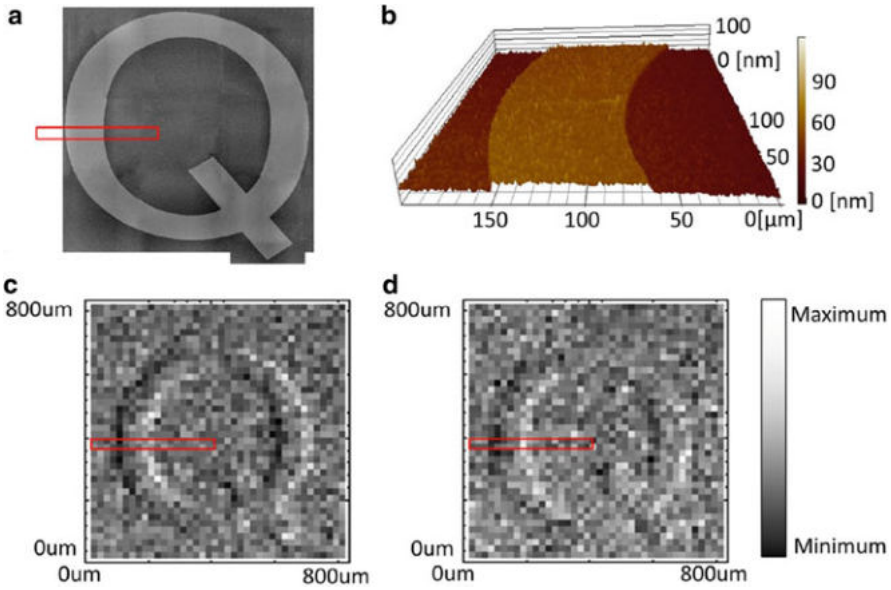

Fig. 7.8 Experimental results for the entanglement-enhanced microscope [2]. (**a**) Atomic force microscope (AFM) image of a glass plate sample (BK7), the surface of which has a Q shape carved in relief with an ultra-thin step using optical lithography. (**b**) The section of the AFM image of the sample, which is the area outlined in *red* in (**a**). The height of the step is estimated to be 17.3 nm from this data. (**c**) An image of the sample using an entanglement-enhanced microscope where a two-photon entangled state is used to illuminate the sample. (**d**) An image of the sample using single photons (a classical light source)

number of photons contributing to these data is set to 920 per position assuming a detection efficiency of unity. A detailed analysis revealed that the SNR of Fig. 7.8c is 1.35 ± 0.12 times better than Fig. 7.8d, which agrees well with the theoretical prediction of 1.35, taking the visibility of the single and two-photon interferences into account.

7.5 Quantum Optical Coherence Tomography

In this subsection, we introduce another application of novel quantum states for optical metrology: QOCT, where the time-frequency entangled states of photons can exceed the depth resolution of their classical counterpart and provide tolerance of the phase dispersion in optical paths.

Figure 7.9a, b temporally depict the two-photon wave function. For the state shown in Fig. 7.9a, the signal photon and idler photon are independent and have no specific correlation in time. In other words, the distribution of the detection time for the signal photon t_s has no correlation to the detection time for the idler photon t_i.

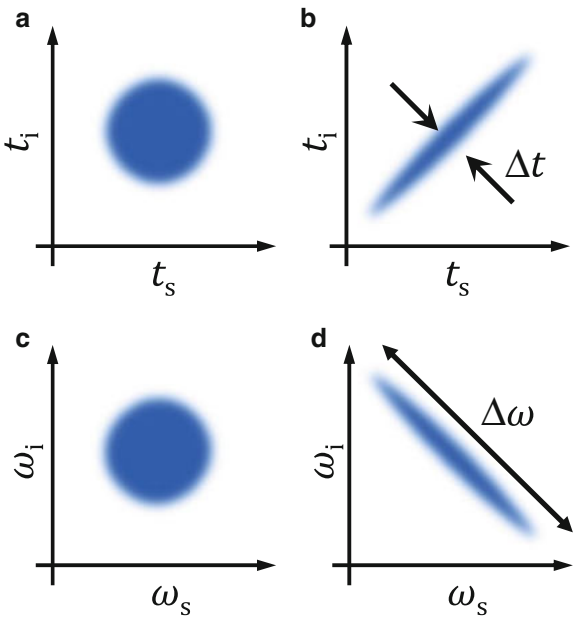

Fig. 7.9 Two photon wave functions. (**a**) Non-entangled two-photon states. (**b**) Two photon states strongly correlated in time. (**c**) Non-entangled two-photon states in frequency space. (**d**) The two-photon wave function of the state in (**b**) in frequency space

On the other hand, for the state shown in Fig. 7.9b, the distribution of t_s strongly correlates with t_i; the signal photon and idler photons are detected at almost the same time $t_s \sim t_i$ with a short correlation time Δt.

Figure 7.9c, d are the wave functions shown in (a) and (b), respectively, in frequency space, which can be obtained through a two-dimensional Fourier transformation. The non-correlated photon pair does not show any correlation (Fig. 7.9c). On the other hand, the state correlated in time shows strong correlation in frequency space also (Fig. 7.9d). It can also be seen that to shorten the correlation time Δt, the frequency correlation $\Delta\omega$ has to be broader.

Recently, the generation and application of photons entangled in time and frequency has been attracting attention. One of these applications is QOCT.

First, let us look at (classical) OCT (Fig. 7.10a) [13]. A classical light field generated from a source is divided by a beam splitter. One light beam is radiated onto the sample, and the other is radiated onto a reference mirror. The reflected beams then interfere as they pass through the beam splitter for a second time and the result is measured by a detector. When the coherent length of the light is short enough, the interference signal is obtained only when the optical path lengths of the sample-path and reference-path are the same. Thus, by scanning the position of the reference mirror, one can obtain an image of the structure inside the sample. This technology is now widely used to observe the eyeground in ophthalmology.

In general, the probe light pass through an optical medium (ex. water in eyeball). In order to improve the resolution along the optical axis (depth resolution), the bandwidth of the low-coherence light has to be broadened in order to make the

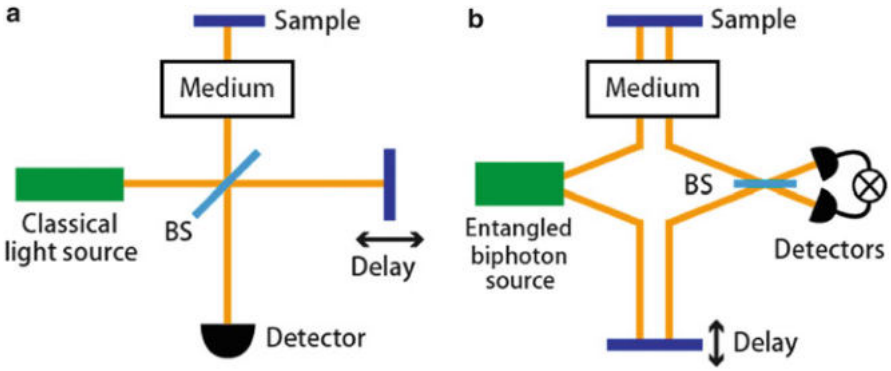

Fig. 7.10 Schematic of LCI (**a**) and TPI (**b**) [3]. BS stands for beam splitter

interference width of the interference fringe smaller. However, due to the group velocity dispersion in the optical medium, the width of the interference fringe becomes even broader. Due to this trade-off relation, the depth resolution of the OCT is limited to around $5 \sim 10\,\mu$m.

QOCT, which was first proposed [14] and demonstrated [15] by Teich and his collaborators, is a method whose resolution is tolerant of the dispersion in the medium (Fig. 7.10b). Time-frequency entangled states, which are usually generated via spontaneous parametric down conversion (SPDC), are used. The frequency ω_s, ω_i of such photon pairs (signal photon and idler photon) has the following relation with the frequency of the pump laser ω_p used for SPDC as follows:

$$\omega_p = \omega_s + \omega_i, \tag{7.17}$$

which can be seen in Fig. 7.9d.

Similarly to OCT, the signal and idler photons are radiated to a sample and a reference mirror, respectively, and the two-photon interference between the reflected components, which interfered at the beam splitter, is detected by a pair of detectors at the output. As we have observed in Fig. 7.3a, the coincidence probability becomes 0 when the optical path lengths of the two arms are the same. On the other hand, the coincidence probability is 1/2 when the lengths are different. For this reason, a dip in the coincidence count rate is observed when the two optical path lengths are the same (Fig. 7.11b). This is known as the Hong-Ou-Mandel dip, or the HOM dip. QOCT uses this HOM dip in place of the low-coherence interference fringe in OCT.

The depth-resolution of QOCT is determined by the width of the HOM-dip. It is known that the dip-width is not affected by the even-order phase dispersion of the medium in the optical path. Recently, we verified the perfect dispersion tolerance of the HOM-dip width in a high-resolution regime ($3 \sim 4\,\mu$m) [3]. A low-coherence interference (LCI) fringe (Fig. 7.11a) and a two-photon interference (TPI) fringe (Fig. 7.11b) are obtained using the single-photon/entangled photon sources with a Gaussian-shaped spectrum of 75 nm in bandwidth with a center wavelength of

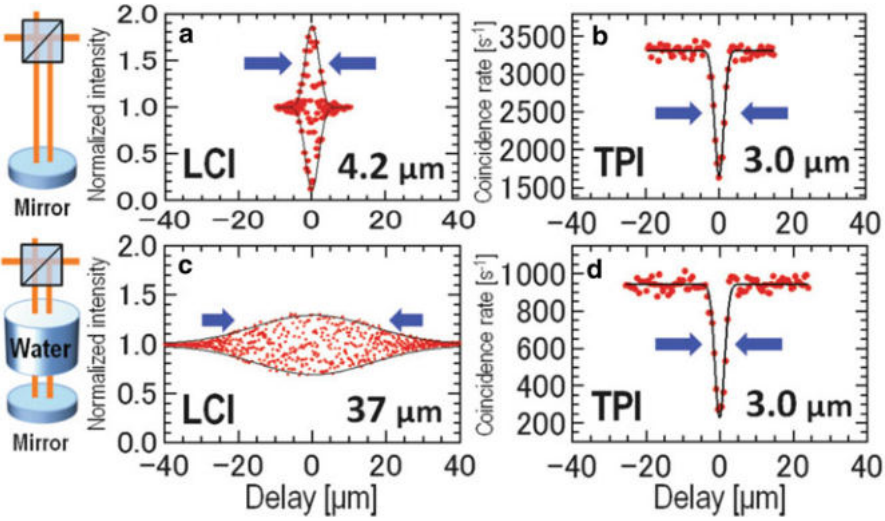

Fig. 7.11 Experimental LCI and TPI interferograms for a Gaussian shaped spectrum [3]: The 4.2 μm LCI (**a**) and 3.0 μm TPI (**b**) widths with no medium, the broadened 37 μm LCI (**c**) and unchanged 3.0 μm TPI (**d**) widths using 25 mm of water as a dispersive medium

808 nm. We found that for a light source with a Gaussian shaped spectrum, the width of the TPI is $1/\sqrt{2}$ that of the LCI, resulting in a $\sqrt{2}$ times better resolution. Figure 7.11c, d show the LCI and TPI fringes with 25 mm of water in the optical path. The width of the LCI fringe becomes much broader (37 μm), while the width of the TPI fringe is 3.0 μm, exactly the same as the case where no water is present (Fig. 7.11b). These experimental results clearly show the advantage of using QOCT for high-resolution tomography.

In order to improve the resolution further, the bandwidth of the entangled-photon pairs has to be broadened. Harris proposed an interesting idea to use chirped quasi-phase-matched (QPM) crystal to realize time-frequency entangled photons with ultra-broad bandwidth [16]. Following on from this idea, we recently succeeded in the generation of ultra-broad parametric fluorescence, the wavelength of which spanned from 790 to 1610 nm [17].

7.6 Summary

In this chapter, we introduced quantum metrologies that utilize entangled photons. We have shown that the sensitivity of phase measurements using an N-photon NOON state interference can exceed that achieved using a classical light source by a factor of $\sqrt{N}$. We also introduced our recent experiments in which the SQL was surpassed using a four-photon interferometer. We demonstrated the

application of this technology to microscopy with experimental verification. Finally, we explained the concept of quantum optical coherence tomography using time-frequency entangled photons and presented recent experimental results showing that a high-resolution (3 μm) HOM-dip is achieved even when 25 mm of water lies in the optical path.

Currently, increasing the number of photons is of the utmost importance. When we are able to use a ten-photon NOON state ($N = 10$) the SNR will be more than three times higher than the SQL. In other words, the same SNR can be achieved with just 10 % of the photon flux. To this end, the development of efficient single-photon sources [18], efficient photon number detectors, and integrated photonic quantum circuits is important. Note that the sensitivity beyond SQL requires quantum resources for input, and thus can be seen as a signature of quantumness of the input state [9]. For QOCT, it is expected that novel technologies like the fabrication of QPM devices using nano-size electrodes will dramatically improve the bandwidth and flux of time-frequency entangled photons. There are some other recent works using non-classical light for quantum metrologies [19–21].

Acknowledgements I would like to thank my collaborators, especially Ryo Okamoto, Tomohisa Nagata, Masayuki Okano, Takafumi Ono, Keiji Sasaki, Jeremy O'Brien, Holger Hofmann, Norihiko Nishizawa, Sunao Kurimura, and my students for their contribution to the works explained here. The works reported in this chapter were supported in part by the FIRST Program by the Japan Society for the Promotion of Science (JSPS), Core Research for Evolutionary Science and Technology (CREST) of the Japan Science and Technology Corporation (JST), the Quantum Cybernetics Project of JSPS, Grants-in-Aid from JSPS, the Project for Developing Innovation Systems run by the Ministry of Education, Culture, Sports, Science and Technology (MEXT), the Global Center of Excellence program run by MEXT, and the Research Foundation for Opto-Science and Technology.

References

1. T. Nagata, R. Okamoto, J.L. O'Brien, K. Sasaki, S. Takeuchi, Science **316**, 726 (2007)
2. T. Ono, R. Okamoto, S. Takeuchi, Nat. Commun. **4**, 2426 (2013)
3. M. Okano, R. Okamoto, A. Tanaka, S. Ishida, N. Nishizawa, S. Takeuchi, Phys. Rev. A **88**, 043845 (2013)
4. L. Mandel, E. Wolf, Chapter 10, in *Optical Coherenece and Quantum Optics* (Cambridge University Press, Cambridge, 1995)
5. H. Lee, P. Kok, J.P. Dowling, J. Mod. Opt. **49**, 2325 (2002)
6. C.K. Hong, Z.Y. Ou, L. Mandel, Phys. Rev. Lett. **59**, 2044 (1987)
7. J. Jacobson, G. Björk, I. Chuang, Y. Yamamoto, Phys. Rev. Lett. **74**, 4835 (1995)
8. M.W. Mitchell, J.S. Lundeen, A.M. Steinberg, Nature **429**, 161 (2004)
9. V. Giovannetti, S. Lloyd, L. Maccone, Phys. Rev. Lett. **96**, 010401 (2006)
10. K.J. Resch, K.L. Pregnell, R. Prevedel, A. Gilchrist, G.J. Pryde, J.L. O'Brien, A.G. White, Phys. Rev. Lett. **98**, 223601 (2007)
11. R. Okamoto, H.F. Hofmann, T. Nagata, J.L. O'Brien, K. Sasaki, S. Takeuchi, New J. Phys. **10**, 073033 (2008)
12. G. Sazaki, S. Zepeda, S. Nakatsubo, E. Yokoyama, Y. Furukawa, Proc. Natl. Acad. Sci. USA **107**, 19702 (2010)

13. D. Haung, E.A. Swanson, C.P. Lin, J.S. Schuman, W.G. Stinson, W. Chang, M.R. Hee, T. Flotte, K. Gregory, C.A. Puliafito, J.G. Fujimoto, Science **254**, 1178 (1991)
14. A.F. Abouraddy, M.B. Nasr, B.E.A. Saleh, A.V. Sergienko, M.C. Teich, Phys. Rev. A **65**, 053817 (2002)
15. M.B. Nasr, B.E.A. Saleh, A.V. Sergienko, M.C. Teich, Phys. Rev. Lett. **91**, 083601 (2003)
16. S.E. Harris, Phys. Rev. Lett. **98**, 063602 (2007)
17. A. Tanaka, R. Okamoto, H.H. Lim, S. Subashchandran, M. Okano, L. Zhang, L. Kang, J. Chen, P.H. Wu, T. Hirohata, S. Kurimura, S. Takeuchi, Opt. Express **20**, 25228 (2012)
18. S. Takeuchi, Jpn. J. Appl. Phys. **53**, 030101 (2014)
19. A. Crespi et al., Appl. Phys. Lett. **100**, 233704 (2012)
20. F. Wolfgramm, C. Vitelli, F.A. Beduini, N. Godbout, M.W. Mitchell, Nat. Photon. **7**, 28 (2013)
21. M.A. Taylor et al., Nat. Photon. **7**, 229 (2013)

Chapter 8
Counting Statistics of Single-Electron Transport

Toshimasa Fujisawa

8.1 Introduction to Counting Statistics

Intriguing quantum dynamics can be studied by determining the electron transport characteristics in nanostructures [1, 2]. In contrast to the averaged electrical current, a statistical analysis of current fluctuation or noise provides rich information on the electrical transport [3, 4]. Frequency spectrum is the standard way of characterizing the noise. Low-frequency ($1/f$) noise often arises from thermally activated impurities [5, 6]. Fundamental white noise, albeit its featureless spectrum, comprises a Johnson Nyquist thermal noise that arises from the Brownian motion of electrons and a shot noise associated with the tunneling of elementary charge. Shot noise measurements have successfully characterized correlated transport, such as the sub-Poissonian statistics in single-electron tunneling [7] and fractional-charge tunneling in the fractional quantum Hall regime [8, 9]. In addition to the frequency spectrum, various statistical methods developed in the field of quantum optics are expected to highlight the correlations [10]. For example, intensity correlation can identify bunching or anti-bunching of indistinguishable particles. The statistical distributions of transporting particles (electrons) in a given time period can exhibit a Poisson or Gaussian function depending on the origin of the fluctuations. The distribution can be characterized by its variance, skewness for asymmetric distribution, sharpness for fourth order term, and so on. Since the thermal noise has a symmetric Gaussian distribution, odd-order noise can be used to exclusively probe the shot noise component. While second-order shot noise measurements are restricted to strongly non-equilibrium conditions, where transport can be considered unidirectional, third-order noise measurements show advantages when evaluating the shot noise, even at

T. Fujisawa (✉)
Department of Physics, Tokyo Institute of Technology, Meguro, Tokyo, Japan
e-mail: fujisawa@phys.titech.ac.jp

Y. Yamamoto, K. Semba (eds.), *Principles and Methods of Quantum Information Technologies*, Lecture Notes in Physics 911, DOI 10.1007/978-4-431-55756-2_8

a small bias voltage close to the equilibrium conditions. Such statistical analyses are useful in studying correlated electron transport in nanostructures.

Several experimental techniques have been developed to evaluate current fluctuations. The distribution function around the averaged current can be directly investigated using a current voltage converter and an analog digital converter with a high precision [11, 12]. However, non-linearity in the amplifiers and converters has to be carefully corrected to remove artifacts from the measurement system. The resolution of the noise is not always sufficient to study intriguing correlation effects. In a frequency domain experiment, third-order noise can be obtained by multiplying three frequency components [13, 14]. The finite bandwidth in the measurement system has to be considered in the analysis. More importantly, a higher-order moment may arise from the connection of the measurement circuit to the finite impedance [15]. All extrinsic effects have to be excluded from the analysis.

In this section, we emphasize on an alternative approach, which counts the passage of single electrons through a quantum dot (QD). Single-electron transport through a QD can be investigated in real time using an integrated charge detector [16–20]. Since all the electron-tunneling events can be stored in a fast and sensitive electrometer attached to the QD, the technique is capable of performing various statistical analyses. For example, a double quantum dot (DQD) can be used with a charge sensor to determine the direction of the electron transport, which will be useful in acquiring all tunneling events and determining the transport characteristics [21].

8.2 Single-Electron Counting with a Quantum Dot

8.2.1 Charge Detection of a Quantum Dot

Single-electron tunneling through a small conductive island has been studied using the Coulomb blockade effect with a significant on-site Coulomb energy [2]. Conductance exhibit oscillatory changes with the electrochemical potential of the QD. The number of electrons in the QD takes a well-defined integer value in the Coulomb blockade region, where the current is well suppressed. Transport is allowed when the electrochemical potential is adjusted between the chemical potentials of the adjacent leads (the transport window). An electron that has entered a QD has to go out before another electron is allowed to enter. This correlated electron transport can be well characterized by the counting scheme, as shown in the following sections. The charge state can be read by using a charge sensor coupled to the QD. A single-electron transistor (SET) or QPC can be used as a charge sensor [22]. Time-resolved counting measurements must be performed with sufficient bandwidth. A wide bandwidth beyond 100 MHz can be obtained with a RF carrier signal and an impedance transformer, known as RF-SET or RF-QPC [23]. However, the practical bandwidth for real-time detection required for counting purposes is limited by the noise floor of the amplifier or current meter. When a cold

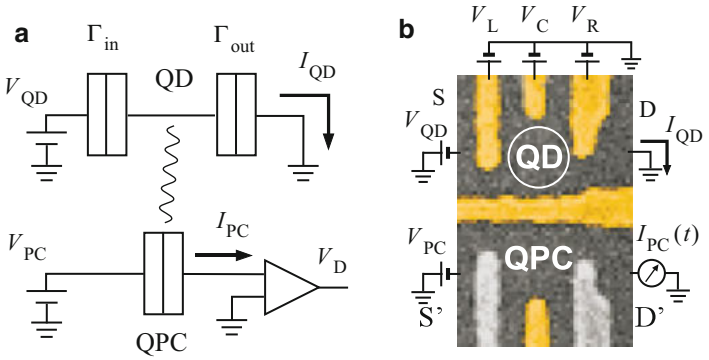

Fig. 8.1 (**a**) Schematic circuit for charge sensing of a single QD. The *double boxes* represent tunneling barriers. Current through a QD, I_{QD}, is dominated by single-electron transport. Current through a QPC, I_{PC}, is sensitive to the charge or number of electrons in the QD. (**b**) Scanning electron micrograph of a device comprising a QD coupled with a QPC

amplifier is used for low-noise operation, the bandwidth can reach 1 MHz, which allows us to count all the tunneling events with currents of the order of 100 fA [24].

Figure 8.1a shows a schematic circuit for detecting charge in a QD by using a QPC. A unidirectional current flow from the left lead, through the QD, and to the right lead is established with a finite bias voltage, eV_{QD}, greater than thermal energy, k_BT. The presence of an excess electron in the QD raises the tunneling barrier of the QPC, and thus lowers the conductance and detector current, I_{PC}. Therefore, the charge state of the QD can be detected by monitoring I_{PC}. This kind of device can be fabricated in a standard AlGaAs/GaAs heterostructure using electron-beam lithography, as shown in Fig. 8.1b [16, 25]. In this device, the two-dimensional electron system (2DES) with a density of $3 \times 10^{11}\,\mathrm{cm}^{-2}$ and a mobility of $1.9 \times 10^6\,\mathrm{cm}^2/\mathrm{Vs}$ is located 95 nm below the surface. The horizontal metal gate isolates the channels for QD and QPC, but a significant electrostatic coupling is obtained between them. The QD is defined by the three upper vertical gates, where tunneling barriers are formed between the outer gates and the horizontal isolation gate with the small gaps (∼50 nm). By adjusting the voltages applied to the fine surface gates, we define a conductive channel through a QD with electron number N ($= 0 - 10$). A QPC is known to show a quantized conductance, ne^2/h, with integer n (even numbers for the spin-degenerated case at zero magnetic field) [26]. For charge detection, the QPC has to be adjusted to the tunneling regime, where the current through the QPC, I_{PC}, is sensitive to the charge state of the QD. Maximum charge sensitivity is obtained at the maximum slope dI_{PC}/dV_g. Charge detection is exclusively efficient, especially when the direct current (I_{QD}) is too small to be investigated.

Nonlinear unidirectional transport through the QD can be induced by a finite bias $V_{QD} = 0.5$ mV. Figure 8.2a shows that the QPC current (I_{PC}) traces as a function of V_C at several V_{QD} values. I_{PC} changes stepwise from the high level corresponding to $N = 0$ to the low level corresponding to $N = 1$. The value of N must be

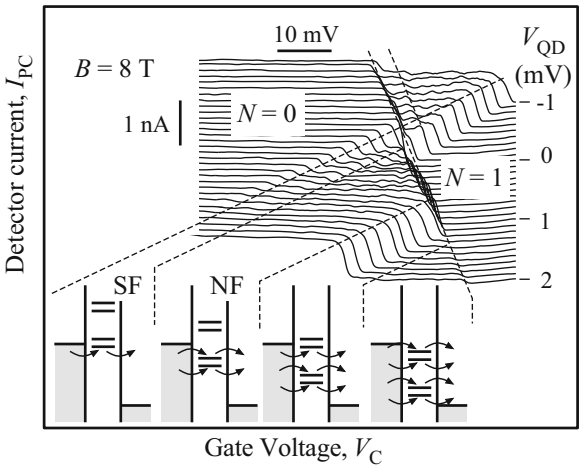

Fig. 8.2 Excitation spectrum obtained by charge detection. The current shows characteristic levels for empty ($N = 0$) and occupied ($N = 1$) states, and intermediate values for single-electron transport. The *insets* show energy diagrams for some current levels

fluctuating between 0 and 1 in the transport region between these Coulomb blockade regions, but the averaged current level in this figure measures the average electron number $\langle N \rangle = \Gamma_i / (\Gamma_i + \Gamma_o)$ given by the incoming/outgoing rate $\Gamma_{i/o}$. Multiple current levels are associated with the inclusion of the ground and excited states in the incoming/outgoing process. In the example measured at $B = 8$ T, a Zeeman splitting of the lowest and first orbital states for $N = 1$ QD is clearly seen. Transport characteristics can be investigated using the charge detection scheme [16]. More detailed information can be obtained by time-resolved charge detection.

Time-resolved charge detection measurements can be performed with a sufficient bandwidth for acquiring single-electron tunneling events. The time trace of I_{PC}, shown in Fig. 8.3a, was taken with an I-V converter with 50 kHz bandwidth operated at room temperature. An additional low-pass filter with a cutoff frequency of 3 kHz is used to obtain a reasonable signal-to-noise ratio [27]. A clear two-level fluctuation between the empty (high current level) and occupied (low current level) states is seen [16]. The dwell times, T_H and T_L, for the empty and occupied states, respectively, are randomly distributed, as seen in Fig. 8.3b, c. The distribution is well described by an exponential profile $\sim \exp(-\Gamma'_{i/o} T_{H/L})$, which originates from a random Poisson process with tunneling rates Γ_i and Γ_o. The slope $\Gamma'_{i/o}$ is obtained from the mean and standard deviations of T_H and T_L. The total transport rate $\Gamma_{cur} = \Gamma_i \Gamma_o / (\Gamma_i + \Gamma_o)$ for the current $I_{QD} = e\Gamma_{cur}$ can also be obtained from the number of switching events per unit time.

8.2.2 Data Correction for Finite Bandwidth

Noted that some fast tunneling events with short dwell time have been removed using low-pass filters in the measurement system. The effect of the finite frequency bandwidth has to be corrected. Error correction is addressed by Naaman and

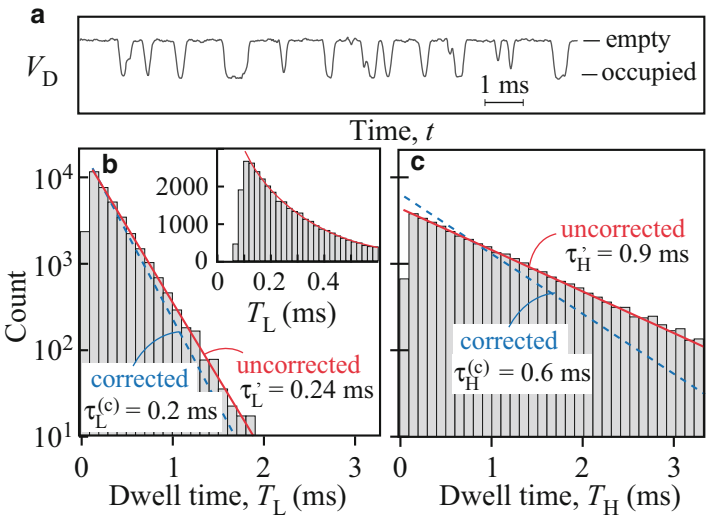

Fig. 8.3 (**a**) Typical random telegraph signal for single-electron tunneling through a QD. (**b–c**) Histograms of dwell times in the empty, T_H (**b**), and occupied, T_L (**c**), states

Aumentado, who have developed a correction scheme for a stochastic detector characterized by a Poisson process with a transition rate Γ_{det} [28, 29]. In this model, the detector responds to the charge with a random delay time with a mean $\tau_{det} \equiv 1/\Gamma_{det}$, which allows us to use the rate equation on the dynamics. However, the detection error is not always given by a stochastic response. Here, we describe an deterministic response when the distortion arises from a first-order frequency filter [27].

As shown in Fig. 8.4a, the true detector current, $I_D(t)$, fluctuates between the high and low levels. This current is converted into a voltage $V_D(t)$ using an I-V converter and appropriate filters, which are necessary to remove unwanted high-frequency noise and obtain a sufficiently high signal-to-noise ratio. Here we assume that the overall response function is expressed as a standard first-order low-pass filter characterized by a time constant τ_f. The $V_D(t)$ waveform would be somewhat distorted like in Fig. 8.4b. The waveform is digitized into two values with hysteretic thresholds, $V_{th,H}$ and $V_{th,L}$, set between the two voltages, $V_{D,H}$ and $V_{D,L}$, respectively, for the high and low levels [30]. A typical response time, τ_{th}, between a tunneling event and the reaching of their threshold values is given by $\tau_{th} = -\tau_f \ln \eta$ with a threshold factor $\eta = (V_{th,L} - V_{D,L})/(V_{D,H} - V_{D,L})$ $(0 < \eta < 1/2)$. The digitized data, as shown in Fig. 8.4c, is often regarded as real-time variation of the dot charge $Q_d(t)$ in an experiment.

However, the obtained dwell times T_H' and T_L', shown in Fig. 8.4c, are not identical to the true dwell times T_H and T_L presented in Fig. 8.4a. The first dwell time in the figure $T_{H,1}'$ is slightly different from the true one ($T_{H,1}$), but this error is usually acceptable as it is less than $\tau_f \ln 2$ for $\eta = 1/2$ and can be reduced for hysteretic

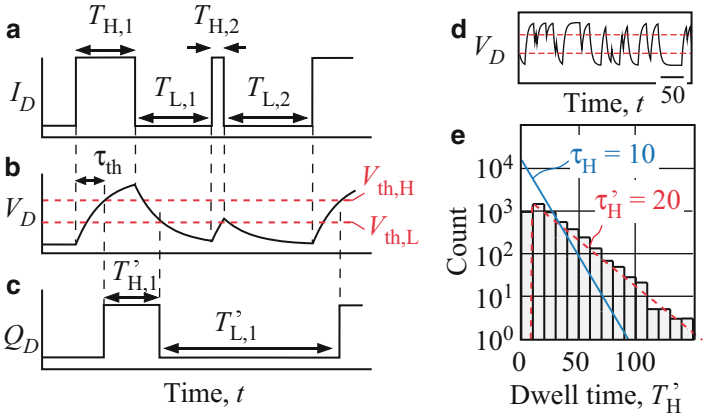

Fig. 8.4 (**a**) Schematic of the detector current $I_D(t)$ with true dwell times $T_{H,i}$ and $T_{L,i}$. (**b**) Distorted voltage $V_D(t)$ through a low-pass filter. (**c**) Digitized data $Q_d(t)$ with recognized dwell times $T'_{H,i}$ and $T'_{L,i}$. (**d**, **e**) Simulated $V_D(t)$ waveform and counting statistics for symmetric tunneling barriers ($\tau_H = \tau_L = 10$) and a filter time constant $\tau_f = 5$ in the time-step unit used in the simulation (Adapted from Ref. [27])

thresholds. Serious errors come from undetected events like the second dwell time $T_{H,2}$ in Fig. 8.4a, which has been removed in Fig. 8.4c. Thus, the original two low-level dwell times $T_{L,1}$ and $T_{L,2}$ are misinterpreted as a long single dwell time $T'_{L,1}$. Such errors alter the statistics of the dwell time, and give incorrect tunneling rate values.

A correction scheme has been developed by considering a Poissonian tunneling process in which the true dwell time $T_{H/L}$ is distributed with the probability distribution function

$$P_{H/L}(T_{H/L}) = \frac{1}{\tau_{H/L}} e^{-T_{H/L}/\tau_{H/L}}, \tag{8.1}$$

where the mean, $m_{H/L}$, and the standard deviation, $\sigma_{H/L}$, are identical to the tunneling time constant $\tau_{H/L}$, which is the inverse of the tunneling rate $\Gamma_{H/L}$; $m_{H/L} = \sigma_{H/L} = \tau_{H/L} = \Gamma_{H/L}^{-1}$ [31]. The low-pass filter removes all the events with short dwell times below τ_{th}. The corresponding error probability can be expressed as $(1 - \beta_{H/L})$ with $\beta_{H/L} = e^{-\tau_{th}/\tau_{H/L}}$ for the high/low level. First, we consider the case where undetected events only exist for the high level, that is, $\beta_H > 0$ and $\beta_L = 0$, corresponding to $\tau_L \gg \tau_H \sim \tau_f$. If the measurement shows a dwell time T'_L, there might be n hidden undetected events with short dwell time $T_{H,i}$ ($i = 1 \ldots n$) in the period. Thus, there should be actual low-level dwell times $T_{L,i}$ ($i = 0 \ldots n$) constituting the fake dwell time ($T'_L = \sum_{i=0}^{n} T_{L,i} + \sum_{i=1}^{n} T_{H,i} \simeq \sum_{i=0}^{n} T_{L,i}$). Here, the high-level dwell times, $T_{H,i}$, are much shorter ($< \tau_f \ln 2$) and are ignored for simplicity. The number of hidden events, n, is randomly distributed, and the probability of having n hidden events in a measured single dwell time is

$p(n) = (1-\beta_{\rm H})^n\beta_{\rm H}$. The corresponding distribution function of $T'_{\rm L}$ comprising $(n+1)$ low-level dwell times can be constituted from each distribution function of hidden events, $T_{{\rm L},i}$, and is given as follows:

$$P_{\rm L}^{(n)}(T'_{\rm L}) = \int_0^\infty dT_{{\rm L},0} \cdots \int_0^\infty dT_{{\rm L},n} \prod_{i=0}^{n} \left[P_{\rm L}\left(T_{{\rm L},i}\right)\right] \delta(T'_{\rm L} - \sum_{i=0}^{n} T_{{\rm L},i}), \tag{8.2}$$

where $\delta(x)$ is the Dirac delta function. The overall distribution function of $T'_{\rm L}$ is found to be as follows:

$$P'_{\rm L}(T'_{\rm L}) = \sum_n^\infty p(n) P_{\rm L}^{(n)}(T'_{\rm L}) = \frac{\beta_{\rm H}}{\tau_{\rm L}} e^{-\beta_{\rm H} T'_{\rm L}/\tau_{\rm L}} \tag{8.3}$$

This is the distribution function measured with a low-pass filter. It has the same form as the original $P_{\rm L}(T_{\rm L})$ function represented by Eq. 8.1, but a different time constant, $\tau'_{\rm L} = \tau_{\rm L}/\beta_{\rm H}$, longer by the factor $\beta_{\rm H}$ (< 1). The above formula can be used to obtain the true tunneling rate, $\Gamma_{\rm out} = \tau_{\rm L}^{-1} = (\tau'_{\rm L}/\beta_{\rm H})^{-1}$, from the measured $\tau'_{\rm L}$ value.

In practice, such errors can occur in both high and low levels, which makes the microscopic analysis difficult. We assume that the above formula can be applied even in such cases. Considering the dead time of $\tau_{\rm th}$, the distribution function of the measurable dwell time $T'_{\rm H/L}$ is given by

$$P'_{\rm H/L}(T'_{\rm H/L}) = 0 \qquad (T'_{\rm H/L} < \tau_{\rm th}) \tag{8.4}$$

$$\propto \frac{1}{\tau'_{\rm H/L}} e^{-T'_{\rm H/L}/\tau'_{\rm H/L}} \quad (T'_{\rm H/L} > \tau_{\rm th}), \tag{8.5}$$

where the measured time constants, $\tau'_{\rm H}$ and $\tau'_{\rm L}$, are related to the true values, $\tau_{\rm H}$ and $\tau_{\rm L}$, by the following relations:

$$\tau_{\rm L} = \tau'_{\rm L} e^{-\tau_{\rm th}/\tau_{\rm H}}, \tau_{\rm H} = \tau'_{\rm H} e^{-\tau_{\rm th}/\tau_{\rm L}}. \tag{8.6}$$

These relations can be used to obtain the true tunneling rates, $\Gamma_{\rm in} = \tau_{\rm H}^{-1}$ and $\Gamma_{\rm out} = \tau_{\rm L}^{-1}$, from the measurement outcomes $\tau'_{\rm H}$ and $\tau'_{\rm L}$. This is the correction scheme we propose for practical experiments.

The validity of the correction scheme can be verified by numerical simulations. A random telegraph signal is generated with time constants $\tau_{\rm H}$ and $\tau_{\rm L}$ and processed using a first-order filter with the time constant $\tau_{\rm f}$. The resultant distorted $V_{\rm D}(t)$ waveform is digitized into two values with a hysteretic threshold ($\eta = 1/4$). The distributions of the dwell times $T'_{\rm H}$ and $T'_{\rm L}$ are evaluated by plotting their histograms. Figure 8.4d, e show the typical results for the symmetric tunneling time constants $\tau_{\rm H} = \tau_{\rm L} = 10$ in the time-step unit used in the random number generator. As seen in Fig. 8.4d, the $V_{\rm D}(t)$ trace is significantly distorted. Corresponding histogram for $T'_{\rm H}$, shown in Fig. 8.4e, deviates from the true distribution function (solid lines labeled

τ_H) and has missing events with dwell time less than τ_{th}. The resulting profile can be well reproduced by solving Eq. 8.4. This ensures that Eq. 8.6 can be used even if both τ_H and τ_L are close to τ_f. The correction introduced by Eq. 8.6 is effective for extracting the true time constants (tunneling rates) even in such a situation. Such a sharp dead time is seen in the experimental data shown in the inset of Fig. 8.3b, which is different from what the stochastic detector model predicts [28].

We examined the influence of the finite bandwidth on the experimental data taken from a GaAs QD-QPC device [27, 32]. A large in-plane magnetic field ($B = 8$ T) is applied to induce a significant Zeeman splitting and realize single-electron transport through the ground state (the spin-up Zeeman sublevel of the lowest orbital) [33–35]. This is the simplest case to study the counting effect. We also performed post-measurement digital data processing by applying a first-order low-pass filter, which allowed us to examine the effects of varying time constants for the same data. Figure 8.5a shows typical waveforms without post-measurement filter (i) and with digital filtering (ii). Although the filtering reduces the noise, it also results in a strong distortion of the telegraph signal. As a result, when the data is digitized with a hysteretic threshold as in (ii), some switching events with short dwell times are filtered out, as shown in (iii). The dwell-time histogram shows exponential characteristics [$\sim \exp(-T'/\tau')$].

We need to determine the response time τ_{th} to apply the correction scheme to the data. Although τ_{th} ($= -\tau_f \ln \eta$) can be determined from the filtering characteristics, one can conveniently estimate τ_{th} from the dead time of the statistics, where short-period events are missing in the histogram. A clear dead time is seen in the inset of Fig. 8.3b. Here, we note that τ_{th} can approximately be estimated by subtracting the standard deviation from the mean value of the dwell time ($\tau'_{th} = m' - \sigma'$). From the numerical simulations, we confirmed that τ'_{th} obtained in this way is close to $-\tau_f \ln \eta$

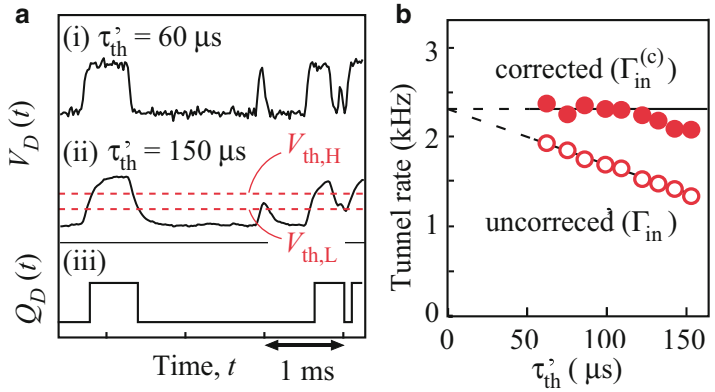

Fig. 8.5 (**a**) Typical waveform of a charge detector with (ii) and without (i) post-measurement filters, and digitized trace (iii) for (ii). (**b**) The uncorrected and corrected tunnel rates, Γ'_{in} and $\Gamma'^{(c)}_{in}$, respectively (Adapted from Ref. [27])

with good accuracy (less than 10 %). In the experiments, $\tau'_{\rm th}$ changes with the time constant of the digital filter, but not with the tunneling time constant τ'.

We applied the above correction scheme using Eq. 8.6 to the measured values $\tau'_{\rm H}$ and $\tau'_{\rm L}$ to extract the corrected time constants $\tau^{(c)}_{\rm H}$ and $\tau^{(c)}_{\rm L}$. Figure 8.5c shows the uncorrected rate $\Gamma'_{\rm in} = \left(\tau'_{\rm H}\right)^{-1}$ as well as the corrected tunneling rate $\Gamma^{(c)}_{\rm in} = \left(\tau^{(c)}_{\rm H}\right)^{-1}$ obtained from the same data, and plotted as a function of the response time $\tau_{\rm th}$. In contrast to $\Gamma'_{\rm in}$, which decreases with increasing $\tau_{\rm th}$, the corrected value $\Gamma^{(c)}_{\rm in}$ remains almost constant when $\tau_{\rm th}$ is less than 120 μs. The parameters $\Gamma'_{\rm in}$ and $\Gamma^{(c)}_{\rm in}$ extrapolate to the same value at $\tau_{\rm th} \sim 0$, which is consistent with the model. In this way, the correction scheme is shown to be effective for analyzing the experimental data.

8.2.3 *Counting Multiple Tunneling Processes*

In the above sections, we focused on analyzing unidirectional tunneling events through a single level. If more tunneling processes are involved, one has to consider the total incoming and outgoing rates in the charge detection measurement.

First, we show the case in which a reverse tunneling process is involved. The electrochemical potential of the dot, $\mu_{\rm d}$, is brought closer to the chemical potential of one lead, $\mu_{\rm L}$, as shown in the insets of Fig. 8.6. In the unidirectional transport region at $\mu_{\rm L} - \mu_{\rm d} \gg k_{\rm B}T$ (right inset), the incoming and outgoing rates measure the tunneling rate across the left and right barriers, respectively ($\Gamma_{\rm in} = \Gamma_{\rm L}$ and $\Gamma_{\rm out} = \Gamma_{\rm R}$). In contrast, if the dot is prepared in the Coulomb blockade region at $\mu_{\rm d} - \mu_{\rm L} \gg k_{\rm B}T$, the incoming rate significantly decreases because the thermal-excitation process (denoted by a dashed arrow) is less probable. Even in such a case with a finite excitation probability, the counting scheme can measure the outgoing rate, which should be the total rate across the left and right barriers ($\Gamma_{\rm out} = \Gamma_{\rm L} + \Gamma_{\rm R}$).

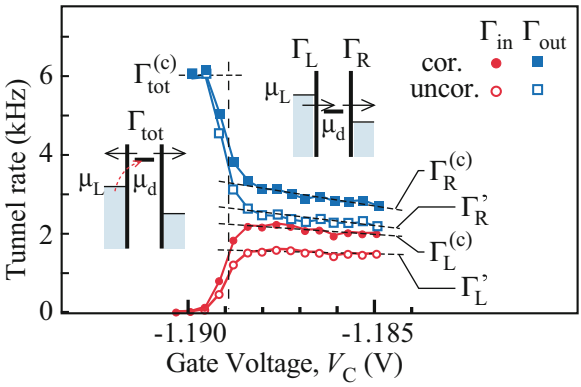

Fig. 8.6 Gate voltage, $V_{\rm C}$, dependence of the incoming and outgoing tunnel rates. $\Gamma^{(c)}_{\rm L}$ and $\Gamma^{(c)}_{\rm R}$ were corrected with the filter response time, $\tau'_{\rm th} = 86\,\mu$s. The *dashed lines* are guides to the eyes. The *insets* show energy diagrams for the unidirectional transport (*right inset*) and thermally activated (*left inset*) regimes (Adapted from Ref. [27])

A smooth transition between the two conditions can be seen in the data plots in Fig. 8.6, where the uncorrected tunneling rates [$\Gamma'_{\rm in} = \left(\tau'_{\rm H}\right)^{-1}$, $\Gamma'_{\rm out} = \left(\tau'_{\rm L}\right)^{-1}$ (open symbols)] and corrected rates [$\Gamma^{\rm (c)}_{\rm in} = \left(\tau^{\rm (c)}_{\rm H}\right)^{-1}$, $\Gamma^{\rm (c)}_{\rm out} = \left(\tau^{\rm (c)}_{\rm L}\right)^{-1}$ (solid symbols)] at various gate voltages $V_{\rm C}$ are shown. One can check the accuracy of the measurement by comparing the individual rates [$\Gamma'_{\rm L}$, $\Gamma^{\rm (c)}_{\rm L}$, $\Gamma'_{\rm R}$, and $\Gamma^{\rm (c)}_{\rm R}$] on the high-$V_{\rm C}$ side, and the total rate [$\Gamma'_{\rm tot} \simeq \Gamma^{\rm (c)}_{\rm tot}$] on the low-$V_{\rm C}$ side [27]. The sum of the individual rates changes from the uncorrected value, $\Gamma'_L + \Gamma'_R = 4.2\,{\rm kHz}$, to the corrected one, $\Gamma^{\rm (c)}_{\rm L} + \Gamma^{\rm (c)}_{\rm R} = 5.5\,{\rm kHz}$, and as a result, it gets closer to the measured total rate $\Gamma'_{\rm tot} \simeq \Gamma^{\rm (c)}_{\rm tot} = 6\,{\rm kHz}$. This demonstrates that the correction scheme is effective. The small residual difference might come from the energy dependence of the rate or higher-order error neglected in the model.

Next, we consider the case where two energy states with spin-up and -down are involved in the transport. The spin-dependent tunneling rate can be studied by considering the transport through the Zeeman sublevels of the lowest orbital for the first electron ($N = 1$) in the QD. As shown in the simplified energy diagram of Fig. 8.7a, only spin-up electrons can tunnel through the QD when a spin-up sublevel is located in the transport window. Under these spin-filtering (SF) conditions, the charge-detection measurement determines the spin-up tunneling rates, $\Gamma_{\rm i/o} = \Gamma_{\rm i/o,\uparrow}$ from incoming/outgoing events. In contrast, both spin-up and -down electrons can participate in the transport when both spin sublevels are in the transport window, as

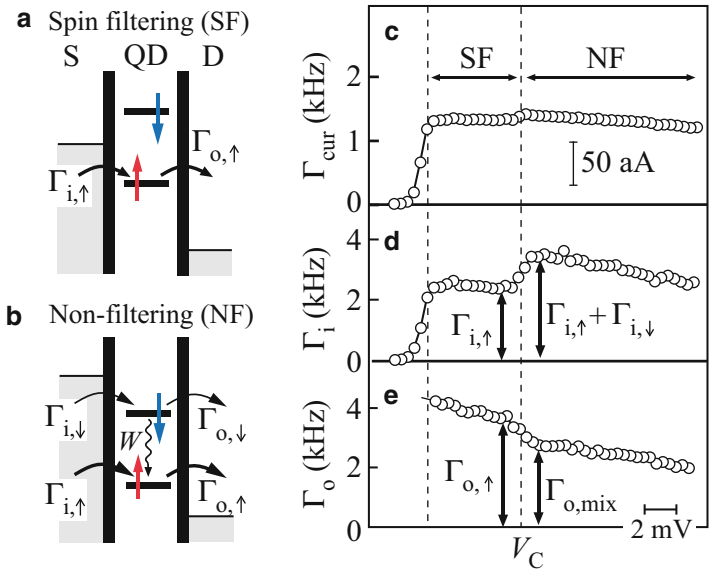

Fig. 8.7 (**a**) and (**b**) Schematic energy diagrams for (**a**) spin-filtering transport and (**b**) non spin-filtering transport. (**c**)–(**e**) Gate voltage dependence of tunneling rates $\Gamma_{\rm cur}$, $\Gamma_{\rm i}$ and $\Gamma_{\rm o}$ (Adapted from Ref. [32])

shown in Fig. 8.7b. Under these non-filtering (NF) conditions, the measurement is also sensitive to the spin-down rates $\Gamma_{i,\downarrow}$ and $\Gamma_{o,\downarrow}$. The incoming rate is simply additive, i.e., $\Gamma_i = \Gamma_{i,\uparrow} + \Gamma_{i,\downarrow}$, as both tunneling events are always allowed. Therefore, $\Gamma_{i,\uparrow}$ and $\Gamma_{i,\downarrow}$ can be determined from the two measurements under the SF and NF conditions. However, the outgoing rate is not additive ($\Gamma_o \neq \Gamma_{o,\uparrow} + \Gamma_{o,\downarrow}$), and is given by the statistical average (denoted by $\Gamma_{o,mix}$) of $\Gamma_{o,\uparrow}$ and $\Gamma_{o,\downarrow}$ weighted by the occupation probabilities of the Zeeman sublevels. Thus, $\Gamma_{o,mix}$ is also influenced by the spin relaxation rate W in the QD. $\Gamma_{o,mix}$, can approximately be denoted as follows:

$$\Gamma_{o,mix} \simeq \frac{\left(\Gamma_{i,\uparrow} + \Gamma_{i,\downarrow}\right)\Gamma_{o,\uparrow}\left(\Gamma_{o,\downarrow} + W\right)}{\Gamma_{i,\uparrow}\left(\Gamma_{o,\downarrow} + W\right) + \Gamma_{i,\downarrow}\left(\Gamma_{o,\uparrow} + W\right)}. \tag{8.7}$$

Therefore, $\Gamma_{o,\downarrow}$ can be determined by solving the above equation if W is known [36].

Figure 8.7c–e show the V_C dependences of Γ_{cur}, Γ_i, and Γ_o, where the SF and NF regions are identified. The data in Fig. 8.7d shows that the first step entering the SF region is larger than the second step entering the NF region, indicating a spin-dependent rate, $\Gamma_{i,\uparrow} > \Gamma_{i,\downarrow}$. A similar spin dependency is found for the outgoing rate. As described above, $\Gamma_{o,mix}$ is a measure of the average values of $\Gamma_{o,\uparrow}$ and $\Gamma_{o,\downarrow}$. The data in Fig. 8.7e shows that $\Gamma_{o,\uparrow} > \Gamma_{o,mix}$, indicating that the spin-up tunneling rate is greater than the spin-down one; $\Gamma_{o,\uparrow} > \Gamma_{o,\downarrow}$ [32, 37, 38].

The observed spin-dependent rate could be attributed to the exchange-enhanced spin splitting in the low-density regions near the tunneling barrier. The electron spins can be spontaneously polarized when only a few one-dimensional channels are occupied [39–42]. The exchange interaction raises the effective potential for minority spins but lowers it for majority spins, giving rise to different tunneling probabilities. Although more detailed experiments are required to identify the origin of this behavior, spin-dependent single-electron counting experiments provide a deep insight into the spin correlations [43, 44].

8.3 Bidirectional Counting with a Double Quantum Dot

8.3.1 Charge Detection of a Double Quantum Dot

DQDs have been extensively studied in various fields such as artificial two-level systems for realizing quantum bits, single-electron pumps for carrying one electron per cycle of potential modulation, and correlated charge and spin transport [45–49]. Here, we utilize charge-detection scheme on DQD to demonstrate a bidirectional single-electron counting (B-SEC) device, in which forward and reverse tunneling processes can be identified through all three junctions [21]. A statistical analysis of the forward and reverse tunneling events allows us to obtain information on the transport characteristics.

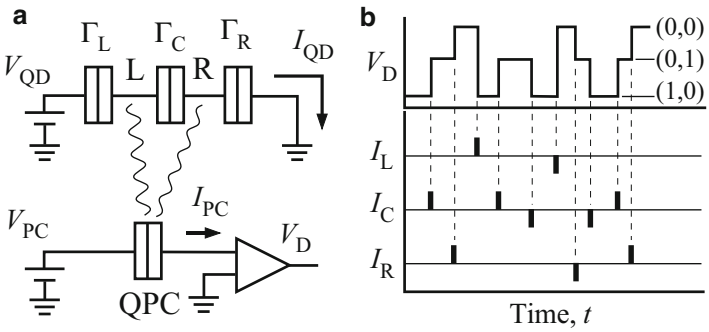

Fig. 8.8 (**a**) Schematic of the B-SEC device, consisting of a double dot (L and R) and a charge detector (PC). The *double boxes* represent tunneling barriers, and the wavy lines illustrate Coulomb interaction. (**b**) Schematic of the fluctuations in the detector current, I_{PC}, corresponding to the charge states (n, m) with n and m excess electrons in dots L and R, respectively. Pulsed currents I_L, I_C, and I_R across the left, central, and right barriers, respectively, are shown. Each current pulse can be considered to have a height e/t_0 for duration t_0, being a time step of the measurement, and constitutes a transport of elementary charge e

Operation of the B-SEC device is based on charge detection in a DQD in the Coulomb blockade regime, where higher-order tunneling processes can be neglected [2]. As shown schematically in Fig. 8.8a, the device consists of a DQD (dots L and R) and a QPC for charge detection. The QPC is asymmetrically coupled to the dots (i.e., more strongly coupled to dot L than to dot R), so that the detector current I_{PC} varies with respect to the electron numbers (n, m) in dots L and R [47]. Current flow through the DQD results in temporal changes in the electron numbers (n, m), which appear as fluctuations in the PC current, as shown in the top panel of Fig. 8.8b. One can translate the multiple-level fluctuations into current through the left, central, and right barriers, as shown in the lower panel of Fig. 8.8b.

Figure 8.9a shows a scanning electron micrograph of a B-SEC device fabricated in an AlGaAs/GaAs heterostructure. The application of appropriate negative voltages on the metal gates depletes the nearby conductive electrons and forms the B-SEC device [16]. The QPC is adjusted in the tunneling regime, where I_{PC} is sensitive to the charge state (n, m) of the DQD. The charge stability diagram of the DQD can be obtained by plotting $d\langle I_{PC}\rangle/dV_R$ as a function of the voltages V_L and V_R respectively applied to gates G_L and G_R, as shown in Fig. 8.9b. The honeycomb pattern is associated with the inter-dot Coulomb energy in the DQD. The clear separation of the (n, m) and $(n + 1, m + 1)$ charge domains indicates an electrostatic coupling energy of $\sim$200 μeV for this DQD.

Time-resolved measurements are performed under specific condition, where all the tunneling rates of the DQD are within the bandwidth ($\sim$10 kHz) of the current amplifier. The average current $\langle I_{PC}\rangle$ shown in Fig. 8.10a indicates four discrete current levels depending on (n, m). Individual tunneling events can be seen in the time domain, as shown in Fig. 8.10b. The three-level fluctuation observed near the

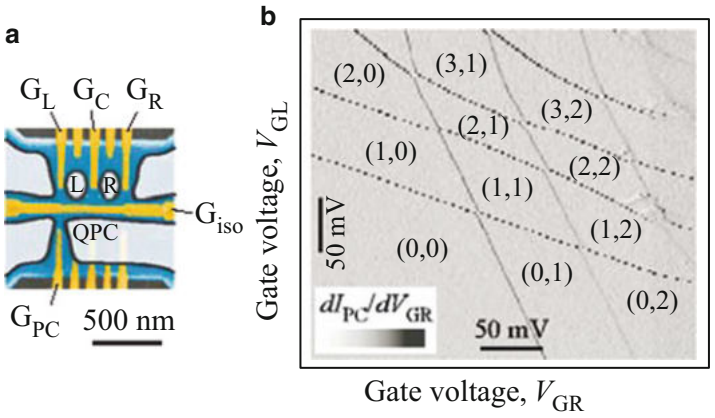

Fig. 8.9 (**a**) Scanning electron micrograph of a B-SEC device with a double dot (L and R) and QPC. (**b**) Charge stability diagram (n, m) of the device

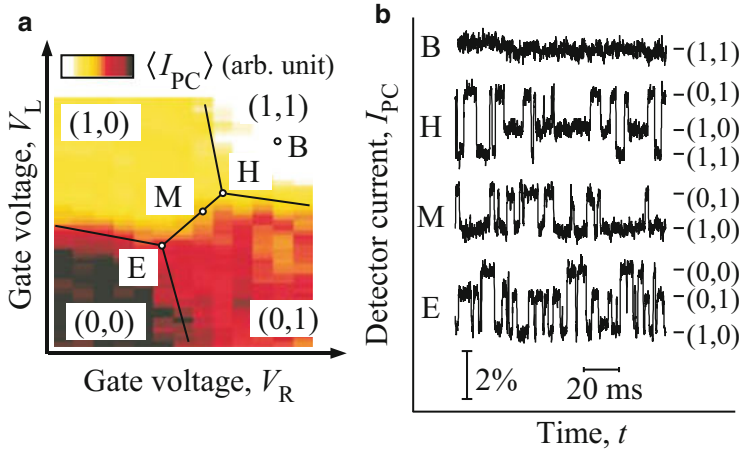

Fig. 8.10 (**a**) Color plot of the averaged QPC current, $\langle I_{PC} \rangle$, in the $V_L - V_R$ plane measured at $V_{QD} = 0$ and $V_{PC} = 0.8$ mV, with a stability diagram (n, m) of the DQD. (**b**) Fluctuation of I_{PC} measured at points, B, H, M, and E, shown in (**a**). Typically $\langle I_{PC} \rangle \sim 12$ nA (Adapted from Ref. [21])

charge triple points E and H, the two-level fluctuation between $(1, 0)$ and $(0, 1)$ at M, and the absence of fluctuation in blockade region B, are consistent with the expectations [49].

We record I_{PC} traces over a period $T_p = 1.3$ s with a time resolution of $t_0 = 20\,\mu$s and digitize the current into four values, corresponding to the (n, m) states of interest, with appropriate filtering and threshold. From the measured statistics, we can obtain all the information needed to characterize the electron transport. The dwell time $T_{(n,m)}$, which indicates how long a QD stays in a particular charge state

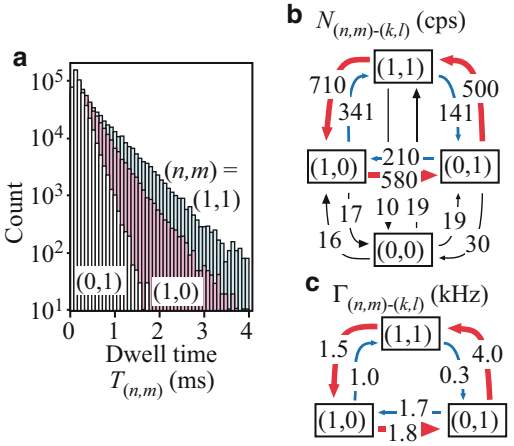

Fig. 8.11 (**a**) Distribution of dwell times for the (0, 1), (1, 0) and (1, 1) states. (**b**) Example of the number of transition events $N_{nm\to ij}$. (**c**) Example of tunneling rates $\Gamma_{nm\to kl}$. The same data set measured at $V_{QD} = 300\,\mu V$ was used for (**a**), (**b**), and (**c**) (Adapted from Ref. [21])

(n, m) before changing to another one, is randomly distributed with an exponential function, as shown in Fig. 8.11a, indicating a random Poisson process characterized by a single lifetime $\tau_{nm} = \langle T_{(n,m)} \rangle$ [16, 31], that is related to the sum of all possible tunneling rates $\Gamma_{nm\to kl}$ from (n, m) to (k, l):

$$\tau_{nm}^{-1} = \sum_{k,l} \Gamma_{nm\to kl}. \tag{8.8}$$

One can also count the number of transition events $N_{nm\to kl}$ from (n, m) to (k, l), which should be proportional to the rates according the following relation

$$N_{nm\to kl} = p_{nm}^0 \Gamma_{nm\to kl} T_p, \tag{8.9}$$

where p_{nm}^0 is the occupation probability for (n, m) under steady conditions. By solving these relations, all the relevant rates $\Gamma_{nm\to kl}$ and populations p_{nm}^0 can be determined.

Figure 8.11b shows $N_{nm\to kl}$ results obtained using the same data set. The transport is dominated by a cyclic transition (thick arrows) from (1, 1), through (1, 0), to (0, 1), and back to (1, 1), which carries an electron from the left to the right, at a positive bias voltage. Note that non-negligible reverse processes (thin arrows) are also observed in the present measurements. The very low counting rate (< 30 cps) is attributed to noise in the PC current (dark counting) and should be disregarded; transitions between (0, 0) and (1, 1) are unphysical in the sequential tunneling regime. We should note that, because of the finite bandwidth, our measurement fails to count very fast successive transitions within $100\,\mu s$. This error can be corrected by using a scheme similar to that described earlier, but it is neglected in this analysis. The obtained rates $\Gamma_{nm\to kl}$ are summarized in Fig. 8.11c. In this way, all tunneling rates can be determined from multi-level charge fluctuations.

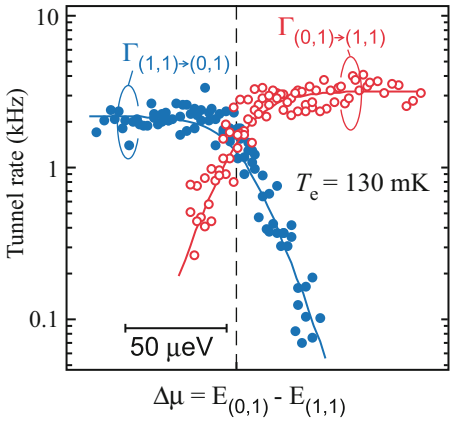

Fig. 8.12 Gate voltage dependence of the tunneling rates, $\Gamma_{01\to 11}$ and $\Gamma_{11\to 01}$. The horizontal axis is converted into electrochemical potential $\Delta\mu_{01-11} = E_{01} - E_{11}$ (Adapted from Ref. [21])

A similar analysis can be made at various points in the $V_L - V_R$ plane, and we investigate how the forward and reverse tunneling rates change. We examine dot-lead tunneling processes across the left barrier by comparing $\Gamma_{01\to 11}$ and $\Gamma_{11\to 01}$, which are plotted in Fig. 8.12 as a function of the electrochemical potential, $\Delta\mu_{01-11} = E_{01} - E_{11}$, where E_{nm} is the total energy of the (n, m) state [49]. The dependence can be well fitted to the Fermi distribution in the electrode with an electron temperature $T_e = 130\,\mathrm{mK}$ in the lead [50]. The behaviors of the forward and reverse rates are almost symmetric with respect to $E_{10} = E_{11}$ (dashed line). The small difference of a factor $\sim$1.5 between the maximum saturated rates for the forward and reverse tunneling may be related to spin degeneracy; a factor-2 difference is expected for transitions between different charge states having total spins of 0 and $1/2$ [51]. The tunneling rate shows detailed balance, in which the ratio between the forward and reverse rates is determined by the electrochemical potential, $\Gamma_{01\to 11}/\Gamma_{11\to 01} = \exp[\Delta\mu_{01-11}/kT_e]$, up to degeneracy. Provided that the detailed balance conditions are met for all the junctions, the electrochemical potentials $\Delta\mu_{nm-kl} = kT_e \log(\Gamma_{nm\to kl}/\Gamma_{kl\to nm})$ can be estimated in the unit of thermal energy just from the statistics. This is an example of how informative the counting statistics is.

8.3.2 Correlated Tunneling Current Through a DQD

Although each tunneling process characterized by $\Gamma_{nm\to kl}$ is Poisson random, Coulomb interaction prohibits double occupancy in a small island and correlates the overall electron transport. Such a correlated transport can be described by statistical quantities. Charge transport in the sequential tunneling regime can be described by the following rate equation:

$$\frac{d}{dt}\mathbf{p}(t) = \mathbf{M}\mathbf{p}(t), \tag{8.10}$$

where $\mathbf{p}(t)$ is an array of time-dependent occupation probabilities $\{p_{nm}(t)\}$ [52]. The matrix $\mathbf{M}$ describes the transition rates consisting of the diagonal and off-diagonal terms, $-\tau_{nm}^{-1}$ and $\Gamma_{nm\to kl}$, respectively. Since we have already obtained $\mathbf{M}$, as shown in Fig. 8.11c, we can calculate the expected average current, noise spectrum, and higher-order moments of noise [53], which are more suitable for describing the correlated transport. These quantities can be obtained from the statistical analysis in the following way, if the available information for $\mathbf{M}$ is incomplete.

Here, we define three pulsed currents, I_L, I_C, and I_R, which exhibit B-SECs at the left, central, and right barriers, respectively. They are obtained by considering the corresponding tunneling processes, as discussed for Fig. 8.8b. The average currents obtained for a long period always agree with each other, i.e., $\langle I_\mathrm{L}\rangle = \langle I_\mathrm{C}\rangle = \langle I_\mathrm{R}\rangle$, as a result of current conservation. Figure 8.13a shows the average current $\langle I\rangle$ in the $V_L - V_R$ plane. The triangular conductive regions around E and H, with a resonant tunneling peak on one side of the triangles, are consistent with conventional current measurements through a DQD [49].

The noise power spectra, S_L, S_C and S_R, shown in the top panel of Fig. 8.13b, are obtained from numerical Fourier transforms of the corresponding pulsed currents. The spectra are qualitatively the same as those calculated from $\mathbf{M}$ (bottom panel of Fig. 8.13b) [52], indicating the validity of our statistical analysis. The enhanced spectrum in the high-frequency part (> 1 kHz, the characteristic frequency set by non-zero eigenvalues of $\mathbf{M}$) is related to how frequently an electron experiences back-scattering across the barrier. The low-frequency part, identical for the three spectra, is almost flat except for the excess dark-counting noise below 10 Hz. Background charge fluctuation (1/f noise), which often dominates the low-frequency noise, is significantly suppressed in our scheme. The noise level in the 10–100 Hz range is suppressed below the full shot noise $2e\langle I\rangle$ (dashed line), indicating a correlated transport [7].

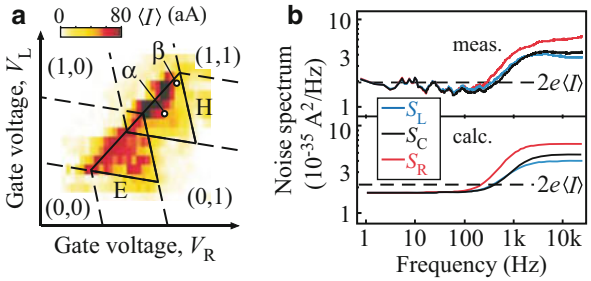

Fig. 8.13 (**a**) Average current $\langle I\rangle$ in the $V_\mathrm{L} - V_\mathrm{R}$ plane at $V_\mathrm{QD} = 300\,\mu$V. The triangles E and H define conductive regions. (**b**) Noise power spectra of the current, S_L, S_C and S_R. The *upper panel* shows the power spectrum of the pulsed current, while the *lower one* shows the spectrum of the correlation function derived by solving the rate equations. The *dashed line* shows the full shot noise $2e\langle I\rangle$ (Adapted from Ref. [21])

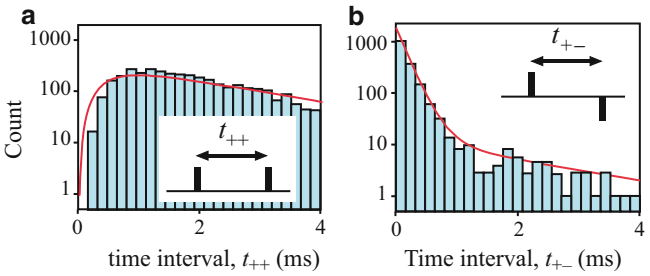

Fig. 8.14 (**a**) Distribution of the time interval between successive forward tunneling events in I_C. (**b**) Distribution of the time interval, t_{+-}, between forward and reverse current pulses. The *solid lines* show the calculated occurrence of the conditional event derived from the corresponding rate equations. The *insets* illustrate the time intervals, t_{++} or t_{+-} (Adapted from Ref. [21])

More importantly, we find that the B-SEC device provides better statistics that allow us to directly identify the anti-bunching correlation. Figure 8.14a shows the distribution of the time interval, t_{++}, between two successive forward current pulses. The distribution is no longer a simple exponential, and the suppression of consecutive forward pulses at $t_{++} \sim 0$ (anti-bunching) is directly identified and is consistent with a rate-equation calculation (solid line). Note that the broad peak in the distribution indicates that a quasi-periodic current is the precursor of the single-electron tunneling oscillations [18]. The back scattering can directly be investigated in the distribution of the time interval, t_{+-}, between forward and reverse current pulses. As shown in Fig. 8.14b, reverse tunneling is enhanced near the zero interval.

We can also extract other statistical data that is often used in quantum optics, such as the electron (photon) number distribution [10, 54, 55]. The third-order moment of the distribution, which is called skewness, is of particular interest because of its insensitivity to thermal distribution [11, 13, 56] and is considered to be a new tool for investigating correlated transport, valid even under nearly-equilibrium conditions. Gustavsson et al. performed charge-detection measurements on a single dot to identify the correlated transport from the second- and third-order noise [19]. Taking advantage of the bidirectional counting in our device, we have demonstrated that the third-order noise is insensitive to the thermal noise.

Note that the B-SEC with single-electron resolution is too precise to see the overall correlated transport. The electron number distribution of interest should be obtained in the zero-frequency limit, where the current is conserved at all points in the circuit ($<$100 Hz in Fig. 8.13b). A sort of coarse graining can be performed by averaging the pulsed current for a moderate period T_{avr}, which should be chosen to be longer than the correlation time of the transport. Then the net electron number N transferred during the averaging time can fluctuate more than one, as shown in the distribution plot of Fig. 8.15a. The mean and variance of the distribution correspond to the average current, $\langle I \rangle = e\langle N \rangle / T_{avr}$, and second-order noise, $S = e^2\langle \delta N^2 \rangle / T_{avr}$, respectively, where $\delta N = N - \langle N \rangle$. The small asymmetric distribution indicates the presence of skewness and a corresponding third-order noise, $C = e^3\langle \delta N^3 \rangle / T_{avr}$,

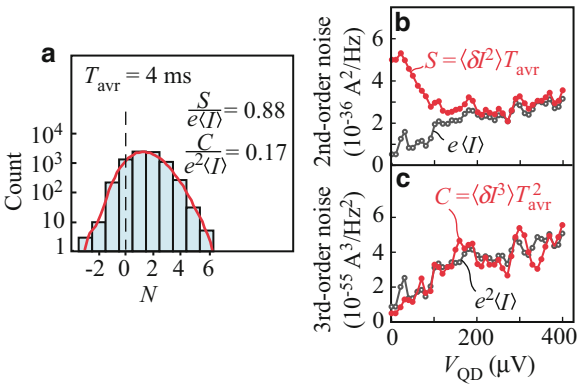

Fig. 8.15 (**a**) Electron number distribution for I_C. N is the net electron number transferred across the central barrier during the averaging time, $T_{avr} = 4$ ms. (**b**) and (**c**) Bias voltage dependences of second- (**b**) and third-order (**c**) noises in the linear conductance regime (Adapted from Ref. [21])

whose relative value to the full shot noise, $C/(e^2\langle I\rangle)$, is a measure of the correlation of the transport [56, 57]. The ratio of 0.17 for Fig. 8.15a indicates an anti-bunching correlation (< 1) that is consistent with the calculation ($\sim$0.2) based on Ref. [53]. To test how closely the measurement can be performed under equilibrium conditions at zero bias, the second- and third-order noise are plotted as a function of the bias voltage in Fig. 8.15b, c. Here, we have chosen the linear conductance region around the triple point H, where the current is restricted by one of the barriers (equivalent to the single barrier case for the noise). In this case, the second- and third-order noises should coincide with the full shot noise $e\langle I\rangle$ and $e^2\langle I\rangle$, respectively, if no other noises contribute to the signal. The second-order noise is significantly higher than $e\langle I\rangle$ at small voltages $V_{QD} < 100\,\mu$V, where the thermal noise is dominant ($k_B T_e = 15\,\mu$eV). In contrast, the third-order noise agrees with $e^2\langle I\rangle$ in the whole range, and no additional noise is observed. Insensitivity to thermal noise is desirable for measuring any meaningful non-Gaussian noise even at high temperatures.

One can use this B-SEC device to identify unknown currents and their correlation in many cases. The top part of Fig. 8.16a illustrates a circuit for counting electrons from a test device. Although it is impossible to obtain all the information about the device, one can obtain useful information by means of time, frequency, and momentum analyses with a B-SEC device. For this purpose, the impedance of the B-SEC device should be smaller and its correlation time shorter than that of the test device [15]. Our B-SEC device can be applied to investigate extremely small currents from a high-impedance test device, and this is precisely what conventional electronics cannot achieve. We demonstrate the performance of our device as a current meter using another single QD as a test device as shown in Fig. 8.16a. The average current $\langle I\rangle$ obtained from the B-SEC device reasonably depends on two gate voltages (V_A and V_B) of the test device as shown in Fig. 8.16b, indicating that the observed Coulomb blockade peaks are associated with the test device. The peak-to-peak noise level in the blockade region is 3 aA for a 1.3 s averaging time, which is about three orders of magnitude smaller than that in conventional current meters.

The demonstrated B-SEC device enables various statistical analyses for characterizing the correlation, and is also useful for investigating extremely small currents.

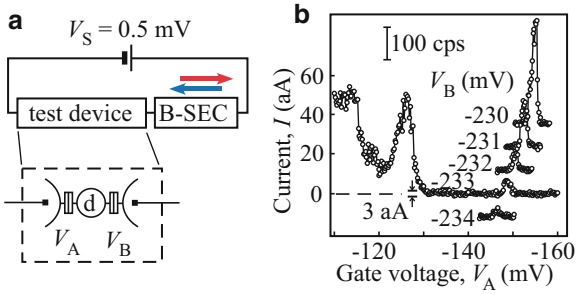

Fig. 8.16 (**a**) Experimental setup for evaluating a test device using a B-SEC device. The test device involves a QD (d) with tunable tunneling barriers via voltages V_A and V_B. (**b**) Average current obtained from the B-SEC device. Current ranging from −10 to 50 aA can be measured with a voltage drop of about 200 μV across the present B-SEC device. The observed Coulomb blockade peaks changes with V_B. Each trace is offset for clarity (Adapted from Ref. [21])

Integration with other mesoscopic electron devices, such as beam splitters or interferometers, could lead to various techniques for exploring non-trivial intensity correlation and entanglement processes in mesoscopic electron systems [58].

8.4 Summary

Counting statistics of single-electron transport provide a very sensitive tool for measuring electrical currents with single-electron resolution. Various statistical analyses, such as frequency spectrum, time correlation functions, or higher-order moments of the current noise, can be applied to highlight the correlated electron transport. Although we focused on measurements for single and double quantum dots, the technique is not limited to these cases but can be applied to other correlated electron sources, too.

Acknowledgements We thank J. C. H. Chen, M. Hashisaka, T. Hayashi, Y. Hirayama, K. Muraki, Y. Tokura, R. Tomita, M. Ueki, N. Watase, and M. Yamagushi for valuable discussions and supports. This work was supported by FIRST "Quantum Information Processing" project, JSPS Grants-in-Aid for Scientific Research (KAKENHI) Grant Numbers 21000004 and 26247051, and GCOE project "Nanoscience and Quantum Physics" at Tokyo Institute of Technology.

References

1. Yu.V. Nazarov, Y.M. Blanter, *Quantum Transport: Introduction to Nanoscience* (Cambridge University Press, Cambridge/New York, 2009)
2. H. Grabert, M.H. Devoret (eds.), *Single Charge Tunneling, Coulomb Blockade Phenomena in Nanostuctures*. NATO ASI Series B, vol. 0294, (Plenum Press, New York, 1991)

3. Yu.V. Nazarov (ed.), *Quantum Noise in Mesoscopic Physics*. NATO Science Series II, vol. 97 (Kluwer, Dordrecht, 2003)
4. Ya.M. Blanter, M. Büttiker, Phys. Rep. **336**, 1 (2000)
5. P. Dutta, P.M. Horn, Rev. Mod. Phys. **53**, 497 (1981)
6. M.J. Kirton, M.J. Uren, Adv. Phys. **38**, 367 (1989)
7. H. Birk, M.J.M. de Jong, C. Schönenberger, Phys. Rev. Lett. **75**, 1610 (1995)
8. L. Saminadayar, D.C. Glattli, Y. Jin, B. Etienne, Phys. Rev. Lett. **79**, 2526 (1997)
9. R. de-Picciotto, M. Reznikov, M. Heiblum, V. Umansky, G. Bunin, D. Mahalu, Nature **389**, 162 (1997)
10. R. Loudon, *The Quantum Theory of Light* (Oxford University Press, New York, 1973)
11. Yu. Bomze, G. Gershon, D. Shovkun, L.S. Levitov, M. Reznikov, Phys. Rev. Lett. **95**, 176601 (2005)
12. G. Gershon, Y. Bomze, E.V. Sukhorukov, M. Reznikov, Phys. Rev. Lett. **101**, 016803 (2008)
13. B. Reulet, J. Senzier, D.E. Prober, Phys. Rev. Lett. **91**, 196601 (2003)
14. J. Gabelli, B. Reulet, J. Stat. Mech. **2009**, P01049 (2009)
15. C.W.J. Beenakker, M. Kindermann, Yu.V. Nazarov, Phys. Rev. Lett. **90**, 176802 (2003)
16. T. Fujisawa, T. Hayashi, Y. Hirayama, H.D. Cheong, Y.H. Jeong, Appl. Phys. Lett. **84**, 2343 (2004)
17. W. Lu, Z. Ji, L. Pfeiffer, K.W. West, A.J. Rimberg, Nature **423**, 422 (2003)
18. J. Bylander, T. Duty, P. Delsing, Nature **434**, 361 (2005)
19. S. Gustavsson, R. Leturcq, B. Simoviv, R. Schleser, T. Ihn, P. Studerus, K. Ensslin D.C. Driscoll, A.C. Gossard, Phys. Rev. Lett. **96**, 076605 (2006)
20. S. Gustavsson, R. Leturcq, M. Studer, I. Shorubalko, T. Ihn, K. Ensslin, D.C. Driscoll, A.C. Gossard, Surf. Sci. Rep. **64**, 191 (2009)
21. T. Fujisawa, T. Hayashi, R. Tomita, Y. Hirayama, Science **312**, 1634 (2006)
22. M. Field, C.G. Smith, M. Pepper, D.A. Ritchie, J.E.F. Frost, G.A.C. Jones, D.G. Hasko, Phys. Rev. Lett. **70**, 1311 (1993)
23. R.J. Schoelkopf, P. Wahlgren, A.A. Kozhevnikov, P. Delsing, D.E. Prober, Science **280**, 1238 (1998)
24. I.T. Vink, T. Nooitgedagt, R.N. Schouten, L.M.K. Vandersypen, W. Wegscheider, Appl. Phys. Lett. **91**, 123512 (2007)
25. G. Shinkai, T. Hayashi, T. Ota, T. Fujisawa, Phys. Rev. Lett. **103**, 056802 (2009)
26. B.J. van Wees, H. van Houten, C.W.J. Beenakker, J.G. Williamson, L.P. Kouwenhoven, D. van der Marel, C.T. Foxon, Phys. Rev. Lett. **60** (1988) 848
27. N. Watase, M. Hashisaka, K. Muraki, T. Fujisawa, Jpn. J. Appl. Phys. **53**, 04EJ01 (2014)
28. O. Naaman, J. Aumentado, Phys. Rev. Lett. **96**, 100201 (2006)
29. O. Naaman, J. Aumentado, Phys. Rev. B **73**, 172504 (2006)
30. O.H. Schmitt, J. Sci. Instr. **15**, 24 (1938)
31. N.G. van Kampen, *Stochastic Processes in Physics and Chemistry* (Elsevier, Amsterdam, 1992)
32. M. Yamagishi, N. Watase, M. Hashisaka, K. Muraki, T. Fujisawa, Phys. Rev. B **90**, 035306 (2014)
33. R. Hanson, B. Witkamp, L.M.K. Vandersypen, L.H.W. van Beveren, J.M. Elzerman, L.P. Kouwenhoven, Phys. Rev. Lett. **91**, 196802 (2003)
34. R. Hanson, L.M.K. Vander-sypen, L.H.W. van Beveren, J.M. Elzerman, I.T. Vink, L.P. Kouwenhoven, Phys. Rev. B **70**, 241304 (2004)
35. B. Jouault, M. Gryglas, M. Baj, A. Cavanna, U. Gennser, G. Faini, D.K. Maude, Phys. Rev. B **79**, 041307 (2009)
36. T. Fujisawa, T. Hayashi, S. Sasaki, Rep. Prog. Phys. **69**, 759 (2006)
37. S. Amasha, K. MacLean, I.P. Radu, D.M. Zumbühl, M.A. Kastner, M.P. Hanson, A.C. Gossard, Phys. Rev. B **78**, 041306 (2008)
38. M.G. House, M. Xiao, G. Guo, H. Li, G. Cao, M.M. Rosenthal, H. Jiang, Phys. Rev. Lett. **111**, 126803 (2013)
39. C.-K. Wang, K.F. Berggren, Phys. Rev. B **54**, R14257 (1996)

40. A. Lassl, P. Schlagheck, K. Richter, Phys. Rev. B **75**, 045346 (2007)
41. H. Lind, I.I. Yakimenko, K.F. Berggren, Phys. Rev. B **83**, 075308 (2011)
42. P. Stano, P. Jacquod, Phys. Rev. B **82**, 125309 (2010)
43. A. Di Lorenzo, Y.V. Nazarov, Phys. Rev. Lett. **93**, 046601 (2004)
44. T.L. Schmidt, A. Komnik, A.O. Gogolin, Phys. Rev. B **76**, 241307 (2007)
45. T. Fujisawa, T.H. Oosterkamp, W.G. van der Wiel, B.W. Broer, R. Aguado, S. Tarucha, L.P. Kouwenhoven, Science **282**, 932 (1998)
46. T. Hayashi, T. Fujisawa, H.D. Cheong, Y.H. Jeong, Y. Hirayama, Phys. Rev. Lett. **91**, 226804 (2003)
47. J.R. Petta, A.C. Johnson, J.M. Taylor, E.A. Laird, A. Yacoby, M.D. Lukin, C.M. Marcus, M.P. Hanson, A.C. Gossard, Science **309**, 2180 (2005)
48. C.W.J. Beenakker, D.P. DiVincenzo, C. Emary, M. Kindermann, Phys. Rev. Lett. **93**, 020501 (2004)
49. W.G. van der Wiel, S. De Franceschi, J.M. Elzerman, T. Fujisawa, S. Tarucha, L.P. Kouwenhoven, Rev. Mod. Phys. **75**, 1 (2003)
50. D.H. Cobden, B.A. Muzykantskii, Phys. Rev. Lett. **75**, 4274 (1995)
51. D.H. Cobden, M. Bockrath, P.L. McEuen, A.G. Rinzler, R.E. Smalley, Phys. Rev. Lett. **81**, 681 (1998)
52. S. Hershfield, J.H. Davies, P. Hyldgaard, C.J. Stanton, J.W. Wilkins, Phys. Rev. B **47**, 1967 (1993)
53. D.A. Bagrets, Yu.V. Nazarov, Phys. Rev. B **67**, 085316 (2003)
54. L.S. Levitov, H. Lee, G.B. Lesovik, J. Math. Phys. **37**, 4845 (1996)
55. M. Ueda, Phys. Rev. A **40**, 1096 (1989)
56. L.S. Levitov, M. Reznikov, Phys. Rev. B **70**, 115305 (2004)
57. G. Kießlich, P. Samuelsson, A. Wacker, E. Schöll, Phys. Rev. B **73**, 033312 (2006)
58. P. Samuelsson, E.V. Sukhorukov, M. Büttiker, Phys. Rev. Lett. **92**, 026805 (2004)

Part III
Coherent Computing

Chapter 9
Some Recent Progress for Approximation Algorithms

Ken-ichi Kawarabayashi

9.1 Introduction

Many optimization problems that need to take inputs globally into account are, most likely, NP-hard. So one cannot hope that there is a polynomial time algorithm to solve these problems, assuming the widely believed conjecture "$P \neq NP$". Therefore approximation (polynomial time) algorithms for these problems are the main focus in the theoretical computer science research community in these 30 years.

Following the development of basic combinatorial (and graph theoretical) techniques in 1970s and 1980s, in the 1990s, parallel developments in techniques for designing approximation algorithms as well as methods for showing hardness of approximation algorithms result in a beautiful theory. This survey focuses on very recent developments in the former. More specifically, we only survey the following problems that have some recent breakthroughs:

1. The edge disjoint paths problem.
2. Graph coloring problem.

The edge disjoint paths problem has attracted attention in the contexts of networking; for example, VLSI layout, transportation networks, virtual circuit routing in high-speed networks (cf. Internet). It is certainly a central problem in

Research partly supported by Japan Society for the Promotion of Science, Grant-in-Aid for Scientific Research, and by Mitsubishi Foundation.

K.-i. Kawarabayashi (✉)
National Institute of Informatics, JST ERATO Kawarabayashi Project, 2-1-2, Hitotsubashi, Chiyoda-ku, Tokyo, Japan
e-mail: k_keniti@nii.ac.jp

Y. Yamamoto, K. Semba (eds.), *Principles and Methods of Quantum Information Technologies*, Lecture Notes in Physics 911, DOI 10.1007/978-4-431-55756-2_9

algorithmic graph theory and combinatorial optimization, and there are a lot of work on this topic. See the next paragraph and the surveys [16, 36].

Graph coloring is arguably the most popular subject in graph theory. Also, it is one of the central problems in combinatorial optimization, since it is one of the hardest problems to approximate. In general, the optimal coloring is inapproximable in polynomial time within factor $n^{1-\epsilon}$ for any $\epsilon > 0$, unless $coRP = NP$, cf. Feige and Kilian [14] and Håstad [22].

The main reason why we focus on these two problems is that the recent development involves the following three ingredients that are quite central in approximation algorithms:

- Combinatorial (graph theoretical) approach.
- LP based approach.
- Semi-definite programming approach.

The development of the edge disjoint paths problem involves the first and the second ingredients, while that of the graph coloring problem involves the first and the third ones.

Let us first look at the edge-disjoint paths problem.

9.2 The Edge-Disjoint Paths Problem

In the edge-disjoint paths problem, we are given a graph $G = (V, E)$ with n vertices and m edges and a set of k pairs of vertices (called *terminals*) in G. The objective is to decide whether or not G has k edge-disjoint paths connecting given pairs of terminals. Let us mention some previously known results.

Known results: If k is a part of the input of the problem, this is a classical NP-complete problem [13], and it remains NP-complete even if an input graph G is constrained to be planar [33]. Early work on this problem focused on characterizing classes of graphs for which the edge-disjoint paths problem can be solved in polynomial time. For example, the seminal work of Robertson and Seymour [34] says that there is a polynomial-time algorithm for the edge-disjoint paths problem when the number of terminals, k, is fixed. Actually, this algorithm is one of the spin-offs of their groundbreaking work on graph minor project, spanning 23 papers and taking more than 20 years, and giving several deep and profound results and techniques in discrete mathematics. The time complexity is improved to $O(n^2)$ in [30]. Also, the half-integral (edge-)disjoint paths problem for the fixed number of terminals has been studied in [25, 27, 32].

Approximation algorithms The focus has recently shifted to the *maximum edge-disjoint paths problem* (MEDP), in which we find a maximum number of edge-disjoint paths connecting terminal pairs. This is because, in the real world under

the situation where there is a limited network capacity but with many requests, we need to optimize over the choice of which requests to satisfy. A *c-approximation* algorithm for this problem is a polynomial-time algorithm that connects at least OPT^*/c terminal pairs using the edge-disjoint paths, where OPT^* is the maximum possible.

Despite significant research in the recent years, there is wide gap in understanding the approximability of the maximum edge-disjoint paths problem. For *directed* graphs, no polynomial-time algorithm can achieve an approximation guarantee of $O(m^{1/2-\epsilon})$ for any $\epsilon > 0$, unless $P = NP$ [21]. But this result is based on the fact that the directed two edge-disjoint paths problem is NP-hard, which apparently does not hold for the undirected case. Currently, the strongest hardness result is due to [1], which shows a lower bound of $\Omega((\log m)^{1/2-\epsilon})$ for any $\epsilon > 0$. This may be the right upper bound, but then we would certainly need a far reaching approximation that there may be a corresponding poly-logarithmic upper bound. In fact, the recent breakthrough by Chuzhoy and Li [11] says the following:

Theorem 1. *If we allow each edge to be in at most two of paths, then there is a poly-logarithmic approximation algorithm for this problem.*

However the best known upper bound for the integral case is $O(\sqrt{n})$ [8].

All or nothing problem In order to tackle the maximum edge-disjoint paths problem, one has the following natural Linear programming relaxation, which can be solved in polynomial time.

Multicommodity Flow Problem (MFP)

$$\begin{aligned}
\text{maximize} \quad & \sum_{i=1}^{k} x_i \\
\text{subject to} \quad & \sum_{P \in \mathcal{P}_i} f(P) = x_i \qquad 1 \le i \le k \\
& \sum_{P: e \in \mathcal{P}} f(P) \le w(e) \qquad \forall e \in E \\
& x_i, f(P) \in [0,1] \qquad 1 \le i \le k, \forall P \in \mathcal{P}
\end{aligned}$$

Note that $\mathcal{P}_i$ is the set of all paths connecting s_i and t_i, and $\mathcal{P} = \bigcup_i \mathcal{P}_i$. Note also that if we require the integrality of x_i and $f(P)$, then it is certainly equivalent to MEDP. Let OPT be the optimal value of this Linear programming (LP). Since OPT is an upper bound of the optimal bound of MEDP, we want to find a feasible integral solution that guarantees a large fraction of OPT. Unfortunately it has been well-known that the integrality gap (i.e., the gap between the integral solution and the fractional solution of LP) for this LP is $\Omega(\sqrt{n})$, even for planar graphs.

The difficulty of MEDP perhaps comes from two types of integrality: one is the integrality of x_i (i.e. the selection of which subset of demands to try to route).

The other is the integrality of $f(P)$ (i.e. finding an integral flow). To understand the difficulty of the selection of the subset (i.e., the former), it is natural to consider the problem of finding a maximum fractionally routable subset of the demand pairs, which is stated as follows.

All-or-Nothing Multicommodity Flow Problem (ANF)

Input. A graph $G = (V, E)$ with integral capacity $w(e)$ for each $e \in E$, and k pairs of vertices $(s_1, t_1), (s_2, t_2), \ldots, (s_k, t_k)$ in G.

Find. A largest subset W of $\{1, \ldots, k\}$ such that for every i in W, we can send one unit of flow between s_i and t_i.

In other words, ANF is obtained from MFP by replacing $x_i \in [0, 1]$ with $x_i \in \{0, 1\}$, which implies that MFP is also a natural LP-relaxation of ANF.

Known results for ANF: Chekuri et al. [7] obtain a poly-logarithmic factor approximation algorithm for ANF and prove that the integrality gap between ANF and MFP is poly-logarithmic. Notice that this is in a big contrast with the $\Omega(\sqrt{n})$ integrality gap for MEDP.

In trees, ANF coincides with the maximum integer multicommodity flow problem, which is known to be APX-hard [18]. A 2-approximation algorithm for trees is also provided in [18]. We also note that there are no simple or obvious algorithms that can take advantage of the fractional routing, because of the APX-hardness on trees demonstrates.

Planar graphs The inapproximability bounds for MEDP [1] mentioned before also apply to ANF, and hence the upper and lower bounds are separated by only a poly-logarithmic factor. However, for planar graphs (which are paid much attention in the algorithmic graph theory research community), no super-constant integrality gap is known for ANF and MEDP with congestion 2 (i.e. each edge is allowed to be in two paths). Motivated by this fact, Chekuri et al. [9] showed that if G is planar and every edge capacity is at least 4, then the LP-relaxation of MEDP, which is MFP, has a constant integrality gap. Moreover, there is a polynomial-time algorithm that converts a fractional solution of MFP with total flow F into an integral congestion 4 solution with total flow $\Omega(F)$. This result is improved by [37] that shows that the congestion 4 is replaced by 2.

Thus what is left is ANF for planar graphs (note that [37] does not imply the corresponding result for the all-or-nothing multicommodity flow problem). The following result by Kawarabayashi and Kobayashi [26] considerably strengthens the above mentioned poly-logarithmic integrality gap by [7].

Theorem 2. *There exists a constant factor approximation algorithm for the all-or-nothing multicommodity flow problem in planar graphs. In particular, in polynomial time, we can find an index set W with $|W| = \Omega(\mathrm{OPT})$ and eight s_i-t_i paths for each $i \in W$ such that each edge is used at most eight times in these paths, where OPT is the optimal value of the LP-relaxation MFP.*

9.3 Semi-definite Programming and Coloring

In this section, we shall look at the graph coloring problem. The key is *semi-definite programming*.

Semi-definite programming (SDP) is probably the most exciting development in mathematical programming in the last 20 years. SDP has applications in such diverse fields as traditional convex constrained optimization, control theory, and combinatorial optimization. Because SDP is solvable via interior-point methods (and usually requires about the same amount of computational resources as linear optimization), most of these applications can usually be solved fairly efficiently in practice as well as in theory.

Semi-definite programming, as a generalization of linear programming, allows us to specify in addition to a set of linear constraints a "semi-definite" constraint, a special form of nonlinear constraints. We now introduce the basic concept of semi-definite programming.

First let us define a positive semi-definite $n \times n$ matrix A. It is positive semi-definite if and only if (1) A is symmetric, and (2) for all $x \in R_n$, $x^T Ax = \sum_{i=1}^{n} \sum_{j=1}^{n} A_{ij} x_i x_j \geq 0$. Then we can define a semi-definite program (SDP) as follows. An SDP is a mathematical program with four components:

- a set of variables x_{ij};
- linear objective function to minimize/maximize;
- a set of linear constraints over x_{ij};
- a semi-definite constraint of the matrix X with element x_{ij}.

The semi-definite constraint is what exactly differentiates SDPs from LPs. This can be interpreted as an infinite class of linear constraints. This is because by the definition of SDP, if a matrix A is semi-definite, then for all $v \in R_n$, $v^T Av \geq 0$. Each possible real vector v clearly gives us one linear constraint. Altogether, we have an infinite number of linear constraints.

Coloring via semi-definite programming A *k-coloring* of an undirected graph assigns k colors to the vertices. The coloring is only valid if no two adjacent vertices get the same color. This validity of coloring is trivially checked in linear time so the deciding if a graph is k-colorable is clearly in NP.

The semidefinite programming relaxation for graph coloring assigns a unit vector to each vertex of a graph G such that certain separation properties are satisfied for vectors corresponding to each pair of adjacent vertices. More precisely, we have the following constraints:

- for any integer $k \leq n + 1$ there exist k unit vectors in R_n such that their pairwise inner products are $\frac{-1}{k-1}$.
- Given a k-coloring of the graph G, we can assign one of these k vectors to each color class such that $< v_i, v_i >= \frac{-1}{k-1}$ for all edges $ij \in E(G)$ where v_i is the vector assigned to the vertex $i \in V$.

SDP coloring

$$\begin{aligned} &\text{minimize } t \\ &\text{subject to } < v_i, v_i > \leq t \qquad \forall ij \in E(G) \\ &\qquad\qquad < v_i, v_i > = 1 \qquad \forall i \in V(G) \\ &\qquad\qquad v_i \in R_n, \qquad \forall i \in V. \end{aligned}$$

Lemma 3. *If t^* is the optimal of the above SDP and G is k-colorable, then $t^* \leq \frac{-1}{k-1}$.*

If $t^* = \frac{-1}{k-1}$, then the function $\theta(G) = 1 - \frac{1}{t^*} = k^*$. In this case, G has a *vector k-colorable* and the corresponding optimal solution is called a *vector k-coloring* for G. k^* is exactly $\theta_{1/2}(\overline{G})$ where $\overline{G}$ is the complement of G and $\theta_{1/2}$ is the variant of the Lovász θ-function introduced by Schrijver [35] (see more details there). The gap between the vector k-coloring and the chromatic number (i.e., the optimal coloring number) is demonstrated in Karger et al. [15] by constructing Kneser graphs with vector chromatic number 3 and chromatic number n^{ϵ}.

We now look at some results about approximating graph coloring using semi-definite programming.

Coloring 3-colorable graphs It is well-known that a graph is 2-colorable if and only if it is bipartite. However, it is also well-known that deciding 3-colorability is a classic NP-hard problem. It was proved hard by Garey et al. [17], and was the prime example of NP-hardness mentioned by Karp in 1975 [24].

The most fundamental problem in approximating graph coloring is therefore coloring 3-colorable graphs. So here is a problem; given a 3-colorable graph, that has some (unknown) 3-coloring (it is important to emphasis that any 3-coloring is unknown when we obtain the input graph G. Otherwise the problem is trivial), we try to color it in polynomial time using as few colors as possible. The algorithm is allowed to fail or give up if the input graph was not 3-colorable. If a coloring is produced, we can always check if it is valid even if the input graph is not 3-colorable. This challenge has emerged many researchers. Wigderson [39] was the first to tackle this problem and give a polynomial time algorithm for $O(n^{1/2})$ colors for a graph with n vertices. Berger and Rompel [4] improved this to $O((n/(\log n))^{1/2})$. Blum [5] came with the first polynomial improvements to $\tilde{O}(n^{3/8})$ colors. These algorithms mentioned so far are based on *combinatorial approach*.

The next big improvement was given by Karger et al. [23] using SDP. This came in the wake of Goemans and Williamson's use of SDP for the max-cut problem [19]. For a graph with maximum degree $\Delta_{\max}$, Karger et al. got down to $O(\Delta_{\max}^{1/3})$ colors. Combining this with Wigderson's algorithm, they got down to $O(n^{1/4})$ colors.

Blum and Karger [6], later, combined the SDP from [23] with Blum's [5] algorithm, which yields an improved bound of $\tilde{O}(n^{3/14}) = \tilde{O}(n^{0.2142})$, where $\tilde{O}$ hides poly-logarithmic factor. Recent improvements on SDP have also been combined

with Blum's algorithm. Indeed, Arora et al. [2] got down to $\tilde{O}(n^{0.2111})$ colors. The proof in [2] is based on the breakthrough by Arora et al. [3] who gave an $O(\sqrt{\log n})$ algorithm for the sparsest cut problem. Chlamtac [10] finally got down to $O(n^{0.2072})$ colors.

Very recently, Kawarabayashi and Thorup [28] presented a purely combinatorial approach (for the first time since Blum [5]), which results in getting down to $\tilde{O}(n^{4/11})$ colors. Combining it with Chlamtac's SDP [10], they got down to $O(n^{0.2049})$ colors. Finally Kawarabayashi and Thorup[29] showed the following. This result is also combining combinatorial approach with SDP.

Theorem 4. *$O(n^{0.19996})$ colors suffices to color 3-colorable graphs in polynomial time.*

This is the biggest single improvement in the exponent since 1997 [6], and in particular, they pass the $n^{1/5}$ milestone.

How good the above theorem is? It is perhaps far from best possible. Indeed only a few lower bounds are known for coloring of 3-colorable graphs. We know that it is NP-hard to get down to 5 colors [20, 31]. Recently, Dinur et al. [12] showed that it's hard to color with any constant number of colors (i.e., $O(1)$ colors) based on a variant of the Unique Games Conjecture.

Integrality gap results [23, 38] show that understanding of SDP coloring [3, 10, 23] is almost optimal, and it is therefore natural to go back and see if we can improve combinatorially.

How to combine SDP with combinatorial approach? As mentioned above, the current best known result follows from a combination of SDP with combinatorial approach. We now show the interplay between combinatorial and semi-definite methods in the above mentioned papers. A parameter Δ is first chosen. By standard reductions, it suffices to work with graphs that either have minimum degree Δ or maximum degree Δ. A high minimum degree is good for *combinatorial* approaches while a low maximum degree is good for *semi-definite* approaches. Therefore, the best bounds are obtained choosing Δ to balance between the best semi-definite and combinatorial approaches.

On the combinatorial side, the coloring bounds have followed the sequence $\tilde{O}((n/\Delta)^{i/(2i-1)})$ for $i = 1, 2, 3, 4$. Indeed $i = 1$ is from Wigderson [39], $i = 2, 3$ from Blum [5], and $i = 4$ is from Kawarabayashi and Thorup[28], respectively. For $i \to \infty$, the sequence approaches its limit $\tilde{O}((n/\Delta)^{1/2})$. Each of the above steps is based on a new combinatorial coloring idea.

For a purely combinatorial algorithm, we balance the above bounds with the trivial Δ-coloring; this takes any vertex v with $< \Delta$ neighbors, and then we color the rest of the graph inductively, and give v the first color not used in its neighborhood.

The first semi-definite solution of Karger et al. [23], implies $O(\Delta^{1/3})$ colors. Balancing this with yet not to be found an $\tilde{O}((n/\Delta)^{1/2})$ coloring, would yield $\tilde{O}(n^{1/5})$ colors, which should be thus a natural milestone. Later semi-definite approaches of Arora et al. [2] and Chlamtac [10], have pin down to $O(\Delta^{1/3-\varepsilon(n,\Delta)})$

colors where $\varepsilon(n, \Delta) > 0$ is a small bound that decreases as very complicated function of Δ. The above mentioned integrality gap implies that $\varepsilon(n, \Delta) = o(1)$ for $\Delta = n^{o(1)}$.

9.4 Conclusion

In this survey, we focus the following two problems that have some recent breakthroughs for approximation algorithms; the edge-disjoint paths problem and the graph coloring problem. These breakthroughs involve the following three ingredients that are quite central in approximation algorithms: (1) Combinatorial (graph theoretical) approach, (2) LP based approach and (3) Semi-definite programming approach.

There are a few other problems that have some recent development. These include TSP, the Steiner tree problem, and the sparsest cut problem. The first one involves (1), the second one is mainly based on (2), and the third one is connected to (3). Therefore, we expect that these three ingredients would lead to more breakthroughs in the next decade.

References

1. M. Andrews, J. Chuzhoy, S. Khanna, L. Zhang, Hardness of the undirected edge-disjoint paths problem with congestion, in *Proceedings of the 46th IEEE Symposium on Foundations of Computer Science (FOCS)*, Pittsburgh (2005), pp. 226–244
2. S. Arora, E. Chlamtac, M. Charikar, New approximation guarantee for chromatic number, in *Proceedings of the 38th STOC*, Seattle (2006) pp. 215–224
3. S. Arora, S. Rao, U. Vazirani, Expanders, geometric embeddings and graph partitioning. J. ACM **56**(2), 1–37 (2009). Announced at STOC'04
4. B. Berger, J. Rompel, A better performance guarantee for approximate graph coloring. Algorithmica, **5**(3), 459–466 (1990)
5. A. Blum, New approximation algorithms for graph coloring. J. ACM **41**(3), 470–516 (1994). Announced at STOC'89 and FOCS'90
6. A. Blum, D. Karger, An $\tilde{O}(n^{3/14})$-coloring algorithm for 3-colorable graphs. Inf. Process. Lett. **61**(1), 49–53 (1997)
7. C. Chekuri, S. Khanna, B. Shepherd, The all-or-nothing multicommodity flow problem, in *Proceedings of the 36th ACM Symposium on Theory of Computing (STOC)*, Chicago (2004), pp. 156–165
8. C. Chekuri, S. Khanna, B. Shepherd, An $O(\sqrt{n})$ approximation and integrality gap for disjoint paths and unsplittable flow. Theory Comput. **2**, 137–146 (2006)
9. C. Chekuri, S. Khanna, B. Shepherd, Edge-disjoint paths in planar graphs with constant congestion. SIAM J. Comput. **39**, 281–301 (2009)
10. E. Chlamtac, Approximation algorithms using hierarchies of semidefinite programming relaxations, in *Proceedings of the 48th FOCS*, Providence (2007), pp. 691–701
11. J. Chuzhoy, S. Li, A polylogarithimic approximation algorithm for edge-disjoint paths with congestion 2, in *Proceedings of the 53rd IEEE Symposium on Foundations of Computer Science (FOCS)*, New Brunswick (2012), pp. 233–242

12. I. Dinur, E. Mossel, O. Regev, Conditional hardness for approximate coloring. SIAM J. Comput. **39**(3), 843–873 (2009). Announced at STOC'06
13. S. Even, A. Itai, A. Shamir, On the complexity of timetable and multicommodity flow problems. SIAM J. Comput. **5**, 691–703 (1976)
14. U. Feige, J. Kilian, Zero-knowledge and the chromatic number. J. Comput. Syst. Sci. **57**, 187–199 (1998)
15. U. Feige, M. Langberg, G. Schechtman, Graphs with tiny vector chromatic numbers and huge chromatic numbers, In *Proceedings of the 43rd FOCS*, Vancouver (2002), pp. 283–292
16. A. Frank, Packing paths, cuts and circuits – a survey, in *Paths, Flows and VLSI-Layout*, ed. by B. Korte, L. Lovász, H.J. Promel, A. Schrijver (Springer, Berlin, 1990), pp. 49–100
17. M. Garey, D. Johnson, L. Stockmeyer, Some simplified NP-complete graph problems. Theor. Comput. Sci. **1**(3), 237–267 (1976). Announced at STOC'74
18. N. Garg, V. Vazirani, M. Yannakakis, Primal-dual approximation algorithms for integral flow and multicut in trees. Algorithmica **18**, 3–20 (1997)
19. M. Goemansl, D. Williamson, Improved approximation algorithms for maximum cut and satisfiability problems using semidefinite programming. J. ACM **42**(6), 1115–1145 (1995). Announced at STOC'94
20. V. Guruswami, S. Khanna, On the hardness of 4-coloring a 3-colorable graph. J. Discret. Math. **18**(1), 30–40 (2004)
21. V. Guruswami, S. Khanna, R. Rajaraman, B. Shepherd, M. Yannakakis, Near-optimal hardness results and approximation algorithms for edge-disjoint paths and related problems. J. Comput. Syst. Sci. **67**, 473–496 (2003)
22. J. Håstad, Clique is hard to approximate within $n^{1-\varepsilon}$. Acta Math. **182**, 105–142 (1999)
23. D. Karger, R. Motwani, M. Sudan, Approximate graph coloring by semidefinite programming. J. ACM **45**(2), 246–265 (1998). Announced at FOCS'94
24. R.M. Karp, On the computational complexity of combinatorial problems. Networks **5**, 45–68 (1975)
25. K. Kawarabayashi, Y. Kobayashi, An improved algorithm for the half-disjoint paths problem. SIAM J. Discret. Math. **25**, 1322–1330 (2011)
26. K. Kawarabayashi, Y. Kobayashi, All-or-nothing multicommodity flow problem with bounded fractionality in planar graphs, in *The 54th Annual Symposium on Foundations of Computer Science (FOCS 2013)*, Berkeley (2013), pp.187–196
27. K. Kawarabayashi, B. Reed, A nearly linear time algorithm for the half integral disjoint paths packing, in *Proceedings of the ACM-SIAM Symposium on Discrete Algorithms (SODA)*, San Francisco (2008), pp. 446–454
28. K. Kawarabayashi, M. Thorup, Combinatorial coloring of 3-colorable graphs, in *Proceedings of the 53rd FOCS*, New Brunswick (2012)
29. K. Kawarabayashi, M. Thorup, Coloring 3-colorable graphs with $o(n^{1/5})$ colors, in *The 31st Symposium on Theoretical Aspects of Computer Science (STACS'14)*, Lyon (2014), pp. 458–469
30. K. Kawarabayashi, Y. Kobayashi, B. Reed, The disjoint paths problem in quadratic time. J. Combin. Theory Ser. B **102**, 424–435 (2012)
31. S. Khanna, N. Linial, S. Safra, On the hardness of approximating the chromatic number. Combinatorica **20**(3), 393–415 (2000)
32. J. Kleinberg, Decision algorithms for unsplittable flow and the half-disjoint paths problem, in *Proceedings of the 30th ACM Symposium on Theory of Computing (STOC)*, Dallas (1998), pp. 530–539
33. M.R. Kramer, J. van Leeuwen, The complexity of wire-routing and finding minimum area layouts for arbitrary VLSI circuits. Adv. Comput. Res. **2**, 129–146 (1984)
34. N. Robertson, P.D. Seymour, Graph minors. XIII. The disjoint paths problem. J. Combin. Theory Ser. B **63**, 65–110 (1995)
35. A. Schrijver, A comparison of the Delsarte and Lovász bounds. IEEE Trans. Inf. Theory **25**, 425–429 (1979)

36. A. Schrijver, in *Combinatorial Optimization: Polyhedra and Efficiency*. Algorithm and Combinatorics, vol. 24 (Springer, Berlin/New York, 2003)
37. L. Séguin-Charbonneau, B.F. Shepherd, Maximum edge-disjoint paths in planar graphs with congestion 2, in *Proceedings of the 52nd IEEE Symposium on Foundations of Computer Science (FOCS)*, Palm Springs (2011), pp. 200–209
38. M. Szegedy, A note on the θ number of Lovász and the generalized Delsarte bound, in *Proceedings of the 35th FOCS*, Santa Fe (1994), pp. 36–39
39. A. Wigderson, Improving the performance guarantee for approximate graph coloring. J. ACM **30**(4), 729–735 (1983). Announced at STOC'82

Chapter 10
Coherent Computing with Injection-Locked Laser Network

S. Utsunomiya, K. Wen, K. Takata, S. Tamate, and Yoshihisa Yamamoto

10.1 Introduction

Combinatorial optimization problems are ubiquitous in our modern life. The classic examples include the protein folding in biology and medicine, the frequency assignment in wireless communications, traffic control and routing in air and on surface, microprocessor circuit design, computer vision and graph cut in machine learning, and social network control. They often belong to NP, NP-complete and NP-hard classes, for which modern digital computers and future quantum computers cannot find solutions efficiently, i.e. in polynomial time [1].

S. Utsunomiya (✉)
National Institute of Informatics, 2-1-2 Hitotsubashi, Chiyoda-ku, Tokyo 101-8430, Japan
e-mail: shoko@nii.ac.jp

K. Wen
E. L. Ginzton Laboratory, Stanford University, Stanford, CA 94305, USA
e-mail: kwen07@gmail.com

K. Takata
The University of Tokyo, 7-3-1 Hongo, Bunkyo-ku, Tokyo 113-8654, Japan

National Institute of Informatics, Hitotsubashi 2-1-2, Chiyoda-ku, Tokyo 101-8403, Japan
e-mail: takata.kenta@lab.ntt.co.jp

S. Tamate
Center for Emergent Matter Science, RIKEN, 2-1 Hirosawa, Wako-shi, Saitama 351-0198, Japan
e-mail: shuhei.tamate@riken.jp

Y. Yamamoto
ImPACT Program, Council for Science Technology and Innovation, Tokyo, Japan
e-mail: yyamamoto@stanford.edu

Y. Yamamoto, K. Semba (eds.), *Principles and Methods of Quantum Information Technologies*, Lecture Notes in Physics 911, DOI 10.1007/978-4-431-55756-2_10

A Ising model described by the Hamiltonian

$$\mathscr{H} = -\sum_{i<j} J_{ij}\sigma_{iz}\sigma_{jz} - \sum_{i} h_i\sigma_{iz} \tag{10.1}$$

is a mathematical abstraction for spin glasses [2]. Here σ_{iz} is a z-projection of Pauli spin operator and takes either $+1$ or -1 eigenvalue. The Ising coupling J_{ij} represents either a ferromagnetic coupling $\left(J_{ij} > 0\right)$ or an anti-ferromagnetic coupling $\left(J_{ij} < 0\right)$. The Zeeman term h_i corresponds to a local field. While the one-dimensional and two-dimensional Ising models belong to the class P [3, 4], the three-dimensional Ising model is NP-hard [5]. Many combinatorial optimization problems can be mapped onto the Ising model with polynomial resource. This is the basic motivation for searching a physical machine which solves the Ising model.

A standard quantum computer utilizes unitary rotation of state vectors of localized spin-$1/2$ particles (qubits) in closed Hilbert space [6], while a quantum annealing machine employs adiabatic evolution of a system Hamiltonian in closed Hilbert space [7, 8]. On the other hand, a novel coherent computer which is the subject of this chapter uses a laser phase transition for non-local electromagnetic fields in open-dissipative setting [9].

An unstructured data search is one of the most difficult problems from the energy landscape viewpoint, in which there is one and only one target state with a lowest energy and all the other states of $2^N - 1$ have degenerate higher energies. A celebrated Grover algorithm can find the target file with a reasonable success probability by $\sim O\left(\sqrt{2^n}\right)$oracle operations [10]. This is the square-root speedup over the classical brute force search which requires $\sim O\left(2^n\right)$ calculations in the worst case. Bad news is that this Grover algorithm is the optimum solution by quantum computers based on blackbody (oracle) inquiry routine [11]. A quantum annealing machine (or rather adiabatic quantum computer) can achieve this square-root speedup if the Hamiltonian sweep is optimized at each time by somehow consulting with the energy gap between the ground state and first excited states [12, 13]. It is conjectured that these two quantum machines cannot overcome the exponential scaling of computational time for NP, NP-complete and NP-hard problems.

In this chapter we will describe the recent effort to elucidate the computational power of coherent computers against NP-hard Ising problems. In Sect. 10.2, we will review the laser phase transition from the viewpoint of Gottesman-Knill theorem and introduce the operational principle of a laser network coherent Ising machine. Section 10.3 will present the theory of injection-locked laser network and obtain the mapping protocol. Section 10.4 will discuss the numerical benchmark study against NP-hard problems. The proof-of-concept experiment using semiconductor lasers will be presented in Sect. 10.5 and finally the scalable system based on higher harmonic mode-locked fiber lasers will be proposed as a XY machine in Sect. 10.6.

10.2 Concept and Basic Principle

10.2.1 Gottesman-Knill Theorem

What is the ultimate origin for quantum speedup over classical computing is an intriguing question not only from a fundamental viewpoint but also from a practical viewpoint of devising a new computing machine. The Gottesman-Knill theorem provides an insightful clue to address this question [14]. The statement of the theorem is summarized as follows:

If a quantum algorithm starts with

1. computational basis states such as $|0\rangle_1, |0\rangle_2, \ldots, |0\rangle_N$,
2. employs a limited set of unitary gates such as Hadamard gate, controlled-NOT gate and phase gate which belong to a so-called Clifford group,
3. and ends with projection measurements along computational basis states,

such an algorithm can be simulated efficiently by classical computers. This means that many important quantum operations, including entanglement generation and purification, quantum error correction and quantum teleportation, are not considered as the origin of quantum speed-up. In fact, the Shor's factoring algorithm cannot be implemented by the Clifford group only. It is known that addition of fractional phase rotations for state vectors would make a universal gate set for quantum algorithm.

The equivalent to Gottesman-Knill theorem for a continuous variable (harmonic oscillator) quantum algorithm also gives a useful insight for this point [15]. The statement of the theorem is summarized as follows:

If a harmonic oscillator quantum algorithm starts with

1. gaussian states such as coherent states $|\alpha\rangle_1, |\alpha\rangle_2, \ldots, |\alpha\rangle_N$,
2. employs a limited set of unitary gates such as squeezing operation and displacement operation,
3. and ends with projective measurements of quadrature amplitudes, $\hat{a} + \hat{a}^\dagger$or $i(\hat{a} - \hat{a}^\dagger)$,

such an algorithm can be simulated efficiently by classical computers. This means that many important quantum operations for continuous variables, such as squeezing, entanglement generation and quantum teleportation, are not considered as the origin of quantum speed-up, either. It is known that addition of photon counting detections or third order (Kerr) nonlinear process to the above gaussian processes would make a universal gate set for continuous variable quantum algorithm.

10.2.2 Laser Phase Transition

A laser is an open dissipative system consisting of the two coupled systems, cavity photon fields and inverted atoms, and the reservoirs, i.e. external vacuum fields with

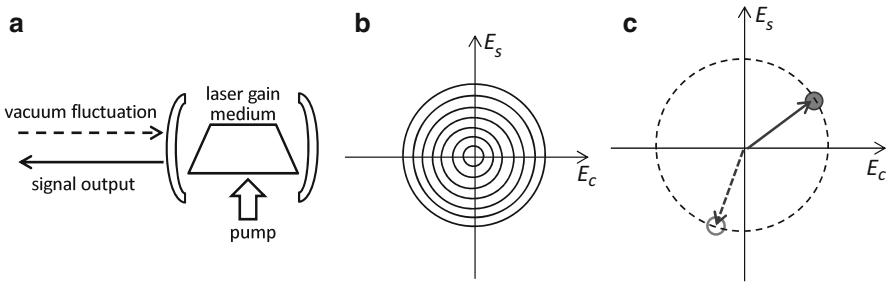

Fig. 10.1 Laser phase transition. (**a**) A laser accepts a vacuum field as an input and reflects it as a signal output. (**b**) A thermal state with a maximum entropy is produced at below oscillation threshold. (**c**) A coherent state with zero entropy is produced at above oscillation threshold

continuous spectra for the photon fields and the invented atoms, and an external pump source for the inverted atoms. If we neglect the details of quantum dynamics of a laser and consider it as a black box, this system accepts vacuum fields as inputs and reflect them as signal outputs as shown in Fig. 10.1a. If the pump rate is just below its oscillation threshold, the reflected signal is in a multimode thermal state,

$$\begin{aligned} \rho &= \prod_{i=1}^{M} \rho_i \\ \rho_i &= \sum_n \left(\frac{1}{1+n_{th}} \right) \left(\frac{n_{th}}{1+n_{th}} \right)^n |n\rangle\langle n| , \end{aligned} \tag{10.2}$$

where the index i denotes a cavity mode within the gain bandwidth and n_{th} is the average photon number per mode. It is known that (2) is a blackbody radiation at an effective temperature of $T_{eff} = {}^{\hbar w}/_{k_B T} \ln 2 \sim 10^4\,\mathrm{K}$ for $\omega \sim 10^{15}$(rad/s) and $T \sim 300\,\mathrm{K}$, as shown in Fig. 10.1b. This multimode thermal state realizes a maximum randomness (entropy),

$$\begin{aligned} S &\equiv Tr\,(\rho \ln \rho) \\ &= M \left[\ln (1+n_{th}) + \frac{1}{1+n_{th}} \ln \left(1 + \frac{1}{n_{th}} \right) \right], \end{aligned} \tag{10.3}$$

under the constraint of constant average photon number $\langle n_{th} \rangle$, where M is the total number of cavity modes within the gain bandwidth.

At a pump rate above its oscillation threshold, however, such randomness disappears. The reflected signal is a single mode coherent state,

$$\rho_i = |\alpha\rangle\langle\alpha|, \tag{10.4}$$

while all the other modes stay in a thermal state. The absolute amplitude $|\alpha|$ of the complex eigenvalue is equal to the square-root of the mean photon number,

$|\alpha| = \sqrt{n}$, which is uniquely determined by the balance between external pumping and out-coupling loss. The phase ϕ of the complex eigenvalue is randomly chosen by the internal and external quantum noise, as shown in Fig. 10.1c. The selection of a particular phase is called "spontaneous breaking of gauge symmetry" associated with laser phase transition. A chosen coherent state has a zero entropy (pure state). It is known that this nonlinear quantum dynamics cannot be simulated efficiently by classical computers and we hope such a laser phase transition is powerful enough to find a right answer from numerous candidates in notorious NP problems. From the viewpoint of harmonic oscillator Gottesman-Knill theorem, the nonlinear gain saturation of a laser distinguishes this system from the above mentioned simple gaussian processes.

10.2.3 Downward Search, Laternal Search and Upward Search

The injection-locked laser network implements the energy landscape, i.e. eigen-energy vs. spin configuration, of the Ising Hamiltonian (1) in terms of the effective loss of the whole network. We will show this one-to-one correspondence between the (original) Ising energy landscape and the (mapped) loss landscape in the next section. The cartoon of Fig. 10.2 illustrates such an energy/loss landscape.

A proposed computational concept is in sharp contrast to the classical (simulated) annealing and quantum annealing. Classical annealing employs a downward search, in which the thermal equilibrium state is searched during the temperature is gradually decreased. For a hard instance of NP problems, there are numerous local

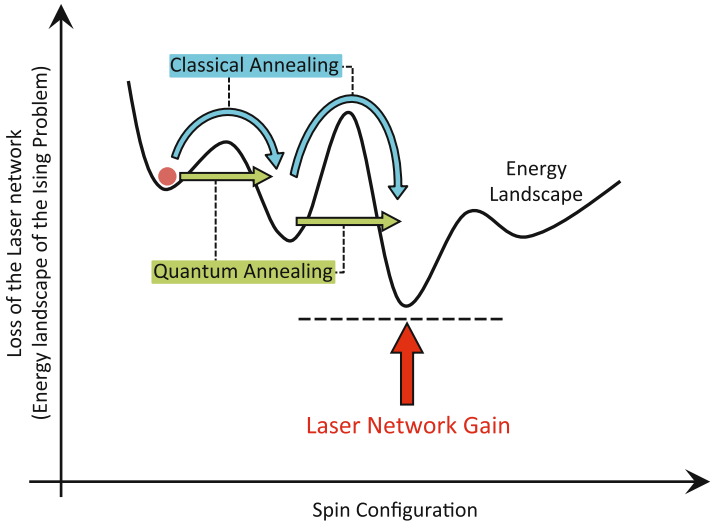

Fig. 10.2 Comparison of the search mechanism between the laser network, classical (simulated) annealing, and quantum annealing

minima that may trap a system in a deep potential barrier so that a thermal excitation cannot allow the system to escape from a metastable state. In order to overcome this problem, the repeated cooling and heating are introduced. Quantum annealing exerts a horizontal search with quantum tunneling. When such quantum tunneling is introduced by a transverse field, simultaneous multi-spin flip and resulting global search are possible. However, even with these methods, the computational time of finding the ground state increases with the number of metastable excited states (local minima), which increases exponentially for a hard instance of NP problems.

In contrast, the injection-locked laser network searches for the ground state in an upward direction. The energy, the ordinate of Fig. 10.2, is now replaced by the network loss. The ground state has now a minimum loss. If we put a laser gain medium into such a network and increase the pump rate gradually, the first touch to the network loss happens always at the ground state so that only the ground state oscillates with all the other modes including local minima suppressed by nonlinear gain saturation. If we use the terminology of "negative temperature" to represent the inverted gain medium, this upward search corresponds to the heating process from $T = -\infty$ (no gain) to $T = -0$ (high gain). Since there is no structure below the ground state as shown in Fig. 10.2, the injection-locked laser network is less susceptible to being trapped in metastable excited states.

10.3 Analysis of Injection-Locked Laser Network

In this section, we present the c-number Langevin equations for injection-locked laser network. The combinational optimisation problems can be formulated as a computational mission of minimising a cost function $E(\sigma_1, \sigma_2, \ldots \sigma_M)$ by choosing the particular combination of M discrete variables $\sigma_1, \sigma_2, \ldots \sigma_M$ under some constraints. The Graph Partition Problem (GPP) or MAX-CUT problem, which are representative NP-hard problems, can be mapped to an Ising spin model (10.1). circuits with one master laser and M mutually injection-locked slave lasers. A spin degree of freedom σ_{iz} at each site is now represented by right or left circular polarization states of each slave laser in the laser network. The ground state of an Ising model emerges spontaneously through the mode competition induced by cross-gain saturation among all candidate polarization configurations. The cost function $E(\sigma_1, \sigma_2, \ldots, \sigma_M)$ mentioned above corresponds to the overall photon decay rate in the laser network. The injection-locked laser network oscillates with a specific polarization configuration which minimizes the cost function.

10.3.1 Proposed System

An effective spin state σ_{iz} at site i is determined by a majority vote using photodetection signals at the final step of this computational scheme, i.e.,

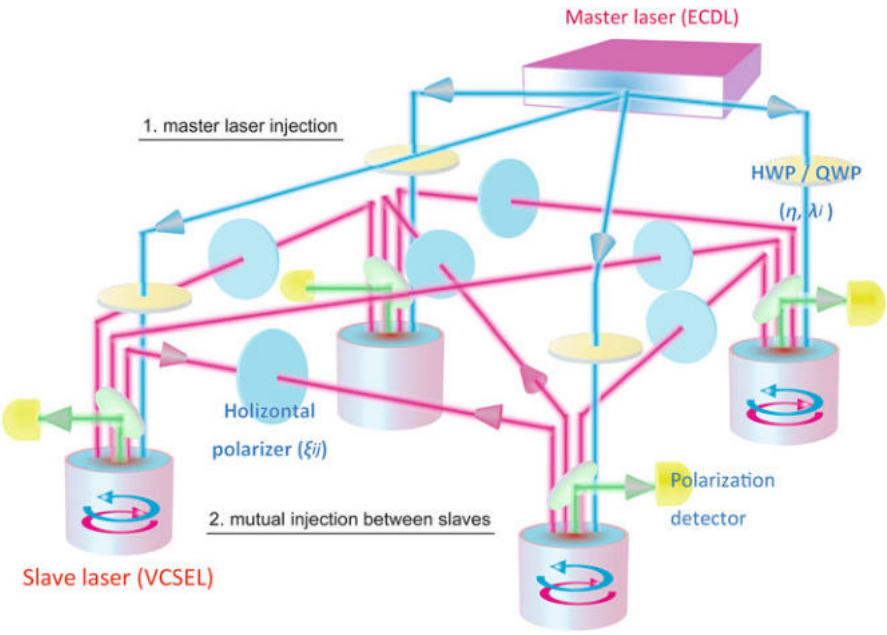

Fig. 10.3 A proposed injection-locked laser system for finding the ground state of an Ising model Eq. (10.1). A master laser output is equally split into M paths and injected into M slave lasers via an optical isolator. At a time $t < 0$ (initialization), the injection signal from the master laser has a vertical linear polarization so that all slave lasers are initialized in vertical linear polarization states $|V\rangle_1|V\rangle_2 \ldots |V\rangle_M$. At a time $t = 0$, the combined attenuator, HWP and QWP can implement the Zeeman term λ_i. Also at a time $t = 0$, each slave laser output is injected to other slave lasers via a horizontal linear polarizer, phase shifter, and attenuator but without an isolator. This mutual injection-locking can implement the Ising interaction term J_{ij}. After a steady state condition is reached, the two polarization components of each slave laser are detected by a polarization beam splitter (PBS) and two photodetectors

$$\sigma_{iz} = \begin{cases} 1 & (\text{if } n_{Ri} > n_{Li}) \\ -1 & (\text{if } n_{Ri} < n_{Li}), \end{cases} \tag{10.5}$$

where n_{Ri} and n_{Li} are the number of photons with right and left circular polarizations from i-th slave laser. We assume that all slave lasers are driven to have the same photon number.

A proposed injection-locked laser network is shown in Fig. 10.3. All slave lasers, which play a role of respective Ising spin sites, are injection-locked by a single master laser with vertical linear polarization.

A master laser output is split into M paths and injected into M slave lasers. To implement the Zeeman term λ_i, the master laser output is injected into the i-th slave laser with a horizontal linear polarization component (as well as a vertical polarization component.) The amplitude and phase of the horizontally polarized

injection signal is controlled with half-wave plates (HWP) and quarter-wave plates (QWP) as shown in Fig. 10.3. The Ising interaction term between site i and site j is implemented with the mutual injection of the slave laser outputs via an attenuator, phase shifter and horizontal linear polarizer. In total, $\frac{1}{2}M(M-1)$ paths must be optically connected between all slave lasers in order to implement a complete graph.

10.3.2 Theoretical Model

We start with the quantum mechanical Langevin equation for an injection-locked laser [16, 17]. The Heisenberg-Langevin equation for a (non-Hermitian) cavity field operator is described as,

$$\frac{d}{dt}\hat{A}(t) = -i\omega_c\hat{A}(t) - \frac{1}{2}\Big[\frac{\omega}{Q} - \frac{\omega}{\mu^2}(\tilde{\chi}_i - i\tilde{\chi}_r)\Big]\hat{A}(t) + \sqrt{\frac{\omega}{Q}}F_0 e^{-i\omega t} + \tilde{f}_G + \hat{f}_L. \quad (10.6)$$

Here the photon field operators are designated by hats and the electronic operators are denoted by tildes. The electric dipole operator is adiabatically eliminated by assuming the electric dipole moment decay rate is faster than the photon decay rate and the electronic population decay rate [18, 19]. $\frac{\omega}{Q}$ describes the cavity photon loss rate through an output coupling mirror (we neglect an internal loss rate) and μ is a non-resonant refractive index. ω_c is the empty cavity resonance frequency of the slave laser, while ω is the frequency of the injection signal. The operator $\tilde{\chi}_i$ represents the net stimulated emission gain and $\tilde{\chi}_r$ represents the nonlinear dispersion, both of which depend on the population operator. $\tilde{f}_G$ is the Langevin noise operator for the electric dipole moment which is associated with random photon emission and absorption by the gain medium. $\hat{f}_L$ is the Langevin noise operator for the cavity field, which is associated with the injection signal noise including a vacuum fluctuation. F_0 is a c-number injection signal amplitude.

The net gain operator $\frac{\omega}{\mu^2}\tilde{\chi}_i = \tilde{E}_{CV} - \tilde{E}_{VC}$ is composed of the photon emission rate operator $\tilde{E}_{CV}$ into a lasing mode and absorption rate operator $\tilde{E}_{VC}$. We assume the absorption loss is negligible so that $\tilde{E}_{CV} - \tilde{E}_{VC} \simeq \tilde{E}_{CV}$. Using the relation between a photon number operator and field operator, $\hat{n}(t) = \hat{A}^\dagger(t)\hat{A}(t)$, in Eq. (10.6), a quantum mechanical rate equation for photon number operator $\hat{n}(t)$ is derived as follows [16, 19]:

$$\frac{d}{dt}\hat{n}(t) = -\frac{\omega}{Q}\hat{n}(t) + \tilde{E}_{CV}\hat{n}(t) + \tilde{E}_{CV} + \sqrt{\frac{\omega}{Q}}(F_0^*\hat{A}(t) + \hat{A}^\dagger(t)F_0) + \hat{F}_n(t). \quad (10.7)$$

Quantum mechanical rate equation for the total electron number operator $\tilde{N}$ in a slave laser is [16, 19],

$$\frac{d}{dt}\tilde{N}(t) = P - \frac{\tilde{N}(t)}{\tau_{sp}} - \tilde{E}_{CV}\hat{n}(t) - \tilde{E}_{CV} + \tilde{F}_c(t), \quad (10.8)$$

where P is an average pump rate, $\frac{\tilde{N}}{\tau_{sp}}$ a total spontaneous emission term, τ_{sp} a spontaneous emission lifetime. If we define β as a fractional coupling efficiency of spontaneous emission into a lasing mode, then a photon emission rate operator into a lasing mode is redefined as $\tilde{E}_{CV} = \beta \frac{\tilde{N}}{\tau_{sp}}$.

When the noise operator $\hat{f}_L$ in Eq. (10.6) represents a vacuum fluctuation, this means the quantum state of the injection signal is a coherent state. In such a case, the amplitude (or photon number) noise of the injection-locked slave laser output is squeezed to below the standard quantum limit (SQL) under quiet (sub-Poisson) pumping [20], while the phase noise is above the SQL due to random walk phase diffusion [16]. The product of the photon number noise and the phase noise is close to the Heisenberg minimum uncertainty product [16]. That is, the output field of the injection-locked laser is close to the minimum uncertainty wavepacket. The amplitude and phase noise of the output-field as well as the electron number noise are small compared to their average values and we can safely neglect the quantum noise in the first-order approximation and replace the operators $\hat{A}(t)$, $\hat{n}(t)$ and $\hat{N}(t)$ by the corresponding c-numbers.

We now expand the c-number photon field amplitude as

$$A(t) = A_0(t)e^{-i[\omega t + \phi_0(t)]}, \tag{10.9}$$

where $A_0(t)$ is the slowly varying amplitude (positive real) and $\phi_0(t)$ is a slowly varying phase. Substituting Eq. (10.9) into Eqs. (10.6) and (10.7) in which the operators $\hat{A}$ and $\hat{n}$ are replaced by the corresponding c-numbers and the noise terms are neglected, we obtain the following three rate equations:

$$\frac{d}{dt}A_0(t) = -\frac{1}{2}\left[\left(\frac{\omega}{Q}\right) - E_{CV}\right]A_0(t) + \sqrt{\frac{\omega}{Q}}F_0\cos[\phi_0(t)], \tag{10.10}$$

$$\frac{d}{dt}n(t) = -\left(\frac{\omega}{Q} - E_{CV}\right)n(t) + E_{CV} + 2\sqrt{\frac{\omega}{Q}}F_0A_0(t)\cos[\phi_0(t)], \tag{10.11}$$

$$\frac{d}{dt}\phi_0(t) = -(\omega - \omega_0) - \sqrt{\frac{\omega}{Q}}\frac{F_0}{A_0(t)}\sin[\phi_0(t)], \tag{10.12}$$

where $\omega_0 = \omega_c + \frac{\omega}{2\mu^2}\chi_r$ is the self-oscillation frequency of the slave laser, $E_{CV} = \langle\tilde{E}_{CV}\rangle$ and $\chi_r = \langle\tilde{\chi}_r\rangle$. Notice that the third term E_{CV} of R. H. S. in Eq. (10.11) represents the spontaneous emission rate into the lasing mode induced by the quantum noise [18, 19], which we keep in our analysis. In the following discussions, we assume $\omega = \omega_0$ so that the slave laser phase is identically equal to the master laser phase $\phi_0(t) = \phi_M = 0$.

Since the phase of a slave laser is locked to that of the dominant vertically polarized master laser signal, the phases of right and left circular polarization modes in all slave lasers are identical to that of the master laser. Then, the last term of R. H. S. of Eq. (10.11) can be rewritten as $2\sqrt{\frac{\omega}{Q}n(t)}F_0$. If an injection signal is only

from the master laser with vertical linear polarization $F_0 = \zeta\sqrt{\frac{\omega}{Q_M}}\sqrt{n_M}$, where $\frac{\omega}{Q_M}$ is the master laser photon decay rate, n_M is the average photon number of the master laser and ζ is an amplitude attenuation coefficient including a factor of $\frac{1}{\sqrt{2}}$ for the projection factor from the vertical linear polarization to the right (or left) circular polarization. For simplicity, we assume that the cavity quality factor of the master laser Q_M is equal to that of the slave lasers, $Q_M = Q$. Then Eq. (10.11) can be simplified as,

$$\frac{d}{dt}n(t) = -\left(\frac{\omega}{Q}\right)n(t) + E_{CV}n(t) + E_{CV} + 2\frac{\omega}{Q}\sqrt{n(t)}\zeta\sqrt{n_M}. \tag{10.13}$$

We now consider two sets of coupled rate equations for the right and left circularly polarized modes of each slave laser. In a proposed injection-locked laser network before the Hamiltonian, Eq. (10.1), is turned on ($t < 0$), the rate equations are

$$\frac{d}{dt}n_{Ri} = -\left(\frac{\omega}{Q} - E_{CVRi}\right)n_{Ri} + E_{CVRi} + 2\frac{\omega}{Q}\sqrt{n_{R_i}}\zeta\sqrt{n_M}, \tag{10.14}$$

$$\frac{d}{dt}n_{Li} = -\left(\frac{\omega}{Q} - E_{CVLi}\right)n_{Li} + E_{CVLi} + 2\frac{\omega}{Q}\sqrt{n_{L_i}}\zeta\sqrt{n_M}, \tag{10.15}$$

where i designates a specific slave laser. The vertically polarized injection signal from the master laser into the slave laser i achieves the proper initialization, i.e., $n_{Ri} = n_{Li}$ and $\phi_{Ri} = \phi_{Li} = 0$.

If the right and left circular polarization modes couple to the inverted electronic population with identical strength, the rate equation for the electronic population is

$$\frac{d}{dt}N_i(t) = P - \frac{N_i(t)}{\tau_{sp}} - E_{CVi}\left[n_{Ri}(t) + n_{Li}(t) + 2\right]. \tag{10.16}$$

At $t = 0$, we inject a small amount of horizontally polarized master laser signal to the slave laser i to implement the Zeeman term λ_i in Eq. (10.1). At $t = 0$, we also inject a small amount of horizontally polarized signal from a slave laser i to a slave laser j and vice versa to implement the Ising interaction term J_{ij} in Eq. (10.1). Then the rate equations for n_{Ri} and n_{Li} after $t = 0$ are given as,

$$\begin{aligned}\frac{d}{dt}n_{Ri} = &-\left(\frac{\omega}{Q} - E_{CVi}\right)n_{Ri} + E_{CVi} \\ &+2\frac{\omega}{Q}\sqrt{n_{R_i}}\left[(\zeta - \eta_i)\sqrt{n_M} - \sum_{j\neq i}\frac{1}{2}\xi_{ij}(\sqrt{n_{Rj}} - \sqrt{n_{Lj}})\right]\end{aligned} \tag{10.17}$$

$$\frac{d}{dt}n_{Li} = -\left(\frac{\omega}{Q} - E_{CVi}\right)n_{Li} + E_{CVi} + 2\frac{\omega}{Q}\sqrt{n_{L_i}}\left[(\zeta + \eta_i)\sqrt{n_M} + \sum_{j\neq i}\frac{1}{2}\xi_{ij}(\sqrt{n_{Rj}} - \sqrt{n_{Lj}})\right]. \tag{10.18}$$

Here an amplitude attenuation coefficient is η_i for the horizontally polarized injection signal from the master laser. The mutual injection term is optically implemented by inserting a horizontal polarizer, attenuator and phase shifter in the optical path between two slave lasers i and j. The amplitude attenuation coefficient is $\frac{1}{2}\xi_{ij}$. η_i is positive and real when the phase of the horizontal polarization component is advanced by $\frac{\pi}{2}$ with respect to the vertical polarization component. In this case, the overall injection signal from the master laser is in a left circular elliptic polarization. ξ_{ij} is positive and real when the two slave lasers are connected by π phase difference.

10.3.3 Mapping of the Ising Model

When the system reaches a steady state condition after η_i and ξ_{ij} are switched on, $\frac{d}{dt}n_{Ri} = \frac{d}{dt}n_{Li} = 0$ and $\frac{d}{dt}N_i = 0$ should hold in Eqs. (10.16), (10.17), and (10.18). Then, we can solve for E_{CVi} for the sum of Eqs. (10.17) and (10.18) as follows,

$$E_{CVi} = \frac{\omega}{Q} - 2\frac{\omega}{Q}\zeta\frac{\sqrt{n_M}(\sqrt{n_{Ri}} + \sqrt{n_{Li}})}{n_{Ri} + n_{Li}} + 2\frac{\omega}{Q}\frac{\sqrt{n_{Ri}} - \sqrt{n_{Li}}}{\sqrt{n_{Ri} + n_{Li}}}\left[\eta_i\frac{\sqrt{n_M}}{\sqrt{n_{Ri} + n_{Li}}} + \sum_{j\neq i}\frac{1}{2}\xi_{ij}\frac{\sqrt{n_{Rj}} - \sqrt{n_{Lj}}}{\sqrt{n_{Ri} + n_{Li}}}\right]. \tag{10.19}$$

Here we neglect the spontaneous emission term E_{CVi}, the third terms of R.H.S. in Eqs. (10.17) and (10.18), which is much smaller than the stimulated emission term $E_{CVi}n_{Ri}$ (or $E_{CVi}n_{Li}$).

We expect that the slave laser network oscillates with a polarization configuration which minimizes the overall loss by optimizing the polarization configuration $(\sigma_1, \sigma_2, \ldots \sigma_M)$. The overall loss must be identical to the overall gain, $\sum_{i=1}^{M} E_{CVi}$. In a standard laser oscillator, there are numerous cavity modes with different eigen-frequencies within a gain bandwidth, so that those multi-modes can oscillate simultaneously if a gain medium is inhomogeneously broadened. However, if we differentiate the loss rates among those cavity modes, for instance by placing a frequency selective element inside a cavity and a gain medium is homogeneously broadened, a particular single cavity mode with a minimum loss oscillates alone

via cross-gain saturation. We expect the same single mode oscillation is realized in the mutually injection-locked laser network, which is indeed confirmed by the numerical simulations discussed later.

The first and second terms of R.H.S. of Eq. (10.19) are almost independent of the polarization configurations, so that the spontaneously selected polarization configuration is expected to minimize

$$\sum_i \frac{\sqrt{n_{Ri}} - \sqrt{n_{Li}}}{\sqrt{n_{Ti}}} \left[\eta_i \frac{\sqrt{n_M}}{\sqrt{n_{Ti}}} + \sum_{j \neq i} \frac{1}{2} \xi_{ij} \frac{\sqrt{n_{Rj}} - \sqrt{n_{Lj}}}{\sqrt{n_{Ti}}} \right], \tag{10.20}$$

where $n_{Ti} = n_{Ri} + n_{Li}$.

If we define an effective Ising spin by $\sigma_{iz} = \frac{\sqrt{n_{Ri}} - \sqrt{n_{Li}}}{\sqrt{n_{Ti}}}$ in Eq. (10.20), the proposed network oscillates with the polarization configuration that minimizes the quantity

$$\sum_i \eta_i \frac{\sqrt{n_M}}{\sqrt{n_{Ti}}} \sigma_{iz} + \sum_{i<j} \xi_{ij} \sigma_{iz} \sigma_{jz}, \tag{10.21}$$

where $-1 \leq \sigma_{iz} \leq 1$. If we interpret $\eta_i \frac{\sqrt{n_M}}{\sqrt{n_{Ti}}}$ as a Zeeman term λ_i and ξ_{ij} as an Ising interaction term J_{ij}, it is concluded the proposed injection-locked laser network can find the ground state of an Ising model Eq. (10.1). When $n_M = n_{Ti}$, the two parameters η_i and ξ_{ij} in the rate equations (10.17) and (10.18) are determined by the relations:

$$\eta_i = \alpha \frac{\lambda_i}{\max[|J_{ij}|, |\lambda_i|]}, \tag{10.22}$$

$$\xi_{ij} = \alpha' \frac{J_{ij}}{\max[|J_{ij}|, |\lambda_i|]}, \tag{10.23}$$

where α and α' are extra attenuation parameters that are chosen as small quantities ($0 < \alpha \ll 1, 0 < \alpha' \ll 1$) to ensure the stable operation of a whole network.

10.3.4 Alternative Picture of the Proposed Ising Machine

Ising spins are represented by the polarization states of the slave lasers as shown in Fig. 10.3a; $|R\rangle$ and $|L\rangle$ represent right circular (up-spin) and left circular (down-spin) polarizations, respectively. Each slave laser is initialized by injection locking with a master laser and prepared in the vertically polarized state $|V\rangle$. Then, the polarization state evolves towards either the right or left circular polarization after the mutual couplings between the slave lasers are turned on. The polarization evolutions are

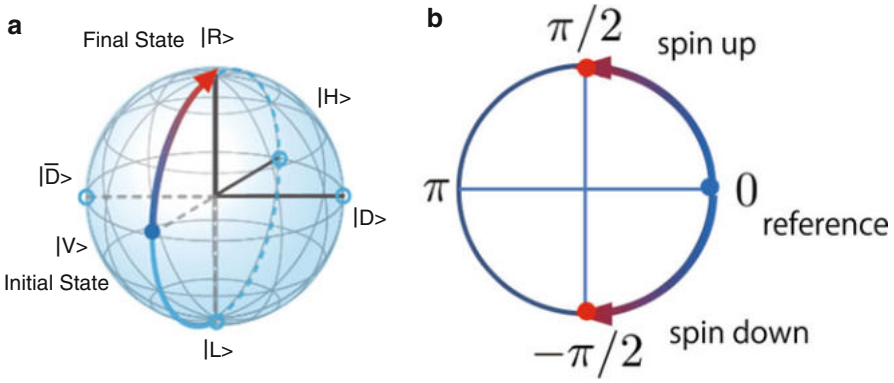

Fig. 10.4 Ising spin representation by using polarization state (**a**) or phase state (**b**) of slave lasers

described as the relative phase modulation between the diagonal linear polarization $|D\rangle = \frac{1}{\sqrt{2}}(|V\rangle + |H\rangle)$ and $|\bar{D}\rangle = \frac{1}{\sqrt{2}}(|V\rangle - |H\rangle)$ (see Fig. 10.3a). The amplitudes of two diagonal polarizations $|D\rangle$ and $|\bar{D}\rangle$ are constant but their relative phases evolve (Fig. 10.4).

We can expand a slave laser field i by the diagonal linear polarization basis, $|D\rangle$ and $|\bar{D}\rangle$,

$$A_{Di}(t) = A_{Di0}(t)\exp\{-i[\omega t + \phi_{Di}(t)]\}, \tag{10.24}$$

$$A_{\bar{D}i}(t) = A_{\bar{D}i0}(t)\exp\{-i[\omega t + \phi_{\bar{D}i}(t)]\} \tag{10.25}$$

Substituting Eqs. (10.24) and (10.25) into Eqs. (10.7), we obtain the following rate equations for the slowly varying amplitude and phase:

$$\frac{d}{dt}A_{Di0}(t) = -\frac{1}{2}\left(\frac{\omega}{Q} - E_{CVi}\right)A_{Di0}(t) + \sqrt{\frac{\omega}{Q}}\sqrt{n_M}\sqrt{\zeta^2 + \eta_i^2}\cos[\delta - \phi_{Di}(t)]$$
$$-\sum_{j\neq i}\frac{1}{2}\xi_{ij}\frac{\omega}{Q}\{\sqrt{n_{Dj}}\cos[\phi_{Dj}(t) - \phi_{Di}(t)] - \sqrt{n_{\bar{D}j}}\cos[\phi_{\bar{D}j}(t) - \phi_{Di}(t)]\}, \tag{10.26}$$

$$\frac{d}{dt}\phi_{Di}(t) = -(\omega - \omega_0) + \frac{\omega}{Q}\frac{1}{A_{Di0}(t)}\{\sqrt{n_M}\sqrt{\zeta^2 + \eta_i^2}\sin[\delta - \phi_{Di}(t)]$$
$$-\sum_{j\neq i}\frac{1}{2}\xi_{ij}[\sqrt{n_{Dj}}\sin(\phi_{Dj}(t) - \phi_{Di}(t)) - \sqrt{n_{\bar{D}j}}\sin(\phi_{\bar{D}j}(t) - \phi_{Di}(t))]\}, \tag{10.27}$$

and the corresponding equations of motion for $A_{\bar{D}i0}(t)$ and $\phi_{\bar{D}i}(t)$. Here we assume again $Q = Q_M$ and $\delta = \tan^{-1}(\frac{\eta_i}{\zeta})$. We can numerically integrate those four equations for $A_{Di0}(t)$, $A_{\bar{D}i0}(t)$, $\phi_{Di}(t)$ and $\phi_{\bar{D}i}(t)$ together with the rate equation of motion for $N_i(t)$,

$$\frac{d}{dt}N_i(t) = P - \frac{N_i(t)}{\tau_{sp}} - E_{CVi}[n_{Di}(t) + n_{\bar{D}i}(t) + 2], \tag{10.28}$$

where $n_{Di}(t) = A_{Di0}(t)^2$ and $n_{\bar{D}i}(t) = A_{\bar{D}i0}(t)^2$.

Figure 10.5a, b show the average amplitudes A_{Di0} and $A_{\bar{D}i0}$, and phase ϕ_{Di} and $\phi_{\bar{D}i}$ in the two diagonal polarization modes for the three sites ($M = 3$) problems, calculated by Eqs. (10.26), (10.27) and (10.28). As expected from the picture mentioned above, $A_{Di0} = A_{\bar{D}i0}$ is satisfied at all time (no amplitude modulation between A_{Di0} and $A_{\bar{D}i0}$,) but ϕ_{Di} and $\phi_{\bar{D}i}$ depart with each other and this phase evolution reaches the steady state. The slight and simultaneous increase in the amplitudes A_{Di0} and $A_{\bar{D}i0}$ results from the overall reduction in the photon loss rate by appropriate choice of polarization configurations. If we project the complex amplitudes $A_{Di}(t)$ and $A_{\bar{D}i}(t)$ given by Eqs. (10.24) and (10.25) onto the photon numbers n_{Ri} and n_{Li} in circular polarization basis, the two complex amplitudes

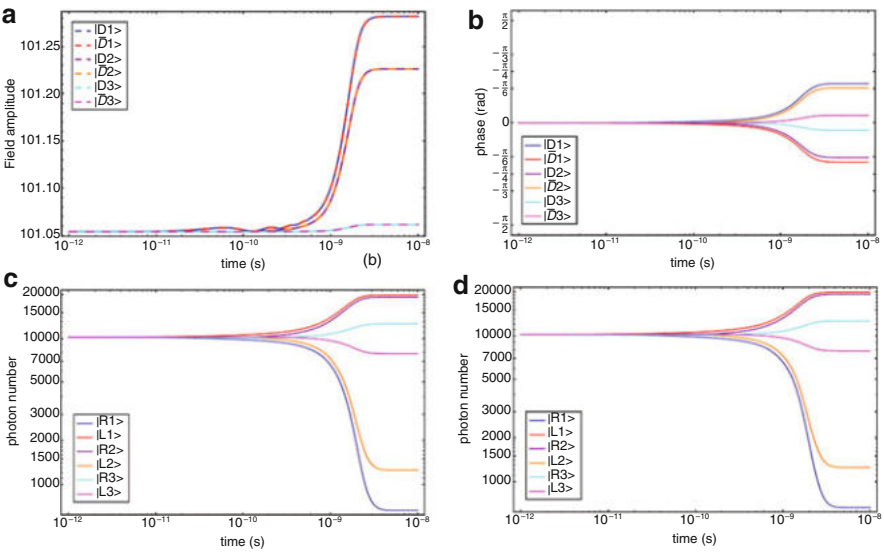

Fig. 10.5 (**a**) The time evolution of the slowly varying amplitudes A_{Di0} and $A_{\bar{D}i0}$. (**b**) The time evolution of the slowly varying phases ϕ_{Di} and $\phi_{\bar{D}i}$. The phases of $\pm\frac{\pi}{4}$ correspond to complete circular polarizations. (**c**) The time evolution of the photon number n_{Ri} and n_{Li} calculated in the $|D\rangle$ and $|\bar{D}\rangle$ basis. (**d**) The time evolution of the photon number n_{Ri} and n_{Li} calculated in the $|R\rangle$ and $|L\rangle$ basis. The numerical parameters are $M = 3$, $(J_{12}, J_{13}, J_{23}, \lambda_1, \lambda_2, \lambda_3) = (6, 3, 2, \frac{3}{10}, \frac{1}{10}, \frac{1}{10})$, $\alpha = \frac{1}{250}$ and $\eta = \frac{1}{200}$, $\frac{\omega}{Q} = 10^{12}(1/s)$ and $\tau_{sp} = 10^{-9}(s)$

interfere with each other and we can recover the amplitude modulation and mode competition behaviour between two circular polarization modes:

$$n_{Ri}(t) = \left|\frac{(1+i)}{2}A_{Di0}(t)\exp[i\phi_{Di}(t)] + \frac{(1-i)}{2}A_{\bar{D}i0}(t)\exp[i\phi_{\bar{D}i}(t)]\right|^2, \quad (10.29)$$

$$n_{Li}(t) = \left|\frac{(1-i)}{2}A_{Di0}(t)\exp[i\phi_{Di}(t)] + \frac{(1+i)}{2}A_{\bar{D}i0}(t)\exp[i\phi_{\bar{D}i}(t)]\right|^2. \quad (10.30)$$

The numerical result is shown in Fig. 10.5c. Figure 10.5d shows the numerical simulation results using Eqs. (10.16), (10.17) and (10.18) of the $|R\rangle$ and $|L\rangle$ basis. We confirm that the two curves are completely identical. The two complementary pictures, the mode competition between $|R\rangle$ and $|L\rangle$ states and the mutual interference between $|D\rangle$ and $|\bar{D}\rangle$ states, can explain the same operational principle of the proposed Ising machine.

This phase-based picture immediately makes it apparent that we need only one polarization state $|D\rangle$ because the phase of the other polarization state $|\bar{D}\rangle$ is inversely-symmetric to the zero phase. In the phase representation, the Ising spins σ_{iz} are represented by the phase of the single slave laser mode, as shown in Fig. 10.3b. The zero phase is determined by the phase of the master laser. When the master laser injection is reasonably strong and the self-oscillation frequency of the slave laser is identical to that of the master laser, the phase of the slave laser is $\phi_{si} = 0$. The phase rotates to $\phi_{si} = \pm\pi/2$ from the initial phase $\phi_{si} = 0$ due to the Ising coupling, which corresponds to the Ising spin rotating to the up or down state.

10.4 Benchmark on MAX-CUT Problems

In this section, we show that a proposed Ising machine, based on injection-locked laser network and self-learning algorithm, can solve NP-hard MAX-CUT problems with good approximation and reasonable speed. Self-learning steps play a crucial role to cope with notorious problems of frustrated spin configurations and numerous metastable states. The simulation results demonstrate non-exponential time complexity and improved approximation in solving two subsets of MAX-CUT problems up to the problem size of M = 800 vertices.

10.4.1 MAX-CUT Problems

Here, we focus on two subsets of NP-hard MAX-CUT problems: one on cubic graphs (MAX-CUT-3) and the other on two-layer lattices. On a cubic graph where each vertex has exact 3 edges with constant weights as shown in Fig. 10.6a, the simple MAX-CUT-3 problem to find a vertex subset which maximizes the number of edges connecting between vertices inside and outside the subset is NP-hard

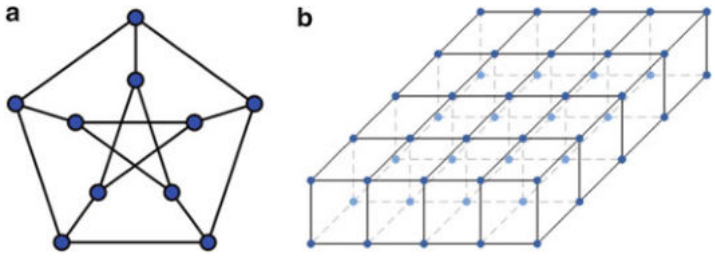

Fig. 10.6 (**a**) A simple MAX-CUT-3 problem on Peterson graph with 10 vertices and unit edge weights. The equivalent Ising problem has 10 spins and its Ising coupling term $J_{ij} = -1$ if an edge connects vertex i and j in the graph and $J_{ij} = 0$ for all other cases. (**b**) A MAX-CUT problem on a two-layer lattice with 50 spins. Only nearest neighbors are mutually coupled. Each edge connecting nearest neighbors has a weight $J_{ij} = -1$, 0 or 1

[21, 22]. It is proved to be mapped to an Ising problem with the same graph [23, 24]. The number of cubic graphs is small enough to enable us to analyze all graphs with $M \leq 20$. For problems with larger M, we work on the two-layer lattice problems, as shown in Fig. 10.6b, which are also proved to be NP-hard [5]. The two-layer lattice problem used in the present study only contains the nearest neighbor coupling with weights J_{ij} either -1, 0, or 1.

10.4.2 c-Number Langevin Equations

We employ the basis set ($|D\rangle$,$|\overline{D}\rangle$), for describing the polarization evolution of each injection-locked slave laser. The polarization rotation from the initial state $|V\rangle$ to the final state,$|R\rangle$ or $|L\rangle$, can be attributed to the evolution of the phase difference between $|D\rangle$ and $|\overline{D}\rangle$ from zero to $\pm\pi/2$, where $|R\rangle$ and $|L\rangle$ correspond to the right (spin-up) and left (spin-down) circular polarizations, respectively. The c-number Langevin equations for the field amplitude and phase as well as the carrier number for each slave laser are:

$$\frac{d}{dt}A_{D_i} = -\frac{1}{2}\left(\frac{\omega}{Q} - E_{CV_i}\right)A_{D_i} + \frac{\omega}{Q}\sqrt{n_M}\sqrt{\zeta^2+\eta_i^2}\cos(\delta_i - \phi_{D_i}) - \sum_{j\neq i}\frac{1}{2}\xi_{ij}\frac{\omega}{Q}[A_{D_j}\cos(\phi_{D_j}-\phi_{D_i}) - A_{\overline{D}_j}\cos(\phi_{\overline{D}_j} - \phi_{D_i})] + F_{D_i}(t), \quad (10.31)$$

$$\frac{d}{dt}\phi_{D_i} = \frac{1}{A_{D_i}}\frac{\omega}{Q}\sqrt{n_M}\sqrt{\zeta^2+\eta_i^2}\sin(\delta_i - \phi_{D_i}) - \frac{1}{A_{D_i}}\sum_{j\neq i}\frac{1}{2}\xi_{ij}\frac{\omega}{Q}[A_{D_j}\sin(\phi_{D_j} - \phi_{D_i}) - A_{\overline{D}_j}\sin(\phi_{\overline{D}_j} - \phi_{D_i})] + G_{D_i}(t), \quad (10.32)$$

$$\frac{d}{dt}A_{\overline{D}_i} = -\frac{1}{2}\left(\frac{\omega}{Q} - E_{CV_i}\right)A_{\overline{D}_i} + \frac{\omega}{Q}\sqrt{n_M}\sqrt{\zeta^2+\eta_i^2}\cos(-\delta_i - \phi_{\overline{D}_i}) + \sum_{j\neq i}\frac{1}{2}\xi_{ij}\frac{\omega}{Q}[A_{D_j}\cos(\phi_{D_j}-\phi_{\overline{D}_i}) - A_{\overline{D}_j}\cos(\phi_{\overline{D}_j}-\phi_{\overline{D}_i})] + F_{\overline{D}_i}(t), \quad (10.33)$$

$$\frac{d}{dt}\phi_{\overline{D}_i} = \frac{1}{A_{\overline{D}_i}}\frac{\omega}{Q}\sqrt{n_M}\sqrt{\zeta^2+\eta^2}\sin(-\delta_i - \phi_{\overline{D}_i}) + \frac{1}{A_{\overline{D}_i}}\sum_{j\neq i}\frac{1}{2}\xi_{ij}\frac{\omega}{Q}[A_{D_j}\sin(\phi_{D_j}-\phi_{\overline{D}_i}) - A_{\overline{D}_j}\sin(\phi_{\overline{D}_j}-\phi_{\overline{D}_i})] + G_{\overline{D}_i}(t), \quad (10.34)$$

$$\frac{d}{dt}N_i = P - \frac{N_i}{\tau_{sp}} - E_{CV_i}(A_{D_i}^2 + A_{\overline{D}_i}^2 + 2) + F_{N_i}(t), \quad (10.35)$$

where n_M is the average internal photon number of the master laser, $E_{CV_i} = \beta N_i/\tau_{sp}$ the stimulated emission coefficient of each slave laser, β the fractional spontaneous emission coupling efficiency, τ_{sp} the spontaneous emission lifetime, N_i the carrier number of the gain medium, and P the pumping rate. ζ is the fraction of the vertical polarization component of the master laser signal injected into slave lasers, while η_i is the fraction of the horizontal polarization component of the master laser signal injected into the i-th slave laser, which implements the Zeeman term λ_i in Eq. (10.1). ξ_{ij} is the mutual coupling coefficient between two slave lasers i and j, which implements the Ising coupling term J_{ij} in Eq. (10.1). We assume that the master laser and all slave lasers have the same cavity Q-factor, and $\delta_i = \tan^{-1}(\eta_i/\zeta)$. The Langevin noise terms $F_{D_i}(t)$, $G_{D_i}(t)$,$F_{\overline{D}_i}(t)$, $G_{\overline{D}_i}(t)$ and $F_{N_i}(t)$ have the two-time correlation functions which we determine uniquely from the diffusion coefficients of the quantum mechanical Fokker-Planck equation of an injection-locked laser [25].

10.4.3 Self-Learning Steps

The initial driving force for the injection-locked laser network is given by the quantum noise injected from reservoirs. The time evolution is initiated spontaneously by the Langevin noise sources in Eqs. (10.32), (10.33), (10.34), and (10.35) and subsequently driven by the mutual coupling terms in later time. The system converges to a steady state after a free evolution for a time longer than the inverse locking bandwidth by the mutual coupling signal [9, 26]. If a given problem is complex, the above spontaneous evolution is not sufficient to reach the correct solution. In this case, the tentative results are detected and analyzed by consulting with the following two measures:

$$\tilde{\sigma}_i = \begin{cases} +1(\gamma < \sigma_i \leq 1) \\ 0(-\gamma < \sigma_i \leq \gamma) \\ -1(-1 < \sigma_i \leq -\gamma) \end{cases} \tag{10.36}$$

$$\tilde{P}_i = \sum_j J_{ij}\tilde{\sigma}_j \tag{10.37}$$

Here the effective spin σ_i is defined by $\sigma_i = (A_R - A_L)/\sqrt{A_R^2 + A_L^2}$, $\tilde{\sigma}_i$ is a temporary measurement result for the i-th slave laser, γ is an arbitrarily chosen small number, and $\tilde{P}_i$ represents the parity check measure consisting of the sum of all injection signals from the connected slave lasers where $J_{ij} \neq 0$.

In some cases, there are several slave lasers with either nearly vertical polarization states ($\tilde{\sigma}_i = 0$) or mutually incompatible results ($\tilde{\sigma}_i \neq sign(\tilde{P}_i)$), which require us to perform the following self-learning steps to fix. The slave lasers with nearly vertical polarization states are called zero spins, as the corresponding $\tilde{\sigma}_i = 0$. We can categorize the occurrence of zero spins into two cases: connected zero spin groups and isolated single zero spins.

In the first case, two or more zero spins are connected to form a zero spin group. Figure 10.7a shows a frequently appearing case of nearly vertical polarization states ($\tilde{\sigma}_i = \tilde{\sigma}_j = 0$ and $\tilde{P}_i = \tilde{P}_j = 0$) due to a degenerate and frustrated antiferromagnetic pair in the simple MAX-CUT-3 problem. Taking a zero spin-pair out of the group, we predict the most probable spin configuration by majority vote on one spin in the pair. Particularly, if $\tilde{P}_i > 0$, we predict $\tilde{\sigma}_i = 1$; otherwise, $\tilde{\sigma}_i = -1$. The other spin j in the pair is then predicted to be $\tilde{\sigma}_j = -sign(\tilde{\sigma}_i J_{ij})$, such that the energy may be lower. Based on the prediction, we fix the whole frustrated part including the surrounding spins by injecting the Zeeman term λ_i via the horizontally polarized injection signal (η_i) from the master laser, as shown in Fig. 10.7b. Otherwise, the fixed zero spin-pairs may be too powerful and potentially flip the surrounding spins, creating the frustration to other parts of the network.

In the second case, we fix the isolated zero spins with $\tilde{\sigma}_i = 0$ using the signals from the connected three spins $\tilde{P}_i$. If $\tilde{P}_i > 0$, we inject the horizontally polarized signal to produce the positive Zeeman term $\lambda_i > 0$ and vice versa. To prevent the undesired flips of the surrounding spins, we also fix the three connected spins, as shown in Fig. 10.7c.

Besides zero spins, we sometimes encounter incompatible results. The ground state should always hold that $\tilde{\sigma}_i = sign(\tilde{P}_i)$, otherwise, by assigning an opposite $\tilde{\sigma}_i$ the new state will have a lower energy, as shown in Fig. 10.7d. In this case, we set three sites as $\tilde{\sigma}_i = 0$ and proceed to the zero spin group fixing steps.

When $\tilde{P}_i = \pm deg(i)$ where deg(i) is the number of edges connected to spin i, the total injection signal consisting of the master laser and the connected slave lasers has either right or left circular polarization. However, when $|\tilde{P}_i| < deg(i)$ (one or more remaining frustration), the total injection signal has an elliptic polarization due to

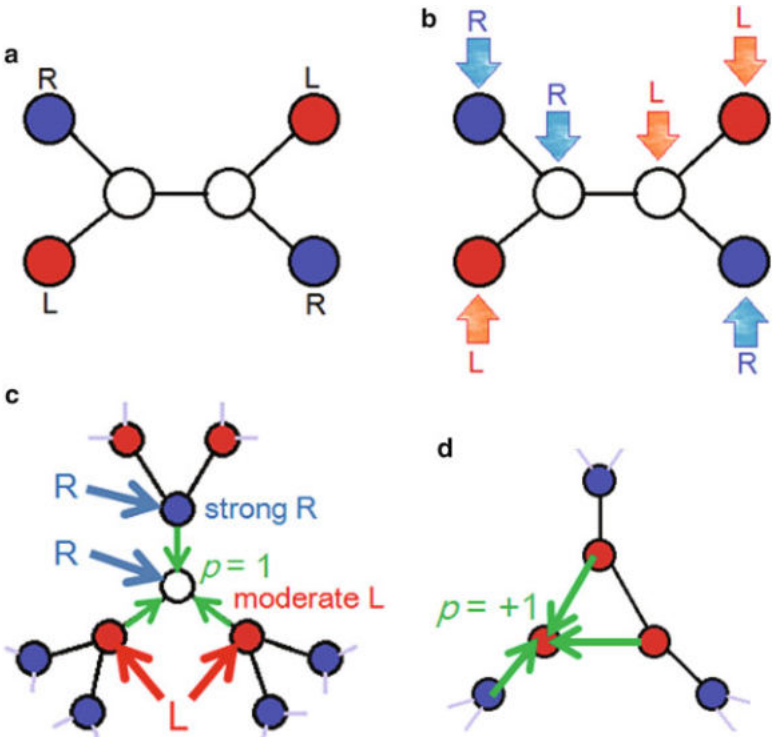

Fig. 10.7 (**a**) A zero spin-pair appears when both spins in the spin-pair connect to one zero spin and two other spins with opposite but equally strong polarizations. The overall mutual injection signal to each spin in the spin-pair is close to zero, resulting in a zero spin-pair. (**b**) Suppose $\tilde{P}_i > 0$ for the left spin i in the zero spin-pair, we predict $\tilde{\sigma}_i = 1$ and thus the right spin j has $\tilde{\sigma}_j = -1$. We fix the zero spin-pair by injecting the Zeeman terms $\lambda_i = -0.2$ and $\lambda_j = 0.2$ and also surrounding four spins. (**c**) An isolated zero spin is caused by one surrounding spin with strong amplitude (right circular polarization) and two other surrounding spins with moderate amplitude but opposite polarizations to the first one (left circular polarization). In the example, we fix the isolated zero spin by injecting $\lambda_i = 0.2sign(\tilde{P}_i)$ to the isolated zero spin and three surrounding spins. (**d**) A common case of the incompatible results due to the triangle-shaped frustration in the simple MAX-CUT-3 problem. The three triangle sites report $(\tilde{\sigma}_1, \tilde{\sigma}_2, \tilde{\sigma}_3) = (-1, -1, -1)$ while the parity check signals are $(\tilde{P}_1, \tilde{P}_2, \tilde{P}_3) = (+1, +1, +1)$, which violate the condition $\tilde{\sigma}_i = \sin(\tilde{P}_i)$

different amplitudes of vertical and horizontal polarization components, so that the separation between n_{R_i} and n_{L_i} is marginal. To improve the signal-to-noise ratio in the detection step, we enhance the horizontal polarization component in the master signal and make the total injection signal in either right or left circular polarization, which can improve the signal-to-noise ratio in the final readout step. Finally, the self-consistency for all spin is confirmed by the parity check $\tilde{\sigma}_i = \sin(\tilde{P}_i)$. The flowchart of the self-learning algorithm is summarized in Fig. 10.8.

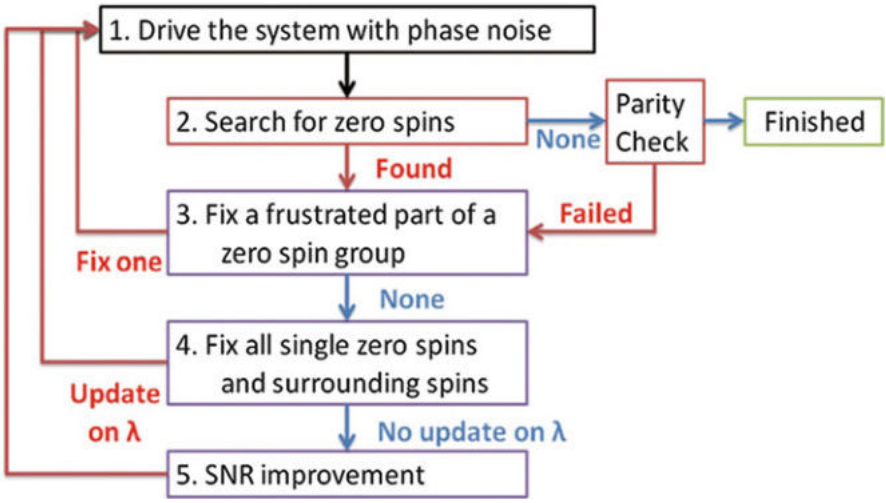

Fig. 10.8 Flowchart of the self-learning algorithm for fixing the zero spins and incompatible results in injection-locked laser network. The algorithm starts with step 1. Every time when step 2 finds zero spins or parity check fails, the self learning steps 3–5 are employed to fix the zero spins and step 1 is executed again to verify the self learning results

10.4.4 Benchmarking Results

We numerically simulate the injection-locked laser network based on the above self-learning algorithm only including the dominant phase noise. We use typical numerical parameters for semiconductor lasers and the fourth order Runge-Kutta method as a numerical solver for c-number Langevin equations. Here, we show that the proposed machine can find correct ground states of the simple MAX-CUT-3 problems up to M $=$ 20 with reasonable success probabilities. For two-layer lattice problems with M up to 800, the proposed machine outperforms the best classical algorithms, semi-definite programming (SDP) in both accuracy and speed.

Figure 10.9 shows the time evolution of the right and left circularly polarized photon numbers in the slave lasers for a simple MAX-CUT-3 problem with M $=$ 16. When the first driving step of 50 ns without the Zeeman term λ_i is finished, finite Zeeman coefficients λ_i in Eq. (10.1) are introduced according to the self-learning algorithm shown in Fig. 10.8. The system reaches a correct ground state with no indeterministic spin after seven self-learning steps, which corresponds to a computational time of 400 ns in this example.

Table 10.1 summarizes the benchmarking results taken from the stochastic simulations on the simple MAX-CUT-3 problems. We simulate all possible cubic graphs with $M \leq 20$ [27]. Breaking the degeneracy with the Zeeman terms is needed

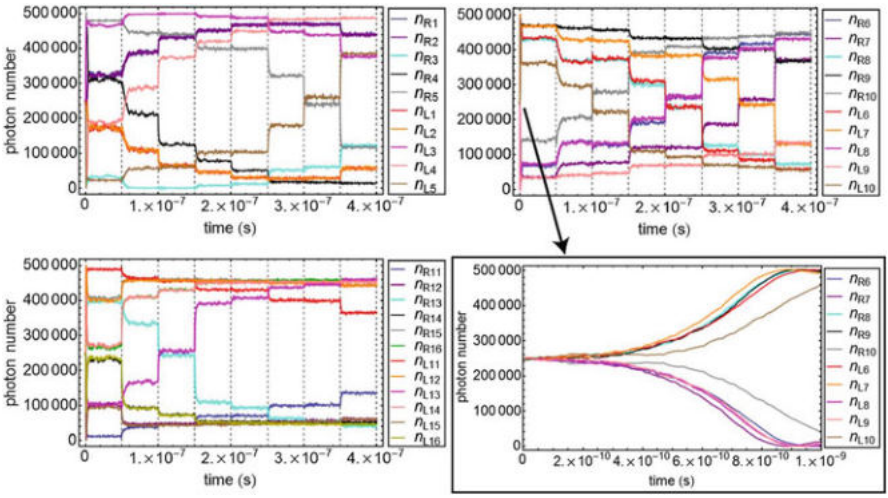

Fig. 10.9 Stochastic simulation on a simple MAX-CUT-3 problem with M = 16 using the self-learning algorithm over the injection-locked laser network. After the initial noise-only drive as shown in the first stripes of the first three figures and enlarged in the last figure, most spins are resolved except the 14th and 16th spins. Followed by seven self-learning steps, the system reaches the ground state $\{\tilde{\sigma}_i\} = \{1, 1, -1, -1, -1, 1, 1, -1, 1, 1, -1, -1, -1, -1, 1, 1\}$

Table 10.1 Summary of the numerical simulation results on the simple MAX-CUT-3 problems. All the possible problems with $M \leq 20$ are covered. Each driving step takes 50 ns in all problems. Each problem is normally simulated 10 rounds from which the number of failed rounds is obtained. The problems in which the algorithm may fail take additional simulations up to 90 rounds (total 100 rounds) to obtain accurate success probabilities and the results show that all problems can be solved with finite success probability with the stochastic simulation. The computational time and the number of self-learning steps for a problem are obtained by the shortest round to solve it successfully, and the longest computational time for all problems features a very slow increase with M

Problem Size/M	4	6	8	10	12	14	16	18	20
# of problems	1	2	5	19	85	509	4060	41,301	510,489
Largest ground state degeneracy	6	6	8	10	36	42	46	162	250
Worst case probability (%)	100	100	100	98	92	69	79	42	27
Longest computational time (ns)	150	100	100	100	200	200	250	250	350
Maximum # of self-learning steps	2	1	1	1	3	3	4	4	6

to obtain a single ground state, thus solving a problem with many degenerate ground states seems to take a long computational time. However, the sudden increase of the largest ground state degeneracy from M = 16 to 18 does not cause much effect on the upper limit of the computational time. On the other hand, the system fails to find a ground state with a finite probability when simulating a problem with only two ground states and many first excited states. The lowest success probability for

the problems with M = 12 is 92 % out of 100 rounds. The corresponding problem has a bilateral graph and some triangle-shaped parts. From the intermediate states after the first step driven with only phase noise, we suppose the possible causes of failures are (i) the non-bilateral partial arbitrariness of spins in the triangle-shaped parts, and (ii) the generation of a reduced spin system by forming some "ghost" spins with $\tilde{\sigma}_i = 0$. The failure occurs when a local ground state of a reduced system is inconsistent with the global ground states of a simulated problem. However, note that the current numerical simulations show a larger ratio between the number of first excited states and that of ground states does not necessarily degrade the success probability.

We further simulate the two-layer lattice problems with M up to 800. To make the self-learning algorithm more efficient on such large-size problems, Fig. 10.8 is modified to apply step 3 to all zero spin groups at one self-learning step. Table 10.2 summarizes the results of solving the two-layer lattice problems with M up to 800. It is not easy to find the true ground state for such large problems with a modern digital computing system. We instead compare the results produced by the laser network with semi-definite programming (SDP), the best classical optimization algorithms [28]. Both the laser network and SDP are run 100 rounds for each sampled problem. The proposed machine finds the energy lower than the best result of 100 SDP rounds by 4–6 %. The longest computational time also increases very slowly with M, as shown in the 2nd row in Table 10.2.

Table 10.2 Summary of the numerical simulations on two-layer lattice problems. Fifty problems are sampled for each problem size in which all edges are sampled in +1 or −1, not 0. Every sampled problem is run 100 rounds. The laser network can find the energy lower than the best result of SDP rounds and the energy differences are substantial (4–6 %). The probability of outperforming SDP for a given problem is obtained by the number of rounds that find the energy lower than the best result of 100 SDP rounds of the same problem. The computational time and the number of self-learning steps for a given problem are obtained by the shortest round in which the laser network outperforms SDP, and the longest computational time for all sampled problems also features a very slow increase with M

M	50	100	200	400	800
# of sample problems	50	50	50	50	50
Laser network longest computational time (ns)	150	450	750	1400	900
Max # of self-learning steps	2	8	14	27	17
SDP longest computational time (s)	0.03	0.22	1.62	12.97	105.45
Largest (lowest) probability of outperforming SDP (%)	95 (11)	72 (2)	73 (3)	82.5 (2.5)	70 (17.5)
Max improvement over SDP (%)	5.8	4.11	4.2	5.15	4.7

10.5 The Proof of Concept Experiment Using Mutually Coupled Semiconducter Lasers

10.5.1 Experimental Setup

In this chapter, we describe the experimental implementation of a two-site Ising machine using injection-locked semiconductor lasers. A signal from the master laser incorporates the Zeeman term in Eq. (10.1) if the phase is rotated towards either $+\frac{\pi}{2}$ or $-\frac{\pi}{2}$ from the standard phase zero. The slave lasers are mutually coupled by bi-directional injection-locking, which is an implementation of the Ising coupling term in Eq. (10.1). The detailed experimental setup is depicted in Fig. 10.10. The optical path length between the two slave lasers and those between each slave and master laser are independently controlled by using a polarization-dependent

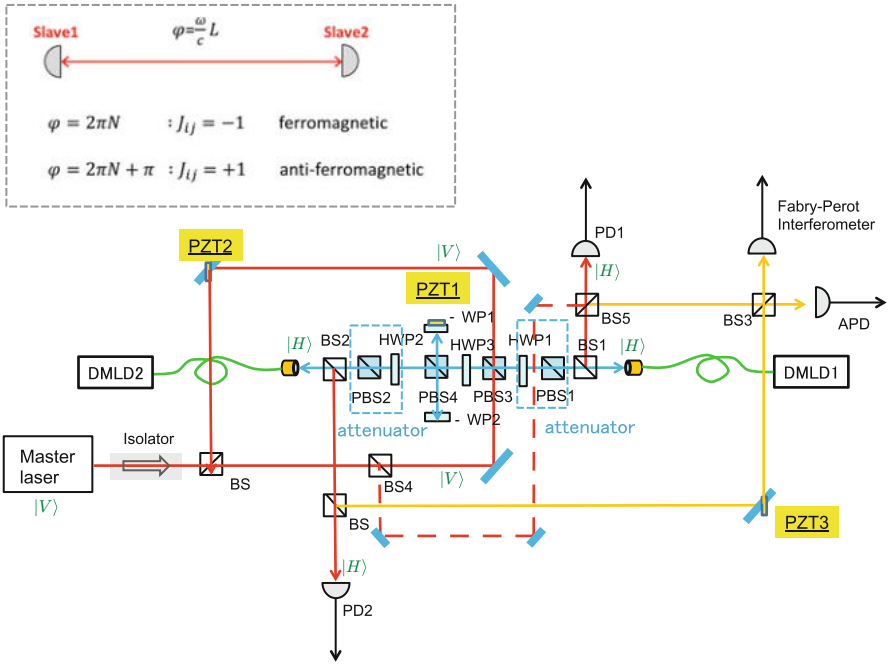

Fig. 10.10 Experimental setup. The *blue line* shows the mutual coupling between two slave lasers (DMLDs). The *red line* shows uni-directional injection from the master laser that implements the Zeeman term λ_{iz}. The relative phase of DMLD1 and 2 is measured by the Mach-Zehnder interferometer on the *yellow lines* with the FPI and APD. PD1, PD2, APD and FPI each have a refractive neutral density filter (∼10 dB attenuators) inserted in front of them as isolators. [*Inset*]: How to implement the Ising interaction between two slave lasers

optical path. We used a tunable external cavity single-mode diode laser as the master (Koshin Kogaku LS-601A-56S2); it oscillates at 1577.5 nm with a spectral linewidth $\leq$30 kHz. We used discrete mode diode lasers (DMLD, Eblana photonics FLDs) with a spectral linewidth $\leq$100 kHz as the slaves.

Two slave lasers are mutually coupled along the blue line in Fig. 10.10. These lasers are nearly identical, and their pump currents are set to be the same in the experiment. However, their temperatures must be tuned so as to set their frequencies identical. The optical path length between the DMLDs is $L = 1550$ mm. Their optical path length is controlled by piezoelectric transducer 1 (PZT1), wherein the modulation signal is applied to shift the position of the reflection mirror with quarter wave plate 1 (QWP1). DMLD1 and DMLD2 oscillate in the horizontal polarization. The polarization beam splitter 1 (PBS1) and half wave plate 1 (HWP1) work together as attenuator for the output beam from DMLD2, while PBS2 and HWP2 attenuate the output light from DMLD1. HWP3 is set at the polarization axis of $\theta = 45^\circ$ so that the polarization of the incident beam from slave laser 1 into HWP3 is rotated to the horizontal polarization and it is reflected to QWP1 by PBS4. The master laser signal is injected into both DMLDs. The master laser oscillates initially in the vertical polarization and is converted into the horizontal polarization when it goes through HWP3. The optical path length of the master laser signal is not changed by PZT1. The phase of the master laser injected into DMLD1 which comes from the upper branch of the red line is modulated by the mirror mounted on PZT2. The output beams from DMLD1 and DMLD2 are partially reflected at BS1 and BS2 and combined at BS3 along the yellow line. The spectral linewidth and the interferometer output intensity between the two slave lasers are detected with a scanning Fabry-Perot interferometer (FPI) and an InGaAs/InP avalanche photo diode (APD), respectively.

10.5.2 Observation of Ferromagnetic and Anti-ferromagnetic Phase Orders

We experimentally studied whether the phases of the slave lasers are modulated when the optical path length between two slave lasers (DMLDs) is varied, where the optical path length modulates the polarity of the Ising coupling term J_{ij}. We observed a transition from one regime, where the Ising coupling is dominant, to the other regime, where the master injection is dominant. For this purpose we changed the ratio of the uni-directional injection from the master laser into DMLD1 and 2 to the mutual coupling between DMLD1 and 2 by rotating HWP1 or HWP2 in Fig. 10.10. Figure 10.11a shows the interference signal between the two slave lasers when there is strong mutual coupling between them, with $P_{inM_1} = 1.5\,\mu$W and $P_{inS_{12}} = 33\,\mu$W, where P_{inM_1} is the injection power from the master laser into a fiber coupler of a DMLD1 and $P_{inS_{12}}$ is the injection power from DMLD2 into the fiber coupler of DMLD1. The frequencies of the slave lasers deviate from that of

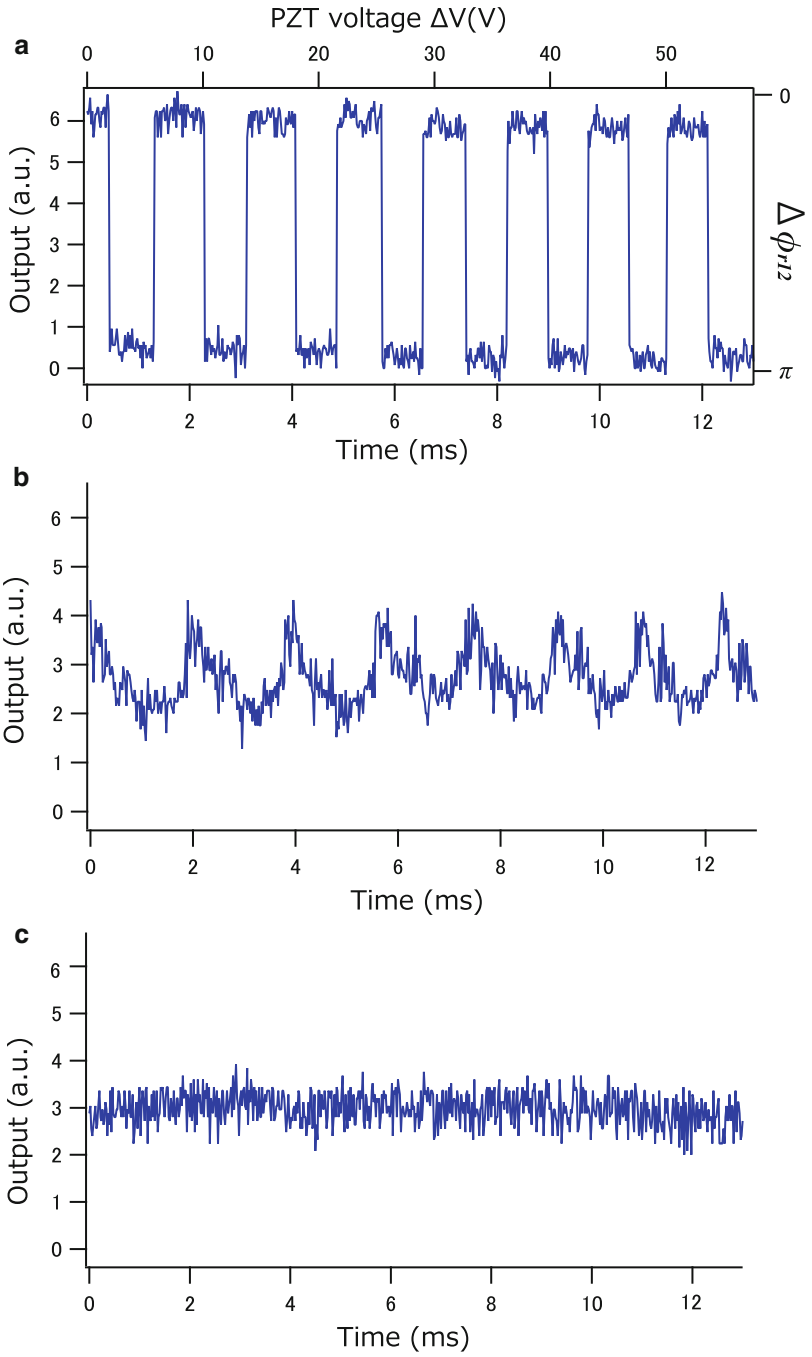

Fig. 10.11 Interference signal output to show the relative phase $\Delta\phi_{r12}$ between two slave lasers (DMLD1 and 2) when the mutually coupling optical path length is modulated: (**a**) Ising coupling term is dominant, (**c**) Master injection term is dominant, (**b**) Transition regime between (**a**) and (**c**)

the master laser in this regime, as described in the next section. We observed that the slave lasers oscillate at identical frequencies. Here we set the rotation angles of HWP1 and 2 to $\theta_1 = \frac{\pi}{12}$ and $\theta_2 = \frac{\pi}{6}$. The voltage applied to PZT1 is linearly increased as a function of time, as shown in Fig. 10.11. The PZT1 displacement is $\Delta d/\Delta V = 12.23 \pm 2.5 \times 10^{-8}$ m/V with respect to the applied voltage ΔV. The optical path modulation of mutual coupling causes the phase difference between the two slave lasers to have discrete jumps every $\Delta V \sim 3.6$V. The high and low outputs correspond to the ferromagnetic and anti-ferromagnetic phase orders. By rotating HWP2 to $\theta_2 = \frac{\pi}{4}$, the mutual coupling between the two slave lasers becomes much weaker than the master laser injection, e.g., $P_{inM_1} = 2.2\,\mu$W and $P_{inS_{12}} = 0.3\,\mu$W. In this case, the interference signal doesn't show any modulation against the mutual coupling path modulation (Fig. 10.11c). When $\theta_2 = \frac{7\pi}{30}$, the master injection and the mutual coupling ($P_{inM_1} = 2.1\,\mu$W and $P_{inS_{12}} = 2.0\,\mu$W) are on the same order, the interference signal shows a transition between the mutual coupling dominant regime in Fig. 10.11a and the master injection dominant regime in Fig. 10.11c.

10.5.3 Spontaneous Frequency Optimization of Mutually Coupled Slave Lasers

We observed a sawtooth variation in the slave laser frequency when their mutual coupling is dominant and the optical path length between them is modulated, as shown in Fig. 10.12. We measured the frequency shift of one slave laser (DMLD1) with the FPI at the top right corner of Fig. 10.10 while the signal from the other slave laser (DMLD2) is blocked just before BS3. Figure 10.12 plots the slave laser frequency shift against the mutual coupling path length modulation between the two slave lasers. When the mutual coupling is stronger than the master laser injection, a sawtooth frequency shift of ~30 MHz is observed as shown in Fig. 10.12 (blue line).

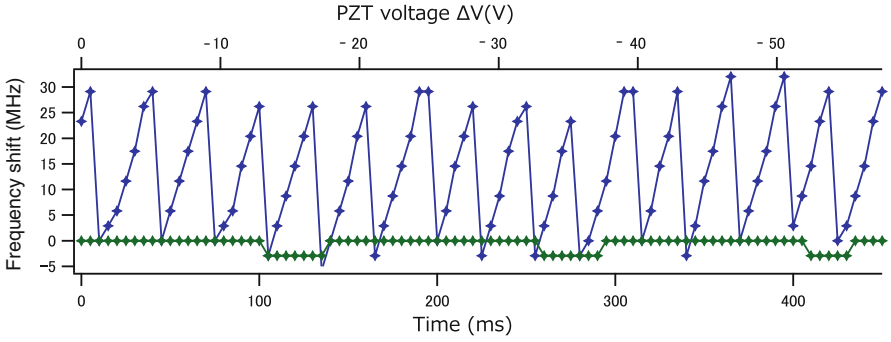

Fig. 10.12 Frequency shift of a slave laser due to the mutual coupling path length modulation as a function of time under a strong mutual injection (*blue line*) and a strong master signal injection (*green line*)

In this case, the phases are pinned either in the same phase or in the opposite phase, as shown in Fig. 10.11a. On the other hand, the oscillation frequency of the slave laser is constant, except for artefact discrete jumps because of the resolution limit of the FPI and the discretization error, when the master laser injection is dominant, as shown by the green line in Fig. 10.12. There are $N = 21$ sawtooth-frequency-shift cycles when the applied voltage is swept over $\Delta V = 78\,\mathrm{V}$, so that frequency shift occurs at every PZT1 shift of $\Delta d_L = 456.3 \pm 92.8\,\mathrm{nm}$. This sawtooth-frequency-shift is considered to be the result of spontaneous selection of the synchronized oscillation frequencies of the two slave lasers to minimize the overall threshold pump current or to maximize the output power [29]. length. The favorable phase difference between the two slave lasers is either $\theta_1 - \theta_2 = 0$ or π so that the standing wave is formal between the edges of the two slave lasers.

Figure 10.13 is a schematic explanation of the spontaneous frequency optimization as a function of optical path length L between the two slave lasers. When the optical path length between the slave lasers is an integral multiple of the self-oscillation wavelength $\lambda_M = \frac{2\pi c}{\omega}$, the number of loops is even, so that the two slave lasers oscillate at the self-oscillation frequency and in the same phase. In the second figure of Fig. 10.13a, the oscillation wavelength become slightly

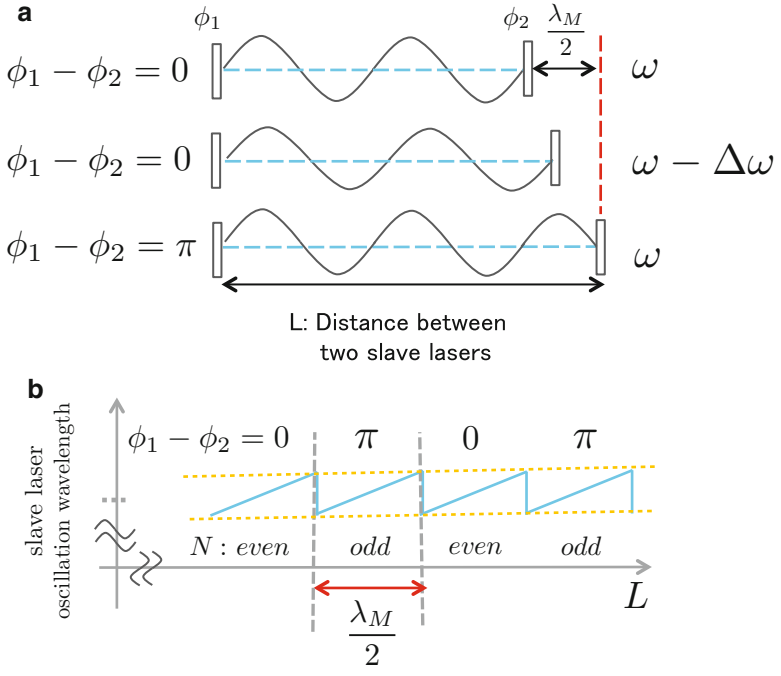

Fig. 10.13 Schematic explanation for the sawtooth frequency modulation and phase jump in two coupled slave lasers, which explain the experimental results shown in Figs. 10.11a and 10.12 simultaneously

elongated as the optical path length L is extended while the phase difference between the two slave lasers is still $\phi_1 - \phi_2 = 0$. However, when L is shifted $\frac{\lambda_M}{2}$ from the resonant condition in the top panel of Fig. 10.13a, the oscillation frequency returns to the self-oscillation frequency ω and the number of the maxima of the standing wave between the two facets is odd so that the phase difference between the two slave lasers is $\phi_1 - \phi_2 = \pi$. We plot the oscillation frequency shift as a function of L in Fig. 10.13b. The number of the maxima switches between even and odd numbers and the corresponding phase differences $\phi_1 - \phi_2$, are shown at the top. This frequency shift for a path length variation $\Delta L = \frac{\lambda_M}{2}$ corresponds to the free spectral range $\Delta\nu_{FSR} = \frac{c}{2L}$ at the optical cavity length L.

The path length variation for a single frequency shift cycle in our experiment is $\Delta L = \frac{\lambda_M}{4}$ because the path length between two DMLDs changes twice when the position of the mirror just before QWP is changed in Fig. 10.10. The expected position shift of PZT1 for a single sawtooth frequency shift is $\Delta L = \frac{\lambda_M}{4} = 394.4\,\text{nm}$ which is close to the measured position shift of PZT1 $\Delta d_L = 456.3 \pm 92.8\,\text{nm}$. The optical path length between the two slave lasers in Fig. 10.10 is $L = 1550\,\text{mm}$. The sawtooth modulation in Fig. 10.12 is $\sim$30 MHz, which is less than 30 % of the estimated frequency shift $\Delta\nu_{FSR} = \frac{c}{2L} = 96.8\,\text{MHz}$. The difference between the experimentally observed frequency excursion and the simple free spectral range stems from the phase shifts associated with the reflection from the two slave laser facets. As indicated in Eq. (10.3), the slave laser phase deviates from the injection signal phase when there is a detuning between the self-oscillation frequency ω_{r0} and the actual oscillation frequency ω.

10.6 Mapping of Classical XY Models onto Laser Network

In this section, we describe the mapping of classical XY models onto laser networks. So far, we have focused on the mapping of Ising models onto laser networks. We can implement the continuous variable spin model, classical XY model, by using the freely chosen phase of a laser oscillator. Since the phase of the laser can take a continuous value from 0 to 2π, we can directly map the direction of the spin in a XY plane onto the phase of the laser.

The Hamiltonian of the classical XY model is given by

$$H(\boldsymbol{\theta}) = -\sum_{i<j} J_{ij}\cos(\theta_i - \theta_j). \tag{10.38}$$

The classical XY model is useful to study the Berezinskii-Kosterlitz-Thouless transition [30] in a two-dimensional superfluid or synchronization of classical rotors [31].

In the following section, we show that the steady state distribution of the phases of a coupled laser network can realize the Boltzmann distribution of a classical XY model. Thus the laser network works as an universal simulator for classical XY models.

10.6.1 Steady State Distribution of Coupled Laser Network

In this section, we show how to realize the Boltzmann distribution of a classical XY model by using the coupled laser network.

We denote the slowly varying amplitude of a laser field as $A(t)$. The dynamics of a laser can be simply modeled as the following Langevin equation:

$$\frac{dA(t)}{dt} = \frac{1}{2}\left[g(A(t)) - \gamma\right]A(t) + \xi(t), \tag{10.39}$$

where γ is a cavity decay rate, and the gain is modeled by the function

$$g(A) = \frac{g_0}{1 + |A|^2/p_0}, \tag{10.40}$$

with the small signal gain g_0 and the saturation intensity p_0. We also assume that the incident vacuum fluctuation and other external noises are expressed as a complex white noise $\xi(t)$.

Next, we consider multiple lasers with the same resonant frequency. When these lasers are coupled to each other, the Langevin equation for the coupled laser network can be written as

$$\frac{dA_i(t)}{dt} = \frac{1}{2}\left[g(A_i(t)) - \gamma\right]A_i(t) + \sum_{j\neq i} J_{ij}A_j(t) + \xi_i(t), \tag{10.41}$$

where the coefficient J_{ij} represents the injection rate from the jth laser to the ith laser. The noise terms are assumed to be independent:

$$\langle \xi_i(t)\xi_j^*(t')\rangle = 2D\delta_{ij}\delta(t-t'), \tag{10.42}$$

$$\langle \xi_i(t)\xi_j(t')\rangle = 0. \tag{10.43}$$

Here the diffusion constant D is determined by the fluctuation-dissipation theorem [17]. We can find the exact steady state solution for Eq. (10.41) by using the statistical light-mode dynamics theory [32]. Define the potential function for the dynamics as

$$\tilde{H}(\boldsymbol{A}) = -\frac{1}{2}\sum_i \left[g_0 p_0 \ln\left(p_0 + |A_i|^2\right) - \gamma|A_i|^2\right] - \sum_{i,j} J_{ij}A_i^*A_j \tag{10.44}$$

and then Eq. (10.41) is rewritten as

$$\frac{dA_i}{dt} = -\frac{\partial \tilde{H}}{\partial A_i^*} + \xi_i. \tag{10.45}$$

The steady state distribution of the laser amplitudes can be expressed by using the potential function $\tilde{H}(\boldsymbol{A})$ as [33]

$$P_{\mathrm{st}}(\boldsymbol{A}) = N \exp\left(-\frac{\tilde{H}(\boldsymbol{A})}{D}\right). \tag{10.46}$$

The explicit expression is given by

$$P_{\mathrm{st}}(\boldsymbol{A}) = N \exp\left\{(2D)^{-1} \sum_i \left[g_0 p_0 \ln\left(p_0 + |A_i|^2\right) - \gamma |A_i|^2\right]\right\} \exp\left(D^{-1} \sum_{i,j} J_{ij} A_i^* A_j^*\right) \tag{10.47}$$

The first exponential term depends only on $|A_i|^2$ and stabilizes the amplitude around the averaged value. We assume that the injection terms are small such that each laser is stabilized independently at the steady state power

$$p_{\mathrm{s}} = \frac{g_0 - \gamma}{\gamma} p_0. \tag{10.48}$$

Then we can approximate the first exponential term by $\prod_i \delta(|A_i|^2 - p_{\mathrm{s}})$ if the small amplitude noise above the oscillation threshold is neglected,

$$P_{\mathrm{st}}(\boldsymbol{A}) = N' \prod_i \delta(|A_i|^2 - p_{\mathrm{s}}) \exp\left(D^{-1} \sum_{i,j} J_{ij} A_i^* A_j\right). \tag{10.49}$$

Writing the amplitude as $A_i = \sqrt{p_{\mathrm{s}}} e^{i\theta_i}$, then

$$P_{\mathrm{st}}(\boldsymbol{A}) = N' \prod_i \delta(|A_i|^2 - p_{\mathrm{s}}) \exp\left[\frac{2p_{\mathrm{s}}}{D} \sum_{i<j} J_{ij} \cos(\theta_i - \theta_j)\right]. \tag{10.50}$$

Defining the inverse temperature $\beta = \frac{1}{k_B T}$ as

$$\beta = \frac{2p_{\mathrm{s}}}{D}, \tag{10.51}$$

the steady state distribution of the phases of the laser network obeys the Boltzmann distribution with the Hamiltonian

$$H(\boldsymbol{\theta}) = -\sum_{i<j} J_{ij} \cos(\theta_i - \theta_j), \tag{10.52}$$

which is the Hamiltonian of a classical XY model. From Eq. (10.51), the effective temperature for the XY model can be tuned by changing the strength of the white noise or the pumping power of the lasers.

10.6.2 Towards Large-Scale Implementation

In this section, we explain an idea of making a large-scale coherent Ising machine and XY computer.

A simple method to prepare many lasers with identical oscillation frequencies is to use a single fiber ring cavity to generate multiple lasers. Such an experiment have already been done in Ref. [34]. In their experiments, they placed the mask of apertures inside a cavity, and generated more than one thousand lasers in a spatially separated manner.

Here, we propose alternative implementation that use the time-division multiplexing technique. Figure 10.14 shows the schematics of our setup to implement a large-scale coherent computer. In this setup, temporally separated pulses are generated in a fiber ring cavity by using so-called harmonic mode locking. The

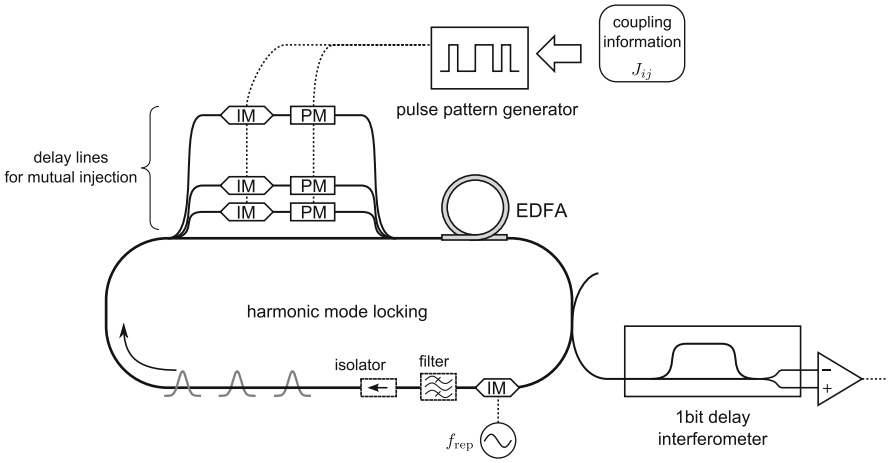

Fig. 10.14 Schematics of coherent computer based on harmonic mode-locked fiber laser. Each pulse corresponds to a spin of a statistical model. The pulses are mutually injected through multiple delay lines, and thereby are coupled to each other. The coupling coefficients are programmed onto the electrical pulse patterns applied to the intensity and phase modulators (IM and PM) placed on the delay lines

phase of each pulse corresponds to the direction of a spin in a statistical model. The coupling between the pulses is implemented by mutual injection from a pulse to another pulse through multiple delay lines. For this purpose, the length of delay lines are adjusted to an integer multiple of the interval of pulses. Each delay line has a pair of intensity and phase modulators. We can implement arbitrary coupling coefficients by changing the electrical pulse patterns applied to these modulators. Finally, the relative phases of pulses are read out by the 1-bit delay interferometer.

One of the distinguished properties of this implementation is its programmability. The coupling coefficients can be arbitrary tuned by only changing the electrical signal to the modulators. Therefore, it works as a general-purpose simulator for classical Ising and XY models.

10.7 Conclusion

We have implemented a two-site Ising model by using the optical phases of two mutually coupled slave lasers that are injection-locked by a single master laser. The transition from the Ising-term dominant regime to the master-injection dominant regime was observed. The phase of the slave laser is continuously synchronized with that of a master laser when the master laser injection is stronger than the mutual coupling between the slave lasers. On the other hand, when the mutual coupling is stronger than the master laser injection, the phases of the two slave lasers jump discretely and the oscillation frequencies continuously shift with the optical path length modulation between the two slave lasers. In that case, the mutually coupled slave lasers communicate with each other and oscillate at the optimum frequency, where a standing wave develops between them that results in either a ferromagnetic or anti-ferromagnetic phase order.

We concludes this chapter with mentioning the achievable problem size of the coherent computer with time domain multiplexing optical pulses. If we use a fiber-based mode-locked laser of repetition rate $f_{\mathrm{rep}} = 10\,\mathrm{GHz}$ and cavity length $L = 200\,\mathrm{m}$, the number of Ising spins implemented by optical pulses inside the cavity is $N = 10{,}000$.

References

1. M.R. Garey, D.S. Johnson, *Computers and Intractability: A Guide to the Theory of NP-Completeness* (W. H. Freeman, New York, 1979)
2. K. Binder, A.P. Young, Spin glasses: experimental facts, theoretical concepts, and open questions. Rev. Mod. Phys. **58**, 801–976 (1986)
3. E. Ising, Beitrag zur theorie des ferromagnetismus. Z. Phys. **31**, 253 (1925)
4. L. Onsager, Crystal statistics. I. A two-dimensional model with an order-disorder transition. Phys. Rev. **65**, 117 (1944)
5. F. Barahona, On the computational complexity of Ising spin glass models. J. Phys. A Math. Gen. **15**, 3241–3253 (1982)

6. M. Nielson, I. Chuang, *Quantum Computation and Quantum Information* (Cambridge University Press, Cambridge/New York, 2000)
7. T. Kadowaki, H. Nishimori, Quantum annealing in the transverse Ising model. Phys. Rev. E **58**, 5355 (1998)
8. E. Farhi, J. Goldstone, S. Gutmann, J. Lapan, A. Lundgren, D. Preda, A quantum adiabatic evolution algorithm applied to random instances of an NP-complete problem. Science **292**(5516), 472–475 (2001)
9. S. Utsunomiya, K. Takata, Y. Yamamoto, Mapping of Ising models onto injection-locked laser systems. Opt. Express **19**, 18091–18108 (2011)
10. L.K. Grover, A fast quantum mechanical algorithm for database search, in *Proceedings of the Twenty-Eighth Annual ACM Symposium on Theory of Computing*, Philadelphia (1996), p. 212
11. C.H. Bennett, E. Bernstein, G. Brassard, U.V. Vazirani, Strengths and weaknesses of quantum computing. SIAM J. Comput. **26**, 1510 (1997)
12. J. Roland, N. Cerf, Quantum search by local adiabatic evolution. Phys. Rev. A **65**, 042308 (2002)
13. D. Aharonov, W. van Dam, J. Kempe, Z. Landau, S. Lloyd, O. Regev, Adiabatic quantum computation is equivalent to standard quantum computation. quant-ph/0405098 v2 (2005)
14. D. Gattesman, The Heisenberg representation of quantum computers. quant-ph/9807006 (1998)
15. S.D. Bartlett, B.C. Sanders, S.L. Braunstein, K. Nemoto, Efficient classical simulation of continuous variable quantum information processes. quant-ph/0109047 (2001)
16. L. Gillner, G. Bjork, Y. Yamamoto, Quantum noise properties of an injection-locked laser oscillator with pump-noise suppression and squeezed injection. Phys. Rev. A **41**(9), 5053–5065 (1990)
17. H.A. Haus, Y. Yamamoto, Quantum noise of an injection-locked laser oscillator. Phys. Rev. A **29**, 1261–1274 (1984)
18. M. Surgent, M.O. Scully, W.E. Lamb, Chapter 20, in *Laser Physics* (Westview Printing, Colorado, 1978), pp. 331–335
19. H. Haug, Quantum-mechanical rate equations for semiconductor lasers. Phys. Rev. **184**, 338–348 (1969)
20. Y. Yamamoto, S. Machida, O. Neilsson, Amplitude squeezing in a pump-noise-suppressed laser oscillator. Phys. Rev. A **34**, 4025–4042 (1986)
21. M. Yannakakis, Edge-deletion problems. SIAM J. Comput. **10**, 297–309 (1981)
22. R. Greenlaw, R. Pedreschi, Cubic graphs. ACM Comput. Surv. **27**, 471–495 (1995)
23. F. Barahona, M. Grotschel, M. Junger, R. Reinelt, An application of combinatorial optimization to statistical physics and circuit layout design. Oper. Res. **36**(3), 493–513 (1988)
24. A. Galluccio, M. Loebl, J. Vondrak, New algorithm for the Ising problem: partition function for finite lattice graphs. Phys. Rev. Lett. **84**, 5924–5927 (2000)
25. C.W. Gardiner, P. Zoller, *Quantum Noise* (Springer, Berlin, 1991)
26. K. Takata, S. Utsunomiya, Y. Yamamoto, Transient time of an Ising machine based on injection-locked laser network. New J. Phys. **14**, 013052 (2012)
27. B.D. McKay, G.F. Royle, Constructing the cubic graphs on up to 20 vertices. Ars Combin. **21**, 129–140 (1986)
28. M.X. Goemans, D.P. Williams, J. ACM **42**, 1115 (1995)
29. S. Saito, O. Nilsson, Y. Yamamoto, Oscillation center frequency tuning, quantum FM noise, and direct frequency characteristics in external grating loaded semiconductor lasers. IEEE J. Quant. Electron. **18**, 6 (1982)
30. H. Nishimori, G. Ortiz, *Elements of Phase Transitions and Critical Phenomena* (Oxford University Press, Oxford, 2011)
31. J.A. Acebrón, L.L. Bonilla, C.J.P. Vicente, F. Ritort, R. Spigler, Rev. Mod. Phys. **77**, 137 (2005)
32. A. Gordon, B. Fischer, Phys. Rev. Lett. **89**, 103901 (2002)
33. H. Risken, *The Fokker-Planck Equation*, 2nd edn. (Springer, Berlin, 1989)
34. M. Nixon, E. Ronen, A.A. Friedman, N. Davidson, Phys. Rev. Lett. **110**, 184192 (2013)

Chapter 11
A Degenerate Optical Parametric Oscillator Network for Coherent Computation

Zhe Wang, Alireza Marandi, Kenta Takata, Robert L. Byer, and Yoshihisa Yamamoto

11.1 Introduction

Combinatorial optimization problems are of great interest in diverse areas including computer science, physics, biology, information processing, and social network. Despite the variety of applications and formulations of these problems, many of them are equivalently hard to solve and are in the NP-hard class in computational complexity.

The Ising problem, which is to find a ground state of the Ising Hamiltonian[1]

[1] An Ising Hamiltonian generally also includes Zeeman terms $-\sum_{j=1}^{N} b_j \sigma_j$ to take account of external magnetic fields. These Zeeman terms can be written in the form of two-body interaction as $-\sum_{j=1}^{N} b_j \sigma_j \sigma_{N+1}$, where σ_{N+1} is introduced as an additional Ising spin and its coupling coefficient with the jth spin is given by b_j. It can be easily proven that solutions to the original Ising problem with Zeeman terms can be obtained from the ground states of the new Ising Hamiltonian only with two-body interaction terms.

Z. Wang (✉) • R.L. Byer
E. L. Ginzton Laboratory, Stanford University, Stanford, CA 94305, USA
e-mail: zhewang@stanford.edu; rlbyer@stanford.edu

A. Marandi
E. L. Ginzton Laboratory, Stanford University, Stanford, CA 94305, USA

National Institute of Informatics, Hitotsubashi 2-1-2, Chiyoda-ku, Tokyo 101-8403, Japan
e-mail: marandi@stanford.edu

K. Takata
The University of Tokyo, 7-3-1 Hongo, Bunkyo-ku, Tokyo 113-8654, Japan

National Institute of Informatics, Hitotsubashi 2-1-2, Chiyoda-ku, Tokyo 101-8403, Japan
e-mail: takata.kenta@lab.ntt.co.jp

Y. Yamamoto
ImPACT Program, Council for Science Technology and Innovation, Tokyo, Japan
e-mail: yyamamoto@stanford.edu

Y. Yamamoto, K. Semba (eds.), *Principles and Methods of Quantum Information Technologies*, Lecture Notes in Physics 911, DOI 10.1007/978-4-431-55756-2_11

$$H = -\sum_{1 \le j < l \le N} J_{jl}\sigma_j\sigma_l, \tag{11.1}$$

is one of these NP-hard problems [1] arising in the study of disordered magnetic systems such as spin glasses [2]. The above Hamiltonian represents the energy of a spin glass with N frustrated spins, where $\sigma_j = \pm 1$ are the two states that each spin can take, and J_{jl} denotes the coupling coefficient of the two-body interaction between the jth and the lth spin. The coupling is called ferromagnetic if $J_{jl} > 0$ and antiferromagnetic if $J_{jl} < 0$. Although simple, this mathematical model serves as a useful prototype for explaining experimental observations of spin glasses [3].

Once a polynomial time algorithm is available for one member of the NP-hard problems, all the problems in this class can be solved efficiently because they are reducible to each other by polynomial transformations [4]. The MAX-CUT problem is one of the first known NP-hard problems in graph theory [5]. Given an undirected graph $G = (V, E)$ with an edge weight function $w : E \to \mathbb{R}$, where V and E denote the sets of vertices and edges, respectively, the goal is to find a cut $(S, V \setminus S)$ such that the sum of the weight of the edges with one endpoint in $S \subset V$ and the other in $V \setminus S$ is maximized over all possible cuts. Let $w_{jl} = w_{lj}$ be the edge weight if $(j, l) \in E$ and $w_{jl} = 0$ if $(j, l) \notin E$, and $\sigma_j = +1$ if the jth vertex is in S and $\sigma_j = -1$ if not. The weight of a cut S is thus given by

$$w(S) = \sum_{j \in S,\, l \in V \setminus S} w_{jl} = \frac{1}{4}\sum_{j,\, l \in V} w_{jl} - \frac{1}{4}\sum_{j,\, l \in V} w_{jl}\sigma_j\sigma_l. \tag{11.2}$$

When the coupling coefficient J_{jl} in the Ising problem is chosen to be $-w_{jl}$, any maximum cut of the given graph can be converted to a ground state of the corresponding Ising Hamiltonian and vice versa.

So far no method is known to solve NP-hard problems in polynomial time and these problems are commonly believed to be intractable. Nevertheless, many attempts have still been undertaken to tackle them. The simulated annealing algorithm is designed by mimicking the thermal annealing procedure in metallurgy [6]. Making use of the quantum tunneling process, quantum annealing technique was also formulated [7] and is shown to have superior performance over simulated annealing [8]. As a variant of quantum annealing, quantum adiabatic computation was devised according to the adiabatic theorem of quantum mechanics [9], with computational power equivalent to that of a quantum computer based on unitary gates [10, 11]. Despite the fact that none of these methods are generally proven to be efficient, taking advantage of fundamental principles in physics has shed new light on solving NP-hard problems. In this regard, it is worthwhile studying the computational ability of other promising physical systems to search for alternative approaches.

Lasers are open dissipative systems that undergo second-order phase transition at the oscillation threshold. Multiple cavity modes in a laser compete for the

available gain. Once a particular mode oscillates, the gain accessible to other modes is suppressed below the threshold value due to the cross-saturation effect [12]. Since the mode with the minimum threshold gain is more likely to oscillate first, it has the advantage over other modes to spontaneously emerge through the mode competition. This phenomenon is to be referred to as the *minimum gain principle* in the following. It is demonstrated that the overall photon decay rate in a mutually injection-locked laser network can be engineered to be in the form of an Ising Hamiltonian [13]. Each laser in the network is polarization degenerate, and it represents Ising spin $+1$ in the case that right circularly polarized photons outnumber left circularly polarized photons and Ising spin -1 in the opposite case. A combination of the polarization of all lasers is considered to be a global mode of the whole network. Numerical simulations have shown evidence in favor of the minimum gain principle. For the selected Ising problems, the network is likely to oscillate in a global mode with the minimum photon decay rate. Moreover, the transient time of the network to the steady state is estimated to be determined by the mutual injection signals among the lasers, which does not scale with the number of spins in the Ising problem [14].

Degenerate parametric oscillators are also open dissipative systems that undergo second-order phase transition at the oscillation threshold [15]. Due to the phase-sensitive amplification effect, however, an oscillator operating above the threshold can only oscillate with one of two possible phases. In the early development of digital computers, logic circuits were built from electrical oscillators of this type utilizing the bistability of their output phases [16]. The phase that an oscillator would take from the two equally preferred outcomes is randomly determined by the noise. In the case of a degenerate optical parametric oscillator (OPO), the vacuum field fluctuation incident on the output mirror and the pump field fluctuation during the oscillation build-up take the charge [17]. Based on this property, a quantum random number generator was implemented by taking XOR of the phases of two independently oscillating degenerate OPOs [18].

This chapter is concerned with the collective computational ability of a degenerate OPO network [19, 20]. In the proposed network, each degenerate OPO is identified as an Ising spin by its binary output phase. Each particular overall phase configuration of the network becomes a global mode and represents an eigenstate of the Ising Hamiltonian. In order to solve an Ising problem, the output fields of the degenerate OPOs are coherently injected to others with the amplitudes and phases governed by the coupling coefficients in the given problem. Under appropriate implementation, the overall photon decay rate of the global mode is proportional to the energy of the corresponding Ising eigenstate. Since the minimum gain principle is also applicable to the OPO mode selection, the network is expected to give a solution to the NP-hard Ising problem.

Section 11.2 prepares the theoretical groundwork for examination of the proposed network through the study of a single degenerate OPO. Section 11.3 presents the dynamical equations of the network and analyzes steady-state properties which

are essential for its computational ability. To illustrate the situations that the network solves the Ising problem, the case of two coupled degenerate OPOs are discussed in Sect. 11.4. Performance of the network is numerically evaluated in Sect. 11.5 by conducting computational experiments against the NP-hard MAX-CUT problem. Section 11.6 describes the experimental implementation of the network and demonstrates the results of solving a small instance of the MAX-CUT problem. Possible quantum features in the two coupled oscillators are discussed in Sect. 11.7. Finally, Sect. 11.8 concludes the chapter.

11.2 A Single Degenerate OPO

A degenerate OPO consists of a second-order nonlinear crystal placed in an optical cavity. Under the drive of a coherent external pump F_p at frequency ω_p, a pump field is excited inside the cavity. Due to the second-order susceptibility of the nonlinear crystal, a signal field at frequency ω_s is generated from the pump field such that $\omega_p = 2\omega_s$. Assume that F_p is classical and its phase is the reference phase of the oscillator. The Hamiltonian of a degenerate OPO is hence given by

$$\begin{aligned} H &= H_0 + H_{\text{int}} + H_{\text{irr}}, \\ H_0 &= \hbar\omega_s \hat{a}_s^\dagger \hat{a}_s + \hbar\omega_p \hat{a}_p^\dagger \hat{a}_p, \\ H_{\text{int}} &= i\hbar\frac{\kappa}{2}\left(\hat{a}_s^{\dagger 2}\hat{a}_p - \hat{a}_s^2\hat{a}_p^\dagger\right) + i\hbar\sqrt{\gamma_p}\left(\hat{a}_p^\dagger F_p \mathrm{e}^{-i\omega_p t} - \hat{a}_p F_p \mathrm{e}^{i\omega_p t}\right), \\ H_{\text{irr}} &= i\hbar\sqrt{\gamma_s}\left(\hat{a}_s^\dagger \hat{B}_s - \hat{a}_s \hat{B}_s^\dagger\right) + i\hbar\sqrt{\gamma_p}\left(\hat{a}_p^\dagger \hat{B}_p - \hat{a}_p \hat{B}_p^\dagger\right). \end{aligned} \tag{11.3}$$

Here, H_0 represents the energies of the signal and the pump fields inside the cavity, where $\hat{a}_s^\dagger, \hat{a}_s$ are the creation and annihilation operators for the signal field and $\hat{a}_p^\dagger, \hat{a}_p$ are the counterparts for the pump field. Also, the first term in H_{int} describes the nonlinear coupling between the signal and the pump fields, where κ is the parametric gain due to the second-order susceptibility of the nonlinear crystal; the second term shows the excitation of the internal pump field by the external pump. Finally, H_{irr} denotes the irreversible interaction between cavity fields and the reservoir, where $\hat{B}_s, \hat{B}_p$ are reservoir operators with continuous spectra in the frequency domain, and γ_s, γ_p are the signal and the pump photon decay rates from the cavity [21].

From the Hamiltonian in Eq. (11.3), the Heisenberg-Langevin equations of a degenerate OPO can be derived as

$$\begin{aligned} \frac{d}{d\tau}\hat{A}_s &= -\frac{\gamma_s}{2}\hat{A}_s + \kappa\hat{A}_s^\dagger\hat{A}_p + \sqrt{\gamma_s}\hat{f}_s, \\ \frac{d}{d\tau}\hat{A}_p &= -\frac{\gamma_p}{2}\hat{A}_p - \frac{\kappa}{2}\hat{A}_s^2 + \sqrt{\gamma_p}\left(F_p + \hat{f}_p\right), \end{aligned} \tag{11.4}$$

where $\hat{A}_s = \hat{a}_s e^{i\omega_s \tau}$, $\hat{A}_p = \hat{a}_p e^{i\omega_p \tau}$ denote the slowly varying signal and pump operators in the rotating frame and $\hat{f}_s, \hat{f}_p$ are the time-dependent noise operators to the signal and the pump fields, respectively [22].

The c-number Langevin equations subsequently follow from converting each operator in the above equations to a complex number. Moreover, under the condition $\gamma_s \ll \gamma_p$, the pump field can be adiabatically eliminated since it immediately follows the change of the signal field. With this slaving principle, the c-number Langevin equations reduce to a single stochastic differential equation

$$\frac{d}{d\tau}\tilde{A}_s = -\frac{\gamma_s}{2}\tilde{A}_s + \kappa\left(\frac{2}{\sqrt{\gamma_p}}F_p - \frac{\kappa}{\gamma_p}\tilde{A}_s^{\,2}\right)\tilde{A}_s^{\,*} + \frac{2\kappa}{\sqrt{\gamma_p}}\tilde{A}_s^{\,*}\tilde{f}_p + \sqrt{\gamma_s}\tilde{f}_s, \tag{11.5}$$

which describes the dynamics of the complex amplitude $\tilde{A}_s$ of the signal field. Here, the superscript * denotes the operation of complex conjugate and $\tilde{f}_s = f_{s,1} + if_{s,2}$, $\tilde{f}_p = f_{p,1} + if_{p,2}$ are quantum noises to the signal and pump fields, respectively, whose real and imaginary components $f_{k,j}$, $k \in \{s, p\}$, $j \in \{1, 2\}$ are independent white Gaussian noises with the ensemble averaged means and correlations satisfying

$$\begin{aligned} \langle f_{k,j}(\tau)\rangle &= 0, \\ \langle f_{k,j}(\tau) f_{k',j'}(\tau')\rangle &= \frac{1}{4}\delta_{kk'}\delta_{jj'}\delta(\tau - \tau'). \end{aligned} \tag{11.6}$$

The real and imaginary parts of the complex amplitude are called the in-phase and quadrature components of the signal field, respectively. Dynamical equations for the in-phase and the quadrature components can be easily derived from Eq. (11.5).

Despite the classical nature of the c-number Langevin equation, it produces a prediction on statistical quantities of the signal field identical to that of a quantum mechanical approach. Figure 11.1 displays the second central moments of the in-phase and the quadrature components at the steady state. The normalized pump rate is defined as $p = F_p/F_{th}$, where $F_{th} = \gamma_s\sqrt{\gamma_p}/4\kappa$ is the threshold external pump

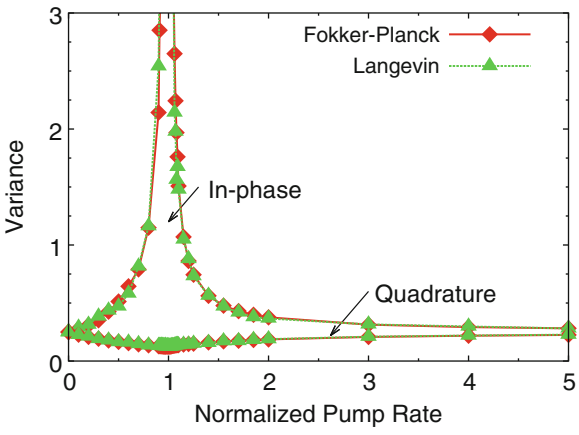

Fig. 11.1 Variances of the in-phase and the quadrature components of the signal field at the steady state at different pump levels when $\gamma_s = 1$, $\gamma_p = 100$, and $\kappa = 0.1$. The numerical values are calculated from two theoretical models: the quantum mechanical Fokker-Planck approach and the classical c-number Langevin approach

flux. It can be easily seen that the c-number Langevin approach successfully predicts the generation of squeezed states around the threshold [23]. Meanwhile, the numerical values are in good agreement with the results calculated from the quantum mechanical Fokker-Planck equation obtained from the generalized P-representation [21]. Therefore, this classical approach is adopted for the investigation of the proposed degenerate OPO network.

11.3 A Degenerate OPO Network

In order to solve an Ising problem with N spins, a network composed of N degenerate OPOs needs to be constructed. Each degenerate OPO in the network corresponds to an Ising spin, and its signal output is coherently injected to another according to the coupling coefficient between the spins involved. Let $\xi_{jl}/2$ denote the scaling factor for the complex signal field $\tilde{A}_j$ of the jth degenerate OPO when it is coupled to the lth degenerate OPO. Since the coupling coefficients in the Ising problem are always symmetric, it follows that $\xi_{jl} = \xi_{lj}$. By further adding terms representing the mutual coupling of the signal fields to Eq. (11.5), the c-number Langevin equations of the network are obtained as

$$\begin{aligned}\frac{d}{d\tau}\tilde{A}_j = &-\frac{\gamma_s}{2}\tilde{A}_j + \kappa\left(\frac{2}{\sqrt{\gamma_p}}F_p - \frac{\kappa}{\gamma_p}\tilde{A}_j{}^2\right)\tilde{A}_j{}^* \\ &+\frac{1}{2}\sum_{l=1,\, l\neq j}^{N}\xi_{jl}\gamma_s\tilde{A}_l + \frac{2\kappa}{\sqrt{\gamma_p}}\tilde{A}_j{}^*\tilde{f}_{p,j} + \sqrt{\gamma_s}\tilde{f}_{s,j},\end{aligned} \tag{11.7}$$

where $\tilde{f}_{s,j}$ and $\tilde{f}_{p,j}$ are the associated quantum noises to the j-th degenerate OPO.

For a single degenerate OPO pumped above the threshold, Eq. (11.5) implies that the mean of its quadrature component at the steady state is zero. Therefore, the phase of the oscillating field on average is either zero or π determined by the sign of its in-phase component. It is favorable if all degenerate OPOs in the coupled network operating above the threshold still possess the bistability of their output phases. This is because the phase configuration of the network can be naturally converted to an Ising state by assigning $\sigma_j = +1$ to the jth degenerate OPO if its in-phase component is positive or $\sigma_j = -1$ if it is negative. Due to the mutual coupling, however, it is not self-evident that this feature is available to the network. In the following, required conditions are explored through analyzing steady-state properties of the network.

Dynamical equations for the in-phase components C_j and the quadrature components S_j of the complex signal amplitudes $\tilde{A}_j$ provide a description of the network equivalent to Eq. (11.7). Since the theoretical investigation is mainly interested in the mean signal fields at the steady state, noise terms are neglected in the dynamical equations. For ease of analysis, normalized equations for the in-phase and quadrature components

$$\begin{aligned}\frac{d}{dt}c_j &= (-1+p-(c_j^2+s_j^2))c_j + \sum_{l=1,\,l\neq j}^{N}\xi_{jl}c_l,\\ \frac{d}{dt}s_j &= (-1-p-(c_j^2+s_j^2))s_j + \sum_{l=1,\,l\neq j}^{N}\xi_{jl}s_l,\end{aligned} \tag{11.8}$$

are utilized, where $t = \gamma_s\tau/2$ is the unitless time normalized to twice of the signal photon cavity lifetime, and $c_j = C_j/A_s$, $s_j = S_j/A_s$ are normalized in-phase and quadrature components where $A_s = \sqrt{\gamma_s\gamma_p/2\kappa^2}$ is the signal amplitude of a single degenerate OPO when $p = 2$. The above equations indicate that the dynamics of the network are influenced by the values of p and ξ_{jl}.

11.3.1 Oscillation Threshold

The in-phase and the quadrature components of the N coupled degenerate OPOs satisfy

$$\begin{aligned}c_j^3 + (1-p+s_j^2)c_j - \sum_{l=1,\,l\neq j}^{N}\xi_{jl}c_l &= 0,\\ s_j^3 + (1+p+c_j^2)s_j - \sum_{l=1,\,l\neq j}^{N}\xi_{jl}s_l &= 0\end{aligned} \tag{11.9}$$

at the steady state. The oscillation threshold of the network is defined as the normalized pump rate p_{th} above which the network cannot arrive at the trivial steady state $c_j = s_j = 0$, $\forall j \in \{1, 2, \ldots, N\}$. For any hermitian matrix A, let $\lambda_{\min}(A)$ and $\lambda_{\max}(A)$ be the smallest and the largest eigenvalues, respectively. Since the largest eigenvalue of the corresponding Jacobian matrix

$$J_0 = \begin{pmatrix} -(1-p)I_N - G & 0 \\ 0 & -(1+p)I_N - G \end{pmatrix} \tag{11.10}$$

has to be positive above the threshold, the threshold of the network is obtained as

$$p_{\text{th}} = 1 + \lambda_{\min}(G) < 1, \tag{11.11}$$

where I_N is the $N \times N$ identity matrix and

$$G = \begin{pmatrix} 0 & -\xi_{12} & \ldots & -\xi_{1N} \\ -\xi_{21} & 0 & \ldots & -\xi_{2N} \\ \vdots & \vdots & \ddots & \vdots \\ -\xi_{N1} & -\xi_{N2} & \ldots & 0 \end{pmatrix} \tag{11.12}$$

is the hermitian matrix showing the coupling relation of the network. Since $\mathrm{Tr}(G) = 0$, it follows that $\lambda_{\min}(G) < 0$ and the threshold of the network is lower than that of an individual degenerate OPO. This phenomenon is similar to the so-called self-ignition effect well known in the study of neural networks [24].

11.3.2 Quadrature Components

It follows from the quadrature component equations in Eq. (11.9) that

$$\sum_{j=1}^{N} s_j^4 + \sum_{j=1}^{N} a_j s_j^2 - \sum_{j=1}^{N} \sum_{l=1,\, l\neq j}^{N} \xi_{jl} s_j s_l = 0, \tag{11.13}$$

where $a_j = 1 + p + c_j^2, j \in \{1, 2, \ldots, N\}$. The last two terms of the above equation is in the quadratic form of the matrix

$$Q = \begin{pmatrix} a_1 & -\xi_{12} & \ldots & -\xi_{1N} \\ -\xi_{21} & a_2 & \ldots & -\xi_{2N} \\ \vdots & \vdots & \ddots & \vdots \\ -\xi_{N1} & -\xi_{N2} & \ldots & a_N \end{pmatrix}. \tag{11.14}$$

If Q is positive definite, the only possible solution to the quadrature components in Eq. (11.9) will be $s_j = 0$, $\forall j \in \{1, 2, \ldots, N\}$. Since dynamics of the in-phase components are affected by the square of the quadrature components, local behaviors of the in-phase and the quadrature components around this solution can be separated. The corresponding Jacobian matrix for the quadrature components is $J_s = -Q$. Thus, a steady state with all quadrature components being 0 is stable if its corresponding Jacobian matrix for the in-phase components is negative definite.

The smallest eigenvalue of Q is still unknown without solving Eq. (11.9) to obtain the steady-state values of the in-phase components. However, a lower bound can be easily evaluated. The hermitian matrix Q can be written as the sum of the hermitian matrix G and a diagonal matrix whose diagonal components are $a_1, a_2, \ldots, a_N$. From Weyl's theorem [25], the eigenvalues $\lambda(Q)$ are bounded as

$$\min(G) + \min_j a_j \leq \lambda(Q) \leq \max_j a_j + \lambda_{\max}(G). \tag{11.15}$$

Since $\lambda_{\min}(G) < 0$, a sufficient condition for Q to be positive definite is

$$|\lambda_{\min}(G)| < 1 + p \leq \min_j a_j. \tag{11.16}$$

The above requirement together with the oscillation threshold in Eq. (11.11) establish guidelines for choosing appropriate combinations of the normalized pump rate p

and the coupling strength ξ_{jl} to identify the degenerate OPOs in the network as Ising spins. Yet it is noteworthy that combinations of p and ξ_{jl} not satisfying Eq. (11.16) may also be preferred in some cases because of its sufficient nature.

11.3.3 Overall Photon Decay Rate

The term $p-(c_j^2+s_j^2)$ in Eq. (11.8) represents the saturated gain for the jth degenerate OPO. At the steady state, the total saturated gain of the network equals the overall photon decay rate Γ. In the case that all the quadrature components of the degenerate OPOs are 0, $\Gamma = \sum_{j=1}^{N}(p - c_j^2)$.

When mutual coupling of the degenerate OPOs is weak enough and $p > 1$, the in-phase component c_j in Eq. (11.9) can be expressed in the formal expansion

$$c_j = c_j^{(0)} + \epsilon c_j^{(1)} + \epsilon^2 c_j^{(2)} + \ldots, \tag{11.17}$$

where $\epsilon = \max_{1\le j,\, l\le N} |\xi_{jl}|$, according to the perturbation theory. Each term $c_j^{(n)}$, $n \ge 0$ can be analytically obtained by substituting the above expansion to Eq. (11.9) and setting the coefficient of the ϵ^n term to be 0. The zeroth-order term $c_j^{(0)} = \pm\sqrt{p-1}$ is the signal amplitude of the jth degenerate OPO operating above the threshold when there is no mutual coupling. Since the formal expansion for c_j can be viewed as a local modification to $c_j^{(0)}$, the Ising spin value σ_j that the jth degenerate OPO represents equals $\mathrm{sgn}(c_j^{(0)})$. The overall photon decay rate is thus given by

$$\Gamma = N - \sum_{1\le j\ne l\le N} \xi_{jl}\sigma_j\sigma_l + O\left(\frac{\epsilon^3 N^4}{(p-1)^3}\right), \tag{11.18}$$

where the higher-order correction term is evaluated in the case when coupling of the same strength exists between any two of the degenerate OPOs. For a particular phase configuration of the degenerate OPOs, the difference of the overall photon decay rates between cases with and without mutual coupling is exactly the energy of its corresponding spin configuration in an Ising problem where the coupling coefficients between spins are $2\xi_{jl}$. Therefore, a global mode that achieves the minimum Γ provides a ground state of the Ising problem.

Given any Ising problem, scaling all the coupling coefficients by the same positive factor does not change its solutions. In this regard, some degree of flexibility is available in choosing the coupling strength of the network. For a fixed pump rate, the gaps among the overall photon decay rates of different modes decrease with weaker coupling strength. As a consequence, the possibility that the network evolves into steady states corresponding to excited states of the Ising Hamiltonian may be increased. On the other hand, the mapping from the overall photon decay rate to the Ising Hamiltonian becomes more inaccurate when the coupling strength gets stronger, which may also cause probable errors in solving the Ising problem. This

intuitive observation indicates that the choice of p and ξ_{jl} can significantly influence the performance of the network as a computing machine. As an example, the system of two coupled degenerate OPOs is examined in the next section.

11.4 Two Coupled Degenerate OPOs

Dynamical behaviors of two coupled degenerate OPOs offer meaningful insight into how the system finds candidate solutions to an Ising problem. Due to the relative simplicity of the system, many steady-state properties can be expressed as functions of the normalized pump rate p and coupling coefficient ξ, which enables the examination of the dependence of solutions on these parameters.

The threshold of the system is $p_{\text{th}} = 1 - |\xi|$ by Eq. (11.11). When $|\xi| \leq 1 + p$, all the quadrature components of the system are zero at the steady state according to the sufficient condition in Eq. (11.16). Expressions of the in-phase components c_1 and c_2 at the steady state can also be easily obtained, which further allows the investigation of their linear stability. As shown in Table 11.1, the possible steady states that the system can evolve into depends considerably on the values of p and ξ. Indeed, it is the phase diagram of the in-phase components being modified. Figure 11.2 displays the variation of the phase diagram with p when ξ is fixed:

(a) When the system is pumped below or at the threshold, the only possible steady state is the trivial one $c_1 = c_2 = 0$.
(b) As the pump rate is slightly increased, the trivial steady state becomes unstable while two additional stable steady states are developed. For the case being displayed, the two degenerate OPOs have the same amplitude but opposite phases at both the two newly developed stable steady states. Therefore, they

Table 11.1 Linear stability of steady states with all quadrature components being zero of two coupled degenerate OPOs

		(c_1, c_2)			
p	ξ	$(0, 0)$	(c_g, c_g)[a]	$(c_u, -c_u)$[b]	(c_s, c_a)[c]
$p \leq 1$	$(1-p, 1+p)$	Unstable	Stable	NA[d]	NA
	$(p-1, 1-p)$	Stable	NA	NA	NA
	$(-1-p, p-1)$	Unstable	NA	Stable	NA
$p > 1$	$(p-1, p+1)$	Unstable	Stable	NA	NA
	$(\frac{p-1}{2}, p-1)$	Unstable	Stable	Unstable	NA
	$(-\frac{p-1}{2}, \frac{p-1}{2})$	Unstable	Stable	Stable	Unstable
	$(1-p, -\frac{p-1}{2})$	Unstable	Unstable	Stable	NA
	$(-1-p, 1-p)$	Unstable	NA	Stable	NA

[a] $c_g^2 = p - 1 + \xi$
[b] $c_u^2 = p - 1 - \xi$
[c] $c_s^2 = \frac{p-1 \pm \sqrt{(p-1)^2 - 4\xi^2}}{2}$, $c_a c_s = -\xi$
[d] *NA* not available

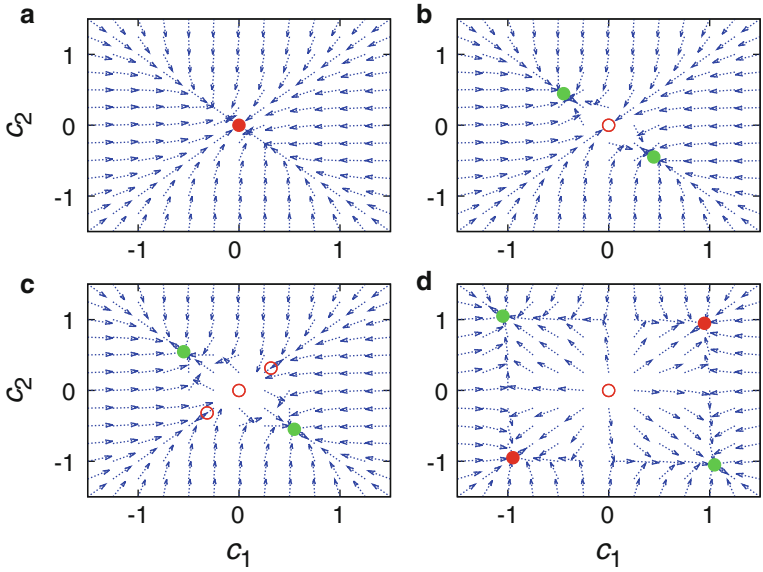

Fig. 11.2 Phase diagrams for the in-phase components of two coupled degenerate OPOs when $\xi = -0.1$. The normalized pump rate for each diagram is (**a**) $p = p_{\text{th}} = 0.9$; (**b**) $p = 1.1$; (**c**) $p = 1.2$; (**d**) $p = 2.0$. The *dots* and *circles* mean stable and unstable steady states, while the colors *green* and *red* denote correct and incorrect solutions, respectively

correspond to the correct solutions to the Ising problem of two spins with an antiferromagnetic coupling. Since these two steady states are the only stable ones available, the system can always arrive at the correct answers irrespective of its initial state.

(c) As the pump rate is further increased, two more steady states begin to exist in the system. Since the two degenerate OPOs have the same amplitude and phase at these two steady states, they correspond to the wrong solutions to the Ising problem. However, at this pump level these two steady states are unstable ones so that the system can still solve the Ising problem with certainty.

(d) When the pump rate is raised up over the critical point $1 + 2|\xi|$ according to Table 11.1, the steady states corresponding to the wrong answers also become stable. Since the system can evolve into these steady states as well, errors may occur for the system in solving the Ising problem.

As a result, the choice of p and ξ affects, to a large extent, the efficiency of the system as a computing machine. Figure 11.3 displays the ξ dependence of its success probability when p is fixed in solving the Ising problem of two spins with a ferromagnetic coupling. A candidate answer can be obtained from the system by numerically solving its dynamical equations under a random noise input. The details of the numerical method are described in Sect. 11.5.1. For each coupling coefficient, 100 groups of 100 random trials are conducted to estimate the success probability and the standard deviation. The success probability asymptotically approaches 0.5

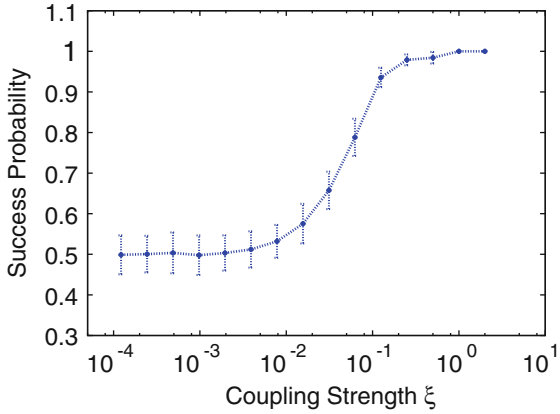

Fig. 11.3 The success probability of two coupled degenerate OPOs in solving the Ising problem of two spins with a ferromagnetic coupling when $p = 2.0$. The error bars are standard deviations

as the coupling strength decreases. This is because in the limit of no coupling each degenerate OPO can choose its phase independently so that correct and incorrect solutions are equally likely. On the other hand, when ξ is above the critical point $(p-1)/2$, the system outputs a correct solution for every trial.

11.5 Computational Experiments

Performance of the degenerate OPO network as a computing machine is evaluated using two sets of instances of the NP-hard MAX-CUT problem. The first set consists of all cubic graphs of order up to 20. These small instances are chosen because the correctness of the network's output solution can be verified by checking all possible cuts by brute force. In addition, the MAX-CUT problem remains NP-hard when restricted to cubic graphs [26]. The factor that limits the maximum input size under consideration is the total number of instances in each graph order, which is irrelevant to the properties of the network. As shown in Table 11.2, it grows even faster than an exponential function with respect to the input size [27]. Thus, the time it takes to exhaust all cubic graphs of the same order climbs commensurately. The second set contains 71 benchmark instances of the so-called G-set graphs. These instances are randomly constructed by a machine-independent graph generator written by G. Rinaldi with the number of vertices ranging from 800 to 20 000, edge density from 0.02 % to 6 %, edge weight being ± 1, and geometry from random, almost planar to toroidal.

11.5.1 Numerical Method

Solution outputs from the network can be obtained by solving the c-number Langevin equations in Eq. (11.7) with the signal field of each degenerate OPO

Table 11.2 Number of cubic graphs

	Order											
	4	6	8	10	12	14	16	18	20	22	24	26
Cubic graphs	1	2	5	19	85	509	4060	41301	510489	7319447	117940535	2094480864

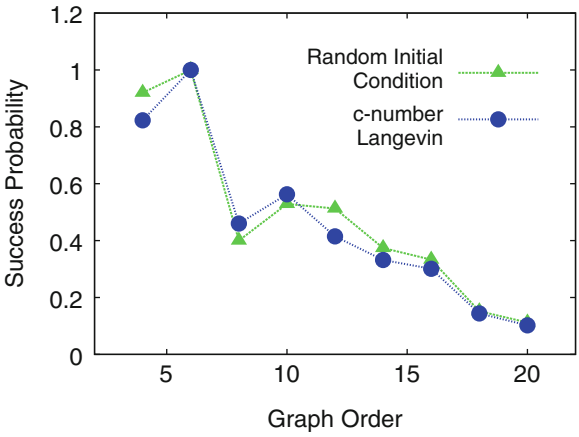

Fig. 11.4 The success probability of the network in solving the MAX-CUT problem on the worst-case instances listed in Table 11.3 when $p = 1.1$ and $\xi = -0.1$. The parameters used in the calculation are $\gamma_s = 1$, $\gamma_p = 100$ and $\kappa = 10^{-4}$ for the c-number Langevin approach, and $A_{\text{ini}} = 10^{-5}$ for the random initial condition approach

starting from the vacuum state. However, the existence of quantum noise inputs in these equations makes the computation relatively expensive. To avoid this issue, the following alternative method is used, which ignores the quantum noise terms and replaces them with a random initial condition.

For a graph with N vertices, the $2N$ classical dynamical equations of the in-phase and quadrature components in Eq. (11.8) are solved instead to obtain candidate cuts. The Dormand-Prince algorithm is chosen as the differential equation solver, which allows adaptive integration step length by evaluating the local truncation error [28]. In order to simulate the quantum noise, initial conditions to Eq. (11.8) are randomly generated in the neighborhood of the trivial steady state $c_j = s_j = 0$, $\forall j \in \{1, 2, \ldots, N\}$. In the current simulation, the degenerate OPOs initially have the same normalized amplitude $A_{\text{ini}} = 10^{-5}$ but different random phases. The simulation continues until the network approaches a stable steady state.

In this way, the differential equations to be dealt with switch from stochastic ones to deterministic ones, which considerably improves the efficiency of the numerical simulation. More importantly, as shown in Fig. 11.4, these two methods provide approximately identical results in terms of the success probability of the network in finding a correct answer when the random initial amplitude of the degenerate OPOs is selected to be the same order of magnitude as the quantum noise strength of the network. Since the number of equations required to be solved only increases linearly with the number of vertices, this method can also be applied to large-scale instances.

11.5.2 Results

As a first attempt to solve the MAX-CUT problem using the degenerate OPO network, the normalized pump rate and the coupling coefficient are fixed at $p = 1.1$, $\xi = -0.1$ for all the instances. This choice of p and ξ reflects the realistically achievable experimental condition. In addition, it guarantees for all instances that the network is operating above its threshold defined by Eq. (11.11) and the steady-state phases of the degenerate OPOs are either 0 or π according to the sufficient condition in Eq. (11.16).

11.5.2.1 Solution Quality

For the small cubic graphs, success probability of the network in finding a maximum cut is estimated by examining its approached steady states under 100 random initial conditions. For instances where the success probability is below 0.25 or in the 10 lowest instances among the cubic graphs of the same order, additional 10000 trials are conducted to refine the estimation. As shown in Fig. 11.5, the network is able to output a maximum cut with a high success rate for most of the instances. The average success probability for cubic graphs of order 20 is about 0.682. Even in the worst cases where the minimum success probability is attained, the network still substantially outperforms a random guess. For the worst-case instance with 20 vertices listed in Table 11.3, the network amplifies the success rate of picking one of the only 2 correct answers out of $2^{20} \approx 10^6$ candidates by about 60 000 times.

For the large G-set graphs, since optimal solutions are unknown, performance of the network are evaluated by making comparisons with the well-celebrated Goemans-Williamson (GW) algorithm based on semidefinite programming (SDP) [29]. The outcomes of running the network 100 times for sample G-set graphs and the GW algorithm implemented by the dual-scaling interior-point method

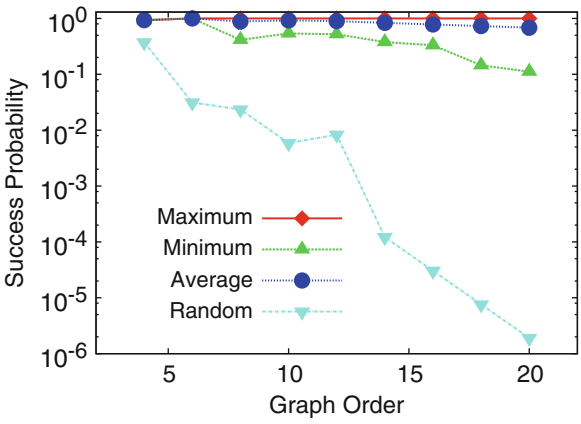

Fig. 11.5 The success probability of the network in solving the MAX-CUT problem on cubic graphs when $p = 1.1$ and $\xi = -0.1$. The maximum, minimum and average success probabilities are evaluated over instances of the same order. The success probability of a random guess for the worst-case instances is also included for comparison

Table 11.3 Worst-case performance of the network in solving the MAX-CUT problem on cubic graphs. Here, $q_{\min}$ denotes the worst-case success probability for each graph order when $p = 1.1$ and $\xi = -0.1$, and q^* is the achieved success probability at the optimal pump rate p^* when $\xi = -0.1$ for each worst-case instance

	Order								
	4	6	8	10	12	14	16	18	20
$q_{\min}$	0.932	1.000	0.413	0.538	0.522	0.378	0.330	0.145	0.111
q^*	1.000	1.000	0.699	0.739	1.000	1.000	1.000	0.158	0.741
p^*	1.05	1.30	1.30	1.30	1.00	0.85	0.85	1.15	0.82

[30] are summarized in Table 11.4. To facilitate the comparison, each cut value O generated from the network and the GW algorithm is normalized according to $(O + E_{\text{neg}})/(U_{\text{SDP}} + E_{\text{neg}})$, where U_{SDP} denotes the SDP upper bound of the optimal solution and E_{neg} the number of negative edges. It can be easily seen that both the network's best and average outputs are about 2–6 % better than the 0.878-performance guarantee of the SDP algorithm. Meanwhile, on 49 out of 71 instances the best output from the network gives a larger cut value than the GW algorithm. Since the average difference between the best and the average values is within 0.7 %, reasonable performance is expected for the network even in a single run, which makes the network favorable for applications when computation time is the utmost priority.

11.5.2.2 Computation Time

Given the randomness of the initial conditions, the computation time is estimated to be the average oscillation build-up time of the network. Figure 11.6 displays the worst-case results of solving the MAX-CUT problem on the cubic and G-set graphs. In addition, the computational complexities of best-known implementations for the GW algorithm are also plotted for reference. If a graph with n vertices and m edges is regular, the SDP in the GW algorithm can be approximately solved in almost linear time as $\tilde{\mathcal{O}}(m) = \mathcal{O}(m \log^2(n)\epsilon^{-4})$ using the matrix multiplicative weights method [31], where ϵ represents the accuracy of the obtained solution. However, slower algorithms are required for general graphs. If a graph is not regular but with all edges positive-weighted, the fastest algorithm available runs in $\tilde{\mathcal{O}}(nm) = \mathcal{O}(nm \log^2(n)\epsilon^{-3})$ time based on a Lagrangian relaxation-based method [32]. For graphs with both positive- and negative-weighted edges, the SDP is commonly solved using the interior-point method which scales as $\tilde{\mathcal{O}}(n^{3.5}) = \mathcal{O}(n^{3.5} \log(1/\epsilon))$ [33]. As can be seen in Fig. 11.6, the GW algorithm is generally not scalable due to the superlinear time scaling. On the other hand, the network's worst-case computation time fits well to a sublinear function $\mathcal{O}(n^{0.2})$. Since the degenerate OPO network can deal with all types of graphs, it has unparalleled advantage over the GW algorithm in solving large-scale instances.

Table 11.4 Performance of the network in solving the MAX-CUT problem on sample G-set graphs compared to the GW algorithm. Here, V denotes the number of vertices in the graph, E the number of edges, $O_{\max}$ and O_{avg} the network's best and average normalized cut values in 100 runs, respectively, and V_{SDP} the GW algorithm's outputs given by the dual-scaling interior-point implementation

Graph	V	E	E_{neg}	$O_{\max}$	O_{avg}	U_{SDP}	V_{SDP}
G1	800	19176	0	0.9591	0.9516	12083	0.9457
G6	800	19176	9511	0.9559	0.9506	2656	0.9448
G11	800	1600	783	0.9384	0.9254	629	0.9327
G14	800	4694	0	0.9367	0.9274	3191	0.9336
G18	800	4694	2315	0.9308	0.9223	1166	0.9282
G22	2000	19990	0	0.9349	0.9277	14136	0.9191
G27	2000	19990	10016	0.9321	0.9270	4141	0.9174
G32	2000	4000	1989	0.9328	0.9260	1567	0.9272
G35	2000	11778	0	0.9264	0.9202	8014	0.9292
G39	2000	11778	5875	0.9214	0.9152	2877	0.9226
G43	1000	9990	0	0.9373	0.9309	7032	0.9292
G48	3000	6000	0	0.9463	0.9292	6000	1.0000
G51	1000	5909	0	0.9333	0.9242	4006	0.9333
G55	5000	12498	0	0.9070	0.9009	11039	0.9006
G57	5000	10000	5019	0.9305	0.9259	3885	0.9237
G59	5000	29570	14737	0.9114	0.9074	7312	0.9148
G60	7000	17148	0	0.9037	0.8995	15222	0.8989
G62	7000	14000	7040	0.9295	0.9256	5431	0.9228
G64	7000	41459	20466	0.9129	0.9092	10466	0.9143
G65	8000	16000	8041	0.9284	0.9252	6206	0.9217
G66	9000	18000	8960	0.9285	0.9251	7077	0.9220
G67	10000	20000	10071	0.9285	0.9260	7744	0.9215
G70	10000	9999	0	0.9433	0.9379	9863	0.9633
G72	10000	20000	10003	0.9284	0.9256	7809	0.9215
G77	14000	28000	13896	0.9281	0.9256	11046	0.9205
G81	20000	40000	19983	0.9268	0.9250	15656	0.9195

11.5.3 Performance Improvement

The above results obtained with the normalized pump rate and coupling coefficient fixed at $p = 1.1$, $\xi = -0.1$ are by no means the optimum performance of the network. Another proper choice of p and ξ can boost the solution quality significantly. As an example, the improvement in the success probability for the worst-case instance among cubic graphs with 20 vertices is demonstrated in Fig. 11.7. It can be easily seen that the success rate is raised above 0.7 when the network is operated at the optimal pump rate p^* for the chosen coupling coefficient. The results for worst-case instances of other graph orders are listed in Table 11.3.

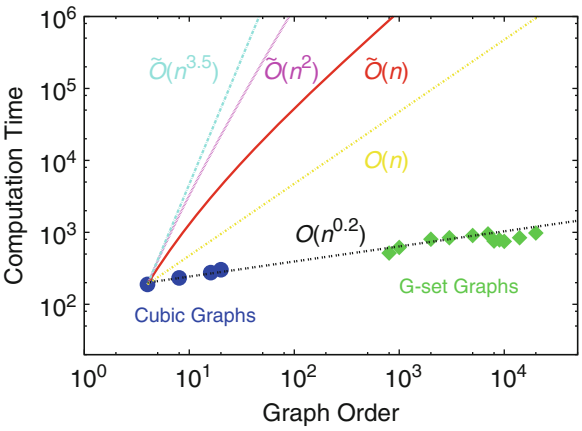

Fig. 11.6 The worst-case computation time of the network in solving the MAX-CUT problem on the cubic and G-set graphs when $p = 1.1$ and $\xi = -0.1$. Here, the time unit is the degenerate OPO cavity photon lifetime

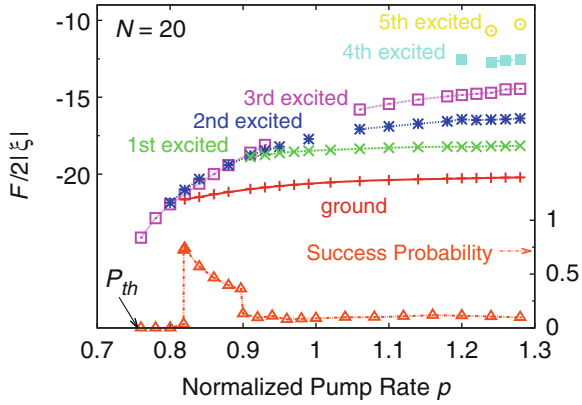

Fig. 11.7 The dependence of the success probability and the reachable steady states of the network on the normalized pump rate p when $\xi = -0.1$ for the worst-case instance among cubic graphs with 20 vertices

Except for the case with 18 vertices, simply adjusting the normalized pump rate has been effective in improving the solution quality.

The variation of the success probability with the normalized pump rate is closely related to the reachable steady states of the network. This relation is demonstrated in Fig. 11.7 as well. The approached steady states of the network are classified according to the weight of the cuts they represent. Since the Ising problem and the MAX-CUT problem are mutually reducible, the maximum cut classification is labeled "ground", and the second-largest cut classification is labeled "first excited" and so on. Each classification is then associated with a function $F = \Gamma - N$. Physically, F means the increased amount of the overall photon decay rate of a global mode due to the mutual coupling. If the approximation in Eq. (11.18) holds, $F/2|\xi|$ is exactly the Ising Hamiltonian corresponding to the MAX-CUT problem. For the shown instance, when the network is pumped just above its threshold, the first appearing steady states represent incorrect solutions. The success probability therefore vanishes because of the large discrepancy between $F/2|\xi|$ and

the energy of the corresponding Ising spin states. The normalized pump rate p has to rise to a certain level before steady states corresponding to the correct solutions can be developed. The success probability increases until p reaches p^* but drops again when the network is further pumped. This is because more and more newly reachable steady states are mapped to the incorrect solutions.

11.6 Experimental Implementation

Mismatch and phase decoherence noise are two main technical difficulties in building a network of coupled degenerate OPOs. In order to resolve these issues, a time division multiplexing (TDM) technique is exploited. In this scheme, spatially separated oscillators in the theoretical description are replaced by temporally separated oscillators in a single ring cavity. Degenerate OPOs are distinguished by the time slots that their signal fields are amplified, and mutual couplings among them are implemented by coherently feeding back the output signals through optical delay lines.

11.6.1 A Network of Four Degenerate OPOs

Figure 11.8 displays the system that implements a 4-OPO network using the TDM technique. The system is pumped with a mode-locked pulse laser with a repetition period T_R. To accommodate four independent temporally separated degenerate OPOs in the ring resonator, the round-trip time is designed to be $T_{RT} = 4T_R$. The couplings among these degenerate OPOs are realized by three delay lines. As shown in Fig. 11.8, delay line $i \in \{1, 2, 3\}$ introduces lag iT_R to the cavity so that delay 1 implements the couplings ξ_{12}, ξ_{23}, ξ_{34}, ξ_{41}, delay 2 the couplings ξ_{13}, ξ_{24}, ξ_{31}, ξ_{42}, and delay 3 the couplings ξ_{14}, ξ_{21}, ξ_{32}, ξ_{43} for the network. The output from the resonator is sent to a Michelson interferometer with time delay $T_d = T_R$ between the two arms. From the differential phases between adjacent signal pulses measured by the interferometer, phase states of the degenerate OPO network are recovered.

When all the delay lines are blocked, one of the four possible pulse patterns shown in Fig. 11.9a is detected by a fast detector at the interferometer output after the system is turned on. The pulses in these patterns are separated by 4 ns, which is exactly the pump repetition period T_R, and each pulse has either a low or a high intensity corresponding to destructive or constructive interference of the consecutive OPO signal fields, respectively. The low-level pulses are non-zero because of the diffraction mismatch of the interferometer arms. Figure 11.9b shows the histogram of the eight phase states obtained from the pulse patterns after running the system 1000 times. The result indicates uniform distribution of the phase states confirming that four temporally separated OPOs are operating independently in the same resonator.

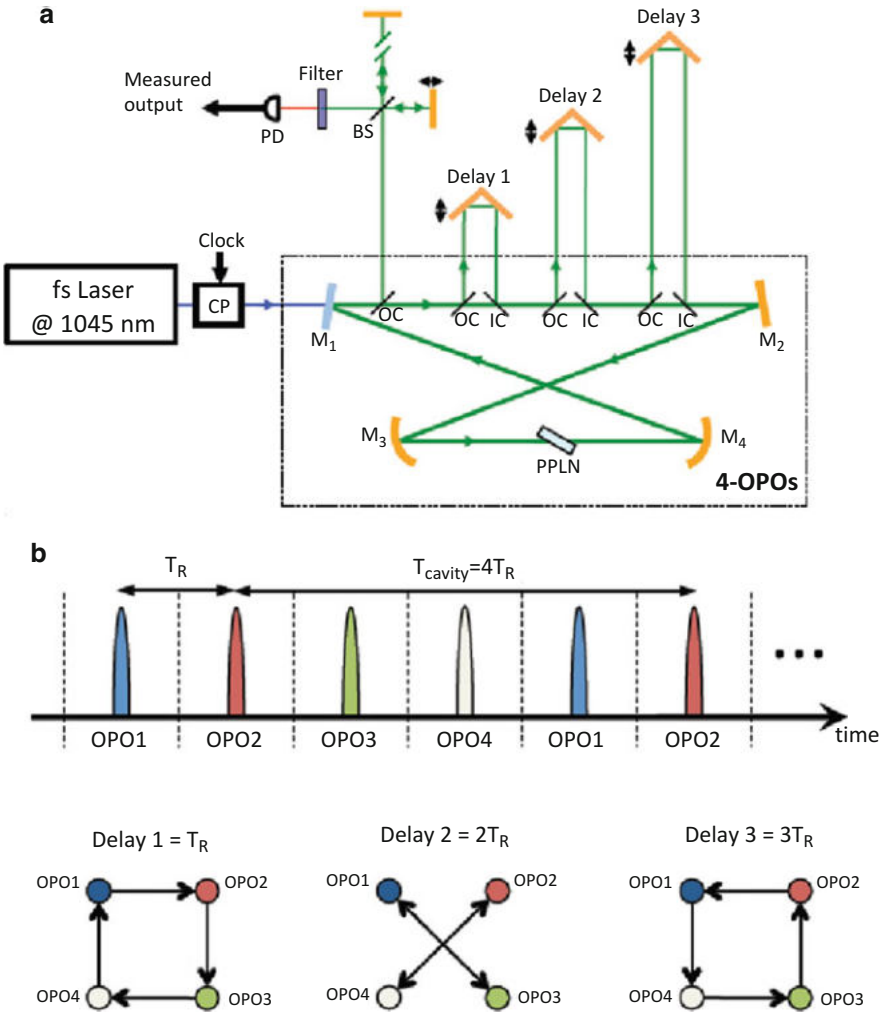

Fig. 11.8 (**a**) Experimental setup for a network of four degenerate OPOs. The nonlinear crystal inside the ring resonator is periodically poled lithium niobate (PPLN). The femtosecond pump laser has a wavelength of 1045 nm and repetition period $T_R = 4$ ns. A chopper (CP) restarts the system every 1 ms and gradually increases the pump field from below to about two times above the oscillation threshold in about 180 µs. Each of the output couplers (OCs) and input couplers (ICs) provides $4 \pm 2\,\%$ of power reflection. The cavity photon lifetime is about 60 ns. (**b**) Illustration of the time slot assignment to the output pulse train to represent four degenerate OPOs and the couplings provided by the delay lines

When all the delay lines are open and introduce π phase shifts to the injection signals, the system becomes a setup to solve the MAX-CUT problem on the cubic graph with 4 vertices. All the coupling coefficients among the degenerate OPOs are the same with the value $\xi \approx -0.08$. The correct solutions to this instance

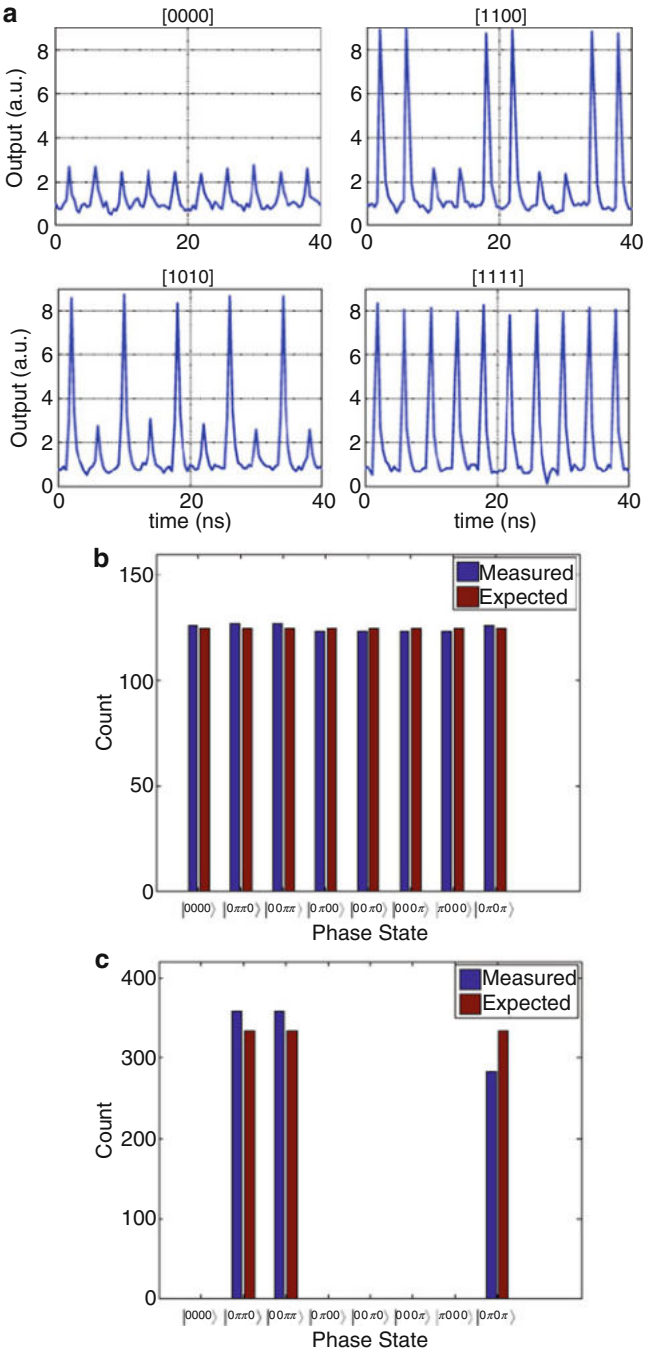
a
[0000]
[1100]
[1010]
[1111]
Output (a.u.)
time (ns)
b
Measured
Expected
Count
Phase State
c
Measured
Expected
Count
Phase State

corresponds to phase states of the network with two degenerate OPOs with zero phases and the remaining two with π phases. Figure 11.9c shows the histogram of the obtained phase states for 1 000 trials. It can be easily seen that no incorrect solution is detected, and the distribution of correct solutions is close to uniform. Therefore, the error rate of computation for this instance is expected to be less than 10^{-3}, and the current estimation is limited by the length of measurements.

11.6.2 Towards the Implementation of Large-Scale Network

An arbitrary large-scale network may also be implemented by extending the idea of using the TDM technique. Meanwhile, exploiting optical fiber technologies and planar light wave circuits can enable compact implementation. A schematic diagram of such fiber-based implementation is illustrated in Fig. 11.10. The single ring resonator whose round-trip time T_{RT} is N times the pump repetition period T_{R} is utilized to represent N degenerate OPOs. The $N-1$ delay lines with delay time T_{R}, $2T_{\mathrm{R}}$, ... $(N-1)T_{\mathrm{R}}$ are to introduce mutual couplings among the degenerate OPOs. In order to implement all the N^2-N number of possible couplings using the $N-1$ delay lines, electrooptic phase and amplitude modulators (EOM) are used to synchronously control the delay lines depending on the phases and the strength of the desired couplings. In this way, the physical size of the implementation scales linearly with N. To avoid effects of nonlinearities and dispersion in optical fibers, picosecond pump pulses can be used in a long resonator and long delay lines comprising optical fiber components.

As an example, for a pump with a repetition period $T_R = 100$ ps, a resonator with 200 m of optical fiber results in 10 000 temporally separated degenerated OPOs. The expected photon lifetime of such a fiber-based network is about 6×10^{-6}s. From the result shown in Fig. 11.6, it will take less than 1 ms for the network to find a reasonably good solution to MAX-CUT instances with 10 000 vertices. The main challenge is to stabilize the phases of all these fiber links. Advancement of extremely low-noise phase-stabilized long optical fibers [34] is promising in terms of overcoming this challenge using the existing technologies. Moreover, the

Fig. 11.9 (**a**) Pulse patterns at the interferometer output with a fast detector. Since no phase and time references are used in the measurement, each pattern corresponds to multiple phase states. Because complimentary phase states such as $|0\pi 0\pi\rangle$ and $|\pi 0\pi 0\rangle$ correspond to the same solution and phase pattern, one representative is selected on behalf of the pair. Then, the [0000] pulse pattern represents the state $|0\pi 0\pi\rangle$; the [1100] pattern the states $|0\pi 00\rangle$, $|00\pi 0\rangle$, $|000\pi\rangle$ and $|\pi 000\rangle$; the [1010] pattern the states $|0\pi\pi 0\rangle$ and $|00\pi\pi\rangle$; the [1111] pattern the state $|0000\rangle$. (**b**) Histogram of the phase states when all the delay lines are blocked for 1000 runs. (**c**) Histogram of the phase states when all the delay lines are on and their phases are locked to π for 1 000 runs. The count of each phase state is estimated by assuming that phase states corresponding to the same interferometer pulse pattern appear equiprobably

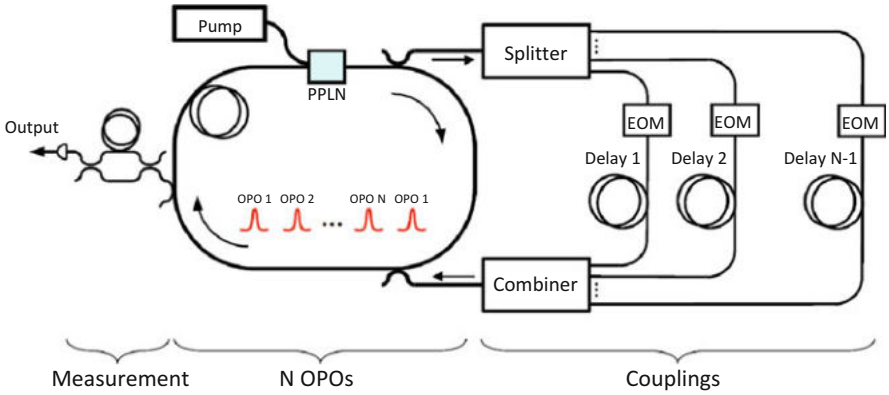

Fig. 11.10 A schematic diagram of a fiber-based large-scale degenerate OPO network

regenerative behavior of a degenerate OPO suggests that the network can tolerate relatively large phase noise in the couplings.

11.7 Quantum Mechanical Simulation

Given the promising results demonstrated in both numerical and experimental examinations, an ensuing question to ask is whether any quantum feature intrinsic to the degenerate OPO network has contributed to its computational ability. In quantum computing, superposition and entanglement are two typical quantum features that make speed-up of computation possible. As to the degenerate OPO network, the macroscopic quantum mechanical superposition of and quantum non-local correlation between field states can be considered as the counterparts. It has been theoretically reported that transient superposition state exists in a single degenerate OPO [35] and entanglement occurs in two oscillators with evanescent coupling [36, 37]. In the following, these properties are studied for the system of two degenerate OPOs with mutual injection.

11.7.1 Theoretical Model

The theoretical formulation is based on the positive *P*-representation [38]. This representation results from non-diagonal expansion of the density operator. For a single degenerate OPO, it gives positive semidefinite diffusion terms in the Fokker-Planck equation [21], which enables quantum mechanical simulation by solving corresponding stochastic differential equations (SDEs).

The positive P-representation for a single degenerate OPO is defined as

$$\hat{\rho} = \int P(\boldsymbol{\alpha}, \boldsymbol{\beta}) \frac{|\boldsymbol{\alpha}\rangle\langle\boldsymbol{\beta}|}{\langle\boldsymbol{\beta}|\boldsymbol{\alpha}\rangle} d^4\boldsymbol{\alpha} d^4\boldsymbol{\beta}, \tag{11.19}$$

where $\boldsymbol{\alpha} = (\alpha_p, \alpha_s)$, $\boldsymbol{\beta} = (\beta_p, \beta_s)$, and α_p, α_s represent the c-number eigenvalues of the annihilation operators on the pump and signal fields of the OPO, respectively, and β_p, β_s are the counterparts for the creation operators. It can be easily observed from Eq. (11.19) that the ensemble averages of $\boldsymbol{\alpha}$ and $\boldsymbol{\beta}$ under this representation are equal to those of corresponding annihilation and creation operators. Although it follows that $\langle\boldsymbol{\alpha}\rangle^* = \langle\boldsymbol{\beta}\rangle$, $\boldsymbol{\alpha}$ and $\boldsymbol{\beta}$ are distinct variables so that off-diagonal components of ρ can be treated. Equation (11.19) is substituted into the master equation under the Hamiltonian (11.3) and the Born-Markov approximation to get the corresponding Fokker-Planck equation for $P(\boldsymbol{\alpha}, \boldsymbol{\beta})$. Eventually, the SDEs for $\boldsymbol{\alpha}$ and $\boldsymbol{\beta}$ obeying the distribution $P(\boldsymbol{\alpha}, \boldsymbol{\beta})$ are derived via the Ito rules [21].

To obtain the positive P-representation for two coupled degenerate OPOs, phenomenological mutual injection terms $\xi\gamma_s\alpha_{sj}/2$ for α_{si} and $\xi\gamma_s\beta_{sj}/2$ for β_{si} are introduced into the SDEs according to Eq. (11.7). Here, $\{i, j\} = \{1, 2\}, \{2, 1\}$ are the indices of the oscillators, ξ is the coupling coefficient including the loss and coupling phase of the injection, and $\gamma_s/2$ is the cavity decay rate for the signal field. These terms result from somewhat lengthy derivation based on a quantum-mechanical model and the details will be reported elsewhere. The resulting normalized Ito SDEs [39] for the c-number signal variables η_i and μ_i are

$$\begin{aligned} \mathrm{d}\eta_i &= \left[-\eta_i + \mu_i\left(p - \eta_i^2\right) + \xi\eta_j\right]\mathrm{d}t + \frac{1}{A_s}\sqrt{p - \eta_i^2}\,\mathrm{d}W_{\eta i}, \\ \mathrm{d}\mu_i &= \left[-\mu_i + \eta_i\left(p - \mu_i^2\right) + \xi\mu_j\right]\mathrm{d}t + \frac{1}{A_s}\sqrt{p - \mu_i^2}\,\mathrm{d}W_{\mu i}. \end{aligned} \tag{11.20}$$

Here, $\eta_i \equiv \alpha_i/A_s$, $\mu_i \equiv \beta_i/A_s$ and $A_s = \sqrt{\gamma_s\gamma_p/2\kappa^2}$ is the normalization amplitude serving as a noise parameter. κ expresses the nonlinear gain, and $\gamma_p/2$ is the cavity decay rate for the pump. $p = F_p/F_{th}$ is the normalized pumping rate, where F_p is the real amplitude of the external pump flux and $F_{th} = \gamma_s\sqrt{\gamma_p}/4\kappa$. The time is scaled with the signal cavity lifetime, i.e. $t = \gamma_s\tau/2$. $\mathrm{d}W_{\eta i}$ and $\mathrm{d}W_{\mu i}$ are independent real Wiener increments. Assuming the condition $\gamma_p \gg \gamma_s$, we have adiabatically eliminated the pump variables with the steady state values, i.e. $\alpha_{pi(ss)} = (2F_p/\sqrt{\gamma_p} - \kappa\alpha_i^2)/\gamma_p$, $\beta_{pi(ss)} = (2F_p/\sqrt{\gamma_p} - \kappa\beta_i^2)/\gamma_p$. Since the positive P-representation can treat any quantum states even when the eigenvalues $\boldsymbol{\alpha}$ and $\boldsymbol{\beta}$ are small [38], these c-number variables are expected to appropriately represent the quantum states of the cavity OPO fields in a single-shot stochastic simulation.

We consider the quadrature amplitudes $\hat{X}_i \equiv (\hat{a}_i + \hat{a}_i^\dagger)/2$ and $\hat{P}_i \equiv (\hat{a}_i - \hat{a}_i^\dagger)/2i$ which can be measured experimentally, and simulate the probability distributions of them. It has been shown that the fringe in P distribution indicates a macroscopic

quantum superposition of two out-of-phase coherent states [40]. The distribution functions can be obtained by unrestricted random sampling for α_i and β_i obeying Eq. (11.20) with [35]

$$P(Z_i) = \mathrm{Tr}_j\langle Z_i|\rho|Z_i\rangle = \int P(\boldsymbol{\alpha},\boldsymbol{\beta})\frac{\langle Z_i|\alpha_i\rangle\langle\beta_i|Z_i\rangle}{\langle\beta_i|\alpha_i\rangle}d^4\boldsymbol{\alpha}d^4\boldsymbol{\beta}, \quad Z = X, P, \tag{11.21}$$

where $\langle X_i|\alpha_i\rangle = \pi^{-1/4}\exp(-X_i^2/2 + \sqrt{2}X_i\alpha_i - \alpha_i^2/2 - |\alpha_i|^2/2)$, $\langle P_i|\alpha_i\rangle = \pi^{-1/4}\exp(-P_i^2/2 - i\sqrt{2}P_i\alpha_i + \alpha_i^2/2 - |\alpha_i|^2/2)$ and $\langle\beta_i|\alpha_i\rangle = \exp\{-(|\alpha_i|^2 + |\beta_i|^2)/2 + \beta_i^*\alpha_i\}$. Here, the trace Tr_j is on the signal variables for OPOj ($\neq i$). The pump variables have been omitted due to the adiabatic elimination.

In the positive P-representation, the normally ordered moments can also be obtained by Monte Carlo integration with [38]

$$\langle\hat{a}_i^{\dagger n}\hat{a}_i^m\rangle = \int P(\{\alpha_i\},\{\beta_i\})\ \beta_i^n\alpha_i^m\ \mathrm{d}^2\alpha_1\mathrm{d}^2\alpha_2\mathrm{d}^2\beta_1\mathrm{d}^2\beta_2. \tag{11.22}$$

Also, we consider the pair of Einstein-Podolsky-Rosen (EPR) [41] type operators $\hat{u} \equiv \hat{X}_1 + \hat{X}_2$ and $\hat{v} \equiv \hat{P}_1 - \hat{P}_2$ for the two OPO fields and the total variance of them to estimate the quantum correlation in the system. The quadrature amplitudes defined here satisfies the commutation relation $[\hat{X}_i, \hat{P}_j] = i\delta_{i,j}/2$, thus the condition for the entanglement (inseparability) between the two cavity modes [42] is

$$\langle\Delta\hat{u}^2\rangle + \langle\Delta\hat{v}^2\rangle < 1, \tag{11.23}$$

where $\Delta\hat{u} \equiv \hat{u} - \langle\hat{u}\rangle$ and $\Delta\hat{v} \equiv \hat{v} - \langle\hat{v}\rangle$. The ensemble averages and variances of the EPR type operators including the vacuum fluctuation can be obtained with Eq. (11.22), though their detailed expressions are omitted because of space limitations.

11.7.2 Simulation Result

We show the result of the numerical simulation on the system with the out-of-phase mutual injection, i.e. $\xi < 0$. Here, the system is initialized with the vacuum state and is gradually pumped [43], that is, the pump parameter p is slowly increased so that the OPO field states are continuously driven from below to above the threshold to hold the state with the minimum photonic loss. We set the linear schedule as $p(t) = p_f t/t_f$, where p_f and t_f are the pump and time parameters for the final state. The state of the system is always transient because the pump parameter is continuously changed. However, the sweeping is sufficiently slow so that the system keeps itself near to the stablest steady state. $p_f = 1.1$ and $t_f = 100$ is used in the simulation below. We adopt a second-order weak scheme [44] with a time step $\Delta t = 2 \times 10^{-3}$ for the stochastic simulation.

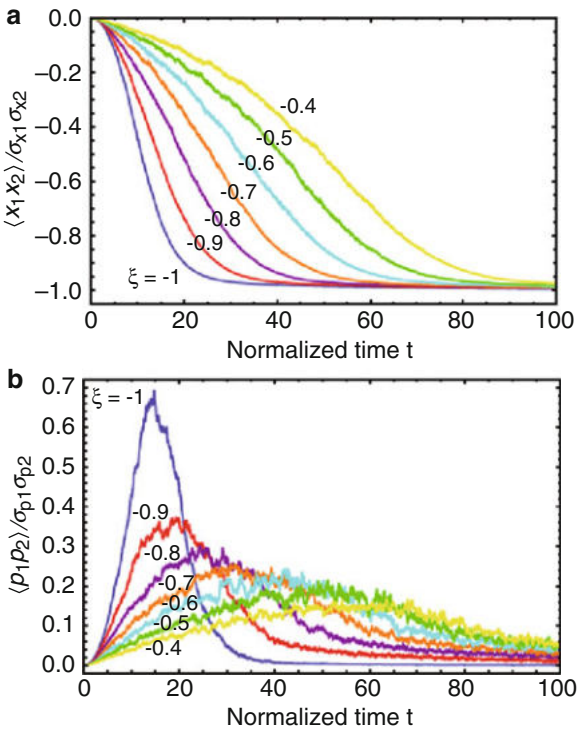

Fig. 11.11 Second-order moments (**a**) $\langle \hat{X}_1 \hat{X}_2 \rangle / \sqrt{\langle \Delta \hat{X}_1^2 \rangle \langle \Delta \hat{X}_2^2 \rangle}$ and (**b**) $\langle \hat{P}_1 \hat{P}_2 \rangle / \sqrt{\langle \Delta \hat{P}_1^2 \rangle \langle \Delta \hat{P}_2^2 \rangle}$ dependent on the normalized time t for different mutual injection magnitudes ξ. Here, the pump parameter is swept linearly with the time, i.e. $p(t) = p_f t / t_f$, where $p_f = 1.1$ and $t_f = 100$. The normalization amplitude is $A_s = 5$. In (**a**), X_1 and X_2 shows the negative correlation soon after the beginning of the pumping. (**b**) shows the mutual injection holds the positive correlation between P_1 and P_2 induced by the quantum noise below the threshold and the mutual injection. Note that the threshold depends on ξ

Figure 11.11 shows the second-order moments for the quadrature amplitudes. Here, they are normalized with the products of the standard deviations of the relevant amplitudes. X_1 and X_2 are negatively correlated from the beginning of the pumping as shown in Fig. 11.11a. It means that the coherent Ising machine can find a ground state for the minimal anti-ferromagnet model. Note that the signal photon numbers in the OPOs $\langle \hat{a}_1^\dagger \hat{a}_1 \rangle \approx \langle \hat{a}_2^\dagger \hat{a}_2 \rangle$ vary from 12 to 27 dependent on the mutual injection strength $|\xi|$. The semiclassical oscillation threshold also depends on $|\xi|$, as $p_{th} = 1 - |\xi|$. In Fig. 11.11b, P_1 and P_2 have some positive correlation, because the mutual injection stimulates the damping of the fluctuation in $P_1 + P_2$ while restricts that in $P_1 - P_2$. This can be seen by the drift matrix for them.

Figure 11.12 presents the distribution functions of the quadrature amplitudes for the two different time: $t = 24.72$ then $p = 0.27192$ for Fig. 11.12a and $t = 25.54$, $p = 0.28094$ for Fig. 11.12b. Here, $A_s = 100$ and $\xi = -1$. The distributions $P(X_i)$ are broadened compared to that of the initial vacuum state with the variance of $1/2$ as seen in both Fig. 11.12a, b. They can be fitted with Gaussian functions, while have some roughness mostly coming from the large fluctuation around the critical point. $P(P_2)$ in Fig. 11.12a and $P(P_1)$ in Fig. 11.12b show the deviation from the Gaussian fitting curves on their sides, not as in the momentum distributions of the other OPOs. This indicates individual formation of the macroscopic superposition components in the OPOs. However, these states

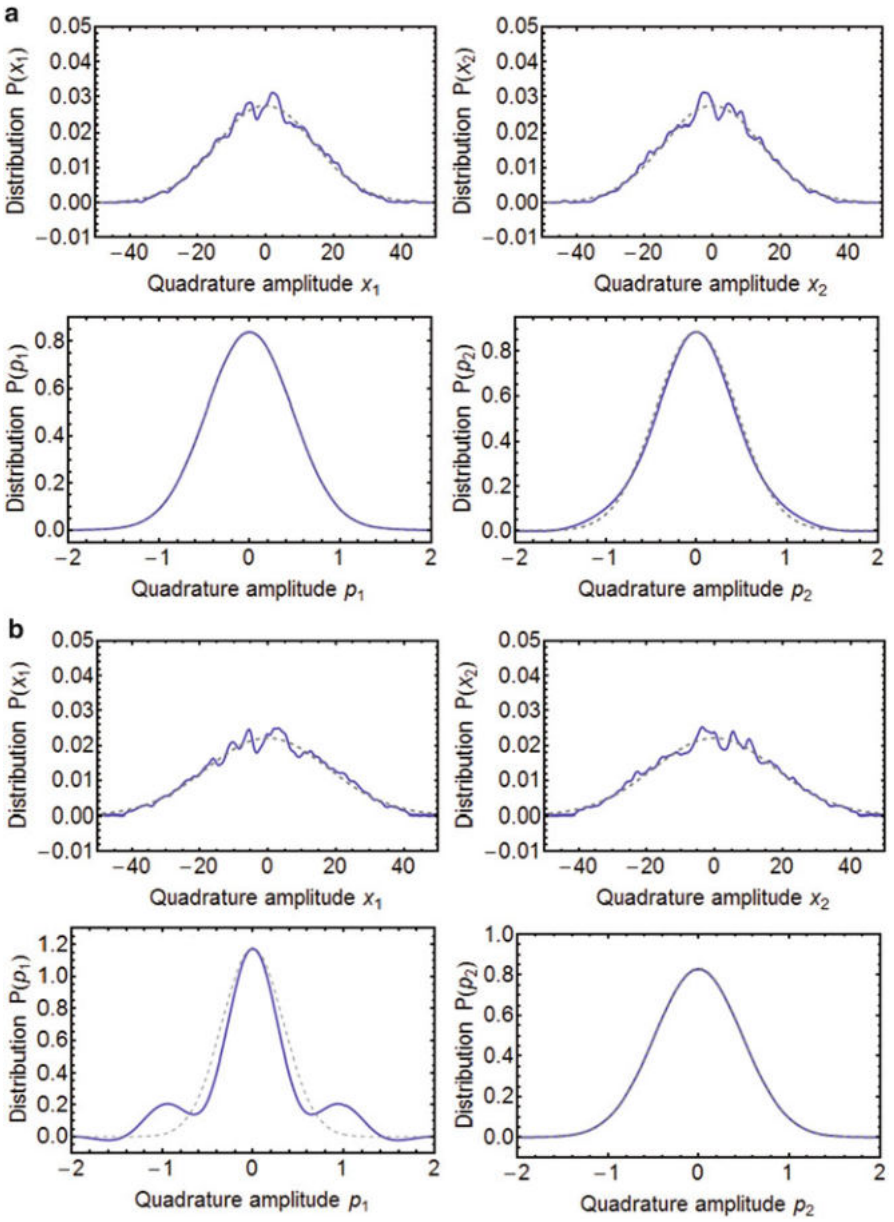

Fig. 11.12 Distribution functions for the quadrature amplitudes for different times near to the oscillation threshold. (**a**) $t = 24.72$ and (**b**) $t = 25.54$. $A_s = 100$ and $\xi = -1$. The *dashed lines* are the Gaussian fitting curves. $P(X_1)$ and $P(X_2)$ can be fitted with the Gaussian functions with the standard deviations of 14.5 for (**a**) and 18.0 for (**b**). The roughness of them comes from the critical fluctuation. $P(P_2)$ in (**a**) and $P(P_1)$ in (**b**) show deviation and humps off the Gaussian curves, not as the Gaussian momentum distributions of the other OPOs. This indicates the existence of transient macroscopic quantum superposition components in the OPOs. Note that the slightly negative region of $P(P_1)$ in (**b**) is attributed to numerical errors due to the strong oscillation components

are transient and shortly vanish with about or less than one tenth of the cavity lifetime. Also, it is difficult to refer to the possibility of the synchronized formation of these states, because the simulation is highly probabilistic due to the critical fluctuation. The superposition comes from the quantum noise around the critical point erasing the which-path information and inducing the tunneling among the states with finite X_i. This is possibly contributed to also by the mutual injection and the third order effect of μ_i and η_i in Eq. (11.20), physically involving a pump photon and two signal photons. Note that Eq. (11.21) indicates the fringe in $P(P_i)$ comes from the integration of $\exp\{-i\sqrt{2}P_i\,\mathrm{Re}(\alpha_i-\beta_i)\}$, thus the Glauber-Sudarshan $P(\alpha)$ representation cannot treat states with such quantum interference in principle because of its restriction $\beta = \alpha^*$. A larger A_s and ξ tend to give a clearer fringe in $P(P_i)$. However, the lossless mutual injection can lead to an unphysical data for the system very near to the threshold due to numerical errors, such as a slightly negative variance in a quadrature amplitude, which is not the case for the time points in Fig. 11.12.

Figure 11.13 displays the time dependence of the fluctuation on the sum and difference of the quadrature amplitudes: (a) for $\langle \Delta u^2 \rangle$, (b) for $\langle \Delta v^2 \rangle$ and (c) for $\langle \Delta u^2 \rangle + \langle \Delta v^2 \rangle$. As shown in Fig. 11.13a, a large mutual injection can suppress the fluctuation on $u = X_1 + X_2$ up nearly to the vacuum level (1/2) around the threshold in spite of the critical fluctuation on each X_i. We see in Fig. 11.13b that the noise in $v = P_1 - P_2$ gets less than 1/2 there, indicating the quantum correlation between the two OPOs. The curves for the total noise $\langle \Delta u^2 \rangle + \langle \Delta v^2 \rangle$ in Fig. 11.13c have the portions which satisfy the condition Eq. (11.23), i.e. the noise level lower than the value of 1 for the vacuum state. This clearly indicates the inseparability between the cavity OPO field states with large mutual injections and means that the mutual injection can be a quantum communication channel. Note that the entanglement is totally attributed to P_i, and the correlation in X_i does not fall below the vacuum level. Thus, this does not mean the EPR paradox [41] and in this sense the quantum correlation in this system is not complete. A smaller mutual injection gives a larger variance in u, leading to destruction of the entanglement. The result here shows that an amplitude coupling coefficient larger than $\xi \sim 0.5$, i.e. 25 % in the feedback power is needed for the single-mode OPO network to hold the entanglement before the macroscopic bifurcation in X_i due to the oscillation.

We simulated the system of two OPOs with the out-of-phase mutual injection in the framework of the positive P-representation. As a result, we have found that the simplest coherent computing system based on OPOs can exhibit the transient macroscopic superposition components and the entanglement of a quadrature amplitude between the separate OPO cavity fields, which are expected to be resources for quantum computing. We can extend this approach based on the quantum expectation values to investigate the quantumness in larger systems. To expect the result of each experimental trial with the large machine exhibiting probabilistic behavior in quantum mechanics, another scheme like the Monte Carlo wave-function method [45] will need to be explored. Also, the theory covering quantum and chaotic systems might lead to findings about the performance of the system.

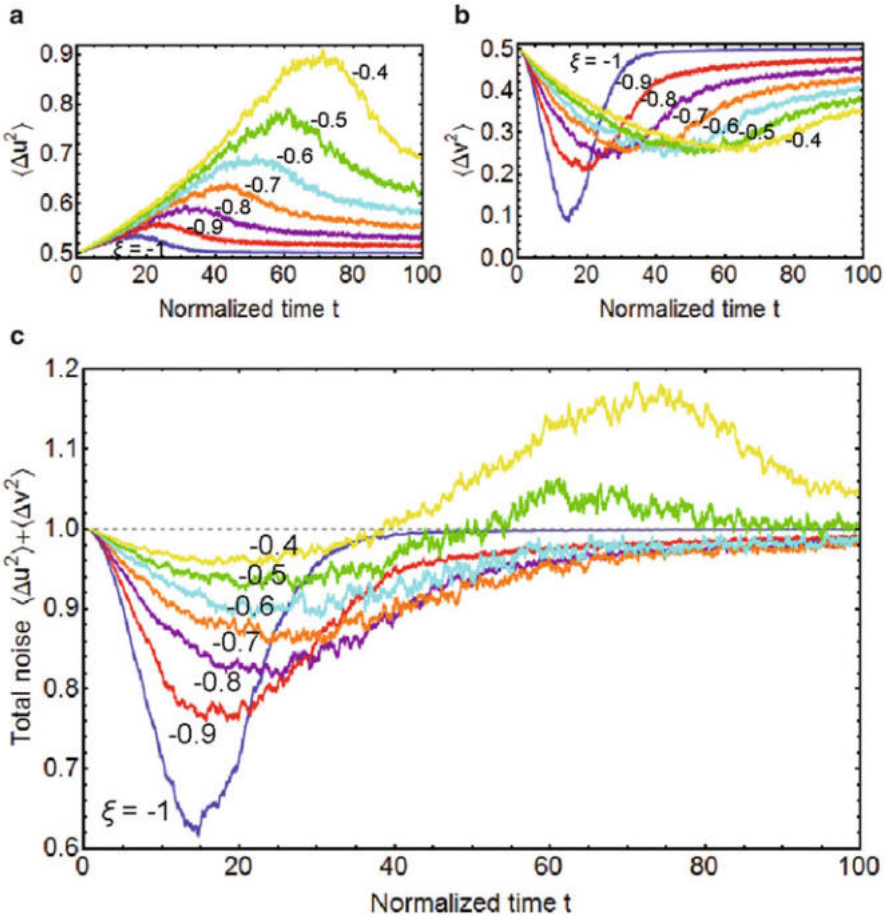

Fig. 11.13 Fluctuation of the sum and difference of the quadrature amplitudes (**a**) $\langle \Delta u^2 \rangle$, (**b**) $\langle \Delta v^2 \rangle$ and (**c**) $\langle \Delta u^2 \rangle + \langle \Delta v^2 \rangle$ dependent on the time for different ξ. $A_s = 5$. (**a**) shows that the mutual injection decreases $\langle \Delta u^2 \rangle$ nearly to the vacuum level (1/2) around the critical point. In (**b**), $\langle \Delta v^2 \rangle$ falls below the vacuum level and shows the quantum mechanical correlation. The *dashed line* in (**c**) is the vacuum fluctuation level and means the bound for the entanglement. The curves of $\langle \Delta u^2 \rangle + \langle \Delta v^2 \rangle$ in (**c**) have the parts which are clearly below the bound, thus indicates the entanglement there, i.e. the quantum communication channel between the two OPO fields

11.8 Conclusion

The computational ability of a degenerate OPO network to solve NP-hard problems has been investigated. When the network is pumped well above its threshold as defined by Eq. (11.11) and the condition given by Eq. (11.16) is also satisfied, phase configurations of the network are in one-to-one correspondence with eigenstates of the Ising Hamiltonian. If the mutual coupling among the constituent degenerate

OPOs is sufficiently weak, the overall photon decay rate from the network is proportional to the eigenenergy of the corresponding eigenstate, as demonstrated in Eq. (11.18).

Performance of the network has been numerically studied against the NP-hard MAX-CUT problem on small cubic graphs and large random graphs in the G-set. Reasonable success probability has been achieved for cubic graphs with number of vertices up to 20. At the time of writing, whether the worst-case success probability starts to decrease exponentially for larger graphs is not known. On the other hand, the results for the G-set graphs demonstrate promising evidence for the degenerate OPO network as an approximate solver. The network can most of the time find better solutions with a much faster speed than the celebrated GW algorithm based on semidefinite programming as shown in Table 11.4 and Fig. 11.6.

The proof-of-concept experiment has been conducted with a TDM scheme using a multi-pulse optical cavity and coherent optical feedback. A network is realized to solve the MAX-CUT problem on the cubic graph with four vertices, and it finds a correct solution in all 1000 runs. It is anticipated that a medium-size network with 5000–10000 degenerate OPOs can be practically implemented using a pulse pump laser with a clock frequency of 1 GHz and a fiber ring cavity of 1–2 km. Such a medium-size network will find a practical application already in searching for an optimum solution in dynamically varying graphs.

References

1. F. Barahona, On the computational complexity of Ising spin glass model. J. Phys. A Math. Gen. **15**, 3241–3253 (1982)
2. V. Dotsenko, *Introduction to the Replica Theory of Disordered Statistical Systems* (Cambridge University Press, Cambridge, 2000)
3. K. Binder, A.P. Young, Spin glasses: experimental facts, theoretical concepts and open questions. Rev. Mod. Phys. **58**, 801–976 (1986)
4. M.R. Garey, D.S. Johnson, *Computers and Intractability: A Guide to the Theory of NP-Completeness* (Freeman, San Francisco, 1979)
5. R.M. Karp, Reducibility among combinatorial problems, in *Complexity of Computer Computations*, ed. by R.E. Millera, J.W. Thatcher (Plenum Press, New York, 1972), pp. 85–103
6. S. Kirkpatrick, C.D. Gelatt Jr., M.P. Vecchi, Optimization by simulated annealing. Science **220**, 671–680 (1983)
7. T. Kadowaki, H. Nishimori, Quantum annealing in the transverse Ising model. Phys. Rev. E **58**, 5355–5363 (1998)
8. G.E. Santoro, R. Martonak, E. Tosatti, Theory of quantum annealing of an Ising spin glass. Science **295**, 2427–2430 (2002)
9. E. Farhi, J. Goldstone, S. Gutmann, J. Lapan, A. Lundgren, D. Preda, A quantum adiabatic evolution algorithm applied to random instances of an NP-complete problem. Science **292**, 472–476 (2001)
10. W. van Dam, M. Mosca, U.V. Vazirani, How powerful is adiabatic quantum computation, in *Proceedings of the 42nd IEEE Symposium on Foundation of Computer Science*, Las Vegas (IEEE Computer Society, 2001)
11. D. Aharonov, W. van Dam, J. Kempe, Z. Landau, S. Lloyd, O. Regev, Adiabatic quantum computation is equivalent to standard quantum computation. SIAM J. Comput. **37**(1), 166–194 (2007)

12. A.E. Siegman, *Lasers* (University Science Books, Mill Valley, 1986)
13. S. Utsunomiya, K. Takata, Y. Yamamoto, Mapping of Ising models onto injection-locked laser systems. Opt. Express **19**, 18091–18108 (2010)
14. K. Takata, S. Utsunomiya, Y. Yamamoto, Transient time of an Ising machine based on injection-locked laser network. New J. Phys. **12**, 013052–013073 (2012)
15. J.W.F. Woo, R. Landauer, Fluctuations in a parametrically excited subharmonic oscillator. IEEE J Quantum Electron. **7**, 435–440 (1971)
16. E. Goto, The parametron, a digital computing element utilizes parametric oscillation. Proc. IRE **47**, 1304–1316 (1959)
17. W.H. Louisell, A. Yariv, A.E. Siegman, Quantum fluctuations and noise in parametric processes i. Phys. Rev. **124**, 1646–1654 (1961)
18. A. Marandi, N.C. Leindecker, K.L. Vodopyanov, R.L. Byer, All-optical quantum random bit generation from intrinsically binary phase of parametric oscillator. Opt. Express **20**, 19322–19330 (2012)
19. Z. Wang, A. Marandi, K. Wen, R.L. Byer, Y. Yamamoto, Coherent Ising machine based on degenerate optical parametric oscillators. Phys. Rev. A **88**, 063853 (2013)
20. A. Marandi, Z. Wang, K. Takata, R.L. Byer, Y. Yamamoto, Network of time-multiplexed optical parametric oscillators as a coherent Ising machine. Nat. Photon. **8**, 937–942 (2014)
21. P.D. Drummond, K.J. McNeil, D.F. Walls, Non-equilibrium transitions in sub/second harmonic generation ii. quantum theory. Opt. Acta **28**, 211–225 (1981)
22. M. Orszag, *Quantum Optics: Including Noise Reduction, Trapped Ions, Quantum Trajectories, and Decoherence* (Springer, Berlin/New York, 2000)
23. G. Milburn, D.F. Walls, Production of squeezed states in a degenerate parametric amplifier. Opt. Commun. **39**, 401–404 (1981)
24. J.M. Kowalski, G.L. Albert, B.K. Rhoades, G.W. Gross, Neuronal networks with spontaneous, correlated bursting activity: theory and simulations. Neural Netw. **5**, 805–822 (1992)
25. J.N. Franklin, *Matrix Theory* (Prentice-Hall, Inc., Englewood Cliffs, NJ, 1968)
26. M. Yannakakis, Node-and edge-deletion np-complete problems, in *Proceedings of the Tenth Annual ACM Symposium on Theory of Computing*, San Diego (IEEE Computer Society, 1978)
27. G. Royle, Cubic graphs, http://www.easybib.com/reference/guide/mla/website. Oct 1996
28. J.D. Lambert, *Numerical Methods for Ordinary Differential Systems: The Initial Value Problem* (Wiley, Chichester/New York, 1991)
29. M.X. Goemans, D.P. Williams, Improved approximation algorithms for max-cut and satisfiability problems using semidefinite programming. J. ACM **42**, 1115–1145 (1995)
30. Y.Y. Steven, J. Benson, X. Zhang, Mixed linear and semidefinite programming for combinatorial and quadratic optimization. Optim. Mehtods Softw. **11**, 515–544 (1999)
31. S. Arora, S. Kale, A combinatorial, primal-dual approach to semidefinite programs, in *Proceedings of the Thirty-Ninth Annual ACM Symposium on Theory of Computing*, San Diego (2007)
32. P. Klein, H.-I. Lu, Efficient approximation algorithms for semidefinite programs arising from max cut and coloring, in *Proceedings of the Twenty-Eighth Annual ACM Symposium on Theory of Computing*, El Paso (1996), pp. 338–947
33. F. Alizadeth, Interior point methods in semidefinite programming with applications to combinatorial optimization. SIAM J. Optim. **5**(1), 13–51 (1995)
34. G. Grosche, O. Terra, K. Predehl, R. Holzwarth, B. Lipphardt, F. Vogt, U. Sterr, H. Schnatz, Optical frequency transfer via 146 km fiber link with 10^{-19} relative accuracy. Opt. Lett. **34**, 2270–2272 (2009)
35. L. Krippner, W.J. Munro, M.D. Reid, Transient macroscopic quantum superposition states in degenerate parametric oscillation: calculations in the large-quantum-noise limit using the positive p representation. Phys. Rev. A **50**, 4330–4338 (1994)
36. M.K. Olsen, P.D. Drummond, Entanglement and the Einstein-Podolsky-Rosen paradox with coupled intracavity optical down-converters. Phys. Rev. A **71**, 053803 (2005)
37. N. Olivier, M.K. Olsen, Bright entanglement and the Einstein–Podolsky–Rosen paradox with coupled parametric oscillators. Opt. Commun. **259**, 781–788 (2006)

38. P.D. Drummond, C.W. Gardiner, Generalized p-representaions in quantum mechanics. J. Phys. A Math. Gen. **13**, 2353–2368 (1980)
39. M. Wolinski, H.J. Carmichael, Quantum noise in the parametric oscillator: from squeezed states to coherent state superpositions. Phys. Rev. Lett. **60**, 1836–1839 (1988)
40. B. Yurke, D. Stoler, Generating quantum mechanical superpositions of macroscopically distinguishable states via amplitude dispersion. Phys. Rev. Lett. **57**, 13–16 (1986)
41. A. Einstein, B. Podolsky, N. Rosen, Can quantum-mechanical description of physical reality be considered complete? Phys. Rev. **47**, 777–780 (1935)
42. L.-M. Duan, G. Giedke, J. Cirac, P. Zoller, Entanglement purification of Gaussian continuous variable quantum states. Phys. Rev. Lett. **84**, 4002–4005 (2000)
43. K. Takata, Y. Yamamoto, Data search by a coherent Ising machine based on an injection-locked laser network with gradual pumping or coupling. Phys. Rev. A **89**, 032319 (2014)
44. H.P. Breuer, F. Petruccione, *The Theory of Open Quantum Systems* (Oxford University Press, Oxford/New York, 2007)
45. K. Mlmer, Y. Castin, J. Dalibard, Monte carlo wave-function method in quantum optics. J. Opt. Soc. Am. B **10**, 524–538 (1993)

Chapter 12
A Coherent Ising Machine for MAX-CUT Problems: Performance Evaluation against Semidefinite Programming and Simulated Annealing

Yoshitaka Haribara, Shoko Utsunomiya, and Yoshihisa Yamamoto

12.1 Introduction

The Ising model is a mathematical abstraction of spin glasses composed of frustrated spins, which feature various peculiar properties [1, 2]. The Hamiltonian of the Ising model with N spins is given by $H = -\sum_{i<j} J_{ij}\sigma_i\sigma_j$, with J_{ij} being the coupling between the i-th and j-th spins. σ_i and σ_j represent the z-components of the spins, which take the eigenvalues of $+1$ or -1. The Ising model is also used as a cost function for many combinatorial optimization problems in life-science, drug discovery, wireless communications, machine learning, artificial intelligence and social network. The three-dimensional Ising model and many important combinatorial optimization problems are intractable in modern digital computers, since they belong to the NP-hard class [3]. So far no efficient classical nor quantum algorithm has been discovered for them. Thus, simulated annealing [4] and various heuristic or semi-definite programming algorithms for approximate solutions [5–7] are widely used. Recently, quantum annealing [8–10] and adiabatic quantum computation [11] have been proposed as an alternative, but their comprehensive study on the potentials are yet to be explored [12, 13].

The previous two sections introduce the novel computing systems based on the laser network [14, 15] and the degenerate optical parametric oscillator (DOPO) network [16, 17]. Such coherent Ising machines (CIM) need to employ multiple optical coupling paths for implementing the Ising coupling terms and thus have an

Y. Haribara • S. Utsunomiya (✉)
National Institute of Informatics, 2-1-2 Hitotsubashi, Chiyoda-ku, Tokyo 101-8430, Japan
e-mail: haribara@nii.ac.jp; shoko@nii.ac.jp

Y. Yamamoto
ImPACT Program, Council for Science Technology and Innovation, Tokyo, Japan
e-mail: yyamamoto@stanford.edu

Y. Yamamoto, K. Semba (eds.), *Principles and Methods of Quantum Information Technologies*, Lecture Notes in Physics 911, DOI 10.1007/978-4-431-55756-2_12

inherent problem for scalability. The number of optical coupling paths increases in proportion to a problem size for a sparse graph and quadratically to a problem size for a dense graph, even though the multiple Ising spins are implemented as a time-division-multiplexing pulse train in a simple ring cavity [17].

In this section we will describe a novel scheme to implement the Ising coupling terms using a quantum feedback control circuit. The new scheme has two additional advantages that a three-body or higher-order Ising coupling terms can be easily implemented without any modification of the feedback circuit and that a strong coupling coefficient ($\xi_{ij} > 1$) can be implemented without additional optical amplifiers. As a demonstration of this new capability, we show some numerical results for the MAX-CUT problems and higher-order Ising problems.

12.2 A Multiple-pulse DOPO with Quantum Measurement-Feedback Control

12.2.1 Outline

A proposed computing system is shown in Fig. 12.1. A fiber ring resonator installs the three components: a PPLN waveguide optical parametric amplifier and two directional couplers I and II, which are used as an out-coupling port to the homodyne

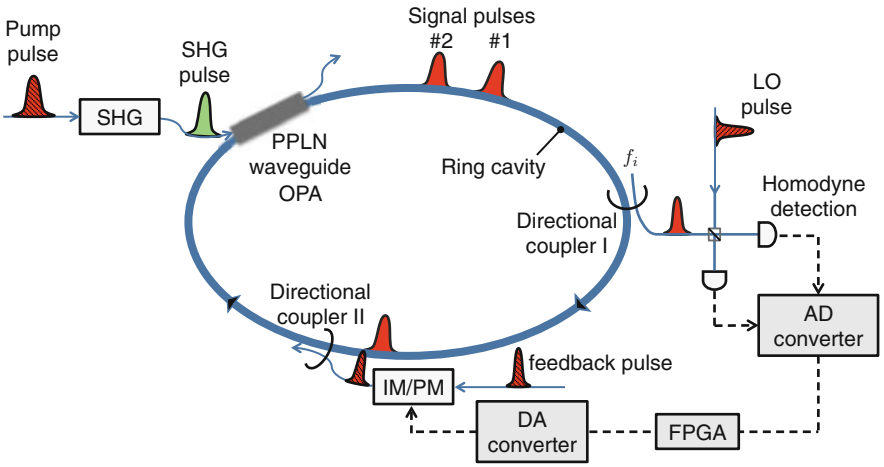

Fig. 12.1 A multiple-pulse DOPO with quantum feedback control. A small portion of each signal pulse is picked off by a directional coupler I and its in-phase component is measured by optical homodyne detectors, where a LO pulse is directly taken from a master laser. The two detector outputs are converted to the digital signals and input into a FPGA circuit, where the feedback signal $\sum_j \xi_{ij}\tilde{c}_j$ for the i-th signal pulse is computed. An independently taken IL pulse from the master laser is modulated in its intensity and phase to realise such an optical pulse and coupled into the i-th signal pulse by the directional coupler II. The flows of optical fields and electrical signals are shown by *solid lines* and *dashed lines*, respectively

detectors and as a mutual coupling port between the DOPO pulses, respectively. A second harmonic generation (SHG) pulse train at a wavelength of 0.78 μm generates multiple DOPO pulses at a wavelength of 1.56 μm inside a fiber ring cavity. The local oscillator (LO) pulse for the homodyne detection and the injection locking (IL) pulse for the mutual coupling are directly taken from the master laser at a wavelength of 1.56 μm.

If the fiber length (or round trip time) inside a ring resonator is properly adjusted to the multiple integer (N) times the pump pulse interval, we can simultaneously generate N independent DOPO pulses inside a cavity [17]. Instead of connecting those pulses with optical delay lines, we can measure the in-phase amplitude $\tilde{c}_j$ of the j-th pulse and compute the proper coupling field amplitude for the i-th pulse, $\sum_j \xi_{ij}\tilde{c}_j$ by the FPGA circuit, where the coupling coefficient ξ_{ij} is proportional to the Ising coupling J_{ij}. This electrical signal drives the intensity and phase modulators to generate an IL pulse for the i-th pulse. Such a hybrid optoelectric coupling scheme is equivalent to the purely optical coupling scheme except for the subtle difference in the noise penalty, which we will discuss in the next section.

A clear advantage of the new scheme is that all the Ising coupling J_{ij} of the order of N^2 can be implemented by a single quantum measurement-feedback control circuit. If N approaches $\sim 10^6$, which corresponds to the realistic clock frequency of 10 GHz and fiber length of 20 km, the above advantage is substantial in practical implementation.

12.3 c-Number Langevin Equations for the Multiple-pulse DOPO with Quantum Feedback Control

The in-phase and quadrature-phase amplitudes of a single isolated DOPO obey the following c-number Langevin equations [17]:

$$dc = (-1 + p - c^2 - s^2)c\,dt + \frac{1}{A_s}\sqrt{c^2 + s^2 + \frac{1}{2}}dW_1, \tag{12.1}$$

$$ds = (-1 - p - c^2 - s^2)s\,dt + \frac{1}{A_s}\sqrt{c^2 + s^2 + \frac{1}{2}}dW_2, \tag{12.2}$$

Equations (12.1) and (12.2) are derived by expanding the field density matrix with the truncated Wigner function. The two quadrature components c and s correspond to $\frac{1}{2A_s}(\alpha_s + \beta_s)$ and $\frac{1}{2A_s i}(\alpha_s - \beta_s)$ where α_s and β_s are the eigenvalues of two coherent states in the generalized (off-diagonal) $P(\alpha_s, \beta_s)$-representation for the field density matrix [18]. The two approaches based on the truncated Wigner function and the generalized P-representation are equivalent and produce identical results. The pump field is adiabatically eliminated already in (12.1) and (12.2) by assuming the pump decay rate γ_p is much larger than the signal decay rate γ_s. $A_s = (\gamma_s\gamma_p/2\kappa^2)^{1/2}$ is the DOPO field amplitude at a normalised pump rate $p = F_p/F_{th} = 2$, γ_s and γ_p are the signal and pump intensity decay rates and κ is

the second order nonlinear coefficient associated with the PPLN waveguide DOPA. As shown in Eq. (12.1) and (12.2), A_s is an important parameter to determine the effective strength of quantum noise. $t = \frac{\gamma_s}{2}\tau$ is a normalized time, while τ is a real time in sec. F_p is the pump field amplitude and $F_{th} = \gamma_s\gamma_p/4\kappa$ is the threshold pump field amplitude. Finally, dW_1 and dW_2 are two independent Gaussian noise processes which represent the incident vacuum fluctuations at signal channel and at pump channel, respectively. The former contributes to 1/2 and the latter contributes to $c^2 + s^2$ in the square-root bracket in (12.1) and (12.2). The c-number Langevin equations (12.1) and (12.2) are fully equivalent to the master equation for the signal field density matrix and the corresponding Fokker-Planck equation for the truncated Wigner function [17, 18], so that the following discussions based on the c-number Langevin equations (12.1) and (12.2) are compatible with rigorous quantum mechanical treatment.

When the i-th signal pulse is incident upon the directional coupler I, the output-coupled field and remaining cavity field are written as

$$c_{i,out} = \sqrt{T}c_i - \sqrt{1-T}\frac{f_i}{A_s}, \tag{12.3}$$

$$c_{i,re} = \sqrt{1-T}c_i + \sqrt{T}\frac{f_i}{A_s}, \tag{12.4}$$

where T is the power transmission coefficient of the directional coupler I and f_i is the incident vacuum fluctuation from the open port of the directional coupler I. The optical balanced homodyne detection for the out-coupled-field "measures" an inferred signal amplitude

$$\tilde{c_i} = c_i - \sqrt{\frac{1-T}{T}}\frac{f_i}{A_s}. \tag{12.5}$$

Note there is no additional noise in Eq. (12.5) except for the intrinsic vacuum field fluctuation f_i. A balanced homodyne detector with a 3 dB coupler (50–50 % beam splitter) and two photodetectors followed by a subtraction circuit can suppress the intensity noise of the LO pulse. Starting with the part of the master laser output, the intensity and phase modulators driven by the FPGA output with those measurement results produces the mutual coupling field $\sum_i \xi_{ij}\tilde{c}_j$, which is actually added to the i-th signal pulse by the directional coupler Ⅱ. Here ξ_{ij} is the effective coupling coefficient from the j-th pulse to the i-th pulse, including the transmission coefficient $\sqrt{T'}$ of the directional coupler Ⅱ.

Since the transmission coefficient $\sqrt{T'}$ of the directional coupler Ⅱ should be much smaller than one in order to keep the ring cavity Q-value high enough, we don't need to consider any additional noise in the combined signal and IL pulses. The c-number Langevin equation (12.1) can now be rewritten to include the mutual coupling terms:

$$dc_i = \left[(-1 + p - c_i^2 - s_i^2)c_i\right] dt + \sum_j \xi_{ij}\tilde{c}_j$$

$$+\frac{1}{A_s}\sqrt{c_i^2 + s_i^2 + \frac{1}{2}}dW_i. \tag{12.6}$$

Here the summation in Eq. (12.6) represents the quantum feedback term consisting of the signal part (proportion to c_j) and the noise part (proportion to f_j). The vacuum fluctuation coupled to the i-th pulse in the directional coupler I is already taken into account in the last term of R. H. S. together with the pump noise.

Note that the coupling coefficient $|\xi_{ij}|$ can be greater than one since we start with a high-intensity IL pulse directly from the master laser. If we do not use a quantum feedback control scheme, we must introduce a laser amplifier with a power gain of G in the optical coupling path in order to realize $|\xi_{ij}| > 1$. In this case, the quantum feedback term of Eq. (12.6) is replaced by

$$\sum_j \xi_{ij}(c_j - \sqrt{\frac{1-T}{T}}\frac{f_j}{A_s} + \sqrt{\frac{1}{T'}}\frac{f_a}{A_s}), \tag{12.7}$$

where $\xi_{ij} = \sqrt{G}T'$, T' is the transmission coefficient of the two directional couplers which pick off a part of the j-th signal pulse and add the amplified optical pulse to the i-th signal pulse, and f_a is the internal noise of the amplifier. When $T' \ll 1$, the added noise power is at least doubled because a laser amplifier needs to add the internal noise which is equal to or greater than the vacuum noise level.

In the following section, the numerical simulation of the coupled c-number Langevin equations (12.6) is employed to study the performance of a new coherent Ising machine with quantum feedback control.

12.4 Numerical Studies for a Simple MAX-CUT-3 Problem

If the Ising coupling coefficient J_{ij} is -1 (anti-ferromagnetic coupling) and each vertex has exactly three edges, such a simple Ising model is equivalent to the graph of a NP-hard simple MAX-CUT problem in a cubic graph (MAX-CUT-3). In this case we are asked to find the way to divide all vertices into two subgroups in order to maximize the edge weights cut between the two subgroups. The solution to the simple MAX-CUT-3 problem is identical to the ground state search problem of the Ising Hamiltonian [16].

$$min(H_{Ising}) = \sum_{i<j} J_{ij} - 2max(G). \tag{12.8}$$

The smallest simple MAX-CUT-3 problem has four vertices and six edges, as shown in Fig. 12.2a The solution to this problem is to divide the four vertices into the two subgroups with two vertices, which correspond to the six degenerate ground states

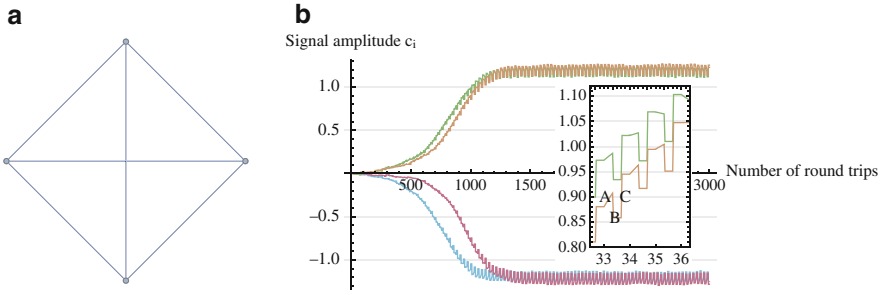

Fig. 12.2 (**a**) A simple MAX-CUT-3 problem with the number of vertices $N = 4$. (**b**) Normalized DOPO signal amplitudes as a function of cavity round trip numbers against $N = 4$ MAX-CUT-3. Small window is enlarged to indicate effects of three components; A: OPA gain, B: out-coupling loss, and C: injection of feedback pulse

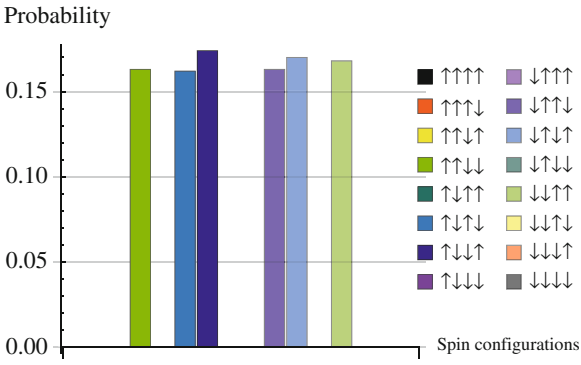

Fig. 12.3 Distribution of output spin configurations in 1000 trials of numerical simulations against simple MAX-CUT-3 problem of graph order $N = 4$. All trials were successful

of the Ising Hamiltonian, i.e. $|\uparrow\uparrow\downarrow\downarrow\rangle$, $|\uparrow\downarrow\uparrow\downarrow\rangle$, $|\uparrow\downarrow\downarrow\uparrow\rangle$, $|\downarrow\uparrow\downarrow\uparrow\rangle$, $|\downarrow\downarrow\uparrow\uparrow\rangle$ and $|\downarrow\uparrow\uparrow\downarrow\rangle$.

Figure 12.2b shows the time evolution of c_i $(i = 1, ..., 4)$ when the pump power is linearly increased from a below-threshold to above-threshold values. A correct solution spontaneously emerges after several tens of round trips. The histogram of obtaining different states against 1000 sessions of such numerical simulation is shown in Fig. 12.3, in which six correct solutions appear with almost equal probabilities and no error was detected.

12.5 Computational Experiments Against G-Set Graphs and Complete Graphs

A computational power of a coherent Ising machine (CIM), the DOPO network with quantum measurement-feedback control, is evaluated against two sets of instances of the NP-hard MAX-CUT problem. The first set includes 81 benchmark instances of the G-set graphs, which are randomly created by a machine-independent graph

generator written by G. Rinaldi. Those graphs have the vertices ranging from 800 to 20,000, the edge density from 0.02 % to 6 % and the edge weight of ± 1. There are three topology of the graphs, i.e. random, nearly planar and toroidal. While the G-set graphs are rather sparse, the second set consists of 5 complete graphs, in which all vertices are fully connected with edge weight of ± 1.

12.5.1 G-Set Graphs

The celebrated Goemans-Williamson algorithm based on semidefinite programming (SDP) has the performance guarantee of 0.87856 to the optional solution of the MAX-CUT problems. Table 12.1 compares the maximum and average numbers of cut, i.e. the sum of edge weights between two sub-groups of vertices normalized by the upper bound of cut by SDP and CIM. The average approximation rate of CIM is 0.93124 to SDP upper bound, whereas the performance of Goemans-Williamson SDP is 0.93025. The worst performance by CIM is 0.90442 while that for SDP is 0.8989. A computational time of SDP scales in $\sim O(N^{3.5})$ if the given graph has both positive and negative-weighted edges. Table 12.1 shows the computational time normalized by the round trip time for CIM, which features a sublinear scaling in $\sim O(N^{0.4})$.

12.5.2 Complete Graphs

Next, we study the computational times for complete graphs by SDP, simulated annealing (SA) and CIM. Figure 12.4 shows the Ising energy vs. evolution time for CIM, SA and SDP for the complete graph with $N = 800$ and $N = 4000$. The codes were running on the Linux machine with two 6 core Intel Xeon(2.67 GHz) processor and 94 GB memory. We assumed the CIM has a clock frequency of 2 GHz, fiber length of 2 km and total number of intra-cavity pulses of 20,000. The computational times for $N = 4000$ are $\sim 10^4$ s, ~ 10 s and $\sim 10^{-3}$ s for SDP, SA and CIM, respectively. Figure 12.5 compares the computational time T(sec) vs. the problem size N for SDP, SA and CIM. The computational time is defined as a time required to reach the same accuracy achieved by SDP. The computational time for complete graphs scales $\sim O(N^{3.5})$ and $\sim O(N^2)$ for SDP and SA. On the other hand, CIM realizes a problem-size independent computational time of the order of ~ 1 ms.

12.6 Numerical Studies for Higher-Order Ising Problems

If the Ising interaction is not a standard two-body interaction but rather a four-body interaction such as

$$H = -J\sigma_1\sigma_2\sigma_3\sigma_4, \tag{12.9}$$

Table 12.1 Performance of the coherent Ising machine and the Goemans-Williamson SDP algorithm in solving the MAX-CUT problems on sample G-set graphs. $\#V$ is the number N of vertices in the graph, $\#E$ is the number m of edges, U_{SDP} is the optimal solution to the semidefinite relaxation of the MAX-CUT problem, C_{GW} is the best solution obtained by $N(=\#V)$ projections after SDP. $C_{\max}$ and C_{avg} are the best and average values in CIM 100 runs, respectively, and T is the average computational time of the CIM normalized to the DOPO cavity round trip time, i.e., 10 μs. To make comparisons with each other, every cut value C generated from the CIM or GW algorithm is normalized according to $(C + E_{\mathrm{neg}})/(U_{\mathrm{SDP}} + E_{\mathrm{neg}})$, where $E_{\mathrm{neg}} \geq 0$ is the number of negative edges

Graph	$\#V$	$\#E$	U_{SDP}	C_{GW}	$C_{\max}$	C_{avg}	T
g1	800	19,176	12,083	0.94571	**0.95506**	0.94902	133.9
g2	800	19,176	12,089	0.94367	**0.95417**	0.94838	138.1
g3	800	19,176	12,084	0.94505	**0.95357**	0.94819	131.4
g4	800	19,176	12,111	0.94509	**0.95583**	0.94819	134.0
g5	800	19,176	12,099	0.94578	**0.95644**	0.94886	137.9
g6	800	19,176	2656	0.94477	**0.95628**	0.94828	131.4
g7	800	19,176	2489	0.94462	**0.95622**	0.94772	128.0
g8	800	19,176	2506	0.94433	**0.95435**	0.94750	126.4
g9	800	19,176	2528	0.94518	**0.95489**	0.94885	128.1
g10	800	19,176	2485	0.94438	**0.95400**	0.94814	126.1
g11	800	1600	629	**0.93272**	0.93130	0.91576	128.3
g12	800	1600	623	**0.93333**	0.93193	0.91830	130.1
g13	800	1600	647	0.93357	**0.93636**	0.91877	129.9
g14	800	4694	3191	0.93356	**0.94798**	0.93930	121.7
g15	800	4661	3171	0.93977	**0.94923**	0.93953	124.9
g16	800	4672	3175	0.93638	**0.94583**	0.93926	125.2
g17	800	4667	3171	0.93756	**0.94607**	0.93904	129.8
g18	800	4694	1166	0.92818	**0.94140**	0.93099	116.7
g19	800	4661	1082	0.92793	**0.93918**	0.92919	119.2
g20	800	4672	1111	0.93545	**0.94121**	0.92974	120.6
g21	800	4667	1104	0.92855	**0.94238**	0.92987	118.0
g22	2000	19,990	14,136	0.91914	**0.93350**	0.92661	204.9
g23	2000	19,990	14,145	0.91877	**0.93079**	0.92628	198.4
g24	2000	19,990	14,140	0.91860	**0.93317**	0.92622	189.7
g25	2000	19,990	14,144	0.91827	**0.93142**	0.92584	197.9
g26	2000	19,990	14,132	0.91735	**0.93242**	0.92610	196.4
g27	2000	19,990	4141	0.91743	**0.93247**	0.92659	192.8
g28	2000	19,990	4100	0.91822	**0.93158**	0.92662	195.5
g29	2000	19,990	4208	0.91668	**0.93186**	0.92631	188.8
g30	2000	19,990	4215	0.91893	**0.93376**	0.92664	204.9
g31	2000	19,990	4116	0.91810	**0.93174**	0.92693	196.7
g32	2000	4000	1567	0.92717	**0.93335**	0.92557	178.0
g33	2000	4000	1544	0.92751	**0.93369**	0.92495	174.0
g34	2000	4000	1546	0.92773	**0.93725**	0.92644	177.0

(continued)

Table 12.1 (continued)

Graph	#V	#E	U_{SDP}	C_{GW}	C_{max}	C_{avg}	T
g35	2000	11,778	8014	0.92925	**0.94285**	0.93780	173.6
g36	2000	11,766	8005	0.92817	**0.94166**	0.93794	174.3
g37	2000	11,785	8018	0.93103	**0.94188**	0.93719	170.9
g38	2000	11,779	8014	0.92912	**0.94223**	0.93805	181.9
g39	2000	11,778	2877	0.92265	**0.93407**	0.92747	157.6
g40	2000	11,766	2864	0.92246	**0.93156**	0.92700	159.9
g41	2000	11,785	2867	0.92302	**0.93328**	0.92679	167.6
g42	2000	11,779	2946	0.92296	**0.93345**	0.92545	174.4
g43	1000	9990	7032	0.92918	**0.93444**	0.92758	143.9
g44	1000	9990	7027	0.92515	**0.93710**	0.92854	147.4
g45	1000	9990	7024	0.92454	**0.93764**	0.92883	146.2
g46	1000	9990	7029	0.92232	**0.93626**	0.92868	148.0
g47	1000	9990	7036	0.92609	**0.93576**	0.92838	144.1
g48	3000	6000	6000	**1.00000**	0.96000	0.93181	228.4
g49	3000	6000	6000	**1.00000**	0.95333	0.93267	231.4
g50	3000	6000	5988	**0.98196**	0.95157	0.93281	228.8
g51	1000	5909	4006	0.93335	**0.94658**	0.93907	136.1
g52	1000	5916	4009	0.93265	**0.94537**	0.93958	130.8
g53	1000	5914	4009	0.93465	**0.94338**	0.93824	138.3
g54	1000	5916	4006	0.93809	**0.94508**	0.93935	137.8
g55	5000	12,498	11,039	0.90063	**0.91023**	0.90499	272.1
g56	5000	12,498	4760	0.90078	**0.91274**	0.90509	272.8
g57	5000	10,000	3885	0.92374	**0.93295**	0.92808	225.8
g58	5000	29,570	20,136	0.92387	**0.93956**	0.93711	244.7
g59	5000	29,570	7312	0.91483	**0.93006**	0.92432	219.0
g60	7000	17,148	15,222	0.89890	**0.90908**	0.90470	285.1
g61	7000	17,148	6828	0.89909	**0.90868**	0.90442	279.2
g62	7000	14,000	5431	0.92278	**0.93208**	0.92842	243.5
g63	7000	41,459	28,244	0.92299	**0.93942**	0.93725	262.5
g64	7000	41,459	10,466	0.91426	**0.93010**	0.91580	213.0
g65	8000	16,000	6206	0.92167	**0.93220**	0.92880	259.7
g66	9000	18,000	7077	0.92199	**0.93322**	0.92881	266.6
g67	10,000	20,000	7744	0.92153	**0.93298**	0.92991	269.2
g70	10,000	9999	9863	**0.96330**	0.94860	0.94391	290.7
g72	10,000	20,000	7809	0.92146	**0.93358**	0.92957	271.5
g77	14,000	28,000	11,046	0.92046	**0.93280**	0.92990	285.0
g81	20,000	40,000	15,656	0.91947	**0.93165**	0.92984	298.3

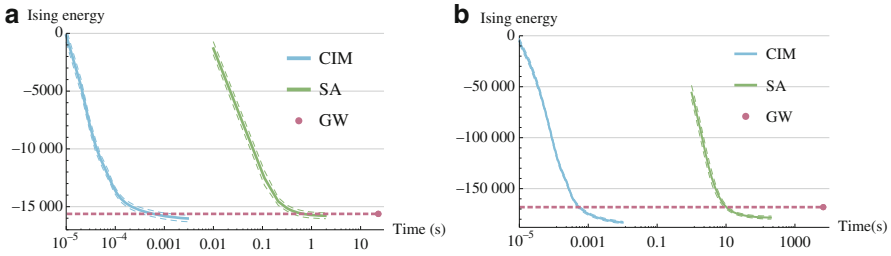

Fig. 12.4 Performance comparison of CIM, SA, and GW in solving complete graphs (**a**) K_{800} and (**b**) K_{4000}, where each edge was randomly weighted ± 1. Each time, bundle of curves depicted average energy (*solid line*) $\pm$ and standard deviations (*dashed line*) in 100 runs. *Dotted line* was obtained using GW algorithm, which is shown with *dot*. The number of flips in SA algorithm were 10^5 for K_{800} and 10^6 for K_{4000}, respectively, to optimize computational time

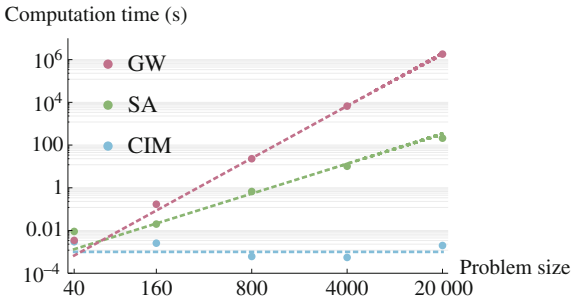

Fig. 12.5 Computational time of coherent Ising machine, simulated annealing algorithm, and Goemans-Williamson SDP algorithm fitted to lines indicating $O(1)$, $O(N^2)$, and $O(N^{3.5})$, respectively. Data points of CIM and SA were calculated by averaging 100 samples, except for $N = 40$. (Since the optimal energy of graph obtained using GW is regarded as ground state, half of the 100 samples of stochastic algorithms were post-selected to reach that value)

the coupled field into the i-th pulse is not given by $\sum_j \xi_{ij}\tilde{c}_j$ any more but is given by $\xi\tilde{c}_j\tilde{c}_k\tilde{c}_l$, where $(j,k,l) \neq i$. In this case the c-number Langevin equation (12.1) can be rewritten to include four body coupling term:

$$dc_i = (-1 + p - c_i^2 - s_i^2)c_i dt + \frac{1}{A_s}\sqrt{c_i^2 + s_i^2 + \frac{1}{2}}dW_i + \xi[c_j c_k c_l + \sqrt{\frac{1-T}{T}}\frac{c^2}{A_s}(f_j + f_k + f_l)]. \quad (12.10)$$

Here we assume $|c_i| = |c_j| = |c_k| = |c_l| = c$.

If the four-body Ising coupling coefficient J is -1 (multi-body anti-ferromagnetic coupling), there are eight degenerate ground state, i.e. $|\uparrow\uparrow\uparrow\downarrow\rangle$, $|\uparrow\uparrow\downarrow\uparrow\rangle$, $|\uparrow\downarrow\uparrow\uparrow\rangle$, $|\downarrow\uparrow\uparrow\uparrow\rangle$ and their inverse spin configurations. Figure 12.6 shows the time evolution of c_i ($i = 1 \sim 4$) when the pump power is linearly increased from a below-threshold to above threshold values. One of the eight degenerate ground states

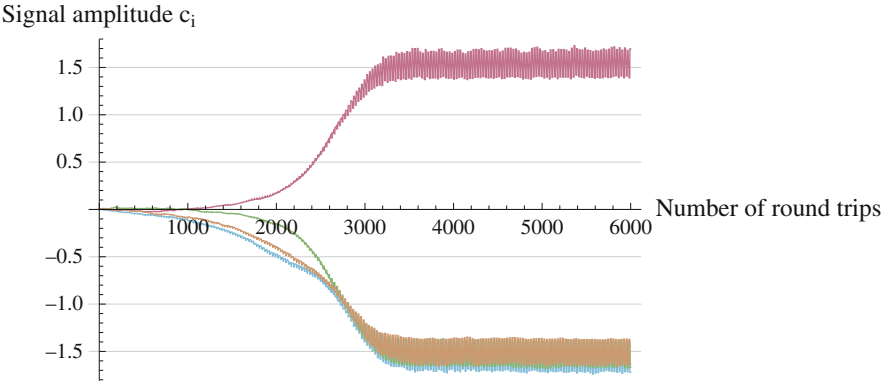

Fig. 12.6 Normalized DOPO pulse amplitudes c_i ($i = 1, \ldots, 4$) in Eq. (12.10) describe interaction between four-body Ising coupling expressed by Eq. (12.9)

Fig. 12.7 Distribution of output spin configurations in 1000 trials of numerical simulation against four-body Ising model of $N = 4$. All trials were successful

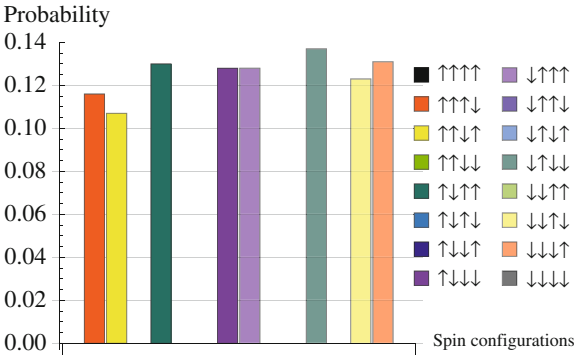

emerges spontaneously after several ten round trips. The statistics of observing different states in 1000 independent sessions of numerical simulation of Eq. (12.9) is shown in Fig. 12.7, in which eight correct solutions are obtained with almost equal probabilities and no error was detected.

12.7 Conclusion

A scalable coherent Ising machine with quantum feedback control is proposed and studied for the MAX-CUT problems. The scalability stems from replacing $\sim O(N)$ optical coupling paths by a single quantum measurement-feedback circuit. The potential for solving NP-hard Ising problems using a CIM was numerically studied by conducting computational experiments using the MAX-CUT problems on sparse graphs (G-set) and fully connected complete graphs of order up to 2×10^4. With the normalized pump rate and coupling coefficient $p = 0.2$ and $\xi = -0.06$, the CIM

achieved a good approximation rate of 0.93124 on average and found better cut compared to the GW for 65 out of 71 graphs in G-set. The computation time for this sparse graph set was $\sim$1 ms. The time scaling was also tested against complete graphs of number of vertices up to 2×10^4 and number of edges up to 10^8. The results imply that CIM achieves almost constant time scaling, while SA scales as $O(N^2)$. The new scheme has two additional advantages: (1) a very large coupling coefficient $\xi_{ij} > 1$ can be implemental without excess amplifier noise and (2) a higher-order Ising coupling can be easily implemented. The second advantage may find new applications of the proposed machine to other types of hard problems such as factoring problems and 3-SAT problems.

References

1. K. Binder, A.P. Young, Spin glasses: experimental facts, theoretical concepts, and open questions. Rev. Mod. Phys. **58**, 801 (1986)
2. V. Dotsenko, *Introduction to the Replica Theory of Disordered Statistical Systems* (Cambridge University Press, Cambridge/New York, 2005)
3. F. Barahona, On the computational complexity of Ising spin glass models. J. Phys. A Math. Gen. **15**, 3241 (1982)
4. S. Kirkpatrick, D. Gelatt Jr., M.P. Vecchi, Optimization by simulated annealing. Science **220**, 4598 (1983)
5. C.H. Papadimitriou, K. Steiglitz, *Combinatorial Optimization: Algorithms and Complexity* (Courier Dover, Mineola, 1998)
6. D.S. Hochbaum, *Approximation Algorithms for NP-Hard Problems* (PWS, Boston, 1996)
7. M.X. Goemans, D.P. Williams, Improved approximation algorithms for maximum cut and satisfiability problems using semidefinite programming. J. ACM **42**, 1115 (1995)
8. T. Kadowaki, H. Nishimori, Quantum annealing in the transverse Ising model. Phys. Rev. E **58**, 5355 (1998)
9. G.E. Santoro, R. Martoak, E. Tosatti, R. Car, Theory of quantum annealing of an Ising spin glass. Science **295**, 2427 (2002)
10. M.W. Johnson et al., Quantum annealing with manufactured spins. Nature **473**, 194 (2011)
11. E. Farhi, J. Goldstone, S. Gutmann, J. Lapan, A. Lundgren, D. Preda, A quantum adiabatic evolution algorithm applied to random instances of an NP-complete problem. Science **292**, 472 (2001)
12. N.G. Dickson et al., Thermally assisted quantum annealing of a 16-qubit problem. Nat. Commun. **4**, 1903 (2013)
13. Q. Deng, D.V. Averin, M.H. Amin, P. Smith, Decoherence induced deformation of the ground state in adiabatic quantum computation. Sci. Rep. **3**, 01479 (2013)
14. S. Utsunomiya, K. Takata, Y. Yamamoto, Mapping of Ising models onto injection-locked laser systems. Opt. Express **19**, 18091 (2011)
15. K. Takata, S. Utsunomiya, Y. Yamamoto, Transient time of an Ising machine based on injection-locked laser network. New J. Phys. **14**, 013052 (2012)
16. Z. Wang, A. Marandi, K. Wen, R.L. Byer, Y. Yamamoto, Coherent Ising machine based on degenerate optical parametric oscillators. Phys. Rev. A. **88**, 063853 (2013)
17. A. Marandi, Z. Wang, K. Takata, R.L. Byer, Y. Yamamoto, *Network of Time-Multiplexed Optical Parametric Oscillators as a Coherent Ising Machine* (2014). arXiv:1407.2871v1
18. P.D. Drummond, K.J. McNeil, D.F. Walls, Non-equilibrium transitions in sub/second harmonic generation. II. Quantum theory. Opt. Acta **28**, 211 (1981)

Part IV
Quantum Simulation

Chapter 13
Bose-Einstein Condensation: A Platform for Quantum Simulation Experiments

Yoshihisa Yamamoto and Yoshiro Takahashi

13.1 Introduction

Since the Bose-Einstein (BEC) condensation of dilute atomic gases was realized in 1995 [1, 2], the study of highly degenerate quantum gases has attracted considerable interest from theoretical and experimental researchers from various fields.

The quantum statistical properties of massless Bose particles were first studied by Bose in 1924, and these properties are known today as photon statistics [3]. Einstein extended this work to a system of non-interacting massive Bose particles and proposed the basic concept of BEC in 1925 [4]. The BEC phase transition is achieved by condensation of a macroscopic number of particles into a ground state with the lowest energy when the temperature is low enough. However, for more than ten years, Einstein's prediction was considered to be a purely mathematical conclusion for a theoretical system composed of a noninteracting (ideal) gas with little relevance to the real physics of interacting Bose particles.

In 1938, Kapitza and, independently, Allen and Misener discovered the phenomenon of superfluidity, i.e., the frictionless flow of fluids, in liquid ^{4}He [5, 6]. In the same year, London published the intuitive idea that superfluidity could be an experimental manifestation of BEC [7]. However, superfluid ^{4}He is a strongly interacting system that is far from the ideal gas studied by Einstein, so it was not at all straightforward to connect the concepts of BEC and superfluidity. The first microscopic theory of interacting Bose gases in the context of BEC was formulated by Bogoliubov [8] in 1947. Independently, Landau developed the phenomenological

Y. Yamamoto (✉)
ImPACT Program, Council for Science Technology and Innovation, Tokyo, Japan
e-mail: yyamamoto@stanford.edu

Y. Takahashi
Department of Physics, Graduate School of Science, Kyoto University, Kyoto, Japan
e-mail: yitk@scphys.kyoto-u.ac.jp

Y. Yamamoto, K. Semba (eds.), *Principles and Methods of Quantum Information Technologies*, Lecture Notes in Physics 911, DOI 10.1007/978-4-431-55756-2_13

theory of superfluidity in terms of the excitation spectrum [9], and this theory was later supported by experimental confirmation. Despite successes in the theoretical understanding of superfluidity in the early years, e.g., the work of Feynman [10], it was only after the realization of atomic BEC in 1995 that the theoretical concepts of BEC proposed by Einstein [4] and Bogoliubov [8] could be experimentally tested.

One of the most significant features of BEC, and a key factor in understanding the connection between BEC and superfluidity, is the off-diagonal long-range order. This subject has been extensively studied by many theorists, including Landau and Lifshitz [11], Penrose [12], and Penrose and Onsager [13]. Another important aspect for the understanding of BEC and superfluidity is the quantized vortices that were predicted by Onsager [14] and Feynman [15]; these vortices were first observed in superfluid ^{4}He, and were observed more recently in atomic BEC and exciton-polariton condensates.

The BEC phase is unstable because the true thermal equilibrium state under BEC pressure and temperature conditions is the solid phase. At such low temperatures, the BEC gas phase decays to form a stable crystal phase by the three-body scattering process. This seems to rule out the possibility of experimental realization of the BEC phase. However, the BEC phase can indeed exist as a "metastable" state if the following conditions are satisfied:

1. The density of the gas is so low that three-body collisions are rare and thus the time taken for the system to enter a stable solid state is much longer than the escape time of these particles.
2. Internal thermal equilibrium of the gas can nevertheless be established efficiently and quickly by sizable two-body collisions, and the established gas temperature is low enough for quantum statistics to play a role in the formation of the metastable gaseous BEC state.
3. The time required to reach the BEC phase and the time required for the Bose particles to escape from the trap are very different, which means that we can experimentally probe the various properties of the BEC phase. This third condition is satisfied in atomic BEC but is not necessarily satisfied in exciton-polariton BEC.

Before experimental studies of atomic BEC began, the semiconductor physics community had already investigated the possibility of BEC of excitons in the 1960s [16, 17]. Excitons are elementary excitations in semiconductors but can also be considered as compound bosonic particles consisting of two fermions: an electron in the conduction band and a hole in the valence band.

Despite both experimental and theoretical efforts lasting for more than four decades, the evidence for exciton BEC remains elusive. The main obstacles to exciton BEC experiments are two-fold:

1. Excitons either dissociate into an electron and hole plasma or decay nonradiatively by the Auger recombination process at the high density limit, which means that it is very difficult to accumulate exciton densities up to the critical BEC density at experimentally accessible temperatures.

2. Excitons are easily localized by crystal defects or impurities and suffer from relatively large inhomogeneous broadening. Thus, an ensemble of excitons in a real crystal cannot be considered as delocalized bosonic waves, even at low temperatures, but this is an indispensable prerequisite for BEC.

In 1996, a proposal was made with regard to BEC of exciton-polaritons, which are hybrid quasi-particles consisting of quantum well (QW) excitons and microcavity (MC) photons in semiconductor planar structures [18]. Dressing the QW excitons with the MC photons produces a new quasi-particle with an extremely light effective mass. These exciton-polaritons can overcome both localization and inhomogeneous broadening through their spatially-extended photonic wavefunctions. Insertion of multiple QWs inside a MC means that the exciton density per QW can be reduced while a sufficiently high two-dimensional polariton density is maintained. The exciton-polariton BEC has been demonstrated in several laboratories around the world [19–22].

There are three distinct regimes for the degenerate Bose gas system, which are determined by the ratio of the thermalization time to the escape time of the ground state particles.

1. If the internal thermalization time τ_{th} is much longer than the particle escape time τ_0, thermal equilibrium is not reached. Nevertheless, some of the BEC signatures, such as the off-diagonal long-range order and the macroscopic population of the ground state, can still exist. This non-equilibrium regime is known as the "matter-wave laser".
2. If the internal thermalization time is comparable to or shorter than the particle escape time, then the thermal equilibrium BEC phase is formed, but only as a transient effect. Many of the BEC signatures can be probed experimentally using various stroboscopic measurement techniques. This transient regime is called the "dynamic condensation".
3. If the internal thermalization time is much shorter than the particle escape time, then the BEC phase exists as a steady state from an experimental viewpoint. We refer to this steady state regime as "thermal equilibrium BEC" [23].

Section 13.2 introduces several fundamental concepts of BEC, including the order parameter, spontaneous symmetry breaking, Nambu-Goldstone modes, the off-diagonal long range order and higher-order coherence. A simple model of a non-interacting Bose gas is presented in Sect. 13.3. Despite its simplicity, the model still captures the basic properties of BEC, including the critical temperature/density and the condensate fraction. Section 13.4 describes the Bogoliubov theory of a weakly interacting Bose gas. We then derive the Gross-Pitaevskii equation, the Bogoliubov excitation spectrum, the sound velocity and the first-order coherence function. Superfluidity is discussed in Sect. 13.5. We present the Landau criterion for superfluidity, quantized vortices, and bound vortex-antivortex pairs, and finally present the Berezinskii-Kosterlitz-Thouless (BKT) theory of superfluidity in a uniform two-dimensional system. Finally, in Sect. 13.6, several important experimental systems for the quantum simulation experiments are reviewed.

13.2 Fundamental Concepts of Bose-Einstein Condensation

13.2.1 Order Parameter, Spontaneous Symmetry Breaking and Coherent State

The field operator $\hat{\psi}(r)$, which annihilates a particle at position r, can be written in the form

$$\hat{\psi}(r) = \sum_i \varphi_i(r)\hat{a}_i, \tag{13.1}$$

where $\hat{a}_i$ $\left(\hat{a}_i^+\right)$ are the annihilation (creation) operators of a particle in the single particle state $\varphi_i(r)$, and they obey the standard bosonic commutation relations

$$\left[\hat{a}_i, \hat{a}_j^+\right] = \delta_{ij}, \quad \left[\hat{a}_i, \hat{a}_j\right] = \left[\hat{a}_i^+, \hat{a}_j^+\right] = 0. \tag{13.2}$$

The $c-$number Schrödinger wavefunction $\varphi_i(r)$ satisfies the following orthonormal condition:

$$\int \varphi_i^*(r)\varphi_j(r)dr = \delta_{ij}. \tag{13.3}$$

It is then straightforward to show that the field operator follows the communication relation

$$\left[\hat{\psi}(r), \hat{\psi}^+(r')\right] = \delta(r - r') \tag{13.4}$$

If the lowest energy single particle state, which is called the ground state in this chapter, has macroscopic occupation, then we can separate the field operator (13.1) into the condensate term ($i = 0$: ground state) and the noncondensate components ($i \neq 0$: excited states):

$$\hat{\psi}(r) = \varphi_0(r)a_0 + \sum_{i\neq 0} \varphi_i(r)\hat{a}_i. \tag{13.5}$$

This expression of the field operator has already been introduced in the Bogoliubov approximation [8], in which the operator $\hat{a}_0$ is replaced by the c-number amplitude $a_0 = \sqrt{N_0}$, where $N_0 = \langle \hat{a}_0^+ \hat{a}_0 \rangle$. By defining $\psi_0 = \sqrt{N_0}\varphi_0$ and $\delta\hat{\psi} = \sum_{i\neq 0} \varphi_i \hat{a}_i$, we obtain the Bogoliubov ansatz:

$$\hat{\psi}(r) = \psi_0(r) + \delta\hat{\psi}(r). \tag{13.6}$$

The separation (13.6) is justified if the ground state is occupied by a macroscopic number of particles ($N_0 \gg 1$) and is useful for description of the ensemble averaged nonlinear dynamics of the condensate using the classical field $\psi_0(r)$ and the small fluctuations $\delta\hat{\psi}(r)$ around the averaged value.

The classical field $\psi_0(r)$ is called an order parameter, and is characterized by a modulus and a phase:

$$\psi_0(r) = |\psi_0(r)|e^{iS(r)} \tag{13.7}$$

The modulus $|\psi_0(r)|$ determines the particle density $n(r) = |\psi_0(r)|^2$ of the condensate, while the phase $S(r)$ characterizes the coherence and the superfluid phenomena. The order parameter can take a particular phase factor. In a real BEC phase transition, a condensate system spontaneously selects a particular phase $S(r)$. An explicit selection of the phase $S(r)$ despite the lack of a preferred phase value is referred to as spontaneous breaking of the gauge symmetry.

The Bogoliubov ansatz (13.6) of the field operator suggests that the expectation value $\langle\hat{\psi}(r)\rangle$ is not zero. This would not be possible if the condensate was in a particle number eigenstate $|N_0\rangle$. From a quantum field theoretical viewpoint, the condensate state is close to the coherent state defined by [24]

$$\hat{a}|\alpha\rangle = \alpha|\alpha\rangle \tag{13.8}$$

where $|\alpha|^2 = N_0$ is the average particle number of the condensate. The coherent state $|\alpha\rangle$ defined by (13.8) can be expanded using the particle number eigenstates [24]:

$$|\alpha\rangle = \sum_n \frac{e^{-|\alpha|^2/2}}{\sqrt{n!}}\alpha^n|n\rangle \tag{13.9}$$

If we recall that the time dependence of the particle number eigenstate is $e^{-iE(n)t/\hbar}|n\rangle$, where $E(n)$ is the total energy of n particles, then we can show that the time dependence of the order parameter is given by [24]

$$\psi_0(r,t) \equiv \langle\alpha|\varphi_0(r)\hat{a}_0|\alpha\rangle = \psi_0(r)e^{-i\mu t}, \tag{13.10}$$

Here, $\hbar\mu = E(n) - E(n-1) \sim \frac{\partial E(n)}{\partial n}$ is the chemical potential of the system. It is important to note that the time evolution of the order parameter is not governed by the total energy $E(n)$ but is in fact governed by the chemical potential μ. This is strongly connected to the spontaneous symmetry breaking mentioned earlier. The difference between the time evolution of a particle number eigenstate $|n\rangle$ and that of a coherent state is explained schematically in Fig. 13.1. A coherent state localizes its phase to a particular value through destructive and constructive interference between the different particle number eigenstates, as shown in Fig. 13.1. Above the BEC phase transition temperature, the ground state is occupied by a statistical mixture of the different particle number eigenstates, in which the entropy is maximum under the constraint of a fixed average particle number [25]. Below the BEC phase transition temperature, the ground state approaches a pure coherent state with zero entropy.

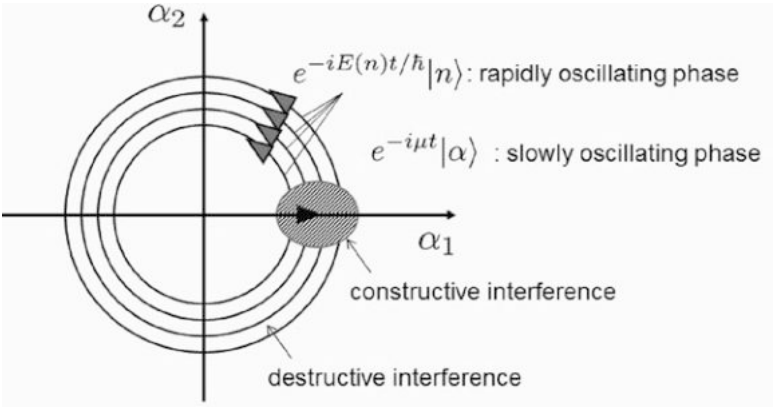

Fig. 13.1 Time evolution of particle number eigenstates $|n\rangle$ and a coherent state $|\alpha\rangle$ in the $\alpha_1 - \alpha_2$ phase space. α_1 and α_2 are the two quadrature amplitudes of the eigenvalue of α. A coherent state is a pure state that consists of linear superposition of particle number eigenstates. The phase is localized by destructive and constructive interference among the different particle number eigenstates in the phase space

13.2.2 Nambu-Goldstone Modes

The Bose particles in the condensate interact with each other via the repulsive potential. This interaction induces low-energy and long-wavelength fluctuations in the condensate. To show this, we begin with the Gross-Pitaevskii equation for the order parameter:

$$i\frac{d}{dt}\psi(r,t) = \left\{-\frac{\hbar\nabla^2}{2m} + g|\psi(r,t)|^2\right\}\psi(r,t), \tag{13.11}$$

where $g(>0)$ is the repulsive interaction potential. The solution of (13.11) is expanded as

$$\psi(r,t) = \psi_0(r)e^{-i\mu t} + \sum_k \left\{u_k e^{i(kr-(\mu+\omega)t)} + v_k e^{-i(kr+(\mu-\omega)t)}\right\}, \tag{13.12}$$

where $u_k(r)$ and $v_k(r)$ are the excitation amplitudes of the forward-propagating and backward-propagating excitation waves with wavenumbers of $\pm k$. The chemical potential is now written as $\hbar\mu = \hbar g|\psi_0(r)|^2$. If we substitute (13.12) into (13.11), we obtain the following eigenvalue equations for the two excitation amplitudes:

$$\begin{pmatrix} \frac{\hbar k^2}{2m} + \mu & \mu \\ -\mu & -\frac{\hbar k^2}{2m} - \mu \end{pmatrix}\begin{pmatrix} u_k \\ v_k \end{pmatrix} = \omega\begin{pmatrix} u_k \\ v_k \end{pmatrix}. \tag{13.13}$$

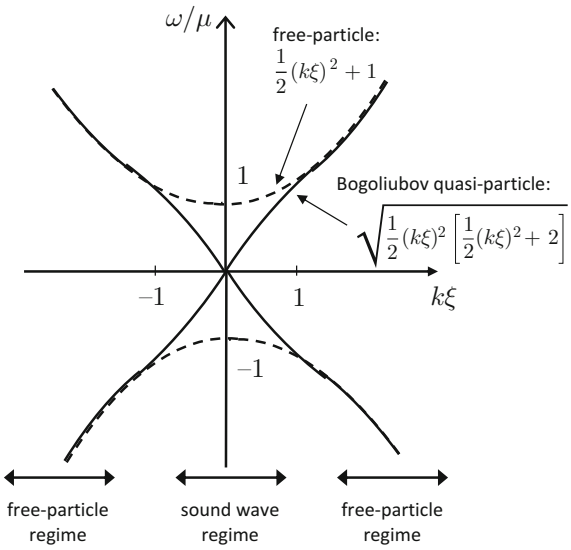

Fig. 13.2 Dispersion relations ω/μ vs $k\xi$ for a free particle and a Bogoliubov quasi-particle

To give a nontrivial solution for u_k and v_k, the eigenvalue ω must satisfy

$$\omega^2 - \left(\mu + \frac{\hbar k^2}{2m}\right)^2 \omega + \mu^2 = 0 \tag{13.14}$$

The solution of (13.14) is easily obtained as

$$\omega = \pm\sqrt{\omega_k\left(\omega_k + 2\mu\right)}, \tag{13.15}$$

where $\hbar\omega_k = \frac{(\hbar k)^2}{2m}$ is the kinetic energy of a noninteracting free particle. Figure 13.2 shows the normalized excitation energy ω/μ vs. the normalized wavenumber $k\xi$, where $\xi = \sqrt{\frac{\hbar}{m\mu}}$ is the healing length. At the low-energy and small-wavenumber (or long-wavelength) limit, $k\xi < 1$, the excitation modes follow a linear dispersion similar to a sound wave:

$$\omega = \pm ck, \tag{13.16}$$

where $c = \sqrt{\frac{\hbar\mu}{m}}$ is the effective sound velocity. The important consequence of this linear dispersion (13.16) will be discussed in Sect. 13.5.

Equation (13.15) is the celebrated Bogoliubov dispersion law [8]. In general, long-wavelength phase fluctuation modes appear universally in spontaneous symmetry breaking processes in both particle and condensed matter physics, and are called the Nambu-Goldstone modes [26–28]. The Bogoliubov dispersion law represents a special case of the Nambu-Goldstone modes for weakly interacting

Bose particles. The repulsive interaction represented by the parameter $g(>0)$ forces the condensate to accumulate in a single state rather than fragment into several degenerate or nearly degenerate states, and also to acquire a specific phase as a coherent state rather than have a random phase. In this way, the Nambu-Goldstone modes play a crucial role at the heart of the BEC phase transition with spontaneous symmetry breaking.

13.2.3 Off-Diagonal Long Range Order

The first-order coherence function for the field operator is defined by [24]

$$G^{(1)}(r,t;r',t') = \langle \hat{\psi}^{+}(r,t)\hat{\psi}(r',t')\rangle \tag{13.17}$$

Equation (13.17) provides a very general definition of coherence that applies to any system, independent of the statistics, both in equilibrium and out of equilibrium. In an equilibrium system, any time dependence is suppressed so that only the concept of spatial coherence exists. In this case, the first-order spatial coherence function is expressed in terms of the single particle wavefunctions:

$$G^{(1)}(r,r') = \sum_i n_i \varphi_i^*(r)\varphi_i(r'), \tag{13.18}$$

where $\langle \hat{a}_i^{+}\hat{a}_j\rangle = \delta_{ij}n_i$ is used. The normalized coherence function is defined as

$$g^{(1)}(r,t;r',t') = \frac{G^{(1)}(r,t;r',t')}{\left[G^{(1)}(r,t;r,t)G^{(1)}(r',t';r',t')\right]^{1/2}}. \tag{13.19}$$

In a three-dimensional system, the scalar product of the momentum $|p\rangle$ and position $|r\rangle$ eigenstates is written as [29]

$$\begin{aligned}\langle p|r\rangle &= (2\pi\hbar)^{-\frac{3}{2}} \exp\left(-i\frac{p\cdot r}{\hbar}\right) \\ &= \langle r|p\rangle^*\end{aligned} \tag{13.20}$$

Using the completeness relation $\int |r\rangle\langle r|dr = \hat{I}$, the field operator $\hat{\psi}(p)$ in the momentum space can thus be written as

$$\hat{\psi}(p) = (2\pi\hbar)^{-\frac{3}{2}} \int dr \hat{\psi}(r) \exp\left(i\frac{p\cdot r}{\hbar}\right). \tag{13.21}$$

The inverse relation to (13.21) is obtained by using another completeness relation, $\int |p\rangle\langle p|dp = \hat{I}$, to give

$$\hat{\psi}(r) = (2\pi\hbar)^{-\frac{3}{2}} \int dp \hat{\psi}(p) \exp\left(-\frac{ip \cdot r}{\hbar}\right). \tag{13.22}$$

Using (13.21) and (13.22), we can calculate the first-order coherence function as follows:

$$G^{(1)}(r, r') = \frac{1}{V} \int dp n(p) \exp\left[\frac{i}{\hbar} p(r - r')\right]. \tag{13.23}$$

Here, $n(p)$ is the particle density in the momentum space, and satisfies the normalization condition $\int dp n(p) = N$.

Consider the case of a uniform and isotropic system of N identical bosons occupying a volume V. In the limit where $N, V \to \infty$, while the density $n = \frac{N}{V}$ remains constant, (13.23) is not dependent on specific positions r, r' but does depend on the modulus of the relative position $s = |r - r'|$, so we can write

$$G^{(1)}(r, r') = G^{(1)}(s) = \frac{1}{V} \int dp n(p) e^{-ip \cdot s/\hbar}, \tag{13.24}$$

For a thermal state above the BEC critical temperature, the momentum distribution is smooth at small momenta, and the first-order coherence function $G^{(1)}(r, r')$ consequently vanishes when $s \to \infty$. The situation differs if instead the momentum distribution features the macroscopic occupation N_0 at the single particle ground state with the momentum $p = 0$

$$n(p) = N_0 \delta(p) + \tilde{n}(p). \tag{13.25}$$

This macroscopic occupation of the single particle state at $p = 0$ is a general feature of BEC, and the quantity $N_0/N < 1$ is called the condensate fraction. Using (13.25) in the integral of (13.24), we find that the first-order coherence function does not vanish when $s \to \infty$ but instead approaches a finite value:

$$g^{(1)}(s)|_{s\to\infty} \longrightarrow \frac{N_0}{N}. \tag{13.26}$$

This asymptotic behavior of the first-order coherence function was discovered by Landau and Lifshitz [30], Penrose [12], and Penrose and Onsager [13], and is often referred to as the off-diagonal long-range order (ODLRO), because it involves the off-diagonal elements ($r \neq r'$) of the first-order coherence function. The first-order coherence function $g^{(1)}(s)$ has been measured using various single particle interferometers [31]. The initial reduction of $g^{(1)}(s)$ for a small s value is governed by $\tilde{n}(p)$ in (13.25). The low-s expansion of (13.24) results in the following quadratic reduction in $g^{(1)}(s)$ in the limit where $s \to 0$:

$$g^{(1)}(s)|_{s\to 0} = 1 - \frac{1}{2}\langle \hat{p}^2 \rangle \frac{s^2}{\hbar^2} + \cdots, \tag{13.27}$$

where $\langle \hat{p}^2 \rangle = \frac{1}{N} \int dp n(p) p^2$ is the second order moment of the momentum distribution and is equal to the variance of the momentum distribution $\langle \Delta \hat{p}^2 \rangle = \langle \hat{p}^2 \rangle - \langle \hat{p} \rangle^2$, because $\langle \hat{p} \rangle = 0$.

If all particles condense into the ground state, i.e., $\frac{N_0}{N} \to 1$, the first-order coherence function $g^{(1)}(s)$ is independent of s and is equal to one. The first-order coherence function $g^{(1)}(s)$ is thus a measure of the degree of condensation in momentum space. If only the ground state is occupied and there are negligible populations in the excited states, then we always obtain $g^{(1)}(s) \simeq 1$.

Thus, the $g^{(1)}(s)$ measurements do not provide any information about the quantum statistical properties of the condensate particles. To distinguish the various possible candidate quantum states [32], we must study the higher-order coherence functions, which are defined by [24]

$$g^{(n)}(s) = \frac{\langle \hat{\psi}^+(r_1, t_1) \cdots \hat{\psi}^+(r_n, t_n) \hat{\psi}(r_n, t_n) \cdots \hat{\psi}(r_1, t_1) \rangle}{\left[\langle \hat{\psi}^+(r_1, t_1) \hat{\psi}(r_1, t_1) \rangle \cdots \cdots \langle \hat{\psi}^+(r_n, t_n) \hat{\psi}(r_n, t_n) \rangle \right]^{1/n}} \tag{13.28}$$

The higher-order coherence function is the joint probability of detection of n particles at $(r_1, t_1), (r_2, t_2) \cdots$ and (r_n, t_n) time-space points, and can be measured using the Hanbury-Brown and Twiss interferometer [33] or its variants. For instance, if the Bose particles in a single spatial mode are in the coherent state $|\alpha\rangle$, the particle number eigenstate $|N\rangle$ or the thermal state $\hat{\rho}_{\text{mix}}$, then the n-th order coherence function takes the following values [34–36]:

$$g^{(n)}(\tau = 0) = \begin{cases} 1 : \text{coherent state} \\ 1 - \frac{n-1}{N} : \text{particle number eigenstate,} \\ n! : \text{thermal state} \end{cases} \tag{13.29}$$

where $\tau = 0$ indicates the simultaneous detection of n particles, i.e., $t_1 = t_2 = \cdots = t_n$.

13.3 Bose-Einstein Condensation of an Ideal Gas

13.3.1 The Physical Picture Behind BEC

In a Bose gas at thermal equilibrium, the chemical potential must satisfy $\mu < \varepsilon_0$, where ε_0 is the lowest energy eigenvalue of the single particle states. Violation of this inequality would result in negative occupation number values for states with energies lower than μ. When μ approaches ε_0 from lower values, the occupation number $n_0 = \frac{1}{e^{\beta(\varepsilon_0 - \mu)} - 1}$ of the ground state becomes increasingly large. Here, $\beta = 1/k_B T$ is a temperature parameter. We can split the total number of particles into

$$N = N_0 + N_{th}, \tag{13.30}$$

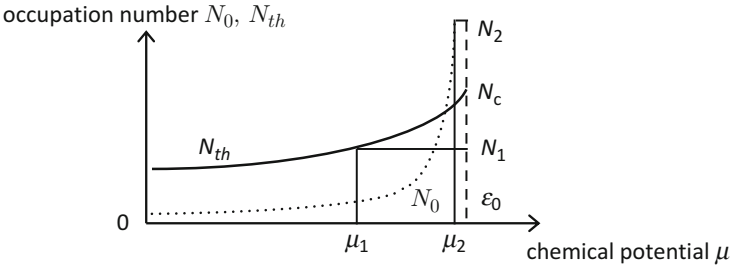

Fig. 13.3 Occupation number N_0 in the ground state and N_{th} in all excited states vs. chemical potential μ. If $N > N_c$, then the system forms a Bose-Einstein condensate

where

$$N_{th} = \sum_{i \neq 0} n_i(T, \mu), \tag{13.31}$$

is the number of particles in all excited states. For a finite temperature T and large volume V, N_{th} shows smooth behavior as a function of μ and reaches a maximum $N_c = N_{th}(T \neq 0, \mu = \varepsilon_0)$ asymptotically, as shown in Fig. 13.3. In contrast, N_0 diverges when μ approaches ε_0. Because the ground state population is given by $N_0 = \left[e^{\beta(\varepsilon_0 - \mu)} - 1\right]^{-1}$, the difference between the ground state energy and the chemical potential is substantially smaller than $k_B T$ when $N_0 \gg 1$:

$$\varepsilon_0 - \mu = k_B T ln\left(1 + \frac{1}{N_0}\right) \simeq \frac{k_B T}{N_0}. \tag{13.32}$$

The critical temperature T_c for BEC is operationally defined by the relation

$$N_{th}(T_c, \mu = \varepsilon_0) = N. \tag{13.33}$$

13.3.2 BEC Threshold in a Uniform System

For a system with finite volume V, the total number of single particle states in the energy range of $k_B T$ measured from the ground state energy ε_0 is finite, and thus $N_{th}(T_c, \mu = \varepsilon_0)$ remains a finite value. This means that (13.33) is always satisfied at finite temperatures, and that the BEC critical temperature exists irrespective of the dimensionality. This is in sharp contrast to the opposite conclusions that were previously drawn for uniform 2D or 1D systems [37].

13.3.2.1 Energy Density of States

The energy density of states for a free particle with mass m in a $d-$dimensional system with system size L is

$$\rho^{(d)}(\varepsilon) = \Omega_d \left(\frac{L}{2\pi}\right)^d \frac{1}{2} \left(\frac{2m}{\hbar^2}\right)^{\frac{d}{2}} \varepsilon^{\frac{d}{2}-1}, \tag{13.34}$$

where

$$\Omega_d = \begin{cases} 4\pi & (d=3) \\ 2\pi & (d=2) \\ 1 & (d=1) \end{cases} \tag{13.35}$$

$\rho^{(3)}(\varepsilon)$ vanishes when $\varepsilon \to 0$, while $\rho^{(2)}(\varepsilon)$ remains constant and $\rho^{(1)}(\varepsilon)$ diverges in the same limits. This difference in the asymptotic behaviors of $\rho^{(d)}(\varepsilon \to 0)$ results in the important consequence that the finite BEC critical temperature T_c only exists in a three-dimensional system [37].

13.3.2.2 BEC Critical Temperature and Density

The BEC critical temperature for a uniform 3D system is given by the condition where the number of particles that are accommodated in single particle excited states at $\mu = \varepsilon_0 = 0$ is equal to the total number of particles in the system:

$$N = \frac{V}{4\pi^2} \left(\frac{2m}{\hbar^2}\right)^{\frac{3}{2}} \int_0^\infty \sqrt{\varepsilon} \frac{d\varepsilon}{e^{\beta\varepsilon} - 1}. \tag{13.36}$$

We can then evaluate the energy integral to obtain the BEC critical density for a uniform 3D system:

$$n_c \equiv \frac{N}{V} \simeq 2.612 \frac{1}{\lambda_{T_c}^3}. \tag{13.37}$$

Here, $\lambda_{T_c} = \sqrt{\frac{2\pi\hbar^2}{mk_B T_c}}$ is the thermal deBroglie wavelength. Because $n_c^{-1/3}$ is the average distance between the particles, the BEC condition (13.37) means that BEC occurs when the inter-particle distance becomes comparable to the thermal deBroglie wavelength of the particle at a specific temperature. When the temperature is lower than T_c (or, equivalently, the density is higher than n_c), a mixture of the condensate at $\varepsilon_0 = 0$ and the thermal population at $\varepsilon > 0$ is formed:

$$n = \frac{2.612}{\lambda_T^3} + n_0. \tag{13.38}$$

13.3.2.3 Condensate Fraction

The BEC condition is often expressed in terms of the Bose function $g_p(Z)$, which is defined by

$$g_p(Z) = \frac{1}{\Gamma(p)} \int_0^\infty dx x^{p-1} \frac{1}{Z^{-1}e^x - 1} \tag{13.39}$$

where $Z = e^{\beta\mu}$ is a fugacity, and $\Gamma(p) = (p-1)!$. The energy integrals for uniform 3D, 2D and 1D systems are then reduced to the Bose functions of $Z = 1$ and $p = \frac{3}{2}, p = 1$ and $p = 1/2$, respectively. Among these functions, only $g_{\frac{3}{2}}(1)$ converges, while $g_1(1)$ and $g_{1/2}(1)$ diverge, which means that a finite critical temperature $T_c \neq 0$ only exists for a 3D system as long as the system is uniform and infinite [37].

At the critical temperature T_c in a uniform 3D system, all particles are in the thermal population, i.e. the particles are distributed over the single particle excited states at $\varepsilon > 0$:

$$\frac{V}{\lambda_{T_c}^3} g_{\frac{3}{2}}(1) = N, \tag{13.40}$$

while at lower temperatures, the thermal population is lower than (13.40)

$$\frac{V}{\lambda_T^3} g_{\frac{3}{2}}(1) = N_T < N. \tag{13.41}$$

From the ratio of (13.40) to (13.41), we obtain $\frac{\lambda_T^3}{\lambda_{T_c}^3} = \frac{N}{N_T}$. From this relationship, the number of particles in the condensate can be expressed as

$$N_0 = N - N_T = N\left[1 - \left(\frac{T}{T_c}\right)^{\frac{3}{2}}\right]. \tag{13.42}$$

If an ideal gas is trapped in a 3D harmonic potential, the argument above must be modified to take the new boundary condition into account. The condensate fraction in this case is given by $N_0/N = 1 - (T/T_c)^3$, which has been confirmed experimentally [38].

13.3.2.4 Volume Requirement for BEC

In a relatively small system, the energy difference between the first excited state and the ground state, $\varepsilon_1 - \varepsilon_0 = \hbar^2/2mV^{2/3}$, becomes appreciable. If the thermal energy k_BT becomes much smaller than $\varepsilon_1 - \varepsilon_0$, almost all particles occupy the ground state, i.e. $N_T \ll N$. This should not be considered to be BEC. For a system with a sufficiently large volume, a temperature range that satisfies

$$\hbar^2/2mV^{2/3} \ll k_BT \ll k_BT_c, \tag{13.43}$$

can be found, where $N_T \ll N$ is realized because of the quantum statistical properties of Bose particles. From (13.43), we obtain the following volume requirement for BEC:

$$V \gg V_c = \left(\frac{2mk_BT_c}{\hbar^2}\right)^{\frac{3}{2}} \sim \lambda_{T_c}^3. \tag{13.44}$$

This means that the system volume must be much larger than the cube of the thermal de Broglie wavelength at the critical temperature. The use of the inequality $\hbar^2/2mV^{2/3} \ll k_BT$ is actually crucial to the above theory of BEC, which is based on a continuous energy integral rather than a discrete sum over the single particle excited states.

13.4 Bogoliubov Theory of a Weakly Interacting Bose Gas

A noninteracting Bose gas has a constant pressure against volume variation, so that the system features infinite compressibility. This pathological feature originates from the absence of particle-particle interactions. It is unsurprising that the interactions between particles affect the properties of the Bose gas dramatically, even for very dilute samples. This problem was first addressed by Bogoliubov [8]. The Bogoliubov theory has provided the theoretical framework for modern approaches to BEC in dilute gases.

13.4.1 Hamiltonian of a Weakly Interacting Bose Gas and the Lowest-Order Approximation

The Hamiltonian of the system is expressed in terms of the field operators $\hat{\psi}$:

$$\hat{\mathcal{H}} = \int \left(\frac{\hbar^2}{2m}\nabla\hat{\psi}^+(r)\nabla\hat{\psi}(r)\right)dr + \frac{1}{2}\int \hat{\psi}^+(r)\hat{\psi}^+(r')V(r'-r)\hat{\psi}(r)\hat{\psi}(r')dr'dr, \tag{13.45}$$

where $V(r'-r)$ is the two-body scattering potential. For a uniform gas that occupies a volume L^3, the field operator $\hat{\psi}$ can be expanded by the plane waves:

$$\hat{\psi}(r) = \frac{1}{\sqrt{L^3}}\sum_p \hat{a}_p e^{ip\cdot r/\hbar}, \tag{13.46}$$

where $\hat{a}_p$ is the annihilation operator for a single particle plane wave with momentum p. By substituting (13.46) into (13.45), we obtain

$$\hat{\mathcal{H}} = \sum_p \frac{p^2}{2m}\hat{a}_p^+\hat{a}_p + \frac{1}{2L^3}\sum_{p_1,p_2,q} V_q \hat{a}_{p_1+q}^+ \hat{a}_{p_2-q}^+ \hat{a}_{p_1}\hat{a}_{p_2}. \tag{13.47}$$

Here, $V_q = \int V(r)\exp(-iq\cdot r/\hbar)\,dr$ is the Fourier transform of the two-body scattering potential. The macroscopic properties of a dilute gas can be explained by the small momentum exchange that occurs between the particles, which means that we can replace V_q with V_0 [23] to give

$$\hat{\mathcal{H}} = \sum_p \frac{p^2}{2m}\hat{a}_p^+\hat{a}_p + \frac{V_0}{2L^3}\sum_{p_1,p_2,q} \hat{a}_{p_1+q}^+ \hat{a}_{p_2-q}^+ \hat{a}_{p_1}\hat{a}_{p_2}. \tag{13.48}$$

Because the lowest energy state is occupied by a macroscopic number of particles in BEC, we can neglect the quantum fluctuation and replace the operator $\hat{a}_0$ with a c-number: $a_0 = \sqrt{N}$.

In the lowest-order approximation, we can neglect all terms with $p \neq 0$ in (13.48), and the ground state energy thus takes the form

$$E_0 = \frac{V_0}{2L^3}N_0^2, \tag{13.49}$$

where V_0 can be expressed in terms of the $s-$wave scattering length a using the Born approximation [23] as

$$V_0 = \frac{4\pi\hbar^2 a}{m} = g. \tag{13.50}$$

13.4.2 Bogoliubov Quasi-particles

If we split the operators $\hat{a}_0$ for the ground state and $\hat{a}_p$ for the excited states in (13.48), the Hamiltonian can be decomposed to:

$$\begin{aligned}\hat{\mathcal{H}} = {} & \frac{V_0}{2L^3}\hat{a}_0^+\hat{a}_0^+\hat{a}_0\hat{a}_0 + \sum_p \frac{p^2}{2m}\hat{a}_p^+\hat{a}_p \\ & + \frac{V_0}{2L^3}\sum_{p\neq 0}\left(4\hat{a}_0^+\hat{a}_p^+\hat{a}_0\hat{a}_p + \hat{a}_p^+\hat{a}_{-p}^+\hat{a}_0\hat{a}_0 + \hat{a}_0^+\hat{a}_0^+\hat{a}_p\hat{a}_{-p}\right).\end{aligned} \tag{13.51}$$

The momentum conservation retains only the quadratic terms in $\hat{a}_p$ when $p \neq 0$. Specifically, a factor of 4 in front of the third term on the right-hand side of (13.51) corresponds to the cases where (i) $p_1 = 0, p_2 = p, q = 0$, (ii) $p_1 = 0, p_2 = p, q = p$, (iii) $p_1 = p, p_2 = 0, q = 0$, and (iv) $p_1 = p, p_2 = 0, q = -p$ in (13.48). Cases (i)

and (iii) do not involve the transfer of momentum between two particles, so these two terms are called "direct terms". The other two cases, (ii) and (iv), do involve the transfer of momentum between two particles, so these terms are called "exchange terms".

We can replace $\hat{a}_0^+$ and $\hat{a}_0$ with $\sqrt{N}$ in the third term of (13.51), but in the first term, we must work with greater accuracy by using the normalization relation, $\hat{a}_0^+\hat{a}_0 + \sum_{p\neq 0}\hat{a}_p^+\hat{a}_p = N$, or

$$\hat{a}_0^+\hat{a}_0^+\hat{a}_0\hat{a}_0 \simeq N^2 - 2N\sum_{p\neq 0}\hat{a}_p^+\hat{a}_p. \tag{13.52}$$

The substitution of (13.50) and (13.52) into (13.51) yields the following Hamiltonian:

$$\hat{\mathcal{H}} = \frac{1}{2}gnN + \sum_p \frac{p^2}{2m}\hat{a}_p^+\hat{a}_p + \frac{1}{2}gn\sum_{p\neq 0}\left(2\hat{a}_p^+\hat{a}_p + \hat{a}_p^+\hat{a}_{-p}^+ + \hat{a}_p\hat{a}_{-p}\right). \tag{13.53}$$

The third term of this Hamiltonian represents the self-energy of the excited states due to the interaction, simultaneous creation and annihilation of excited states at the momenta p and $-p$.

Equation (13.53) can be diagonalized using the linear transformation

$$\hat{a}_p = u_p\hat{b}_p + v_{-p}\hat{b}_{-p}^+. \tag{13.54}$$

This is known as the Bogoliubov transformation. The two parameters, u_p and v_{-p}, are uniquely determined based on the following requirements. The new quasi-particle operators, $\hat{b}_p$ and $\hat{b}_p^+$, are assumed to obey the bosonic commutation relation as real particle operators, $\hat{a}_p$ and $\hat{a}_p^+$:

$$\left[\hat{b}_p, \hat{b}_{p'}^+\right] = \delta_{pp'}. \tag{13.55}$$

This commutation relation imposes the following constraint for the two parameters, u_p and v_{-p}:

$$u_p^2 - v_{-p}^2 = 1, \tag{13.56}$$

and thus we can write

$$u_p = \cosh(\alpha_p), v_{-p} = \sinh(\alpha_p). \tag{13.57}$$

The value of α_p must be chosen to ensure that the coefficients of the nondiagonal terms $\hat{b}_p^+\hat{b}_{-p}^+$ and $\hat{b}_p\hat{b}_{-p}$ in (13.53) disappear. This condition can be rewritten as

$$\coth\left(2\alpha_p\right) = -\frac{p^2/2m + gn}{gn}, \tag{13.58}$$

from which the two coefficients can be determined uniquely as

$$u_p, v_{-p} = \pm\left(\frac{p^2/2m + gn}{2\varepsilon(p)} \pm \frac{1}{2}\right)^{1/2}, \tag{13.59}$$

where

$$\varepsilon(p) = \left[\frac{gn}{m}p^2 + \left(\frac{p^2}{2m}\right)^2\right]^{1/2} \tag{13.60}$$

is the well-known dispersion law of the Bogoliubov excitation spectrum. By substitution for the Bogoliubov transformation (13.54) with the expressions (13.59) for the two coefficients u_p and v_{-p}, the Hamiltonian (13.53) is finally diagonalized:

$$\mathcal{H} = E_0 + \sum_{p\neq 0}\varepsilon(p)\hat{b}_p^+\hat{b}_p. \tag{13.61}$$

The results of (13.60)–(13.61) have the following physical meaning. The original system of interacting particles can be mapped onto the Hamiltonian for noninteracting quasi-particles with the dispersion law $\varepsilon(p)$. In this case, a real particle $\hat{a}_p$ can be described as a superposition of the forward-propagating many-body quasi-particles $u_p\hat{b}_p$ and the backward-propagating many-body quasi-particles $v_{-p}\hat{b}_{-p}^+$. When the momentum is small, $p \ll \sqrt{mgn}, |u_p| \simeq |v_{-p}| \gg 1$ and $\hat{a}_p \sim u_p\left(\hat{b}_p - \hat{b}_{-p}^+\right)$. However, when the momentum has a larger value, $p \gg \sqrt{mgn}, |u_p| \simeq 1$ and $|v_{-p}| \simeq 0$, and the quasi-particle $\hat{b}_p$ becomes indistinguishable from the real particle $\hat{a}_p$, i.e., $\hat{a}_p \sim \hat{b}_p$.

The ground state of the interacting Bose gas at $T = 0$ can now be defined as the vacuum state for the Bogoliubov quasi-particle annihilation operator:

$$\hat{b}_p|0\rangle = 0 \quad {}^\forall p \neq 0. \tag{13.62}$$

13.4.3 Excitation Spectrum

13.4.3.1 Phase and Amplitude Modulation Modes

The excitation spectrum at each wavenumber k is split into positive and negative branches. The eigenstate in the positive branch with positive eigen-frequency $\omega_+ =$

$\sqrt{\left(\frac{\hbar k^2}{2m}\right)\left[\left(\frac{\hbar k^2}{2m}+\mu\right)\right]}$ consists of the two plane waves $\psi_k^{(+)}$ and $\psi_{-k}^{(+)}$, and satisfies

$$\psi_k^{(+)} = \frac{-\mu}{\frac{\hbar k^2}{2m}+\mu-\omega_+}\psi_{-k}^{(+)} = -\frac{\mu}{\Delta}\psi_{-k}^{(+)}. \tag{13.63}$$

Here, $\Delta = \frac{\hbar k^2}{2m} + \mu - \omega_+$ is a positive quantity. When combined with the normalization condition, $\psi_k^{(+)_2} + \psi_{-k}^{(+)_2} = 1$, $\psi_k^{(+)}$ and $\psi_{-k}^{(+)}$ are expressed as

$$\psi_k^{(+)} = \frac{\mu}{\sqrt{\mu^2+\Delta^2}}, \tag{13.64}$$

$$\psi_{-k}^{(+)} = \frac{-\Delta}{\sqrt{\mu^2+\Delta^2}}. \tag{13.65}$$

For small wavenumbers, $\Delta \simeq \mu$ holds, meaning that the eigenstate in the positive branch is reduced to

$$\psi_{r,t}^{(+)} = i\sqrt{2}\sin(k\cdot r)e^{-i(\mu+\omega_+)t}. \tag{13.66}$$

Because $\psi_0(r)$ is a real-number order parameter, the purely imaginary term in (13.66) indicates that the positive branch of the excitation spectrum represents spatial phase modulation of the condensate order parameter.

The eigenstate in the negative branch with negative eigen-frequency $\omega = -\sqrt{\left(\frac{\hbar k^2}{2m}\right)\left[\left(\frac{\hbar k^2}{2m}\right)+2\mu\right]}$ consists of two plane waves, $\psi_k^{(-)}$ and $\psi_{-k}^{(-)}$, which satisfies

$$\psi_k^{(-)} = \frac{\mu}{\Delta}\psi_{-k}^{(-)}. \tag{13.67}$$

When combined with the normalization condition, $\psi_k^{(-)2} + \psi_{-k}^{(-)2} = 1$, $\psi_k^{(-)}$ and $\psi_{-k}^{(-)}$ are expressed as

$$\psi_k^{(-)} = \frac{\mu}{\sqrt{\mu^2+\Delta^2}}, \tag{13.68}$$

$$\psi_{-k}^{(-)} = \frac{\Delta}{\sqrt{\mu^2+\Delta^2}}. \tag{13.69}$$

At small wavenumbers, $\Delta \simeq \mu$ holds, meaning that the eigenstate in the negative branch is reduced to

$$\psi^{(-)}(r,t) = \sqrt{2}\cos(k\cdot r)e^{-i(\mu+\omega_-)t}. \tag{13.70}$$

The negative branch of the excitation spectrum corresponds to spatial amplitude modulation of the condensate order parameter.

13.4.3.2 Healing Length and Mean-Field Energy Shift

For small momenta $p \ll mc = \sqrt{mgn}$, the Bogoliubov dispersion law (13.15) can be approximated well by the phonon-like linear dispersion (13.16). According to the Bogoliubov theory, the long wavelength (small momentum) excitations of an interacting Bose gas are sound waves. These excitations can also be regarded as the Nambu-Goldstone modes associated with the spontaneous breaking of the gauge symmetry [39]. In this small momentum regime, a real particle can be represented by coherent superposition of the forward- and backward-propagating many-body quasi-particles: $\hat{a}_p = u_p \hat{b}_p + v_{-p} \hat{b}^+_{-p}$, where $|u_p| \sim |v_{-p}| \sim \sqrt{mc/2p} \gg 1$.

For the opposite limit $p \gg mc$, the Bogoliubov dispersion law (13.15) can be reduced to the free-particle form:

$$\varepsilon(p) = \frac{p^2}{2m} + gn. \tag{13.71}$$

The (additional) interaction energy gn in (13.71) can be traced back to the third term of the Hamiltonian (13.53). The interaction energy between the two particles in the condensate is calculated using the first term of (13.53). In contrast, the interaction energy between a particle in the condensate and another particle in the excitation spectrum, which is given by the third term of (13.53), is twice as large. The factor of 2 comes from the equal contributions of the direct and exchange terms for the identical bosons. In this large momentum regime, a forward-propagating real particle is almost identical to a forward-propagating quasi-particle: $\hat{a}_p \sim \hat{b}_p \left(u_p \simeq 1, v_{-p} \simeq 0\right)$.

The transition from the phonon regime to the free particle regime occurs when $\frac{p^2}{2m} = gn$ is satisfied. If we use $p = \hbar/\xi$ in this equation, the healing length ξ can then be obtained as

$$\xi = \sqrt{\frac{\hbar^2}{2mgn}} = \frac{1}{\sqrt{2}} \frac{\hbar}{mc}, \tag{13.72}$$

This is the length scale at which the density and phase fluctuations in the condensate are removed by the interactions between the condensed particles.

13.4.3.3 Observation of the Bogoliubov Excitation Spectrum

The Bogoliubov excitation spectrum was first observed in 1998, using the two-photon Bragg scattering spectroscopy technique in an atomic BEC [40], and was

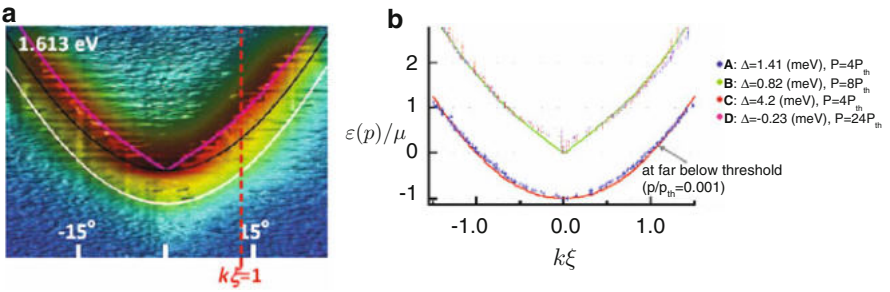

Fig. 13.4 (**a**) Observed energy vs. emission angle for the leakage photons from an exciton-polariton condensate in a logarithmic plot of intensity. The *white*, *black* and *pink solid lines* represent the dispersion laws, $\frac{p^2}{2m} - \mu$, $\frac{p^2}{2m}$ and $\varepsilon(p)$, which were given by (13.15). (**b**) Normalized energy $\varepsilon(p)/\mu$ vs. normalized wavenumber $k\xi$ for four exciton-polariton condensates with different detuning parameters (particle masses) [41]

observed later in polariton condensates [41]. Figure 13.4a shows the observed excitation energy vs. (in-plane) momentum for an exciton-polariton condensate [41]. Angle-resolved energy spectroscopy for the leakage photons from a semiconductor microcavity provided the dispersion law of the excitation spectrum directly. The white solid line represents the quadratic dispersion law for a single exciton-polariton far below the BEC critical density, while the black solid line indicates the quadratic dispersion law displaced by the interaction energy μ (chemical potential). The Bogoliubov excitation spectrum is indicated by the pink solid line in Fig. 13.4a, and shows remarkably good agreement with the experimental results.

The Bogoliubov dispersion law (13.16) can be rewritten in a normalized form:

$$\varepsilon(p)/\mu = \sqrt{(k\xi)^2\,[(k\xi)^2 + 2]}, \tag{13.73}$$

The relationship between $\varepsilon(p)/\mu$ and $k\xi$ is independent of the interaction strength, the particle mass and the particle density. This universal scaling law was confirmed experimentally for four exciton-polariton condensates with different masses, as shown in Fig. 13.4b [41].

13.4.4 Condensate Fragmentation

The standard argument for BEC leaves one central question unanswered: Why do the condensate particles accumulate in a single state, rather than be shared between several states that are degenerate or nearly degenerate, even when it makes no difference to the kinetic energy at thermal equilibrium? The answer is nontrivial: it is the exchange interaction energy (i.e., the Fock term) that makes the condensate fragmentation costly [42].

Consider the interaction Hamiltonian (the second term on the right-hand side of (13.48)) for two cases:

Case 1: Single state condensation

If all N particles are condensed into the single state

$$|\psi_0\rangle = \frac{1}{\sqrt{N!}} \left(\hat{a}_0^+\right)^N |0\rangle = |N\rangle, \tag{13.74}$$

the corresponding interaction energy is

$$E_0 \equiv \left\langle \psi_0 | \hat{\mathcal{H}}_I | \psi_0 \right\rangle = \simeq \frac{V_0}{2L^3} N^2. \tag{13.75}$$

Case 2: Two-state condensation

If the condensate is fragmented into two states, 1 and 2, with populations N_1 and N_2 ($N_1 + N_2 = N$), respectively, then

$$|\psi_{12}\rangle = \frac{1}{\sqrt{N_1! N_2!}} \left(\hat{a}_1^+\right)^{N_1} \left(\hat{a}_2^+\right)^{N_2} |0\rangle = |N_1\rangle_1 |N_2\rangle_2. \tag{13.76}$$

The interaction energy involves all possible contractions of the operators, and consists of the Hartree (direct) terms with (i) $p = p' = p_1, q = 0$, (ii) $p = p' = p_2, q = 0$, (iii) $p = p_1, p' = p_2, q = 0$, and (iv) $p = p_2, p' = p_1, q = 0$, and the Fock (exchange) terms with (v) $p = p_1, p' = p_2, q = p_2 - p_1$, and (vi) $p = p_2, p' = p_1, q = p_1 - p_2$. Therefore

$$\begin{aligned} E_{12} \equiv \left\langle \psi_{12} | \hat{\mathcal{H}}_I | \psi_{12} \right\rangle &= \left(\underbrace{\frac{1}{2} V_0 N_1^2 + \frac{1}{2} V_0 N_2^2 + V_0 N_1 N_2}_{\text{Hartree term}} + \underbrace{V_q N_1 N_2}_{\text{Fock term}} \right) / L^3 \\ &\simeq \frac{1}{2L^3} V_0 N^2 + \frac{1}{L^3} V_q N_1 N_2. \end{aligned} \tag{13.77}$$

Because $V_0 \simeq V_q > 0$ (repulsive interaction), the condensate fragmentation costs the macroscopic exchange energy. Genuine Bose-Einstein condensation is not an ideal gas effect, but is in fact a unique property of an interacting gas.

It may be debated that the use of the particle number state as the ground state is not justified in this case. Indeed, the repulsive interaction leads to quantum depletion, i.e., $N_0 < N$ even at $T = 0$, and the ground state is complicated. The argument above against condensate fragmentation nevertheless remains true, because it relies on a comparison of two situations with the same amount of quantum depletion. The exchange interaction energy is reduced slightly by the quantum depletion, but it remains substantial.

However, if a Bose system is dynamic because of a finite particle lifetime, the thermodynamic argument above does not apply. Instead, condensate fragmentation is often unavoidable. This is indeed the case for exciton-polariton condensates.

13.4.5 Population Fluctuations and Phase Locking

We gain exchange interaction energy by avoiding the condensate fragmentation. We can actually further reduce the exchange interaction energy by allowing population fluctuations and, in return, introducing a stabilized phase into the condensate [42]. Let us introduce a Glauber coherent state [24] for the ground state:

$$|\phi\rangle = e^{\phi \hat{a}_0^+}|0\rangle, \tag{13.78}$$

where ϕ is a c-number excitation amplitude with a phase, $\theta = \arg(\phi)$, that is stabilized to a specific value. The population and phase of the coherent state have finite variances:

$$\left\langle \Delta \hat{N}^2 \right\rangle = \left\langle \hat{N} \right\rangle = |\phi|^2, \tag{13.79}$$

$$\left\langle \Delta \hat{\theta}^2 \right\rangle = \frac{1}{4\left\langle \hat{N} \right\rangle} = \frac{1}{4|\phi|^2}. \tag{13.80}$$

$\hat{N}$ and $\hat{\theta}$ are canonically conjugate observables, and the phase is thus stabilized, i.e., $\left\langle \Delta \hat{\theta}^2 \right\rangle \ll 1$, at the cost of increased population fluctuation, $\left\langle \Delta \hat{N}^2 \right\rangle \gg 1$. We compare this coherent state with the particle number eigenstate:

$$|N\rangle = \int_0^{2\pi} d\theta e^{-iN\theta}|\phi\rangle. \tag{13.81}$$

Equation (13.81) shows that the particle number state $|N\rangle$ is constructed as a linear superposition of the coherent states with the different eigenvalues, as shown in Fig. 13.5. The constructive and destructive interferences result in a fixed particle number, but the phase is completely spread out. Similarly, the coherent state is expanded by coherent superposition of the particle number eigenstates, as shown in Fig. 13.1. The interaction energy in the condensate is the same for the two states, because both states have identical average particle numbers, i.e., $\left\langle \hat{N} \right\rangle = N$. There seems to be no preference for the quantum state of the ground state.

However, the story changes dramatically when we consider the quantum depletion into the Bogoliubov excitation spectrum, which allows virtual excitation of two particles out of the condensate, and vice versa. To take this quantum depletion into account, we consider a variational state:

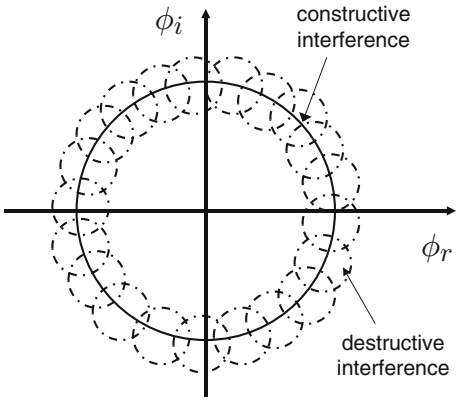

Fig. 13.5 Particle number eigenstate $|N\rangle_0$ constructed by coherent superposition of the coherent states

$$
\begin{aligned}
|\psi_0\rangle &= e^{\phi \hat{a}_0^+ + \sum_q \lambda_q \hat{a}_q^+ \hat{a}_{-q}^+} |0\rangle \\
&= |\phi\rangle_0 \otimes \sum_q \left[|0\rangle_q |0\rangle_{-q} + \lambda_q |1\rangle_q |1\rangle_{-q} + \cdots \right], \qquad (13.82)
\end{aligned}
$$

where the variational parameter λ_q is determined such that the interaction energy is minimized. The modulus $|\lambda_q|$ is determined from

$$
\begin{aligned}
|\lambda_q|^2 \simeq N_q &= \frac{q^2/2m + V_0}{2\varepsilon(q)} - \frac{1}{2} \\
&= \frac{1}{2\sqrt{2}k\xi} \qquad (13.83)
\end{aligned}
$$

The Bogoliubov interaction energy is given by

$$
E_B \equiv \left\langle \psi_0 | \hat{\mathcal{H}}_I | \psi_0 \right\rangle = \sum_q \frac{V_q}{2L^3} \left(\phi_0^{*2} \lambda_q + c.c. \right), \qquad (13.84)
$$

If we express the complex excitation amplitudes as $\phi = |\phi| e^{i\theta_0}$ and $\lambda_q = |\lambda_q| e^{i\theta_q}$, then (13.84) becomes

$$
E_B = \sum_q \frac{V_q}{L^3} |\phi|^2 |\lambda_q| \cos\left(2\theta_0 - \theta_q\right). \qquad (13.85)
$$

The Bogoliubov interaction energy is at a minimum when $2\theta_0 - \theta_q = \pi$. It is energetically favorable that the condensate has a well-defined phase (e.g., $\theta_0 = 0$,) and the excitations are phase-locked to the condensate phase with a 180° phase difference. The reduced energy is macroscopic, since $\frac{V_q}{L^3} |\phi|^2 |\lambda_q| \sim g n_0 \sqrt{N_q}$, where $n_0 = |\phi|^2 / L^3$ and N_q is the average population of the excitation

modes. From (13.83), N_q is of the order of 1 if $k\xi \lesssim 1$. In fact, quantum depletion is bound to occur because of the interaction Hamiltonian. Then, phase stabilization of the condensate is preferred, and the phase locking $2\theta_0 - \theta_q = \pi$ is implemented simultaneously. However, this argument does not answer the following question: if (13.85) is negative and is proportional to $|\lambda_q|$, does the system prefer continuous growth of the excitations at a cost of substantial quantum depletion of the condensate? Actually, the π-phase difference between the condensate and the excitations guarantees that this does not occur, and the quantum depletion is kept to a minimum.

Condensate population fluctuations and phase stabilization, which are caused by phase locking between the condensate and the excitations , are genuine signatures of spontaneous symmetry breaking [26], and this is distinct from the standard picture of Bose-Einstein condensation of a noninteracting ideal gas.

13.5 Superfluidity

Superfluidity is closely related to BEC. On a phenomenological level, a superfluid can flow through narrow capillaries or slits without friction. The superfluid ^{4}He was discovered independently by Kapitza [5] and by Allen and Misener [6]. Soon after this discovery, Landau explained that if the excitation spectrum satisfies certain specific criteria, the motion of the fluid does not cause energy dissipation [9]. These Landau criteria are met by the Bogoliubov excitation spectrum associated with Bose-Einstein condensates, which consists of an interacting Bose gas and thus establishes the first connection between superfluidity and BEC. The connection between the two phenomena is strengthened through the relationship between the irrotationality of the superfluid and the global phase of the BEC order parameter. After we discuss these aspects of superfluidity, we will conclude this section with a study of superfluidity in a uniform 2D system, which is known as the Berezinskii-Kosterlitz-Thouless phase transition.

13.5.1 Landau's Criteria of Superfluidity

Let E and $\mathbf{P}$ be the energy and the momentum of a fluid in a laboratory frame K. If we describe the energy and momentum of the same fluid in a moving frame K', which has a relative velocity $\mathbf{V}$ with respect to the laboratory frame K, we derive the following relations:

$$\mathbf{P}' \equiv \mathbf{P} - M\mathbf{V}, \tag{13.86}$$

$$E' = E - \mathbf{P}\cdot\mathbf{V} + \frac{1}{2}M|\mathbf{V}|^2, \tag{13.87}$$

where $E = \frac{|P|^2}{2M}$ and M is the total mass of the fluid.

Consider a fluid at zero temperature, at which all particles are in the ground state and are flowing along a capillary at a constant velocity $\mathbf{v}$. If the fluid is viscous, then the motion will produce energy dissipation via friction with the capillary wall and will thus reduce the kinetic energy. We assume that these dissipative processes occur through the creation of elementary excitation. Let us first describe this process in the laboratory frame K, which, rather confusingly, moves with the same velocity v as the fluid. In this laboratory frame, the fluid is at rest. If a single elementary excitation with momentum $\mathbf{p}$ appears in the fluid, then the total energy of the fluid in the laboratory frame K is $E_0 + \varepsilon(\mathbf{p})$, where E_0 and $\varepsilon(\mathbf{p})$ are the ground state energy and the elementary excitation energy, respectively. We now consider the moving frame K', in which the fluid moves with velocity $\mathbf{v}$, but the capillary is at rest. In this moving frame K', which moves with velocity $-\mathbf{v}$ relative to the fluid, the energy and momentum of the fluid can be expressed as

$$\mathbf{p}' = \mathbf{p} + M\mathbf{v}. \tag{13.88}$$

$$E' = E_0 + \varepsilon(\mathbf{p}) + \mathbf{p}\cdot\mathbf{v} + \frac{1}{2}M|\mathbf{v}|^2, \tag{13.89}$$

The results above indicate that the changes in the energy and momentum caused by the appearance of a single elementary excitation are $\varepsilon(\mathbf{p}) + \mathbf{p}\cdot\mathbf{v}$ and $\mathbf{p}$, respectively.

Spontaneous creation of elementary excitations, i.e. energy dissipation, can occur if and only if the required process is energetically favorable. This means that if the energy of an elementary excitation in the moving frame K', where the capillary is at rest, is negative, i.e.,

$$\varepsilon(\mathbf{p}) + \mathbf{p}\cdot\mathbf{v} < 0, \tag{13.90}$$

then energy dissipation occurs. The above condition is satisfied when $|\mathbf{v}| > \frac{\varepsilon(\mathbf{p})}{|\mathbf{p}|}$ and $\mathbf{p}\cdot\mathbf{v} < 0$, i.e., when the elementary excitation has momentum $\mathbf{p}$ opposite to the fluid velocity $\mathbf{v}$ and the fluid velocity $|\mathbf{v}|$ exceeds a critical value,

$$v_c = \min_{\mathbf{p}} \frac{\varepsilon(\mathbf{p})}{|\mathbf{p}|}, \tag{13.91}$$

where the minimum is calculated over all values of $\mathbf{p}$. If, instead, the fluid velocity $\mathbf{v}$ is smaller than (13.91), no elementary excitation will spontaneously form.

By studying the Bogoliubov excitation spectrum, we can easily conclude that the weakly interacting Bose gas at zero temperature satisfies Landau's criteria of superfluidity, and that the critical velocity is provided by the sound velocity. It is easily understood that the critical velocity decreases with reduction of the particle-particle interaction and disappears at the limit of an ideal gas because $v_c = \min_p \frac{\varepsilon(p)}{|p|} = 0$ for $\varepsilon(p) = \frac{p^2}{2m}$. Particle-particle interaction is a crucial requirement for the appearance of superfluidity.

13.5.2 Superfluid Velocity and Phase of the BEC Order Parameter

In the case of BEC, the local density of the particles is related to the squared order parameter by

$$n(r,t) = |\psi_0(r,t)|^2, \tag{13.92}$$

and thus the total number of particles is equal to $N = \int |\psi_0(r)|^2 dr$. If we multiply (13.11) by $\psi_0^*(r,t)$ and subtract the complex conjugate of the resulting equation, we then obtain the following continuity equation:

$$\frac{d}{dt} n(r,t) + \mathrm{div}\,[j(r,t)] = 0 \tag{13.93}$$

where the particle current density is

$$j(r,t) = -\frac{i\hbar}{2m}\left(\psi_0^* \nabla\psi_0 - \psi_0 \nabla\psi_0^*\right). \tag{13.94}$$

From (13.93), we can conclude that the Gross-Pitaevskii equation guarantees conservation of the total particle number $N = \int n(r) dr$. If we express the $c-$number order parameter $\psi_0(r,t)$ in terms of its amplitude and phase,

$$\psi_0(r,t) = \sqrt{n(r,t)} e^{iS(r,t)}, \tag{13.95}$$

then the particle current density (13.94) can be rewritten as $j(r,t) = n(r,t)\frac{\hbar}{m}\nabla S(r,t)$. This result shows that the superfluid velocity v_s of the condensate particles is related to the gradient of the phase S of the order parameter:

$$v_s(r,t) = \frac{\hbar}{m}\nabla S(r,t). \tag{13.96}$$

The phase of the order parameter plays the role of the velocity potential, and v_s is referred to as a velocity field.

13.5.3 Quantized Vortices in Superfluids

The history of quantized vortices provides an important insight into the problems of rotations in superfluids. Quantized vortices were first predicted by Onsager [14] and Feynman [15]. It is well known that a superfluid cannot rotate. In conventional rigid systems, the tangential velocity that corresponds to a rotation is given by $\mathbf{v} = \boldsymbol{\Omega} \times \mathbf{r}$,

where $\mathbf{\Omega}$ is the angular velocity vector and r is the distance vector from the origin of the rotation. Such a rigid rotator has $\text{curl}(\mathbf{v}) = \nabla \times (\mathbf{\Omega} \times \mathbf{r}) = \mathbf{\Omega} \neq 0$. In contrast, the superfluid velocity given by (13.96) satisfies

$$\text{curl}(\mathbf{v_s}) = \frac{\hbar}{m} \nabla \times \nabla S = 0. \tag{13.97}$$

This means that a superfluid must be irrotational and is thus expected to rotate in a completely different manner to a rigid rotator.

Consider a superfluid confined in a macroscopic cylinder of radius R and length L. The solution to the Gross-Pitaevskii equation for rotation around the $z-$axis of this cylinder is

$$\psi_0(r) = \sqrt{n(r)} e^{is\varphi}, \tag{13.98}$$

where we have used the cylindrical coordinates (r, φ and z), and $|\psi_0(r)| = \sqrt{n(r)}$. Because of the symmetry of the problem, the modulus of the order parameter $|\psi_0(r)|$ depends solely on the radial variable r. The parameter s should be an integer to ensure that the order parameter $\psi_0(r)$ has a single value. From (13.96) and (13.98), the tangential velocity is

$$v_s = \frac{\hbar}{m} |\nabla S| = \frac{\hbar}{m} \frac{\partial}{r \partial \varphi} S = \frac{\hbar}{m} \frac{s}{r}. \tag{13.99}$$

This result is completely different to the tangential velocity $\mathbf{v} = \mathbf{\Omega} \times \mathbf{r}$ of the rigid rotator, which has a modulus that increases linearly with r. At large distances from the $z-$axis, the tangential velocity v_s of the superfluid approaches zero and the irrotationality of the superfluid (13.97) is satisfied. The circulation of the tangential velocity over a closed contour around the $z-$axis is given by

$$\oint v_s dl = \frac{h}{m} s, \tag{13.100}$$

which is quantized in units of h/m, and is independent of the radius of the contour. This is called the "Onsager-Feynman quantization condition".

By substituting (13.98) into the time-independent Gross-Pitaveskii equation, we obtain the following equation for the modulus of the order parameter:

$$-\frac{\hbar^2}{2m} \frac{1}{r} \frac{d}{dr} \left(r \frac{d}{dr} |\psi_0| \right) + \frac{\hbar^2 s^2}{2mr^2} |\psi_0| + g|\psi_0|^3 - \hbar\mu|\psi_0| = 0. \tag{13.101}$$

The normalized modulus $f = |\psi_0|/\sqrt{n}$ as a function of the normalized position $\eta = r/\xi$ tends to obey $f \sim \eta^{|s|}$, which means that the superfluid density $n(r) = |\psi_0(r)|^2$ tends to zero on the vortex axis. Perturbation of the density occurs in a

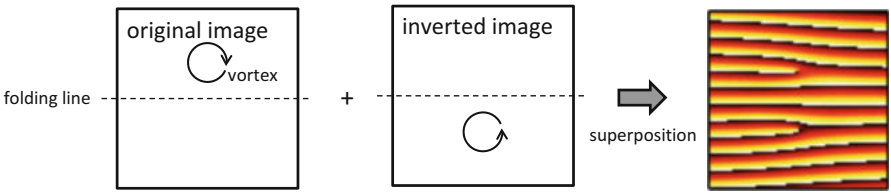

Fig. 13.6 Interference pattern of a quantized vortex with $s = 1$. The lower folk pattern is a mirror image of the upper folk pattern

spatial region of the order of the healing length ξ from the vortex line ($z-$axis). If the order parameter $\psi_0(r)$ for $s = 1$ is superposed to the ground state order parameter for $s = 0$, then a characteristic fork pattern emerges, as shown in Fig. 13.6, which manifests a 2π phase rotation along the vortex axis. This unique interference pattern can be used to identify the existence of a quantized vortex experimentally.

13.5.4 Berezinskii-Kosterlitz-Thouless (BKT) Phase Transition

13.5.4.1 Bound Vortex-Pairs

In uniform 2D systems, an off-diagonal long range order is destroyed at any finite temperature, in contrast to the uniform 3D systems [37, 43]. In a 3D superfluid, the energy cost associated with a quantized vortex is macroscopic, which means that the thermal creation of vortices is prohibited at low temperatures. However, in a 2D system, the creation of vortices is energetically favorable because the free energy is reduced by the appearance of entropy. This is the Hohenberg-Mermin-Wagner theorem [37, 43]. However, the 2D system can form a quasi-long-range order and become a superfluid below a finite critical temperature. This is referred to as the BKT phase transition [44, 45]. When the temperature decreases below a certain point T_{MF}, the macroscopic occupation of the ground state occurs, but with free vortices as fundamental excitations. With a further reduction in temperature below the BKT transition point T_{BKT}, a quasi-long-range order is formed through the pairing of vortices with opposite circulations. Formation of such bound vortex-pairs allows the global phase order to be recovered.

Proliferation of free vortices above the transition temperature T_{BKT} has been observed in a two-dimensional atomic Bose gas [46]. The onset of free vortex proliferation with increasing temperature coincides with a loss of quasi-long-range coherence [46].

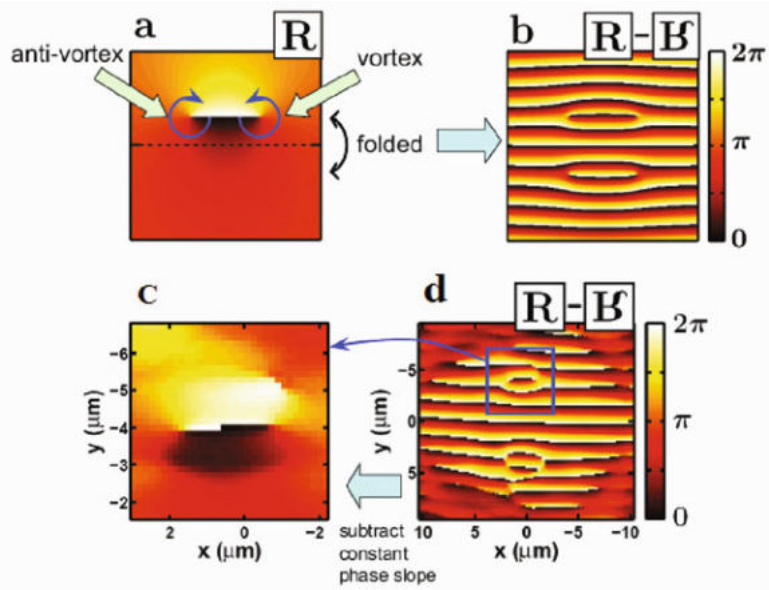

Fig. 13.7 Theoretical phase distribution (**a**) and interference pattern (**b**) of a vortex-pair, compared with the observed phase distribution (**c**) and interference pattern (**d**) [47]

A bound pair of vortices with opposite circulations has been observed directly in an exciton-polariton condensate, which is intrinsically 2D [47]. Figure 13.7 shows the observed phase distribution and the interference pattern of the vortex-pair in comparison to their theoretically predicted counterparts. The phase disturbance is indeed localized by formation of a bound pair and the global phase is recovered.

13.5.4.2 BKT Phase Transition Temperature

The creation of a quantized vortex is thermodynamically profitable if the total free energy of the system would be reduced by the appearance of a quantized vortex. The free energy is expressed as

$$F = E_v - TS, \tag{13.102}$$

where the 2D vortex energy cost and the entropy are given by

$$E_v = \pi \rho_{2s} \left(\frac{\hbar}{m}^2 \right) ln \left(\frac{R}{r_c} \right), \tag{13.103}$$

$$S = k_B ln\left(\frac{R^2}{r_c^2}\right). \tag{13.104}$$

Here, $r_c \simeq \xi$ is the vortex core size, ρ_{2s} is the 2D superfluid mass density, and R^2/r_c^2 is the number of possible states for the creation of a single vortex in a 2D condensate with a size of R.

The condition where $F < 0$ produces the BKT phase transition temperature:

$$T \geq \frac{\pi}{2k_B}\rho_{2s}\left(\frac{\hbar}{m}\right)^2 = T_{BKT}, \tag{13.105}$$

or

$$n_s\lambda_{T,BKT}^2 < 4. \tag{13.106}$$

When $T < T_{BKT}$ or $n_s\lambda_{T,BKT}^2 > 4$, the creation of free vortices is thermodynamically unfavorable, which means that pairs of vortices form and a quasi-long-range order is restored.

13.5.4.3 Algebraic Decay of the First-Order Coherence Function

If the order parameter of the BKT phase is expressed as $\psi(r) = \sqrt{n(r)}e^{iS(r)}$, then the phase correlation function is given by [48]

$$\begin{aligned}\chi(s) &= \langle S(s)S(0)\rangle \\ &= \frac{mc^2}{\rho_{2s}}\int N_p \cdot \frac{e^{ip\cdot s/\hbar}}{p}\frac{d^2p}{(2\pi\hbar)^2},\end{aligned} \tag{13.107}$$

where

$$N_p \simeq \frac{1}{e^{cp/k_BT} - 1} \simeq \frac{k_BT}{cp} \tag{13.108}$$

is the equilibrium particle distribution at temperature T for the Nambu-Goldstone phase mode. By introducing a lower cut-off momentum $\hbar/s$ and a higher cut-off momentum k_BT/c, we can evaluate the integral (13.107) as [48]

$$\chi(s) = \frac{k_BTm^2}{\rho_{2s}}\int_{\hbar/s}^{k_BT/c}\frac{e^{ips/\hbar}}{p^2}\cdot\frac{d^2p}{(2\pi\hbar)^2}, \tag{13.109}$$

and

$$\chi(0) - \chi(s) = \frac{k_BTm^2}{2\pi\hbar^2\rho_{2s}}ln\left(\frac{s}{s_T}\right). \tag{13.110}$$

Here, S_T is a characteristic length that is defined by

$$s_T = \frac{\hbar c}{k_B T} = \frac{\lambda_T^2}{2\pi\xi}. \tag{13.111}$$

The first-order spatial correlation function is obtained as:

$$\begin{aligned} g^{(1)}(s) &\simeq e^{-[\chi(0)-\chi(s)]} \\ &\simeq \left(\frac{s_T}{s}\right)^{a_p}, \end{aligned} \tag{13.112}$$

where the exponent is

$$a_p = \frac{k_B T m}{2\pi\hbar^2 \rho_{2s}} = \frac{1}{n_s \lambda_T^2}. \tag{13.113}$$

This algebraic decay of the first-order correlation function is an unmistakable evidence for the BKT phase and is indeed observed in a 2D exciton-polariton condensate, as shown in Fig. 13.8a, b [49]. The exponent a_p is plotted against the inverse phase space density $1/n_s\lambda_T^2$ in Fig. 13.9 [50]. These experimental results fully confirms the theoretical BKT prediction.

13.6 Useful Techniques for Quantum Simulation Experiments

To finish up this chapter, we will review several experimental techniques that are useful when performing quantum simulation with BEC.

13.6.1 Production of Atomic BEC

13.6.1.1 Cooling and Trapping

There are two kinds of mechanical forces on neutral atoms produced by laser light [51]. The first is a dissipative force called the radiation pressure or scattering force, which originates from the momentum transfer of photons during the photon absorption process. While the amount of momentum carried by a single photon is very small, we can exert a sizable mechanical force on atoms by repetition of absorption and subsequent emission cycles, which, for example, resulted in the stopping of a sodium atom with an initial velocity of 1 km/s in about 1 ms over a distance of approximately 0.5 m.

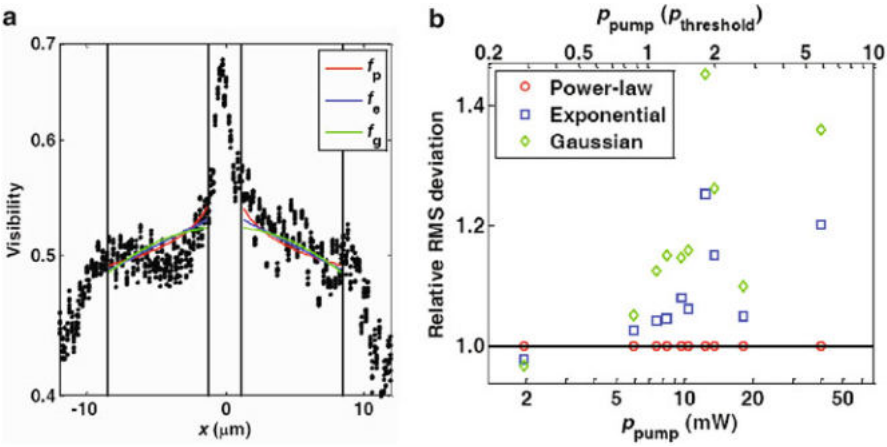

Fig. 13.8 The decay of a first-order coherence function for exciton-polariton condensates. (**a**) The fitting functions used are a power-law of the form $f_p(x) = c_p|x/\mu m|^{-a_p}$, an exponential decay function $f_e(x) = c_e \exp(-a_e|x/\mu m|)$, and a Gaussian $f_g(x) = c_g \exp\left[-a_e(x/\mu m)^2\right]$. Fitting has been performed by minimization of the root-mean-square (RMS) deviation $D_i = \sqrt{\sum_n [f_i(x_n) - V_n]^2 / N}$ between the fitted functions f_i (with $i \in \{p, e, g\}$) and the N measured data points $(x_n; V_n)$ for both position and visibility with $x_{\min} < |x_n| < x_{\max}$, where the intermediate range limits $x_{\min}$ and $x_{\max}$ (indicated by the *black vertical lines*) have been chosen manually. Here, we use the same fitting for both the $x < 0$ and the $x > 0$ regions. The visibility shown here has been measured at $\delta \approx -1$ meV and $p_{\text{pump}} = 18$ mW. (**b**) The relative RMS deviations $R_i = \frac{D_i}{D_p}$, measured at $\delta \approx -1$ meV. Above the condensation threshold, we always observed $D_p < D_e < D_g$, which shows that the power-law fit provides the best match, and that the Gaussian fit provides the worst match

The second mechanical force is called a dipole force, which originates from the momentum transfer of photons in the photon scattering process, or in the virtual photon absorption and emission process [51, 52]. This is a conservative force, and is also understood as a force caused by the potential gradient of the AC Stark shift $V_{ACS} = -(1/2)\alpha(\omega)E(r)^2$, where $\alpha(\omega)$ is the polarizability at the laser frequency ω, and $E(r)$ is the applied electric field amplitude at the atom position r. When atoms are confined by a periodic potential produced by a standing wave of laser light, then the system is called an optical lattice.

Various cooling techniques based on these two types of forces have been developed, and atoms at very low temperatures have been produced [51]. As a typical example, atoms from an atomic oven with high initial velocity have been decelerated with a Zeeman slower and cooled and trapped by magneto-optical trapping, and, in some cases, by polarization-gradient cooling. This process can produce up to 10^{10} atoms at microkelvin temperatures.

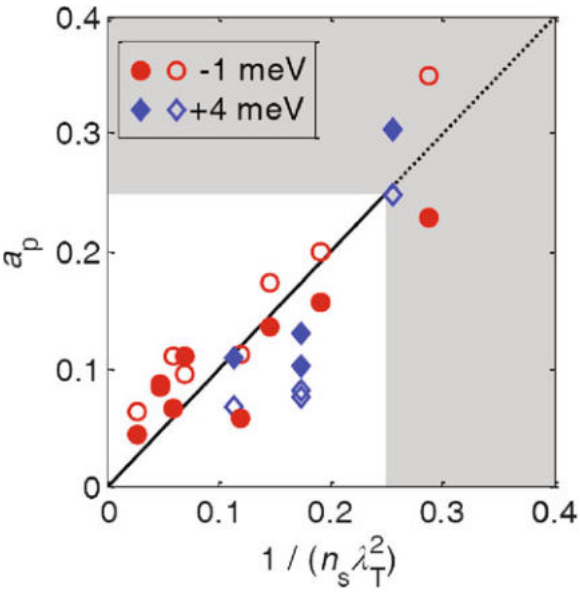

Fig. 13.9 Measured exponents a_p as a function of the estimated inverse superfluid phase-space-density $1/\left(n_s\lambda_T^2\right)$. The *black line* shows the predicted $a_p^{\text{calculated}} = 1/\left(n_s\lambda_T^2\right)$, and the region above the expected threshold of 0.25 is shaded in *gray*. Although we did not vary the temperature during the measurement, the abscissa can be interpreted as the dimensionless temperature (in units of $2\pi m_{\text{eff}} k_B n_s^{-1} h^{-2}$), and the BKT phase transition occurs at a dimensionless temperature of 0.25 in these units

The temperature of an atomic gas can be accurately measured using a time-of-flight (TOF) technique, in which the velocity distribution of the atoms, after ballistic expansion during a specific time period caused by the sudden turning off of a trap, is measured by an absorption imaging method.

Figure 13.10 illustrates some cooling and trapping methods for neutral atoms. Figure 13.10a shows the setup of the laser beams used for cooling and the magnetic field gradient coils used for the magneto-optical trapping of, for instance, ytterbium (Yb) atoms. A typical fluorescence image of the laser cooled and trapped Yb atoms is also shown. Figure 13.10b shows a setup used for optical trapping of rubidium (Rb) atoms based on optical dipole-force trapping. A typical absorption image of the trapped Rb atoms is also shown. Figure 13.10c shows a setup used for magnetic trapping, in which a combination of coils produces the necessary magnetic field gradients.

13.6.1.2 Evaporative Cooling to Quantum Degeneracy

Cold atoms in the microkelvin regime are easily trapped using conservative traps such as an optical dipole-force trap or a magnetic trap, which realize a well isolated atomic ensemble within a vacuum chamber. By selectively removing the energetic atoms from the trap, it is possible to obtain a lower temperature for the remaining atoms; this is called evaporative cooling [53]. This relies solely on the elastic collisions of the atoms, and is not limited by single-photon recoil. To reach the quantum degenerate regime, this method must always be used as a final step. The

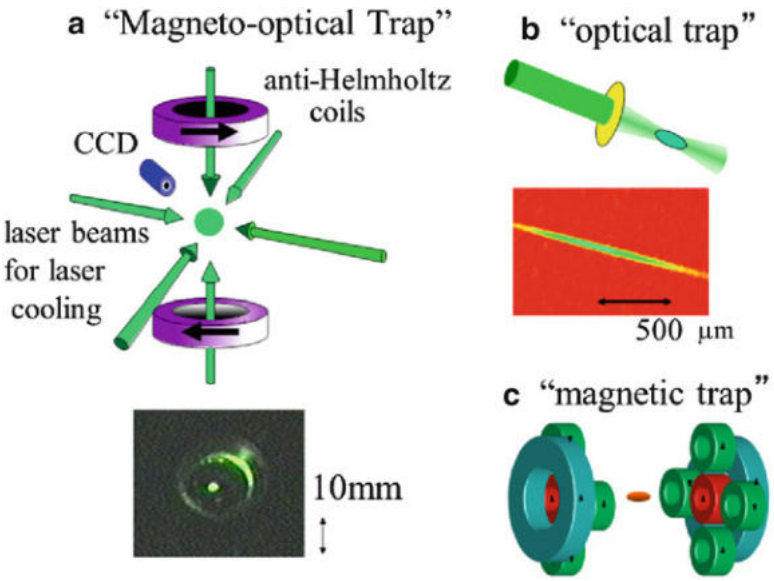

Fig. 13.10 Cooling and trapping of neutral atoms by (**a**) magneto-optical trapping, (**b**) optical dipole-force trapping, and (**c**) magnetic trapping

most important point for successful evaporative cooling is a large ratio of the elastic collision rate, which promotes evaporation and thermalization in a trap, to the inelastic collision rate, which removes the cold and high density atoms from a trap and thus results in heating.

13.6.1.3 Quantum Gases

Various quantum gases have been successfully produced since the initial realization using ^{87}Rb atoms [1]. Almost all of the alkali-metal atoms have been successfully cooled into the quantum degenerate regime, along with atomic hydrogen and metastable helium atoms. Additionally, many two-electron atoms such as alkali-earth-metal-atoms and Yb atoms have been successfully cooled to quantum degeneracy by all-optical means. Quantum degenerate gases of magnetic atoms such as chromium, dysprosium, and erbium have also been produced.

13.6.2 Production of Exciton-Polariton Condensates

An exciton-polariton is a hybridized mode that consists of two bosonic particles: excitons (bound electron-hole pairs) trapped in a quantum well (QW) potential

and photons confined in a planar microcavity. Therefore, the exciton-polaritons are trapped in the vertical direction but can propagate freely in the horizontal directions, i.e., they are two-dimensional systems.

13.6.2.1 Cooling and Trapping

Exciton-polaritons can be cooled efficiently by phonons emitted into the host crystal lattices, where the vertical confinement of the excitons by the QW potential removes the momentum conservation requirement along the vertical direction. However, at the transition in-plane momentum value, where the energy-momentum dispersion relationship changes dramatically from exciton-like to polariton-like behavior, the phonon emission rate drops rapidly, and the so-called bottleneck effect, i.e., the accumulation of polaritons at a finite in-plane momentum, is observed. The bottleneck effect is usually suppressed by increasing the particle density, because the two-body scattering process creates a new cooling channel for the bottleneck polaritons [54].

To trap exciton-polaritons in the lateral directions, some forms of photon or exciton confinement mechanisms can be introduced into the planar microcavity structures. Figure 13.11 shows several representative schemes, including a metallic thin film evaporated on the top layer of a microcavity [55], a modulated optical cavity layer thickness scheme [56], an etched post structure scheme [57], a mechanical strain scheme [22] and a laser pump interference pattern scheme [58]. Various lattice structures can be formed using these techniques.

13.6.2.2 Polariton Fluids

Exciton-polariton condensates have been produced in various materials, including GaAs [59], CdTe [21], GaN [60], ZnO [61], and organic materials [62]. The last three materials allow the production of exciton-polariton condensates even at room temperature, because of their small dielectric constants and large binding energies, while GaAs offers the highest material quality, which means that most of the fundamental physics have been explored using this system.

13.6.3 Inter-atomic Interaction

13.6.3.1 Quantum Collision Regime

Because the typical temperature range is in the sub-microkelvin regime for atomic quantum degenerate gases and the centrifugal barriers for higher partial waves are much higher than such a temperature or energy scale, the collision is in a quantum regime, in which only a few of the lowest orders (typically one) of the partial

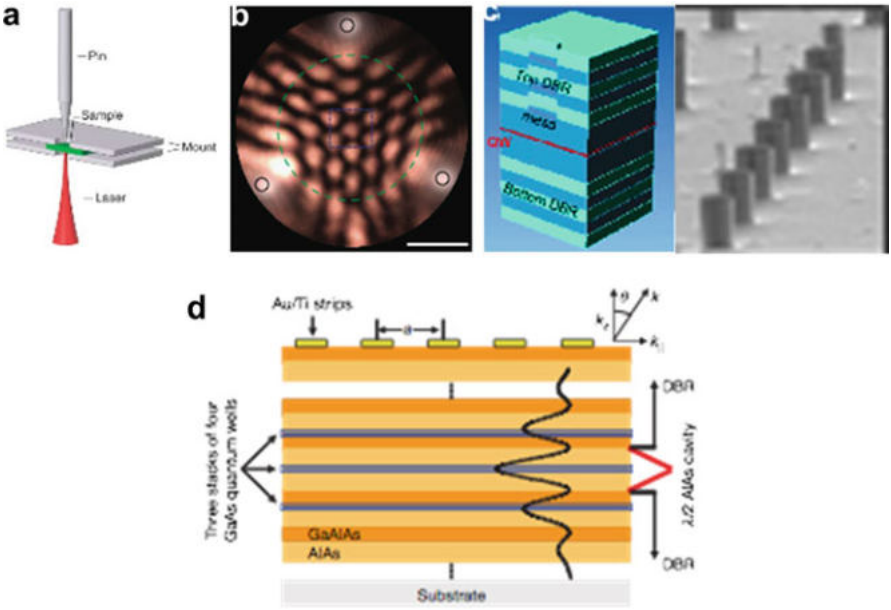

Fig. 13.11 Methods of trapping potential generation for microcavity exciton-polaritons. (**a**) Applied mechanical strain using a pin near the sample to change the exciton energy, as depicted in [22]. (**b**) A honeycomb lattice of exciton-polaritons induced by a three-spot laser pump profile [58]. (**c**) Partial (*left*, [56]) and complete etching (*right*, [57]) to form a photonic trap. (**d**) A weakly modulated in-plane one-dimensional photon lattice with a thin metal film technique on the grown wafer fabricated in [55]

waves contribute to the collision [53]. For bosons in a BEC, s-wave scattering is thus usually dominant, and the s-wave scattering length a_s is the most important parameter in characterization of the collision in the atomic BECs.

13.6.3.2 Scattering Length

While the s-wave scattering length a_s is crucially important, it is usually very difficult to theoretically predict the scattering length, because we need an accurate potential curve for all inter-atomic distance ranges. We need to determine the information on the inter-atomic potential from experimental measurements, such as photoassociation. In the mean-field approximation, the inter-atomic interaction $V(x)$ can be written using the scattering length as $V(x) = 4\pi n\hbar^2 a_s \delta(x)/m$, where n is the atomic density, m is the mass of an atom, and $\hbar$ is the Planck constant divided by 2π. Note that a positive (negative) scattering length a_s represents a repulsive (attractive) interaction.

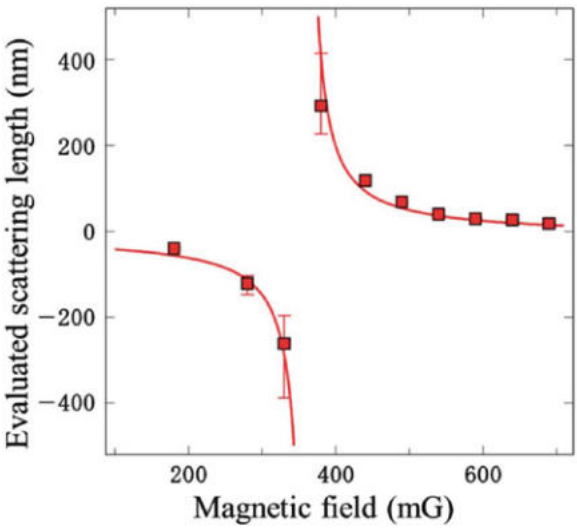

Fig. 13.12 Example of Feshbach resonance in the Yb atom case, in which Feshbach resonance is induced by anisotropic inter-atomic interaction between the ground and metastable states

13.6.3.3 Feshbach Resonance

Usually, if we select an atom with a specific state, the scattering length a_s is determined. However, in certain cases, we can vary the scattering length a_s with a magnetic field; this phenomenon is known as Feshbach resonance [63, 64]. This resonance is induced by coupling between an open or entrance channel of a two-atom scattering state and a closed channel of a molecular bound state, which has a different magnetic moment to that of the entrance channel. By tuning the magnetic field, the energy levels of the open and closed channels can be tuned to coincide, which results in resonant control of the scattering length with a dispersive curve as a function of the magnetic field, and is given as follows:

$$a(B) = a_{bg}(1 - \Delta B/(B - B_0)) \tag{13.114}$$

Here, a_{bg} is the scattering length at a magnetic field far from the resonant value B_0, and is called the background scattering length. An example of Feshbach resonance is shown in Fig. 13.12 for the case of Yb atoms, in which the Feshbach resonance is induced by an anisotropic inter-atomic interaction between the ground and metastable states [65]. This novel ability to tune the interaction is quite powerful, and is only possible when using an atomic quantum gas system. When the Feshbach resonance technique is applied to a bosonic system, we can study the novel Bosenova phenomenon, in which a stable BEC with a repulsive interaction is suddenly subjected to a collapse with an attractive interaction, e.g., [66]. Another interesting example is the case for fermions, with which we can create a Bardeen-Cooper-Schrieffer (BCS) state [67] and molecular BEC, and study BEC-BCS crossover and unitary gases [68].

13.6.4 Quantum Gases in an Optical Lattice

13.6.4.1 Optical Lattice

When atoms are subjected to a periodic potential produced, for example, by a standing laser light wave like $\sin^2(k_L x)$, then the system is called an optical lattice [52]. Here, $k_L = 2\pi/\lambda$ is the wavenumber of the laser for an optical lattice. A typical example is shown in Fig. 13.13 for a 3D cubic optical lattice produced by three orthogonal standing wave light beams with retro-reflecting mirrors and lattice constants of $\lambda/2$. Note that we can use various lattice geometries. For example, by superimposing several laser beams and/or by using the interference of the laser beams, we can successfully produce not only a simple super-lattice, but also more exotic nonstandard triangular, honeycomb, Kagome, and Lieb lattices. It should also be noted that one particular optical lattice configuration can be continuously changed into another by varying the optical lattice laser parameters. Additionally, a quantum gas of various dimensions can easily be produced, including the formation of a 2D gas by loading into an optical lattice in one direction, and formation of a 1D gas using two orthogonal optical lattices.

13.6.4.2 Hubbard Model

A Hubbard model is considered to describe the essence of a system of interacting electrons in condensed matter. A system of ultracold atoms in an optical lattice and exciton-polaritons under a periodic potential are described well by a Bose-Hubbard model [69, 70]:

$$H = -J \sum_{i,j} a_i^\dagger a_j + U/2 \sum_i n_i(n_i - 1) + \sum_i \epsilon_i n_i. \tag{13.115}$$

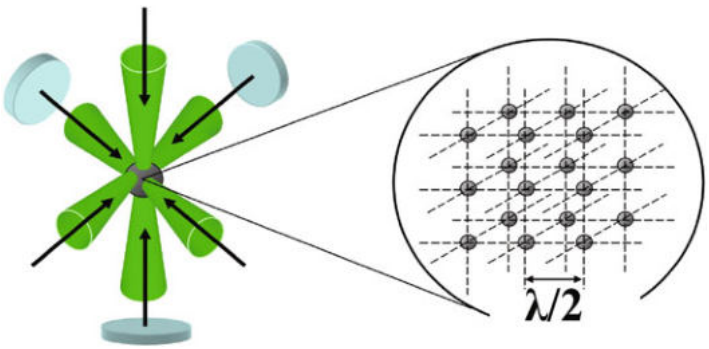

Fig. 13.13 Three-dimensional optical lattice produced by three orthogonal standing wave light beams, with a lattice constant of $\lambda/2$

Here, a_i and $a_i^\dagger$ describe the annihilation and creation operators of a particle, respectively. The first term, which is proportional to J, represents the hopping between the adjacent lattice sites, and the second term, which is proportional to U, represents the on-site interaction when more than two particles occupy the same lattice site. In addition to these two terms for hopping, and on-site interaction there is a third term that represents an inhomogeneous energy shift caused by a weak harmonic confinement or crystal imperfection. The important parameters J and U can be described approximately using the parameters of the atoms and the optical lattice as follows:

$$J = -E_R(2/\sqrt{\pi})s^{3/4}\exp(-2\sqrt{s}), \tag{13.116}$$

and

$$U = E_R a_s k_L \sqrt{8/\pi}s^{3/4}. \tag{13.117}$$

Here, $s = V/E_R$ is the nondimensional parameter that represents the optical lattice depth V normalized with respect to the recoil energy $E_R = (\hbar k_L)^2/(2m)$, which is a typical energy scale for an optical lattice system with a typical 100 nK range. The corresponding expressions for the exciton-polaritons can be found in [71].

In particular, the ratio of U/J, which determines the system behavior, is precisely and continuously tuned by changing the intensity of the laser light used for the optical lattice. Independent control of the on-site interaction U can also be possible when using the Feshbach resonance technique described in the preceding section.

In the case of ultracold fermions in an optical lattice, we can consider the Fermi-Hubbard model:

$$H = -J\sum_{i,j} c_i^\dagger c_j + U\sum_i n_{i,\uparrow}n_{i,\downarrow} + \sum_i \epsilon_i n_i. \tag{13.118}$$

Here, c_i and $c_i^\dagger$ describe the annihilation and creation operators of a Fermi atom, respectively. $n_{i,\uparrow}$ and $n_{i,\downarrow}$ describe the number operators of a Fermi atom at the $i-$th site with up and down spins, respectively.

13.6.4.3 Two Ultimate Bose-Hubbard Model Regimes: Superfluid and Mott Insulator States

When the hopping J is dominant over the on-site interaction U, as realized in the case of relatively shallow lattice depths, the system is called a superfluid state, which is described as follows:

$$|\Psi_{SF}\rangle \propto (\frac{1}{\sqrt{M}}\sum_i^M a_i^\dagger)^N |0\rangle \tag{13.119}$$

Here, M is the number of the optical lattice sites, N is the number of atoms, and $|0\rangle = \prod_{i=1}^{M} |0\rangle_i$ is the product of the vacuum states of each site $|0\rangle_i$. If N and M are large enough, with a ratio $n = N/M$, we can express the state approximately as a product of a coherent state in each optical lattice site:

$$|\Psi_{Coh}\rangle \propto \prod_{i=1}^{M} \exp(\sqrt{n} a_i^{\dagger}) |0\rangle_i . \tag{13.120}$$

In contrast, when U is dominant over J, which is realized in the case where the lattice depths are relatively deep, the system is called a Mott insulating state and is described as the product of the number states in the optical lattice sites:

$$|\Psi_{MI}\rangle \propto \prod_{i=1}^{M} (a_i^{\dagger})^n |0\rangle . \tag{13.121}$$

It is important that this state is a strongly-correlated state and it should be distinguished from a simple band insulating state in which the atoms occupy all the lower energy bands and do not occupy a higher band separated by the band gap energy. Repulsive interaction plays a crucial role in formation of a Mott insulating state. Even if the hopping energy J is finite, the formation of multiply-occupied sites caused by hopping is energetically unfavorable because of the large onsite interaction U, and thus the hopping is suppressed and the atoms are localized, or the insulating state is formed.

References

1. M.H. Anderson, J.R. Ensher, M.R. Matthews, C.E. Wieman, E.A. Cornell, Observation of Bose-Einstein condensation in a dilute atomic vapor. Science **269**, 198–201 (1995)
2. K.B. Davis, M.O. Mewes, M.R. Andrews, N.J. van Druten, D.S. Durfee, D.M. Kurn, W. Ketterle, Bose-Einstein condensation in a gas of sodium atoms. Phys. Rev. Lett. **75**, 3969–3973 (1995)
3. S.N. Bose, Plancks law and light quantum hypothesis. Z. Phys. **26**, 178 (1924)
4. A. Einstein, Quantum theory of ideal monoatomic gases. Sitzber. Preuss. Akad. Wiss. **23**, 3 (1925)
5. P. Kapitza, Viscosity of liquid helium below the λ-point. Nature **141**, 74 (1938)
6. J.F. Allen, A.D. Misener, Flow of liquid helium II. Nature **141**, 75–75 (1938)
7. F. London, The lambda-phenomenon of liquid helium and the Bose-Einstein degeneracy. Nature **141**, 643 (1938)
8. N.N. Bogoliubov, On the theory of superfluidity. J. Phys. (USSR) **11**, 23 (1947)
9. L.D. Landau, The theory of superfluidity of helium II. J. Phys. USSR **5**, 71 (1941)
10. R.P. Feynman, Atomic theory of the 2-fluid model of liquid helium. Phys. Rev. **94**, 262 (1954)
11. L.D. Landau, E.M. Lifshitz, *Statisticheskai Fizika* (Fizatgiz, Moscow, 1951)
12. O. Penrose, On the quantum mechanics of helium II. Philos. Mag. **42**, 1373 (1951)
13. O. Penrose, L. Onsager, Bose-Einstein condensation and liquid helium. Phys. Rev. **104**, 576–584 (1956)

14. L. Onsager, Statistical hydrodynamics. Nuovo Cimento **6**, 279–287 (1949)
15. R.P. Feynman, *Progress in Low Temperature Physics, vol. 1* (North-Holland, Amsterdam, 1955)
16. S.A. Moskalenko, Reversible optico-hydrodynamic effects in nonideal exciton gas. Fiz. Tverd. Tela **4**, 276 (1962)
17. I.M. Blatt, W. Brandt, K.W. Boer, Bose-Einstein condensation of excitons. Phys. Rev. **126**, 1691 (1962)
18. A. Imamoglu, R.J. Ram, S. Pau, Y. Yamamoto, Nonequilibrium condensates and lasers without inversion: Exciton-polariton lasers. Phys. Rev. A **53**, 4250–4253 (1996)
19. H. Deng, G. Weihs, C. Santori, J. Bloch, Y. Yamamoto, Condensation of semiconductor microcavity exciton polaritons. Science **298**, 199–202 (2002)
20. H. Deng, D. Press, S. Goetzinger, G. Solomon, H. Rudolf, K.H. Ploog, Y. Yamamoto, Quantum degenerate exciton-polaritons in thermal equilibrium. Phys. Rev. Lett. **97**, 146402 (2006)
21. J. Kasprzak, M. Richard, S. Kundermann, A. Baas, P. Jeambrun, J.M.J. Keeling, F.M. Marchetti, M.H. Szymanska, R. Andre, J.L. Staehli, V. Savona, P.B. Littlewood, B. Deveaud, L. Si Dang, Bose-Einstein condensation of exciton polaritons. Nature **443**, 409 (2006)
22. R. Balili, V. Hartwell, D. Snoke, L. Pfeiffer, K. West, Bose-Einstein condensation of microcavity polaritons in a trap. Science **316**, 1007 (2007)
23. L. Pitaevskii, S. Stringari, *Bose-Einstein Condensation* (Clarendon Press, Oxford, 2003)
24. R.J. Glauber, The quantum theory of optical coherence. Phys. Rev. **130**(6), 2529–2539 (1963)
25. Y. Yamamoto, H.A. Haus, Preparation, measurement and information capacity of optical quantum states. Rev. Mod. Phys. **58**, 1001–1020 (1986)
26. Y. Nambu, Quasi-particles and gauge invariance in the theory of superconductivity. Phys. Rev. **117**, 648–663 (1960)
27. J. Goldstone, Field theories with superconductor solutions. Nuovo Cimento **19**, 154–164 (1961)
28. J. Goldstone, S. Weinberg, A. Salam, Broken symmetries. Phys. Rev. **127**, 965 (1962)
29. W.H. Louisell, *Quantum Statistical Properties of Radiation* (Wiley, New York, 1973)
30. L.D. Landau, E.M. Lifshitz, *Statistical Physics*, 3rd edn. (Butterworth-Heinemann, Oxford, 1951)
31. I. Bloch, T.W. Hänsch, T. Esslinger, Measurement of the spatial coherence of a trapped Bose gas at the phase transition. Nature **403**, 166 (2000)
32. Y. Yamamoto, A. Imamoglu, *Mesoscopic Quantum Optics* (Wiley-Interscience, New York, 1999)
33. R. Hanbury Brown, R.Q. Twiss, A test of a new type of stellar interferometer on sirius. Nature **178**, 1046–1048 (1956)
34. L. Mandel, E. Wolf, *Optical Coherence and Quantum Optics* (Cambridge University Press, Cambridge, 1995)
35. R. Loudon, *The Quantum Theory of Light* (Clarendon Press, Oxford, 1973)
36. T. Horikiri, P. Schwendimann, A. Quattropani, S. Hofling, A. Forchel, Y. Yamamoto, Higher order coherence of exciton-polariton condensates. Phys. Rev. B **81**, 0333307 (2010)
37. P.C. Hohenberg, Existence of long-range order in one and two dimensions. Phys. Rev. **158**, 383–386 (1967)
38. J.R. Ensher, D.S. Jin, M.R. Matthews, C.E. Wieman, E.A. Cornell, Bose-Einstein condensation in a dilute gas: measurement of energy and ground-state occupation. Phys. Rev. Lett. **77**, 4984–4987 (1996)
39. T.D. Lee, K. Huang, C.N. Yang, Eigenvalues and eigenfunctions of a Bose system of hard spheres and its low-temperature properties. Phys. Rev. **106**, 1135–1145 (1957)
40. D.M. Stamper-Kurn, A.P. Chikkatur, A. Görlitz, S. Inouye, S. Gupta, D.E. Pritchard, W. Ketterle, Excitation of phonons in a bose-einstein condensate by light scattering. Phys. Rev. Lett. **83**, 2876–2879 (1999)
41. S. Utsunomiya, L. Tian, G. Roumpos, C.W. Lai, N. Kumada, T. Fijisawa, M. Kuwata-Gonokami, A. Löffler, A. Höfling, A. Forchel, Y. Yamamoto, Observation of bogoliubov excitations in exciton-polariton condensates. Nat. Phys. **4**, 700–705 (2008)

42. P. Nozieres, *Bose-Einstein Condensation* (Cambridge University Press, Cambridge, 1995), p. 15
43. N.D. Mermin, H. Wagner, Absence of ferromagnetism or antiferromagnetism in one- or 2-dimensional isotropic Heisenberg models. Phys. Rev. Lett. **17**, 1133 (1966)
44. V.L. Berezinskii, Destruction of long-range order in one-dimensional and two-dimensional systems possessing a continuous symmetry group ii. Sov. Phys. JETP **34**, 610 (1972)
45. J.M. Kosterlitz, D.J. Thouless, Ordering, metastability and phase-transitions in 2 dimensional systems. J. Phys. C **6**, 1181 (1973)
46. Z. Hadzibabic, P. Kruger, M. Cheneau, B. Battelier, J. Dalibard, Berezinskii-kosterlitz-thouless crossover in a trapped atomic gas. Nature **441**, 1118–1121 (2006)
47. G. Roumpos, M.D. Fraser, A. Löfler, S. Höfling, A. Forchel, Y. Yamamoto, Single vortex-antivortex pair in an exciton polariton condensate. Nat. Phys. **7**, 129 (2011)
48. Z. Hadzibabic, J. Dalibard, Two-dimensional bose-fluids: an atmic physics perspective. Rivista de Nuovo Cimento **34**, 389 (2011)
49. G. Roumpos, M. Lohse, W.H. Nitsche, J. Keeling, M.H. Szymanska, P.B. Littlewood, A. Löfler, L. Worschech, A. Forchel, Y. Yamamoto, Power-law decay of the spatial correlation function in exciton-polariton condensates. Proc. Nat. Aca. Sci. **109**, 6467 (2012)
50. W.H. Nitsche, N.Y. Kim, G. Roumpos, C. Schmeiden, M. Kama, S. Hoerling, A. Forchel, Y. Yamamoto, Algebraic order at the Berezinskii-Kosterlitz-Thouless transition in an exciton-polariton gas. Phys. Rev. **B90**, 205430 (2014)
51. H.J. Metcalf, P. van der Straten, *Laser Cooling and Trapping* (Springer, 1999)
52. R. Grimm, M. Weidemüller, Y.B. Ovchinikov, Optical dipole traps for neutral atoms. Adv. At. Mol. Opt. Phys. **42**, 95 (2000)
53. C. Pethick, H. Smith, *Bose-Einstein Condensation in Dilute Gases* (Cambridge University Press, Cambridge/New York, 2002)
54. F. Tassone, Y. Yamamoto, Exciton-exciton scattering dynamics in a semiconductor microcavity and stimulated scattering into polaritons. Phys. Rev. B **59**, 10830–10842 (1999)
55. C.W. Lai, N.Y. Kim, S. Utsunomiya, G. Roumpos, H. Deng, M.D. Fraser, T. Bynes, P. Recher, N. Kumada, T. Fijisawa, Y. Yamamoto, Coherent zero-state and π-state in an exciton-polariton condensate array. Nature **450**, 529–533 (2007)
56. G. Nardin, Y. Leger, B. Pietka, F. Morier-Genoud, B. Deveaud-Pledran, Phase-resolved imaging of confined exciton-polariton wave functions in elliptical traps. Phys. Rev. B **82**, 045304 (2010)
57. D. Bajoni, P. Senellart, E. Wertz, I. Sagnes, A. Miard, A. Lemaître, J. Bloch, Polariton laser using single micropillar gaas-gaalas semiconductor cavities. Phys. Rev. Lett. **100**, 047401 (2008)
58. G. Tosi, G. Christmann, N.G. Berloff, P. Tsotsis, T. Gao, Z. Hatzopoulos, P.G. Savvidis, J.J. Baumberg. Geometrically locked vortex lattices in semiconductor quantum fluids. Nat. Commun. **3**, 1243 (2012)
59. H. Deng, G. Weihs, G. Snoke, J. Bloch, Y. Yamamoto, Polariton lasing vs. photon lasing in a semiconductor microcavity. Proc. Natl. Acad. Sci. **100**, 15318–15323 (2003)
60. S. Christopoulos, G. Baldassarri Höger von Högersthal, A.J.D. Grundy, P.G. Lagoudakis, A.V. Kavokin, J.J. Baumberg, G. Christmann, R. Butté, E. Feltin, J.-F. Carlin, N. Grandjean, Room-temperature polariton lasing in semiconductor microcavities. Phys. Rev. Lett. **98**, 126405 (2007)
61. T. Guillet, M. Mexis, J. Levrat, G. Rossbach, C. Brimont, T. Bretagnon, B. Gil, R. Butte, N. Grandjean, L. Orosz, F. Reveret, J. Leymarie, J. Zuniga-Perez, M. Leroux, F. Semond, S. Bouchoule, Polariton lasing in a hybrid bulk zno microcavity. Appl. Phys. Lett. **99**, 161104 (2011)
62. S. Kena-Cohen, S.R. Forrest, Room-temperature polariton lasing in an organic single-crystal microcavity. Nat. Photonics **4**, 371 (2010)
63. T. Köhler, K. Goral, P.S. Julienne, Production of cold molecules via magnetically tunable Feshbach resonances. Rev. Mod. Phys. **78**, 1311 (2006)

64. C. Chin, R. Grimm, P.S. Julienne, E. Tiesinga, Feshbach resonances in ultracold gases. Rev. Mod. Phys. **82**, 1225–1286 (2010)
65. Y. Yakahashi, Chapter 14 in this book
66. E.A. Donley, N.R. Clausen, S.L. Cornish, J.L. Roberts, E.A. Cornell, C.E. Wieman, Dynamics of collapsing and exploding Bose-Einstein condensates. Nature **412**, 295–299 (2001)
67. C. Regal, M Greiner, D.S. Jin, Observation of resonance condensation of fermionic atom pairs. Phys. Rev. Lett. **92**, 040403 (2004)
68. M. Inguscio, W. Ketterle, C. Salomon, Ultracold fermi gases. In *International School of Physics, Enrico Fermi, Course CLXIV* (IOS, Amsterdam, 2006)
69. D. Jaksch, C. Bruder, J.I. Cirac, C.W. Gardiner, P. Zoller, Cold bosonic atoms in optical lattices. Phys. Rev. Lett. **81**, 3108–3111 (1998)
70. I. Bloch, J. Dalibard, W. Zwerger, Many-body physics with ultracold gases. Rev. Mod. Phys. **80**, 885–964 (2008)
71. T. Byrnes, P. Recher, Y. Yamamoto, Mott transitions of exciton polaritons and indirect excitons in a periodic potential. Phys. Rev. B. **81**, 205312 (2010)

Chapter 14
Quantum Simulation Using Ultracold Ytterbium Atoms in an Optical Lattice

Yoshiro Takahashi

14.1 Quantum Simulation Using Ultracold Atoms in an Optical Lattice: Background

Since the development of the laser cooling technique in 1980, laser-cooled atoms have been actively used in many scientific fields. In particular, the research field of quantum degenerate gases has been developing rapidly. The physics of weakly-interacting Bose gases has been clarified since the Bose-Einstein condensation (BEC) of alkali atoms was realized in 1995. Significant progress has also been made in the physics of ultracold fermions, including realization of the Bardeen-Cooper-Schrieffer (BCS) state and crossover between the BCS state and molecular BEC.

Among the many interesting research areas that use quantum gases, the quantum simulation of quantum many-body systems described by the so-called Hubbard model using ultracold atoms in an optical lattice, which is a periodic potential for atoms, is especially interesting. Here, we use the term "quantum simulation" in the same sense that Richard Feynman first used the term to represent the simulation of one quantum many-body system using another quantum many-body system with high controllability. The quantum simulation of the Hubbard model is very important because the Hubbard model is the basis on which we explain the novel magnetism and unconventional superconductivity that is observed in condensed matter systems, and it is also difficult to solve this model numerically without any approximations. The extremely high controllability that is available for systems of ultracold atoms in optical lattices has already allowed very impressive work to have been done using alkali atoms in optical lattices, such as a superfluid-Mott insulator transition for bosons (the Bose-Hubbard model), a metal-Mott insulator

Y. Takahashi (✉)
Department of Physics, Graduate School of Science, Kyoto University, Kyoto, Japan
e-mail: yitk@scphys.kyoto-u.ac.jp

Y. Yamamoto, K. Semba (eds.), *Principles and Methods of Quantum Information Technologies*, Lecture Notes in Physics 911, DOI 10.1007/978-4-431-55756-2_14

transition for fermions (the Fermi-Hubbard model), and also the effect of fermions on the superfluidity of bosons in a Bose-Fermi mixture (the Bose-Fermi-Hubbard model).

In these situations, rather than use popular alkaline atoms, we have studied quantum degenerate gases using the two-electron atoms of ytterbium (Yb), because Yb atoms have many unique features that are advantageous in quantum simulation studies. In this chapter, we will describe the basic properties of the two-electron Yb atoms. It is noted that some of these properties are common to all two-electron atoms of alkaline earth metal atoms. Detailed information on how to generate ultracold Yb atoms and molecules can be found, for example, in Refs. [1] and [2].

14.2 Basic Properties of Two-Electron Atoms of Yb

14.2.1 Rich Variety of Isotopes

One of the unique features of Yb atoms is the existence of a rich variety of isotopes: two fermions (^{171}Yb and ^{173}Yb) and five bosons (^{168}Yb, ^{170}Yb, ^{172}Yb, ^{174}Yb, and ^{176}Yb). Because the natural abundances of these isotopes are fairly equally distributed, we can in principle create and study various interesting quantum degenerate gases using Yb atoms, such as a gas of a BEC and a Fermi degeneracy, and also quantum degenerate mixtures of Bose-Bose, Fermi-Fermi, and Bose-Fermi combinations, by simply changing the laser frequency for laser cooling by only a few GHz. To date, we have successfully created BECs of ^{168}Yb, ^{170}Yb, ^{174}Yb, and ^{176}Yb, Fermi degenerate gases of ^{171}Yb and ^{173}Yb, Bose-Bose mixtures of ^{168}Yb–^{174}Yb, and ^{174}Yb–^{176}Yb, a Fermi-Fermi mixture of ^{171}Yb–^{173}Yb, and Bose-Fermi mixtures of ^{170}Yb–^{173}Yb, ^{174}Yb–^{173}Yb, and ^{174}Yb–^{171}Yb [1, 2].

One of the important advantages of working with Yb isotope mixtures is that the gravitational sag in a trapping potential, which often introduces the problem of undesirable spatial separation in a trap for different species, is negligibly small, because the masses of the isotopes are almost the same. For the same reason, when the Yb atoms are loaded into an optical lattice, the hopping energy has almost the same value for each of the different isotopes, which significantly simplifies the experimental and theoretical conditions. This contrasts favorably with the case of alkaline atoms, in which special care is generally required when performing mixture experiments.

14.2.2 Novel Energy Structure

Another unique feature of Yb atoms is related to the novel energy structure that is associated with two valence electrons. The two valence electrons result in both

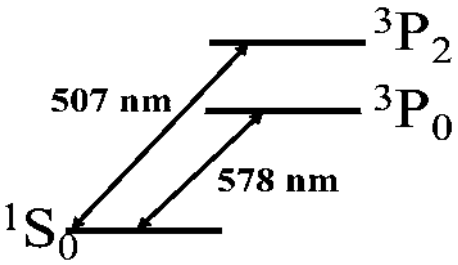

Fig. 14.1 Energy level diagram with the ground state and the metastable states, which are connected by ultra-narrow optical transitions

singlet and triplet states. In addition to the ground state $^1S_0$, there are two metastable states $^3P_0$ and $^3P_2$, as shown in Fig. 14.1. The lifetimes of these metastable states are of the order of 10 s, and thus are long enough to perform most cold atom experiments. Therefore, these metastable states can be considered as being useful orbital states in the Hubbard model, similar to the hyperfine state in the case of alkali metal atoms.

Additionally, between the ground state $^1S_0$ and these long-lived metastable states, only weakly-allowed intercombination transitions exist. The linewidths are of the order of 10 mHz, and have sufficiently high resolution for most cold atom experiments to be performed. In fact, we have successfully performed high-resolution laser spectroscopy of quantum many-body states in an optical lattice, including superfluids and Mott insulator states; the details of these measurements are described in a later section.

14.2.3 Interatomic Interaction

In Sect. 14.2.1, we mentioned that the rich variety of Yb isotopes was a major advantage. However, the existence of multiple isotopes is not important by itself, and what is truly important is the rich variety of interatomic interactions. Previously, information on the interatomic interactions of Yb atoms was scarcely known, even theoretically, which caused great difficulty when working with Yb atoms. However, a combination of our two-color photoassociation experiments and theoretical works has resulted in accurate determination of the interatomic interactions of all pairs of Yb isotopes [3].

The most important parameter that is used to describe a quantum degenerate gas is the s-wave scattering length, which characterizes an interatomic interaction at an ultracold temperature. Figure 14.2 shows the scattering lengths obtained. From these values, we can see that the scattering length actually has a variety of values, ranging from a large negative value, which represents a strong attractive interaction, to a large positive value, which represents a strong repulsive interaction, along with values that are almost zero, which represents almost no interaction. The scattering length value obeys the mass-scaling law, and the isotope-related variation

Fig. 14.2 Scattering lengths of Yb isotopes

of the scattering length comes solely from the reduced mass. Therefore, using the system of Yb atoms, we can enjoy the interesting possibility of *isotopic tuning* of the scattering length, in which a specific scattering length value can be chosen by selecting the appropriate Yb isotope. This isotope tuning concept was used in the experiments with Bose-Fermi mixtures in an optical lattice, which are described in detail in a later section.

14.2.4 SU(N) Symmetry

Among the seven stable Yb isotopes, the ^{173}Yb isotope is especially unique. This isotope has a nuclear spin of 5/2, and thus the interatomic interaction is independent of the spin. This system is known to have a high spin symmetry of SU(6) [4]. Here we can define nuclear spin permutation operators that satisfy SU(6) algebra and that are commutable with the Hamiltonian of the system. This property implies that the spin population should be conserved, even in the presence of interatomic collisions. Experimentally, we have confirmed that the spin population is actually conserved in a harmonic trap [5].

Notably, strontium (Sr), which is an alkali earth metal atom, also has a fermionic isotope of ^{87}Sr with a nuclear spin of 9/2, and offers another example of the high spin symmetry of SU(10).

Before the cold atom realization, the theoretical aspects of the physics of SU(N) with N of more than two had already been investigated several times in the literature, basically from purely theoretical interest, and various novel quantum magnetic states have been predicted. However, it is very difficult to realize an ideal SU(N) system in physical systems other than the cold alkali earth metal-like atom system.

14.3 Yb Atoms in an Optical Lattice

Using these novel possibilities, we have conducted several works using Yb atoms in an optical lattice [1, 6]. In the following sub-sections, we discuss the details of some of these experiments.

14.3.1 Strongly Interacting Bose-Fermi Mixtures in an Optical Lattice

Because of the rich variety of available isotopes, we prepare and study two different types of Bose-Fermi mixture [1, 2]. The first is an attractively interacting pair of ^{170}Yb–^{173}Yb, and the other is a repulsively interacting pair of ^{174}Yb–^{173}Yb. After creation of the quantum degenerate mixture in an optical trap with sympathetic evaporative cooling, we adiabatically load the mixture into a 3D optical lattice. When the optical lattice depth is sufficient, the boson system superfluidity is lost, and both the bosons and the fermions enter the Mott insulating state [7]. Note that the relative strength of the onsite interactions is given as $U_{FF} > |U_{BF}| > U_{BB}$ for both mixtures. The temperature is higher than the hopping energy, but is lower than these onsite interactions, and thus the bosons and the fermions enter the Mott insulating regime.

14.3.1.1 Photoassociation Method for Probing of Pair Occupancies

To investigate the behavior of these atoms, we use the photoassociation technique. If there are two atoms in the same optical lattice site, then irradiation using the resonant photoassociation beam results in the creation of excited state molecules, which eventually escape from the optical lattice. Thus, the loss associated with photoassociation is the signature of two atoms in the same optical lattice site, or pair occupancy.

In general, we can consider many possible pair occupancies in the optical lattice for this system, including boson-boson (boson double occupancy), fermion-fermion (fermion double occupancy), and boson-fermion pair occupancies. Because we can already find the corresponding photoassociation resonances using different laser frequencies, we can thus selectively measure each pair occupancy using this technique.

As an illustrative example of the strong interaction property of this system, which can be revealed by photoassociation measurements, we demonstrate its novel behavior in Fig. 14.3. When we prepare a pure sample of ^{170}Yb bosons in a sufficiently deep optical lattice, the system enters the Mott insulating state with one boson in each lattice site, in which we do not observe bosonic double occupancy.

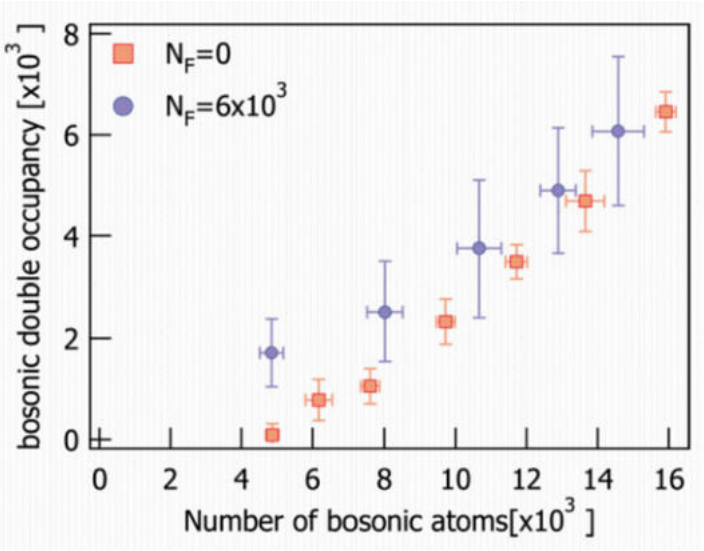

Fig. 14.3 Bosonic double occupancy for pure bosons (*squares*) and bosons with fermions (*circles*)

When we add a small fraction of ^{173}Yb fermions, which interact attractively with ^{170}Yb bosons, to this bosonic Mott insulator, then the admixture induces a dramatic increase in bosonic double occupancy, which indicates the dramatic change in the system.

14.3.1.2 Formation of Novel Quantum States

After changing the relative filling of the fermions, we perform systematic measurements of the double occupancies of both bosons and fermions, as well as the boson and fermion pair occupancies for both attractively and repulsively interacting Bose-Fermi mixtures.

From the results of these experiments and theoretical calculations based on the Bose-Fermi-Hubbard model, we confirm that various interesting quantum states are created in these strongly interacting Bose-Fermi mixtures. For example, in an attractively interacting Bose-Fermi mixture, various combinations of composite particles such as BF, BBF, BBFF, and BFF are created in an optical lattice, depending on the relative filling of the fermions, where B represents the boson (^{170}Yb) and F represents the fermion (^{173}Yb). In contrast, in the repulsively interacting Bose-Fermi mixture, a phase separation is formed between the bosons and the fermions where the doubly-occupied bosonic Mott insulator around the center of the trap is surrounded by a spherical shell of fermions with a relatively high fermion filling level. In the relatively low filling case, a novel mixed Mott insulator

system of bosons and fermions is formed. In this state, neither the bosons nor the fermions alone form a Mott insulator state, but the bosons and fermions together can form a Mott insulator state with unit filling, or one particle in each site. This can be also regarded as a system of composite particles of fermions and holes of bosons in the vacuum of the bosonic Mott insulator with unit filling, and has triggered further theoretical studies.

14.3.2 SU(6) Mott Insulator and Enhanced Atomic Pomeranchuk Cooling

14.3.2.1 Optical Stern-Gerlach Spin Separation

As described in the previous section, the fermionic isotope of ^{173}Yb has a novel high spin symmetry of SU(6). We have successfully created a deeply Fermi-degenerate gas of ^{173}Yb with temperature T that is approximately 14 % of the Fermi temperature T_F for each spin component, which was confirmed by time-of-flight measurements [4]. It is quite important to measure each spin component separately to explore the behavior of this system with its high SU(6) spin symmetry. However, it is also true that the conventional method of the Stern-Gerlach spin separation technique, which uses a magnetic field gradient with a typical value of several 10^{-1} T/m, is not applicable to ^{173}Yb, because the origin of the spin degrees of freedom is a nuclear spin, which has a magnetic moment that is about a 1000 times smaller than that of an electron spin, and therefore we need a magnetic field gradient that is a 1000 times greater. For this purpose, we recently developed a powerful optical Stern-Gerlach spin separation technique using off-resonant circularly-polarized light that produces a nuclear spin-dependent light shift [4]. Using this technique, we successfully performed separate imaging of each of the nuclear spin components, and can obtain accurate information on the nuclear spin population of an atomic sample, as shown in Fig. 14.4.

14.3.2.2 Formation of the SU(6) Mott Insulator

By adiabatically loading a deeply Fermi-degenerate gas of ^{173}Yb with spin components into an optical lattice, we successfully created a strongly correlated system of a Mott insulator state with SU(6) symmetry [5]. To investigate the behavior of the atoms in this optical lattice, we performed several measurements.

The first was the measurement of the number of double occupancies as a function of the characteristic density. One important parameter used to characterize the Mott insulator is the incompressibility of the system. We find that the system that we created actually shows suppression of double occupancies, even with increased characteristic density, which is the signature of incompressibility.

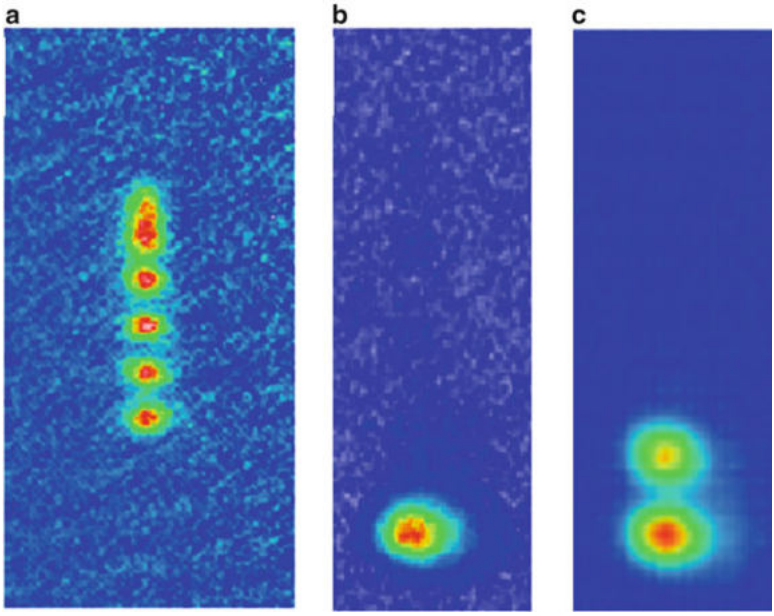

Fig. 14.4 Optical Stern-Gerlach technique for separate imaging of spin components, which clearly shows the existence of (**a**) six, (**b**) one, and (**c**) two spin components

The second was the measurement of the Mott gap. By modulating the optical lattice depth at a specific frequency, we can produce a doublon, which is detected as a loss due to photoassociation. The spectrum obtained, i.e., the number of doublons created as a function of the modulation frequency, shows a region of no doublon creation, which is the signature of the Mott gap.

The third was the doublon production rate measurement, which provides a sensitive probe of the temperature of the atoms in an optical lattice. In this measurement, we also modulate the optical lattice depth slightly at a specific frequency and measure the number of doublons produced; however, what is of interest is not the number of doublons produced but the production rate, which is proportional to the nearest-neighbor correlator of the atoms in the optical lattice. This can be understood as follows. At low lattice temperatures, high-density atoms are concentrated around the center of the trap with almost no holes, and thus each atom can easily find neighbors to produce doublons, which results in a high doublon production rate. In contrast, at high temperatures, the atom cloud expands in the trap, and the resulting atomic density is low, with many holes and doublons; it is thus more difficult for each atom to find neighbors and produce doublons, which results in a low doublon production rate. Using the highest production rate obtained for the lowest initial temperature in a harmonic trap before loading into the optical lattice, we can reproduce the Mott plateau in the atom density distribution using numerical calculations based on high-temperature second-order perturbation theory.

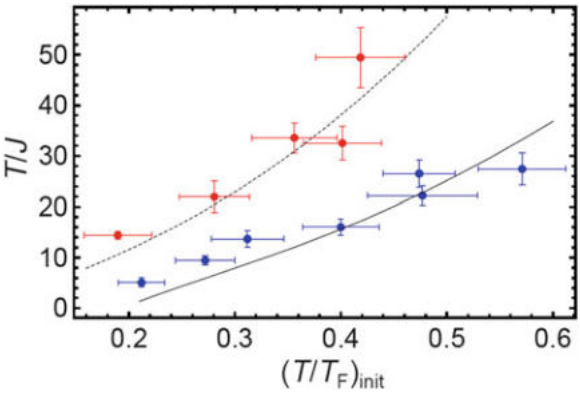

Fig. 14.5 Enhanced Pomeranchuk cooling, which shows a more powerful cooling effect for a larger spin system

We also find that the lowest entropy for a single site almost reaches a value of k_B log(6) (where k_B is the Boltzmann constant), which is the value expected for an uncorrelated spin, and this indicates that this temperature regime brings us close to observation of the onset of the quantum magnetism of the SU(6) system.

14.3.2.3 Enhanced Pomeranchuk Cooling for an Atomic Gas

With the adiabatic loading of the SU(6) fermionic atoms into an optical lattice, we find an interesting effect that is associated with the spin degrees of freedom [5]. We compare the temperature of the SU(6) atoms in the optical lattice with that of an SU(2) atom, which was created by an optical pumping technique and was confirmed by the optical Stern-Gerlach technique mentioned earlier.

Lower temperatures are obtained for the SU(6) system than for SU(2) when starting with the same initial entropy in a harmonic trap, as shown in Fig. 14.5. This effect can be explained as the atomic analogue of Pomeranchuk cooling, which is known as an important cooling method for liquid ^{3}He. In Pomeranchuk cooling of ^{3}He, the initial state, which is a spin-depolarized and quantum degenerate liquid state of ^{3}He, is adiabatically compressed and, as a final state, solid ^{3}He, in which the spin is depolarized with atom localization, is created. Because the atoms are localized in the solid ^{3}He, the spin degrees of freedom of solid ^{3}He become free, carrying entropy of k_B log(2). During adiabatic compression, the entropy flows from the motional degrees of freedom into those of the spin, which results in cooling of the system. In this situation, the temperature is not actually determined by the spin, but by the motional degrees of freedom.

In our atomic system, the initial state is a spin-depolarized and quantum degenerate gas of ^{173}Yb with six spin components in a harmonic trap, and the final state is a spin-depolarized atomic Mott insulator state, in which each atom is localized with full spin degrees of freedom. The liquid and solid ^{3}He in the original Pomeranchuk cooling concept therefore correspond to a Fermi degenerate gas in a harmonic trap and an atomic Mott insulator, respectively.

14.3.3 High-Resolution Laser Spectroscopy

14.3.3.1 Spectroscopy for the Mott Insulating State

The ultranarrow optical transition of the Yb atoms is used to provide a high-resolution probe of the behavior of these atoms [8, 9]. An illustrative example of such high-resolution laser spectroscopy in an optical lattice is the occupancy-resolving spectroscopy of a Mott insulating state of ^{174}Yb atoms [10, 11]. Under our experimental conditions for the harmonic trap and the atom numbers, there are many sites with various occupancies that range from single to triple. Because the on-site interaction is different for different numbers of atom occupancies, we can successfully resolve the resonances that originate from the different occupancies with typical frequency separations of several tens of kHz. It is noted that only single atoms are excited, even in multiply-occupied sites with double and triple occupancies, because of the collision blockade, in which excitation of the second atom becomes off-resonant with respect to that of the first atom because of a collision frequency shift.

Additionally, we can separately induce Rabi oscillation for different occupancies. We clearly observed that the Rabi frequency is enhanced for higher occupancies because of bosonic enhancement.

14.3.3.2 Spectroscopy for the Superfluid-Mott Insulator Transition

Both the Mott insulating state and the transition from a superfluid to the Mott insulating state can be investigated with this high-resolution spectroscopy method. Previously, high-resolution microwave spectroscopy was applied only to a Mott insulating state or a Bose condensate, and no systematic study across the two quantum states has been reported. At a shallow lattice depth, the spectrum shows a broad peak, reflecting the phase coherence of the superfluidity. In contrast, at deeper lattice depths, the spectrum shows multiple narrow peaks, reflecting the existence of multiple number states, as described in the previous sub-section. In the intermediate regime, we observe the co-existence of both features. Because this system is inhomogeneous, it is natural for several quantum states to co-exist in the trap.

14.3.4 Yb-Li Atomic Mixture

14.3.4.1 Controlled Impurity System

We studied a quantum degenerate mixture of Yb atoms and fermionic isotopes of lithium (^{6}Li) atoms in an optical lattice. One of the most important properties of this mixture is its large mass ratio of approximately 29. Because Yb is well localized

in the optical lattice, it can be considered to be a localized impurity. In contrast, ^{6}Li is highly delocalized in the optical lattice, and can be considered to be an itinerant carrier. If we consider the example of an optical lattice with a wavelength of 1064 nm, the effective mass ratio exceeds 10^3 at a lattice depth of 20 recoil energy units of the optical lattice potential. Therefore, this offers an ideal controlled impurity system for a Fermi system.

Additionally, as explained in the previous section, the internal states of Yb atoms in an optical lattice can be precisely controlled using a resonant laser beam, which offers great possibilities for use of the dynamical aspects of the impurity response. Therefore, using this system, we can study the nonequilibrium behavior of the Fermi sea, which is known as an Anderson orthogonality catastrophe problem. In addition, if we can prepare a sufficiently deep optical lattice for the ^{6}Li atoms such that the tight-binding treatment with the Hubbard model is valid, we can perform a quantum simulation of the Anderson Hubbard model using random potentials offered by the localized impurities of the Yb atoms.

14.3.4.2 Quantum Degenerate Mixture of Yb and Li in an Optical Lattice

In our experiments, we successfully created a quantum degenerate mixture of ^{174}Yb atoms and ^{6}Li atoms in a harmonic trap using the sympathetic evaporative cooling technique [12, 13], and then loaded this mixture into an optical lattice with a wavelength of 1064 nm [14].

We have observed matter-wave interference of ^{174}Yb atoms that is suddenly released from the optical lattice, as shown in Fig. 14.6. The coherence properties were compared for the cases of ^{174}Yb atoms with and without the ^{6}Li atoms, and no significant differences were found. Thermalization measurements between the ^{174}Yb and ^{6}Li atoms in an optical trap showed minimal interaction between the ground states of the ^{174}Yb atoms and the ^{6}Li atoms, which could be one reason why only small differences were observed. Spatial separation due to gravitational sag would also make a contribution. It is possible to compensate for this sag, e.g., by irradiation with an inhomogeneous optical dipole-force beam at 532 nm, which produces an attractive force for Yb and a repulsive force for Li.

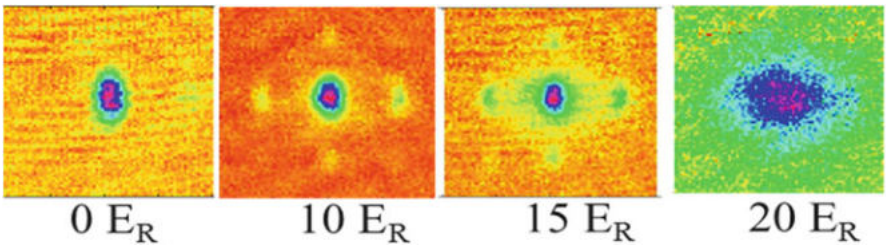

Fig. 14.6 Matter-wave interference pattern of ^{174}Yb atoms in an optical lattice with a ^{6}Li Fermi sea

We have also performed high-resolution laser spectroscopy of Yb atoms using the ultranarrow $^1S_0$–$^3P_2$ transition for both cases, i.e., with and without the ^{6}Li Fermi sea [14]. While we have observed the resonant peak of the spectrum, the observed spectrum does not show any significant difference between the two cases, and can be explained by neglecting the Yb-Li interaction.

14.3.4.3 Molecules with Spin Degrees of Freedom

This atomic mixture can provide a good starting point to produce an interesting type of molecule with electron-spin degrees of freedom in the electronic ground state [12]. This is in favorable contrast with the case of the molecules produced from the two alkali metal atoms. Using these molecules with their spin degrees of freedom loaded in an optical lattice, we can then perform a quantum simulation of the lattice spin model.

14.4 Realization of Nonstandard Optical Lattices

All experiments that were reported in the previous parts of this section were conducted using the standard cubic optical lattice. Using several lasers, we can create various nonstandard optical lattices, including triangular, honeycomb, and kagome lattices, which have been successfully demonstrated for alkali metal atoms.

14.4.1 Superlattice

By combining an optical lattice with a laser wavelength of 532 nm and another lattice with a wavelength of 1064 nm, we can successfully create two-dimensional optical superlattices for Yb atoms. By appropriate detuning of the relative laser frequencies, we can control the phases of the superlattice. The matter-wave interference pattern of a Bose condensate released from the superlattice acts as a good measure of the superlattice pattern that has been realized.

14.4.2 Lieb Lattice

In particular, by additional combination of the optical lattice produced by the interference of two laser beams with wavelengths of 532 nm, we have successfully realized an optical Lieb lattice, in which there are three sites per unit cell, as shown in Fig. 14.7. The Lieb lattice is unique in that it has a flat band and a Dirac cone in

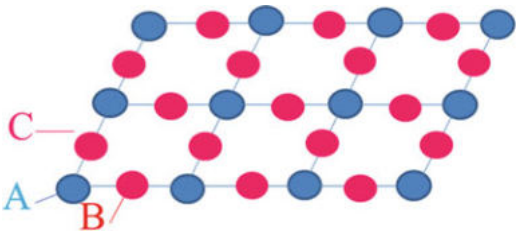

Fig. 14.7 Optical Lieb Lattice, consisting of three sites, *A*, *B*, and *C*, in a unit cell

the band structure, and it is thus especially important to explore the physics of the flat-band ferromagnetism. The Lieb lattice configuration is basically the same as that of the CuO_2 two-dimensional plane of high-T_c cuprate superconductors. Therefore, we can perform a good quantum simulation of the d–p model of high-T_c cuprates.

Successful formation of the Lieb lattice is confirmed by the characteristic matter-wave interference pattern. Successful loading of the ^{173}Yb fermions is also confirmed by measuring the band populations using an adiabatic band-mapping technique.

14.5 Development of Methods for Manipulation of Yb Interatomic Interaction

While the proposed system of an optical lattice of Yb atoms can provide unique possibilities for quantum simulation of the Hubbard model, there is one important missing ingredient: independent control of the on-site interactions. In the alkali metal atoms case, this is easily done using a magnetic Feshbach resonance between the hyperfine levels in the ground state. Unfortunately, in the case of the Yb atoms, there are no hyperfine states in the ground state $^1S_0$, and therefore we cannot expect a magnetic Feshbach resonance.

14.5.1 Optical Feshbach Resonance

However, we can produce an optical Feshbach resonance, in which a laser beam with a photoassociation resonance frequency enables us to couple the ground scattering states of two atoms to a molecular bound state in an electronic excited state. In this optical Feshbach resonance, we can tune the scattering length by changing the laser frequency, rather than the magnetic field in the magnetic Feshbach resonance case. The coupling strength can be varied by varying the laser intensity. In particular, the use of a narrow optical line, which is characteristic of two-electron atoms, provides the advantage of suppressed atom loss.

To date, we have demonstrated an efficient optical Feshbach resonance technique for thermal gases using the $^1S_0$–$^3P_1$ narrow optical transition with a $^3P_1$ lifetime of approximately 875 ns [15]. This technique has been successfully applied to a Bose condensate [16]. The novel advantages of the optical Feshbach resonance method of sub-micron spatial modulation ability and high-speed modulation of the interatomic interaction have been successfully demonstrated using a pulsed lattice diffraction method. More recently, we have extended this technique to control the p-wave interatomic interaction of the ultracold ^{171}Yb fermionic isotope [17].

We also have recently observed a photoassociation resonance associated with the ultranarrow $^1S_0$–$^3P_2$ transition, which will provide a powerful optical Feshbach resonance effect with low losses because of its very long radiative lifetime of more than 10 s.

14.5.2 Magnetic Feshbach Resonance

While no magnetic Feshbach resonance exists in the ground state of the Yb atoms, the existence of long-lived metastable states offers another interesting possibility for magnetic Feshbach resonance between the ground $^1S_0$ state and the metastable $^3P_2$ states. In fact, we have successfully observed magnetic Feshbach resonances for ^{170}Yb and ^{174}Yb atoms under low magnetic fields, which were revealed by high-resolution laser spectroscopy of these atoms in an optical lattice [11].

In addition, we have recently observed magnetic Feshbach resonances for the ^{171}Yb and ^{173}Yb fermionic isotopes by atom loss spectroscopy in a harmonic trap and by high-resolution laser spectroscopy of these atoms in an optical lattice. These magnetic Feshbach resonances for fermionic isotopes will be useful for exploration of the novel superfluidity of Cooper pairs of atoms with different electronic orbitals. Another interesting possibility is the creation of topological superfluids by combination with a spin-orbit interaction [18, 19].

14.6 Conclusion

In this chapter, we describe several important results related to quantum simulations of the Hubbard model using ultracold Yb atoms in an optical lattice. We describe in detail the formation of strongly interacting Bose-Fermi mixtures and a novel SU(N) Mott insulator, a high-resolution laser spectroscopic method for the superfluid-Mott insulator transition, and a quantum simulator for the impurity system with a Yb-Li atomic mixture.

Additionally, recent work on the realization of a nonstandard optical lattice and the development of methods to manipulate Yb interatomic interactions are also described in detail; these methods would provide a basis for further exploration of strongly-correlated quantum many-body states.

It is also shown that the cold Yb atoms are useful for the studies of spin-squeezing and quantum feedback that have been described in the literature [20–22]. By working with the ultracold atoms in an optical lattice, we could also enjoy the advantages of this system.

Acknowledgement The author would like to thank all the members of Quantum Optics group of Kyoto University for their great contributions in performing the experiments described in this paper. Additionally, the author would like to thank M. Yamashita and K. Inaba for their collaboration in the theoretical analysis of atoms in an optical lattice.

References

1. S. Sugawa, Y. Takasu, K. Enomoto, Y. Takahashi, Chapter 1 "Ultracold ytterbium: Generation, many-body physics, and molecules", in *Annual Review of Cold Atoms and Molecules: Volume 1*, ed. by K.W. Madison, Y. Wang, R. Ana Maria, K. Bongs (World Scientific, Singapore, 2013)
2. Y. Takasu, Y. Takahashi, Quantum degenerate gases of ytterbium atoms. J. Phys. Soc. Jpn. **78**, 012001-1-11 (2009)
3. M. Kitagawa, K. Enomoto, K. Kasa, Y. Takahashi, R. Ciurylo, P. Naidon, P.S. Julienne, Two-color photoassociation spectroscopy of ytterbium atoms and the precise determinations of s-wave scattering lengths. Phys. Rev. A **77**, 012719-1-8 (2008)
4. S. Taie, Y. Takasu, S. Sugawa, R. Yamazaki, T. Tsujimoto, R. Murakami, Y. Takahashi, Realization of a SU(2) x SU(6) system of fermions in a cold atomic gas. Phys. Rev. Lett. **105**, 190401 (2010)
5. S. Taie, S. Sugawa, R. Yamazaki, Y. Takahashi, An SU(6) Mott insulator of an atomic Fermi gas realized by large-spin Pomeranchuk cooling. Nat. Phys. **8**, 2430 (2012)
6. T. Fukuhara, S. Sugawa, M. Sugimoto, S. Taie, Y. Takahashi, Mott insulator of ultracold alkaline-earth-metal-like atoms. Phys. Rev. A **79**, 041604 (2009)
7. S. Sugawa, K. Inaba, S. Taie, R. Yamazaki, M. Yamashita, Y. Takahashi, Interaction and filling induced quantum phases of dual Mott insulators of bosons and fermions. Nat. Phys. **7**, 2028 (2011)
8. A. Yamaguchi, S. Uetake, S. Kato, H. Ito, Y. Takahashi, High-resolution laser spectroscopy of a Bose-Einstein condensate using the ultranarrow magnetic quadrupole transition. New J. Phys. **12**, 1367–2630 (2010)
9. M. Yamashita, S. Kato, A. Yamaguchi, S. Sugawa, T. Fukuhara, S. Uetake, Y. Takahashi, Strongly interacting array of Bose-Einstein condensates trapped in a one-dimensional optical lattice. Phys. Rev. A **87**, 041604-1-4 (2013)
10. S. Kato, R. Yamazaki, K. Shibata, R. Yamamoto, H. Yamada, Y. Takahashi, Observation of long-lived van der Waals molecules in an optical lattice. Phys. Rev. A **86**, 043411-1-4 (2012)
11. S. Kato, S. Sugawa, K. Shibata, R. Yamamoto, Y. Takahashi, Control of resonant interaction between electronic ground and excited states. Phys. Rev. Lett. **110**, 173201-1-4 (2013)
12. M. Okano, H. Hara, M. Muramatsu, K. Doi, S. Uetake, Y. Takasu, Y. Takahashi, Simultaneous magneto-optical trapping of lithium and ytterbium atoms towards production of ultracold polar molecules. Appl. Phys. B **98**, 691–696 (2009)
13. H. Hara, Y. Takasu, Y. Yamaoka, J.M. Doyle, Y. Takahashi, Quantum degenerate mixtures of alkali and alkali-earth-like atoms. Phys. Rev. Lett. **106**, 205304-1-4 (2011)
14. H. Hara, H. Konishi, S. Nakajima, Y. Takasu, Y. Takahashi, A three-dimensional optical lattice of ytterbium and lithium atomic gas mixture. J. Phys. Soc. Jpn. **83**, 014003 (2014)
15. K. Enomoto, K. Kasa, M. Kitagawa, Y. Takahashi, Optical feshbach resonance using the intercombination transition. Phys. Rev. Lett. **101**, 203201-1-4 (2008)

16. R. Yamazaki, S. Taie, S. Sugawa, Y. Takahashi, Submicron spatial modulation of an interatomic interaction in a Bose-Einstein condensate. Phys. Rev. Lett. **105**, 050405-1-4 (2010)
17. R. Yamazaki, S. Taie, S. Sugawa, K. Enomoto, Y. Takahashi, Observation of a p-wave optical feshbach resonance. Phys. Rev. A **87**, 010704-1-4 (2013)
18. M. Sato, Y. Takahashi, S. Fujimoto, Non-Abelian topological order in s-wave superfluids of ultracold fermionic atoms. Phys. Rev. Lett. **103**, 020401 (2009)
19. M. Sato, Y. Takahashi, S. Fujimoto, Non-Abelian topological orders and Majorana fermions in spin-singlet superconductors. Phys. Rev. B **82**, 134521 (2010)
20. T. Takano, M. Fuyama, R. Namiki, Y. Takahashi, Spin squeezing of a cold atomic ensemble with the nuclear spin of one-half. Phys. Rev. Lett. **102**, 033601-1-4 (2009)
21. T. Takano, S. Tanaka, R. Namiki, Y. Takahashi, Manipulation of nonclassical atomic spin states. Phys. Rev. Lett. **104**, 013602-1-4 (2010)
22. R. Inoue, S. Tanaka, R. Namiki, T. Sagawa, Y. Takahashi, Unconditional quantum-noise suppression via measurement-based quantum feedback. Phys. Rev. Lett. **110**, 163602-1-4 (2013)

Chapter 15
Quantum Simulation with Trapped Ions—Experimental Realization of the Jaynes-Cummings-Hubbard Model—

Shinji Urabe, Kenji Toyoda, and Atsushi Noguchi

15.1 Introduction

One purpose of quantum simulation is to elucidate the fundamental process of a strong correlated many-body system in solid state physics and to predict new phenomena by replacing it with a system that can be manipulated easily and has well-known fundamental process in quantum optics and atomic physics [1]. The quantum simulation of the Ising model with trapped ions [2–4] and of the Bose-Hubbard (BH) model with ultra cold atoms in an optical lattice [5] are successful examples. Phase transitions have been demonstrated from the paramagnetic to ferromagnetic order in the former experiments and from Mott-insulator into superfluid states in the latter. As a new model for a strongly correlated many-body system, an array of optical cavities containing two-level atoms or multilevel atoms (QED-cavity arrays) has been proposed [6, 7]. Since neighbor sites are separated by several tens of micrometers and each site can be accurately accessed by optical methods, measurements of local properties and simulations of inhomogeneous systems are possible in this system. Thus, it is expected to complement the optical lattice system, and many theoretical analyses have already been performed [8–14]. If the cavities contain four-level atoms, the model can be mapped onto the Bose-Hubbard Hamiltonian [8]. If the cavities contain two-level atoms, the system is called the Jaynes-Cummings-Hubbard (JCH) model [9, 10]. This is a combination of two well-known systems, namely, the Jaynes-Cummings (JC) model, which

S. Urabe (✉) • K. Toyoda
Graduate School of Engineering Science, Osaka University, Toyonaka, Japan
e-mail: urabe@ee.es.osaka-u.ac.jp

A. Noguchi
Graduate School of Engineering Science, Osaka University, Toyonaka, Japan

RCAST, University of Tokyo, Bunkyo, Japan

Y. Yamamoto, K. Semba (eds.), *Principles and Methods of Quantum Information Technologies*, Lecture Notes in Physics 911, DOI 10.1007/978-4-431-55756-2_15

describes coupling a single two-level system to a bosonic mode, and the Bose Hubbard model, which describes the interaction of bosons on a lattice. In the JCH model, the anharmonicity of the energy levels of the dressed states of a JC Hamiltonian induces a photon blockade and acts as an effective on-site interaction [15, 16]. Furthermore the dressed atoms or polaritons transform into various kinds of excitations depending on externally controllable parameters. As a result, the JCH model has a richer phase structure than the BH model. Although many methods have been proposed to demonstrate the JCH model [6], including photonic band-gap structures, coupled-cavity waveguides, arrays of superconducting strip-line cavities and an ion chain in a linear trap, an experimental demonstration had not been done until recently.

A trapped-ion system is one of the most promising systems for quantum simulation since it offers high controllability and individual access [17, 18]. This system enables us to manipulate and measure internal electronic or vibrational quantum states at a single particle level [19, 20]. To demonstrate the JCH model in a linear trap, it is necessary to generate local phonons at each site in an ion chain. In an ion chain, there are phonons in axial modes that oscillate along the chain direction and phonons in radial modes that oscillate perpendicular to the chain direction. When the radial confinement is strong and its potential is much larger than the Coulomb potential, radial phonons are localized to an ion at each site and they hop between sites due to the Coulomb interaction [21]. These phonons can play a role of the photons in the cavity-array system. If an on-site phonon-phonon interaction is added to this system, it can simulate the Bose-Hubbard model [22]. However, it is not easy to generate a direct interaction of this sort in an actual experiment. By contrast, the JC interaction can be generated more easily. Irradiating ion qubits with a laser, which induces red sideband transitions, generate a JC coupling between internal states (qubit states) and phonon states, and the JCH model can be demonstrated [14].

We have recently demonstrated the JCH model experimentally using two trapped ions in a linear trap [23]. The present article describes the theoretical and experimental aspects of this demonstration. In Sect. 15.2, the local phonons in a linear trap and observation of phonon hopping are discussed, while Sect. 15.3 presents the JCH interaction, phase diagram of the JCH model and observation of quantum phase transitions.

15.2 Local Phonons in a Linear Trap and Phonon Hopping

The motion of ions in a linear Paul trap is governed by a harmonic potential due to trap electrodes and by the Coulomb interaction between ions. The Hamiltonian is given by [21, 24]

$$H_0 = \sum_{i=1}^{N} \frac{\overrightarrow{P}_i^2}{2m} + \frac{1}{2} m \sum_{i=1}^{N} \sum_{\alpha=x,y,z} \omega_\alpha^2 R_{i,\alpha}^2 + \sum_{\substack{i,j=1 \\ i>j}}^{N} \frac{e^2}{4\pi\varepsilon_0 \left| \overrightarrow{R}_i - \overrightarrow{R}_j \right|}. \tag{15.1}$$

where N is the number of ions and m is their mass. $\overrightarrow{P}_j$ and $\overrightarrow{R}_j$ are the momenta and absolute positions of ions, respectively. ω_α is the trapping frequency in each spatial direction. We assume that the ions are cooled sufficiently so that they form a crystalline structure. We choose the condition, $\omega_z \ll \omega_x, \omega_y$, so that the ion chain is along the z axis. The positions of ions are given in terms of small displacements, x_i, y_i, z_i, from the equilibrium position $(0, 0, z_i^0)$ as $R_{i,x} = x_i$, $R_{i,y} = y_i$, $R_{i,z} = z_i^0 + z_i$. z_i^0 are given by the minima of the trapping potential and the Coulomb repulsion. In the harmonic approximation, H_0 is expanded up to second order in the displacement of the ions around the equilibrium positions and divided into three independent Hamiltonians that represent independent vibration modes corresponding to each spatial direction.

The Hamiltonian that governs motion in one of the radial directions (which we take to be the x direction in this case) can be given by [24]

$$H_{x0} = \sum_{i=1}^{N} \frac{P_{i,x}^2}{2m} + \frac{1}{2} m\omega_x^2 \sum_{i=1}^{N} x_i^2 - \frac{1}{2} \sum_{\substack{i,j=1 \\ i>j}}^{N} \frac{e^2}{4\pi\varepsilon_0 \left| z_i^0 - z_j^0 \right|^3} \left(x_i - x_j\right)^2 . \tag{15.2}$$

where $P_{i,x}$ are the momenta corresponding to the displacement x_i. The second quantized form of this Hamiltonian is

$$H_{x0} = \sum_{i=1}^{N} \hbar\omega_{x,i} a_i^\dagger a_i + \sum_{\substack{i,j=1 \\ i>j}}^{N} \frac{\hbar\kappa_{i,j}}{2} \left(a_i^\dagger + a_i\right)\left(a_j^\dagger + a_j\right) . \tag{15.3}$$

$a_i^\dagger (a_i)$ are creation (annihilation) operators for local phonons in the radial direction. The effective trapping frequency $\omega_{x,i}$ contains the corrections induced by the Coulomb interaction,

$$\omega_{x,i} = \omega_x - \frac{1}{2} \sum_{j=1, j\neq i}^{N} \kappa_{i,j}, \tag{15.4}$$

where $\kappa_{i,j}$ are hopping rates expressible as follows:

$$\kappa_{i,j} = \frac{e^2}{4\pi\varepsilon_0 m\omega_x^2 \left| z_i^0 - z_j^0 \right|^3} \omega_x . \tag{15.5}$$

The characteristics of the vibrational modes are governed by the following parameters, which quantify the relative values of the Coulomb interaction and trapping potentials [21].

$$\beta_\alpha = |c_\alpha| e^2/4\pi\varepsilon_0 m\omega_\alpha^2 d_0^3 \approx \frac{\kappa_{i,j}}{\omega_\alpha}, \tag{15.6}$$

where $c_{x,y} = 1$, $c_z = -2$, and d_0 is the mean distance between ions. If $\beta_\alpha \ll 1$, the second term in Eq. (15.3) becomes a small perturbation. The phonons are close to being localized at each ion (stiff limit) and can be considered local phonons. When the ion chain is along the z axis, radial phonons in the x and y directions can easily satisfy this condition. These local phonons are used for quantum simulation experiments of the Ising model [25] and Hubbard model [22]. By contrast, if $\beta_\alpha \gtrsim 1$, phonons have a strong collective character that has the ability to mediate interactions within the whole trap region. In this limit phonons are well described as collective modes. The axial mode in the z direction usually satisfies this condition and is used as a bus bit in quantum gate experiments to communicate between ion qubits. When the stiff limit is satisfied, $\beta_x \ll 1$, the phonon non-conserving terms, $a_i^\dagger a_j^\dagger + a_i a_j$, in the second term of Eq.(15.3) can be neglected in a rotating wave approximation [24]. Since the second term of Eq.(15.3) is considered to be an excitation exchange term, phonons are mainly localized at each ion site and hop between sites at a low rate of $\kappa_{i,j}$.

The Hamiltonian of two trapped ions in the stiff limit can be written as,

$$H_{x0} = \sum_{i=1,2} \hbar \left(\omega_x - \frac{\kappa}{2}\right) a_i^\dagger a_i + \frac{\hbar\kappa}{2}\left(a_1 a_2^\dagger + a_1^\dagger a_2\right), \tag{15.7}$$

$$\text{where} \quad \kappa = \frac{e^2}{4\pi\varepsilon_0 m d_0^3 \omega_x}. \tag{15.8}$$

Phonon hopping can be explained easily by using collective modes which are eigen modes of the above Hamiltonian. We introduce the creation operators of these modes,

$$a_c^\dagger = \frac{\left(a_1^\dagger + a_2^\dagger\right)}{\sqrt{2}}, \; a_r^\dagger = \frac{\left(a_1^\dagger - a_2^\dagger\right)}{\sqrt{2}}, \tag{15.9}$$

which correspond to the center-of-mass (c.m.) mode and the rocking mode, respectively. The above Hamiltonian becomes

$$H_{x0} = \hbar\omega_x a_c^\dagger a_c + \hbar\left(\omega_x - \kappa\right) a_r^\dagger a_r. \tag{15.10}$$

The two eigenstates of the center-of-mass mode and the rocking mode for one phonon excitation are $|\phi_c\rangle = \left(|1\rangle_1|0\rangle_2 + |0\rangle_1|1\rangle_2\right)/\sqrt{2}$, $|\phi_r\rangle = \left(|1_1\rangle\,|0_2\rangle - |0_1\rangle\,|1_2\rangle\right)/\sqrt{2}$, respectively, where $|n_i\rangle$ are the Fock states of the local phonon at the i th ion and n is the phonon number. When one phonon is excited

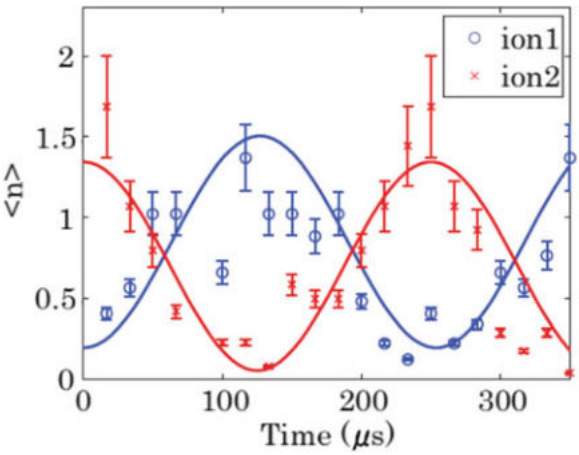

Fig. 15.1 Observed phonon hopping dynamics. The *horizontal* and *vertical axes* represent the hopping time and the mean phonon number of each ion, respectively. The trap frequency is $\omega_x = 2\pi \times 3.23$ MHz and the ion separation is 18.9 μm which correspond to $\omega_z = 2\pi \times 161$ kHz. By fitting the data the hopping rate is estimated to be $\kappa = 2\pi \times 4.0$ KHz [26]

in one of the local modes, the non-stationary state, $|0_1\rangle\,|1_2\rangle = (|\phi_c\rangle - |\phi_r\rangle)/\sqrt{2}$, evolves into the state,

$$\begin{aligned} |\psi(t)\rangle &= e^{-i\omega_x t}\,|\phi_c\rangle - e^{-i(\omega_x-\kappa)t}\,|\phi_r\rangle \\ &= e^{-i(\omega_x-\kappa/2)t}\left[-i\sin(\kappa t/2)\,|1\rangle_1|0\rangle_2 + \cos(\kappa t/2)\,|0\rangle_1|1\rangle_2\right]. \end{aligned} \tag{15.11}$$

The probability finding a phonon at site1 and site2 are $\sin^2(\kappa t/2)$ and $\cos^2(\kappa t/2)$, respectively. This means that the phonon hops at a rate of κ, moving from one site to the other. This phenomenon resembles the well-known oscillation transfer between two weakly coupled mechanical oscillators in classical mechanics.

Figure 15.1 shows hopping of a radial phonon observed experimentally [26]. Two ions are trapped in a linear trap. All six vibrational modes of the two ions are cooled to near the ground state by sideband cooling at ion distance of 6.4 μm where the Lamb-Dicke criterion is satisfied for all modes. Then the distance between ions is adiabatically increased to 18.9 μm to satisfy the stiff limit condition for local phonons. The initial phonon state of $|0\rangle_1|1\rangle_2$ is prepared by applying a blue sideband π pulse to one of the ions with a different ac-Stark-shift method for individual addressing [27]. After pumping the ion back to the ground state, a delay time with no laser interaction is inserted in order for the phonon to undergo hopping. Then a laser pulse for exciting the sideband transition is applied to the ions to estimate the mean phonon number of each ion by comparing the excitation probabilities of the red and blue sideband transitions. The internal state of the individual ions is detected with an intensified CCD camera. The horizontal and vertical axes of Fig. 15.1 represent the hopping time and the mean phonon number at each ion, respectively. The results show sinusoidal oscillations in the mean phonon number of each ion. The oscillations of ion 1 and 2 are out of phase, indicating an exchange of phonon energy between the two ions as expected from Eq. (15.11). By fitting the data with a sinusoidal function, the hopping rate is estimated to be $\kappa = 2\pi \times 4.0(2)$ kHz

which is in good agreement with the value calculated from Eq. (15.8). The offset in the residual phonon number in Fig. 15.1 is mainly due to ion heating induced, during the dynamical change in the ion distance. Details of the experiment are described in reference [26]. A similar phenomenon has been observed by using individual traps [28, 29].

15.3 Simulation of a JCH Model with Two Trapped Ions

15.3.1 JCH Model

To demonstrate the JCH model with a chain of trapped ions, we add the Jaynes-Cummings interaction to the system by using a laser [14]. Each ion in the chain has a qubit with a transition frequency ω_0. We irradiate the whole chain equally along the x-direction with a common traveling laser having as frequency ω_L. After the optical rotating-wave approximation, the Hamiltonian of the system in the Lamb-Dicke limit is given by

$$\begin{aligned} H_{x0} = &\sum_{i=1}^{N} \hbar\omega_{x,i} a_i^\dagger a_i + \sum_{\substack{i,j=1 \\ i>j}}^{N} \frac{\hbar\kappa_{i,j}}{2}\left(a_i^\dagger a_j + a_i a_j^\dagger\right) + \hbar\omega_0 \sum_{i=1}^{N} |e_i\rangle\langle e_i| \\ &+ \frac{\hbar\Omega_0}{2}\sum_{i=1}^{N}\left[\sigma_i^+\left\{1 + i\eta\left(a_i^\dagger + a_i\right)\right\} e^{-i\omega_L t} + \text{H.C.}\right]. \end{aligned} \tag{15.12}$$

$\sigma_i^+ = |e_i\rangle\langle g_i|$, $\sigma_i^- = |g_i\rangle\langle e_i|$ are spin flip operators, $|e_i\rangle, |g_i\rangle$ are the qubit state of the i-th ion, Ω_0 is the Rabi frequency, and $\eta = k_x x_0$ is the Lamb-Dicke parameter, where k_x is the x component of the laser wave vector and $x_0 = \sqrt{\hbar/2m\omega_x}$ is the spread of the ground state wave function. After transforming into the rotating frame by the unitary transformation $U = e^{-iH_{0e}t/\hbar}$, with $H_{0e} = \hbar\omega_L \sum_{i=1}^{N} |e_i\rangle\langle e_i|$, and tuning the laser frequency near the red motional sideband, we can get the following JCH Hamiltonian,

$$\begin{aligned} H_{x0} = &\sum_{i=1}^{N} \hbar\omega_{x,i} a_i^\dagger a_i + \hbar\Delta\sum_{i=1}^{N} |e_i\rangle\langle e_i| + \hbar g\sum_{i=1}^{N}\left(\sigma_i^+ a_i + \sigma_i^- a_i^\dagger\right) \\ &+ \sum_{\substack{i,j=1 \\ i>j}}^{N} \frac{\hbar\kappa_{i,j}}{2}\left(a_i^\dagger a_j + a_i a_j^\dagger\right) \end{aligned} \tag{15.13}$$

where $g = \eta\Omega_0/2$. This Hamiltonian is valid for $\kappa_{i,j}, g \ll \omega_{x,i}$, which ensures higher terms can be neglected. The first three terms in (15.13) describe the Jaynes-Cummings (JC) interaction. The first two terms are the energies of local phonons and ions, which correspond to the photons and atoms in the cavity in the coupled cavity-array model, respectively. In the above Hamiltonian, since it is represented in the rotating frame, the energy of the qubit is transformed into $\Delta = \omega_0 - \omega_L$. The third term describes the phonon-ion interaction mediated by the laser-ion interaction. The fourth term describes the non-local hopping of phonons between ions which corresponds to the hopping between cavities in the coupled cavity-array model. In the system described by the above Hamiltonian, the total number of excitations is conserved since the total excitation operator, $\widehat{N} = \sum_{i=1}^{N} \widehat{N}_i$, commutes with the Hamiltonian, where $\widehat{N}_i = a_i^\dagger a_i + |e_i><e_i|$ is the total excitation operator at each site.

In the coupled cavity array model, the JCH model can be demonstrated under the strong coupling condition that the JC coupling coefficient g is much larger than the atomic decay rate γ and the leakage rate of photons from the cavity ζ, $g \gg \gamma, \zeta$. In the trapped-ion system, this condition can be easily satisfied since $g \sim 10^4\ \mathrm{s}^{-1}$, $\gamma \sim 1\ \mathrm{s}^{-1}$, $\zeta \sim 10\ \mathrm{s}^{-1}$ under the typical experimental conditions where we use electric quadrupole transitions for qubit transitions.

15.3.2 JCH Model Using Two Trapped Ions with Two Excitations

The JCH Hamiltonian of two trapped ions is given by

$$H_{x0} = \sum_{i=1,2} \hbar\omega_x' a_i^\dagger a_i + \hbar\Delta \sum_{i=1,2} |e_i\rangle\langle e_i| + \hbar g \sum_{i=1,2} \left(\sigma_i^+ a_i + \sigma_i^- a_i^\dagger\right) + \frac{\hbar\kappa}{2}\left(a_1^\dagger a_2 + a_1 a_2^\dagger\right), \tag{15.14}$$

where $\omega_x' = \omega_x - \kappa/2$. The externally controllable parameters are the laser detuning Δ, the JC coupling coefficient g and the hopping rate κ. The hopping rate and coupling coefficient can be varied with the distance between ions and the laser amplitude, respectively. When the ground state of the above Hamiltonian is discussed, the detuning between the "atomic resonance frequency" Δ and phonon frequency $\omega_x^{'}$, $\Delta' = \Delta - \omega_x' = \left(\omega_0 - \omega_x'\right) - \omega_L$, is used as an external parameter, rather than the detuning Δ itself. Depending on these parameters, the ground state of the system changes and several quantum phases appear. For an order parameter characterizing these quantum phases, the variance of the total excitation number per site, $\Delta\widehat{N}_i^2 = \left\langle \widehat{N}_i^2 \right\rangle - \left\langle \widehat{N}_i \right\rangle^2$, is used [10]. The atomic excitation number variance, $\Delta\widehat{N}_{a,i}^2 = \left\langle \widehat{N}_{a,i}^2 \right\rangle - \left\langle \widehat{N}_{a,i} \right\rangle^2$, where $\widehat{N}_{a,i} = |e_i\rangle\langle e_i|$, is also used, as an additional order parameter [12]. The expectation value of the annihilation operator which is usually

Table 15.1 Eigen states and corresponding eigen energies of the unperturbed Hamiltonian for the condition $g \gg \kappa$

Eigen state	Eigen energy
$\left\|1_1^-\right\rangle \left\|1_2^-\right\rangle$	$2\omega_x' + \Delta' - \sqrt{\Delta'^2 + 4g}$
$\left\|2_1^-\right\rangle \left\|0_2\right\rangle, \left\|0_1\right\rangle \left\|2_2^-\right\rangle$	$2\omega_x' + \Delta'/2 - (1/2)\sqrt{\Delta'^2 + 8g}$
$\left\|1_1^+\right\rangle \left\|1_2^-\right\rangle, \left\|1_1^-\right\rangle \left\|1_2^+\right\rangle$	$2\omega_x' + \Delta'$
$\left\|2_1^+\right\rangle \left\|0_2\right\rangle, \left\|0_1\right\rangle \left\|2_2^+\right\rangle$	$2\omega_x' + \Delta'/2 + (1/2)\sqrt{\Delta'^2 + 8g}$
$\left\|1_1^+\right\rangle \left\|1_2^+\right\rangle$	$2\omega_x' + \Delta' + \sqrt{\Delta'^2 + 4g}$

used in the mean-field limit cannot be used here as the order parameter, since it is always zero for a closed system with no particle exchange with the outside.

The quantum phases that appear in a two-site and two-excitation system were analyzed extensively in reference [12]. What follows is based on reference [12]. We consider the following two extreme cases:

1. The hopping rate is much smaller than the JC coupling coefficient, $g \gg \kappa$.

In this case, the forth term describing hopping in Eq. (15.14) can be regarded as a small perturbation. We can discuss the ground state of the system on the basis of the dressed states that appear in the JC model. The eight eigen states and corresponding eigen energies of the unperturbed Hamiltonian are listed in Table 15.1. $|n_i^{\pm}\rangle$ in the Table 15.1 are dressed states defined as follows:

$$
\begin{aligned}
|0_i\rangle &= |g_i\rangle\,|0_i\rangle\,, \\
\left|n_i^-\right\rangle &= \sin(\theta_n/2)\,|e_i\rangle\,|n-1_i\rangle - \cos(\theta_n/2)\,|g_i\rangle\,|n_i\rangle\,, \\
\left|n_i^+\right\rangle &= \cos(\theta_n/2)\,|e_i\rangle\,|n-1_i\rangle + \sin(\theta_n/2)\,|g_i\rangle\,|n_i\rangle\,,
\end{aligned}
$$

where $i = 1,\ 2$ and $\tan\theta_n = 2g\sqrt{n}/\Delta$. The corresponding eigen energies are given by

$$
\begin{aligned}
E_i^0 &= 0, \\
E_i^{n\pm} &= n\omega_x' + \Delta'/2 \pm (1/2)\sqrt{\Delta'^2 + 4ng^2}.
\end{aligned}
$$

When the detuning takes on large negative values ($-\Delta'/g \gg 1$), the internal energy of each atom becomes smaller than the phonon energy, so that the excitations localize to each atom and the lowest state $\left|1_1^-\right\rangle\left|1_2^-\right\rangle$ approaches $|e_1\rangle|0_1\rangle|e_2\rangle|0_2\rangle$. This ground state is an "atomic insulator" state: $|\psi_{al}\rangle = |e_1\rangle\,|0_1\rangle\,|e_2\rangle\,|0_2\rangle$. The order parameters for this state become $\Delta\widehat{N}_i^2 = 0,\ \Delta\widehat{N}_{a,i}^2 = 0$. Near the resonance, $\Delta'/g \approx 0$, the interaction between atoms and phonons is strong. Owing to the anharmonicity of the dressed-state energy, a phonon-blockade effect occurs. Each phonon localizes at each site and couples with an atom strongly to generate a "polaritonic insulator" state. The ground state can be approximated by $\left|\psi_{pol}\right\rangle = (|e_1\rangle\,|0_1\rangle - |g_1\rangle\,|1_1\rangle)\,(|e_2\rangle\,|0_2\rangle - |g_2\rangle\,|1_2\rangle)\,/2$. This state is analogous to the Mott insulator state in the Bose-Hubbard model. The order parameters for this state

become $\Delta\widehat{N}_i^2 = 0, \quad \Delta\widehat{N}_{a,i}^2 > 0$. When the detuning takes on large positive values ($\Delta'/g \gg 1$), the phonon energy becomes smaller than that of atoms and the excitations transfer to phonons. The three eigen states $\left|1_1^-\right\rangle\left|1_2^-\right\rangle, \left|2_1^-\right\rangle|0_2\rangle, |0_1\rangle\left|2_2^-\right\rangle$ become degenerate, furthermore, owing to the hopping term, these states are coupled together to generate a nonlocal "phonon superfluid" state. In the limit $\Delta'/g \to \infty$, the ground state, which can be obtained by diagonalizing the hopping term within the above degenerate subspace, becomes

$$\left|\psi_{phSF}\right\rangle = |g_1\rangle\,|g_2\rangle\,a_r^{\dagger 2}|0\rangle_1|0\rangle_2 = |g_1\rangle\,|g_2\rangle\left[\frac{|1\rangle_1|1\rangle_2}{\sqrt{2}} - \frac{|2\rangle_1|0\rangle_2 + |0\rangle_1|0\rangle_2}{2}\right].$$

The order parameters for this state become $\Delta\widehat{N}_i^2 > 0, \quad \Delta\widehat{N}_{a,i}^2 = 0$.

2. The hopping rate is much larger than the JC coupling coefficient, $g \ll \kappa$.

In this case, the third term describing the JC interaction in Eq. (15.14) can be regarded as a small perturbation. We can discuss the ground state of the system on the basis of the direct product of collective phonon states and bare states of atoms. The eight eigen states and corresponding eigen energies of the unperturbed Hamiltonian are listed in Table 15.2. $a_c^\dagger$ and $a_r^\dagger$ in Table 15.2 are the creation operators of the c.m. mode and rocking mode, respectively, as defined in Eq. (15.9).

When the detuning is smaller than $-\kappa/2$, ($\Delta' < -\kappa/2$), the ground state can be approximated by the "atomic insulator" state $|\psi_{aI}\rangle = |e_1\rangle\,|0_1\rangle\,|e_2\rangle\,|0_2\rangle$. The order parameters for this state become $\Delta\widehat{N}_i^2 = 0, \quad \Delta\widehat{N}_{a,i}^2 = 0$.. The ground state becomes complex when $\Delta' \approx -\kappa/2$. The four unperturbed eigen states,

$$\left|\psi_{phSF}\right\rangle == |g_1\rangle\,|g_2\rangle a_r^{\dagger 2}\,|0_1\rangle\,|0_2\rangle\,, |\psi_{aI}\rangle = |e_1\rangle\,|e_2\rangle\,|0_1\rangle\,|0_2\rangle$$
$$\left|\psi'_{i1}\right\rangle = |g_1\rangle\,|e_2\rangle a_r^\dagger\,|0_1\rangle\,|0_2\rangle\,, \left|\psi'_{i2}\right\rangle = |e_1\rangle\,|g_2\rangle a_r^\dagger\,|0_1\rangle\,|0_2\rangle\,,$$

become degenerate. The ground state, which can be obtained by diagonalizing the JC interaction term within the above degenerate subspace, is given by

$$\left|\psi_{poSF}\right\rangle = \left|\psi_{phSF}\right\rangle/\sqrt{3} + |\psi_{aI}\rangle/\sqrt{6} + \left(\left|\psi'_{i1}\right\rangle + \left|\psi'_{i2}\right\rangle\right)/2$$

Table 15.2 Eigen states and corresponding eigen energies of the unperturbed Hamiltonian for the condition $g \ll \kappa$

Eigen state	Eigen energy
$\|g_1\rangle\|g_2\rangle a_r^{\dagger 2}\|0_1\rangle\|0_2\rangle$	$2\omega\prime_x - \kappa$
$\|g_1\rangle\|g_2\rangle a_c^\dagger a_r^\dagger\|0_1\rangle\|0_2\rangle$	$2\omega\,'_x$
$\|g_1\rangle\|g_2\rangle a_c^{\dagger 2}\|0_1\rangle\|0_2\rangle$	$2\omega\prime_x + \kappa$
$\|e_1\rangle\|e_2\rangle\|0_1\rangle\|0_2\rangle$	$2\omega\prime_x + 2\Delta'$
$\|e_1\rangle\|g_2\rangle a_r^\dagger\|0_1\rangle\|0_2\rangle, \|g_1\rangle\|e_2\rangle a_r^\dagger\|0_1\rangle\|0_2\rangle$	$2\omega\prime_x - \kappa/2 + \Delta'$
$\|e_1\rangle\|g_2\rangle a_c^\dagger\|0_1\rangle\|0_2\rangle, \|g_1\rangle\|e_2\rangle a_c^\dagger\|0_1\rangle\|0_2\rangle$	$2\omega\prime_x + \kappa/2 + \Delta'$

This is a "polaritonic superfluid" state where the atomic and phonon components are mixed by hopping. The order parameters for this state become $\Delta\widehat{N}_i^2 > 0$, $\Delta\widehat{N}_{a,i}^2 > 0$. When the detuning is larger than $-\kappa/2$, $(\Delta' > -\kappa/2)$, the ground state can be approximated by the "phonon superfluid" state $|\psi_{phSF}\rangle$ and the order parameters for this state become $\Delta\widehat{N}_i^2 > 0$, $\Delta\widehat{N}_{a,i}^2 = 0$.

This analysis of the ground state in the two extreme limits suggests that there exist four quantum phases, *viz*., "atomic insulator" $\left(\Delta\widehat{N}_i^2 = 0,\ \Delta\widehat{N}_{a,i}^2 = 0\right)$, "polaritonic insulator" $\left(\Delta\widehat{N}_i^2 = 0,\ \Delta\widehat{N}_{a,i}^2 > 0\right)$, "polaritonic superfluid" $\left(\Delta\widehat{N}_i^2 > 0,\ \Delta\widehat{N}_{a,i}^2 > 0\right)$ and "phonon superfluid" $\left(\Delta\widehat{N}_i^2 > 0,\ \Delta\widehat{N}_{a,i}^2 = 0\right)$. In the intermediate region between the two limits, the ground state must be calculated numerically and the order parameters $\Delta\widehat{N}_i^2$ and $\Delta\widehat{N}_{a,i}^2$ must be obtained. The order parameters, $\Delta\widehat{N}_i^2$ and $\Delta\widehat{N}_{a,i}^2$, obtained from the above analysis are shown in Fig. 15.2a, b, respectively. The horizontal and vertical axes represent Δ'/g and κ/g, respectively. The color red (blue) indicates a large (small) variance. Figure 15.2c shows the four regions of quantum phases, as estimated from Fig. 15.2a, b. There are the "polaritonic insulator" and "polaritonic superfluid" phases around the boundary between the "atomic insulator" and "phonon superfluid" phases where $\Delta' + \kappa/2 \approx 0$ is satisfied.

15.3.3 Experimental

15.3.3.1 Experimental Setup

The experimental setup is shown in Fig. 15.3a. Details are described in reference [30]. Two Ca^+ ions are used in this experiment. The linear trap is composed of four stainless blades. An rf field (frequency: 24 MHz) is applied to a diagonal pair of blades. The other diagonal pair is divided into three segments and a dc electric field is applied to the two end pairs. To lift the degeneracy between two radial frequencies, a small dc field is applied to the diagonal pair of the center dc electrodes. The distance between the ions and the surface of the electrodes is 0.6 mm. The secular frequencies are $(\omega_x, \omega_y, \omega_z)/2\pi = (2.1, 1.7, 0.17)$ MHz and the distance between ions in the axial direction is 18–20 μm, which corresponds to the hopping rate $\kappa/2\pi$ of 5–7 KHz. The relevant energy levels of the Ca^+ ions are shown in Fig. 15.3b. All vibrational modes are cooled by Doppler cooling using the $S_{1/2} - P_{1/2}$ (397 nm) and $D_{3/2} - P_{1/2}$ (866 nm) transitions, and then the radial modes are cooled by sideband cooling using the $S_{1/2} - D_{5/2}$ (729 nm) and $D_{5/2} - P_{3/2}$ (854 nm) transitions. The excitation beam at 729 nm, which is used for sideband cooling, generating the JC coupling and other operations, is illuminated from the radial direction. This direction is chosen to couple the beam only to the radial directions and to ignore the

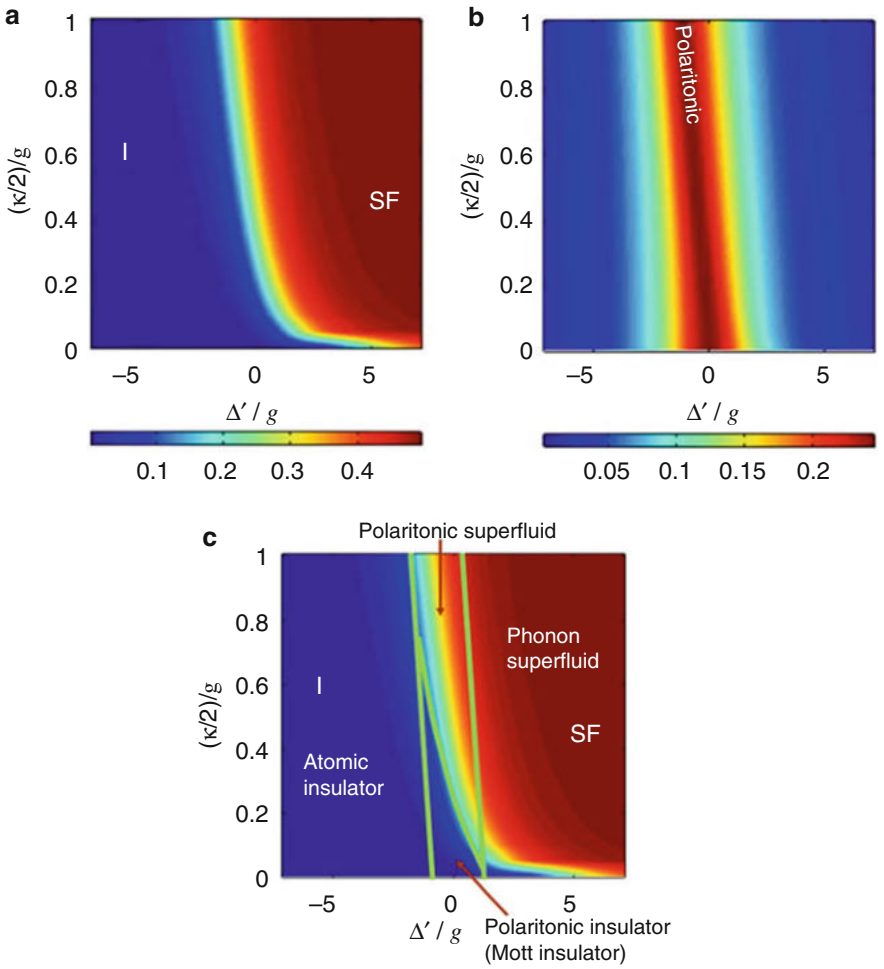

Fig. 15.2 (**a**) Calculated total excitation number variance $\Delta\hat{N}_1^2$, plotted against the two normalized parameters Δ'/g and $(\kappa/2)/g$. High values of this quantity indicate the existence of superfluid states. These values are calculated by obtaining the ground states of JCH Hamiltonian. (**b**) Calculated atomic excitation number variance $\Delta\hat{N}_{a,1}^2$. High values of this quantity indicate the existence of polaritonic excitations. (**c**) The four phase regions estimated from Fig. 15.2a, b

axial direction whose frequency is relatively small for effective sideband cooling. The average quantum numbers of the radial motion after sideband cooling are $\left(\langle n_{x,c.m.}\rangle, \langle n_{x,rock}\rangle, \langle n_{y,c.m.}\rangle, \langle n_{y,rock}\rangle\right) = (0.04, 0.03, 0.57, 0.08)$. Intermittently, ions are optically pumped to $S_{1/2}$ ($m_J = -1/2$) by using a 397-nm beam with the σ^+ polarization during and after sideband cooling. Ions are equally illuminated with the 729-nm laser within an error of less than 5 %. The internal state of ions is determined by irradiating them with lasers at 397 nm and 866 nm and by detecting

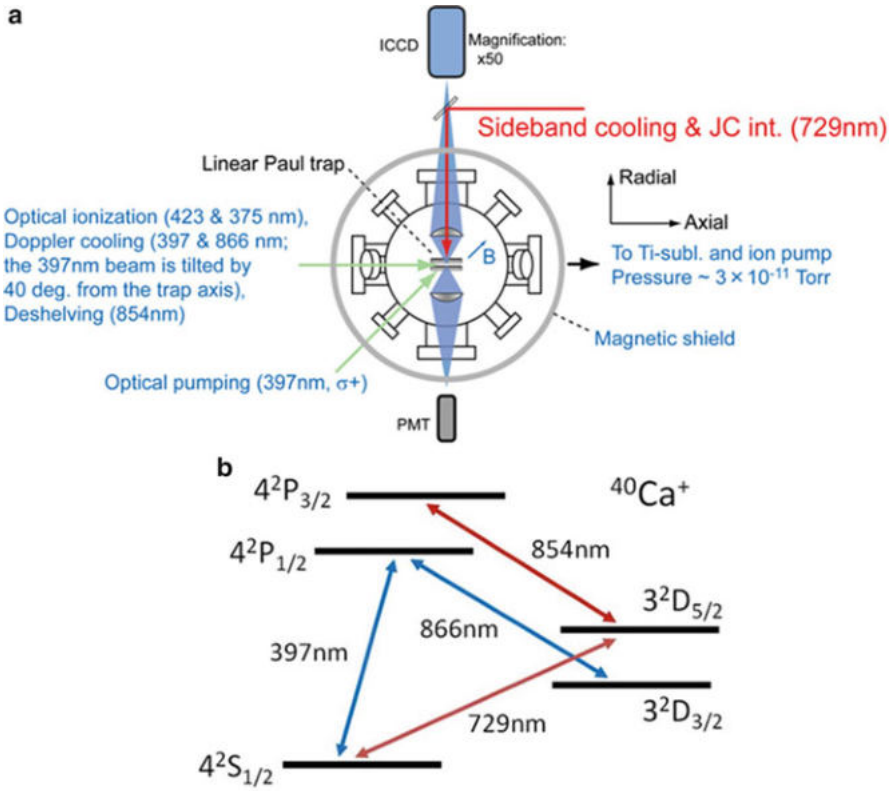

Fig. 15.3 (**a**) Experimental setup used to demonstrate the JCH model with two trapped ions. (**b**) Energy levels of $^{40}Ca^{+}$ relevant to laser cooling and induction of JC coupling

fluorescence photons with a photomultiplier and an intensified charge-coupled-device (ICCD).

15.3.3.2 Results

As a demonstration of a quantum phase transition, the system is transferred adiabatically from the ground state of an "atomic-insulator" region to the ground state of a "phonon superfluid" region and the excited-state population of two ions is observed. The trajectory of this process on the phase diagram is shown in Fig. 15.4a. It starts from a point where $-\Delta'/g$ is large, where the ground state is approximately the "atomic insulator" state $|\psi_{aI}\rangle$. Then, Δ'/g increases, exceeds zero, and becomes a large positive value, where the ground state is approximately the "phonon superfluid" state $|\psi_{phSF}\rangle$. In the intermediate region around $\Delta'/g \approx 0$, the system is in the "polaritonic superfluid" state $|\psi_{poSF}\rangle$. The measured variation of the average internal-state population during the adiabatic transfer is shown in

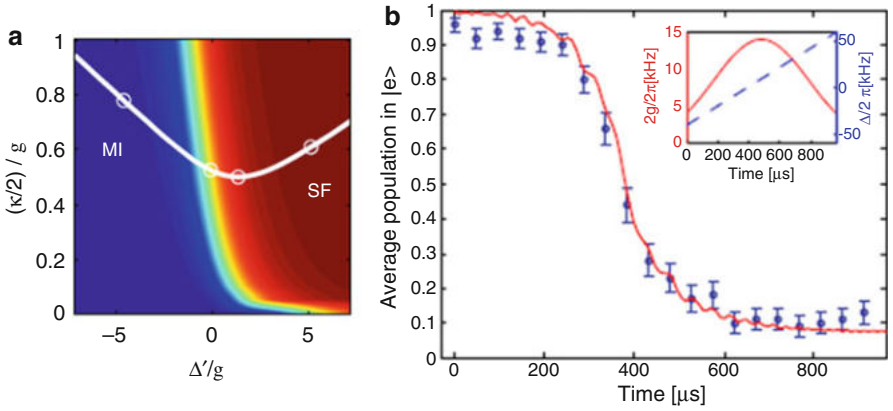

Fig. 15.4 (**a**) The trajectory of the adiabatic transfer on the phase diagram for this experiment. (**b**) Variation of the average internal-state population during the adiabatic transfer. Each data point is the average of 50 measurements. The inset shows the time dependence of the JC coupling coefficient $2g/2\pi$ (the solid curve with the vertical axis on the *left*) and the detuning $\Delta'/2\pi$ (the dashed curve with the vertical axis on the *right*) [23]

Fig. 15.4b. The initial state $|\psi_{aI}\rangle$ is prepared by cooling, optical pumping and applying a carrier π pulse. The adiabatic transfer is realized by shining the excitation laser and sweeping its detuning Δ' over the red-sideband resonance from negative to positive values. The amplitude is also modulated in a Gaussian shape to ensure that $|\Delta'|/g$ is large at the beginning and end of the pulse so that the overlap of the initial (final) state and $|\psi_{aI}\rangle$ ($|\psi_{phSF}\rangle$) is optimized. The explicit values of the parameters are as follows. $\Delta'/2\pi$ is swept linearly from -41 to 59 kHz in 960 μs, and the JC coupling coefficient $2g/2\pi$ is varied from 0.29×14 to 14 kHz and back to 0.29×14 kHz in a Gaussian shape over the same period. The hopping rate $\kappa/2\pi$ is 7.0 kHz. The imperfect preparation in the initial population in Fig. 15.4b is the result of infidelity in the carrier π pulse for preparation. The 10 % offset in the final population is due to infidelity in the adiabatic transfer process caused by the laser frequency fluctuation in addition to the imperfect initialization. The red curve in Fig. 15.4b is a numerically simulated result. These results show that the excitations in the internal state of atoms transfer to phonons in this process.

The realization of the "phonon superfluid" state at the end of this transfer is confirmed by measuring the phonon numbers of the radial c.m. mode and rocking mode at the beginning and end of the process. To this end, the spectra of the radial red- and blue-sideband transitions are observed at each time. From these results, the average phonon numbers for the c.m. and rocking modes at the beginning and end are estimated to be $(\langle n_{c.m.}\rangle, \langle n_{rock}\rangle) = (0.09, 0.04)$, and $(\langle n_{c.m.}\rangle, \langle n_{rock}\rangle = (0.15, 1.58)$, respectively. At the beginning, both of the phonon modes are almost in the ground state, while at the end, a state that has rocking-mode quanta close to 2 is realized and the c.m. mode is almost intact. These results support the

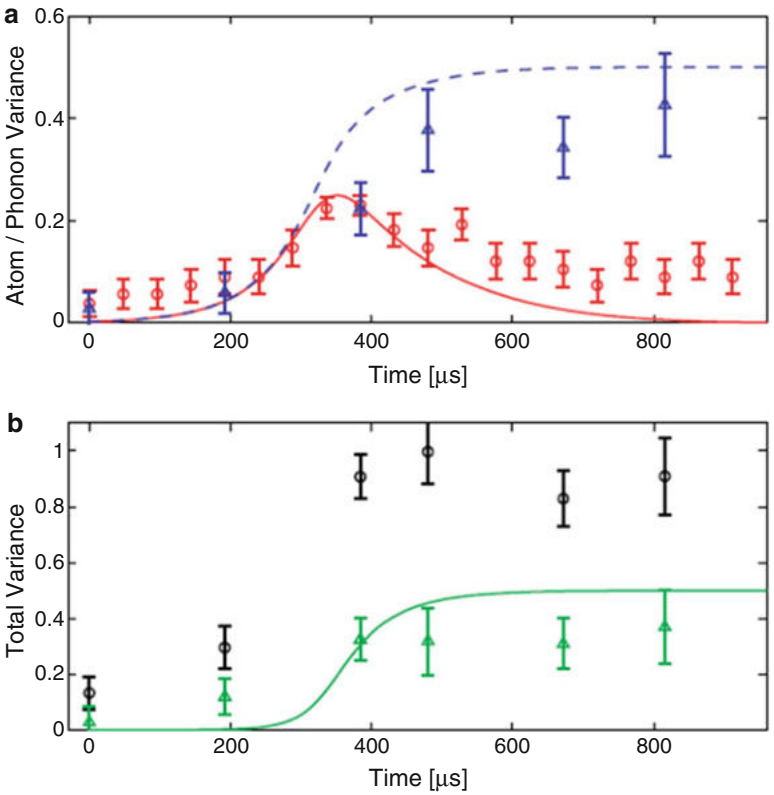

Fig. 15.5 Estimated experimental and calculated values for the excitation number variances (atomic, photon and total) during the adiabatic transfer. The data points are experimental values and the curves are calculated from exact ground states against the actual time dependence of the experimental parameters. (**a**) Values for the atomic excitation number variance $\Delta\hat{N}^2_{a,1}$ (*circles* and *solid curve*) and the phonon- number variance $\Delta\hat{N}^2_{p,1}$ (*triangles* and *dashed curve*). Each data point is the average of 50 measurements. (**b**) Values for the total excitation number variance $\Delta\hat{N}^2_1$. Instead of estimating the experimental values for this quantity directly, the upper and lower bounds are estimated along with the error, and shown by the *circles* and *triangles* [23]

occurrence of a quantum phase transition from the "atomic-insulator" state $|\psi_{aI}\rangle = |e_1\rangle\,|0_1\rangle\,|e_2\rangle\,|0_2\rangle$ to the "phonon-superfluid" state $\left|\psi_{phSF}\right\rangle = |g_1\rangle\,|g_2\rangle a_r^{\dagger 2}\,|0_1\rangle\,|0_2\rangle$.

The transfer process is further analyzed by estimating the excitation number variances (atomic, phonon, and total). The red circles in Fig. 15.5a show the atomic excitation number variances $\Delta\widehat{N}^2_{a,1}$ estimated from atomic populations measured with the photomultiplier tube. Individual detection is possible with the photomultiplier owing to the unequal illumination intensity of the two ions with the 397-nm laser. The peak at the center indicates the presence of polaritonic excitations. The red solid curve is the numerically simulated result. The blue triangles in Fig. 15.5a show the phonon-number variances $\Delta\widehat{N}^2_{p,1}$ with $\widehat{N}_{p,i} = a_i^\dagger\, a_i$. These values are obtained

from the average phonon numbers of the rocking mode and atomic variances measured during the process. The result also supports the realization of phonon superfluid state at the end of the adiabatic transfer. Figure 15.5b shows the upper and lower bounds of the total excitation number variance $\Delta\widehat{N}_1^2$. Details of the derivation of the phonon-number variances and inequalities for estimating these bounds are given in reference [23]. The expected qualitative behavior of the phase transition is reproduced in these results.

15.4 Conclusion

The JCH model has been demonstrated with two trapped ions. In the above experiment, the "polaritonic superfluid" phase is only confirmed during the adiabatic transfer from the "atomic insulator" phase to the "phonon superfluid" phase. By increasing the distance between ions and hence decreasing the hopping rate, it is expected that the "polaritonic insulator" (Mott insulator) phase can be observed clearly.

Scaling up this model to include large numbers of sites is the next problem. For this purpose, certain points must be considered. When we use an ion chain in a linear trap for this model, the trap anisotropy must satisfy the condition, $\omega_{x,y}/\omega_z > 0.77N_{ions}/\sqrt{\log N_{ions}}$, where N_{ions} is the number of ions, to prevent the linear chain from transitioning to a zigzag configuration [31]. Under the above condition, as increasing number of ions in the chain, the spacing at the center separation d_{min} decreases in proportion to $(N_{ions})^{-0.559}$ and thus the hopping rate κ increases in proportion to $(N_{ions})^{1.677}$. To explore the phase diagram of the JCH model widely, it is desirable to change the value of κ/g as widely as possible. Although a large trap anisotropy $\omega_{x,y}/\omega_z$ is advantageous for this purpose, it is not a sufficient condition. It is advantageous to be able to control d_{min} without being restricted by the dependence on the number of ions via the term $(N_{ions})^{-0.559}$. This problem can be overcome by using an anharmonic linear trap that contains a quartic potential term in the axial direction [32]. A nearly uniform spacing between ions is achieved, and a large linear structure can be stabilized in this trap. Another approach is to use an array of independent traps [33–35]. In this case the spacing between ions and the magnitude of confinement can be chosen independently and also two-dimensional arrays can be realized.

In the above experiment, the phonon and total variances are not measured directly but rather estimated from measured values. It is possible to measure these values directly by using individual addressing of the exciting laser beams. For a large number of ions the use of micro-mirrors for individual addressing has been proposed [36].

References

1. R.P. Feynman, Int. J. Theor. Phys. **21**, 467 (1982)
2. A. Friedenauer, H. Schmitz, J.T. Glueckert, D. Porras, T. Schaetz, Nat. Phys. **4**, 757 (2008)
3. K. Kim, M.-S. Chang, S. Korenblit, R. Islam, E.E. Edwards, J.K. Freericks, G.-D. Lin, L.-M. Duan, C. Monroe, Nature **465**, 590 (2010)
4. R. Islam, E.E. Edwards, K. Kim, S. Korenblit, C. Noh, H. Carmichael, D.-G. Lin, L.-M. Duan, C.-C. Joseph Wang, J.K. Freericks, C. Monroe, Nat. Commun. **2**, 377 (2011)
5. M. Greiner, O. Mandel, T. Esslinger, T.W. Hansch, I. Bloch, Nature **415**, 39 (2002)
6. M.J. Hartmann, F. Brandao, M.B. Plenio, Laser & Photon. Rev. **2**, 527 (2008)
7. A. Tomadin, R. Fazio, J. Opt. Soc. Am. B **27**, A130 (2010)
8. M.J. Hartmann, F. Brandao, M.B. Plenio, Nat. Phys **2**, 849 (2006)
9. A.D. Greentree, C. Tahan, J.H. Cole, L.C.L. Hollenberg, Nat. Phys. **2**, 856 (2006)
10. D.G. Angelakis, M.F. Santos, S. Bose, Phys. Rev. A **76**, 031805 (2007)
11. D. Rossini, R. Fazio, Phys. Rev. Lett. **99**, 186401 (2007)
12. E.K. Irish, C.D. Ogden, M.S. Kim, Phys. Rev. A **77**, 033801 (2008)
13. M.I. Makin, J.H. Cole, C. Tahan, L.C.L. Hollenberg, A.D. Greentree, Phys. Rev. A **77**, 053819 (2008)
14. P.A. Ivanov, S.S. Ivanov, N.V. Vitanov, A. Mering, M. Fleischhauer, K. Singer, Phys. Rev. A **80**, 060301 (2009)
15. A. Imamoglu, H. Schmidt, G. Woods, M. Deutsch, Phys. Rev. Lett. **79**, 1467 (1997)
16. K.M. Birnbaum, A. Boca, R. Miller, A.D. Boozer, T.E. Northup, H.J. Kimble, Nature **436**, 87 (2005)
17. M. Johanning, A.F. Varon, C. Wunderlich, J. Phys. B: At. Mol. Opt. Phys. **42**, 154009 (2009)
18. R. Blatt, C.F. Roos, Nat. Phys. **8**, 277 (2012)
19. D.M. Meekhof, C. Monroe, B.E. King, W.M. Itano, D.J. Wineland, Phys. Rev. Lett. **76**, 1796 (1996)
20. D. Leibfried, R. Blatt, C. Monroe, D. Wineland, Rev. Mod. Phys. **75**, 281 (2003)
21. X.-L. Deng, D. Porras, J.I. Cirac, Phys. Rev. A **72**, 063407 (2005)
22. D. Porras, J.I. Cirac, Phys. Rev. Lett. **93**, 263602 (2004)
23. K. Toyoda, Y. Matsuno, A. Noguchi, S. Haze, S. Urabe, Phys. Rev. Lett. **111**, 160501 (2013)
24. X.-L. Deng, D. Porras, J.I. Cirac, Phys. Rev. A **77**, 033403 (2008)
25. K. Kim, M.-S. Chang, R. Islam, S. Korenblit, L.-M. Duan, C. Monroe, Phys. Rev. Lett. **103**, 120502 (2009)
26. S. Haze, Y. Tateishi, A. Noguchi, K. Toyoda, S. Urabe, Phys. Rev. A **85**, 031401(R) (2012)
27. K. Toyoda, T. Watanabe, T. Kimura, S. Nomura, S. Haze, S. Urabe, Phys. Rev. A **83**, 022315 (2011)
28. K.R. Brown, C. Ospelkaus, Y. Colombe, A.C. Wilson, D. Leibfried, D.J. Wineland, Nature **471**, 196 (2011)
29. M. Harlander, R. Lechner, M. Brownnutt, R. Blatt, W. Hansel, Nature **471**, 200 (2011)
30. K. Toyoda, S. Haze, R. Yamazaki, S. Urabe, Phys. Rev. A **81**, 032322 (2010)
31. D.F.V. James, Appl. Phys. B **66**, 181 (1998)
32. G.-D. Lin, S.-L. Zhu, R. Islam, K. Kim, M.-S. Chang, S. Korenblit, C. Monroe, L.-M. Duan, Euro. Phys. Lett. **86**, 60004 (2009)
33. R.J. Clark, T. Lin, K.R. Brown, I.L. Chuang, J. Appl. Phys. **105**, 013114 (2009)
34. M. Kumph, M. Brownnutt, R. Blatt, New J. Phys. **13**, 073043 (2011)
35. J.D. Siverns, S. Weidt, K. Lake, B. Lekitsch, M.D. Hughes, W. Hensinger, New J. Phys. **14**, 085009 (2012)
36. S. Korenblit, D. Kafri, W.C. Campbell, R. Islam, E.E. Edwards, Z.-X. Gong, G.-D. Lim, L.-M. Duan, J. Kim, K. Kim, C. Monroe, New J. Phys. **14**, 095024 (2012)

Chapter 16
Equilibrium to Nonequilibrium Condensation in Driven-Dissipative Semiconductor Systems

Makoto Yamaguchi and Tetsuo Ogawa

16.1 Introduction

In a semiconductor system, it is known that electron-hole (e-h) bound pairs can be formed by their Coulomb attraction when the conduction and valence band effectively reach an equilibrium state after the carriers are generated e.g. by laser excitation (Fig. 16.1). An exciton polariton is a quasi-bosonic particle composed of such a Coulomb-bound e-h pair (exciton) and a photon [1, 2], the behaviors of which have attracted much attention due to their potential apprications through the Bose-Einstein condensation (BEC) [3–5], i.e. a macroscopic occupation of a single exciton-polariton state by a thermodynamic phase transition.

A typical exciton-polariton system is shown in Fig. 16.2. The system basically consists of semiconductor quantum wells (QWs) and a microcavity, the same structure as a vertical cavity surface emitting laser (VCSEL). In this context, a conventional lasing phase[1] is involved in this system as well as the exciton-polariton BEC [9]. At high densities, moreover, the Bardeen-Cooper-Schrieffer (BCS) – like

[1]In this contribution, the terms 'lasing' and 'laser' are used only when the condensation is inherently governed by non-equilibrium kinetics, according to [6, 7]. In other words, thermodynamic variables of the system, such as temperatures, cannot be defined for lasing phases. However, we note that these terms are occasionally used even for a condensation dominated by the thermodynamics of the electron-hole-photon system [8] if the interest is in fabricating a device.

M. Yamaguchi • T. Ogawa (✉)
Department of Physics, Osaka University, 1-1 Machikaneyama, Toyonaka, Osaka 560-0043, Japan
e-mail: yamaguchi@acty.phys.sci.osaka-u.ac.jp; ogawa@acty.phys.sci.osaka-u.ac.jp

Y. Yamamoto, K. Semba (eds.), *Principles and Methods of Quantum Information Technologies*, Lecture Notes in Physics 911, DOI 10.1007/978-4-431-55756-2_16

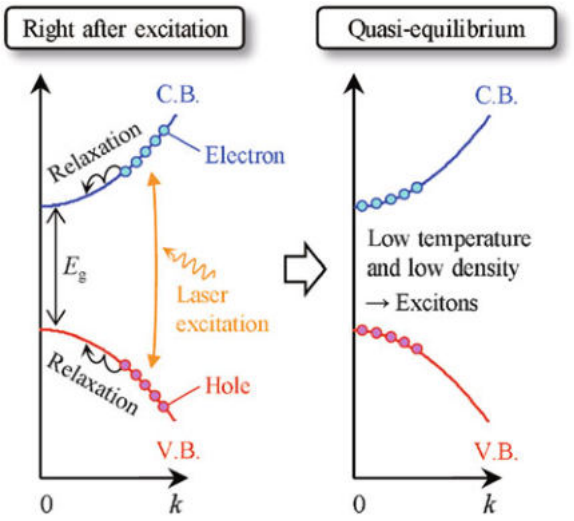

Fig. 16.1 Excitation and thermalization process in a semiconductor. Electrons and holes generated by laser excitation subsequently undergo immediate intraband relaxations and redistributions in the conduction band (*C.B.*) and valence band (*V.B.*) to effectively reach an equilibrium state. Coulomb-bound e-h pairs (excitons) are formd when the equilibrium state is at sufficiently low temperature and low carrier density

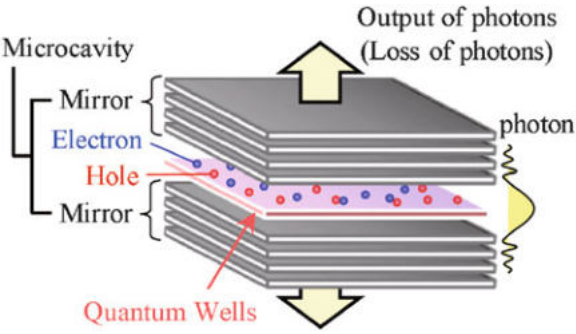

Fig. 16.2 Schematic illustration of a typical exciton-polariton system. Exciton-polaritons are formed by the electrons and holes in the QWs and the photons confined between the two mirrors (microcavity)

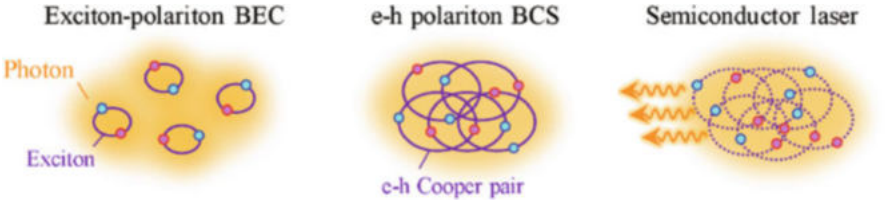

Fig. 16.3 Schematic illustration of several ordered phases involved in the exciton-polariton system

ordered phase can potentially be caused where electrons and holes form the "Cooper pairs" [10, 11], as is discussed in the BCS-BEC crossover in cold atom systems with Feshbach resonances [12, 13]. These ordered phases are schematically shown in Fig. 16.3.

However, the BEC and BCS phases are in equilibrium, the situation of which is quite different from the semiconducotor laser in nonequilibrium. As a result, approaches for describing the BEC and BCS phases based on equilibrium statistical

mechanics, e.g. the BCS theory [14, 15], are not applicable to the semiconductor laser because any nonequilibrium effects cannot be taken into account, such as pumping and loss. Conversely, past theories for describing the lasing operation, e.g. the Maxwell-Semiconductor-Bloch equations (MSBEs) [16, 17], cannot recover such equilibrium statistical approaches.[2] The difficulty shown here has been one of problems to understand the underlying physics in exciton-polariton systems.

In such a situation, we have recently proposed a framework which can treat the phases of the BEC, BCS and laser in a unified way [19, 20]. This framework is an extention of a nonequilibrium Green's function approach developed in Refs. [21–23] in which excitons are simply modeled by localized noninteracting two-level systems without internal e-h structures. Our formalism results in the BCS theory when the system can be regarded as in equilibrium, while it recovers the MSBE when nonequilibrium features become important. The internal e-h structures as well as the Coulomb interactions can also be taken into account within the mean-field approximation. In this contribution, we would like to give an introduction to such a "BEC-BCS-LASER crossover theory".

16.2 BCS Theory and MSBE for Exciton-Polariton Systems

In exciton-polariton systems, the equilibrium phases (the BEC and BCS phases) can be described by the BCS theory while the nonequilibrium phase (the lasing phase) can be described by the MSBE. In this section, we give an overview of the BCS theory and the MSBE to highlight their similarities and differences. For simplicity, we set $\hbar = k_{\mathrm{B}} = 1$ in the followings.

16.2.1 Model

We first describe the Hamiltonian for the exciton-polariton system where electrons and holes in the QWs and photons in the microcavity are taken into account. The system Hamiltonian $\hat{H}_{\mathrm{S}}$ is then given by $\hat{H}_{\mathrm{S}} = \hat{H}_0 + \hat{H}_{\mathrm{Coul}} + \hat{H}_{\mathrm{dip}}$. Here, $\hat{H}_0$ is the Hamiltonian for free particles without interactions and written as

$$\hat{H}_0 = \sum_k \left(\epsilon_{\mathrm{e},k} \hat{e}_k^\dagger \hat{e}_k + \epsilon_{\mathrm{h},k} \hat{h}_k^\dagger \hat{h}_k + \epsilon_{\mathrm{ph},k} \hat{a}_k^\dagger \hat{a}_k \right), \tag{16.1}$$

[2] We note that theories for describing dynamics of equilibrium phases, e.g. the Gross-Pitaevskii equation, can asymptotically be derived from Maxwell-Bloch equations [18] even though these theories still do not recover equilibrium statistical approaches.

where $\hat{e}_k$, $\hat{h}_k$, and $\hat{a}_k$ are annihilation operators for electrons, holes, and photons with in-plane wave number k, respectively. $\epsilon_{\mathrm{e(h)},k} = k^2/2m_{\mathrm{e(h)}} + E_\mathrm{g}/2$ is the energy dispersion of electrons (holes) with an effective mass $m_{\mathrm{e(h)}}$, while $\epsilon_{\mathrm{ph},k} = k^2/2m_\mathrm{cav} + E_\mathrm{cav}$ is that of photons with an effective mass m_cav. E_g is the bandgap and E_cav is the energy of the cavity mode for $k = 0$ [24].

In contrast, $\hat{H}_\mathrm{Coul}$ and $\hat{H}_\mathrm{dip}$ denote the Coulomb interaction and the light-matter interaction within the dipole approximation, respectively written as

$$\hat{H}_\mathrm{Coul} = \frac{1}{2}\sum_{k,k',q} U'_q \left(\hat{e}^\dagger_{k+q}\hat{e}^\dagger_{k'-q}\hat{e}_{k'}\hat{e}_k + (\hat{e} \leftrightarrow \hat{h}) - 2\hat{e}^\dagger_{k+q}\hat{h}^\dagger_{k'-q}\hat{h}_{k'}\hat{e}_k\right), \quad (16.2)$$

$$\hat{H}_\mathrm{dip} = -\sum_{k,q}\left(g\hat{a}^\dagger_q\hat{h}_{-k}\hat{e}_{k+q} + g^*\hat{a}_q\hat{e}^\dagger_{k+q}\hat{h}^\dagger_{-k}\right), \quad (16.3)$$

where $U'_q = U'_{-q}$ and $U'_{q=0} \equiv 0$. Note that $[\hat{H}_\mathrm{S}, \hat{N}_\mathrm{S}] = 0$ is satisfied when an excitation number of the system $\hat{N}_\mathrm{S}$ is defined as $\hat{N}_\mathrm{S} \equiv \sum_k[\hat{e}^\dagger_k\hat{e}_k/2 + \hat{h}^\dagger_k\hat{h}_k/2 + \hat{a}^\dagger_k\hat{a}_k]$. For later convenience, therefore, we redefine $\hat{H}_\mathrm{S} - \mu\hat{N}_\mathrm{S}$ as $\hat{H}_\mathrm{S}$. This means that a grand canonical ensemble is assumed with a chemical potential μ if we are interested in equilibrium phases. In contrast, for time-dependent problems, this means that dynamics of physical quantities is captured on a rotating frame with the frequency μ. Thus, μ is a given parameter identical to the chemical potential for the BEC and BCS phases (Sect. 16.2.3), whereas it becomes a unknown variable equivalent to the lasing frequency for the semiconductor laser in a steady state (Sect. 16.2.4).

16.2.2 Mean-Field Approximation

The Hamiltonians shown in Sect. 16.2.1 give a starting point for theories of the exciton-polariton system. However, in practice, it is difficult to exactly treat $\hat{H}_\mathrm{Coul}$ and $\hat{H}_\mathrm{dip}$ because these Hamiltonians cause many-body problems. In this subsection, therefore, we discuss the mean-field (MF) approximation in order to reduce the problems to single-particle problems.

In general, the MF approximation is performed by writing a specific operator $\hat{O}$ as $\hat{O} = \langle\hat{O}\rangle + \delta\hat{O}$ and by neglecting quadratic terms with respect to $\delta\hat{O}$ in the Hamiltonians.[3] Here, $\langle\hat{O}\rangle \equiv \mathrm{Tr}[\hat{O}\hat{\rho}]$ denotes the expectation value for the density operator $\hat{\rho}$ and the operator $\delta\hat{O}$ corresponds to a fluctuation around the expectation value. In our case, the interaction Hamiltonians of $\hat{H}_\mathrm{Coul}$ and $\hat{H}_\mathrm{dip}$ can easily be reduced to a single-particle problem by employing $\hat{O} \in \{\hat{a}_k, \hat{h}_{-k}\hat{e}_{k'}, \hat{e}^\dagger_k\hat{e}_{k'}, \hat{h}^\dagger_k\hat{h}_{k'}\}$. As

[3] We note, however, that physical guesses are required for the determination of what operator(s) should be chosen as $\hat{O}$, e.g. from experiments.

a result, with definitions of the photon field $\langle \hat{a}_k \rangle \equiv \delta_{k,0} a_0$, the polarization function $\langle \hat{h}_{-k} \hat{e}_{k'} \rangle \equiv \delta_{k,k'} p_k$, and the distribution functions of electrons $\langle \hat{e}_k^\dagger \hat{e}_{k'} \rangle \equiv \delta_{k,k'} n_{\mathrm{e},k}$ and holes $\langle \hat{h}_k^\dagger \hat{h}_{k'} \rangle \equiv \delta_{k,k'} n_{\mathrm{h},k}$, the mean-field Hamiltonian $\hat{H}_{\mathrm{S}}^{\mathrm{MF}}$ is obtained as

$$\hat{H}_{\mathrm{S}}^{\mathrm{MF}} = \sum_k \left(\tilde{\xi}_{\mathrm{e},k} \hat{e}_k^\dagger \hat{e}_k + \tilde{\xi}_{\mathrm{h},k} \hat{h}_k^\dagger \hat{h}_k - [\Delta_k \hat{e}_k^\dagger \hat{h}_{-k}^\dagger + \mathrm{H.c.}] \right) + \sum_k \left(\xi_{\mathrm{ph},k} \hat{a}_k^\dagger \hat{a}_k - [g p_k \hat{a}_0^\dagger + g^* p_k^* \hat{a}_0] \right). \tag{16.4}$$

Here, constants are ignored because the following discussion is not affected. $\tilde{\xi}_{\mathrm{e(h)},k}$ and $\xi_{\mathrm{ph},k}$ are respectively defined as $\tilde{\xi}_{\mathrm{e(h)},k} \equiv \tilde{\epsilon}_{\mathrm{e(h)},k} - \mu/2$ and $\xi_{\mathrm{ph},k} \equiv \epsilon_{\mathrm{ph},k} - \mu$, where $\tilde{\epsilon}_{\mathrm{e(h)},k} \equiv \epsilon_{\mathrm{e(h)},k} - \sum_{k'} U'_{k-k'} n_{\mathrm{e(h)},k'}$ denotes the energy dispersion of electrons (holes) renormalized by the repulsive electron-electron (hole-hole) Coulomb interaction, the first (second) term in Eq. (16.2). The well-known bandgap renormalization (BGR) in semiconductor physics is included in $\tilde{\epsilon}_{\mathrm{e(h)},k}$. In contrast, $\Delta_k \equiv g^* a_0 + \sum_{k'} U'_{k-k'} p_{k'}$ results from the attractive electron-hole Coulomb interaction, the third term in Eq. (16.2), and is called the generalized Rabi frequency [25]. Δ_k has a role in forming e-h pairs as can be seen in Eq. (16.4).

The mean-field Hamiltonian is thus obtained. However, note that the expectation values of $\langle \hat{O} \rangle$ (i.e. a_0, p_k, $n_{\mathrm{e},k}$, and $n_{\mathrm{h},k}$) are included in $\hat{H}_{\mathrm{S}}^{\mathrm{MF}}$. For self-consistensy, therefore, the following relation should be satisfied :

$$\langle \hat{O} \rangle = \mathrm{Tr}[\hat{O} \hat{\rho}^{\mathrm{MF}}(\langle \hat{O} \rangle)]. \tag{16.5}$$

Here, $\hat{\rho}^{\mathrm{MF}}$ is the density operator determiend by using $\hat{H}_{\mathrm{S}}^{\mathrm{MF}}$. The BCS theory and the MSBE shown below are obtained from this self-consistent equation.

16.2.3 BCS Theory for Exciton-Polariton Condensation

First, we assume that the exciton-polariton system is in equilibrium. According to the equilibrium statistical mechanics, the density operator $\hat{\rho}^{\mathrm{MF}}$ at temperature T can be described as

$$\hat{\rho}^{\mathrm{MF}} = \hat{\rho}_{\mathrm{eq}}^{\mathrm{MF}} \equiv \frac{1}{Z} \exp(-\beta \hat{H}_{\mathrm{S}}^{\mathrm{MF}}), \tag{16.6}$$

where $Z \equiv \mathrm{Tr}[\exp(-\beta \hat{H}_{\mathrm{S}}^{\mathrm{MF}})]$ and $\beta \equiv 1/T$. In this case, μ is a given parameter equivalent to the chemical potential, as mentioned above. With $\epsilon_{\mathrm{e},k} = \epsilon_{\mathrm{h},k}$ for simplicity, the self-consistent equations obtained from Eq. (16.4) to (16.6) are

$$a_0 = \sum_{k'} \frac{g}{\xi_{\mathrm{ph},0}} p_{k'}, \; p_k = \frac{\Delta_k}{2E_k} \tanh\left(\frac{\beta E_k}{2} \right), \tag{16.7}$$

$$n_{\mathrm{e},k} = n_{\mathrm{h},k} = \frac{1}{2}\left\{1 - \frac{\tilde{\xi}^{+}_{\mathrm{eh},k}}{E_k}\tanh\left(\frac{\beta E_k}{2}\right)\right\}, \tag{16.8}$$

where $\tilde{\xi}^{\pm}_{\mathrm{eh},k} \equiv (\tilde{\xi}_{\mathrm{e},k} \pm \tilde{\xi}_{\mathrm{h},k})/2$ and $E_k \equiv [(\tilde{\xi}^{+}_{\mathrm{eh},k})^2 + |\Delta_k|^2]^{1/2}$. In the derivation, Bogoliubov transformations of $\hat{e}_k$ and $\hat{h}_k$ can be applied to the first line in Eq. (16.4) for diagonalization, while a displacement of $\hat{a}_0$ to the second line, because the Hilbert space of the first (second) line of Eq. (16.4) is spanned only by the electron and hole (photon) degrees of freedom.

The gap equation, which is formally equivalent to the BCS theory for superconductors, can then be obtained by substituting Eq. (16.7) into the definition of Δ_k:

$$\Delta_k = \sum_{k'} U^{\mathrm{eff}}_{k',k}\frac{\Delta_{k'}}{2E_{k'}}\tanh\left(\frac{\beta E_{k'}}{2}\right). \tag{16.9}$$

In this context, Δ_k is an order parameter in the exciton-polariton system as well as in the superconducting system. $U^{\mathrm{eff}}_{k',k} \equiv |g|^2/\xi_{\mathrm{ph},0} + U'_{k'-k}$ represents an effective attractive e-h interaction, from which one can find that photon-mediated process also contributes the attractive interaction. Notice that Eqs. (16.8) and (16.9) are simultaneous equations with the unknown variables $n_{\mathrm{e},k}(= n_{\mathrm{h},k})$ and Δ_k. Especially for $T = 0$, this treatment is known to cover the equilibrium phases from the BEC to the BCS states [14, 15, 26].

16.2.4 MSBE for Semiconductor Lasers

Next, a treatment based on the MSBE is explained for the discussion of the semiconductor laser, which is characterized by nonequilibrium. In contrast to the BCS theory, therefore, the effects of environments (Fig. 16.4) cannot be neglected for lasing; the excitation and thermalization of the e-h system and the loss of photons from the microcavity. For this reason, the dynamics of the total density operator $\hat{\rho}^{\mathrm{MF}}$ is discussed by writing the total mean-field Hamiltonian $\hat{H}^{\mathrm{MF}} \equiv \hat{H}^{\mathrm{MF}}_{\mathrm{S}} + \hat{E}$ with the couplings to the environments $\hat{E}$. Since $\mathrm{i}\partial_t\hat{\rho}^{\mathrm{MF}} = [\hat{H}^{\mathrm{MF}}, \hat{\rho}^{\mathrm{MF}}]$ in the Schrödinger picture, a time drivative of Eq. (16.5) yields

$$\mathrm{i}\partial_t\langle\hat{O}\rangle = \mathrm{Tr}[[\hat{O}, \hat{H}^{\mathrm{MF}}_{\mathrm{S}}]\hat{\rho}^{\mathrm{MF}}] + \mathrm{Tr}[[\hat{O}, \hat{E}]\hat{\rho}^{\mathrm{MF}}], \tag{16.10}$$

where $\mathrm{Tr}[\hat{A}\hat{B}] = \mathrm{Tr}[\hat{B}\hat{A}]$ is used. The MSBE is then obtained when the first term is derived from Eq. (16.4) and the second term is replaced by phenomenological relaxation terms:

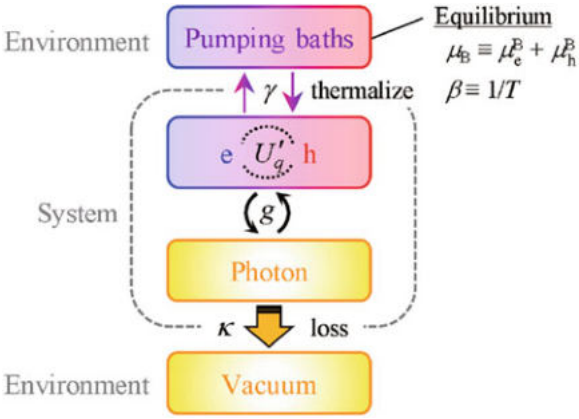

Fig. 16.4 A schematic picture of the model including environments. The e-h system is excited and thermalized by the pumping baths by exchanging carriers. Photons in the system are lost into the vacuum

$$\partial_t a_0 = -\mathrm{i}\xi_{\mathrm{ph},0} a_0 + \mathrm{i}g\textstyle\sum_k p_k - \kappa a_0, \tag{16.11}$$

$$\partial_t p_k = -2\mathrm{i}\tilde{\xi}^{+}_{\mathrm{eh},k} p_k - \mathrm{i}\Delta_k N_k - 2\gamma(p_k - p_k^0), \tag{16.12}$$

$$\partial_t n_{\mathrm{e(h)},k} = -2\mathrm{Im}[\Delta_k p_k^*] - 2\gamma(n_{\mathrm{e(h)},k} - n^0_{\mathrm{e(h)},k}), \tag{16.13}$$

where the last term in each equation is the relaxation term and $N_k \equiv n_{\mathrm{e},k} + n_{\mathrm{h},k} - 1$ denotes the degree of the population inversion.[4] p_k^0 and $n^0_{\mathrm{e(h)},k}$ are defined as

$$p_k^0 \equiv 0, \quad n^0_{\mathrm{e(h)},k} \equiv f_{\mathrm{e(h)},k} \tag{16.14}$$

where $f_{\mathrm{e(h)},k} \equiv [1 + \exp\{\beta(\tilde{\epsilon}_{\mathrm{e(h)},k} - \mu^{\mathrm{B}}_{\mathrm{e(h)}})\}]^{-1}$ is the Fermi distribution with the chemical potential $\mu^{\mathrm{B}}_{\mathrm{e(h)}}$ of the electron (hole) pumping bath. The phenomenological approximation shown here is called the relaxation approximation [27]. Each relaxation term suggests that the photon field a_0 decays with a rate of κ, the distribution function $n_{\mathrm{e(h)},k}$ is driven to approach the Fermi distribution $f_{\mathrm{e(h)},k}$ (Fig. 16.5), i.e. thermalization (Fig. 16.1), and p_k decays due to thermalization-induced dephasing.

Solutions for the laser action can then be obtained by determining the unknown variables a_0, p_k, $n_{\mathrm{e},k}$, $n_{\mathrm{h},k}$, and μ in Eqs. (16.11), (16.12) and (16.13) under a steady-state condition $\partial_t\langle\hat{O}\rangle = 0$. Again, we emphasize that μ is a unknown variable corresponding to the laser frequency in the steady-state MSBE, in contrast to the BCS theory. This is equivalent to find an appropriate frequency with which the lasing oscillation of a_0 and p_k seems to remain stationary on the rotating frame.

[4] Here, $-1 \leq N_k \leq +1$ because $0 \leq n_{\mathrm{e(h)},k} \leq 1$. Population inversion is formed in k-resions with $N_k > 0$.

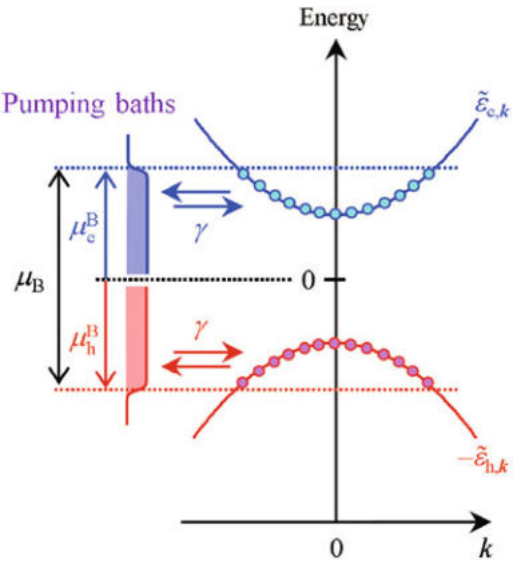

Fig. 16.5 Energy dispersions of electrons and holes. The distribution functions $n_{e,k}$ and $n_{h,k}$ are driven to approach the Fermi distributions by the respective pumping baths

16.3 BEC-BCS-LASER Crossover Theory

In the exciton-polariton system, as shown in Sect. 16.2, the BCS theory and the MSBE are theoretical frameworks starting from the common Hamiltonians with the same mean-field approximation. However, the difference is the way of deriving the self-consistent equations. In the case of the BCS theory, $\hat{\rho}^{\rm MF}$ is directly described by $\hat{H}_{\rm S}^{\rm MF}$ (Eq. (16.6)). In contrast, in the case of the MSBE, Eq. (16.10) is used to introduce the phenomenological relaxation terms. We note, however, that any assumption is not used for $\hat{\rho}^{\rm MF}$ in Eq. (16.10), which indicates that the MSBE may incorporate the BCS theory at least in principle.

In this context, an approach to derive the BCS theory from the MSBE should be discussed briefly. We first consider a situation where the effects of the environments are completely neglected, which is equivalent to set $\kappa = \gamma = 0$ in the MSBE. However, in this case, the BCS theory cannnot be derived because there is no term to drive the system into equilibrium in the MSBE.[5] A natural condition to consider is physically a limit of $\gamma \to 0^+$ after $\kappa \to 0$ because the system should be thermalized even though the effects of environments are decreased. Unfortunately, however, the MSBE does not recover the BCS theory even by taking this limit. The relationship between the BCS theory and the MSBE is thus discontinuous in spite of

[5]For $\kappa = \gamma = 0$, the steady state of the MSBE becomes identical to the BCS theory if the solution of the BCS theory is chosen as an initial condition in the MSBE because $[\hat{\rho}_{\rm eq}^{\rm MF}, \hat{H}_{\rm S}^{\rm MF}] = 0$. However, this is a special case.

the similarities of the two frameworks. Obviously, the phenomenological relaxation approximation causes such a problem.

In regard to this problem, we have recently constructed a unified framework [19] by using a nonequilibrium Green's function approach [21–23]. The framework, at first, takes an integral form of simultaneous equations and seems quite different from the MSBE (see also Appendix 2). However, by rearranging the equations with particular attention to the problem mentioned above, all of important changes can successfully be incorporated in the relaxation terms in the MSBE [20]. The result simply replaces Eq. (16.14) by

$$p_k^0 \equiv \mathrm{i}\int \frac{\mathrm{d}\nu}{2\pi}\left[G^{\mathrm{R}}_{12,k}(\nu)\{1-f^{\mathrm{B}}_{\mathrm{h}}(-\nu)\} - G^{\mathrm{R}*}_{21,k}(\nu)f^{\mathrm{B}}_{\mathrm{e}}(\nu)\right],$$
$$n^0_{\mathrm{e(h)},k} \equiv \int \frac{\mathrm{d}\nu}{2\pi} f^{\mathrm{B}}_{\mathrm{e(h)}}(\nu)A_{11(22)}(\pm\nu;k), \qquad (16.14')$$

where $f^{\mathrm{B}}_{\mathrm{e(h)}}(\nu) \equiv [\exp\{\beta(\nu-\mu^{\mathrm{B}}_{\mathrm{e(h)}}+\mu/2)\}+1]^{-1}$ is the Fermi distribution of the electron (hole) pumping bath. $G^{\mathrm{R}}_{\alpha\alpha',k}(\nu)$ is called the retarded Green's function and described by elements of a matrix

$$G^{\mathrm{R}}_k(\nu) = \begin{pmatrix} \nu-\tilde{\xi}_{\mathrm{e},k}+\mathrm{i}\gamma & \Delta_k \\ \Delta_k^* & \nu+\tilde{\xi}_{\mathrm{h},k}+\mathrm{i}\gamma \end{pmatrix}^{-1}. \qquad (16.15)$$

On the other hand, $A_{11(22)}(\nu;k)$ is called the single-particle spectral function and defined as

$$A_{\alpha\alpha'}(\nu;k) \equiv \mathrm{i}(G^{\mathrm{R}}_{\alpha\alpha',k}(\nu) - G^{\mathrm{R}*}_{\alpha'\alpha,k}(\nu)). \qquad (16.16)$$

Here, $A_{11(22)}(\nu;k)$ means the density of states for electron-like (hole-like) quasi-particles with the energy ν and wave number k.

Some readers might feel difficult to understand the formalism because the above definitions are unique to the Green's function approach. However, all we have to do is the replacement of Eq. (16.14) by Eq. (16.14′). The unknown variables are still a_0, p_k, $n_{\mathrm{e},k}$, $n_{\mathrm{h},k}$, and μ, that is, the same as the MSBE. In this sense, the obtained equations are quite simple, which is one of strong points of this formalism. From the viewpoint of the Green's funciton, it is relatively easy to understand the physical meaning of Eq. (16.14′) due to the clear form; the energy integral of (distribution)×(density of states).[6] We refer to such a formalism as the BEC-BCS-LASER crossover theory.

Now, this formalism enables us to cleary understand the standpoint of the BCS theory. For this purpose, let us discuss the limit of equilibrium, based on the idea described above. In the followings, however, $\epsilon_{\mathrm{e},k} = \epsilon_{\mathrm{h},k}$ and a charge neutrality

[6]The retarded Green's funcition is also seen as a kind of density of states.

$\mu_{\rm e}^{\rm B} = \mu_{\rm h}^{\rm B}$ are assumed for simplicity. First, in the limit of $\kappa \to 0$, one can prove $\mu = \mu_{\rm B} (\equiv \mu_{\rm e}^{\rm B} + \mu_{\rm h}^{\rm B})$. This is the same as treating μ as a given parameter, and physically, means that the system reaches in chemical equilibrium with the pumping baths because there is no photon loss. The BCS theory is then derived after taking the limit of $\gamma \to 0^+$, where the integrals in Eq. (16.14′) can be performed analytically. In this derivation, $\gamma \neq 0$ is required to be canceled down even though γ does not appear in the final expression. This means that thermalization is essential to recover the equilibrium theory.

Thus, the BCS theory can be derived from the presented theory in the equilibrium limit. However, in some sense, this situation is physically trivial; the situation is not limited to such a trivial one for the system to be in equilibrium. Even under a condition where photons are continuously lost, it may be still possible to identify the system as being in equilibrium (quasi-equilibrium) as long as the e-h system is excited and thermalized. A true advantage of the above-presented framework becomes obvious in such a situation rather than in the trivial one. In this case, μ is still equivalent to the chemical potential but $\mu_{\rm B} > \mu$ because the system is influenced by the photon loss. As a result, μ becomes a unknown variable again. Furthermore, such a quasi-equilibrium condition can easily be obtained from Eqs. (16.14′) to (16.16) as[7]

$$\text{(I)} \ \ \min[2E_k] \gtrsim \mu_{\rm B} - \mu + 2\gamma + 2T.$$

Here, $\min[2E_k]$ is the minimum energy required for breaking e-h bound pairs and $\mu_{\rm B} - \mu > 0$ suggests that there is continuous particle flow from the pumping baths into the system.[8] We can then interpret the condition (I); this is a condition that the particle flux, thermalization-induced dephasing (= 2γ), and temperature effect (= $2T$), do not contribute to the dissociations of the e-h pairs.

However, the system can no longer be in quasi-equilibrium when nonequilibrium effect becomes significant. Let us therefore consider a situation where the MSBE, i.e. the physics of the semiconductor laser, becomes important. Such a condition can be found from Eqs. (16.14′) to (16.16) as

$$\text{(II)} \ \ \mu_{\rm B} - \mu \gtrsim \min[2E_k] + 2\gamma + 2T,$$

because $f_{\rm e(h)}^{\rm B}(\pm\nu) \simeq f_{\rm e(h)}^{\rm B}(\tilde{\xi}_{{\rm eh},k}^{+})$ turns out to be a good approximation in Eq. (16.14′) for k-resions satisfying

$$\text{(II}') \ \ \mu_{\rm B} - \mu \gtrsim 2E_k + 2\gamma + 2T.$$

[7] Under the condition (I), $f_{\rm e(h)}^{\rm B}(\nu)$ in Eq. (16.14′) can be approximated by the values at $\nu = \pm E_k$ because $A_{\alpha\alpha'}(\nu; k)$ and $G_{\alpha\alpha',k}^{\rm R}(\nu)$ have peaks around $\nu = \pm E_k$, as seen in Eqs. (16.17) and (16.33).

[8] This means that the system is chemically non-equilibrium with the pumping baths even if the system is in quasi-equilibrium.

Note that there are such k-resions whenever the condition (II) is fulfilled. As a result, we can obtain $p_k^0 \cong 0$ and $n_{\mathrm{e(h)},k}^0 \cong f_{\mathrm{e(h)},k}$ which recovers the MSBE. However, we stress that the condition (II′) depends on the wave number k; there remain k-regions still described by the BCS theory. The MSBE and the BCS theory are, thus, coupled with each other in a strict sense. In this context, the lasing can be referred to as the BCS-coupled lasing when this viewpoint is emphasized. At the same time, the physical meaning of μ changes into the oscillating frequency of the laser action.

16.4 Second Thresholds, Band Renormalization, and Gain Spectra

Figure 16.6 shows the number of coherent photons in the cavity $|a_0|^2$ and the frequancy μ as a function of μ_{B} calculated by our formalism.[9] Plots are colour coded by red (blue) when the quasi-equilibrium condition (I) (the lasing condition (II)) is satisfied, while by green when neither of the conditions is satisfied. In Fig. 16.6a, $|a_0|^2$ arises with increasing μ_{B}, the point of which is called the first threshold. In this situation, the system is in quasi-equilibrium regime (red) and μ is around the lower polariton level[10] E_{LP} in Fig. 16.6b. The first threshold therefore means that the exciton-polariton BEC is caused because the chemical potential of the system reaches the lowest energy of the exciton polariton, E_{LP}.

With further increase of μ_{B}, the system changes from the quasi-equilibrium regime (red) into the lasing regime (blue) through a crossover regime (green). Around the crossover regime in Fig. 16.6a, a second threshold can be seen where the number of coherent photons grows rapidly again. μ is then blue-shifted from E_{LP} into the bare cavity level E_{cav}. Furthermore, the kinetic hole burning can be seen in the distribution function of electrons $n_{\mathrm{e},k}$ (the blue arrow in the inset to Fig. 16.6a). These resuls demonstrate that the exciton-polariton BEC has smoothly changed into the semiconductor laser with the second threshold.

In experiments [28–34], the second threshold and the blue shift has been reported since more than 10 years ago, the mechanism of which has been attributed to a

[9] In the numerical calculations, the k-dependence of Δ_k is eliminated by using a contact potential $U'_{q\neq 0} = U = 2.66 \times 10^{-10}\,\mathrm{eV}$ with cut-off wave number $k_{\mathrm{c}} = 1.36 \times 10^9\,m^{-1}$. The other parameters are $m_{\mathrm{e}} = m_{\mathrm{h}} = 0.068 m_0$ (m_0 is the free electron mass), $\mu_{\mathrm{e}}^{\mathrm{B}} = \mu_{\mathrm{h}}^{\mathrm{B}}$, $T = 10\,\mathrm{K}$, $g = 6.29 \times 10^{-7}\,\mathrm{eV}$, $\gamma = 4\,\mathrm{meV}$, and $\kappa = 100\mu\mathrm{eV}$. In this context, our calculations are not quantitative but qualitative even though the parameters are taken as realistic as possible. In this situation, the exciton level ($\equiv E_{\mathrm{ex}}$) is formed at 10 meV below E_{g} ($E_{\mathrm{ex}} = E_{\mathrm{g}} - 10\,\mathrm{meV}$) and the lower polariton level E_{LP} is created at 20 meV below E_{g} ($E_{\mathrm{LP}} = E_{\mathrm{g}} - 20\,\mathrm{meV}$) under the resonant condition $E_{\mathrm{cav}} = E_{\mathrm{ex}}$ [20].

[10] For E_{LP} and E_{ex}, see also Appendix 1. Excitonic effects are discussed in the low density limit.

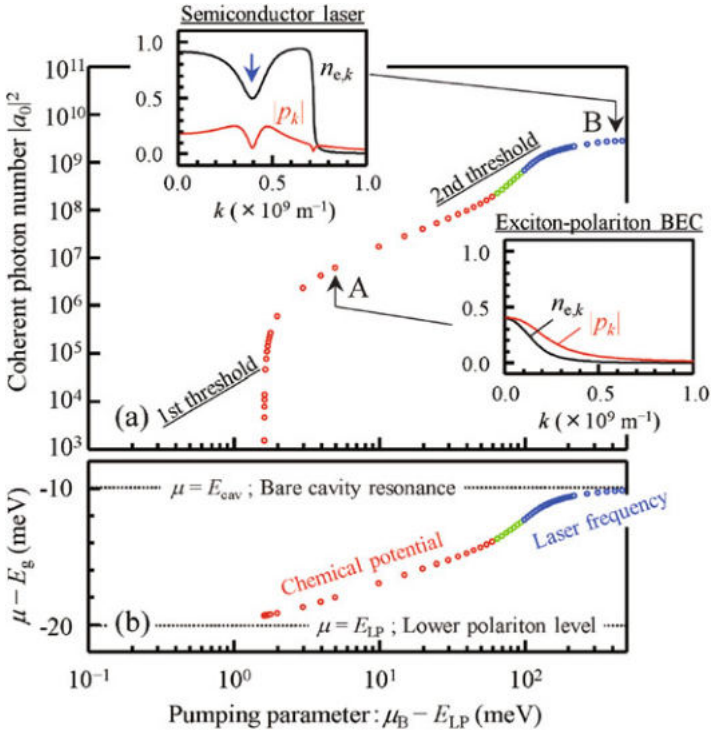

Fig. 16.6 Numerical results of (**a**) the coherent photon number in the cavity $|a_0|^2$ and (**b**) the frequency μ as a function of μ_B. Plots are colour coded by *red* and *blue* when satisfying the quasi-equilibrium condition (I) and the lasing condition (II), respectively. *Green colours* are used when neither of them are satisfied. μ represents the chemical potential in the quasi-equilibrium regime (*red*) but the laser frequency in the lasing regime (*blue*). *Inset*: the distribution function of electrons $n_{e,k}$ (*black*) and the polarization p_k (*red*). In the lasing regime (*B*), a characteristic dip can be seen in the distribution (the *bule arrow*), which is known as one of the signatures of lasing and called the kinetic hole burning

shift into the weak coupling regime due to dissociations of Coulomb-bound e-h pairs (excitons); the lasing phase is then achieved as a result. However, there is no convincing discussion why such dissociations lead to nonequilibration essential for lasing.

According to our formalism, this empirical picture can be investigated and shown to be incorrect. This is because, even in the lasing regime, there are gaps around $\pm\mu/2$ in the renormalized band structure as shown in the left of Fig. 16.7. An analytical form of $A_{11(22)}(\nu;k)$, obtained by Eqs. (16.15) and (16.16), enables us to conveniently study the renormalized band:

$$A_{11(22)}(\nu;k) = 2|u_k|^2 \frac{\gamma}{(\nu - \tilde{\xi}^-_{\mathrm{eh},k} \mp E_k)^2 + \gamma^2} + 2|v_k|^2 \frac{\gamma}{(\nu - \tilde{\xi}^-_{\mathrm{eh},k} \pm E_k)^2 + \gamma^2}. \tag{16.17}$$

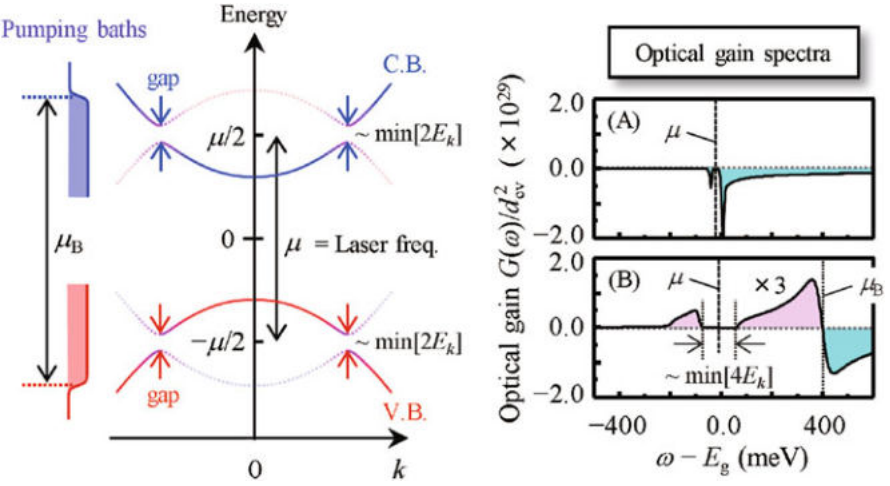

Fig. 16.7 *Left*; A renormalized band structure in a lasing phase (the point B in Fig. 16.6). The gaps are opened around $\pm\mu/2$ with the magnitude of $\min[2E_k]$. *Right*; Optical gain spectra for the exciton-polariton BEC (**A**) and for the lasing phase (**B**). Panels (**A**) and (**B**) correspond to the point A and B in Fig. 16.6, respectively. Aqua (*pink*) represents the gain (absorption) (Panels (**A**) and (**B**) are reproduced with permission from [20])

Here, u_k and v_k are the Bogoliubov coefficients defined as

$$u_k \equiv \sqrt{\frac{1}{2} + \frac{\tilde{\xi}^{+}_{\mathrm{eh},k}}{2E_k}}, \qquad v_k \equiv e^{\mathrm{i}\theta_k}\sqrt{\frac{1}{2} - \frac{\tilde{\xi}^{+}_{\mathrm{eh},k}}{2E_k}}, \tag{16.18}$$

with $\theta_k \equiv \arg(\Delta_k)$. These equations have remarkable similarities to the BCS theory in superconductors [20, 35]. Therefore, it is clear that the gaps are opened around $\pm\mu/2$ with the magnitude of $\min[2E_k]$ when $\tilde{\xi}^{-}_{\mathrm{eh},k} = 0$ i.e. $\epsilon_{\mathrm{e},k} = \epsilon_{\mathrm{h},k}$ with $\mu^{\mathrm{B}}_{\mathrm{e}} = \mu^{\mathrm{B}}_{\mathrm{h}}$. Note, however, that the unknown variables contained in Eqs. (16.17) and (16.18) are determined by the BEC-BCS-LASER crossover theory (Eqs. (16.11), (16.12) and (16.13) with Eqs. (16.14′), (16.15) and (16.16)) rather than the BCS theory. In the BCS phase, the existence of the gap around $\pm\mu/2$ means the formation of Cooper pairs around the Fermi level because $\pm\mu/2$ is equivalent to the Fermi level. In contrast, in the lasing phase, $\pm\mu/2$ corresponds to the laser frequency.[11] Thus, the gap indicates the formation of bound e-h pairs by mediating photons around the laser frequency. The semiconductor laser in Fig. 16.3 is drawn along this picture, where the e-h pairs are explicitly depicted.

Such a "lasing gap" is, at least in principle, measureable in the optical gain spectrum $G(\omega)$ by irradiating probe light with frequency ω because $G(\omega)$ is

[11] The origin of the gap is analogous to the Rabi splitting in resonance fluorescence [20, 27, 36, 37].

strongly affected by the renormalized band structure in general. As a result, in the gain spectrum of the lasing phase (Fig. 16.7B), there appears a transparent region originating from the gap. The optical gain spectrum is thus one of important ways for the verification of the lasing gap.

In addition, we note that behaviors of the gain spectra vary drastically when the exciton-polariton BEC is changed to the laser phase. By comparing Fig. 16.7A, B, for example, one can find only absorption but no gain in Fig. 16.7A. This is mainly because there is no k-region with inverted population $N_k > 0$ ($\Leftrightarrow n_{\mathrm{h},k} = n_{\mathrm{e},k} > 0.5$) in Fig. 16.6A. In contrast, optical gain is caused in Fig. 16.7B because there are k-regions with $N_k > 0$ in Fig. 16.6B. Thus, the existence of the gain after the second threshold gives us important information to identify the phases in the system.[12]

16.5 Conclusions and Perspectives

In this contribution, we have presented a brief explanation of the BCS theory and the MSBE in the exciton-polariton system, to highlight their similarities and differences. We have then shown a framework of describing the BCS theory (the BEC and BCS phases) and the MSBE (the semiconductor laser) in a unified way. As a result, the existence of bound e-h pairs in the lasing phase as well as the lasing gap have been pointed out. The results presented here are the physics elucidated for the first time by considering the BEC, BCS, and Laser phases in a unified way. However, for example, effects of spontaneous emission [36] and pure dephasing [38] are still unclear. In this respect, further studies are needed for a full understanding of this system. Experimantal studies are also important, in particular, in a high density regime [28–34, 39].

Although we have focused on the exciton-polariton system in this contribution, we finally would like to emphasize that this system has a close relationship with superconductors and the Feshbach resonance in cold atom systems because interacting Fermi and Bose particles play important roles in the formation of ordered phases. In this sense, it would be interesting to study the lasing gap by terahertz pulses in a manner similar to superconductors [40, 41]. Inclusions of the e-h center-of-mass fluctuations with mass imbalance are also important, as discussed in the cold atom systems [42], because these effects cannot be taken into account within the mean-field approximation. We further note that fundamental problems of the nonequilibrium statistical physics are also included in this system in the sense of providing a bridge between the equilibrium and the nonequilibrium phases. We hope that our approach also stimulates new studies in a wide range of such fields.

[12] In fact, the second threshold and the blue-shift can also be caused by a different mechanism even if the system remains in quasi-equilibrium. In this situation, however, the gain spectrum shows only absorption [19].

Acknowledgements The authors are grateful to K. Kamide, R. Nii, Y. Yamamoto, T. Horikiri, Y. Shikano, Y. Matsuo, T. Yuge, and M. Bamba for fruitful discussions. This work is supported by the JSPS through its FIRST Program, and DYCE, KAKENHI No. 20104008.

Appendix 1: Excitonic Effects in the Low Density Limit

In semiconductor exciton-polariton systems, the excitonic effects play quite important roles in the formation of Coulomb-bound e-h pairs (excitons) and exciton-polaritons. In this Appendix, we, therefore, confirm the excitonic effects in our formalism.[13]

For this purpose, we now assume that the density of electrons and holes are sufficiently low ($n_{e,k}, n_{h,k} \ll 1$ or $N_k \cong -1$) with no pumping and loss ($\gamma = 0$ and $\kappa = 0$). Under this condition, $2\tilde{\xi}^{+}_{eh,k}$ in Eq. (16.12) can be written as

$$2\tilde{\xi}^{+}_{eh,k} = \epsilon_{e,k} + \epsilon_{h,k} - \mu = \frac{k^2}{2m_r} + E_g - \mu, \tag{16.19}$$

where $1/m_r = 1/m_e + 1/m_h$. Then, Eqs. (16.11) and (16.12) can be described as

$$0 = -(\epsilon_{ph,0} - \mu)a_0 + g\sum_k p_k, \tag{16.20}$$

$$0 = -\left(\frac{k^2}{2m_r} + E_g - \mu\right)p_k + g^* a_0 + \sum_{k'} U'_{k'-k}p_{k'}, \tag{16.21}$$

where the definition of $\Delta_k \equiv g^* a_0 + \sum_{k'} U'_{k-k'}p_{k'}$ is used. Especially, for $g = 0$ in Eq. (16.21), we obtain

$$\frac{k^2}{2m_r}p_k - \sum_{k'} U'_{k'-k}p_{k'} = -(E_g - \mu)p_k, \tag{16.22}$$

which is nothing but the Schrödinger equation in k-space for the single exciton bound state [19, 25, 26]. This means that the Coulomb-bound e-h pairs (excitons) can be formed in the low density limit in the presented formalism. In such a case, p_k can be described by the bound state e-h pair wave-function ϕ_k ($p_k = \eta\phi_k$ with $\sum_k |\phi_k|^2 = 1$) with $\mu = E_{ex}$, where E_{ex} is the energy level of the exciton and the binding energy corresponds to $E_g - E_{ex}$. The formation of the exciton is, thus, includeed in the theory.

[13] Discussion in Appendix 1 is reproduced from the supplemental material in Ref. [20].

Although p_k is changed from the exciton wave-function ϕ_k by the photon-mediated attraction in the case of $g \neq 0$, it is instructive to consider the case where such an effect is not so large. In this limit, by substituting $p_k \cong \eta\phi_k$ into Eqs. (16.20) and (16.21), we obtain

$$0 = (\mu - E_{\rm cav})a_0 + g_{\rm ex}\eta, \tag{16.23}$$

$$0 = (\mu - E_{\rm ex})\eta + g^*_{\rm ex}a_0, \tag{16.24}$$

where $g_{\rm ex} \equiv g\sum_k \phi_k = g\phi_{\rm ex}(r = 0)$ is the coupling constant renormalized by the exciton wave-function. Then, μ is given by one of the eigenvalues of these two coupled equations, which are the eigen-energies of the upper and lower polaritons:

$$E_{\rm UP/LP} = \frac{E_{\rm cav} + E_{\rm ex} \pm \sqrt{(E_{\rm cav} - E_{\rm ex})^2 + 4|g_{\rm ex}|^2}}{2}. \tag{16.25}$$

Here, $E_{\rm UP}$ and $E_{\rm LP}$ in Eq. (16.25) are the well-known expressions obtained when the excitons are treated as simple bosons [25]. This means that the formation of exciton-polaritons are also included in the theory. The excitonic effects are, thus, taken into account in our formalism within the mean-field approximation. We note that the procedure shown here is basically the same as Section 2.1.2 in Ref. [19].

Appendix 2: Proof of Equivalence

In the main text, we have mentioned that the formalism in Ref. [19] seems quite different from the MSBE. This formalism can be described by the follwoing simultaneous equations with the unknown variables of Δ_k, $n_{{\rm e},k}$, $n_{{\rm h},k}$, and μ:

$$\Delta_k = \sum_{k'} U^{{\rm eff},\kappa}_{k',k}\Delta_{k'}\int_{-\infty}^{\infty}\frac{{\rm d}\nu}{2\pi}L_{k'}(\nu) \times\left\{(F^{\rm B}_{\rm e}(\nu) + F^{\rm B}_{\rm h}(\nu))(\nu - \tilde{\xi}^-_{{\rm eh},k'}) + (F^{\rm B}_{\rm e}(\nu) - F^{\rm B}_{\rm h}(\nu))(\tilde{\xi}^+_{{\rm eh},k'} + {\rm i}\gamma)\right\}, \tag{16.26}$$

$$n_{{\rm e(h)},k} = \frac{1}{2} \mp \int_{-\infty}^{\infty}\frac{{\rm d}\nu}{2\pi}L_k(\nu)\left\{F^{\rm B}_{\rm e(h)}(\nu)[(\nu \pm \tilde{\xi}_{{\rm h(e)},k})^2 + \gamma^2] + F^{\rm B}_{\rm h(e)}(\nu)|\Delta_k|^2\right\}, \tag{16.27}$$

where $U^{{\rm eff},\kappa}_{k',k} \equiv |g|^2/(\xi_{{\rm ph},0} - {\rm i}\kappa) + U'_{k'-k}$ and

$$L_k(\nu) \equiv \frac{\gamma}{[(\nu - \tilde{\xi}^-_{{\rm eh},k} - E_k)^2 + \gamma^2][(\nu - \tilde{\xi}^-_{{\rm eh},k} + E_k)^2 + \gamma^2]}. \tag{16.28}$$

$F_{\rm e}^{\rm B}(\nu)$ and $F_{\rm h}^{\rm B}(\nu)$ are respectively defined as

$$F_{\rm e}^{\rm B}(\nu) \equiv \tanh\left(\frac{\beta[\nu-\mu_{\rm e}^{\rm B}+\mu/2]}{2}\right) = 1-2f_{\rm e}^{\rm B}(\nu), \tag{16.29}$$

$$F_{\rm h}^{\rm B}(\nu) \equiv \tanh\left(\frac{\beta[\nu+\mu_{\rm h}^{\rm B}-\mu/2]}{2}\right) = 2f_{\rm h}^{\rm B}(-\nu)-1. \tag{16.30}$$

In this Appendix 2, therefore, we prove that Eqs. (16.26), (16.27), (16.28), (16.29) and (16.30) are equivalent to Eqs. (16.11), (16.12) and (16.13) with Eqs. (16.14′), (16.15) and (16.16) under the steady-state condition $\partial_t\langle\hat{O}\rangle = 0$.

For this purpose, we here note that the following sum rule is satisfied for the single-partice spectral function:

$$\int_{-\infty}^{\infty}\frac{{\rm d}\nu}{2\pi}A_{\alpha\alpha'}(\nu;k) = \delta_{\alpha,\alpha'}. \tag{16.31}$$

This relation can be confirmed by the direct integration of $A_{\alpha\alpha'}(\nu;k)$ described by elements of a matrix

$$\begin{aligned} A(\nu;k) &= \frac{-2}{|D_k(\nu)|^2}\begin{pmatrix} {\rm Im}[D_k^*(\nu)(\nu+\tilde{\xi}_{{\rm h},k}+{\rm i}\gamma)] & {\rm Im}[D_k(\nu)]\Delta_k \\ {\rm Im}[D_k(\nu)]\Delta_k^* & {\rm Im}[D_k^*(\nu)(\nu-\tilde{\xi}_{{\rm e},k}+{\rm i}\gamma)] \end{pmatrix} \\ &= \frac{-2\gamma}{|D_k(\nu)|^2}\begin{pmatrix} -[(\nu+\tilde{\xi}_{{\rm h},k})^2+\gamma^2+|\Delta_k|^2] & 2\Delta_k(\nu-\tilde{\xi}_{{\rm eh},k}^-) \\ 2\Delta_k^*(\nu-\tilde{\xi}_{{\rm eh},k}^-) & -[(\nu-\tilde{\xi}_{{\rm e},k})^2+\gamma^2+|\Delta_k|^2] \end{pmatrix}, \end{aligned} \tag{16.32}$$

which is obtained from the definition of Eq. (16.16) with Eq. (16.15):

$$G_k^{\rm R}(\nu) = \frac{1}{|D_k(\nu)|^2}\begin{pmatrix} D_k^*(\nu)(\nu+\tilde{\xi}_{{\rm h},k}+{\rm i}\gamma) & -D_k^*(\nu)\Delta_k \\ -D_k^*(\nu)\Delta_k^* & D_k^*(\nu)(\nu-\tilde{\xi}_{{\rm e},k}+{\rm i}\gamma) \end{pmatrix}, \tag{16.33}$$

where

$$D_k(\nu) \equiv (\nu-\tilde{\xi}_{{\rm eh},k}^-+E_k+{\rm i}\gamma)(\nu-\tilde{\xi}_{{\rm eh},k}^--E_k+{\rm i}\gamma). \tag{16.34}$$

The diagonal element $A_{11(22)}(\nu;k)$ can then be described as Eq. (16.17). In the following, by using thse expressions, Eqs. (16.26) and (16.27) are derived from Eqs. (16.11), (16.12) and (16.13) with Eqs. (16.14′), (16.15) and (16.16).

ν-integral forms of N_k and p_k: First, we discuss ν-integral forms of the population inversion $N_k \equiv n_{{\rm e},k}+n_{{\rm h},k}-1$ and the polarization function p_k because Eqs. (16.26) and (16.27) are described by the integration with respect to ν. From Eqs. (16.13) and (16.14′) with $\partial_t n_{{\rm e(h)},k} = 0$, we obtain

$$N_k = -\frac{2}{\gamma}\,\mathrm{Im}[\Delta_k p_k^*] + \int_{-\infty}^{\infty}\frac{\mathrm{d}\nu}{2\pi}\left\{f_{\mathrm{e}}^{\mathrm{B}}(\nu)A_{11}(\nu;k) - (1-f_{\mathrm{h}}^{\mathrm{B}}(-\nu))A_{22}(\nu;k)\right\}. \tag{16.35}$$

where Eq. (16.31) is used. In a similar manner, from Eqs. (16.12) and (16.14′) with $\partial_t p_k = 0$,

$$p_k = -\frac{\Delta_k}{2(\tilde{\xi}^+_{\mathrm{eh},k} - \mathrm{i}\gamma)}N_k + \frac{\gamma}{\tilde{\xi}^+_{\mathrm{eh},k} - \mathrm{i}\gamma}\int_{-\infty}^{\infty}\frac{\mathrm{d}\nu}{2\pi}\left\{[1-f_{\mathrm{h}}^{\mathrm{B}}(-\nu)]G_{12}^{\mathrm{R}}(\nu;k) - f_{\mathrm{e}}^{\mathrm{B}}(\nu)G_{21}^{\mathrm{R}*}(\nu;k)\right\}. \tag{16.36}$$

Therefore, with Eqs. (16.32) and (16.33), substitution of Eq. (16.36) into Eq. (16.35) yields

$$N_k = \int_{-\infty}^{\infty}\frac{\mathrm{d}\nu}{2\pi}\frac{2\gamma}{|D_k(\nu)|^2}\Big\{f_{\mathrm{e}}^{\mathrm{B}}(\nu)[(\nu+\tilde{\xi}_{\mathrm{h},k})^2 - |\Delta_k|^2 + \gamma^2] + [f_{\mathrm{h}}^{\mathrm{B}}(-\nu) - 1][(\nu-\tilde{\xi}_{\mathrm{e},k})^2 - |\Delta_k|^2 + \gamma^2]\Big\}. \tag{16.37}$$

By substituting Eq. (16.37) into Eq. (16.36), we also find

$$p_k = \Delta_k\int_{-\infty}^{\infty}\frac{\mathrm{d}\nu}{2\pi}\frac{2\gamma}{|D_k(\nu)|^2}\Big\{[f_{\mathrm{h}}^{\mathrm{B}}(-\nu) - 1](\nu - \tilde{\xi}_{\mathrm{e},k} - \mathrm{i}\gamma) - f_{\mathrm{e}}^{\mathrm{B}}(\nu)(\nu + \tilde{\xi}_{\mathrm{h},k} + \mathrm{i}\gamma)\Big\}. \tag{16.38}$$

Although the derivation of Eqs. (16.37) and (16.38) is straightforward, the following equations would be useful in the derivation:

$$\pm|\Delta_k|^2\,\mathrm{Im}[D_k(\nu)(\tilde{\xi}^+_{\mathrm{eh},k} - \mathrm{i}\gamma)] + ([\tilde{\xi}^+_{\mathrm{eh},k}]^2 + \gamma^2)\,\mathrm{Im}[D_k^*(\nu)(\nu \mp \tilde{\xi}_{\mathrm{e(h)},k} + \mathrm{i}\gamma)] = -\gamma(E_k^2 + \gamma^2)((\nu \mp \tilde{\xi}_{\mathrm{e(h)},k})^2 - |\Delta_k|^2 + \gamma^2), \tag{16.39}$$

$$(\nu + \tilde{\xi}_{\mathrm{h}})^2 - |\Delta_k|^2 + \gamma^2 - D_k(\nu) = 2(\tilde{\xi}^+_{\mathrm{eh},k} - \mathrm{i}\gamma)(\nu + \tilde{\xi}_{\mathrm{h}} + \mathrm{i}\gamma), \tag{16.40}$$

$$(\nu - \tilde{\xi}_{\mathrm{e}})^2 - |\Delta_k|^2 + \gamma^2 - D_k^*(\nu) = -2(\tilde{\xi}^+_{\mathrm{eh},k} - \mathrm{i}\gamma)(\nu - \tilde{\xi}_{\mathrm{e}} - \mathrm{i}\gamma). \tag{16.41}$$

The ν-integral forms of N_k and p_k are thus obtained as Eqs. (16.37) and (16.38), respectively. These expressions are helpful to find the ν-integral forms of Δ_k, $n_{\mathrm{e},k}$, and $n_{\mathrm{h},k}$, which turn out to be the same as Eqs. (16.26), (16.27), (16.28), (16.29), and (16.30), as shown below.

Derivation of $\boldsymbol{\Delta_k}$: From the definition of $\Delta_k \equiv g^* a_0 + \sum_{k'} U'_{k-k'} p_{k'}$ and Eq. (16.11) with $\partial_t a_0 = 0$, Δ_k can be described as

$$\Delta_k = \sum_{k'} \left\{ \frac{|g|^2}{\xi_{\mathrm{ph},0} - \mathrm{i}\kappa} + U'_{k'-k} \right\} p_{k'} = \sum_{k'} U^{\mathrm{eff},\kappa}_{k',k} p_{k'}. \tag{16.42}$$

Therefore, after the substitution of Eq. (16.38) into Eq. (16.42), we obtain

$$\Delta_k = \sum_{k'} U^{\mathrm{eff},\kappa}_{k',k} \Delta_{k'} \int_{-\infty}^{\infty} \frac{\mathrm{d}\nu}{2\pi} L_{k'}(\nu) \Big\{ [F^{\mathrm{B}}_{\mathrm{h}}(\nu) - 1][\nu - \tilde{\xi}_{\mathrm{e},k'} - \mathrm{i}\gamma] + [F^{\mathrm{B}}_{\mathrm{e}}(\nu) - 1][\nu + \tilde{\xi}_{\mathrm{h},k'} + \mathrm{i}\gamma] \Big\}, \tag{16.43}$$

where the definitions of Eqs. (16.28), (16.29) and (16.30) are used with $L_k(\nu) = \gamma/|D_k(\nu)|^2$. This equation can be rewritten as

$$\Delta_k = \sum_{k'} U^{\mathrm{eff},\kappa}_{k',k} \Delta_{k'} \int_{-\infty}^{\infty} \frac{\mathrm{d}\nu}{2\pi} L_{k'}(\nu) \Big\{ (F^{\mathrm{B}}_{\mathrm{e}}(\nu) + F^{\mathrm{B}}_{\mathrm{h}}(\nu) - 2)(\nu - \tilde{\xi}^{-}_{\mathrm{eh},k'}) + (F^{\mathrm{B}}_{\mathrm{e}}(\nu) - F^{\mathrm{B}}_{\mathrm{h}}(\nu))(\tilde{\xi}^{+}_{\mathrm{eh},k'} + \mathrm{i}\gamma) \Big\}. \tag{16.44}$$

By noting $\int \frac{\mathrm{d}\nu}{2\pi} L_{k'}(\nu)(\nu - \tilde{\xi}^{-}_{\mathrm{eh},k'}) = 0$, we thus find that Eq. (16.44) is equivalent to Eq. (16.26).

Derivation of $n_{\mathrm{e},k}$ and $n_{\mathrm{h},k}$: Our remaining task is now to derive the ν-integral forms of $n_{\mathrm{e},k}$ and $n_{\mathrm{h},k}$. By multiplying Δ_k by the complex conjugate of Eq. (16.38),

$$\frac{1}{\gamma} \mathrm{Im}[\Delta_k p^*_k] = |\Delta_k|^2 \int_{-\infty}^{\infty} \frac{\mathrm{d}\nu}{2\pi} \frac{2\gamma}{|D_k(\nu)|^2} \{ f^{\mathrm{B}}_{\mathrm{e}}(\nu) + f^{\mathrm{B}}_{\mathrm{h}}(-\nu) - 1 \}, \tag{16.45}$$

can be obtained. The substitution of Eq. (16.45) into Eq. (16.13) with $\partial_t n_{\mathrm{e(h)},k} = 0$, then, yields

$$n_{\mathrm{e(h)},k} = \int_{-\infty}^{\infty} \frac{\mathrm{d}\nu}{2\pi} \frac{2\gamma}{|D_k(\nu)|^2} \Big\{ [(\nu \pm \tilde{\xi}_{\mathrm{h(e)},k})^2 + \gamma^2] f^{\mathrm{B}}_{\mathrm{e(h)}}(\pm\nu) - |\Delta_k|^2 [f^{\mathrm{B}}_{\mathrm{h(e)}}(\mp\nu) - 1] \Big\}, \tag{16.46}$$

which can be rewritten as

$$n_{\mathrm{e(h)},k} = \int_{-\infty}^{\infty} \frac{\mathrm{d}\nu}{2\pi} L_k(\nu) \Big\{ [(\nu \pm \tilde{\xi}_{\mathrm{h(e)},k})^2 + \gamma^2 + |\Delta_k|^2] \mp [(\nu \pm \tilde{\xi}_{\mathrm{h(e)},k})^2 + \gamma^2] F^{\mathrm{B}}_{\mathrm{e(h)}}(\nu) \mp |\Delta_k|^2 F^{\mathrm{B}}_{\mathrm{h(e)}}(\nu) \Big\}. \tag{16.47}$$

We then find that Eq. (16.47) is identical to Eq. (16.27) because, from Eqs. (16.31) and (16.32),

$$\int_{-\infty}^{\infty} \frac{\mathrm{d}\nu}{2\pi} L_k(\nu)[(\nu \pm \tilde{\xi}_{\mathrm{h(e)},k})^2 + \gamma^2 + |\Delta_k|^2] = \frac{1}{2}. \tag{16.48}$$

Thus, we have shown that Eqs. (16.26) and (16.27) are derived from Eqs. (16.11), (16.12) and (16.13) with Eqs. (16.14), (16.14′), (16.15) and (16.16). This means that the formalism in Ref. [19] is equivalent to Eqs. (16.11), (16.12) and (16.13) with Eqs. (16.14′), (16.15) and (16.16).

References

1. C. Weisbuch, M. Nishioka, A. Ishikawa, Y. Arakawa, Phys. Rev. Lett. **69**, 3314 (1992)
2. J. Bloch, T. Freixanet, J.Y. Marzin, V. Thierry-Mieg, R. Planel, Appl. Phys. Lett. **73**, 1694 (1998)
3. A. Imamoglu, R.J. Ram, S. Pau, Y. Yamamoto, Phys. Rev. A **53**, 4250 (1996)
4. H. Deng, G. Weihs, C. Santori, J. Bloch, Y. Yamamoto, Science **298**, 199 (2002)
5. J. Kasprzak, M. Richard, S. Kundermann, A. Baas, P. Jeambrun, J.M.J. Keeling, F.M. Marchetti, M.H. Szymanska, R. Andre, J.L. Staehli, V. Savona, P.B. Littlewood, B. Deveaud, L.S. Dang, Nature **443**, 409 (2006)
6. D. Bajoni, P. Senellart, E. Wertz, I. Sagnes, A. Miard, A. Lemaître, J. Bloch, Phys. Rev. Lett. **100**, 047401 (2008)
7. H. Deng, G. Weihs, D. Snoke, J. Bloch, Y. Yamamoto, Proc. Natl. Acad. Sci. USA **100**, 15318 (2003)
8. J. Kasprzak, D.D. Solnyshkov, R. André, L.S. Dang, G. Malpuech, Phys. Rev. Lett. **101**, 146404 (2008)
9. D. Snoke, in *Exciton Polaritons in Microcavities*, ed. by D. Sanvitto, V. Timofeev. Springer Series in Solid-State Sciences, vol. 172 (Springer, Berlin/Heidelberg, 2012), pp. 307–327
10. L.V. Keldysh, Y.V. Kopaev, Sov. Phys. Solid State **6**, 2219 (1965)
11. P.B. Littlewood, P.R. Eastham, J.M.J. Keeling, F.M. Marchetti, B.D. Simons, M.H. Szymanska, J. Phys.: Condens. Matter **16**(35), S3597 (2004)
12. Y. Ohashi, A. Griffin, Phys. Rev. Lett. **89**, 130402 (2002)
13. Y. Ohashi, A. Griffin, Phys. Rev. A **67**, 063612 (2003)
14. K. Kamide, T. Ogawa, Phys. Rev. Lett. **105**, 056401 (2010)
15. T. Byrnes, T. Horikiri, N. Ishida, Y. Yamamoto, Phys. Rev. Lett. **105**, 186402 (2010)
16. W. Chow, H. Schneider, S. Koch, C.H. Chang, L. Chrostowski, C. Chang-Hasnain, IEEE J. Quantum Electron. **38**, 402 (2002)
17. K. Kamide, T. Ogawa, Phys. Status Solidi (c) **8**, 1250 (2011)
18. N. Berloff, J. Keeling, in *Physics of Quantum Fluids*, ed. by A. Bramati, M. Modugno. Springer Series in Solid-State Sciences, vol. 177 (Springer, Berlin/Heidelberg, 2013), pp. 19–38
19. M. Yamaguchi, K. Kamide, T. Ogawa, Y. Yamamoto, New J. Phys. **14**, 065001 (2012)
20. M. Yamaguchi, K. Kamide, R. Nii, T. Ogawa, Y. Yamamoto, Phys. Rev. Lett. **111**, 026404 (2013)
21. M.H. Szymańska, J. Keeling, P.B. Littlewood, Phys. Rev. Lett. **96**, 230602 (2006)
22. M.H. Szymańska, J. Keeling, P.B. Littlewood, Phys. Rev. B **75**, 195331 (2007)
23. J. Keeling, M.H. Szymańska, P.B. Littlewood, in *Optical Generation and Control of Quantum Coherence in Semiconductor Nanostructures*, ed. by G. Slavcheva, P. Roussignol. NanoScience and Technology (Springer, Berlin/Heidelberg, 2010), pp. 293–329

24. H. Deng, H. Haug, Y. Yamamoto, Rev. Mod. Phys. **82**, 1489 (2010)
25. H. Haug, S. Koch, *Quantum Theory of the Optical and Electronic Properties of Semiconductors* (World Scientific, Singapore/River Edge, 2004)
26. C. Comte, P. Nozieres, J. Phys. France **43**, 1069 (1982)
27. K. Henneberger, F. Herzel, S.W. Koch, R. Binder, A.E. Paul, D. Scott, Phys. Rev. A **45**, 1853 (1992)
28. R. Balili, B. Nelsen, D.W. Snoke, L. Pfeiffer, K. West, Phys. Rev. B **79**, 075319 (2009)
29. B. Nelsen, R. Balili, D.W. Snoke, L. Pfeiffer, K. West, J. Appl. Phys. **105**, 122414 (2009)
30. L.S. Dang, D. Heger, R. André, F. Boeuf, R. Romestain, Phys. Rev. Lett. **81**, 3920 (1998)
31. J.S. Tempel, F. Veit, M. Aßmann, L.E. Kreilkamp, A. Rahimi-Iman, A. Löffler, S. Höfling, S. Reitzenstein, L. Worschech, A. Forchel, M. Bayer, Phys. Rev. B **85**, 075318 (2012)
32. J.S. Tempel, F. Veit, M. Aßmann, L.E. Kreilkamp, S. Höfling, M. Kamp, A. Forchel, M. Bayer, New J. Phys. **14**, 083014 (2012)
33. P. Tsotsis, P.S. Eldridge, T. Gao, S.I. Tsintzos, Z. Hatzopoulos, P.G. Savvidis, New J. Phys. **14**, 023060 (2012)
34. E. Kammann, H. Ohadi, M. Maragkou, A.V. Kavokin, P.G. Lagoudakis, New J. Phys. **14**, 105003 (2012)
35. A.A. Abrikosov, L.P. Gorkov, I.E. Dzyaloshinski, R.A. Silverman, *Methods of Quantum Field Theory in Statistical Physics* (Pergamon Press, New York, 1975)
36. M.O. Scully, M.S. Zubairy, *Quantum Optics* (Cambridge University Press, New York, 1997)
37. S. Schmitt-Rink, D.S. Chemla, H. Haug, Phys. Rev. B **37**, 941 (1988)
38. M. Yamaguchi, T. Asano, S. Noda, Rep. Prog. Phys. **75**(9), 096401 (2012)
39. T. Horikiri, Y. Matsuo, Y. Shikano, A. Löffler, S. Höfling, A. Forchel, Y. Yamamoto, J. Phys. Soc. Jpn. **82**(8), 084709 (2013)
40. R. Matsunaga, Y.I. Hamada, K. Makise, Y. Uzawa, H. Terai, Z. Wang, R. Shimano, Phys. Rev. Lett. **111**, 057002 (2013)
41. T. Papenkort, V.M. Axt, T. Kuhn, Phys. Rev. B **76**, 224522 (2007)
42. R. Hanai, T. Kashimura, R. Watanabe, D. Inotani, Y. Ohashi, Phys. Rev. A **88**, 053621 (2013)

Chapter 17
High-Orbital Exciton-Polariton Condensation: Towards Quantum-Simulator Applications

Na Young Kim, Kenichiro Kusudo, Tim Byrnes, Naoyuki Masumoto, and Yoshihisa Yamamoto

17.1 Introduction

Indistinguishable quantum particles are divided into two groups according to spin statistics: fermions and bosons [1]. As known as the Pauli exclusion principle, two fermions, spin-half-integer particles, can not occupy the same quantum state simultaneously according to Fermi-Dirac statistics. In contrast, spin-integer particles, bosons can, under suitable circumstances, accumulate in one quantum state predominantly, a phenomenon generally called "condensation" governed by Bose-Einstein statistics.

In atomic physics, electronic orbital and spin configurations are explained by the fermionic statistics and exclusion principle. Physical and chemical properties of electronic material systems are closely linked to the orbital and spin nature of valence electrons, and thus many theories, ranging from a simple to a sophisticated level, have been developed to capture key features of various material systems [2]. Despite the success of these theories, some materials still elude complete understanding, for example, high temperature superconductors, transitional metal oxides, magnetic materials and topological materials. The difficulty of these materials is

N.Y. Kim (✉)
Edward L. Ginzton Laboratory, Stanford University, 348 Via Pueblo Mall, Stanford, CA 94305, USA
e-mail: nayoungstanford@gmail.com

K. Kusudo • T. Byrnes • N. Masumoto
National Institute of Informatics, 2-1-2 Hitotsubashi, Chiyoda-ku, Tokyo 101-8430, Japan
e-mail: kusudo@nii.ac.jp

Y. Yamamoto
ImPACT Program, Council for Science Technology and Innovation, Tokyo, Japan
e-mail: yyamamoto@stanford.edu

Y. Yamamoto, K. Semba (eds.), *Principles and Methods of Quantum Information Technologies*, Lecture Notes in Physics 911, DOI 10.1007/978-4-431-55756-2_17

thought to originate from the coupling among orbital, spin degrees of freedom as well as many-body interactions [2, 3]. Understanding these effect is one of the core problems in condensed matter physics at present.

The study of many-body bosonic systems have an equally varied and interesting history. In the early 1920s, Einstein predicted using a quantum statistical approach, noninteracting identical bosons would occupy a unique quantum state of the system, a phenomenon referred to as Bose-Einstein condensation (BEC) [1, 4–6]. The physics of BEC is deep and rich. It has been anticipated that it would be fundamentally related to fascinating effects such as superfluidity in Helium-4 liquid [7, 8] and superconductivity [9]. Since its prediction, 70 years passed before it was actually observed in a laboratory setting for a weakly interacting dilute gas of bosonic atoms [10, 11] by harnessing laser cooling and magnetic evaporative cooling techniques [12–14]. Experimental evidence of the atomic BEC is found from the velocity distribution of particles. Below the transition critical temperature, the population of atoms with the close-to-zero velocity values surges, whereas the velocity distribution of atoms above the transition temperature is thermally populated [10, 11]. The atoms in the lowest state share the same macroscopic quantum phase to exhibit quantum interference [10, 11]. This collective quantum state obeys Bose-Einstein statistics with a chemical potential much smaller than thermal energy. The BEC state is described by a macroscopic order parameter with an average density and a fixed phase as a consequence of spontaneous symmetry breaking.

Besides dilute cold atom gases, BEC also appears in elementary excitations (or quasiparticles) in solids. Superconductivity can be understood as a BEC of Cooper pairs, composite quasi-bosonic particles consisting of two electrons [9]. Magnons, quanta of magnetic excitations, also exhibit BEC resulting in magnetic ordering [15, 16]. Photon BEC has been recently observed in dye-filled cavities [17]. In solid state systems, there has been a long history of realizing BEC with quasiparticles. In this regard, excitons and exciton-polaritons in semiconductors are the most studied systems [4, 18]. This chapter focuses on the exciton-polariton condensation in GaAs-based semiconductors, reviewing its fundamental properties as well as unique dynamic nature of condensation. In particular, we give an overview of recent efforts to demonstrate coherent exciton-polaritons with different orbital symmetries by placing them to various two-dimensional lattice potentials. We envision that the polariton-lattice system would be a promising solid-state platform for quantum simulation applications [19, 20], which would address unresolved quantum phenomena in various fields including condensed matter physics, high energy physics and chemistry [21, 22].

The chapter is constructed as follows: Sect. 17.2 introduces the basics of exciton-polaritons and their fundamental condensation properties without any external lattices, followed by the technical probes to identify condensation properties. In Sect. 17.3, we explain our methods to engineer exciton-polariton condensation with various lattice potential geometries, and the experimental signatures of the exciton-polartions in artificial band structures are shown. Our current understanding on the physics of the polariton-lattice system is presented. Finally, we remark

on perspectives of this newly established solid-state particle-lattice system in the context of quantum simulation and the insights of unknown phenomena in Sect. 17.4.

17.2 Microcavity Exciton-Polaritons

In semiconductors, the crystal ground state in thermal equilibrium, namely the vacuum state, has all electrons in the valence band and none in the conduction band with an energy gap (E_g) separating two bands. Electrically it is insulating due to the lack of free electrons, and optically it is dark. Suppose that the system is disturbed by an external energy source either electrically or optically, and the energy of the external stimulation is equal to or bigger than E_g. The system then departs from equilibrium and responds to the disturbance such that electrons in the valence band are promoted to the conduction band, leaving positively-charged holes behind in the valence band. An electron (e) and a hole (h), which are oppositely charged particles, experience a Coulomb attraction to form a bound state. Its bound state is the elementary electronic excitation in semiconductors. This excitation behaves a quasiparticle, that may freely move within the semiconductor and is called an *exciton*.

Exciton As a bound e-h pair, the relative coordinate wavefunction is hydrogen (H)-like, whereas the center-of-mass wavefunction is a plane wave. In semiconductors, we should consider the effect of many electrons, which forms bands. A mean-field treatment is successful to handle many-body problems in terms of a single particle description by averaging the effect of all individual particles. In this approximation, two physical quantities to describe excitons, the Bohr radius (a_B) and the binding energy (E_B), have the same forms of those in the hydrogen atom except for the effective mass (m^*) of the particle and the relative permittivity (ϵ_r) of the medium: $a_B = \epsilon_r\epsilon_0\hbar^2/e^2m^* \sim 0.53\epsilon_r/(m^*/m_0)$ in unit of Å, and $E_B = m^*e^4/h^2\epsilon_r^2\epsilon_0^2 = \hbar^2/2m^*(a_B)^2 \sim 13.6(m^*/m_0)/\epsilon_r^2$ in unit of eV, where ϵ_0 is the vacuum permittivity, and $\hbar$ is the planck constant h divided by 2π. For example, the effective mass of a heavy-hole exction in bulk GaAs is around $0.06m_e$, much lighter than the bare electron mass m_e and ϵ_r is 12.9, yielding that E_B is around 5 meV and a_B is around 11.4 nm. Excitons are composite bosons consisting of two fermions, and in the dilute density limit where excitons do not overlap, they are predicted to undergo BEC phase transition [4, 18]. Excitonic condensation has been intensely studied both in theory and experiments [18, 23, 24].

The excitonic effect is significantly magnified in confined structures. Thanks to recent semiconductor growth techniques such as molecular beam epitaxy and MOCVD, low-dimensional structures (a quantum-well (QW), a quantum wire and a quantum dot) are readily made, where quantum confinement effects are essential. A QW is a thin layer of a small bandgap semiconductor surrounded by a large bandgap semiconductors such that charge carriers are free in a transverse plane but confined in the growth direction. The enhanced excitonic effect in the QW can be

qualitatively understood as follows: in contrast to the bulk, the exciton Bohr radius is often smaller than the QW thickness so that excitons are squeezed inside the QW, reducing the average distance of electrons and holes. The stronger Coulomb interaction between electrons and holes binds the excitons more tightly, leading to a bigger binding energy of QW excitons and a reduced Bohr radius. The GaAs QW exciton has a binding energy $E_B \sim 10\,\text{meV}$ and a Bohr a_B around 6 nm.

Cavity photon Using the same growth techniques, a cavity (or a resonator) to confine photons can be prepared monolithically in the same semiconductors. By alternating $\lambda/4$-thick semiconductors with different refractive indices multiple times (λ is the wavelength of light in semiconductors), a dielectric mirror can be constructed. It is called a *distributed Bragg reflector* (DBR), where optical fields with wavelengths close to λ are reflected owing to the constructive interference of the partial refections at the interfaces of two semiconductors. A stop band is the wavelength range where the reflectance is close to 1. While there are many shapes and sizes of microcavities [25], a pair of the DBRs form a simple 2D Fabry-Perot resonator, where the light can bounce back and forth for a characteristic time determined by the quality factor of the resonator. This planar resonator has advantages in semiconductor photonic devices since it can be monolithically grown with aforementioned quantum confined structures, quantum wires, quantum dots and QWs. The microcavity size is on the order of the wavelength λ, where only one longitudinal mode is allowed. The quality factor Q of the microcavity is a dimensionless quantity, defined as the ratio between the full-width at half maximum of a cavity mode and the mode center frequency. A high Q value means the narrow linewidth, equivalently a long photon lifetime. A typical $Q \sim 1000$ in GaAs-based semiconductor corresponds to a photon lifetime, roughly a few ps. The record Q value in the Fabry-Perot is on the order of 1 million, confining photons close to $1\,\mu\text{s}$.

The 2D microcavity modifies the character of confined photons: first, the photon density of states is quantized similar to the quantization of the electron density of states in nanostructures; second, the ordinarily massless photons gain an effective mass. The effective mass of a cavity photon can be understood in a following way. The confined photon energy E_c satisfies $E_c = \hbar v|k|$, which is the same relation as a photon in vacuum except the light velocity v in the medium of a refractive index n_c is $v = c/n_c$ in terms of the speed of light in vacuum c. In the 2D microcavity, the longitudinal component of the wave vector, k_c, is given by $k_c = n_c 2\pi/\lambda$. Typically, for a sub-micrometer λ, k_c is on the order of 10^7 1/m, bigger than typical values of the transverse component $k_\parallel$ near the zero momentum value. In the region $k_\parallel << k_c$ the cavity photon energy can be approximated as:

$$E_c = \hbar v|k| = \hbar v\sqrt{k_c^2 + k_\parallel^2} = \hbar v k_c \sqrt{1 + \left(\frac{k_\parallel}{k_c}\right)^2},$$

$$\sim \hbar v k_c \left(1 + \frac{k_\parallel^2}{2k_c^2}\right) \equiv E_{c0} + \frac{\hbar^2 k_\parallel^2}{2m_c},$$

where the effective photon mass m_c is set to $m_c = \hbar v/c^2$, and E_{c0} is the cavity photon energy at $\mathbf{k} = 0$. Graphically, the cavity photon dispersion becomes parabolic as shown in Fig. 17.1b, whose curvature is related to the effective mass.

Now consider a microcavity, where a QW is placed at the maximum of the cavity photon mode amplitude(Fig. 17.1a). If the QW exciton energy is on resonance with the cavity photon energy, a reversible energy exchange between the two can occur. When the conversion rate is much faster than the decay rates of photon and QW exciton, the system enters in a so-called strong coupling regime. One manifestation of the strong coupling is an anti-crossing feature in energy-momentum dispersion, where two hybridized modes appear. These hybridized modes in the microcavity with the embedded QW are called *microcavity exciton-polaritons*, *cavity polaritons* or *exciton-polaritons* in the literature since the first observation of the strongly coupled exciton-photon modes [26]. In this chapter, either exciton-polaritons or

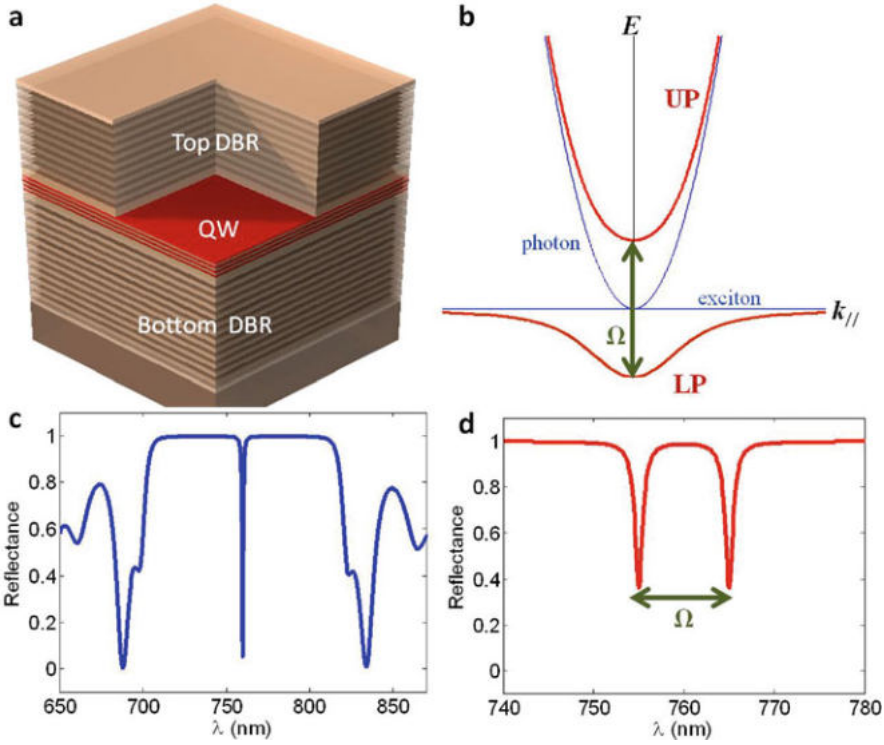

Fig. 17.1 (**a**) Schematic microcavity structure with embedded quantum-well (*QW*) layers surrounded by two top and bottom distributed Bragg reflectors (*DBRs*). (**b**) The energy dispersion relations of cavity photon (*blue*), QW exciton (*blue*), upper polariton (*UP*, *red*) and lower polariton (*LP*, *red*) in a microcavity with a QW. (**c**) Reflectance spectrum of an empty cavity. A center sharp dip is a longitudinal cavity mode and the region between two reflectance minima is called a stop band. (**d**) Reflectance spectrum of the strongly-coupled exciton-polariton. The energy difference between two dips is a photon-QW exciton coupling strength denoted as Ω

polaritons are used for 2D quasi-particles as an admixture of the cavity photon and QW-exciton. Section 17.2 begins with the basics of exciton-polaritons and their properties arising from their bosonic nature followed by the experimental techniques to identify the polariton properties.

17.2.1 Exciton-Polaritons: Fundamentals

An exciton-polariton is a quasiparticle resulting from the strong coupling between the cavity photon and the QW exciton [27–29]. The basic physics of exciton-polariton in the low-density regime is captured by a simple 2-by-2 matrix Hamiltonian, where the bases are the constituent particles, $|X_{k_\parallel}\rangle$ with an QW exciton energy $E^X_{k_\parallel} = \hbar\omega^X_{k_\parallel}$ and $|C_{k_\parallel}\rangle$ with a cavity energy $E^c_{k_\parallel}$ where $k_\parallel$ is the in-plane momentum. By momentum conservation, excitons with momentum $k_\parallel$ only couple to photons with the same momentum. Parameterizing the interaction energy between two modes by $\hbar\Omega$, the system Hamiltonian matrix at momentum $k_\parallel$ is

$$\hat{H} = \begin{pmatrix} E^X_{k_\parallel} & \hbar\Omega \\ \hbar\Omega^* & E^c_{k_\parallel} \end{pmatrix}.$$

The Hamiltonian can be diagonalized by a new basis, $|UP_{k_\parallel} >= -v_{k_\parallel}|X_{k_\parallel} > +u_{k_\parallel}|C_{k_\parallel} >$ and $|LP_{k_\parallel} >= u_{k_\parallel}|X_{k_\parallel} > +v_{k_\parallel}|C_{k_\parallel} >$ with coefficients $u_{k_\parallel}$ and $v_{k_\parallel}$ giving the photon and exciton amplitudes respectively. We call these new eigenmodes the upper polariton (UP) and lower polariton (LP) with energies

$$E^{UP,LP}_{k_\parallel} = \frac{E^X_{k_\parallel} + E^c_{k_\parallel}}{2} \pm \frac{\sqrt{(E^X_{k_\parallel} - E^c_{k_\parallel})^2 + (2\hbar\Omega)^2}}{2}.$$

The energy and in-plane momentum dispersion relations of four modes are drawn in Fig. 17.1b: cavity photon and QW excitons in blue, UP and LP in red. Two normal modes anti-cross near $k_\parallel = 0$, and the doublet is separated by the strength of the interaction energy $\hbar\Omega$. The curvature of the dispersions relates to the effective mass of the particles and the density of states. For small values of $k_\parallel$, the LP is more like a photon, but the LP is more a exciton for large $k_\parallel$.

Experimentally, we characterize the system parameters by reflection and luminescence spectroscopy. Figure 17.1c shows the reflectance of an empty microcavity, where the dip inside the stop band corresponds to the longitudinal cavity mode. An exciton energy state is readily identified in photoluminescence as a recombination process. The loaded cavity with the QW has a distinctive reflectance spectrum taken along the $k_\parallel = 0$, featuring double dips in Fig. 17.1d. The separation between two dips is the direct measure of the interaction energy, referred to be vacuum Rabi splitting analogous to an atom-cavity system.

Figure 17.1b illustrates the particular case of zero detuning ($\Delta = 0$), where $E^X_{k_\parallel}$ and $E^c_{k_\parallel}$ are on resonance at $k_\parallel = 0$, resulting in the LP and UP with equal exciton and photon fractions of $|C_{k_\parallel}|^2 = |X_{k_\parallel}|^2 = 1/2$. The detuning parameter $\Delta = E^c_{k_\parallel=0} - E^X_{k_\parallel=0}$ quantifies the energy difference between two individual modes. By shifting the cavity photon energy branch with respect to the exciton energy, the LP can be more photon-like (red detuning) or more exciton-like (blue detuning).

17.2.2 Experimental Techniques

This subsection briefly summarizes the experimental setup and the standard experimental procedure to characterize a microcavity-QW wafer. Exciton-polaritons have a finite lifetime, leaking as photons through the microcavity. According to energy and momentum conservations in 2D, the energy and momentum of leaked photons have a direct relation to those of the exciton-polaritons inside the cavity. Thus, capturing the leaked photons and analyzing the information allow us to study the state of exciton-polaritons.

We build a free-space Fourier optics setup [30]. Each lens performs a Fourier transform, converting the real space coordinate into the momentum space coordinate and vice versa, depending on the lens location. Figure 17.2a, b illustrate the schematic of the setup to access the information in the real space and the momentum space, respectively. The signals are analyzed by a spectrometer, which provides the energy-resolved information in the real and momentum spaces. Furthermore, the temporal dynamics of exciton-polaritons is characterized by a streak camera. Figure 17.2c is a Mach-Zehnder interferometer for the first-order correlation measurement.

The following is a typical protocol to characterize a grown microcavity-QW wafer. Making a wedged cavity, whose cavity length is spatially varying, we are able to access exciton-polaritons at different detuning values. First, we measure the detuning parameters in space via reflectance spectroscopy as a broadband white light scans the wafer. By tracing the doublet dips like Fig. 17.1d, we construct the spatial map of the UP and LP energy values as well as the detuning values. Next, the photoluminescence imaging and spectroscopy provide the polariton density distribution as well as the energy values in the real and momentum spaces.

The GaAs- and CdTe-based samples are studied at low temperatures around 4–10 K in a cryostat for protecting excitons from thermal energy. Resorting to large bandgap semiconductors such as GaN [31–33], ZnO [34, 35], and organic material [36–38], measurements are done at room temperatures.

17.2.3 Exciton-Polariton Condensation

As composite bosons, the dynamics of exciton-polaritons are governed by Bose-Einstein statistics, and are expected to be condensed at sufficiently low tem-

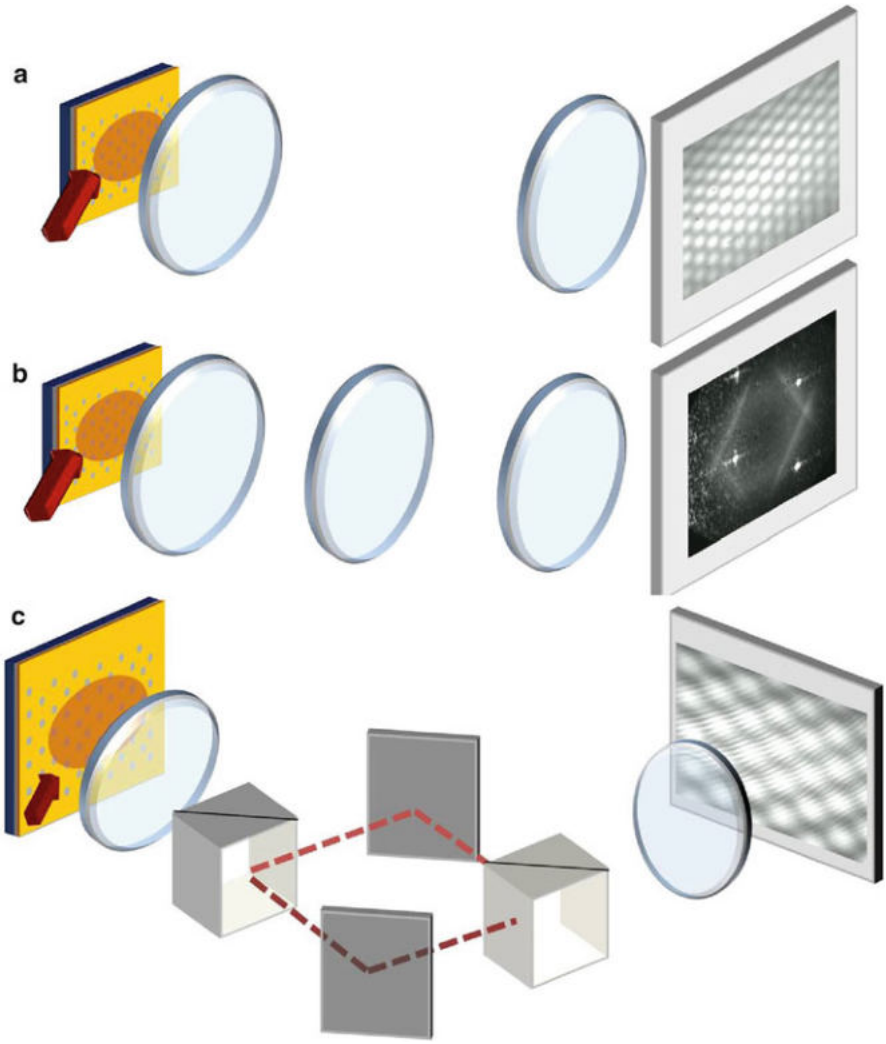

Fig. 17.2 Sketches of photoluminescence setup for a near-field (**a**) and a far-field (**b**) measurements. (**c**) A Mach-Zehnder interferometer used for mapping a phase information in space

peratures [27–29]. Whereas the BEC is a thermodynamic phase transition at equilibrium [1, 39], it is crucial to understand the non-equilibrium nature of exciton-polariton condensation due to their finite lifetime. Since exciton-polaritons decay as photons out of the cavity, the system has to be continuously replenished if a constant condensate population is desired. This highly open-dissipative setting makes exciton-polariton condensation in the non-equilibrium regime.

In the microcavity-QW structure, we vary the particle density, which is an alternative route towards condensation as lowering the temperature. The polariton density as a function of in-plane momentum values is measured by examining the

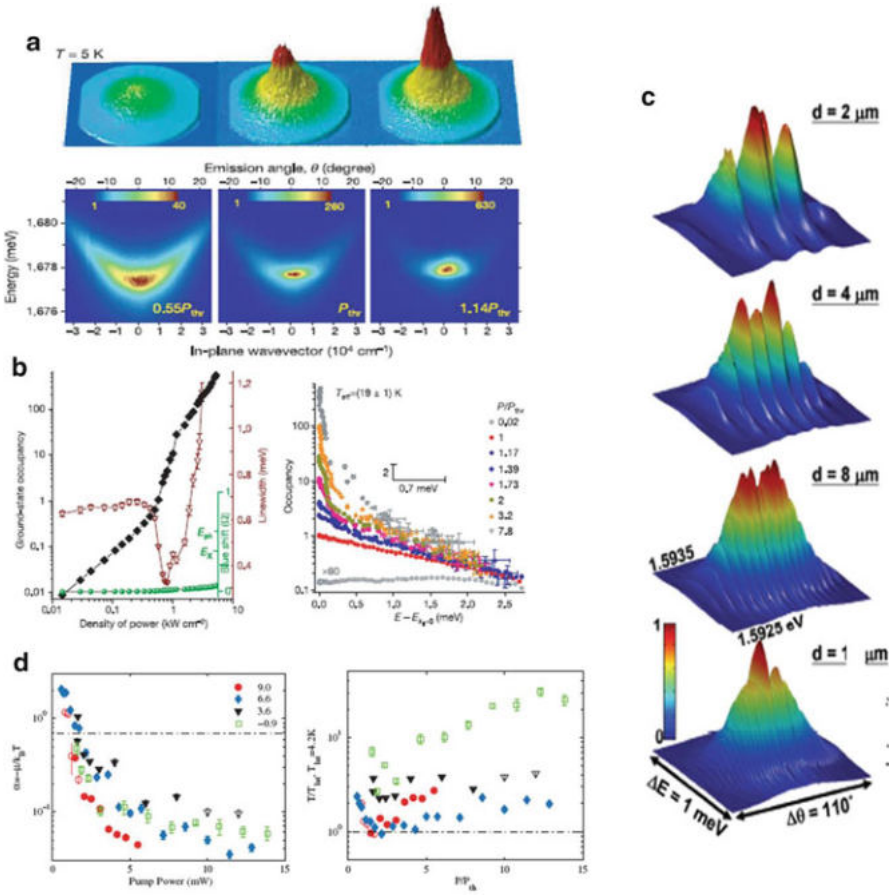

Fig. 17.3 Properties of exciton-polariton condensations. (**a**) A lower polariton (LP) population distribution (*top*) and LP energy spectra (*bottom*) in the momentum space as a function of pump power values. (**b**) (*Left*) Characteristics of the LP ground state as a function of pump power: the intensity (*black*), spectral linewidth (*red*), energy shift (*green*). (*Right*) A LP occupancy in energy as a function of pump power, exhibiting quantum degeneracy threshold. Figures (**a**) and (**b**) are taken from Ref. [44] and permission is granted. (**c**) Interference of LP condensates to exhibit spatial coherence from Young's double slit measurements reported in Ref. [40]. (**d**) Quantum degeneracy behavior of LPs in the LP momentum distribution at various detuning and pump power values, computing normalized chemical potential (*left*) and LP temperature with respect to the lattice temperature (*right*) captured from in Ref. [41]

captured photon intensity (Fig. 17.3a). In a typical experiment where condensation is realized, the polariton density at the lowest energy state shows a threshold behavior as shown in Fig. 17.3b. The off-diagonal long range order, one of the important concepts in BEC and superfluidity, is directly related to spatial coherence. Figure 17.3c collects Young's double-slit interferograms at different slit distances when condensates are created by a laser whose energy is much higher (a non-

resonant excitation) [40]. The coherence among exciton-polaritons above threshold is spontaneously built in this case. Furthermore, the statistical analysis from Bose-Einstein distribution fitting to the LP momentum distribution provides the information of a chemical potential and an effective gas temperature at various detuning and pump power values, exhibiting quantum degeneracy in thermal equilibrium in Fig. 17.3d [41].

Since the first discovery of exciton-polariton in 1992 [26], coherent matter waves based on exciton-polaritons were predicted [42], and a huge amount of research efforts have been put both in theories and experiments using different materials. The dynamical nature of exciton-polariton condensation was first reported in GaAs semiconductors by Deng et al. [43]. Subsequently, polariton condensation was reported in CdTe semiconductors with a series of evidence by Dang and Deveaud and their colleagues [44], and a trap by strain in GaAs system facilitates polariton condensation [45].

This nature of the exciton-polariton condensation becomes much richer when they are subjected to artificial lattices and the next section we will describe the dynamics of coherent exciton-polaritons in a variety of two-dimensional geometries.

17.3 Exciton-Polaritons in Two-Dimensional Lattices

Section 17.3 reviews our progress on band engineering, meta-stable condensates above band gap, and their dynamical formation of exciton-polariton condensates in two-dimensional (2D) lattices. In the presence of an energy gap in lattice band structures, polariton relaxation is highly suppressed for states above the band gap so that polaritons condense in the meta-stable states. The states are further populated by bosonic final state stimulation. When the relaxation rate exceeds the loss rate mainly due to the radiative decay, the polariton population can reach quantum degeneracy threshold. Such a state is prone to meta-stable condensation, exhibiting distinct spatial profiles due to high-orbital states. The system also shows multi-mode condensates at several orbital states.

17.3.1 Lattice Formation

First, we describe how 2D lattice potentials are implemented in our polariton system. We deposit a thin metal film (Au/Ti $\sim$ 23/5 nm) on the top of the sample surface. Lattice geometries and dimensions are designed and patterned by electron beam lithography followed by a metal liftoff. A basic principle of spatially modulated potentials can be understood as follows. A thin metal imposes a zero photon field amplitude at the metal-semiconductor interface, while a semiconductor-air interface supports a non-zero photon field amplitude. Therefore, the wavelength of the cavity resonance under the metal is slightly shorter than that in bare (no metal) region. It only affects photon modes, and this photon potential modulation is about

400 μeV in our GaAs-based microcavity with 16(20) top (bottom) DBRs. The actual potential for LPs would vary around 100–200 μeV, taking into account of photon fractions. Using this method, we made four different lattice types: square [46], honeycomb [47], triangular [48, 49], and kagome [50] geometries with the center-to-center distances between 2 and 20 μm.

17.3.2 Band Structure Calculation

When a particle is in a crystalline structure, a first thing is to construct a band structure of periodic potentials. In this subsection, we briefly explain the band structure calculation of the polariton-lattice systems. Let us take an example of a simplest square lattice, whose unit vectors are orthogonal $\mathbf{a_1} = (a, 0)$ and $\mathbf{a_2} = (0, a)$ and corresponding reciprocal lattice vectors are $\mathbf{b_1} = (2\pi/a, 0)$ and $\mathbf{b_2} = (0, 2\pi/a)$, where a is the lattice constant equal to the center-to-center distance between nearest neighbor sites. In reciprocal space, Brillouin zones are defined as shown in Fig. 17.4b and high-symmetry points are denoted as Γ, X and M according to rotational symmetry.

Near zero-detuning area, the effective mass of exciton-polaritons is extremely light, $m_p \sim 10^{-5} m_e$ in unit of bare electron mass m_e. The characteristic kinetic energy E_0 at the first Brillouin zone boundaries $\pm\pi/a$ is given $E_0 = \hbar^2(\pi/a)^2/2m_p$. For the devices of $a = 2, 4$ μm, E_0 ranges 0.3–1 meV, much larger than the potential energy depth $V \sim 200$ μeV. Hence, we can use the single-particle plane wave expansion method for the band calculation. Figure 17.4c shows the calculated band structure for a weak potential $V = 0.2E_0$. Four-fold degeneracies at M-points are lifted by the lattices, and band gaps open between the fourth band and the lower bands. We also calculate corresponding real space wavefunctions at high symmetry points, and we label them analogous to atomic orbital wavefunctions. At

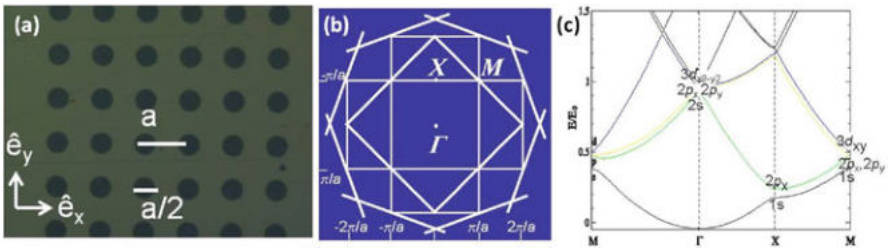

Fig. 17.4 (**a**) A picture of a square lattice device. Dark area corresponds to trap region (no metal), and bright area is the potential wall (with metal film). (**b**) Brillouin Zones and high symmetry points of the square lattice. (**c**) Calibrated band structures of square lattice (All figures are adapted from Ref. [46])

M-points, they are $3d_{xy}$, $2p_x$, $2p_y$ and, $1s$-orbital nature. We apply this band structure calculation to all four lattices, and we are able to understand characteristics of meta-stable high-orbital condensates in the following subsections.

17.3.3 Experimental Setup

Before explaining our experimental observation, we here recapitulate our experimental conditions. A focused pump laser beam is shined from 60 degree ($\sim 7.4 \times 10^4\ \mathrm{cm}^{-1}$) onto the sample, which is kept in a cryostat at a temperature around 4.2 K. We use a tunable Ti:sapphire laser in a pulsed operation, sending a 3-ps pulse at a 76 MHz repetition rate. The laser wavelength is tuned at exciton resonance, roughly 6 meV higher than the energy of the LP ground state. This incoherent non-resonant pumping scheme is particularly chosen in order to make sure that coherence in exciton-polaritons is not from excitation laser coherence.

Photoluminescence signals are collected by an object lens with 0.55 numerical aperture and converted to near- and far-field images by the following lenses as described in Sect. 17.2.2. We place a CCD camera for energy-integrated imaging in both real and momentum spaces. Position-resolved and angle-resolved spectra are taken by a 750 mm-long spectrometer with a resolution of 20 μeV. For complex-valued order parameters with high-orbital symmetries, Michelson and Mach-Zehnder interferometers are built to extract the relative phase map and coherence functions.

17.3.4 High-Orbital Condensates

17.3.4.1 *d*-Wave Condensation in the Square Lattice

Figure 17.5a displays the evolution of LP population distributions in momentum space from far-field (FF) imaging as a function of the pump power values in the square lattice device with $a = 4\,\mu\mathrm{m}$. Below the threshold pump power ($P/P_{th} < 1$), broad ring shaped distribution is observed in momentum space which results from the so-called bottleneck effect. Just above the threshold, distinct diffraction peaks are developed at M-points, which clearly indicate M-point condensation. We also observed nonlinear intensity increase and the spectral linewidth shrink across the threshold, which are the standard characteristics of polariton condensation. With further increase of the pump power, polariton distribution moves to X-points and finally to Γ – point, a global ground state.

The dynamics can be understood from the band structure. As we discussed earlier in the previous subsection, the fourth band at M-points is separated by a band gap from the lower bands. It becomes meta-stable momentum valley, where coherent polaritons are accumulated to form a condensate. The M-point state in the fourth

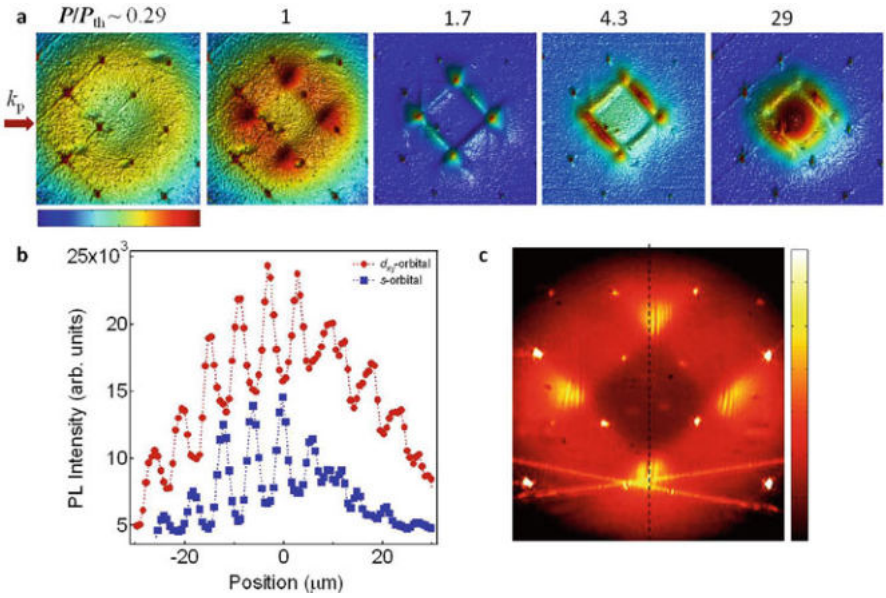

Fig. 17.5 (**a**) Lower polariton (LP) distributions in momentum space from far-field imaging as normalized pump power values with threshold $P_{th} \sim 7$ mW. (**b**) Near-field LP polariton distribution of *s*- and *d*-orbital states across lattices. Intensities of *s*- and *d*-orbital wavefunctions are clearly anti-correlated in space as expected since *d*-wavefunctions have node at the trap center, where *s*-wavefunctions are at maximum. (**c**) Michelson interferometry in momentum space showing macroscopic coherence between the *M*-points. For clarity, the square lattice is rotated by 45 degrees from the vertical line (All figures are adapted from Ref. [46], whose permission is granted by Nature Physics)

band $|\Psi\rangle$ can be described by a superposition of four plane wave components of the *M*-points and it is arranged as anti-phased d_{xy} configurations at sites. The spatial profile of the *d*-wave condensate is directly measured through the energy-resolved near-field (NF) imaging and their cross-sectional cuts are plotted in Fig. 17.5b. The data tell us that the *d*-wave condensate has its intensity peaks outside the trap centers, while the Γ-point condensate with *s*-wave symmetry has its intensity peaks in the traps. It is clear to observe the *anti-correlated* intensity distribution in space between two orbital symmetries. Theoretical calculation of wavefunctions for the strongly trapped case clearly elucidate these NF orbital symmetry, and our plane-wave basis calculations also confirm it.

The coherence between four plane wave components is confirmed through the Michelson interferometry in momentum space, as shown in Fig. 17.5c. Although the coherence between four *M*-points already exists in the single particle state, the observed mutual coherence is a direct manifestation of condensation. Finally, we discuss the formation dynamics of multi-condensates, *d*-wave (at *M*-points), *p*-wave (at *X*-points), and the *s*-wave (at the Γ-points) condensates in terms of evolution time. Since polaritons have short lifetime (a few ps), there always exist a radiative

loss from each state and gain from the upper energy excited states,which also works as a loss mechanism for the excited states. Such gain-loss dynamics explains the observed multi-condensates dynamics through the rate equations analysis [46].

17.3.4.2 Vortex-Antivortex Order in the Honeycomb Lattice

We next describe two degenerate p-wave condensates with vortex-antivortex phase order and their population correlation in the honeycomb lattice. The calculated band structure exhibits a band gap between the third band and the lower bands at K- and K'points. Note that the first Brillouin zone of the honeycomb lattice has two inequivalent K and K'-points depicted in Fig. 17.6b, which are related to inversion symmetry. K and K'-points have three-fold rotational symmetry. We denote $|\Psi_K^3\rangle$ and $|\Psi_{K'}^3\rangle$ as corresponding two degenerate states in the third band (Fig. 17.6c). These wavefunctions exhibit vortex-antivortex order as a linear combination of three K or K'-point plane waves (Fig. 17.7e, f). A modified Mach-Zehnder interferometer enables us to directly measure the phase order of the K-point condensates. In one

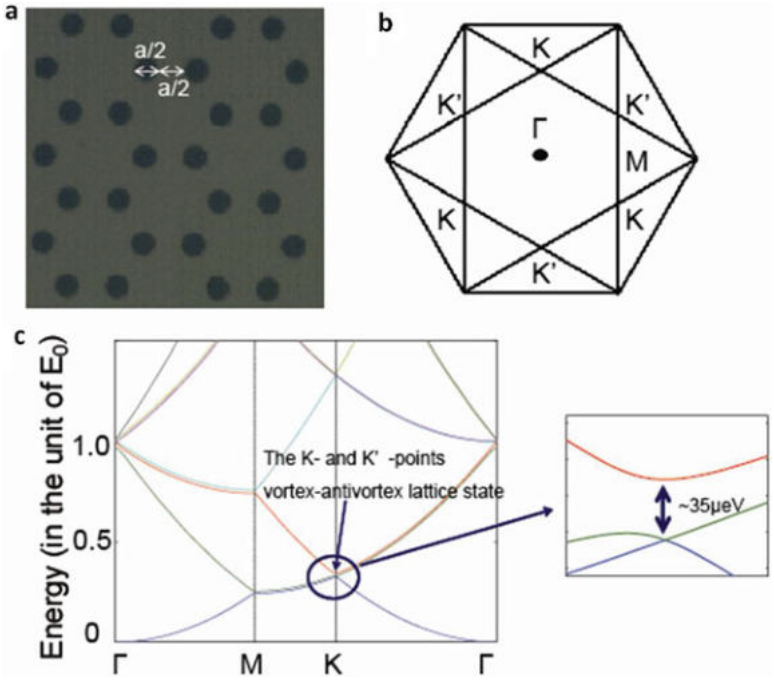

Fig. 17.6 (**a**) A photograph of the honeycomb lattice sample. (**b**) Corresponding Brillouin Zones (up to the 3rd) with high symmetry points Γ, M, K and K'. (**c**) Calculated band structures with the potential amplitude $V = 0.10E_0$, where $E_0 = \frac{\hbar^2}{2m_p}(\frac{4\pi}{3a})^2$ (All figures are taken from Ref. [47]. Copyright, 2013 American Institute of Physics)

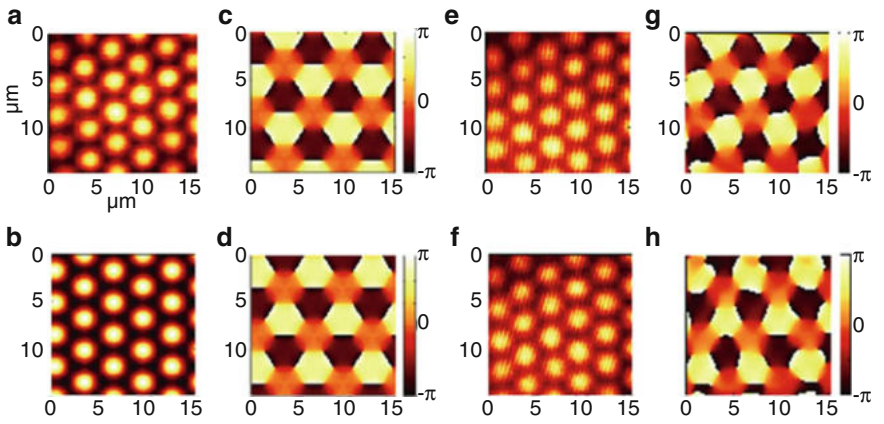

Fig. 17.7 Time-integrated interferogram for the K- and K'–points condensate at $P/P_{th} \sim 2$. The theoretical near-field intensity and phase map of $|\Psi_3^K\rangle$ (**a**,**c**) and $|\Psi_3^{K'}\rangle$ (**b**,**d**). (**e**,**f**) The experimental interferogram between the signal from all the K and K′-points in the one arm of the Mach-Zehnder interferometer, and the signal from only one K-point or one K'-point in the other arm. (**g**,**h**) The reconstructed phase order of $|\Psi_3^K\rangle$ (**g**) and $|\Psi_3^{K'}\rangle$ (**h**) condensates from the off-axis components (All figures are rearranged from Ref. [47])

arm, one plane wave component is excluded by a filtering mask in FF plane, and in the other arm all signals are contained. By selecting a plane wave component from K or K'-points, we can map out the phase order of the condensates at K- or K'-points from the off-axis analysis of interferograms. Experimental interferograms are displayed in Fig. 17.7 at K and K'-points together with theoretical results, which confirm alternative vortex-antivortex order.

In contrast to the square lattice, two K and K'-points condensates are formed in two degenerate K- and K'-points states. We have carried out the second order correlation measurement to study the formation dynamics of these degenerate condensates. Figure 17.8 compiles experimental results of K and K'-auto- and cross-correlations at different pump powers. Interestingly we observe two distinct behaviors in the second-order auto-correlation functions $g^{(2)}(K, K, 0)$ and $g^{(2)}(K', K', 0)$ and cross-correlation functions between K- and K'-point condensates $g^{(2)}(K, K', 0)$. The former ones exhibit a bunching behavior, which is well-known in polariton condensates, originating from the polariton-polariton interaction and excess intensity noise due to their open-dissipative nature. We interpret the observed bunching in high-orbital condensates in the same way. However, the cross-correlation functions have an opposite feature of anti-correlation above threshold.

We assume such anti-correlation is brought from the competition between the one reservoir and two condensates, and simulate the following complex-number Langevin equations for the system,

$$\frac{d}{dt}\Psi_\sigma = \frac{1}{2}\left[-\Gamma - \gamma_c\left(|\Psi_G|^2 + 1\right) + \gamma N_R\right]\Psi_\sigma + \theta_\sigma(t),$$

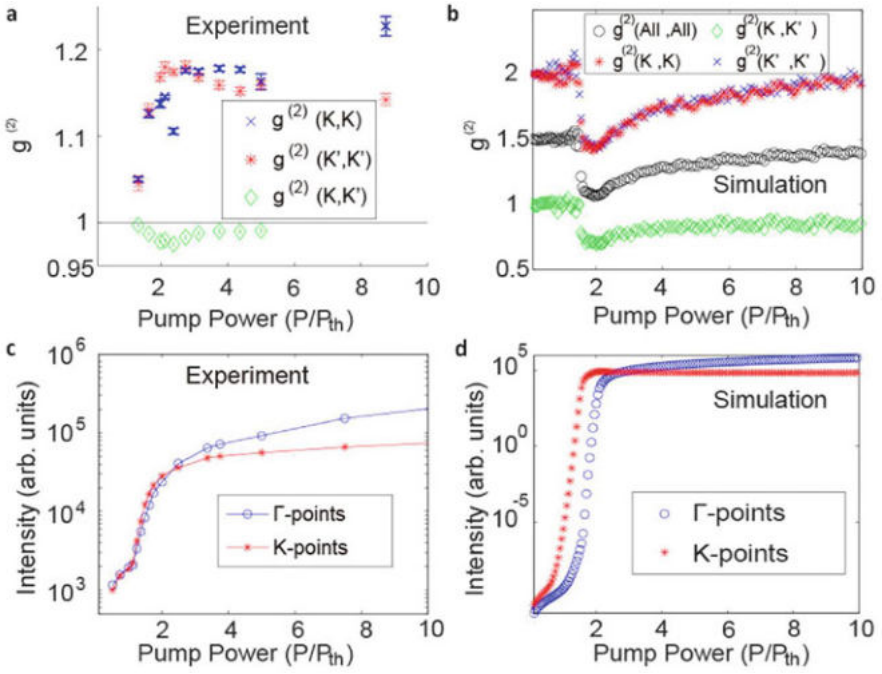

Fig. 17.8 Multi-mode condensates dynamics through the polariton population and second order correlation measurement. (**a**) Experimental and (**b**) theoretical results for the normalized second order auto correlation, $g^{(2)}(K, K', \tau = 0)$, $g^{(2)}(K, K', \tau = 0)$ and the cross correlation $g^{(2)}(K, K', \tau = 0)$. Simulation also shows $g^{(2)}(\text{All}, \text{All}, \tau = 0)$. (**c**) Experimental and (**d**) simulation results of the pump power dependence of the polariton population at Γ-point and the K-point condensate. (**c**) The peak intensity values at the Γ-point and one K-point are plotted. (**d**) The Γ-point intensity ($|\Psi_G|^2$) and the K-point total intensity ($|\Psi_K|^2 + |\Psi_{K'}|^2$) are plotted (All figures are taken from Ref. [47])

$$\frac{d}{dt}\Psi_G = \frac{1}{2}\left[-\Gamma_G + \gamma_G N_R + \gamma_c\left(|\Psi_K|^2 + |\Psi_{K'}|^2\right)\right] + \theta_{GR}(t) + \theta_{GK}(t) + \theta_{GK'}(t),$$

$$\frac{d}{dt}N_R = P - \Gamma_R N_R - \gamma N_R\left(|\Psi_K|^2 + 1\right) - \gamma N_R\left(|\Psi_{K'}|^2 + 1\right) - \gamma_G N_R\left(|\Psi_G|^2 + 1\right).$$

We also include the ground state Ψ_G at Γ-point in the calculation, into which LPs in K and $K\prime$ points are relaxed. Here Ψ_σ is either Ψ_K or $\Psi_{K'}$, and Ψ_K, $\Psi_{K'}$ and Ψ_G are order parameters of $|\Psi_3^K\rangle$, $|\Psi_3^{K'}\rangle$ and $|\Psi_G\rangle$, respectively. Γ is the radiative decay rate of LPs in $|\Psi_3^K\rangle$ and $|\Psi_3^{K'}\rangle$ states, Γ_G is the ground state decay rate and Γ_R for the reservoir decay rate. A stimulated scattering rate for each relaxation process is characterized by γ (from reservoir to $|\Psi_3^K\rangle$ and $|\Psi_3^{K'}\rangle$), γ_G (from reservoir to the ground state) and γ_c (from $|\Psi_3^K\rangle$ and $|\Psi_3^{K'}\rangle$ to the ground state) respectively. Langevin noise terms are responsible for the spontaneous scattering process, and characterized as $< \theta_\eta(t)\theta_{\eta'}(t') >= 0$ and $< \theta_\eta(t)\theta^*_{\eta'}(t') >= A(\eta)\delta_{\eta\eta'}\delta(t - t')$, where $\eta = K, K', GR, GK$ and GK' and $A(K) = A(K') = \frac{1}{2}\gamma N_R$, $A(GR) = \frac{1}{2}\gamma_G N_R$,

$A(GK) = \frac{1}{2}\gamma_c|\Psi_K|^2$ and $A(GK') = \frac{1}{2}\gamma_c|\Psi_{K'}|^2$. Because the pump field is a short pulse, we put $N_R(0) = \int dtP(t)$ and set $P = 0$ for all times for $t > 0$. The parameters which we use are $\Gamma = 0.2\,\mathrm{ps}^{-1}$, $\Gamma_G = 0.2\,\mathrm{ps}^{-1}$, $\Gamma_R = 1/200\,\mathrm{ps}^{-1}$, $\gamma = 5 \times 10^{-4}\mathrm{ps}^{-1}$, $\gamma_c = 10\gamma$ and $\gamma_G = 0.6\gamma$. Simulation results are summarized in Fig. 17.8b, d, which explain experimental results qualitatively. Although the total particle number injected into the system is fixed at a certain pump power, the relaxation into each condensate from the reservoir is initiated by spontaneous polariton scattering and that the relaxation dynamics may change from pulse-to-pulse.

17.3.5 Band Engineering

In addition to the observation of high-orbital condensations reviewed in previous two subsections, we engineer Dirac cones in lattices with triangular-symmetry [48]. In the triangular and honeycomb lattices, linear dispersions appear near high symmetry points. Figure 17.9a is a band structure of the triangular lattice in a reduced zone scheme, indicating a Dirac point at K. This linear dispersion with the gapless crossing point is called as a Dirac cone as an analog of the Dirac dispersion in the relativistic field theory.

We prepare for the triangular lattice potentials in exciton-polariton systems, and probe the dispersion relation directly near K- and K'-points. The spectral linewidth of emitted signals ($\sim$250 μeV) limits our capability to resolve all three individual bands with a gap at low pump power (Fig. 17.9b). We have compared the Dirac velocity estimated from the linear regression analysis on the measured band from K-M section (Fig. 17.9c) with the theoretical value $v = h/3m_p a$. The extracted velocity is 1.0×10^8 cm s^{-1} for $P/P_{\mathrm{th}} \sim 1.3$, and 2.1×10^8 cm s^{-1} for $P/P_{\mathrm{th}} \sim 2$. Both values are in the same order with theoretical velocity values, 1.5×10^8 cm s^{-1}.

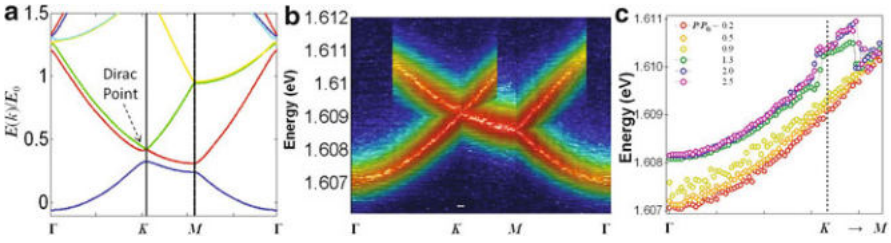

Fig. 17.9 (**a**) A band structure calculated for triangular lattices. E_0 is the characteristic kinetic energy $\frac{\hbar^2}{2m_p}(\frac{2\pi}{a})^2 \sim 4.5$ meV, $a = 2$ μm and the potential energy V = 200 μeV. (**b**) Experimentally constructed band structures well below threshold pump power $P/P_{\mathrm{th}} \sim 0.2$ in the triangular lattice. (**c**) The extracted energy values at the maximum LP emission intensity at the several pump powers. We have estimated the Dirac velocity from the linear regression analysis from the K-M section. Each pump power is normalized by the threshold pump power where condensation effect has been observed around the M-points (All figures are reproduced from Ref. [48])

In the kagome lattice, we attempt to engineer the flat bands in order to study lattice frustration and localization effect. Flat bands mean a quenching of kinetic energy and it would have a signature of localized distributions in real space. It turned out that exciton-polaritons are rather spread over many sites in our weak potential modulation, which keeps us from reaching a complete flatness of the bands [50]. The combination of long-lived polaritons (around 100 ps) and deeper potential modulation (a few meV) would allow us to have clear band engineering in lattices. Recently, linear dispersion and flat bands in the honeycomb geometries of micro-pillar arrays by etching are indeed observed [51].

17.4 Exciton-Polariton Quantum Simulation

A remark on the applications of the exciton-polariton-lattice systems is given in the context of quantum simulation. A quantum simulator (QS) is a specially designed quantum device, which may simulate a certain class of quantum problems efficiently in a controllable environment [19–21]. Establishing a quantum simulator in various platforms is one of the major research activities in quantum information science since the seminal paper in 2002, which reported the superfluid- Mott insulator phase transition in ultracold Bose atoms in an optical lattice [52]. For the last decade, QSs have been built in various systems from the ultracold atoms in optical lattice [53], trapped ions [54], superconducting qubits in a microwave cavity array [55], and 2D electron gases in artificial lattices [56].

One of the early targets of the QS is to study a mathematical toy model, which is pertinent to capture the key features in condensed matter systems. One famous prototypical Hamiltonian is the Hubbard model with the nearest-neighbor hopping kinetic energy and an on-site interaction energy [57]. Despite the simplicity of the model, analytical solutions for 2D and 3D systems are unavailable, and the numerical solutions of a relatively small number of sites require extremely large computing resources. The key idea of a QS is to use a simple quantum device to simulate such quantum many-body problems. Our discussions in previous sections suggest that the polariton-lattice system will provide a solid-state QS platform in the optical domain to address condensed matter physics problems. We recapitulate the present status of our polariton-lattice system as a QS platform followed by a discussion how to extract many-body physics, as would appear in real materials.

17.4.1 Present Status

We have successfully implemented various 2D lattice potentials to trap exciton-polaritons using the thin-metal film technique. The band structures of a given lattice geometry are created, and we are able to directly map out the band structures of exciton-polaritons in the 2D lattices. The experimental results are well described by a single particle picture. Due to the interplay of the finite lifetime and the

relaxation time to the lower energy states, coherent exciton-polaritons can be made to temporarily reside at finite-momentum values of the Brillouin zone boundaries. This enables us to select the high orbital symmetry of exciton-polariton condensates.

The study of high-orbital condensation is interesting from the perspective that they give a complementary view to high-orbital fermion physics in strongly correlated systems like high temperature superconductors (copper d-orbital and oxygen p-orbital) or transition metal oxides with d and f-orbital electrons. The interferometry techniques allow us to access the phase information of the system order parameter in real space. In the end, it enables us to observe the orbital symmetry of the meta-stable condensate states at finite momentum values. High-orbital states have degeneracies, for examples, p_x and p_y-orbital states are degenerate in 2D. These orbital states are not distributed isotropically in space, which is distinct from the non-degenerate s-orbital state. The degeneracy and anisotropy of high-orbital condensates would be compliment to the nature of high-orbital electrons [58]. In this aspect, the inherent non-equilibrium nature of exciton-polariton condensation grants us to readily select the orbital symmetry of the band structures as shown in previous section. However, the major limitation of the present polariton-lattice system is the controllability of the lattice potentials. Since the thin-metal-film technique creates a shallow lattice potential, which is much smaller or comparable to the kinetic energy of exciton-polaritons, the physics explored by this system is limited to the single-particle physics.

17.4.2 Beyond the Single-Particle Physics

In order for the exciton-polariton-lattice QS system to study the many-body physics problems, we first seek a different method to produce the artificial lattice potential. Etching a pillar as a single trap [59] or pillar-arrays [60] has shown stronger trapping potentials. However, a micron-sized site is still not strong enough to induce a noticeable two-particle interaction energy at the level of one or a few particles at the site. Therefore, it is a great demand to find right material and methods for stronger interaction energy.

Another physics we can study in the polariton-lattice QS is spin and its dynamics. The polariton spin degrees of freedom can be controlled by the light polarization, and they are regarded as a pseudo-spin 1/2 [61]. When the spin physics is combined with to high-orbital states in lattice geometries, we expect to simulate the spin-orbital interaction and topological states in condensed matter systems.

17.5 Conclusion

We have made progress in the preparation of dynamically condensed polaritons with high-orbital symmetries in 2D artificial lattices. The powerful experimental advantages in optical spectroscopy and correlation measurements allow us to

directly measure the band structures, macroscopic condensate wavefunctions in real space with both amplitude and phase information as well as dynamical formation of completely degenerate condensates. This exciton-polariton-lattice system would be an interesting QS candidate, with which we search for an 2D exotic quantum order associated with orbital and spin degrees of freedom.

Acknowledgements We acknowledge Navy/SPAWAR Grant N66001-09-1-2024, the Japan Society for the Promotion of Science (JSPS) through its "Funding Program for World-Leading Innovative R&D on Science and Technology (FIRST Program)". We deeply thank all our collaborators: Prof. Alfred Forchel, Dr. Sven Höfling, Dr. Andreas Löffler for providing the wafer; Prof. T. Fujisawa, Dr. N. Kumada for supporting the device fabrication; Prof. C. Wu, Dr. Z. Cai for theoretical discussions.

References

1. F. Reif, Fundamentals of Statistical and Thermal Physics (Waveland Press, Long Grove, 1982)
2. G.D. Mahan, *Many-Particle Physics* (Kluwer Academic/Plenum Publishers, New York, 1981)
3. Y. Tokura, N. Nagaosa, Orbital physics in transition-metal oxides. Science **288**, 462–468 (2000)
4. A. Griffin, D.W. Snoke, S. Stringari, *Bose-Einstein Condensation* (Cambridge University Press, Cambridge/New York, 1996)
5. L. Pitaevskii, S. Stringari, *Bose-Einstein Condensation* (Oxford University Press, 2003)
6. C.J. Pethick, H. Smith, *Bose-Einstein Condensation in Dilute Gases* (Cambridge University Press, Cambridge/New York, 2008)
7. P. Kapitza, Viscosity of liquid helium below the λ-point. Nature **141**, 74 (1938)
8. J.F. Allen, A.D. Misener, Flow of liquid helium II. Nature **141**, 75 (1938)
9. M. Tinkham, *Introduction to Superconductivity* (McGraw-Hill, New York, 1975)
10. E. Cornell, C.E. Wieman, Bose-Einstein condensation in a dilute gas, the first 70 years and some recent experiments. Rev. Mod. Phys. **74**, 875 (2002)
11. W. Ketterle, When atoms behave as waves: Bose-Einstein condensation and the atom laser. Rev. Mod. Phys. **74**, 1131 (2002)
12. S. Chu, The manipulation of neutral particles. Rev. Mod. Phys. **70**, 685 (1998)
13. C.N. Cohen-Tannoudji, Manipulating atoms with photons. Rev. Mod. Phys. **70**, 707 (1998)
14. W.D. Phillips, Laser cooling and trapping of neutral atoms. Rev. Mod. Phys. **70**, 721 (1998)
15. T. Nikuni, M. Oshikawa, A. Oosawa, H. Tanaka, Bose-Einstein condensation of dilute magnons in $TlCuCl_3$. Phys. Rev. Lett. **84**, 5868 (2000)
16. A.A. Serga, V.S. Tiberkevich, C.W. Sandweg, V.I. Vasyuchka, D.A. Bozhko, A.V. Chumak, T. Neumann, B. Obry, G.A. Melkov, A.N. Slavin, B. Hillebrands, Bose-Einstein condensation in an ultra-hot gas of pumped magnons. Nat. Commun. **5**, 3452 (2014)
17. J. Klaers, J. Schmitt, F. Vewinger, M. Weitz, Bose-Einstein condensation of photons in an optical microcavity. Nature **468**, 545 (2010)
18. S.A. Moskalenko, D.W. Snoke, *Bose-Einstein Condensation of Excitons and Biexcitons. And Coherent Nonlinear Optics with Excitons* (Cambridge University Press, Cambridge/New York, 2000)
19. R. Feynman, Simulating physics with computers. Int. J. Theor. Phys. **21**, 467–488 (1982)
20. S. Lloyd, Universal quantum simulators. Science **273**, 1073–1078 (1996)
21. I. Buluta, F. Nori, Quantum simulators. Science **326**, 108–111 (2009)
22. I.M. Georgescu, S. Ashhab, F. Nori, Quantum simulation. Rev. Mod. Phys. **86**, 153 (2014)
23. L.V. Butov, C.W. Lai, A.L. Ivanov, A.C. Gossard, D.S. Chemla, Towards Bose-Einstein condensation of excitons in potential traps. Nature **417**, 47 (2002)

24. J.P. Eisenstein, A.H. MacDonald, Bose-Einstein condensation of excitons in bilayer electron systems. Nature **432**, 691 (2004)
25. K.J. Vahala, Optical microcavities. Nature **424**, 839 (2003)
26. C. Weisbuch, M. Nishioka, A. Ishikawa, Y. Arakawa, Observation of the coupled exciton-photon mode splitting in a semiconductor quantum microcvity. Phys. Rev. Lett. **69**, 3314–3317 (1992)
27. A. Kavokin, J. Baumberg, G. Malpuech, F.P. Laussy, *Microcavities* (Clarendon Press, Oxford, 2006)
28. D. Snoke, P. Littlewood, Polariton condensates. Phys. Today **63**(8), 42–47 (2010)
29. H. Deng, H. Haug, Y. Yamamoto, Exciton-polariton Bose-Einstein condensation. Rev. Mod. Phys. **82**, 1490–1537 (2010)
30. E. Hecht, *Optics* (Addison-Wesley, 2001)
31. S. Christopoulos et al., Room-temperature polariton lasing in semiconductor microcavities. Phys. Rev. Lett. **98**, 126405 (2007)
32. G. Christmann, R. Butté, E. Feltin, J.-F. Carlin, N. Grandjean, Room temperature polariton lasing in a GaN/AlGaN multiple quantum well microcavity. Appl. Phys. Lett. **93**, 051102 (2008)
33. J.J. Baumberg, A.V. Kavokin, S. Christopoulos, A.J.D. Crundy, R. Butté, G. Christmann, D.D. Solnyshkov, G. Malpuech, G.B. von Högersthal, El Feltin, J.-F. Carlin, N. Grandjean, Spontaneous polarization buildup in a room-temperature polariton laser. Phys. Rev. Lett. **101**, 136409 (2008)
34. M. Zamfirescu, A. Kavokin, B. Gil, G. Malpuech, M. Kaliteevski, ZnO as a material mostly adapted for realization of room-temperature polariton laser. Phys. Rev. B **65**, 161205 (2002)
35. J.R. Chen, T.-C. Lu, Y.-C. Wu, S.-C. Lin, W.-R. Liu, W.-F. Hsieh, C.-C. Kuo, C.-C. Lee, Large vacuum splitting in ZnO-based hybrid microcavities observed at room temperature. Appl. Phys. Lett. **94**, 061103 (2009)
36. M. Litinskaya, P. Reineker, V.M. Agranovich, Exciton-polaritons in a crystalline anisotropic organic microcavity. Phys. Status Solidi A **201**, 646 (2004)
37. S. Kéna-Cohen, M. Davanço, S.R. Forrest, Strong exciton-photon coupling in an organic single crystal microcavity. Phys. Rev. Lett. **101**, 116401 (2008)
38. S. Kéna-Cohen, S.R. Forrest, Room-temperature polariton lasing in an organic single-crystal microcavity. Nat. Photon. **4**, 371 (2010)
39. K. Huang, *Statistical Mechanics* (Wiley, New York, 1987)
40. C.W. Lai et al., Coherent zero-state and π-state in an exciton-poalriton condensate array. Nature **450**, 529–533 (2007)
41. H. Deng, D. Press, S. Götzinger, G.S. Solomon, R. Hey, K.H. Ploog, Y. Yamamoto, Quantum degenerate exciton-polaritons in thermal equilibrium. Phys. Rev. Lett. **97**, 146402 (2006)
42. A. Imamoglu, R.J. Ram, S. Pau, Y. Yamamoto, Nonequilibrium condensates and lasers without inversion: exciton-polariton lasers. Phys. Rev. A **53**, 4250–4253 (1996)
43. H. Deng, G. Weihs, C. Santori, J. Bloch, Y. Yamamoto, Condensation of semiconductor microcavity exciton polaritons. Science **298**, 199–202 (2002)
44. J. Kapsrzak et al., Bose-Einstein condensation of exciton polaritons. Nature **443**, 409–414 (2006)
45. R.B. Balili, V. Hartwell, D. Snoke, L. Pfeiffer, K. West, Bose-Einstein condensation of microcavity polaritons in a trap. Science **316**, 1007–1010 (2010)
46. N.Y. Kim, K. Kusudo, C. Wu, N. Matsumoto, A. Löffler, S. Höfling, N. Kumada, L. Worschech, A. Forchel, Y. Yamamoto, Dynamic d-wave condensation of exciton-polaritons in a two-dimensional square-lattice potential. Nat. Phys. **7**, 681–686 (2011)
47. K. Kusudo, N.Y. Kim, A. Löffler, S. Höfling, A. Forchel, Y. Yamamoto, Stochastic formation of polariton condensates in two degenerate orbital states. Phys. Rev. B **87**, 214503 (2011)
48. N.Y. Kim, K. Kusudo, A. Löffler, S. Höfling, A. Forchel, Y. Yamamoto, Exciton-polariton condensates near the DIrac point in a triangular lattice. New J. Phys. **15**, 035032 (2013)
49. N.Y. Kim, K. Kusudo, A. Löffler, S. Höfling, A. Forchel, Y. Yamamoto, f-band condensates in exciton-polariton lattice systems. Phys. Rev. B **89**, 085306 (2014)

50. N. Masumoto, N.Y. Kim, T. Byrnes, K. Kusudo, A. Löffler, S. Höfling, A. Forchel, Y. Yamamoto, Exciton-polariton condensates with flat bands in a two-dimensional kagome lattice. New J. Phys. **14**, 065002 (2012)
51. T. Jacqmin, I. Carusotto, I. Sagnes, M. Abbarchi, D.D. Solnyshkov, G. Malpuech, E. Galopin, A. Lemaître, J. Bloch, A. Amo, Direct observation of Dirac cones and a flatband in a honeycomb lattice for polaritons. Phys. Rev. Lett. **112**, 116402 (2014)
52. M. Greiner, O. Mandel, T. Esslinger, T. Hänsch, I. Bloch, Quantum phase transition from a superfulid to a Mott insulator in a gas of ultracold atoms. Nature **415**, 39–44 (2002)
53. I. Bloch, J. Dalibard, S. Nascimbéne, Quantum simulations with ultracold quantum gases. Nat. Phys. **8**, 267–276 (2012)
54. R. Blatt, C.F. Roos, Quantum simulations with trapped ions. Nat. Phys. **8**, 277–284 (2012)
55. A.A. Houck, H. Türeci, J. Koch, On-chip quantum simulation with superconducting circuits. Nat. Phys. **8**, 292–299 (2012)
56. A. Singha, M. Gibertini, B. Karmakar, S. Yuan, M. Polini, G. Vignale, M.I. Katsnelson, A. Pinczuk, L.N. Pfeiffer, K.W. West, V. Pellegrini, Two-dimensional Mott-Hubbard electrons in an artificial honeycomb lattice. Science **332**, 1176–1179 (2011)
57. J. Hubbard, Electron correlations in narrow energy bands. Proc. R. Soc. Lond. A **276**, 238–257 (1963)
58. C. Wu, Unconventional Bose-Einstein condensation beyond the "No-node" theorem. Mod. Phys. Lett. **23**, 1 (2009)
59. J. Bloch, F. Boeuf, J.M. Gérard, B. Legrand, J.Y. Marzin, R. Planel, V. Thierry-Mieg, E. Costard, Strong and weak coupling regime in pillar semiconductor microcavities. Physica E **2**, 915 (1998)
60. T. Jacqmin et al., Direct observation of Dirac cones and a flatband in a honeycomb lattice for polartions. arXiv:1310.8105 (2013)
61. I.A. Shelykh, A.V. Kavokin, Y.G. Rubo, T.C.H. Liew, G. Malpuech, Polariton polarization-sensitive phenomena in planar semiconductor microcavities. Semicond. Sci. Technol. **25**, 013001 (2010)

Part V
Quantum Computing

Chapter 18
Layered Architectures for Quantum Computers and Quantum Repeaters

Nathan C. Jones

18.1 Introduction to Quantum Architectures

A computer architecture defines and organizes the components of a system, their roles, and the interfaces between them. In computer systems, the architecture of a system determines its performance, the difficulty of implementation, and its flexibility. A good architecture exposes the strengths of its underlying technologies while avoiding unnecessary dependence on a specific technology, allowing independent evolution over time, and occasionally wholesale replacement of components or subsystems. Developing a flexible framework is particularly important for the nascent field of quantum computing, where relatively little work on architecture has been performed. This problem is important since an architecture provides structure, not only for the quantum computer itself but also for the designers—organizing the system design can also serve to organize the conceptual and logistical problems of engineering a computer.

Here, we propose layered architectures for quantum computing and quantum communication which strive to be *modular* and *fault-tolerant*. The objective is to develop a framework for building up a quantum computer from individual components, while also providing a means to compare different approaches to quantum computing, such as nitrogen-vacancy centers in diamond, quantum dots, trapped ions, or atoms in optical lattices [1]. The layered framework can be adapted to different forms of quantum hardware, but to make this discussion concrete, we analyze specific instances of the architectures that are based on optical quantum dots [2–4]. The organizing principles of the architecture are explained as these specific implementations are developed step-by-step.

N.C. Jones (✉)
Edward L. Ginzton Laboratory, Stanford University, Stanford, CA 94305-4088, USA
e-mail: ncodyjones@gmail.com

Y. Yamamoto, K. Semba (eds.), *Principles and Methods of Quantum Information Technologies*, Lecture Notes in Physics 911, DOI 10.1007/978-4-431-55756-2_18

18.1.1 Prior Work on Quantum Computer Architecture

Many prospective quantum computing technologies have been demonstrated in experiment [1]. These technologies are guided by fundamental theory results, such as DiVincenzo's criteria for a viable quantum computing technology [5] and Steane's analysis of the complex systems need to run quantum error correction (QEC) adequately [6, 7]. More recently, architectural requirements for operating large-scale systems have been examined [8, 9]. For many technologies, small-scale interconnects have been proposed, but the problems of organizing subsystems using these techniques into a complete architecture for a large-scale system have been addressed by only a few researchers.

Some problems of quantum architecture have been examined for specific hardware, such as ion-trap proposals that uses separate memory and computing areas [10], or system designs tailored for particular error correction schemes [11, 12]. Oskin et al. consider the issues of classical control and movement of quantum data in scalable systems [13]. Duan and Monroe proposed long-range interconnects in the form of "flying" photonic qubits to distribute entanglement between ions located in distant traps [14], and such photonic channels could be utilized to realize quantum repeaters or distributed quantum computers [15]. Fowler et al. [16] investigated a Josephson junction flux qubit architecture considering the extreme difficulties of routing both the quantum couplers and large numbers of classical control lines, producing a structure with support for quantum codes and logical qubits organized in a line. Whitney et al. [17, 18] have investigated automated layout and optimization of circuit designs specifically for ion trap architectures, and Isailovic et al. [19, 20] have studied interconnection and data throughput issues in similar ion trap systems.

Recent advances in the operation of the topological quantum codes have yielded schemes for fault tolerance that require only nearest-neighbor connectivity in two dimensions, yet are still functional with error rates as high as 1 % per physical operation [21, 22]. The fact that these codes are readily adapted to solid-state quantum devices was the subject of several recent architecture analyses [23, 24]. As quantum hardware steadily improves in both accuracy and number of qubits, early forms of experimental quantum error correction are now being demonstrated [25–27]

18.1.2 Layered Framework

The layered architecture consists of five layers, where each layer is devoted to a closely related group of tasks. Two layers interact through defined functional behavior. To execute an operation, the upper layer issues commands to the layer

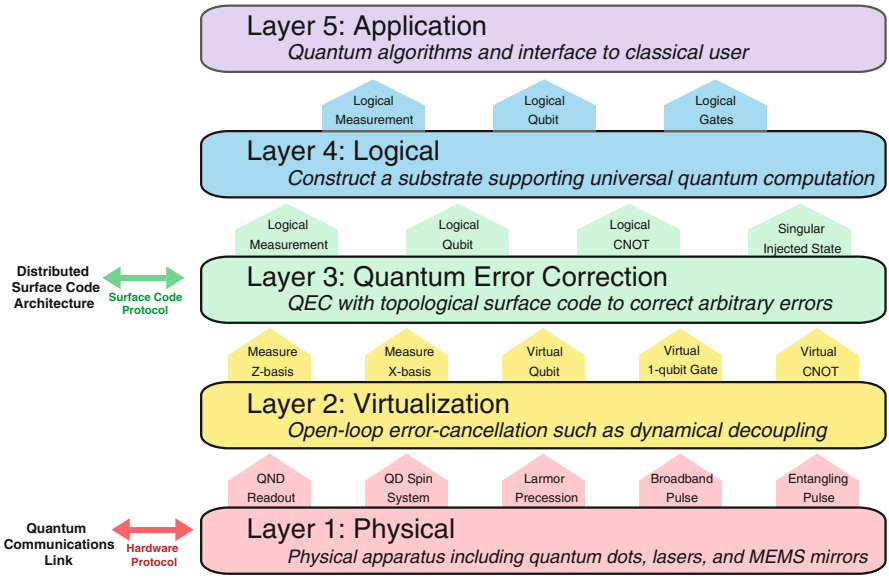

Fig. 18.1 Example of layered control stack quantum computer based on quantum dots [23]. Vertical arrows show what resources the lower layer provides to the upper. *Arrows* on the left margin indicate communication protocols for quantum repeaters or distributed quantum computing

below, then later processes the results. This modular design allows one layer to be changed (such as adopting a new error correction scheme) without significant change to the rest of the system.

The layered framework is represented with a control stack, as in Fig. 18.1, that shows the functions of each layer and the relationships between layers. This example is based on the quantum-dot architecture considered here, so the specific behavior of each layer could be different in another system. The top layer is the Application layer, which implements a quantum algorithm and returns output to the user. The bottom Physical layer contains the quantum hardware. The middle layers (Virtualization, Quantum Error Correction, and Logical) are used to suppress errors, converting the faulty hardware of the Physical layer into fault-tolerant qubits and quantum gates used by the Application layer.

Just as modern digital computers are frequently networked together, quantum computers may need to share a quantum information connection. To communicate quantum information between two devices, as in quantum repeaters [28] or in a distributed architecture [29], an appropriate communication protocol for Layer 1 (Physical) must be devised. These two quantum computers could be of wholly different technologies (say ion trap vs. quantum dot) if a practicable protocol exists. Moreover, a distributed surface code architecture [29] would also require a communication control protocol [30] in Layer 3. The location of these protocols in the layered framework is indicated in Fig. 18.1.

18.2 Physical Layer

The physical layer is the foundation of the quantum computer. All truly quantum effects happen here, with higher layers building complicated operations from sequences of processes performed at the physical layer. As a result, the physical layer exists solely to provide services to layers above, and no decision- or branching-based controls run here, as they occur in the upper layers. Implementing a quantum computer architecture begins at Layer 1, where basic hardware for storing and manipulating quantum information is constructed. We illustrate this process with a quantum computer based on the optical control of charged quantum dots known as QuDOS [23].

18.2.1 Spin Qubits in Quantum Dots

A quantum computer stores information in quantum bits, or qubits. The physical qubit in QuDOS is the spin state of an electron-charged InGaAs self-assembled quantum dot (QD) [31–36]. A QD can be excited to a "trion" state, consisting of an electron and an exciton, using light of wavelength around 900 nm. A transverse magnetic field separates the spin energy levels into two distinguishable ground states for use as a qubit [37]. The energy separation serves two purposes for quantum gates: (1) the energy splitting facilitates control with optical pulses as explained in Sect. 18.2.2; and (2) Larmor precession of the electron spin is continuous Z-axis rotation around the Bloch sphere, which together with selective timing of optical pulses provides complete single-qubit control of the electron spin state.

Accessing the quantum properties of a single electron spin system requires an enhanced interaction with light, and so an optical microcavity is necessary. To provide the two-dimensional geometry of gates required for error correction, this microcavity is planar and consists of two distributed Bragg reflector (DBR) mirrors grown vertically on a semiconductor wafer, which can be fabricated using molecular beam epitaxy (MBE). The QDs are positioned vertically at the center of this cavity to maximize interaction with the optical mode of the cavity. Figure 18.2 illustrates quantum dots arranged at the center of a planar cavity.

18.2.2 Optical Spin Control

The ability to perform fast manipulations of the quantum states stored in a quantum computer is essential for performing operations faster than decoherence processes can corrupt them, as well as for ensuring a fast overall algorithm execution time [9]. In QuDOS, ultrafast optical pulses centered 900–950 nm rotate the spin vector of an electron within a QD [3, 4]. By virtue of being short in duration, these pulses

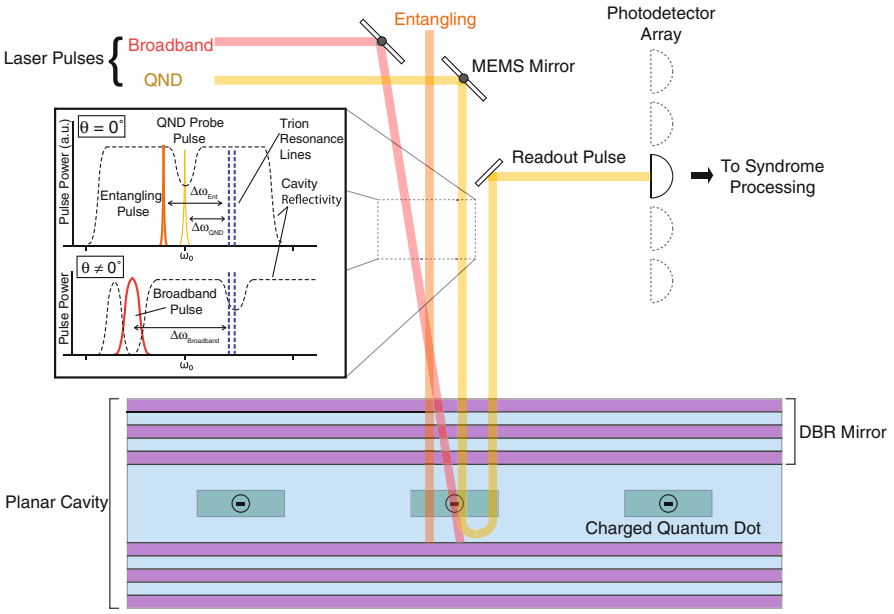

Fig. 18.2 Schematic diagram showing the primary components of the Physical Layer. Spins states are manipulated with laser pulses, which could be controlled by using MEMS micromirrors to dynamically direct laser pulses toward or away from each spin qubit [15, 38, 39]. The quantum non-demolition (*QND*) measurement and entangling pulses are modulated continuous-wave laser pulses, which are narrow in frequency bandwidth; these pulses are sent at normal incidence. The broadband pulses which rotate the electron spin state are angled relative to normal incidence, which shifts the cavity reflectivity response to higher frequencies. This enables the red-detuned pulse to enter the cavity at the first dip in the reflectivity. Each of the different laser pulses has a detuning relative to the trion (excited state) resonance frequency. The entangling pulse is also detuned from cavity resonance in a manner prescribed in Ref. [40]. The *inset image* shows the spectrum for the various laser pulses that implement different quantum operations

are broad in frequency, facilitating stimulated Raman transitions between the spin levels through excited-state trion levels. Therefore, the complete dynamics of the state rotation depends on a four-level system (consisting of the two metastable spin ground states and two excited trion states).

Other control pulses in QuDOS described below require a high-Q microcavity which has a narrow transmission window at the cavity resonance. The cavity can be problematic if the bandwidth of the broadband pulses is significantly larger than the transmission bandwidth of the cavity resonance. As a result, the broadband pulse cannot be sent directly into the microcavity. This problem is circumvented by sending the broadband pulses at angled (rather than normal) incidence. The cavity response is shifted to higher frequencies, so that a red-detuned pulse can enter the cavity at the first minimum in the cavity reflectivity as a function of frequency. Alternatively, one could send red-detuned pulses at normal incidence, sacrificing the majority of each pulse which is reflected; this approach is only viable if significantly

more optical power is available. Figure 18.2 shows the three laser pulses used in QuDOS, as well as their power spectrums.

A two-qubit gate that couples spins in two separate quantum dots is essential for both quantum computers and quantum repeaters, but challenging to implement. In quantum dots with transverse confinement provided by electrostatic gates, electronic manipulation of the electron wavefunction allows control over the exchange interaction, providing fast ($\sim$100 ps) quantum gates, as proposed some time ago [41] and demonstrated in numerous experiments [42]. Employing such gates for a hybrid system with both optical and electrical control is certainly possible, but requires further development of the optical control of electrically defined quantum dots [43]. Entanglement of directly tunnel-coupled vertically stacked InAs quantum dots has also been demonstrated [44], but the scalability of this coupling mechanism is uncertain. An exotic but promising possibility includes optically inducing longer-range, exciton-mediated exchange interactions [45, 46].

The QuDOS architecture would implement an all-optical entangling gate employing the optical nonlinearities provided by the planar microcavity. One proposal suggests using two lasers for both single-qubit and two-qubit gates [47]. However, recent experiments in single-qubit gates [2, 3] and theoretical proposals for two-qubit gates [40] suggest that complete spin control can be achieved with one laser for each type of operation. However, the demands on the optical microcavity system are challenging. The figure of merit for nonlinear optics using cavity QED is the cooperativity factor C, which is proportional to the cavity quality factor Q divided by the cavity volume V. Large values of this can be achieved via cavities with strong transverse confinement, such as the microdisk cavities proposed in Ref. [47]. This arrangement poses challenges for scalability. An obvious modification is to couple these cavities with waveguides; an architecture employing this approach was discussed in Ref. [29], and in this case substantial additional physical resources are needed to mitigate optical losses at the cavity-waveguide interfaces.

For the present architecture, we propose to confine light vertically using the planar microcavity and in transverse directions through angle-dependence of the cavity response, which is enhanced with high refractive-index contrast between alternating DBR mirrors [31]. Whether a microplanar microcavity arrangement will offer sufficient nonlinearity for an all-optically controlled dot architecture or whether electronically controlled gates will be employed will depend on forthcoming experimental developments. However, for the purposes of the present architecture, both gates are short range, a constraint handled by the surface code quantum error correction we employ (see Sect. 18.4), which demands only nearest-neighbor interactions. For comparison, short range gates can severely limit the efficacy of other quantum error correction schemes [48]. Long range couplings, for example to form bridges over optically inactive regions of a single chip or for chip-to-chip connections, will likely employ a variety of different quantum optical techniques which sacrifice speed for tolerance to optical loss; for a discussion, see Refs. [29, 49]. Incorporating such long-distance links into the present architecture must occur at both the Physical and QEC layers; the inclusion of such interconnections into QuDOS is the subject of future work.

18.2.3 Dispersive Non-demolition Measurement

The essential measurement operation in QuDOS consists of an optical pulse which uses dispersive quantum non-demolition (QND) readout based on Faraday/Kerr rotation. An optical probe pulse is reflected off of the cavity containing the quantum dot, and reflected pulse receives a phase shift that depends on the spin state of the quantum dot. Measuring the phase shift, such as by homodyne detection, performs projective measurement on the quantum-dot spin.

The physics of such a QND measurement has favorable properties for system integration. The fact that the probe pulse is off-resonant means that inhomogeneity among various quantum dots can be tolerated to a higher degree than is true in schemes involving resonant pulses. Moreover, the probe pulse can have a relatively high photon count, resulting in less stringent detector requirements. Experiments building toward such a measurement technique have recently been demonstrated, such as multi-shot readout of the spin state of a charged quantum dot [50, 51] and observation of a large phase shift induced by a neutral quantum dot in a photonic crystal cavity [52].

There are however several challenges related to this scheme. First, the measurement needs to be "single shot"—after just one probe pulse is applied, the measurement result via photodetection is correct with high probability. For a sufficiently large detuning, the ability to complete a single-shot QND measurement depends on the cooperativity factor C of the cavity. The phase shift in the probe pulse, θ, scales as the detuning, as well as with C. However, the probability for a photon to create a trion state, which decays by spontaneous emission, scales as C/Δ^2 [53]. For an input probe pulse that is in a coherent state, the number of photons required to resolve a phase shift θ scales as $1/\theta^2 \propto \Delta^2/C^2$, indicating that the probability of spontaneous emission during a single-shot measurement (which would spoil its QND character by introducing measurement error) scales as $1/C$, independent of Δ. Consequently, a large cooperativity factor of the cavity (e.g. $C \sim 10^3$) may allow single-shot dispersive QND measurements to be carried out with low measurement error.

18.3 Virtualization Layer

Quantum information systems are very sensitive to imperfections in their environment and control, which manifest as errors in the stored information. These errors can be systematic or random. Layer 2 sharply reduces systematic errors since this can be accomplished without measuring the system state, which is inherently faster and simpler than error-correcting methods which extract information about errors. Quantum error correction is implemented in Layer 3 to correct general errors, but doing so requires syndrome extraction circuits which operate at longer timescales. The purpose of Layer 2 is to reduce the error rate in virtual qubits and gates to the levels sufficient for Layer 3 to function.

18.3.1 Virtual Qubit

The virtual qubit is an abstraction of the underlying physical system. It approximates an ideal qubit as a two-level system whose state is constant until purposefully manipulated. However, the virtual qubit is modeled with physically relevant decoherence. In QuDOS, the virtual qubit is defined by the two spin states of an electron bound to a quantum dot. Without refocusing techniques, the electron spin has dephasing time $T_2^* \approx 1\,\text{ns}$ [54] caused by an inhomogeneous distribution of nuclear spins in the environment of the electron. This dephasing time is too short for error correction, but the coherence time can be extended to microseconds using dynamical decoupling (DD) techniques [54–56]. The electron spin resides in a magnetic field to facilitate optical control (see Sect. 18.2.2), so it precesses continuously at the Larmor frequency about the Z-axis on the Bloch sphere. Conversely, the idealized virtual qubit is unchanging when gates are not applied. This abstraction is achieved by appropriately timing measurement and control optical pulses in a frame rotating with the Larmor frequency. Measurement of the virtual qubit is achieved by the QND measurement of the spin state from Layer 1. In principle, multiple measurements could be performed in Layer 1 in order to increase measurement fidelity, but this architecture uses single-shot readout for the sake of speed.

18.3.2 Virtual Gates

Quantum operations must be implemented by physical hardware which is ultimately faulty to some extent. Many errors are *systematic*, so that they are repeatable, even if they are unknown to the quantum computer designer. In Layer 2, virtual gates manipulate the state of the virtual qubit using control operations in the Physical layer. When systematic errors are present, they can be suppressed using advanced control techniques in order to satisfy the demands of the error correction system, such as around 0.1 % error per gate [23, 24, 57]. For example, in QuDOS, the ultrafast pulses in the Physical layer may cause coherent over-rotation in the spin basis. Such errors may be correctable if action is taken faster than the relevant decoherence timescales.

The QuDOS architecture uses compensation sequences to correct systematic errors in the state rotation operations [58, 59]. Examples of systematic errors relevant to this system include laser intensity fluctuations over long timescales or the coupling strength of the electron to the optical field (caused by variations in the fabrication process). Since these errors are systematic over the timescales of operations in this architecture, a compensation sequence is effective for generating a virtual gate with lower net error than each of the constituent gates in the sequence. Moreover, many compensation sequences are capable of suppressing error for a range of error magnitudes, meaning the error does not have to be characterized exactly [58, 59].

18.4 Quantum Error Correction Layer

Error correction schemes remove entropy, which manifests as errors, from an information system. In contrast to Layer 2, quantum error correction schemes [60–65] such as the surface code [24, 57, 66, 67] can correct arbitrary errors in the underlying quantum information, assuming the probability of such errors is bounded below a certain threshold [68]. This process of information protection is achieved by continually consuming fresh ancilla states prepared to extract entropy from the quantum computer (via syndrome measurement). Layer 3 of this architecture framework is devoted to quantum error correction (QEC), which is vitally important to the successful operation of the quantum computer.

Like many quantum hardware proposals, optical quantum dots have faulty control, so the surface code is needed to provide logical qubits and gates with the exceptionally low error demanded of a large-scale quantum algorithm such as simulating quantum chemistry [69]. We will not review the entirety of the surface code here, but instead refer the interested reader to several key works in the field [24, 57, 67, 70]. This section is devoted to the important architecture-related matters of surface code QEC, such as estimating the resource overhead.

18.4.1 Surface Code in the Layered Architecture

The QEC layer uses error correction to provide fault-tolerant logical qubits, logical gates, and logical measurement to Layer 4. We explain the salient aspects of the surface code, the error correction scheme in QuDOS, but in general the processes in Layer 3 can vary significantly between different forms of QEC. The surface code provides the ability to correct arbitrary errors with quantum error correction [24, 57, 67, 70]. Virtual qubits in a broad 2-dimensional array are encoded into a single surface code via single-qubit operations and nearest-neighbor (CNOT) gates. Logical qubits are produced by forming "defects" in the surface code. A defect is a rectangular connected region of virtual qubits in the lattice which have been measured, so that the resulting surface code lattice has an SU(2) subspace of freedom, equivalent to a qubit. References [24, 67] gives an overview of the steps needed to construct the surface code. For practical matters (explained in Ref. [57]), a logical qubit is constructed from two defects. In contrast to Layer 2, the surface code gathers information on the system state by periodically measuring an error syndrome and using this knowledge to correct errors in post-processing. The probability of an undetected error decreases exponentially as a function of the "distance" [71] of the code, so that logical qubits and gates with arbitrarily low error are possible with a sufficiently large code. However, the virtual qubits and gates must have error rates below the threshold of the surface code (around 1 % [24, 72]), so that often error-reduction techniques in Layer 2 are necessary for Layer 3 to function. The error rate in virtual qubits and gates needs to be about an order of magnitude below the threshold, or approximately 0.1 %, for the surface code to be manageable in size.

In contrast to some other QEC schemes, the surface code has some key advantages for a quantum-dot architecture. In particular, the surface code requires only nearest-neighbor gates between qubits in a square lattice. Within this architecture framework, the necessary Layer 2 components for the surface code to function are the injection of single-qubit states needed for non-Clifford gates, a two-dimensional array of qubits with nearest-neighbor coupling (CNOT), and measurement in the X and Z bases [67, 73]. The two-dimensional arrangement with nearest-neighbor CNOT gates is most readily achieved in QuDOS with a physical 2D array of quantum dots, each supporting a virtual qubit. Although the single-qubit Pauli rotations are needed to form a complete set for universal quantum computation, we may neglect these in the present context by simply maintaining a continually-changing Pauli frame in a classical computer and modifying the final measurement results of the quantum computation [74].

18.4.2 Pauli Frames

A Pauli frame [74, 75] is a technique for tracking classically any Pauli gates needed during quantum computation without having to implement them explicitly, which is implied by the Gottesman-Knill theorem [76]. Quantum codes, such as the surface code, use projective measurement to identify Pauli errors on physical qubits within a code block. The syndrome reveals what these Pauli errors are, and error correction is achieved by applying those same Pauli gates to the appropriate qubits (Pauli gates are self-inverse). With the Pauli frame, one can avoid the unnecessary errors which could result from applying these Pauli gates in the quantum computation.

The Pauli frame works as follows. Classical hardware keeps a record of each Pauli gate instead of implementing this gate in quantum hardware. When a measurement is made, the binary outcome might be changed depending on which Pauli gates were associated with this qubit. This stored Pauli gate is called the Pauli frame [74, 75], because the reference frame for this qubit is changed. The way this works is that one implicitly relabels the axes on the Bloch sphere, rather than changing the state of the qubit. The computation proceeds normally, and the modified measurement results are equivalent to what would have been observed if the Pauli gates were explicitly implemented.

18.4.3 Resource Overhead for Error Correction

Estimates for the resource overhead in quantum error correction are critically important to architecture design. This overhead factor exists because QEC schemes embed "logical qubits" within a larger Hilbert space formed by many virtual qubits. The cost for protecting information through redundancy is the number of qubits is multiplied by an overhead factor. This overhead is an important quantity to understand and optimize, and it depends on several parameters of the quantum

Table 18.1 Parameters determining the size of the surface code in QuDOS

Parameter	Symbol	Value
Threshold error per virtual gate	$\varepsilon_{\text{thresh}}$	1.4×10^{-2}
Error per virtual gate	ε_{V}	1×10^{-3}
Logical circuit depth (in lattice refresh cycles)	K	6.8×10^{12}
Number of logical qubits	Q	600
Error per lattice refresh cycle	ε_{L}	2.7×10^{-18}
Surface code distance	d	27
Virtual qubits per logical qubit	VQ/LQ	4830

computer, such as error per virtual gate (ε_{V}), threshold error rate for the quantum code ($\varepsilon_{\text{thresh}}$), distance ($d$) of the code, and error per logical gate (ε_{L}), which depends on the algorithm being implemented.

We use the "KQ product" approximation [77] to determine ε_{L}. For a quantum algorithm with K gates in depth (allowing parallelism) and Q logical qubits, then the probability of logical error is given by

$$P_{\text{fail}} = 1 - (1 - \varepsilon_{\text{L}})^{KQ} \approx KQ\varepsilon_{\text{L}}, \tag{18.1}$$

where approximation applies for small ε_{L}. To ensure high probability of computation succeeding, we set $\varepsilon_{\text{L}} \ll 1/KQ$. The average error per logical gate in the surface code can be approximated [24, 71] with

$$\varepsilon_{\text{L}} \approx C \left(\frac{\varepsilon_{\text{V}}}{\varepsilon_{\text{thresh}}} \right)^{\lfloor \frac{d+1}{2} \rfloor}, \tag{18.2}$$

where C is a constant determined by the implementation of the surface code. The data in Ref. [71] suggests $C \approx 3 \times 10^{-2}$. Therefore, given a known ε_{V}, $\varepsilon_{\text{thresh}} = 1.4 \times 10^{-2}$, and $C \approx 0.03$, one can determine the necessary distance d such that the probability of failure of an entire quantum algorithm is sufficiently small. Table 18.1 provides an example of these calculations for the QuDOS architecture. Error per virtual qubit (ε_{V}) is also assumed to be 10^{-3}, and the K and Q values are for problems typical of quantum chemistry [69, 78]. To have a probability of logical error below 1 %, we set $\varepsilon_{\text{L}} \leq 10^{-2}/KQ$.

Solving Eq. (18.2) for the required code distance also indicates the number of virtual qubits needed to produce one logical qubit, which consists of two defects separated from each other and any other defects or boundaries by the distance of the code. Table 18.1 calculates this number for QuDOS, but we emphasize that a complete surface code quantum computer will need additional virtual qubits to facilitate movement of defects (braiding) and the distillation of magic states needed for non-Clifford logical gates [23, 24, 57, 79]. As a result, the total number of virtual qubits from Layer 2 is larger than simply the product of [*virtual qubits per logical qubit*] × [*logical qubits*]. Accounting for these additional virtual qubits is crucial to accurately estimating the resource requirements for QuDOS. More generally, the

quantity of these additional qubits depends significantly on the algorithm executed by the computation, since the number of magic states is related to the types of logical gates one must implement [78].

18.5 Logical Layer

The Logical layer bridges the gap between error correction and the algorithm at the top Application layer. The QEC layer provides logical qubits and a limited set of logical gates; however, the Application layer may request any arbitrary quantum gate, and it is the task of Layer 4 to create this gate. A specific implementation of the Logical layer depends on what services Layer 3 provides. We develop Layer 4 in the context of using the surface code in Layer 3, which provides logical qubits, logical `CNOT`, and injected magic states. In another quantum computer where the QEC layer provides different outputs, a different set of processes in the Logical layer may be needed.

18.5.1 Functions of the Logical Layer

The function of the logical layer is to provide the logical qubits and gates needed for the quantum algorithm in the Application layer. The surface code produces logical qubits and gates with arbitrarily high accuracy. However, the only fault-tolerant gates provided by the surface code are the Pauli 1-qubit gates (trivially performed by updating the logical Pauli frame), initialization and measurement in the X and Z bases, the CNOT gate and the identity gate (i.e. memory). Rotations about the X and Z Bloch sphere axes are produced using ancilla states of the form $\frac{1}{\sqrt{2}}\left(|0\rangle + e^{i\theta}\,|1\rangle\right)$. These so-called magic states come from faulty qubits that are injected into the code, then subsequently distilled using specialized circuits [24, 57, 67, 79]. Specific cases of importance to the surface code are $\theta = \pi/2, \pi/4$. By the Solovay-Kitaev theorem [80], these gates are sufficient to efficiently approximate arbitrary single-qubit logical unitary gates.

Just as in Layer 3, it is unnecessary to implement logical Pauli gates. Instead, a logical Pauli frame exists in Layer 4 which functions exactly like its counterpart in Layer 3 (see Sect. 18.4.2). Whenever a logical Pauli gate would be applied, the corresponding entry in the Layer 4 Pauli frame is modified. However, the performance requirements of this Pauli frame are not as strict as the one in Layer 3, because logical gates operate on slower timescales than virtual gates.

18.5.2 Magic State Distillation

Magic states are special ancillas that are used to produce a universal set of logical gates in the surface code. Faulty copies of the desired state are injected into the

surface code, then purified to high fidelity using distillation circuits [24, 57, 67, 79]. This process consumes a great deal of resources in the quantum computer since many logical qubits are required for distillation. If states are injected with an approximate error of 0.1 %, then distilling an $|A\rangle$ state ($\theta = \pi/4$) requires at least two levels of distillation, or at least 225 injected $|A\rangle$ states, to produce one logical $|A\rangle$ qubit with error probability low enough for the algorithm considered in Table 18.1. Consequently, distillation must be performed continuously in parallel with other logical operations to ensure that these purified states are available on demand. References [23, 24, 57, 67] discuss the resource cost and error scaling of this process in more detail. Importantly, distillation is probabilistic, but the probability of success is high for high-fidelity injected states.

18.6 Application Layer

The Application layer is responsible for executing the quantum algorithm, such as simulating chemistry [69], using fault-tolerant qubits and gates provided by the Logical layer. Logical gates constructed in Layer 4 are performed on the logical qubits provided by the QEC layer, and the end result is communicated to the classical user. The Application layer is completely unaware of the underlying hardware, since it interfaces only with Layer 4. Since the lower layers have provided all the resources for quantum computing, the figures of merit in Layer 5 are the number of available qubits and the speed of logical operations, which implies the time required to implement a certain quantum algorithm.

Timing of control operations at all layers is critically important to running an algorithm. In order to successfully correct errors faster than they occur, many operations must be executed in parallel [6]. Realizing this parallelism requires understanding the interdependence of the different layers in the architecture, which is depicted in Fig. 18.3. The plot depicts the timescales on which operations occur, and arrows are used to indicate where a lower-level process dictates the speed of an upper-level process. Because operations are performed on timescales that vary by orders of magnitude, the horizontal axis is a logarithmic scale. The large variation in timescales is a consequence of the overhead required for fault tolerance, including dynamical decoupling, error correction, and magic-state distillation.

18.7 Quantum Repeaters

Quantum repeaters are distinct from quantum computers, as repeaters are used for communication instead of computation. Nevertheless, the two machines may be constructed from many of the same components, including physical qubits and gates, error correction to accommodate faulty components, and control protocols for parallel operation. The systems are so similar that the layered architecture developed for computation can be adapted to communication by adding the

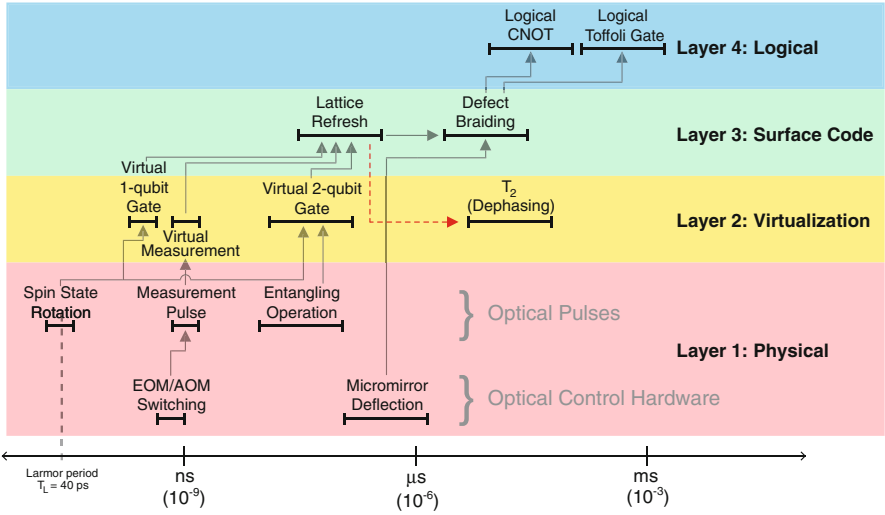

Fig. 18.3 Execution time for operations in QuDOS, according to layer in the architecture [23]. The *arrows* show how lower-level operations affect the speed of higher-level operations. The *red arrow* is a crucial relationship for error correction, and it signifies that the surface code lattice refresh must be much faster than the dephasing time. For generality, the Application layer is not shown since quantum algorithms can vary widely in complexity

appropriate communication interfaces, as shown in Fig. 18.1. A defining feature of a repeater is the ability to transmit quantum information over long distances, which almost surely requires coupling into photons. Quantum dots are naturally suited to photonic interfaces at the physical layer [81], and a modified version of surface code error correction is specifically designed for repeaters [30]. There are some notable differences between computer and repeater. Magic-state distillation is not necessary for communication, but a similar technique known as entanglement purification might be needed [82]. Additionally, a repeater could be smaller in size and complexity than a computer, because a repeater may only require ten or fewer logical qubits for temporary storage, instead of thousands that may be required for a large-scale algorithm.

18.8 Conclusion

This chapter examined how to organize quantum computers and repeaters in a systematic way that is modular and facilitates fault tolerance. Importantly, the layers are chosen in a way that encapsulates important subroutines for fault-tolerant quantum information. By separating important tasks like hardware control or error correction into distinct layers, this approach to architecture readily adapts to changes from new technologies or different design requirements.

The layered architecture is purposefully designed to implement fault-tolerant information processing, and the order of the layers in Fig. 18.1 reflects this. Layer 2 implements "open-loop control" to mitigate systematic errors, meaning there is no feedback from the hardware. The lack of feedback means operations in Layer 2 can be fast because there are no decisions to be made, and Fig. 18.3 shows that speed in Layer 2 is important. By contrast, Layer 3 implements error correction, which does require feedback in the form of syndrome measurement. Putting error correction in a layer above the open-loop control of the Virtualization layer is prudent because the processing of many rounds of measurement can be slow [22]. Layer 4 distills specialized magic states that are required for universal, fault-tolerant quantum computing. The distillation circuits themselves require error corrected gates, so this layer must be positioned above QEC in Layer 3. The Logical layer provides any arbitrary gate that might be required by the Application layer.

To demonstrate a layered architecture, we considered the QuDOS hardware platform. The physical quantum information consists of quantum-dot spin qubits that can be controlled and measured using optical pulses. These quantum dots can be arranged in a two-dimensional array inside a microplanar cavity, all of which is consistent with solid-state fabrication technology. Importantly, control operations in this technology can be very fast. Figure 18.3 shows that each logical operation requires many physical qubits and gates, so technologies like QuDOS that support large arrays of qubits and fast operations are a promising development path for quantum-information technology.

Acknowledgements This work was supported by the National Science Foundation CCF-0829694, the Univ. of Tokyo Special Coordination Funds for Promoting Science and Technology, NICT, and the Japan Society for the Promotion of Science (JSPS) through its "Funding Program for World-Leading Innovative R&D on Science and Technology (FIRST Program)."

References

1. T.D. Ladd, F. Jelezko, R. Laflamme, Y. Nakamura, C. Monroe, J.L. O'Brien, Quantum computers. Nature **464**, 45–53 (2010)
2. S.M. Clark, K.-M.C. Fu, T.D. Ladd, Y. Yamamoto, Quantum computers based on electron spins controlled by ultrafast off-resonant single optical pulses. Phys. Rev. Lett. **99**, 040501 (2007)
3. D. Press, T.D. Ladd, B. Zhang, Y. Yamamoto, Complete quantum control of a single quantum dot spin using ultrafast optical pulses. Nature **456**, 218–221 (2008)
4. J. Berezovsky, M.H. Mikkelsen, N.G. Stoltz, L.A. Coldren, D.D. Awschalom, Picosecond coherent optical manipulation of a single electron spin in a quantum dot. Science **320**(5874), 349–352 (2008)
5. D.P. DiVincenzo, The physical implementation of quantum computation. Fortschritte der Physik **48**(9–11), 771–783 (2000)
6. A.M. Steane, Quantum computer architecture for fast entropy extraction. Quantum Inf. Comput. **2**, 297 (2002)
7. A.M. Steane, How to build a 300 bit, 1 Giga-operation quantum computer. Quantum Inf. Comput. **7**, 171 (2007)

8. T.P. Spiller, W.J. Munro, S.D. Barrett, P. Kok, An introduction to quantum information processing: applications and realizations. Contemp. Phys. **46**(6), 407–436 (2005)
9. R. Van Meter, M. Oskin, Architectural implications of quantum computing technologies. ACM J. Emerg. Technol. Comput. Syst. **2**(1), 31–63 (2006)
10. D. Kielpinski, C. Monroe, D. Wineland, Architecture for a large-scale ion-trap quantum computer. Nature **417**, 709–711 (2002)
11. D. Copsey, M. Oskin, T. Metodiev, F.T. Chong, I. Chuang, J. Kubiatowicz, The effect of communication costs in solid-state quantum computing architectures, in *Proceedings of the Fifteenth Annual ACM Symposium on Parallel Algorithms and Architectures (SPAA'03)* (ACM, New York, 2003), pp. 65–74
12. K.M. Svore, A.V. Aho, A.W. Cross, I. Chuang, I.L. Markov, A layered software architecture for quantum computing design tools. Computer **39**(1), 74–83 (2006)
13. M. Oskin, F.T. Chong, I.L. Chuang, J. Kubiatowicz, Building quantum wires: the long and the short of it, in *30th International Symposium on Computer Architecture, 2003 (ISCA'03)*, San Diego (2003), pp. 374–385
14. L.-M. Duan, C. Monroe, Colloquium: quantum networks with trapped ions. Rev. Mod. Phys. **82**(2), 1209–1224 (2010)
15. J. Kim, C. Kim, Integrated optical approach to trapped ion quantum computation. Quantum Inf. Comput. **9**, 181–202 (2009)
16. A.G. Fowler, W.F. Thompson, Z. Yan, A.M. Stephens, B.L.T. Plourde, F.K. Wilhelm, Long-range coupling and scalable architecture for superconducting flux qubits. Phys. Rev. B **76**(17), 174507 (2007)
17. M. Whitney, N. Isailovic, Y. Patel, J. Kubiatowicz, Automated generation of layout and control for quantum circuits, in *Proceedings of the 4th International Conference on Computing Frontiers*, Ischia (2007), pp. 83–94
18. M.G. Whitney, N. Isailovic, Y. Patel, J. Kubiatowicz, A fault tolerant, area efficient architecture for shor's factoring algorithm, in *36th International Symposium on Computer Architecture, 2009 (ISCA'09)*, Austin (2009)
19. N. Isailovic, Y. Patel, M. Whitney, J. Kubiatowicz, Interconnection networks for scalable quantum computers, in *33rd International Symposium on Computer Architecture, 2006 (ISCA'06)*, Boston (2006), pp. 366–377
20. N. Isailovic, M. Whitney, Y. Patel, J. Kubiatowicz, Running a quantum circuit at the speed of data, in *35th International Symposium on Computer Architecture, 2008 (ISCA'08)*, Beijing (2008)
21. R. Stock, D.F.V. James, Scalable, high-speed measurement-based quantum computer using trapped ions. Phys. Rev. Lett. **102**(17), 170501 (2009)
22. S.J. Devitt, A.G. Fowler, T. Tilma, W.J. Munro, K. Nemoto, Classical processing requirements for a topological quantum computing system. Int. J. Quantum Inf. **8**(1–2), 121–147 (2010)
23. N. Cody Jones, R. Van Meter, A.G. Fowler, P.L. McMahon, J. Kim, T.D. Ladd, Y. Yamamoto, Layered architecture for quantum computing. Phys. Rev. X **2**, 031007 (2012)
24. A.G. Fowler, M. Mariantoni, J.M. Martinis, A.N. Cleland, Surface codes: towards practical large-scale quantum computation. Phys. Rev. A **86**, 032324 (2012)
25. M.D. Reed, L. DiCarlo, S.E. Nigg, L. Sun, L. Frunzio, S.M. Girvin, R.J. Schoelkopf, Realization of three-qubit quantum error correction with superconducting circuits. Nature **482**, 382 (2012)
26. R. Barends, J. Kelly, A. Megrant, A. Veitia, D. Sank, E. Jeffrey, T.C. White, J. Mutus, A.G. Fowler, B. Campbell, Y. Chen, Z. Chen, B. Chiaro, A. Dunsworth, C. Neill, P. O'Malley, P. Roushan, A. Vainsencher, J. Wenner, A.N. Korotkov, A.N. Cleland, J.M. Martinis, Superconducting quantum circuits at the surface code threshold for fault tolerance. Nature **508**, 500 (2014)
27. D. Nigg, M. Mueller, E.A. Martinez, P. Schindler, M. Hennrich, T. Monz, M.A. Martin-Delgado, R. Blatt, Quantum computations on a topologically encoded qubit. Science **345**, 302 (2014)

28. W. Dür, H.-J. Briegel, J.I. Cirac, P. Zoller, Quantum repeaters based on entanglement purification. Phys. Rev. A **59**(1), 169–181 (1999)
29. R. Van Meter, T.D. Ladd, A.G. Fowler, Y. Yamamoto, Distributed quantum computation architecture using semiconductor nanophotonics. Int. J. Quantum Inf. **8**, 295–323 (2010) Preprint available as arXiv:quant-ph/0906.2686v2
30. A.G. Fowler, D.S. Wang, C.D. Hill, T.D. Ladd, R. Van Meter, L.C.L. Hollenberg, Surface code quantum communication. Phys. Rev. Lett. **104**(18), 180503 (2010)
31. G. Björk, S. Pau, J. Jacobson, Y. Yamamoto, Wannier exciton superradiance in a quantum-well microcavity. Phys. Rev. B **50**(23), 17336–17348 (1994)
32. A. Imamoglu, D.D. Awschalom, G. Burkard, D.P. DiVincenzo, D. Loss, M. Sherwin, A. Small, Quantum information processing using quantum dot spins and cavity qed. Phys. Rev. Lett. **83**(20), 4204–4207 (1999)
33. N.H. Bonadeo, G. Chen, D. Gammon, D.G. Steel, Single quantum dot nonlinear optical spectroscopy. Physica Status Solidi B **221**(1), 5–18 (2000)
34. J.R. Guest, T.H. Stievater, X. Li, J. Cheng, D.G. Steel, D. Gammon, D.S. Katzer, D. Park, C. Ell, A. Thränhardt, G. Khitrova, H.M. Gibbs, Measurement of optical absorption by a single quantum dot exciton. Phys. Rev. B **65**(24), 241310 (2002)
35. J. Hours, P. Senellart, E. Peter, A. Cavanna, J. Bloch, Exciton radiative lifetime controlled by the lateral confinement energy in a single quantum dot. Phys. Rev. B **71**(16), 161306 (2005)
36. Y. Yamamoto, T.D. Ladd, D. Press, S. Clark, K. Sanaka, C. Santori, D. Fattal, K.M. Fu, S. Höfling, S. Reitzenstein, A. Forchel, Optically controlled semiconductor spin qubits for quantum information processing. Physica Scripta **2009**(T137), 014010 (2009)
37. M. Bayer, G. Ortner, O. Stern, A. Kuther, A.A. Gorbunov, A. Forchel, P. Hawrylak, S. Fafard, K. Hinzer, T.L. Reinecke, S.N. Walck, J.P. Reithmaier, F. Klopf, F. Schäfer, Fine structure of neutral and charged excitons in self-assembled in(ga)as/(al)gaas quantum dots. Phys. Rev. B **65**(19), 195315 (2002)
38. C. Kim, C. Knoernschild, B. Liu, J. Kim, Design and characterization of mems micromirrors for ion-trap quantum computation. IEEE J. Sel. Top. Quantum Electron. **13**(2), 322–329 (2007)
39. C. Knoernschild, C. Kim, B. Liu, F.P. Lu, J. Kim, Mems-based optical beam steering system for quantum information processing in two-dimensional atomic systems. Opt. Lett. **33**(3), 273–275 (2008)
40. T.D. Ladd, Y. Yamamoto, Simple quantum logic gate with quantum dot cavity QED systems. Phys. Rev. B **84**, 235307 (2011)
41. D. Loss, D.P. DiVincenzo, Quantum computation with quantum dots. Phys. Rev. A **57**, 120–126 (1998)
42. R. Hanson, L.P. Kouwenhoven, J.R. Petta, S. Tarucha, L.M.K. Vandersypen, Spins in few-electron quantum dots. Rev. Mod. Phys. **79**(4), 1217–1265 (2007)
43. M. Kuwahara, T. Kutsuwa, K. Ono, H. Kosaka, Single charge detection of an electron created by a photon in a g-factor engineered quantum dot. Appl. Phys. Lett. **96**(16), 163107 (2010)
44. D. Kim, S.G. Carter, A. Greilich, A.S. Backer, D. Gammon, Ultrafast optical control of entanglement between two quantum dot spins. arXiv:quant-ph/1007.3733 (2010, preprint)
45. C. Piermarocchi, P. Chen, L.J. Sham, D.G. Steel, Optical RKKY interaction between charged semiconductor quantum dots. Phys. Rev. Lett. **89**, 167402 (2002)
46. G.F. Quinteiro, J. Fernandez-Rossier, C. Piermarocchi, Long-range spin-qubit interaction mediated by microcavity polaritons. Phys. Rev. Lett. **97**(9), 097401–097404 (2006)
47. A. Imamo̅glu, D.D. Awschalom, G. Burkard, D.P. DiVincenzo, D. Loss, M. Shermin, A. Small, Quantum information processing using quantum dot spins and cavity QED. Phys. Rev. Lett. **83**, 4204 (1999)
48. T. Szkopek, P.O. Boykin, H. Fan, V.P. Roychowdhury, E. Yablonovitch, G. Simms, M. Gyure, B. Fong, Threshold error penalty for fault-tolerant quantum computation with nearest neighbor communication. IEEE Trans. Nanotechnol. **5**(1), 42–49 (2006)
49. T.D. Ladd et al., High-speed quantum computer with semiconductor spins, in *Semiconductor Quantum Bits*, eds. F. Henneberger, O. Benson, vol. 453 (Pan Stanford Publishing, Singapore, 2009)

50. J. Berezovsky, M.H. Mikkelsen, O. Gywat, N.G. Stoltz, L.A. Coldren, D.D. Awschalom, Nondestructive optical measurements of a single electron spin in a quantum dot. Science **314**(5807), 1916–1920 (2006)
51. M. Atatüre, J. Dreiser, A. Badolato, A. Imamoglu, Observation of faraday rotation from a single confined spin. Nat. Phys. **3**, 101–106 (2007)
52. I. Fushman, D. Englund, A. Faraon, N. Stoltz, P. Petroff, J. Vuckovic, Controlled phase shifts with a single quantum dot. Science **320**(5877), 769–772 (2008)
53. R. Long, T. Steinmetz, P. Hommelhoff, W. Hänsel, T.W. Hänsch, J. Reichel, Magnetic microchip traps and single-atom detection. Philos. Trans.: Math. Phys. Eng. Sci. **361**(1808), 1375–1389 (2003)
54. D. Press, K. De Greve, P.L. McMahon, T.D. Ladd, B. Friess, C. Schneider, M. Kamp, S. Höfling, A. Forchel, Y. Yamamoto, Ultrafast optical spin echo in a single quantum dot. Nat. Photonics **4**, 367–370 (2010)
55. L. Viola, E. Knill, Robust dynamical decoupling of quantum systems with bounded controls. Phys. Rev. Lett. **90**(3), 037901 (2003)
56. H.K. Ng, D.A. Lidar, J. Preskill, Combining dynamical decoupling with fault-tolerant quantum computation. Phys. Rev. **A84**, 012305 (2011)
57. R. Raussendorf, J. Harrington, K. Goyal, Topological fault-tolerance in cluster state quantum computation. New J. Phys. **9**(6), 199 (2007)
58. K.R. Brown, A.W. Harrow, I.L. Chuang, Arbitrarily accurate composite pulse sequences. Phys. Rev. A **70**, 052318 (2004)
59. Y. Tomita, J.T. Merrill, K.R. Brown, Multi-qubit compensation sequences. New J. Phys. **12**(1), 015002 (2010)
60. P.W. Shor, Scheme for reducing decoherence in quantum computer memory. Phys. Rev. A **52**(4), R2493–R2496 (1995)
61. A.M. Steane, Error correcting codes in quantum theory. Phys. Rev. Lett. **77**(5), 793–797 (1996)
62. A.R. Calderbank, P.W. Shor, Good quantum error-correcting codes exist. Phys. Rev. A **54**(2), 1098–1105 (1996)
63. D. Gottesman, Stabilizer codes and quantum error correction. PhD thesis, California Institute of Technology, Pasadena, 1997
64. P. John, Fault-tolerant quantum computation, in *Quantum information and computation*, ed. by H.-K. Lo, T. Spiller, S. Popescu (World Scientific, Singapore, 1998)
65. A. Kitaev, Fault-tolerant quantum computation by anyons. arXiv:quant-ph/9707021 (1997, preprint)
66. S.B. Bravyi, A.Y. Kitaev, Quantum codes on a lattice with boundary. arXiv:quant-ph/9811052 (1998, preprint)
67. A.G. Fowler, A.M. Stephens, P. Groszkowski, High-threshold universal quantum computation on the surface code. Phys. Rev. A **80**(5), 052312 (2009)
68. D. Aharonov, M. Ben-Or, Fault-tolerant quantum computation with constant error, in *Proceedings of the Twenty-Ninth Annual ACM Symposium on Theory of Computing (STOC'97)* (ACM, New York, 1997), pp. 176–188
69. A. Aspuru-Guzik, A.D. Dutoi, P.J. Love, M. Head-Gordon, Simulated quantum computation of molecular energies. Science **309**(5741), 1704–1707 (2005)
70. R. Raussendorf, J. Harrington, Fault-tolerant quantum computation with high threshold in two dimensions. Phys. Rev. Lett. **98**(19), 190504 (2007)
71. A.G. Fowler, D.S. Wang, L.C.L. Hollenberg, Surface code quantum error correction incorporating accurate error propagation. Quantum Inf. Comput. **11**, 8 (2011)
72. D.S. Wang, A.G. Fowler, L.C.L. Hollenberg, Surface code quantum computing with error rates over 1%. Phys. Rev. **A83**, 020302(R) (2011)
73. S.J. Devitt, A.G. Fowler, A.M. Stephens, A.D. Greentree, L.C.L. Hollenberg, W.J. Munro, K. Nemoto, Architectural design for a topological cluster state quantum computer. New J. Phys. **11**(8), 083032 (2009)
74. E. Knill, Quantum computing with realistically noisy devices. Nature **434**, 39–44 (2005)

75. D.P. DiVincenzo, P. Aliferis, Effective fault-tolerant quantum computation with slow measurements. Phys. Rev. Lett. **98**(2), 020501 (2007)
76. S. Anders, H.J. Briegel, Fast simulation of stabilizer circuits using a graph-state representation. Phys. Rev. A **73**(2), 022334 (2006)
77. M.A. Nielsen, I.L. Chuang, *Quantum Computation and Quantum Information*, 1 edn. (Cambridge University Press, Cambridge/New York, 2000)
78. N.C. Jones, J.D. Whitfield, P.L. McMahon, M.-H. Yung, R. Van Meter, A. Aspuru-Guzik, Y. Yamamoto, Faster quantum chemistry simulation on fault-tolerant quantum computers. New J. Phys. **14**(11), 115023 (2012)
79. S. Bravyi, A. Kitaev, Universal quantum computation with ideal clifford gates and noisy ancillas. Phys. Rev. A **71**(2), 022316 (2005)
80. C.M. Dawson, M.A. Nielsen, The solovay-kitaev algorithm. Quantum Inf. Comput. **6**, 81 (2006)
81. K. De Greve, L. Yu, P.L. McMahon, J.S. Pelc, C.M. Natarajan, N. Young Kim, E. Abe, S. Maier, C. Schneider, M. Kamp, S. Höfling, R.H. Hadfield, A. Forchel, M.M. Fejer, Y. Yamamoto, Quantum-dot spin–photon entanglement via frequency downconversion to telecom wavelength. Nature **491**, 421 (2012)
82. D. Deutsch, A. Ekert, R. Jozsa, C. Macchiavello, S. Popescu, A. Sanpera, Quantum privacy amplification and the security of quantum cryptography over noisy channels. Phys. Rev. Lett. **77**, 2818–2821 (1996)

Chapter 19
Analysis of an Atom-Optical Architecture for Quantum Computation

Simon J. Devitt, Ashley M. Stephens, William J. Munro, and Kae Nemoto

19.1 Introduction

The last century saw the discovery and development of a set of principles that describes physical reality at the atomic level of matter. These principles known as quantum mechanics has been extensively tested and is now being used to develop todays advantaged technologies. Quantum mechanics has played a vital support role for modern conventional information technology, improving the building blocks, through, for example, providing better understanding of material properties and of the functioning of components such as transistors, memory elements and GPS based location devices. Such technologies need to take into account the effects of quantum physics to operate correctly. However quantum mechanics allows much much more, it allows a new paradigm for the processing of information known as quantum information processing [5, 40, 54, 63, 76]. Since 1995, there has been a large worldwide effort to explore and develop quantum-based devices and technologies [23, 75]. Quantum key distribution (QKD) [26, 40], the technology by which one can create unconditionally secure (according to the laws of quantum mechanics) keys for classical cryptography is already commercially available. QKD is in a sense a communication tasks yet it has been long known that these quantum principles of superposition and entanglement can be used for computation tasks [14, 27, 41, 74]. One of the most famous examples is Shor's algorithm [74], which allows one to

S.J. Devitt • A.M. Stephens • K. Nemoto (✉)
National Institute of Informatics, 2-1-2 Hitotsubashi, Chiyoda-ku, Tokyo 101-8430, Japan
e-mail: devitt1@mac.com; astephens@nii.ac.jp; nemoto@nii.ac.jp

W.J. Munro
NTT Basic Research Laboratories, NTT Corporation, 3-1 Morinosato-Wakamiya, Atsugi, Kanagawa 243-0198, Japan
e-mail: william.munro@lab.ntt.co.jp

Y. Yamamoto, K. Semba (eds.), *Principles and Methods of Quantum Information Technologies*, Lecture Notes in Physics 911, DOI 10.1007/978-4-431-55756-2_19

factor large number of polynomial time (of order $O(\log N)^3$ for an N bit number) and will require a large quantum computer. This however is not an easy task to accomplish.

The problem of designing large scalable quantum computer architectures has been a major focus since the first introduction of physical architectures for QIP in the mid to late 1990s [1, 11, 12, 38, 47, 52, 56, 59, 60]. The development of a quantum computer not only capable of achieving a universal set of gates, but also incorporating the necessary flexibility to implement extensive quantum error correction is somewhat summarised in David DiVincenzo's famous criterion for a scalable quantum architecture [21, 22]. The five criterion (later amended to seven [22] to include QC Networkability) can be briefly summarised as,

1. *System is comprised of well characterized qubits and allows for scalability.*
2. *Ability to initialize the state of the qubits.*
3. *System provides long coherence times, much longer than a gate operation time.*
4. *A universal set of gates is experimentally feasible.*
5. *Qubit specific measurement capability.*
6. *Ability to interconvert stationary and flying qubits.*
7. *Faithful transmission of flying qubits between specified locations.*

This list of properties, unarguably necessary for any system proposed as a large scale quantum computer, does not encapsulate the subtleties required when one is attempting to design and operate a large-scale quantum architecture.

Since 2007 there has been rapid development of architectural designs that allows us to specify the structure and operation of a fully error-corrected quantum computer containing millions if not billions of components. These new designs generally have one common feature in that they all utilise new forms of error correction based on topological quantum codes [7–9, 13, 35, 48, 70]. While many other error correction codes exist, these topologically based ones have several important properties that make them applicable to many physical systems. These properties are

- They are geometrically local, i.e. interactions can be restricted to physically 2- or 3-dimensional nearest neighbour systems.
- They exhibit high fault-tolerant thresholds, up to 2 % per gate depending on underlying assumptions [3, 32, 68, 70, 78, 80, 86]. A number of physical systems including ion-traps [4, 42], superconducting systems [2], liquid-state nuclear magnetic resonance [72], and several solid state systems have demonstrated operational error rate well below this.
- Implementation of algorithms can be detached from the operation of the physical hardware and resource optimisation can be performed at a more abstract level, applicable to all system based on these codes.

The elegance of such coding models allows us, with great specificity, to design an arbitrarily large quantum computer. Comparatively simple modular elements can be designed to implement fully error corrected, topological computation. This method of architecture design is not necessarily always the choice for all major hardware

systems [17, 33, 46, 57, 58, 61, 81, 88], but it does suit our purpose here for the design of a module based atom-optical system. The basic module is composed of an atom (or artificial atom) embedded in an optical cavity. Photons that have never directly interacted with one another can be routed through the cavity to deterministically entangle one another [81].

In this chapter we will present a detailed summary of one such design, ranging from the fundamental physical building blocks all the way to optimisation and implementation of Shor's factoring algorithm [74] within the topological model. Such a detailed formulation will allow us to provide an accurate resource estimate of the number of quantum devices (modules) and the computational time required for very large factoring problems. We begin this discussion in Sect. 19.2 with a description of a photonic module, a device used to deterministically create entanglement between individual photonic qubits. Such a device forms the building block for the topological architecture. We will then in Sect. 19.3 describe the design of a photonic module architecture, how it prepares an appropriate cluster state for topological computation and how this cluster is used to correct errors. Section 19.4 then summarises how quantum logic is achieved in the topological model, ranging from how encoded gates are realised and how the size of the algorithm relates to the size of the topological cluster prepared by our hardware. Using this designs we will then conclude by providing resource estimates for Shor's factoring algorithm with respect to the total number of photonic modules and real computational time. The contents of this chapter are derived from the work in Refs. [15–18, 20, 29, 34, 79] and readers are encouraged to examine these papers for further details.

19.2 The Photonic Module

As was mentioned in the introduction, the photonic module is a simple device that allows us to deterministically entangle photons together mediated via an atomic system [16]. This device forms the building block of the entire computational architecture and no other quantum components are necessary. The design of this device is such that expanding the size of the computer only requires fabricating and then connecting additional photonic modules in a well defined way.

Let us now consider its operation in detail. The basis of the scheme, depicted in Fig. 19.1 is a mechanism to deterministically entangle the atomic system and a single photon. The atomic system considered is an L level systems with basis states $|1\rangle$, $|2\rangle$ and $|3\rangle$ where the $|2\rangle \leftrightarrow |3\rangle$ is (or near) resonant with the cavity (Fig. 19.1). We will assume the $|1\rangle \leftrightarrow |3\rangle$ transition is forbidden (or far off resonance). Now there are a number of techniques that can be used to entangle the photon and atom [6, 16, 37, 66, 77, 82, 87, 90], but here we will focus based on a state-dependent reflectivity technique [44, 45, 73, 83, 89]. This is where our photon picks up a phase shift dependent on which of the two lower level basis states the atomic system is in.

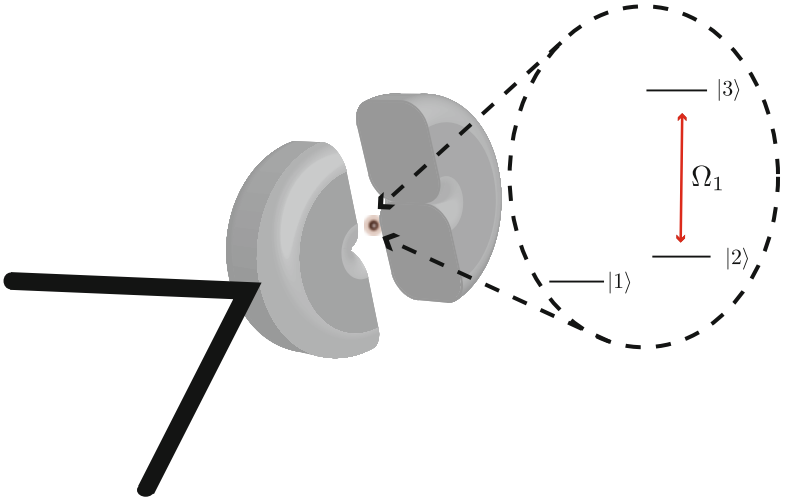

Fig. 19.1 Schematic representation of photonic module composed of a three level atoms embedded in an optical cavity. The three level system is in an L level configuration with the $|2\rangle \leftrightarrow |3\rangle$ resonant or near resonant with the cavity. We assume the $|1\rangle \leftrightarrow |3\rangle$ is forbidden

We can describe our combined system by the Hamiltonian

$$H = \hbar\omega_c a^\dagger a + E_1|1\rangle\langle 1| + E_2|2\rangle\langle 2| + E_3|3\rangle\langle 3| + \hbar g\left(a^\dagger|2\rangle\langle 3| + a|3\rangle\langle 2|\right) \quad (19.1)$$

which includes free energy terms for both the optical field and three level atoms as well as an interaction terms coupling the two together. In Eq. 19.1, ω_c is the cavity frequency, E_1, E_2, E_3 are the energy eigenvalues of the levels $|1\rangle$, $|2\rangle$ and $|3\rangle$ respectively, while g is the coupling strength between the cavity mode and the $|2\rangle \rightarrow |3\rangle$ transition ($\hbar\Omega_1 = E_3 - E_2$). For such a system [84], we can write the Langevin equations of motion for a and $\sigma_- = |2\rangle\langle 3|$ as,

$$\dot{a} = -\left\{i\Delta + \frac{\kappa}{2}\right\} a - ig\sigma_- + \sqrt{\kappa}a_{in} \quad (19.2)$$

$$\dot{\sigma}_- = -\left\{i\delta + \frac{\gamma}{2}\right\} \sigma_- + ig\sigma_z a + \text{Noise}(t) \quad (19.3)$$

where $\Delta = \omega_c - \omega$ is the detuning between the optical field and cavity while $\delta = \Omega_1 - \omega$ is the detuning between the atom center and cavity. κ is the damping rate of the cavity while γ the spontaneous emission rate of the atom (from $|3\rangle \rightarrow |2\rangle$). a_{in} is the signal incident field on the cavity, while Noise(t) is a noise operator related to the reservoirs of the atom. We also assume that the excited state $|3\rangle$ is never significantly populated, so $\langle\sigma_z\rangle \sim -1$ [44]. Using input-output theory [36, 84] we can straightforwardly show that the output field a_{out} is given by,

$$a_{out} = \frac{\kappa - 2i\Delta - \frac{4g^2}{\gamma + 2i\delta}}{\kappa + 2i\Delta + \frac{4g^2}{\gamma + 2i\delta}} a_{in} \tag{19.4}$$

We immediately see that our output field a_{out} depends heavily on the state of the atom. If the atom was in the $|1\rangle$ state then $g \sim 0$ and so we effectively have an empty cavity giving $a_{out} = (\kappa - 2i\Delta)\, a_{in} / (\kappa + 2i\Delta) \sim a_{in}$ if $\kappa \gg \Delta$. Alternatively for the atom in the $|2\rangle$ state we can have $a_{out} = \sim -a_{in}$ if $C = 4g^2/(\kappa\gamma) \gg 1$. This means we have a differential phase shift of π on the photon dependent on the state of the atom. For instance with a photon field in a superposition state $\left(|0\rangle_p + |1\rangle_p\right)/\sqrt{2}$ and the atom in a superposition of $\left(|1\rangle_a + |2\rangle_a\right)/\sqrt{2}$, then our interaction gives

$$\frac{1}{2}\left(|0\rangle_p + |1\rangle_p\right)\left(|1\rangle_a + |2\rangle_a\right) \rightarrow \frac{1}{2}\left(|0\rangle_p + |1\rangle_p\right)|1\rangle_a + \frac{1}{2}\left(|0\rangle_p - |1\rangle_p\right)|2\rangle_a \tag{19.5}$$

This CZ operation thus creates a maximally entangled state between the photon and atom. While we considered the photon state as a superposition of no photon and a single photon, the gate also works for the polarisation state $\left(|H\rangle_p + |V\rangle_p\right)/\sqrt{2}$, that is we can straight forwardly achieve

$$\begin{aligned}\frac{1}{2}\left(|H\rangle_p + |V\rangle_p\right)\left(|1\rangle_a + |2\rangle_a\right) &\rightarrow \frac{1}{2}\left(|H\rangle_p + |V\rangle_p\right)|1\rangle_a + \frac{1}{2}\left(|H\rangle_p - |V\rangle_p\right)|2\rangle_a \\ &= \frac{1}{2}\left(|1\rangle_a + \hat{Z}_p|2\rangle_a\right)\left(|H\rangle_p + |V\rangle_p\right)\end{aligned} \tag{19.6}$$

by either having the $|3\rangle \rightarrow |2\rangle$ polarisation sensitive or transforming the polarisation encoded photons to path encoded photons. Here $\hat{Z}_p = |H\rangle_p\langle H| - |V\rangle_p\langle V|$. In such a case, our effective unitary operation is $U = \exp\left[i\pi|2\rangle_a\langle 2| \otimes |V\rangle_p\langle V|\right]$. By performing a Hadamard operation on the atom state before and after U, we can generate an interaction of the form $U_{\text{eff}} = \exp\left[i\frac{\pi}{2}\sigma_{x,a} \otimes |V\rangle_p\langle V|\right]\exp\left[-i\frac{\pi}{2}|V\rangle_p\langle V|\right]$, that is a conditional bit-flip instead of the CZ gate plus a linear phase shift on the photon (such a phase shift can simply be undone with a phase shifter – either before the interaction is applied or after). Both interactions U and U_{eff} are very useful for generating large cluster states [67], however before we turn to look at this, let us first consider creating entanglement (Bell states) between photons that have never directly interacted [16].

The entangling gate U can be used simply to mediate the generation of entangled Bell states between temporally separated photons (in such a case the first photon interacts with the atom in the cavity initially and then the second photon). This is important because it means the photons do not have to be identical in the Hong-Ou-Mandel [43] sense as there is no direct interaction. Non identical photons can be used as long as the cavity interactions are the same. To illustrate the generation of this Bell state, consider two photons prepared individually in the $\left(|H\rangle_p + |V\rangle_p\right)/\sqrt{2}$ state sequentially interacting with the atom in the cavity (again the atom is prepared in the state $\left(|1\rangle_a + |2\rangle_a\right)/\sqrt{2}$). After such interactions we have

$$\frac{1}{4}\left(|H\rangle_{p1}+|V\rangle_{p1}\right)\otimes\left(|H\rangle_{p2}+|V\rangle_{p2}\right)|1\rangle_a + \frac{1}{4}\hat{Z}_{p1}\hat{Z}_{p2}\left(|H\rangle_{p1}+|V\rangle_{p1}\right)\otimes\left(|H\rangle_{p2}+|V\rangle_{p2}\right)|2\rangle_a \quad (19.7)$$

Performing a Hadmard operation on the $|1\rangle_a \rightarrow |1\rangle_a + |2\rangle_a, |2\rangle_a \rightarrow |1\rangle_a - |2\rangle_a$ gives

$$\frac{1}{4}\left(|H\rangle_{p1}|H\rangle_{p2}+|V\rangle_{p1}|V\rangle_{p2}\right)|1\rangle_a + \frac{1}{4}\left(|H\rangle_{p1}|V\rangle_{p2}+|V\rangle_{p1}|H\rangle_{p2}\right)|2\rangle_a, \quad (19.8)$$

and so by measuring the atom, we get either $\left(|H\rangle_{p1}|H\rangle_{p2}+|V\rangle_{p1}|V\rangle_{p2}\right)/\sqrt{2}$ or $\left(|H\rangle_{p1}|V\rangle_{p2}+|V\rangle_{p1}|H\rangle_{p2}\right)/\sqrt{2}$ depending on the measurement result (we label the $|1\rangle_a$ outcome an even parity (+1) result, while the $|2\rangle_a$ outcome an odd parity (-1) result). This shows we can sequentially entangle two photons that have never interfered directly with one another. Additionally unlike other schemes, the measurement result of the atom-cavity system never collapses the photons to unentangled states. Now since the even and odd parity Bell states differ only through local bit flips, either result is acceptable and an even parity state can be prepared by applying a local, classically controlled bit flip on any photon once the atomic system is measured. The preparation of the Bell state is therefore completely deterministic, with the classical result only giving parity information of the entangled state. As the even and odd parity states are interchangeable through local Clifford gates, correction can be fed forward to the end of subsequent operations on the photonic state.

The same technique used to create Bell state can be generalised to entanglement of multiple photons (as is illustrated in Fig. 19.2). For an initial N separable photon state of the form $|\psi\rangle^{\otimes N} = \left[|H\rangle_p + |V\rangle_p\right]^{\otimes N}/\sqrt{2^N}$ we can show

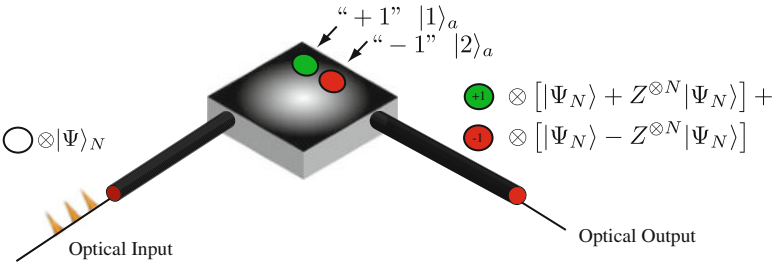

Fig. 19.2 Photonic module used to entangle a series of polarisation encoded photons. The atom-photon interaction based on the L level system in a cavity is polarisation sensitive to only the vertical component of each single photon. The measurement of the atom projects the photonic state into one of two locally equivalent states. For a measurement result $+1$ (associated with the detection result from the $|1\rangle_a$ state) we have the photonic state $\left(|\psi_N\rangle + \hat{Z}_p^{\otimes N}|\psi_N\rangle\right)/\sqrt{2}$ while for the -1 result (associated with the detection result from the $|2\rangle_a$ state) we have the photonic state $\left(|\psi_N\rangle - \hat{Z}_p^{\otimes N}|\psi_N\rangle\right)/\sqrt{2}$

$$\frac{1}{\sqrt{2^{N+1}}}\left[|H\rangle_p + |V\rangle_p\right]^{\otimes N}(|1\rangle_a + |2\rangle_a) \rightarrow \frac{1}{\sqrt{2}}|\psi\rangle^{\otimes N}|1\rangle_a + \frac{1}{\sqrt{2}}\hat{Z}_p^{\otimes N}|\psi\rangle^{\otimes N}|2\rangle_a.$$

Performing a Hadamard operation on the atom, we have

$$\frac{1}{2}\left[|\psi\rangle^{\otimes N} + \hat{Z}_p^{\otimes N}|\psi\rangle^{\otimes N}\right]|1\rangle_a + \frac{1}{2}\left[|\psi\rangle^{\otimes N} - \hat{Z}_p^{\otimes N}|\psi\rangle^{\otimes N}\right]|2\rangle_a \tag{19.9}$$

We can thus see that the natural operation of the module is to project the train of photons into a ± 1 eigenstate of the $\hat{Z}_p^{\otimes N}$ operator. Further we do not need to send into the module a separable state of the form $|\psi\rangle^{\otimes N}$, instead we can consider a general N photon state $|\psi_N\rangle$ (such a state could already be entangled). In the case we can show that after the operation of the module (including the Hadamard operations)

$$\begin{aligned}\frac{1}{\sqrt{2}}|\psi_N\rangle(|1\rangle_a + |2\rangle_a) \rightarrow \tfrac{1}{2}\left[|\psi_N\rangle + \hat{Z}_p^{\otimes N}|\psi_N\rangle\right]|1\rangle_a \\ + \tfrac{1}{2}\left[|\psi_N\rangle - \hat{Z}_p^{\otimes N}|\psi_N\rangle\right]|2\rangle_a\end{aligned} \tag{19.10}$$

The measurement outcome from the atomic system (± 1) will determine which eigenstate (either $\left(|\psi_N\rangle + \hat{Z}_p^{\otimes N}|\psi_N\rangle\right)/\sqrt{2}$ or $\left(|\psi_N\rangle - \hat{Z}_p^{\otimes N}|\psi_N\rangle\right)/\sqrt{2}$) one is projected into, with local operations applied to switch between eigenstates. We are also not restricted to Z based operations, instead for instance by applying a Hadamard operation on the atomic system before and after the photon-atom interaction, we can instead do X based operations [16]. Thus we could perform an overall operation like

$$\begin{aligned}\frac{1}{\sqrt{2}}|\psi_N\rangle(|1\rangle_a + |2\rangle_a) \rightarrow \tfrac{1}{2}\left[|\psi_N\rangle + \hat{X}_p^{\otimes N}|\psi_N\rangle\right]|1\rangle_a \\ + \tfrac{1}{2}\left[|\psi_N\rangle - \hat{X}_p^{\otimes N}|\psi_N\rangle\right]|2\rangle_a\end{aligned} \tag{19.11}$$

or another general interaction where some photons are associated with Z operations, others with X or Y or any of the single qubit clifford operators. A remarkable property of the module is that the number of entangled photons that are prepared depends only on the number sent through the module, we do not need to alter any internal structure of the module to entangle more photons [16].

We can immediately see the potential of these modules to create interesting photonic states. By adding appropriate single-photon routing and local operations to the module (as illustrated in Fig. 19.3) we can prepare any entangled photon state that can be expressed in terms of stabilisers [41].

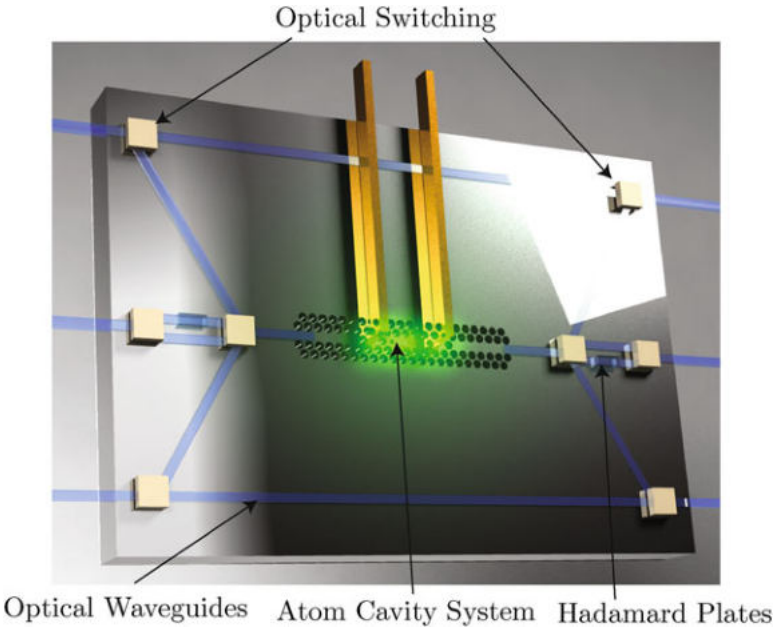

Fig. 19.3 Schematic design of a photonic chip. The chip is a 3-in 3-out integrated circuit containing one photonic module, classical single photon routing and two optical wave-plates allowing for the optional application of single photon Hadamard gates (or other Pauli gates) to specific photons

Stabilized states are a class of multi-qubit states that are eigenstates of a group of multi-qubit Pauli operators. Stabiliziers are a very simple framework for describing multi-qubit states and provide an efficient description of entangled states commonly used in cluster state quantum computing [67, 70] and quantum error correction [19]. Cluster states (an more generally quantum graph states) have a particularly elegant stabiliser description.

$$\mathscr{K}_a = X_a \bigotimes_b Z_{b\in m(a)} \qquad a \in [1, 2, \ldots, N]. \tag{19.12}$$

For each of the N-qubits in the graph, a, a stabiliser operator $\mathscr{K}_a$ is formed as the tensor product of X on qubit a and Z on any qubit that is connected to a, $b \in m(a)$. The graph state is then defined as the quantum state that is a simultaneous eigenstate of all N of these operators. For a general N-photon graph, N parity checks need to be performed. This can either be done by using N separate modules, or sequentially using only one. If multiple modules are available, many parity checks can be done in parallel without waiting for atomic readout, potentially speeding up state preparation.

An N-qubit stabiliser state is fully characterised by N Pauli operators and include states such as Bell states, higher order GHZ states and cluster states [67]. To prepare such states using the module, we perform a parity check of the N stabilisers describing the state. As each of the stabilisers for an N-photon stabilised state are described via an N-fold tensor product of the operators $\{I, X, Y, Z\}$, the ability to perform a parity check of the operator $Z^{N'}$ for $N' \ll N$ and then apply local operations is sufficient to perform a parity check on an arbitrary state with respect to any operator of that form. Given this, if we can selectively route photons within the train and apply local operations to any photon, the parity measurement performed by the module is sufficient to prepare any stabiliser state.

As the stabiliser structure of the desired state dictates the number of photons passed through the module for each atomic measurement, the coherence time of the atom-cavity system does not depend on the total number of photons in the entangled state. Instead, the atomic system must only maintain coherence until the parity of a specific stabilizer operator is measured, The number of non identity operators in any given stabiliser operator dictates the number of photons passed through the module in any one step and therefore the coherence time required for the atom-cavity system. For instance, an N-photon cluster state appropriate for quantum computation has a well-known stabiliser structure, with a maximum of five photons passing through the module before measurement. Regardless of the total size of the cluster, the atomic system only needs to maintain coherence long enough for five photons to pass through the module between initialisation and measurement.

Now making use of our module we can deterministically prepare large photonics states, the next section examines how an array of these devices can be used to make states appropriate for large-scale quantum computation [62, 69, 70].

19.3 Towards Fault-Tolerant Quantum Computation

So far, we have introduced a device to prepare arbitrary stabilizer states from unentangled photons. Combined with adaptive single-qubit rotations and single-photon detectors, this is sufficient for universal quantum computation [62]. However, without error correction, errors due to decoherence and various imperfections will accumulate and may compromise the scalability of the architecture. To overcome these errors, our architecture is designed to implement topological error correction [13, 49]. In particular, we use a network of photonic modules to prepare a topological cluster state, which is a resource for universal *fault-tolerant* quantum computation [69, 70].

The three-dimensional topological cluster state is a cluster state on the lattice with an elementary unit cell shown in Fig. 19.4a. Qubits are located at the centre of faces and edges of the unit cell. The stabilizer group is generated by weight-five operators, as described in the previous section.

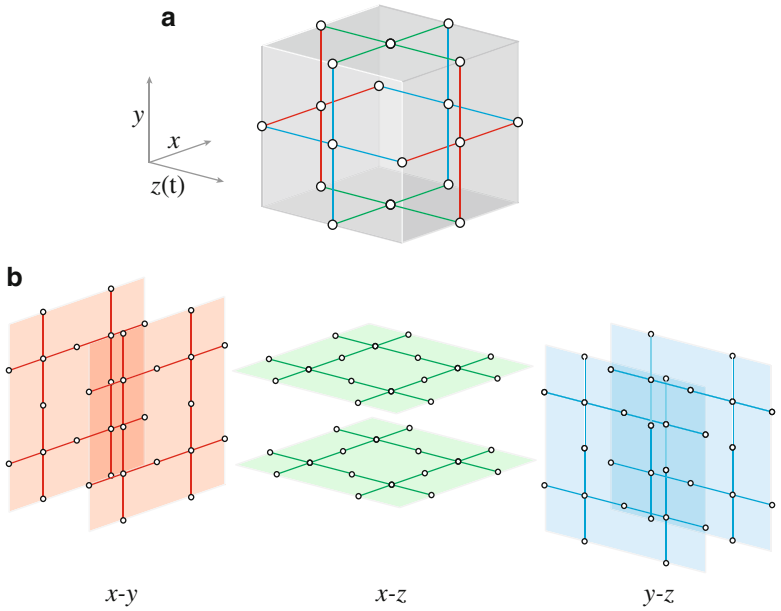

Fig. 19.4 **(a)** Unit cell of the three-dimensional topological cluster state. Each vertex represents a qubit and edges represent entanglement specified by the stabilizer group. The stabilizer generators can be divided into three distinct types according to their orientation $x - y$, $x - z$, and $y - z$, as illustrated in *red*, *green*, and *blue* respectively. **(b)** Extending the lattice, we see the pattern of stabiliser measurements required to prepare the topological cluster state. The order of measurements is fixed by the association of the z axis with time

The significance of the topological cluster state is revealed by associating one of its spatial dimensions with simulated time [69, 70]. Then, the topological cluster state simulates the evolution of a two-dimensional array of qubits encoded in the surface code [9, 35]. As we will see, this property allows the state to be used a resource to encode logical information, perform a universal set of gates on the logical information, and detect and correct errors affecting the physical qubits. Moreover, this encoding inherits the remarkable features of the surface code – namely, a high tolerance to errors (around one percent per physical qubit) and the ability to manipulate the logical information using local measurements [32, 68]. We will return to describe this encoding in detail, but for now we focus on how the architecture is designed to prepare and then measure the topological cluster state.

19.3.1 A Modular Quantum Computer Architecture

The architecture is designed to prepare the topological cluster state from unentangled photons by measuring each of the stabilizer generators. These measurements

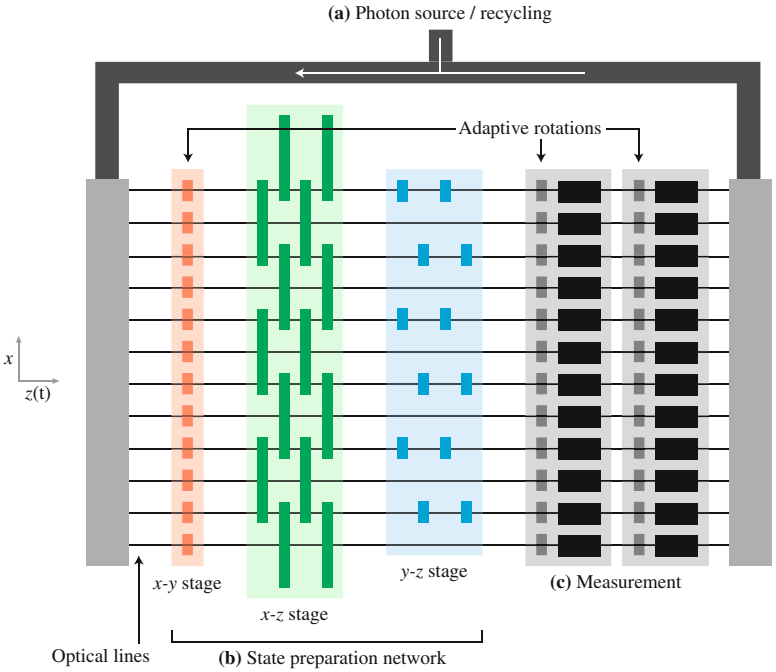

Fig. 19.5 Cross-sectional schematic of the architecture. The architecture consists of a reliable source of unentangled single photons, a network of photonic modules to prepare the topological cluster state, and additional modules to measure the photons to enact the computation. These elements are connected by optical lines and classical switches, and photons flow through the network along the z axis. **(a)** An array of photonic modules (not shown) provides single photons distilled from a weak coherent-light source. These photons combine with photons recycled from the output of the network to provide the input state. **(b)** An array of waveplates adjusts the input state as required and two arrays of photonic modules measure stabilizer generators to prepare the topological cluster state, where the coloration corresponds to Fig. 19.4b. **(c)** A final array of photonic modules non-destructively measures the output state, where waveplates adjust the measurement basis as required. The measurements are repeated to detect photon loss

are performed using a network of photonic modules. Motivated by the natural 2+1-dimensional interpretation of the topological cluster state, the concept of simulated time dictates the order of the measurements. Furthermore, photons leaving a photonic module can proceed to subsequent modules before the outcome of the measurement is known. These concepts are combined, leading to a *flowing* architecture in which photons that are initially unentangled cascade through a series of photonic modules and emerge as the successive two-dimensional planes of the topological cluster state [17, 79].

Figure 19.5 gives an overview of the architecture. In greater detail, the architecture consists of a two-dimensional array of common optical waveguides carrying photons along the z axis. To reflect the structure of the lattice on which the topological cluster state is defined, there are two groups of waveguides distinguished

by the repetition rate of the photons, which we denote as half-rate and full-rate lines. The temporal spacing of the photons is parametrized by an interval T, which is bounded below by the minimum interaction time required for the operation of the photonic module and bounded above by the coherence time of the atomic system [79].

Photonic modules are arranged along the $x-y$ plane to perform the stabilizer measurements required to prepared the topological cluster state [17]. Each module is connected to three adjacent waveguides, oriented according to the different orientations of the stabilizer generators, illustrated in Fig. 19.4b. The photonic module also enables the non-destructive measurement of photons, and thus an array of modules performs the single-qubit measurements required to enact the computation after the topological cluster state is prepared. Adaptive waveplates perform single-qubit rotations, adjusting the initial state of the photons and the final measurement basis as required. Lastly, to eliminate the need for high-frequency single-photon sources, the outgoing photons are recycled to be used as incoming photons at a later time [18]. As the photonic module also enables the heralded distillation of single photons from a weak coherent-light source (with low probability), an array of photonic modules provides the photons that initialize the network [18]. These modules (and appropriate classical routing) also serve to replace photons that are lost due to fiber attenuation or coupling inefficiency.

The primary task in preparing the topological cluster state is imposing the stabilizer conditions that specify the topological cluster state. Reflecting the three distinct types of stabilizer generators, illustrated in Fig. 19.4b, these conditions are satisfied by three distinct stages of the architecture, outlined below:

- $x-y$ **stabilizer stage:** For an arbitrary input state, measurements are required to the impose the stabilizer conditions in the $x-y$ plane. However, we are free to specify an input (product) state that already satisfies these conditions. Thus, the $x-y$ stabilizer stage consists of an array of waveplates to rotate the incoming photons are required. Only this stage of the three can be done by adaptive rotations, whereas the rest two stages serves as the entanglement sequence for the cluster state. Photons in the half-rate lines are prepared in the $+1$ eigenstate of X, and photons in the full-rate lines are prepared in the $+1$ eigenstate of Z. This ensures that the input state satisfies the stabilizer conditions in the $x-y$ plane as it enters the next stage of the network.
- $x-z$ **stabilizer stage:** The $x-z$ stabilizer stage consists of an array of photonic modules oriented along the x axis, each connected to three adjacent waveguides. Each photonic module periodically measures stabilizer generators centered at a particular $x-y$ coordinate, as illustrated in Fig. 19.6. To perform these measurements whilst maintaining synchronicity and avoiding collisions between photons, photonic modules are required to have several settings to control incident photons. At different times, incident photon will interact with the atomic system, be delayed by the atomic system, or bypass the atomic system

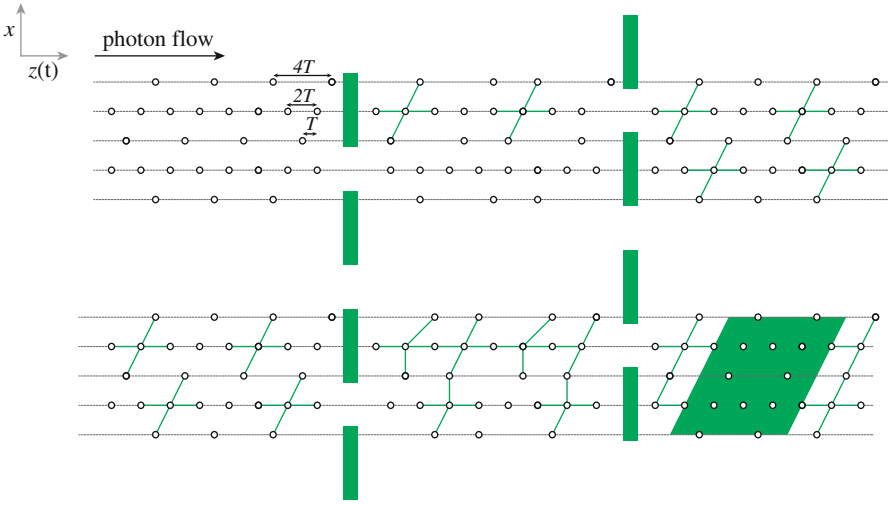

Fig. 19.6 Action of the $x-z$ stabilizer stage. Photons flow from left to right through the network with the temporal spacing parameterized by the atom-photon interaction time T. The photonic modules perform stabilizer measurements, imposing the stabilizer conditions in the $x-z$ plane

entirely with no delay. Additionally, in some cases, a Hadamard operation will be applied before and after a photon interacts with the atomic system. These various requirements are satisfied by the classical routing illustrated in Fig. 19.3. Photon delay is achieved by preparing the atomic system in the $|1\rangle$ state, preventing it from entangling with the photon during the interaction time [17]. Lastly, the atomic system will be periodically measured and re-prepared. The switching sequence to control these various settings during the $x-z$ stabilizer state is detailed in Ref. [17]. Following this stage the stabilizer conditions in the $x-z$ plane are satisfied.

- $y-z$ **stabilizer stage:** The $y-z$ stabilizer stage is identical to the $x-z$ stage, but now the photonic modules oriented along the y axis. This reflects the 90°-rotational symmetry of the topological cluster state.

Following these three stages, the state of the photons emerging from the network satisfies all of the stabilizer conditions of the topological cluster state. As incoming photons are continually entangled with the state, outgoing photons are immediately measured to enact the computation. This limits the propagation time of each photon to a constant time independent of the extent of the topological cluster state. To increase the extent of the topological cluster state, we simply extend the $x-y$ dimension of the architecture in a modular fashion, allowing us to continuously prepare an abitrarily large topological cluster state. In general, $4N^2+4N$ photonic modules are required to continuously prepare a topological cluster state with an $N \times N$ cross section of unit cells [17].

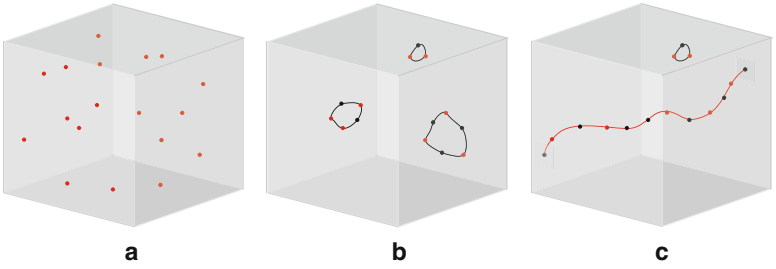

Fig. 19.7 Error correction. **(a)** An example of a distribution of errors affecting a set of physical qubits in the bulk of the topological cluster state. **(b)** The state after a set of corrections has been applied. Some of the initial errors were corrected, others combined with corrections to form closed cycles. As these are homological trivial operators equivalent to the identity operator, error correction has succeeded in restoring the system to its initial state. **(c)** The state after a different set of corrections has been applied. In this case, the errors and corrections combined to form an open cycle. As this is a homological non-trivial operator equivalent to a logical operator, error correction has failed

19.3.2 Topological Error Correction

With a sufficiently large topological cluster state, logical qubits can be introduced and then manipulated to execute an arbitrary quantum algorithm. However, for the output of the algorithm to be reliable, we require an effective procedure to detect and correct the various errors that are likely to arise as the topological cluster state is prepared from unentangled single photons. This is the role of topological error correction [13, 49]. In principle, the task is to ensure that any errors affecting the states of the physical qubits are unlikely to lead to errors affecting the states of the logical qubits. In effect, we are required to suppress the probability that non-trivial homological cycles of errors are established in the topological cluster state [30, 70]. Figure 19.7 gives an overview of the task at hand. To illustrate, we will assume a uncorrelated single-qubit noise model in which each physical qubit in the topological cluster state is affected by a discrete Z error with probability p.

Error correction is based on the well-defined stabilizer group of the topological cluster state. Consider the stabilizer operator that is the bitwise tensor product of the six stabilizer generators associated with the six centre qubits on each face of a unit cell. To determine its eigenvalue, it is sufficient to independently measure each qubit in the X basis and then classically compute the parity of the six measurement results. If there are no errors affecting the qubits, then the eigenvalue will equal $+1$. However, due to the commutation relation $XZ = -ZX$, if there are an odd number of Z errors affecting the six qubits, then the eigenvalue will equal -1. Identical stabilizer operators are associated with every unit cell of the topological cluster state, so by measuring the eigenvalue of each of these operators we are able to detect Z errors affecting the physical qubits [30, 70].

An isolated Z error will result in two adjacent cells having eigenvalue equal to -1. Connected chains of errors will result in the cells at the endpoints having

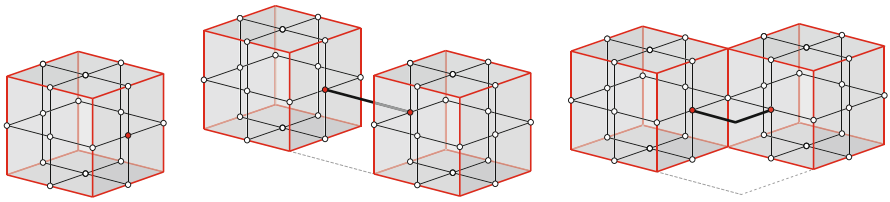

Fig. 19.8 Examples of how chains of errors (indicated by *red circles* connected by *solid black lines*) are revealed by stablilizers with eigenvalue equal to -1 at the endpoints (indicated by the associated unit cells, outlined in *red*)

eigenvalue equal to -1, illustrated in Fig. 19.8. It is these the locations of these cells that make up the error syndrome, from which we must infer the location of the errors [13, 24]. If errors occur independently with probability $p \ll 1$, then the most likely set of errors consistent with the syndrome is a set of chains that connects the cells in pairs in the shortest length. To find this set, we express the syndrome as a weighted graph and find the minimum-weight set of edges using Edmonds' perfect matching algorithm [25, 53]. This is not an optimal strategy, but it leads to a computationally efficient algorithm for decoding the error syndrome [13, 86]. An identical procedure occurs on the primal lattice, either independently or in conjunction to account for correlations between the noise on the two lattices.

If the error rate is sufficiently low, then errors will typically be well isolated and easily identified. In this case, enlarging the topological cluster state will make it less likely that long cycles of errors will arise. On the other hand, if the error rate is too high, then enlarging the topological cluster state will make this more likely. The threshold error rate that separates these two regimes is critical, as the effective physical error rate in the architecture must be below this value for error correction to be effective.

To determine the threshold error rate, we undertake a series of Monte Carlo simulations of topological cluster states of various sizes, parameterized by the linear dimension of the topological cluster state in unit cells d. We estimate the logical error rate (the probability that a homologically non-trivial cycle of errors remains after error correction) as a function of the single-qubit physical error rate p. Our numerical results are shown in Fig. 19.9, indicating that the threshold error rate is 0.0290(1) per qubit. This value is consistent with other studies of topological error correction and the associated random-plaquette gauge model [64, 70, 85]. We also probe the performance of the scheme for error rates well below the threshold. These results are shown in Fig. 19.10. In this regime, we confirm that increasing the extent of the topological cluster state results in an exponential suppression of the logical error rate as required.

The threshold error rate sets an error budget which must account for a variety of noise sources during the preparation and measurement of the topological cluster state. For example, if the topological cluster state is prepared using a standard quantum circuit based on controlled-phase gates, then the threshold error rate is

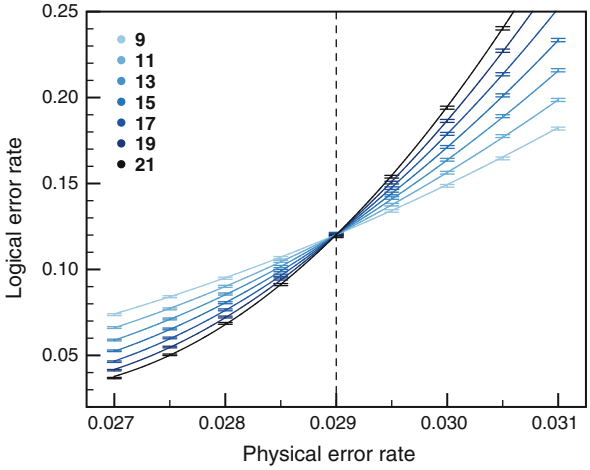

Fig. 19.9 Numerical simulations of topological cluster-state error correction for lattices of various size d under a phenomenological noise model where each qubit is affected by a Z error with probability p. For given values of p and d, the logical error rate is estimated from an average of at least 10^6 independent trials. Error bars indicate $\pm 2\sigma$ statistical error due to finite sample size. Curves are derived from a universal scaling function fit to the data. From this fitting, the value of the threshold error rate is found to be 0.0290(1) and is indicated by the *dashed vertical line*

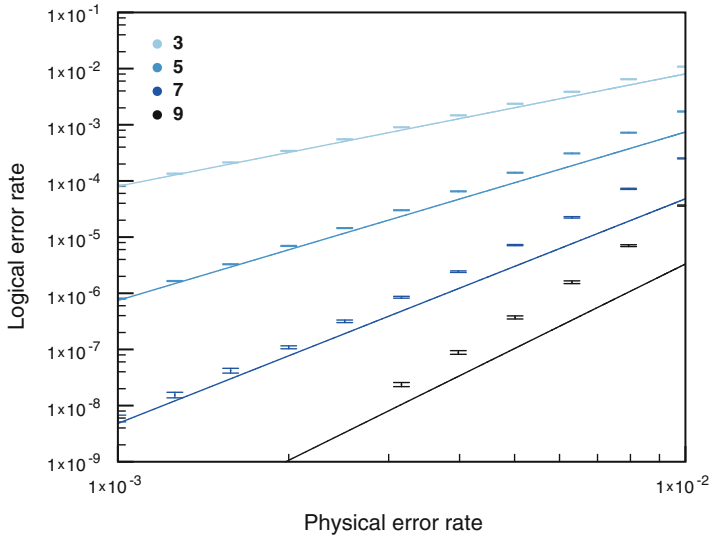

Fig. 19.10 Numerical simulations of topological cluster-state error correction for lattices of various size d. Error bars indicate $\pm 2\sigma$ statistical error due to finite sample size. Curves are leading-order approximations of the form $R_d p^{(d+1)/2}$, which are valid for low physical error rates. Values of R_d are estimated by sampling from all possible combinations of $(d+1)/2$ errors

0.0063 per gate [3, 70, 78]. Topological error correction is robust against more general correlated errors and qubit loss, with a corresponding reduction in the threshold error rate [3, 55]. Importantly, no modification of the architecture is required provided that the cumulative noise satisfies the threshold condition. The architecture can be efficiently scaled in the $x - y$ dimension to prepare a sufficiently large topological cluster state to achieve the desired logical error rate.

19.4 Topological Computation and Performance

The previous sections have detailed the structure and operation of the quantum hardware that is needed to create a large 3-dimensional lattice of entangled qubits. This section details how this lattice is used in order to perform fault-tolerant, error corrected quantum computation and how we ultimately calculate resource costs (in terms of physical devices and computational time) for a large-scale quantum algorithm.

The topological cluster state model of quantum computation is a measurement based model and therefore operations are realised via the consumption of the entangled state [67]. The quantum hardware does not care what the final computational application is [15]. The only condition on the quantum hardware is that it produces a large enough lattice for the given application and that all physical error rates lie below the fault-tolerant threshold of the code.

In this section we summarise the important operations necessary for utilising the cluster to perform computation and what quantum algorithms look like in this model. We conclude this section with a brief discussion about how resources are estimated (in terms of the number of photonics modules and the total computational time) for a large scale quantum algorithm run on the architecture we have detailed. This section will only contain a brief review, for more details please see Refs. [15, 20, 30, 70]

19.4.1 Defining Qubits and Gates

Previously we had examined how to perform error correction on a perfect lattice (i.e. one that does not contain any encoded information). However, this is useless for computation. We need a method of introducing degrees of freedom (which will be used to store encoded information) into the lattice. This is done by creating a hole (or defect) in the lattice by removing, or disentangling, specific qubits at specific points in time (Fig. 19.11). As noted in the previous section. The lattice is produced by the hardware one cross-section at a time. The *flow* of the topological computation takes place as each cross-sectional sheet of the cluster is measured. Each time a cross-section of the lattice is measured, information is teleported to the next successive cross-sectional sheet and the information processing can be performed by changing how each cross-sectional sheet is measured.

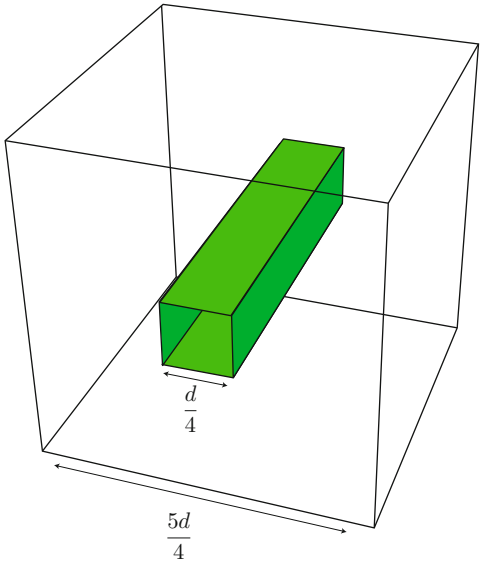

Fig. 19.11 A Logical Volume. This element is a scale independent way to measure the size of a topological quantum circuit. The size of the cell and the size of the defect are determined by the error correction strength, d. Constructing cells in this manner ensures that proper defect separation occur to maintain error correction properties

If every qubit in the cluster is simply measured in the X-basis, we do not perform any computation at all, and the only thing we can do is detect (and correct) physical errors that have occurred on qubits (Sect. 19.3). However, if certain physical qubits are measured in the Z-basis. They are effectively removed from the lattice and introduce a degree of freedom that can be used to encode information. A Z-basis measurement of a given physical qubit essentially removes it from the cluster [67]. We omit the details here, but if you examine the lattice carefully, the removal of a single qubit will reduce the total number of qubits in the lattice by *one*, but reduce the total number of independent stabilisers describing the lattice by *two* [19, 30, 70]. This reduction of the number of constraints (stabilisers) introduces a single-qubit degree of freedom, and hence two unique quantum states can satisfy the remaining constraints of the $N-2$ stabilisers. These two quantum states can now be used as the logical $|0\rangle$ and $|1\rangle$ states. On the cluster state, we can define two types of logical qubits: primal and dual qubits. In a cell in Fig. 19.4a, the eight qubits between two faces coloured red locate on a *dual* lattice, while the qubits on the red dagger are on *primal* face. The dual face and the primal face are the exactly same shape with a half lattice shifted in all three directions. Performing Z-basis measurements on the centre qubits on primal face creates a primal logical qubit, and the same on the dual face generates a dual logical qubit. Note that primal and dual logical qubits cannot coexist at the same location in the lattice and they can never touch each other. The distinction between primal and dual qubits becomes important when we consider quantum logic.

We now extend the idea of a *unit cell* of the cluster to the idea of a *logical volume*. This unit of measure, represented as d in Fig. 19.11, is used to define the minimum volume of cluster necessary to perform error correction on one of these encoded

qubits. As error chains can move in all three dimension (the spatial cross section plus the temporal axis of the cluster), this volume is a cuboid of fixed edge length related to the *strength* of error correction needed for computation. Situated in the centre of this volume is a *defect*. Outside the boundary of the defect, all qubits are measured in the X-basis for error correction, while all qubits inside the boundary of the defect are measured in the Z-basis and removed from the cluster. The defect itself is not a fixed size and it's perimeter increases with the strength of the error correction code.

Before explaining how the logical volume relates to the error correction strength of the cluster, we need to explain some details regarding the properties of the defects. We define a logical qubit with a pair of defects (of the same type), and there are three sets of physical qubits that are relevant to the logical qubit. These qubits can be divided into *defect sets*, *correlation sets* and *logic sets*, which are marked in three different colours in Fig. 19.12. In this figure we illustrate two defects that are a single unit cell in cross section and are defined for two cells in the temporal direction. Qubits not directly relevant to these sets have been omitted. The first set are the centre qubit of each face of a unit cell, indicated in green, which are measured in the Z-basis. These defects *define* the defect geometry (in this case two straight pieces that are each two unit cells long). The second set of qubits marked in orange is the logic set. In Fig. 19.14a, the logic sets define rings around each of the two defects. If these qubits were measured in the Z-basis, the parity of these measurements would determine the locally encoded state. If the defect is of *primal* type, we would be performing a projective measurement on the logical $|0, 1\rangle$ states, while if the defect is of *dual* type, we would be measuring in the logical $|+, -\rangle$ state. In Fig. 19.12b the conjugate operator is defined with a *chain* of Z measurements connecting the two defects. For primal type this parity determines the measurement result in the X-basis and for dual type the parity determines the measurement in the Z-basis. These ring or chain operators determine the encoded logic state at each point in time. The purpose of each cross-sectional measurement of the cluster is to teleport the information encoded with these operators to the next layer in the cluster and to perturb them in accordance with an algorithm. The final set of qubits relevant to defects are illustrated in blue and are known as the correlation sets. The correlation sets relate how the logic operators at time step t are related to identical operators are time-step t'. They in effect connect the logic state of a defect from input to output along the temporal axis of the cluster. In the upper cluster of Fig. 19.12, measuring the blue qubits in the X-basis and the input logical ring operator in the X-basis, you will teleport the parity of the ring operator from the input side to the output side of the defect. There is a byproduct correction to the logical state that depends on the total parity of all these X measurements. Similar is true for the chain operator, but instead the relevant correlation set is a sheet of X-basis measurements between the two defects that connect a chain operator at the input to a chain operator at the output. In Fig. 19.12 we are essentially describing the identity operation. As the cluster is measured, certain qubits are measured in the Z-basis to define the geometry of a defect and the other qubits measured in the X-basis are used for error correction and correctly propagating the logical state of the qubit from the input side of the cluster to the output.

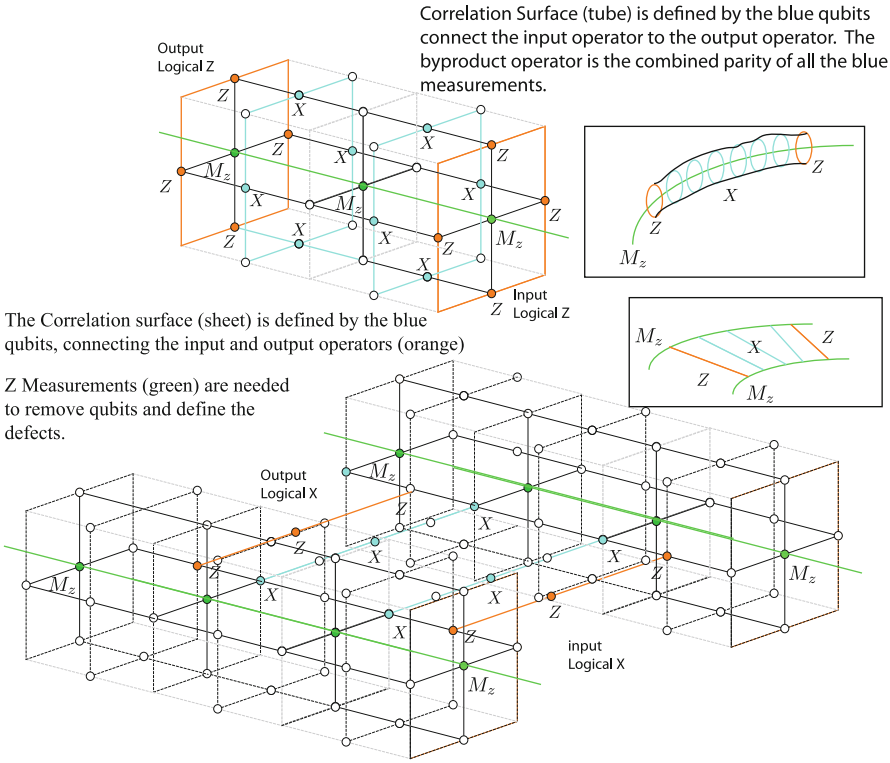

Fig. 19.12 Relavant sets of physical qubits to define the structure and propagation of a defect. Illustrated here is a defect for $d = 4$ for a simple identity operation. Three sets of qubits are defined. The first, illustrated in *green* are measured in the Z-basis and define the geometric structure of the defect. The second, illustrated in *orange*, are the logic sets that define the X and Z eigenstates of a particular encoded qubits. The third, illustrated in *blue* are correlation sets that connect the input and output logic operators as the cluster is measured. Two types of logic operators and correlation sets are defined, consisting of rings and tubes (*upper*) or chains and sheets (*lower*). For a primal type defect, the ring operators define the Z logic state while the chain operators define the X logic state. For a dual type defect these definitions are reversed. physical qubits

Given these definitions we can now go back to the logical volume. As the logic sets consists of the parity of either a ring of physical qubits encircling a defect or a chain that connects two defects together, the strength of error correction is related to the *weight* of these operators. If either the ring or the chain consists of many more physical qubits, it takes more errors to potentially corrupt the encoded state. The distance of the error correction code specifies the minimum number of errors to create a logical error. Therefore, the distance d of the underlying quantum code is related to the perimeter of a defect and the distance they are separated from each other. The logical volume illustrated in Fig. 19.11 is defined with respect to d. A

defect is defined with a total perimeter of d unit cells in the lattice and the defect is $d/2$ unit cells away from the edge of the unit cell (ensuring that two logical cells placed next to each other have a total separation between defects of d). By defining the logical volume with respect to d now gives us a way to define topological circuits independently of the underlying error correction strength. A circuit can be specified in terms of the number of logical volumes and then simply converted to an actual lattice volume once the error correction strength has been specified.

19.4.1.1 Gates

As with any other model of error corrected computation, the topological model does not have a universal set of gates that can be directly implemented in a fault-tolerant manner. In fact only a small number of operations are directly allowed. This set includes state preparation and measurement in the X and Z bases and the CNOT operation. To complete a universal set we generally append to further protocols to fault-tolerantly enact $P = R_z(\pi/4)$ and $T = R_z(\pi/8)$ gates which will be described in a moment.

Initialisation and measurement in the cluster can be described using simple geometric structures illustrated in Fig. 19.13. In Fig. 19.13a initialises an encoded qubit into the Z (X)-basis for the primal (dual) qubit, while Fig. 19.13b initialises an encoded qubit into the X (Z)-basis for the primal (dual) qubit. The temporal axis runs from left to right in the image. Measurement in the Z or X basis is achieved by inverting these geometric structures with respect to the temporal axis.

The final intrinsic gate that can be implemented in the model is the two qubit CNOT, which occurs by altering the trajectory of defects and performing a braid. A CNOT operation can only be performed between primal and dual logical qubits (where the dual qubit always acts as control). How this braid achieves the CNOT can be seen when examining how the correlation sets (the physical qubits that

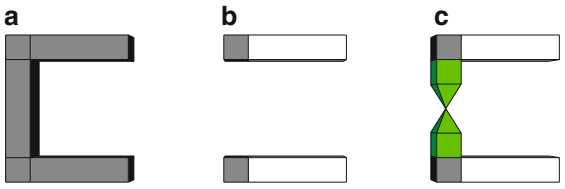

Fig. 19.13 Geometric structures for initialisation. For primal (dual) type defects, (**a**) initialises into the $|0\rangle$ ($|+\rangle$) state, (**b**) initialises into the $|+\rangle$ ($|0\rangle$) state and (**c**) initialises a defect into the $|A\rangle$ or $|Y\rangle$ state depending on the measurement of the physical quit at the apex of the pyramid. The way in which these structures are created within the cluster is by measuring *any* quit *inside* the defect structures in the Z-basis as the cluster is consumed along the temporal axis (i.e. quits are measured in cross sectional layers from left to right). The parity of the X-basis measurements on the *surface* of these structures will dictate the actual (e.g. $|0\rangle$ or $|1\rangle$ when initialised in the Z-basis). Measurement in the topological model occurs by mirroring these structures along the temporal axis

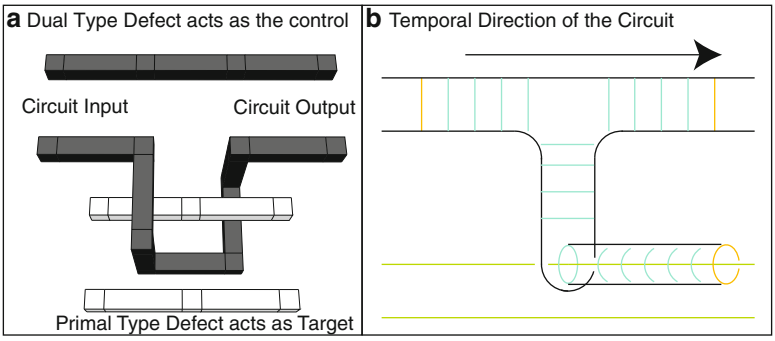

Fig. 19.14 Defect and correlation surface propagation for a braided CNOT. (**a**) illustrates the actual braid, where the dual qubit (*grey*) interacts with the primal (*white*) to perform the gate. The dual qubit *always* acts as the control qubit for the gate. (**b**) illustrates the perturbation of one of the four relevant correlation surfaces. In this case we illustrate the mapping of the stabiliser $XI \rightarrow XX$ which occurs during a CNOT. The correlation surface of the control qubit (the sheet) is perturbed by the braid to form a ring around the target qubit, therefore the output is stabilised by the XX operator if the input is stabilised by XI

connect the inputs and outputs of a topological circuit are perturbed), as illustrated in Fig. 19.14. In this figure, we examine what happens during the CNOT for a pair of qubits stabilised by the operator XI (i.e. when the control qubit is in the $|+\rangle$ state). If the control qubit is in the $|+\rangle$ state there is a correlation surface that connects the logical chain operator (the X operator for the dual defects) from input to output. A correlation surface that starts on a dual type defect *cannot* terminate on a primal defect and visa versa, hence when the primal defect intersects with this correlation surface it is perturbed into a ring around the primal defect. A ring around a primal defect corresponds to the X logic operator and consequently a system initially stabilised by the XI operator at input will be stabilised by the XX operator at output. This is exactly the behaviour of the CNOT (three other basis operators need to be checked to fully specify the gate and this is discussed in Ref. [30]).

The final gates to be described are the P and T gates. These are rotations about the Z axis by the angles $\pi/4$ and $\pi/8$ respectively and combined with the native gates in the topological model constitutes a universal set. The way we achieve these gates is through a process known as injection, distillation and teleportation. The first step is injection, where we introduce the states $|Y\rangle = |0\rangle + i|1\rangle$ and $|A\rangle = |0\rangle + e^{i\pi/4}|1\rangle$ into the cluster. This is done via the structure shown in Fig. 19.13c. In this figure a single *physical* qubit is measured in the desired rotated basis and then expanded into two encoded defects. The problem with injection is that the error rate associated with that *physical* measurement is propagated to the encoded state. Given that the physical measurement has a much higher error rate (compared with the other encoded qubits), the encoded state by the expansion inherits the same high error rate, these injected states therefore need to be *cleaned*. Reducing the error rates of these injected qubits can be done via state distillation protocols [10]. This is where either 7 (for the $|Y\rangle$ state) or 15 (for the $|A\rangle$ state) copies of the injected

state with an error rate of p are used to distill one higher fidelity state of error $O(p^3)$. This can be done recursively in order to achieve the desired encoded error rate. Once this purification is complete, these states can be used to enact teleported gates on encoded information. The resource requirements for state distillation protocols mean that the single qubit P and T gates are the most resource hungry gates in quantum algorithms and minimising especially T gates is of great importance when designing effective quantum algorithms.

19.4.2 Resource Optimisation and Estimation

The topological nature of error corrected quantum circuits allows for interesting avenues in algorithmic optimisation, and given the detailed computational architecture and circuits, we are able to make very accurate resource estimates of large-scale quantum algorithms. For these circuits, provided the topology of the braiding is maintained we can change the geometric structure of the circuit in order to minimise its physical volume and hence the resources needed to implement them. There are a number of techniques to achieve this [28, 29, 65, 70], and though we omit the specific discussions of these techniques, Fig. 19.15 shows a specific example of the minimisation for a state distillation circuit. Illustrated in Fig. 19.15a is a direct, canonical, implementation of the quantum circuit in the insert diagram at the top right corner, which is the circuit to perform state distillation of the $|Y\rangle$ state. This circuit has a volume of 192 logical cells and via several optimisation protocols can be reduced to the structure shown in Fig. 19.15b which has a volume of 18, achieving a reduction of over 90 %. This type of classical optimisation has a drastic effect in the final resources required, as the cross section of this cluster determines the number of physical photonic chips required, while the reduction along the third dimension will shorten the computational depth.

To give an explicit example, we consider the resources required for Shor's algorithm. For Shor's algorithm we use a linearised version of the algorithm [31]. For the algorithm, we need to decompose each gate into the universal set compatible for the code using techniques developed in Refs. [39, 51, 71]. Essentially the decomposed algorithm consists of T gates interspersed with CNOTS and Hadamard gates (which are constructed using three P gates). As the T gate is the most resource intensive, we assume that *all* gates are T gates. Therefore, given an L-bit number and a physical error rate of each component, p, the strength of error correction is given by [20],

$$d \geq \left\lceil \frac{2\log(640C_1L^4\Gamma V)}{\log(p_{th}) - \log(C_2 p)} - 1 \right\rceil \tag{19.13}$$

where $C_1 \approx 0.13$, $C_2 \approx 0.61$, $\Gamma = 6.42\log_2(640L^4) - 13.86$, $p_{th} \approx 0.62\,\%$ is the threshold for the topological code and V is the volume of topological cluster

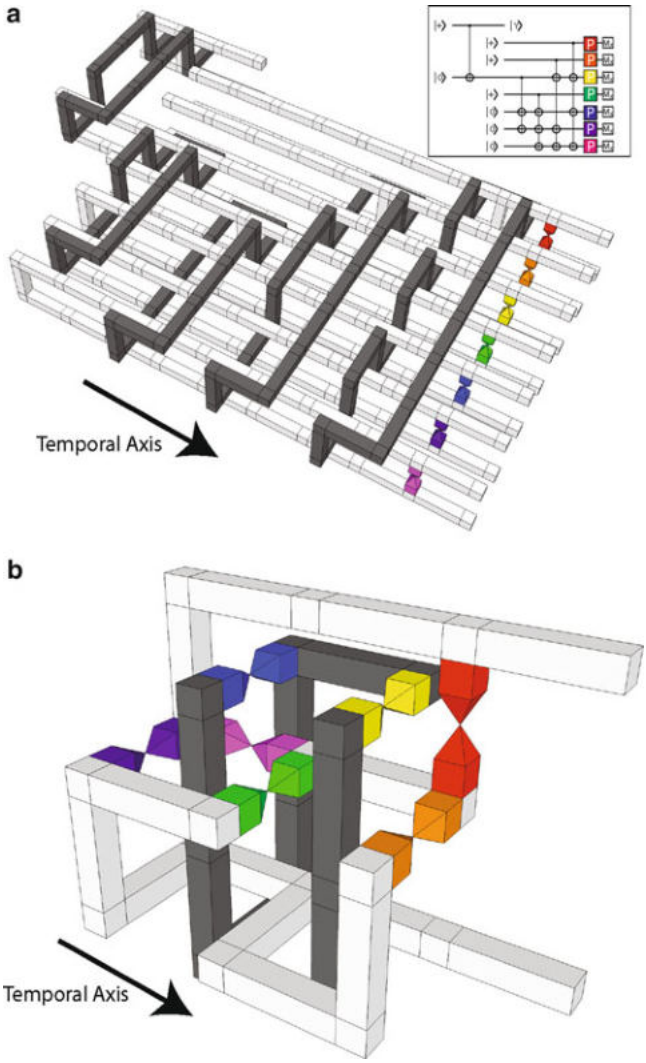

Fig. 19.15 Optimisation of a topological circuit. The structure in (**a**) is a un-optimal canonical topological construction of the circuit shown in the insert to distill $|Y\rangle$ states. Through various optimisation techniques this structure can be compressed in size by over 90 %, decreasing physical resources while maintaining the same functionality and error correction properties

(in terms of logical cells) needed to implement a T gate [20], where the volume is related to its cross section, A, and depth, D. In Fig. 19.16 we illustrate the T gate and all it's ancillary distillation protocols for one and two levels of state distillation. The data qubits, which are ones used for the actual algorithm, are shown in the green defect structure in Fig. 19.16, linearly lining on the close-section of the cluster between the $|Y\rangle$ state distillation region above and the $|A\rangle$ state distillation region

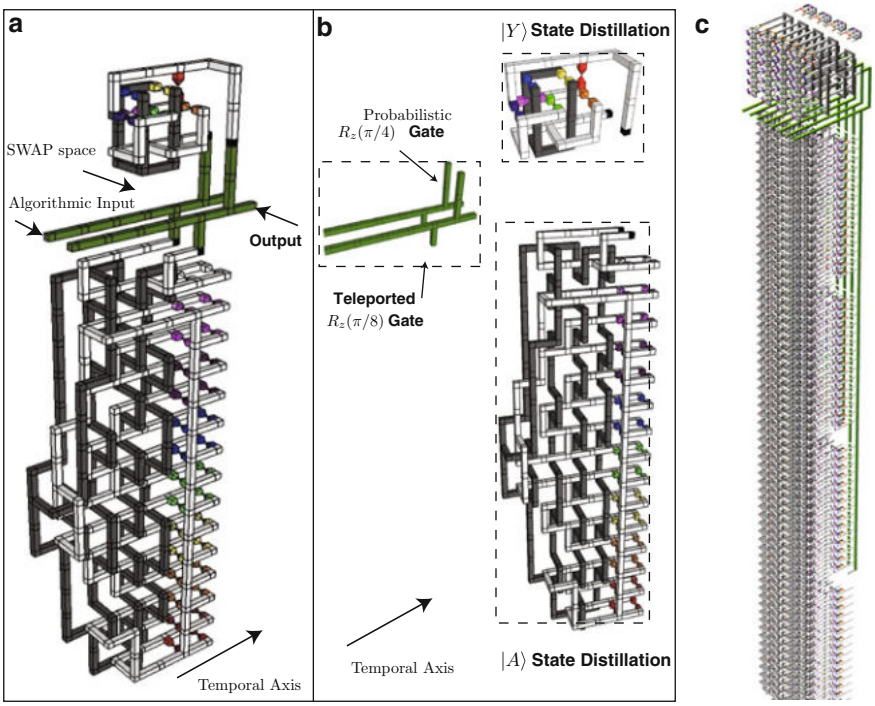

Fig. 19.16 Topological circuits to Implement a logical $T = R_z(\pi/8)$ rotation. In (**a**) and (**b**) we illustrate the circuit and individual components for one level of $|A\rangle$ state distillation. In (**b**) we illustrate the much larger structure needed for two recursive levels of $|A\rangle$ state distillation. The logical volumes can be calculated and used to estimate resources for an algorithm. (**c**) Illustrates the entire gate, over four algorithmic qubits and utilising two concatenated layers of state distillation

below [20]. These structures have a cross section and depth given by $A_1 = 21 \times 2$, $A_2 = 77 \times 2$, $D_1 = 5$ and $D_2 = 9$. We can use this information to now calculate the total size of the cluster needed to implement the algorithm for various error rates, p, and problem sizes, L. The cross sectional size, A, is related to the total number of photonic chips, Λ, as $\Lambda = 25Ld^2A + 30d\sqrt{LA} + 8$ and the depth of the cluster is related to the total computation time as, $T_{comp} = 160L^3\Gamma Dtd$, where t is the operational time of the photonic module. Figure 19.17 illustrates the total computational time (assuming $t = 10$ ns) and the number of devices needed to factor an L-bit number at an error rate of p. The results shown in Fig. 19.17 suggest that we can factor a $L \approx 810$-bit number in approximately 1 year with a physical error rate of $p \approx 0.07\,\%$. This is only slightly better than the current record of $L = 768$-bits using classical techniques [50]. The discontinues in the plot is where the number of recursive layers of state distillation increases from one to three. These results lead us to an important conclusion. The resource saving that can be achieved by reducing the error associated with quantum components is minimal compared to the savings that can be achieved using classical optimisation techniques. We could potentially

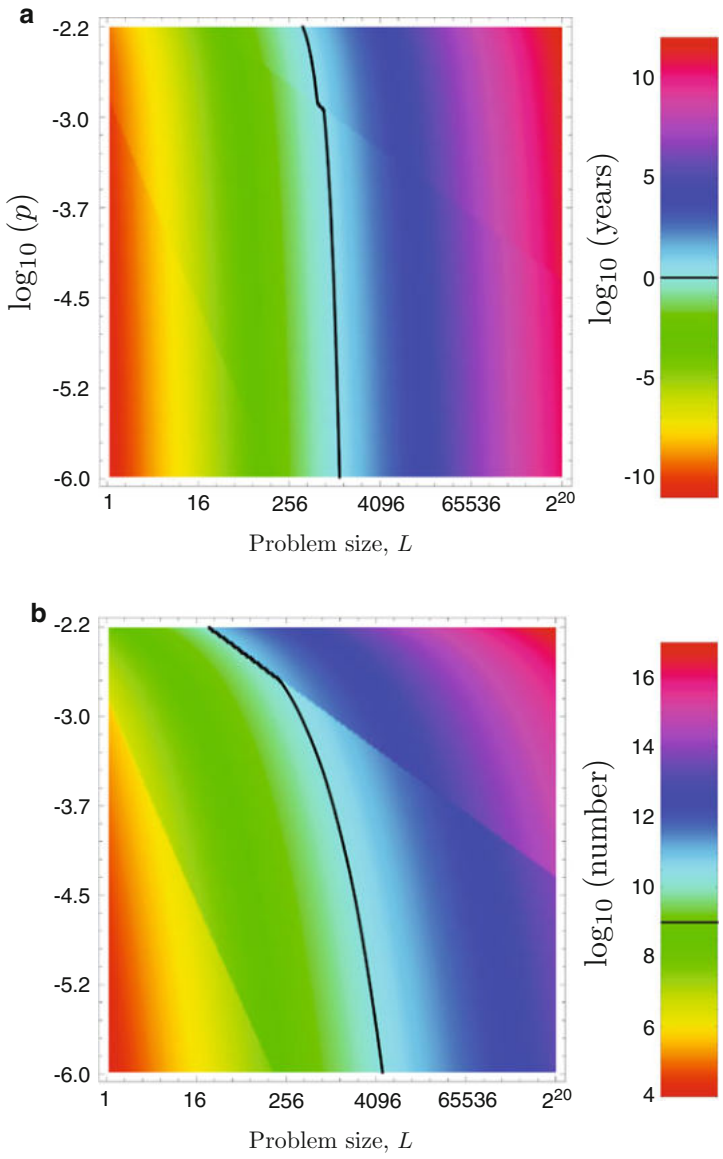

Fig. 19.17 Resource estimates for Shor's algorithm for the atom-optics architecture. (**a**) illustrates the number of photonic chips needed as a function of problem size, L, and physical error rate, p. (**b**) illustrates the total computational time assuming the photonic module operates on a timescale of $t = 10$ ns. On both plots we illustrate where the number of devices reaches one billion and the computational time reaches one year

speed up Shor's algorithm by *either* reducing the volume of circuit components by a further 40 % or by decreasing error rates by a factor of 10. As topological optimisation is purely a classical problem, this appears to be much more preferable.

Resource estimates for Shor's algorithm for the atom-optics architecture are summarised in Fig. 19.17a plotting the number of photonic chips needed as a function of problem size, L, and physical error rate, p and Fig. 19.17b indicating the total computational time assuming the photonic module operates on a timescale of $t = 10$ ns. On both plots we illustrate where the number of devices reaches one billion and the computational time reaches one year.

19.5 Summary

In this chapter we have presented an example of a complete architecture for topologically error corrected quantum computation. We have constructed an arbitrarily large array of photonic modules that produce a specific type of cluster state that can be utilised for error corrected quantum computation. We examined how this state can be used for both error correction and encoded logic and what fault-tolerant quantum circuits look like in this model. Finally we discussed how an accurate resource analysis for large-scale algorithms must be performed. Accurate system benchmarking must take into account the way in which a quantum algorithm is implemented in an error corrected system and what the fundamental building blocks are for the hardware itself. Many quantum architectures now follow a similar method of construction and further work on algorithmic optimisation will help reduce resource costs for all hardware models based on topological codes.

Acknowledgements This work was supported by the Funding Program for World-Leading Innovative R&D on Science and Technology (FIRST Program), a Scientific Research of Specially Promoted Research (grant no.18001002) by MEXT and a Quantum Cybernetics grant.

References

1. ARDA, Quantum information science and technology roadmap project (2004), http://qist.lanl.gov
2. R. Barends, J. Kelly, A. Megrant, A. Veitia, D. Sank, E. Jeffrey, T. White, J. Mutus, A. Fowler, B. Campbell, Y. Chen, Z. Chen, B. Chiaro, A. Dunsworth, C. Neill, P. O'Malley, P. Roushan, A. Vainsencher, J. Wenner, A. Korotkov, A. Cleland, J. Martinis, Logic gates at the surface code threshold: superconducting qubits poised for fault-tolerant quantum computing. Nature **508**, 500–503 (2014)
3. S. Barrett, T. Stace, Fault tolerant quantum computation with very high threshold for loss errors. Phys. Rev. Lett. **105**, 200,502 (2010)
4. J. Benhelm, G. Kirchmair, C. Roos, R. Blatt, Towards fault-tolerant quantum computing with trapped ions. Nat. Phys. **4**, 463 (2008)

5. C. Bennett, G. Brassard, C. Crépeau, R. Jozsa, A. Peres, W. Wooters, Teleporting an unknown quantum state via dual classical and Einstein-Podolsky-Rosen channels. Phys. Rev. Lett. **70**, 1895 (1993)
6. B.B. Blinov, D.L. Moehring, L.M. Duan, C. Monroe, Observation of entanglement between a single trapped atom and a single photon. Nature **428**(6979), 153–157 (2004). http://dx.doi.org/10.1038/nature02377
7. H. Bombin, M. Martin-Delgato, Topological quantum distillation. Phys. Rev. Lett. **97**, 180,501 (2006)
8. H. Bombin, M. Martin-Delgato, Topological computation without braiding. Phys. Rev. Lett. **98**, 160,502 (2007)
9. S. Bravyi, A. Kitaev, Quantum codes on a lattice with boundary (1998). quant-ph/9811052
10. S. Bravyi, A. Kitaev, Universal quantum computation with ideal clifford gates and noisy ancillas. Phys. Rev. A **71**, 022,316 (2005)
11. J. Cirac, P. Zoller, Quantum computations with cold trapped ions. Phys. Rev. Lett. **74**, 4091 (1995)
12. D. Cory, A. Fahmy, T. Havel, Ensemble quantum computing by NMR spectroscopy. Proc. Natl. Acad. Sci. **94**, 1634–1639 (1997)
13. E. Dennis, A. Kitaev, A. Landahl, J. Preskill, Topological quantum memory. J. Math. Phys. **43**, 4452 (2002)
14. D. Deutsch, Quantum computational networks. Proc. R. Soc. Lond. Ser. A, Math. Phys. Sci. **425**, 73 (1989)
15. S. Devitt, K. Nemoto, Programming a topological quantum computer, in *2012 IEEE 21st Asian Test Symposium (ATS)*, Niigatta (2012), pp. 55–60
16. S. Devitt, A. Greentree, R. Ionicioiu, J. O'Brien, W. Munro, L. Hollenberg, The photonic module: an on-demand resource for photonic entanglement. Phys. Rev. A **76**, 052312 (2007)
17. S. Devitt, A. Fowler, A. Stephens, A. Greentree, L. Hollenberg, W. Munro, K. Nemoto, Architectural design for a topological cluster state quantum computer. New. J. Phys. **11**, 083,032 (2009)
18. S. Devitt, A. Stephens, W. Munro, K. Nemoto, Integration of highly probabilistic sources into optical quantum architectures: perpetual quantum computation. New J. Phys. **13**, 095,001 (2011)
19. S. Devitt, W. Munro, K. Nemoto, Quantum error correction for beginners. Rep. Prog. Phys. **76**, 076,001 (2013)
20. S. Devitt, A. Stephens, W. Munro, K. Nemoto, Requirements for fault-tolerant factoring on an atom-optics quantum computer. Nat. Commun. **4**, 2524 (2013)
21. D. DiVincenzo, Topics in quantum computers. in *Mesoscopic Electron Transport*, ed. by L. Kowenhoven, G. Schon, L. Sohn. NATO ASI Series E (Kluwer Academic, Dordrecht, 1997)
22. D. DiVincenzo, The physical implementation of quantum computation. Fortschr. Phys. **48**, 771 (2000)
23. J. Dowling, G. Milburn, Quantum technology: the second quantum revolution (2002). quant-ph/0206091
24. G. Duclos-Cianci, D. Poulin, Fault-tolerant renormalization group decoded for Abelian topological codes. Quantum Inf. Comput. **14**, 0721 (2014)
25. J. Edmonds, Paths, trees, and flowers. Can. J. Math. **17**, 449 (1965)
26. A. Ekert, Quantum cryptography based on Bell's theorem. Phys. Rev. Lett. **67**, 661 (1991)
27. R. Feynman, Simulating physics with computers. Int. J. Theor. Phys. **21**, 467 (1982)
28. A. Fowler, Low overhead surface code logical H. Quantum Inf. Comput. **12**, 970 (2012)
29. A. Fowler, S. Devitt, A bridge to lower overhead quantum computation (2012). arXiv:1209.0510
30. A. Fowler, K. Goyal, Topological cluster state quantum computing. Quantum Inf. Comput. **9**, 721 (2009)
31. A. Fowler, S. Devitt, L. Hollenberg, Implementation of Shor's algorithm on a linear nearest neighbour qubit array. Quantum Inf. Comput. **4**, 237–251 (2004)

32. A. Fowler, A. Stephens, P. Groszkowski, High threshold universal quantum computation on the surface code. Phys. Rev. A **80**, 052,312 (2009)
33. A. Fowler, M. Mariantoni, J. Martinis, A. Cleland, Surface codes: towards practical large-scale quantum computation. Phys. Rev. A **86**, 032,324 (2012)
34. A. Fowler, S. Devitt, C. Jones, Surface code implementation of block code state distillation. Sci. Rep. **3**, 1939 (2013)
35. M. Freedman, D.A. Meyer, Projective plane and planar quantum codes. Found. Comput. Math. **1**, 325 (2001)
36. C.W. Gardiner, P. Zoller, *Quantum Noise: A Handbook of Markovian and Non-Markovian Quantum Stochastic Methods with Applications to Quantum Optics*. Springer Series in Synergetics (Springer, Berlin/Heidelberg, 2004)
37. C. Gerry, P.L. Knight, *Introductory Quantum Optics* (Cambridge University Press, Cambridge, 2004)
38. N. Gershenfeld, I. Chuang, Bulk spin resonance quantum computing. Science **275**, 350 (1997)
39. B. Giles, P. Selinger, Exact synthesis of multiqubit Clifford+T circuits. Phys. Rev. A **87**, 032,332 (2013)
40. N. Gisin, G. Ribordy, W. Tittel, H. Zbinden, Quantum cryptography. Rev. Mod. Phys. **74**, 145 (2002)
41. L. Grover, Quantum mechanics helps in searching for a needle in a haystack. Phys. Rev. Lett. **79**, 325 (1997)
42. T. Harty, D. Allcock, C. Ballance, L. Guidoni, H. Janacek, N. Linke, D. Stacey, D. Lucas, High-fidelity preparation, gates, memory and readout of a trapped-ion quantum bit (2014). arXiv:1403.1524
43. C.K. Hong, Z.Y. Ou, L. Mandel, Measurement of subpicosecond time intervals between two photons by interference. Phys. Rev. Lett. **59**(18), 2044–2046 (1987)
44. C. Hu, A. Young, J. O'Brien, W. Munro, J. Rarity, Giant optical Faraday rotation induced by a single-electron spin in a quantum dot: applications to entangling remote spins via a single photon. Phys. Rev. B **78**, 085,307 (2008)
45. C. Hu, W. Munro, J. O'Brien, J. Rarity, Proposed entanglement beam splitter using a quantum-dot spin in a double-sided optical microcavity. Phys. Rev. B **80**, 025,326 (2009)
46. N.C. Jones, R.V. Meter, A. Fowler, P. McMahon, J. Kim, T. Ladd, Y. Yamamoto, A layered architecture for quantum computing using quantum dots. Phys. Rev. X **2**, 031,007 (2012)
47. B. Kane, A silicon-based nuclear spin quantum computer. Nature (London) **393**, 133 (1998)
48. A. Kitaev, Quantum computations: algorithms and error correction. Russ. Math. Serv. **52**, 1191 (1997)
49. A. Kitaev, Fault-tolerant quantum computation by anyons. Ann. Phys. **303**, 2 (2003)
50. T. Kleinjung, K. Aoki, J. Franke, A.K. Lenstra, E. Thomé, J.W. Bos, P. Gaudry, A. Kruppa, P.L. Montgomery, D.A. Osvik, H. te Riele, A. Timofeev, P. Zimmermann, Factorization of a 768-bit RSA modulus, in *Advances in Cryptology – CRYPTO 2010*, ed. by T. Rabin. IACR International Association for Cryptologic Research (Springer, Berlin, 2010), pp. 333–350
51. V. Kliuchnikov, D. Maslov, M. Mosca, Asymptotically optimal approximation of single qubit unitaries by Clifford and T circuits using a constant number of ancillary qubits. Phys. Rev. Lett. **110**, 190,502 (2013)
52. E. Knill, R. Laflamme, G. Milburn, A scheme for efficient quantum computation with linear optics. Nature (London) **409**, 46 (2001)
53. V. Kolmogorov, Blossom V: a new implementation of a minimum cost perfect matching algorithm. Math. Program. Comput. **1**, 43 (2009)
54. H.K. Lo, S. Popescu, T. Spiller (eds.), *Introduction To Quantum Computation and Information* (World Scientific, Singapore, 1998)
55. C. Lorenz, R. Ziff, Precise determination of the bond percolation thresholds and finite-size scaling corrections for the sc, fcc, and bcc lattices. Phys. Rev. E. **57**, 230 (1998)
56. D. Loss, D. DiVincenzo, Quantum computation with quantum dots. Phys. Rev. A **57**, 120 (1998)

57. R.V. Meter, T. Ladd, A. Fowler, Y. Yamamoto, Distributed quantum computation architecture using semiconductor nanophotonics. Int. J. Quantum Inf. **8**, 295 (2010)
58. C. Monroe, R. Raussendorf, A. Ruthven, K. Brown, P. Maunz, L.M. Duan, J. Kim, Large scale modular quantum computer architecture with atomic memory and photonic interconnects. Phys. Rev. A **89**, 022,317 (2014)
59. J. Mooij, T. Orlando, L. Levitov, L. Tian, C. van der Wal, S. Lloyd, Josephson persistent-current qubit. Science **285**, 1096–1039 (1999)
60. Y. Nakamura, Y.A. Pashkin, J. Tsai, Coherent control of macroscopic quantum states in a cooper-pair box. Nature (London) **398**, 786 (1999)
61. K. Nemoto, M. Trupke, S. Devitt, A. Stephens, K. Buczak, T. Nobauer, M. Everitt, J. Schmiedmayer, W. Munro, Photonic architecture for scalable quantum information processing in NV-diamond. arXiv:1309.4277 (2013)
62. M. Nielsen, Optical quantum computation using cluster states. Phys. Rev. Lett. **93**, 040,503 (2004)
63. M. Nielsen, I. Chuang, *Quantum Computation and Information*, 2nd edn. (Cambridge University Press, Cambridge/New York, 2000)
64. T. Ohno, G. Arakawa, I. Ichinose, T. Matsui, Phase structure of the random-plaquette image gauge model: accuracy threshold for a toric quantum memory. Nucl. Phys. B **697**, 462 (2004)
65. A. Paetznick, A. Fowler, Quantum circuit optimization by topological compaction in the surface code (2013). arXiv:1304.2807
66. S.J.D. Phoenix, P.L. Knight, Establishment of an entangled atom-field state in the jaynes-cummings model. Phys. Rev. A **44**, 6023–6029 (1991). doi:10.1103/PhysRevA.44.6023. http://link.aps.org/doi/10.1103/PhysRevA.44.6023
67. R. Raussendorf, H.J. Briegel, A one way quantum computer. Phys. Rev. Lett. **86**, 5188 (2001)
68. R. Raussendorf, J. Harrington, Fault-tolerant quantum computation with high threshold in two dimensions. Phys. Rev. Lett. **98**, 190,504 (2007)
69. R. Raussendorf, J. Harrington, K. Goyal, A fault-tolerant one way quantum computer. Ann. Phys. **321**, 2242 (2006)
70. R. Raussendorf, J. Harrington, K. Goyal, Topological fault-tolerance in cluster state quantum computation. New J. Phys. **9**, 199 (2007)
71. N. Ross, P. Selinger, Optimal ancilla-free Clifford+T approximation of z-rotations (2014). arXiv:1403.2975
72. C. Ryan, M. Laforest, R. Laflamme, Randomized benchmarking of single-and multi-qubit control in liquid-state NMR quantum information processing. New J. Phys. **11**, 013,034 (2009)
73. C. Santori, D. Fattal, Y. Yamamoto, *Single-Photon Devices and Applications* (Whiley-VCH, Weinheim, 2010)
74. P. Shor, Polynomial-time algorithms for prime factorization and discrete logarithms on a quantum computer. SIAM J. Sci. Statist. Comput. **26**, 1484 (1997)
75. T. Spiller, W. Munro, Towards a quantum information technology industry. J. Phys.: Condens. Matter **18**, 1–10 (2006)
76. T. Spiller, W. Munro, S. Barrett, P. Kok, An introduction to quantum information processing: applications and realizations. Contemp. Phys. **46**, 407 (2005)
77. T.P. Spiller, K. Nemoto, S.L. Braunstein, W. Munro, P. van Loock, G.J. Milburn, Quantum computation by communication. New J. Phys. **8**, 30 (2006)
78. A. Stephens, Fault-tolerant thresholds for quantum error correction with the surface code. Phys. Rev. A **89**, 022,321 (2014)
79. A. Stephens, Z. Evans, S. Devitt, A. Greentree, A. Fowler, W. Munro, J. O'Brien, K. Nemoto, L. Hollenberg, Deterministic optical quantum computer using photonic modules. Phys. Rev. A **78**, 032,318 (2008)
80. A. Stephens, W. Munro, K. Nemoto, High-threshold topological quantum error correction against biased noise. Phys. Rev. A **88**, 060,301(R) (2013)
81. R. Stock, D. James, A scalable, high-speed measurement based quantum computer using trapped ions. Phys. Rev. Lett. **102**, 170,501 (2009)

82. E. Togan, Y. Chu, A.S. Trifonov, L. Jiang, J. Maze, L. Childress, M.V.G. Dutt, A.S. Sorensen, P.R. Hemmer, A.S. Zibrov, M.D. Lukin, Quantum entanglement between an optical photon and a solid-state spin qubit. Nature **466**(7307), 730–734 (2010). http://dx.doi.org/10.1038/nature09256
83. E. Waks, J. Vuckovic, Dipole induced transparency in drop-filter cavity-waveguide systems. Phys. Rev. Lett. **96**, 153,601 (2006)
84. D. Walls, G. Milburn, *Quantum Optics* (Springer, Berlin, 1994)
85. C. Wang, J. Harrington, J. Preskill, Confinement-Higgs transition in a disordered gauge theory and the accuracy threshold for quantum memory. Ann. Phys. **303**, 31 (2003)
86. D. Wang, A. Fowler, A. Stephens, L. Hollenberg, Threshold error rates for the toric and surface codes. Quantum Inf. Comput. **10**, 456 (2010)
87. T. Wilk, S.C. Webster, A. Kuhn, G. Rempe, Single-atom single-photon quantum interface. Science **317**(5837), 488–490 (2007). doi:10.1126/science.1143835. http://www.sciencemag.org/content/317/5837/488.abstract
88. N. Yao, L. Jiang, A. Gorshkov, P. Maurer, G. Giedke, J. Cirac, M. Lukin, Scalable architecture for a room temperature solid-state quantum information processor. Nat. Commun. **3**, 800 (2012)
89. A. Young, C. Hu, L. Marseglia, J. Harrington, J. O'Brien, J. Rarity, Deterministic photon entangler using a charged quantum dot inside a microcavity. Phys. Rev. B **78**, 125,318 (2008)
90. S.B. Zheng, G.C. Guo, Efficient scheme for two-atom entanglement and quantum information processing in cavity qed. Phys. Rev. Lett. **85**, 2392–2395 (2000). doi:10.1103/PhysRevLett.85.2392. http://link.aps.org/doi/10.1103/PhysRevLett.85.2392

Chapter 20
Optical Hybrid Quantum Information Processing

Shuntaro Takeda and Akira Furusawa

20.1 Introduction

Optical quantum systems are one of the most promising candidates for quantum information processing (QIP) since their decoherence is almost negligible under ambient conditions at room temperatures. This advantage, together with mature optical technologies such as beam splitters and nonlinear optical crystals, enabled significant progress in the field of optical quantum communication and quantum computing. This progress was made by two complementary approaches, each exploiting only one aspect of the wave-particle duality of light (Fig. 20.1). One utilizes the particle-like discrete nature of light to encode quantum information based on quantum bits (qubits) [1, 2]. The other, which harnesses wave-like continuous nature of light, is based on continuous variables (CVs) [3]. The conceptual difference between these two approaches is analogous to classical digital (discrete) and analog (continuous) signal processing.

Both approaches have advantages and disadvantages in terms of the practical realization of optical QIP. Qubit QIP enables high fidelity of operations, but experimental realizations have been probabilistic and mostly required post-selection of successful events. This is due to the low creation and detection efficiencies of

S. Takeda (✉)
Department of Applied Physics, School of Engineering, The University of Tokyo, 7-3-1 Hongo, Bunkyo-ku, Tokyo 113-8656, Japan

Department of Photo-Molecular Science, Institute for Molecular Science, National Institutes of Natural Sciences, Myodaiji, Okazaki 444-8585, Japan
e-mail: takeda@alice.t.u-tokyo.ac.jp; takeda@ims.ac.jp

A. Furusawa
Department of Applied Physics, School of Engineering, The University of Tokyo, 7-3-1 Hongo, Bunkyo-ku, Tokyo 113-8656, Japan
e-mail: akiraf@ap.t.u-tokyo.ac.jp

Y. Yamamoto, K. Semba (eds.), *Principles and Methods of Quantum Information Technologies*, Lecture Notes in Physics 911, DOI 10.1007/978-4-431-55756-2_20

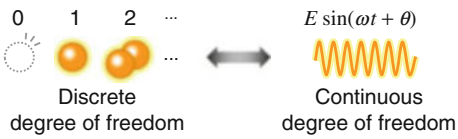

Fig. 20.1 Discrete and continuous degrees of freedoms of light

Table 20.1 Comparison between qubit and CV QIP

	Qubit QIP	Continuous-variable QIP
Carrier	Degrees of freedom of a photon	Quadratures of a light field
Basis	Photon number basis: $\{\|n\rangle\}$	Quadrature basis: $\{\|x\rangle\}$ or $\{\|p\rangle\}$
Encoding	$\|\psi\rangle = \alpha\|0,1\rangle + \beta\|1,0\rangle$	$\|\psi\rangle = \int_{-\infty}^{\infty}\psi(x)\|x\rangle\, dx$
Source	Photons by PDC (weak pump)	Squeezed light by PDC (strong pump)
Detector	Photon detector (measures $\hat{n}$)	Homodyne detector (measures $\hat{x}$ or $\hat{p}$)
Difficulty	Two-qubit gate (e.g. CNOT gate)	Non-Gaussian gate (e.g. cubic phase gate)

photonic qubits. On the other hand, CV QIP is deterministic, thanks to on-demand entanglement resources and efficient homodyne measurement; however, the fidelity of operations is limited by the imperfection of the entanglement. In recent years, there has been significant progress in combining both technologies with a view to realizing hybrid protocols that overcome the current limitations of optical QIP [4, 5]. This hybrid approach is analogous to the digital and analog hybrid signal processing in classical information processing: we set thresholds to digitize the originally continuous voltage signals. In optical QIP, this threshold was given by nature as the wave-particle duality of light. Therefore it naturally follows to take advantage of both features in optical QIP as well.

In this chapter, we start by reviewing the basic concepts of qubit and CV QIP in Sect. 20.2. We then focus on quantum teleportation as an elementary protocol in qubit and CV QIP, and explain its applications to quantum computing in Sect. 20.3. Finally in Sect. 20.4, we summarize our recent accomplishment of combining both technologies to realize "hybrid" quantum teleportation, and describe its application to hybrid QIP that potentially overcomes the current limitations in optical QIP.

20.2 Qubits and Continuous Variables

Here we briefly review the encoding method, basic technologies, and difficulties in qubit and CV QIP. The comparison between these two approaches are summarized in Table 20.1.

20.2.1 Qubits

The basic unit of information in the classical digital information processing is a bit, which can have only one of two values, '0' or '1'. The quantum analogue of

the classical bit is called a qubit, which is a superposition of the two values. Qubit operations in optics, which exploits the particle-like discrete nature of light, can be represented by photon number basis $\{|n\rangle\}$. This is the eigenstate of the number operator $\hat{n} = \hat{a}^\dagger \hat{a}$ ($\hat{n}\,|n\rangle = n\,|n\rangle$ for $n = 0, 1, 2, \ldots$), where $\hat{a}$ and $\hat{a}^\dagger$ are annihilation and creation operators of a quantized electromagnetic field ($[\hat{a}, \hat{a}^\dagger] = 1$). Usually a qubit is encoded in the degrees of freedom of a single photon (such as polarization, time of arrival or spatial modes); it can be described using two optical modes as

$$|\psi\rangle = \alpha\,|0\rangle\,|1\rangle + \beta\,|1\rangle\,|0\rangle = \alpha\,|\bar{0}\rangle + \beta\,|\bar{1}\rangle\,. \tag{20.1}$$

Here $|0\rangle$ and $|1\rangle$ are vacuum (zero photon) and single photon states, while $|\bar{0}\rangle$ and $|\bar{1}\rangle$ denote logical '0' and '1', respectively. The information is encoded in the complex amplitudes α and β ($|\alpha|^2 + |\beta|^2 = 1$); this is processed by sequential quantum logic gates to realize quantum computation. A quantum logic gate can be described by the transformation $|\psi\rangle \rightarrow \hat{U}\,|\psi\rangle$, where $\hat{U}$ is an unitary transformation (Fig. 20.2a).

Let us now move on to the physical implementation of qubit QIP. Generation and measurement techniques of photonic qubits are well developed [2]. The most standard source for single photons is parametric down conversion (PDC), where a pump photon is probabilistically converted into two photons via a nonlinear crystal. Measurements in the logical basis can be readily implemented with photon detectors. The next question to follow is how to implement quantum logic gates. In order to realize universal qubit QIP, arbitrary single-qubit gates and at least one two-qubit gate are required [6]. The former is easily implemented with simple linear optics, such as beam splitters and phase shifters (Fig. 20.2b). One example of the latter is the controlled-NOT (CNOT) gate, which flips the state of a target qubit only if the control qubit is in the state '1'. This is equivalent to the state of a single photon being controlled by another single photon via optical Kerr interaction (third-order nonlinear optical effect [4]); very large nonlinearity is required to induce this effect on a single photon. This makes the implementation of such two-qubit gates a major difficulty in qubit QIP.

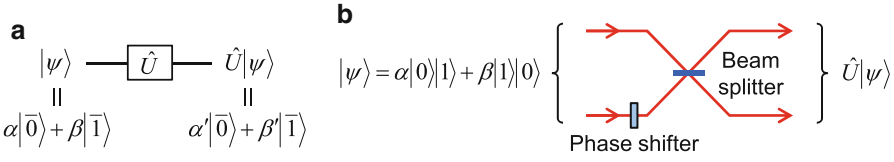

Fig. 20.2 Quantum logic gate for qubits. (**a**) Circuit of a single-qubit gate $|\psi\rangle \rightarrow \hat{U}\,|\psi\rangle$. (**b**) Implementation of a single-qubit gate for a photonic qubit encoded in two paths (spatial modes). Appropriate choice of the phase shift and beam splitter transmissivity enables arbitrary single-qubit gates $\hat{U}$

20.2.2 Continuous Variables

The alternative way to encode quantum information is to use continuous basis. This idea is similar to classical analog information processing, such as AM/FM radios, where continuous values are encoded in amplitude and phase modulations of radio waves. In CV QIP, quadratures $\hat{x}$ and $\hat{p}$ of optical waves [3]

$$\hat{x} = (\hat{a}^\dagger + \hat{a})/\sqrt{2}, \quad \hat{p} = i(\hat{a}^\dagger - \hat{a})/\sqrt{2} \quad (\hbar = 1) \tag{20.2}$$

are used to encode the superposition of continuous values. An intuitive definition of quadrature values would be the sine and cosine components of an oscillating wave (Fig. 20.3a):

$$E\sin(\omega t + \theta) = E\cos\theta\sin\omega t + E\sin\theta\cos\omega t \propto x\sin\omega t + p\cos\omega t. \tag{20.3}$$

The commutation relation $[\hat{x}, \hat{p}] = i$ can be derived from $[\hat{a}, \hat{a}^\dagger] = 1$. Therefore all quantum states satisfy the uncertainty relation $\Delta x \Delta p \geq 1/2$. Even the vacuum state has a so-called zero-point fluctuation of $\Delta x = \Delta p = 1/\sqrt{2}$, though its quadratures are zero on average $\langle\hat{x}\rangle = \langle\hat{p}\rangle = 0$ (Fig. 20.3b). The eigenstates of $\hat{x}$ and $\hat{p}$ form continuous bases $\{|x\rangle\}$ and $\{|p\rangle\}$ ($\hat{x}\,|x\rangle = x\,|x\rangle$, $\hat{p}\,|p\rangle = p\,|p\rangle$ for $x, p \in \mathbb{R}$). An example of CV quantum information described in the $\hat{x}$-quadrature basis reads

$$|\psi\rangle = \int_{-\infty}^{\infty} \psi(x)\,|x\rangle\,dx. \tag{20.4}$$

Here the information is represented by the wave function $\psi(x) = \langle x|\psi\rangle$; which is to be processed by CV quantum logic gates $|\psi\rangle \to \hat{U}\,|\psi\rangle$. Note that the state in Eq. (20.4) can also be expanded in the photon number basis as $|\psi\rangle = \sum_{n=0}^{\infty} c_n\,|n\rangle$

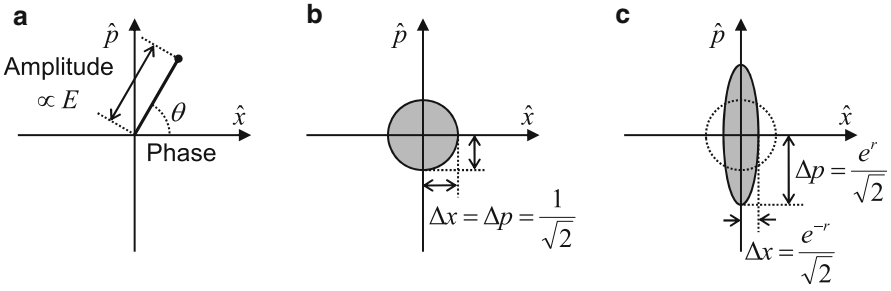

Fig. 20.3 Phase space description. (**a**) Quadratures $\hat{x}$ and $\hat{p}$ correspond to $E\cos\theta$ and $E\sin\theta$ (Eq. (20.3)), and these relations can be illustrated in the phase space spanned by $\hat{x}$ and $\hat{p}$. (**b**) Quadrature distribution of a vacuum state. (**c**) Quadrature distribution of a squeezed state. The degree of squeezing is often characterized by the squeezing parameter r

with $c_n = \langle n|\psi\rangle$. Therefore, CV QIP includes qubit QIP as a special case when the infinite dimensional Hilbert space is limited to a smaller subspace.

The key resource in implementing CV QIP is squeezed light. The quantum noise level of one of the quadratures (Δx or Δp) of squeezed light is below the vacuum noise level, with infinitely squeezed light $\Delta x \to 0$ ($\Delta p \to 0$) corresponding to the quadrature eigenstate $|x = 0\rangle$ ($|p = 0\rangle$) (Fig. 20.3c). The squeezed light can be deterministically generated using the same mechanism as PDC but with a strong pump beam. Furthermore, measurement of $\hat{x}$ and $\hat{p}$ values can be carried out with high efficiency by homodyne detectors. Now let us move on to how to implement universal CV QIP. In order to construct an arbitrary unitary transformation $\hat{U} = \exp(-i\hat{H}t)$, Hamiltonians $\hat{H}$ of arbitrary polynomials of $\hat{x}$ and $\hat{p}$ are required [7]. Unitary transformations which involves Hamiltonians of linear or quadratic in $\hat{x}$ and $\hat{p}$ are called "Gaussian" gates, which can be readily implemented by standard techniques such as beam splitters, phase shifters, squeezing and modulation. However, CV universality requires at least one "non-Gaussian" gate which involves a higher order Hamiltonian, such as the cubic phage gate $\hat{U} = \exp(i\chi\hat{x}^3)$ ($\hat{H} \propto \hat{x}^3$) [7]. Implementation of non-Gaussian gates is a major problem in CV QIP as they require at least third-order optical nonlinearity; this is hard to implement for arbitrary quantum states of light. In this sense, non-Gaussian gates share the same difficulty as the CNOT gate in DV QIP.

20.3 Quantum Teleportation and Quantum Computing

In optical QIP, "quantum teleportation", the transfer protocol of quantum information, plays the central role in building quantum logic gates. This section discusses the basics and applications of quantum teleportation.

20.3.1 Quantum Teleportation

Quantum teleportation [8] is the act of transferring quantum information to distant places without direct transmission of the physical entity itself. Its basic concepts and implementations are as follows.

20.3.1.1 Basic Concept

It is impossible to transfer unknown quantum superposition states from a sender to a spatially distant receiver only via classical communications (e.g. phone and e-mail) [8]. However, this can be accomplished by following the quantum teleportation protocol which utilizes quantum entanglement shared between the two parties. This idea was first proposed for qubits in 1993 by Bennett et al. [8], and later

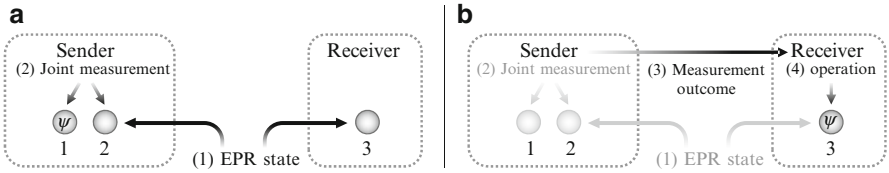

Fig. 20.4 Procedure of quantum teleportation. An unknown quantum state $|\psi\rangle$, originally possessed by mode 1, is teleported to mode 3 after the four steps (1–4) illustrated in the figure. (**a**) The first two steps. (**b**) The latter two steps

extended to CVs by Vaidman [9]. The basic procedure of quantum teleportation is the same for both schemes. Here we define the mode of the quantum state $|\psi\rangle$ to be teleported as mode 1. As shown in Fig. 20.4, quantum teleportation consists of the following four steps:

(1) The sender and receiver share an ancillary entangled state in modes 2 and 3 (Einstein-Podolsky-Rosen state, EPR state).
(2) The sender performs a joint measurement on modes 1 and 2 (Bell-state measurement).
(3) The sender sends the measurement outcome to the receiver via classical communications.
(4) The receiver performs an unitary operation on mode 3 based on the measurement outcome; as a result $|\psi\rangle$ appears in mode 3.

In this way, the quantum state $|\psi\rangle$ is transferred from mode 1 to 3 by means of the shared entanglement and classical communications. The nomenclature of "teleportation" comes from the fact that the initial quantum state in mode 1 inevitably vanishes, and the same quantum state reappears in mode 3. In this way, quantum teleportation evades violating the no-cloning theorem, which prohibits making an exact copy of a quantum state.

20.3.1.2 Qubit Teleportation

After the original proposal, Bouwmeester et al. reported the first experimental realization of quantum teleportation using photonic qubits in 1997 [10]. This experiment used the polarization modes of photon 1 in Fig. 20.5 to encode the qubit:

$$|\psi\rangle_1 = \alpha\,|1\rangle_{1H}\,|0\rangle_{1V} + \beta\,|0\rangle_{1H}\,|1\rangle_{1V} = \alpha\,|H\rangle_1 + \beta\,|V\rangle_1\,, \tag{20.5}$$

where $|H\rangle_1$ and $|V\rangle_1$ denote the horizontal and vertical polarization of the photon respectively. In this case, the ancillary EPR state in step (1) is polarization-entangled photons 2 and 3, written as

$$|\mathrm{EPR}\rangle_{23} = (|H\rangle_2\,|V\rangle_3 - |V\rangle_2\,|H\rangle_3)/\sqrt{2}. \tag{20.6}$$

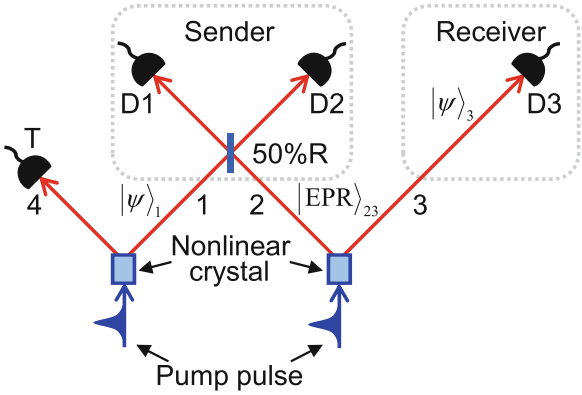

Fig. 20.5 Schematic of quantum teleportation of photonic qubits demonstrated in Ref. [10]. A polarization qubit $|\psi\rangle$ in mode 1 is prepared when T detects a photon, and then teleported to mode 3 on condition that all of D1, D2 and D3 each detect a photon

These two photons have the following correlation: when one photon has horizontal (vertical) polarization, the other photon has vertical (horizontal) polarization. Both the input qubit $|\psi\rangle_1$ and the EPR state $|\mathrm{EPR}\rangle_{23}$ are probabilistically created by PDC with a weak pump pulse, as shown in Fig. 20.5. The photon detector T is used to verify whether the input qubit had been prepared properly. Bell-state measurement in step (2) is then performed using a 50:50 beam splitter and two photon detectors D1 and D2. When the two detectors simultaneously detect photons, photons 1 and 2 are projected onto the state $|\Psi\rangle_{12} = (|H\rangle_1 |V\rangle_2 - |V\rangle_1 |H\rangle_2)/\sqrt{2}$. In this case the final state of photon 3 would read

$$ {}_{12}\langle\Psi|\psi\rangle_1 |\mathrm{EPR}\rangle_{23} = -(\alpha |H\rangle_3 + \beta |V\rangle_3) , \tag{20.7}$$

which turns out to be the same polarization qubit as in Eq. (20.5), and the teleportation is completed without the operation step (4).

However, this scheme withholds two important drawbacks in terms of applications. One is its low transfer efficiency due to the probabilistic nature of the PDC and Bell-state measurement. The success probability is estimated to be far below 1 %, which does not meet the requirements for practical applications. Another is that this scheme requires post-selection of successful events by confirming the existence of the output qubit with detector D3 [11]. This removes the unwanted events when there is no output photon (this event corresponds to the case when two photon pairs are created in the left nonlinear crystal of Fig. 20.5 and no photons in the right). The transferred qubits are destroyed in this process, and thus cannot be used for further information processing. Despite these inefficiencies, the transfer fidelity of the post-selected successful events are high with the potential to reach 100 % in principle.

20.3.1.3 CV Teleportation

In 1998, Furusawa et al. demonstrated teleportation of the quadratures of a light beam [12], following the proposal by Braunstein and Kimble [13]. Here the input

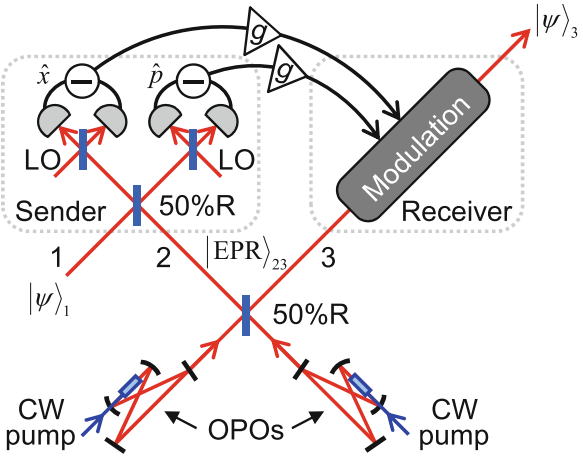

Fig. 20.6 Schematic of quantum teleportation of CVs demonstrated in Ref. [12]. A quantum state $|\psi\rangle$ of a light beam is deterministically teleported from mode 1 to 3 by on-demand EPR beams and complete Bell-state measurement followed by modulation. *CW* continuous wave, *OPO* optical parametric oscillator, *LO* local oscillator, *g* classical channel gain. In the standard protocol as in Ref. [12], the gain is set to unity. However, it is shown that gain tuning is quite effective for the hybrid approaches (see Sect. 20.4.1)

quantum state to be teleported is encoded in beam 1 as $|\psi\rangle_1 = \int_{-\infty}^{\infty} \psi(x)\,|x\rangle_1\,dx$ (Fig. 20.6). Teleportation of such states require the following ancillary EPR beam 2 and 3, entangled in quadrature basis:

$$|\text{EPR}\rangle_{23} \propto \int_{-\infty}^{\infty} |x\rangle_2\,|x\rangle_3\,dx = \int_{-\infty}^{\infty} |p\rangle_2\,|-p\rangle_3\,dp. \tag{20.8}$$

The quadratures of each of the EPR beam are quite noisy, but these two beams behave in a correlated way: when beam 2 has a $\hat{x}$-quadrature value of x ($\hat{p}$-quadrature value of p), beam 3 has the value of x ($-p$). The strength of CV teleportation is that approximated EPR beams can be prepared on-demand by mixing two orthogonally squeezed beams (approximated states of $|x = 0\rangle$ and $|p = 0\rangle$) on a 50:50 beam splitter. These squeezed beams are deterministically generated using an optical parametric oscillator (OPO), a cavity-enhanced version of the PDC pumped by a strong continuous-wave beam. Furthermore, CV Bell-state measurement can be performed completely by two homodyne detectors that each measure either $\hat{x}$ or $\hat{p}$. These measurements are followed by amplitude and phase modulations for step (4) to displace (shift) the quadratures of beam 3 in the phase space according to the measured values of $\hat{x}$ and $\hat{p}$. Intuitively, this measurement-and-modulation process cancels out the correlated quadrature noise between beams 2 and 3 in Eq. (20.8). If the quadratures are perfectly correlated, the noise is completely canceled out, and beam 3 becomes the same quantum state as the input state $|\psi\rangle_1$. Since all these steps can be performed in a deterministic fashion, a CV teleportation device

can always teleport the input state, and outputs the corresponding state in beam 3. This deterministic nature is a clear advantage over the probabilistic scheme of qubit teleportation (see Refs. [3, 13] for more detailed mathematical description of CV teleportation).

The major drawback of CV teleportation is that the transfer fidelity is limited due to the imperfect EPR beams generated from finitely-squeezed light. More specifically, the output state is always degraded by excess noise contamination due to the imperfect quadrature correlation between beams 2 and 3. The fidelity approaches unity in the limit of infinite squeezing, which would require infinite energy. Though efforts were made to circumvent this drawback using higher squeezing levels, transfer errors were not eradicated.

20.3.2 Quantum Computing Based on Quantum Teleportation

Quantum teleportation was originally proposed for transferring quantum information as it is ($|\psi\rangle \rightarrow |\psi\rangle$), but later works have revealed a more auspicious potential: quantum teleportation can work a quantum logic gates ($|\psi\rangle \rightarrow \hat{U}|\psi\rangle$) only with slight modification. Below we deal with two main schemes to realize logic gates based on the CV teleportation circuit. A similar discussion can be made for the qubit teleportation circuit.

20.3.2.1 Cluster-State Quantum Computation

Let us first consider an elementary CV teleportation circuit shown in Fig. 20.7a [14]. The original CV teleportation in Fig. 20.6 is equivalent to the case when this elementary circuit is cascaded twice. In this circuit, an arbitrary input state $|\psi\rangle$ is first coupled with an ancillary state $|p = 0\rangle$ via a controlled-phase gate $\hat{C}_Z$, and then its $\hat{p}$ quadrature is measured by a homodyne detector. The measurement outcome s decides the amount of the $\hat{x}$-displacement operation $\hat{X}(-s)$ on the other mode. After this operation, the Fourier transformed input state $\hat{F}\,|\psi\rangle$ appears.

Suppose an unitary operation $\hat{U} = \exp[if(\hat{x})]$ is applied to the input state before teleportation as shown in Fig. 20.7b. In this case, the input of the teleportation circuit is replaced by $\hat{U}|\psi\rangle$, and therefore the output should be $\hat{F}\hat{U}|\psi\rangle$. Since $\hat{U}$ and $\hat{C}_Z$ commute, $\hat{U}$ may be performed after the $\hat{C}_Z$ gate. Furthermore, $\hat{U}$ can be incorporated into the measurement part by changing the measurement from $\hat{p}$ to $\hat{U}^\dagger\hat{p}\hat{U}$. In this way, Fig. 20.7b can be transformed into Fig. 20.7c. This shows that an arbitrary unitary operation $\hat{U}$ can be applied to an input state only by appropriately changing the measurement basis of the elementary teleportation circuit. By cascading this circuit as in Fig. 20.7d, we can perform unitary operations sequentially to obtain the desired output state $\hat{F}\hat{U}_3\hat{F}\hat{U}_2\hat{F}\hat{U}_1|\psi\rangle$. This process can be understood as follows. A three-mode entangled state is prepared in advance (surrounded by a gray dashed line), and coupled to the input state $|\psi\rangle$ by $\hat{C}_Z$

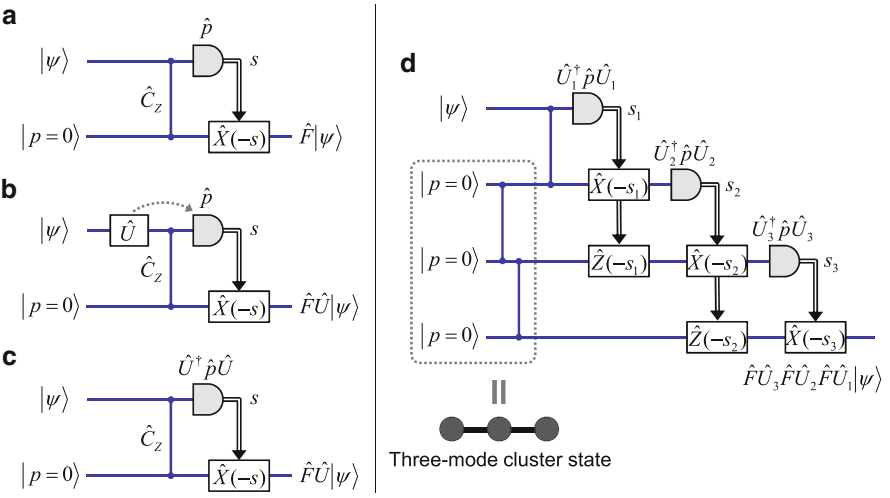

Fig. 20.7 Cluster-state quantum computation. $\hat{C}_Z = \exp(i\hat{x}_1\hat{x}_2)$, controlled-phase gate; $\hat{F} = \exp\left[i\pi(\hat{x}^2+\hat{p}^2)/4\right]$, Fourier transform; $\hat{U} = \exp[if(\hat{x})]$, a desired unitary transformation; $\hat{X}(s) = \exp(-is\hat{p})$, $\hat{x}$-displacement operation; and $\hat{Z}(s) = \exp(is\hat{x})$, $\hat{p}$-displacement operation. (**a**) An elementary CV teleportation circuit. (**b**) $\hat{U}$ is applied to the input state to obtain the output $\hat{F}\hat{U}\,|\psi\rangle$. (**c**) Measured variable is changed from $\hat{p}$ to $\hat{U}^\dagger\hat{p}\hat{U}$ to obtain the output $\hat{F}\hat{U}\,|\psi\rangle$. (**d**) Quantum computation using a three-mode cluster state

gate. Then quantum computation is performed only by appropriate choice of the measurement. The initial multi-mode entangled state is called a cluster state. This cluster-state quantum computation is totally different from the conventional model for quantum computation. The conventional model requires preparation of each quantum circuit for every unitary operation, and therefore requires different optical circuits (hardware) for different quantum computations. In contrast, in the cluster model, the required circuit for preparing cluster states (hardware) is always the same, but different computations can be realized by simply choosing a different measurement basis (different software). This software-based quantum computer is the quantum analogue of the current general-purpose computer.

Cluster-state quantum computation was originally proposed for qubit QIP by Raussendorf and Briegel in 2001 [15]. To date, preparation of few-qubit cluster states and cluster-based quantum logic gates for qubits have been reported in several experiments [16–18]. However, due to the probabilistic nature of PDC, preparation of large-scale cluster states are too demanding. In contrast, CV cluster states can be generated deterministically by a scheme proposed by van Loock et al. in 2007 [19], which requires only mixing squeezed beams (approximated states of $|p=0\rangle$) at beam splitters with appropriate transmissivities and phases. Figure 20.8a shows the schematic of generating a four-mode CV cluster state in four optical beams, demonstrated by Yukawa et al. in 2008 [20]. This cluster state was later used for demonstrating cluster-based one- and two-mode Gaussian

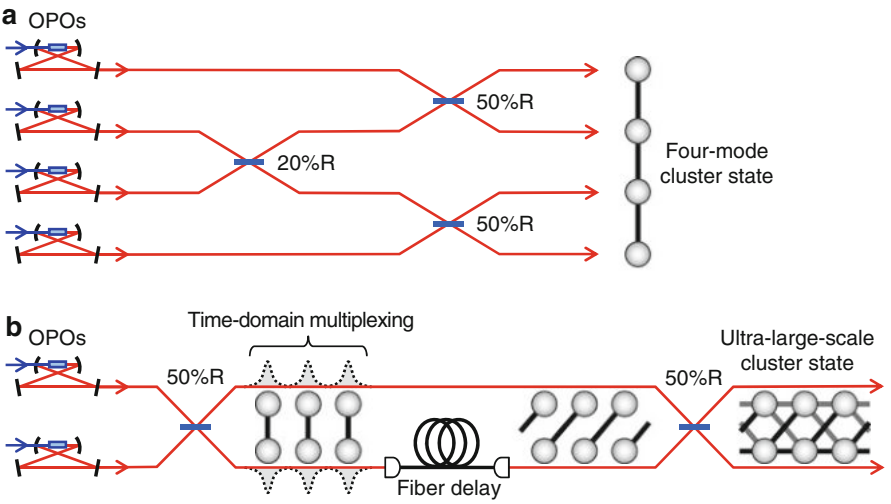

Fig. 20.8 Generation scheme of CV cluster states. (**a**) A four-mode cluster state in four optical beams generated from four squeezed beams [20]. (**b**) An ultra-large-scale cluster state multiplexed in the time domain generated from two squeezed beams [23]

gates by Ukai et al. in 2011 [21, 22]. Though CV cluster-state computation is deterministic, the configuration of Fig. 20.8a still lacks scalability as each additional mode to the cluster state requires more OPOs and beam splitters. In 2013, Yokoyama et al. took a different approach to generate an ultra-large-scale CV cluster state containing more than 10,000 modes [23]. Here, the modes entangled are wave packets of light in two beams, multiplexed in the time domain (Fig. 20.8b). These experimental achievements show that the CV cluster state is a promising platform for CV QIP. However, it should be noted that errors accumulate during CV cluster-state computation, because experimentally generated cluster states are generated from finitely-squeezed states. In addition, non-Gaussian gates required for universal CV QIP, cannot be achieved using only homodyne measurement (solutions to this problem will be mentioned in Sect. 20.4.2).

20.3.2.2 Quantum Gate Based on Off-Line Scheme

Another important application of the elementary teleportation circuit are quantum gates based on off-line prepared ancillary states. In this scheme, quantum teleportation allows fault-tolerant implementation of difficult quantum gates that would otherwise corrupt fragile quantum information [6, 24, 25]. This idea dates back to the proposal of so-called "gate teleportation", which was originally introduced for qubits by Gottesman and Chuang in 1999 [24], and then extended to CVs by Bartlett and Munro in 2003 [25]. Let us explain the basic idea by starting from the circuit of Fig. 20.7a again. This circuit is first extended to Fig. 20.9a, where the unitary

operation $\hat{U} = \exp[if(\hat{x})]$ is added to the final step. The output state in this case is $\hat{U}\hat{F}|\psi\rangle$. By replacing $\hat{X}(-s)$ by $\hat{U}\hat{X}(-s)\hat{U}^\dagger$ and using the commutation of $\hat{U}$ and $\hat{C}_Z$, we can move $\hat{U}$ prior to the $\hat{C}_Z$ gate, as in Fig. 20.9b.

Importantly, when $\hat{U}$ involves a Hamiltonian of a n-th order polynomial of $\hat{x}$, $\hat{U}\hat{X}(-s)\hat{U}^\dagger$ is shown to involve a Hamiltonian of $(n-1)$-th order [25]. In the case of $n \leq 3$, $\hat{U}\hat{X}(-s)\hat{U}^\dagger$ is a Gaussian gate which is within reach of current technology. Therefore, Fig. 20.9b implies the following; once an ancillary state $\hat{U}|p=0\rangle$ is prepared, gate $\hat{U}$ can be deterministically applied to an arbitrary input state $|\psi\rangle$ with homodyne measurement followed by a Gaussian gate, as long as $\hat{U}$ involves a third- or lower-order Hamiltonian. Here, the task of directly applying $\hat{U}$ to arbitrary states *on-line* is replaced by another task of preparing a specific ancillary state $\hat{U}|p=0\rangle$ *off-line* prior to the actual gate, which is much easier in experimental implementation. In this case, gate $\hat{U}$ for $|p=0\rangle$ may be implemented in a probabilistic fashion for multiple trials until it succeeds. Then, only the successfully prepared ancillary states $\hat{U}|p=0\rangle$ are stored in optical memories and consumed on demand as a resource for the logic gate (see Sect. 20.4.2 for a scheme to prepare ancillary states on demand). Note that, in contrast to the cluster-state computation where only Gaussian displacement gates are required for arbitrary $\hat{U}$ (Fig. 20.7c), the off-line scheme requires the gate $\hat{U}\hat{X}(-s)\hat{U}^\dagger$ and the difficulty of implementing such gate depends on $\hat{U}$.

One important example of the CV off-line scheme is the universal squeezer, a Gaussian gate which deterministically performs a squeezing gate to arbitrary input states $|\psi\rangle$ by means of an off-line prepared squeezed state (Fig. 20.9c). The universal squeezer and quantum non-demolition (QND) sum gate based on

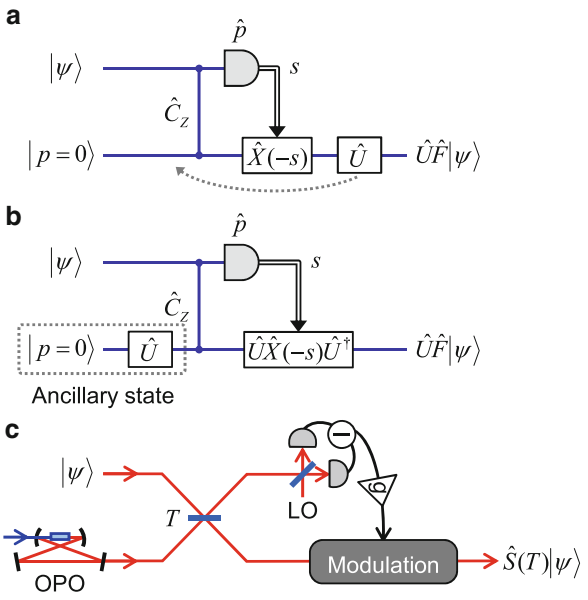

Fig. 20.9 Quantum gates based on off-line scheme. (**a**) $\hat{U}$ is applied to the output state to obtain $\hat{U}\hat{F}|\psi\rangle$. (**b**) Ancillary state $\hat{U}|p=0\rangle$ is used to realize the desired gate $|\psi\rangle \rightarrow \hat{U}\hat{F}|\psi\rangle$. (**c**) Schematic of the universal squeezer demonstrated in Ref. [26]. Beam splitter transmissivity T and gain g are chosen to perform desired degree of squeezing operation $\hat{S}(T)$ to the input state $|\psi\rangle$

the squeezers were already demonstrated by Yoshikawa et al. in 2007 and 2008, respectively [26, 27]. Importantly, the cubic phase gate $\hat{U} = \exp(i\chi\hat{x}^3)$ (third order, non-Gaussian) can be implemented only with Gaussian gates if a nonlinear cubic phase state $\exp(i\chi\hat{x}^3)\,|p = 0\rangle$ can be prepared off-line [28, 29]. However, the experimental realization of the cubic phase gate has not yet been reported (progress towards its realization will be mentioned in Sect. 20.4.2). In the case of qubit QIP, Gottesman and Chuang showed that the CNOT gate can also be implemented using the qubit teleportation circuit and off-line prepared ancillary states [24]. Linear optics quantum computing proposed by Knill, Laflamme and Milburn (KLM) in 2001 [30] also uses the teleportation circuit and special ancillary states to perform two-qubit gates with near-unit success probability. A probabilistic CNOT gate based on the KLM scheme was demonstrated by Okamoto et al. in 2011 [31]. Despite these proposals and demonstrations, the requirement for scalable qubit QIP will continue to be demanding, as long as it is based on the probabilistic generation and detection of photonic qubits.

20.4 Towards Hybrid Quantum Information Processing

As mentioned above, both qubit and CV QIP come with technical problems. The problem of qubit QIP is the low success rate, while CV QIP has limited fidelity due to finite squeezing. Here we introduce the recent research progress and future possibilities of "hybrid" QIP [5], which has the potential to overcome current limitations.

20.4.1 Hybrid Quantum Teleportation

Considering the fact that quantum teleportation now plays a central role in qubit and CV QIP, quantum teleportation using a hybrid technique should be an important first step towards more advanced hybrid protocols.

20.4.1.1 Proposal and Difficulties

One promising solution to the inefficiency of the conventional qubit teleportation scheme is to teleport photonic qubits via a CV teleportation device. This hybrid setting enables deterministic teleportation of qubits by exploiting the on-demand squeezing resources and complete Bell-state measurements in the quadrature bases. In principle, CV teleportation can be straightforwardly applied to any optical quantum state, let alone photonic qubits. However, experimental realization of the hybrid teleportation was too demanding when the proposal was made in around 2000 [32, 33].

There were three main obstacles to the experimental realization. First was the high squeezing level requirements for the resource EPR states; these highly non-classical states were beyond the technology of that time. Squeezing is typically quantified by the reduction in noise level of the squeezed quadrature below the shot noise level. The world record for squeezing had been 6 dB [34], which was not enough for such teleportation. Takeno et al. overcame this limitation by turning to a new nonlinear crystal, periodically poled $KTiOPO_4$; this produced 9 dB of squeezing in 2007 [35]. The current world record for high-level-squeezing is 13 dB, reported with the same nonlinear medium by Eberle et al. [36].

Second was the bandwidth incompatibility. The typical photonic qubit has a broad bandwidth in frequency domain because it is a wave packet, i.e., a pulse. In contrast, the conventional CV teleportation device only worked for narrow frequency sidebands [12] (Fig. 20.10a). Therefore it was impossible to teleport a wave packet by using the conventional setup of CV teleportation. In order to break through such difficulty, the bandwidth of CV teleporter had to be broadened. Takei et al. first broadened the bandwidth of the EPR resource in 2006 [37], and then Lee et al. used the broadband and highly entangled EPR resource to teleport highly non-classical wave packets of light in 2011 [38] (Fig. 20.10b).

Third, a narrow-band qubit compatible with the CV teleporter was needed. Although the original proposals for CV teleportation of qubits were for polarization qubits [32, 33], time-bin qubits were later found to be more technically compatible. This qubit consists of two optical pulses separated temporally, and described as a superposition of a photon in either pulse $|\psi\rangle = \alpha\,|0,1\rangle + \beta\,|1,0\rangle$ (Fig. 20.10d). The advantage of time-bin qubits is that they can be teleported using one CV teleporter, since the two pulses have the same polarization; polarization qubit teleportation requires two CV teleporters (one for each polarization) as in Fig. 20.10c. In 2013,

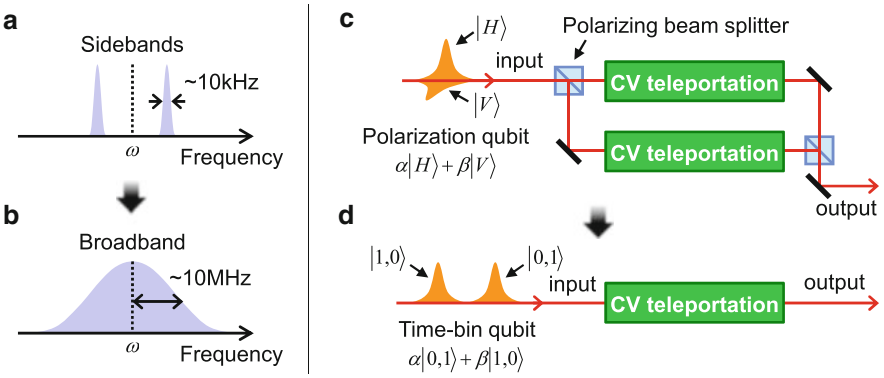

Fig. 20.10 Technologies towards hybrid quantum teleportation. (**a**) Conventional CV teleportation device works on only narrow frequency sidebands around laser carrier frequency ω. (**b**) Broadband CV teleportation device works on frequency band with up to around 10 MHz of half-width at half maximum. (**c**) CV teleportation of polarization qubits requires two teleportation devices. (**d**) CV teleportation of time-bin qubits requires only one teleportation device

Takeda et al. developed a generation and characterization technique for time-bin qubits with a compatible frequency spectrum, thereby completing the last piece of the hybrid teleportation system [39]. Now it is time for the hybrid teleportation.

20.4.1.2 Demonstration of Hybrid Teleportation

The combination of all these state-of-the-art technologies enabled CV quantum teleportation of time-bin qubits. Using this hybrid setup, Takeda et al. demonstrated, for the first time, deterministic quantum teleportation of photonic qubits in 2013 [40]. This experiment demonstrated that, even with finite squeezing resources, qubit information can be teleported faithfully by adjusting the classical channel gain in CV teleportation (g in Fig. 20.6). The mechanism is as follows. For finite squeezing parameter r (defined in Fig. 20.3c), the standard CV teleportation protocol with $g = 1$ yields a largely distorted output qubit with additional photons in general. In contrast, a CV teleporter with $g = \tanh r$ becomes equivalent to a pure loss channel, which only adds extra loss of $(1-\tanh^2 r)$ to the input state [32]. Moreover, the single-photon-based qubit $|\psi\rangle = \alpha\,|0,1\rangle + \beta\,|1,0\rangle$ represents a quantum error detection code against photon loss, where either a photon-loss error occurs, erasing the qubit, or a symmetric amplitude damping leaves the input qubit state completely intact [6]. These two facts together mean that the CV teleporter transforms the initial qubit state as

$$|\psi\rangle\langle\psi| \longrightarrow \tanh^2 r\,|\psi\rangle\langle\psi| + (1-\tanh^2 r)\,|0,0\rangle\langle 0,0|\,. \tag{20.9}$$

Importantly, no additional photons are created, and the qubit information $|\psi\rangle$ remains undisturbed regardless of the squeezing level. The teleporter only adds an extra two-mode vacuum term. Thus the weakness of CV teleportation due to the finite squeezing can be circumvented to a great extent by gain tuning.

One of the experimental results are shown in Fig. 20.11. The qubit components in the subspace spanned by $\{|0,1\rangle, |1,0\rangle\}$ decrease from 69 % at the input state to 42 % at the output, due to the extra loss added by the teleporter. However, the output qubit components still retain the original phase information of the superposition of $|0,1\rangle$ and $|1,0\rangle$ at input, demonstrating that the qubit information is faithfully teleported. The overall transfer fidelity ranged from 79 % to 82 % for four different qubits, all of which exceed the classical limit of teleportation. It was later shown that these experimental results are in good agreement with its corresponding theoretical model [41]. By extension of this setup, Takeda et al. also performed CV quantum teleportation of discrete-variable entanglement in the form of a photon split by a beam splitter; this demonstrated the genuine quantum nature of the hybrid teleportation system [42].

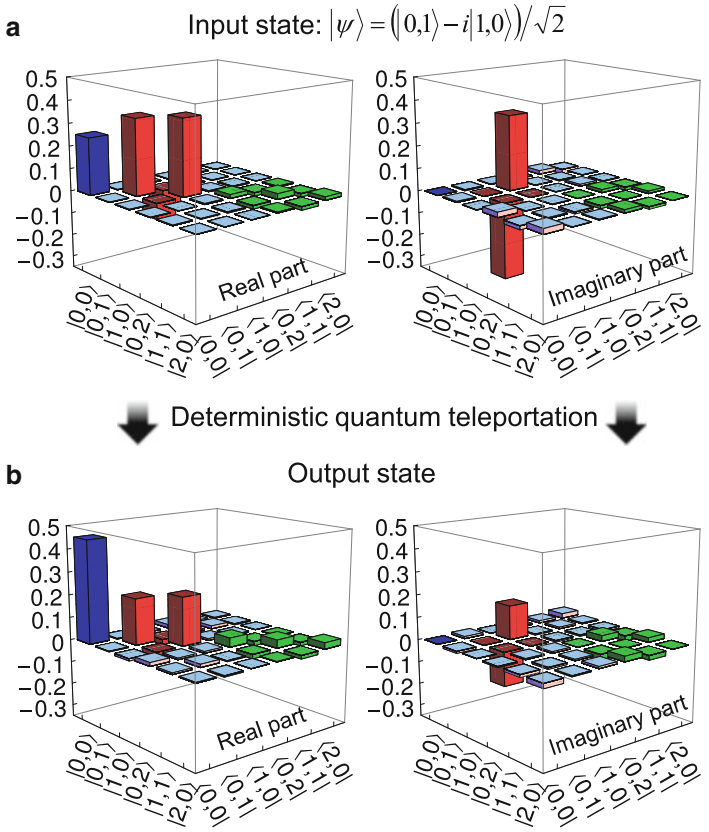

Fig. 20.11 Experimental results of hybrid quantum teleportation in Ref. [40]. CV quantum teleportation is performed for qubit $|\psi\rangle = (|0,1\rangle - i\,|1,0\rangle)/\sqrt{2}$ at squeezing parameter $r = 1.01$ and gain $g \approx \tanh r$. The two-mode density matrices are reconstructed both for the input and the output qubit states in the photon-number basis: $\hat{\rho} = \sum_{k,l,m,n=0}^{\infty} \rho_{klmn} |k,l\rangle \langle m,n|$. (**a**) Density matrix of the input state. (**b**) Density matrix of the output state

20.4.2 Hybrid Quantum Computing

The CV teleportation circuit has now become compatible with the basic technologies of qubit QIP, such as pulsed single photons and photon counting measurements. The combination of deterministic gates based on CV teleportation and nonlinear optical resources in qubit QIP potentially gives us great benefit for implementing universal quantum computers in both CV and qubit regimes.

20.4.2.1 Hybrid Approach to CV Universality

One challenging task towards universal CV QIP is the implementation of non-Gaussian gates, such as the cubic phase gate $\hat{U} = \exp(i\chi\hat{x}^3)$. One non-Gaussian gate, together with already well-developed Gaussian gates, is sufficient for realizing universal CV QIP, in principle [7]. In order to generate the ancilla for the cubic phase gate, Gottesman, Kitaev and Preskill (GKP) proposed an approximate version of the cubic phase state, generated by squeezed states and photon counting measurements as in Fig. 20.12a [28]. The generated cubic phase state can be used to perform the cubic phase gate to an arbitrary input state $|\psi\rangle$ through the circuit of Fig. 20.12b. These two circuits together can be interpreted as a CV cluster-state computation using homodyne measurement and photon counting measurement as in Fig. 20.12c [43]. Therefore the hybrid technology developed thus far may be beneficial for realizing universal CV cluster-state computation.

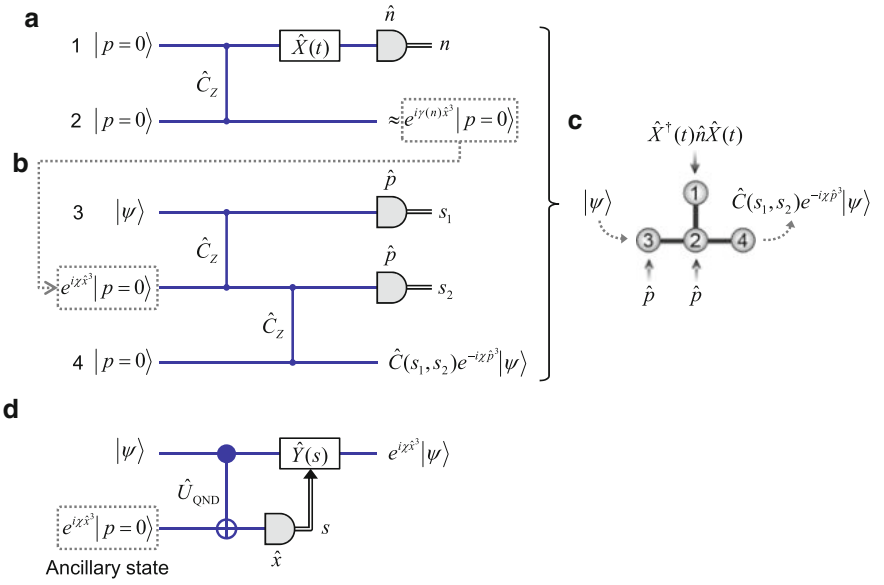

Fig. 20.12 Implementation of a cubic phase gate. (**a**) Displacement operation $\hat{X}(t)$ with sufficiently large t and photon number measurement produces an approximate version of a cubic phase state [28]. The cubic phase state depends on the measurement outcome n, and for the desired cubic phase gate, additional squeezing operations are needed. (**b**) The prepared cubic phase state is used to perform the cubic phase gate to an arbitrary input state $|\psi\rangle$. Gaussian operations can undo the operator $\hat{C}(s_1, s_2)$ depending on the homodyne results s_1 and s_2. (**c**) The cubic phase gate can be implemented based on a CV cluster state, homodyne measurement and a nonlinear measurement onto the displaced number basis $\{\hat{X}^\dagger(t)\,|n\rangle\}$ [43]. (**b**) Cubic phase gate can be performed on the input state $|\psi\rangle$ by the off-line scheme with an ancillary cubic phase state and a Gaussian gate $\hat{Y}(s)$ [28]

Another approach to the cubic phase gate is based on the off-line scheme using an ancillary cubic phase state $\exp(i\chi\hat{x}^3)\,|p=0\rangle$, as already mentioned in Sect. 20.3.2.2. Figure 20.12d shows one possible implementation proposed by GKP [28]. In this implementation, all the components except for the cubic phase state are already technologically available. When the desired gate is weak ($\chi \ll 1$), a certain superposition state of up-to three photons becomes enough for the ancillary state, as proposed by Marek et al. in 2011[29]. This type of ancillary state has already been generated experimentally by Yukawa et al. in 2013, albeit probabilistically [44, 45]. For a deterministic cubic phase gate, this ancillary state needs to be prepared on demand. The on-demand generation technique of non-classical optical states has been reported by Yoshikawa et al. in 2013 [46]. In this experiment, single photons are created and stored inside an OPO, and finally released on demand through a dynamical tuning of the output coupling. This scheme can be potentially used to prepare cubic phase states on demand. All the ingredients essential for a deterministic cubic phase gate have become available in principle, awaiting for their future ingratiation.

20.4.2.2 Hybrid Approach to Qubit Universality

Once the deterministic cubic phase gate is realized, in combination with other Gaussian gates, the CNOT gate for qubits may be implemented deterministically. This is because the unitary transformation of optical Kerr interaction $\hat{U} = \exp(i\chi\hat{a}_1^\dagger\hat{a}_1\hat{a}_2^\dagger\hat{a}_2)$, which is the essence of the CNOT gate, can be decomposed into the sequence of several cubic phase gates and other Gaussian gates [47]. Therefore, hybrid technologies ultimately lead to universal qubit QIP, where photonic qubits are processed by CV cluster-state computation or CV off-line scheme. Such a hybrid implementation should be much more efficient and faster than the previous counterpart of qubit QIP, which is solely based on probabilistic and post-selective resources and measurements. Furthermore, the limitation of gate fidelity, which had been the weak point inherent in CV QIP, may be circumvented by effective gain tuning used in the hybrid teleportation experiment. As an example of hybrid quantum computing, the squeezing operation (Gaussian) on single photons was demonstrated by Miwa et al. in 2012 [48] using the CV universal squeezer in Fig. 20.9c. Future technical developments would enable deterministic logic gates for photonic qubits by a CV scheme.

In order to perform universal QIP fault-tolerantly, GKP proposed to encode a logical qubit into the superposition of $\hat{x}$-eigenstates as $|\bar{j}\rangle \propto \sum_{s=-\infty}^{\infty} |x = (2s+j)\sqrt{\pi}\rangle$ $(j = 0, 1)$ [28]. This hybrid encoding is intended to protect a logical qubit against small errors such as random shift in the quadrature variables $\hat{x}$ and $\hat{p}$. A later work by Menicucci showed that fault-tolerant quantum computation based on the GKP encoding is possible by using finitely-squeezed resources above a threshold value of 20.5 dB and performing CV cluster-state computation with error correction [49]. Though the GKP encoding may still be far from implementable, it offers unique and interesting concepts to optical QIP and reveals a high potential of the hybrid approach.

20.5 Conclusion

Until recent years, qubit and CV QIP had developed separately each utilizing the quantum teleportation circuit as a key building block. The gap between these two approaches had been wide due to the incompatibilities in experimental technologies. However, these recent advances in combining both technologies have changed the situation. Especially, the realization of hybrid quantum teleportation in 2013 [40] must be a significant turning point in the development of optical QIP. This work presents a prototype technology for hybrid QIP systems, and will stimulate the further development of hybrid protocols to overcome the current limitations in optical QIP.

In our opinion, the hybrid approach to optical QIP will be the most promising one in the near future. In principle, universal and fault-tolerant quantum computing can be attained by using CV cluster-state computation and off-line schemes, while introducing nonlinearity through photon-counting measurement and nonlinear optical resources such as photon number states. For scalable implementations of hybrid QIP, multiplexing quantum modes in the time domain may be a key technology. This idea has already been used for generating ultra-large-scale CV cluster states [23], as well as for implementing hybrid quantum teleportation using time-bin encoding of a qubit [40]. In addition, hybrid QIP using on-chip integrated photonic circuits [50] would be desirable. Such an integrated architecture will decrease the size and complexity of the experimental setup, leading to a low-loss, robust and scalable hybrid QIP.

References

1. P. Kok, W.J. Munro, K. Nemoto, T.C. Ralph, J.P. Dowling, G.J. Milburn, Rev. Mod. Phys. **79**, 135 (2007)
2. J.-W. Pan, Z.-B. Chen, C.-Y. Lu, H. Weinfurter, A. Zeilinger, M. Żukowski, Rev. Mod. Phys. **84**, 777 (2012)
3. S.L. Braunstein, P. van Loock, Rev. Mod. Phys. **77**, 513 (2005)
4. P. van Loock, Laser Photonics Rev. **5**, 167 (2011)
5. A. Furusawa, P. van Loock, *Quantum Teleportation and Entanglement: A Hybrid Approach to Optical Quantum Information Processing* (Wiley, New York, 2011)
6. M.A. Nielsen, I.L. Chuang, *Quantum Computation and Quantum Information Processing* (Cambridge University Press, Cambridge, 2000)
7. S. Lloyd, S.L. Braunstein, Phys. Rev. Lett. **82**, 1784 (1999)
8. C.H. Bennett, G. Brassard, C. Crépeau, R. Jozsa, A. Peres, W.K. Wootters, Phys. Rev. Lett. **70**, 1895 (1993)
9. L. Vaidman, Phys. Rev. A **49**, 1473 (1994)
10. D. Bouwmeester, J.-W. Pan, K. Mattle, M. Eibl, H. Weinfurter, A. Zeilinger, Nature **390**, 575 (1997)
11. S.L. Braunstein, H.J. Kimble, Nature **394**, 840 (1998)
12. A. Furusawa, J.L. Sørensen, S.L. Braunstein, C.A. Fuchs, H.J. Kimble, E.S. Polzik, Science **282**, 706 (1998)
13. S.L. Braunstein, H.J. Kimble, Phys. Rev. Lett. **80**, 869 (1998)
14. N.C. Menicucci, P. van Loock, M. Gu, C. Weedbrook, T.C. Ralph, M.A. Nielsen, Phys. Rev. Lett. **97**, 110501 (2006)

15. R. Raussendorf, H.J. Briegel, Phys. Rev. Lett. **86**, 5188 (2001)
16. P. Walther, K.J. Resch, T. Rudolph, E. Schenck, H. Weinfurter, V. Vedral, M. Aspelmeyer, A. Zeilinger, Nature **434**, 169 (2005)
17. R. Prevedel, P. Walther, F. Tiefenbacher, P. Böhi, R. Kaltenbaek, T. Jennewein, A. Zeilinger, Nature **445**, 65 (2007)
18. Y. Tokunaga, S. Kuwashiro, T. Yamamoto, M. Koashi, N. Imoto, Phys. Rev. Lett. **100**, 210501 (2008)
19. P. van Loock, C. Weedbrook, M. Gu, Phys. Rev. A **76**, 032321 (2007)
20. M. Yukawa, R. Ukai, P. van Loock, A. Furusawa, Phys. Rev. A **78**, 012301 (2008)
21. R. Ukai, N. Iwata, Y. Shimokawa, S.C. Armstrong, A. Politi, J. Yoshikawa, P. van Loock, A. Furusawa, Phys. Rev. Lett. **106**, 240504 (2011)
22. R. Ukai, S. Yokoyama, J. Yoshikawa, P. van Loock, A. Furusawa, Phys. Rev. Lett. **107**, 250501 (2011)
23. S. Yokoyama, R. Ukai, S.C. Armstrong, C. Sornphiphatphong, T. Kaji, S. Suzuki, J. Yoshikawa, H. Yonezawa, N.C. Menicucci, A. Furusawa, Nat. Photon. **7**, 982 (2013)
24. D. Gottesman, I.L. Chuang, Nature **402**, 390 (1999)
25. S.D. Bartlett, W.J. Munro, Phys. Rev. Lett. **90**, 117901 (2003)
26. J. Yoshikawa, T. Hayashi, T. Akiyama, N. Takei, A. Huck, U.L. Andersen, A. Furusawa, Phys. Rev. A **76**, 060301(R) (2007)
27. J. Yoshikawa, Y. Miwa, A. Huck, U.L. Andersen, P. van Loock, A. Furusawa, Phys. Rev. Lett. **101**, 250501 (2008)
28. D. Gottesman, A. Kitaev, J. Preskill, Phys. Rev. A **64**, 012310 (2001)
29. P. Marek, R. Filip, A. Furusawa, Phys. Rev. A **84**, 053802 (2011)
30. E. Knill, R. Laflamme, G.J. Milburn, Nature **409**, 46 (2001)
31. R. Okamoto, J.L. O'Brien, H.F. Hofmann, S. Takeuchi, Proc. Natl. Acad. Sci. USA **108**, 11067 (2011)
32. R.E.S. Polkinghorne, T.C. Ralph, Phys. Rev. Lett. **83**, 2095 (1999)
33. T. Ide, H.F. Hofmann, T. Kobayashi, A. Furusawa, Phys. Rev. A **65**, 012313 (2001)
34. E.S. Polzik, J. Carri, H.J. Kimble, Appl. Phys. B **55**, 279 (1992)
35. Y. Takeno, M. Yukawa, H. Yonezawa, A. Furusawa, Opt. Express **15**, 4321 (2007)
36. T. Eberle, S. Steinlechner, J. Bauchrowitz, V. Händchen, H. Vahlbruch, M. Mehmet, H. Müller-Ebhardt, R. Schnabel, Phys. Rev. Lett. **104**, 251102 (2010)
37. N. Takei, N. Lee, D. Moriyama, J.S. Neergaard-Nielsen, A. Furusawa, Phys. Rev. A **74**, 060101(R) (2006)
38. N. Lee, H. Benichi, Y. Takeno, S. Takeda, J. Webb, E. Huntington, A. Furusawa, Science **332**, 330 (2011)
39. S. Takeda, T. Mizuta, M. Fuwa, J. Yoshikawa, H. Yonezawa, A. Furusawa, Phys. Rev. A **87**, 043803 (2013)
40. S. Takeda, T. Mizuta, M. Fuwa, P. van Loock, A. Furusawa, Nature **500**, 315 (2013)
41. S. Takeda, T. Mizuta, M. Fuwa, H. Yonezawa, P. van Loock, A. Furusawa, Phys. Rev. A **88**, 042327 (2013)
42. S. Takeda, M. Fuwa, P. van Loock, A. Furusawa, Phys. Rev. Lett. **114**, 100501 (2015)
43. M. Gu, C. Weedbrook, N.C. Menicucci, T.C. Ralph, P. van Loock, Phys. Rev. A **79**, 062318 (2009)
44. M. Yukawa, K. Miyata, T. Mizuta, H. Yonezawa, P. Marek, R. Filip, A. Furusawa, Opt. Express **21**, 5529 (2013)
45. M. Yukawa, K. Miyata, H. Yonezawa, P. Marek, R. Filip, A. Furusawa, Phys. Rev. A **88**, 053816 (2013)
46. J. Yoshikawa, K. Makino, S. Kurata, P. van Loock, A. Furusawa, Phys. Rev. X **3**, 041028 (2013)
47. S. Sefi, V. Vaibhav, P. van Loock, Phys. Rev. A **88**, 012303 (2013)
48. Y.Miwa, J. Yoshikawa, N. Iwata, M. Endo, P.Marek, R. Filip, P. van Loock, A. Furusawa, Phys. Rev. Lett. **113**, 013601 (2014)
49. N.C. Menicucci, Phys. Rev. Lett. **112**, 120504 (2014)
50. A. Politi, M.J. Cryan, J.G. Rarity, S. Yu, J.L. O'Brien, Science **320**, 646 (2008)

Part VI
Superconducting Qubits

Chapter 21
Microwave Photonics on a Chip: Superconducting Circuits as Artificial Atoms for Quantum Information Processing

Franco Nori and J.Q. You

21.1 Introduction

Superconducting circuits with Josephson junctions, behaving as nonlinear inductors, can act like artificial atoms [1–114]. This nonlinearity in quantum circuits is important because it produces an unequal separation between energy levels, allowing external fields to address the lowest energy states. These circuits are made in the laboratory on a micrometer scale and work at 10–50 mK temperatures. In order for these circuits to be quantum mechanical, it is important to greatly reduce the noise acting on them, and this can be achieved due to various factors, such as: the superconducting gap, the circuit reduced dimensionality, and by operating these circuits at very low temperatures, while isolating these from electromagnetic noise sources.

Superconducting circuits using Josephson junctions are being studied intensely because these can be utilized as qubits for quantum information processing (see, e.g., Refs. [1–4] for earlier reviews and [101–113] for more recent reviews). These circuits can be thought of as superconducting artificial atoms [103]. There are insightful analogies [103] between natural atoms and the artificial atoms produced with superconducting circuits. These show discrete energy levels and coherent quantum oscillations. Natural atoms are driven using visible or microwave photons,

F. Nori (✉)
CEMS, RIKEN, Saitama 351-0198, Japan

Physics Department, The University of Michigan, Ann Arbor, MI 48109-1040, USA
e-mail: fnori@riken.jp

J.Q. You
Beijing Computational Science Research Center, Beijing 100094, China

Y. Yamamoto, K. Semba (eds.), *Principles and Methods of Quantum Information Technologies*, Lecture Notes in Physics 911, DOI 10.1007/978-4-431-55756-2_21

while the artificial atoms in the circuits are controlled by voltages, currents, and microwave photons, exciting the qubit from one macroscopic quantum state to another.

There are obvious differences [103] between natural atoms and superconducting circuits. These include the different energy scales in these systems, and how strongly each system couples to its environment (atoms have a weak coupling, whereas circuits have a strong coupling). Artificial atoms can be manufactured with designed characteristics and lithographically made on a chip. This flexibility is not available with natural atoms and it provides an important advantage over natural atoms [103]. Therefore, superconducting circuits can be used to test fundamental quantum mechanics at a macroscopic scale, and to study atomic physics and quantum optics in a circuit. Furthermore, these artificial atoms can be produced to display novel properties which do not appear in natural atoms [103]. These circuits provide an unprecedented level of control over quantum states, and this can be useful for future quantum information processors.

In this review we discuss the atomic-physics and quantum-optics aspects of superconducting circuits. New physics, not occurring in natural atoms, in these artificial atoms will also be presented. This chapter is a much shorter version of our review in Ref. [101]. To simplify the presentation, no equations will be displayed here. Additional references, mostly to recent reviews, have been added. Of course, this chapter does not present original research. This is just a brief overview of the research work done by very many groups in this exciting interdisciplinary field, which is currently attracting considerable attention. For further information, we refer the reader to several much longer reviews, listed at the end of this chapter.

21.2 Basic Types of Superconducting Qubit Circuits

The energy scales which influence the quantum mechanics of a Josephson-junction circuit are: The Josephson coupling energy E_J and the electrostatic energy $E_C = (2e)^2/2C$. There are three basic kinds of superconducting circuits corresponding to different values of E_J/E_C. These are: (i) the Cooper-pair box for a charge qubit [5], (ii) the flux qubit [6], and (iii) the current-driven junction for a phase qubit [7, 8]. Furthermore, several hybrid superconducting qubits have been studied, based on variations of these three basic designs. These hybrid circuits can involve various aspects of the three basic types of qubits. For instance, a charge qubit can act like a charge-flux qubit [9] when $E_J/E_C \approx 1$. For the flux-driven three-junction loop, by making the ratio E_J/E_C smaller, the charge noise increases above the level of the flux noise [10], acting more like a charge qubit instead of the original three-juntion loop. For a flux qubit, when $\alpha < 0.5$, the double-well potential collapses to a single-well potential and the circuit acts like a phase qubit [10, 11].

Note that here α refers to the pre-factor of one of the three values of E_J in a flux qubit loop. If a large capacitance shunts the small junction [10, 11] this reduces the charge noise in the flux qubit. Moreover, when this large capacitance shunts the junction, then this can suppress the charge noise in a charge qubit [12], effectively transforming this shunted charge qubit into a phase one. Experiments have also studied flux qubits with a different number of Josephson junctions, e.g., one [89] or four junctions [90]. Moreover, a single current-driven junction by itself conveniently provides a phase qubit, with energy levels in a tilted potential well [91].

Hereafter, we briefly describe various aspects of the atomic-physics and quantum-optics phenomena of superconducting circuits. These circuits are expected to be important building blocks for quantum information processors.

21.3 Cavity Quantum Electrodynamics

A two-level system inside a tiny cavity can exchange energy coherently with a quantized electromagnetic field. This exchange of energy is known as Rabi oscillations, in which the field and the qubit exchange a quantum of energy at each Rabi cycle. The simplest example refers to the coupling between a qubit and one photon inside the cavity. This type of coupling between atoms and photons has been achieved experimentally, and this area of study is referred to as cavity quantum electrodynamics, abbreviated as cavity QED. Cavity quantum electrodynamics with superconducting circuits has been proposed [13, 14] and experimentally realized [15, 16], with superconducting qubits as two-level fabricated atoms. A single-mode *LC* resonator [15] and a multi-mode coplanar waveguide resonator [16] have been employed for the cavity. It is important to stress that the atom-photon coupling is much stronger (about a million times larger) for a superconducting qubit inside a cavity than for a natural atom inside a cavity [4, 14]. This very strong coupling permits to observe interesting phenomena like the Lamb shift for a superconducting qubit in the cavity [17]. Furthermore, both the cavity and the superconducting qubit can be made on the same integrated circuit. Reference [4] presents a review on cavity quantum electrodynamics with superconducting qubits.

Superconducting quantum circuits can also reach the so-called ultrastrong-coupling regime, in which the strength of the photon-qubit coupling is comparable to the energies of the photon and the qubit [18]. Various theoretical studies of this ultra-strong regime have explored some of its remarkable properties (see, e.g., Refs. [19–22]). Moreover, experiments have realized the ultrastrong coupling between a flux qubit and a coplanar waveguide [23] or an *LC* resonator [24]. This ultrastrong-coupling regime is very difficult to achieve using natural atoms, and exhibits new physics which is not available in the more usual weak- and medium-coupling regimes.

21.4 Selecting Quantum Transitions

The electronic state at each orbital level of natural atoms has a well-defined parity symmetry, either being odd or even. The Hamiltonian operator between the atom and the time-dependent electric field has an odd parity, in the usual dipole approximation. A non-zero dipole transition matrix element requires a change of parity between the initial and final states, beyond the usual constraints on the azimuthal and magnetic quantum numbers of the electron states. This optical selection rule implies that there are only three kinds of three-level systems, denoted as Λ-, V-, and Ξ-type atoms. This applies for natural atoms, in which no dipole transitions are allowed between electronic states with the same parity. Nevertheless, different selection rules can hold for superconducting artificial atoms. For example, the interaction Hamiltonian between a flux qubit and a time-dependent magnetic field does not have a well-defined parity, besides when the normalized (or reduced) magnetic flux $f \equiv \Phi/\Phi_0 = 1/2$. For this value of the applied field, the Hamiltonian has an odd parity. Considering the parity symmetries of the artificial-atom states at $f = 1/2$, the three lowest-energy levels of the circuit act like a Ξ-type or ladder-type artificial atom [25]. When this holds, the dipole transition between the ground state $|g\rangle$ and the auxiliary state $|a\rangle$ is forbidden, while the other two transitions (between the states $|g\rangle$ and $|e\rangle$, and also between $|e\rangle$ and $|a\rangle$) are allowed. The situation changes when $f \neq 1/2$, which breaks the parity symmetry for the interaction Hamiltonian. Thus, in this case, all the three dipole transitions (among $|g\rangle$, $|e\rangle$, and $|a\rangle$) are possible, and the circuit acts like a Δ-type atom because of the triangle-shaped transitions between these three energy levels. Therefore, when $f \neq 1/2$ the superconducting circuit acts like a cyclic Δ-type artificial atom, on which one- and two-photon processes coexist [25].

This novel Δ-type artificial atom is suitable for the upconversion and down-conversion of photon frequencies. Furthermore, when performing these frequency conversions, all transitions only require linear processes. This is quite different from the conventional frequency conversion in nonlinear optics, in which a nonlinear medium is used and the nonlinear effect converts the photon frequencies. Using a flux-biased three-junction loop [26], an experiment has demonstrated the frequency upconversion of a microwave photon. This experimental circuit observed the coexistence of one- and two-photon processes because of the symmetry-breaking of the Hamiltonian, when the applied magnetic flux was shifted away from $f = 1/2$.

Two microwave fields were applied at the same time to a superconducting circuit [27] with two coupled flux qubits. A given electronic transition can be activated or suppressed due to the interference between processes corresponding to an excitation selected by the applied microwave fields. Thus, artificial electronic selection rules can be effectively created with superconducting circuits.

21.5 Electromagnetically Induced Transparency

Quantum interference can control the light propagation through three-level atoms. For Λ-type three-level atoms, the goal here is to control the propagation of a probe light field in resonance with the dipole transition between the ground state, $|g\rangle$, and an auxiliary state, $|a\rangle$. To achieve this, the Λ-type three-level atom must also be driven by another field, called control field, which is in resonance with the transition between the excited state, $|e\rangle$, and the auxiliary state, $|a\rangle$. Driving the atom with these two fields directs the atom to a so-called dark state, which is a coherent superposition of the ground and excited states. When these conditions are met, the two applied fields cancel each other, due to destructive quantum interference. In this case, the auxiliary state is not occupied, and the absorption becomes zero, even when these two fields pump the atom. This electromagnetically induced transparency, or EIT, is well-known in quantum optics [28, 29] and it is also applicable to Ξ- and V-type atoms, both natural and artificial. This effect is quite remarkable, and has interesting consequences, including slowing down and sometimes trapping or stopping light.

When the applied reduced magnetic flux $f = 1/2$, then the flux qubit can be considered as a Ξ-type artificial atom [25, 30]. With appropriate parameters, the circuit can also turn into a Λ-type artificial atom when $f \neq 1/2$, when the dipole transition rate between the ground state $|g\rangle$ and the excited state $|e\rangle$ is considerably smaller than the rates for the other two transitions [30]. As mentioned in the previous section, on selecting quantum transitions, these selection rules are determined by the parity symmetries of the artificial-atom states. In stark contrast to natural atoms, the controllability of a superconducting qubit circuit can prepare the artificial atom in an initial state which is close to the dark state of the system, for arbitrary driving strengths of the pump and control fields. Thus, electromagnetically induced transparency in a superconducting atom can be produced for either weak or strong control and probe fields. This is a remarkable benefit of superconducting circuits compared to the usual natural atoms. Superconducting circuits displaying electromagnetically induced transparency have been explored both theoretically (e.g., Refs. [31–33]) and experimentally [34, 35].

21.6 State Population Inversion and Lasing

A common laser requires an amplifying medium inside a resonant optical cavity. With a suitable pumping or drive, a state population inversion (SPI) can be obtained for the molecules or atoms in the amplifying medium. Furthermore, there is a positive feedback between the amplifying medium and the emitted light. Several works studied lasing using one single artificial atom, both theoretically [30, 36–38] and experimentally [39, 40].

To build up a lasing field, two conditions, described in Refs. [30] and [36–40], are needed for quickly establishing state population inversion and then achieving a strong circuit-cavity coupling. Moreover, the cavity must have a high Q, meaning that it has a small decay or leak rate. Experimentally this can be achieved with a coplanar waveguide resonator [16].

Using a charge qubit in an on-chip cavity [39], lasing was experimentally observed. In contrast with the proposal [30] employing a flux qubit, this experiment [39] used a different three-level system: the two lowest superconducting states and a quasi-particle state which acts as an auxiliary state. Lasing was achieved continuously [39] and escaped out of the cavity from one of its ends.

21.7 Cooling

Natural atoms can be cooled by various means, including Sisyphus cooling, Doppler cooling, subrecoil cooling, side-band cooling, and evaporative cooling [41]. These approaches must be greatly modified in order to cool a solid-state artificial atom. For example, the so-called Sisyphus cooling technique has been experimentally used to cool a flux qubit [40]. Side-band cooling has also been reported experimentally [40]. Doppler, sub-recoil, and evaporative cooling do not seem suitable for artificial atoms, because these are fixed and cannot move.

The experimental cooling of a flux qubit has been made using side-band cooling, i.e., using the inverse process of state population inversion. The temperature of a superconducting flux qubit [42] was lowered by up to two orders of magnitude when its environment reached a temperature of tens of mK. This flux qubit was cooled when the applied flux was moved away from $f = 1/2$, which is the special point where the dipole transition rates for the lowest three levels of the flux qubit satisfy certain relations. The noise sources surrounding the qubit were not cooled when the superconducting qubit in Ref. [42] was cooled experimentally, quickly heating the qubit. To avoid this problem, it would be desirable to increase the controllability of the superconducting qubit by replacing the small Josephson junction in the flux-driven loop with a tunable SQUID [43]. This allows the cooling of both the qubit and also nearby two-level systems.

21.8 Nanomechanical Resonators

Several experimental groups have recently fabricated nano-mechanical resonators (NAMRs) with a high quality factor Q and also high frequencies, near the usual frequencies of superconducting circuits [44]. These developments motivated research on various superconducting circuits in order to reach the ground-state cooling of coupled nano-mechanical resonators [37, 43, 45–48]. Furthermore, by coupling it to a superconductor single-electron transistor [49] or to a microwave-frequency

superconducting resonator [50], the experimental cooling of nano-mechanical resonators has also been achieved. A nano-mechanical resonator cooled to the ground state [51] allows the direct study of various quantum phenomena and also the classical-to-quantum transition of macroscopic objects. These developments are creating the new subject of quantum acoustics.

21.9 Photon Generation

The quantum states of superconducting qubits can be controlled. Various fixed qubits, which are spatially separated, can communicate with each other using single photons in an extended cavity, behaving as a quantum bus. This type of quantum communication process can be achieved on a chip which has a cavity in it. A single-photon source can be produced experimentally via a superconducting qubit plus an on-chip cavity [52–55].

Going beyond single-photon generation, it is also possible to produce, as proposed in Refs. [56] and [57], many-photon Fock states $|n\rangle$ (where n is the number states of photons) and also arbitrary superposition states $\sum_n c_n |n\rangle$. A remarkable experiment [58] achieved the controlled generation of pure Fock states with up to 15 photons, via a superconducting phase qubit coupled to a microwave cavity. Furthermore, complex superpositions of states with various numbers of photons were also produced in a deterministic way [55], in a remarkable experimental realization of the proposal described in Ref. [56]. These exciting experiments further showed the quantum nature of the cavity and opened the way for future on-demand multi-photon sources for quantum-technology applications.

21.10 Quantum State Tomography

Quantum information processing requires the measurement of the final quantum states. On the other hand, a general quantum state cannot be fully characterized by one quantum measurement, due to the uncertainty relations. Nevertheless, all the complementary aspects of a general state can be obtained by several measurements on many identically-prepared copies of the quantum system. From this complete set of measurements of the system observables it is possible to reconstruct an unknown quantum state. This approach of reconstructing quantum states is known as quantum state tomography (QST). Using this state tomography, it is possible to characterize the noisy channel of the quantum system. This way of obtaining information on the dynamics of an open quantum system is known as quantum process tomography (QPT).

It has been proposed [60] how to perform tomographic measurements on the quantum states of superconducting qubits. Several experiments have been performed on the quantum state tomography of single superconducting phase qubits

[61, 62] and two coupled superconducting phase [63] and charge [64] qubits. Moreover, experimental realizations of quantum process tomography have been performed on single [65] and two [66] phase qubits. Quantum state tomography is important for qubit-state measurements, and quantum process tomography can be useful to monitor the noise properties and the temporal dynamics of qubit systems.

21.11 Dynamical Casimir Effect

Moving mirrors create vacuum modes which do not match well at various times. It has been predicted that real photons could be produced from vacuum fluctuations. This effect is known as the dynamical Casimir effect and it can also apply for one accelerated mirror in a vacuum. Prior to 2011 there was no experimental verification of the dynamical Casimir effect. The main reason for the difficultly in observing this effect is because the mirror velocity must be exceedingly high. Of course, this task becomes problematic when employing mirrors that have a mass. A proposal [67] considered using a coplanar waveguide terminated by a SQUID, and this method was used to observe this effect experimentally [114]. A key idea [67] is to modify the magnetic field through the SQUID circuit, and this changes the boundary condition of the waveguide, which determines its effective length. In this set-up [67, 114] there are no moving massive mirrors, so the speed of the effective magnetic boundary can approach the speed of light. This experiment [114] produced enough photons from the vacuum and these can be detected. This experiment [114] and various related phenomena are reviewed in Ref. [107].

21.12 Coherent Population Transfer

Very many precise resonant pulses are needed to produce elementary logic gates in quantum computing networks. This is a very challenging task because imperfections and fluctuations, which are unavoidable in experiments, make it very difficult to produce many precise resonant pulses. Moreover, it is very difficult to turn on and off the interbit couplings. Therefore, this makes it exceeding challenging to generate the very-precise pulse sequences needed for two-qubit gates. Using Stark-chirped rapid adiabatic passages, Ref. [68] puts forward a method to transfer coherently the populations of qubit states. If made adiabatically, the transfers of populations produced are not sensitive to the dynamics of the qubits. The required Stark effect could be generated via, for instance, two-photon excitations of the qubit [69]. This approach, called rapid adiabatic passage, provides an enticing way to make high-fidelity single-qubit and two-qubit gates. This proposal based on rapid adiabatic passage has been experimentally implemented via the passage of one photon in a superconducting qubit [70].

21.13 Tunable Mirrors and Interferometers

Landau-Zener-Stuekelberg interferometry [71, 106] can be studied using superconducting circuits. There are also other kinds of interferometry, like Fano and Fabry-Perot interferometry [72, 73]. These explorations can be performed by linking a coplanar waveguide to superconducting qubits. The photons inside the waveguide couple with the qubits, which can be tuned by the applied magnetic and electric fields. These qubits can behave like tunable mirrors, modifying the transmission and reflection coefficients of the photons inside the waveguide.

An array of coupled cavities linked to a superconducting qubit exhibit a nonlinear photonic dispersion relation. Thus, the photon transmission shows a more versatile line shape [72], more general and complex than the Fano and Breit-Wigner line shapes. When the lattice constant is commensurate with the photon wavelength [72], the photon transmission can exhibit a Breit-Wigner line shape, similarly to an open transmission line [74], because the photonic dispersion relation can then become linear. This effect was recently seen experimentally using a flux qubit linked to a resonator [75].

21.14 Quantum Nondemolition Measurements

Measurements perturb quantum states, which are known to be delicate. A so-called quantum non-demolition measurement does not disturb much a given quantum system. This can be realized via a special system-detector interaction that does not change the eigenstates of the quantum system. Quantum non-demolition measurements had been done earlier in quantum optics (see, e.g., Ref. [29]).

An early quantum non-demolition measurement on a superconducting qubit was performed via a dispersive (atom-field coupling) technique [16, 76]. Other experiments [77, 78] have demonstrated that quantum non-demolition measurements can also be performed for one qubit via a nonlinear resonator acting like a detector. A detector made of capacitance-shunted-SQUID was studied in Ref. [77], while Ref. [78] used a bifurcation amplifier [79]. Moreover, using a hysteretic dc SQUID detector [80], a quick fast quantum non-demolition measurement of a flux qubit was performed in the weakly projective region. How to best perform weakly-perturbing measurements is a very active area of research, due to its basic-science interest and also for its potential applications.

21.15 Generating Squeezed States

Squeezed states are well known in quantum optics and are currently being explored in solid state systems. *LC* oscillators in superconducting circuits can be used for quantum control and readout together with qubits. Superconducting resonant

tank circuits (parametric transducers acting as radio-frequency auto-oscillators) have been used to measure the quantum state of flux qubits [81]. Squeezed states would allow the reduction of the noise of detectors below the standard quantum limit. Theoretically [82], a superconducting parametric transducer can be used to generate squeezed states which would reduce quantum fluctuations. This would allow reducing the effective noise temperature of the amplifier appearing on the next stage, at least to the nominal temperature of the cooling container.

21.16 Topological Phases

Any local perturbation [83] cannot lift the degeneracy of a topologically-protected quantum state. Therefore topological phases are suitable for applications requiring a large degree of quantum coherence. Many artificial lattices, using superconducting circuits, can be designed to have interesting topological phases. For example, a proposal predicts that a triangular array of Josephson junctions may have a twofold degenerate ground state, and this could be employed for constructing qubits which are topologically-protected [84]. A recent prototype device [85] of this type was fabricated, and it is made of twelve Josephson junction qubits. After some tuning, this circuit appeared not to be affected by magnetic flux variations, even beyond the linear order. This preliminary test suggests that larger-scale topologically-protected superconducting qubits could be realized in the future. Furthermore, a proposal [86], based on superconducting circuits, implement the Kitaev honeycomb model, which involves three different types of interactions [87] at each node of a honeycomb lattice; the spins (natural or artificial) interact with their three nearest neighbors. For different bond parameters, this anisotropic spin model exhibits both Abelian and non-Abelian anyons. If this were to be experimentally studied, this could experimentally demonstrate anyons, which can exhibit fractional quantum statistics.

21.17 Bell Inequality

If one looks at correlations between spatially-separated measurements, then the Bell inequality implies that the predictions of quantum mechanics can contradict those of local hidden variable theories (see, for instance, Ref. [92]). Theoretical proposals for Bell inequality tests have been put forward using charge [93] and phase qubits [94]. The experimental violation of the Bell inequality has been verified [95] using phase qubits. This experiment gives strong evidence that these macroscopic circuits behave quantum mechanically, because Bell's inequality was violated by a quantum mechanical prediction. Other experimental results [96, 97] of Greenberger-Horne-Zeilinger states do not require statistical arguments to observe a violation of this theorem.

21.18 Leggett-Garg Inequality

An inequality [111] was derived by Leggett and Garg which can be considered as a temporal version of Bell's inequality and it should be violated by a quantum two-level system. This inequality applies for a degree of freedom exhibiting coherent oscillations and being measured at consecutive times [98]. This inequality has been tested experimentally [99] using a charge qubit, suggesting that the time correlations at the output of the detector violate the inequality.

21.19 Kochen-Specker Theorem

The conflict between quantum mechanics and noncontextual hidden-variable theories [92] was studied by Kochen and Specker. To study this non intuitive phenomenon macroscopically, a proposal [100] was made to use two charge qubits, controllably coupled by phase qubit acting as a two-level data-bus. The proposal [100] showed that joint nondestructive quantum measurements of two distinct qubits could prove quantum contextuality for a macroscopic circuit.

21.20 Nonlinear Optics

Superconducting circuits contain Josephson junctions and these can behave as nonlinear inductors. Thus, these could act as field-controlled nonlinear resonators to produce the Kerr effect, either the quadratic electro-optic or the quadratic magneto-optic versions of this effect. Employing these circuits as a Kerr medium, one could explore different nonlinear optics experiments, including: implementing quantum gates for photon qubits, coupling microwave photons, and performing quantum non-demolition experiments.

21.21 Final Summary

Superconducting circuits can have numerous additional applications. For example, a proposal to simulate Hawking radiation [88, 107] considers using a coplanar waveguide, with the center conductor replaced by an array of SQUIDs. In fact, superconducting circuits provide a very versatile platform for exploring complex controllable quantum dynamics [102, 107, 113]. These studies would enable exciting on-chip both quantum simulations and also studying many-body physics [102, 113]. Superconducting circuits allow the finding of many novel physical effects, and these will have potential applications in future quantum technologies.

In particular, these circuits provide an unprecedented level of control over quantum states, and this can be useful for future quantum information processors.

Acknowledgments We acknowledge partial support from the RIKEN iTHES Project, the MEXT Kakenhi on Quantum Cybernetics, a Grant-in-Aid for Scientific Research (A), and especially the JST "Funding Program for Innovative R&D on S&T" (FIRST).

References

1. Y. Makhlin, G. Schön, A. Shnirman, Quantum-state engineering with Josephson-junction devices. Rev. Mod. Phys. **7**, 357–400 (2001)
2. J.Q. You, F. Nori, Superconducting circuits and quantum information. Phys. Today **58**(11), 42–47 (2005)
3. J. Clarke, F.K. Wilhelm, Superconducting quantum bits. Nature **453**, 1031–1042 (2008)
4. R.J. Schoelkopf, S.M. Girvin, Wiring up quantum systems. Nature **451**, 664–669 (2008)
5. Y. Nakamura, Y.A. Pashkin, J.S. Tsai, Coherent control of macroscopic quantum states in a single-Cooper-pair box. Nature **398**, 786–788 (1999)
6. C.H. van der Wal et al., Quantum superposition of macroscopic persistent-current states. Science **290**, 773–777 (2000)
7. Y. Yu, S.Y. Han, X. Chu, S.I. Chu, Z. Wang, Coherent temporal oscillations of macroscopic quantum states in a Josephson junction. Science **296**, 889–892 (2002)
8. J.M. Martinis, S. Nam, J. Aumentado, C. Urbina, Rabi oscillations in a large Josephson-junction qubit. Phys. Rev. Lett. **89**, 117901 (2002)
9. D. Vion et al., Manipulating the quantum state of an electrical circuit. Science **296**, 886–889 (2002)
10. J.Q. You, X. Hu, S. Ashhab, F. Nori, Low-decoherence flux qubit. Phys. Rev. B **75**, 140515 (2007)
11. M. Steffen et al., High-coherence hybrid superconducting qubit. Phys. Rev. Lett. **105**, 100502 (2010)
12. J. Koch et al., Charge-insensitive qubit design derived from the Cooper pair box. Phys. Rev. A **76**, 042319 (2007)
13. J.Q. You, F. Nori, Quantum information processing with superconducting qubits in a microwave field. Phys. Rev. B **68**, 064509 (2003)
14. A. Blais, R.-S. Huang, A. Wallraff, S.M. Girvin, R.J. Schoelkopf, Cavity quantum electrodynamics for superconducting electrical circuits: An architecture for quantum computation. Phys. Rev. A **69**, 062320 (2004)
15. I. Chiorescu et al., Coherent dynamics of a flux qubit coupled to a harmonic oscillator. Nature **431**, 159–162 (2004)
16. A. Wallraff et al., Strong coupling of a single photon to a superconducting qubit using circuit quantum electrodynamics. Nature **431**, 162–167 (2004)
17. A. Fragner et al., Resolving vacuum fluctuations in an electrical circuit by measuring the Lamb shift. Science **28**, 1357–1360 (2008)
18. M.H. Devoret, S. Girvin, R. Schoelkopf, Circuit-QED: How strong can the coupling between a Josephson junction atom and a transmission line resonator be? Ann. Phys. (Leipzig) **16**(767–779) (2007)
19. E.K. Irish, J. Gea-Banacloche, I. Martin, K.C. Schwab, Dynamics of a two-level system strongly coupled to a high-frequency quantum oscillator. Phys. Rev. B **72**, 195410 (2005)
20. D. Zueco, G.M. Reuther, S. Kohler, P. Hänggi, Qubit-oscillator dynamics in the dispersive regime: Analytical theory beyond the rotating-wave approximation. Phys. Rev. A **80**, 033846 (2009)

21. S. Ashhab, F. Nori, Qubit-oscillator systems in the ultrastrong-coupling regime and their potential for preparing nonclassical states. Phys. Rev. A **81**, 042311 (2010)
22. P. Nataf, C. Ciuti, Vacuum degeneracy of a circuit QED system in the ultrastrong coupling regime. Phys. Rev. Lett. **104**, 023601 (2010)
23. T. Niemczyk et al., Circuit quantum electrodynamics in the ultrastrong-coupling regime. Nat. Phys. **6**, 772–776 (2010)
24. P. Forn-Diaz et al., Observation of the Bloch-Siegert shift in a qubit-oscillator system in the ultrastrong coupling regime. Phys. Rev. Lett. **105**, 237001 (2010)
25. Y.X. Liu, J.Q. You, L.F. Wei, C.P. Sun, F. Nori, Optical selection rules and phase-dependent adiabatic state control in a superconducting quantum circuit. Phys. Rev. Lett. **95**, 087001 (2005)
26. F. Deppe et al., Two-photon probe of the Jaynes-Cummings model and controlled symmetry breaking in circuit QED. Nat. Phys. **4**, 686–691 (2008)
27. P.C. de Groot et al., Selective darkening of degenerate transitions demonstrated with two superconducting quantum bits. Nat. Phys. **6**, 763–766 (2010)
28. S.E. Harris, Electromagnetically induced transparency. Phys. Today **50**(7), 36–42 (1997)
29. M.O. Scully, M.S. Zubairy, *Quantum Optics* (Cambridge University Press, Cambridge, 1997)
30. J.Q. You, Y.X. Liu, C.P. Sun, F. Nori, Persistent single-photon production by tunable on-chip micromaser with a superconducting quantum circuit. Phys. Rev. B **75**, 104516 (2007)
31. K.V.R.M. Murali, Z. Dutton, W.D. Oliver, D.S. Crankshaw, T.P. Orlando, Probing decoherence with electromagnetically induced transparency in superconductive quantum circuits. Phys. Rev. Lett. **93**, 087003 (2004)
32. Z. Dutton, K.V.R.M. Murali, W.D. Oliver, T.P. Orlando, Electromagnetically induced transparency in superconducting quantum circuits: Effects of decoherence, tunneling, and multilevel crosstalk. Phys. Rev. B **73**, 104516 (2006)
33. H. Ian, Y.X. Liu, F. Nori, Tunable electromagnetically induced transparency and absorption with dressed superconducting qubits. Phys. Rev. A **81**, 063823 (2010)
34. M.A. Sillanpää et al., Autler-Townes effect in a superconducting three-level system. Phys. Rev. Lett. **103**, 193601 (2009)
35. A.A. Abdumalikov Jr. et al., Electromagnetically induced transparency on a single artificial atom. Phys. Rev. Lett. **104**, 193601 (2010)
36. D.A. Rodrigues, J. Imbers, A.D. Armour, Quantum dynamics of a resonator driven by a superconducting single-electron transistor: A solid-state analogue of the micromaser. Phys. Rev. Lett. **98**, 67204 (2007)
37. J. Hauss, A. Fedorov, C. Hutter, A. Shnirman, G. Schön, Single-qubit lasing and cooling at the Rabi frequency. Phys. Rev. Lett. **100**, 037003 (2008)
38. S. Ashhab, J.R. Johansson, A.M. Zagoskin, F. Nori, Single-artificial-atom lasing using a voltage-biased superconducting charge qubit. New J. Phys. **11**, 023030 (2009)
39. O. Astafiev et al., Single artificial-atom lasing. Nature **449**, 588–590 (2007)
40. M. Grajcar et al., Sisyphus cooling and amplification by a superconducting qubit. Nature Phys. **4**, 612–616 (2008)
41. C.J. Foot, *Atomic Physics* (Oxford University Press, Oxford, 2004)
42. S.O. Valenzuela et al., Microwave-induced cooling of a superconducting qubit. Science **314**, 1589–1592 (2006)
43. J.Q. You, Y.X. Liu, N. Nori, Simultaneous cooling of an artificial atom and its neighboring quantum system. Phys. Rev. Lett. **100**, 047001 (2008)
44. X.M.H. Huang, C.A. Zorman, M. Mehregany, M.L. Roukes, Nanodevice motion at microwave frequencies. Nature **421**, 496 (2003)
45. I. Martin, A. Shnirman, L. Tian, P. Zoller, Ground-state cooling of mechanical resonators. Phys. Rev. B **69**, 125339 (2004)
46. P. Zhang, Y.D. Wang, C.P. Sun, Cooling mechanism for a nonmechanical resonator by periodic coupling to a Cooper pair box. Phys. Rev. Lett. **95**, 097204 (2005)
47. F. Marquardt, J.P. Chen, A.A. Clerk, S.M. Girvin, Quantum theory of cavity-assisted sideband cooling of mechanical motion. Phys. Rev. Lett. **99**, 093902 (2007)

48. M. Grajcar, S. Ashhab, J.R. Johansson, F. Nori, Lower limit on the achievable temperature in resonator-based sideband cooling. Phys. Rev. B **78**, 035406 (2008)
49. A. Naik et al., Cooling a nanomechanical resonator with quantum back-action. Nature **443**, 193–196 (2006)
50. T. Rocheleau et al., Preparation and detection of a mechanical resonator near the ground state of motion. Nature **463**, 72–75 (2010)
51. A.D. O'Connell et al., Quantum ground state and single-phonon control of a mechanical resonator. Nature **464**, 697–703 (2010)
52. M.A. Sillanpää, J.I. Park, R.W. Simmonds, Coherent quantum state storage and transfer between two phase qubits via a resonant cavity. Nature **449**, 438–442 (2007)
53. A.A. Houck et al., Generating single microwave photons in a circuit. Nature **449**, 328–331 (2007)
54. M. Hofheinz et al., Generation of Fock states in a superconducting quantum circuit. Nature **454**, 310–314 (2008)
55. M. Hofheinz et al., Synthesizing arbitrary quantum states in a superconducting resonator. Nature **459**, 546–549 (2009)
56. C.K. Law, J.H. Eberly, Arbitrary control of a quantum electromagnetic field. Phys. Rev. Lett. **76**, 1055–1058 (1996)
57. Y.X. Liu, L.F. Wei, F. Nori, Generation of nonclassical photon states using a superconducting qubit in a microcavity. Europhys. Lett. **67**, 941–947 (2004)
58. H. Wang et al., Measurement of the decay of Fock states in a superconducting quantum circuit. Phys. Rev. Lett. **101**, 240401 (2008)
59. H. Wang et al., Deterministic entanglement of photons in two superconducting microwave resonators. Phys. Rev. Lett. **106**, 060401 (2011)
60. Y.X. Liu, L.F. Wei, F. Nori, Tomographic measurements on superconducting qubit states. Phys. Rev. B **72**, 014547 (2005)
61. M. Steffen et al., State tomography of capacitively shunted phase qubits with high fidelity. Phys. Rev. Lett. **97**, 050502 (2006)
62. N. Katz et al., Coherent state evolution in a superconducting qubit from partial-collapse measurement. Science **312**, 1498–1500 (2006)
63. M. Steffen et al., Measurement of the entanglement of two superconducting qubits via state tomography. Science **313**, 1423–1425 (2006)
64. S. Filipp et al., Two-qubit state tomography using a joint dispersive readout. Phys. Rev. Lett. **102**, 200402 (2009)
65. M. Neeley et al., Process tomography of quantum memory in a Josephson-phase qubit coupled to a two-level state. Nat. Phys. **4**, 523–526 (2008)
66. R.C. Bialczak et al., Quantum process tomography of a universal entangling gate implemented with Josephson phase qubits. Nat. Phys. **6**, 409–413 (2010)
67. J.R. Johansson, G. Johansson, C.M. Wilson, F. Nori, Dynamical Casimir effect in a superconducting coplanar waveguide. Phys. Rev. Lett. **103**, 147003 (2009)
68. L.F. Wei, J.R. Johansson, L.X. Cen, S. Ashhab, F. Nori, Controllable coherent population transfers in superconducting qubits for quantum computing. Phys. Rev. Lett. **100**, 113601 (2008)
69. A.A. Rangelov et al., Stark-shift-chirped rapid-adiabatic-passage technique among three states. Phys. Rev. A **72**, 053403 (2005)
70. B.R. Johnson et al., Quantum non-demolition detection of single microwave photons in a circuit. Nat. Phys. **6**, 663 (2010)
71. S.N. Shevchenko, S. Ashhab, F. Nori, Landau-Zener-Strückelberg interferometry. Phys. Rep. **492**, 1–30 (2010)
72. L. Zhou, Z.R. Gong, Y.X. Liu, C.P. Sun, F. Nori, Controllable scattering of a single photon inside a one-dimensional resonator waveguide. Phys. Rev. Lett. **101**, 100501 (2008)
73. L. Zhou, H. Dong, Y.X. Liu, C.P. Sun, F. Nori, Quantum supercavity with atomic mirrors. Phys. Rev. A **78**, 063827 (2008)

74. J.T. Shen, S. Fan, Coherent single photon transport in a one-dimensional waveguide coupled with superconducting quantum bits. Phys. Rev. Lett. **95**, 213001 (2005)
75. O. Astafiev et al., Resonance fluorescence of a single artificial atom. Science **327**, 840–843 (2010)
76. A. Wallraff et al., Approaching unit visibility for control of a superconducting qubit with dispersive readout. Phys. Rev. Lett. **95**, 060501 (2005)
77. A. Lupascu et al., Quantum non-demolition measurement of a superconducting two-level system. Nat. Phys. **3**, 119–125 (2007)
78. N. Boulant et al., Quantum nondemolition readout using a Josephson bifurcation amplifier. Phys. Rev. B **76**, 014525 (2007)
79. I. Siddiqi et al., RF-driven Josephson bifurcation amplifier for quantum measurement. Phys. Rev. Lett. **93**, 207002 (2004)
80. T. Picot, R. Schouten, C.J.P.M. Harmans, J.E. Mooij, Quantum nondemolition measurement of a superconducting qubit in the weakly projective regime. Phys. Rev. Lett. **105**, 040506 (2010)
81. E. Il'ichev et al., Continuous monitoring of Rabi oscillations in a Josephson flux qubit. Phys. Rev. Lett. **91**, 097906 (2003)
82. A.M. Zagoskin, E. Il'ichev, M.W. McCutcheon, J.F. Young, F. Nori, Controlled generation of squeezed states of microwave radiation in a superconducting resonant circuit. Phys. Rev. Lett. **101**, 253602 (2008)
83. C. Nayak, S.H. Simon, A. Stern, M. Freedman, S. Das Sarma, Non-Abelian anyons and topological quantum computation. Rev. Mod. Phys. **80**, 1083 (2008)
84. L.B. Ioffe et al., Topologically protected quantum bits using Josephson junction arrays. Nature **415**, 503–506 (2002)
85. S. Gladchenko et al., Superconducting nanocircuits for topologically protected qubits. Nat. Phys. **5**, 48–53 (2009)
86. J.Q. You, X.F. Shi, X. Hu, F. Nori, Quantum emulation of a spin system with topologically protected ground states using superconducting quantum circuits. Phys. Rev. B **81**, 014505 (2010)
87. A. Kitaev, Anyons in an exactly solved model and beyond. Ann. Phys. (N.Y.) **321**, 2–111 (2006)
88. P.D. Nation, M.P. Blencowe, A.J. Rimberg, E. Buks, Analogue Hawking radiation in a dc-SQUID array transmission line. Phys. Rev. Lett. **103**, 087004 (2009)
89. J.R. Friedman, V. Patel, W. Chen, S.K. Tolpygo, J.E. Lukens, Quantum superposition of distinct macroscopic states. Nature **406**, 43–46 (2000)
90. P. Bertet et al., Dephasing of a superconducting qubit induced by photon noise. Phys. Rev. Lett. **95**, 257002 (2005)
91. R.W. Simmonds et al., Decoherence in Josephson phase qubits from junction resonators. Phys. Rev. Lett. **93**, 077003 (2004)
92. M. Genovese, Research on hidden variable theories: A review of recent progresses. Phys. Rep. **413**, 319–396 (2005)
93. L.F. Wei, Y.X. Liu, F. Nori, Testing Bell's inequality in a constantly coupled Josephson circuit by effective single-qubit operations. Phys. Rev. B **72**, 104516 (2005)
94. A.G. Kofman, A.N. Korotkov, Analysis of Bell inequality violation in superconducting phase qubits. Phys. Rev. A **77**, 104502 (2008)
95. M. Ansmann et al., Violation of Bell's inequality in Josephson phase qubits. Nature **461**, 504–506 (2009)
96. M. Neeley et al., Generation of three-qubit entangled states using superconducting phase qubits. Nature **467**, 570–573 (2010)
97. D. DiCarlo et al., Preparation and measurement of three-qubit entanglement in a superconducting circuit. Nature **467**, 574–578 (2010)
98. A.J. Leggett, A. Garg, Quantum mechanics versus macroscopic realism: Is the flux there when nobody looks? Phys. Rev. Lett. **54**, 857–860 (1985)

99. A. Palacios-Laloy et al., Experimental violation of a Bell's inequality in time with weak measurement. Nat. Phys. **6**, 442–447 (2010)
100. L.F. Wei, K. Maruyama, X.B. Wang, J.Q. You, F. Nori, Testing quantum contextuality with macroscopic superconducting circuits. Phys. Rev. B **81**, 174513 (2010)
101. J.Q. You, F. Nori, Atomic physics and quantum optics using superconducting circuits. Nature **474**, 589 (2011)
102. I. Buluta, F. Nori, Quantum simulators. Science **326**, 108 (2009)
103. I. Buluta, S. Ashhab, F. Nori, Natural and artificial atoms for quantum computation. Rep. Prog. Phys. **74**, 104401 (2011)
104. F. Nori, Atomic physics with a circuit. Nat. Phys. **4**, 589 (2008)
105. F. Nori, Quantum football. Science **325**, 689 (2009)
106. S.N. Shevchenko, S. Ashhab, F. Nori, Landau-Zener-Stuckelberg interferometry. Phys. Rep. **492**, 1 (2010)
107. P.D. Nation, J.R. Johansson, M.P. Blencowe, F. Nori, Stimulating uncertainty: Amplifying the quantum vacuum with superconducting circuits. Rev. Mod. Phys. **84**, 1–24 (2012)
108. I. Georgescu, F. Nori, Quantum technologies: An old new story. Phys. World **25**, 16–17 (2012)
109. A.G. Kofman, S. Ashhab, F. Nori, Weak pre- and post-selected measurements. Phys. Rep. **520**, 43–133 (2012)
110. Z.-L. Xiang, S. Ashhab, J.Q. You, F. Nori, Hybrid quantum circuits: Superconducting circuits interacting with other quantum systems. Rev. Mod. Phys. **85**, 623 (2013)
111. C. Emary, N. Lambert, F. Nori, Leggett-Garg inequalities. Rep. Prog. Phys. **77**, 016001 (2014)
112. J. Ma, X. Wang, C.P. Sun, F. Nori, Quantum spin squeezing. Phys. Rep. **509**, 89 (2011)
113. I. Georgescu, S. Ashhab, F. Nori, Quantum simulation. Rev. Mod. Phys. **86**, 153 (2014)
114. C.M. Wilson, G. Johansson, A. Pourkabirian, J.R. Johansson, T. Duty, F. Nori, P. Delsing, Observation of the dynamical Casimir effect in a superconducting circuit. Nature **479**, 376–379 (2011)

Chapter 22
Achievements and Outlook of Research on Quantum Information Systems Using Superconducting Quantum Circuits

Jaw-Shen Tsai

22.1 Introduction

Research of quantum information processing currently underway is expected to lead to the new paradigm of information processing of the future. Among the possible technologies, the development of quantum computers using superconducting circuits is a particularly intensively investigated field of research, and many notable progresses have been made.

The heart of the fundamental physics of this superconducting technology is the coherent control of superconducting macroscopic quantum states. This breakthrough in science and technology was originated in our laboratory 15 years ago [1]. The puzzle of whether a macroscopically extended complex object can have quantum coherence, such as quantum wave superposition, has implications, which include the possible identification of boundary between classical world and quantum world. Our experimental result provided a definite and positive solution to this longstanding challenging research topic in physics.

On the other hand, in an engineering context, a qubit (quantum bit) consists of a superconducting circuit. It is a solid-state device, and is a technology that is expected to lead to quantum computers, which require the integration of a huge number of bits. The degrees of freedom intrinsic to solid-state devices, such as design flexibility and ease of control using gates, are expected to offer a promising avenue for research and development in this area.

A superconducting qubit circuit with quantized multiple energy levels can be considered an artificial atom. This "atom" is a massive solid-state device that allows

J.-S. Tsai (✉)
The RIKEN Center for Emergent Matter Science Smart Energy Research Laboratories, NEC Corporation, Tokyo, Japan
e-mail: tsai@riken.jp

Y. Yamamoto, K. Semba (eds.), *Principles and Methods of Quantum Information Technologies*, Lecture Notes in Physics 911, DOI 10.1007/978-4-431-55756-2_22

control of the quantum state of the circuit by performing amplitude and phase control as desired on an eigenstate at each energy level with quantum coherence preserved.

Our laboratory has developed several key technologies for quantum information processing, including creation of entanglement using a macroscopic quantum state [2], a quantum logic operation [3], a single-shot readout [4], a universal quantum gate [5], extended life of qubits with echo pulses [6], and high-precision control with microwave pulses [7].

The above work marked the birth of artificial atom quantum optics, which is a field of research related to the interaction between superconducting artificial atoms and microwave photons. Artificial atom quantum optics, which can easily create strong coupling conditions, has many advantages over naturally occurring atoms, including ease of design, ease of integration and strong coupling with light, and has the potential for many other new applications. We have developed a lasing process with a single artificial atom [8], resonance fluorescence [9], electromagnetically induced transparency [10], and a single atom quantum amplifier [11]. This paper describes the background to the development of this technology and the progress made on key research activities, as well as innovative achievements, particularly in research focusing on quantum computers and their prospects. Our research activities on quantum optics with a superconducting artificial atom are described by Yasunobu Nakamura in this issue.

22.2 Superconducting State and Josephson Junction

A macroscopic superconducting quantum state has outstanding characteristics. In a normal-state metal, a large number of conduction electrons move around in clusters with very high degrees of freedom. Once a superconducting transition occurs in the metal, most of the conduction electrons form Cooper pairs (electron pairs) and condense into a single macroscopic quantum state. This state is described by the macroscopic wave function (order parameter) $\psi(x) = \psi_0(x)e^{i\phi(x)}$. Consequently, all the degrees of freedom of the conduction electrons are frozen, except the phase φ of the macroscopic quantum state and the charge number, which remain effective degrees of freedom.

In nature, a completely new hierarchy of order is occasionally created by a relatively simple mechanism. This phenomenon, which is sometimes called an emergent order, very often exhibits remarkable and unexpected capabilities. The superconducting state is a typical emergent order that occurs in a solid.

A Josephson junction is useful for the observation and control of a macroscopic phase in a superconductor. A supercurrent can flow through the Josephson junction and is given by $I = I_0 sin\theta$, where $\theta = \phi_1 - \phi_2$ is the macroscopic phase difference between the ends of the junction, and I_0 is a constant called the maximum Josephson current. This is called the direct current Josephson Effect.

When a voltage V is applied to the junction, the phase difference causes a Josephson oscillation, and the correlation $V = \frac{h}{2e}\frac{d\theta}{dt}$ holds, where h is Planck's constant and e is the elementary charge. This is called the alternating current Josephson correlation. More precisely, the voltage V is a gauge-invariant electrochemical potential detected by the Cooper pair.

The phase and charge degrees of freedom of a superconductor can be observed and controlled only when a Josephson junction is present. This device is a key component of both a superconducting classical bit and a superconducting qubit.

22.3 Eve of Josephson Qubit Realization

There is very little dissipation in a macroscopic superconducting state, and this is considered a suitable environment for creating a coherent state in quantum mechanics (there is dissipation at a finite temperature due to excited quasiparticles).

In the 1980s, a novel proposal of macroscopic quantum tunneling in a Josephson junction, in particular, in experiment uses a superconducting quantum interference device (SQUID) [12]. A subsequent verification experiment confirmed that the superconducting macroscopic quantum state tunneled through the Josephson confinement potential (see below) [13].

Subsequently, a quantized excited state other than the ground state was confirmed to exist in the macroscopic quantum state of the Josephson junction. Discrete energy levels were confirmed in a photon-assisted macroscopic quantum tunnel experiment [14]. In a Josephson junction where $I_B < I_0$, the macroscopic quantum phase θ is trapped in a certain phase space by the confinement potential $U(\theta) = E_J\left(1 - \cos\theta - \frac{I_B}{I_0}\theta\right)$ ($E_J =$ Josephson energy, $I_B =$ bias current) created by the junction.

The spatial degrees of freedom of the electrons confined in the atomic potential are constrained, resulting in discrete energy levels. Similarly, the phase degrees of freedom of the macroscopic quantum state confined in the potential $U(\theta)$ of the Josephson junction are constrained, resulting in discrete energy levels. A superconducting ground state is usually formed in a superconductor. In the Josephson junction, due to its nonlinearity, several anharmonic macroscopic energy levels can be generated. Quantized multiple energy levels can be generated by enhancing the quantum characteristics of quantum quantities θ and N and this is called the secondary macroscopic quantum effect [15].

Of the two degrees of freedom of the superconducting macroscopic state, the phase degree of freedom is primarily involved in the Josephson Effect. The single Cooper-pair tunneling effect was also investigated, which primarily involves the other degree of freedom, namely the charge degree of freedom. As the capacitance C of a tunneling junction is minimized, the charge energy $E_C = \frac{2e^2}{C}$ of the junction increases. As a result, this effect becomes more pronounced for $E_c > E_J$ than for the Josephson energy $E_J = I_0\Phi_0$.

A single-Cooper-pair box is a circuit in which small superconducting islands are connected to an external circuit through a small Josephson junction. This is a circuit dual to an RF-SQUID circuit consisting of a superconducting loop containing a Josephson junction. When a gate field is applied to the Cooper-pair box, each electron pair can be moved into and out of an island through the junction. This is equivalent to the ability to move a quantum flux into and out of a superconducting loop by applying an external magnetic field to the SQUID circuit. It was theoretically predicted that in a single-Cooper-pair box, an energy gap would open up near a bias point with a gate charge of e/2 in a state with n electron pairs in an island and in a state with $(n \pm 1)$ electron pairs [15]. This gap is caused by the presence of a coherent macroscopic quantum superposition between charge quantum states $|n\rangle$ and $|v + 1\rangle$.

In 1997 we were studying a series of superconducting single electron-pair circuits. As part of the study, we conducted a microwave spectroscopy experiment on a single-Cooper-pair box and confirmed the existence of the energy gap [16]. For the first time, we showed the presence of quantum coherence in a macroscopic superconducting circuit experimentally. The discrete energy levels generated by the energy gap are required if a qubit is to be used for quantum information processing.

Subsequently, in an experiment where the excess charge was controlled by the gate of a single-Cooper-pair box, a gradual change in the average charge reflecting the opening of the energy gap was observed [17], indicating the presence of a macroscopic quantum superposition of the charge states. Similarly, in a SQUID circuit, an energy gap that was opened by the macroscopic quantum superposition of flux states was observed spectroscopically [18, 19].

At the end of the last century, successive pieces of evidence were found that confirmed the presence of quantum coherence in a superconducting circuit. In a Josephson circuit, the superconducting state was shown to exist in the BCS ground state as well as in its excited state, and expectations for the development of a superconducting qubit were gradually mounting.

22.4 Development of Josephson Qubit

Quantum information cannot be processed by the above-mentioned static superposition of eigenstates. To process quantum information, a qubit must be realized that allows a quantum state to be dynamically changed, two quantum states to be superposed, and their phase and amplitude to be freely controlled. In 1999, in an experiment using a superconducting Cooper-pair box, Yasunobu Nakamura, Yuri Pashkin and the author successfully controlled the phase and amplitude at will through the quantum oscillation of the charge states of the system. This inspired research on a solid-state device qubit [1]. In this experiment, quantum oscillation was induced by non-adiabatically changing the external electric field of the circuit. Figure 22.1 shows a photograph of the circuit used in the experiment and the

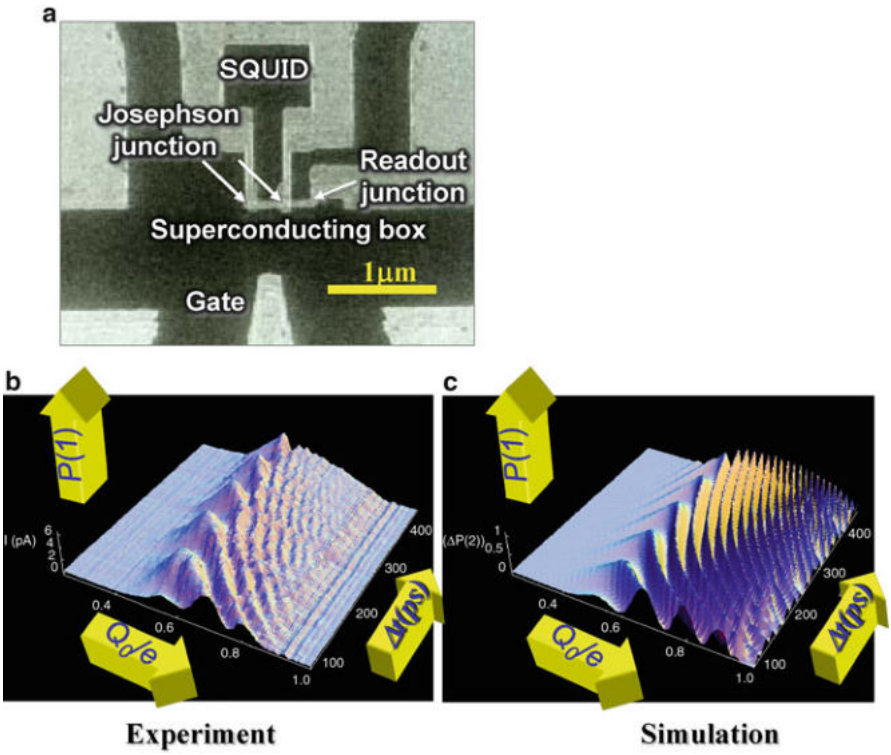

Fig. 22.1 Photograph of a charge qubit (**a**); observed quantum oscillation (**b**); and its simulation (**c**). The device is made of aluminum thin film. In the quantum oscillation graphs, the z-axis represent the probability of the state in $|1\rangle$ state, x-axis is the external bias charge, and y-axis is the time

observed quantum oscillation. A thin aluminum film, which allows a Josephson junction tunnel barrier to be easily made, was used for the superconductor.

When the gate field of the superconducting Cooper-pair box is changed non-adiabatically, the charge-number state of the box (island) oscillates between $|\mathrm{v}\rangle$ and $|\mathrm{v} + 1\rangle$. These two states correspond to the $|0\rangle$ and $|1\rangle$ states of the quantum bit. This is the quantum oscillation with a period $\frac{h}{\Delta E}$ ($h =$ Planck's constant, $\Delta E =$ energy difference between the $|0\rangle$ and $|1\rangle$ states) observed in the experiment. The qubit state of any phase was generated by controlling the bias electric field in this way, and single-qubit control was achieved.

Subsequently, instead of a non-adiabatic bias operation, we developed a technique for controlling qubit state oscillation, which is called Rabi oscillation in an atomic system, in a superconducting qubit [20]. This is a phenomenon where the state changes between $|0\rangle$ and $|1\rangle$ and the transition probability oscillates in time when microwaves with a wavelength equivalent to qubit energy ΔE are directed at

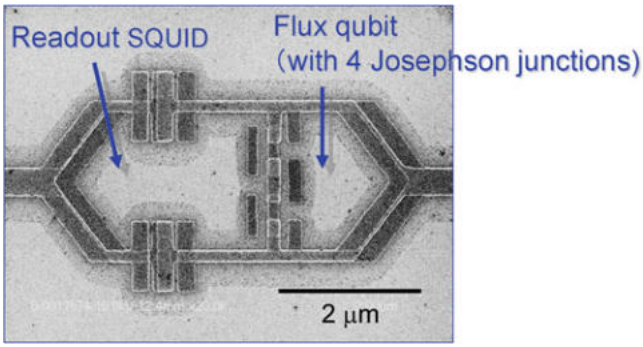

Fig. 22.2 Photograph of a flux qubit. It was made of aluminum thin film. A readout SQUID is attached to the side which latches to a voltage state when reading out $|1\rangle$ state

a qubit. The oscillation frequency is given by $\omega_{Rabi} = J\,(V_{AC})\,\frac{\Delta E}{\hbar}$. This is a general correlation. $J(V_{AC})$ is a Bessel function that depends on the microwave intensity.

Subsequently, qubit-control-based Rabi oscillation has been used in a number of experiments on different types of superconducting qubits. The results of experiments on quantronium charge qubits [21] (a qubit with the same structure as the charge qubit in Fig. 22.1 but with a lower charge energy), flux qubits [22, 23], and phase qubits [26, 27] have been reported successively. They all used this microwave. This method has advantages over the non-adiabatic control method as regards the precision of state control and the reduction in the decoherence effects of ambient noise described in the following.

In an experiment on a charge qubit called a transmon, the gradient of the energy band was successfully flattened by reducing the charge energy to an extremely low level from the normal level of $E_C \gg E_J$ to $E_C \ll E_J$ [24]. A charge qubit that can preserve quantum coherence for a relatively long time was realized by reducing various effects of the fluctuation of the operating point as a result of these improvements.

Figure 22.2 is a photograph of a typical flux qubit that is using the degrees of freedom of the flux quantum state (the number of flux qubits) in a superconducting loop. Aluminum is used for the superconducting film. This flux qubit has four Josephson junctions. A flux qubit with more than three junctions provides larger qubit energy (the energy difference between the $|0\rangle$ and $|1\rangle$ states) [25]. This type has been used in almost all the experiments performed on flux qubits, including the first ever flux qubit [22].

In addition to charge and flux qubits, there is a device called a phase qubit. As a qubit, this device employs a quantized state that does not use charge and flux degrees of freedom, and appears in a single Josephson junction [26, 27]. The most prominent characteristic of this qubit is that it has a simple structure and can be realized with a relatively large Josephson junction without the need to rely on a submicron fabrication technique.

As described above, various types of superconducting qubits have been realized. The diversity of qubits is due to their being solid-state devices, which will be very advantageous when fabricating complex computer circuits. The macroscopic quantum state of a Josephson junction can be accurately described by relatively simple physics, and a desired energy band can be created by adjusting circuit parameters. This is another factor that contributes significantly to the design of a superconducting qubit.

22.5 Progress on Gate Operation Accuracy and Decoherence

The quantum computation process is performed while quantum errors are being corrected. Qubit operation with reasonable fidelity is required in order to correct quantum errors. The operation has a maximum allowable limit as regards the error rate. The surface code quantum error correction method [28] has an upper limit of about 0.1 % for the error rate of the quantum gate operation (the threshold gate fidelity $F =$ about 0.999). Therefore, in an environment where the accuracy of a qubit is constantly compromised by decoherence, the gate operation time must be as short as 0.1 % of the decoherence time.

As mentioned above, a superconducting qubit uses only two macroscopic degrees of freedom, phase (flux) and charge number. However, in actual experimental environments, there are a number of microscopic degrees of freedom in the qubit environment in addition to these two macroscopic degrees of freedom. These microscopic degrees of freedom interact with the qubit, resulting in a gradual loss of the qubit's coherence (decoherence). This is intrinsic to quantum computers but not to classical computers, and is one of the biggest impediments to the realization of a quantum computer.

Decoherence has two types of time constants: the energy relaxation time T_1, during which a transition occurs from a higher energy state $|1\rangle$ to a lower energy state $|0\rangle$, and the dephasing time T_2, during which the phase becomes unclear. They are related as follows, $\frac{1}{T_2} = \frac{1}{2T_1} + \frac{1}{T_\varphi}$, where T_φ is called the pure dephasing time.

The gate time is mainly controlled by the qubit energy. Its maximum value is of the order of nanoseconds. Therefore, the decoherence time must at least exceed a microsecond for surface code quantum error correction. An even longer decoherence time is advantageous when various factors are considered. This requirement in decoherence time has been established for superconducting qubits.

Figure 22.3 shows the progress made on the decoherence time of a superconducting qubit. In the figure, the green circles represent the energy relaxation time, the yellow circles represent T_2 from a Ramsey interference experiment, and the red circles represent T_2 obtained by the echo technique (a technique for eliminating slow noise fluctuations) [6].

The decoherence time of a superconducting qubit has been improved by more than six orders of magnitude since the first experiment in 1999. The qubits within the

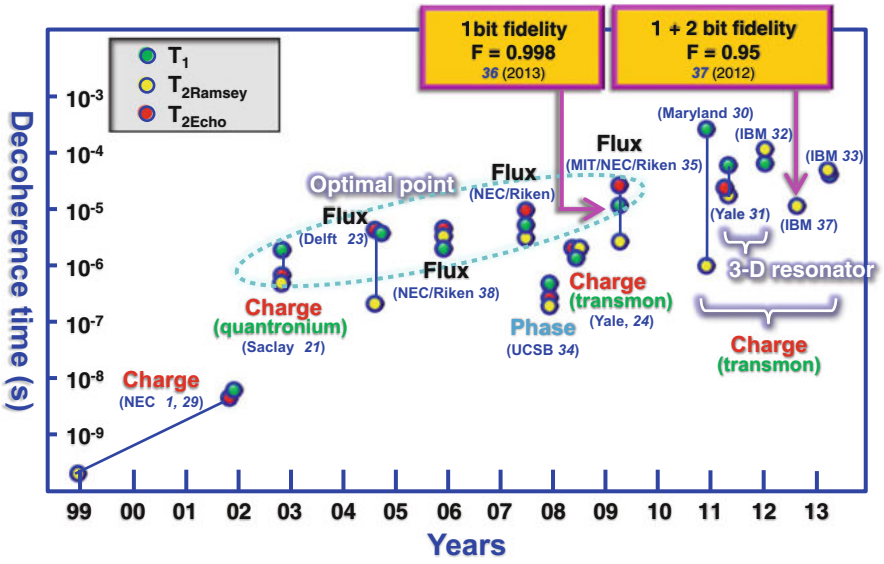

Fig. 22.3 The progress in the decoherence time. *Green circles* are energy relaxation time T1, *yellow circles* are dephasing time T2 from Ramsey interference experiments, *red circules* are T2 from echo experiments. In the past 15 years, improvement of about six orders of magnitudes has been achieved. Quantum gate operations achieved with high fidelity were also marked. Reference numbers are given

light blue dashed line in Fig. 22.3 represent operations at an operating point in the flat energy band. Since the effect of external microscopic low-frequency oscillations is sufficiently reduced, the decoherence time can be effectively improved. This operating point is called the optimal operating point. [21] However, the decoherence time decreases rapidly when the operating point is slightly displaced. Therefore, the allowable operation range is limited for this type of qubit. There is no optimal operating point for transmon and phase qubits. Figure 22.3 shows that the decoherence time of the transmon qubit has improved significantly, particularly in recent years, due to the improvements made on resonators [29–32]. In contrast, there has been little improvement in the decoherence time of the phase qubit [33].

In an experiment where the fidelity of long-lived flux qubits [34] was evaluated by performing a gate operation at a high speed, a fidelity F of 0.998 was achieved [35]. This value is close to the threshold gate fidelity required with the above-mentioned surface code quantum error correction method. The flux qubits used in the experiment are indicated in Fig. 22.3. A fidelity F of 0.95 (actually $F > 0.98$) has also been achieved for a more complex two-bit logic gate operation [36], which is described later.

It is important to identify the factors limiting the decoherence time of qubits to make it possible to increase it further. We have shown that the low-frequency oscillations causing phase relaxation are predominantly charge fluctuations [38] for

a charge qubit and flux fluctuations [37] for a flux qubit. It has been indicated that the fluctuations of the degrees of freedom are involved in the energy relaxation of a charge qubit [38]. In recent years, charge qubit experiments with a resonator and their analysis [39] have indicated that a dielectric loss on the surface of a substrate or on the surface of a superconducting film is the cause of the energy relaxation of this type of qubit.

In conclusion, the obstacle of achieving a "high gate fidelity" for quantum computers is being overcome as the result of significant improvements in the decoherence time of a superconducting qubit.

22.6 Quantum Logic Gates and Integration

To perform a manipulated quantum operation, it is necessary to realize a universal quantum gate operation by combining a one-qubit operation and a two-qubit quantum logic operation gate. A two-qubit system is a physical system of great interest where quantum entanglement occurs during a quantum logic operation.

Being a solid-state device, a superconducting quantum qubit offers significant flexibility in design the coupling of the qubits, compared to a microscopic qubit. The first coupled solid-state qubit was realized in a two-qubit system that we demonstrated where the coupling was achieved via a capacitance. In this experiment, quantum entanglement had been achieved in a macroscopic system for the first time [2]. Subsequently, using the two coupled phase qubits, the state of each of the qubit was read out and quantum entanglement in a macroscopic system was clearly shown by quantum state tomography [40].

We also achieved the operation of the first two-bit quantum logic operation gate with a fixed-coupled charge qubit circuit similar to the one mentioned above [3]. We achieved a controlled-NOT (CNOT) operation with this circuit. A CNOT circuit is a typical two-qubit operation circuit, consisting of a control qubit and a target qubit. When a CNOT operation is performed, the target qubit flips if the control qubit is $|0\rangle$ but does not flip if it is $|1\rangle$. If the control qubit is a superposition of $|0\rangle$ and $|1\rangle$, the CNOT operation results in entanglement. A CNOT operation based on fixed-coupled flux qubits was subsequently reported [41].

Both the accurate state control of one qubit and a two-qubit operation must be achieved in quantum computation. A means of controlling the ON/OFF of qubit coupling is the easiest way to achieve this. Controlling the coupling of qubits makes it possible to realize a universal quantum gate, which is a fundamental component of a quantum computer. This means placing a switch between qubits in such a way that it is possible to control the coupling. It is physically impossible to make such switches with microscopic atom- or molecule-based qubits. Since a superconducting qubit is a solid-state device, we can make such coupling switches and simplify information processing operations. We proposed a method for the operation of a two-qubit quantum gate with a variable coupling switch [42] and succeeded in an experiment using the method [5, 43] (Fig. 22.4).

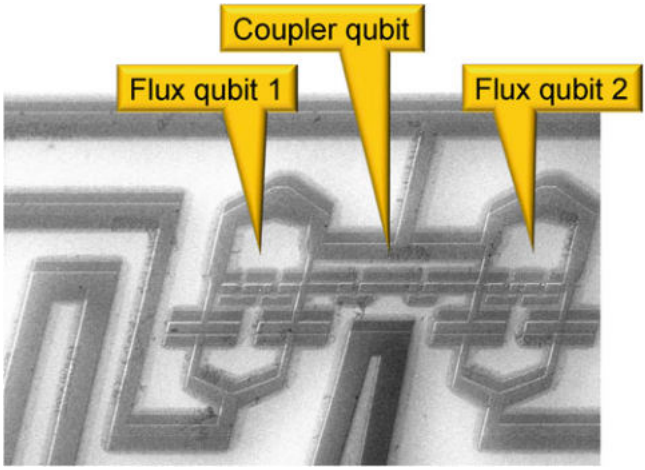

Fig. 22.4 Photograph of 2-qubit system couple with a similar qubit-based coupler (Ref 44)

In the experiment, we used two flux qubits and demonstrated that a third flux qubit could be used as a variable coupler with each of the two qubits being biased at its optimal operating point. In the photograph in Fig. 22.4, the two qubits are at either end and the coupling qubit is in the middle. The coupling qubit has a qubit energy sufficiently higher than the energies Δ_1 and Δ_2 of the two qubits and therefore will not be excited during a normal gate operation. Inductive coupling can be approximated as zero when the qubit is biased at the optimal operating point. Therefore, a one-qubit operation can be easily performed. Two qubits can be coupled and a logic operation can be performed by applying microwaves with an energy $\Delta_1 + \Delta_2$ or $\Delta_1 - \Delta_2$ at the coupling qubit. A state transition of $|00\rangle \iff |11\rangle$ or $|01\rangle \iff |10\rangle$ was observed during this operation. This is a logic operation called iSWAP (exchange with a phase). A 3-step quantum state protocol consisting of two one-qubit operations and one two-qubit operation was performed using this two-qubit system. The expected results were obtained, showing that the coupling switch worked properly and effectively [5].

Since then, we have continued research on this nonlinear coupling switch. As a result, circuit design has advanced to a level that makes it theoretically possible to realize the large two-dimensional qubit array required for surface code quantum error correction. This new design allows one- and two-qubit control to be easily performed with adequate fidelity [44]. This coupling method has a significant advantage in that sufficiently high crosstalk immunity can be obtained if attention is paid to frequency detuning between qubits. A coupler has been reported that turns on/off DC coupling with high precision through the high-speed control of quantum inductance [45].

Variable coupling methods using a linear superconducting microwave resonator are being researched, in addition to those using a nonlinear coupling circuit. This

method is sometimes called circuit quantum electrodynamics (Circuit QED). The electromagnetic resonator is usually a superconducting coplanar waveguide-type transmission line circuit and is used as a qubit coupling bus. Among operations that use this type of resonator, a qubit operation using non-adiabatic DC pulses has produced good results. The first successful experiments consisted of one [46] where two phase qubits were coupled via a resonator, and one [47] where two transmon qubits (charge qubits with extremely low charge energy) were coupled via a resonator.

Coupling methods using microwave pulses, such as the one mentioned above, which uses a nonlinear coupler [5], are advantageous for integration. Among coupling methods using a linear resonator, one has been realized that uses microwave pulses. With this approach, qubit states were coupled via the photon state in the resonator using sideband transitions [48]. A CNOT gate has been realized that selectively controls quantum state transitions based on the microwave intensity and the phase difference [49]. A universal quantum gate that performs a CNOT gate operation with high fidelity $F = 0.95$ has been realized by a microwave coupling method called cross coupling [36].

Experiments for implementing several quantum algorithms based on quantum logic operation using the various coupling methods mentioned above were performed as described below.

22.7 Implementation of Quantum Algorithm

Experimental studies of the implementation of a practical quantum algorithm using superconducting qubits have been conducted. The Grover and Deutsch-Jozsa algorithms were successfully implemented in an experiment using two transmon qubits and a linear coupling bus [50]. The operation of a two-qubit information processing circuit with an independent readout circuit has been reported [51]. Using the DC pulse method, entanglement was achieved in a three-qubit quantum circuit [52, 53]; three-qubit quantum error correction was performed recently [54]; and a Toffoli gate was realized [55] Bell's inequality violation was successfully observed in a system with two phase qubits coupled via a resonator [56] showing that the classical realism does not hold in such macroscopic systems.

In some experiments, a quantum algorithm was implemented using a microwave resonator coupled to a qubit as a quantum memory device. An experiment to perform a quantum Fourier transform using two phase qubits and three resonators (two for storage and one for coupling) has been reported [57]. Here, the resonators were used as quantum memories, to compensate for the relatively short coherence lifetime of a phase qubit. A larger-scale experiment was conducted where four phase qubits were coupled via four resonator memories and one resonator bus [58]. In the experiment, the prime factoring of 15 was successfully computed by a three-qubit compiled version of Shor's algorithm.

A quick overview shows that multi-qubit quantum operation has already been realized, reflecting the diverse array of the coupling method of this solid state device, and simple quantum algorithms can be implemented. The coupling methods are largely divided into those that use a nonlinear coupler and those that use a linear resonator. It is worth noting that a number of results have been achieved by the latter method (in combination with non-adiabatic DC pulses), which has a relatively simple structure. However, a small nonlinear coupling switch, three orders of magnitude (one dimension) smaller than the resonator, is expected to play an important role in large-scale two-dimensional integration in the future. This will be further discussed later.

22.8 Qubit Readout

A readout technique for determining, at any desired moment, whether the quantum state is $|0\rangle$ or $|1\rangle$ is very important in qubit experiments. Quantum error correction requires that an accurate readout be performed. The readout fidelity is considered to be in the order of 99.9 %, which is the same as for gate operations. A single-shot readout is important. A fast readout in less than 10 ns is needed to increase the fidelity (three orders of magnitude faster than T_1). A quantum nondemolition qubit readout is desirable that can preserve the projected quantum state. Significant progress has been reported on this technology.

When quantum states are observed, an average is often taken over several experimental sessions because the observed signals are weak. Over the years, various improvements have been made to a single-shot readout technique that does not need to take an average. For example, in the early stages of our research, we achieved a single-shot readout via a charge trap when reading out a charge qubit [4]. The readout fidelity was $F = 0.93$ for the $|0\rangle$ state and $F = 0.87$ for the $|1\rangle$ state.

A high-fidelity single-shot readout technique called dispersive readout was later developed. This is a quantum nondemolition qubit readout. With this technique, a qubit is coupled to a resonator and the qubit state is determined based on the change in the resonance frequency of the whole system. To express this simply, the change in the resonance frequency can be understood as a reflection of the change in the quantum capacitance or inductance of the qubit. Normally, a change in the resonance frequency can be observed as a change in the phase of the AC signal used to drive the resonant circuit. A charge qubit has been read out with high fidelity using a linear resonator [59].

However, this is insufficient for a single-shot readout. Only a weak signal is input into the resonator (for example, an average of one photon) to prevent any excitation of the qubit. Therefore, an averaged observation is required to observe the phase change. A low-noise amplifier with low dissipation needs to be developed to improve this situation. Experiments have been successfully conducted using a Josephson bifurcation amplifier and a Josephson parametric amplifier for this purpose.

The Josephson bifurcation amplifier uses dynamical bifurcation, a phenomenon associated with the nonlinearity of the Josephson junction, as a dissipationless amplifying switch [60]. In an experiment where bifurcation amplifier was used to read out a flux qubit, non-destructive single-event readout fidelity $F > 0.854$ was achieved [61]. A single-shot readout with readout fidelity $F > 0.94$ has been reported in a similar experiment where a transmon qubit was read out [62].

Parametric amplification can be realized using the nonlinear inductance of a Josephson junction. Fidelity $F = 0.7$ was observed in a single-shot readout of a transmon qubit with a Josephson parametric amplifier [63]. In this experiment, the relaxation of the qubit was detected as a quantum jump under continuous observation, showing that this readout technique is highly quantum nondemolition in nature. We conducted a readout experiment in a system where a flux qubit was capacitively coupled to a resonator, using a flux-driven Josephson parametric amplifier of our own design [64]. Characteristically, this system produced a surprisingly large dispersive shift in the resonant frequency [65]. A single-shot readout with fidelity $F = 0.74$ was achieved and a quantum jump was successfully observed [66]. The fidelity limit in these experiments can be explained by the relatively short relaxation time of the qubit used. A readout with $F = 1$ will be achieved by extending the qubit lifetime.

Quantum feedback experiments using a single-shot readout with a Josephson parametric amplifier have been reported [67, 68]. An experiment was successfully performed that allowed the highly efficient active initialization of a qubit using a similar readout [69] and a change in the readout intensity [70]. In both of the last two experiments, fidelity F as high as 0.98 was achieved.

Thus, the readout efficiency of a superconducting qubit is gradually approaching the level required for quantum error correction. The major issue that must be addressed if we are to realize a quantum computer is how to achieve large-scale integration of the microwave resonators used for a high-efficiency single-shot readout or, as a separate issue, whether a small high-efficiency readout circuit can be developed.

22.9 Outlook

Ever since we realized the first solid-state qubit with a superconducting circuit about 14 years ago [1], we had been wondering about the possibility of realizing a quantum computer. At first, we had no clear idea how to get started. As we continued our research, we developed a two-bit logic circuit [2, 3] and began to feel that we were actually starting to climb a mountain. As a result of the subsequent tremendous efforts of many researchers throughout the world, as described in this paper, the summit of the faraway mountain of quantum information processing is becoming visible, and the research path leading towards it has begun to take shape (although the possibility of a shortcut cannot be denied).

The aim is to realize a machine that performs quantum operations while continuously repeating the quantum error correction (a surface code [28] is the most promising). We still have a very long way to go before we can reach our goal. Quantum computing involves a hierarchy of computation resources. As solid-state physicists, we have been looking for a way to realize a large two-dimensional array of qubits which corresponds to the physical resources at the bottom of the hierarchy.

A major issue is which of the many qubit coupling methods we should use. One relatively successful method uses a linear resonator, which has a simple structure but a size of centimeters. In theory, methods that use a nonlinear coupler can realize a compact two-dimensional qubit array, although the coupler will have a complex structure. The surface code quantum error correction architecture requires only that adjacent qubits be coupled. A nonlinear coupler meets this requirement. Similarly, there is the issue of the integration of a single-shot, high-precision qubit readout circuit that requires a resonator.

Existing silicon large-scale integrated (LSI) circuit technology can be used to produce a large two-dimensional qubit array. A Josephson qubit circuit is made of a thin aluminum film. This is the wiring material used for the present semiconductor LSI circuits, therefore it has good material compatibility. The minimum line width is about 100 nm and this is much larger than the limit for the current silicon LSC process. The number of qubits in a two-dimensional array is expected to be 10^8–10^9. Therefore, the circuit size is within the range of the current largest LSI production technology. However, the above discussion does not exactly apply to circuit that involving large resonators.

The integration of peripheral circuits and packaging of a qubit array pose significant technical problems, in addition. All of the 10^8–10^9 qubits in the array must be individually coupled by microwaves and DC wire and manipulated externally. This requires 10^8–10^9 microwave pulse sources and DC/pulse sources and an interface module to connect them to the qubit chip.

A conventional LSI circuit requires only that external wires be connected to the periphery of the chip. A quantum LSI circuit will require external wires to be connected to the entire chip. New components, such as the three-dimensional interface module shown in Fig. 22.5, will be needed. The figure is a schematic of a qubit chip using a small nonlinear qubit coupler. Three-dimensional integration will be necessary for coupling with a microwave resonator as well as for the large-scale integration of readout circuits.

An error correction architecture that allows the use of multiplexing to reduce the number of wires is needed if we are to reduce the resources employed for such peripheral circuits, packaging and cooling. It is quite possible to place a classical superconducting digital circuit in the interface module as a part of the peripheral circuit. The interface with the peripheral circuit has been little studied. However, abundant resources are available.

The realization of a quantum computer will take information processing technology to another dimension. In this paper, we have presented research achievements that are moving us towards the realization of a superconducting quantum computer and the outlook of large-scale qubit LSI chips, peripheral circuits and packaging

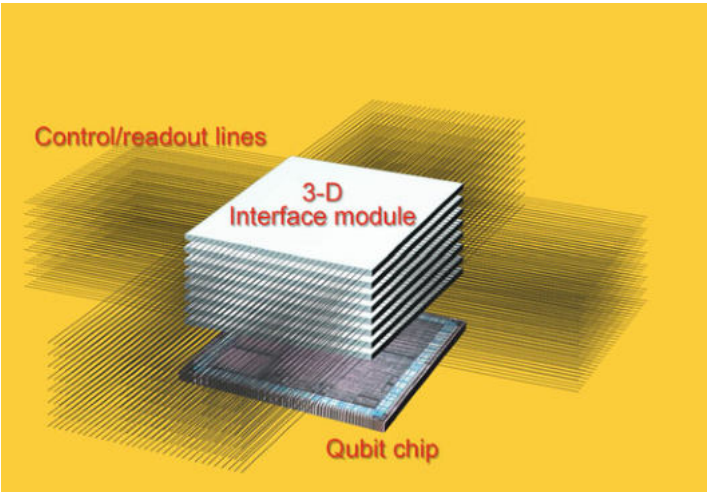

Fig. 22.5 Image of qubit chip and interface module to connect control and readout lines to outside

technology. Several solutions have been developed for some difficult problems, but there are still many areas that require research. We hope that further research will be conducted and, in the near future, more concrete plans for quantum computers will be produced.

Acknowledgements I would like to thank Yasunobu Nakamura, Yuri Pashkin, Tsuyoshi Yamamoto, Oleg V. Astafiev, Fumiki Yoshihara, Antti Niskanen, Khalil Harrabi, Michio Watanabe, Kunihiro Inomata, Pierre-Marie Billangeon, and Zhirong Lin, who are the main co-authors of the achievements presented in this paper. I am grateful for the support provided by our two JST CREST projects, the Cabinet Office FIRST Project on Quantum Information Processing and the JSPS Scientific Research on Innovative Areas, Quantum Cybernetics Project.

References

1. Y. Nakamura, Y.A. Pashkin, J.S. Tsai, Nature **398**, 786 (1999)
2. Y.A. Pashkin, T. Yamamoto, O. Astafiev, Y. Nakamura, D.V. Averin, J.S. Tsai, Nature **421**, 823 (2003)
3. T. Yamamoto, Y.A. Pashkin, O. Astafiev, Y. Nakamura, J.S. Tsai, Nature **425**, 941 (2003)
4. O. Astafiev, Y.A. Pashkin, T. Yamamoto, Y. Nakamura, J.S. Tsai, Phys. Rev. B **69**, 180507 (2004)
5. A.O. Niskanen, K. Harrabi, F. Yoshihara, Y. Nakamura, J.S. Tsai, S. Lloyd, Science **316**, 723 (2007)
6. Y. Nakamura, Y.A. Pashkin, T. Yamamoto, J.S. Tsai, Phys. Rev. Lett. **88**, 047901 (2002)
7. Y. Nakamura, Y.A. Pashkin, J.S. Tsai, Phys. Rev. Lett. **87**, 246601 (2001)
8. O. Astafiev, K. Inomata, A.O. Niskanen, T. Yamamoto, Y.A. Pashkin, Y. Nakamura, J.S. Tsai, Nature **449**, 588 (2007)

9. O. Astafiev, A.M. Zagoskin, A.A. Abdumalikov Jr., Y.A. Pashkin, T. Yamamoto, K. Inomata, Y. Nakamura, J.S. Tsai, Science **327**, 840 (2010)
10. A.A. Abdumalikov Jr., O. Astafiev, A.M. Zagoskin, Y.A. Pashkin, Y. Nakamura, J.S. Tsai, Phys. Rev. Lett. **104**, 193601 (2010)
11. O.V. Astafiev, A.A. Abdumalikov Jr., A.M. Zagoskin, Y.A. Pashkin, Y. Nakamura, J.S. Tsai, Phys. Rev. Lett. **104**, 183603 (2010)
12. J. Leggett, Prog. Theor. Phys., Suppl. **69**, 80 (1980)
13. R.F. Voss, R.A. Webb, Phys. Rev. Lett. **47**, 647 (1981); L.D. Jackel, J.P. Gordon, E.L. Hu, R.E. Howard, L.A. Fetter, D.M. Tennant, R.W. Epworth, J. Kurkijarvi, Phys. Rev. Lett. **47**, 697 (1981); S. Washburn, R.A. Webb, R.F. Voss, S.M. Faris, Phys. Rev. Lett. **54**, 2712 (1985)
14. J.M. Martinis, M.H. Devoret, J. Clarke, Phys. Rev. Lett. **55**, 1543 (1985)
15. K.K. Likharev, *Dynamics of Josephson Junctions and Circuits* (Gordon and Breach Science Publications, New York, 1986)
16. Y. Nakamura, C.D. Chen, J.S. Tsai, Phys. Rev. Lett. **79**, 2328 (1997)
17. V. Bouchiat, D. Vion, P. Joyez, D. Esteve, M.H. Devoret, Phys Scr T **76**, 165 (1998)
18. J.R. Fridman, V. Patel, W. Chen, S.K. Tolpygo, J.E. Lukens, Nature **406**, 43 (2000)
19. C.H. van der Wal, A.C.J. ter Haar, F.K. Wilmhelm, R.N. Schouten, C.J.P.M. Harmans, T.P. Orando, S. Lloyd, J.E. Mooij, Science **290**, 773 (2000)
20. The first superconducting qubit experiment:Y. Nakamura, Yu. A. Pashkin, J.S. Tsai, Phys. Rev. Lett, **87**, 246601 (2002)
21. D. Vion, A. Assime, A. Cottet, P. Joyez, H. Pothier, C. Urbina, D. Esteve, M.H. Devoret, Science **296**, 886 (2002)
22. I. Chioreseu, Y. Nakamura, C.J.P.M. Harmans, J.E. Mooij, Science **299**, 1869 (2003)
23. P. Bertet, I. Chiorescu, G. Burkard, K. Semba, C.J.P.M. Harmans, D.P. DiVincenzo, J.E. Mooij, Phys. Rev. Lett. **95**, 257002 (2005)
24. J.A. Schreier, A.A. Houck, J. Koch, D.I. Schuster, B.R. Johnson, J.M. Chow, J.M. Gambetta, J. Majer, L. Frunzio, M.H. Devoret, S.M. Girvin, R.J. Schoelkopf, Phys. Rev. B **77**, 180502(R) (2008)
25. J.E. Mooij, T.P. Orlando, L. Levitov, L. Tian, C.H. van der Wal, S. Lloyd, Science **285**, 1036 (1999)
26. Y. Yu, S. Han, X. Chu, S. Chu, Z. Wang, Science **296**, 889 (2002)
27. J.M. Martinis, S. Nam, J. Aumentado, C. Urbina, Phys. Rev. Lett. **89**, 117901 (2002)
28. R. Raussendorf, J. Harrington, K. Goyal, Ann. Phys. (N. Y.) **321**, 2242 (2006)
29. Z. Kim, B. Suri, V. Zaretskey, S. Novikov, K.D. Osborn, A. Mizel, F.C. Wellstood, B.S. Palmer, Phys. Rev. Lett. **106**, 120501 (2011)
30. H. Paik, D.I. Schuster, L.S. Bishop, G. Kirchmair, G. Catelani, A.P. Sears, B.R. Johnson, M.J. Reagor, L. Frunzio, L.I. Glazman, S.M. Girvin, M.H. Devoret, R.J. Schoelkopf, Phys. Rev. Lett. **107**, 240501 (2011)
31. C. Rigetti, J.M. Gambetta, S. Poletto, B.L.T. Plourde, J.M. Chow, A.D. Córcoles, J.A. Smolin, S.T. Merkel, J.R. Rozen, G.A. Keefe, M.B. Rothwell, M.B. Ketchen, M. Steffen, Phys. Rev. B **86**, 100506(R) (2012)
32. J.B. Chang, M.R. Vissers, A.D. Córcoles, M. Sandberg, J. Gao, D.W. Abraham, J.M. Chow, J.M. Gambetta, M.B. Rothwell, G.A. Keefe, M. Steffen, D.P. Pappas, Appl. Phys. Lett. **103**(012602) (2013)
33. J. Clarke, F.K. Wilhelm, Nature **453**, 1031 (2008)
34. J. Bylander, J. Gustavsson, F. Yan, F. Yoshihara, K. Harrabi, G. Fitch, D.G. Cory, Y. Nakamura, J.-S. Tsai, W.D. Oliver, Nat. Phys. (2011). doi:10.1038/nphys1994
35. S. Gustavsson, O. Zwier, J. Bylander, F. Yan, F. Yoshihara, Y. Nakamura, T.P. Orlando, W.D. Oliver, Phys. Rev. Lett. **110**, 040502 (2013)
36. J.M. Chow, J.M. Gambetta, A.D. Córcoles, S.T. Merkel, J.A. Smolin, C. Rigetti, S. Poletto, G.A. Keefe, M.B. Rothwell, J.R. Rozen, M.B. Ketchen, M. Steffen, Phys. Rev. Lett. **109**, 060501 (2012)
37. F. Yoshihara, K. Harrabi, A.O. Niskanen, Y. Nakamura, J.S. Tsai, Phys. Rev. Lett. **97**, 167001 (2006)

38. O. Astafiev, Y.A. Pashkin, T. Yamamoto, Y. Nakamura, J.S. Tsai, Phys. Rev. Lett. **93**, 267007 (2004)
39. J. Wenner, R. Barends, R.C. Bialczak, Y. Chen, J. Kelly, E. Lucero, M. Mariantoni, A. Megrant, P.J.J. O'Malley, D. Sank, A. Vainsencher, H. Wang, T.C. White, Y. Yin, J. Zhao, A.N. Cleland, J.M. Martinis, Appl. Phys. Lett. **99**, 113513 (2011)
40. M. Steffen, M. Ansmann, R.C. Bialczak, N. Katz, E. Lucero, R. McDermott, M. Neeley, E.M. Weig, A.N. Cleland, J.M. Martinis, Science **313**, 1423 (2006)
41. J.H. Plantenberg, P.C. de Groot, J.C. Hammons, J.E. Mooij, Nature **447**, 836 (2007)
42. A.O. Niskanen, Y. Nakamura, J.-S. Tsai, Phys. Rev. B **73**, 094506 (2006)
43. K. Harrabi, F. Yoshihara, A.O. Niskanen, Y. Nakamura, J.S. Tsai, Phys. Rev. B **79**, 020507(R) (2009)
44. P.-M. Billangeon, J.S. Tsai, Y. Nakamura, Phys. Rev. B **91**, 094517 (2015)
45. R.C. Bialczak, M. Ansmann, M. Hofheinz, M. Lenander, E. Lucero, M. Neeley, A.D. O'Connell, D. Sank, H. Wang, M. Weides, J. Wenner, T. Yamamoto, A.N. Cleland, J.M. Martinis, Phys. Rev. Lett. **106**, 060501 (2011)
46. M.A. Sillanpaa, J.I. Park, R.W. Simmonds, Nature **449**, 438 (2007)
47. J. Majer, J.M. Chow, J.M. Gambetta, J. Koch, B.R. Johnson, J.A. Schreier, L. Frunzio, D.I. Schuster, A.A. Houck, A. Wallraff, A. Blais, M.H. Devoret, S.M. Girvin, R.J. Schoelkopf, Nature **449**, 443 (2007)
48. A. Wallraff, D.I. Schuster, A. Blais, J.M. Gambetta, J. Schreier, L. Frunzio, M.H. Devoret, S.M. Girvin, R.J. Schoelkopf, Phys. Rev. Lett. **99**, 050501 (2007)
49. P.C. de Groot, J. Lisenfeld, R.N. Schouten, S. Ashhab, A. Lupascu, C.J.P.M. Harmans, J.E. Mooij, Nat. Phys. **6**, 763 (2010)
50. L. DiCarlo, J.M. Chow, J.M. Gambetta, L.S. Bishop, B.R. Johnson, D.I. Schuster, J. Majer, A. Blais, L. Frunzio, S.M. Girvin, R.J. Schoelkopf, Nature **460**, 240 (2009)
51. A. Dewes, F.R. Ong, V. Schmitt, R. Lauro, N. Boulant, P. Bertet, D. Vion, D. Esteve, Phys. Rev. Lett. **108**, 057002 (2012)
52. M. Neeley, R.C. Bialczak, M. Lenander, E. Lucero, M. Mariantoni, A.D. O'Connell, D. Sank, H. Wang, M. Weides, J. Wenner, Y. Yin, T. Yamamoto, A.N. Cleland, J.M. Martinis, Nature **467**, 570 (2010)
53. L. DiCarlo, M.D. Reed, L. Sun, B.R. Johnson, J.M. Chow, J.M. Gambetta, L. Frunzio, S.M. Girvin, M.H. Devoret, R.J. Schoelkopf, Nature **467**, 574 (2010)
54. M.D. Reed, L. DiCarlo, S.E. Nigg, L. Sun, L. Frunzio, S.M. Girvin, R.J. Schoelkopf, Nature **482**, 382 (2012)
55. A. Fedorov, L. Steffen, M. Baur, M.P. da Silva, A. Wallraff, Nature **481**, 170 (2012)
56. M. Ansmann, H. Wang, R.C. Bialczak, M. Hofheinz, E. Lucero, M. Neeley, A.D. O'Connell, D. Sank, M. Weides, J. Wenner, A.N. Cleland, J.M. Martinis, Nature **461**, 504 (2009)
57. M. Mariantoni, H. Wang, T. Yamamoto, M. Neeley, R.C. Bialczak, Y. Chen, M. Lenander, E. Lucero, A.D. O'Connell, D. Sank, M. Weides, J. Wenner, Y. Yin, J. Zhao, A.N. Korotkov, A.N. Cleland, J.M. Martinis, Science **334**, 61 (2011)
58. E. Lucero, R. Barends, Y. Chen, J. Kelly, M. Mariantoni, A. Megrant, P. O'Malley, D. Sank, A. Vainsencher, J. Wenner, T. White, Y. Yin, A.N. Cleland, J.M. Martinis, Nat. Phys. **8**, 719 (2012)
59. A. Wallraff, D.I. Schuster, A. Blais, L. Frunzio, J. Majer, M.H. Devoret, S.M. Girvin, R.J. Schoelkopf, Phys. Rev. Lett. **95**, 060501 (2005)
60. I. Siddiqi, R. Vijay, M. Metcalfe, E. Boaknin, L. Frunzio, R.J. Schoelkopf, M.H. Devoret, Phys. Rev. B **73**, 054510 (2006)
61. A. Lupacu, S. Saito, T. Picot, P.C. de Groot, C.J.P.M. Harmans, J.E. Mooij, Nat. Phys. **3**, 119 (2007)
62. F. Mallet, F.R. Ong, A. Palacios-Laloy, F. Nguyen, P. Bertet, D. Vion, D. Esteve, Nat. Phys. **5**, 791–795 (2009)
63. R. Vijay, D.H. Slichter, I. Siddiqi, Phys. Rev. Lett. **106**, 110502 (2011)
64. T. Yamamoto, K. Inomata, M. Watanabe, K. Matsuba, T. Miyazaki, W.D. Oliver, Y. Nakamura, J.S. Tsai, Appl. Phys. Lett. **93**, 042510 (2008)

65. K. Inomata, T. Yamamoto, P.-M. Billangeon, Y. Nakamura, J.S. Tsai, Phys. Rev. B **86**, 140508(R) (2012)
66. Z.R. Lin, K. Inomata, W.D. Oliver, K. Koshino, Y. Nakamura, J.S. Tsai, T. Yamamoto, Appl. Phys. Lett. **103**, 132602 (2013)
67. R. Vijay, C. Macklin, D.H. Slichter, S.J. Weber, K.W. Murch, R. Naik, A.N. Korotkov, I. Siddiqi, Nature **490**, 77 (2012)
68. D. Ristè, C.C. Bultink, K.W. Lehnert, L. DiCarlo, PRL **109**, 240502 (2012)
69. D. Ristè, J.G. van Leeuwen, H.-S. Ku, K.W. Lehnert, L. DiCarlo, PRL **109**, 050507 (2012)
70. M. Hatridge, S. Shankar, M. Mirrahimi, F. Schackert, K. Geerlings, T. Brecht, K.M. Sliwa, B. Abdo, L. Frunzio, S.M. Girvin, R.J. Schoelkopf, M.H. Devoret, Science **339**, 178 (2013)

Chapter 23
Parametric Amplifier and Oscillator Based on Josephson Junction Circuitry

T. Yamamoto, K. Koshino, and Y. Nakamura

23.1 Introduction

The parametric amplifier has a unique noise property. When the amplifier operates in the degenerate mode, the gain depends on the relative phase between the pump and the signal. Because of this phase sensitivity, the amplifier can, in principle, amplify one quadrature of the signal without adding any noise, which is called noiseless amplification [1, 2]. This is in sharp contrast to the phase-insensitive amplifier case, where the amplifier must add at least half a photon of noise (the standard quantum limit, or SQL). Superconducting circuits are suitable for the realization of these low-noise amplifiers, because the Josephson junction serves as a lossless nonlinear inductor. There have been numerous studies of parametric amplifiers using superconductors since the 1950s [3]. In the late 1980s, pioneering works were published by Yurke et al. that demonstrated the squeezing of thermal [4, 5] and vacuum [6] noise.

T. Yamamoto (✉)
NEC Smart Energy Research Laboratories, Tsukuba, Ibaraki 305-8501, Japan
e-mail: t-yamamoto@fe.jp.nec.com

K. Koshino
College of Liberal Arts and Sciences, Tokyo Medical and Dental University, 2-8-30 Konodai, Ichikawa, Chiba 272-0827, Japan
e-mail: kazuki.koshino@osamember.org

Y. Nakamura
Research Center for Advanced Science and Technology (RCAST), The University of Tokyo, 4-6-1 Komaba, Tokyo 153-8904, Meguro-ku, Japan

RIKEN Center for Emergent Matter Science (CEMS), 2-1 Hirosawa, Wako, Saitama 351-0198, Japan
e-mail: yasunobu@ap.t.u-tokyo.ac.jp

Y. Yamamoto, K. Semba (eds.), *Principles and Methods of Quantum Information Technologies*, Lecture Notes in Physics 911, DOI 10.1007/978-4-431-55756-2_23

Despite the successful demonstrations of these amplifiers, they were not often used in practice, because there were only a limited number of applications that needed such good noise performance. However, this situation has changed because of the emergence of the field of quantum information processing using superconducting circuits [7]. More specifically, in one qubit-readout scheme called a dispersive readout, where the qubit is dispersively coupled to an inductor-capacitor (LC) resonator, it is necessary to detect a small microwave signal leaking from the resonator with content of the order of a single photon to minimize back-action on the qubit [8]. Additionally, this detection process must be performed within a time that is much shorter than the lifetime of the qubit. This is so challenging that even with the state-of-the-art cryogenic high-electron-mobility transistor (HEMT) amplifiers, the signal-to-noise ratio typically remains less than unity, which hampers our efforts to achieve single-shot (i.e., without ensemble averaging) readout of the qubit. This has strongly motivated the development of amplifiers with better noise performance.

In the mid-2000s, several groups independently started studies of parametric amplifiers [9–12], and vacuum noise squeezing and noise temperatures below the SQL were demonstrated [13]. Shortly thereafter, a parametric amplifier was applied to position measurements for a nanomechanical resonator, and achieved an imprecision that was below the SQL [14]. A few years later, a parametric amplifier was applied for the first time to the dispersive readout of a qubit by Vijay et al., and the quantum jump of the qubit was subsequently observed [15].

Another interesting aspect of the use of the parametric amplifier in the context of quantum optics using electrical circuits (which is known as circuit quantum electrodynamics [16]) is that it can generate squeezed microwaves. Reconstruction of the state of the squeezed vacuum that is generated by the parametric amplifier has been reported by Mallet et al. in [17]. This research was extended further to the study of two-mode correlation [18, 19], and the path entanglement of continuous-variable microwaves [20].

When a parametric amplifier is pumped strongly (above a specific threshold) it generates an output field even without the presence of an input field. This phenomenon is classically well-known as parametric oscillation [21]. Using a superconducting device, Wilson et al. first demonstrated parametric oscillation in this context [22, 23]. Using a similar device, they also reported observation of the dynamical Casimir effect [24]. While the parametric oscillator generates an output field without any input field, it is the external signal injection that actually controls the state of the output field. The device called the parametron [25], which is also known as the parametric phase-locked oscillator [26] is based on this property, and was used as a basic element of digital computers in the 1950s and 1960s. Recently, we have implemented a superconducting circuit version of the parametron, and have demonstrated high-fidelity single-shot readout of a flux qubit using this device as a sensitive phase detector [27].

In this chapter, we present the quantum-optical theory of the two devices that we implemented: the flux-driven Josephson parametric amplifier (JPA) [11] and the Josephson parametric phase-locked oscillator (PPLO) [27], which are both modeled using a parametrically-modulated nonlinear oscillator. We derive several formulae that characterize our devices, including the gain and the noise temperature of the

JPA, and the locking properties of the PPLO. The rest of this chapter is organized as follows. We first review the device structure and the operating principle of the flux-driven JPA. Then, we model the device using the parametrically-modulated Duffing oscillator. Using the input-output formalism [28], we derive the Heisenberg equation for the resonator photon operator. From this, we derive formulae for both the gain and the noise temperature of the JPA. We also derive the master equation for the resonator field, and calculate its Q function. From this, we can calculate the probability of obtaining one of the two dynamical states of the PPLO.

23.2 Quantum Description of the Parametrically-Modulated Duffing Oscillator

23.2.1 Review of the Flux-Driven Josephson Parametric Amplifier

Here, we explain how the flux-driven JPA works [11]. Figure 23.1a shows a schematic diagram of the flux-driven JPA. The primary component of the device is a coplanar waveguide (CPW) resonator with a direct current superconducting quantum interference device (dc-SQUID) termination [29]. The dc-SQUID works as a variable inductor that sets the boundary condition of the transmission-line resonator. The inductance is controlled by a magnetic flux threading the loop of the dc-SQUID, and changes from the minimal value of $\frac{\Phi_0}{4\pi I_c}$ to infinity, where Φ_0 is the flux quantum, and I_c is the critical current for each of the two junctions, which are assumed to be identical. The resonant frequency of the lowest resonator mode depends on the magnetic flux, as shown schematically in Fig. 23.1c.

We apply a static dc flux bias of Φ_{dc}/Φ_0 to set the static resonant frequency of the resonator at Ω_0 (Fig. 23.1c). Then, we apply a pump field at a frequency of $\alpha\Omega_0$ ($\alpha \sim 2$). Because the pump line is inductively coupled to the loop of the dc-SQUID, the pump field modulates the flux, and thus the resonant frequency is also modulated at the frequency of $\alpha\Omega_0$, where we assume that the resonant frequency depends linearly on the flux as shown in Fig. 23.1c. This temporal modulation performs parametric work for the signal that comes into the resonator and is then reflected back along the same line (Fig. 23.1a).

This scheme has several advantages. First, the band center can be controlled by a static magnetic field. Second, it is a straightforward process to separate the signal from the pump, because their frequencies differ by a factor of 2. Additionally, because the resonator is of the $\lambda/4$ type and there is no resonance around $2\Omega_0$, any pump leakage into the signal line is also suppressed.

We can also consider the flux-driven JPA using a lumped element circuit, as shown in Fig. 23.1b [30]. The operating scheme is essentially the same as that using a distributed element circuit, but this device is advantageous because it is free from the higher resonant modes, and the participation ratio of the Josephson inductance to the total inductance is also easy to control while maintaining a constant resonant frequency. Lumped element JPAs with slightly different designs (i.e., without the

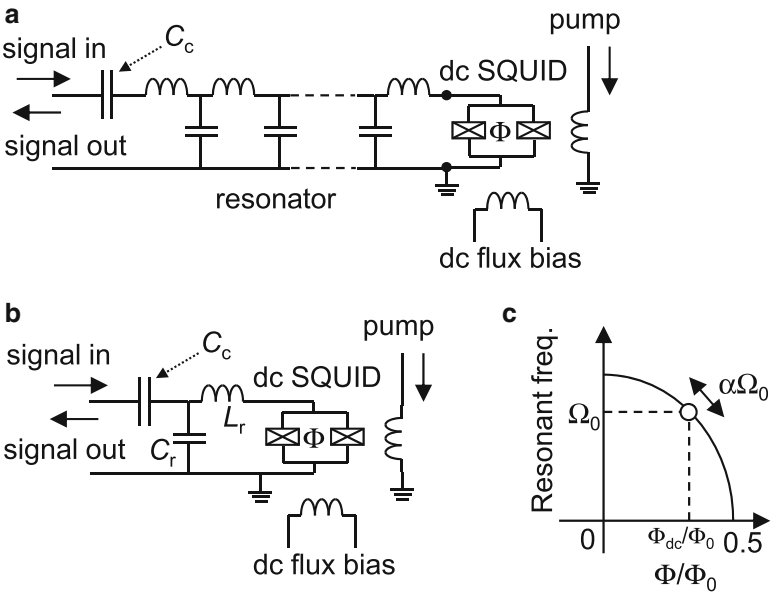

Fig. 23.1 Schematic diagram of the flux-driven Josephson parametric amplifier. (**a**) Distributed element version. (**b**) Lumped element version. (**c**) Schematic diagram representing the resonant frequency of the resonator as a function of the magnetic flux through the SQUID loop. C_c represents the coupling capacitor between the resonator and the feedline. Φ represents the magnetic flux that penetrates the loop of the SQUID

coupling capacitor) have been developed by groups at University of California, Berkeley (UCB) and University of California, Santa Barbara (UCSB) [31, 32] and were operated successfully to provide qubit readout [33].

When operated with a pump power below a specific threshold, the device shown in Fig. 23.1a works as a JPA. We have reported the single-shot readout of a superconducting flux qubit and the observation of quantum jumps [34]. The noise temperature below the SQL has been confirmed using a calibrated noise source [35]. The generation of squeezed states and the path entanglement have also been demonstrated [20, 35]. However, when operated with a pump power above the given threshold, the device works as a PPLO. We have demonstrated that we can use this device as a sensitive phase detector. We applied this device to the dispersive readout of a qubit, and achieved high-fidelity single-shot readout [27].

23.2.2 Hamiltonian and Equations of Motion

We start from an equation of motion for a harmonic oscillator,

$$\frac{d^2q}{dt^2} + \Omega_0^2 q = 0, \tag{23.1}$$

and then introduce a modulation of the resonant frequency Ω_0 at a frequency $\alpha\Omega_0$ with an amplitude of $\epsilon/2$, i.e., $\Omega_0 \to \Omega_0[1 + \epsilon/2\cos(\alpha\Omega_0 t)]$. Then,

$$\frac{d^2q}{dt^2} + \Omega_0^2[1 + \epsilon\cos(\alpha\Omega_0 t)]q = 0, \tag{23.2}$$

where we neglected the term that is proportional to ϵ^2. The Hamiltonian that gives this equation of motion is

$$\mathscr{H}(t) = \frac{p^2}{2m} + \frac{m}{2}\Omega_0^2\big[1 + \epsilon\cos(\alpha\Omega_0 t)\big]q^2. \tag{23.3}$$

By introducing the creation and annihilation operators for the modulated oscillator defined by

$$q = \frac{a + a^\dagger}{2}\sqrt{\frac{2\hbar}{m\Omega_0}}, \tag{23.4}$$

$$p = \frac{a - a^\dagger}{2i}\sqrt{2\hbar m\Omega_0}, \tag{23.5}$$

$$\big[a, a^\dagger\big] = 1, \tag{23.6}$$

we arrive at the Hamiltonian of the parametrically-modulated harmonic oscillator,

$$\mathscr{H}(t) = \hbar\Omega_0\big[a^\dagger a + \epsilon\cos(\alpha\Omega_0 t)(a + a^\dagger)^2\big]. \tag{23.7}$$

Now, we consider a signal and a fictitious loss port connected to the oscillator. We also include the nonlinearity of the oscillator. The Hamiltonian of the system is given by

$$\mathscr{H}(t) = \mathscr{H}_{\rm sys}(t) + \mathscr{H}_{\rm sig} + \mathscr{H}_{\rm loss}, \tag{23.8}$$

$$\mathscr{H}_{\rm sys}(t)/\hbar = \Omega_0\big[a^\dagger a + \epsilon\cos(\alpha\Omega_0 t)(a + a^\dagger)^2\big] + \gamma(a + a^\dagger)^4, \tag{23.9}$$

$$\mathscr{H}_{\rm sig}/\hbar = \int dk\Big[v_b k b_k^\dagger b_k + {\rm i}\sqrt{\frac{v_b\kappa_1}{2\pi}}\Big(a^\dagger b_k - b_k^\dagger a\Big)\Big], \tag{23.10}$$

$$\mathscr{H}_{\rm loss}/\hbar = \int dk\Big[v_c k c_k^\dagger c_k + {\rm i}\sqrt{\frac{v_c\kappa_2}{2\pi}}\Big(a^\dagger c_k - c_k^\dagger a\Big)\Big], \tag{23.11}$$

where γ is the nonlinearity parameter, and b_k (c_k) is the annihilation operator for a photon in the signal (loss) port with wave number k and velocity v_b (v_c). κ_1 (κ_2) represents the coupling strength between the resonator and the signal (loss) port, which are related to the external and internal quality factors of the resonator as follows: $\kappa_1 = \Omega_0/Q_{\rm e}$ and $\kappa_2 = \Omega_0/Q_{\rm i}$. The operators b_k and c_k satisfy the following

commutation rules: $\left[b_k, b_{k'}^\dagger\right] = \delta(k-k')$, and $\left[c_k, c_{k'}^\dagger\right] = \delta(k-k')$. Hereafter, we assume that $v_b = v_c$ for simplicity and denote both by v.

Below, we consider the case of $\alpha \sim 2$. From the Heisenberg equations of motion for b_k, we obtain

$$\frac{db_k(t)}{dt} = -\mathrm{i}vkb_k(t) - \sqrt{\frac{v\kappa_1}{2\pi}}a(t). \tag{23.12}$$

By formally solving this differential equation, we have

$$b_k(t) = e^{-\mathrm{i}vkt}b_k(0) - \sqrt{\frac{v\kappa_1}{2\pi}}\int_0^t e^{-\mathrm{i}vk(t-t')}a(t')dt'. \tag{23.13}$$

We introduce the real-space representation of the waveguide field as $\tilde{b}_r = (2\pi)^{-1/2}\int dke^{\mathrm{i}kr}b_k$. In this representation, the waveguide field interacts with the resonator at $r = 0$, and the $r < 0$ ($r > 0$) region corresponds to the incoming (outgoing) field. From Eq. 23.13, we have

$$\tilde{b}_r(t) = \tilde{b}_{r-vt}(0) - \sqrt{\frac{\kappa_1}{v}}\theta(r)\theta(t-r/v)a(t-r/v), \tag{23.14}$$

where $\theta(r)$ is the Heaviside step function. We define the input and output operators as

$$b_{\mathrm{in}}(t) \equiv \tilde{b}_{-0}(t) = \tilde{b}_{-vt}(0), \tag{23.15}$$

$$b_{\mathrm{out}}(t) \equiv \tilde{b}_{+0}(t) = b_{\mathrm{in}}(t) - \sqrt{\frac{\kappa_1}{v}}a(t). \tag{23.16}$$

Using Eqs. 23.14 and 23.15, the field operator $\tilde{b}_r(t)$ at the resonator position ($r = 0$) is given by

$$\tilde{b}_0(t) = \frac{1}{\sqrt{2\pi}}\int b_k(t)dk = b_{\mathrm{in}}(t) - \frac{1}{2}\sqrt{\frac{\kappa_1}{v}}a(t). \tag{23.17}$$

From the Heisenberg equations of motion for a, we then obtain

$$\frac{da}{dt} = -\mathrm{i}[\mathscr{H}_{\mathrm{sys}}(t), a] + \sqrt{v\kappa_1}\tilde{b}_0 + \sqrt{v\kappa_2}\tilde{c}_0. \tag{23.18}$$

Using Eq. 23.17 and its counterpart for $\tilde{c}_0$, Eq. 23.18 is rewritten as

$$\frac{da}{dt} = -\mathrm{i}[\mathscr{H}_{\mathrm{sys}}(t), a] - \frac{\kappa}{2}a + \sqrt{v\kappa_1}b_{\mathrm{in}}(t) + \sqrt{v\kappa_2}c_{\mathrm{in}}(t) \tag{23.19}$$

$$= -\left(\mathrm{i}\Omega_0 + \frac{\kappa}{2}\right)a - \mathrm{i}\Omega_0\epsilon e^{-\mathrm{i}\alpha\Omega_0 t}a^\dagger - 12\mathrm{i}\gamma a^\dagger aa$$
$$+\sqrt{v\kappa_1}b_{\mathrm{in}}(t) + \sqrt{v\kappa_2}c_{\mathrm{in}}(t), \tag{23.20}$$

where $\kappa = \kappa_1 + \kappa_2$, and we dropped the term $-12\mathrm{i}\gamma a$ because it can be regarded as a renormalization to Ω_0.

23.2.3 JPA Characteristics

By solving Eq. 23.20, we can then calculate the properties of the amplifier, including its gain, bandwidth, and noise temperature. For simplicity here, we neglect the nonlinearity ($\gamma = 0$), although it does determine practically important parameters such as the 1-dB-compression point [36]. First, we switch to a frame rotating at $\alpha\Omega_0/2$, and define the following operators:

$$A = e^{\mathrm{i}\frac{\alpha}{2}\Omega_0 t}a, \tag{23.21}$$
$$B_{\mathrm{in}} = e^{\mathrm{i}\frac{\alpha}{2}\Omega_0 t}b_{\mathrm{in}}, \tag{23.22}$$
$$C_{\mathrm{in}} = e^{\mathrm{i}\frac{\alpha}{2}\Omega_0 t}c_{\mathrm{in}}. \tag{23.23}$$

By substituting this into Eq. 23.20, we obtain

$$\frac{dA}{dt} + \left[\left(1 - \frac{\alpha}{2}\right)\mathrm{i}\Omega_0 + \frac{\kappa}{2}\right]A + \mathrm{i}\epsilon\Omega_0 A^\dagger = e^{\mathrm{i}\frac{\alpha}{2}\Omega_0 t}F(t), \tag{23.24}$$

where

$$F(t) = \sqrt{v\kappa_1}B_{\mathrm{in}}(t) + \sqrt{v\kappa_2}C_{\mathrm{in}}(t). \tag{23.25}$$

The Hermitian conjugate of this equation is

$$\frac{dA^\dagger}{dt} + \left[-\mathrm{i}\left(1 - \frac{\alpha}{2}\right)\Omega_0 + \frac{\kappa}{2}\right]A^\dagger - \mathrm{i}\epsilon\Omega_0 A = F^\dagger(t). \tag{23.26}$$

The Fourier transform of Eqs. 23.24 and 23.26 leads to

$$\begin{pmatrix} -\mathrm{i}\omega - \mathrm{i}\left(\frac{\alpha}{2} - 1\right)\Omega_0 + \frac{\kappa}{2} & \mathrm{i}\epsilon\Omega_0 \\ -\mathrm{i}\epsilon\Omega_0 & -\mathrm{i}\omega + \mathrm{i}\left(\frac{\alpha}{2} - 1\right)\Omega_0 + \frac{\kappa}{2} \end{pmatrix}\begin{bmatrix} A(\omega) \\ A^\dagger(-\omega) \end{bmatrix} = \begin{bmatrix} F(\omega) \\ F^\dagger(-\omega) \end{bmatrix}, \tag{23.27}$$

where we defined the Fourier transform of $A(t)$ as

$$A(\omega) = \frac{1}{\sqrt{2\pi}}\int_{-\infty}^{\infty} dt A(t)e^{\mathrm{i}\omega t}. \tag{23.28}$$

From this equation, we obtain

$$A(\omega) = \frac{-\mathrm{i}\omega + \mathrm{i}\left(\frac{\alpha}{2} - 1\right)\Omega_0 + \frac{\kappa}{2}}{-\left(\omega + \mathrm{i}\frac{\kappa}{2}\right)^2 + \left(\frac{\alpha}{2} - 1\right)^2\Omega_0^2 - \epsilon^2\Omega_0^2} F(\omega) + \frac{-\mathrm{i}\epsilon\Omega_0}{-\left(\omega + \mathrm{i}\frac{\kappa}{2}\right)^2 + \left(\frac{\alpha}{2} - 1\right)^2\Omega_0^2 - \epsilon^2\Omega_0^2} F^\dagger(-\omega). \tag{23.29}$$

From Eq. 23.16,

$$B_{\mathrm{out}}(\omega) = B_{\mathrm{in}}(\omega) - \sqrt{\frac{\kappa_1}{v}} A(\omega). \tag{23.30}$$

By substituting Eq. 23.29 into Eq. 23.30, we finally arrive at

$$B_{\mathrm{out}}(\omega) = J_{\mathrm{b}}(\omega)B_{\mathrm{in}}(\omega) + K_{\mathrm{b}}(\omega)B_{\mathrm{in}}^\dagger(-\omega) + J_{\mathrm{c}}(\omega)C_{\mathrm{in}}(\omega) + K_{\mathrm{c}}(\omega)C_{\mathrm{in}}^\dagger(-\omega), \tag{23.31}$$

where

$$J_{\mathrm{b}}(\omega) = 1 + \kappa_1 \frac{-\mathrm{i}\omega + \mathrm{i}\left(\frac{\alpha}{2} - 1\right)\Omega_0 + \frac{\kappa}{2}}{\left(\omega + \mathrm{i}\frac{\kappa}{2}\right)^2 - \left(\frac{\alpha}{2} - 1\right)^2\Omega_0^2 + \epsilon^2\Omega_0^2}, \tag{23.32}$$

$$K_{\mathrm{b}}(\omega) = -\frac{\mathrm{i}\epsilon\kappa_1\Omega_0}{\left(\omega + \mathrm{i}\frac{\kappa}{2}\right)^2 - \left(\frac{\alpha}{2} - 1\right)^2\Omega_0^2 + \epsilon^2\Omega_0^2}, \tag{23.33}$$

$$J_{\mathrm{c}}(\omega) = \sqrt{\kappa_1\kappa_2} \frac{-\mathrm{i}\omega + \mathrm{i}\left(\frac{\alpha}{2} - 1\right)\Omega_0 + \frac{\kappa}{2}}{\left(\omega + \mathrm{i}\frac{\kappa}{2}\right)^2 - \left(\frac{\alpha}{2} - 1\right)^2\Omega_0^2 + \epsilon^2\Omega_0^2}, \tag{23.34}$$

$$K_{\mathrm{c}}(\omega) = -\frac{\mathrm{i}\epsilon\sqrt{\kappa_1\kappa_2}\Omega_0}{\left(\omega + \mathrm{i}\frac{\kappa}{2}\right)^2 - \left(\frac{\alpha}{2} - 1\right)^2\Omega_0^2 + \epsilon^2\Omega_0^2}. \tag{23.35}$$

Note that Eq. 23.29 corresponds to a special solution of Eqs. 23.24 and 23.26. We neglected the general solution of the corresponding homogeneous equation [$F(t) = F^\dagger(t) = 0$], which takes the form of $C_1 e^{\lambda_1 t} + C_2 e^{\lambda_2 t}$. Here, C_1 and C_2 are time-independent operators, and λ_1 and λ_2 are given by

$$\lambda_1 = -\frac{\kappa}{2} + \Omega_0\sqrt{\epsilon^2 - \left(\frac{\alpha}{2} - 1\right)^2}, \tag{23.36}$$

$$\lambda_2 = -\frac{\kappa}{2} - \Omega_0\sqrt{\epsilon^2 - \left(\frac{\alpha}{2} - 1\right)^2}. \tag{23.37}$$

This solution vanishes in the steady state (i.e., $\mathrm{Re}\lambda_1, \mathrm{Re}\lambda_2 < 0$), provided that

$$\epsilon \leq \sqrt{\left(\frac{\kappa}{2\Omega_0}\right)^2 + \left(\frac{\alpha}{2} - 1\right)^2} \equiv \epsilon_{\mathrm{c}}. \tag{23.38}$$

If $\epsilon > \epsilon_c$, then the output signal with frequency λ_1 exists even without an input. This is called parametric oscillation, which will be discussed later in the chapter.

23.2.3.1 Parametric Gain

Equation 23.31 implies that the output field at a frequency of $\omega+\alpha\Omega_0/2$ is generated from the input field at the same frequency and from the conjugate of the input field at $-\omega + \alpha\Omega_0/2$ (which are the first and second terms on the right-hand side of Eq. 23.31, respectively). These terms are the signal and the idler of the parametric amplifier, and their coefficients $J_b(\omega)$ and $K_b(\omega)$ are related to the signal gain (G_s) and the intermodulation gain (G_i), respectively:

$$G_s = \left|J_b(\omega)\right|^2, \tag{23.39}$$

$$G_i = \left|K_b(\omega)\right|^2. \tag{23.40}$$

Note that in the lossless case ($\kappa_2 = 0$),

$$\left|J_b(\omega)\right|^2 - \left|K_b(\omega)\right|^2 = 1. \tag{23.41}$$

Figure 23.2 shows the signal and intermodulation gains, where both are given as a function of the signal frequency β and the modulation amplitude ϵ. Here, β is the normalized signal frequency measured from half of the pump frequency, i.e., $\beta\Omega_0 = \omega + \frac{\alpha}{2}\Omega_0$.

When we operate the amplifier in the degenerate mode, i.e., when the signal frequency is half of the pump frequency ($\omega = 0$), then the signal and idler frequencies become identical. The signal and the idler components of the output field should then be superposed, and thus the output field amplitude becomes sensitive to the phase θ_s of the input signal field. The phase-dependent degenerate gain G_d is given by

$$G_d = \left|J_b(0)e^{i\theta_s} + K_b(0)e^{-i\theta_s}\right|^2. \tag{23.42}$$

When half of the pump frequency is exactly equal to the resonator frequency ($\alpha = 2$), Eq. 23.42 reads,

$$G_d = \frac{\left(\frac{\kappa_1^2-\kappa_2^2}{4} + \epsilon^2\Omega_0^2\right)^2 + \epsilon^2\kappa_1^2\Omega_0^2 - 2\epsilon\kappa_1\Omega_0\left(\frac{\kappa_1^2-\kappa_2^2}{4} + \epsilon^2\Omega_0^2\right)\sin 2\theta_s}{\left(\frac{\kappa^2}{4} - \epsilon^2\Omega_0^2\right)^2}. \tag{23.43}$$

From this formula, G_d for $\epsilon = 0$ (i.e., pump-off level) is given by

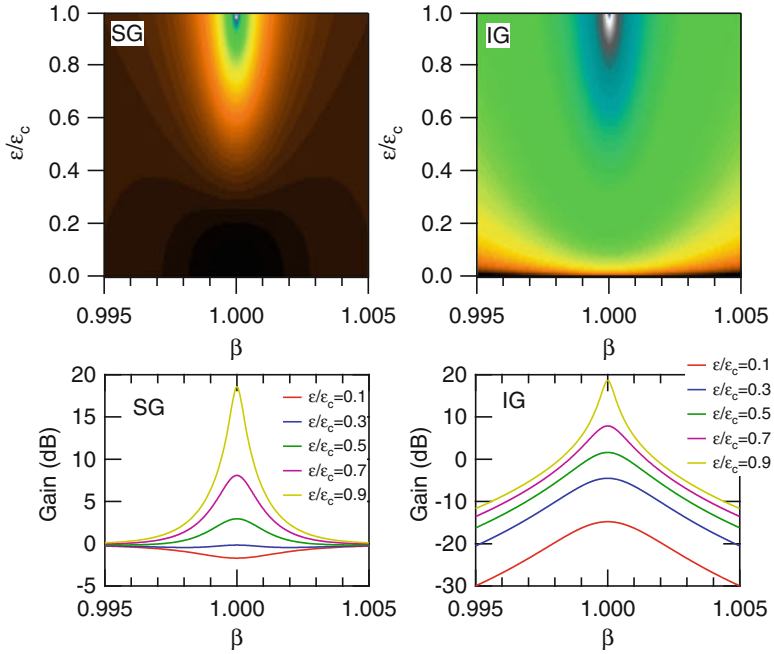

Fig. 23.2 Signal and intermodulation gains, where both are given as a function of the signal frequency and the modulation amplitude. The parameters used for the calculations were $Q_{\mathrm{ext}} = 240$, $Q_{\mathrm{int}} = 2200$, and $\alpha = 2$

$$G_{\mathrm{d}}^{0} = \left(\frac{\kappa_1 - \kappa_2}{\kappa_1 + \kappa_2}\right)^2. \tag{23.44}$$

Assuming that $(\kappa_1^2 - \kappa_2^2)/4 + \epsilon^2\Omega_0^2 > 0$, the minimum gain is achieved when $\theta_{\mathrm{s}} = \pi/4 + n\pi$, and is given by

$$G_{\mathrm{d}}^{\mathrm{min}} = \left(\frac{\epsilon\Omega_0 - \frac{\kappa_1-\kappa_2}{2}}{\epsilon\Omega_0 + \frac{\kappa_1+\kappa_2}{2}}\right)^2. \tag{23.45}$$

The maximum gain is achieved when $\theta_{\mathrm{s}} = 3\pi/4 + n\pi$, and is given by

$$G_{\mathrm{d}}^{\mathrm{max}} = \left(\frac{\epsilon\Omega_0 + \frac{\kappa_1-\kappa_2}{2}}{\epsilon\Omega_0 - \frac{\kappa_1+\kappa_2}{2}}\right)^2. \tag{23.46}$$

Figure 23.3 shows a numerical example of the degenerate gain. Figure 23.3a represents the phase-dependent gain, which is a hallmark of the degenerate parametric amplifier. The gain can be larger (amplification) or smaller (deamplification) than unity, depending on the relative phase between the pump and the signal. In

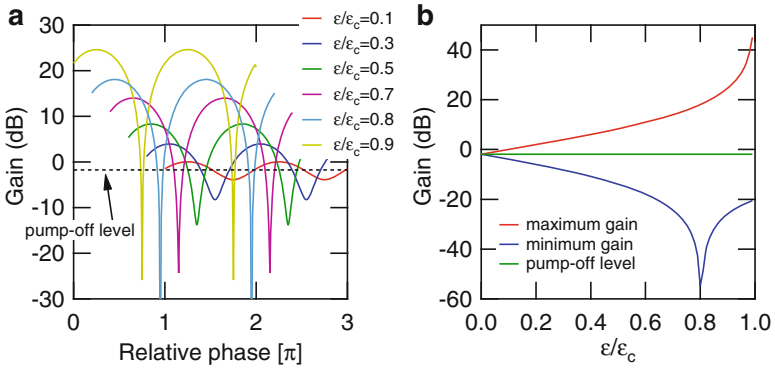

Fig. 23.3 (**a**) The gain of the amplifier when operating in the resonant degenerate mode ($\alpha = 2\beta = 2$) as a function of the relative phase between signal and pump for different modulation amplitudes. The traces are offset from each other along the horizontal axis. The parameters that were used for the calculation are $Q_{\rm ext} = 240$, and $Q_{\rm int} = 2200$. (**b**) The maximum and the minimum of the phase-dependent gain as a function of modulation amplitude. The pump-off level is also shown. The parameters that were used for the calculation are the same as those in (**a**)

Fig. 23.3b, we plot the maximum and minimum values of the phase-dependent gain as a function of ϵ. While the maximum gain increases monotonically as ϵ increases and diverges at $\epsilon = \epsilon_{\rm c}$, the minimum gain becomes zero at $\epsilon/\epsilon_{\rm c} = (\kappa_1 - \kappa_2)/\kappa$ because of the perfectly destructive interference. If $\kappa_1 = \kappa_2$, this occurs at $\epsilon = 0$, which represents the critical coupling condition (a zero reflection coefficient).

23.2.3.2 Noise Temperature

In this section, we consider the case where the inputs to the signal and loss ports consist of the Nyquist noise, i.e.,

$$\left\langle B_{\rm in}(\omega)\right\rangle = \left\langle C_{\rm in}(\omega)\right\rangle = 0, \tag{23.47}$$

$$\left\langle B_{\rm in}^{\dagger}(\omega)B_{\rm in}(\omega')\right\rangle \sim \frac{e^{-\hbar\alpha\Omega_0/2k_{\rm B}T_{\rm b}}}{1-e^{-\hbar\alpha\Omega_0/2k_{\rm B}T_{\rm b}}}\delta(\omega-\omega'), \tag{23.48}$$

$$\left\langle C_{\rm in}^{\dagger}(\omega)C_{\rm in}(\omega')\right\rangle \sim \frac{e^{-\hbar\alpha\Omega_0/2k_{\rm B}T_{\rm c}}}{1-e^{-\hbar\alpha\Omega_0/2k_{\rm B}T_{\rm c}}}\delta(\omega-\omega'), \tag{23.49}$$

where $T_{\rm b}$ and $T_{\rm c}$ are the temperatures of the bath for the input and loss ports, respectively. Assuming that $\omega \ll \alpha\Omega_0/2$, we used the approximation $\hbar(\alpha\Omega_0/2 + \omega) \simeq \hbar\alpha\Omega_0/2$ in Eqs. 23.48 and 23.49. If the output of the parametric amplifier is delivered to the mixer, the mixer output is then given by [37, 38]

$$I_{\rm D}(\omega) = B_{\rm out}^{\dagger}(-\omega)e^{-{\rm i}\phi_{\rm LO}} + B_{\rm out}(\omega)e^{{\rm i}\phi_{\rm LO}}, \tag{23.50}$$

where ϕ_{LO} is the local oscillator phase. The noise power spectral density of the mixer output is given by

$$\begin{aligned} P(\omega) = {} & \left|e^{-\mathrm{i}\phi_{\mathrm{LO}}} J_{\mathrm{b}}^{*}(\omega) + e^{\mathrm{i}\phi_{\mathrm{LO}}} K_{\mathrm{b}}(-\omega)\right|^2 \frac{e^{-\hbar\alpha\Omega_0/2k_{\mathrm{B}}T_{\mathrm{b}}}}{1-e^{-\hbar\alpha\Omega_0/2k_{\mathrm{B}}T_{\mathrm{b}}}} \\ & + \left|e^{\mathrm{i}\phi_{\mathrm{LO}}} J_{\mathrm{b}}(-\omega) + e^{-\mathrm{i}\phi_{\mathrm{LO}}} K_{\mathrm{b}}^{*}(\omega)\right|^2 \frac{1}{1-e^{-\hbar\alpha\Omega_0/2k_{\mathrm{B}}T_{\mathrm{b}}}} \\ & + \left|e^{-\mathrm{i}\phi_{\mathrm{LO}}} J_{\mathrm{c}}^{*}(\omega) + e^{\mathrm{i}\phi_{\mathrm{LO}}} K_{\mathrm{c}}(-\omega)\right|^2 \frac{e^{-\hbar\alpha\Omega_0/2k_{\mathrm{B}}T_{\mathrm{c}}}}{1-e^{-\hbar\alpha\Omega_0/2k_{\mathrm{B}}T_{\mathrm{c}}}} \\ & + \left|e^{\mathrm{i}\phi_{\mathrm{LO}}} J_{\mathrm{c}}(-\omega) + e^{-\mathrm{i}\phi_{\mathrm{LO}}} K_{\mathrm{c}}^{*}(\omega)\right|^2 \frac{1}{1-e^{-\hbar\alpha\Omega_0/2k_{\mathrm{B}}T_{\mathrm{c}}}}. \end{aligned} \tag{23.51}$$

The first two terms on the right-hand side represent the input noise amplified (or deamplified) by the parametric amplifier, and the last two terms represent the extra noise that was added by the parametric amplifier. This formula allows us to calculate the noise temperature of the amplifier, or the achievable degree of squeezing. As an example, we consider the special case where $\alpha = 2$ and $\omega = 0$. In this case,

$$\begin{aligned} P(0) = {} & \left|J_{\mathrm{b}}(0) + |K_{\mathrm{b}}(0)| e^{\mathrm{i}(2\phi_{\mathrm{LO}} - \frac{\pi}{2})}\right|^2 \coth\left(\frac{\hbar\Omega_0}{2k_{\mathrm{B}}T_{\mathrm{b}}}\right) \\ & + \left|J_{\mathrm{c}}(0) + |K_{\mathrm{c}}(0)| e^{\mathrm{i}(2\phi_{\mathrm{LO}} - \frac{\pi}{2})}\right|^2 \coth\left(\frac{\hbar\Omega_0}{2k_{\mathrm{B}}T_{\mathrm{c}}}\right), \end{aligned} \tag{23.52}$$

where

$$J_{\mathrm{b}}(0) = \frac{\epsilon^2\Omega_0^2 + \frac{\kappa_1^2-\kappa_2^2}{4}}{\epsilon^2\Omega_0^2 - \frac{\kappa^2}{4}}, \tag{23.53}$$

$$K_{\mathrm{b}}(0) = \frac{-\mathrm{i}\epsilon\kappa_1\Omega_0}{\epsilon^2\Omega_0^2 - \frac{\kappa^2}{4}}, \tag{23.54}$$

$$J_{\mathrm{c}}(0) = \frac{\frac{\kappa}{2}\sqrt{\kappa_1\kappa_2}}{\epsilon^2\Omega_0^2 - \frac{\kappa^2}{4}}, \tag{23.55}$$

$$K_{\mathrm{c}}(0) = \frac{-\mathrm{i}\epsilon\sqrt{\kappa_1\kappa_2}\Omega_0}{\epsilon^2\Omega_0^2 - \frac{\kappa^2}{4}}. \tag{23.56}$$

Thus, the minimum of $P(0)$ (i.e., the maximum squeezing) is achieved when ϕ_{LO} is chosen such that $2\phi_{\mathrm{LO}} - \frac{\pi}{2} = -\pi$, and is given by

$$P(0)^{\min} = \left(J_{\mathrm{b}}(0) - |K_{\mathrm{b}}(0)|\right)^2 \coth\left(\frac{\hbar\Omega_0}{2k_{\mathrm{B}}T_{\mathrm{b}}}\right) + \left(J_{\mathrm{c}}(0) - |K_{\mathrm{c}}(0)|\right)^2 \coth\left(\frac{\hbar\Omega_0}{2k_{\mathrm{B}}T_{\mathrm{c}}}\right). \tag{23.57}$$

The noise temperature T_n referred to the input is given by

$$T_\mathrm{n} = \frac{\hbar\Omega_0}{k_\mathrm{B}} \frac{\left|J_\mathrm{c}(0) + |K_\mathrm{c}(0)|e^{\mathrm{i}(2\phi_\mathrm{LO}-\frac{\pi}{2})}\right|^2}{\left|J_\mathrm{b}(0) + |K_\mathrm{b}(0)|e^{\mathrm{i}(2\phi_\mathrm{LO}-\frac{\pi}{2})}\right|^2} \coth\left(\frac{\hbar\Omega_0}{2k_\mathrm{B}T_\mathrm{c}}\right), \tag{23.58}$$

$$= \frac{\hbar\Omega_0}{k_\mathrm{B}} \frac{\kappa_1\kappa_2\left|\frac{\kappa}{2} + \epsilon\Omega_0 e^{\mathrm{i}(2\phi_\mathrm{LO}-\frac{\pi}{2})}\right|^2}{\left|\epsilon^2\Omega_0^2 + \frac{\kappa_1^2-\kappa_2^2}{4} + \epsilon\kappa_1\Omega_0 e^{\mathrm{i}(2\phi_\mathrm{LO}-\frac{\pi}{2})}\right|^2} \coth\left(\frac{\hbar\Omega_0}{2k_\mathrm{B}T_\mathrm{c}}\right). \tag{23.59}$$

When $2\phi_\mathrm{LO} - \frac{\pi}{2} = 0$ is satisfied (i.e., the maximum gain), this leads to

$$T_\mathrm{n} = \frac{\hbar\Omega_0}{k_\mathrm{B}} \frac{\kappa_1\kappa_2\left(\frac{\kappa}{2} + \epsilon\Omega_0\right)^2}{\left(\epsilon^2\Omega_0^2 + \frac{\kappa_1^2-\kappa_2^2}{4} + \epsilon\kappa_1\Omega_0\right)^2} \coth\left(\frac{\hbar\Omega_0}{2k_\mathrm{B}T_\mathrm{c}}\right). \tag{23.60}$$

Alternatively, the noise number N_n is given by

$$N_\mathrm{n} \equiv \frac{k_\mathrm{B}T_\mathrm{n}}{\hbar\Omega_0} = \frac{\kappa_1\kappa_2\left(\frac{\kappa}{2} + \epsilon\Omega_0\right)^2}{\left(\epsilon^2\Omega_0^2 + \frac{\kappa_1^2-\kappa_2^2}{4} + \epsilon\kappa_1\Omega_0\right)^2} \coth\left(\frac{\hbar\Omega_0}{2k_\mathrm{B}T_\mathrm{c}}\right). \tag{23.61}$$

In Fig. 23.4, we show the calculation of N_n as a function of both ϵ and Q_int for a fixed Q_ext of 240. If we assume a Q_int of 2200, for example, a G_d of 20 dB (see Fig. 23.3) with a noise temperature below the SQL for the phase-insensitive amplifier is expected at $\epsilon/\epsilon_\mathrm{c} \sim 0.8$.

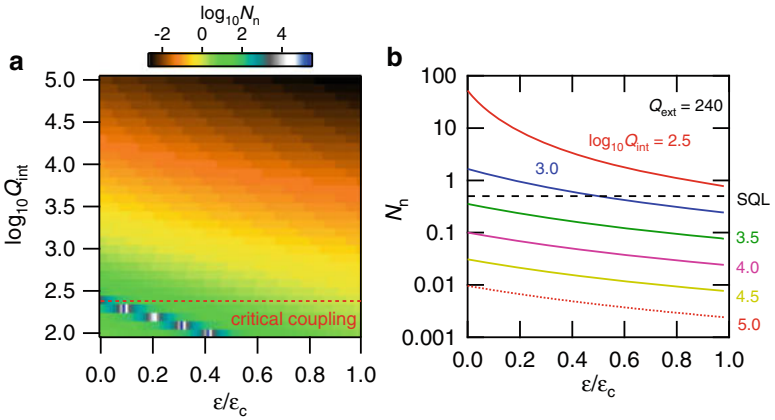

Fig. 23.4 (**a**) Noise number as a function of modulation amplitude and Q_int, calculated from Eq. 23.61. The parameters used for the calculation were $\frac{\Omega_0}{2\pi} = 10.41$ GHz, $Q_\mathrm{ext} = 240$, $\alpha = 2\beta = 2$, and $T_b = T_c = 0.01$ K. (**b**) shows a cross-section of (**a**) at different values of Q_int. SQL represents the standard quantum limit for a phase-insensitive amplifier, i.e., $N_\mathrm{n} = 0.5$

23.2.4 Parametric Oscillator

For a more comprehensive quantum-mechanical description of the resonator field, we introduce the resonator transition operator given by $s_{mn} = |m\rangle\langle n|$, where $|m\rangle$ and $|n\rangle$ are the resonator Fock states. In this section, we consider the case where the parametric modulation frequency is exactly double the resonant frequency of the resonator (i.e., $\alpha = 2$). The Heisenberg equation for s_{mn} in a frame rotating at Ω_0 $[s_{mn}(t)e^{i\Omega_0(n-m)t} \to S_{mn}(t)]$ is given by

$$\begin{aligned}\frac{d}{dt}S_{mn} = {} & \frac{\mathrm{i}}{\hbar}[\mathscr{H}'_{\mathrm{sys}}, S_{mn}] + \frac{\kappa}{2}(2A^\dagger S_{mn}A - S_{mn}A^\dagger A - A^\dagger A S_{mn}) \\ & + \sqrt{v\kappa_1}[S_{mn}, A^\dagger]B_{\mathrm{in}}(t) - \sqrt{v\kappa_1}B^\dagger_{\mathrm{in}}(t)[S_{mn}, A] \\ & + \sqrt{v\kappa_2}[S_{mn}, A^\dagger]C_{\mathrm{in}}(t) - \sqrt{v\kappa_2}C^\dagger_{\mathrm{in}}(t)[S_{mn}, A]. \end{aligned} \tag{23.62}$$

where the static system Hamiltonian $\mathscr{H}'_{\mathrm{sys}}$ is

$$\mathscr{H}'_{\mathrm{sys}}/\hbar = \frac{\epsilon\Omega_0}{2}(A^2 + A^{\dagger 2}) + 6\gamma A^\dagger A^\dagger AA. \tag{23.63}$$

Note that $\mathscr{H}'_{\mathrm{sys}}$ can be derived from $\mathscr{H}_{\mathrm{sys}}$ (Eq. 23.9) in the rotating frame. We consider the application of an external signal field, $E_{\mathrm{s}}(r,t) = E^*_{\mathrm{s}}e^{i\Omega_0(r/v-t)}$, from the signal port. Then, we can rigorously claim the following equations: $\langle B_{\mathrm{in}}(t)\rangle = E^*_{\mathrm{s}}$ and $\langle C_{\mathrm{in}}(t)\rangle = 0$. Using these relations, $\langle S_{mn}\rangle$ evolves as

$$\begin{aligned}\frac{d}{dt}\langle S_{mn}\rangle = {} & \frac{\mathrm{i}\Omega_0\epsilon}{2}\Big(\sqrt{m(m-1)}\langle S_{m-2,n}\rangle + \sqrt{(m+1)(m+2)}\langle S_{m+2,n}\rangle \\ & - \sqrt{n(n-1)}\langle S_{m,n-2}\rangle - \sqrt{(n+1)(n+2)}\langle S_{m,n+2}\rangle\Big) \\ & + 6\mathrm{i}\gamma[m(m-1) - n(n-1)]\langle S_{mn}\rangle \\ & + \frac{\kappa}{2}\Big[2\sqrt{(m+1)(n+1)}\langle S_{m+1,n+1}\rangle - (m+n)\langle S_{mn}\rangle\Big] \\ & + \sqrt{\kappa_1}E_{\mathrm{s}}\Big(\sqrt{n}\langle S_{m,n-1}\rangle - \sqrt{m+1}\langle S_{m+1,n}\rangle\Big) \\ & - \sqrt{\kappa_1}E^*_{\mathrm{s}}\Big(\sqrt{n+1}\langle S_{m,n+1}\rangle - \sqrt{m}\langle S_{m-1,n}\rangle\Big), \end{aligned} \tag{23.64}$$

where we have used $A^\dagger S_{mn}A = \sqrt{(m+1)(n+1)}S_{m+1,n+1}$ and similar equalities.

Because $\langle S_{mn}\rangle = \mathrm{Tr}[\rho S_{mn}] = \rho_{nm}$, Eq. 23.64 is equivalent to the following master equation:

$$\frac{d\rho}{dt} = -\frac{\mathrm{i}}{\hbar}[\mathscr{H}_{\mathrm{int}}, \rho] + \frac{\kappa}{2}(2A\rho A^\dagger - A^\dagger A\rho - \rho A^\dagger A), \tag{23.65}$$

where

$$\mathscr{H}_{\rm int}/\hbar = \frac{\epsilon\,\Omega_0}{2}(A^2 + A^{\dagger 2}) + 6\gamma A^\dagger A^\dagger A A + {\rm i}\sqrt{\kappa_1}|E_{\rm s}|(e^{{\rm i}\theta_{\rm s}}A^\dagger - e^{-{\rm i}\theta_{\rm s}}A), \quad (23.66)$$

and $E_{\rm s} = |E_{\rm s}|e^{-{\rm i}\theta_{\rm s}}$. By introducing the dimensionless time $\tau = t\kappa/2$, Eq. 23.65 becomes

$$\frac{d\rho}{d\tau} = -{\rm i}[\mathscr{H}'_{\rm int}, \rho] + (2A\rho A^\dagger - A^\dagger A\rho - \rho A^\dagger A). \quad (23.67)$$

Here, the dimensionless Hamiltonian $\mathscr{H}'_{\rm int}$ is given by

$$\mathscr{H}'_{\rm int} = \mathscr{H}_{\rm int}/(\hbar\kappa/2) = \gamma' A^\dagger A^\dagger A A + \frac{\epsilon}{2\epsilon_{\rm c}}(A^2 + A^{\dagger 2}) + {\rm i}\sqrt{N}(e^{{\rm i}\theta_{\rm s}}A^\dagger - e^{-{\rm i}\theta_{\rm s}}A), \quad (23.68)$$

where $\gamma' = 12\gamma/\kappa$, $\epsilon_{\rm c} = \kappa/(2\Omega_0)$, and $\sqrt{N} = \sqrt{\kappa_1}|E_{\rm s}|/(\kappa/2)$. Here, $\epsilon_{\rm c}$ represents the modulation amplitude threshold required to induce parametric oscillation (Eq. 23.38 with $\alpha = 2$), and N represents the mean photon number in the resonator.

Equation 23.67 can be solved numerically by expanding ρ on a number state basis, i.e., $\rho = \sum_{m,n=0}^{N} \rho_{mn}|m\rangle\langle n|$. Using ρ, we can then calculate the time evolution of, e.g., the resonator field $\langle A + A^\dagger\rangle = {\rm Tr}[\rho(A + A^\dagger)]$ or the Q function $Q(z) = \langle z|\rho|z\rangle/\pi$, where $|z\rangle$ is a coherent state [28].

Figure 23.5 shows an example of the calculated Q function [39]. We assumed that the resonator was in the ground state at $\tau = 0$. In the figure, two distribution peaks can be seen. These peaks correspond to the two dynamical states of the parametric oscillation, which were used in the parametron as a classical bit [25]. As shown in the figure, the peaks have equal amplitudes, but are phase shifted by π, and are called the 0π-state and the 1π-state. The figure thus shows that the probabilities of these states depend on the phase of the external signal.

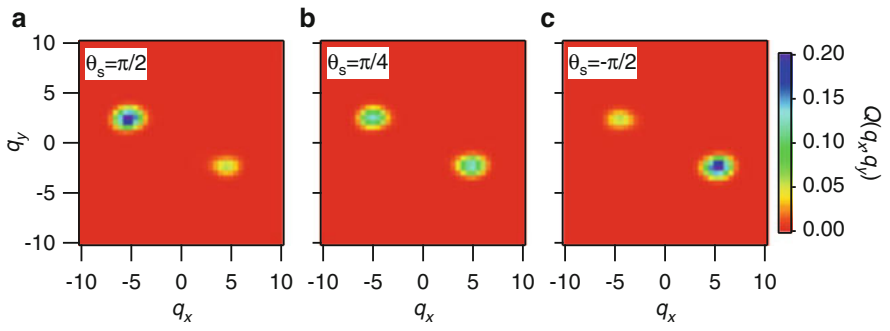

Fig. 23.5 Q function at $\tau = 20$. The parameters used for the calculation were $\Omega_0/2\pi = 10.5$ GHz, $\gamma = -2.3 \times 10^5$ Hz, $Q_{\rm ext} = 336$, $Q_{\rm int} = 5300$, $N = 0.10$, $\epsilon/\epsilon_{\rm c} = 1.29$, and the number of basis states was 80. $\theta_{\rm s}$ is fixed at $\pi/2$ in (**a**), $\pi/4$ in (**b**), and $-\pi/2$ in (**c**)

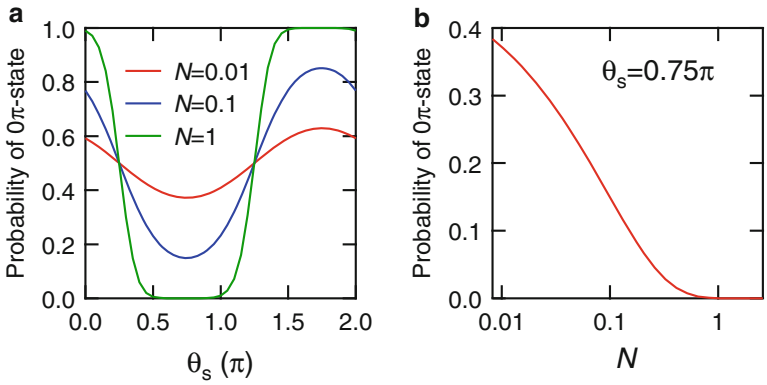

Fig. 23.6 Probability of obtaining the 0π state as a function of (**a**) signal phase and (**b**) signal amplitude. The parameters used for the calculation were $\Omega_0/2\pi = 10.5\,\text{GHz}$, $\gamma = -2.3\times10^5$ Hz, $Q_{\text{ext}} = 336$, $Q_{\text{int}} = 5300$, $\epsilon/\epsilon_c = 1.29$, and the number of basis states was 80

In Fig. 23.6a, the probability of obtaining the 0π-state is calculated as a function of the signal phase θ_s for different magnitudes of N. As N increases, the modulation amplitude also increases. When $N = 1$, the probability of the 0π-state is fully modulated from zero to unity. Figure 23.6b shows the probability of the 0π-state as a function of N at $\theta_s = 0.75\pi$. The probability of the 0π-state decreases monotonically as N increases, and vanishes when $N \gtrsim 1$. This property indicates the parametric oscillator's capability to act as a sensitive phase detector. For example, a signal that has been digitally modulated by binary phase-shift keying (BPSK) can be reliably demodulated using this device as long as the signal is sufficiently intense to satisfy $N \gtrsim 1$.

Finally, Fig. 23.7 shows the calculated evolution of the resonator field with time. The expectation value of $A + A^\dagger$ is plotted as a function of the dimensionless time τ. The resonator field builds up because of parametric modulation above the threshold $\epsilon/\epsilon_c > 1$, and saturates after a certain time. As shown in the figure, the build-up time depends on both ϵ and N. The time becomes shorter as ϵ and/or N increase, and becomes comparable to the lifetime of a resonator photon ($\tau = 1$). This behavior is consistent with that reported in the literature on the parametron [40]. This build-up time, combined with the integration time required to extract the phase, determines the bandwidth of the PPLO when it is acting as a phase detector [27].

23.3 Conclusions

We presented a quantum description of a parametrically-modulated nonlinear resonator that is coupled to external ports. This is a model for both the flux-driven Josephson parametric amplifier (JPA) and the Josephson parametric phase-locked

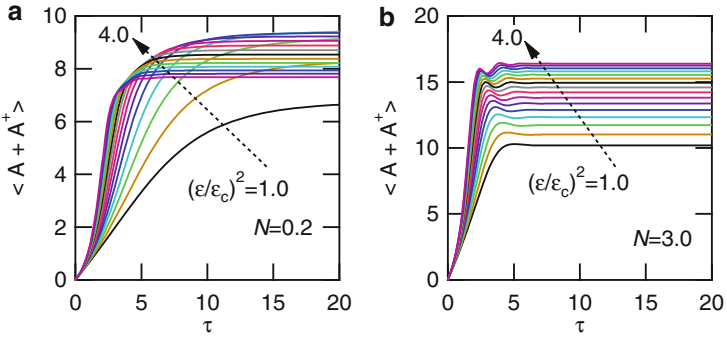

Fig. 23.7 Time evolution of the cavity field $\langle A + A^{\dagger} \rangle$. The parameters used for the calculation were $\Omega_0/2\pi = 10.5\,\mathrm{GHz}$, $\gamma = -2.3 \times 10^5\,\mathrm{Hz}$, $Q_{\mathrm{ext}} = 336$, $Q_{\mathrm{int}} = 5300$, $\theta_{\mathrm{s}} = 1.75\pi$, and the number of basis states was 80. N is fixed at 0.2 in (**a**) and 3.0 in (**b**). In both panels, $(\epsilon/\epsilon_{\mathrm{c}})^2$ changes from 1.0 to 4.0 with steps of 0.2

oscillator (PPLO). Numerical calculations using practical device parameters show that a flux-driven JPA with a noise temperature that is below the SQL is readily achievable. Also, the Josephson PPLO will work as a sensitive binary phase detector that can discriminate the phase of a weak microwave field, and can be used to perform a high-fidelity single-shot readout of a superconducting qubit.

Superconducting parametric amplifiers have already been shown to be useful tools for quantum information processing experiments in the microwave frequency range. These amplifiers could also be indispensable for the realization of practical quantum computers. One crucial issue in that respect is scalability, i.e., the number of qubits that can be read out with a single parametric amplifier. Although the multiplexed readout of five qubits has recently been demonstrated [41], further improvements in terms of both bandwidth and dynamic range are needed. Traveling wave parametric amplifiers using transmission lines with high nonlinear inductances [42, 43] could be useful in this respect. Another important issue is the integration of the parametric amplifier into the qubit chip to eliminate signal losses during propagation between separate chips. The reflection-type parametric amplifier necessitates the use of microwave components with directivity, such as a directional coupler and a circulator to separate the incoming and outgoing signals, and this has prevented on-chip integration of the parametric amplifier to date. Traveling wave parametric amplifiers or coupled Josephson parametric converters [44] could, in principle, solve this problem.

Acknowledgements The authors gratefully acknowledge the support of the Funding Program for World-Leading Innovative R&D on Science and Technology (FIRST). This work was also supported in part by the Project for Developing Innovation Systems of MEXT, MEXT KAKENHI (grant nos. 21102002 and 25400417), SCOPE (111507004) and the National Institute of Information and Communications Technology (NICT).

References

1. H. Takahashi, in *Advances in Communication Systems*, ed. by A.V. Balakrishnan (Academic, New York, 1965), p. 227
2. C.M. Caves, Phys. Rev. D **26**, 1817 (1982)
3. A. Barone, G. Paterno, *Physics and Applications of the Josephson Effect* (Wiley, New York, 1982), chap. 11
4. B. Yurke, P.G. Kaminsky, R.E. Miller, E.A. Whittaker, A.D. Smith, A.H. Silver, R.W. Simon, Phys. Rev. Lett. **60**, 764 (1988)
5. B. Yurke, L.R. Corruccini, P.G. Kaminsky, L.W. Rupp, A.D. Smith, A.H. Silver, R.W. Simon, E.A. Whittaker, Phys. Rev. A **39**, 2519 (1989)
6. R. Movshovich, B. Yurke, P.G. Kaminsky, A.D. Smith, A.H. Silver, R.W. Simon, M.V. Schneider, Phys. Rev. Lett. **65**, 1419 (1990)
7. Y. Nakamura, Y.A. Pashkin, J.S. Tsai, Nature **398**, 786 (1999)
8. A. Blais, R.S. Huang, A. Wallraff, S.M. Girvin, R.J. Schoelkopf, Phys. Rev. A **69**, 062320 (2004)
9. E.A. Tholén, A. Ergül, E.M. Doherty, F.M. Weber, F. Grégis, D.B. Haviland, Appl. Phys. Lett. **90**, 253509 (2007)
10. M.A. Castellanos-Beltran, K.W. Lehnert, Appl. Phys. Lett. **91**, 083509 (2007)
11. T. Yamamoto, K. Inomata, M. Watanabe, K. Matsuba, T. Miyazaki, W.D. Oliver, Y. Nakamura, J.S. Tsai, Appl. Phys. Lett. **93**, 042510 (2008)
12. N. Bergeal, R. Vijay, V.E. Manucharyan, I. Siddiqi, R.J. Schoelkopf, S.M. Girvin, M.H. Devoret, Nat. Phys. **6**, 296 (2010)
13. M.A. Castellanos-Beltran, K.D. Irwin, G.C. Hilton, L.R. Vale, K.W. Lehnert, Nat. Phys. **4**, 928 (2008)
14. J.D. Teufel, T. Donner, M.A. Castellanos-Beltran, J.W. Harlow, K.W. Lehnert, Nat. Nanotech. **4**, 820 (2009)
15. R. Vijay, D.H. Slichter, I. Siddiqi, Phys. Rev. Lett. **106**, 110502 (2011)
16. A. Wallraff, D.I. Schuster, A. Blais, L. Frunzio, R.S. Huang, J. Majer, S. Kumar, S.M. Girvin, R.J. Schoelkopf, Nature **431**, 162 (2004)
17. F. Mallet, M.A. Castellanos-Beltran, H.S. Ku, S. Glancy, E. Knill, K.D. Irwin, G.C. Hilton, L.R. Vale, K.W. Lehnert, Phys. Rev. Lett. **106**, 220502 (2011)
18. C. Eichler, D. Bozyigit, C. Lang, M. Baur, L. Steffen, J.M. Fink, S. Filipp, A. Wallraff, Phys. Rev. Lett. **107**, 113601 (2011)
19. E. Flurin, N. Roch, F. Mallet, M.H. Devoret, B. Huard, Phys. Rev. Lett. **109**, 183901 (2012)
20. E.P. Menzel, R. Di Candia, F. Deppe, P. Eder, L. Zhong, M. Ihmig, M. Haeberlein, A. Baust, E. Hoffmann, D. Ballester, K. Inomata, T. Yamamoto, Y. Nakamura, E. Solano, A. Marx, R. Gross, Phys. Rev. Lett. **109**, 250502 (2012)
21. A.H. Nayfeh, D.T. Mook, *Nonlinear Oscillations* (Wiley-Interscience, New York, 1995)
22. C.M. Wilson, T. Duty, M. Sandberg, F. Persson, V. Shumeiko, P. Delsing, Phys. Rev. Lett. **105**, 233907 (2010)
23. C.W. Wilson, T. Duty, P. Delsing, in *Fluctuating Nonlinear Oscillators: From Nanomechanics to Quantum Superconducting Circuits*, ed. by M. Dykman (Oxford University Press, Oxford, 2012), chap. 15
24. C.M. Wilson, G. Johansson, A. Pourkabirian, M. Simoen, J.R. Johansson, T. Duty, F. Nori, P. Delsing, Nature **376**, 479 (2011)
25. E. Goto, Proc. Inst. Radio Eng. **47**, 1304 (1959)
26. L.S. Onyshkevych, W.F. Kosonocky, A.W. Lo, Trans. Inst. Radio Engrs. **EC-8**, 277 (1959)
27. Z.R. Lin, K. Inomata, K. Koshino, W.D. Oliver, Y. Nakamura, J.S. Tsai, T. Yamamoto, Nat. Commun. **5**, 4480 (2014)
28. D.F. Walls, G.J. Milburn, *Quantum Optics* (Springer, Berlin/Tokyo, 1994)
29. M. Wallquist, V.S. Shumeiko, G. Wendin, Phys. Rev. B **74**, 224506 (2006)
30. T. Ojanen, J. Salo, Phys. Rev. B **75**, 184508 (2007)

31. M. Hatridge, R. Vijay, D.H. Slichter, J. Clarke, I. Siddiqi, Phys. Rev. B **83**, 134501 (2011)
32. J.Y. Mutus, T.C. White, E. Jeffrey, D. Sank, R. Barends, J. Bochmann, Y. Chen, Z. Chen, B. Chiaro, A. Dunsworth, J. Kelly, A. Megrant, C. Neill, P.J.J. O'Malley, P. Roushan, A. Vainsencher, J. Wenner, I. Siddiqi, R. Vijay, A.N. Cleland, J.M. Martinis, Appl. Phys. Lett. **103**, 122602 (2013)
33. E. Jeffrey, D. Sank, J.Y. Mutus, T.C. White, J. Kelly, R. Barends, Y. Chen, Z. Chen, B. Chiaro, A. Dunsworth, A. Megrant, P.J.J. O'Malley, C. Neill, P. Roushan, A. Vainsencher, J. Wenner, A.N. Cleland, J.M. Martinis, Phys. Rev. Lett. **112**, 190504 (2014)
34. Z.R. Lin, K. Inomata, W.D. Oliver, K. Koshino, Y. Nakamura, J.S. Tsai, T. Yamamoto, Appl. Phys. Lett. **103**, 132602 (2013)
35. L. Zhong, E.P. Menzel, R.D. Candia, P. Eder, M. Ihmig, A. Baust, M. Haeberlein, E. Hoffmann, K. Inomata, T. Yamamoto, Y. Nakamura, E. Solano, F. Deppe, A. Marx, R. Gross, New J. Phys. **15**, 125013 (2013)
36. B. Abdo, A. Kamal, M. Devoret, Phys. Rev. B **87**, 014508 (2013)
37. B. Yurke, in *Quantum Squeezing*, ed. by P.D. Drummond, Z. Ficek (Springer, Berlin/New York, 2004)
38. B. Yurke, E. Buks, J. Lightwave Tech. **24**, 5054 (2006)
39. J. Johansson, P. Nation, F. Nori, Comput. Phys. Commun. **184**, 1234 (2013)
40. K. Beer, Radio Electron. Eng. **25**, 432 (1963)
41. R. Barends, J. Kelly, A. Megrant, A. Veitia, D. Sank, E. Jeffrey, T.C. White, J. Mutus, A.G. Fowler, B. Campbell, Y. Chen, Z. Chen, B. Chiaro, A. Dunsworth, C. Neill, P. O'Malley, P. Roushan, A. Vainsencher, J. Wenner, A.N. Korotkov, A.N. Cleland, J.M. Martinis, Nature **508**, 500 (2014)
42. B.H. Eom, P.K. Day, H.G. LeDuc, J. Zmuidzinas, Nat. Phys. **8**, 623 (2012)
43. O. Yaakobi, L. Friedland, C. Macklin, I. Siddiqi, Phys. Rev. B **87**, 144301 (2013)
44. B. Abdo, K. Sliwa, L. Frunzio, M. Devoret, Phys. Rev. X **3**, 031001 (2013)

Chapter 24
Superconductor-Diamond Hybrid Quantum System

Kouichi Semba, Fumiki Yoshihara, Jan E.S. Johansson, Xiaobo Zhu, Norikazu Mizuochi, William J. Munro, Shiro Saito, Kosuke Kakuyanagi, and Yuichiro Matsuzaki

24.1 Introduction

The recent emergence of the superconducting artificial atom (a macroscopic quantum system), has made research on light and matter at the single-photon interaction level possible using only superconducting circuits [1]. The interaction between a single microwave photon and a macroscopic superconducting artificial atom is huge, and more than several orders of magnitude stronger than the interaction between a natural atom and a photon. So, the high-Q cavity, which is an indispensable ingredients of strong coupling experiments in cavity quantum electrodynamics (QED), is not really necessary to achieve strong coupling [2]. Nevertheless, the strong

K. Semba (✉) • F. Yoshihara
National Institute of Information and Communication Technology, 4-2-1, Nukui-Kitamachi, Koganei, Tokyo 184-8795, Japan
e-mail: semba@nict.go.jp; fumiki@nict.go.jp

J.E.S. Johansson
Faculty of Engineering and Science, University of Agder, Postboks 422, 4604 Kristiansand, Norway
e-mail: jan.johansson@uia.no

X. Zhu
Chinese Academy of Sciences, The Institute of Physics, P.O.Box 603, Beijing 100190, China
e-mail: xbzhu@aphy.iphy.ac.cn

N. Mizuochi
Graduate School of Engineering Science, Osaka University, Toyonaka, Osaka 560-8531, Japan
e-mail: mizuochi@mp.es.osaka-u.ac.jp

W.J. Munro • S. Saito • K. Kakuyanagi • Y. Matsuzaki
NTT Basic Research Laboratories, 3-1, Morinosato-Wakamiya, Atsugi, Kanagawa 243-0198, Japan
e-mail: william.munro@lab.ntt.co.jp; saito.shiro@lab.ntt.co.jp; kakuyanagi.kosuke@lab.ntt.co.jp; matsuzaki.yuichiro@lab.ntt.co.jp

Y. Yamamoto, K. Semba (eds.), *Principles and Methods of Quantum Information Technologies*, Lecture Notes in Physics 911, DOI 10.1007/978-4-431-55756-2_24

non-linearity and low dissipative nature of a Josephson circuit makes quantum non-demolition (QND) measurement possible [3–5]. Moreover, relevant physical parameters, such as the energy level spacing of a single quantum system, can be controlled in-situ by the combination of synchronized dc-pulses [6, 7]. Relevant coherence properties, such as the power spectrum density of the electromagnetic noise environment of a superconducting artificial atom, can also be studied over a wide frequency range [8]. In addition to describing the strong coupling dynamics of a superconducting artificial atom LC harmonic oscillator system [2], we have also successfully performed a quantum memory type experiment in a hybrid quantum system composed of a superconducting artificial atom and the electron spin ensemble of nitrogen-vacancy color centers in diamond [9–11].

24.2 Superconducting Flux Qubit

Quantum bits (qubits) based on superconducting Josephson junctions are attracting increasing attention because of their potential for use in quantum information processing. In addition, they offer an ideal testing ground for studying fundamental interactions between matter and light. A superconducting flux qubit is a superconductor loop that incorporates sub micrometer scale multiple (typically three or four) Josephson junctions [12, 13]. According to the strict requirement that the order parameter of the superconducting state is single valued, the fluxoid associated with each hole in a multiply connected superconductor should be quantized so that it is an integer multiple of the flux quantum ($\phi_0 = \frac{h}{2e} \approx 2.07 \times 10^{-15}$ Wb). Using this property, we intentionally tune the magnetic field strength so that number of magnetic fluxes through the loop is approximately half an odd integer multiple of the flux quantum for example, $0.5\phi_0$. Then, a clockwise (counterclockwise) supercurrent flows over the surface of the loop, that forms total fluxoid 0 (ϕ_0). In general, a linear combination of these states will be the energy eigenstates of the system, so we can use these energy eigenstates as a quantum two-level system (qubit).

24.2.1 Superconducting Flux Qubit with Tunable Quantum Level Spacing

A flux qubit is decoupled from low frequency flux noise at degeneracy point. It achieves maximum coherence times exceeding 10 μs compared with nanoseconds at the off-degeneracy point, which is why this is the optimal operation point. Implementing a quantum processor based on flux qubits requires operation at this optimal point, especially when coupling to other quantum systems is required. We aim to overcome these limitations by replacing the smallest junction of the flux

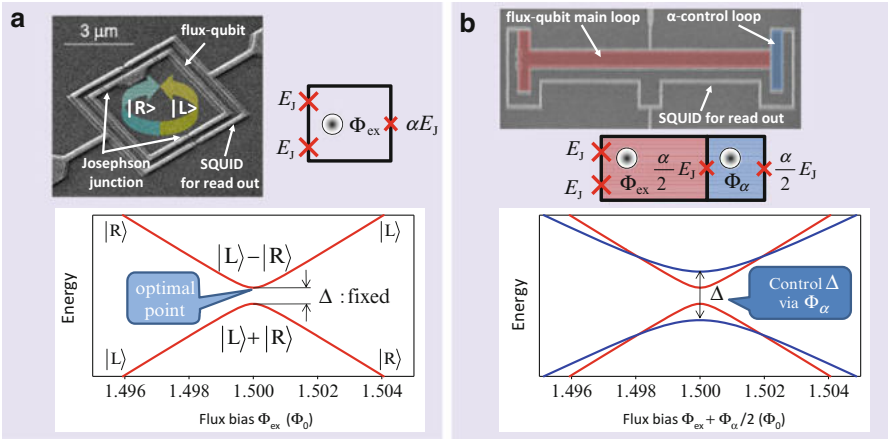

Fig. 24.1 (**a**) A conventional flux qubit with three Josephson junctions. (**b**) A flux qubit with tunable in-situ quantum level spacing

qubit with a low inductance direct current superconducting quantum interference device (dc-SQUID) loop. Varying the magnetic flux through this loop is equivalent to changing the critical current of the smallest junction, thus we succeeded in making a flux qubit with in-situ tunability of the quantum level spacing during the experiment [6, 7]. Using this tuning parameter we can control the coupling to an arbitrary quantum system by tuning to or away from the resonant frequency while operating at the optimal point.

Figure 24.1a shows a conventional flux qubit. In contrast, Fig. 24.1b shows a flux qubit with a tunable quantum energy level spacing. Two identical junctions with Josephson energy E_J in series with a symmetric dc-SQUID (shown as the α-control loop in Fig. 24.1b) in which each junction has a Josephson energy of $\alpha_0 E_J$ are enclosed in a superconducting loop. The effective Josephson energy of the dc-SQUID is $\alpha E_J = 2\alpha_0 \cos(\frac{\pi\phi_\alpha}{\phi_0})E_J$, where ϕ_α is the flux through the dc-SQUID and ϕ_0 is the flux quantum. The main loop is threaded by a flux ϕ_{ex}. The phase drop caused by ϕ_α constitutes an effective magnetic flux $\phi_t = \phi_{ex} + \frac{\phi_\alpha}{2}$ threading the qubit. We operate the qubit at fluxes close to $\phi_t = \phi_0(n + 1/2)$, where n is an integer. Near these flux bias points, the system can be regarded as a quantum two-level system (qubit) with the Hamiltonian:

$$H = \frac{h}{2}[\varepsilon(\phi_t)\sigma_z + \Delta(\phi_\alpha)\sigma_x], \tag{24.1}$$

where $\varepsilon = 2I_p(\phi_t - \phi_0(n + 1/2))$ is the energy difference between the two different classical persistent current states $|L\rangle$ and $|R\rangle$ induced by the external magnetic field, I_p is the persistent current circulating in the qubit loop, $\Delta(\phi_\alpha) \equiv 2\Delta\cos(\frac{\pi\phi_\alpha}{\phi_0})$ is the transition energy between these two states, and σ_x and σ_z are the Pauli matrices. In our design, we place two control lines adjacent to the qubit structure. The fluxes

in the qubit loops are related to the control currents by the mutual inductances between the respective lines. The mutual inductances of control line 1 to the dc-SQUID loop and main loop are 85 fH and 64 fH, and those of control line 2 are 1 fH and 84 fH, respectively. In the experiment, first we pre-bias the effective qubit flux ϕ_t close to the operating point $(n + 1/2)\phi_0$ by using the external magnetic coil. Applying current to the control lines tunes ϕ_t and ϕ_α in situ away from their prebiased values. The coupling to the effective qubit loop induced by control line 1 can be compensated for by applying the corresponding current to control line 2, thus giving full control over the two-dimensional parameter space. By combining the synchronized dc current pulses, it is possible to control the qubit level spacing without changing the qubit flux bias on a sub-ns time scale.

24.2.2 Coherence Property

A superconducting flux qubit is realized in superconducting electric circuits, and is positioned in the middle of the surrounding circuit and on top of the substrate. The qubit interacts with various degrees of freedom which decohere the qubit. The transition frequency is described as $\omega_{01} = \sqrt{\Delta^2 + \varepsilon^2}$, where Δ is the tunnel splitting between two states with opposite persistent current directions along the qubit loop I_p, and $\hbar\varepsilon = 2I_\mathrm{p}\phi_0 n_\phi$ is the energy bias between the two states. Here, the flux bias is normalized by the superconducting flux quantum ϕ_0 as $n_\phi = \phi_\mathrm{ex}/\phi_0 - 0.5$. We find $\partial\omega_{01}/\partial n_\phi = 0$ at $n_\phi = 0$; this is the optimal flux bias condition where dephasing due to n_ϕ fluctuations is minimal. The decoherence time measured with the spin-echo method is $T_{2\mathrm{echo}} = 23\,\mu\mathrm{s}$, which is about twice as long as the energy relaxation time $T_1 = 12\,\mu\mathrm{s}$ [14]. This result indicates that pure dephasing measured with the spin-echo method is largely suppressed. On the other hand, at $n_\phi \neq 0$, $\partial\omega_{01}/\partial n_\phi \neq 0$ and n_ϕ fluctuations causes dephasing. To understand and suppress the flux fluctuations mechanisms, it is important to identify and characterize the dominant noise sources among the many possibilities.

The power spectral density (PSD) of flux fluctuations typically follows $1/f$ frequency dependence with a spectral density of $1\text{–}10\,\mu\phi_0/\sqrt{\mathrm{Hz}}$ at 1 Hz. The accessible frequency range of the PSD was limited to approximately 10 MHz in the spin-echo measurements and was extended to a few tens of megahertz using Carr-Purcell-Meiboom-Gill pulse sequences [14]. The spectrum in a higher-frequency range would provide further information for a better understanding of the microscopic origin of the flux fluctuations.

The high-frequency flux noise spectrum in a superconducting flux qubit can be inferred by studying the decay of Rabi oscillations under strong driving conditions [8]. The Rabi frequency is proportional to the amplitude of the driving field for weak to moderate driving at the qubit transition frequency, and Rabi frequencies in the gigahertz range are also achieved. The fluctuations at the Rabi frequency cause the Rabi oscillation to decay. We measured Rabi oscillations over a wide range of

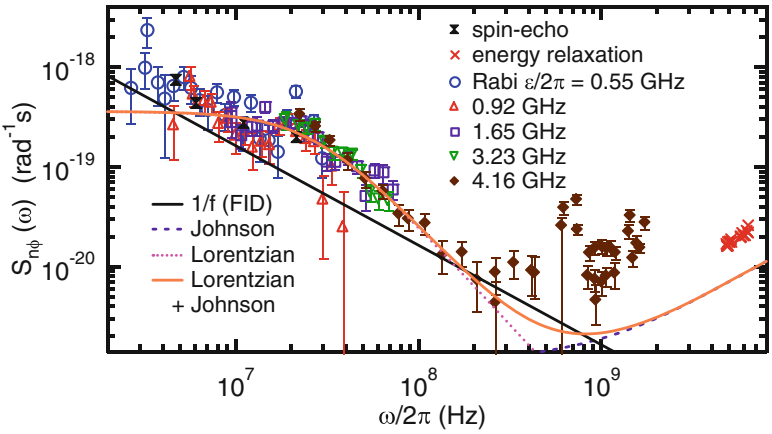

Fig. 24.2 Power spectrum density (PSD) of flux fluctuations, $S_{n_\phi}(\omega)$, extracted from the Rabi oscillation measurements. The PSDs obtained from the spin-echo and energy relaxation measurements are also plotted. The *black solid line* is the $1/f$ spectrum extrapolated from the FID measurements. The *purple dashed line* is the estimated Johnson noise from a 50 Ω microwave line coupled to the qubit by a mutual inductance of 1.2 pH and nominally cooled to 35 mK. The *pink dotted line* is a Lorentzian, $S_{n_\phi}^{\text{model}}(\omega) = S_{\text{h}}\omega_{\text{w}}^2/(\omega^2 + \omega_{\text{w}}^2)$, and the *orange solid line* is the sum of the Lorentzian and the Johnson noise. Here the parameters are $S_{\text{h}} = 3.6 \times 10^{-19}\,\text{rad}^{-1}\,\text{s}$ and $\omega_{\text{w}}/2\pi = 2.7 \times 10^7\,\text{Hz}$ (Reprinted with permission from Yoshihara et al. (2014). ©*American Physical Society*)

Rabi frequencies ($\Omega_{\text{R}}/2\pi$) from 2.7 MHz to 1.7 GHz, and evaluated the PSD of the flux fluctuations at each Rabi frequency.

The PSD of the flux fluctuations, $S_{n_\phi}(\omega)$, evaluated from the Rabi oscillation measurements is plotted in Fig. 24.2. PSDs from the spin-echo and energy relaxation measurements, and the $1/f$ spectrum extrapolated from the free induction decay (FID) measurements, $S_{n_\phi}(\omega) = (3.2\times10^{-6})^2/\omega$, are also plotted. Several points are worth mentioning. (i) $S_{n_\phi}(\omega)$ obtained from the spin-echo measurements is consistent with that obtained from the Rabi-oscillation measurements. (ii) $S_{n_\phi}(\omega)$ obtained from the energy relaxation measurements is 2.5 times larger than expected for the decay into a 50 Ω microwave line coupled to the qubit by a mutual inductance of 1.2 pH and nominally cooled to 35 mK. (iii) There can be an additional decoherence induced by strong driving. Therefore, it is not surprising to see the increased and scattered $S_{n_\phi}(\omega)$ from the Rabi oscillation measurements above 300 MHz. These data points should be considered the upper limit of the noise. (iv) $S_{n_\phi}(\omega)$ from the Rabi oscillation measurements is roughly parallel to the $1/f$ spectrum extrapolated from the FID measurements, but it is generally larger and has more structures. The deviation is largest at 25 MHz, and the slope at approximately 100 MHz is steeper than $1/f$. (v) $S_{n_\phi}(\omega)$ around 300 MHz is approximately $10^{-20}\,\text{rad}^{-1}\text{s}$, demonstrating that the noise level is not very far from the extrapolation of the $1/f$ spectrum, even at such high frequencies.

24.2.3 Strong Coupling to a Quantum Harmonic Oscillator

As an example of strong coupling between superconducting quantum circuits, in this section, we report the observation of vacuum Rabi oscillations in a macroscopic superconducting solid-state system. In our strongly coupled system, the qubit state and the qubit interaction time with the oscillator are controlled by a combination of microwave and dc-shift pulses, resulting in a measuring sequence analogous to atomic cavity quantum electrodynamics (QED). In our experiment, a superconducting qubit plays the role of the atom. A superconducting qubit is characterized with a huge magnetic dipole moment produced by a circulating superconducting persistent current ($I_p \sim 0.35\,\mu\mathrm{A}$), which is several orders of magnitude larger than that of the natural atom. So, in order to achieve a strong coupling condition, and unlike with atomic cavity QED, we do not have to use a high-Q microwave cavity. This is noteworthy feature of a macroscopic superconducting artificial atom (qubit).

As shown in Fig. 24.3a–c, the qubit is spatially separated from the rest of the circuitry. The qubit is enclosed by a superconducting quantum interference device (SQUID) that is inductively coupled to the qubit (Fig. 24.3b). The switching current of the SQUID is sensitive to the flux produced by the current in the qubit. The qubit is also enclosed by a larger loop containing on-chip capacitors that provide a well-defined electromagnetic environment for the SQUID and filtering of the measurement leads. The lead inductance L and capacitance C in the outer loop constitute an LC oscillator (see Fig. 24.3c) with resonance frequency $\omega_r = \frac{1}{\sqrt{LC}}$. We observed the LC resonance at $\nu_r = 4.35\,\mathrm{GHz}$. The LC oscillator is described by a simple harmonic oscillator Hamiltonian: $H_{osc} = \hbar\omega_r(a^\dagger a + \frac{1}{2})$, where $a^\dagger$ (a) is the creation (annihilation) operator of the LC-mode (plasmon). The qubit is coupled to the LC oscillator via the mutual inductance M, giving an interaction Hamiltonian $H_I = h\lambda\sigma_z(a^\dagger + a)$, where the coupling constant is $h\lambda = MI_p\sqrt{\frac{\hbar\omega_r}{2L}}$. The total system is thus described by a Jaynes-Cummings type Hamiltonian $H = \frac{h}{2}(\varepsilon\sigma_z + \Delta\sigma_x) + \hbar\omega_r(a^\dagger a + \frac{1}{2}) + h\lambda\sigma_z(a^\dagger + a)$. We denote the state of the system by $|Q, i\rangle$ with the qubit either in the ground ($Q = g$) or excited ($Q = e$) state, and the oscillator in the Fock state ($i = 0, 1, 2, \ldots$). The parameters of the system can readily be engineered during fabrication; Δ is determined by α and the junction ω_r by L and C, and λ can be tuned by M.

We investigated the dynamics of the coupled system in the time domain. We performed a measurement cycle. We first excited the qubit and then brought the qubit and the LC oscillator into resonance where the exchange of a single energy quantum between the qubit and LC oscillator manifests itself as a vacuum Rabi oscillation $|e, 0\rangle \rightleftharpoons |g, 1\rangle$ (see Fig. 24.3). Figure 24.3f is a schematic of the pulse sequence. We start by fixing the qubit operating point far from the resonance point (point 3 in Fig. 24.3f) and prepare the qubit in the excited state by employing a π pulse. The π pulse is followed by a shift pulse, which brings the qubit into resonance with the LC oscillator. After the shift pulse the qubit and the LC

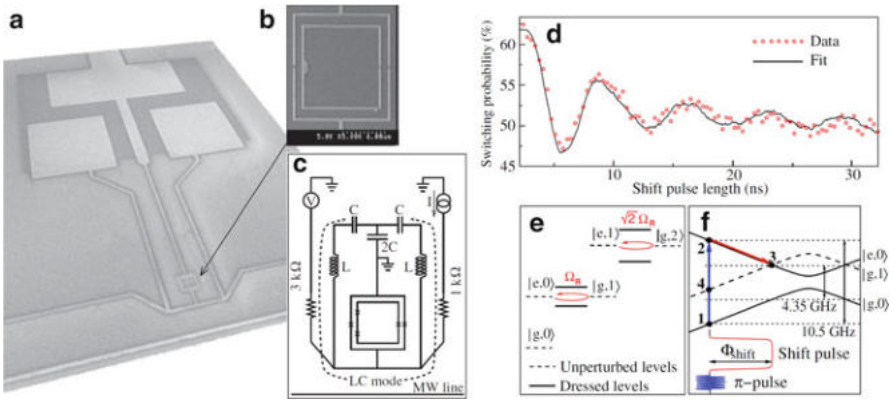

Fig. 24.3 (**a**) scanning electron micrograph of the sample. The square plates at the top of the picture are the top plates of the onchip capacitors separated by an insulator from the large bottom plate. (**b**) A close up of the qubit and the SQUID. (**c**) Equivalent circuit of the sample. The Josephson junctions are indicated by *crosses*: three in the inner qubit loop and two in the SQUID. The LC mode is indicated by the *dashed line*. The inductance and capacitances are calculated from the geometry to be $L = 140\,\text{pH}$ and $C = 10\,\text{pF}$, and the qubit LC oscillator mutual inductance to be $M = 5.7\,\text{pH}$. (**d**) Vacuum Rabi oscillations (*symbols*) and a numerical fit (*solid line*). (**e**) The few lowest unperturbed and dressed energy levels when the system is in resonance. (**f**) The qubit energy level diagram and pulse sequence for the vacuum Rabi measurements. The π pulse (4.6 ns long) on the qubit brings the system from state 1 to 2 and the shift pulse changes the flux in the qubit by ϕ_{shift}, which, in turn, changes the operating point from 2 to 3 where the system undergoes free evolution between $|e,0\rangle$ and $|g,1\rangle$ at the vacuum Rabi frequency Ω_R, until the shift pulse ends and the system returns to the initial operating point where the state is measured to be either in 2 or 4 (Reprinted with permission from Johansson et al. (2006). ©*American Physical Society.*)

oscillator are returned to off-resonance and the measurement pulse is employed to detect the state of the qubit. The rise time of our shift pulse, $\tau_{rise} = 0.8\,\text{ns}$, is adiabatic with respect to both the qubit and the oscillator, $\tau_{rise} > 1/E, 2\pi/\omega_r$, but nonadiabatic with respect to the coupling of the two systems, $\tau_{rise} < 1/\lambda$. Hence, when the system reaches the resonant point, it is in the state $|e,0\rangle$, which is not an eigenstate of the total Hamiltonian and therefore free evolution between the states $|e,0\rangle$ and $|g,1\rangle$ begins. The physics behind the vacuum Rabi oscillations is thus different from that of normal Rabi oscillations where the system is driven by an external classical field and oscillates between two energy eigenstates. Also, with normal Rabi oscillations the Rabi frequency is determined by the drive amplitude, whereas the vacuum Rabi oscillation frequency is determined solely by the intrinsic parameters of the system. The vacuum Rabi frequency obtained from the fits varies between 137 and 147 MHz, which is within the accuracy of the fitting (solid line in Fig. 24.3d).

24.2.4 Readout and Measurement Based Control via Josephson Bifurcation Amplifier

To realize quantum computation using superconducting qubits, we have to avoid quantum information loss caused by decoherence. A quantum error correction technique is a method we can employ to avoid quantum information loss. As regards quantum error collections, we should measure an ancillary qubit, and perform gate operations depending on the measurement result. So a qubit for quantum computing needs good controllability and a fast accurate readout method. The Hamiltonian of a superconducting qubit can be approximately described as a quantum two-level system: $H = \frac{h}{2}(\varepsilon\sigma_z + \Delta\sigma_x)$. We can control the ε value by applying an external magnetic field. By establishing magnetic coupling between a resonant microwave and a qubit, we can control the transition of the qubit. The $|L\rangle$ and $|R\rangle$ states are eigenstates of σ_z. These states correspond to the clockwise and anticlockwise supercurrent states on a superconducting loop. The supercurrent generates a small magnetic field, and we can measure the qubit state by detecting this magnetic field. In our experiments, we usually use a superconducting quantum interference device (SQUID) as a small magnetic field detector. The critical current of a SQUID depends on the magnetic field. A voltage will be induced, if the bias current exceeds the critical current. So by applying the optimum bias current, we can obtain information about the magnetic field by detecting the switching voltage of a SQUID. This method allows us to read a qubit state easily, but the measurement destroys the qubit state because the voltage state of a Josephson junction generates many quasi-particles. We cannot detect the qubit state until the quasi-particles disappear, so it is difficult to perform the fast readout needed for quantum error correction.

However, we can solve these problems by using another readout method, which employs the non-linearity of the superconducting circuit. A Josephson junction works as a non-linear inductor, and so the resonator, which includes a Josephson junction, also exhibits non-linearity. The resonance frequency of this non-linear resonator depends on the driving current. Specifically, when we apply a characteristic driving current to a non-linear resonator, a bistable state appears. The realization of coupling between a superconducting qubit and a superconducting non-linear resonator, allow us to choose the optimum driving condition where the convergent resonator states reflect the coupled qubit state. When we apply an optimum driving microwave, the resonance state bifurcates to one of the bistable states depending on the coupled qubit state. With this readout method we can measure a qubit state without quasi-particles appearing. This method is called Josephson bifurcation amplifier (JBA) readout, and known to be capable of quantum non-demolition (QND) measurement [3]. In principle this JBA readout method can perform QND measurements not only on superconducting qubits but also on spin ensemble systems. It is therefore a promising readout method for various types of quantum information processing.

We fabricated a co-planar waveguide resonator including a SQUID structure that exhibits non-linearity (Fig. 24.4). A measured superconducting flux qubit is

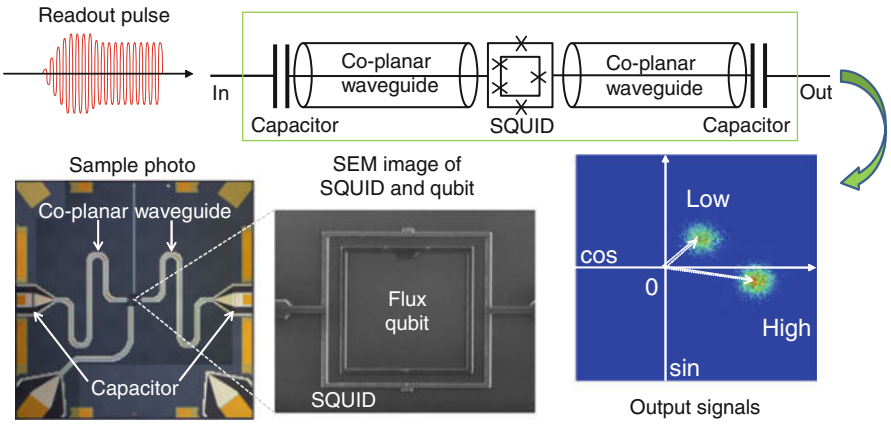

Fig. 24.4 A schematic image and sample photograph of our JBA sample. The co-planar waveguide is separated by capacitors. In the middle of the co-planar waveguide, we prepare a SQUID and a superconducting flux qubit. When we apply a microwave readout pulse, a bifurcation phenomenon occurs and a resonator state converges with the high or low amplitude state. Output signal shows high or low amplitude, and these amplitudes correspond to the qubit excited state or ground state

magnetically coupled to the SQUID. We input two pulses into a readout line, and then succeeded in reading out the qubit state, which was projected by the first pulse [4]. QND measurement has also been performed in superconducting qubit JBA readout systems [5]. This fast and low backaction readout method makes it possible to realize qubit state control depending on the readout result (measurement based control). This measurement-based control is the first step towards quantum error correction. The system has the characteristics required for a physical quantum computation system.

24.3 Single Spin, Photon and Charge Manipulation of NV Center in Diamond

24.3.1 NV Center in Diamond

Recently, nitrogen-vacancy (NV) defect centers in diamond (Fig. 24.5a) have attracted significant attention [15]. The NV center is a joint defect in the carbon lattice of diamond, which consists of a substitutional nitrogen atom and an adjacent vacancy. Its spin triplet (S = 1) ground state can be polarized and read out optically (Fig. 24.5b), so that electron-spin resonance experiments can be performed on a single spin under ambient conditions. A lot of important research has been carried out on the manipulation of single electron and nuclear spin. NV centers

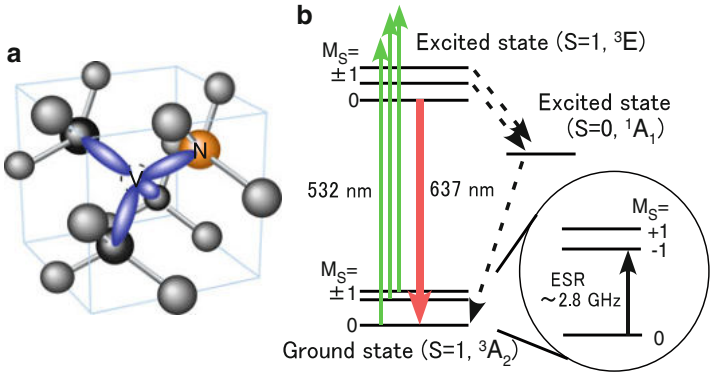

Fig. 24.5 (**a**) Atomic structure of NV center. (**b**) Energy levels of ground and excited states of the NV center

are thus promising candidates as solid-state room-temperature quantum bits and as quantum sensors with various applications in quantum information, magnetometry and biosensing.

The properties of the NV center make it an excellent candidate to play the role of a quantum interface. One important example of such a property is the quantum coupling between the flux qubit and the spin of the NV center [9]. Another example is the generation of entanglement between the spin and a photon [16]. In these studies, spin is expected to be used for quantum memory and processing. In the next section, we introduce the spin property of the NV center. In addition to those, we expect a role of quantum interface by using charge, which is very important from a viewpoint of electrical control of qubit. In Sect. 24.3.3, we will show the recent research about it.

24.3.2 Spin Coherence Time of NV Center

In the last decade, the coherence time T_2 of NV centers has been significantly increased [15]. In 2009, T_2 for a single NV center was reported to be 0.65 ms, which is, to the best of our knowledge, the longest room-temperature T_2 for a diamond with a natural abundance of ^{13}C (1.1 %) [17]. This extension of T_2 is attributed to the removal of nitrogen, and other impurities and defects by development of chemical vapour deposition (CVD). Given that $T_2 = 0.65$ ms is the longest coherence time available for high-quality diamond in which the impurities and defects have been removed, the next question becomes: what is the dominant mechanism that determines T_2 in this diamond. We will see how T_2 depends on the ^{13}C concentration [17, 18].

We analyzed T_2 for a diamond made by CVD and for a diamond with a ^{13}C concentration of 0.3 %. The T_2 of the electron spin was measured using two-pulse

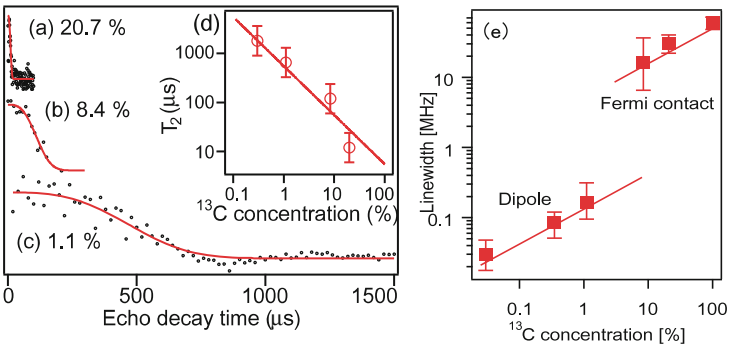

Fig. 24.6 Echo decays of electron spin in (**a**) 20.7 %, (**b**) 8.4 %, and (**c**) 1.1 % ^{13}C diamond. The microwave pulse sequence is $\pi/2$-τ-π-τ-$\pi/2$ where τ is the interpulse delay. *Red lines* are fits to $\exp(-(t/T_2)^3)$. (**d**) T_2 as a function of ^{13}C concentration n. The *solid line* is fitted with a $1/n$ dependence. (**e**) Inhomogeneous linewidth as a function of ^{13}C concentration

Hahn echo decay curves (see Fig. 24.6). The diamond with a ^{13}C concentration of 0.3 % was found to have an even longer T_2 of 1.8 ms [17, 18]. This is the longest T_2 at room temperature measured using a two-pulse Hahn echo technique. It is noteworthy that extension of T_2 to more than 2 ms ($T_2 > 2$ ms) has been reported in cases where measurement was instead performed using the dynamical decoupling technique [19]. T_2 is found to be inversely proportional to ^{13}C concentration, as shown in Fig. 24.6a–d. This benchmark may allow the observation of coherent coupling between spins separated by a few tens of nanometres. Single electron spins in the same isotopically engineered CVD diamond have been used to detect external magnetic fields with a sensitivity reaching 4 nT/$\sqrt{\text{Hz}}$ and with sub-nanometer spatial resolution [18]. It should be noted that the longest T_2 at room temperature is limited by T_1 of electron spin (∼6 ms) [20]. By decreasing temperature, T_1 can be extended, so $T_2 = 0.6$ s at 77 K for electron spin is reported [21].

The T_2 for nuclear spin is potentially much longer than that for electron spin. However, T_2 for nuclear spin states is measured to be approximately 6 ms because it is limited by T_1 for electron spin (∼6 ms) [22]. Recently, T_2 for nuclear spin was significantly extended to over 1 s by decoupling the single nuclear spin from its local environment [23]. In the experiments, the decoupling was performed using irradiation by a high-powered laser (532 nm, >10 mW). The report shows that the decoupling is caused by rapid ionization and deionization, the rate of which is proportional to the laser's intensity.

In addition to T_2, it is also important to elucidate upon T_2^* as a spin coherence property of the NV center. We measured T_2^*, the inhomogeneous electron spin resonance linewidth, and investigated a static interaction between the single NV electron spin and the environment for different ^{13}C concentrations. It was observed that with decreasing ^{13}C concentration, T_2^* increased, the linewidth narrowed as shown in Fig. 24.2e. In diamond with 0.03 % ^{13}C, an extremely long T_2^* of 30 μs was found. In the region of high ^{13}C concentration (>1.1 %), the linewidth of

electron spin appeared to be dominated by the hyperfine coupling of Fermi-contact interaction in ^{13}C. At low ^{13}C concentration, the linewidth appeared to be dominated by dipole-dipole interactions. Recently, T_2^* of more than 30 μs was reported in diamond with a natural abundance of ^{13}C [24], and one of more than 470 μs was reported in ^{12}C-enriched diamond [23]. Both measurements were taken under μ-metal shielded environments. The ^{12}C concentration of the latter sample is reported to be 99.99 % [23]. In Ref. [24], it was reported that T_2^* of NV centers depends upon the axial component of the magnetic field. T_2^* clearly attained a maximum when the applied axial magnetic field was reduced to zero.

24.3.3 Electrical Control of Single Photon Emission and Charge State in Single NV Center

Recently, significant progress in realizing highly efficient nonclassical light sources has been seen in semiconductor quantum dots. However, a major obstacle in semiconductor structures so far has been the cryogenic temperatures due to necessary to confine the carriers within the dots. Recently, we realized a stable room temperature electrically driven single-photon source based on the single NV center in diamond.

Diamonds were doped with large amounts of boron (B) and phosphorous (P) to create semiconducting properties. However, these implantations also caused color centers. Therefore, an extremely high quality undoped region (*i*-layer), in which the concentration of color centers was reduced to substantially less than 0.1 ppb (10^{13}/cm^3), was introduced into the structure, resulting in a *p*-*i*-*n* diamond diode, as shown in Fig. 24.7a. The NV centers were measured in the *i*-layer close to the edge of mesa structures. A homebuilt confocal microscope was used to address single defect centers. All experiments were conducted under ambient conditions. After the injection of current, electroluminescence (EL) was observed. The value of autocorrelation function at $\tau = 0$ ($g^{(2)}(0)$) was estimated to be 0.45, which confirms that the photon originated from single NV centers. From the EL spectrum, the charge was indicated to be in the neutral state (NV^0) [20].

Remarkably, the generation of EL follows fundamentally different kinetics than photoluminescence (PL) with intra-bandgap excitation. This fact, our analysis of dynamics, and the theoretical calculation suggest that EL is generated by electron-hole recombination at the defect [20]. Our results indicate that defects in diamond semiconductors can be used as stable room temperature electrically driven single-photon sources that are crucial for large-scale applications in quantum information technology.

In this research [20], we observed changes of charge state in PL spectra by injecting current in the *p*-*i*-*n* diode. Recently, it was reported that stochastic transitions between negatively charged NV (NV^-) and NV^0 are induced by laser illumination, surface termination, and combined optical and electrical operation. Fast and deterministic charge state control of single NV centers is essential for quantum

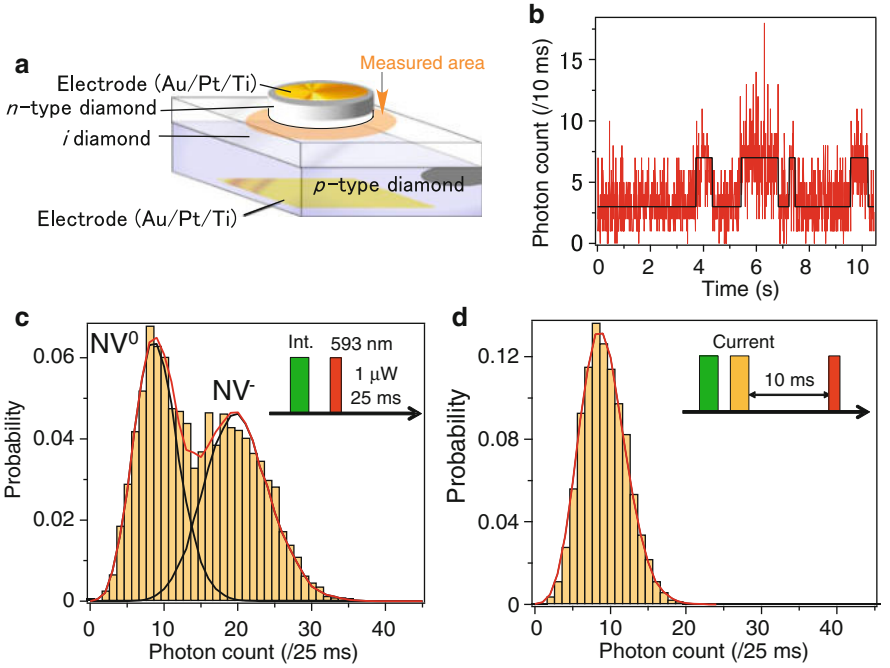

Fig. 24.7 Device structure and single-shot readout measurement of the charge states. (**a**) Schematic diagram of the single-photon-emitting diamond diode. (**b**) Time trace of the fluorescence of a single NV under continuous illumination with 593 nm, 1 μW laser light, showing the abrupt jumps between the two distinct states: high (NV^-) and low count rates (NV^0). (**c**) Histogram of photon counts during the 593 nm measurement pulse after illuminating the NV with 532 nm, 100 μW laser light for 20 ms. *Two solid black carves* are obtained by curve fitting of the Poisson distribution. The *red solid curve* is their sum. (**d**) Histogram of photon counts for the 593 nm measurement pulse, after illuminating the NV with a 532 nm laser and injecting a 0.1 mA current. The waiting time between the injected current and detection laser pulse (593 nm) is set at 10 ms

applications: for example, charge state stabilization improves qubit initialization and readout. Furthermore, stochastic charge state changes lead to spectral diffusion of the NV^- zero-phonon line, which is detrimental to the efficiency of two-photon quantum interference and related quantum communication applications. Stochastic, optically induced charge state switching using a high laser power ($\sim$5 MW/cm^2) can be exploited to decouple nuclear spins from the NV electron spin, yielding very long nuclear spin coherence times ($T_2 > 1$ s) in diamond at room temperature [23]. Potentially, the T_2 of the nuclear spin could be longer than 1 h; however, high-power laser illumination heats the diamond surface, which reduces T_2 [23]. In contrast, the electrical change in the charge state occurs in a single step, such as the capture or release of a carrier, which is important for control efficiency, heat suppression, and fast operation speeds (tens of MHz–GHz). Furthermore, electrical controls of carriers and charge of qubit are important for scalable and integrated devices, which are well investigated in quantum dot systems.

Recently, progress on the combined optical and electrical manipulation of charge states between NV^0 and possibly NV^+ of a single NV center and between NV^- and NV^0 of an NV ensemble has been reported. Grotz et al. reported the use of a diamond solution-gated field-effect transistor with a hydrogen-terminated p-type surface for the electrical manipulation of single NV centers [25]. Simultaneously, a 532 nm laser irradiation was applied, which causes fluorescence and prevents charge state identification. However, it was obvious that the laser application actually induced severe stochastic and ongoing charge state switching between NV^- and NV^0. Furthermore, this switching can lead to NV^0 fluorescence when NV^- is the stable charge state in the dark or vice versa. Consequently, extrapolating about the action of a purely electrical control is hardly possible because the displayed fluorescence spectra and concluded charge states are properties of a dynamic steady state under illumination and electrical control.

The charge state dynamics of the single NV center were investigated using time-resolved measurements and *nondestructive single-shot readouts* of the charge state [26]. In this measurement, illumination by a low-power 593 nm laser ($\sim$1 μW) allows the direct and nondestructive observation of the NV charge state. The fluorescence time trace of the single NV under such continuous illumination is shown in Fig. 24.7b. Abrupt varies between high and low count rates (NV^- and NV^0, respectively) are observed. By appropriately choosing both the power and the duration of the single laser pulse (593 nm), the number of fluorescence photons in this pulse allows the single-shot determination of the charge state. The histogram of the measurements shows two Poisson distributions corresponding to the fluorescence of NV^0 and NV^-. We repeated the single-shot charge state measurements 2,000 times to obtain each histogram shown in Fig. 24.7c–d.

After the laser was switched off, the charge state was measured using the 593 nm laser pulse. The obtained population ratio was $p_{eqNV-} : p_{eqNV^0} = 0.514 : 0.486$ as shown in Fig. 24.7c. We investigated the NV charge state after the application of the bare current injection (i.e., in the dark without simultaneous 532 nm illumination). The Poisson distribution peak of NV^- completely disappeared after the 0.1 mA current was injected (Fig. 24.7d), showings the deterministic electrical charge state control in the dark. We obtained the same results in the current range from 0.1 to 0.4 mA. Figures 24.7d shows nearly 100 % fidelity for the charge state initialization [26].

Furthermore, fast charge state switching rates (from negative to neutrally charged defects), greater than $0.72 \pm 0.10\,\mu s^{-1}$, were realized. In the non-operative mode, the realized charge states were stable for presumably much more than 0.45 s [26]. We believe that the results obtained are useful not only for ultrafast electrical control of qubits, long T_2 quantum memory, and quantum sensors associated with single NV centers but also for classical memory devices based on single atomic storage bits working under ambient conditions.

24.4 Superconducting Flux Qubit NV Center in a Diamond Hybrid Quantum System

During the past decade, research into superconducting quantum bits (qubits) based on Josephson junctions has made rapid progress. Many foundational experiments have been performed, and superconducting qubits are now considered one of the most promising systems for quantum information processing. However, the experimentally reported coherence times are likely to be insufficient for future large-scale quantum computation. A natural solution to this problem is a dedicated engineered quantum memory based on atomic and molecular systems. The question of whether coherent quantum coupling is possible between such natural systems and a single macroscopic artificial atom has attracted considerable attention since the first demonstration of macroscopic quantum coherence in Josephson junction circuits. In this subsection, we report evidence of coherent strong coupling between a single macroscopic superconducting artificial atom (a flux qubit) and an ensemble of electron spins in the form of nitrogen-vacancy color centers in diamond[9]. Furthermore, we have observed the coherent exchange of a single quantum of energy between a flux qubit and a macroscopic ensemble consisting of about 3×10^7 such color centers.

With the early successes of single-atom quantum state manipulation, research in quantum information processing with atomic systems has largely progressed independently from that using solid-state systems. In recent years, considerable effort has been devoted to coupling atomic and molecular systems to solid-state qubits to form hybrid quantum devices. Hybrid devices involving the integration of an ensemble of atomic spin systems with a transmission line resonator have been realized. Such schemes have the potential to couple superconducting solid-state qubits to optical fields via atomic systems, thus allowing quantum media conversion. The coupling strength, g, of an individual atomic system to one electromagnetic mode in a resonator circuit is usually too small for the coherent exchange of quantum information. However, the coupling strength of an ensemble of N such atomic systems will be enhanced by a factor of $\sqrt{N}$, making it possible to reach the strong-coupling regime ($g\sqrt{N} \gg \kappa$ and $g\sqrt{N} \gg \gamma$, where κ and γ are the respective damping rates of the resonator circuit and the atomic system). Of the many possible hybrid systems, coupling a flux qubit to a nitrogen-vacancy color center (NV^- center) in diamond is particularly appealing. First, the magnetic coupling strength between a flux qubit and a single NV^- center can be three orders of magnitude larger than that between a superconducting transmission line resonator and an NV^- center [27]. Second, the ground state of a NV^- center is a triplet ($S = 1$) owing to its C_{3V} symmetry (Fig. 24.5a). The $S = 1$ state $|m_s = 0\rangle$ is separated by 2.88 GHz from the excited states $|m_s = \pm1\rangle$ under zero magnetic field (Fig. 24.5b). This energy separation is ideal in terms of allowing a quantum-level-tunable flux qubit to be brought into and out of resonance with it.

24.4.1 Preparation of NV Center in Diamond

A sample of diamond containing NV^- centers was prepared by the ion implantation of $^{12}C^{2+}$ at 700 keV in a high vacuum into single-crystal, type-1b diamond synthesized under high pressure and at high temperature (HPHT) and with a (001) surface orientation. The $^{12}C^{2+}$ ions, implanted with a surface density of $3 \times 10^{13}\,cm^{-2}$, were stopped at a depth of about 600 nm. This generated vacancies with a concentration of about $5 \times 10^{18}\,cm^{-3}$ over a depth of $\sim$0.7 μm. After implantation, the crystals were annealed at 900 °C in a vacuum for 3 $\sim$ 10 h. This high-dose carbon implantation method enhances the NV^- center yield. Photoluminescence optical spectroscopy established that NV^- centers were generated with a concentration of $\sim 1.1 \times 10^{18}\,cm^{-3}$ over a depth of 1 μm [9].

24.4.2 Coherent Coupling Between Flux Qubit and NV Spin Ensemble

The total Hamiltonian of the coupled system is

$$H = \frac{h}{2}(\Delta\sigma_x + \epsilon\sigma_z) + h\sum_i (DS_{z,i}^2 + E(S_{x,i}^2 - S_{y,i}^2)) + \frac{h}{2}\sum_i g_i \sigma_z S_{x,i}, \qquad (24.2)$$

where i runs over the NV^- centers that couple to the flux qubit. The corresponding coupling constant can be estimated using the Biot-Savart law as $g_i \approx 8.8$ kHz [9]. In this set-up, the $|m_s = \pm 1\rangle$ states of the electronic spin are nearly degenerate so our flux qubit couples to the $|0\rangle \leftrightarrow \frac{1}{\sqrt{2}}[|-1\rangle + |+1\rangle]$ transition.

From the spectroscopic measurements, a clear anticrossing was observed (Fig. 24.8b) near the degeneracy point of the flux qubit, whereas no such gap was observed in the same flux qubit before mounting the NV-diamond crystal (Fig. 24.3a, inset). We also note a narrow resonance, with a width of less than 1 MHz, at 2.878 GHz near this anticrossing. This resonance is evidence of a collective dark state in the NV^--ensemble [11]. In Sect. 24.4.4, we will focus on this dark state in detail. From the high-resolution spectrum, a vacuum Rabi splitting near $2g_{ens} \simeq 70$ MHz was clearly observed, confirming strong coupling (two broad resonance peaks are present in the cross-sectional view) between the flux qubit and the NV^--ensemble. The ensemble can be seen as an effective harmonic oscillator strongly coupled to the flux qubit. Next, from the measured vacuum Rabi splitting and our calculated g_i, we estimate the number of NV^- centers in the coupled ensemble to be $N \sim g_{ens}^2/2g^2 \approx 3.2 \times 10^7$, where the factor of 2 in the denominator is due to the twofold degeneracy of the excited states $|\pm 1>_i$ of an NV^- center. This estimate gives reasonable agreement with the density of NV^- centers measured by using photoluminescence spectroscopy for the whole sample ($1.1 \times 10^{18}\,cm^{-3}$) multiplied by the volume of centers coupling to the flux qubit

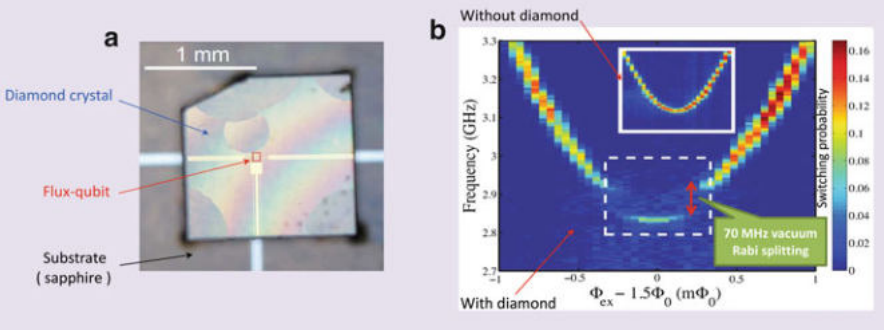

Fig. 24.8 Experimental set-up of an NV diamond sample attached to a flux qubit system. (**a**) Diamond crystal glued on top of a flux qubit (*red box*). (**b**) Energy spectrum of a flux qubit coupled to an NV-ensemble. Resonant frequencies indicated by the SQUID detector switching probability (when a 500-ns microwave pulse excites the system before the read-out pulse) versus the external magnetic flux, $\phi_{ex} = \phi_m + \phi_\alpha/2$, where ϕ_m and ϕ_α are the fluxes through the qubit main loop and the qubit a-loop, respectively. *Inset*, spectrum over the same region before the diamond crystal was mounted

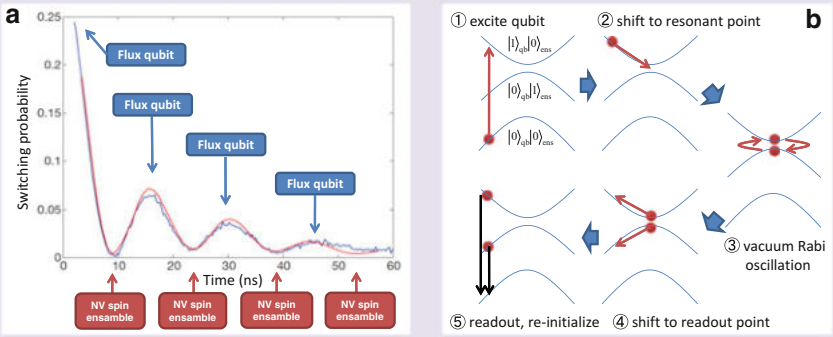

Fig. 24.9 (**a**) Vacuum Rabi oscillations of the flux qubit/NV$^-$ ensemble coupled system. (**b**) measurement sequence

($40\,\mu m^2$ (area) $\times\, 0.7\,\mu m$ (effective thickness)). This spectroscopy approach gives the number of coupled centers as $\sim 3 \times 10^7$.

Next we investigated the dynamics of our system in the time domain, using a measurement cycle similar to that used in systems of qubits coupled with LC (inductor-capacitor) resonators (Fig. 24.9b). We first excited the flux qubit and then brought it into resonance with the NV$^-$-ensemble. Single-energy quantum exchange between the flux qubit and the NV$^-$-ensemble at resonance manifests itself as the vacuum Rabi oscillations $|1\rangle_{qb}|0\rangle_{ens} \rightleftharpoons |0\rangle_{qb}|1\rangle_{ens}$ where $|0\rangle_{qb}$ and $|1\rangle_{qb}$ are respectively the ground and excited states of the qubit; $|0\rangle_{ens} = |00\cdots0\rangle$ is the ground state of the ensemble, with each individual NV$^-$ center in the state $|m_s = 0\rangle$; and $|1\rangle_{ens}$ is the Dicke state of the spin ensemble with one excitation, written as

$|1\rangle_{ens} = (\frac{1}{\sqrt{N}}) \sum_i S_{+,i}|00\cdots0\rangle$. Here the operator $S_{+,i} = (\frac{1}{\sqrt{2}})(|1\rangle_i\langle 0|_i + |-1\rangle_i\langle 0|_i)$ excites the ith NV^- spin into a superposition of states $|1\rangle$ and $|-1\rangle$. Figure 24.9a shows vacuum Rabi oscillations between the flux qubit and the ensemble of electronic spins at the 2.878-GHz resonance. However, the decay time of the oscillations is approximately 20 ns. This is much shorter than the relaxation times of both the flux qubit ($T_{1,qb} < 150$ ns) and the NV^--ensemble ($T_{1,NV} \gg 10\,\mu$s). We cannot improve the vacuum Rabi decay time even by tuning the qubit degeneracy point closer to the NV^- resonance frequency. As we tune the flux qubit away from the 2.878-GHz resonance, by changing ϕ_m, the coherence time associated with this measurement scheme becomes considerably longer. From these results, we conclude that there is a strong source of dephasing of unknown origin in the system near resonance.

24.4.3 Quantum Memory Operations in the Hybrid Quantum System

In the previous section we showed how vacuum Rabi oscillations could be experimentally realized in a hybrid quantum system [9]. However, we could not store quantum information in the NV center ensemble at that stage as its coherence time was too short. The origin of this decoherence was primarily the inhomogeneous broadening of the centers stemming from internal magnetic field fluctuation and strain distribution in the diamond crystal. To reduce the former effect, we prepared a diamond with a lower NV center concentration of $4.7 \times 10^{17}\,\mathrm{cm}^{-3}$, which reduces the dipole interaction between electron spins, NV centers and P1 centers (substitutional nitrogen defect atoms). To further reduce the latter effect, we then applied an in-plane magnetic field of 2.6 mT along the [100] crystal axis of the diamond. This magnetic field lifts the degeneracy between the $|\mathrm{m_s} = \pm 1\rangle$ energy levels, causing a Zeeman splitting of approximately 80 MHz. Under this condition, the Zeeman term of the NV spin becomes dominant and the strain effect is greatly reduced.

Given that our flux qubit can only couple to one transition at a time ($|0\rangle \leftrightarrow |+1\rangle + |-1\rangle$ for instance when there is no applied magnetic field), the splitting of the NV spin ensemble into two by the magnetic field therefore reduces the collective coupling strength by a factor of $1/\sqrt{2}$, but a longer coherence time would be expected. To utilize one of the two new ensemble transitions ($|0\rangle \leftrightarrow |+1\rangle$ or $|0\rangle \leftrightarrow |-1\rangle$) for our quantum memory operations we tuned our qubit gap frequency $\Delta/2\pi$ to 2.92 GHz corresponding to the NV center transition between $|0\rangle$ and $|+1\rangle$. We have observed a clear vacuum Rabi splitting of 18 MHz in the spectrum of the hybrid system (not shown) confirming strong coupling between the flux qubit and the NV ensemble. The possibility now exists of storing quantum information in the ensemble.

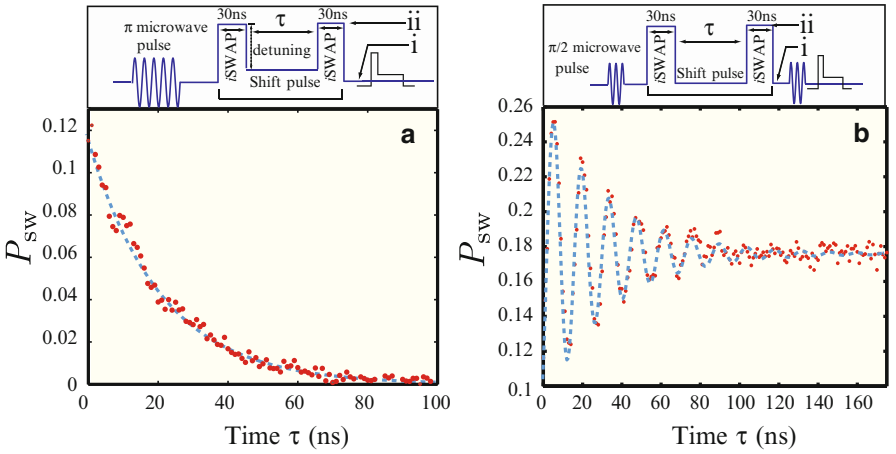

Fig. 24.10 Quantum memory operations for (**a**) a single excitation and (**b**) an equal superposition state. The *upper panels* represent the pulse sequences for the memory operations

The first step in demonstrating the memory capabilities of NV centers is the storage of a single quantum excitation in a spin ensemble (memory). The pulse sequence, depicted in the upper panel of Fig. 24.10a, shows how to transfer the qubit excited state $|1\rangle_{qb}|0\rangle_{ens}$ to the memory $|0\rangle_{qb}|1\rangle_{ens}$, store it there for a time τ and then retrieve it. Here $|0\rangle_{ens}$ is the ground state of the ensemble while $|1\rangle_{ens}$ is a single excitation spread collectively over all the electron spins in the ensemble. This is a very similar pulse sequence to the one we used to observe the vacuum Rabi oscillations in the previous section. The main difference is that we replace the shift pulse inducing the oscillation with two iSWAP pulses separated by time τ. The length of the iSWAP pulse is half that of the vacuum Rabi period. We can thus use this pulse sequence to transfer a single excitation from the qubit to the ensemble memory, store it for a time and later retrieve it. Figure 24.10a shows the switching probability (proportional to the population in the qubit excited state) as a function of the storage time τ [10]. We observed the expected monotonic decay curve, which means that the information was successfully stored in the memory independently of the qubit. The memory time of this excitation was estimated to be $T^*_{1ens} = 20.8 \pm 0.7$ ns by fitting a simple exponential to this curve.

The next essential step is to demonstrate the storage of phase information for a quantum state. For this purpose, first we prepare our flux qubit in the superposition state $(1/\sqrt{2})(|0\rangle_{qb} + |1\rangle_{qb})|0\rangle_{ens}$ by applying a $\pi/2$ pulse to the qubit (the upper panel in the Fig. 24.10b). Then we perform the memory operation as described above. We next employ a $\pi/2$ pulse to transfer the phase information of the qubit superposition state to the population information. Finally, the qubit excited state population is read out. Such a sequence corresponds to a Ramsey fringe experiment for the spin ensemble and enables us to estimate the memory time of the phase

information $T^*_{2\mathrm{ens}}$. The fitting of an exponential decaying sinusoid to the data in Fig. 24.10b yields $T^*_{2\mathrm{ens}} = 33.6 \pm 2.3$ ns [10] (similar to [28]).

Although the memory times are shorter than the flux qubit coherence time of 150 ns, these results demonstrate convincingly that we can store population and phase information, namely an arbitrary quantum state, in the spin ensemble. This is a significant step towards the realization of a long-lived quantum memory for superconducting flux qubits.

24.4.4 Observation of a Dark State with a Hybrid System Consisting of a Superconducting Flux Qubit and an Electron Spin Ensemble in Diamond

Although we have demonstrated quantum memory operations in our superconductor diamond hybrid system, the quantum memory lifetime was very short, at around 20 ns [10]. This is shorter than that of a flux qubit at 150 ns. For practical quantum information processing applications, the lifetime of the quantum memory must be increased by at least several orders of magnitude. Our previously reported experiments were limited by randomized magnetic fields from the spin bath of the substituted nitrogen atom (P1 center). This can of course be further suppressed if we use single crystal diamond with a lower P1 center density [9, 10, 29]. However, reducing the P1 center density has a significant drawback since it also reduces the number of NV centers in the diamond and so reduces the collective coupling strength between the flux qubit and the ensemble. The coupling strength could be maintained in two ways, either by reducing the distance between the flux qubit and the ensemble or by increasing the persistent current of the flux qubit. Both approaches are challenging and so it is natural to look for alternative ways of improving the lifetime of the NV center ensemble.

Interestingly, a narrow resonance of unknown origin was observed in the first spectroscopy experiments with a superconductor diamond hybrid system under zero external magnetic field [9, 29]. The line-width of this peak was much smaller than that of the states that we used for quantum memory operation [10]. Given that a narrow resonance implies a long lifetime, the state associated with this resonance could be an attractive candidate for a quantum memory. However, the origin of such a peak was not investigated during the first experiments. If it is to be a candidate for a longer-lived quantum memory, it is essential to understand the origin of such a state.

We have investigated this sharp resonance both experimentally and theoretically [11] to understand its nature. A theoretical model [11] was developed to reproduce the experimental spectroscopy results of coupling the flux qubit to an ensemble containing $\sim 10^7$ NV centers including the effects of the inhomogeneous broadening of the NV centers caused by randomized magnetic fields, strain distributions in the diamond crystal, and fluctuations of the zero-field splitting (models for the earlier

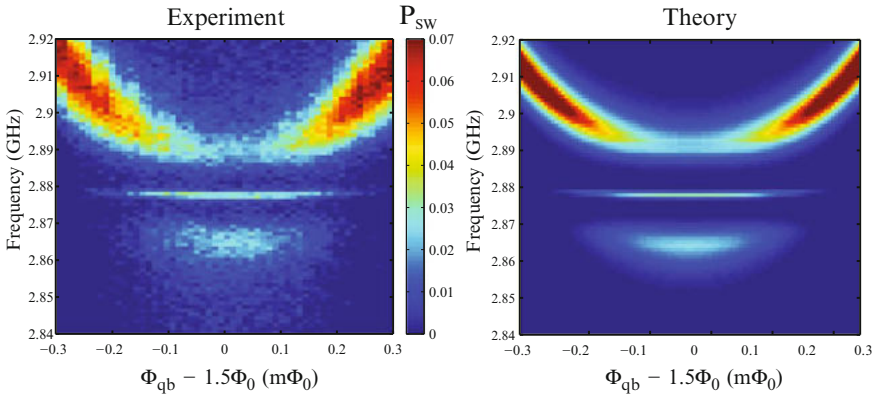

Fig. 24.11 Spectroscopy of the flux qubit coupled with the ensemble of NV centers with a zero magnetic field, indicated by the switching probability of the SQUID detector. The horizontal axis denotes an applied magnetic flux, and the vertical axis denotes the frequency of the microwave driving signal. We have observed a vacuum Rabi splitting of 28 MHz, and also a sharp resonance in the middle of the vacuum Rabi splitting

experiments did not include all these effects [27, 29–33]). In Fig. 24.11, we show the experimentally obtained spectroscopy results and the results obtained with our theoretical model. The results were in excellent agreement.

We have shown how the sharp resonance observed in the middle of the vacuum Rabi splitting is strong evidence of a collective dark state [11]. Since the NV centers have a spin 1 structure, both a bright state and dark state naturally exist. As there is significant hybridization between the flux qubit and the bright state via the collective enhancement, the flux qubit cannot be directly coupled with the dark state of the NV center due to the destructive interference of the phase of the dark state. However, owing to the perturbations caused by the environmental magnetic field and the diamond strain, the destructive interference of the dark state is weakened and a non-negligible coupling with the flux qubit can occur. Such a coupling provides us with a detectable resonance from the dark state in the spectroscopy results. The lifetime of this dark state is estimated from the width of the peak at around 150 ns, which is much larger than that of the bright state (20 ns). This clearly shows the robustness of the dark states against inhomogeneous broadening. Therefore, our results have opened a possible new way of realizing a long-lived quantum memory for hybrid system based quantum information processing.

24.5 Conclusions

The twentieth century saw the discovery of quantum mechanics, a set of principles describing physical reality at the atomic level of matter. These principles have been used to develop much of today's advanced technology, including, for example,

microprocessors. Quantum physics also allows a new paradigm for the processing of information known as quantum information processing. Over the last decade there has been a huge worldwide effort to develop and explore quantum information based devices and technologies. Devices for quantum key distribution (1-bit devices) are already commercially available. The challenge is now to design and build larger scale devices. No single approach seems to be able to address all the problems. The development of electronic technologies based on the principles of quantum mechanics, such as quantum computing, requires the coupling and integration of quantum objects of various kinds on the same electronic chip, namely a hybrid approach[34]. For such integration to succeed, each object needs to be among the best in its class.

The hybrid system approach is very powerful, as shown by our previous demonstration of coherent coupling between a superconducting qubit and NV centers in diamond [9–11]. Superconducting flux (or persistent current) qubits are an excellent choice among superconducting qubits. This is because their magnetic flux produced by the current circulating in the loop, couples directly to quantum magnets (atomic spins) that either exist in crystals or are artificially induced in them. Superconducting qubits are excellent devices for the fast processing of information but they have short coherences times. NV centers on the other hand have long coherence times but it is difficult to make them interact with one another [17, 22, 23]. This hybrid combination thus has the potential to provide a device, that can process information rapidly but also store it for a long time.

Furthermore, NV centers have an optical transition that could allow us to bridge the microwave and optical worlds. This opens up new fields of science and technology. We could use optical fields to indirectly control our flux qubits and even read them out. Alternatively, we could take information stored in the microwave regime, convert it to optical information, and transmit it to remote locations (some that would be totally impossible if one stays in the microwave regime). The potential here is enormous and ground breaking.

This work was supported by the Funding Program for World-Leading Innovative R&D on Science and Technology (FIRST Program) initiated by the Council for Science and Technology Policy (CSTP), Scientific Research of Specially Promoted Research (grant no.18001002) by MEXT, a Grant-in-Aid for Scientific Research on Innovative Areas (grant no.22102502), Scientific Research (A) grant no. 22241025, and Scientific Research (S) grant no. 25220601 from the Japanese Society for the Promotion of Science (JSPS).

References

1. J. Clarke, F.K. Wilhelm, Superconducting quantum bits. Nature **453**, 1031–1042 (2008)
2. J. Johansson, S. Saito, T. Meno, H. Nakano, M. Ueda, K. Semba, H. Takayanagi, Vacuum Rabi oscillations in a macroscopic superconducting qubit LC oscillator system. Phys. Rev. Lett. **96**, 127006 (2006)

3. I. Siddiqi, R. Vijay, F. Pierre, C.M. Wilson, M. Metcalfe, C. Rigetti, L. Frunzio, M.H. Devoret, RF-driven Josephson bifurcation amplifier for quantum measurement. Phys. Rev. Lett. **93**, 207002 (2004)
4. K. Kakuyanagi, S. Kagei, R. Koibuchi, S. Saito, A. Lupaşcu, K. Semba, H. Nakano, Experimental analysis of the measurement strength dependence of superconducting qubit readout using a Josephson bifurcation readout method. New J. Phys. **15**, 043028 (2013)
5. A. Lupaşcu, S. Saito, T. Picot, P.C. de Groot, C.J.P.M. Harmans, J.E. Mooij, Quantum non-demolition measurement of a superconducting two-level system. Nat. Phys. **3**, 119–123 (2007)
6. F.G. Paauw, A. Fedorov, C.J.P.M. Harmans, J.E. Mooij, Tuning the gap of a superconducting flux qubit. Phys. Rev. Lett. **102**, 090501 (2009)
7. X. Zhu, A. Kemp, S. Saito, K. Semba, Coherent operation of a gap-tunable flux qubit. Appl. Phys. Lett. **97**, 102503 (2010)
8. F. Yoshihara, Y. Nakamura, F. Yan, S. Gustavsson, J. Bylander, W.D. Oliver, J.S. Tsai, Flux qubit noise spectroscopy using Rabi oscillations under strong driving conditions. Phys. Rev. B **89**, 020503(R) (2014)
9. X. Zhu, S. Saito, A. Kemp, K. Kakuyanagi, S. Karimoto, H. Nakano, W.J. Munro, Y. Tokura, M. Everitt, K. Nemoto, M. Kasu, N. Mizuochi, K. Semba, Coherent coupling of a superconducting flux qubit to an electron spin ensemble in diamond. Nature **478**, 221–224 (2011)
10. S. Saito, X. Zhu, R. Amsüss, Y. Matsuzaki, K. Kakuyanagi, T. Shimo-Oka, N. Mizuochi, K. Nemoto, W.J. Munro, K. Semba, Towards realizing a quantum memory for a superconducting qubit: storage and retrieval of quantum states. Phys. Rev. Lett. **111**, 107008 (2013)
11. X. Zhu, Y. Matsuzaki, R. Amsüss, K. Kakuyanagi, T. Shimo-Oka, N. Mizuochi, K. Nemoto, W.J. Munro, K. Semba, S. Saito, Observation of dark states in a superconductor diamond quantum hybrid system. Nat. Commun. **5**, 3424 (2014)
12. J.E. Mooij, T.P. Orlando, L. Levitov, L. Tian, C.H. van der Wal, S. Lloyd, Josephson persistent-current qubit. Science **285**, 1036–1039 (1999)
13. T.P. Orlando, J.E. Mooij, L. Tian, C.H. van der Wal, L.S. Levitov, S. Lloyd, J.J. Mazo, Superconducting persistent-current qubit. Phys. Rev. B **60**, 15398–15413 (1999)
14. J. Bylander, S. Gustavsson, F. Yan, F. Yoshihara, K. Harrabi, G. Fitch, D.G. Cory, Y. Nakamura, J.S. Tsai, W.D. Oliver, Noise spectroscopy through dynamical decoupling with a superconducting flux qubit. Nat. Phys. **7**, 565–570 (2011)
15. M.W. Dohert, N.B. Manson, P. Delaney, F. Jelezko, J. Wrachtrup, L.C.L. Hollenberg, The nitrogen-vacancy colour centre in diamond. Phys. Rep.-Rev. Sect. Phys. Lett. **528**, 1–45 (2013)
16. E. Togan, Y. Chu, A.S. Trifonov, L. Jiang, J. Maze, L. Childress, M.V.G. Dutt, A.S. Sørensen, P.R. Hemmer, A.S. Zibrov, M.D. Lukin, Quantum entanglement between an optical photon and a solid-state spin qubit. Nature **466**, 730 (2010)
17. N. Mizuochi, P. Neumann, F. Rempp, J. Beck, V. Jacques, P. Siyushev, K. Nakamura, D. Twitchen, H. Watanabe, S. Yamasaki, F. Jelezko, J. Wrachtrup, Coherence of single spins coupled to a nuclear spin bath of varying density. Phys. Rev. B **80**, 041201(R) (2009)
18. G. Balasubramanian, P. Neumann, D. Twitchen, M. Markham, R. Kolesov, N. Mizuochi, J. Isoya, J. Achard, J. Beck, J. Tissler, V. Jacques, F. Jelezko, J. Wrachtrup, Ultralong spin coherence time in isotopically engineered diamond. Nat. Mater. **8**, 383 (2009)
19. L.M. Pham, N. Bar-Gill, C. Belthangady, D. Le Sage, P. Cappellaro, M.D. Lukin, A. Yacoby, R.L. Walsworth, Enhanced solid-state multispin metrology using dynamical decoupling. Phys. Rev. **86**, 045214 (2012)
20. N. Mizuochi, T. Makino, H. Kato, D. Takeuchi, M. Ogura, H. Okushi, M. Nothaft, P. Neumann, A. Gali, F. Jelezko, J. Wrachtrup, S. Yamasaki, Electrically driven single photon source at room temperature in diamond. Nat. Photonics **6**, 299–303 (2012)
21. N. Bar-Gill, L.M. Pham, A. Jarmola, D. Budker, R.L. Walsworth, Solid-state electronic spin coherence time approaching one second. Nat. Commun. **4**, 1743 (2013)
22. P. Neumann, N. Mizuochi, F. Rempp, P. Hemmer, H. Watanabe, S. Yamasaki, V. Jacques, T. Gaebel, F. Jelezko, J. Wrachtrup, Multipartite entanglement among single spins in diamond. Science **320**, 1326 (2008)

23. P.C. Maurer, G. Kucsko, C. Latta, L. Jiang, N.Y. Yao, S.D. Bennett, F. Pastawski, D. Hunger, N. Chisholm, M. Markham, D.J. Twitchen, J.I. Cirac, M.D. Lukin, Room-temperature quantum bit memory exceeding one second. Science **336**, 1283 (2012)
24. F. Dolde, H. Fedder, M.W. Doherty, T. Nobauer, F. Rempp, G. Balasubramanian, T. Wolf, F. Reinhard, L.C.L. Hollenberg, F. Jelezko, J. Wrachtrup, Electric field sensing using single diamond spins. Nat. Phys. **7**, 459 (2011)
25. B. Grotz, M.V. Hauf, M. Dankerl, B. Naydenov, S. Pezzagna, J. Meijer, F. Jelezko, J. Wrachtrup, M. Stutzmann, F. Reinhard, J.A. Garrido, Charge state manipulation of qubits in diamond. Nat. Commun. **3**, 729 (2012)
26. Y. Doi, T. Makino, H. Kato, D. Takeuchi, M. Ogura, H. Okushi, H. Morishita, T. Tashima, S. Miwa, S. Yamasaki, J. Wrachtrup, Y. Suzuki, N. Mizuochi, Deterministic electrical charge state initialization of single nitrogen-vacancy center in diamond. Phys. Rev. X **4**, 01107 (2014)
27. D. Marcos, M. Wubs, J.M. Taylor, R. Aguado, M.D. Lukin, A.S. Sørensen, Coupling nitrogen-vacancy centers in diamond to superconducting flux qubits. Phys. Rev. Lett. **105**, 210501 (2010)
28. Y. Kubo, I. Diniz, A. Dewes, V. Jacques, A. Dréau, J.-F. Roch, A. Auffeves, D. Vion, D. Esteve, P. Bertet, Storage and retrieval of a microwave field in a spin ensemble. Phys. Rev. A **85**, 012333 (2012)
29. Y. Kubo, F.R. Ong, P. Bertet, D. Vion, V. Jacques, D. Zheng, A. Dréau, J.-F. Roch, A. Auffeves, F. Jelezko, J. Wrachtrup, M.F. Barthe, P. Bergonzo, D. Esteve, Strong coupling of a spin ensemble to a superconducting resonator. Phys. Rev. Lett. **105**, 140502 (2010)
30. I. Diniz, S. Portolan, R. Ferreira, J.M. Gérard, P. Bertet, A. Auffeves, Strongly coupling a cavity to inhomogeneous ensembles of emitters: potential for long-lived solid-state quantum memories. Phys. Rev. A **84**, 063810 (2011)
31. R. Houdré, R.P. Stanley, M. Ilegems, Vacuum-field Rabi splitting in the presence of inhomogeneous broadening: resolution of a homogeneous linewidth in an inhomogeneously broadened system. Phys. Rev. A **53**, 2711 (1996)
32. A. Imamoğlu, Cavity qed based on collective magnetic dipole coupling: spin ensembles as hybrid two-level systems. Phys. Rev. Lett. **102**, 083602 (2009)
33. J.H. Wesenberg, A. Ardavan, G.A.D. Briggs, J.J.L. Morton, R.J. Schoelkopf, D.I. Schuster, K. Mølmer, Quantum computing with an electron spin ensemble. Phys. Rev. Lett. **103**, 070502 (2009)
34. Z.-L. Xiang, S. Ashhab, J.Q. You, F. Nori, Hybrid quantum circuits: superconducting circuits interacting with other quantum systems. Rev. Mod. Phys. **85**, 623–653 (2013)

Part VII
Semiconductor and Molecular Spin Qubits

Chapter 25
Spin Qubits with Semiconductor Quantum Dots

Seigo Tarucha, Michihisa Yamamoto, Akira Oiwa, Byung-Soo Choi, and Yasuhiro Tokura

25.1 Spin Qubit Made of Quantum Dots

The research aiming the manipulation of the individual electrons in semiconductor quantum dots (QDs) starts about 25 years ago when the single electron tunneling phenomena had been discovered. Initial QDs had contained many and uncertain numbers of electrons. Various improvements of fabrication technologies and electrical manipulation have enabled the first report of the precise control of the electron numbers starting from zero to one, two, and so on in 1996 [43]. In addition to the control of numbers, the electronic states of quantum mechanical confinement and spin states were steered with the precision as if for real atoms (artificial atom) [20]. In 1998, a new architecture of quantum computing was proposed using the electron spins in such QDs by purely electrical means [23]. Subsequent findings of very long spin relaxation time [8], control of the exchange coupling of pairs of neighboring spins in adjacent QDs [12], and the discovery of Pauli spin blockade, which is now used to initialize and read-out spins [31] have triggered the active field of electron spin qubits [24, 42]. First demonstration of electrically controlled single spin qubit

S. Tarucha (✉) • M. Yamamoto • B.-S. Choi
Department of Applied Physics, University of Tokyo, Hongo, Bunkyo-ku, Tokyo 113-8656, Japan
e-mail: tarucha@ap.t.u-tokyo.ac.jp

A. Oiwa
The Institute of Scientific and Industrial Research, Osaka University, Mihogaoka, Ibaraki, Osaka 567-0047, Japan

Y. Tokura
Graduate School of Pure and Applied Sciences, University of Tsukuba, 1-1-1 Tennodai, Tsukuba, Ibaraki 305-8571, Japan
e-mail: tokura.yasuhiro.ft@u.tsukuba.ac.jp

Y. Yamamoto, K. Semba (eds.), *Principles and Methods of Quantum Information Technologies*, Lecture Notes in Physics 911, DOI 10.1007/978-4-431-55756-2_25

was reported in 2005 [32] and after a while, two spin qubits and the control of their entanglement were realized [4, 39]. Coherent control of single qubit and entangling two qubits are fundamental elements of quantum algorithm, and now the research of quantum computing with spins is shifting to the proof of various algorithms with error corrections and fault tolerant large scale quantum computing.

In parallel, rapid developments of various quantum technologies other than quantum computing have been witnessed. For example, quantum interface between single photons and single spins, which will be an indispensable ingredient of quantum repeaters, solid state quantum optics experiments including single electron generation and beam splitters, and the coupling of microwave photons in a superconducting cavity circuit and electron spins.

This section summarizes the progress of electrical manipulation of electron spins in quantum dots, based on our recent researches. Section 25.2 briefly summarizes the initialization and detection of spin states. Coherent manipulation of individual electron spins is discussed in Sect. 25.3 and two spin operations are in Sect.25.4. Section 25.5 is on the architecture for spin-qubit quantum computers considering the scalability and other techniques for manipulating single electrons are discussed in Sect. 25.6. Finally, Sect. 25.7 is the conclusion.

25.2 Electron Spin Initialization and Detection

The electron spins in quantum dots are protected from various environmental disturbances and can be assumed an ideal carrier of useful information, especially, a quantum bit of information, or qubit for short. The two basis states of a spin $1/2$ electron are $|\uparrow\rangle$ and $|\downarrow\rangle$, which can be decoded into a classical bit "0" and "1" – e.g. magnetic moments in hard drives. In contrast to classical bits, an electron can be brought to a state, $|\psi\rangle = \alpha\,|\uparrow\rangle + \beta\,|\downarrow\rangle$ with two complex numbers α, β satisfying $|\alpha|^2+|\beta|^2 = 1$, where its spin points in two opposite directions simultaneously. This section discusses the important ingredients of quantum computation, initialization and reading of individual spins.

The basic strategy for the detection of single spins is *spin-charge-convergence*, where we utilize high sensitive charge or current measurements combined with spin dependent tunneling mechanisms. Under a large magnetic field where Zeeman energy is much larger than thermal energy, the tunneling probability is spin dependent when the chemical potential of the reservoir locates in-between the Zeeman splitted levels. When the higher energy spin sub-level, say the spin down state in a negative g-factor material, is occupied, tunneling-out processes to the reservoir are allowed. In contrast, if the spin up state, the ground state, is occupied, the tunneling-out process is energetically unfavored. This change of charge states can be detected using high-speed high-sensitivity charge detector using quantum point contact (QPC) or near-by QD [7]. Another method utilizes series QD system, where one to two electron charge states are available under finite bias condition.

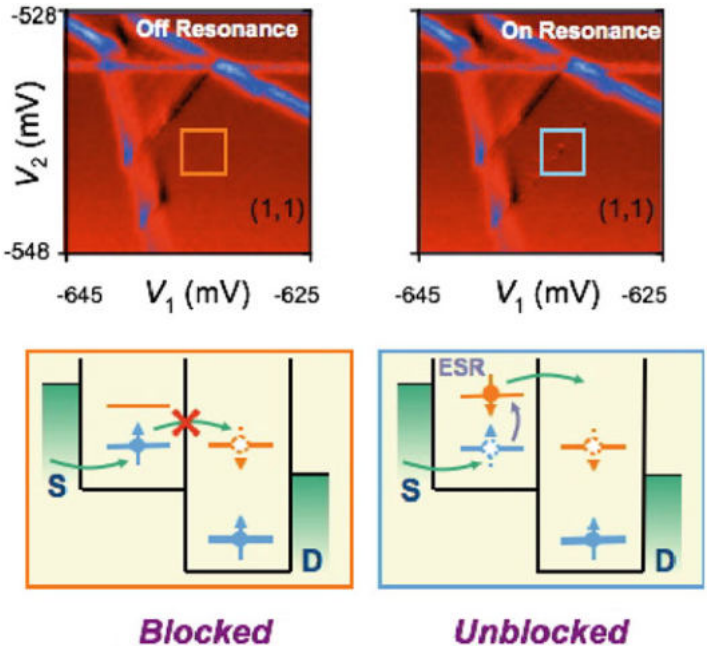

Fig. 25.1 Example of charge stability diagrams of coupled QDs near (1, 1) charge states, where (N_L, N_R) represents the number of the charge in the left and right QD respectively. *Top two panels* show the spin flip signal by ESR (EDSR) mechanism. *Lower panels* show the principle of the spin detection with Pauli-spin blockade mechanism

Because of Pauli spin blockade, once spin triplet states are realized, further charge fluctuation is strongly suppressed (Pauli-spin blockade (PSB)) [31], see Fig. 25.1. This mechanism is now widely used as a handy initialization and detection scheme of two electron states. Series QDs with different Zeeman energies realized by controlling g-factors or/and local magnetic fields are also proposed to resolve spins [2, 14, 38].

25.3 Electrical Manipulation of Single Electron Spins

The coherent manipulation, or unitary operation, should be completed within a characteristic time, T_2, so that the superposition states are maintained. The long T_2 time of the spin in quantum dots combined with the ease with which electron charges can be localized and transported in scalable solid-state devices make electron spin qubits one of the most promising systems for quantum information processing applications.

25.3.1 Single Spin Manipulation

25.3.1.1 One-Qubit Gates

Single-spin manipulations implement the basic one-qubit gates needed for universal quantum computation in combination with two-qubit gates, known as controlled-NOT (CNOT), for example. Single-spin states and their dynamics are easily understood using the Bloch representation of quantum mechanical two-level systems, $|\psi\rangle = \cos\theta\,|\uparrow\rangle + e^{i\phi}\sin\theta\,|\downarrow\rangle$ where two polar-coordinate angles θ, ϕ assign a point on the Bloch sphere of unit radius (Fig. 25.2). For example, a rotation of 180 degrees along the x-axis will take the spin from the north pole (corresponding to state $|\uparrow\rangle$) to the south pole (corresponding to state $|\downarrow\rangle$). For quantum information processing, the spin must however reach any specified point on the Bloch sphere by a unitary operation U [28]. In general, for any single-qubit U, there are real numbers α, β, γ and δ such that $U = e^{i\alpha}R_z(\beta)R_y(\gamma)R_z(\delta)$. Here $R_\nu(\theta)$ represents a rotation of angle θ around the $\nu = x, y, z$ axis defined by $R_\nu(\theta) \equiv \exp[-\frac{i\theta\sigma_\nu}{2}]$, where σ_ν is the ν element of Pauli spin matrices. The Pauli spin matrices themselves are quantum logic gates, for example, $\sigma_x = iR_x(\pi)$ is analogous to the classical NOT gate, which flips $|\uparrow\rangle$ to $|\downarrow\rangle$ and vice versa. Other useful quantum gates are the Hadamard gate, $H = e^{\frac{i\pi}{2}}R_z(\pi)R_y(-\frac{\pi}{2})$, and the phase gate, $Z_\phi = e^{\frac{i\phi}{2}}R_z(\phi)$. An electron spin under a static magnetic field $\boldsymbol{B}_0$ pointing in the z direction is subject to the Hamiltonian $\mathcal{H} = \frac{\hbar\omega_Z}{2}\sigma_z$, where $\hbar\omega_Z = g\mu_B B_0$ is the Zeeman energy with the Bohr magneton μ_B and electron g-factor g. The unitary time-evolution of the spin is defined by the operator $U(t) \equiv R_z(\omega_Z t)$. Therefore, a static field drives an electron spin rotating around the z axis (spin precession) and $\omega_Z/2\pi$ is called the Larmor frequency.

In principle, any one-qubit operation is achieved by successive applications of magnetic field pulses pointing in the z or y direction. However, when we want to control the spin using electrical methods, we find that the vectorial control of magnetic fields is difficult in practice. Instead, electron spin resonance (ESR) is the tool of choice for rotating spins [40].

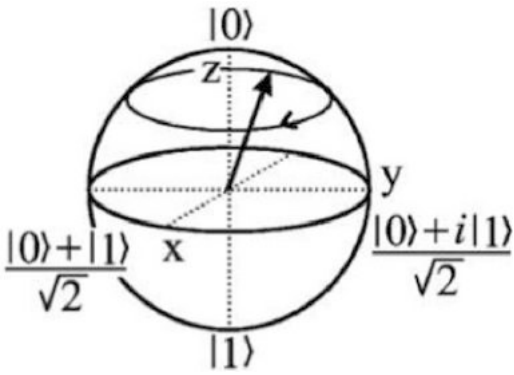

Fig. 25.2 Bloch sphere representation of an electron spin qubit. State $|0\rangle$ corresponds to $|\uparrow\rangle$ and $|1\rangle$ to $|\downarrow\rangle$ (From [48])

25.3.1.2 Principle of Electron Spin Resonance

The ESR technique consists of applying an oscillating magnetic field $\boldsymbol{B}_{AC}$, of angular frequency ω, pointing in a direction (say along $\hat{\boldsymbol{x}}$) perpendicular to the static field $\hat{\boldsymbol{B}}_0$ pointing to $\hat{\boldsymbol{z}}$. The motion of the spin subject to both static and a.c. magnetic fields is rather complex when described using the usual laboratory coordinate system (the lab frame). However, it is greatly simplified by describing the motion in a coordinate system rotating about $\hat{\boldsymbol{z}}$ at ω (the rotating frame) and the spin state becomes $|\psi\rangle^{rot} = \exp[\frac{i\omega t}{2}\sigma_z]\,|\psi\rangle$. In the rotating frame, the Hamiltonian reduces to

$$H^{rot} = \frac{\hbar(\omega_Z - \omega)}{2}\sigma_z + \frac{\hbar\omega_1}{2}[\sigma_x \cos\varphi - \sigma_y \sin\varphi], \tag{25.1}$$

where we assume $\boldsymbol{B}_{AC} = \hat{\boldsymbol{x}} B_{AC}\cos(\omega t + \varphi)$ and define $\omega_1 \equiv g\mu_B B_{AC}/2$ while neglecting fast oscillating terms such as $e^{\pm 2i\omega t}$ (rotating wave approximation). Naturally, the a.c. field lies along a fixed axis in the rotating frame. Furthermore, if the frequency of the a.c. field $f_{AC} = \omega/2\pi$ matches the Larmor frequency, the first term in Eq. (25.1) vanishes. In this case, an observer in the rotating frame will see the spin precessing around the vector $(\cos\varphi, \sin\varphi, 0)$ on the $x-y$ plane. If we adjust the phase of the oscillations φ to zero, a rotation occurs along the x-axis. Shifting the phase by $\pi/2$ changes the rotation axis to the y-axis. As can be seen in Eq. (25.1), we can flip a spin from $|\uparrow\rangle$ to $|\downarrow\rangle$ by applying an a.c. field burst for $T_\pi = \pi/\omega_1$ (π pulse). Moreover, the probability of the spin $|\uparrow\rangle$ oscillates between 0 and 1 with a frequency of $f_{Rabi} = \omega_1/2\pi$ (Rabi oscillation). In general, a one-qubit gate will consist of a sequence of a.c. magnetic field pulses of various durations (to control the amount of rotation) as well a sequence of phases (to select the rotation axis). The duration, phase and even frequency are relatively easy to control using signal modulation techniques.

If the a.c. field is off-resonance with respect to the Larmor precession frequency by $\Delta\omega \equiv \omega_Z - \omega$, the spin precesses in the rotating frame about an axis tilted from the $x-y$ plane by an angle $\chi = \arctan(\Delta\omega/\omega_1)$ and with frequency $\omega' \equiv \sqrt{\Delta\omega^2 + \omega_1^2}$. It follows that the a.c. field has virtually no effect on spins that are far off resonance $|\Delta\omega| \gg \omega_1$, since $\chi \sim \pm\pi/2$. If all spins have well separated Larmor frequencies, we can in principle selectively rotate any given qubit without rotating the other spins. This feature can be used to manipulate several spins selectively as discussed below. The first demonstration of the ESR of individual spins used a micro-coil with a.c. electric current [17].

25.3.2 Electric Dipole Spin Resonance

In comparison to the local a.c. magnetic field generated by a micro-coil, strong and local a.c. *electric* fields can be generated by exciting a tiny gate electrode near

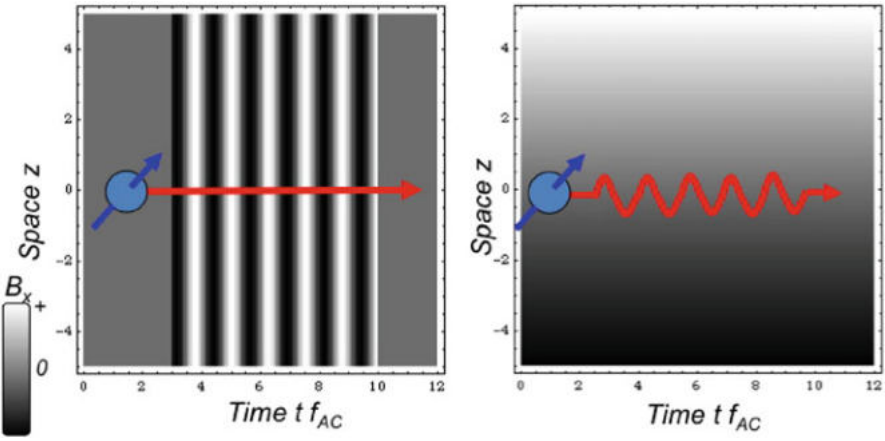

Fig. 25.3 Schematics of the ESR (*left*) and EDSR (*right*)

the target spin with a low voltage. For scalability purposes, it is therefore highly desirable to manipulate electron spins with electric fields instead of magnetic fields. To benefit from the advantages of electrical excitation, a mediating mechanism must be in place to couple the electric field to the electron spin, which usually responds only to magnetic fields. Electric dipole spin resonance (EDSR) is the above mentioned process, which has been investigated for bulk systems of strong spin-orbit interaction since the 1960s [3, 25, 36] (Fig. 25.3). The application of EDSR to the coherent manipulation of single spins in a quantum dot was first argued theoretically with and an inhomogeneous magnetic field [45] and spin-orbit coupling [10] as the mediating mechanisms. Moreover, a hyperfine interaction and g-factor tensor modulation also work as the mediating mechanism.

To manipulate spin coherently, we introduce a driving electric field and the Hamiltonian is

$$\mathcal{H}_{el} = e\boldsymbol{E}(t)\cdot\boldsymbol{r}, \tag{25.2}$$

where $\boldsymbol{E}(t) = \boldsymbol{E}_{AC}\cos\omega t$. To simplify the following arguments, we consider a two-dimensional quantum dot confined by a parabolic potential such that $V(x,y) = m\omega_0^2\boldsymbol{r}^2/2$ where ω_0 is the confinement frequency and the electric field is in-plane. Using a time-dependent canonical transformation [35],

$$\Psi_0(\boldsymbol{r},t) = e^{-i\boldsymbol{k}\cdot\boldsymbol{R}(t)}\Psi_0^{osc}(\boldsymbol{r},t),$$

with $\boldsymbol{k} \equiv -i\boldsymbol{\partial}$, the electric field Hamiltonian H_{el} can be eliminated by choosing $\boldsymbol{R}(t) = -e\boldsymbol{E}(t)/m\omega_0^2$ and neglecting the correction proportional to $\omega/\omega_0 \ll 1$. This canonical transformation changes the position operator $\boldsymbol{r}$ as follows

$$e^{i\boldsymbol{k}\cdot\boldsymbol{R}(t)}\boldsymbol{r}e^{-i\boldsymbol{k}\cdot\boldsymbol{R}(t)} = \boldsymbol{r} + \boldsymbol{R}(t). \tag{25.3}$$

Now we assume that uniform magnetic field $\boldsymbol{B}_0$ is applied in the x direction, and (inhomogeneous) slanting field directing

$$\boldsymbol{B}_{sl}(x) = b_{sl} x\, \hat{z}, \tag{25.4}$$

where $\hat{z}$ is the unit vector normal to the plane and $b_{sl} \equiv \partial B_z/\partial x$ characterizes the steepness of the field gradient in the x-direction. Hence the periodical displacement of the electron center-of-mass by the a.c. electric field around its equilibrium position in the slanting field induces an oscillating effective transverse magnetic field, as shown in Fig. 25.3,

$$\begin{aligned} \boldsymbol{B}_{AC}(t) &= b_{sl} R_x(t) \hat{z} \\ &= -b_{sl} \ell_0 \frac{eE_{AC}(t)\ell_0}{\hbar\omega_0} \hat{z}, \end{aligned} \tag{25.5}$$

where $\ell_0 \equiv \sqrt{\hbar/(m\omega_0)}$. As discussed in the previous section, this allows transitions between the electron spin states when the driving frequency, f_{AC}, matches the Larmor frequency.

How can the slanting magnetic field in semiconductor QDs as shown in Eq. (25.4) be realized? In the following, we discuss three approaches, (1) using spin orbit interaction (SOI), (2) on-chip micro-magnet, and (3) g-tensor modulation.

Spin-orbit interaction: We argue that a 2D quantum dot with SOI with in-plane magnetic field can be subjected to an effective Hamiltonian of a quantum dot with a uniform magnetic field and an inhomogeneous transversal field [10, 21, 22]. The original Hamiltonian is $\mathcal{H} = \mathcal{H}_{DOT} + \mathcal{H}_Z + \mathcal{H}_{SOI}$, with $\mathcal{H}_{DOT} = (p_x^2 + p_y^2)/(2m) + V(x, y)$, $\mathcal{H}_Z = \frac{1}{2} g\mu_B \boldsymbol{B}_0 \cdot \boldsymbol{\sigma}$ where $V(x, y)$ is the 2D confinement potential and the magnetic field is applied in-plane $(x-y)$ with $\boldsymbol{\sigma} = (\sigma_x, \sigma_y, 0)$. The SOI Hamiltonian for a 2D electron system without spatial- and bulk-inversion symmetry is $\mathcal{H}_{SOI} = \alpha(p_x\sigma_y - p_y\sigma_x) + \beta(-p_x\sigma_x + p_y\sigma_y)$, where α and β are the coupling constants for Rashba and Dresselhaus SOI, respectively. We took the 2D plane to be (001) and the [100] ([010]) crystal axis to be in the x (y) direction. Applying unitary operation $\mathcal{U} = \exp[-i\frac{m}{\hbar}\{(\alpha x + \beta y)\sigma_y - (\beta x + \alpha y)\sigma_x\}]$, to the total Hamiltonian, $\tilde{\mathcal{H}} = \mathcal{U}^\dagger \mathcal{H} \mathcal{U}$, we obtain an effective Hamiltonian to the lowest order of the spin-orbit interaction

$$\tilde{\mathcal{H}} = \mathcal{H}_{DOT} + \mathcal{H}_Z + \frac{1}{2} g\mu_B \tilde{B}_z(x, y)\sigma_z, \tag{25.6}$$

It is convenient to rotate the x-axis, which is parallel to the external magnetic field along [110] or [1$\bar{1}$0] direction, and we found the effective field $\tilde{B}_z$ is given by

$$\tilde{B}_z(x) = 2|\boldsymbol{B}_0| \frac{x}{\ell_{SO}}. \tag{25.7}$$

where we defined spin-orbit length $\ell_{SO}^{-1} = m(\alpha \pm \beta)/\hbar$. Therefore, the spin experiences an effective transverse magnetic field, which depends linearly on its position and is proportional to the external magnetic field B_0.

On-chip micro-magnet Inhomogeneous field is realized when we place a micrometer-size ferromagnet near the quantum dot. The magnetic field with a uniform in-plane ($\hat{x}$) field is [34]

$$\boldsymbol{B} = [B_0 + \delta B_0 + b_{sl} z]\hat{x} + b_{sl} x\hat{z}, \tag{25.8}$$

where b_{sl} characterizes the gradient of the transverse magnetic field and δB_0 is an offset field provided by the ferromagnet. The counter-term field $b_{sl}z$ parallel to the external field is needed if $\boldsymbol{B}$ is to obey Maxwell's equation but is not effective for a strongly confined electron in the $x-y$ plane, $z = 0$.

g-tensor modulation Electrical control of the spin Larmor frequency in a g-factor modulated parabolic quantum well has been demonstrated [37]. However, the modulation of a scalar g-factor cannot flip spins, and it only provides Larmor frequency modulation. Fortunately, the electron g-factor in a quantum well is known to be anisotropic and must be treated as a tensor, $\hat{g}$. Therefore, the Hamiltonian reads

$$\mathcal{H}_Z = \frac{1}{2}\mu_B \boldsymbol{\sigma} \cdot \hat{g} \cdot \boldsymbol{B} = \boldsymbol{S} \cdot \boldsymbol{\Omega}, \tag{25.9}$$

where $\boldsymbol{\Omega}$ and $\boldsymbol{S} = \frac{\hbar}{2}\sigma$ are the precession axis vector and the spin operator, respectively. The g-tensor is designed as a function of position z in the growth direction and to be uniform in the $x-y$ plane. By applying a magnetic field B_0 with an angle θ from the z axis, the precession axis vector is

$$\boldsymbol{\Omega}(z) = \frac{\mu_B}{\hbar} \begin{pmatrix} g_\pi(z) & 0 & \\ 0 & g_\pi(z) & 0 \\ 0 & 0 & g_0(z) \end{pmatrix} \cdot \begin{pmatrix} B_0 \sin\theta \\ 0 \\ B_0 \cos\theta \end{pmatrix}, \tag{25.10}$$

where g_π and g_0 are the in-plane and out-of-plane components of the g-tensor, respectively. Then we expand the axis vector in a power series in z,

$$\boldsymbol{\Omega}(z) = \boldsymbol{\Omega}_0 + \boldsymbol{\omega}_\parallel z + \boldsymbol{\omega}_\perp z,$$

where $\boldsymbol{\omega}_\parallel$ and $\boldsymbol{\omega}_\perp$ are the parallel and perpendicular components of the first Taylor series of the precession axis vector around $z = 0$, which is set at the electron's stable position. The perpendicular component, explicitly

$$\boldsymbol{\omega}_\perp = \frac{\mu_B}{\hbar} B_0 \frac{\partial(g_\pi - g_0)}{\partial z} \sin\theta\cos\theta \begin{pmatrix} \cos\theta \\ 0 \\ -\sin\theta \end{pmatrix}, \tag{25.11}$$

flips the spin.

First single spin EDSR was demonstrated by the Delft group [29] using spin-orbit interaction in a GaAs quantum dot system, (Eq. (25.7)). Microwaves of $\sim$10 GHz are applied to one of the side gates and a resonant dot current peak with a width of a few mT is observed at the resonant condition $g\mu_B B_0 = hf_{AC}$ where $|g| = 0.39$.

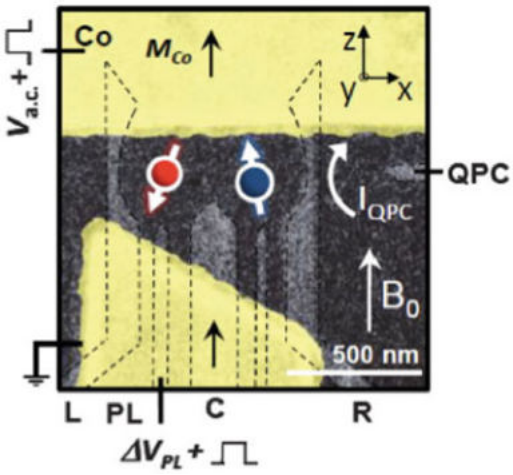

Fig. 25.4 Scanning electron microscopy image of the device fabricated on top of an AlGaAs/GaAs heterostructure showing the Ti/Au gates (*light gray*) and the split cobalt (*Co*) magnet (upper/lower) separated from the gate contacts by a calixarene layer. Gates *R* (right) and *L* (left) control number of electrons; *C* (center) controls the inter dot tunnel coupling *t*. A microwave voltage V_{ac} is applied to the upper part of the magnet (From [4])

As with the on-chip stripline experiment, Rabi oscillations of the dot current as a function of microwave burst time are observed. The linear dependence of the Rabi frequency on the applied microwave amplitude is also confirmed.

The use of an inhomogeneous magnetic field allows greater flexibility, because the method is applicable to any semiconductor material. The scheme has recently been demonstrated using on-chip micro-magnets [4, 30, 34]. Two electrons are confined and spatially separated from each other in a gate-defined double quantum dot (Fig. 25.4). The a.c. electric field, $E_{AC}(t)$, is generated by exciting a nearby gate that couples to both spins. The magnetic-field gradient is obtained by using a ferromagnetic strip integrated on top of the double-dot structure. The strip is magnetized uniformly along its hard axis by applying an in-plane magnetic field, B_0, that is stronger than the micro-magnet's saturation field ($\sim$2 T). In this condition, the resulting stray magnetic field has an out-of-plane component that varies linearly with position. The expected field gradient is as large as $b_{sl} \sim 1$ T/μm. The effective a.c. transverse magnetic field defined in Eq. (25.8) drives one of the two electron spins flip in a resonant condition and allows a finite dot current I_{dot} or a signal in the nearby QPC, G_{QPC}. In addition, the inhomogeneity of the in-plane component yields two different quantum-dot Zeeman fields, B_{0L} and B_{0R}. This feature is used to probe each spin separately as shown in Fig. 25.5. Two independent Rabi oscillations, from the two quantum dots, 1 and 2, were observed for different resonant magnetic fields as a function of the microwave burst time as shown in Fig. 25.6 [4, 30]. The linear dependence of each resonance on the external magnetic field shown in Fig. 25.6 (right) is a key signature of ESR because the Larmor frequency is proportional to B_0, which determines $|g| = 0.39$.

Electron spin manipulation by modulating the g-tensor electrically has been reported for optically generated electron spins in a specially designed quantum well [16]. By applying a DC voltage of several volts to the surface gate, g-factor can be controlled for a wide range and even its sign can be changed [37]. The short T_2^* time ($\sim$300 ps) of extended electron spins limited the tipping angle to $\sim$2 degrees.

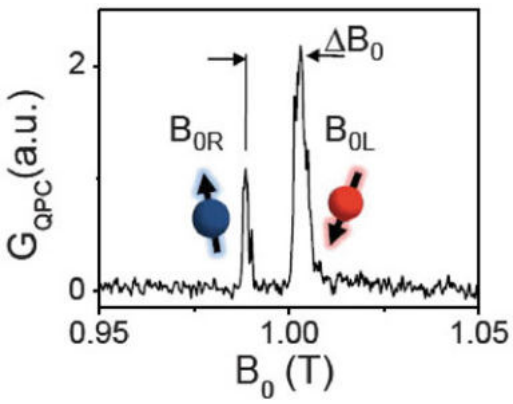

Fig. 25.5 cw EDSR for the left and right spin. PSB is lifted on resonance for the left (*red*) and right (*blue*) QD spin. EDSR peak separation: $\Delta B_0 \sim 5\,\mathrm{mT}$ (From [4])

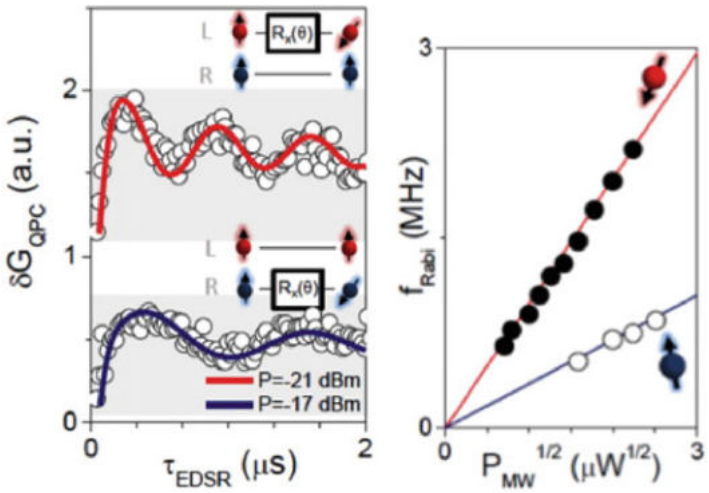

Fig. 25.6 (*Left*) Rabi oscillations for the left QD (*red*) and right QD (*blue*) ($B_{0L} = 2\,\mathrm{T}$ and $B_{0R} = 1.985\,\mathrm{T}$, $f_{AC} = 11\,\mathrm{GHz}$). δG_{QPC} is the difference in G_{QPC} between the on-resonance and off-resonance conditions. (*Right*) Rabi oscillation frequency f_{Rabi} as a function of the square root of MW power, for the left (*closed*) and right (*open*) QD spin (From [4])

There has been no report of single spin coherent manipulation using a g-tensor modulation mechanism, however its feasibility was confirmed recently in a self-assembled QDs [6].

25.3.3 Strongly Driven EDSR

The Rabi frequency f_{Rabi} shown in Fig. 25.6 (right) was limited to several MHz. The amplitude dumps with time which is approximated as an exponential form

$\propto \exp -\tau_{EDSR}/T_2^*$. It is also pointed out that the phase of the oscillation shows $\pi/4$ shift [18]. The primary source of this "decoherence" is the quasi-static modulation of nuclear spin polarization, which is hyperfine-coupled to the electron spins. Since T_2^* is limited to be less than 100 ns, the fidelity of π- or $\pi/2$ operation cannot be high. As can be seen in Eq. (25.5), larger Rabi frequency can be achieved by increasing the magnetic field gradient b_{sl} and microwave amplitude, E_{AC}. In addition, increasing ℓ_0 (or equivalently decreasing $\hbar\omega_0$, smaller confinement potential strength) is effective. Recently, by improving the macro-magnet design and increasing the microwave amplitude, Rabi frequency more than 100 MHz has been achieved and Rabi oscillation does not show $\pi/4$ shift and clear Chevron pattern had been observed with spin flip gate fidelity more than 96 % [50].

Since Rabi frequency is linearly proportional to B_{AC}, from Eq. (25.5), we expect linear dependence of f_{Rabi} on E_{AC}. However, for very large microwave amplitude condition, clear sub-linear behavior of f_{Rabi} on E_{AC} was observed [50]. Possible origins of this behavior are the non-parabolicity of the confinement potential $V(x, y)$ [46] or the deviation from the linear behavior of the field gradient assumed in Eq. (25.8).

Other type of fast single operation was proposed and demonstrated by Yoneda, [50], where rapid change of the combination of gate voltages shifts the center position of QD, and then modifies the Larmor frequency. This realizes z-rotation operation up to 100 MHz range.

25.4 Two Spin Operations

25.4.1 Reduced Spin Dynamics Made of Two Spins

To realize the necessary unitary operations for the quantum computation algorithm, CNOT or a SWAP operation is essential for the two qubits. Following the original proposal [23], we rely on the exchange interaction that is allowed by the finite tunnel coupling between two quantum dots. The low energy spin dynamics is described by an isotropic Heisenberg interaction

$$\mathcal{H}_S = J\mathbf{S}_1 \cdot \mathbf{S}_2 + g\mu_B \mathbf{B}_0 \cdot (\mathbf{S}_1 + \mathbf{S}_2), \tag{25.12}$$

where $\mathbf{S}_\nu$ ($\nu = 1/2$) represents a localized electron spin in the dot 1 and 2. Therefore, an estimation of the exchange coupling J is vital to the two spin qubit operation. The estimation of J in symmetric double dots with a Gaussian confinement potential and a magnetic field has already been reported in Refs. [5, 15]. In a two-qubit gate in combination with the EDSR mechanism, the effect of spin-orbit coupling [41] and inhomogeneous field [45] deviate the exchange coupling from a simple Heisenberg form.

25.4.1.1 Exchange Qubits

Petta et al. [32] used this knob to coherently control an 'effectively single qubit' made of two spins. The effective random hyperfine magnetic field $\boldsymbol{B}_n$ (Overhauser field) induced by the interaction with nuclear spins is of the order of 1–5 mT. When the external field B_0 pointing in the z direction is much larger than $|\boldsymbol{B}_n|$, two of the triplet states, $T_{\pm}$, are well separated from the S_0 and T_0 states, that are energetically different in $J(\varepsilon)$. The difference between the random hyperfine fields along $\boldsymbol{B}_0$ of the two dots, ΔB_n^z induces coupling between T_0 and S_0 states [44]. This can be seen by rewriting the second term of Eq. (25.12) as $g\mu_B(\boldsymbol{B}_1\cdot\boldsymbol{S}_1+\boldsymbol{B}_2\cdot\boldsymbol{S}_2) = g\mu_B\bar{\boldsymbol{B}}\cdot(\boldsymbol{S}_1+\boldsymbol{S}_2)+\frac{1}{2}g\mu_B\Delta\boldsymbol{B}_n\cdot(\boldsymbol{S}_1-\boldsymbol{S}_2)$ where $\bar{\boldsymbol{B}} = \boldsymbol{B}_0+(\boldsymbol{B}_{n1}+\boldsymbol{B}_{n2})/2$ and $\Delta\boldsymbol{B}_n = \boldsymbol{B}_{n1}-\boldsymbol{B}_{n2}$. At low magnetic fields of $\sim$10 mT and with very weak inter-dot tunnel coupling t, this difference in the nuclear field $\Delta\boldsymbol{B}_n$ induces strong mixing of the spin singlet and triplet states and results in a leakage current from the Pauli spin blockade condition [17]. Using the relation $\langle T_0|\{S_{Lz}-S_{Rz}\}|S(1,1)\rangle = 1$ and the general expression for the singlet ground state $|S_0\rangle \equiv a\,|S(1,1)\rangle + b\,|S(0,2)\rangle + c\,|S(2,0)\rangle$, with $|a|^2+|b|^2+|c|^2 = 1$, we have a nonzero matrix element $\langle T_0|H_S|S_0\rangle = \frac{1}{2}g\mu_B\Delta B_n^z a$. By reading S_0 and T_0 as effective spin up and down, respectively, the exchange energy can be assumed to be Zeeman energy and $\Delta B_n^z a$ is the transverse magnetic field. It is convenient to consider a Bloch sphere with S_0 and T_0 at the north and south poles and $|\uparrow\downarrow\rangle$ and $|\downarrow\uparrow\rangle$ as the poles along the x axis. A small but finite ΔB_n^z makes either of the states in the x axis poles, say $|\uparrow\downarrow\rangle$, the ground state for largely negative detuning where $J \sim 0$. Starting from the well-defined ground state $S(0,2)$ at positive detuning ε, an adiabatic negative shift of ε drives the system to $|\uparrow\downarrow\rangle$. Then a sudden shift of ε to a more positive value realizes a large J and then the state starts rotating around the z axis. The reading stage is again the adiabatic ramping of ε to project the state $|\uparrow\downarrow\rangle$ to $S(0,2)$ and $|\downarrow\uparrow\rangle$ to T_0, which can easily be distinguished by the QPC charge detector. Because of the random distribution of the nuclear spin field, and possibly because of electrical noise in the detuning control signal, the inhomogeneous decoherence time estimated from the damping of the two-electron Rabi oscillation is about 10 ns. Spin-echo experiments have also been successfully demonstrated using a detuning pulse sequence. The estimated lower bound of T_2 time is 1.2 μs. Recently, two-qubit operation using two exchange only qubits had been demonstrated [39].

25.4.1.2 SWAP Operation

Here, we present the realisation of an electron spin based two-qubit gate suitable to prepare a partially entangled state with the degree of entanglement depending on the exchange operation time as well as the micro-magnet induced inhomogeneous Zeeman field. This gate operation allows an entangled singlet included in the output state and provides a novel basis for quantum information processing which can be applied to materials with promising long coherence times.

To demonstrate the modulation and detection of an entangled state as a fraction of the output we use two-qubit gate comprising universal single-qubit control and controlled SWAP operation. Using the exchange energy J_0, the time for SWAP operation is $\tau_{SWAP} \equiv \pi/J_0$. The SWAP operation is based on the manipulation of the exchange interaction in the double quantum dot according to Ref. [23], where the inter-dot potential barrier is tuned thus changing the exchange interaction between the electrons. Coming from stage A, where spins are initialized to spin triplet using Pauli-spin blockade, we rotate the electron spin in the left dot in stage B with $\varepsilon \gg 0$ and control the inter-dot exchange coupling in stage C (Fig. 25.13c). We switch the exchange coupling on by pulsing ε from stage B ($\varepsilon \gg 0$) to C ($\varepsilon > 0$) and switch it off by returning to B (Fig. 25.7 (lower-left)). The sequence of the quantum operation in the experiment at $B_0 = 2.00\,\mathrm{T}$ starting with the spin state evolves in detail by

$$|\uparrow\rangle \otimes |\uparrow\rangle \rightarrow \frac{|\uparrow\rangle - i\,|\downarrow\rangle}{\sqrt{2}} \otimes |\uparrow\rangle \rightarrow |\psi_1\rangle \rightarrow |\psi_2\rangle\,, \tag{25.13}$$

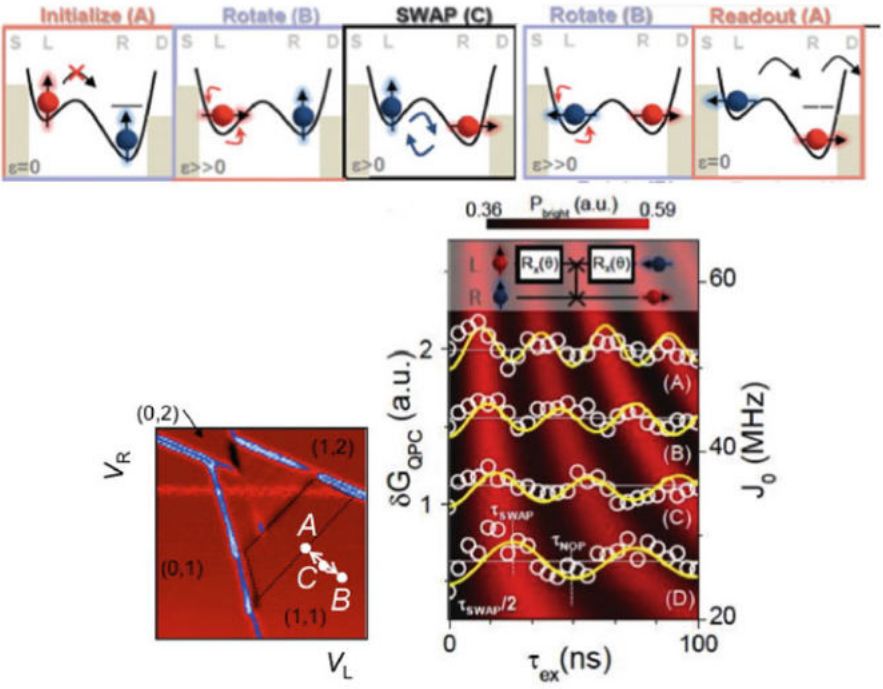

Fig. 25.7 (*Top*) The schematics of the combination of single- and two-qubit operations. The conditions (*A*), (*B*) and (*C*) correspond to the detuning condition shown in the panel in the (*Lower left*). (*Lower right*) Result of two-qubit measurement for four different energy detuning ε. Contour plot showing J_0 vs τ_{ex} indicating P_S. We use the ratio $\delta E_Z/J_0$ as a fitting parameter to reproduce the experimental data and find that all data (*A*) to (*D*) measured for various detuning values are consistent with the calculation by taking $\delta E_Z/J_0 \sim 0.74$ (SWAP$^{n=1,3,5,\cdots}$: *red*; NOP: *black*). $\delta E_Z \equiv |g\mu_B \Delta B_0|$ is the difference of the Zeeman energies of two spins (From [4])

where in the first step, $3\pi/2$ rotation around the x axis for the left qubit, in the second step, two-bit exchange operation for the exchange time τ_{ex}, and in the third step, $\pi/2$ rotation around the x axis for the left qubit again. $|\psi_2\rangle$ is the final two spin wave function, which is for $\tau_{ex} = 2n\tau_{SWAP}$, $|\psi_2\rangle = |\uparrow\rangle \otimes |\uparrow\rangle$ and is for $\tau_{ex} = (2n+1)\tau_{SWAP}$, $|\psi_2\rangle = \frac{1}{2}[|\uparrow\rangle \otimes |\uparrow\rangle + |\downarrow\rangle \otimes |\downarrow\rangle - \sqrt{2}iS(1,1)]$ where $S(1,1)$ is the spin singlet state. Since the non-entangled spin triplet states $|\sigma\rangle \otimes |\sigma\rangle$ are both spin blocked, they induce no detectable change in the charge state from the initial state. In contrast, the singlet component of the wavefunction $|\psi_2\rangle$ is measured by the projection $\langle S|\psi_2\rangle$ resulting in the charge transfer between the two quantum dots, which is detected by the nearby QPC. In Fig. 25.7 (lower-right), we plot the change of the charge state measured by the QPC as a function of τ_{ex} and detuning ε or J_0. The measurement exhibits periodic oscillations as a function of both parameters. The experimental data agree well with a model calculation shown as solid lines.

25.5 Architecture for Spin-Qubit Quantum Computer

Considering the scalability, we should choose a good architecture with a suitable fault-tolerance scheme. Since the architecture and the scheme are very closely related, the analysis of their combination is important. In this section, hence we investigate the two typical architectures with one typical quantum error-correction code.

To make a scalable and universal quantum simulator or computer, the long-time memory should be prepared first. Unfortunately the physical memory time of physical qubit is not so long, it is not sufficient for arbitrary computation. By encoding a logical qubit with multiple qubits and gates with a quantum error-correction code, we can increase the logical memory time arbitrarily long. Note that to make it work, the error rate of qubits and gates should be lower than a predefined value, which is defined by a chosen quantum error-correction code. Meanwhile such value, which is called accuracy threshold value, also depends on the physical architecture. Since the lower accuracy threshold value means that it is getting more difficult, it would be better to find a good combination of an error-correction code and the target qubit architecture.

Since we already have many quantum error-correction codes and it is focused on the architectural issues, we choose a typical error-correction code such as 9-qubit Shor code. Also considering the difficulty of measurement, we focus on the use of measurement-free Shor code as shown in Fig. 25.8. In the circuit, a data qubit $|\psi\rangle$ can be encoded by using nine qubits. After encoding, this state will be used for processing. In this figure, the encoded qubit is used only for memory with potential errors during *error* period. After that the encoded state is checked by the reverse process of encoding, and finally corrected by using Toffoli gate. If there is any single error during *error* period, this circuit can correct such error. More than two errors cannot be corrected. For holding for long time, such encoding, checking, and correction period should repeat. Note that since the circuit has a time slot for

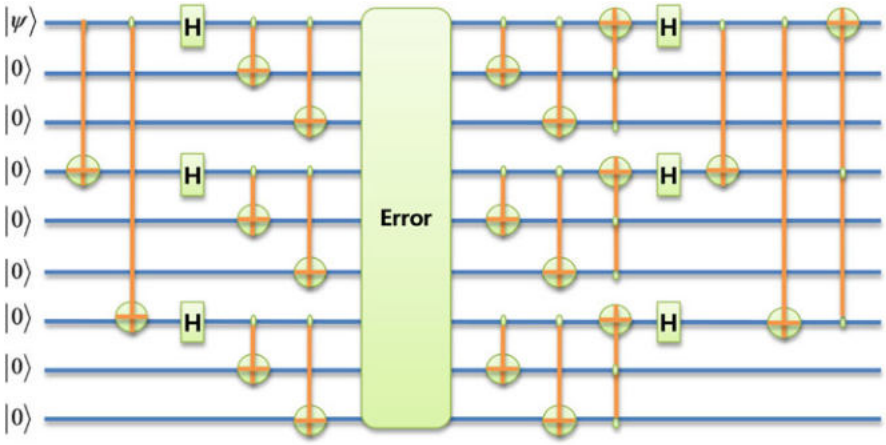

Fig. 25.8 Measurement-free Shor code

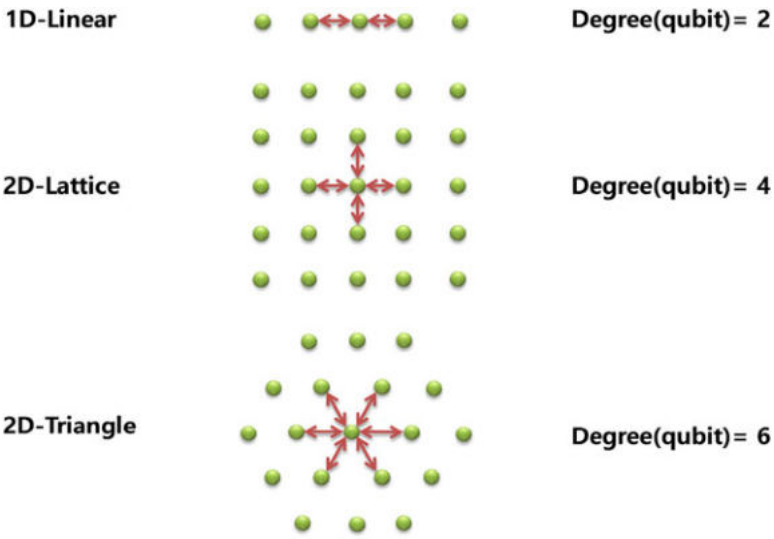

Fig. 25.9 Physical architecture

decoded qubit between error-correction cycles, it is not fully fault-tolerant memory. However, this error-correction code can be used for showing the feasibility of long-time memory, and hence it has been widely used for many experimental results.

Based on the physical capability, we can put the spin qubits in an arbitrary way. For systematic control, however, we usually consider two types of architectures such as the one-dimensional and two-dimensional architectures as shown in Fig. 25.9. For representing arbitrary implementation we assume the node as the qubit and the

edge as the interaction between two qubits. For the one-dimensional architecture, the typical implementation would be the linear structure. Hence a qubit can interact with only two neighbors. On the other hand, we may have several implementations for the two-dimensional architecture as the lattice or the triangle structures as shown in the figure. In general, the lattice structure is chosen for the two-dimensional architecture. In this case, a qubit can interact with four neighbor qubits.

Since we should map the chosen quantum error-correction code, in this case the Shor code, into the target architecture, we need to consider how to map the qubits and to schedule the quantum operations of the circuit. Since the physical architecture has a limitation of interaction distance and the number of qubits which can interact with the chosen qubit, the target circuit cannot be directly mapped into the physical architecture without modification. More specifically we should add multiple SWAP operations to make the non-local two-qubit operations depends on the location of source and target qubits. Therefore, we first need to find a good layout of qubits to minimize the physical distance, and then add additional SWAP operations to relocate the qubits to the neighbor positions. Because of that the quality of the mapping affects the overall performance. Since our main concern is the physical architecture, we assume to use the best layout and scheduling in this analysis. Since the goal of the layout of qubits is to minimize the physical distance of qubits for two-qubit operations, it is usually very hard if the circuit is big. Fortunately since the circuit of the Shor code is very small and has a regular structure it is relatively easy. Figure 25.10 shows the best layout of qubits. Although it is optimal, it still requires 24 SWAP operations to relocate the qubits as shown in Fig. 25.11. On the other hand, as shown in Fig. 25.12, the layout of qubits for the two-dimensional lattice does not require additional SWAP operations. Therefore, the scheduling of quantum gates is the same with the target circuit.

To compare the performance of two architectures, we consider two performance metric: time and error rate. Since the time of SWAP gate of the spin-qubit system

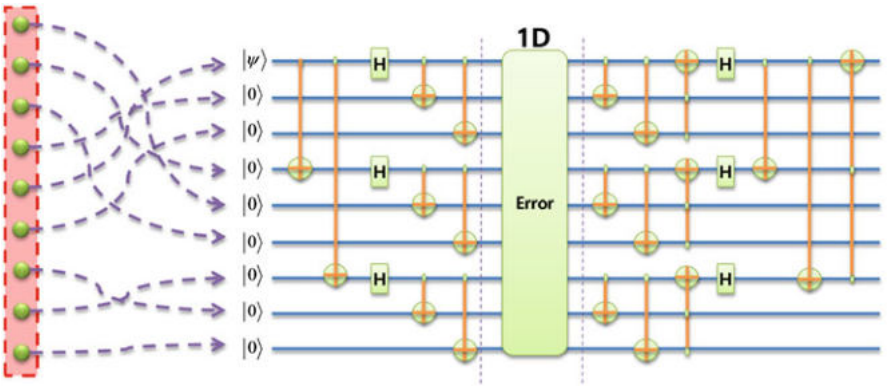

Fig. 25.10 Layout of the Shor code on the one-dimensional architecture

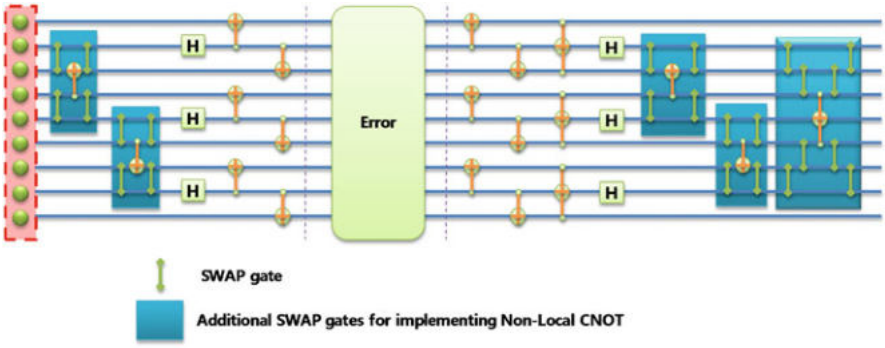

Fig. 25.11 Scheduling of the Shor code on the one-dimensional architecture

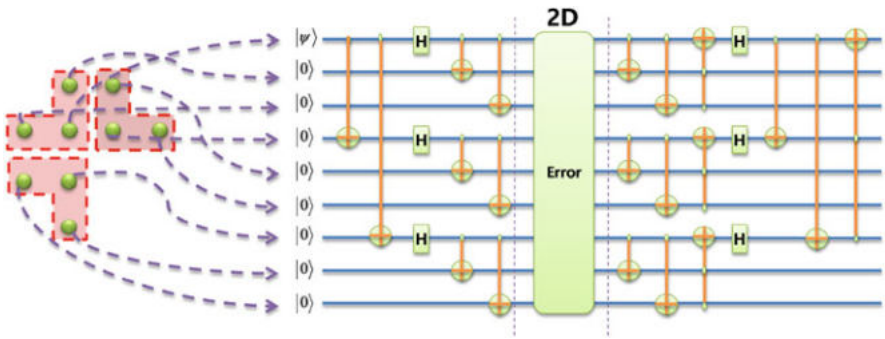

Fig. 25.12 Layout of the Shor code on the two-dimensional architecture

is shorter than single-qubit gate, the additional time caused by 24 additional SWAP gates on the one-dimensional structure is negligible. Therefore, two architectures have almost the same time performance. To compare the error performance, we analyze the number of error instances to make error on the output data qubit. For this analysis, the fault-path counting method is used [47]. Based on the analysis, the number of error instances for the two-dimensional architecture is (36, 40) for X and Z type errors. On the other hand, the number of error instances for the one-dimensional architecture is (64, 62), which is 50 counts more. This analysis implies two issues as follows.

- First, the accuracy threshold value of the one-dimensional architecture is lower than that of two-dimensional. If we assume that the accuracy threshold value is one over the number of error instances, the accuracy threshold values are $\frac{1}{126}$ and $\frac{1}{76}$ for the one- and two-dimensional architectures, respectively. Therefore, the one-dimensional architecture requires two times lower accuracy threshold value.

- Second, if the error rate of SWAP is relatively lower than other gates, the error performance would be same. Since the number of additional SWAP gates for the one-dimensional architecture is 24, if the error rate of the SWAP gate is $\frac{1}{24}$ times lower than that of other gates, the overall error rate of the output qubit would be the same. In addition to that, since the additional time caused by the SWAP gate is negligible, the time performance degradation is also negligible.

In summary, since the one-dimensional architecture supports the lower interaction degree, it causes to use additional SWAP gates over the two-dimensional architecture. However, since the time of SWAP gate is very short, the time performance of the one-dimensional architecture is almost the same with the two-dimensional. On the other hand, the error performance depends on the error rate of the SWAP gate. If the error rate of the SWAP gate is the same with other gates, then the accuracy threshold value of the one-dimensional architecture should be lower than that of the two-dimensional architecture. Or if the error rate of the SWAP gate is relatively lower than that of other gates, the overall error rate still can be the same.

Although the one-dimensional architecture shows comparable performance than the two-dimensional architecture for the chosen quantum error-correction code, the two-dimensional architecture has much practical advantage as follows.

- Many high performance quantum error-correction codes are based on the use of higher degree of interaction with local gates. For example, the Surface code, which shows the highest accuracy threshold value, is based on the use of two-dimensional array of qubits and the local two-qubit operations.
- Universal quantum simulator or computer requires the logical two-qubit operations between encoded blocks. Beyond the quantum memory, we should also consider the implementation of logical gates, specially logical CNOT gate. For making such CNOT gate, the physical location of qubits affects the performance very much. The better layout should support the easier and systematic control of qubits. Unfortunately, the one-dimensional architecture is generally not suitable for such logical CNOT operation.
- The physical size of building block should be minimized. If we consider to use the one-dimensional architecture for universal quantum simulator or computer, the size increases only one direction. Hence the physical size will reach the limit very quickly. On the other hand, the two-dimensional architecture can integrate many more qubits in a smaller area.

25.6 Other Techniques for Manipulating Single Electrons

In this chapter we describe novel techniques of transferring a quantum state between different quantum systems: transfer of single photons to single electrons in a QD in Sect. 25.6.1 and single electron transfer between two quantum dots (QDs) in Sect. 25.6.2.

25.6.1 Photon to Electron Spin Interface

Electron spin in semiconductor QDs has the advantage of having a good match with photons which can be used for optical communication, and therefore it may be a good candidate as a qubit combined with a photon qubit to construct quantum interface which enables long-distance quantum information communication and distributed quantum computing systems. Angular momentum is a good quantum number for both photons and electrons. Consequently conducting electrons are generated in QDs after band to band excitation by circularly polarized photons preserving the angular momentum [27]. Based on this concept quantum media conversion from the photon polarization state to electron spin state was previously proposed [49], and indeed an experiment following this concept was performed using GaAs quantum wells but for a large ensemble of photons and electron spins [19]. However, for applications to quantum information quantum state transfer from single photons to single electron spins is necessary but yet been demonstrated. We have recently used GaAs QDs to experimentally study the quantum state transfer from single photons to single electron spins. Here we describe the experiments on single photoelectron detection and angular momentum transfer from single photons to single electrons.

25.6.1.1 Single Photoelectron Detection with a Single QD

We first used a single GaAs QD equipped with a QPC charge sensor to detect the single photon trapping by the QD. The dot is electrically defined in a 2DEG of n-AlGaAs/GaAs. A 200 nm Au mask with an aperture is placed on top of the dot. A ps-laser pulse is irradiated onto the mask to optically excite the dot through the aperture. The photo-excitation predominantly occurs to generate electron-hole pairs in the GaAs buffer layer. The electron is only collected to the 2DEG interface of n-AlGaAs/GaA or trapped by the dot because of the built-in potential (Fig. 25.13a). The addition of the photo-electron in the dot can be detected by the charge sensor. The pulsed laser light with wavelength of 780 nm is introduced into a 1.5 K cryostat through an optical fiber to irradiate the dot. An estimate of the photon flux onto the aperture is 0.4 photons/pulse so that at most one electron-hole pair is optically generated.

Figure 25.13b is a typical data of charge sensor current I_{QPC} upon the optical excitation. The I_{QPC} instantly decreases after the optical excitation and abruptly increases in 3 ms. This I_{QPC} increase is 0.8 nA consistent with the change of I_{QPC} due to the change in the electron occupation of the dot just by one (measured in a separate experiment), and therefore assigned to the escape of the photo-generated electron to the lead [33]. The initial I_{QPC} decrease is larger than 0.8 nA probably because the gate potential of the sensor QPC is modified by photo-excitation outside the metal mask. (Note the laser beam diameter incident onto the metal mask is larger than the mask size.) From measurement of linear dependence of the photo-electron

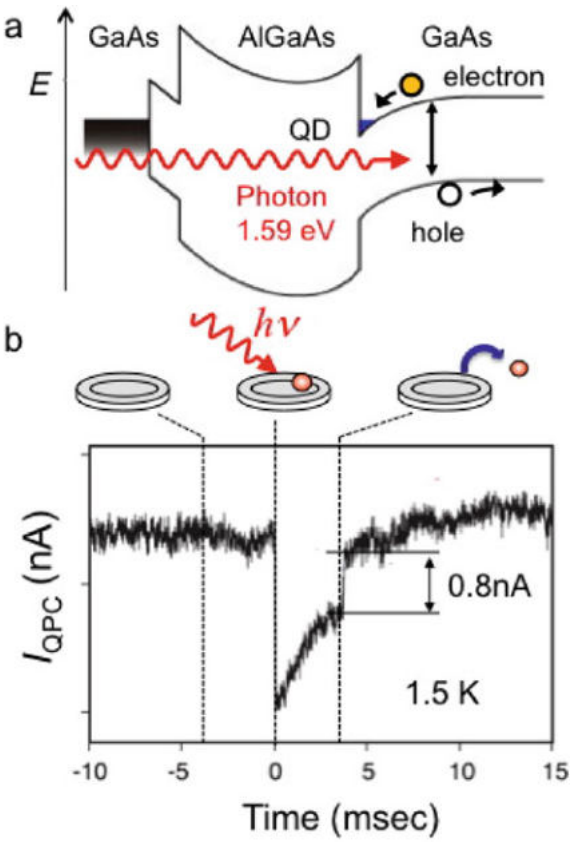

Fig. 25.13 (**a**) Band profile of an n-AlGaAs/GaAs heterostructure. The excitation laser energy is tuned just above the GaAs resonant energy. The excited electron hole pair is separated due to the intrinsic electric field. (**b**) Typical charge sensor current I_{QPC} due to single photoelectron trapping by a single QD. The measurement temperature is 1.5 K. The *upper panel* illustrates trapping of a photoelectron by a dot and escape of the photoelectron to the lead. The photo-excitation is performed with a light pulse of 0.4 photons/pulse

detection probability on the irradiated photon flux we derive the photo-electron detection efficiency of 15 % [33]. This value is consistent with that calculated from the optical absorption in the GaAs buffer layer.

In Fig. 25.14b the photoelectron detection can be complete within 0.3 ms whose time scale is shorter than the spin relaxation time T_1 and therefore the present detection technique can apply for the spin readout. Indeed we used a difference of tunneling rate of electrons from the dot to the spin-resolved edge states in the 2DEG leads to distinguish the spin orientation of single photoelectrons [33].

25.6.1.2 Non-destructive Single Photoelectron Detection

The spin readout using the electron escape to the leads as describe before is performed in a destructive manner. However, a nondestructive spin readout may be more useful in the context of quantum information processing. We have newly developed a technique for nondestructive and robust photo-electron detection using a DQD.

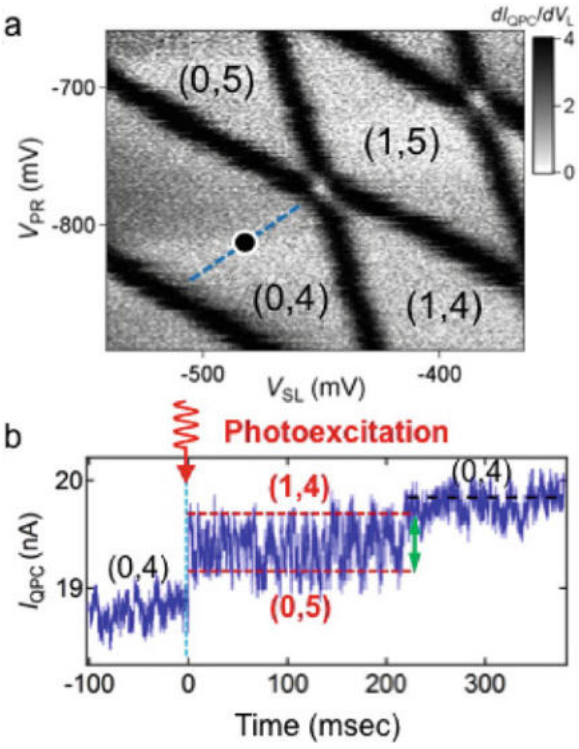

Fig. 25.14 (**a**) Charge stability diagram of the DQD as a function of two plunger gate voltages for the respective dots. The *black dot* indicates the initial bias point before the photo-excitation. (**b**) Charge sensor current I_{QPC} due to single photo-electron trapping by the double QD. The measurement temperature is 0.3 K. The excitation light pulse intensity is 1.0 photon/pulse

The wafer of the DQD used in the experiment is the same as for the dot in Fig. 25.13a but having an aperture in the metal mask only on top of one of the two dots. In this experiment a pulsed laser beam is directly focused onto the DQD placed in a 0.4 K cryostat through an optical window. The beam spot size is 200 μm. The optical polarization is controlled by rotating a quarter wavelength plate placed outside the cryostat.

The DQD charge state is initialized in the Coulomb blockade condition of the (0,4) state before irradiating a linearly polarized beam onto the DQD (See Fig. 25.14a). In addition the excited states of (1,4) and (0,5) are energetically aligned. Figure 25.14b shows a typical charge sensing data of I_{QPC} indicating the single photoelectron detection [9]. Soon after an electron is photo-generated in the dot, it starts resonantly tunneling between the (1,4) and (0,5) states. This gives rise to oscillations of I_{QPC} between two levels corresponding to the two charge states. The oscillation frequency is given by the inter-dot tunneling rate. Finally in about 200 ms the excess electron goes out to the lead and then the (0,4) state is restored. This way of photoelectron detection is more reliable than that using single QD in Fig. 25.13 and in addition nondestructive because the photoelectron does not escape from the DQD. The photoelectron detection efficiency is 15–20 % same as in the single QD experiment [9].

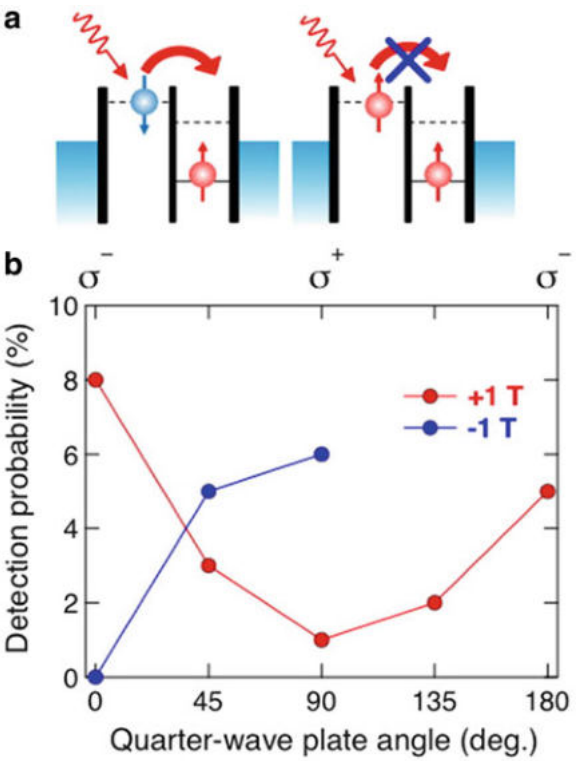

Fig. 25.15 (**a**) Schematic of Pauli spin blockade predicted for a photo-generated electron in a double QD having an up-spin residing electron in the right dot. *Left*: For the photo-excitation of an anti-parallel electron spin to the residing electron the charge state undergoes a (1,1) to (0,2) transition by inter-dot tunneling. *Right*: For the photo-excitation of a parallel spin the (1,1) to (0,2) transition is blocked by Pauli effect. (**b**) Detection probability of blocked photoelectron for parallel spins in the *left right panel* of (**a**) for various incident photon polarization. The residing electron spin in the dot is polarized by the magnetic field of ± 1 T. The excitation light pulse intensity is 0.2 photons/pulse

25.6.1.3 Angular Momentum Transfer from Single Photons to Single Electrons

Pauli-spin blockade (PSB) for DQDs having two electrons has often been used to detect the spin orientation [11]. We apply this method for the photoelectron detection experiment described in Sect. 25.6.1.2 to demonstrate the angular momentum transfer from single photons to single electrons.

The way to judge the spin orientation of photoelectrons is schematically shown in Fig. 25.15a. Suppose an electron is initially trapped by the right dot. A photoelectron spin trapped by the left dot can tunnel to the left dot if it is antiparallel to the electron spin of the right dot. This is not the case if it is parallel to the electron spin of the right dot because the inter-dot tunneling is blocked by Pauli exclusion. The inter-dot tunneling only starts in a time scale (>ms) of spin relaxation after the photo-excitation (blocked inter-dot tunneling). The different processes due to the spin orientation of the photoelectron can be detected by the charge sensor. In the real experiment the inter-dot tunneling time and tunneling time from the right dot to the right lead are both set to the value much shorter than the time resolution of the measurement (0.1 ms). Then the blocked inter-dot tunneling can only be detected by the charge sensor. The non-blocked tunneling cannot be detected because the photoelectron instantly escapes to the right lead.

In the experiment the DQD is initialized to the (0,1) state under a magnetic field of B=±1 T to polarize the residing electron spin along the magnetic field. A quarter wavelength plate is used to change the polarization of incident photons between clockwise (σ_+ polarization for the wavelength plate angle $\theta = 0°$) and anti-clockwise (σ_- polarization for $\theta = 90°$) via the linear polarization states. The detection probability of the blocked inter-dot tunneling of single photoelectrons is plotted for various incident photon polarizations in Fig. 25.15b. We see that the photoelectron spin orientation changes depending on the incident photon polarization [1]. The same result is obtained when the magnetic field direction is reversed with B = −1 T to initialize the residing electron spin in the opposite direction. The photon polarization dependence of the blocked photoelectron detection probability is reversed as expected. These results indicate that the angular momentum is projected from the single photon to the single electron.

In the experiment of Fig. 25.15 photoelectrons are predominantly generated in the GaAs buffer layer. The heavy hole (HH) band with $m_j = \pm 3/2$ and light hole (LH) band with $m_j = \pm 1/2$ are degenerate in the bulk GaAs, therefor σ_+ photons can generate down-spin electrons with $s_z = -1/2$ through the $m_j = -3/2$ HH excitation and up-spin electrons with $s_z = 1/2$ through the $m_j = -1/2$ LH excitation. On the other hand σ_- photons can generate up-spin electrons through the $m_j = 3/2$ HH excitation and down-spin electrons through the $m_j = 1/2$ LH excitation. Because the HH band has the density of states three times larger than the LH band, down-spin (up-spin) electrons are predominantly generated by the $\sigma_+(\sigma_-)$ photon. However, for the quantum state transfer beyond the angular momentum transfer selective excitation of either HH or LH is necessary. For this purpose we use a double heterostructure quantum well of n-AlGaAs/GaAs/AlGaAs instead of a single heterostructure n-AlGaAs/GaAs in which the HH and LH band degeneracy is lifted.

25.6.2 Transfer of Single Electrons Between Distant QDs

To coherently manipulate traveling electrons or paired electrons in solids can provide solid-state quantum information with a new degree of freedom analogous to quantum optics for generating flying qubits and their entanglement. However, the technique has long remained challenging because of strong influence from the environment to collapse the coherence. In this section we describe a newly developed technique for transferring single electrons between distant quantum dots [13, 26].

25.6.2.1 Electron Transfer Using Surface Acoustic Wave

Conducting electrons in Fermi sea become readily admixed with or indistinguishable from other electrons while propagating. This indicates that the electrons as

quantum information carriers easily lose their information. This can only be avoided by transferring single electrons being isolated from the environment just like photons. There may be two possible approaches for it: shuttling electrons through a series of QDs and trapping electrons in a confining potential induced by a surface acoustic wave (SAW). We take the second approach. Then in addition to the SAW a single electron source, an electron propagation waveguide and a single electron trap should be prepared.

Here we use a single QD as the electron source and as the electron trap, a fully depleted one-dimensional (1D) channel as the waveguide, and a SWA burst as the propagation medium. SAW is a crystal strain wave travelling near the surface, and can be generated by applying a microwave to an inter-digital transducer (IDT) placed on the crystal surface in piezo-electric materials like GaAs.

SAW propagates as a periodic potential wave for conducting electrons in a specific crystallographic direction with no substantial dumping. Confined by the SAW induced potential and the 1D waveguide potential in a 2D plane a three-dimensionally confining potential moving at the SAW velocity, i.e. "Moving QD" is established. We use this moving QD to transfer an electron between two distant QDs, while being isolated from the environment. The change of the electron occupation in each dot is precisely detected using a nearby QPC as a charge sensor.

Figure 25.16a is an electron micrograph of the device used for the experiment. Two QDs, source QD and trap QD, and a 3-μm long channel connecting the two dots are defined in a 2DEG by surface Schottky gates. The 1D channel is depleted by applying large negative voltages to the side gates. Just one electron is initially loaded to the source QD while keeping the trap QD empty. Note before sending the SAW burst to the source QD, the junction potentials to the outside are appropriately adjusted so that the residing electron is ejected from the source QD by the SAW and the electron being carried by the SAW is captured by the trap QD.

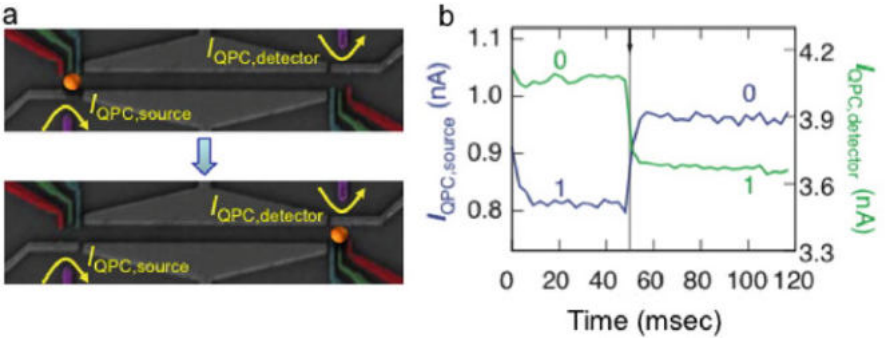

Fig. 25.16 (**a**) Electron micrograph picture of the device used for the experiment of single electron transfer. Two QDs (electron source and trap) are separated by a 3-μm long one-dimensional channel defined by Schottky gates. The electron occupation of each dot is detected by a nearby QPC as a charge sensor. A SAW is generated by applying a microwave to an IDT placed 2 mm to the left of the left dot. (**b**) Temporal change of the charge sensor current showing transfer of a single electron from the source QD to the trap QD by SAW. A 200 ns burst of SAW is irradiated to the IDT at time 50 ms

Figure 25.16b shows the changes of the charge sensors to the source and trap QDs when a burst of SAW is turned on. Upon irradiation of the SAW the source QD becomes empty and the trap QD becomes occupied by one electron. This indicates one electron transfer. The transfer time calculated from the sound velocity in the crystal is about 1 ns for 3 μm, which is much shorter than the spin dephasing time. We find that the probability of success exceeds 90 % after a number of experiments of the single electron transfer. The same SAW technique can apply for picking up one electron out of two electrons residing in the source QD and transferring to the trap QD (not shown) [13]. The success probability is about 90 %. Because the two-electron state is assumed to be a spin single state, this experiment implies formation of a spatially separated singlet state.

The first experiment of Fig. 25.16a demonstrates preparation of a single electron emitter, a 1D waveguide and a single electron detector. When combined with a beam splitter and interferometer, basic elements of quantum electron optics will be established.

25.7 Conclusions and Prospects

We have discussed coherent control of electron spins in quantum dots for possible application as qubits and quantum information processing. Various signatures of spins in single and coupled quantum dots had been revealed because the electron spin is a state quantum number in quantum dot system. Key ingredients for the quantum information are spin Rabi oscillation by electric dipole spin resonance and SWAP gate using exchange interactions. From the viewpoint of scalability, our proposed micro-magnet technology is promising. Recently, multiple qubit systems had been realized in various systems, which had boosted the research and technology in the related fields. Further breakthroughs are definitely still to be explored like controlling quantum entanglement, quantum error correction, suppression of decopherence, and key idea for the scalability.

Acknowledgements Part of this work was supported financially by JSPS MEXT Grant-in-Aid for Scientific Research on Innovative Areas (Grant No. 21102003) and Funding Program for World-Leading Innovative R&D Science and Technology (FIRST).

References

1. T. Asayama, T. Fujita, H. Kiyama, G. Allison, A.D. Wieck, A. Oiwa, S. Tarucha (unpublished)
2. S.D. Barrett, T.M. Stace, Continuous measurement of a microwave-driven solid state qubit. Phys. Rev. Lett. **96**, 017405 (2006)
3. R.L. Bell, Electric dipole spin transition in InSb. Phys. Rev. Lett. **9**, 52–54 (1962)
4. R. Brunner, Y.-S. Shin, T. Obata, Y. Tokura, M. Pioro-Ladrière, T. Kubo, T. Taniyama, S. Tarucha, Realization of a spin two-qubit gate with semiconductor quantum dots using an inhomogeneous Zeeman field. Phys. Rev. Lett. **107**, 146801 (2011)

5. G. Burkard, D. Loss, D.P. DiVincenzo, Coupled quantum dots as quantum gates. Phys. Rev. B **59**, 2070–2078 (1999); G. Burkard, G. Seelig, D. Loss, Spin interactions and switching in vertically tunnel-coupled quantum dots. Phys. Rev. B **62**, 2581–2592 (2000)
6. R.S. Deacon, Y. Kanai, S. Takahashi, A. Oiwa, K. Yoshida, K. Shibata, K. Hirakawa, Y. Tokura, S. Tarucha, Electrically tuned g-tensor in an InAs self-assembled quantum dot. Phys. Rev. B **84**, 041302(R) (2011)
7. J.M. Elzerman, R. Hanson, L.H. Willems van Beveren, B. Witkamp, L.M.K. Vandersypen, L.P. Kouwenhoven, Single-shot read-out of an individual electron spin in a quantum dot. Nature (London) **430**, 431 (2004)
8. T. Fujisawa, D.G. Austing, Y. Tokura, Y. Hirayama, S. Tarucha, Allowed and forbidden transitions in artificial hydrogen and helium atoms. Nature **419**, 278 (2002)
9. T. Fujita, H. Kiyama, K. Morimoto, S. Teraoka, G. Allison, A. Ludwig, A.D. Wieck, A. Oiwa, S. Tarucha, Nondestructive real-time measurement of charge and spin dynamics of photoelectrons in a double quantum dot. Phys. Rev. Lett. **110**, 266803–266807 (2013)
10. V.N. Golovach, M. Borhani, D. Loss, Electric-dipoleinduced spin resonance in quantum dots. Phys. Rev. B **74**, 165319–165322 (2006)
11. R. Hanson, L.P. Kouwenhoven, J.R. Petta, S. Tarucha, L.M.K. Vandersypen, Spins in few-electron quantum dots. Rev. Mod. Phys. **79**, 1217–1265 (2007)
12. T. Hatano, M. Stopa, S. Tarucha, Single-electron delocalization in hybrid vertical-lateral double quantum dots. Science **309**, 268 (2005)
13. S. Hermelin, S. Takada, M. Yamamoto, S. Tarucha, A.D. Wieck, L. Saminadayar, C. Bauerle, T. Meunier, Electrons surfing on a sound wave as a platform for quantum optics with flying electrons. Nature **477**, 435–438 (2011)
14. S.M. Huang, Y. Tokura, H. Akimoto, K. Kono, J.J. Lin, S. Tarucha, K. Ono, Spin bottleneck in resonant tunneling through double quantum dots with different Zeeman splittings. Phys. Rev. Lett. **104**, 136801 (2010)
15. X. Hu, S. Das Sarma, Hilbert-space structure of a solid-state quantum computer: two-electron states of a double-quantum-dot artificial molecule. Phys. Rev. A **61**, 062301–062319 (2000)
16. Y. Kato, R.C. Myers, D.C. Driscoll, A.C. Gossard, J. Levy, D.D. Awschalom, Gigahertz electron spin manipulation using voltage-controlled g-tensor modulation. Science **299**, 1201–1204 (2003)
17. F.H.L. Koppens, C. Buizert, K.J. Tielrooij, I.T. Vink, K.C. Nowack, T. Meunier, L.P. Kouwenhoven, L.M.K. Vandersypen, Driven coherent oscillations of a single electron spin in a quantum dot. Nature **442**, 766–771 (2006)
18. F.H.L. Koppens, D. Klauser, W.A. Coish, K.C. Nowack, L.P. Kouwenhoven, D. Loss, L.M.K. Vandersypen, Universal phase shift and nonexponential decay of driven single-spin oscillations. Phys. Rev. Lett. **99**, 106803 (2007)
19. H. Kosaka, H. Shigyou, Y. Mitsumori, Y. Rikitake, H. Imamura, T. Kutsuwa, K. Arai, E. Edamatsu, Coherent transfer of light polarization to electron spins in a semiconductor. Phys. Rev. Lett. **100**, 096602–096605 (2008)
20. K.P. Kouwenhoven, D.G. Austing, S. Tarucha, Few-electron quantum dots. Rep. Prog. Phys. **64**, 701 (2001)
21. L.S. Levitov, E.I. Rashba, Dynamical spin-electric coupling in a quantum dot. Phys. Rev. B **67**, 115324 (2003)
22. R. Li, J.Q. You, C.P. Sun, F. Nori, Controlling a nanowire spin-orbit qubit via electric-dipole spin resonance. Phys. Rev. Lett. **111**, 086805 (2013)
23. D. Loss, D. DiVincenzo, Quantum computation with quantum dots. Phys. Rev. A **57**, 120 (1998)
24. S. Maekawa, *Concept of Spin Electronics* (Oxford University Press, Oxford/New York, 2006)
25. B.D. McCombe, S.G. Bishop, R. Kaplan, Combined resonance and electron g values in insb. Phys. Rev. Lett. **18**, 748–750 (1967)
26. R.P.G. McNeil, M. Kataoka, C.J.B. Ford, C.H.W. Barnes, D. Anderson, G.A.C. Jones, I. Farrer, D.A. Ritchie, On-demand single-electron transfer between distant quantum dots. Nature **477**, 439–442 (2011)
27. F. Meier, B.P. Zakharchenya (eds.), *Optical Orientation* (Elsevier, Amsterdam, 1984)

28. M.A. Nielsen, I.L. Chuang, *Quantum Computation and Quantum Information* (Cambridge University Press, Cambridge, 2000)
29. K.C. Nowack, F.H.L. Koppens, Y.V. Nazarov, L.M.K. Vandersypen, Coherent control of a single electron spin with electric fields. Science **318**, 1430–1433 (2007)
30. T. Obata, M. Pioro-Ladriere, Y. Tokura, T. Kubo, K. Yoshida, T. Taniyama, S. Tarucha, Coherent manipulation of individual electron spin in a double quantum dot integrated with a micromagnet. Phys. Rev. B **81**, 085317 (2010)
31. K. Ono, D.G. Austing, Y. Tokura, S. Tarucha, Current rectification by Pauli exclusion in a weakly coupled double quantum dot system. Science **297**, 1313 (2002)
32. J.R. Petta, A.C. Johnson, J.M. Taylor, E.A. Laird, A. Yacoby, M.D. Lukin, C.M. Marcus, M.P. Hanson, A.C. Gossard, Coherent manipulation of coupled electron spins in semiconductor quantum dots. Science **309**, 2180 (2005)
33. A. Pioda, E. Totoki, H. Kiyama, T. Fujita, G. Allison, T. Asayama, A. Oiwa, S. Tarucha, Single-shot detection of trapping and resetting single electrons generated by single photons in a lateral quantum dot. Phys. Rev. Lett. **106**, 146804–146807 (2011)
34. M. Pioro-Ladrière, T. Obata, Y. Tokura, Y.-S. Shin, T. Kubo, K. Yoshida, T. Taniyama, S. Tarucha, Electrically driven single-electron spin resonance in a slanting Zeeman field. Nat. Phys. **4**, 776–779 (2008)
35. E.I. Rashba, Theory of electric dipole spin resonance in quantum dots: mean field theory with gaussian fluctuations and beyond. Phys. Rev. B **78**, 195302 (2008)
36. E.I. Rashba, V.I. Sheka, Electron-dipole spin resonance, in *Landau Level Spectroscopy*, chapter 4, ed. by G. Landwehr, E.I. Rashba (Amsterdam, North-Holland, 1991), pp. 131–206
37. G. Salis, Y. Kato, K. Ensslin, D.C. Driscoll, A.C. Gossard, D.D. Awschalom, Electrical control of spin coherence in semiconductor nanostructures. Nature **414**, 619–622 (2001)
38. Y.-S. Shin, T. Obata, M. Pioro-Ladriere, Y. Tokura, R. Brunner, T. Kubo, K. Yoshida, S. Tarucha, Single-spin readout in a double quantum dot integrated with a micromagnet. Phys. Rev. Lett. **104**, 046802 (2010)
39. M.D. Shulman, O.E. Dial, S.P. Narvey, H. Bluhm, V. Umansky, A. Yacoby, Demonstration of entanglement of electrostatically coupled singlet-triplet qubits. Science **336**, 202 (2012)
40. C.P. Slichter, *Principles of Magnetic Resonance*. Springer Series in Solid-State Sciences, 3rd edn. (Cambridge University Press, Cambridge, 1996)
41. D. Stepanenko, N.E. Bonesteel, D.P. DiVincenzo, G. Burkard, D. Loss, Spin-orbit coupling and time-reversal symmetry in quantum gates. Phys. Rev. B **68**, 115306–115314 (2003)
42. S. Tarucha, Y. Tokura, Control over single electron spins in quantum-dots, in *Comprehensive Semiconductor Science and Technology*, ed. by P. Bhattacharya, R. Fornari, H. Kamimura. Physics and Fundamental Theory, vol. 2 (Elsevier, Amsterdam, 2011), pp. 23–67
43. S. Tarucha, D.G. Austing, T. Honda, R.J. van der Hage, L.P. Kouwenhoven, Shell filling and spin effects in a few electron quantum dot. Phys. Rev. Lett. **77**, 3613 (1996)
44. J.M. Taylor, J.R. Petta, A.C. Johnson, A. Yacoby, C.M. Marcus, M.D. Lukin, Relaxation, dephasing, and quantum control of electron spins in double quantum dots. Phys. Rev. B **76**, 035315 (2007)
45. Y. Tokura, W.G. van der Wiel, T. Obata, S. Tarucha, Coherent single electron spin control in a slanting Zeeman field. Phys. Rev. Lett. **96**, 047202–047205 (2006)
46. Y. Tokura, T. Kubo, W.J. Munro, Power dependence of electric dipole spin resonance. JPS Conf. Proc. **1**, 012022 (2014)
47. Y. Tomita, M. Gutiérrez, C. Kabytayev, K.R. Brown, M.R. Hutsel, A.P. Morris, K.E. Stevens, G. Mohler, Comparison of ancilla preparation and measurement procedures for the steane [[7,1,3]] code on a model ion-trap quantum computer. Phys. Rev. A **88**, 042336 (2013)
48. L.M.K. VanderSypen, I.L. Chuang, NMR techniques for quantum control and computation. Rev. Mod. Phys. **76**, 1037–1069 (2004)
49. R. Vrijen, E. Yablonovitch, A spin-coherent semiconductor photo-detector for quantum communication. Physica E **10**, 569–575 (2001)
50. J. Yoneda, T. Otsuka, T. Nakajima, T. Takakura, T. Obata, M. Pioro-Ladriere, H. Lu, C.J. Palmstrom, A.C. Gossard, S. Tarucha, Fast electrical control of single electron spins in quantum dots with vanishing influence from nuclear spins. Phys. Rev. Lett. **113**, 267601 (2014)

Chapter 26
Silicon Quantum Information Processing

Takeharu Sekiguchi and Kohei M. Itoh

26.1 Introduction

As the modern computer is built on the silicon technology, it would be favorable if quantum computation is realized on the same material. Is it possible to build a silicon-based quantum computer? One of the candidates was proposed by Kane in 1998 [1]: The nuclear spin 1/2 of the phosphorus (^{31}P) donor impurity in silicon crystal. In 2002, the present authors' group has proposed an alternative way: all silicon quantum computer employing the nuclear spin 1/2 of ^{29}Si isotope as a qubit [2]. Generally speaking, a spin qubit among many different kinds of qubits is relatively robust to environmental fluctuations so that its quantum state stays intact for a long time. Compared to an electron spin, a nuclear spin has three orders of magnitude smaller magnetic dipole moment and thus much weaker interaction with external perturbations. Accordingly, a nuclear spin has a much longer coherence time than an electron spin, while an electron spin can be manipulated (rotated) in shorter time than a nuclear spin. Hybrid quantum computer architectures are studied very actively. They employ different kinds of qubits with advantages as different components, e.g., quantum memory and quantum processor in a quantum computer. In practice, a quantum error correction (QEC) algorithm needs to be applied in order to store quantum information in qubits. If a minimum set of the QEC can be performed within the coherence time T_2 of the qubits, they serve as a quantum memory by repeated application of the QEC. In this regard, the long-coherence nuclear spins are suited for quantum memory.

One of challenges is the smallness of the magnetic dipole moment of a nuclear spin making it difficult to be polarized (initialized) and measured (readout). In

T. Sekiguchi • K.M. Itoh (✉)
Department of Applied Physics and Physico-Informatics, Keio University, Yokohama, Japan
e-mail: kitoh@appi.keio.ac.jp

Y. Yamamoto, K. Semba (eds.), *Principles and Methods of Quantum Information Technologies*, Lecture Notes in Physics 911, DOI 10.1007/978-4-431-55756-2_26

the solid-state NMR, the thermal equilibrium polarization is less than 0.1 % even at a low temperature 4.2 K and under a high field 10 T for ^{1}H nuclide, whose dipole moment is relatively large among nuclides, and also the magnetic energy is very small so that it is necessary to prepare an ensemble of more than 10^{18} equivalent nuclear spins for measuring a polarized part of spins in the ensemble. However, recent studies have reported that these difficulties can be overcome. Initialization, control, and readout of a single nuclear spin in a silicon wafer have been demonstrated, as shown later. It should be noted that there are defects in other solid-state systems, e.g., nitrogen-vacancy (NV) centers in diamond, whose single nuclear spin state can be optically initialized, optically readout, and manipulated by microwave at room temperature.

In parallel, the scalability is regarded to be one of the crucial challenges for realization of a practical quantum computer architecture. Here a quantum system demonstrated already to serve as one or a few qubits needs to be scaled to a large number of qubits and integrated into a small volume with a limited amount of resources. For example, factoring a 600-digit integer by Shor's algorithm requires 4000 logical qubits [3], and QEC demands a far more number of ancillary qubits. In total, more than 10^{8} qubits are necessary to build a quantum computer [3]. In this regard, silicon has an advantage of established large-scale integrated-circuit technology.

26.2 Single Spin Versus Spin Ensemble

A qubit composed of a single spin would be favorable for quantum computation or quantum memory. It was experimentally demonstrated very recently that a single individual spin in silicon can serve as a qubit [4–6]. A decade ago when we initiated solid-state spin-based quantum computing research, it was necessary to start our research from an ensemble of spins in silicon. Therefore, let us first discuss how one can treat an ensemble of spins as a collection of single qubits whose expectation values indeed represent that of a single qubit and what condition is required to perform a truly quantum-mechanical computation.

The first condition for quantum computation, i.e., a computation that cannot be accomplished by a classical computer, is that the qubits need to be initialized to pure states. In other words, while early NMR quantum computation studies employed only a small, polarized part in an ensemble of nuclear spins for what they called quantum computation, the initial state created by such a pseudo-pure state approach is not sufficiently pure and a quantum algorithm executed on such a pseudo-pure initial state cannot produce true quantum computation. Figure 26.1 shows representative spin qubits in silicon. Focusing on the ^{31}P nuclear spins, Fig. 26.1a, b correspond to single-spin qubit and spin-ensemble qubit. To treat this spin ensemble in an equivalent manner as the single spin, all the ^{31}P nuclear spins in the ensemble need to be indistinguishably equivalent. Even if a perfect silicon crystal that does not contain chemical impurities or structural defects except for

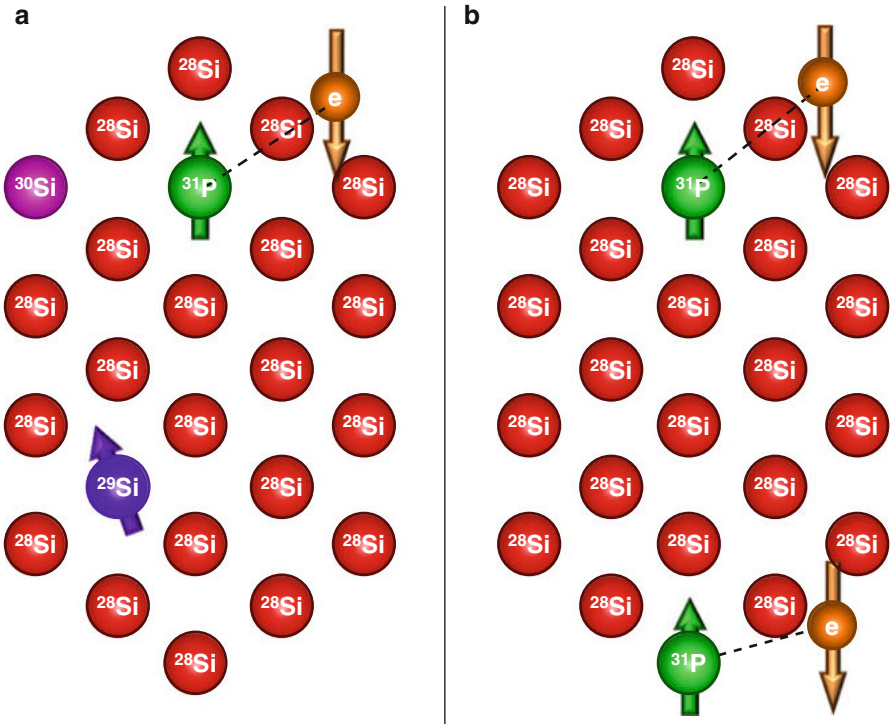

Fig. 26.1 Spin qubits in silicon crystal. (**a**) A qubit of single ^{31}P nuclear spin at a single P atom. (**b**) A qubit composed of ^{31}P nuclear spin ensemble of many P atoms (two shown here). The *green*, *orange*, and *violet arrows* represent the spins of ^{31}P nucleus, donor electron, and ^{29}Si isotope, respectively; The *red* and *pink spheres* represent the no-spin ^{28}Si and ^{30}Si isotopes, respectively

the P donors is employed, the existence of the three kinds of stable Si isotopes (^{28}Si, ^{29}Si, ^{30}Si) causes crucial imperfectness around the P donors, i.e., the spatial inhomogeneity of the isotope mass of the surrounding Si atoms, and the spatial and temporal fluctuations of local magnetic field due to non-zero nuclear spin of ^{29}Si. Such isotopic fluctuations can be removed by employing a Si single-crystal enriched in ^{28}Si. Such enriched silicon results in remarkable enhancement of coherence times of electron and nuclear spins of the P donor. Furthermore, the initialization of the spin-ensemble qubit requires polarization of not only the ^{31}P nuclear spins but also the associated electron spins. (In Fig. 26.1, all the ^{31}P nuclear spins and electron spins are aligned up and down, respectively.) In the following, we review first the nuclear spin polarization, followed by the spin coherence times, and finally the most recent developments.

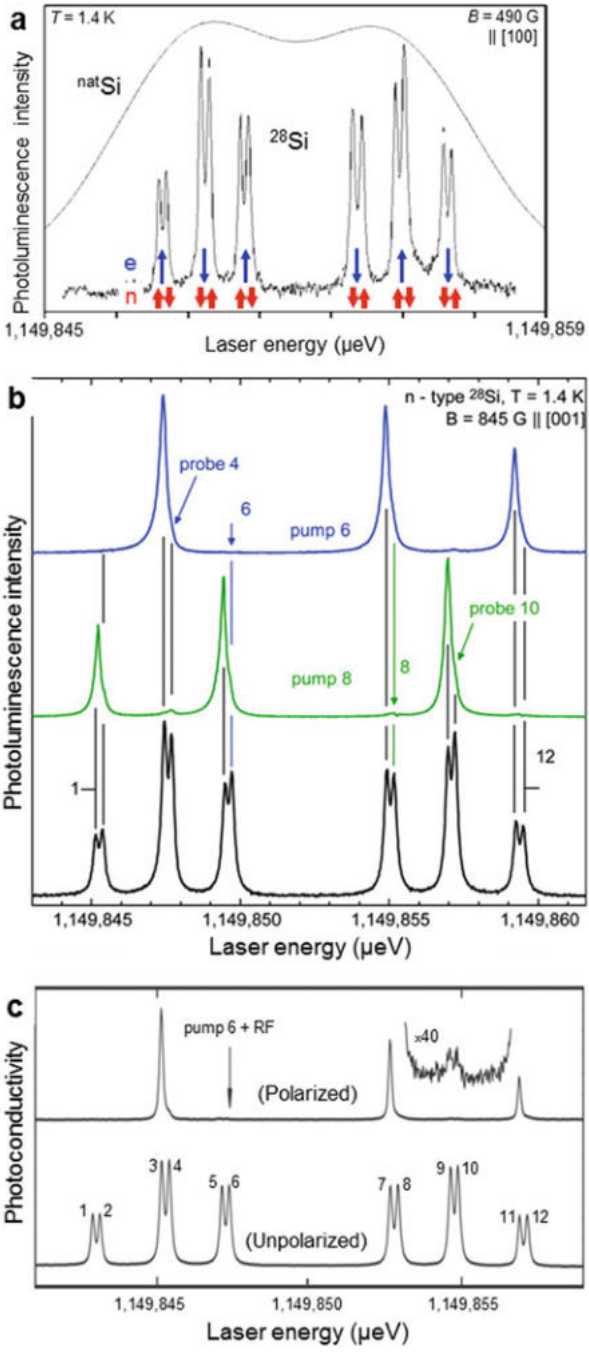
a
T = 1.4 K
B = 490 G
|| [100]
natSi
28Si
e
n
Photoluminescence intensity
1,149,845
1,149,859
Laser energy (μeV)
b
n - type 28Si, T = 1.4 K
B = 845 G || [001]
probe 4
6
pump 6
probe 10
pump 8
8
12
1
Photoluminescence intensity
1,149,845
1,149,850
1,149,855
1,149,860
Laser energy (μeV)
c
pump 6 + RF
×40
(Polarized)
1
2
3
4
5
6
7
8
9
10
11
12
(Unpolarized)
Photoconductivity
1,149,845
1,149,850
1,149,855
Laser energy (μeV)

26.3 Initialization of Nuclear Spins

The straightforward way to obtain higher polarization of spins is to put them at lower temperature and in higher magnetic field. At 2.9 K and 3.4 T, the P donor electron spins have a polarization of 66 % in thermal equilibrium. However, its nuclear spin (^{31}P) has only 0.04 % polarization in the same condition. Therefore, the nuclear spin polarization needs to be greatly enhanced by some nonequilibrium manner. One of such methods is depicted in Fig. 26.4a, b, i.e., When the electron spin is polarized at low temperature and high field, a microwave pulse and a radio-frequency pulse that are resonant to specific ESR and NMR transition, respectively, can transfer the electron spin polarization to the nuclear spin. In the same temperature and field as above, 64 % nuclear spin polarization was achieved [7] Furthermore, nonresonant infrared (IR) laser excitation led to a nuclear spin polarization (for ^{209}Bi donor) essentially equal to the electron spin polarization (more than 99 %) at 1.5 K and 6 T [8]; A visible light excitation yielded 68 % ^{31}P nuclear spin polarization at 1.4 K and 8.5 T [9].

Furthermore, even when the electron spin polarization is very weak, the ^{31}P polarization as high as 90 % was reported by using an infrared laser resonant to the P donor bound exciton (BE) transition [10]. Figure 26.2a shows photoluminescence excitation (PLE) spectra of the P donor bound exciton transition [11]. The upper broad spectrum is from isotopically natural Si crystal (^{nat}Si), and the lower spectrum exhibiting 12 hyperfine-split lines is from ^{28}Si-enriched Si crystal ([^{29}Si] = 50 ppm). Thus, suppression of the spatial inhomogeneity of the Si isotope mass by ^{28}Si enrichment resulted in drastic reduction of the BE linewidth and clear resolution of hyperfine doublets due to ^{31}P nuclear spin ($I = 1/2$). As indicated by red and blue arrows, the two lines in each doublet correspond to up and down nuclear spins ($m_I = +1/2$ and $-1/2$), respectively, and wider six lines are due to different combinations of the ground electron spin and bound-exciton hole spin states. By using this ^{28}Si-enriched silicon, both the electron and nuclear spins can be initialized to a particular state by illuminating a pumping IR resonant to a relevant electron-nuclear spin state, as shown in Fig. 26.2b [12]. The bottom (black) spectrum like

Fig. 26.2 Bound exciton spectra of P donors in silicon crystals. (**a**) Spectra from P donors in ^{nat}Si and ^{28}Si crystals measured by PLE spectroscopy [11]. The ^{28}Si enrichment reduces the linewidth and thus makes the six doublets clearly resolved. The *blue* and *red arrows* represent the orientations of the electron and nuclear spins, respectively, in the donor ground state. (**b**) PLE spectra from an n-type ^{28}Si crystal [12]. The bottom one was measured without pumping laser illumination. The *upper green* and *blue spectra* resulted from the pumping laser at the line 8 and 6, respectively. The selective pumping makes only the three of twelve lines appear, indicating that both the electron and nuclear spins are initialized to a particular state depending on the pumping laser frequency. (**c**) High sensitivity spectra from a p-type ^{28}Si crystal measured by Auger electron detection [10]. The SNR was improved from (**b**) despite the three orders of magnitude lower concentration of P donors. The lower spectrum shows the unpolarized state without pumping, and the upper one exhibits the polarization higher than (**b**) when pumped at the line 6 along with selective RF excitation

Fig. 26.2a is obtained without pumping IR, indicating negligible polarization of both the electron and nuclear spins. (The six doublets have different intensities due to different optical transition probabilities.) The top (blue) and middle (green) spectra are observed with a resonant pumping laser at 6 and 8, respectively, while sweeping the probe laser. In both the spectra, only three lines out of twelve are visible. This demonstrates that the resonant pumping polarizes the electron and nuclear spins in the donor ground state. The Auger relaxation process after the resonant pumping resulted in the initialized state, where only the electron spin is reversed from the ground state. Indeed, this polarizing method yielded polarizations of 90 % for the donor electron and 76 % for ^{31}P nuclear spin [12]. The spin polarizations are improved to 97 % (electron) and 90 % (^{31}P) by further enrichment of ^{28}Si and reduction of P donor concentration combined with RF radiation resonant to particular NMR transitions (See Fig. 26.2c [10]).

On the other hand, a different method is required to hyperpolarize the ^{29}Si nuclear spins as they cannot bind paramagnetic electrons in contrast to ^{31}P. For this purpose, the effects of optical and dynamical nuclear polarizations (ONP and DNP) have been studied utilizing electron and nuclear spin polarizations of paramagnetic centers. Using the P donor ground state and the spin triplet state (SL1 center) of oxygen-vacancy center, the ^{29}Si nuclear polarization was enhanced to 1.5 % [13] and 6.4 % [14], respectively, which are more than three orders of magnitude higher than the thermal polarization. However, these values are not sufficient for quantum memory application. We have investigated the SL1 center in more details and obtained more than 80 % polarization of ^{29}Si nuclear spins (at a specific site) [15], as explained in Sect. 26.5.2.

26.4 Coherence Times

26.4.1 Electron Spin Coherence Times T_{2e}

As mentioned in Sect. 26.2, the ^{29}Si concentration in silicon needs to be minimized to extend the spin coherence times of the donor electron and nucleus to a sufficient level. In 2003, $T_{2e} > 60$ ms (donor concentration of 10^{15} cm^{-3}, temperature of 7 K) was reported for P donors in ^{28}Si-enriched crystal [16]. In 2012, T_{2e} was extended to c.a. 1 s by reducing the ^{29}Si concentration and the P donor concentration to 50 ppm and 1×10^{14} cm^{-3}, respectively, and measuring at 1.8 K [17]. However, this value is still 3 orders of magnitude shorter than the electron spin-lattice relaxation time $T_{1e} = 2000$ s, indicating far below the ideal electron spin coherence. Apart from the magnetic field fluctuation due to surrounding ^{29}Si nuclear spins [18, 19], one of the dominant decoherence sources should be the magnetic dipole-dipole interaction between the donor electrons themselves. Indeed, T_{2e} depends strongly on the donor concentration below 7 K, as shown in Fig. 26.3a [17]. By applying a spatial gradient on the static magnetic field to suppress the effective concentration of the donors that

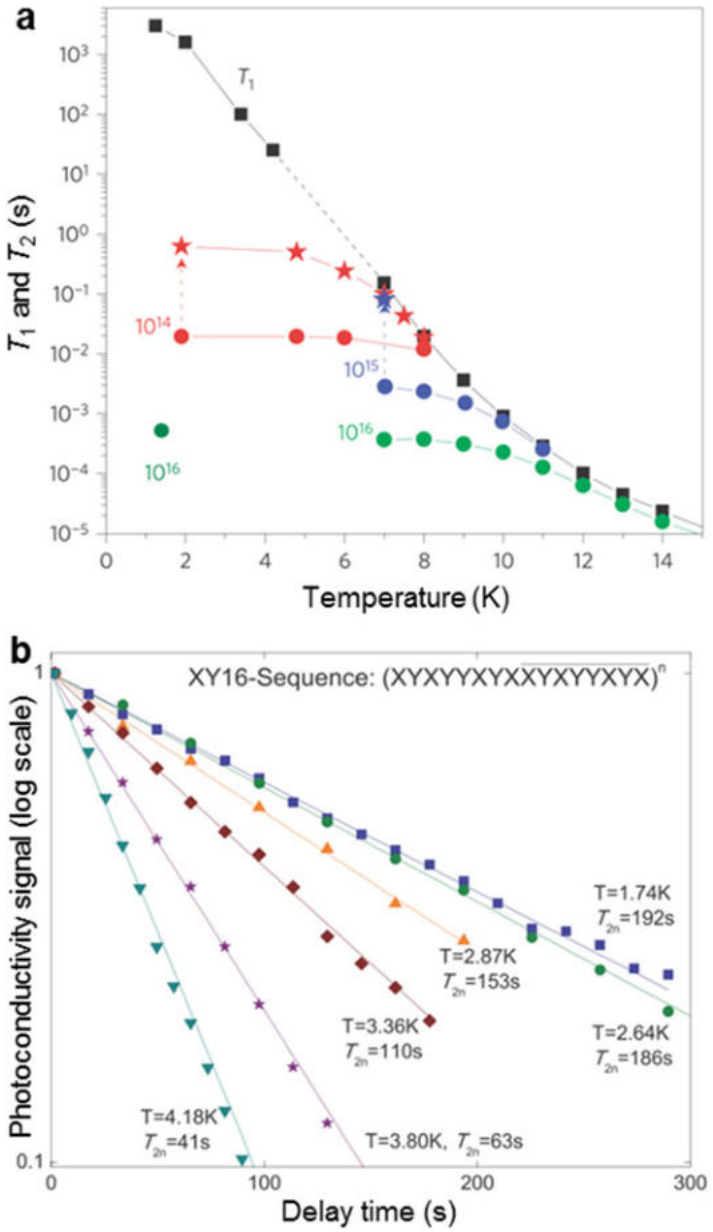

Fig. 26.3 Spin coherence times of P atom ensembles. (**a**) The electron spin coherence time T_{2e} measured by the conventional ESR spectroscopy depends on the temperature and the P concentration. The spin-lattice relaxation time T_{1e} is also plotted as a function of temperature [17]. (**b**) The ^{31}P nuclear spin coherence time T_{2n} measured by the AEDMR also depends on the temperature. The RF pulse sequence (XY16) as given at the upper-right corner is composed of π pulses of four different phases (X, Y, −X, −Y) to decouple from external field fluctuations while keeping arbitrary initial states [10]

are resonant to the microwave pulses, T_{2e} was extended up to 10 s [17]. To extend T_{2e} further, the donor concentration needs to be lowered further. However, the detection in the conventional ESR experiment is very difficult because the electron spin echo intensity would be decreased in proportion to the donor concentration. To overcome this difficulty, the bound exciton transition was combined into the spin coherence experiment, as described in Sect. 26.4.2.

26.4.2 Nuclear Spin Coherence Time T_{2n}

As mentioned in the introduction, the nuclear spin coherence time is expected to be orders of magnitude longer than the electron spin coherence time. While direct detection of the ^{31}P nuclear spins of dilute donors is difficult by the conventional NMR, they can be detected through the donor electron spin signal. The most popular method is the electron nuclear double resonance (ENDOR). The nuclear spin coherence time T_{2n} can be measured as the electron spin echo intensity by transferring the nuclear spin coherence (decaying with a time constant T_{2n}) into the electron spin. In 2008, $T_{2n} = 1.8$ s of ^{31}P was reported at 5.5 K by ENDOR of a ^{28}Si crystal (^{29}Si concentration of 800 ppm and P donor concentration around 10^{14} cm^{-3}) [20]. As for T_{2e}, the concentrations of both ^{29}Si isotopes and P donors need to be lowered to extend T_{2n} further. However, the reduction of the donor concentration makes difficult the nuclear spin echo detection by the conventional ENDOR. An optically detected magnetic resonance (ODMR) method that combines the PLE spectroscopy and NMR spectroscopy (Sect. 26.3) allows for the detection of the donor nuclear spin states. However, since silicon is an indirect band-gap semiconductor, the light emission intensity is much weaker than direct gap semiconductors like GaAs, and thus the nuclear spin detection of low concentration donors is still difficult even by ODMR. In the relaxation from the donor bound exciton state to its ground state, the nonradiative Auger process is four orders of magnitude dominant over the radiative process. By measuring the conduction electron (Auger electron) emitted in the nonradiative relaxation instead of photons in the radiative relaxation, detection sensitivity can be remarkably enhanced. The bound exciton spectrum by this electrical detection method is shown in Fig. 26.2c [10]. In spite of that low donor concentration 5×10^{11} cm^{-3}, the SNR is better than the optically detected PLE spectrum of three orders of magnitude higher concentration donors (7×10^{14} cm^{-3}). Here, since the ^{28}Si enrichment is improved to 99.995 %, the linewidth is even more narrowed to resolve the nuclear spin states more clearly, resulting in the enhancement of the ^{31}P nuclear polarization. By the Auger electron detected magnetic resonance (AEDMR) experiment, which combined the Auger electron detection with the NMR spectroscopy, $T_{2n} = 44$ s was obtained at 1.7 K even with the simplest Hahn echo sequence [10]. This T_{2n} was extended to 3 min by applying a dynamical decoupling pulse sequence that cancelled out the external field fluctuation adaptable to arbitrary initial states (Fig. 26.3b [10]).

26.5 Quantum Memory and Quantum Calculation by Nuclear Spin Ensemble Qubits

26.5.1 Entanglement of the Electron and Nuclear Spins of the ^{31}P Donors

It has been shown that for ^{31}P nuclear spins in silicon crystal, nearly 100 % polarization is achieved, the coherence time is very long (minutes) even in the ensemble, and that their states can be read out by transferring to the electron spin or by detecting the Auger electrons. In order to employ such an ensemble of nuclear spins to a practical quantum computation, one of important issues is the fidelity of the quantum information transfer between the electron spins and the nuclear spins in the ensemble. The fidelity of 97 % was obtained in the ENDOR experiments that determined the T_{2n} of the ^{31}P nuclear spin ensemble [20]. Moreover, an entangled state was created between the electron and nuclear spins in an ensemble of the P donors by ENDOR [7]. Creation of such entanglement requires the electron and nuclear spins to be initialized into a *pure* state with a high fidelity, i.e., it is required to prepare both spins with high enough polarizations. Conversely, if the initial state has only weak polarization, it could give only a separable *pseudo*-entangled state. Simmons et al. [7] prepared more than 60 % polarizations of both the electron and nuclear spins, and then applied an RF pulse rotating the nuclear spin by an angle of $\pi/2$ and a microwave pulse rotating the electron spin by π, and finally obtained an entangled state. These processes (initialization and entanglement creation) are depicted in Fig. 26.4a–c. Figure 26.4d shows the density matrix elements of this entangled state measured by quantum tomography. The observation that only the diagonal elements (1,1), (4,4) and the off-diagonal elements (1,4), (4,1) have significant values indicates a superposition state between the states 1 and 4, i.e., an entanglement between the electron and nuclear spins. Quantitatively speaking, the PPT (positive partial transpose) test[1] gave the minimum eigenvalue of -0.19, and the concurrence value as a measure of quantum entanglement[2] was 0.43. Both values prove a finite entanglement in the created state. The fidelity of the entanglement creation process was better than 98 %, and the fidelity of the entangled state obtained with respect to the ideal Bell state was 68 %. To improve the entanglement fidelity, a purer initial state is required, i.e., even more highly polarized electron and nuclear spins need to be prepared. Such a high polarization will be obtained in a straightforward manner (low temperature and high field) or by combination with other experimental techniques as described in Sect. 26.3.

[1] If the partial transpose of the density matrix for a given quantum state is positive definite, this state is separable and non-entangled (and vice versa). Conversely, if the minimum eigenvalue of the partial transpose is negative, that state is entangled.

[2] The higher the concurrent value is (between 0 and 1), the higher the degree of entanglement is.

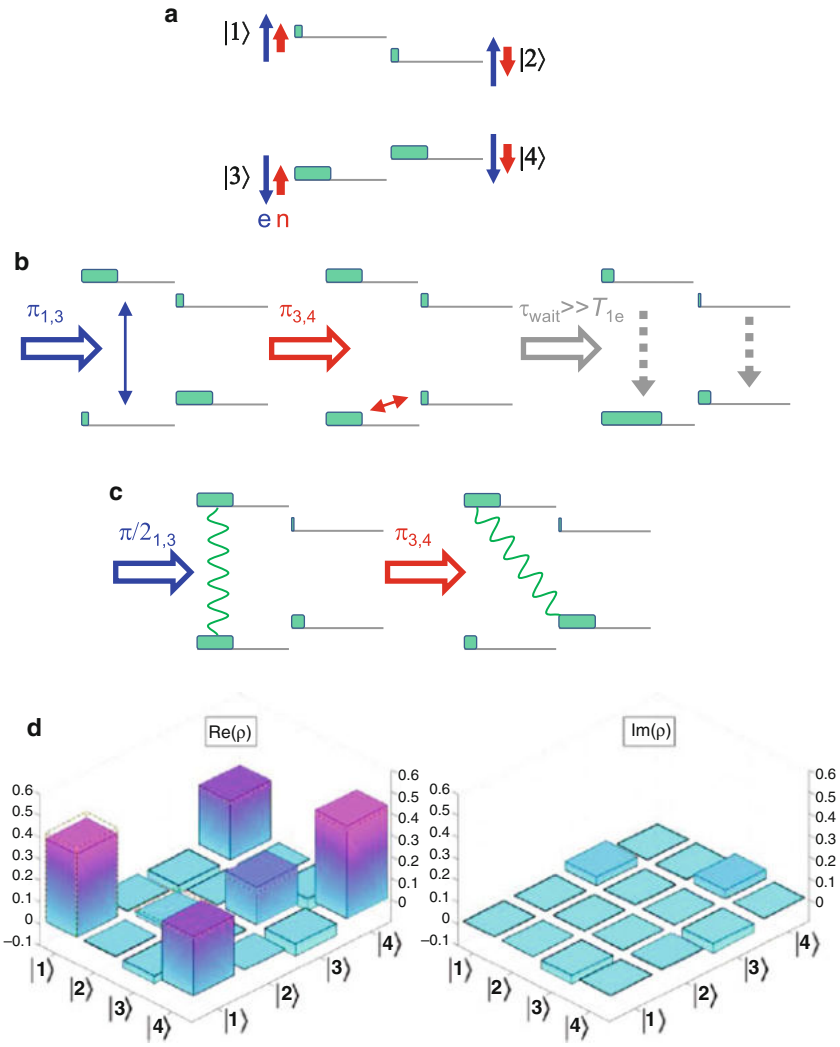

Fig. 26.4 Entanglement between electron spins and nuclear spins of P donor ensemble [7]. (**a**) Energy level diagram for the P donor electron and nuclear spins. The *blue* and *red arrows* indicate the electron and nuclear spin states, respectively, at each level. The *green bar* on each level represents the occupation probability. In the thermal equilibrium at given temperature and field, the electron spin polarization is more than 60 %, but the nuclear spin polarization is negligible. (**b**) Initialization process to polarize the nuclear spins too. The microwave π pulse resonant with the $1 \leftrightarrow 3$ transition ($\pi_{1,3}$) followed by the RF π pulse resonant with the $3 \leftrightarrow 4$ transition ($\pi_{3,4}$) polarizes the nuclear spins upwards, and then waiting longer than the electron spin-lattice relaxation time T_{1e} results in the exclusive occupation in the state 3. (**c**) The pulse sequence applied to the initialized state to create entanglement between the electron spins and the nuclear spins. After the microwave $\pi/2$ pulse resonant with the transition $1 \leftrightarrow 3$ ($\pi/2_{1,3}$) creates the electron spin coherence, the RF $\pi_{3,4}$ pulse creates entanglement. (**d**) The density matrix elements of the entangled states measured by quantum tomography. Entanglement is indicated by the observation that only the (1,1), (4,4), (1,4), and (4,1) elements have significant values

26.5.2 ^{29}Si Nuclear Spin Quantum Memory with a Spin Triplet Center

The oxygen-vacancy (OV) center in silicon has an electron spin triplet state like the negatively charged NV center in diamond. While the NV center has a spin triplet ground state, the spin triple state (SL1 center) of the OV center is optically excited from the spin singlet ground state (named A center). Therefore, to measure the electro spin resonance (ESR) spectrum, one needs to excite the OV center into the triplet state by continuous illumination or to excite by a light pulse followed by detecting the electron spin echo before the relaxation into the ground state. On the other hand, due to different relaxation times (0.2–2 ms) for different spin sublevels in the triplet [15], a simple illumination gives more than 80 % electron spin polarization at 0.3 T and 12 K [15]. The ^{29}Si located at the nearest neighbor site of the vacancy of OV in ^{nat}Si has strong enough hyperfine interaction with the triplet electron spin to be resolved as satellite peaks by ESR spectroscopy [21]. At these satellite peaks (resonance fields), the coherence can be transferred between the triplet electron spin of SL1 and this nearest-neighbor ^{29}Si nuclear spin by a process illustrated with the energy level diagram in Fig. 26.5a [15]. The SL1 is initialized into the T_+ state (the electron spin projection of $m_S = +1$) by optical excitation and partial relaxation, and then a microwave $\pi/2$ pulse creates the electron spin coherence (EC). A pair of RF π pulse and a microwave π pulse transfers this coherence into the nuclear spin (SWAP), to create the nuclear spin coherence (NC). The NC can be swapped back to the EC by the reversed pair of the RF and microwave π pulses, to detect the ^{29}Si nuclear spin coherence time T_{2n}. The electron spin echo decay curves measured by this method is shown in Fig. 26.5b [15]. The apparent decay time constant 0.9 ms is limited by the triplet state lifetime 1.0 ms. Figure 26.5c shows the experimental result with improved pulse sequence to remove the effect of the triplet state lifetime [15]. The echo intensity reduction due to the triplet state lifetime is canceled by fixing the microwave pulse interval in which the RF pulse interval is swept, and the lower bound of the coherence time $T_{2n} > 5$ ms was obtained. This value is close to $T_{2n} = 5.6$ ms [22] that was reported for the ^{29}Si in the absence of the SL1 centers by NMR. While the dominant decoherence source for the latter system is the dipole-dipole interaction between the nuclear spins of equivalent ^{29}Si, which occupies randomly 4.7 % of the total lattice sites due to its natural abundance [22], the decoherence due to this interaction should be suppressed for the ^{29}Si hyperfine-coupled to the SL1 (low concentration) as this ^{29}Si is magnetically inequivalent to other uncoupled ^{29}Si. Therefore, another decoherence mechanism associated with the SL1 electron spins should be dominant for the ^{29}Si coupled with the SL1.

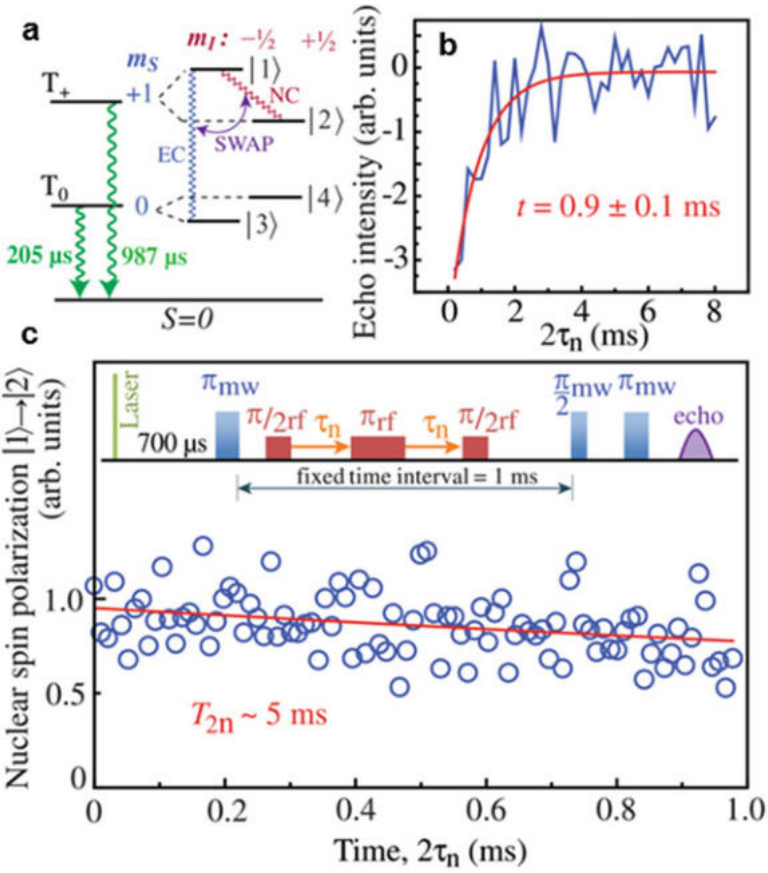

Fig. 26.5 Photoexcited triplet states called SL1 center [15]. (**a**) A partial energy level diagram of the electron spin triplet excited states and singlet ground state. The electron spin is initialized due to the different relaxation times (*green wavy lines*) of the different triplet sublevels. By a SWAP operation, the electron spin coherence (EC) is transferred to the nuclear spin coherence (NC). (**b**) Apparent ^{29}Si nuclear spin coherence time observed by the Davies ENDOR pulse sequence. This is limited by the lifetime 0.99 ms of the T_+ state. (**c**) The improved ENDOR pulse sequence to remove the effect of the triplet state lifetime, and the true T_{2n} obtained by this method

26.6 Single-Spin Qubit

So far we reviewed the spin-ensemble qubits. Below we focus on recent studies of the electron spin and nuclear spin qubits of a single P donor atom performed in University of New South Wales in Australia. Figure 26.6a shows the device structure

for the electron spin qubit and the ^{31}P nuclear spin qubit at a single phosphorus atom in silicon [4]. A single electron transistor (SET) structure tunnel-coupled to a P atom in silicon substrate was fabricated for initialization and readout of the single-atom electron spin state. Phosphorus was doped by a special ion implantation method to put a single P atom at a desired position, which guarantees that the tunneling electron derives from the single P atom instead of an ensemble of P atoms. A broad-band transmission line is also fabricated on the same substrate for oscillating field application to manipulate the spin state. A tunnel current flows depending on the spin state of the electron bound to the P atom, by combination of the electron Zeeman splitting at high field and the electric potential control by gate voltages. This spin blockade mechanism was used to demonstrate the initialization and readout of the electron spin state of the single P atom [4]. Figure 26.6b shows the electron spin Rabi oscillation [4], demonstrating the control of the single electron spin by microwave pulses (30–50 GHz) using the broadband transmission line. Moreover, the coherence time T_{2e} of the single electron spin was measured to be 200 μs with the simplest Hahn echo pulse sequence and extended to 400 μs by the XYXY dynamical decoupling sequences [4]. Like the electron spin ensemble of the P donors in ^{nat}Si, whose T_{2e} is 300 μs measured by the conventional ESR spectroscopy, the decoherence source for this single electron spin should be ^{29}Si nuclear spin fluctuation. The fidelities of the initialization, control (manipulation), readout in this single-spin device were 90 % up, 57 %, 77 %, respectively [4].

Because the ^{31}P nuclear spin is hyperfine-coupled to the donor electron spin, the ESR frequency has two values depending on the nuclear spin state, whose difference was measured to be 114 MHz for this single-spin device [5]. Therefore, when a selective microwave π pulse is applied to excite either ESR transition, the electron spin is flipped only if the nuclear spin occupies a particular state of the two. Combining with the spin blockade used for the single electron-spin state detection, the nuclear spin state can be also read out. Indeed, the nuclear spin readout fidelity reached better than 99.8 % [5]. Moreover, by applying the RF field (20–90 MHz) through the broadband transmission line used for the microwave application, the single nuclear spin control, i.e., NMR spectroscopy is allowed. Apart from NMR spectra, Rabi oscillation [Fig. 26.6c], Ramsey fringe (effective phase relaxation time T_{2n*}), and the Hahn echo (coherence time T_{2n}) experiments were performed [5]. Furthermore, the visibility of the Rabi oscillation, T_{2n*}, and T_{2n} were all improved in the ionized state (D^+) compared to the neutral state (D^0): visibility from about 60 % to almost 100 %, $T_{2n*} = 0.84$ ms to 3.3 ms, $T_{2n} = 3.5$ ms to 60 ms. In particular, T_{2n} in D^+ is limited by the ^{29}Si nuclear spin fluctuation as in the case of T_{2e} of the single electron spin [23].

The advancement of the single-spin experiments using SET has enhanced the prospect for realization of quantum memory employing the individual nuclear spins in silicon. So far, the coherence times T_2 of both the single donor electron spin and

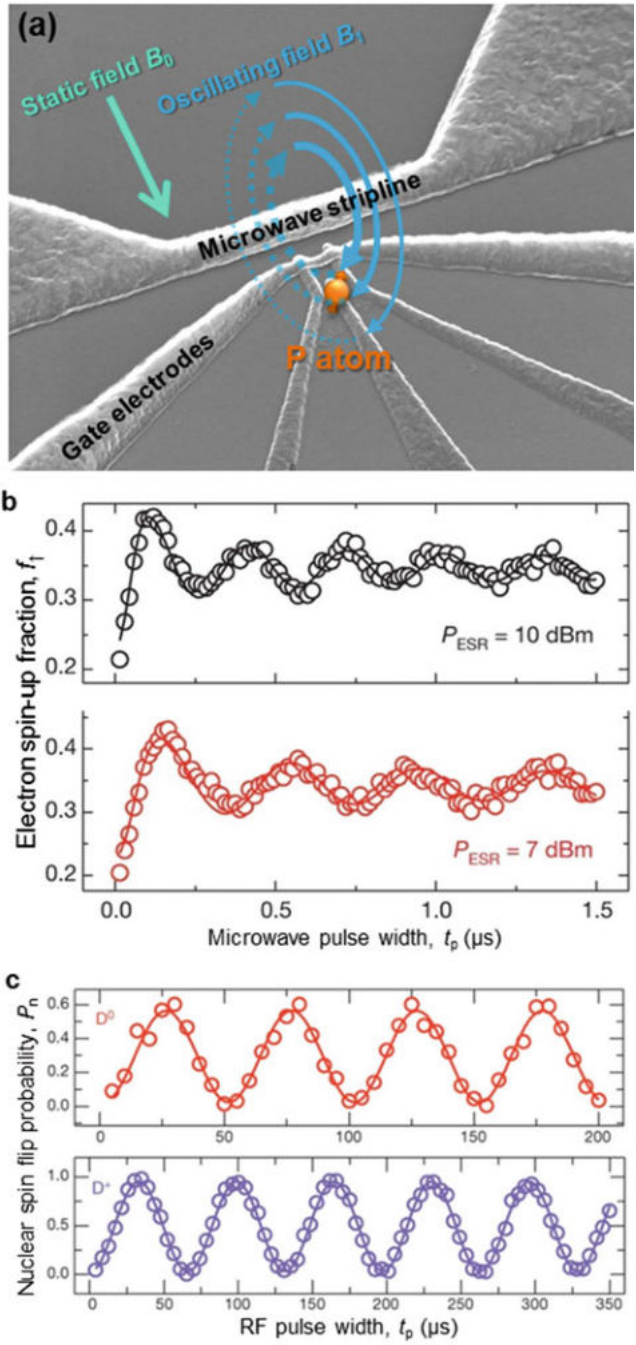
(a)
Static field B_0
Oscillating field B_1
Microwave stripline
P atom
Gate electrodes
b
Electron spin-up fraction, $f_\uparrow$
P_{ESR} = 10 dBm
P_{ESR} = 7 dBm
Microwave pulse width, t_p (μs)
c
Nuclear spin flip probability, P_n
D^0
D^+
RF pulse width, t_p (μs)

the single ^{31}P nuclear spin were limited by the magnetic dipole fluctuation of the ^{29}Si isotopes, whose concentration is 4.7 % in ^{nat}Si substrates. According to the spin ensemble experiments of the same donors, employment of the ^{28}Si-enriched substrate should improve drastically the coherence times of the single spins. In this way, ^{28}Si-enriched wafers will be used to build MOS quantum circuits on them, and thus there will be a growing need for the silicon isotope engineering.

26.7 Summary

We reviewed recent development to utilize electron and nuclear spins in silicon as qubits for quantum computation. In the investigations of electron and nuclear spin properties based on an ensemble, it has been experimentally demonstrated that a sufficiently high polarization can be achieved even for the nuclear spins in the solid state, that ^{28}Si enrichment of the host material can extend the coherence times of both the electron spins and the nuclear spins, and that the quantum information transfer and entanglement are possible between the electron spins and the nuclear spins. While ensemble experiments with low spin concentrations have been conducted to improve the detection sensitivity and the coherence times as an extension of the conventional magnetic resonance experiments, the combination with the SET micro-device has allowed the initialization, manipulation, and readout of not only the single electron spin but also the single nuclear spin. In the coming years, we expect that the single electron and nuclear spin qubit device will be extended to multiple qubits on an isotopically enriched substrates to extend the coherence and demonstrate the entanglement and multi-bit operations. Along with this direction, the scalability in perspective of hybridization with other kinds of quantum systems must be extensively studied to demonstrate it.

Fig. 26.6 Electron-spin and nuclear-spin qubits of single P atom in silicon. (**a**) SEM image of the microdevice for initialization, manipulation, readout of spins of a single P atom in silicon [4]. On the silicon substrate in which a single P atom is embedded at a desired location, the SET structure composed of gate electrodes and the transmission line for the oscillating field application was fabricated. (**b**) Rabi oscillations of the single electron spin [4]. The electron spin polarization calculated from the SET current is plotted as a function of the microwave pulse width. The Rabi frequency is proportional to the square root of the applied microwave power, i.e., the microwave field amplitude. (**c**) Rabi oscillations of the single nuclear spin [5]. The nuclear spin flipping probability is plotted as a function of the RF pulse width. The *upper* and *lower curves* correspond to the neutral donor (D^0) and the ionized donor (D^-), respectively. The visibility of Rabi oscillation is enhanced from the electron spin to the nuclear spin, and further enhanced for the nuclear spin by ionizing the donor, which removes the effect of the electron spin (Note the different scales of the *vertical axes*)

References

1. B.E. Kane, A silicon-based nuclear spin quantum computer. Nature **393**, 133–137 (1998). doi:10.1038/30156
2. T.D. Ladd, J.R. Goldman, F. Yamaguchi, Y. Yamamoto, E. Abe, K.M. Itoh, All-silicon quantum computer. Phys. Rev. Lett. **89**, 017901 (2002). doi:10.1103/PhysRevLett.89.017901
3. A.G. Fowler, Surface codes: Towards practical large-scale quantum computation. Phys. Rev. A **86**, 032324 (2012). doi:10.1103/PhysRevA.86.032324
4. J.J. Pla, K.Y. Tan, J.P. Dehollain, W.H. Lim, J.J.L. Morton, D.N. Jamieson, A.S. Dzurak, A. Morello, A single-atom electron spin qubit in silicon. Nature **489**, 541–545 (2012). doi:10.1038/nature11449
5. J.J. Pla, K.Y. Tan, J.P. Dehollain, W.H. Lim, J.J.L. Morton, F.A. Zwanenburg, D.N. Jamieson, A.S. Dzurak, A. Morello, High-fidelity readout and control of a nuclear spin qubit in silicon. Nature **496**, 334–338 (2013). doi:10.1038/nature12011
6. A. Morello, Quantum Information: Atoms and circuits unite in silicon. Nat. Nanotechnol. **8**, 233–234 (2013). doi:10.1038/nnano.2013.50
7. S. Simmons, R.M. Brown, H. Riemann, N.V. Abrosimov, P. Becker, H.J. Pohl, M.L.W. Thewalt, K.M. Itoh, J.J.L. Morton, Entanglement in a solid-state spin ensemble. Nature **470**, 69–72 (2011). doi:10.1038/nature09696
8. T. Sekiguchi, M. Steger, K. Saeedi, M.L.W. Thewalt, H. Riemann, N.V. Abrosimov, N. Nötzel, Hyperfine structure and nuclear hyperpolarization observed in the bound exciton luminescence of Bi donors in batural Si. Phys. Rev. Lett. **104**, 137402 (2010). doi:10.1103/PhysRevLett.104.137402
9. D.R. McCamey, J. van Tol, G.W. Morley, C. Boehme, Fast nuclear spin hyperpolarization of phosphorus in silicon. Phys. Rev. Lett. **102**, 4 (2009). doi:10.1103/PhysRevLett.102.027601
10. M. Steger, K. Saeedi, M.L.W. Thewalt, J.J.L. Morton, H. Riemann, N.V. Abrosimov, P. Becker, H.-J. Pohl, Quantum information storage for over 180 s using donor spins in a ^{28}Si "semiconductor vacuum". Science **336**, 1280–1283 (2012). doi:10.1126/science.1217635
11. M.L.W. Thewalt, A. Yang, M. Steger, D. Karaiskaj, M. Cardona, H. Riemann, N.V. Abrosimov, A.V. Gusev, A.D. Bulanov, I.D. Kovalev, A.K. Kaliteevskii, O.N. Godisov, P. Becker, H.-J. Pohl, E.E. Haller, J.W. Ager, K.M. Itoh, Direct observation of the donor nuclear spin in a near-gap bound exciton transition: ^{31}P in highly enriched ^{28}Si. J. Appl. Phys. **101**, 081724 (2007). doi:10.1063/1.2723181
12. M. Steger, T. Sekiguchi, A. Yang, K. Saeedi, M.E. Hayden, M.L.W. Thewalt, K.M. Itoh, H. Riemann, N.V. Abrosimov, P. Becker, H.-J. Pohl, Optically-detected NMR of optically-hyperpolarized ^{31}P neutral donors in ^{28}Si. J. Appl. Phys. **109**, 102411 (2011). doi:10.1063/1.3577614
13. H. Hayashi, T. Itahashi, K.M. Itoh, L.S. Vlasenko, M.P. Vlasenko, Dynamic nuclear polarization of ^{29}Si nuclei in isotopically controlled phosphorus doped silicon. Phys. Rev. B **80**, 045201 (2009). doi:10.1103/PhysRevB.80.045201
14. T. Itahashi, H. Hayashi, M.R. Rahman, K.M. Itoh, L.S. Vlasenko, M.P. Vlasenko, D.S. Poloskin, Optical and dynamic nuclear polarization of ^{29}Si nuclei via photoexcited triplet states of oxygen-vacancy complexes in isotopically controlled silicon. Phys. Rev. B **87**, 075201 (2013). doi:10.1103/PhysRevB.87.075201
15. W. Akhtar, V. Filidou, T. Sekiguchi, E. Kawakami, T. Itahashi, L. Vlasenko, J.J.L. Morton, K.M. Itoh, Coherent storage of photoexcited triplet states using ^{29}Si nuclear spins in silicon. Phys. Rev. Lett. **108**, 097601 (2012). doi:10.1103/PhysRevLett.108.097601
16. A.M. Tyryshkin, S.A. Lyon, A.V. Astashkin, A.M. Raitsimring, Electron spin relaxation times of phosphorus donors in silicon. Phys. Rev. B **68**, 193207 (2003). doi:10.1103/PhysRevB.68.193207
17. A.M. Tyryshkin, S. Tojo, J.J.L. Morton, H. Riemann, N.V. Abrosimov, P. Becker, H.-J. Pohl, T. Schenkel, M.L.W. Thewalt, K.M. Itoh, S.A. Lyon, Electron spin coherence exceeding seconds in high-purity silicon. Nat. Mater. **11**, 143–147 (2012). doi:10.1038/nmat3182

18. E. Abe, K.M. Itoh, J. Isoya, S. Yamasaki, Electron-spin phase relaxation of phosphorus donors in nuclear-spin-enriched silicon. Phys. Rev. B **70**, 033204 (2004). doi:10.1103/PhysRevB.70.033204
19. E. Abe, A.M. Tyryshkin, S. Tojo, J.J.L. Morton, W.M. Witzel, A. Fujimoto, J.W. Ager, E.E. Haller, J. Isoya, S.A. Lyon, M.L.W. Thewalt, K.M. Itoh, Electron spin coherence of phosphorus donors in silicon: Effect of environmental nuclei. Phys. Rev. B **82**, 121201 (2010). doi:10.1103/PhysRevB.82.121201
20. J.J.L. Morton, A.M. Tyryshkin, R.M. Brown, S. Shankar, B.W. Lovett, A. Ardavan, T. Schenkel, E.E. Haller, J.W. Ager, S.A. Lyon, Solid-state quantum memory using the ^{31}P nuclear spin. Nature **455**, 1085–1088 (2008). doi:10.1038/nature07295
21. Brower, Electron Paramagnetic Resonance of the Neutral ($S = 1$) One-Vacancy–Oxygen Center in Irradiated Silicon. Phys. Rev. B **4**, 1968–1982 (1971). doi:10.1103/PhysRevB.4.1968
22. A. Dementyev, D. Li, K. MacLean, S. Barrett, Anomalies in the NMR of silicon: Unexpected spin echoes in a dilute dipolar solid. Phys. Rev. B **68**, 153302 (2003). doi:10.1103/PhysRevB.68.153302
23. W.M. Witzel, M.S. Carroll, L. Cywinski, S. Das Sarma, Quantum decoherence of the central spin in a sparse system of dipolar coupled spins. Phys. Rev. B **86**, 035452 (2012). doi:10.1103/PhysRevB.86.035452

Chapter 27
Quantum Information Processing Experiments Using Nuclear and Electron Spins in Molecules

Masahiro Kitagawa, Yasushi Morita, Akinori Kagawa, and Makoto Negoro

27.1 Introduction

Quantum information processing (QIP) using nuclear spins in molecules was proposed in 1996 by Chuang et al. [1] and Cory et al. [2]. Under a static magnetic field, spin-1/2 particles have two energy levels, corresponding to the states that are parallel ($|\uparrow\rangle$) and anti-parallel ($|\downarrow\rangle$) to the magnetic field. These quantum states can be used as the $|0\rangle$ and the $|1\rangle$ of a qubit, respectively. Many nuclei with spin exist in the organic molecules that form many qubit systems. Since the original proposals, various small-scale QIP experiments have been demonstrated. In particular, a demonstration of Shor's factoring algorithm with 7 qubits (Fig. 27.1a) attracted major attention [3]. At present, up to 12 qubits (Fig. 27.1b) can be controlled with sufficient precision to form the Schrödinger's cat state [4].

Nuclear spin energy is very low and a single nuclear spin qubit can be controlled by applying magnetic fields at radio frequencies. Gate operations between nuclear spin qubits can be implemented using J or dipolar interactions. Over the 60-year history of nuclear magnetic resonance (NMR) spectroscopy, vast knowledge of the

M. Kitagawa • A. Kagawa (✉) • M. Negoro
Graduate School of Engineering Science, Osaka University, 1-3 Machikaneyama, Toyonaka, Osaka 560-8531, Japan
e-mail: kitagawa@ee.es.osaka-u.ac.jp; kagawa@ee.es.osaka-u.ac.jp; negoro@ee.es.osaka-u.ac.jp

Y. Morita
Department of Applied Chemistry, Faculty of Engineering, Aichi Institute of Technology, 1247 Yachigusa, Yakusa, Toyota 470-0392, Japan
e-mail: moritay@aitech.ac.jp

Y. Yamamoto, K. Semba (eds.), *Principles and Methods of Quantum Information Technologies*, Lecture Notes in Physics 911, DOI 10.1007/978-4-431-55756-2_27

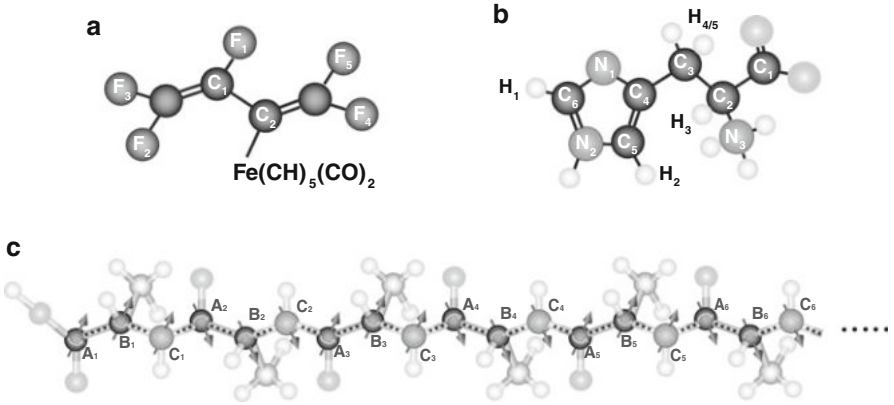

Fig. 27.1 Nuclear spin systems in molecules. **(a)** Perfluorobutadienyl iron complex. **(b)** L-histidine. **(c)** Poly-DL-alanine

control of nuclear spins has been accumulated [5]. Additionally, the nuclear spin qubit has a long decoherence time [6]. The successes of these small-scale QIP experiments can be attributed in part to these advantages.

QIP experiments using the electron spins in organic molecules have also been carried out [7, 8]. The electron spin energy is higher than the nuclear spin energy and the oscillating magnetic field used to control the electron spin is typically in the microwave region, which is more difficult to handle than its radio-frequency counterpart. However, microwave technology has advanced greatly in recent years. It has been found that electron spins also have long decoherence times if they are isolated from any unwanted nuclear spins [9]. These advances have motivated us to apply electron spins as qubits.

The main advantage in the use of a molecular spin system lies in its scalability. In a macromolecular system where n sets of three spin species, A, B, and C, are aligned on a chain, as shown in Fig. 27.1c, it is possible, in principle, to implement arbitrary n qubit unitary operations [10]. It is anticipated that future progress in both macromolecular technology and supramolecular technology [11] will make it possible to array Avogadro numbers of spins periodically in two or three dimensions, let alone the 10^9 spins that are required for fault-tolerant quantum computation to outperform classical computation [12].

However, low energy spin qubits have two disadvantages. The first is the difficulty in detection of the tiny signal from a spin, because it is buried under the thermal noise of the detection apparatus. The other is the difficulty in increasing the polarization of the spin state, because the thermal energy mixes the spin states, which causes difficulty in initialization of the qubit state. Two spins with polarization of less than 41.4 % cannot be entangled with any unitary operations [13, 14]. However, entanglement is a necessary condition for QIP. Most QIP experiments that use spins in molecules have used pseudo-entanglement, which is generated by pseudo-initialization techniques in which resources such as the number of

accumulations or molecules increase exponentially with respect to the number of qubits. Therefore, the QIP performance based on the entanglement power is canceled out in these experiments. An entangled cat state involving more than 13 qubits in a molecular spin system has not yet been reported and its implementation would require a physical initialization technique to increase the spin polarization.

We have been working on the realization of large-scale QIP using the spins in molecules. We have previously proposed a new method for numerical synthesis of pulse sequences to dynamically decouple unwanted interactions [15, 16]. While the computational cost of the conventional numerical synthesis method grows exponentially with respect to the size of a qubit system, our proposal can dramatically reduce the computational cost. We have developed instrumentation for the irradiation of broadband microwave pulses with arbitrary waveforms, including optimized decoupling pulses [16–19], which enables us to control the electron spins as precisely as the nuclear spins. Broadband radio-frequency (RF) or microwave pulses are deformed by a resonator transient phenomenon. We have developed techniques to compensate for this deformation [16, 20, 21]. These studies have further improved the spin qubit controllability. We have studied enhancements of both polarization and sensitivity to enable us to overcome the disadvantages of the spin qubit. For electron spins, the polarization can be increased to 99 % at 150 mK and 0.6 T. For nuclear spins, it is difficult to obtain such hyperpolarization by simply lowering the temperature. However, we have succeeded in producing room-temperature hyperpolarization with dynamic nuclear polarization using photo-excited triplet electrons [22]. We have also studied spin amplification, which enhances the sensitivity of spin detection [23]. In this paper, we summarize our research efforts and discuss the potential use of molecular spin qubits for QIP in particular, analog quantum simulations and digital quantum computation.

27.2 Spin Qubit Control Techniques

In this chapter, we briefly review the conventional techniques used for the control of spin qubits, which are detailed in Ref. [24]. Then, we introduce our research with the aim of controlling spin qubits more precisely.

27.2.1 Conventional Techniques

First, we explain the control of a spin with a gyromagnetic ratio of γ under a static magnetic field of B_0. By irradiation with an oscillating transverse magnetic field of $2B_1 \cos \gamma B_0 t$, we can rotate the spin at an angular frequency γB_1 about the x-axis in the rotating frame at the oscillating field angular frequency, γB_0. Next, we consider two spins with a resonant angular frequency difference of $\Delta\omega$, which is a result of the differences in their gyromagnetic ratios, chemical shifts, or g-factors. One of the

two spins can be selectively rotated with an oscillating field, for which the strength γB_1 is much smaller than $\Delta\omega$. In many spins, single spins can be also selectively controlled if each spin has a different resonant frequency. Two-qubit gate operation can be implemented with spin-spin interactions such as dipolar interaction, J coupling, or Fermi contact interaction. For many spin systems, an interaction between a pair of spins can be decoupled by selectively rotating either of the spins.

A universal set of quantum gates can therefore, in principle, be implemented with the aforementioned techniques. In practice, the fidelity of a quantum gate can be degraded by, e.g. inhomogeneities of B_0 and B_1, dephasing, and unwanted off-resonance effects during selective rotation. To combat the inhomogeneities, a composite rotation technique using phase modulated pulses has been found to be effective [25]. Numerical approaches to find an optimally modulated waveform to reduce the effects of inevitable errors have been studied [26, 27], and will be explained in the next section. These techniques for modulation of an oscillating field have been used in small-scale QIP experiments with spin qubit systems and with other qubit systems.

27.2.2 Numerical Synthesis

For dynamical decoupling (DD) of the interactions between qubit and bath systems to suppress phase decoherence, the CPMG (Carr-Purcell-Meiboom-Gill) pulse sequence, which was developed in NMR spectroscopy [28], and the UDD (Uhrig DD) [29] and QDD (quadratic DD) [30] pulse sequences are used. Most DD sequences provide ideal performances when the pulse shape is a delta function. In practice, the oscillating field pulse has both finite amplitude and bandwidth. Therefore, the decoupling efficiency tends to be degraded from the ideal performance level. If the Hamiltonian of the entire system is fully known, then numerical approaches, e.g. GRAPE (gradient ascent pulse engineering) [27], are useful for DD under practical resource limitation conditions. This approach optimizes the waveform to increase the decoupling efficiency, based on numerical calculations of the unitary evolution of the entire system. In this approach, we can synthesize a modulated waveform that is robust against the inevitable errors under the physical resource limitation by incorporating the errors and the limitations into the calculation of the unitary evolution in the optimization process. However, the computational cost of calculation of the full unitary evolution grows exponentially with increasing system size.

We have previously proposed a new method to numerically synthesize a modulated waveform that can dynamically decouple unwanted interactions [15]. Our method can fully exploit the symmetry of the system to reduce the computational costs. We consider a system of an electron spin and nuclear spins with an internal Hamiltonian $H_{\mathrm{Q-B}}$. Here, we consider the phase decoherence of the electron spin qubit influenced by the nuclear spin bath under physical resource limitations, e.g. the limitations of the oscillating field strength and the inevitable oscillating field

amplitude and phase errors. Under an oscillating field with a periodically modulated waveform, $H_{\mathrm{RF}}(t)$, the time evolution of the whole system, $U(t)$, can be easily described using the Hamiltonian in the so-called toggling frame, $\tilde{H}$. The toggling frame is a type of interaction representation in which time evolution due to the applied oscillating field is canceled out. The Hamiltonian that includes the errors, H_E, of the oscillating field, $H_0 = H_E + H_{\mathrm{Q-B}}$, is rewritten in the toggling frame:

$$\tilde{H}(t) = U_{\mathrm{RF}}(t)^{-1}(t) H_0 U_{\mathrm{RF}}(t), \tag{27.1}$$

$$U_{\mathrm{RF}}(t) = \exp(-iH_{\mathrm{RF}}(t)t). \tag{27.2}$$

If $U_{\mathrm{RF}}(t)$ becomes the identity operator at a specific cycle time t_c, the time evolution of the whole system is described by:

$$U(t_c) = \hat{T} \exp\left\{-i \int_0^{t_c} dt_1 \tilde{H}(t_1)\right\}, \tag{27.3}$$

where $\hat{T}$ is the Dyson time ordering operator. Using the Magnus expansion, this can be rewritten as:

$$U(t_c) = \exp\{-i\bar{H}t_c\}, \quad \bar{H} = \bar{H}^{(0)} + \bar{H}^{(1)} + \cdots, \tag{27.4}$$

$$\bar{H}^{(0)} = \frac{1}{t_c} \int_0^{t_c} dt_1 \tilde{H}(t_1), \tag{27.5}$$

$$\bar{H}^{(1)} = \frac{-i}{2t_c} \int_0^{t_c} dt_2 \int_0^{t_2} dt_1 [\tilde{H}(t_2), \tilde{H}(t_1)]. \tag{27.6}$$

$\bar{H}$ is called the average Hamiltonian. If $1/t_c \gg ||H_0||$, the higher order terms converge to zero, and the time evolution can thus be described using only a few low order terms. For more details of average Hamiltonian theory, see e.g. Slichter's textbook [5].

Using an orthonormal set of operators $\{\Theta_\alpha\}$, H_0 and $H_{\mathrm{RF}}(t)$ can be expressed by

$$H_0 = \sum_\alpha h_\alpha \Theta_\alpha, \tag{27.7}$$

$$H_{\mathrm{RF}}(t) = \sum_\alpha \omega_\alpha(t) \Theta_\alpha. \tag{27.8}$$

The toggling frame Hamiltonian is expressed by

$$\tilde{H}(t) = \sum_\alpha h_\alpha \sum_\beta c_{\beta\alpha}(t) \Theta_\beta, \tag{27.9}$$

$$c_{\beta\alpha}(t) = \mathrm{Tr}[U_{\mathrm{RF}}(t) \Theta_\alpha U_{\mathrm{RF}}^{-1}(t) \Theta_\beta] / \mathrm{Tr}[\Theta_\beta^2]. \tag{27.10}$$

Therefore, the average Hamiltonian is expressed as

$$\bar{H}^{(0)} = \frac{1}{t_c}\sum_{\alpha,\beta} h_\alpha \Big\{ \int_0^{t_c} dt_1 c_{\beta\alpha}(t_1) \Big\} \Theta_\beta, \tag{27.11}$$

$$\bar{H}^{(1)} = \frac{-i}{2t_c}\sum_{\alpha,\alpha'} h_\alpha h_{\alpha'} \sum_{\beta<\beta'} \Big\{ \int_0^{t_c} dt_2 \int_0^{t_2} dt_1$$

$$\times (c_{\beta'\alpha'}(t_2)c_{\beta\alpha}(t_1) - c_{\beta'\alpha}(t_1)c_{\beta\alpha'}(t_2)) \Big\} [\Theta_{\beta'}, \Theta_\beta]. \tag{27.12}$$

In our method, we define the cost functions as the terms of Eqs. (27.11) and (27.12) above that are surrounded by curly brackets. We optimize $\{\omega_\alpha(t)\}$ to minimize these cost functions. By solving a nonlinear programming problem, we can find the optimal DD waveform numerically. The cost functions used in the conventional numerical approaches do not correspond to the terms in the curly brackets described above but do include the coupling coefficients h_α or $h_\alpha h_{\alpha'}$. Because our cost functions do not include detailed information about the spin system, our method can dramatically reduce the computational costs.

An example waveform synthesized using our method is shown in Fig. 27.2. We used a genetic algorithm in addition to the gradient ascent algorithm for the numerical optimization process. By taking the amplitude and phase errors of the oscillating field into consideration, the performance of the synthesized waveform is higher than the performances of both UDD [29] and QDD [30]. We have also synthesized a waveform to dynamically decouple the dipolar interactions between qubits. If the oscillating field strength is limited to a finite value, then the performance of the synthesized waveform is higher than that of the MREV16 sequence [6]. We have previously studied the dependence of the decoupling efficiency on the frequency bandwidth and on the maximum strength of the oscillating field, and detailed results can be found in Ref. [15].

Our numerical synthesis method, which can dramatically reduce the computational cost, will also contribute to improvement of the quantum gate fidelity for spin qubit systems and for other qubit systems.

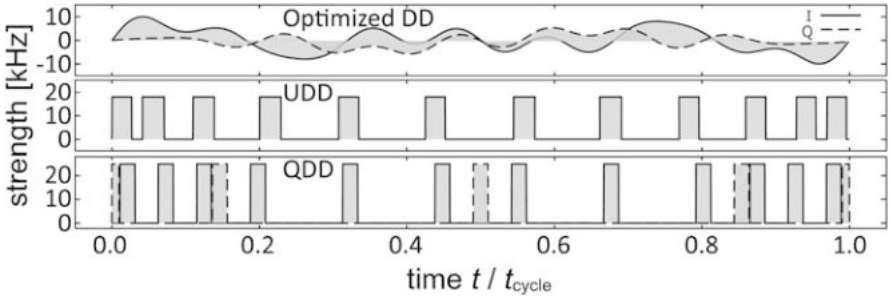

Fig. 27.2 Numerically synthesized DD pulse sequence, UDD pulse sequence, and QDD pulse sequence

27.2.3 Control of the Electron Spins

Typically, the energy of the nuclear spins used as qubits is of the order of 100 MHz, and the interaction energy between these nuclear spins in solids is of the order of 10 kHz or less. For the precise control of nuclear spin systems with such interaction strengths, the maximum amplitudes (in terms of γB_1 frequency) and bandwidths of the RF pulses must be of the order of 100 kHz, in our experience. However, the energy of the electron spins used as qubits is typically of the order of 10 GHz, and the interaction energy between the electron spins in the molecules that we have synthesized is of the order of 10 MHz [8]. Therefore, for precise control of electron spin systems with such interaction strengths, the maximum amplitudes and bandwidths of the microwave pulses are required to be of the order of 100 MHz.

We have developed the 17 GHz stripline resonator shown in Fig. 27.3a to obtain strong pulse irradiation with the required strength and frequency bandwidth [18]. In this design, the current concentrates on the U-shaped part at the center of the half wavelength stripline, and a strong magnetic field is induced inside the U-shaped part. The field-conversion efficiency of this resonator is quite high. In pulsed electron spin resonance (ESR) experiments, we have demonstrated that strong irradiation that drives 210 MHz Rabi oscillation can be obtained with an input power of 1 W. Because the Q factor of the resonator is 85, we can perform the irradiation with a bandwidth of 200 MHz, which meets the requirement mentioned above. Therefore, using this resonator and the modulated pulses, we can control electron spins as precisely as nuclear spins.

To generate the broadband pulses, we have also developed the 17 GHz pulsed ESR spectrometer shown in Fig. 27.3b [17, 19]. In this spectrometer, the arbitrary waveform generator outputs a signal with a center frequency of 2.5 GHz and a bandwidth of 1 GHz. The signal is fed into the mixer with a local oscillator signal at 14.5 GHz, and is then upconverted to the 17 GHz band. The pulses generated can be amplified up to 1 W with low distortion. Using this arbitrary waveform pulsed

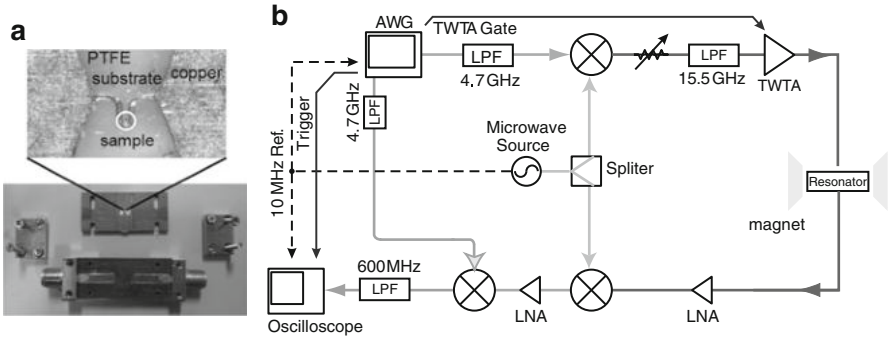

Fig. 27.3 **(a)** Stripline resonator. **(b)** 17 GHz broadband arbitrary waveform pulsed ESR spectrometer

ESR spectrometer, we can generate arbitrary modulated pulses that enable us to fully exploit the broadband stripline resonator and the sophisticated Hamiltonian engineering.

27.2.4 Transient Compensation

If a pulse with a bandwidth of 200 MHz is fed to a resonator with a bandwidth of 200 MHz, the amplitude and phase profiles of the irradiated magnetic field inside the resonator are distorted compared with those of the input pulse waveform because of the resonator transient phenomenon. The distortion of one such rectangular pulse is shown in Fig. 27.4. The phase distortion causes degradation in the fidelity of the quantum gate operation. The amplitude distortion destroys the time-reversal symmetry of the pulse shape and the time-reversal anti-symmetry of the conventional DD pulse sequences [6, 28]. Because time-reversal antisymmetry is a sufficient condition for elimination of odd order terms in the average Hamiltonian, the amplitude distortion thus degrades the efficiency of the DD sequences. The distortions of both the amplitude and phase profiles should be suppressed even for numerically synthesized pulses.

The relationship between the magnetic field $B_1(t)$ inside the resonators, which is irradiated to the spins, and the input waveform $v(t)$ is described using the response function $h(t)$ as

$$B_1(t) = \int_{-\infty}^{t} d\tau h(\tau) v(t-\tau). \tag{27.13}$$

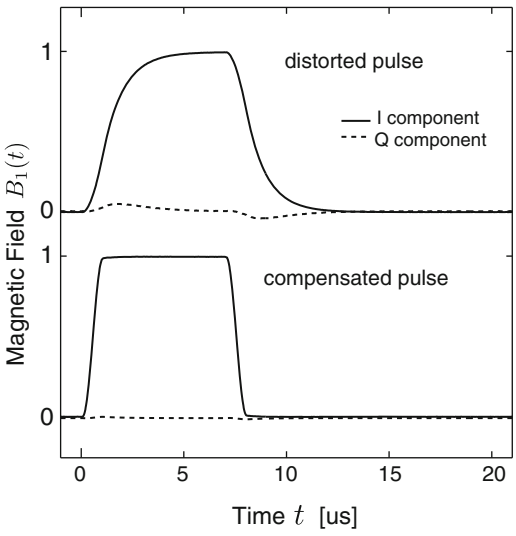

Fig. 27.4 Pulse deformed by resonator transient and compensated pulse

The response function can be determined experimentally by monitoring the irradiated field inside the resonator with respect to the broadband step function input. If the response function is known, we can then calculate the input pulse waveform required to generate the intended magnetic field inside the resonator. Using the Laplace transformations $\tilde{B}_1(s), \tilde{V}(s), \tilde{H}(s)$ of $B_1(t), v(t), h(t)$, respectively, the above equation can be rewritten as

$$\tilde{V}(s) = \frac{\tilde{B}(s)}{\tilde{H}(s)}. \tag{27.14}$$

We can then obtain the input waveform using the inverse-Laplace transformation of the above. Both the Laplace and the inverse-Laplace transformations are calculated numerically. We have therefore succeeded in compensating the resonator transient. The irradiated magnetic field with leading and trailing edges in raised cosine shapes is shown in Fig. 27.4 [21]. This transient compensation technique makes it possible to precisely irradiate the spins inside the resonator with a magnetic field with the intended waveform.

The combination of the numerical synthesis method, the arbitrary waveform pulsed ESR spectrometer, and the transient compensation technique, which have been introduced in this chapter, makes it possible to precisely control both nuclear spin qubits and electron spin qubits. The studies described in this chapter are detailed in the PhD theses of Tabuchi [16] and Yap [19].

27.3 Hyperpolarization of Spins

27.3.1 Hyperpolarization by Cooling

The polarization of spin-1/2 particles is defined by

$$\epsilon = \frac{N_{|\uparrow\rangle} - N_{|\downarrow\rangle}}{N_{|\uparrow\rangle} + N_{|\downarrow\rangle}}, \tag{27.15}$$

where $N_{|\uparrow\rangle}$ and $N_{|\downarrow\rangle}$ are the populations of $|\uparrow\rangle$ and $|\downarrow\rangle$, respectively. In thermal equilibrium under a static magnetic field of B_0 at temperature T, the polarization ϵ_{th} obeys the Maxwell-Boltzmann distribution law as follows:

$$\epsilon_{\mathrm{th}} = \tanh\left(\frac{\gamma\hbar B_0}{2k_B T}\right), \tag{27.16}$$

where γ is the gyromagnetic ratio, $\hbar$ is the Planck constant, and k_B is the Boltzmann constant. For example, the polarization of ^{1}H spins at 11.7 T (where the resonant frequency is 500 MHz) and 300 K is 0.004 %, and the polarization of electron spins at 0.6 T (where the resonant frequency is 17 GHz) and 300 K is 0.1 %.

At 150 mK and 0.6 T, the electron spin polarization reaches 99 %. Such a temperature can be obtained using a dilution refrigerator. In this refrigerator, we must also realize strong and broadband pulse irradiation for precise control, as mentioned in the previous chapter. However strong irradiation using high microwave power generates more Joule heat. This Joule heat must not exceed the cooling power of the refrigerator. To avoid this heating problem, a resonator with a high microwave power to magnetic field conversion efficiency is required. We have developed the U-shaped stripline resonator for this purpose. Although the electron spin polarization also reaches 99 % under higher magnetic fields at higher temperatures, spin control at the higher frequencies becomes more difficult. To obtain a nuclear spin polarization of 99 % under a static field of 11.7 T, the sample must be cooled to below 5 mK. At such a low temperature, the nuclear spin lattice relaxation time is extremely long. The long relaxation time is discouraging for exploratory experiments that require repetitive measurements.

27.3.2 Dynamic Nuclear Polarization Using Photo-Excited Triplet Electrons

Because the sensitivities of NMR spectroscopy and magnetic resonance imaging (MRI) are proportional to the nuclear spin polarization, various methods to obtain hyperpolarization have previously been studied. In particular, dynamic nuclear polarization (DNP) has drawn considerable attention [5, 31, 32]. DNP offers a means of transferring the spin polarization from the electrons to the nuclei. As mentioned in the previous section, it is easier to increase the polarization of electron spins in thermal equilibrium than that of nuclear spins, because the Zeeman energy of the electron spin is 660 times higher than that of the nuclear spin. The polarization and the sensitivity can, in principle, be enhanced by at most this factor through DNP. DNP has been applied not only to sensitivity enhancement in NMR spectroscopy [33] but also to medical science [34] and fundamental physics applications including elementary particle physics [35], nuclear physics [36], and studies of magnetism [32], which will be explained later in the paper. Nuclear spin polarization of 98 % has already been achieved using DNP at 2.5 T and 0.4 K [37].

To obtain nuclear spin polarization of >10 %, conventional DNP, which uses electron spins at thermal equilibrium as the polarizing source, requires cryogenic temperatures (e.g., <17 K under a static magnetic field of 2.5 T). To realize such hyperpolarization at room temperatures, we have studied DNP using the photo-excited triplet states of electron spins, known as triplet-DNP [38–42], rather than the thermal states of electron spins. Some π-conjugated molecules have photo-excited triplet states, where the population distribution is highly biased, as shown in Fig. 27.5a. The electron spin polarization is then determined by the selection rule in the intersystem crossing from the excited singlet state to the triplet state. In the case of pentacene, the electron spin polarization is 73 %, even at room temperature. Thus, the triplet-DNP can achieve nuclear spin hyperpolarization at

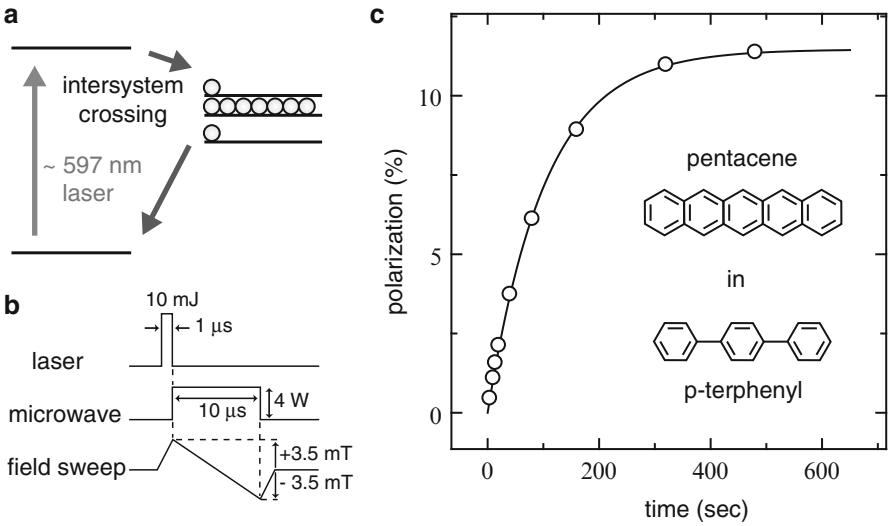

Fig. 27.5 **(a)** Energy diagram of pentacene. **(b)** Triplet-DNP pulse sequence. **(c)** ^{1}H spin polarization buildup behavior of samples under triplet-DNP

room temperature [43, 44]. Owing to the finite lifetime of the triplet electron spins, the nuclear-spin system becomes free from disturbance by the electron paramagnetism causing nuclear spin decohrence.

The triplet-DNP procedure, which was developed by Henstra et al. [43], is shown in Fig. 27.5b. The procedure begins by using a pulsed laser at a wavelength of 597 nm to excite the pentacene in the sample. The hyperpolarization in the photo-excited triplet state is then transferred to the nuclear spins in the vicinity during the triplet lifetime by a pulsed DNP process, the integrated solid effect (ISE) [43]. In this process, the field sweep and the microwave irradiation near the transition frequency between the triplet sublevels are applied simultaneously. The inhomogeneously-broadened electron spin packets are swept over adiabatically, and the effective nutation frequency of the electron spins in the rotating frame is matched with the ^{1}H spin Larmor frequency at some point in the adiabatic process. The photo-excited triplet state decays non-radiatively to a ground singlet state. The hyperpolarized spin state then diffuses from the nuclear spins in the vicinity of the polarizing agent to the entire sample. By repeating this sequence, we can accumulate nuclear spin polarization until the buildup and the nuclear spin-lattice relaxation reach a steady state.

In Ref. [43], at room temperature under a field of 0.35 T, the polarization of ^{1}H spins was increased to 0.66 %, which equated to an enhancement factor of 5,500 in a single crystal of naphthalene doped with 0.01 mol % pentacene. In Ref. [45], the enhancement factor at room temperature was 13,000 under a field of 0.3 T with a ^{1}H spin polarization of 1.3 %, where *p*-terphenyl was used as host material. By carefully optimizing the ISE parameters and avoiding heating of the sample, we attained a ^{1}H

spin polarization of 12 %, as shown in Fig. 27.5c. Recently, we have also achieved a ^{1}H spin polarization of 34 % in a single crystal of regioselectively deuterated *p*-terphenyl-2′,3′,5′,6′-d_4 doped with fully deuterated pentacene- d_{14} [46].

Using triplet-DNP, we can now achieve hyperpolarization at room temperatures. QIP experiments with precise control of the hyperpolarized nuclear spins are showing promise, and will be discussed later in the paper.

27.4 Sensitivity Enhancement by Spin Amplification

The quantum nondemolition (QND) measurement of the Z component of a spin is realized in the following manner. We consider a two spin system, incorporating a spin of interest and an ancilla spin. We can copy the Z component of the spin of interest to the ancilla spin using a controlled-NOT (CNOT) gate, although a copy of an arbitrary unknown state itself is prohibited by the no-cloning theorem [47]. By measuring the Z component of the ancilla spin, we can nondestructively determine the Z component of the spin of interest. If the thermal noise in the detection apparatus is larger than the signal that is obtained from the ancilla spin, then the result may be incorrect. With N repetitions of the CNOT process and the measurement, as shown in Fig. 27.6a, the signal-to-noise ratio (SNR) is improved by a factor of $\sqrt{N}$. In inductive detection, which is the most popular method used for spin detection, the thermal noise is much higher than the induction signal from a

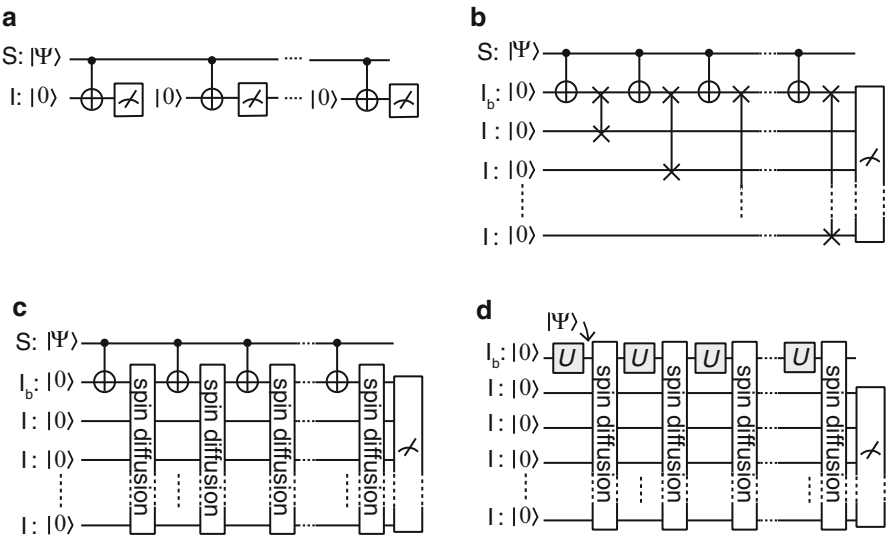

Fig. 27.6 **(a)** Conventional quantum circuit for QND measurement with ancilla spin. **(b)** Quantum circuit for spin amplification with selective control. **(c)** Quantum circuit for spin amplification with spin diffusion. **(d)** Partial circuit section of circuit **(c)**

single spin. The QND measurement of a single spin qubit with inductive detection requires a tremendous number of repetitions, and is therefore practically impossible. In this chapter, we introduce a method to measure a spin component using low sensitivity detection apparatus on the basis of spin amplification.

We consider a system where the spin of interest (S) is surrounded by a buffer spin I_b and m abundant spins I. In this system, using the quantum circuit in shown Fig. 27.6b, we can copy the Z spin component of the S spin to all surrounding spins. By measuring the surrounding spins after the copying process, we can determine the Z component of the S spin from the amplified signal. Using this method, the signal is amplified with a gain of N, corresponding to the number of copies, while it is contaminated by thermal noise only once, in the detection apparatus. Thus, the SNR is improved by a factor of N. This method is called spin amplification and was proposed by DiVincenzo [48]. In the circuit, the Z component of S is copied to the buffer spin I_b by the CNOT gate and then the Z component of I_b is selectively swapped with one of the surrounding spins I. This requirement for a selective swap operation for all surrounding spins makes the realization of a high gain very difficult.

The homonuclear spins (the i-th spin I_i and the j-th spin I_j) in bulk solids composed of organic molecules are coupled with dipolar interactions, $H \propto I_{iZ}I_{jZ} - \frac{1}{2}(I_{i-}I_{j+} + I_{i+}I_{j-})$. The flip-flop term $(I_{i-}I_{j+} + I_{i+}I_{j-})$ causes an exchange of the Z components between the homonuclear spins. Among multiple homonuclear spins, the Z components of the I spins are shuffled by the flip-flop terms, and this behavior is known as spin diffusion [49]. We use this spin diffusion behavior for spin amplification [23]. However, between the heteronuclear spins in a high magnetic field, the flip-flop term is averaged out because of the large Zeeman energy difference. Under a low field, where the dipolar interactions between I_b and some nearby I spins are larger than or comparable to the I-I_b Zeeman energy difference, the flip-flop terms of the I-I_b coupling are not averaged out. If the I-S couplings are much smaller than the I-S Zeeman energy difference under the low field, only the I_b spin attends the I spin diffusion, as shown in the quantum circuit in Fig. 27.6c. In this circuit, we apply a CNOT operation to the control spin S and the target spin I_b under a high field, where the flip-flop terms of the I-I_b couplings are averaged out. After that, we move the sample to a low field to diffuse the Z component of I_b spin to the I spins. By repeating the CNOT operation and spin diffusion process, we can accumulate the excited states $|1\rangle$ on the I spins if the S spin state is $|1\rangle$; otherwise, the I spins are not excited at all. In this way, the spin component is amplified. In this circuit, the S spin component is copied to randomly-selected I spins. An I spin that has already been selected may then be selected again, which leads to errors. The amplification gain can be scaled up linearly by simultaneously increasing the number of copies N and the number of I spins m while maintaining $N = m/2$.

We have also demonstrated that the excited state of the I_b spins can be accumulated in the I spins using the quantum circuit in Fig. 27.6d. We used a sample of a single crystal of naphthalene that was doubly-doped with 0.005 mol % pentacene and 1 mol % 2-fluoronaphthalene, in which a ^{19}F spin (I_b) is surrounded by 799 ^{1}H spins (I) on average. The experimental procedure is as follows. The procedure began with triplet-DNP to increase the polarizations of the ^{1}H and ^{19}F

spins to 12 % at 233 K and 0.4 T. We then applied a unitary gate operation, which was NOT rather than CNOT in this case, to the ^{19}F spin in 0.4 T. Then, we performed field cycling (0.4 T $\rightarrow$ 0.01 T $\rightarrow$ 0.4 T) to transfer the excited state of the ^{19}F spin to the ^{1}H spins by spin diffusion. After repeating the unitary gate and the field-cycling processes, we observed ^{1}H spin magnetization. We successfully demonstrated a gain as large as 140 with 200 repetitions, as detailed in Ref. [23]. Spin amplification that is scalable to produce a higher gain opens the door to single spin measurements and a readout process for spin-based quantum computers.

27.5 Summary: Toward Spin QIP Experiments

In this paper, we have introduced the results of our research on spin control, spin hyperpolarization, and sensitivity enhancement. By these advances, scalable molecular spin qubit systems are more suitable for QIP experiments. In this section, we discuss the kinds of QIP experiments that will be possible with the scalable molecular spin qubit system.

First, we discuss the potential for analog quantum simulations. We begin by briefly describing the notable experiments of Abragam et al. during the 1960s [32]. They attempted to simulate the magnetic phase transitions induced by electron spin interactions, and used nuclear spin systems to investigate these transitions under various conditions. To induce a magnetic phase transition in a nuclear spin system, the temperature should be lower than 1 μK, because nuclear spin interaction energies are typically lower than 30 kHz. They achieved such an extremely low temperature as follows, using paramagnetic-impurity-doped crystal samples containing many nuclear spins, such as calcium fluoride doped with Tm^{2+} ions. First, the environmental temperature was reduced to 0.7 K under a static magnetic field of 2.7 T. Then, submillimeter wave irradiation was performed at the ESR frequency for DNP. The nuclear spin polarization obtained was comparable to the electron spin polarization. The temperature that provides the obtained polarization at thermal equilibrium is defined as the spin temperature. DNP lowers the spin temperature to the millikelvin regime. After DNP, an oscillating field far off-resonant with nuclear spins was applied and the frequency was adiabatically swept to on-resonance. Finally, the oscillating field strength was adiabatically decreased to 0. Because the system entropy is conserved in adiabatic processes, the spin state transits to the ground state of the nuclear spin interactions. The spin temperature is in the sub-microkelvin regime after these processes, which are called adiabatic demagnetization in the rotating frame. A nuclear ordered state, either ferromagnetic or antiferromagnetic, was manifested if the spin temperature was below a specific transition temperature. These researchers also investigated the dependences of the emergent magnetic phases on the spin temperature and the dipolar coupling network, using various samples and changing the sample orientations with respect to the static magnetic field.

After several decades, a vast knowledge of quantum many-body physics and quantum information has been accumulated, and various spin control techniques have been devised, as explained in the preceding sections. Thus, these types of experiments have considerable significance. Roumpos et al. proposed quantum simulation of the so-called XXZ model using multiple pulse sequences based on Abragam's experiment [50]. While they intended to use a nuclear spin system, the electron spin system can also be used for the quantum simulation. The spin control techniques and molecular engineering that we have described here will enable more complicated types of quantum simulations. Some quantum simulation experiments were also demonstrated using pseudo-initialization with small numbers of nuclear spins in molecules [51]. Our aim is to realize true analog quantum simulation using a scalable many-body spin system and our hyperpolarization technique.

Next, we discuss the potential for digital quantum computation. To outperform classical computation, quantum computers must be fault-tolerant, with the help of quantum error correction. Quantum error correction can lower the increased entropy caused by inevitable decoherence without any loss of quantum information. This means that, by repeating the process, we can stop the qubit system accumulating errors caused by decoherence. The implementations proposed to date require feedback operations with measurements of the qubit states and the quantum gate controls. Most fault-tolerant quantum computer architectures are constructed with measurement-based quantum error correction. To outperform classical computation, the number of qubits must be more than 10^9, and each of these 10^9 qubits must be measured simultaneously every 100 ns [12]. The implementation of this architecture using a molecular spin qubit system may seem to be hopeless in practice. Fortunately, two facts encourage the possible realization of a large-scale quantum computer based on the molecular spin qubit system. The first is that quantum error correction can be implemented via feedback operations with quantum gate operation and cooling [52]. If the system entropy that has been increased by errors can be lowered using only translationally-invariant operations and cooling, a large-scale quantum memory can be implemented with a scalable molecular spin qubit system [53]. The other fact is that the arbitrary quantum algorithm can be implemented by slightly breaking the translation symmetry in a way similar to that of the macromolecular system mentioned earlier, where n sets of three spin species, A, B, and C, are aligned on a chain [10]. Based on these two facts, we believe that it will be possible to construct a fault-tolerant quantum computer architecture with the molecular spin qubit system.

We have developed technologies for Hamiltonian engineering, hyperpolarization, and spin amplification. Using state-of-the-art molecular engineering technology, we can array more than 10^9 spin qubits with translational invariance. Using hyperpolarization and precise control, we can implement analog quantum simulation on a scalable molecular spin system with translational invariance. This method uses a top-down approach, whereas artificial atomic qubit systems such as quantum dots and superconducting qubits use a bottom-up approach. In the bottom-up approach, individually addressable and controllable qubits must be integrated bit-by-bit without loss of controllability to eventually reach 10^9 qubits. In the top-down

approach, we begin with a highly-symmetrical quantum many-body system with 10^9 or more spin qubits without individual addressability and measurability. By introducing a microstructure and breaking the symmetry step-by-step, we can increase both controllability and addressability. By progressing in this way, we will soon encounter interesting quantum many-body physics problems. We will then exploit the most promising routes towards the realization of quantum simulation, topological protection of quantum information, and quantum computation.

Acknowledgements The studies in Sects. 27.2.2 and 27.2.4 were mainly performed by Dr. Yutaka Tabuchi. The study in Sect. 27.2.3 was mainly performed by Dr. Yung Szen Yap. The studies in Sects. 27.3.2 and 27.4 were collaborative work performed by Dr. Kenichiro Tateishi and Dr. Shinsuke Nishida. The authors thank Dr. Kazuyuki Takeda for fruitful discussions on DNP. The research described in this paper was supported by a MEXT Grant-in-Aid for Scientific Research on Innovative Areas (no. 21102004), Young Scientist Research B grant nos. 24740273 and 25800230, and the Funding Program for World-Leading Innovative R&D on Science and Technology (FIRST). M.N. and K.T. were also supported by the Global-COE Program of Osaka University.

References

1. N.A. Gershenfeld, I.L. Chuang, Science **275**, 350 (1997)
2. D.G. Cory, A.F. Fahmy, T.F. Havel, Proc. Natl. Acad. Sci. U. S. A. **94**, 1634, (1997)
3. L.M.K. Vandersypen, M. Steffen, G. Breyta, C.S. Yannoni, M.H. Sherwood, I.L. Chuang, Nature **414**, 883 (2001)
4. C. Negrevergne, T.S. Mahesh, C.A. Ryan, M. Ditty, F. Cyr-Racine, W. Power, N. Boulant, T. Havel, D.G. Cory, R. Laflamme, Phys. Rev. Lett. **96**, 170501 (2006)
5. C.P. Slichter, *Principles of Magnetic Resonance, Third Enlarged and Updated Edition* (Springer, Berlin, 1990)
6. T.D. Ladd, D. Maryenko, Y. Yamamoto, E. Abe, K.M. Itoh, Phys. Rev. B **71**, 014401 (2005)
7. M. Mehring, J. Mende, W. Scherer, Phys. Rev. Lett. **90**, 153001 (2003)
8. K. Sato, S. Nakazawa, R. Rahimi, T. Ise, S. Nishida, T. Yoshino, N. Mori, K. Toyota, D. Shiomi, Y. Yakiyama, Y. Morita, M. Kitagawa, K. Nakasuji, M. Nakahara, H. Hara, P. Carl, P. Höfer, T. Takui, J. Mater. Chem. **19**, 3739 (2009)
9. J.J.L. Morton, A.M. Tyryshkin, A. Ardavan, K. Porfyrakis, S.A. Lyon, G.A.D. Briggs, J. Chem. Phys. **124**, 014508 (2006)
10. S. Lloyd, Science **261**, 1569 (1993)
11. Y. Morita, Y. Yakiyama, S. Nakazawa, T. Murata, T. Ise, D. Hashizume, D. Shiomi, K. Sato, M. Kitagawa, K. Nakasuji, T. Takui, J. Am. Chem. Soc. **132**, 6944 (2010)
12. N.C. Jones, R. Van Meter, A.G. Fowler, P.L. McMahon, J. Kim, T.D. Ladd, Y. Yamamoto, Phys. Rev. X **2**, 031007 (2012)
13. A. Peres, Phys. Rev. Lett. **77**, 1413 (1996)
14. R. Rahimi, K. Takeda, M. Ozawa, M. Kitagawa, J. Phys. A **39**, 2151 (2006)
15. Y. Tabuchi, M. Kitagawa, arXiv:1208.5218
16. Y. Tabuchi, On the control of electron spin qubits, PhD thesis (Japanese), Osaka University, 2012
17. Y. Hashimoto, Y. Tabuchi, T. Kishida, I. Yamashina, M. Kitagawa, Toward quantum computation with electron spin multiple resonance, in *International Symposium on Physics of Quantum Technology* (Nara, Japan, 2008)

18. Y.S. Yap, H. Yamamoto, Y. Tabuchi, M. Negoro, A. Kagawa, M. Kitagawa, J. Magn. Reson. **232**, 62 (2013)
19. Y.S. Yap, Precise control and initialization of electron spin qubits, PhD thesis, Osaka University, 2013
20. K. Takeda, Y. Tabuchi, M. Negoro, M. Kitagawa, J. Magn. Reson. **197**, 242 (2009)
21. Y. Tabuchi, M. Negoro, K. Takeda, M. Kitagawa, J. Magn. Reson. **204**, 327 (2010)
22. K. Tateishi, Room temperature nuclear hyperpolarization and hypersensitive NMR spectroscopy of molecules doped in glass using photo-excited triplet electrons, PhD thesis (Japanese), Osaka University, 2013
23. M. Negoro, K. Tateishi, A. Kagawa, M. Kitagawa, Phys. Rev. Lett. **107**, 050503 (2011)
24. L.M.K. Vandersypen, I.L. Chuang, Rev. Mod. Phys. **76**, 1037 (2004)
25. M.H. Levitt, R. Freeman, J. Magn. Reson. **33**, 473 (1979)
26. H. Geen, R. Freeman, J. Magn. Reson. **93**, 93 (1991)
27. N. Khaneja, T. Reiss, C. Kehlet, T. Schulte-Herbruggen, S.J. Glaser, J. Magn. Reson. **172**, 296 (2005)
28. S. Meiboom, D. Gill, Rev. Sci. Instrum. **29**, 688 (1958)
29. G.S. Uhrig, Phys. Rev. Lett. **98**, 100504 (2007)
30. T. Gullion, D.B. Baker, M.S. Conradi, J. Magn. Reson. **89**, 479 (1990)
31. A.W. Overhauser, Phys. Rev. **92**, 411 (1953)
32. A. Abragam, M. Goldman, *Nuclear Magnetism: Order and Disorder* (Clarendon Press, Oxford University Press, Oxford, New York, 1982)
33. T. Maly, G.T. Debelouchina, V.S. Bajaj, K.-N. Hu, C.-G. Joo, M.L. Mak-Jurkauskas, J.R. Sirigiri, P.C.A. van der Wel, J. Herzfeld, R.J. Temkin, R.G. Griffin, J. Chem. Phys. **128**, 052211 (2008)
34. K. Golman, J.H. Ardenaer-Larsen, J.S. Petersson, S. Mansson, I. Leunbach, Proc. Natl. Acad. Sci. U. S. A. **100**, 10435 (2003)
35. D.G. Crabb, W. Meyer, Annu. Rev. Nucl. Part. Sci. **47**, 67 (1997)
36. A. Obertelli, T. Uesaka, Eur. Phys. J. A **47**, 1 (2011)
37. W. de Boer, T.O. Niinikoski, Nucl. Instr. Methods **114**, 495 (1974)
38. A. Kagawa, Y. Murokawa, K. Takeda, M. Kitagawa, J. Magn. Reson. **197**, 9 (2009)
39. A. Kagawa, M. Negoro, K. Takeda, M. Kitagawa, Rev. Sci. Instrum. **80**, 044705 (2009)
40. M. Negoro, K. Nakayama, K. Tateishi, A. Kagawa, K. Takeda, M. Kitagawa, J. Chem. Phys. **133**, 154504 (2010)
41. K. Tateishi, M. Negoro, A. Kagawa, T. Uesaka, M. Kitagawa, J. Phys. Soc. Jpn. **82**, 084005 (2013)
42. K. Tateishi, M. Negoro, A. Kagawa, M. Kitagawa, Angew. Chem. Int. Ed. **125**, 13549 (2014)
43. A. Henstra, T.-S. Lin, J. Schmidt, W.T. Wenckebach, Chem. Phys. Lett. **165**, 6 (1990)
44. K. Takeda, *Triplet State Dynamic Nuclear Polarization* (VDM Verlag, Saarbrücken, 2009)
45. M. Iinuma, Y. Takahashi, I. Shake, M. Oda, A. Masaike, T. Yabuzaki, H.M. Shimizu, J. Magn. Reson. **175**, 235 (2005)
46. K. Tateishi, M. Negoro, S. Nishida, A. Kagawa, Y. Morita, M. Kitagawa, Room-temperature hyperpolarization of nuclear spins in bulk. Proc. Natl. Acad. Sci. U. S. A. **111**, 7527 (2014)
47. W.K. Wooters, W.H. Zurek, Nature (London) **299**, 802 (1982)
48. D.P. DiVincenzo, Fortschr. Phys. **48**, 771 (2000)
49. N. Bloembergen, Physica **15**, 386 (1949)
50. G. Roumpos, C.P. Master, Y. Yamamoto, Phys. Rev. B **75**, 094415 (2007)
51. J. Zhang, M.-H. Yung, R. Laflamme, A. Aspuru-Guzik, J. Baugh, Nat. Commun. **3**, 880 (2012)
52. M. Nielsen, I. Chuang, *Quantum Computation and Quantum Information* (Cambridge University Press, 2000)
53. K. Fujii, M. Negoro, N. Imoto, M. Kitagawa, Phys. Rev. X **4**, 041039 (2014)

Chapter 28
Molecular Spin Qubits: Molecular Optimization of Synthetic Spin Qubits, Molecular Spin AQC and Ensemble Spin Manipulation Technology

Shigeaki Nakazawa, Shinsuke Nishida, Kazunobu Sato, Kazuo Toyota, Daisuke Shiomi, Yasushi Morita, Kenji Sugisaki, Elham Hosseini, Koji Maruyama, Satoru Yamamoto, Masahiro Kitagawa, and Takeji Takui

28.1 Introduction

Molecular spin qubits based on extremely stable open shell compounds [1, 2] are the latest arrival among physically realized matter qubits [2, 3]. Such molecular spin qubits – composed of unpaired spins and nuclei with non-zero nuclear spin quantum numbers in the electronic spin network of molecular frames – are intrinsically synthetic matter spins [4], because the need for molecular optimization to make

S. Nakazawa • K. Sato • K. Toyota • D. Shiomi • K. Sugisaki • E. Hosseini • T. Takui (✉)
Department of Chemistry and Molecular Materials Science, Graduate School of Science, Osaka City University, 3-3-138, Sugimoto, Sumiyoshi, Osaka 558-8585, Japan

FIRST project on "Quantum Information Processing", JSPS, Tokyo 101-8430, Japan
e-mail: takui@sci.osaka-cu.ac.jp

S. Nishida
Department of Chemistry, Graduate School of Science, Osaka University, 1-1 Machikaneyama, Toyonaka, Osaka 560-0043, Japan

Y. Morita
Department of Applied Chemistry, Faculty of Engineering, Aichi Institute of Technology, 1247 Yachigusa, Yakusa, Toyota 470-0392, Japan
e-mail: moritay@aitech.ac.jp

K. Maruyama • S. Yamamoto
Department of Chemistry and Molecular Materials Science, Graduate School of Science, Osaka City University, 3-3-138, Sugimoto, Sumiyoshi, Osaka 558-8585, Japan

M. Kitagawa
Division of Advanced Electronics and Optical Science, Department of System Innovation, Graduate School of Engineering Science, Osaka University, 1-3 Machikaneyama, Toyonaka, Osaka 560-8531, Japan

FIRST project on "Quantum Information Processing", JSPS, Tokyo 101-8430, Japan

Y. Yamamoto, K. Semba (eds.), *Principles and Methods of Quantum Information Technologies*, Lecture Notes in Physics 911, DOI 10.1007/978-4-431-55756-2_28

functioning matter spin qubits requires testing with actual, open shell chemical entities. We emphasize that the molecular optimization has to fulfill all of DiVincenzo's five criteria [5] and additionally to provide material uniformity and stability under strong microwave and RF irradiation. An additional requirement is to establish appropriate crystal engineering for quantum computing and quantum information processing (QC/QIP) [2, 3]. This is important for controlling decoherence of the spin qubits in ensemble, which is partly governed by intermolecular spin-spin interactions and symmetry of the crystal lattice.

Molecular optimization by synthetic chemistry is advantageous to generate scalable spin qubits such as electron spin versions of a Lloyd model system [6, 7], in which three non-equivalent g-tensors, A, B, and C are arranged in a 1D periodic $(ABC)_n$ backbone. A synthetic approach to the Lloyd model has been a materials challenge, but now molecular units for a prototypical Lloyd model have been isolated and chemically identified by X-ray structural analysis and electron magnetic resonance spectroscopy, as described below. Alternative approaches to Lloyd model systems are also briefly described. Molecular spins as qubits resources are composed of both electron spins as bus qubits and nuclear spins as client qubits. This is due to the intrinsic nature of unpaired electron spins, whose molecular wavefunctions are extended and delocalized in such a manner that the electronic structures are governed by both group-theoretical and topological symmetry of the electron network [1, 4]. Thus, gate operations with electron spin qubits only can be achieved by utilizing anisotropic electron spin dipolar interactions between the spin qubits, as shown below. The electron spin qubits connect the client spin qubits via hyperfine (A) interactions, and we emphasize that molecular information about the principal axes of hyperfine qubit A-tensors is important to implement quantum computing in anisotropic media such as solid-state materials, as shown in a later section herein.

28.2 Synthetic Approaches to Lloyd Model Electron Spin Scalable Qubit Systems

We have extended the original Lloyd model – in which qubits resources are *nuclear* spin-1/2 systems, later extended to high spin systems with nuclear-nuclear interactions assumed to be usable for gate operations – to the corresponding *electron* spin versions. Our idea has been underlain by the feasibility of molecular optimization in terms of synthetic strategy for scalability and facile initialization processes compared with the nuclear spin qubit based versions. A remarkable advantage relevant to the Lloyd model is that one needs to prepare only three kinds of addressable spin qubits, say A, B and C, as a one-dimensional array in an $(ABC)_n$ periodic manner. The periodic boundary conditions are strict and relevant to the materials uniformity required for the accuracy of any gate operations in the frequency domain during QC/QIP processes. Materials control of periodicity with uniformity is important in crystal engineering for ensemble solid-state QC/QIP.

The issues can be met by molecular optimization with specific chemical bonding schemes like a DNA-based approach described below.

In an electron spin version of the Lloyd model, the g-tensors of molecular spins play an essential role in building up the $(ABC)_n$ periodic spin chain, in which A, B and C have different g-tensors that are addressable in the frequency domain of current microwave technology. We emphasize that for an electron spin Lloyd model system in isotropic media, the use of significantly non-equivalent isotropic g-values (termed genuine g-tensor approach-2) or a pseudo g-tensor (hyperfine A-tensor) approach is essential to differentiate between the three molecular spin qubits. The genuine g-tensor approach-2 requires particular molecular optimization in which the g-tensor of each molecular spin is tuned by introducing hetero-atoms at a radical site. This is termed electronic tuning of the g-tensor. In molecular spin based solid-state QC/QIP, the spatial orientation of each g-tensor provides non-equivalence of the resonance frequency with respect to an applied static magnetic field, with differentiation of the three molecular spins if the molecular optimization is properly achieved, as described below (genuine g-tensor approach-1). The pseudo g-tensor (hyperfine A-tensor) approach utilizes nuclear spins with sizable hyperfine couplings to a particular electron spin site (e.g., a radical moiety). The hyperfine coupling gives rise to significant additional splitting of the resonance line, which differentiates between two g-tensors having the same principal values and axes. Such A-tensor engineering is a workable method to lift inversion symmetry induced degeneracy of two g-tensors. Isotopic labeling at one radical site in biradical systems having inversion symmetry is one of the applications of this method.

The electronic tuning approach above is also applicable to solid-state QC/QIP. A promising application of this approach is to utilize DNA-like double-stranded structures capable of incorporating non-equivalent open-shell metal ligands at complementary hydrogen bonding sites. This is termed DNA based supramolecular crystal engineering. In the electron spin version of the Lloyd model, anisotropic electron dipolar interactions between neighboring molecular spins are utilized to execute quantum gate operations. This contrasts with the use of small exchange interactions in the case of nuclear spin Lloyd model qubits with closed shell molecular frames, for two main reasons: (1) precise control of exchange interactions to order of MHz is a still-intractable problem in open shell chemical entities [1, 2]; (2) experimental limitations of current microwave spin technology mean that presently available excitation bandwidth cannot cope with sizable exchange couplings. The latter will be sorted out by emerging microwave technology, if the corresponding frequency is not very high (less than 100 GHz).

In this section, we describe the g-tensor-orientation approach to the electron spin version of the Lloyd model, from the viewpoint of materials challenges (genuine g-tensor approach-1) [8], focusing on molecular optimization for a prototypical Lloyd model of the electron spin version. Figure 28.1 shows a prototypical spin chain of electron spin version Lloyd model, in which supramolecular ligands play dual roles in building up 1D spin chains of the proposed periodicity. One is that the ligands are able to incorporate either open or closed shell transition metal cations, and the other is that the ligands can yield triple-stranded 1D structures of metal-ligation to give

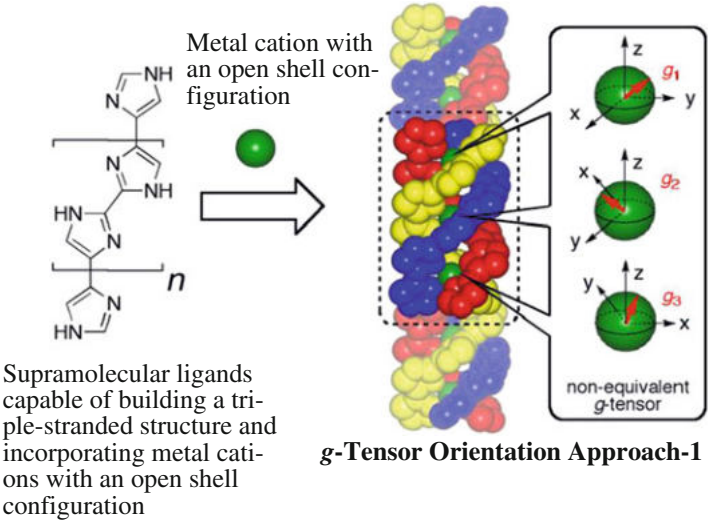

Fig. 28.1 A prototypical model of the electron spin version of the Lloyd model (supramolecular approach). Molecular optimization is based on the g-tensor orientation approach-1. The strength of ligand-metal self-association should be strong enough to keep the triple-stranded helical structure unfolded even in solution at ambient temperature [8]. The supramolecular ligands bind transition metal cations in a pseudo octahedral symmetry with a robust global structure to suppress decoherency of ensemble electron spin qubits when incorporated into crystal lattices with diamagnetic host molecules. Use of various metal cations also allows preparation of magnetically-diluted, mixed single crystals with desired concentration ratios of guest/host molecules. Supramolecular functionality also allows triple-stranded structures, in which the orientations of electron spin qubit g-tensors and other magnetic tensors are governed by the global molecular symmetry

triple-stranded helical symmetry (see the caption of Fig. 28.1 for the dual roles). The metals are located in a pseudo-octahedral symmetry of the local structures. The departure from octahedral symmetry matters in terms of establishing the g-tensor orientation approach. This is because octahedral symmetry cannot generate a non-equivalency of magnetic tensors in the triple-stranded helical environment, so the three molecular spins units would not be distinguishable. One of the crucial points in the supramolecular approach, where the ligands play dual roles, is how to control the *magnitude* of the deviation from strict octahedral symmetry and to increase the axial nature of the relevant magnetic tensors at the transition metal cation sites. Another crucial, practical point is the synthetic feasibility of length extension of the periodicity while strictly keeping the other structural boundary conditions. The present supramolecular approach is subject to two apparent weaknesses that should be improved from the viewpoint of molecular optimization. One is the fact that the method is not applicable for materials syntheses using the genuine g-tensor approach-2 with electronic tuning of the g-tensors in a straight forward manner. To our knowledge, current supramolecular chemistry cannot afford subtle synthetic differentiation between metal cations having non-equivalence of their g-

tensors. In this context, a novel molecular optimization strategy requires functioning modification of ligands combined with control of their metal binding selectivity in terms of theoretical considerations of the contribution to their g-tensors from spin-orbit interactions. The other is the broadened linewidth of electron spin resonance (ESR) transitions compared with those from organic-only open-shell spin qubits. This arises from nuclear electric quadrupolar interactions of transition metal ions. This issue is not intrinsic but relevant to the excitation strength of pulsed microwave irradiation at resonance.

In this context, g-tensor engineering approaches based on the DNA double-stranded $(ABC)_n$ architecture have the advantage of utilizing electronic tuning of the g-tensor, in which the complementary hydrogen bonding scheme can afford 1D periodic chains of non-equivalent g-tensors for molecular spin qubits [9]. The DNA-based approach to g-tensor engineering was tested by introducing molecular spins at mismatched sites of the complementary hydrogen bonds in the DNA oligonucleotides. Both the global and local molecular structures were probed by Q-band pulsed ELectron-electron-DOuble-Resonance (pulsed ELDOR) spectroscopy and by computational molecular mechanics modeling. In DNA-based g-tensor engineering, the molecular rigidity of molecular spin qubits introduced at desired sites of the hydrogen bonding is crucial, and this approach utilizing organic molecular spins is not subject to the two weaknesses for the metal cation approach described above.

28.3 Controlled-NOT Gate Operations by Molecular Spin Qubits

Molecular spins for qubits usage are composed of both electron spins as bus qubits and nuclear spins as client qubits. The client qubits are useful in many aspects of qubits usage (particularly as quantum spin memory), but nuclear spin qubits giving cross-talk in g-tensor engineered molecular spin qubits are an obstacle in executing gate operations composed of electron spin qubits, because they give so many unwanted nuclear sublevels. Toward avoiding this problem, the biradical **1** depicted in Fig. 28.2a is the first synthetic electron spin qubit system which allows Controlled-NOT (CNOT) gate operations by the use of molecular *electron* spins [10].

In the biradical **1**, orientation g-tensor engineering is achieved using the two radical sites with non-equivalent g-tensors denoted by molecular fragments in blue and red in Fig. 28.2. The two radical sites are not related by inversion symmetry, so hyperfine A-tensor engineering is not necessary in the molecular optimization. The two nitrogen nuclei and thirty-four hydrogen atoms in the fragments are ^{15}N- and fully deuterium-labeled, respectively. The isotope labeling enormously enhances the spectral resolution. Particularly, the nitrogen labeling is crucial to identify the magnetic field orientation suitable for QC/QIP experiments. The biradical **1** is diluted

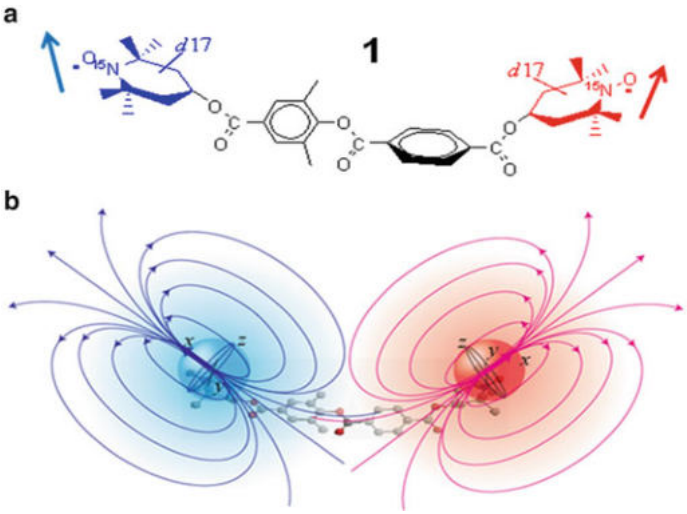

Fig. 28.2 Biradical **1** as a spin qubit that makes Controlled-NOT gate operations implemented in molecular systems. (**a**) Molecular structure: The two nitrogen nuclei are ^{15}N-labeled and all the protons of the two radical fragments deuterium-labeled. There is no inversion symmetry between the two radical sites, so orientation g-tensor engineering is achieved. (**b**) The exchange interaction between the radical sites is <0.2 MHz owing to molecular optimization, in which the two central benzene rings bridging the two radicals govern the relative orientation of the g-tensors. The Controlled-NOT gate operations by electron spin qubits in molecular systems were implemented by utilizing anisotropic spin-dipolar interactions (−9.5 MHz for the zero-field splitting parameter) [10]

to a desired concentration in a diamagnetic host lattice of the related bisketone molecule whose molecular structure is approximately the same as that of **1**. The central benzene rings play an important role to allow a large angle between the two radical fragments, allowing effective orientation g-tensor engineering. After the measurements of angular dependence of fine-structure hypefine-split ESR spectra with respect to crystal coordinate or molecular principal axis orientation, we can identify orientations of the static magnetic field with respect to the crystal and fully determine the magnetic tensors in the spin Hamiltonian. This identification provides conditions for QC/QIP experiments such as initialization, CNOT gate operation, or quantum teleportation between molecular spin qubits, so long as appropriate rf and microwave frequency pulse energies and sequences can be achieved. Obviously, two microwave frequencies with their phases controlled in currently available coherent-dual pulsed ELDOR [3b] are not enough, so Nuclear Magnetic Resonance (NMR) paradigm, pulsed-ESR spin technology using conventional microwave frequencies has been implemented in our laboratory (Osaka City University). This emerging spin technology can afford realistic QC/QIP experiments in which both electron spin bus and nuclear client qubits can be manipulated/controlled in the Bloch sphere in an equal manner. This new spin technology is *not* subject to limitations of the number of irradiation pulses, their relative phase and amplitudes. This was demonstrated

by first CNOT gate operation in the molecular spin qubits of **1**, which were been implemented in the magnetic field direction in which the eigenstates of the nuclear spins are not affected during the electron spin transitions on resonance. Thus, only the four *electron* spin sublevels are involved in the QC experiments, and the gate operations are achieved by utilizing anisotropic *electron* spin dipolar interactions (−9.5 MHz for the zero-field splitting parameter). In biradical **1**, the molecular structure optimization gave effective suppression of the exchange interaction (less than 0.2 MHz). The molecular optimization for shortening the distance between two molecular spin qubits also gives faster gate operations than those for the longer distance, as expected.

28.4 Adiabatic Quantum Computation on a Molecular Spin QC

A molecular spin quantum computer utilizes electron spins as bus qubits which are manipulated by electron spin resonance (ESR) based magnetic resonance techniques in open shell molecules, in which nuclear spins topologically connected play the role of client qubits. In this section, we focus on adiabatic quantum (AQ) computation [11] by utilizing both electron spin bus qubits and nuclear client qubits in as fully controlled a manner as possible using current levels of spin resonance technology. The molecular spin AQ computation is underlain by the recent implementation of NMR-paradigm pulsed ESR technology from the experimental side. A factorization of 21 was chosen for the adiabatic algorithm in order to illustrate the essence of the approach, for comparison with NMR molecular systems. We present for the first time pulse sequences required for ESR QC experiments using molecular spin systems, and possible problems to be encountered in molecular spin AQ computation are pointed out for further development.

Since Shor's algorithm appeared, attempts at realistic QC/QIP have been made from the experimental side [12, 13], with the first experiment performed by utilizing pulsed NMR techniques [14] without invoking quantum entanglement. An experiment proposed by Peng and coworkers factorizes 21 by an Adiabatic Quantum Computer (AQC) with rather small numbers of qubit resources such as three qubits. They performed this QC experiment using solution NMR conditions in which C, H and F nuclear spin states in a dimethylfluoromalonate molecule were manipulated [15]. AQC is one of the computation models of QCs, which processes information in the ground states of a quantum system with variation of the corresponding Hamiltonian [11]. Although AQC has been defined as different from standard QC, it is important that: (1) AQC has the same computational ability as standard QC [16]; (2) AQC can allow performance of error correction [17].

From the viewpoint of spin resonance, it is interesting to identify the difference between NMR and ESR qubit systems in terms of AQC. As already described in the preceding section, in the ESR system molecular spins with open shell electronic

structures are utilized in QC/QIP, and electron spins play the role of bus qubits while nuclear spins are client qubits. Particular magnetic interactions involving electron spins are utilized for computational operations, and thus generally shorter overall computational time is anticipated [18]. Here, we describe the theoretical study of an adiabatic factorization problem, illustrating how a molecular spin AQC works when AQC is implemented in real molecular spin qubits. This gives a foundation to build the implementation of molecular spin based AQC.

AQC requires definition of an adiabatic Hamiltonian path in an algorithm. The initial Hamiltonian, $\hat{H}_{\mathrm{i}}$ and the final Hamiltonian, $\hat{H}_{\mathrm{f}}$ are adopted as Eqs. (28.1) and (28.2) in this study, respectively.

$$\widehat{H}_{\mathrm{i}} = a\sum_{i=1}^{n}\sigma_x^i \tag{28.1}$$

$$\widehat{H}_{\mathrm{f}} = (N - xy)^2 \tag{28.2}$$

where, $a = 30, N = 21, n = 3, x = \left(I - \sigma_z^1\right) + I, y = 2\left(I - \sigma_z^2\right) + \left(I - \sigma_z^3\right) + I$ in the factorization of 21 [15]. In this algorithm, there are unsolvable problems when the solution of (x, y) has the same bit size because the two ground states have the same energy. Nevertheless, there are two advantages to this algorithm: (1) the algorithm easily compares ESR systems (i.e., molecular spins) to NMR systems; (2) this approach requires only a small number of qubits for execution. Applied to molecular spins using pulsed ESR techniques, the time evolution operator of the adiabatic process is approximated in finite time steps and defines the needed, adiabatic path as Eq. (28.3).

$$U = \prod_{m=1}^{5}\exp\left(-i\widehat{H}_m\Delta t\right),\ \widehat{H}_m = (m/5)^2\widehat{H}_{\mathrm{f}} + \left\{1 - (m/5)^2\right\}\widehat{H}_{\mathrm{i}} \tag{28.3}$$

The time evolution operator U is a non-commutative operator in Eq. (28.3). Therefore, U was transformed by the Trotter expansion to commutable operators in the pulse sequences of calculations (see Appendices at the end of this chapter): the theoretical fidelity of this approach is 0.91 [15].

Generally the spin Hamiltonian in a molecular spin QC with the static magnetic field along the z-direction can be written by Eq. (28.4) in the Schrödinger picture.

$$\begin{aligned}\widehat{H}_{\mathrm{MSQC}} = &\sum_{i=1}^{N} S^i g^i \beta^i B - \sum_{j=1}^{M} I^j g^j \beta^j B + \sum_{i<j}^{N,N} S^i (J+D)^{ij} S^j \\ &+ \sum_{i=j=1}^{N,M} S^i A^{ij} I^j + \sum_{i<j}^{M,M} I^i (J+D)^{ij} I^j\end{aligned} \tag{28.4}$$

The first and second terms are Zeeman interactions for electron and nuclear spins, and g^i is a second rank tensor which is related to the Larmor frequency ω_0^i of an ith spin ($\omega_0^i = g_{zz}^i \beta^i B_z/\hbar$ where B_z is the static magnetic field in the ESR system). The interactions between spins are written by second rank tensors of J, D and A which correspond to electron exchange interaction, anisotropic fine-structure (mainly spin-dipolar interaction in organic molecular high spins) and hyperfine interaction, respectively.

The effective Hamiltonian in the time evolution operator is calculated by transforming to an interaction picture of the spin Hamiltonian. Following the common procedure, the unperturbed Hamiltonian is selected for Zeeman terms by assuming the secular approximation with small anisotropy in the g-tensor. This approach is equivalent to adopting the rotational frame in quantum mechanics. Since most experiments of a molecular spin QC have been carried out in single crystal systems incorporating open shell molecules such as radicals or multi-radicals, in this study for designing pulse sequences, either a three-electron system (3e system) or one-electron plus two-nuclear system (1e + 2n system) is adopted, as exemplified in Fig. 28.3. In transforming to the interaction picture, the principal axes of the hyperfine tensors are assumed to be parallel to the static magnetic field, to simplify by eliminating effects from anisotropic terms. We have known that this assumption is special for most of real molecular spin qubits, and that non-linearity of the quantization axes is crucial to acquire better fidelity to the model. Overall, Eqs. (28.5) and (28.6) are obtained as perturbation Hamiltonians in the time evolution operator of the 3e system and 1e + 2n system, respectively,

$$\widehat{H}_{\text{int}}^{\text{3e}} = S_z^1 (J+D)^{12} S_z^2 + S_z^2 (J+D)^{23} S_z^3 + S_z^3 (J+D)^{31} S_z^1 \tag{28.5}$$

$$\widehat{H}_{\text{int}}^{\text{1e+2n}} = S_z^1 A^{12} I_z^2 + I_z^2 (J+D)^{23} I_z^3 + I_z^3 A^{31} S_z^1 \tag{28.6}$$

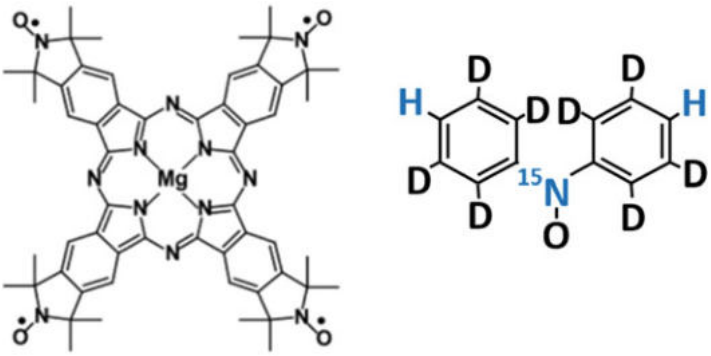

Fig. 28.3 Molecular structures of a phthalocyanine system (four electron (4e) system, *left*) and an isotope-labeled diphenylnitroxide (DPNO) (one-electron and two nuclear-spin (1e + 2n) system without counting ^{15}N nucleus, *right*). In the calculation described in the text, only three electron qubits of the phalocyanine system are treated, so one of the four radical sites should be closed shell. Any nuclear effects mainly arising from the nitrogen nuclei are neglected in the present treatment, for simplicity

where $(J+D)^{ij}$ and A^{ij} are the zz-components of the corresponding tensor. In solution, only the D tensor will vanish on the basis of its traceless character.

Pulse sequences were calculated using two pulse operations (arbitrary angle operations of the x- and y-directions) for each qubit with time evolution (arbitrary time). A phthalocyanine derivative for the 3e system and a diphenyl nitroxide (DPNO) for the 1e + 2n system were adopted as real molecular examples of these (see Fig. 28.3 for the molecules). There are four electron spins in the phtalocyanine system, so we assumed a three-qubit system in which one radical site is chemically reduced. These systems have strong enough isotropic interactions that are needed for establishing constant time in any orientation, and they are workable molecular spin QCs from the previous study [19, 20]. Considering the experimental restrictions, e.g. selecting the axis for the g-tensor while keeping co-linearity of the hyperfine tensors, the average time for an adiabatic calculation can approximately equal the isotropic coupling case ($J^{12} = J^{23} = -22.8$ MHz, $J^{31} = -40.8$ MHz, $A^{12} = -5.56$ MHz and $A^{31} = -37.9$ MHz) [19, 20]. By this assumption, the obtained pulse sequences are the same as those in the solution state of these systems. The 3-qubit interaction on the adiabatic time evolution is replaced by reducing 2-qubit interactions [21]. In the case of the 1e + 2n system, the interactions between nuclei are too weak to manipulate, therefore the interactions are replaced by 3-qubits interactions and the other 2-qubits interactions. We replaced the pulses only when we need to connect two pulses. The pulse sequences were lined up in the 3-qubit interaction, 2-qubit interactions and 1-qubit operations as shown in Fig. 28.4.

The estimated, calculated time and the total operation angles for each spin are shown in Table 28.1. For comparison to a three-*nuclear* system, we have calculated the time for the NMR system to be approximately 50 ms and for the ESR system to be about 0.23 μs. Thus, using a three-*electron* (3e) system can be about 10^5 faster. This is because the nuclear spin system has exchange couplings of the magnitude of 50–200 Hz. On the other hand, in the 3e system couplings are on the order of 20–40 MHz. As expected, an important result is that the calculation speed is not simply proportional to the gyromagnetic ratio between the two systems, but to the interaction strength. From the experimental point of view, if one tries to perform the same adiabatic algorithms in molecular electron spin systems as for the NMR systems, the short time operations (e.g., 0.2 ns) for 2-qubit interactions could be a problem. Even under this condition, we can perform the adiabatic calculation by scaling up the *problem* Hamiltonian, but the required time proportionally increases for the Hamiltonian. Alternatively, one can treat the electron spin systems using accurate and short time operations (below 0.2 ns), which is a technical issue for current microwave technology. We emphasize that this problem appears only in AQC not in a standard QC.

In the 1e + 2n system the required time when ignoring the pulse manipulation time is about 1.57 μs, therefore this system also is faster than for NMR system methodology. In this molecular spin system, the same problem for the short

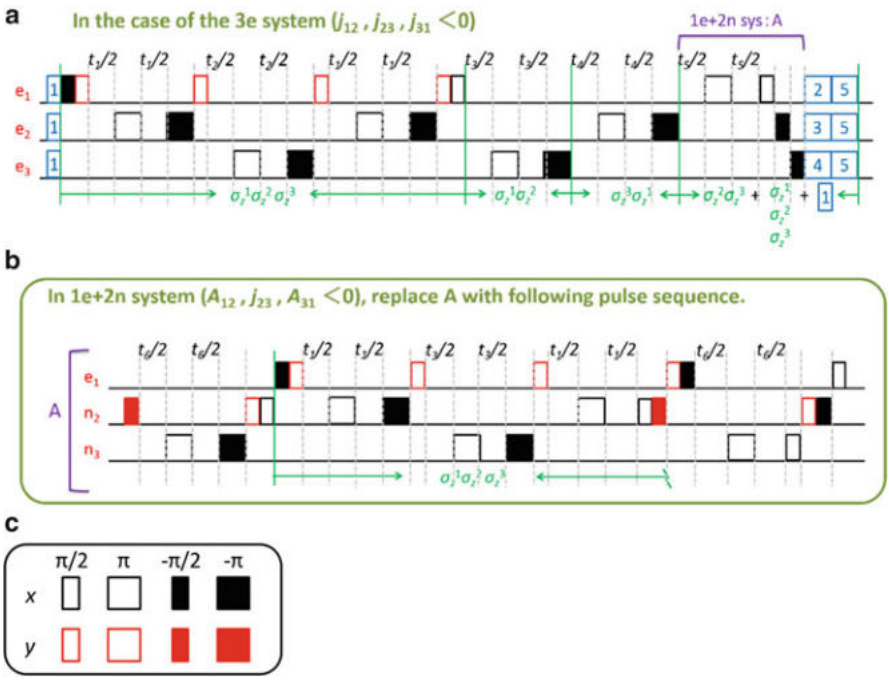

Fig. 28.4 The pulse sequences for the factorization problem of 21. (**a**) The sequence of the 3e-system. The time, t_i and the *green character* indicate the pulse time interval and the operation of the adiabatic Hamiltonian, respectively. The pulse in *blue* including the number is for an arbitrary operation of the *x*- or *y*-direction. In the adiabatic process, the pulse sequences need to loop five times (n = 1 to 5). (**b**) The sequences of the 1e + 2n system. In this case, the pulse sequence basically similar to (**a**) but replace A-block of (**a**) to nuclear cases for (**b**). (**c**) Denotes the types of pulse for easier identifications. *Black* and *red blocks* indicate the *x*- and *y*-direction, and narrow and wide blocks indicate π/2 and π pulses, respectively. The numbered pulses are the *x*- or *y*-operations in a certain angle. The details of the operation time and angle are calculated

Table 28.1 Operation angles and required times in the 3e system and 1e + 2n system are shown

	3e system			1e + 2n system		
	e_1	e_2	e_3	e_1	n_2	n_3
Operation angle/radian	28π	38π	27π	38π	68π	52π
Required time/μs	0.229			1.57		

operation time occurs. Another problem with the 1e + 2n system is the manipulation of nuclear spins. Because of the absolute value of the *g* factor, the Rabi operation for nuclei (e.g., π pulse) in the molecular spin system takes much more time than for electrons (about few μs for nuclear spins) [20], so the time required for this algorithm would depend on the operation time of the nuclear spins. In this case, the

hyperfine interactions which are larger than or as the same order of magnitude as the Rabi frequency need to be taken into account in the pulse formulation.

In terms of operation angles, our pulse sequence requires a larger number of pulses than in the NMR method [15]. The operation angles in the 1e + 2n system need approximately twice the number of pulse operations than the 3e system, due to the replacements of the 2-qubit operation. This difficulty of this adiabatic algorithm mostly arises from the three qubit interaction (Fig. 28.4).

In this section, we have illustrated the factorization problem of 21 treated by AQC by utilizing molecular spin qubits and presented the difference between the NMR and ESR systems. In the 3e system, increased speed depending on the interaction strength has been proven and shorter time operations in the molecular spin systems are suggested. Also, the 1e + 2n system has the possibility for increased speed, although appropriate treatment of the nuclear spin operations is needed. The difficulties in applying the present adiabatic algorithm to molecular spin qubits are identified, and mostly arise from three-qubit interactions. Overall, we have introduced experiments for AQC that utilize molecular spin qubits in which appropriate molecular optimization has been made to solve the problems for correct adiabatic operations in ESR systems.

28.5 Multi-Spin Quantum Control Through Single Spin Manipulation

28.5.1 Theoretical Background

Toward the realization of quantum computing, it suffices if we could fully control a given many-body quantum system. By full control, we mean the implementation of any unitary operation on the system, maintaining its quantum coherence throughout the operation. The system that is the subject of our control typically comprises a number of qubits, and high-fidelity applications of single- and two-qubit operations to arbitrary qubits have been a much-coveted goal for physicists.

Aiming at the implementation of a small number of elementary qubit operations appears to be convenient, since any unitary transformations on many-qubit systems can be decomposed into a sequence of simple operations, or quantum logic gates. Yet, performing a multi-qubit operation usually requires control of *inter*-qubit interactions. In order to switch interactions between qubits, we would need an extra control probe for every qubit pair; it may be a physical electrode to control voltage, or additional electromagnetic waves to induce interactions between degrees of freedom, or even a measurement on auxiliary qubits to cause an effective state change.

Here we primarily focus on the systems of spin-1/2 particles, as they are a naturally very good two-state system, i.e., qubit, and, in many cases they have advantages in terms of scalability and longer coherence times. Although spin-spin

interactions, such as the Heisenberg-type exchange interactions, are capable of realizing useful two-qubit operations, it is hard to switch such inter-spin interactions at will, as described in the earlier sections.

Luckily, the difficulty in performing two-qubit operations in the presence of constant coupling between qubits is not a crucial problem for quantum computing, since the decomposition of a unitary transformation into elementary gates is just for descriptive convenience. All we need to do is to seek the right modulation of external field parameters, where time evolution becomes equal to the desired unitary transformation. We employ this approach here to find a feasible field modulation (pulse sequence) for nontrivial quantum operations using multi-spin systems.

The most generic form of the system Hamiltonian is described as

$$H(t) = H_0 + \sum_m f_m(t) H_m, \tag{28.7}$$

where H_0 represents an unmodulable interaction and H_m represents external fields that can be controlled experimentally by a modulation function $f_m(t)$. For example, if the system is a one-dimensional chain of spins-1/2: H_0 describes the inter-spin couplings, such as $H_0 = \sum_n J_n \sigma_n \cdot \sigma_{n+1}$; H_m represents the Zeeman interaction between the m-th spin and the local magnetic field $\mathbf{b}_m$, i.e., $H_m = \mathbf{b}_m\ \sigma_m$; and $f_m(t)$ denotes the field intensity at time t. Here, $\mathbf{b}_m$ is the unit vector in the direction of the field at the m-th site. As we want to control the entire system by modulating a small number of parameters, we would consider that the number m of controllable Hamiltonians H_m is small, e.g., two or three.

The Schrödinger equation for the time evolution operator under the Hamiltonian Eq. (28.8) is

$$i\tfrac{d}{dt} U(t) = H\left[\mathbf{f}(t)\right] U(t),\ U(0) = I, \tag{28.8}$$

where $\mathbf{f}(t)$ stands for the set $\{f_m(t)\}$. This equation can formally be integrated as

$$U(t) = \mathsf{T} \exp\left(-i \int_0^t H\left[\mathbf{f}(\tau)\right] d\tau\right), \tag{28.9}$$

where T is the time-ordering operator.

We are interested in the set $\{U(t)\}$ with a finite t, each element of which is obtainable by varying the pulse sequence $\mathbf{f}(t)$. Let us define the *reachable set* R to be the unitaries that can be arbitrarily close to the unitary transform $U(T)$ in Eq. (28.9) with a finite T and a right pulse sequence $\mathbf{f}(t)(t\ \varepsilon\ [0,T])$. That is,

$$\forall \Lambda \in \mathcal{R},\ \forall \varepsilon \in 0,\ \exists \mathrm{f}(t) \in,\ \exists T < 0, \text{ such that } ||\, V - U(t)\,|| < \varepsilon. \tag{28.10}$$

If R is equal to U(2^N) or SU(2^N) for an N spin system, then any unitary operation for this system can be realized within a finite time by designing the pulse sequence appropriately, and hence is fully controllable.

Then, how can we characterize R, given a set of Hamiltonians $\{H_m\}(m \varepsilon \{0,1,\ldots,M\})$. A famous theorem of quantum control gives a concise answer to this question [22].

Theorem 28.1 *The reachable set* R *is the connected Lie group associated with the Lie algebra* L *that is generated by taking commutators of elements in* $\{H_m\}$ *repeatedly, i.e.,*

$$\mathrm{R} = e^{\mathrm{L}}. \tag{28.11}$$

In the Lie algebra U(n) (or SU(n)), each element in the algebra is skew-Hermitian. Thus, precisely speaking, L contains $\{iH_m\}$ and their repeated commutators.

The algebra L is often called *dynamical Lie algebra*, and its elements take the form $[A_1,[A_2,[\ldots,[A_k-1, A_k]\ldots]]]$, where $A_1,A_2,\ldots,A_k \varepsilon \{H_m\}$. The linearly independent ones form the basis of the dynamical Lie algebra. Because we are considering a finite dimensional system, this process of taking commutators eventually stops generating a new basis that is linearly independent with respect to those generated before. The maximum number of the independent bases, i.e., the rank, is n^2 or n^2-1, when H_m are $n \times n$ matrices in U(n) or SU(n), respectively.

Therefore, in the context of quantum control, where we disregard the effect of the global phase, if the rank of the dynamical Lie algebra L is equal to n^2-1, R is equal to SU(n), and hence the system is fully controllable through $\{H_m\}$. Even if R does not coincide with SU(n), any unitary in R can be implemented, thus partially controllable. The simplest case of this theorem is the control of a single spin-1/2. If the magnetic field can be controlled in two (orthogonal) directions, say x and y, the modulable Hamiltonians are σ_x and σ_y (through the Zeeman interaction). The commutator of these, $[\sigma_x,\sigma_y]$, gives σ_z (apart from the i factor). This means that we can effectively control σ_z as well, so the rank of L is three. Since SU(2) is three dimensional, the single spin is fully controllable by field control in two directions. This particular simplistic case corresponds to the Euler decomposition of arbitrary rotations, such that any rotation in three dimensions can be expressed as a product of rotations around the two fixed directions.

While Theorem 28.1 is very powerful in judging the controllability of the system, it does not tell anything about how we should design the control pulse sequences, let alone the necessary time duration for a pulse sequence to implement a specific unitary operation. Although some partial results have been obtained to reduce the complexity of this problem [23], finding optimal control pulses is a computationally hard task in general. Thus we still need to rely on some algorithms of numerical calculations that have been developed for these purposes, such as the one developed by Macnes and coworkers [24].

Knowing that all parameters (including the inter-qubit interactions) do *not* necessarily have to be controlled, one can implement some nontrivial quantum operations on a real system in the lab. Molecular spins in molecules, which are the subject of our study, are a good basis for which Theorem 28.1 can be applied nicely;

they are constantly interacting with each other, and in electron-spin-only mediated systems each spin typically has a different g-factor from others if appropriate molecular optimization is made as described in the previous sections, and thus it is not very hard to control a few electron spins or nuclear ones selectively. In the following section, we describe attempts to achieve indirect quantum control practically, using a three-spin system consisting of one electron spin and two nuclear spins, which is termed a bus spin qubit system. Here the electron spin and nuclear spins act as a bus qubit and client qubits, respectively, in the molecular frame.

28.5.2 *Indirect Application of a Quantum Gate on a Three-Spin System*

Typically, in a hybrid molecular system of an electron spin plus nuclear spins, a single electron spin has been used for state preparation, readout and control while the nuclear spins act as qubits for storing and processing information. It has been shown that in such systems, the nuclear spins can be indirectly fully controllable through an electron spin as a spin actuator via hyperfine interactions [25, 26]. In this study, we designed a control pulse sequence numerically to implement a high fidelity gate operating on nuclear spins. Using the pulse sequence, we are currently attempting to implement multi-qubit operations with systems of three and more spins, and we will verify the result of quantum operations (under limited access) using well-established electron nuclear multiple resonance methods. We emphasize that pulse techniques composed of only microwave frequencies to manipulate nuclear spins under certain conditions are novel spin technology that is still under development. This spin technology enables us to rotate nuclear spins faster than pulsed ENDOR based techniques.

We consider a three-spin system composed of an electron spin and two nuclear ones in the presence of an external static magnetic field. For simplicity, the spin Hamiltonian of the system in frequency units is given by Eq. (28.12),

$$\begin{aligned} H_0 = & \frac{g_{zz}\beta_e B_0}{h} S_z - \frac{\gamma_{n_1}}{2\pi} B_0 I_z^1 - \frac{\gamma_{n_2}}{2\pi} B_0 I_z^2 \\ & + A_{zx}^1 S_z I_x^1 + A_{zy}^1 S_z I_y^1 + A_{zz}^1 S_z I_z^1 + A_{zx}^2 S_z I_x^2 + A_{zy}^2 S_z I_y^2 + A_{zz}^2 S_z I_z^2, \end{aligned} \tag{28.12}$$

where β_e is the Bohr magneton, $\gamma_{mi}/2\pi = 42.576$ MHz /T as the gyromagnetic ratio of a hydrogen atom, and B_0 is the external static magnetic field which is applied along the z-direction of the g-tensor, respectively. A_{zz} is the zz component of the hyperfine coupling tensor, while A_{zx} and A_{zy} denote the anisotropic hyperfine coupling coefficients. S and I are the electron spin and nuclear spin operators, respectively. The nuclear spin-dipolar interactions between two nuclear spins is neglected since its strength is almost 1000 times smaller than the hyperfine interactions between electron and nucleus.

If all transitions between the eight states of a 1e + 2n system are accessible, universal control in the system is possible. For different values of the hyperfine coupling coefficients, the probabilities of transitions between all the states can be varied, depending on the direction of the static magnetic field with respect to the molecular principal-axis system in the solid state. In order to control the system efficiently and to realize high fidelity quantum gate behavior, the hyperfine coefficients must carefully be designed to ensure that all the transitions can be accessed with significant transition probabilities. We emphasize that in terms of conventional electron magnetic resonance spectroscopy complex experimental conditions are required in addition to appropriate molecular optimization for molecular spins. Microwave irradiation on the single electron makes it work as an actuator to perform an entangling gate between the two nuclear spins. The Hamiltonian of control can then simply be described by Eq. (28.13), as

$$H_{control} = \frac{g_{zz}\beta_e B_e(t)}{h} S_x \tag{28.13}$$

where B_e is the amplitude of the oscillating microwave magnetic field which is applied on the electron on the x-direction. Thus $g_{zz}\beta_e B_e(t)/h$ corresponds to the strength of the microwave magnetic field.

The actual spin system employed here is a diphenylaminoxyl (DPNO = diphenylnitroxide) derivative, whose molecular structure is given in Fig. 28.5. We emphasize that spin manipulation technology should be based on pulsed electron-nuclear multiple resonance technique with controlled phase of each spin by coherence microwave frequency.

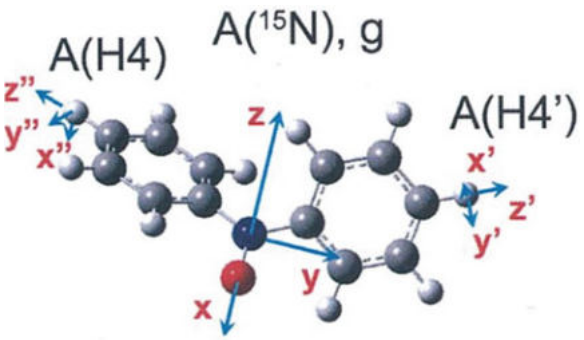

Fig. 28.5 Experimental qubit spin system, diphenylaminoxyl (DPNO). The nitrogen labeling simplifies hyperfine ESR spectra with significantly enhanced spectral resolution. Red, blue, gray and white balls denote oxygen, nitrogen-15, carbon, and proton and deutron atoms, respectively. The principle-axis alignments are shown with corresponding arrows in the figure. The molecular structure is assumed if it is incorporated in a diamagnetic host lattice having a similar molecular structure to diphenylaminoxyl

The hyperfine and g-tensors of DPNO are given by Yoshino [27]. The principal values of the proton hyperfine tensors and g-factor in their principal-axis coordinate system of Fig. 28.5, are summarized in Eqs. (28.14) to (28.15) as follows:

$$g = \begin{pmatrix} 2.0097 & 0 & 0 \\ 0 & 2.0053 & 0 \\ 0 & 0 & 2.0024 \end{pmatrix} \tag{28.14}$$

$$e^{-1}H : \begin{pmatrix} -8.63 & 0 & 0 \\ 0 & -5.56 & 0 \\ 0 & 0 & -2.22 \end{pmatrix} e^{-2}H : \begin{pmatrix} -8.82 & 0 & 0 \\ 0 & -5.76 & 0 \\ 0 & 0 & -2.34 \end{pmatrix} \tag{28.15}$$

The hyperfine couplings can be adjusted by varying the orientation of the static magnetic field with respect to a single crystal doped with DPNO. Transforming the tensors from the principal-axis system to the laboratory-axis reference, the orientation that can differentiate between transitions with suitable transition probabilities between all the states can be chosen for QC experiments. Any rotation of the frame can generally be described by Eq. (28.16) and (28.17), where

$$T_{\text{lab}} = RT_{\text{diag}}R^t \tag{28.16}$$

with

$$R = \begin{pmatrix} \cos\theta_{ax}\cos\theta_{ay}\cos\theta_{az} \\ \cos\theta_{bx}\cos\theta_{by}\cos\theta_{bz} \\ \cos\theta_{cx}\cos\theta_{cy}\cos\theta_{cz} \end{pmatrix} \tag{28.17}$$

where (x,y,z) and (a,b,c) denote the laboratory-axis and principal-axis references, respectively. The g-factor terms of the electron spin and the hyperfine couplings of the hydrogen atoms for the chosen orientation are typically as given below in Eq. (28.18):

$$\begin{aligned} &g_{zz} = 2.00253; \\ &A^1_{zx} = -0.12158\ \text{MHz}; A^1_{zy} = 1.15564\ \text{MHz}; A^1_{zz} = -8.37156\ \text{MHz}; \\ &A^2_{zx} = -0.91001\ \text{MHz}; A^2_{zy} = 1.33327\ \text{MHz}; A^2_{zz} = -7.25018\ \text{MHz}. \end{aligned} \tag{28.18}$$

We have designed numerically a pulse sequence which can performs a C-NOT gate on two nuclei with ^{1}H' being the control qubit and ^{2}H being the target qubit of the gate. Choosing the values $B = 0.35$ T and $g_{zz}\beta_e B_e/h = 10$ MHz for the intensity of the static magnetic field and the energy of the microwave to be employed, the gate can be performed in 5 μs with fidelity 0.81. Since in our experimental setup, the excitation bandwidth is on the order of 100 MHz, we fixed $\triangle t = 0.005$ ns in our numerical calculation, which yields the excitation bandwidth = 200 MHz. In order to get higher fidelity, we need a longer time duration: in the present molecular

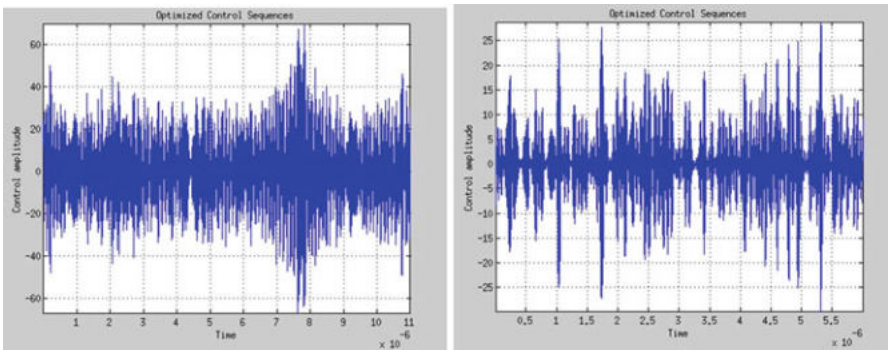

Fig. 28.6 Pulse sequences which perform a C-NOT gate with fidelity 0.99 as a function of time. In the *left/right* panels, the magnetic field is chosen as $B = 0.35$ T/$B = 0.1$ T. The former corresponds to QC experiments at X-band and the latter at L-band

spin $t = 11\ \mu$s leads to a fidelity of 0.99. However, we emphasize that shorter pulse durations are better from the viewpoint of quantum information processing, so QC experiments may be better performed at L-band frequencies. By setting $B_0 = 0.1$ T, the fidelity can be as high as 0.94 for $t = 5\ \mu$s, and 0.99 for $t = 6\ \mu$s. The numerically computed pulse sequences are shown in Fig. 28.6. *One can extend this method to any number of nuclear spins that have resolvable anisotropic hyperfine interactions.*

28.6 Conclusions

In order to manipulate or control both bus and client qubits in an equivalent manner, the implementation of sophisticated microwave pulse technology is essential. Novel microwave pulse technology that enables full control of both the amplitudes and phases of multiple microwave frequencies has already been emerging, indicating that new spin technology based on arbitrary wave generators (AWGs) can be powerful in manipulating ensemble molecular spin systems. The problems described in Sect. 28.5 are relevant to enable appropriate molecular optimizations of spin behavior. We also emphasize that the three-electron spin system under study imposes limitations in terms of its molecular optimization but sophisticated quantum chemical calculations of D tensors are available, which will enable us to design more appropriate three- or multi-electron spin molecular systems. In this quest of achieving practical molecular spin QCs or QIP systems, pulse-based advanced microwave spin technology combined with molecular optimization is essential.

Acknowledgments This work has been supported by Grants-in-Aid for Scientific Research on Innovative Areas "Quantum Cybernetics" and Scientific Research (B) from MEXT, Japan. The support for the present work by the FIRST project on "Quantum Information Processing" from JSPS, Japan and by the AOARD project on "Quantum Properties of Molecular Nanomagnets" (Award No. FA2386-13-1-4030) is also acknowledged.

Appendices

Appendix 28.1

The details of the rotation angle are shown in (a) where a_n and b are $(n/5)^2$ and 0.028, respectively. The operation times are shown in (b).

(a) Rotation angles

	Direction	Angle
1	*x*-	$30(1-a_n)b/2$
2	*y*-	$84a_nb$
3	*y*-	$88a_nb$
4	*y*-	$44a_nb$
5	*x*-	$30(1-a_n)b/2+\pi/2$

(b) Operation times

	3e system	1e + 2n system
t_1	$-\pi/j_{31}$	$-\pi/A_{31}$
t_2	$-64s_n\tau/j_{12}$	$-64s_n\tau/A_{12}$
t_3	$-80s_n\tau/j_{12}$	$-80s_n\tau/A_{12}$
t_4	$-40s_n\tau/j_{31}$	$-40s_n\tau/A_{31}$
t_5	$-80s_n\tau/j_{23}$	–
t_6	–	$-\pi/A_{12}$

Appendix 28.2

The Trotter's formula of the Eq. (28.3) where b is 0.028.

$$U=\prod_{m=1}^{5}\exp\left\{-i\left(1-(m/5)^2\right)\widehat{H}_i\,(b/2)\right\} \times\exp\left\{-i(m/5)^2\widehat{H}_f b\right\}\times\exp\left\{-i\left(1-(m/5)^2\right)\widehat{H}_i\,(b/2)\right\} \tag{28.19}$$

References

1. (a) K. Itoh, M. Kinoshita (ed.), *Molecular Magnetism.* (Kodansha, and Gorden and Breach Scientific Publisher, Tokyo, 2000), pp. 1–347. (b) K. Itoh, T. Takui, Proc. Acad. Soc. Jpn. **41**, 1 (2003)
2. E. Coronado, A.J. Epstein, J. Mater. Chem. **19**, 1670–1770 (2009)
3. (a) M. Mehring, J. Mende, Phys. Rev. A **73**, 052303 (2006). (b) K. Sato, S. Najazawa, Y. Morita, et al, J. Mater. Chem. **19**, 3739–3754 (2009)
4. Y. Morita, S. Suzuki, K. Sato, T. Takui, Nat. Chem. **3**, 197–204 (2011)
5. D.P. DiVincenzo, in *Mesoscopic Electron Transport*, ed. by I. Kowenhoven, G. Shen, I. Shon. NATO ASI Series F (Kluwer, Dordrecht, 1997), p. 657. cond-mat/9612126
6. S. Lloyd, Sci. Am. **73**, 140–145 (1995)
7. Y. Kawano, S. Yamashita, M. Kitagawa, Phys. Rev. A **72**, 20301 (2005)
8. Y. Morita, Y. Yakiyama, S. Nakazawa, T. Murata, T. Ise, D. Hashizume, D. Shiomi, K. Sato, M. Kitagawa, K. Nakasuji, T. Takui, J. Am. Chem. Soc. **132**, 6944–6946 (2010)
9. H. Atsumi, K. Maekawa, S. Nakazawa, D. Shiomi, K. Sato, M. Kitagawa, T. Takui, K. Nakatani, Chem. Eur. J. **18**, 173–183 (2012)
10. S. Nakazawa, S. Nishida, T. Ise, T. Yoshino, N. Mori, R.D. Rahimi, K. Sato, Y. Morita, K. Toyota, D. Shiomi, M. Kitagawa, H. Hara, P. Carl, P. Hoefer, T. Takui, Angew. Chem. Int. Ed. **51**, 9860–9864 (2012)
11. E. Farhi, J. Goldstone, S. Gutman, M. Sipser. arXiv:quant-ph/0001106
12. P.W. Shor, J. SIAM, Sci. Stat. Comput. **26**, 1484–1509 (1997)
13. C-Y. Lu, D.E. Browne, T. Yang, J-W. Pan, Phys. Rev. Lett. **99**, 250504 (2007); B.P. Lanyon, T.J. Weinhold, N.K. Langford, M. Barbieri, D.F.V. James, A. Gilchrist, A.G. White, Phys. Rev. Lett. **99**, 250505 (2007); A. Politi, J.C.F. Matthews, J.L. O'Brien, Science **325**, 1221 (2009); E.L.A. Martine-Lopez, T. Lawson, X.Q. Zhou, J.L. O'Brien, Nat. Photon **6**, 773–776 (2012); E. Lucero, Nat. Phys. **8**, 719–723 (2012).
14. L.M.K. Vandersypen, M. Steffen, G. Breyta, C.S. Yannoni, M.H. Sherwood, I.L. Chung, Nature **414**, 883–887 (2001)
15. X.-H. Peng, Z. Liao, N. Xu, G. Qin, X. Zhou, D. Suter, J. Du, Phys. Rev. Lett. **101**, 220405 (2008)
16. D. Aharonov, W. van Dam, J. Kempe, Z. Landau, S. Lloyd, O. Regev, SIAM J. Comput. **37**, 166–194 (2007)
17. S.P. Jordan, E. Farhi, P.W. Shor, Phys. Rev. A **74**, 052322 (2006)
18. J. Twamley, Phys. Rev. A **67**, 052318 (2003); Blank, A., arXiv:1302.1653
19. A.G.M. Barrett, G.R. Hanson, A.J.P. White, D.J. Williams, A.S. Micallef, Tetrahedron **63**, 5244–5250 (2007)
20. T. Yoshino, S. Nishida, K. Sato, S. Nakazawa, R.D. Rahimi, K. Toyota, D. Shiomi, Y. Morita, M. Kitagawa, T. Takui, J. Phys. Chem. Lett. **2**, 449–453 (2011)
21. C.H. Tseng, S. Somaroo, Y. Sharf, E. Knill, R. Laflamme, T.F. Havel, D.G. Cory, Phys. Rev. A **61**, 012302 (1993)
22. D. D'Alessandro, *Introduction to Quantum Control and Dynamics* (Taylor and Francis, Boca Raton, 2008)
23. D. Burgarth,K. Maruyama, M. Murphy, S. Montangero, T. Calarco, F. Nori, M.B. Plenio, Phys. Rev. A **81**, 040303(R) (2010)
24. S. Machnes, U. Sander, S.L. Glaser, P. de Fouquières, A. Gruslys, S. Schirmer, T. Schulte-Herbrüggen, Phys. Rev. A **84**, 022305 (2011)
25. J.S. Hodges, J.C. Yang, C. Ramanathan, D.G. Cory, Phys. Rev. A **78**, 010303 (2008)
26. Y. Zhang, C.A. Ryan, R. Laflamme, J. Baugh, Phys. Rev. Lett. **78**, 010303 (2008)
27. T. Yoshino, *Quantum-State Manipulation of Molecular Spin-Bus Qubits by Pulsed Electron-Nuclear Multiple Resonance Technique*. Ph.D. Thesis, Osaka City University, 2011